

HIGH-FIDELITY, BROADBAND AMPLIFICATION AND  
FILTERING FOR SPACEBORNE INSTRUMENTATION

A DISSERTATION  
SUBMITTED TO THE DEPARTMENT OF ELECTRICAL  
ENGINEERING  
AND THE COMMITTEE ON GRADUATE STUDIES  
OF STANFORD UNIVERSITY  
IN PARTIAL FULFILLMENT OF THE REQUIREMENTS  
FOR THE DEGREE OF  
DOCTOR OF PHILOSOPHY

Benjamin Joseph Mossawir

December 2009

© Copyright by Benjamin Joseph Mossawir 2010  
All Rights Reserved



I certify that I have read this dissertation and that, in my opinion, it is fully adequate in scope and quality as a dissertation for the degree of Doctor of Philosophy.

---

(Umran S. Inan) Principal Adviser

I certify that I have read this dissertation and that, in my opinion, it is fully adequate in scope and quality as a dissertation for the degree of Doctor of Philosophy.

---

(Ivan R. Linscott)

I certify that I have read this dissertation and that, in my opinion, it is fully adequate in scope and quality as a dissertation for the degree of Doctor of Philosophy.

---

(Robert W. Dutton)

Approved for the University Committee on Graduate Studies.



# Abstract

Recently, there have been increased efforts to investigate wave-particle interactions within the Earth's Van Allen belts using scientific instruments, known as plasma wave receivers, to obtain in-situ measurements of wave electric fields. With such phenomena spanning four decades in frequency, from 100 Hz to 1 MHz, and nine orders of magnitude in power, traditional receivers must trade their range in both dimensions against the desired resolution in frequency, power, and time.

But, to enable the next generation of wideband receiver that is capable of capturing signals throughout the full bandwidth and dynamic range simultaneously, a new type of analog front end is required. This device must meet these objectives while consuming minimal power and withstanding the deleterious effects of the radiation environment in these belts.

This dissertation addresses the design, implementation, and testing of the first fully-integrated analog front-end for satellite-based, wideband plasma wave receivers. The front-end, which is fabricated in a commercial 0.25- $\mu\text{m}$  SiGe BiCMOS process, features both a high-impedance, low-noise amplifier (LNA) and a field-trimmable, 6<sup>th</sup> anti-aliasing filter (AAF). The LNA, whose gain can be programmed in arbitrary steps from 0 dB to 24 dB to accommodate dipole antennae ranging from 6 to 100 meters in length, features 90-dB SFDR and consumes less than 2 mW. With programmable cut-offs at 30, 180, and 1080 kHz, the AAF can be dynamically adapted to compensate for the availability of host resources while maintaining 90-dB odd-harmonic suppression.

Though fabricated in a commercial manufacturing process, rather than a custom one tailored to prevent radiation-induced degradation, both circuits maintain performance for absorbed doses in excess of 100 krad(Si) and exhibit no latchup through

an equivalent LET of  $100 \text{ MeV-cm}^2/\text{mg}$  as a result of radiation-hardness-by-design techniques employed in their architecture, implementation, and layout.

# Acknowledgments

At the outset of this program, the only thing I miscalculated more egregiously than the timing of its conclusion was the number of individual contributions that would be required to get there.

First and foremost, I would like to thank my advisor, Professor Umran Inan, for having not only the vision that made this project possible, but the confidence in me to carry out my part with so much freedom. He may have regretted it at times, but my career will forever benefit from the unique opportunity he afforded a novice co-terminal student to take a complex problem from its nascent outline to a qualified, flight-worthy part and learn about everything in between. I also owe a deep debt of gratitude to Dr. Ivan Linscott, who in his capacity as my co-advisor routinely helped to winnow daunting sets of options into refined solutions. Along the way, his boundless optimism repeatedly taught me how to find the attractive challenge at the heart of an apparent obstacle.

Special appreciation goes to Professor Robert Dutton, who agreed to serve as the third reader of this dissertation and who first fueled my interest in bipolar circuit design in his courses over a decade ago. He merits further commendation for his bravery in allowing me to serve as his teaching assistant on more than one occasion; the satisfaction of helping students succeed on the lab bench is something that I found as rewarding as it was difficult. I would also like to thank Professor Per Enge, who graciously agreed to chair my oral examination committee.

The collaboration with National Semiconductor Corporation that brought my designs to life would not have been possible without the support of Dr. Ahmad Bahai and the efforts of Bijoy Chatterjee. I am also grateful to: Monir El-Diwany and

James Shibley, for conferring their wisdom on device engineering; Peter Misich, who coordinated my final fabrication runs; and Saeed Khosrowbeygi, Babak Matinpour, Ali Kiaei, and Anish Shah, whose technical and logistical support were instrumental in getting my designs onto the shuttles.

For authorizing and coordinating the numerous rounds of radiation testing conducted during this research, I am indebted to Dr. Jim Roeder and Dr. Bernie Blake at the Aerospace Corporation. I would also like to sincerely thank the team in El Segundo—Jon Osborn, Steve Witczak, Everett King, Steve LaLumondiere, Mark Turpin, Bob Garrett, and Stephanie Brown—for their assistance and patience during the testing down there. Likewise I greatly appreciate the expertise and commitment of Rocky Koga, Jeff George, and Van Tran, who spent many a long night with me at the LBNL BASE facility. Speaking of which, the folks who coordinate visitors at the 88-inch cyclotron—Mike Johnson, Patti Kobayashi, and Daphne Trowbridge-Williams—deserve special mention for being a pleasure to work with on every visit.

For teaching me just how difficult it is to build and test satellite equipment, as opposed to research prototypes, and for their assistance in the lab on many occasions, I would like to recognize Dr. Jack Doolittle, Bob Bumala, and Clem Tillier at Lockheed Martin Corporation, which generously provided financial support in the later stages of this dissertation; all are top-notch engineers, in addition to being congenial colleagues.

Over the course of my time at Stanford, there are many people whose efforts have made my work a whole lot easier, but I am particularly grateful to: Keith Gaul and Pat Burke for their help with instruments and computers, respectively; Pauline Prather, who bonded all of my die; and Tharman Patton, who delivered far too many Digikey rush orders. Dr. Steve Conolly and Dr. Greig Scott, members of the pMRI group, contributed intellectually and materially, as well, and always had the time to talk. Fellow graduate students Shu-Jen Han, Hemanth Jagannathan, Scott Kulchycki, and Yinan Zhao provided valuable consultation on technical matters.

I would also like to thank the sundry members of the VLF group as a whole, with particular recognition for the silicon designers: Dr. Charlie Wang (whose meticulous work ethic and relentlessness were boons to this project not easily overstated), Kelin Lee, Sarah Harriman, Carsten Barth, and (by courtesy) Max Klein; each has provided

invaluable technical assistance. Whenever I encountered confusion about a point of plasma science (which was often), I was able try the patience of senior group members Dr. Tim Bell, Dr. Don Carpenter, Dr. Tim Chevalier, and Dr. Maria Spasojević with my inane questions and never received less than gracious assistance. Good office mates are an under-appreciated facet of Ph.D. research, so those whose company I have enjoyed over these many years are owed mention: Dr. Robb Moore, Dr. Joe Payne, Dr. Ryan Said, Ben Cotts, and Geoff Bainbridge. Of course, I would be remiss not to laud the essential contributions of the people who actually enable the group to function: Shaolan Min, Helen Niu, Jeff Chang, and Dan Musetescu.

I am very lucky to have so many great friends who have supported and encouraged me over the years; in addition to the laughs and recreation, many times that succor has taken the form of impressive restraint, with those things left unsaid being as appreciated as those that are. For their loyalty, I would especially like to acknowledge: Anthony Aboseif, James Damasco, Ben and Kim D'Ewart, Fred Jabbour, Kerstin Johnson, Nate Gillespie, Sean Hashimoto, Megan Henry, Chris Hiserman, Jackie Lai, Dr. Nate Matter, Rohit Mishra, Dr. Kiemanh Pham, Sharath and Mili Reddy, Lincoln and Rachel Sanders, Aren Sandersen, Alex Tung, and Dr. Ross Venook.

Finally, as feeble as a single paragraph is for doing justice to their roles, I want to express my abiding love and respect for the limitless patience and support of my parents Mark and Marcy, and my brother Jake. I am truly fortunate for a lifetime of their unconditional love which, along with that of my family-in-law, Walt, Pat, Janette, Tom, and Max, motivates me to represent them well in this and every endeavor of my life.

But, most of all, I want to thank my wife Katy who has earned an honorary doctorate in the field of sanity maintenance and without whom none of this would have been possible. Since I fully realize that these humble words cannot hope to convey my gratitude, admiration, and fondness for all you have done, I will keep it brief: I love you with all my heart.

BENJAMIN JOSEPH MOSSAWIR  
*Stanford University*  
*1 December 2009*

The initial stages of this work were sponsored by the NASA New Technology Initiatives Program, Grant #NAG5-10822, under The Aerospace Corporation subcontract #4600001624-9. More recent efforts were conducted under the aegis of support to Stanford University from the United States Air Force Research Laboratory, contract #FA8178-05-C-0027-20. This research was also made possible by the generous support of National Semiconductor Corporation, in providing all semiconductor fabrication through a collaboration agreement with Stanford University, and The Aerospace Corporation, which graciously provided access to proton testing facilities at Lawrence Berkeley National Laboratory.



*This dissertation is dedicated to the memories of*  
Betty and Landon Bar  
*whose pride in my accomplishments at Stanford has been my utmost reward.*  
*I hope it does not disappoint you.*



# Contents

<b>Abstract</b>	<b>v</b>
<b>Acknowledgments</b>	<b>vii</b>
<b>1 Scientific Application</b>	<b>1</b>
1.1 Space Plasma Science . . . . .	3
1.1.1 Van Allen Radiation Belts . . . . .	5
1.1.1.1 Inner Zone . . . . .	6
1.1.1.2 Outer Zone . . . . .	8
1.1.2 The Geomagnetic Field . . . . .	10
1.1.2.1 Dipole Model . . . . .	12
1.1.2.2 Geomagnetic Coordinates . . . . .	14
1.1.3 Plasma Waves . . . . .	17
1.1.3.1 Theories and Models . . . . .	19
1.1.3.2 Electromagnetic Waves . . . . .	23
1.1.3.3 Electrostatic Waves . . . . .	25
1.1.3.4 Magnetohydrodynamic Waves . . . . .	26
1.2 Space Plasma Instrumentation . . . . .	28
1.2.1 Plasma Wave Receivers . . . . .	30
1.2.1.1 Sweep Frequency Receiver (SFR) . . . . .	38
1.2.1.2 Multichannel Spectrum Analyzer (MSA) . . . . .	40
1.2.1.3 Wideband Receiver . . . . .	42
1.2.2 Target Receiver . . . . .	46

1.3	Organization . . . . .	51
1.4	Contributions . . . . .	54
<b>2</b>	<b>Radiation Effects</b>	<b>57</b>
2.1	Total Dose Effects . . . . .	60
2.1.1	MOS Transistors . . . . .	60
2.1.1.1	Threshold Voltage . . . . .	61
2.1.1.2	Transconductance . . . . .	71
2.1.1.3	Leakage Current . . . . .	75
2.1.1.4	Noise . . . . .	81
2.1.2	Bipolar Transistors . . . . .	84
2.1.2.1	Beta Degradation . . . . .	85
2.1.2.2	Leakage Current . . . . .	93
2.1.2.3	Dose-Rate Effects . . . . .	95
2.2	Single-Event Effects . . . . .	100
2.2.1	Single-Event Latchup . . . . .	104
2.2.2	Single-Event Transients . . . . .	110
2.3	Radiation Hardening . . . . .	115
2.3.1	Van Allen Belt Fluxes . . . . .	115
2.3.2	Mitigation Strategies . . . . .	119
2.3.2.1	Shielding . . . . .	119
2.3.2.2	Radiation-Hardened Process . . . . .	122
2.3.2.3	Advanced Commercial Process . . . . .	123
2.3.2.4	Radiation-Hardening-By-Design . . . . .	129
<b>3</b>	<b>Architecture</b>	<b>133</b>
3.1	Component Specifications . . . . .	134
3.1.1	Programmability . . . . .	135
3.1.1.1	LNA Gain . . . . .	136
3.1.1.2	AAF Bandwidth . . . . .	139
3.1.2	Linearity . . . . .	142
3.1.2.1	Spurious-Free Dynamic Range . . . . .	143

3.1.2.2	Spot Noise . . . . .	148
3.1.2.3	Large Signal Behavior . . . . .	149
3.1.3	Noise . . . . .	153
3.1.3.1	Minimum Detectable Signal . . . . .	154
3.1.3.2	Antenna Noise in Plasmas . . . . .	158
3.1.3.3	Circuit Noise . . . . .	162
3.1.4	Input Impedance . . . . .	169
3.1.4.1	Antenna-LNA Interface . . . . .	170
3.1.4.2	Ideal Voltmeter Operation . . . . .	174
3.1.4.3	LNA Input Impedance . . . . .	175
3.1.5	Specification Summary . . . . .	177
3.2	System-Level Strategies . . . . .	179
3.2.1	Manufacturing Process . . . . .	179
3.2.1.1	CMOS . . . . .	182
3.2.1.2	Vertical npn . . . . .	183
3.2.1.3	Substrate pnp . . . . .	184
3.2.1.4	Lateral pnp . . . . .	185
3.2.2	Feedback . . . . .	187
3.2.2.1	Global versus Local . . . . .	189
3.2.2.2	Passive versus Active . . . . .	190
3.2.2.3	Linear versus Nonlinear . . . . .	193
<b>4</b>	<b>LNA Design</b>	<b>197</b>
4.1	Architecture . . . . .	198
4.1.1	Canonical Inamp . . . . .	199
4.1.1.1	Qualitative Operation . . . . .	201
4.1.1.2	Quantitative Operation . . . . .	202
4.1.1.3	Shortcomings . . . . .	208
4.1.2	Modified Architecture . . . . .	208
4.1.2.1	Differential Output . . . . .	210
4.1.2.2	Current Steering . . . . .	211

4.1.2.3	Gain Programming . . . . .	212
4.2	Implementation . . . . .	215
4.2.1	General Philosophy . . . . .	215
4.2.1.1	Single-Stage OTA . . . . .	216
4.2.1.2	Multi-stage OTA . . . . .	218
4.2.1.3	Extrapolation . . . . .	219
4.2.2	First Stage . . . . .	220
4.2.2.1	Super Emitter-Follower . . . . .	220
4.2.2.2	Hybrid Super Emitter-Follower . . . . .	224
4.2.2.3	Series-Shunt Loop . . . . .	226
4.2.3	Second Stage . . . . .	231
4.2.3.1	Output Buffer . . . . .	232
4.2.3.2	Load Impedance . . . . .	235
4.2.4	Current Sources . . . . .	236
4.2.4.1	Tail Current Sources . . . . .	236
4.2.4.2	Head Current Sources . . . . .	241
4.3	Layout . . . . .	245
4.3.1	Matching . . . . .	246
4.3.1.1	Transistors . . . . .	247
4.3.1.2	Resistors . . . . .	252
4.3.2	Radiation Tolerance . . . . .	254
4.3.2.1	SEL Prevention . . . . .	255
4.3.2.2	ASET Suppression . . . . .	258
<b>5</b>	<b>AAF Design</b>	<b>261</b>
5.1	Filter Architecture . . . . .	265
5.1.1	Filter Approximation . . . . .	266
5.1.2	Ideal Response . . . . .	267
5.1.3	Cascade Topology . . . . .	270
5.1.3.1	Pole Distribution . . . . .	271
5.1.3.2	Gain Assignment . . . . .	272

5.2	Stage Architecture . . . . .	273
5.2.1	Single-Ended Biquads . . . . .	274
5.2.1.1	Sallen-Key . . . . .	274
5.2.1.2	Tow-Thomas . . . . .	277
5.2.2	Canonical 2 <sup>nd</sup> -Order Section . . . . .	280
5.3	Integrator Architecture . . . . .	283
5.3.1	Active Integrators . . . . .	284
5.3.1.1	MOS-C-Opamp . . . . .	285
5.3.1.2	G <sub>m</sub> -C-Opamp . . . . .	286
5.3.2	Hybrid G <sub>m</sub> -C-Opamp . . . . .	289
5.3.2.1	Element Sizing . . . . .	289
5.3.2.2	Ideal Components . . . . .	293
5.3.2.3	Non-Ideal Components, $\alpha$ -error . . . . .	296
5.3.2.4	Non-Ideal Components, $Q$ -enhancement . . . . .	298
5.4	Transconductor Architecture . . . . .	301
5.4.1	Feedforward Transconductors . . . . .	301
5.4.1.1	Triode MOS . . . . .	301
5.4.1.2	Saturated MOS . . . . .	302
5.4.1.3	Cross-Coupled Pair . . . . .	304
5.4.1.4	Hyperbolic Compensation . . . . .	307
5.4.2	Two-Stage Unit Cell . . . . .	311
5.4.2.1	Translinear Principle . . . . .	311
5.4.2.2	Gilbert Gain Cell . . . . .	315
5.5	Implementation . . . . .	319
5.5.1	First Stage . . . . .	320
5.5.1.1	Positive Feedback . . . . .	322
5.5.1.2	Linearization . . . . .	324
5.5.2	Second Stage . . . . .	330
5.5.2.1	Odd-Order Distortion . . . . .	332
5.5.2.2	Even-Order Distortion . . . . .	334
5.5.3	Common-Mode Feedback . . . . .	336

5.5.3.1	Shared Amplifier . . . . .	339
5.5.3.2	pMOS Loads . . . . .	344
5.6	Layout . . . . .	346
5.6.1	Matching . . . . .	348
5.6.1.1	Reference Distribution . . . . .	348
5.6.1.2	Comb Capacitors . . . . .	349
5.6.1.3	Transconductor Array . . . . .	354
5.6.2	Radiation Tolerance . . . . .	355
5.6.2.1	Switch Leakage . . . . .	355
5.6.2.2	SEE Prevention . . . . .	361
<b>6</b>	<b>Measured Results</b>	<b>365</b>
6.1	Experimental Setup . . . . .	366
6.1.1	Devices Under Test . . . . .	366
6.1.1.1	Die Layout . . . . .	367
6.1.1.2	Packaging . . . . .	369
6.1.2	Circuit Boards . . . . .	372
6.1.2.1	Characterization Board . . . . .	372
6.1.2.2	Radiation Bias Board . . . . .	374
6.1.2.3	Burn-In Bias Board . . . . .	375
6.1.3	Instrumentation . . . . .	375
6.2	Test Benches . . . . .	377
6.2.1	Frequency Response . . . . .	378
6.2.1.1	Instrumentation . . . . .	378
6.2.1.2	Configuration . . . . .	379
6.2.1.3	Acquisition . . . . .	384
6.2.1.4	Analysis . . . . .	385
6.2.2	Linearity . . . . .	385
6.2.2.1	Instrumentation . . . . .	385
6.2.2.2	Configuration . . . . .	387
6.2.2.3	Acquisition . . . . .	388



	6.2.2.4	Analysis . . . . .	389
6.2.3	Noise . . . . .		394
	6.2.3.1	Instrumentation . . . . .	394
	6.2.3.2	Configuration . . . . .	396
	6.2.3.3	Acquisition . . . . .	396
	6.2.3.4	Analysis . . . . .	399
6.2.4	Power Dissipation . . . . .		400
	6.2.4.1	Instrumentation . . . . .	402
	6.2.4.2	Configuration . . . . .	402
	6.2.4.3	Acquisition . . . . .	404
	6.2.4.4	Analysis . . . . .	404
6.2.5	Single-Event Effects . . . . .		405
	6.2.5.1	Instrumentation . . . . .	405
	6.2.5.2	Configuration . . . . .	408
	6.2.5.3	Acquisition . . . . .	409
	6.2.5.4	Analysis . . . . .	413
6.3	Baseline Performance . . . . .		417
	6.3.1	Procedure . . . . .	417
	6.3.2	LNA Results . . . . .	417
		6.3.2.1 Bode Response and Programming . . . . .	418
		6.3.2.2 Linearity . . . . .	419
		6.3.2.3 Noise . . . . .	424
		6.3.2.4 Power Dissipation . . . . .	424
	6.3.3	AAF Results . . . . .	426
		6.3.3.1 Bode Response . . . . .	426
		6.3.3.2 Trimming . . . . .	434
		6.3.3.3 Linearity . . . . .	439
		6.3.3.4 Power Dissipation . . . . .	442
6.4	Radiation Performance . . . . .		443
	6.4.1	Procedure . . . . .	445
	6.4.2	LNA Results . . . . .	445

6.4.2.1	Bode Response . . . . .	445
6.4.2.2	Linearity . . . . .	451
6.4.2.3	Power Dissipation . . . . .	451
6.4.2.4	Single-Event Transients . . . . .	452
6.4.3	AAF Results . . . . .	460
6.4.3.1	Bode Response . . . . .	460
6.4.3.2	Linearity . . . . .	462
6.4.3.3	Power Dissipation . . . . .	462
6.4.3.4	Single-Event Latchup . . . . .	466
6.5	Burn-In Performance . . . . .	468
6.5.1	Procedure . . . . .	469
6.5.2	Results . . . . .	469
<b>7</b>	<b>Conclusion</b>	<b>471</b>
7.1	Performance Summary . . . . .	474
7.2	Mission Opportunities . . . . .	477
7.3	Suggestions For Future Research . . . . .	477
<b>A</b>	<b>Space Plasma Physics</b>	<b>481</b>
A.1	The Earth’s Magnetosphere . . . . .	482
A.1.1	Outer Magnetosphere . . . . .	484
A.1.1.1	Solar Wind . . . . .	485
A.1.1.2	Bow Shock . . . . .	487
A.1.1.3	Magnetopause . . . . .	488
A.1.2	Plasmasphere . . . . .	489
A.2	Particle Trapping . . . . .	490
A.2.1	Particle Motion . . . . .	491
A.2.1.1	Cyclotron Motion . . . . .	491
A.2.1.2	Drift Motion . . . . .	492
A.2.1.3	Bounce Motion . . . . .	494
A.2.2	Adiabaticity . . . . .	495
A.2.2.1	Adiabatic Invariants . . . . .	496

A.2.2.2	Adiabatic Motion . . . . .	497
A.2.2.3	Non-Adiabatic Motion . . . . .	499
A.3	Wave-Particle Interactions . . . . .	500
A.3.1	Pitch-Angle Diffusion . . . . .	502
A.3.2	Bounce Resonance . . . . .	503
A.3.3	Cyclotron Resonance . . . . .	503
A.3.3.1	Normal Scattering . . . . .	504
A.3.3.2	Anomalous Scattering . . . . .	509
A.3.3.3	Electrons versus Ions . . . . .	509
A.3.3.4	Scattering versus Diffusion . . . . .	511
<b>B</b>	<b>Plasma Wave Instruments</b>	<b>513</b>
B.1	Hardware Surveys . . . . .	514
B.1.1	Instruments . . . . .	515
B.1.2	Antennas . . . . .	522
B.1.3	Electronics . . . . .	532
B.1.3.1	Sweep Frequency Receivers . . . . .	534
B.1.3.2	Multichannel Spectrum Analyzers . . . . .	540
B.1.3.3	Wideband Receivers . . . . .	546
B.2	Selected Bibliography . . . . .	554
<b>C</b>	<b>Radiological Physics</b>	<b>573</b>
C.1	Dosimetry . . . . .	575
C.1.1	Radiation Types . . . . .	575
C.1.1.1	Alpha Particles . . . . .	576
C.1.1.2	Beta Particles . . . . .	576
C.1.1.3	Gamma Rays . . . . .	577
C.1.1.4	Nucleons and heavy ions . . . . .	578
C.1.2	Radiation Metrics . . . . .	580
C.1.2.1	Linear Energy Transfer . . . . .	580
C.1.2.2	Absorbed Dose . . . . .	582
C.1.2.3	Equivalent Dose . . . . .	583

C.2	Ionizing Radiation . . . . .	587
C.2.1	Generation . . . . .	587
C.2.1.1	Photonic Mechanisms . . . . .	587
C.2.1.2	Particle Mechanisms . . . . .	591
C.2.2	Recombination . . . . .	592
C.2.3	Transport . . . . .	594
C.2.4	Oxide Traps . . . . .	597
C.2.5	Border Traps . . . . .	603
C.2.6	Interface Traps . . . . .	605
C.3	Non-Ionizing Radiation . . . . .	610
C.3.1	Generation . . . . .	610
C.3.1.1	Photonic Mechanisms . . . . .	611
C.3.1.2	Particle Mechanisms . . . . .	611
C.3.2	Recombination and aggregation . . . . .	613
C.3.3	Defect Migration . . . . .	614
C.3.4	Minority Carrier Trapping . . . . .	616
C.3.5	Majority Carrier Trapping . . . . .	619
<b>D</b>	<b>Antenna Noise in a Magnetoplasma</b>	<b>623</b>
D.1	Electric Antennas . . . . .	624
D.1.1	Langmuir Theory . . . . .	625
D.1.1.1	Antenna Currents . . . . .	625
D.1.1.2	Sheath Character . . . . .	629
D.1.1.3	Sheath Resistance . . . . .	630
D.1.1.4	Sheath Capacitance . . . . .	630
D.1.2	Noise Sources . . . . .	633
D.1.2.1	Thermal Noise . . . . .	633
D.1.2.2	Shot Noise . . . . .	634
D.1.2.3	Total Noise . . . . .	635
D.1.3	Dipole Impedance . . . . .	636
D.1.3.1	Low-Frequency Regime . . . . .	638

D.1.3.2	Mid-Frequency Regime . . . . .	639
D.1.3.3	Resonant Regime . . . . .	646
D.1.3.4	High-Frequency Regime . . . . .	646
D.1.4	Summary . . . . .	647
D.2	Magnetic Antennas . . . . .	647
D.2.1	Antenna Basics . . . . .	650
D.2.1.1	Bandwidth . . . . .	650
D.2.1.2	Impedance . . . . .	651
D.2.2	Noise Sources . . . . .	652
D.2.3	Summary . . . . .	653
<b>E</b>	<b>Gate-Controlled Lateral pnp</b>	<b>657</b>
E.1	Bipolar Gain . . . . .	658
E.1.1	Base Decomposition . . . . .	660
E.1.1.1	Homogeneous Base . . . . .	661
E.1.1.2	Space-Charge Regions . . . . .	662
E.1.2	Injection Level . . . . .	663
E.1.2.1	Low-Level Effects . . . . .	663
E.1.2.2	High-Level Effects . . . . .	665
E.2	GCLPNP Basics . . . . .	665
E.2.1	Structure . . . . .	666
E.2.2	Operation . . . . .	667
E.2.2.1	Accumulated Base . . . . .	667
E.2.2.2	Depleted Base . . . . .	668
E.2.3	Radiation Tolerance . . . . .	668
E.2.3.1	Irradiation Bias . . . . .	669
E.2.3.2	Measurement Bias . . . . .	670
E.3	Novel GCLPNP . . . . .	671
E.3.1	Construction . . . . .	671
E.3.1.1	Emitter . . . . .	673
E.3.1.2	Collector . . . . .	675

E.3.1.3	Base . . . . .	677
E.3.1.4	n-Type Tub . . . . .	677
E.3.1.5	Variations . . . . .	682
E.3.2	Measured Results . . . . .	682
E.4	Summary . . . . .	690
<b>F</b>	<b>Filter Theory</b>	<b>693</b>
F.1	Filter Descriptions . . . . .	693
F.1.1	Filter Polynomials . . . . .	694
F.1.1.1	Loss Function . . . . .	695
F.1.1.2	Characteristic Polynomials . . . . .	697
F.1.1.3	Characteristic Function . . . . .	699
F.1.2	Pole-Zero Relationships . . . . .	701
F.1.2.1	Summary . . . . .	702
F.1.3	Filter Approximations . . . . .	703
F.1.3.1	Butterworth . . . . .	703
F.1.3.2	Type I Chebyshev . . . . .	705
F.1.3.3	Type II Chebyshev . . . . .	707
F.1.3.4	Cauer . . . . .	708
F.1.3.5	Bessel . . . . .	709
F.2	Integrator Loss Metrics . . . . .	710
F.2.1	Reactive Losses, Passive . . . . .	711
F.2.1.1	Dissipation . . . . .	712
F.2.1.2	Quality Factor . . . . .	712
F.2.2	Reactive Losses, Active . . . . .	713
F.2.3	Excess Phase . . . . .	714
F.2.3.1	Lossless Integrator . . . . .	715
F.2.3.2	Lossy Integrator . . . . .	716
<b>G</b>	<b>Auxiliary SVEPRE Circuits</b>	<b>717</b>
G.1	AAF Elements . . . . .	717
G.1.1	Operational Amplifier . . . . .	718

G.1.1.1	First Stage . . . . .	718
G.1.1.2	Second Stage . . . . .	719
G.1.1.3	Common-Mode Feedback . . . . .	723
G.1.1.4	Biasing . . . . .	725
G.1.1.5	Summary . . . . .	725
G.2	System Elements . . . . .	728
G.2.1	Voltage Regulator . . . . .	728
G.2.1.1	Feedback Loop . . . . .	729
G.2.1.2	Feedback Amplifier . . . . .	730
G.2.2	Reference Generators . . . . .	732
G.2.2.1	Reference Voltages . . . . .	733
G.2.2.2	Reference Currents . . . . .	734
<b>H</b>	<b>Characterization Board</b>	<b>737</b>
H.1	Signal Path . . . . .	739
H.1.1	Device-Under-Test (DUT) . . . . .	739
H.1.2	Single-Ended Input (INPSE) . . . . .	740
H.1.2.1	Passive Path . . . . .	740
H.1.2.2	Active Path . . . . .	742
H.1.3	Differential Input (INPDF) . . . . .	743
H.1.4	Input Offset Cancellation (INPOS) . . . . .	745
H.1.5	Output Termination (OUTDF and OUTSE) . . . . .	747
H.1.5.1	Differential Output . . . . .	747
H.1.5.2	Single-Ended Output . . . . .	747
H.2	Supplies and References . . . . .	747
H.2.1	Fixed Supply Regulators (SUPF) . . . . .	749
H.2.1.1	Power Measurement . . . . .	750
H.2.2	Adjustable Supply Regulators (SUPA) . . . . .	750
H.2.3	Reference Currents (RCUR) . . . . .	751
H.2.4	Reference Voltages (RVLT) . . . . .	751
H.2.5	Common-Mode Generators (RVCM) . . . . .	754

H.3	Programming and Control . . . . .	754
H.3.1	Gain Programming (GNADJ) . . . . .	754
H.3.2	Bandwidth Programming (BWADJ) . . . . .	754
H.3.3	Digital Subsection (ADC, INPCK, SUPF3, SUPF4) . . . . .	755
H.3.4	Digital Headers (INPHD and OUTHD) . . . . .	755
<b>I</b>	<b>Total-Dose Testing</b>	<b>757</b>
I.1	<sup>60</sup> Co Testing . . . . .	759
I.1.1	Source . . . . .	759
I.1.1.1	Theory . . . . .	760
I.1.1.2	Overview . . . . .	761
I.1.1.3	Dosimetry . . . . .	761
I.1.2	Setup . . . . .	764
I.1.2.1	Device-Under-Test . . . . .	764
I.1.2.2	Circuit Board . . . . .	764
I.1.3	Procedure . . . . .	764
I.1.3.1	Irradiation Schedule . . . . .	765
I.1.3.2	Annealing Schedule . . . . .	765
I.2	Proton Testing . . . . .	767
I.2.1	Source . . . . .	768
I.2.1.1	Overview . . . . .	769
I.2.1.2	Dosimetry . . . . .	771
I.2.2	Setup . . . . .	773
I.2.2.1	Device-Under-Test . . . . .	773
I.2.2.2	Circuit Board . . . . .	773
I.2.3	Procedure . . . . .	774
I.2.3.1	Irradiation Schedule . . . . .	774
I.2.3.2	Annealing Schedule . . . . .	775
<b>J</b>	<b>Single-Event Testing</b>	<b>779</b>
J.1	Pulsed-Laser Testing . . . . .	779
J.1.1	Source . . . . .	780



	J.1.1.1	Theory . . . . .	780
	J.1.1.2	Overview . . . . .	782
	J.1.1.3	Dosimetry . . . . .	784
J.1.2	Setup . . . . .		787
	J.1.2.1	Device-Under-Test . . . . .	787
	J.1.2.2	Circuit Board . . . . .	788
J.1.3	Procedure . . . . .		788
	J.1.3.1	SEL Scans . . . . .	788
	J.1.3.2	SET Scans . . . . .	788
J.2	Heavy-Ion Testing . . . . .		789
	J.2.1	Source . . . . .	790
	J.2.1.1	Overview . . . . .	792
	J.2.1.2	Dosimetry . . . . .	793
J.2.2	Setup . . . . .		796
	J.2.2.1	Device-Under-Test . . . . .	796
	J.2.2.2	Circuit Board . . . . .	796
	J.2.2.3	Instrumentation . . . . .	797
J.2.3	Procedure . . . . .		799
	J.2.3.1	Waveform Runs . . . . .	799
	J.2.3.2	Cross-Section Runs . . . . .	799
<b>K</b>	<b>Burn-In Testing</b>		<b>803</b>
K.1	Setup . . . . .		804
	K.1.1	Thermal . . . . .	804
	K.1.2	Characterization . . . . .	806
K.2	Procedure . . . . .		806
	K.2.1	Thermal . . . . .	807
	K.2.2	Characterization . . . . .	807
	K.2.2.1	Test Vectors . . . . .	808
	K.2.2.2	Frequency Response (FR) . . . . .	809
	K.2.2.3	Linearity (LN), Gain Compression . . . . .	810

K.2.2.4	Linearity (LN), SFDR . . . . .	811
K.2.2.5	Power Dissipation (PD) . . . . .	812
K.3	Results . . . . .	812
K.4	Analysis . . . . .	812
K.4.1	Figure of Merit . . . . .	813
K.4.1.1	Weighting . . . . .	816
K.4.2	Ranking . . . . .	817
K.4.2.1	Delta Acceptance . . . . .	817
K.4.2.2	Epsilon Acceptance . . . . .	818
K.4.2.3	Zeta Acceptance . . . . .	818
K.4.3	Summary . . . . .	819

# List of Tables

1.1	Macroscopic properties and transport equations for fluid theory . . .	21
1.2	Satellites since 1959 with plasma wave receiver payloads . . . . .	37
1.3	Estimated power budget for five-channel receiver . . . . .	51
3.1	Antenna properties predicted by unified noise model . . . . .	161
3.2	Summary of target specifications for front-end . . . . .	178
3.3	Tapeout catalog . . . . .	181
3.4	Comparison of NL1d25x0d6 and NL2d5x5d0 npn devices . . . . .	184
3.5	Select performance comparison of bipolar geometries . . . . .	186
5.1	Pole locations for stages of 6th-order Type I Chebyshev low-pass AAF in each mode . . . . .	269
5.2	Transconductor and capacitor sizes for stage of Figure 5.13(b), Mode B	294
5.3	Configuration of nMOS GGC switches in each AAF mode . . . . .	332
5.4	Configuration of pMOS load switches in each AAF mode . . . . .	342
5.5	Configuration of CMFB amplifier switches in each AAF mode . . . .	342
5.6	Layout variations of unit transconductor cell . . . . .	355
6.1	Flight packaging options for SVEPRE-3 . . . . .	371
6.2	Network analyzer settings for FR test bench . . . . .	384
6.3	INPDF settings for LN test bench . . . . .	388
6.4	Spectrum analyzer settings for NS test bench . . . . .	397
6.5	Function generator settings for NS test bench . . . . .	398
6.6	Oscilloscope settings for SEE test bench during heavy-ion testing . .	410

6.7	Spectrum analyzer settings for NS test bench . . . . .	411
6.8	Total-dose radiation testing performed for this dissertation . . . . .	446
6.9	Single-event radiation testing performed for this dissertation . . . . .	447
6.10	Summary of ASETs observed during pulsed-laser testing of LNA . . . . .	456
6.11	Weibull parameters for LNA heavy-ions cross-sections . . . . .	459
6.12	Summary of performance variation during burn-in testing . . . . .	470
7.1	Summary of measured LNA performance . . . . .	475
7.2	Summary of measured AAF performance . . . . .	476
B.1	Wave instruments payloads of satellites in Table 1.2 . . . . .	521
B.2	Limiting capacitances for dipole and double-probe antennas . . . . .	523
B.3	Properties of electric field antennas and their amplifiers . . . . .	531
B.4	Sweep frequency receivers aboard satellites in Table B.1 . . . . .	539
B.5	Multichannel spectrum analyzers aboard satellites in Table B.1 . . . . .	545
B.6	Wideband receivers aboard satellites in Table B.1 . . . . .	553
C.1	Radiation weighting factors recommended by ICRP . . . . .	584
C.2	Equivalent dose limits recommended by ICRP . . . . .	585
C.3	Hazardous effects of radiation doses for sample population . . . . .	586
D.1	Summary of unified noise model for dipole antenna in magnetoplasma . . . . .	648
D.2	Plasma and antenna parameters invoked by antenna noise simulations . . . . .	649
E.1	Terminal mapping for pMOS and lpnp that comprise GCLPNP . . . . .	666
F.1	Relationship between poles and zeros of filter polynomials . . . . .	704
G.1	Simulated performance of opamp CMFB loop . . . . .	725
G.2	Simulated performance of opamp for AAF integrators . . . . .	727
G.3	Simulated performance of opamp for on-chip regulator . . . . .	733
I.1	Dose-rate calibration table for $^{60}\text{Co}$ chamber . . . . .	762
I.2	Irradiation schedule for $^{60}\text{Co}$ $\gamma$ -ray testing . . . . .	766
I.3	Irradiation schedule for 50-MeV $\text{H}^+$ testing . . . . .	776

I.4	Irradiation schedule for 30-MeV $H^+$ testing . . . . .	777
J.1	Parameters of pulsed dye laser setup at The Aerospace Corporation .	785
J.2	Properties of species in the 10-MeV/nucleon heavy ion cocktail . . . .	790
J.3	Irradiation schedule for waveform acquisitions during heavy-ion testing	800
J.4	Irradiation schedule for 30 mV <sub>PP</sub> acquisitions during heavy-ion testing	801
J.5	Irradiation schedule for 60 mV <sub>PP</sub> acquisitions during heavy-ion testing	801
J.6	Irradiation schedule for DC acquisitions during heavy-ion testing . . .	802
K.1	Burn-in test vectors comprised of select gain and frequency modes . .	808
K.2	Sweep parameters for FR test bench during burn-in testing . . . . .	809
K.3	Sweep parameters for LN test bench during burn-in testing . . . . .	810
K.4	Measured performance of 32-piece lot before burn-in, by serial number	814
K.5	Measured performance of 32-piece lot before burn-in, by serial number	815
K.6	Weighting coefficients for figure-of-merit defined in (K.7) . . . . .	816
K.7	Burn-in rankings of 32-piece lot using delta acceptance method . . . .	820



# List of Figures

1.1	Concentric tori formed by inner and outer zones of Earth's Van Allen radiation belts . . . . .	6
1.2	Omnidirectional, differential flux spectrum of inner zone protons . . .	7
1.3	Omnidirectional, integrated flux of radiation-belt protons with energy greater than 50 MeV . . . . .	8
1.4	Omnidirectional, integrated flux of radiation-belt electrons with energy greater than 1 MeV . . . . .	9
1.5	Equatorial, omnidirectional, integrated flux of outer zone electrons . .	11
1.6	Distortion of the Earth's magnetic field due to the solar wind . . . . .	12
1.7	Schematic depiction of Earth's offset dipole field highlighting the South Atlantic Anomaly (SAA) . . . . .	15
1.8	Geomagnetic coordinate system for dipole field model . . . . .	16
1.9	Electric field spectral density of representative plasma wave phenomena	18
1.10	Magnetic field spectral density of representative plasma wave phenomena	18
1.11	Refractive index versus frequency for parallel and perpendicular plasma wave modes . . . . .	24
1.12	Magnetospheric regions home to the menagerie of plasma waves . . .	25
1.13	Signal space to be acquired by target receiver . . . . .	28
1.14	Exemplary spectrogram generated by Polar PWI instrument . . . . .	32
1.15	Partitioning of target signal space by SFR architecture . . . . .	39
1.16	Sweep frequency receiver front-end architecture . . . . .	39
1.17	Partitioning of target signal space by MSA architecture . . . . .	41
1.18	Multichannel spectrum analyzer front-end architecture . . . . .	41

1.19	Partitioning of target signal space by WBR architecture . . . . .	43
1.20	Wideband receiver front-end architectures . . . . .	44
1.21	Signal space captured by target receiver . . . . .	48
1.22	Architecture of target wideband receiver . . . . .	49
2.1	Decomposition of $I_D$ - $V_{GS}$ curve distortions into $\Delta V_{ot}$ and $\Delta V_{it}$ effects	62
2.2	Dependence of $\Delta V_{thp}$ on static gate bias during irradiation . . . . .	65
2.3	Comparison of $\Delta V_{ot}$ and $\Delta V_{it}$ gate-bias dependencies . . . . .	67
2.4	Dose dependence of $\Delta V_{thn}$ and $\Delta V_{thp}$ highlighting rebound of former .	69
2.5	Measured $\Delta V_{thn}$ of nMOS pairs from target process . . . . .	70
2.6	Measured $\Delta V_{thp}$ of pMOS pair from target process . . . . .	71
2.7	Measured $g_m$ -degradation of nMOS pairs from target process . . . . .	74
2.8	Measured $g_m$ -degradation of pMOS pair from target process . . . . .	75
2.9	MOSFET leakage paths in LOCOS-isolated technology . . . . .	77
2.10	Observed TID-induced leakage for LOCOS isolation . . . . .	78
2.11	MOSFET leakage paths in shallow-trench-isolated technology . . . . .	79
2.12	Observed TID-induced leakage for shallow-trench isolation . . . . .	80
2.13	Dose dependence of $1/f$ noise PSD for an nMOS transistor . . . . .	84
2.14	Dose dependence of $K_F$ in a 0.25- $\mu$ m CMOS technology . . . . .	85
2.15	Beta degradation of npn, substrate pnp, and lateral pnp transistors .	89
2.16	Measured $\beta$ -degradation of representative npn BJT from target process	90
2.17	Measured degradation of peak $\beta$ fit to (2.16) . . . . .	91
2.18	Gummel plot corresponding to measured $\beta$ -degradation at extremes of Figure 2.16 . . . . .	93
2.19	BJT leakage paths in ROX-isolated technology . . . . .	94
2.20	BJT leakage paths in DTI-isolated technology . . . . .	95
2.21	Measured threshold voltage shift of DTI FOXFET . . . . .	96
2.22	Radiation-induced collector-emitter sidewall leakage current . . . . .	97
2.23	Radiation-induced collector-base leakage current . . . . .	98
2.24	Illustration of space-charge fields responsible for ELDRS . . . . .	99
2.25	Funnel formation by charge track of heavy ion strike . . . . .	101



2.26	Charge track, collection mechanisms, and current pulse for an ion strike	102
2.27	Illustration of multi-junction strike for charge track traversing vn timer	104
2.28	Example of potential SEL structure in CMOS layout	106
2.29	Illustrative I-V characteristic of SEL-prone p-n-p-n structure	107
2.30	Representative ASET measured for the LM111 comparator	112
2.31	Ideal cross-sections for SEUs and ASETs as a function of LET	113
2.32	Measured ASET cross-sections for OP-15	114
2.33	5-year accumulated dose for various radiation-belt orbits	116
2.34	Orbit-averaged LET spectrum for circular, geosynchronous orbit	118
2.35	Dose-depth curves for Al and Pb shielding over a 7-year orbit	121
2.36	Scaling of SEU $Q_{crit}$ with feature size	125
2.37	Illustration of SOI device construction, including leakage paths	127
2.38	Example layout and band structure of SiGe HBT	131
3.1	Relationship of LNA input to induced dipole emf	137
3.2	AAF Bode plot for each bandwidth mode	141
3.3	Spectral elements utilized in definitions of noise and linearity metrics	144
3.4	Impact of SFDR on signal discrimination in output power spectrum	147
3.5	Comparison of nonlinear MOSFET behavior for various signal swings	151
3.6	Comparison of nonlinear BJT behavior for various signal swings	152
3.7	Dynamic range specifications for front-end signal path	155
3.8	Illustration of noise floor for sine wave equivalents of broadband inputs	157
3.9	Simulated noise of nominal dipole antenna	160
3.10	Front-end equivalent noise model	163
3.11	Simulated flicker noise of pMOSFETs in target technology	170
3.12	Single-sided impedance model for antenna-LNA coupling	171
3.13	Impedance models attained through reduction of Figure 3.12	173
3.14	Antenna impedance matching at the frequency range extremes	174
3.15	MOSFET schematic symbols	182
3.16	n timer BJT schematic symbols	185
3.17	Cross-section of second-generation prototype GCLP timer layout	188

3.18	Block diagram of canonical negative feedback system . . . . .	189
3.19	Use of global feedback to desensitize LNA . . . . .	191
3.20	Block diagram of passive local feedback within LNA . . . . .	192
3.21	Block diagram of nonlinear negative feedback system . . . . .	194
3.22	Recovery of desensitivity through active feedback loops . . . . .	195
3.23	Equivalent representation of linearization via techniques in Figure 3.22	196
4.1	Classic, discrete inamp built from three opamps . . . . .	199
4.2	Simplified inamp architecture of Brokaw and Timko . . . . .	200
4.3	Degenerated differential pair extracted from first stage of Figure 4.2 .	203
4.4	Flow graph representation of first stage of Figure 4.2 . . . . .	207
4.5	Simplified schematic of LNA architecture . . . . .	209
4.6	Lumped model of parasitic capacitances incurred across off-chip resistor	213
4.7	Potential single-stage and multi-stage OTA implementations . . . . .	217
4.8	Implementation of first stage of Figure 4.5 . . . . .	221
4.9	Simulated transfer function of degenerated differential pair . . . . .	222
4.10	Transconductance gains corresponding to slopes of curves in Figure 4.9	223
4.11	Conversion of Figure 4.3 into super emitter-follower . . . . .	224
4.12	Transconductance gain of super emitter-follower . . . . .	225
4.13	Block diagram of canonical series-shunt feedback . . . . .	227
4.14	Half-circuit of Figure 4.8 (positive side) . . . . .	228
4.15	Small-signal circuit derived from Figure 4.14(b) . . . . .	229
4.16	Simulated magnitude of LNA input impedance for various gain settings	231
4.17	Implementation of second stage of Figure 4.5 . . . . .	233
4.18	Output buffer chain extracted from Figure 4.17 . . . . .	235
4.19	Implementation of LNA tail current sources . . . . .	237
4.20	Mismatch of current sources in Figure 4.19 as a function of $V_{\text{deg}}$ . . .	238
4.21	Dependence of LNA linearity on tail current source $C_{\mu}$ . . . . .	240
4.22	Implementation of bias network for Figure 4.5 . . . . .	242
4.23	Implementation of LNA head current sources . . . . .	243
4.24	Principles and layouts of common-centroid arrays . . . . .	250

4.25	Example of npn and resistor common-centroid layouts . . . . .	251
4.26	Example layout of polysilicon resistor array . . . . .	253
4.27	Illustration of voltage modulation for p-type diffused resistor . . . . .	254
4.28	Example layout of diffused resistor array . . . . .	255
4.29	Examples of RHBD layout techniques applied to Q1/Q2 . . . . .	256
4.30	Possible common centroid arrays, including SET-tolerant configuration	260
5.1	Ideal and actual low-pass filter specifications . . . . .	262
5.2	AAF roll-off necessary to avoid spectral aliasing . . . . .	263
5.3	Bode response of ideal AAF design for Mode B . . . . .	268
5.4	Pole/zero plot of ideal AAF design for Mode B . . . . .	270
5.5	Three-stage cascaded filter architecture . . . . .	272
5.6	Single-ended Sallen-Key biquads . . . . .	275
5.7	Single-ended Tow-Thomas biquads . . . . .	278
5.8	Differential canonical 2 <sup>nd</sup> -order section . . . . .	282
5.9	Breakout of differential Miller integrators that comprise CSOS . . . . .	284
5.10	Differential, lossless MOSFET-C integrator . . . . .	285
5.11	Differential, lossless $G_m$ -C integrator . . . . .	287
5.12	Shaping of opamp noise by integrator architectures . . . . .	290
5.13	Stage architecture employing hybrid $G_m$ -C-Opamp integrators . . . . .	291
5.14	Bode response of realizable AAF design for Mode B . . . . .	295
5.15	Pole/zero plot of realizable AAF design for Mode B . . . . .	296
5.16	Excess phase versus attenuation error for each AAF stage . . . . .	298
5.17	Generic all-pole biquads based on two-integrator loop . . . . .	299
5.18	Popular transconductors based on triode MOS operation . . . . .	303
5.19	Popular transconductors based on saturated MOS operation . . . . .	305
5.20	Popular transconductors based on cross-coupled differential pairs . . . . .	306
5.21	Transconductor linearization using common-mode input voltage . . . . .	308
5.22	Example of multi-tanh principle with two pairs . . . . .	310
5.23	Two-stage architecture of unit transconductor . . . . .	312
5.24	Translinear loop examples . . . . .	313

5.25	Degenerated TLL with feedback linearization via current mirrors . . .	315
5.26	Flow graph representation of first stage of Figure 5.23 . . . . .	316
5.27	Simplified schematic of canonical Gilbert gain cell . . . . .	317
5.28	Illustration of GGC asymmetries responsible for distortion . . . . .	318
5.29	Simplified schematic of first stage of Figure 5.23 . . . . .	320
5.30	Positive feedback loop formed by pMOS mirror on left half of Figure 5.29	322
5.31	Full schematic of first stage of Figure 5.23 . . . . .	325
5.32	Heterogeneous implementation of $R_g$ . . . . .	326
5.33	Complete decomposition of heterogeneous $R_g$ . . . . .	327
5.34	Harmonics of $I_g$ for linearized first-stage TLL . . . . .	329
5.35	Simplified schematic of second stage of Figure 5.23 . . . . .	331
5.36	Simplified schematic of current density matching technique in GGC .	333
5.37	SPDT implementation of GGC current-density-matching switches . .	335
5.38	Linearized GGC with resistive degeneration . . . . .	337
5.39	Monte Carlo analysis of improved GGC mismatch with degeneration .	338
5.40	Simplified schematic of transconductor CMFB network . . . . .	340
5.41	Implementation of CMFB amplifier in Figure 5.40 . . . . .	341
5.42	Common-mode feedback loop for worst-case stability . . . . .	343
5.43	Transconductor loads of Figure 5.40 with simplified switching . . . .	345
5.44	Complete transconductor loads of Figure 5.40 . . . . .	347
5.45	Block diagram of reference shipping techniques . . . . .	350
5.46	Schematic of local reference generators in each stage of Figure 5.45 .	351
5.47	Metal comb capacitor used in SVEPRE . . . . .	352
5.48	Example layout of metal comb capacitor array . . . . .	353
5.49	Block diagram of Stage 1 layout . . . . .	356
5.50	Block diagram of Stage 2 layout . . . . .	357
5.51	Block diagram of Stage 3 layout . . . . .	358
5.52	Examples of low-leakage nMOS transistor layouts . . . . .	359
5.53	Measured leakage suppression of enclosed-source nMOS . . . . .	362
5.54	GGC ground-interrupt switching strategies . . . . .	363
5.55	$G_m$ -C-opamp capacitor drive strategies . . . . .	364

6.1	Photomicrograph of fabricated SVEPRE-3 chip . . . . .	368
6.2	Full pinout of SVEPRE in 68-pin JLDCC package . . . . .	370
6.3	Block diagram of characterization PCB . . . . .	373
6.4	Instrument connectivity for characterization PCB . . . . .	376
6.5	Instrument connectivity for frequency response measurements . . . . .	381
6.6	Instrument connectivity for frequency response calibration . . . . .	383
6.7	Instrument connectivity for linearity measurements of LNA . . . . .	386
6.8	Instrument connectivity for noise measurements of LNA . . . . .	395
6.9	Simplified noise model for NS test bench signal path . . . . .	399
6.10	Single-frequency ( $f_o$ ) slice of $S_{mo}(f)$ surface . . . . .	401
6.11	Instrument connectivity for power dissipation measurements . . . . .	403
6.12	Instrument connectivity for SEE measurements . . . . .	407
6.13	Measured LNA Bode response over gain programming . . . . .	421
6.14	Measured LNA gain programming curve . . . . .	422
6.15	Measured LNA output PSD for multiple fundamentals . . . . .	423
6.16	Measured LNA input-referred noise . . . . .	425
6.17	Predicted and measured magnitude of AAF Bode response . . . . .	429
6.18	Predicted and measured phase of AAF Bode response . . . . .	432
6.19	Measured AAF Bode response over bandwidth programming . . . . .	437
6.20	Measured AAF bandwidth trimming curve . . . . .	438
6.21	Measured AAF Stage 1 PSD for each mode . . . . .	440
6.22	Measured AAF Stage 1 PSD for each mode . . . . .	441
6.23	Measured power-efficiency of AAF trimming . . . . .	444
6.24	Measured magnitude of LNA Bode response for both TID sources . . . . .	449
6.25	Measured change in LNA SFDR for both TID sources . . . . .	452
6.26	Measured change in LNA power dissipation for both TID sources . . . . .	453
6.27	Measured output transients for pulsed-laser illumination of Q1 . . . . .	454
6.28	Measured output transients for pulsed-laser illumination of Q2 . . . . .	455
6.29	Measured output transients for pulsed-laser illumination of M23 . . . . .	457
6.30	Measured heavy-ion cross sections for LNA . . . . .	458
6.31	Measured magnitude of AAF Bode response for 30-MeV $H^+$ exposure . . . . .	461

6.32	Measured AAF attenuation for 30-MeV $H^+$ TID exposure . . . . .	463
6.33	Measured AAF Stage 1 SFDR3 for 30-MeV $H^+$ TID exposure . . . . .	464
6.34	Measured AAF Stage 1 SFDR3 for 30-MeV $H^+$ TID exposure . . . . .	465
6.35	Measured AAF power dissipation for 30-MeV $H^+$ TID exposure . . . . .	466
6.36	Measured SVEPRE-1 latchup sensitivity for heavy-ion exposure . . . . .	467
A.1	Nomenclature for strata of the Earth's upper atmosphere . . . . .	483
A.2	Artist's rendition of Earth's magnetosphere in cross-section . . . . .	485
A.3	Two-dimensional projection of Archimedean spiral formed by solar wind . . . . .	486
A.4	Average equatorial radius of the plasmapause . . . . .	490
A.5	Three periodic orbits executed by geomagnetically trapped particles . . . . .	495
A.6	Geometry of normal-mode electron cyclotron resonant interaction . . . . .	504
A.7	Phase relationships of wave fields and electron velocity perpendicular to ambient field . . . . .	505
A.8	Particle momentum trajectories due to cyclotron-resonant wave inter- actions . . . . .	508
C.1	Range of protons and electrons in aluminum . . . . .	579
C.2	Key steps in radiation-induced oxide damage . . . . .	588
C.3	Relative strength of photoionization mechanisms . . . . .	589
C.4	Gaussian transport model . . . . .	595
C.5	Non-Gaussian hole transport model . . . . .	596
C.6	Comparison of trapping and hopping hole transport models . . . . .	598
C.7	Transport of self-trapped hole (polaron) via tunneling . . . . .	599
C.8	Precursor to $E'$ center . . . . .	601
C.9	Molecular representation of $E'$ center . . . . .	602
C.10	Illustration of trap locations in Si oxide . . . . .	604
C.11	Molecular representation of Pb center . . . . .	609
D.1	Bias-dependent geometry of positive-ion sheath around dipole antenna . . . . .	631
D.2	Generalized model of dipole antenna impedance . . . . .	637
D.3	Simulated noise of magnetic antennas in inner zone ( $L=2$ ) . . . . .	655

D.4	Simulated noise of magnetic antennas in inner zone ( $L=4$ ) . . . . .	656
E.1	Typical variation of $\beta$ with npn bias conditions . . . . .	659
E.2	Decomposition of base regions in lpnp topology . . . . .	662
E.3	Gummel curve corresponding to $\beta$ described in Figure E.1(b) . . . . .	663
E.4	Structure and circuit symbol of simplified GCLPNP . . . . .	666
E.5	Measurements of GCLPNP dependence on irradiation bias . . . . .	669
E.6	Dependence of GCLPNP $\beta$ -degradation on measurement and irradiation bias . . . . .	671
E.7	General structure of GCLPNP . . . . .	672
E.8	Breakout of GCLPNP emitter design . . . . .	674
E.9	Breakout of GCLPNP collector design . . . . .	676
E.10	Breakout of GCLPNP base design . . . . .	678
E.11	Breakout of GCLPNP n-tub design . . . . .	681
E.12	Design of first-generation GCLPNP device . . . . .	683
E.13	Design of second-generation GCLPNP device . . . . .	684
E.14	Measured $I_C$ -vs- $V_{EC}$ curves for first generation GCLPNPs . . . . .	687
E.15	Measured $I_C$ -vs- $V_{EC}$ curves for second generation GCLPNPs . . . . .	689
E.16	Measured performance of GCLPNP under best operating conditions . . . . .	691
F.1	Simple block diagram defining filter transfer function . . . . .	694
F.2	Relationship between $H(j\omega)$ , $K(j\omega)$ , and $\alpha(\omega)$ . . . . .	700
F.3	Relative pole locations of Bessel approximation . . . . .	710
G.1	Simplified schematic of opamp architecture . . . . .	719
G.2	Schematic of first stage of opamp . . . . .	720
G.3	Schematic of second stage of opamp . . . . .	722
G.4	Schematic of opamp common-mode feedback amplifier . . . . .	724
G.5	Schematic of opamp biasing network . . . . .	726
G.6	Simplified schematic of regulator feedback loop . . . . .	729
G.7	Simulated load regulation of on-chip voltage regulator . . . . .	731
G.8	Schematic of regulator opamp . . . . .	732

G.9	Diagram of options for reference voltage generation . . . . .	734
G.10	Schematic of voltage buffer for on-chip references . . . . .	735
G.11	Schematic of global, on-chip reference current generators . . . . .	736
H.1	Block diagram of characterization PCB . . . . .	738
H.2	Schematic of passive and active paths in INPSE block of Figure H.1 .	741
H.3	Schematic of INPDF block of Figure H.1 . . . . .	744
H.4	Schematic of INPOS block of Figure H.1 . . . . .	746
H.5	Schematics of OUTDF and OUTSE output termination paths of Figure H.1 . . . . .	748
H.6	Schematic of dual-mode power sensing circuit within each block of Figure H.1 . . . . .	750
H.7	Schematics of reference-voltage generation blocks of Figure H.1 . . . .	752
I.1	Map of the BASE facility at the LBNL 88-inch cyclotron . . . . .	767
I.2	Example equipment sequence at the beam line terminus in Cave 4A .	770
J.1	Diagram of pulsed-laser apparatus at The Aerospace Corporation . .	783
J.2	Map of the BASE facility at the LBNL 88-inch cyclotron . . . . .	794
J.3	Location of test equipment for heavy-ion SEE testing . . . . .	798
K.1	Schematic of DUT bias configuration for burn-in PCB . . . . .	805



# Chapter 1

## Scientific Application

Despite their critical relevance to fields of study spanning disparate realms from environments solar to subterranean, many underlying processes that govern the plasma electrodynamics of Earth’s outer atmosphere are “still only dimly perceived” [Walt, 1994, p.1]. In particular, the lack of a comprehensive description for the interactions between electromagnetic waves and energetic particles in the magnetosphere has inspired substantial research in recent years (e.g., [Bell *et al.*, 2004; Bortnik, 2004; Platino *et al.*, 2005]), owing to the import it holds for such disciplines as geophysics, astrophysics [Walt, 1994, p.6–7], terrestrial climate and weather [Wilcox, 1976], space weather [Tribble, 2003, p.14–24], spacecraft operations [Tascione, 1994, p.133–144], communications, power transmission systems, geology, and petroleum exploration [Lanzerotti, 1979]. Recent proposals [Inan *et al.*, 2003] even suggest that such an understanding might allow for the controlled mitigation of harmful and/or anthropogenic high-energy particle fluxes trapped by the Earth’s magnetic field.<sup>1</sup>

Given the scope and complexity of these wave-particle interactions, and the

---

<sup>1</sup>An example of the latter class of flux is afforded by the population of greater than 1-MeV electrons which persisted for 2–10 years [Tribble, 2003, p.165] after the Starfish Prime 1.4 megaton high-altitude nuclear detonation 400 km above Johnston Island in the Pacific Ocean [Barth *et al.*, 2003, p.470] on July 9, 1962 [O’Brien *et al.*, 1962]. Its crippling of radiation-susceptible communications satellites was cited by Nikita Krushchev as a potential mechanism for future USSR weaponry [Hughes, 1989, p.47] and is still a threat at the disposal of ‘rogue nations’ today [Pease, 2003, p.539].

concomitant intricacies of the modeling mathematics [[Schulz and Lanzerotti, 1974](#), p.vi], the first thirty years of theoretical advances in their study resembled “a series of unpredicted discoveries followed by interpretations and explanation” [[Walt, 1994](#), p.156]. But, having transitioned from an

...exploratory stage to one in which satellite missions and ground-based observations are planned with the specific-objective of achieving a global understanding and self-consistent quantitative description of the cause-and-effect relationships among the principle dynamical processes involved, [[Roederer, 1979](#), p.3]

current efforts to treat the Earth’s magnetosphere as “a convenient plasma laboratory of cosmic scale in which to perform experiments, active and passive, related to plasma wave processes” [[Shawhan, 1979](#), p.214], are limited by the quality of the instrumentation. Specifically, to conduct experiments aimed at the unresolved physics of wave-particle interactions in the Earth’s radiation belts, which serve as motivation for this research,

...the data most needed now are simultaneous observations made from key locations throughout the magnetosphere. Such measurements will involve multispacecraft observations and as well as multi-instrument measurements of particle fluxes, electric and magnetic fields, and the characteristics of waves over a broad frequency range. [[Walt, 1994](#), p.8]

Thus, to enable the next generation of plasma wave receivers for such high-fidelity, broadband, interferometric, in-situ measurements, a new class of instrument-grade electronics, suitable for sustained operation in the radiation-belt environment, is a prerequisite.

The purpose of this research is to design, implement, and test an application-specific integrated circuit (ASIC), dubbed SVEPRE,<sup>2</sup> to serve as the analog front-end

---

<sup>2</sup>SVEPRE is an initialism for **S**tanford **V**LF **E**-field **P**reamplifier. To distinguish between successive versions of the chip, the version number (counted from one) may be appended with a dash, as in SVEPRE-1 for the initial prototype. Such version numbers are used explicitly in this document when emphasizing revision differences; in their absence, references to SVEPRE should be construed as applying to all versions.

for such a modern, satellite-based, wideband plasma wave receiver. To introduce the design requirements of such a receiver and flow them down to the front-end ASIC, the remainder of this chapter is bifurcated as follows: Section 1.1 summarizes the geophysical background from which the science requirements of the target receiver are derived; Section 1.2 briefly reviews the architectures of canonical plasma wave receivers, providing a context in which the remaining specifications of the target system are explicated and its performance advantages contrasted with existing solutions.

## 1.1 Space Plasma Science

The continual application of heat causes a material to progressively transition through the four states of matter as it becomes increasingly more disordered: from solid, to liquid, to gas, to plasma [Tribble, 2003, p.115]. More formally, this final state, by far the most prevalent in the universe, describes “gases that include a large number of electrons and ionized atoms and molecules as well as the neutral atoms and molecules” [Inan and Inan, 2000, p.440]. Though the volumetric number density of these electrons ( $N_e$ ) and ions ( $N_i$ ) must be large enough for the plasma to exhibit collective behavior,<sup>3</sup> the degree of ionization required to achieve this behavior can be quite low, with greater than 0.01% of the total atom density,  $N_t$ , being sufficient to delineate strongly versus weakly ionized plasmas [Inan and Inan, 2000, p.443].

One key manifestation of their collective behavior is that these electrons(ions), liberated by the available thermal energy, can effectively screen the electrostatic field of a positively(negatively) charged particle introduced into the plasma, so that its influence is felt over only a small distance. This screening distance, known as the Debye length and denoted  $\lambda_D$ , is given by [Bittencourt, 1995, p.8]

$$\lambda_D = \sqrt{\frac{kT\epsilon_0}{NQ^2}} \quad (1.1)$$

---

<sup>3</sup>This property implies that the behavior of the plasma in regions distant from a disturbance is still affected due to the long-range scales of the electromagnetic forces at play and is a primary feature distinguishing plasmas from ordinary fluids [Bittencourt, 1995, p.3].

where  $N$ ,  $Q$ , and  $T$  denote the number density per unit volume, charge, and Kelvin temperature of the particles responsible for the screening.<sup>4</sup> Within a sphere of radius  $\lambda_D$  around the disturbance, this screening results in an excess number of oppositely charged particles as the inter-particle electromagnetic potential energy balances the thermal, or mean kinetic, energy of the screening particles.

But, over a macroscopic region where the dimensions of interest exceed the Debye length (e.g., in space), the plasma can be treated as quasi-neutral ( $N_i \simeq N_e$ ), since its equilibrium thermal energy is well below that required by Coulomb forces to maintain a net separation of space charge over such distances. Instead, in response to any displacement of its equilibrium charge distribution, internal electrostatic forces attempt to restore the macroscopic neutrality of the plasma, giving rise to natural oscillations at a characteristic frequency known as the plasma frequency,  $\omega_p$ , which, from the application of Newton's second law and Gauss's law [*Inan and Inan, 2000*, p.446] is given by

$$\omega_p^2 = \frac{NQ^2}{m\epsilon_0} \quad (1.2)$$

where  $m$  represents the mass of the screening particles.<sup>5</sup> As long as the plasma frequency far exceeds the neutral collision frequency,  $\nu_n$ , which is the rate of collisions between the screening particles and the neutral gas atoms, the inertial motions of the former are not appreciably damped, allowing the plasma to sustain oscillations at this and only this frequency unless external electric fields are imposed.

The response to such extrinsic fields, in the form of stationary or propagating electromagnetic waves known as plasma waves that are further investigated in Section 1.1.3, is governed by the relationship of their frequency to  $\omega_{pe}$  and quantities derived from it. Similarly, it is shown that the Debye length describes the dimensions of the plasma sheath that control the input impedance of the receiver antenna (cf.

---

<sup>4</sup>As usual,  $k$  is the Boltzmann constant and  $\epsilon_0$  is the permittivity of free space.

<sup>5</sup>While the parameters defined in this section are unique to each charged particle species in the plasma, the limiting cases occur for electrons, on account of the high frequency motion associated with their relatively small mass. Thus, unless otherwise noted by explicitly using the subscripts  $e$  (electrons) and  $i$  (ions), it is assumed for the remainder of this document that the terms Debye length and plasma frequency, refer to the characteristics of the electron,  $\lambda_{De}$  and  $\omega_{pe}$ , which are obtained by substituting  $N = N_e$ ,  $T = T_e$ ,  $m = m_e$ ,  $Q = -q$  and  $\nu_n = \nu_{ne}$  into (1.1) and (1.2).

Section 3.1.4). These fundamental plasma parameters depend upon properties of the near-Earth space plasma that vary drastically with altitude, such as number density and temperature. For the unfamiliar but curious reader, a brief review of this environment with emphasis on the composition and particle dynamics of the magnetosphere is offered in Appendix A. Adducing reasons elucidated there, this work is concerned with investigating the portion of the magnetosphere known as the radiation belts, where plasma waves drive a powerful but elusive set of non-adiabatic particle motions.

### 1.1.1 Van Allen Radiation Belts

Serendipitously discovered during the International Geophysical Year (IGY) with Geiger-Müller tubes aboard the U.S. Explorer I and III satellites, and further explored by subsequent missions that year [*Ratcliffe et al.*, 1960, p.551],<sup>6</sup> the Van Allen radiation belts consist of enhanced fluxes of high-energy charged particles that are trapped by Earth’s magnetic field at equatorially measured distances between 1.2 and 7 Earth radii ( $R_E$ ) from its center and latitudes below  $65^\circ$  [*Walt*, 1994, p.4].<sup>7</sup> These energetic particle fluxes,<sup>8</sup> and the altitudes of their maxima, tend to decrease with increasing particle energy [*Walt*, 1994, p.76],<sup>9</sup> to conserve adiabatic momenta with

---

<sup>6</sup>Perhaps misleadingly titled, the international scientific effort known as IGY spanned an eighteen month period from July 1, 1957 to December 31, 1958. Existence of the radiation belts was suggested and subsequently confirmed by data from an array of satellites launched during the 1958 calendar year, beginning with Explorer I (January 31) [*Ratcliffe et al.*, 1960, p.551].

<sup>7</sup>Even though the Earth is not a perfect sphere, having more mass and thus a wider extent near the equator than the poles [*Tribble*, 2003, p.14] its radius, hereafter symbolized by  $R_E$ , can be approximated as 6,378 km. Unless otherwise noted, all distances normalized to  $R_E$  are measured geocentrically at the equator.

<sup>8</sup>In accordance with the conventions of early particle detectors and unless otherwise specified, all radiation-belt particle fluxes cited herein are omnidirectional, integral fluxes, in units of particles/cm<sup>2</sup>/s. Such a quantity, for particles above a given energy  $E_o$ , is obtained by integrating the differential, directional flux—the number of particles within  $dE$  of energy  $E$  that pass through a unit area perpendicular to a directional angle  $\theta$  within a unit solid angle in one second—over all  $E > E_o$  and all angles  $0 < \theta < \pi$ .

<sup>9</sup>In the context of radiation-belt physics, it is typically assumed that the energies of the relevant particles exceed 100 keV, which easily distinguishes them from the cold background plasma of the plasmasphere whose average energies are below 1 eV (cf. Section A.1.2). However, delineating the former, whose motions are governed solely by the drifts of Section A.2.1.2, from the hot-plasma of the ring current, for which such drifts are commensurate with those imposed by the convective and

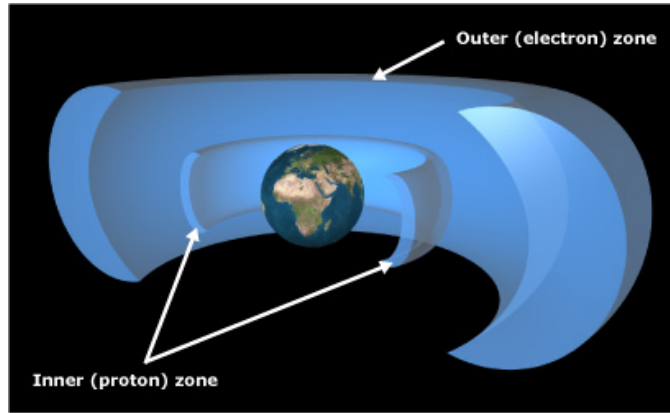


Figure 1.1: Inner and outer zones of Earth’s Van Allen radiation belts. Drawn to scale, the altitudes of these concentric tori reflect those of the maxima in proton and electron flux, respectively. Reproduced *in toto* from [Mazur, 2003].

increasing field strength (cf. Section A.3). Additionally, the populations are not static, constantly responding to the counterbalance of source and loss mechanisms which are in turn subject to interplanetary weather cycles and spontaneous solar phenomena. Although the fluxes of the major constituents,<sup>10</sup> namely protons, electrons, and heavy ions (primarily  $\text{He}^+$  and  $\text{O}^+$ ) [Walt, 1994, p.81],<sup>11</sup> demonstrate diffuse and continuous enhancement patterns [Tascione, 1994, p.51–52], it is customary to divide this region into azimuthally symmetric,<sup>12</sup> discrete toroids known as the inner zone and outer zone, separated by a so-called ‘slot’ region (Figure 1.1) [Walt, 1994, p.75].

#### 1.1.1.1 Inner Zone

The inner zone is composed of both high-energy protons, whose energies range from 100 keV to 500 MeV, averaging 10–50 MeV as shown in Figure 1.2, and electrons from

---

co-rotational electric fields, requires a more rigorous definition that places this boundary near 200 keV [Schulz and Lanzerotti, 1974, p.2–7].

<sup>10</sup>Although it is extremely significant practically and scientifically, even under worst-case conditions “the total mass of the ‘radiation’ material is very small. It may amount to only a few pounds!” [Ratcliffe *et al.*, 1960, p.554].

<sup>11</sup>A heavy ion is defined as a charged atom of any element heavier than helium [Srouer and McGarrity, 1988, p.1458].

<sup>12</sup>This symmetry breaks down over the South Atlantic anomaly, where the offset between the Earth’s magnetic and geographic poles results in weaker local field strengths that produce substantially higher flux levels for a given altitude (cf. Section 1.1.2).

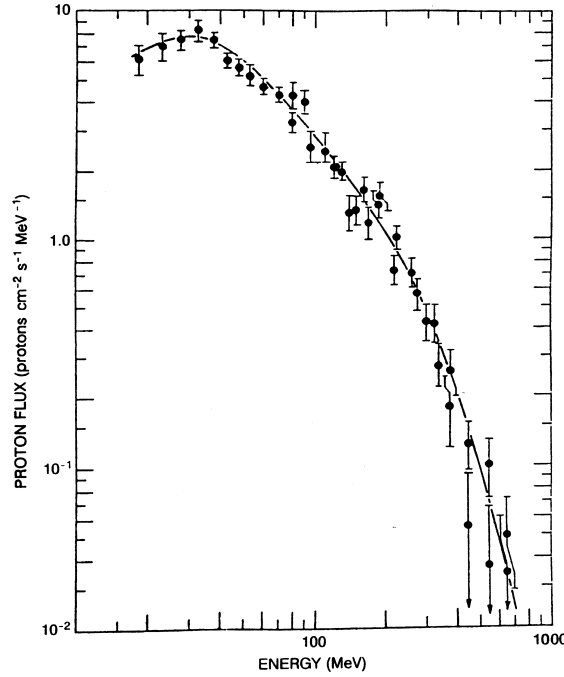


Figure 1.2: Omnidirectional, differential flux spectrum of inner zone protons. Peak fluxes between 10–50 MeV are often used to define zonal center. Reproduced *in toto* from [Walt, 1994, p.78].

100 keV to 3 MeV, averaging 1 MeV [Holmes-Siedle and Adams, 2002, p.20]. These electron populations persist at altitudes from 1.2–2.4  $R_E$ , with the peak concentration of 50-MeV protons, depicted in Figure 1.3 at about 1.5  $R_E$ , generally considered the zonal center [Walt, 1994, p.75].

The topside ionosphere forms a lower boundary below which  $\nu_n$  increases significantly, leading to the removal of these particles through collisions with atmospheric neutrals.<sup>13</sup> But, these same neutral atoms also fuel source mechanisms as they are continually bombarded by galactic cosmic rays (GCRs)—low isotropic fluxes of extremely energetic ( $> 1$  GeV) heavy ions [Holmes-Siedle and Adams, 2002, p.19] described in detail in Section C.1.1.3—which produce secondary, outward radiation in the form of high-energy albedo neutrons [Tascione, 1994, p.53]. Each of these unstable neutrons, whose half-life is just 12 minutes, decays into a proton, electron,

<sup>13</sup>In the absence of such collisions, the particles are geomagnetically trapped, as described in Section A.2.

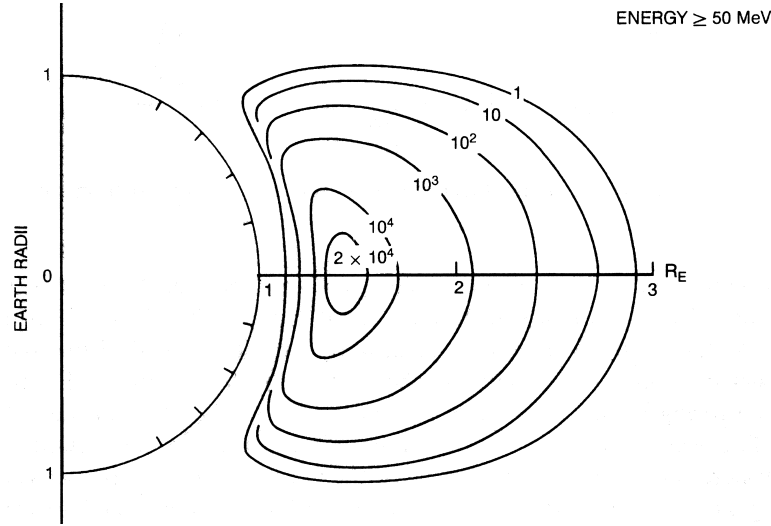


Figure 1.3: Omnidirectional, integrated flux of radiation-belt protons with energy greater than 50 MeV. A cross-section in the meridional plane is obtained by using a dipole model for geomagnetic field and the solar-minimum AP8 model for proton flux. Reproduced *in toto* from [Walt, 1994, p.77].

and neutrino, with the foremost attaining the majority of the momentum. If this spontaneous reaction occurs while the neutron is still in the plasmasphere, its by-products are trapped in the inner zone [Walt, 1994, p.106–108]. This cosmic-ray albedo neutron decay (CRAND) mechanism accounts for the 50-MeV proton fluxes within  $1.5 R_E$ , whereas the source of the lower-energy protons and electrons above  $1.8 R_E$  is radial diffusion from higher altitudes during geomagnetic disturbances [Tascione, 1994, p.54], as discussed in Section A.3. Due to the balance of these source and loss processes, and the isolation afforded at lower altitudes, the inner zone populations are relatively stable, with plasma processes remaining steady for periods of weeks to months, even in the presence of solar and geomagnetic activity such as solar flares and magnetospheric substorms [Lyons, 1979, p.142].

### 1.1.1.2 Outer Zone

By contrast, the particles trapped in the outer zone are very sensitive to such disturbances, since they extend into the outer magnetosphere, occupying the region



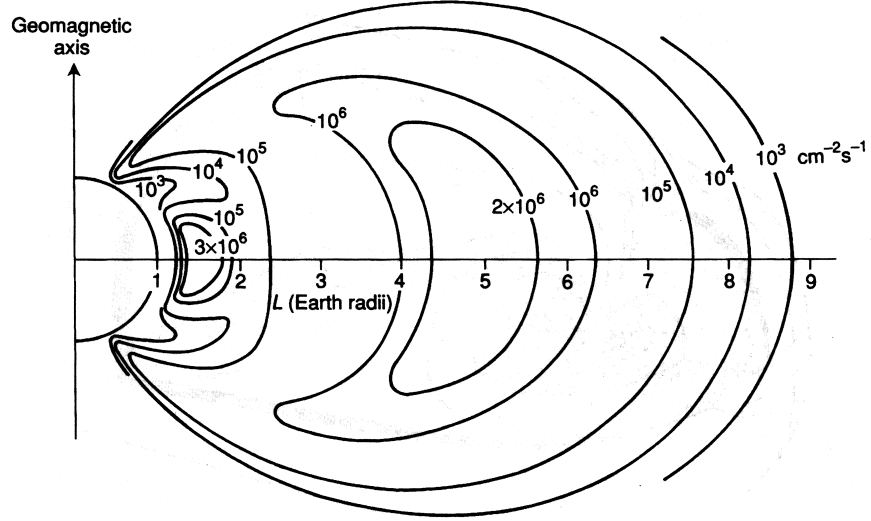


Figure 1.4: Omnidirectional, integrated flux of radiation-belt electrons with energy greater than 1 MeV. A cross-section in meridional plane is obtained using a dipole model for geomagnetic field and the solar-minimum AE8 model for electron flux. Reproduced *in toto* from [Holmes-Siedle and Adams, 2002, p.20].

from 2.8 to 7  $R_E$  [Holmes-Siedle and Adams, 2002, p.18], where fractional changes in the weaker geomagnetic field are more pronounced. For reasons described in Section A.2.1, this outer zone field is unfavorable for proton trapping, ceding the bulk of the particle composition in this region to electrons with energies from 100 keV to 10 MeV, averaging 1 MeV [Holmes-Siedle and Adams, 2002, p.18], and in small part to heavy ions,<sup>14</sup> with energies from 1–10 MeV [Walt, 1994, p.81]. As shown in Figure 1.4, the peak in the 1-MeV electron population from 4–5  $R_E$  defines the center of an outer zone that envelops the entire inner zone described above and is capped with high-flux cusps near the poles known as the ‘polar horns’ [Holmes-Siedle and Adams, 2002, p.18].

These outer zone electrons are injected from the ionosphere into the polar regions by the Birkeland currents [Birkeland, 1908], and from the solar wind into the magnetotail during substorms, with the latter accounting for the strong correlation of their aforementioned variability with the 11-year solar cycle [Tascione, 1994, p.54].

<sup>14</sup>The heavy ions, whose fluxes peak around 3  $R_E$ , only occupy equatorial latitudes [Walt, 1994, p.81].

Regardless of their source, the electrons are ultimately accelerated from tens of keV to much higher energies by means of Very Low Frequency (VLF) whistler-mode plasma waves,<sup>15</sup> through abstruse interactions that are at the heart of this research [*Horne, 2002*]. However, such wave-particle interactions are also capable of reducing the electron flux levels through pitch-angle scattering described in Section A.3.3, and this loss mechanism not only equalizes the above sources in the outer zone, but is responsible for the formation of the slot region between 2 and 2.5  $R_E$  (cf. Figure 1.5) [*Walt, 1994*, p.80]. The means by which this pitch angle scattering dominates the loss rates in the slot region,<sup>16</sup> particularly for higher energy electrons, also remains unresolved at the present time [*Horne, 2002*].

Before addressing these wave-particle interactions at play in the dynamics of the Van Allen belt, it is necessary to further elucidate the role of the Earth's magnetic field in trapping these particles in the first place.

## 1.1.2 The Geomagnetic Field

Although severely distorted near the magnetopause and magnetotail by the magnetic and plasma pressure of the solar wind, as explained in Section A.1 and highlighted by their ‘bullet’ shape at the boundary of Figure 1.6, the terrestrial magnetic field lines in the vicinity of the radiation belts resemble those of a tilted, off-axis dipole. In total, this field is composed of contributions from a variety of geophysical current systems, including all of four of those discussed at the conclusion of Section A.1.2, whose fluctuations in response to magnetospheric disturbances result in rapid, but minor, transient variations in field strength measured on the Earth's surface [*Tascione, 1994*, p.43].<sup>17</sup> But, the self-exciting dynamo at the Earth's core is responsible for bulk of the

---

<sup>15</sup>Strictly connoted, the VLF portion of the electromagnetic spectrum covers waves whose frequency(wavelength) is between 3–30 kHz(10–100 km). However, since its usage in this document is restricted to describing plasma waves, the definition of VLF is expanded to include the entire space of such waves under study, whose spectrum can stretch from 100 Hz to 1 MHz.

<sup>16</sup>When participating in VLF wave-particle interactions, a wave of given energy density has a greater impact on the momentum of an electron than a proton, since the latter is substantially lighter. Hence, the ‘slot’ feature is only observed in the electron population.

<sup>17</sup>Though responsible for non-trivial distortions in the field measured at the Earth's surface, static sources such as permanently magnetized rock and mineral deposits [*Walt, 1994*, p.26] are insignificant

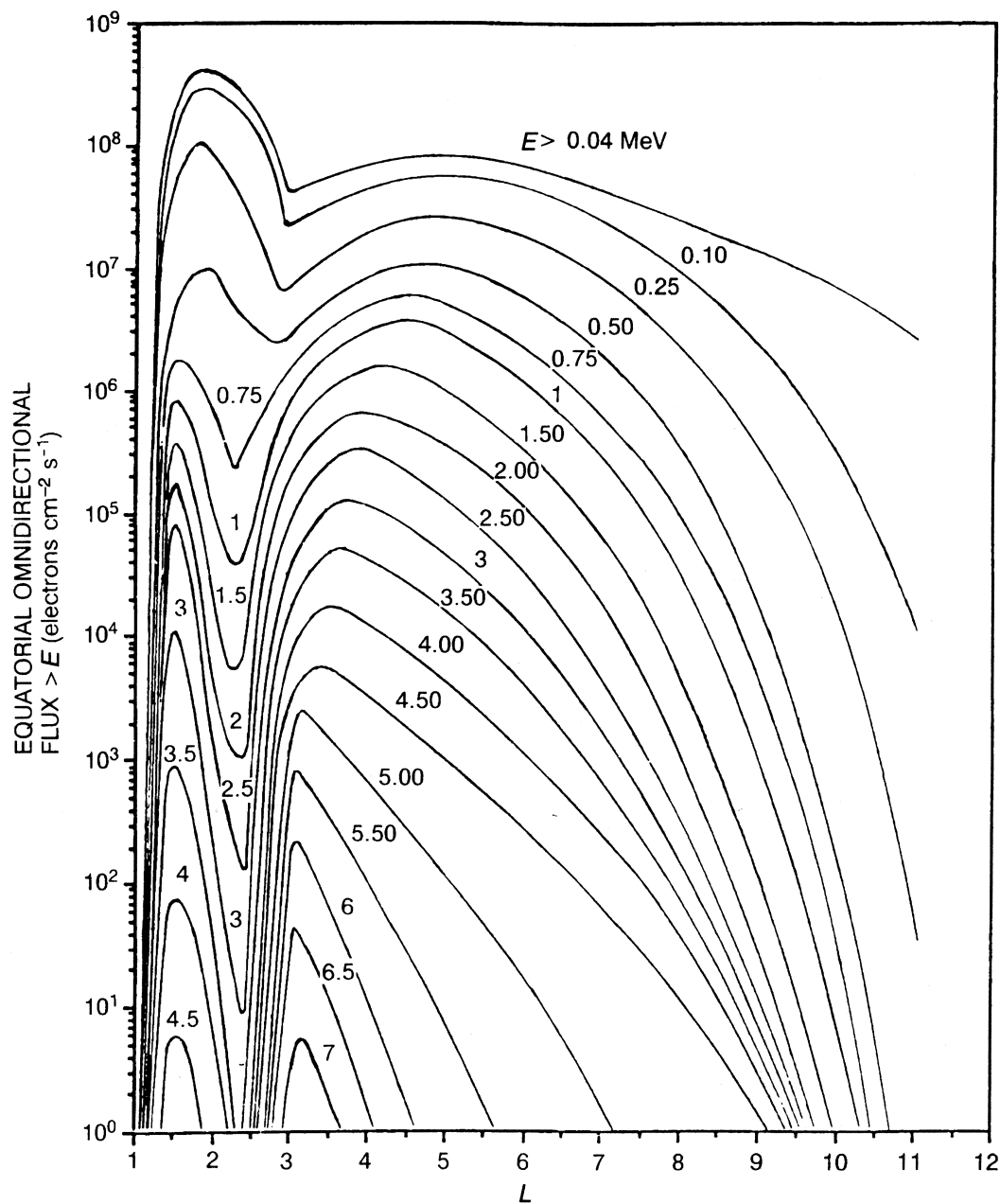


Figure 1.5: Equatorial, omnidirectional, integrated flux of outer zone electrons, clearly evidencing the slot region for all energies between  $2 < L < 2.5$ . Reproduced *in toto* from [Walt, 1994, p.80].

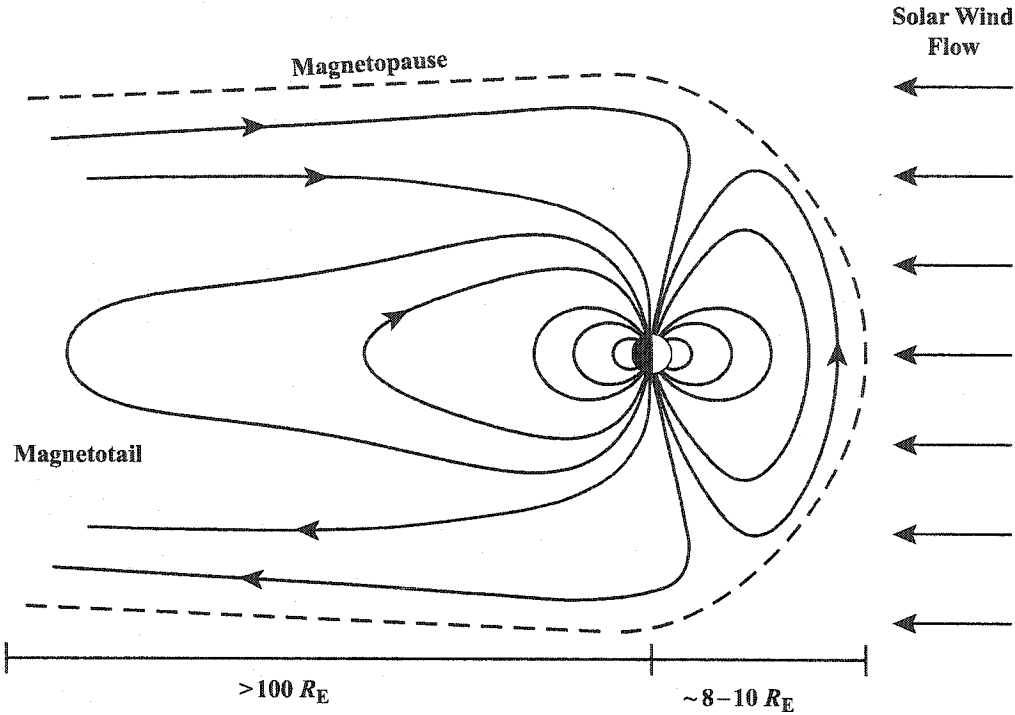


Figure 1.6: Simplified depiction of distortion in the Earth's magnetic field due to the solar wind for a noon-midnight meridional cross-section. Reproduced *in toto* from [Spasojević, 2003, p.3].

field strength [Walt, 1994, p.26], and causes deviations on longer time-scales, such as: year-to-year, or secular, variations observed for centuries; the gradual westward drift of the magnetic poles, as well as their reversal every  $10^5$ – $10^6$  years [Tascione, 1994, p.45]; and a documented waning of the geomagnetic field that, assuming continuation of the trend, projects its quenching in 2000–3000 years [Walt, 1994, p.25].

#### 1.1.2.1 Dipole Model

Although these trends remain enigmatic, as the energy source feeding this core dynamo and its likely connection to planetary rotation are still poorly understood [Tascione, 1994, p.45], it is widely accepted that the circular convection of hot, conducting fluids around the Earth's core generates a self-reinforcing magnetic field

---

at the altitudes considered here.

that sustains the process while simultaneously converting the underlying mechanical energy into that stored in its field configuration. Since these circulating metallic liquids constitute an effective current, they produce a tangential field at Earth's equator,  $\mathbf{B}_0$ , given classically by

$$\mathbf{B}_0 = \frac{\mu_0 I}{4R_E} \left( \frac{a}{R_E} \right)^2 \hat{\mathbf{z}} \quad (1.3)$$

where  $-\hat{\mathbf{z}}$  is in the direction perpendicular to the loop that satisfies the right-hand rule,<sup>18</sup> whereas  $a$  and  $I$  are the assumed radius and amperage of this current, respectively. This simple model allows the magnetic dipole moment,  $\boldsymbol{\mu}_m$ , to be expressed in terms of  $B_0$  (which has been measured at approximately 30  $\mu\text{T}$  [[Tribble, 2003](#), p.12]) as

$$\boldsymbol{\mu}_m = I\mathbf{S} = -\frac{4\pi}{\mu_0} R_E^3 \mathbf{B}_0 = -\frac{4\pi}{\mu_0} M_E \hat{\mathbf{z}} \quad (1.4)$$

Contrasted with the vector quantity  $\boldsymbol{\mu}_m$ , whose magnitude  $\mu_m$  is in units of A-m<sup>2</sup>,  $M_E$  is a scalar quantity often cited as the Earth's magnetic moment and numerically equal to  $B_0 R_E^3$  or  $8.05 \times 10^{15} \text{ T-m}^3$  [[Tascione, 1994](#), p.43].<sup>19</sup>

Deriving a complete description of the Earth's magnetic field from  $\boldsymbol{\mu}_m$  involves the solution of Laplace's equation, which places a condition on the magnetic scalar potential,  $\psi$ , namely  $\nabla^2 \psi = 0$ . Such solutions take the form of a multipole expansion which, though vital in computer modeling, contains upwards of 48 terms, most of which decay rapidly with geocentric distance,  $r$ , going as  $1/r^{(n+1)}$  for terms of higher order  $n$  [[Walt, 1994](#), p.29]. Thus, for the altitudes under consideration it is sufficient to consider only the first-order, or dipole, term in the scalar potential expansion, namely

$$\psi = \frac{\mu_0 \boldsymbol{\mu}_m \cdot \mathbf{r}}{4\pi r^3} = -\frac{M_E}{r^2} \cos \theta \quad (1.5)$$

---

<sup>18</sup>At present, the terrestrial field lines are directed toward(away from) the Earth's surface in the northern(southern) hemisphere, in contrast to the orientation canonically applied to the designation of the north(south) pole of a bar magnet [[Spasojević, 2003](#), p.3]. Thus, the direction of the tangential field at the equator, given as  $+\hat{\mathbf{z}}$  in (1.3), points northward.

<sup>19</sup>To satisfy dimensional analysis, the quantity  $M_E$ , or simply  $M$  in [[Tascione, 1994](#); [Tribble, 2003](#)] must be related to  $\mu_m$ , called  $\mathcal{M}$  in [[Walt, 1994](#)], by  $4\pi/\mu_0$ , as shown in (1.4), rather than its reciprocal, as stated in [[Walt, 1994](#), p.30].

where  $\theta$  is defined as the angle between  $\hat{\mathbf{z}}$  and the radial location of interest. Recall that, according to Ampere's law, under steady-state conditions and in the absence of extrinsic currents,  $\nabla \times \mathbf{B} = 0$ . Since vector identities reveal that any zero-curl field can be expressed as the gradient of a scalar quantity, this condition implies that the dipole field can be obtained from the approximate scalar magnetic potential in (1.5) through [Walt, 1994, p.29]:<sup>20</sup>

$$\mathbf{B} = -\nabla\psi \quad (1.6)$$

Formulating the gradient for spherical coordinates under the assumption of azimuthal symmetry ( $\partial\psi/\partial\phi=0$ ) and with the relationships between  $\hat{\mathbf{z}}$ ,  $\mathbf{r}$ , and  $\theta$  noted above, the components of  $\mathbf{B}$  in (1.6) become [Tribble, 2003, p.11]:

$$B_r = -\frac{\partial\psi}{\partial r} = -\frac{2M_E}{r^3} \cos\theta \quad (1.7a)$$

$$B_\theta = -\frac{1}{r} \frac{\partial\psi}{\partial\theta} = -\frac{M_E}{r^3} \sin\theta \quad (1.7b)$$

$$B = \frac{M_E}{r^3} \sqrt{1 + 3 \cos^2\theta} \quad (1.7c)$$

Note that the total dipole field in (1.7c) falls off as  $1/r^3$  for a given angle and, at a given radius, increases when moving toward the poles, where it reaches a value double that at the equatorial surface,  $2B_0$ , or approximately  $60 \mu\text{T}$ .

### 1.1.2.2 Geomagnetic Coordinates

The preceding description of the geomagnetic field is relative to the  $\hat{\mathbf{z}}$ -axis running perpendicular to the plane of the dynamo currents. This dipole axis is not aligned with the Earth's axis of rotation, but rather is displaced by an angle of  $11.3^\circ$  and offset about 250 miles toward the western Pacific Ocean [Tascione, 1994, p.43]. The resulting geomagnetic poles lie near  $78.5^\circ\text{S}$ – $111^\circ\text{E}$  (near Vostok Station, Antarctica)

---

<sup>20</sup>According to Maxwell's equations, the relation in (1.6) should be expressed as  $B = \mu_0 H = -\mu_0 \nabla\psi$ . But, the permeability constant has already been incorporated into the definition of the scalar magnetic potential in (1.5).

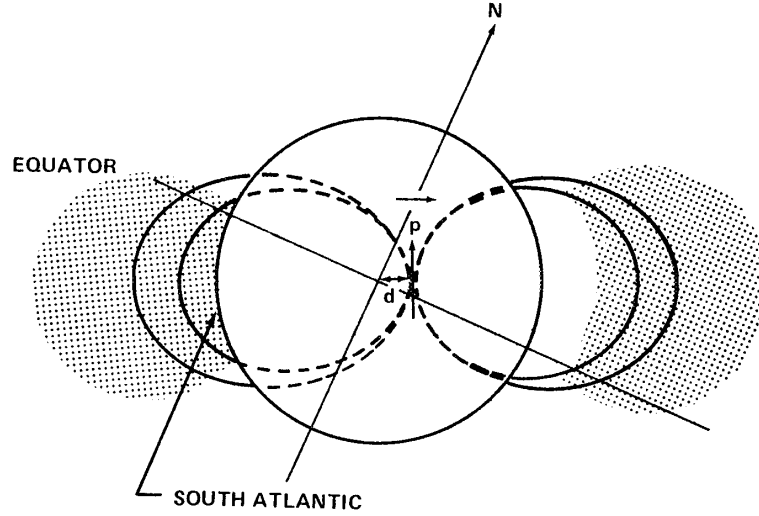


Figure 1.7: Schematic depiction of Earth's offset dipole field highlighting the South Atlantic Anomaly (SAA), above which the inner radiation belt reaches its minimum altitude (200–300 km) [Stassinopoulos and Raymond, 1988, p.1429]. Reproduced *in toto* from [West et al., 1977, p.2-22].

and 78.5°N–69°W (near Thule, Greenland),<sup>21</sup> giving rise to the field asymmetries depicted in Figure 1.7 [Tascione, 1994, p.43]. Note the weaker fields in the South Atlantic, as referenced in Section A.2.2.2 and Footnote 12 in conjunction with the lower altitudes to which radiation-belt fluxes extend above that region.

Since forthcoming analyses of wave behavior, radiation exposure, and antenna impedance exhibit high sensitivity to locality within this oblique magnetic field, it is convenient to introduce a coordinate system that is relative to its field lines, rather than Earth's geographic directions. In a meridional plane, each field line is described by the slope of the dipole field at the corresponding location, given by the ratio of (1.7b) to (1.7a) as

$$\frac{B_\theta}{B_r} = \frac{r \partial \theta}{\partial r} = \frac{\tan \theta}{2} \quad (1.8)$$

<sup>21</sup>The geomagnetic poles should not be confused with the Earth's true magnetic poles. The former represent where the field lines would be orthogonal to the Earth's surface for the simplified dipole model in use here, and therefore are antipodal; the latter mark where the field lines are actually orthogonal to the surface and, given the nonidealities discussed previously, are not antipodal [Tascione, 1994, p.47].

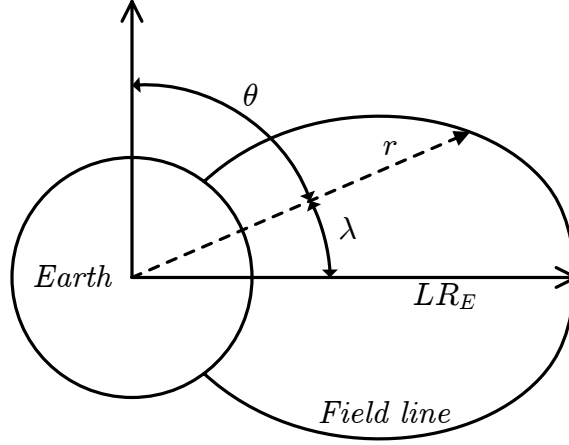


Figure 1.8: Geomagnetic coordinate system for dipole field model. Any point  $\mathbf{r}$  can be equivalently parameterized by  $B$  and  $\theta$  (using (1.7c)) or  $L$  and  $\theta$  (using (1.9)). After [Walt, 1994, p.29].

Integrating both sides of (1.8) parameterizes the field line definition as [Tribble, 2003, p.12]:

$$r = LR_E \sin^2 \theta \quad (1.9)$$

where the  $L$  parameter corresponds to the geocentric distance at which the field line crosses the dipole equator. Thus, the coordinate system for the offset, titled dipole model of the scalar potential has been reduced to simply (1.7c) and (1.9), which employ the parameters  $B$  and  $L$ , respectively, to describe a field strength and a field line trajectory at each point in space. In some cases, it also proves useful to refer to locations relative to the current-loop plane of this model, where the  $B$  reaches  $B_0$ , its minimum field strength on each field line, known as the geomagnetic equator, and to the angle  $\theta$ , which is measured eastward from the geomagnetic north pole and known as the geomagnetic (or invariant) colatitude.<sup>22</sup> The relationships between these geomagnetic coordinates are summarized in Figure 1.8.

<sup>22</sup>Geomagnetic colatitude,  $\theta$ , and latitude,  $\lambda$ , are related through  $90^\circ - \theta = \lambda$ , with the former measured eastward from the dipole axis and the latter northward from the equator.



### 1.1.3 Plasma Waves

Though loosely defined, the term plasma wave is commonly “used to denote all waves which are generated in a plasma or which have their characteristics significantly modified by the presence of the plasma” [Shawhan, 1979, p.213]. The bandwidth and spectral density of the electric and magnetic fields associated with the most prevalent magnetospheric plasma waves are depicted in the cartoons of Figure 1.9 and Figure 1.10, respectively.<sup>23</sup> In addition to these properties, the categorization of these wave phenomena naturally incorporates: the direction of their wave vector relative to the Earth’s magnetic field, with the wave normal angle,  $\theta_k$ , and the parallel and perpendicular components of the wave vector,<sup>24</sup>  $k_{\parallel}$  and  $k_{\perp}$ , being analogous to their particle velocity counterparts,  $\alpha_v$ ,  $v_{\parallel}$ , and  $v_{\perp}$ ; their polarization, which defines the ratios of the various wave components, including the rotational sense of the wave electric field perceived by a receiver as either right-handed (clockwise) or left-handed (counter-clockwise);<sup>25</sup> and, the orientation of the electromagnetic oscillations relative to  $\mathbf{k}$ , either transverse (perpendicular to  $\mathbf{k}$ ) or longitudinal (parallel to  $\mathbf{k}$ ).

---

<sup>23</sup>Since the quantities plotted in Figures 1.9 and 1.10 are simply the squared strengths of the underlying wave fields, they are spectral densities not power spectral densities (PSD); obtaining the latter from the former requires multiplication by a constant factor. Since, electrical engineers are most comfortable expressing PSD in normalized units of  $V^2/\text{Hz}$  rather than true units (e.g.,  $W/\text{Hz}$ ) those factors are  $L_{\text{eff}}^2$  and  $v_p^2 L_{\text{eff}}^2$ , respectively, for the pertinent case of a plane wave incident upon an antenna of effective length,  $L_{\text{eff}}$  (cf. Section 3.1.1.1).

<sup>24</sup>In the context of the electromagnetic plane waves under consideration, the wave vector symbolized by  $\mathbf{k}$  is at all times orthogonal to uniform phase fronts of the wave (and, thus is in the same direction as the wave phase velocity described in Section 1.1.3.2) with magnitude equal to the angular wavenumber  $k=2\pi/\lambda$ .

<sup>25</sup>By convention, in a magnetized plasma the receiver is always located at the terminus of the ambient field line, not that of the wave trajectory. In this way, the wave polarization is relative to  $B$  but independent of the direction of propagation along it, just as is the case for gyrating particles [Tsurutani and Lakhina, 1997, p.495]. But, confusion arises because looking from the field line terminus rather than its origin violates the ‘right-hand rule’ that is applied to particle motion and dictates that, with one’s thumb in the direction of  $B$ , a right-handed wave vector rotation is *counter*-clockwise. Thus, the handedness of particle gyration(wave polarization) is obtained by curling one’s fingers in the direction of rotation of the position(electric field) vector such that the thumb points parallel(anti-parallel) to  $B$ .

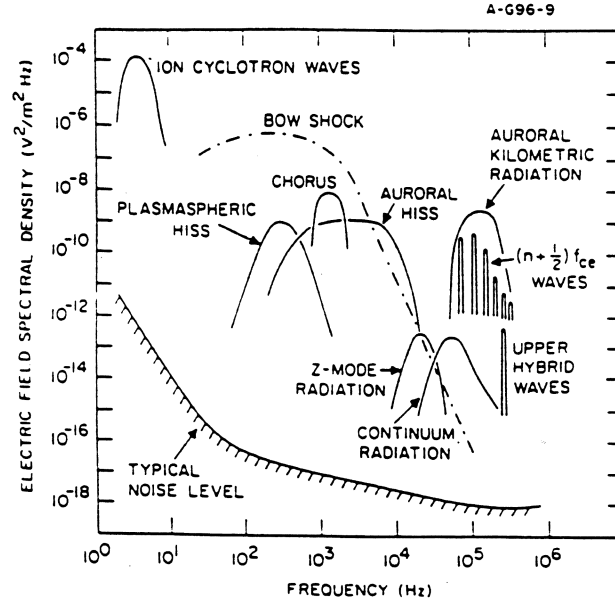


Figure 1.9: Electric field spectral density of representative plasma wave phenomena. Reproduced *in toto* from [Gurnett, 1998, p.123].

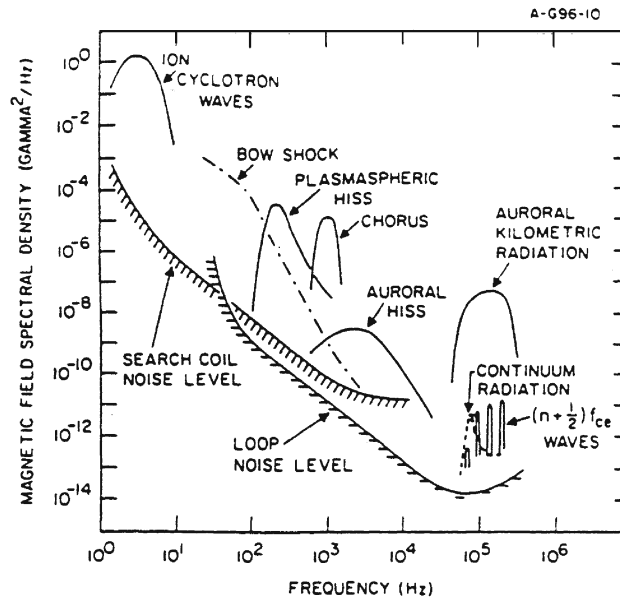


Figure 1.10: Magnetic field spectral density of representative plasma wave phenomena ( $1 \gamma = 1 \text{ nT}$ ). Reproduced *in toto* from [Gurnett, 1998, p.123].

### 1.1.3.1 Theories and Models

As noted when defined,  $\omega_{pe}$  represents the maximum rate which the plasma can behave collectively in response to perturbations—oscillations at  $\omega > \omega_{pe}$  behave as though in free space and, without time for the internal fields associated with the plasma constituents to be established, these constituents respond to the imposed fields according to single-particle motion such as that analyzed in Section A.2.1 [Shawhan, 1979, p.213]. However, for  $\omega < \omega_{pe}$ , forcing fields can, under certain conditions, propagate in the plasma subject to the influences of its collective behavior. To assess these effects on wave properties such as velocity, amplitude, and polarization, and to determine the requirements for propagation, it is necessary, for each plasma constituency  $x$ , to consider the entire population using a distribution function  $f_x(r, v, t)$ . This distribution function completely describes the volumetric density of the species in six-dimensional phase space,<sup>26</sup> any infinitesimal element of which,  $d^3r d^3v$ , is known to be incompressible as it moves along a dynamic phase space trajectory (Liouville's theorem) [Schulz and Lanzerotti, 1974, p.14–16]. In other words, from the perspective of a representative particle moving through this space, the density in its immediate vicinity appears constant in time [Bittencourt, 1995, p.131].<sup>27</sup> This conservation is formally stated by the Vlasov equation, equivalently

---

<sup>26</sup>Since field effects should appear in the description of the waves, not the particles, it is convenient to transform  $f_x$  from the six-dimensional phase space of Section A.2.1, based on canonical momentum ( $\mathbf{p}$ ) and its conjugate position ( $\mathbf{q}$ ), to non-canonical coordinates of kinetic momentum ( $m\mathbf{v}$ ) and position ( $\mathbf{r}$ ) that eliminate  $\mathbf{A}$ . It can be shown that this transformation, given by the set of equations (A.15) and  $\mathbf{q}=\mathbf{r}$ , has unit Jacobian so that, when restricted to the non-relativistic case,  $f(\mathbf{q}, \mathbf{p}, t) = f(\mathbf{r}, \mathbf{v}, t)$  [Schulz and Lanzerotti, 1974, p.15]

<sup>27</sup>This statement of Liouville's theorem, and the successive derivations, presume collisional terms can be neglected. Although not true for all wave domains, this formulation holds for those under consideration and is preferred for its clarity since techniques for incorporating short-range collisions through diffusive models [Bittencourt, 1995, p.589] are beyond the scope of this work.

expressed as:

$$\frac{Df_x}{Dt} = 0 \quad (1.10a)$$

$$\frac{\partial f_x}{\partial t} + \mathbf{v} \cdot \nabla_{\mathbf{r}} f_x + \mathbf{a} \cdot \nabla_{\mathbf{v}} f_x = 0 \quad (1.10b)$$

$$\frac{\partial f_x}{\partial t} + \mathbf{v} \cdot \nabla_{\mathbf{r}} f_x + \frac{Q_x}{m_x} [\mathbf{E} + \mathbf{v} \times \mathbf{B}] \cdot \nabla_{\mathbf{v}} f_x = 0 \quad (1.10c)$$

where the total derivative in phase space, often termed the 'convective' derivative  $D/Dt$  [Bortnik, 2004, p.24], accounts for changes in the local plasma parameters even when  $\partial f_x / \partial t = 0$ , due to motion of the the local volume element along its six gradients. Note that this equation explicitly accounts for the effects of both the externally applied wave fields and internal fields resulting from the motion of the particles themselves, jointly subsumed into the self-consistent  $\mathbf{E}$  and  $\mathbf{B}$  fields, thereby handling long-range Coulomb interactions [Bittencourt, 1995, p.136].

When coupled with Maxwell's equations for these fields, the Vlasov (or Boltzmann) equation yields a complete description of the plasma wave behavior under kinetic theory. However, for the purposes of wave classification it is neither necessary nor straightforward to solve for the complete particle distribution at each point in time and space. Instead, it is sufficient to invoke a simplified model which treats the plasma as a fluid characterized by macroscopic properties that are related to the velocity moments of the distribution.<sup>28</sup> Corresponding moments of the Vlasov equation, known as transport equations, then define the relationships which govern these velocity-averaged properties, according to Table 1.1 [Bittencourt, 1995, p.157,195–209]. Since each higher moment introduces a new macroscopic quantity, it is not possible to solve the system of equations in Table 1.1 without truncating the hierarchy and introducing an approximate, physically based definition for the highest remaining

---

<sup>28</sup>For example, the average fluid velocity,  $\mathbf{u}_x$ , is related to the first moment of  $f_x$  through

$$\mathbf{u}_x(\mathbf{r}, t) = \frac{1}{N_x(\mathbf{r}, t)} \int_{\mathbf{v}} \mathbf{v} f_x(\mathbf{r}, \mathbf{v}, t) d^3v$$

The corresponding transport equation, known as the momentum equation, results from multiplying both sides of (1.10) by  $\mathbf{v}$  and performing the same integral over all of velocity space [Bittencourt, 1995, p.142].

Moment	Moment of $f_x(\mathbf{r}, \mathbf{v}, t)$	Moment of (1.10)
	<i>Macroscopic property<sup>a</sup></i>	<i>Transport equation (quantity)</i>
0 <sup>th</sup> order	$N_x(\mathbf{r}, t) = \int_v f_x(\mathbf{r}, \mathbf{v}, t) d^3v$ $N_x$ : number density	$\frac{\partial n_x}{\partial t} + \nabla \cdot (N_x \mathbf{u}_x) = 0$ <i>conservation of mass (continuity)</i>
1 <sup>st</sup> order	$\mathbf{u}_{x,i}(\mathbf{r}, t) = \frac{1}{N_x(\mathbf{r}, t)} \int_v v_i f_x(\mathbf{r}, \mathbf{v}, t) d^3v$ $\mathbf{u}_x$ : mean flow velocity	$m_x N_x \frac{D\mathbf{u}_x}{Dt} - N_x Q_x (\mathbf{E} + \mathbf{u}_x \times \mathbf{B}) - m_x N_x \mathbf{g} + \nabla \cdot \mathbf{P}_x = 0$ <i>conservation of momentum (motion)<sup>b</sup></i>
2 <sup>nd</sup> order	$\Pi_{x,ij}(\mathbf{r}, t) = m_x \int_v v_i v_j f_x(\mathbf{r}, \mathbf{v}, t) d^3v$ $\mathbf{P}_x = \Pi_x _{u=0}$ : kinetic pressure flow <sup>c</sup>	$\frac{3}{2} \frac{D P_x}{Dt} + \frac{3 P_x}{2} \nabla \cdot \mathbf{u}_x + (\mathbf{P}_x \cdot \nabla) \cdot \mathbf{u}_x + \nabla \cdot \mathbf{q}_x = 0$ <i>conservation of energy (energy)<sup>d</sup></i>
3 <sup>rd</sup> order	$\chi_{x,ijk}(\mathbf{r}, t) = m_x \int_v v_i v_j v_k f_x(\mathbf{r}, \mathbf{v}, t) d^3v$ $\mathbf{Q}_x = \chi_x _{u=0}$ : thermal energy flow <sup>e</sup>	$n/a$

<sup>a</sup>  $i, j$ , and  $k$  are used as dimensional indices for elements of vectors and dyads<sup>b</sup> In contrast to (1.10c), which only accounts for the Lorentz force, here the acceleration due to gravity ( $\mathbf{g}$ ) is also included.<sup>c</sup> The momentum flow dyad  $\Pi_x$  accounts for transport due to both particle thermal velocity ( $\mathbf{v}$ ) and average fluid velocity ( $\mathbf{u}_x$ ); the kinetic pressure dyad  $\mathbf{P}_x$ , only the former.<sup>d</sup> Each element of the heat flow vector  $\mathbf{q}_x$  is the sum of the diagonal elements of the corresponding sheet of the heat flow triad  $\mathbf{Q}_x$ ; that is,  $q_{x,i} = \frac{1}{2} (Q_{x,11i} + Q_{x,22i} + Q_{x,33i})$ .<sup>e</sup> The energy flux triad  $\chi_x$  accounts for transport due to both particle thermal velocity ( $\mathbf{v}$ ) and average fluid velocity ( $\mathbf{u}_x$ ); the heat flow triad  $\mathbf{Q}_x$ , only the former.

Table 1.1: Macroscopic properties and transport equations for fluid theory.

moment of  $f_x$ . Coupled with the necessary subset of Maxwell's equations and the transport equations, this simplified moment definition, or closure relation, yields a complete set of hydrodynamic equations that can be solved for the macroscopic plasma parameters and self-consistent fields. The description of plasma waves has been apportioned into the following subsections according to the closure relation that is necessary to arrive at the corresponding solutions.

In the plasmasphere, and thus much of the radiation belts, it is sufficient to use the closure relation for the ‘cold’ plasma model,<sup>29</sup> in which  $f_x(\mathbf{r}, \mathbf{v}, t) = \delta(\mathbf{v} - \mathbf{u}(\mathbf{r}, t))$ , and therefore  $\mathbf{P}_x \rightarrow 0$ . This assumption is tantamount to assuming  $T_e = T_i = 0$ , thereby condensing the distribution of thermal velocities for each species into a delta function and arriving at a so-called magnetonic formulation that governs the electromagnetic waves to be discussed in Section 1.1.3.2 [Bittencourt, 1995, p.210].

However, for the propagating electrostatic modes of Section 1.1.3.3 to exist, it is necessary to account for finite particle temperatures by using a ‘warm’ plasma model that incorporates all three transport equations from Table 1.1, along with a closure relation that assumes no thermal conductivity or viscosity ( $\mathbf{Q}_x \rightarrow 0$ ) and isotropic pressure ( $\nabla \cdot \mathbf{P}_x \rightarrow \nabla P_x$ ) [Bittencourt, 1995, p.212]. This assumption reduces the conservation of energy equation to the adiabatic energy equation of thermodynamics<sup>30</sup>

$$P_x (m_x N_x)^{-\gamma_a} = \text{constant} \quad (1.11)$$

which is why this warm plasma model is often termed the adiabatic approximation.

Finally, if the populations of all the plasma species are considered as a whole, that is  $f = \sum f_x$ , the resulting conducting fluid reveals unique wave behavior in

---

<sup>29</sup>Recall that the density of hot particles in the radiation belts is quite low, representing an “alien population” [Ratcliffe *et al.*, 1960, p.554] interspersed in an otherwise cold plasmaspheric plasma. It is this latter, described in Section A.1.2, that governs wave behavior [Bortnik, 2004, p.44] and can be treated mathematically as cold since, for  $2 < L < 3$ , the background plasma exhibits  $T_e \simeq 2000$  K [Chevalier, 2007, p.20].

<sup>30</sup>In contrast to its use in Section A.2.2, here the term *adiabatic* inherits its meaning from thermodynamics, wherein it describes a process which changes the pressure or volume of a fluid without any heat transfer. In that case, the product of its pressure ( $P$ ) and volume ( $\mathcal{V}$ ) is constant according to  $P\mathcal{V}^{\gamma_a} = \text{constant}$ , where the adiabatic index,  $\gamma_a$ , is related to the number of molecular degrees of freedom (for a plasma composed of monoatomic ions, its value is 5/3).

cases where time variations are slow or collisions are dominant, and the net plasma is suprathermal, or nearly cold [Bittencourt, 1995, p.234–235]. Such conditions, wherein the first two transport equations can be closed through (1.11) because slow time scales and/or collisions permit  $f$  to reach a Maxwellian equilibrium [Bittencourt, 1995, p.209], beget the magnetohydrodynamic (MHD) waves enumerated in Section 1.1.3.4.

### 1.1.3.2 Electromagnetic Waves

Under the magnetoionic closure relation, there exist a broad set of solutions to the wave equation that can propagate as electromagnetic plane waves depending upon the wave normal angle. In general, waves with  $\theta_k$  near  $0^\circ(90^\circ)$  tend to be circularly(linearly) polarized, with their magnetic(electric) field carrying the majority of the energy [Shawhan, 1979, p.224]. For the extreme cases of parallel ( $\theta_k = 0^\circ$ ) and perpendicular ( $\theta_k = 90^\circ$ ) propagation, into which any oblique wave can be decomposed, Figure 1.11 categorizes the allowable electromagnetic (and, parenthetically, electrostatic) modes for all the waves of Figure 1.9 in terms of their refractive index. Represented by  $n_v$ , where<sup>31</sup> [Shawhan, 1979, p.224]

$$n_v = \frac{c}{v_p} = \frac{ck}{\omega} \quad (1.12)$$

the refractive index indirectly measures phase velocity—the propagation speed for any phase of the wave at a particular frequency  $\omega$  and  $k$ , given by  $v_p = \omega/k$ .<sup>32</sup>

In free space,  $n_v = 1$ , but a magnetized plasma is a dispersive medium, in which the dependence of  $n_v$  on  $\omega$  can be complicated, so that waves at different frequencies may travel at different phase and group velocities, sometimes exhibiting maxima or minima as a function of frequency. For a white tone in the audio bandwidth, this dispersion of the frequency components in the wave packet causes distant receivers to hear a ‘whistling’ tone. Of particular relevance to this work are the right-hand(left-hand) circularly polarized modes permitted below the electron(ion) gyrofrequency in

<sup>31</sup>As usual,  $c$  represents the vacuum speed of light ( $\sim 3 \times 10^8$  m/s).

<sup>32</sup>Phase velocity is traditionally contrasted with group velocity—the rate at which the wave amplitude or envelope, and thus its information content, propagates through space as given by  $v_g = \partial\omega/\partial k$ .

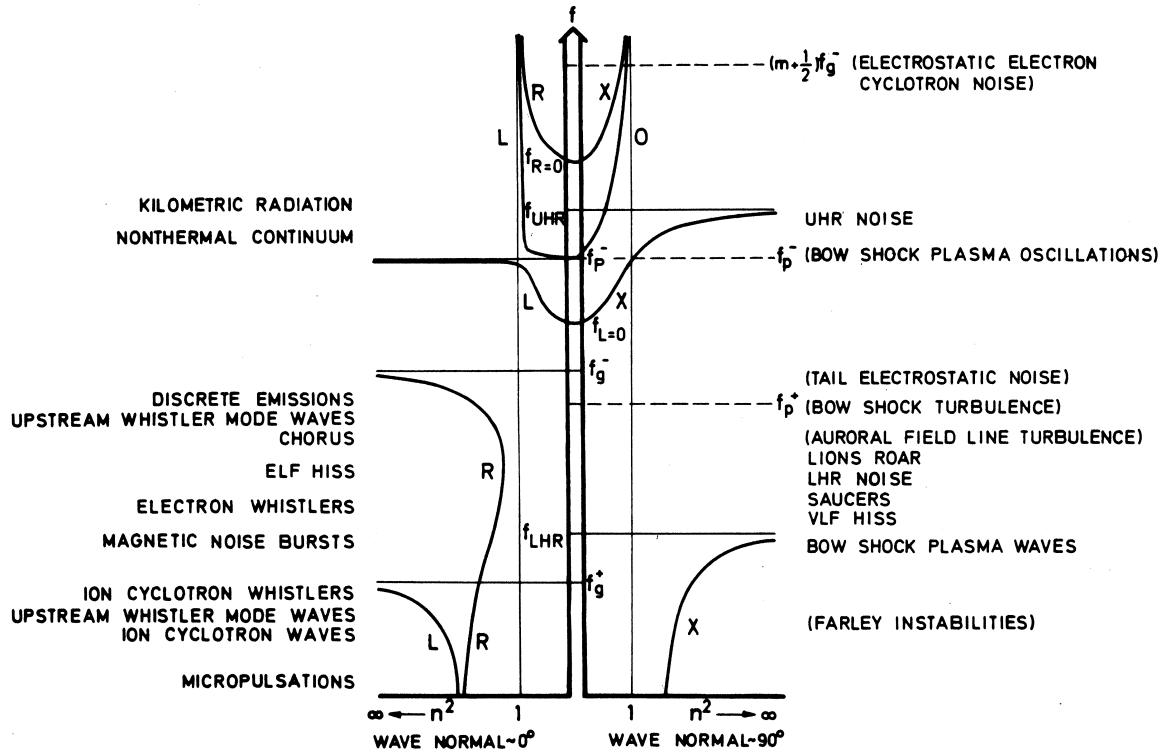


Figure 1.11: Refractive index versus frequency for parallel and perpendicular plasma wave modes. Polarity denoted by  $L$  (left-hand),  $R$  (right-hand),  $O$  (ordinary), and  $X$  (extraordinary). Electrostatic modes in parentheses. Reproduced *in toto* from [Shawhan, 1979, p.225].

Figure 1.11 that are subject to such dispersion and known as electron(ion) whistlers.<sup>33</sup> Their significance derives both from Figure 1.12, which maps the waves of Figure 1.9 and Figure 1.10 to their regions of most probable observation in the magnetosphere, depicting that whistler-mode waves are indigenous to the radiation belts and occur predominantly within the plasmasphere, as well as from their role in the cyclotron resonant wave-particle interactions described in Section A.3.3: these slow waves, propagating at speeds of order  $0.01c$  to  $0.1c$  can significantly interact with energetic

<sup>33</sup>Although there are many classes of whistler-mode wave phenomena in the plasmasphere, stemming from both natural (chorus, hiss) and man-made (VLF transmitters, power-line harmonic radiation) sources, lightning generated electron whistlers represent a particularly important class. For a thorough treatment of their historic discovery and geophysical significance, consult [Helliwell, 1965].



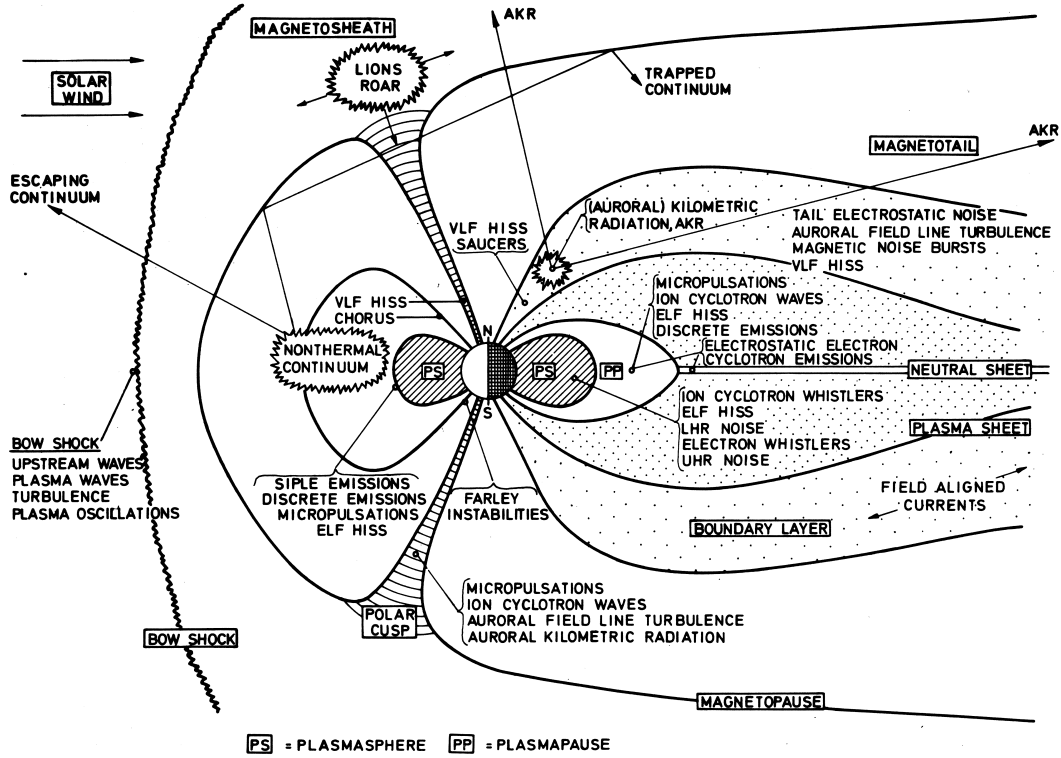


Figure 1.12: Magnetospheric regions home to the menagerie of plasma waves. Amidst the various locales of wave predominance revealed in a noon-night meridional cross-section, the plasmasphere (PS) is home to those of particular import for the radiation-belt study in work. Reproduced *in toto* from [Shawhan, 1979, p.216].

electrons.

### 1.1.3.3 Electrostatic Waves

Even an unmagnetized, cold plasma is subject to natural oscillations at the plasma frequency given in (1.2). Since this expression for  $\omega_{pe}$  is independent of  $\mathbf{k}$ , these oscillations exhibit zero group velocity and do not propagate (cf. Footnote 32). However, when invoking the warm plasma model to account for finite electron and ion temperatures, such natural resonances, near  $\omega_p$  and  $\omega_c$  of both species, give rise to perpendicularly propagating modes whose magnetic field is so small as to be essentially undetectable [Shawhan, 1979, p.217–226].

Since this set of electrostatic waves, including bow shock plasma oscillations and a

subset of electron cyclotron waves, can only be observed by an electric field antenna, and since there exists no dual wave class possessing only a component perceptible by a magnetometers, the former sensor offers a significantly more complete representation of the plasmaspheric wave environment [*Laaspere et al.*, 1969, p.148]. In addition, a low-noise amplifier designed to interface with an electric field antenna inherently possesses the requisite impedance to also receive signals from the preamplifier integrated into most magnetometer assemblies; the reverse is not true for the magnetometer preamplifier itself. For these reasons, the analog front-end at the heart of this effort has been tailored for use with a dipole antenna.<sup>34</sup>

#### 1.1.3.4 Magnetohydrodynamic Waves

MHD waves are very low frequency, dispersionless waves that are akin to free-space sound waves,<sup>35</sup> but travel in a magnetized, conducting fluid in which the corresponding adiabatic ‘sound’ speed is given by the Alfvén velocity:

$$v_A = \frac{B}{\sqrt{\mu_0 N_i m_i}} \quad (1.13)$$

In the ideal MHD formulation, the plasma is treated as a perfectly conducting fluid (cf. the formulation of the solar wind in Section A.1.1.1), so that the static magnetic field lines are ‘frozen-in’ and therefore placed under stress when the fluid is compressed perpendicular to  $\mathbf{B}$ .<sup>36</sup> Such motion gives rise to two circularly polarized wave modes with different  $\mathbf{k}$  vectors and phase velocities  $\mathbf{v}_p$ .

When  $\mathbf{k} \perp \mathbf{B}$ , the wave is longitudinal but it produces both a magnetic field parallel to  $\mathbf{B}$  and an electric field perpendicular to both  $\mathbf{k}$  and  $\mathbf{B}$ . This magnetosonic or magnetoacoustic wave is thus longitudinal in terms of the fluid motion, but

<sup>34</sup>The preference for a dipole over other flavors of electric field antenna is justified in Section B.1.2.

<sup>35</sup>Just as waves with  $\omega > \omega_{pe}$  behave like electromagnetic waves free space, unaffected by the surrounding plasma medium, MHD waves resemble standard sound waves, with the analogy exact only when they are longitudinally propagating parallel to the ambient magnetic field.

<sup>36</sup>As noted in Section A.2.1.3, motion parallel to the magnetic field for a conducting fluid is unaffected by the Lorentz force, so a standard longitudinal sound wave can propagate with  $\mathbf{k} \parallel \mathbf{B}$  at the speed of sound,  $v_s = \gamma_a kT/m$ . But, supporting neither an electric nor magnetic field component, such a wave is not relevant here.

electromagnetically transverse. Due to the stronger restoring forces, and thus greater total pressure, that result from the combination of the kinetic fluid pressure and the compression of the frozen-in field lines, it travels faster than the adiabatic speed, with  $v_p = \sqrt{v_s^2 + v_A^2}$ , and is known as the compressional or fast Alfvén wave [14:382].

By contrast, if  $\mathbf{k} \parallel \mathbf{B}$ , the wave is transverse and, without the fluid pressure, the lines of force are only restored as a result of their magnetic tension.<sup>37</sup> This condition results in a much slower phase velocity of  $v_A$  along the field line and gives rise to the sheer mode or slow Alfvén wave [Bittencourt, 1995, p.384]. It can be shown that the left-hand(right-hand) polarized sheer(compressional) Alfvén wave is simply the low-frequency limit of the ion(electron) cyclotron whistler mode under the ideal MHD model [Tsurutani and Lakhina, 1997, p.495].

Magnetohydrodynamic, or simply hydromagnetic, waves that are responsible for the ‘micro-pulsations’ of the geomagnetic field are believed to arise through wave-particle interactions, magnetospheric convection, and drift instabilities [Lanzerotti and Southwood, 1979, p.115]. However, they are not considered in this research since their low frequencies, typically in or below the extremely low frequency (ELF) range (3–30 Hz), render them difficult to decouple from satellite spin rates on the same order.<sup>38</sup>

Instead, to investigate wave-particle interactions for both the electromagnetic and electrostatic waves defined above, it is typically necessary to measure the electric field components of the waves highlighted in Figure 1.13. The next section introduces the instrumentation required for such measurements.

---

<sup>37</sup>The classical analogy for this mode is to consider the field lines as strings under tension, with the plasma particles acting as an attached load mass under the ‘frozen-in’ condition. A transverse disturbance then propagates down the string as a vibration whose frequency is proportional to the square-root of the tension-to-mass ratio [Bittencourt, 1995, p.376].

<sup>38</sup>Furthermore, MHD waves and micro-pulsations are disregarded because they are invisible to the hot particle populations of the radiation belts in terms of the resonant interactions of Section A.3. For an excellent review of the early observations, magnetospheric conditions, and theoretical underpinnings of these phenomena, the reader is directed to [Lanzerotti and Southwood, 1979].

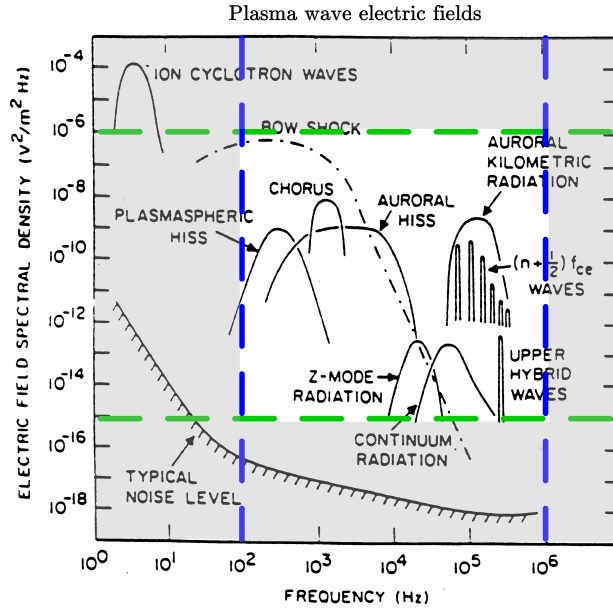


Figure 1.13: Signal space to be acquired by target receiver. The blue(green) lines emphasize the 1-MHz(90-dB) extent in bandwidth(power) spanned by signals of interest, which dictates aggressive specifications for SVEPRE. Modified from [Gurnett, 1998, p.123].

## 1.2 Space Plasma Instrumentation

As noted at the outset of this chapter, a thorough understanding of the intricacies that underlie magnetospheric wave-particle interactions can only be derived through simultaneous and precise measurements of both principal parties; namely, the wave packets and particle distributions at any, and preferably more than one, point in space [Gurnett *et al.*, 1978, p.226]. Although technologies for energetic particle detectors that measure the charged particle fluxes, also known as plasma analyzers, have exhibited remarkable advancement over the last half century, such instruments are subject to fundamental trade-offs, imposed by their physical dimensions, that limit their versatility [Young, 1998]. In particular, their sensitivity, as defined by the geometric factor, is a product of the sensor area and acceptance angle. Improving sensitivity by increasing the former(latter) produces a corresponding increase(decrease) in the detector's overall volume/weight(angular discrimination),

constraining the size, orbit, and attitude of spacecraft upon which it can be deployed [Walt, 1994, p.69].

Therefore, in an effort to develop advanced satellite sensor technology with the broadest possible applicability in terms of both scientific scope and mission compatibility, the research in question is aimed at improving the performance and flight worthiness of instrumentation for detecting waves, known as plasma wave receivers,<sup>39</sup> rather than particles.<sup>40</sup> The remainder of this document concentrates only on plasma wave receivers for use with sensors that can detect the wave electric field components depicted in Figure 1.13. In addition to allowing for the detection of both electromagnetic and electrostatic modes (cf. Section 1.1.3.3), and accommodating a preamplifier that can interface with search coil magnetometers as well as dipole antennae (cf. Section 3.1.4), the choice to sense the wave electric field component rather than its magnetic counterpart is justified by eased sensitivity demands [Gurnett et al., 2004, p.416].<sup>41</sup>

For plane waves with electric(magnetic) field strengths given by  $e(b)$ , such as those propagating in the whistler-mode germane to the wave-particle interactions of

---

<sup>39</sup>Although ground-based observations of plasma wave phenomena predate the space era, and although their hardware can cover the same bandwidth and dynamic range as Figure 1.13, for the purposes of this dissertation such terrestrial receivers are considered distinct from those which can measure the waves *in situ*, with the term *plasma wave receiver* applying only to the latter to signify that since such waves can only exist in a plasma, the sensing of their effects below the ionosphere must be, by definition, indirect.

<sup>40</sup>For a review of the state-of-the-art in particle detectors at the turn of the millennium, as well as an overview of the technological progression for each of the canonical architectures, including Langmuir probes, retarding-potential analyzers, and spectrometers, [Pfaff et al., 1998] is recommended for the reader's consideration.

<sup>41</sup>Although not addressed in detail here, sensors capable of measuring the strength (scalar) and/or direction (vector) of both DC and AC magnetic fields are known as magnetometers and have a long history in space. This lineage and the variety of canonical architectures, including quantum (precession, Overhauser, vapor, etc.), fluxgate, and search coil magnetometers, are expertly summarized by [Primdahl, 1998] and [Snare, 1998], for scalar and vector types, respectively. Though magnetometers were originally used only to measure the geomagnetic DC field, it is common for modern satellites to employ plasma wave receivers whose inputs can be driven by either dipole antennas or AC magnetometers. Recent progress toward versions of the latter that employ novel, integrated architectures [Goldstein, 1998] promise size and mass reductions akin to those achieved by the analog receiver electronics described herein. Such magnetometers are suitable as alternative inputs to the electric-field dipoles employed by the nominal design.

Section A.3, it can be shown that [Walt, 1994, p.120]:

$$\frac{e}{b} = v_p \quad (1.14)$$

So, even in the slowly-traveling whistler-mode, where  $n \geq 10$ ,  $e$  is at least seven orders of magnitude larger than  $b$ , enabling electric field instrumentation to cover the full nine orders of magnitude (90 dB) in power spectral density spanned by the waves of Figure 1.13 without the smallest signals falling into its noise. Note that these waves also extend over a broad range in frequency, covering four decades from 100 Hz to 1 MHz over which the receiver must maintain this sensitivity without distortion.

### 1.2.1 Plasma Wave Receivers

Produced by a typical plasma wave receiver—the Plasma Wave Instrument (PWI) aboard the Polar satellite [Gurnett et al., 1995], whose auroral mission places it on an orbit through the radiation belts of interest—the spectrogram in Figure 1.14 is representative of the data format used to study plasma wave electric fields in general and, specifically, their interactions with Van Allen belt particles.<sup>42</sup> In addition to the spread in the bandwidth and intensity of these waves in accordance with Figure 1.13, this spectrogram, also known as an  $f$ - $t$  diagram, emphasizes a third dimension of fluctuation—their variation in time. As is evident in the five-second interval magnified

---

<sup>42</sup>Standard terminology delineates measurements of the static electric field in a plasma from those of existent wave phenomena by designating instruments addressing the former, such as Langmuir probes, as *DC receivers* and the latter as *wave receivers*. Since DC (and even ELF fields) are not under consideration here, it henceforth suffices to simply omit the *wave* modifier and instead refer to the *electric field* and its *receiver*, as needed, without ambiguity.

Incidentally, a key distinction between DC and wave receivers, namely the AC-coupling of the latter to the electric-field antenna, indurates wave receivers against modulation effects below 10 Hz caused by the rotation of the spacecraft, including: saturation by the spin-induced Doppler-shifting of the relatively large DC electric field [Jones, 1978, p.331] and low-frequency noise [Scarf et al., 1968, p.6672]; sun-oriented spin modulation that results from beating between the spin and sampling frequencies [Scarf et al., 1971, p.500]; and low-frequency radiated interference at the spin frequency and its higher harmonics caused by supply voltage fluctuations as each solar panel group rotates in and out of shadow [Gurnett et al., 1978; Matsumoto et al., 1994, p.230,p.73]. For DC-coupled receivers, which are subject to such phenomena, resolution in excess of 14 bits [Maynard et al., 1981] and signal processing techniques [Scarf et al., 1971, p.500–501] are typically invoked to extract the desired signals.

on the left, these wave exhibit discrete temporal structure,<sup>43</sup> and often both high- and low-power phenomena are present simultaneously. Amongst the transient behaviors central to interpretation of the underlying phenomena are onset delay, onset duration, and recovery, each with a characteristic time constant [Johnson *et al.*, 1999].

Of course, an ideal plasma wave receiver possesses excellent resolution in frequency, power, and time over the full bandwidth and dynamic range of Figure 1.13.<sup>44</sup> But, due to the limitations of their digital back-ends, namely low telemetry rates and limited amounts of on-board data storage, traditional receivers such as PWI are not capable of capturing all of this information simultaneously. Instead, the spectrogram and the enlarged inset in Figure 1.13 are actually produced by two separate receivers within the instrument: one which has high dynamic range and bandwidth, but poor time resolution; the other which has much better time resolution, but only over a narrow bandwidth and power range.

This strategy, of providing “several different types of receivers, each of which has certain advantages, in time and frequency resolution,” [Gurnett *et al.*, 1995, p.602] rather than a single, all-purpose receiver, consumes more of valuable spacecraft resources such as power and mass, reflecting a time when satellites could readily provide such support but were severely constrained in terms of data storage and transmission. As a result, legacy receivers employ a variety of front-end architectures aimed at reducing the total data volume by partitioning the space of Figure 1.13 into a series of smaller segments and only capturing them one at a time. For nearly all plasma wave receivers, as detailed next, these analog front-ends can be classified into three categories, based upon which dimensional partition(s) (frequency, power,

---

<sup>43</sup>The term *impulsive* is often used in the study of ELF/VLF plasma waves to denote features of especially short duration. However, this brevity, on the order of at least a few microseconds, is only relative to the long time-scales over which such waves evolve. So, this term is eschewed here to avoid confusion with the mathematical notion of an impulse.

<sup>44</sup>The terms *bandwidth* and *dynamic range* are blatantly overloaded in this document. As general descriptors, they refer to the full extent(operating range) of the signals(circuit) in question along the dimensions of frequency and power, respectively; put another way, they describe the frequency span or power range of interest. As formal metrics, each can also refer to a fraction of the total span; for example, bandwidth may describe a subset with some minimum gain, as in the  $-3$ -dB bandwidth, whereas the dynamic range may pertain only to a linear operating regime, as in the  $90$ -dB spurious-free dynamic range. To distinguish the latter usage from the former, explicit variables, such as  $f_{-3\text{dB}}$  and  $\text{SFDR}_{100\text{kHz}}$ , are defined and employed in pertinent discussions.



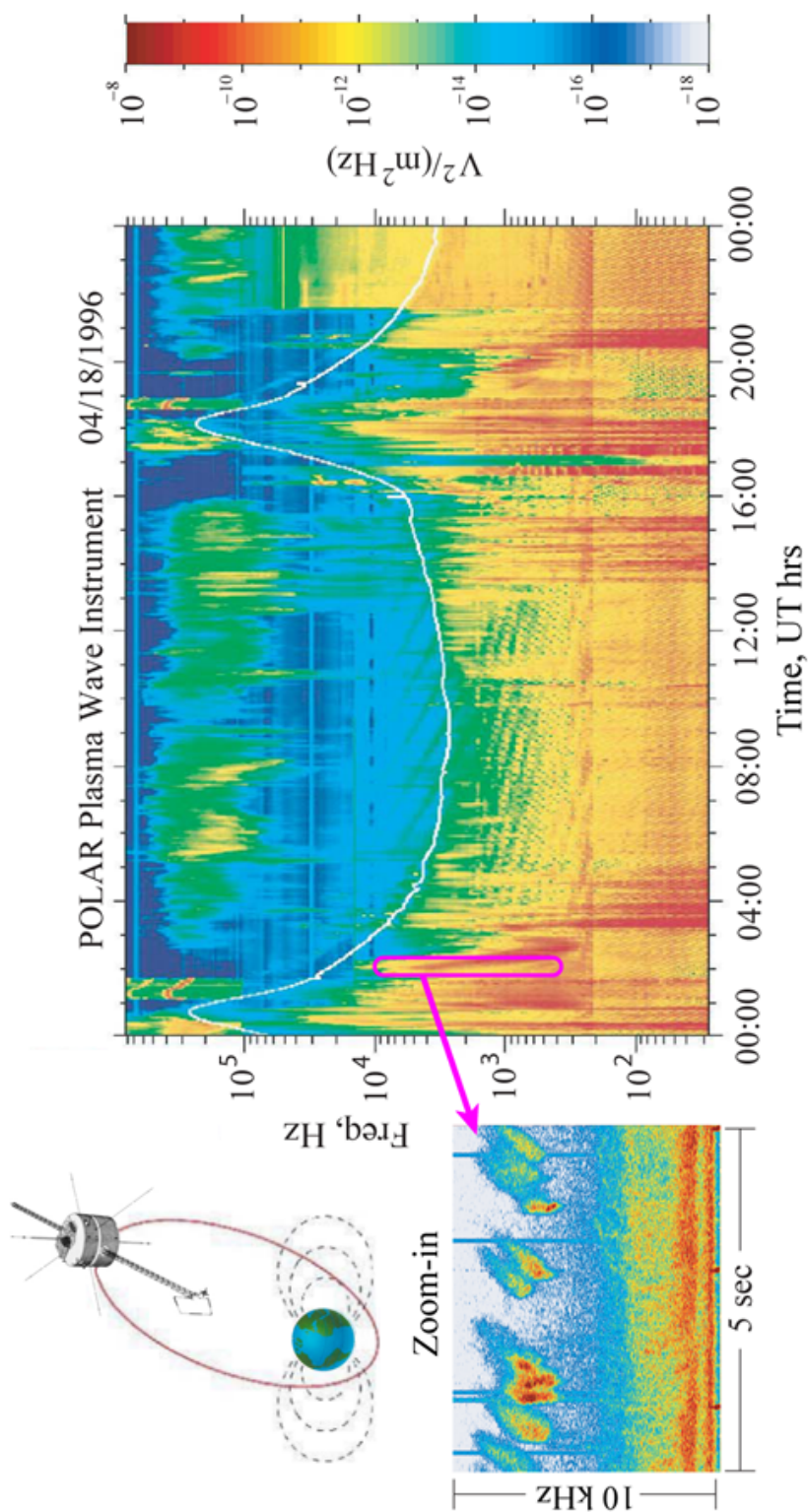


Figure 1.14: Exemplary spectrogram generated by Polar PWI instrument while sensing representative plasma wave phenomena in the radiation belts (note: orbital diagram not to scale). The image on the right was produced from sweep frequency receiver measurements, which afford good frequency resolution, whereas the dynamic behavior of the inset narrowband data required a wideband receiver. Both receiver inputs were multiplexed from the  $E_U$  130-m spherical double-probe antenna.



or time) receives the highest priority.<sup>45</sup>

Table 1.2 summarizes the relevant properties of both US and foreign satellites flown since 1959 whose payload contains one or more plasma wave receivers.<sup>46</sup> In tracking the historical advancement of these receivers, several entries merit specific recognition. Vanguard 3 offered the first satellite-based measurements of naturally occurring VLF whistlers waves in 1961 [*Gurnett and O'Brien*, 1964, p.69],<sup>47</sup> using a magnetometer. Shortly thereafter, in 1962, Alouette 1 carried the first broadband VLF receiver fed by an electric dipole antenna [*Laaspere et al.*, 1969, p.141]. Not only did its data, along with that from the complementary air-core loop magnetic field receiver of Injun 3 in the same year [*Gurnett and O'Brien*, 1964, p.84], form the seminal observations which spawned the modern study of magnetospheric wave-particle interactions [*Singh and Singh*, 1998, p.20727], but its hardware, a wideband receiver for electric field measurements, is the predecessor of the system advanced here (cf. Section 1.2.2).

---

<sup>45</sup>This tripartite classification system is adopted from [*Gurnett*, 1998], though some authors employ slightly different divisions and/or vocabulary.

<sup>46</sup>Although it comprises all such satellites for which sufficiently detailed reports on plasma wave instrumentation are both published and readily available, this table is indicative, not exhaustive. Among those spacecraft known to carry such receivers, the following have been omitted due to a lack of accessible documentation: LOFTI 1, PROGNOZ series, SCATHA (P78-2), Intercosmos 18, Intercosmos 24, Mars-96.

<sup>47</sup>In the same year, though slightly earlier, LOFTI 1 (not tabulated) made the first measurements of magnetospheric VLF waves by sensing the emissions from ground-based naval transmitters [*Scarabucci*, 1970, p.69]; Vanguard 3 measured the first naturally occurring VLF wave phenomena.

Identification			Orbit		Mechanical				Telemetry	
Name	Cntry	Launch	Region <sup>a</sup>	Qty <sup>b</sup>	Spin <sup>c</sup> $f_r$ [rpm]	Mass <sup>d</sup> $M_{\text{tot}}$ [kg]	$M_{\text{pwi}}$ [kg]	Power <sup>e</sup> $P_{\text{tot}}$ [W]	$P_{\text{pwi}}$ [W]	Type <sup>f</sup> $\Upsilon_t$ [bps]
Vanguard 3	USA	09/18/59	Topside IS	1		22.7				A 108.03
Alouette 1	CAN	09/29/62	Topside IS	1	1.4	145.7		23		A 136.86
Injun 3	USA	12/13/62	Auroral IS	1		54.0				A/D 136.86
OGO 1	USA	09/05/64	Equatorial IS	1	5	487.2				A/D 64k
OGO 2	USA	10/14/65	Polar IS	1	0.11	507.1				A/D 64k
OGO 3	USA	06/07/66	Equatorial IS	1	0.6	514.8				A/D 64k
Ariel 3	UK	05/05/67	Ionosphere	1	31	89.8				
OGO 4	USA	07/28/67	Polar IS	1	0.28	514.8				A/D 64k
Pioneer 8	USA	12/13/67	Heliocentric	1	60	146.0				D 512
OGO 5	USA	03/04/68	Equatorial IS	1	< 10	611.0				A/D 64k
Injun 5	USA	08/09/68	Topside IS	1	0.1	71.4				A/D 400.0
Pioneer 9	USA	11/08/68	Heliocentric	1	60	147.0				D 512
ISIS 1	CAN	01/30/69	Topside IS	1	2.9	241.0				A/D 400.0
OGO 6	USA	06/05/69	Polar IS	1	< 10	631.8				A/D 64k
IMP 6	USA	03/13/71	Outer MS	1	5	635.0				D 1600
ISIS 2	CAN	04/01/71	Topside IS	1	2	264.0				A/D 400.0
S <sup>3</sup> A	USA	11/15/71	Magnetosphere	1	7.14	114.0	3.3	34	12	A/D 446
Ariel 4	UK	12/11/71	Ionosphere	1	< 10	99.5				

Identification			Orbit		Mechanical					Telemetry	
Name	Cntry	Launch	Region <sup>a</sup>	Qty <sup>b</sup>	Spin <sup>c</sup> $f_r$ [rpm]	Mass <sup>d</sup> $M_{\text{tot}}$ [kg] $M_{\text{pwi}}$ [kg]	Power <sup>e</sup> $P_{\text{tot}}$ [W] $P_{\text{pwi}}$ [W]	Type <sup>f</sup>	Rate <sup>g</sup> $\Upsilon_t$ [bps]		
Pioneer 10	USA	03/03/72	Jupiter flyby	1		258.0	165	D	2048		
IMP 8	USA	10/26/73	Outer MS	1	23	371.0	150	D	1600		
Hawkeye 1	USA	06/03/74	Outer MS	1	5.45	22.7	22	D	200		
Helios 1	GER	12/10/74	Heliocentric	1	60	371.2		D	4096		
IK-14	USSR	12/11/75	Geocentric	1		700.0		D			
Helios 2	GER	01/15/76	Heliocentric	1	60	371.2		D	4096		
S3-3	USA	07/08/76	Ionosphere	1	3	7.5	4	A/D			
GEOS 1	ESA	04/20/77	Geostationary	1	10	273.6		D	96k		
Voyager 1	USA	09/05/77	Jupiter/Saturn	1	< 10	721.9	1.4	D	128k		
Voyager 2	USA	09/05/77	Jupiter/Saturn	1	< 10	721.9	1.4	D	128k		
ISEE 1 <sup>h</sup>	USA	10/22/77	Outer MS	1	19.75	340.2	8.0	D	16k		
ISEE 2	ESA	10/22/77	Outer MS	1	19.8	165.8	3.4	D	8192		
PVO	USA	05/20/78	Venus flyby	1	< 10	517.0	0.5	D	2048		
GEOS 2	ESA	07/14/78	Geostationary	1	10	571.7		D	96k		
ISEE 3	USA	08/12/78	Liberation pt.	1	20	390.0	8.8	D	2048		
DE 1	USA	08/03/81	Outer MS	1	10	424.0	86	D	16k		
DE 2	USA	08/03/81	Inner MS	1	< 10	420.0	5.3	D	16k		
Aureol 3	USSR	09/21/81	Geocentric	1	< 10	1000	250	D	51200		

Identification			Orbit		Mechanical					Telemetry	
Name	Cntry	Launch	Region <sup>a</sup>	Qty <sup>b</sup>	Spin <sup>c</sup> [rpm]	Mass <sup>d</sup> $M_{\text{tot}}$ [kg]	$M_{\text{pwi}}$ [kg]	Power <sup>e</sup> $P_{\text{tot}}$ [W]	$P_{\text{pwi}}$ [W]	Type <sup>f</sup>	Rate <sup>g</sup> $\Upsilon_t$ [bps]
CCE <sup>i</sup>	USA	08/16/84	Outer MS	1	10	242.0	0.76	140	0.7		
IRM <sup>i</sup>	GER	08/16/84	Outer MS	1	15	705.0	22.6	60	10.9	D	8000
UKS <sup>i</sup>	UK	08/16/84	Outer MS	1	12	77.0				D	32k
Akebono	JAP	02/21/89	Auroral IS	1	7.5		8.8		7.26	D	64k
Galileo	USA	10/18/89	Jupitercentric	1	3.5	2380	3.94	570	6.8	D	806k
CRRES	USA	07/25/90	Outer belt	1	2	4383	5.06		4.9	D	256k
Ulysses	ESA	10/06/90	Heliocentric	1	5	370.0	7.3	285	10	D	
Geotail	JAP	07/24/92	Magnetotail	1	20	980.0	14.0	273	13.9	D	64k
Freja	GER	10/06/92	Auroral IS	1	10	214.0	8.27	168	10.6	D	520k
Wind	USA	11/01/94	Bow shock	1	20	1250	14.5		28	D	11k
Interball 1	USSR	08/02/95	Magnetotail	2	0.5	1250	3.7		0.445	D	32k
Polar	USA	02/24/96	Auroral IS	1	10	1250		333		D	600k
FAST	USA	08/21/96	Auroral IS	1	12	187.0	16.4	60		D	2.25M
Interball 2	USSR	08/29/96	Auroral IS	2	0.5	1250				D	32k
Cassini	USA	10/15/97	Saturncentric	1	< 10	2523	5.59	640	5.0	D	166k
IMAGE	USA	03/25/00	Polar MS	1	0.5	536.0	48.0	250	30.8	D	44k
Cluster <sup>j</sup>	ESA	09/09/00	Outer MS	4	15	550.0	1.67	224	1.57	D	262k
DEMETER	FRA	06/29/04	Ionosphere	1	3	129.0		70		D	16.8M

Identification			Orbit		Mechanical				Telemetry	
Name	Cntry	Launch	Region <sup>a</sup>	Qty <sup>b</sup>	Spin <sup>c</sup> $f_r$ [rpm]	Mass <sup>d</sup> $M_{\text{tot}}$ [kg]	$M_{\text{pwi}}$ [kg]	Power <sup>e</sup> $P_{\text{tot}}$ [W]	Type <sup>f</sup>	Rate <sup>g</sup> $\Upsilon_t$ [bps]
STEREO	USA	10/26/06	Heliocentric	2	< 10	623.0	10.8	475	D	720k
THEMIS	USA	02/17/07	Outer MS	5	20	77.0		37	D	

<sup>a</sup> MS: magnetosphere; IS: ionosphere

<sup>b</sup> For clusters (Qty > 1), all mechanical quantities are given per satellite

<sup>c</sup> Satellites spin-stabilized at unknown rate are denoted with  $\omega_r < 10$

<sup>d</sup>  $M_{\text{tot}}$ : Total mass of spacecraft;  $M_{\text{pwi}}$ : Total mass of plasma wave instrument(s)

<sup>e</sup>  $P_{\text{tot}}$ : Available spacecraft power;  $M_{\text{pwi}}$ : Power consumption of plasma wave instrument(s)

<sup>f</sup> Refers to carrier modulation scheme: analog (A), digital (D), or mixed (A/D)

<sup>g</sup> For analog modulation, decimal carrier frequency ( $f_o$ , in MHz) given in place of maximum rate ( $\Upsilon_t$ )

<sup>h</sup>  $M_{\text{pwi}}$  and  $P_{\text{pwi}}$  pertain to Univ. of Iowa instrument; for Stanford Univ. instrument, the corresponding quantities are 1.3 kg and 0.7 W, respectively.

<sup>i</sup> One of three spacecraft that participated in AMPTE mission whose acronym often prefixes this sobriquet.

<sup>j</sup>  $M_{\text{pwi}}$  and  $P_{\text{pwi}}$  pertain to WBD instrument; for EFW instrument, the corresponding quantities are 1.8 kg and 3.7 W, respectively.

Table 1.2: Satellites since 1959 with plasma wave receiver payloads.

### 1.2.1.1 Sweep Frequency Receiver (SFR)

Though it is not the inaugural class chronologically, the sweep frequency receiver (SFR) whose front-end is depicted in Figure 1.16 is considered first.<sup>48</sup> It uses a super heterodyne architecture such that, at any point in time, it can examine only a narrow window of frequencies, represented by the red-shaded box in Figure 1.15, which it then sweeps across the entire horizontal axis (dotted boxes). For the subset of satellites in Table 1.2 which feature SFRs, the sweep ranges, step sizes, cycle times, dynamic range, and other properties, as well as the experiment(s) with which they are associated, are summarized in Table B.4.

As implied by the rectifier and filter to the end of the signal path in Figure 1.16, the vast majority of these SFRs construct a complete spectrum by measuring the root-mean-square (RMS) average power of the signal within a resolution bandwidth, or RBW, (typically, 2–5000 Hz) centered on each of 4–256 frequency steps within each of their 1–6 bandwidth divisions.<sup>49</sup> The coarseness of these steps and the lengthy cycle times (0.5–64 s/spectrum) prevent the discrimination(acquisition) of simultaneous phenomena that are very closely(broadly) spaced in frequency, including the harmonics of non-linear emissions and power line radiation, not to mention burst phenomena whose duration is a less than one sweep cycle.<sup>50</sup>

Furthermore, with only 8-bit digital resolution in most cases, these SFRs cannot inherently process signals throughout the full power range. One approach to overcoming this limitation, depicted in Figure 1.16, precedes the rectifier and back-end analog-to-digital converter (ADC) (not pictured) with a variable gain amplifier (VGA), thereby allowing the acquisition window to be vertically aligned with the

---

<sup>48</sup>In the last twenty years, superheterodyne stages featuring one or two non-zero intermediate frequencies have encroached upon the formerly exclusive domain of such homodyne or direct-conversion architectures (e.g., [Bougeret *et al.*, 2008, p.507]). Nevertheless, the single-stage heterodyne performed in Figure 1.16 sufficiently captures the relevant design trade-offs of this architecture.

<sup>49</sup>Those SFRs in Table B.4 which output the full wave, rather than just its RMS amplitude, embody an architecture more consistent with a heterodyned wideband receiver (cf. Figure 1.20(a)) and thus are addressed in Section 1.2.1.3.

<sup>50</sup>Additionally, in some architectures, data from each of the bandwidth divisions are sampled sequentially, rather than simultaneously, further eroding the achievable temporal resolution for the entire frequency range.

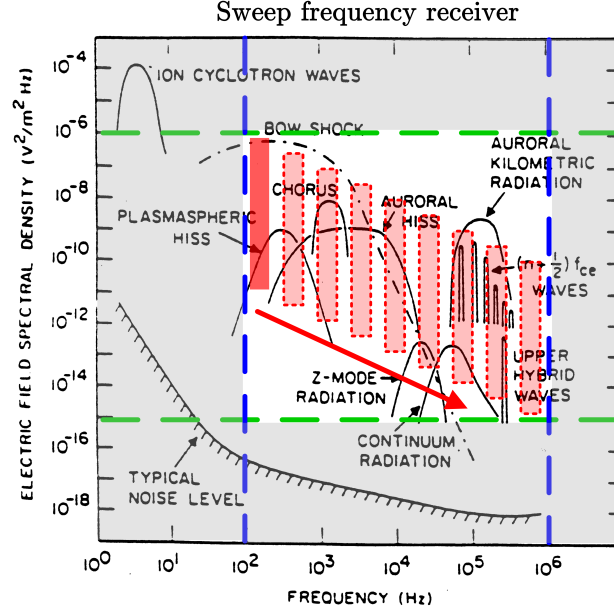


Figure 1.15: Partitioning of target signal space by SFR architecture. Only signals within the dark red box are measured at the depicted point in time; subsequently, the segments within the dashed boxes are acquired in the temporal sequence indicated by the arrow. Modified from [Gurnett, 1998, p.123].

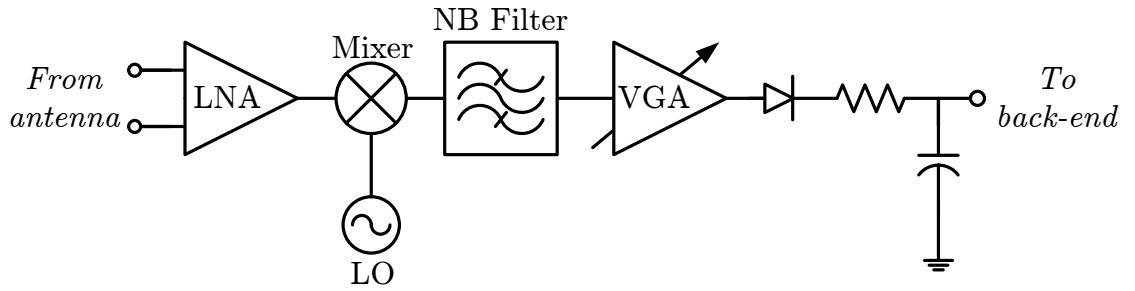


Figure 1.16: Sweep frequency receiver front-end architecture. The frequency of the local oscillator (LO) is tuned so as to translate the desired signal into the bandwidth of the fixed, narrow-bandwidth (NB) filter. The role of the optional variable-gain amplifier (VGA) is described in the main text.

signals of interest during each sweep step, as limned by the progression indicated by the arrow in Figure 1.15. In lieu of this variable gain, or simply to reduce the number of gain steps it requires, it is common for the amplifier to perform a piecewise, quasi-logarithmic compression [Gurnett *et al.*, 2004, 1995, p.615–616,p.444–445]. Thus, while the total dynamic range ( $DR_T$ ) can approach or even exceed the 90-dB target, the instantaneous dynamic range ( $DR_I$ ) is limited to that at a single gain setting, typically less than 70 dB, with a resolution set by the logarithmic compressor at approximately 0.375 dB per least-significant bit (LSB), even for 8-bit systems that quote 100-dB  $DR_I$  [Bougeret *et al.*, 1995, p.245].

The spectrogram to the right of Figure 1.14, which appears continuous in all dimensions, is actually stitched together from a series of such time-sequenced windows, each obtained by the PWI SFR at a particular frequency step and gain setting.

### 1.2.1.2 Multichannel Spectrum Analyzer (MSA)

To improve the time resolution, a second and, as evidenced by the number of entries in Table B.5, more popular approach, the multichannel spectrum analyzer (MSA) whose front-end block diagram is depicted in Figure 1.18, requires much more hardware, but is capable of capturing several wide frequency windows simultaneously,<sup>51</sup> as represented by the red-shaded boxes in Figure 1.17. By processing the input signal(s) through multiple (usually, 4–32) parallel filtering paths, each of which extracts a particular subset of the spectrum, then amplifies, compresses, rectifies, and averages this signal analogously to the SFR path,<sup>52</sup> this architecture produces a coarsely

---

<sup>51</sup>Of the three front-end architectures identified here and in [Gurnett, 1998], the MSA exhibits the most diverse set of aliases. Although the term *spectrum analyzer* predominates today, earlier literature alternatively refers to this architecture as a *filter bank* [*S-300 Experimenters*, 1979] or, more unfortunately, a *step-frequency receiver* [Gurnett *et al.*, 1969]. Despite its lingual similarities, the latter describes an architecture fundamentally distinct from the *sweep frequency receiver* of Section 1.2.1.1.

<sup>52</sup>Some MSAs and SFRs feature a variation of this signal conditioning which extracts the mean and maximum value of the signal over a each sample interval, rather than its average power. Other than suppressing or accentuating large transient phenomena, respectively, these variations only affect the interpretation of the data; the above arguments concerning the instrument trade-offs remain applicable.



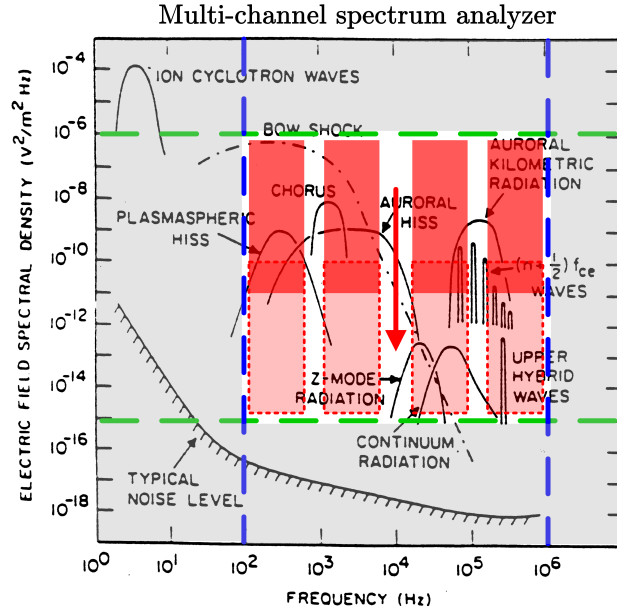


Figure 1.17: Partitioning of target signal space by MSA architecture. Only signals within the dark red box are measured at the depicted point in time; subsequently, the segments within the dashed boxes are acquired in the temporal sequence indicated by the arrow. Modified from [Gurnett, 1998, p.123].

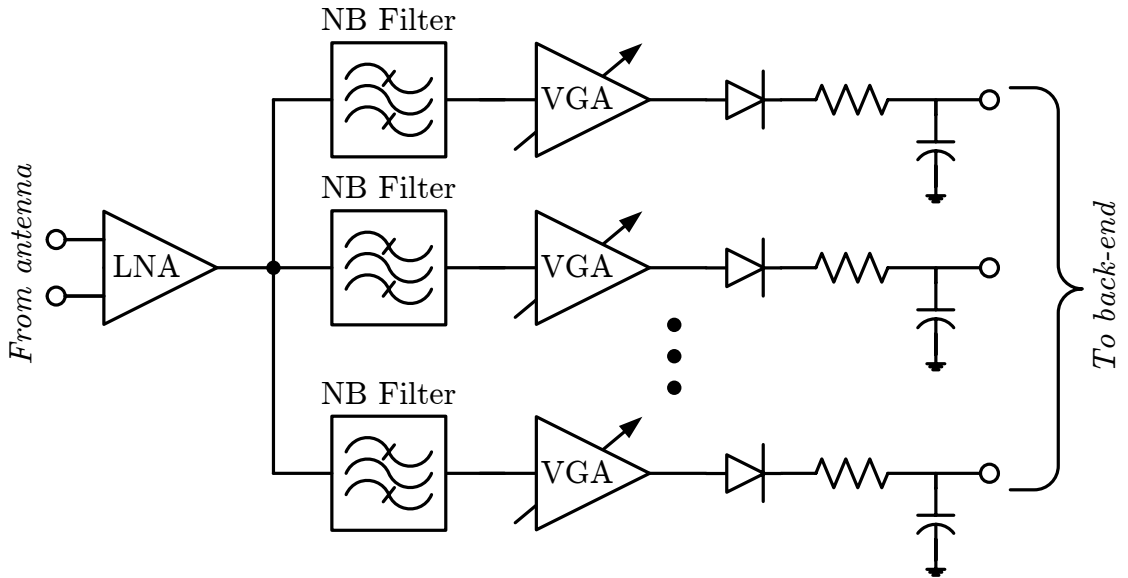


Figure 1.18: Multichannel spectrum analyzer front-end architecture. On occasion, rectifier and filter are replaced with peak/nadir detectors or omitted altogether.

sampled column of the ideal spectrogram at each time step. The extent to which all paths, or bands, are sampled simultaneously is a function of the hardware and data budget, which jointly limit the number of ADCs available. Thus, either a single ADC is commutated between paths [*Scarf and Gurnett, 1977*, p.302], acquiring all the band samples for a given time-step in a round-robin fashion, or each band is sampled by a dedicated ADC, but at the same effective, and thus slow, rate (typically,  $< 1$  kS/s) [*Gurnett et al., 1978*, p.228].

Naturally, increasing the frequency resolution of an MSA directly translates into additional hardware costs (mass, volume, power, etc.), so in practice the ability to observe the entire frequency range with good time resolution comes at the cost of frequency resolution. Hence, as portrayed by the gaps between the windows of Figure 1.17, some frequencies are ignored altogether. Furthermore, the MSA is subject to the same dynamic range limitations as the SFR, so it still requires a VGA and/or logarithmic compressor [*Gurnett et al., 1995*, p.615–616].

### 1.2.1.3 Wideband Receiver

Both of the above analog front-end architectures yield low data-rate approximations to the wave spectrum. But, in so doing, the SFR(MSA) intrinsically, irreversibly, and *a priori* emphasizes frequency resolution,  $\Delta\omega$ (time resolution,  $\Delta t$ ) over  $\Delta t(\Delta\omega)$  in the inescapable  $\Delta\omega\Delta t \simeq 1$  trade-off imposed by the uncertainty principle of Fourier transforms [*Bracewell, 1986*, p.160]. A more flexible solution would allow the scientist to alternately weight the two factors based upon the principal phenomena of interest. In the ideal limit, this evaluation consists of digitizing the time-domain waveform with high resolution at the time of acquisition and allowing the choice of Fourier transform parameters during the computation of the spectrogram itself, to be deferred until data analysis is performed on the ground [*Gurnett, 1998; Gurnett et al., 1997*, p.195,133].

The wideband receiver (WBR) architecture represents a shift toward this idealized paradigm, wherein a fraction of the overall bandwidth consistent with the limitations of the Nyquist sampling theorem [*Nyquist, 1928; Shannon, 1949*] is extracted from the antenna by means of a wideband filter, to prevent aliasing artifacts [*Oppenheim et al., 1999*, p.142–149], and the result sampled at the corresponding rate. Captured in the

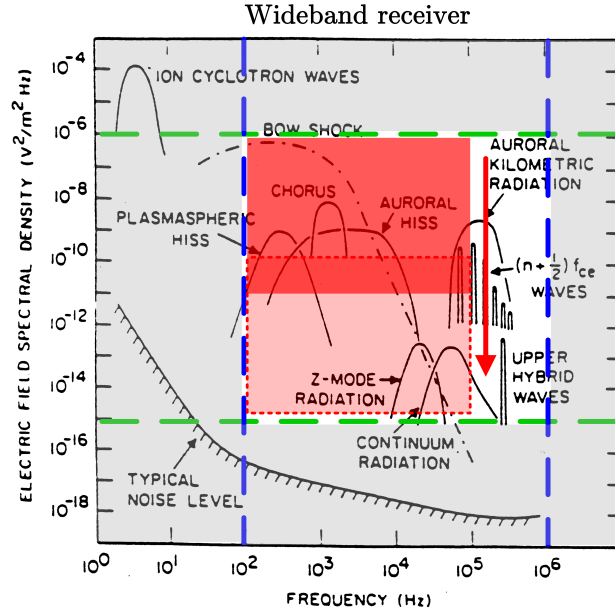


Figure 1.19: Partitioning of target signal space by WBR architecture. Only signals within the dark red box are measured at the depicted point in time; subsequently, the segments within the dashed boxes are acquired in the temporal sequence indicated by the arrow. Modified from [Gurnett, 1998, p.123].

front-end block diagrams of Figure 1.20, this procedure, when followed by spectral post-processing, permits the examination of a much wider range in either frequency or power than afforded by the SFR or MSA front-ends.

However, as indicated by the extent of the red-shaded box in Figure 1.19, the WBR coverage in frequency(power) remains incomplete as a result of constraints on the speed(resolution) of the digitization process. Specifically, modest telemetry rates for magnetospheric satellite orbits, measured in bits/second (bps) and symbolized by  $\Upsilon_t$  (cf. Table 1.2), and insufficient quantities of either tape or solid-state data storage on board previous satellite systems, writable at a rate  $\Upsilon_m$ , impose restrictions on the total data acquisition rate,  $\Upsilon_a$ . Thus encumbered by the need for  $\Upsilon_a \leq \max\{\Upsilon_t, \Upsilon_m\}$ , the WBR front-end must cap  $\Upsilon_a$  by restricting either the signal bandwidth (via the sampling rate) or resolution (via the ADC bit-width), resulting in the partial scope of Figure 1.19.

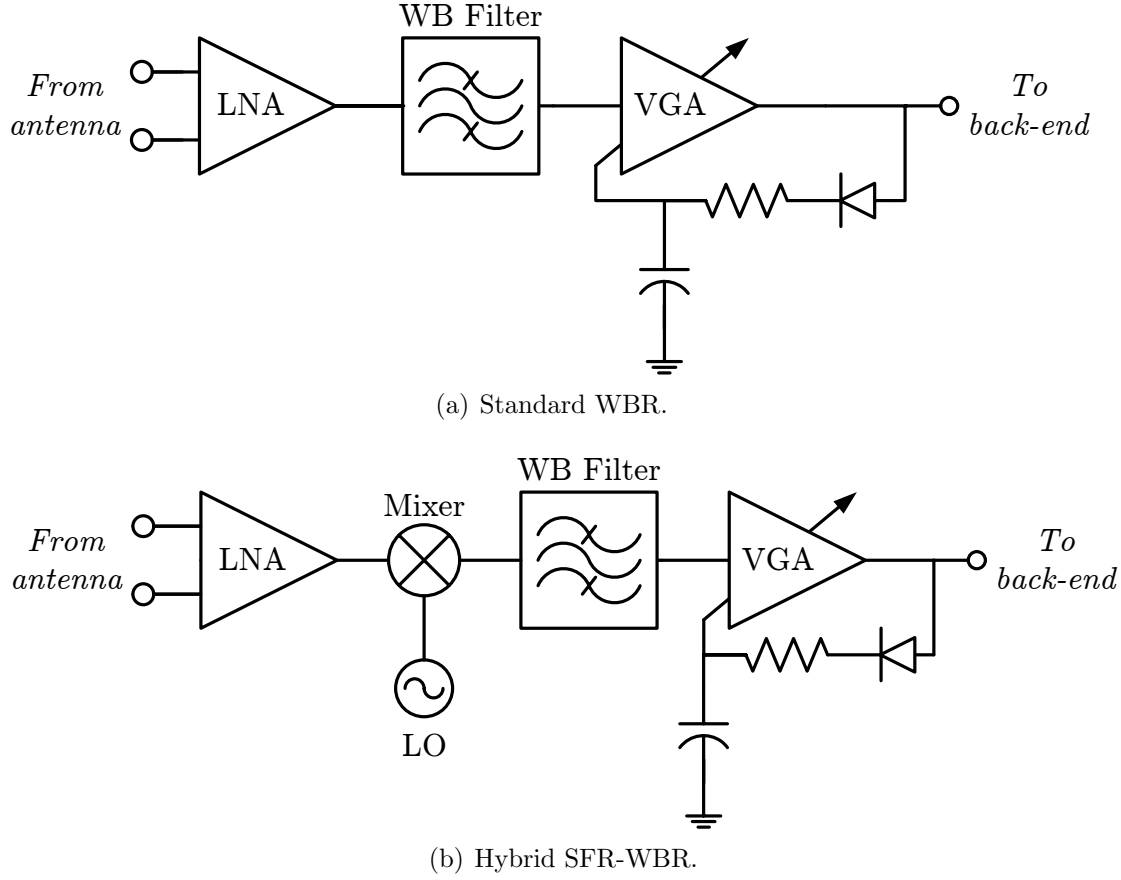


Figure 1.20: Wideband receiver front-end architectures. In both cases, the back-end must also periodically record the level of the AGC control signal alongside the amplitude data (not shown).

Dictated by concessions to these back-end limitations, WBR front-end architectures, such as those of Figure 1.20, have evolved in-step with the historical, ascendant progression of the permitted  $\Upsilon_a$ . The earliest forerunners of the modern WBR, found aboard Alouette 1 [Florida, 1969] and Injun 3 [Gurnett and O'Brien, 1964], lacked any on-board storage (i.e.,  $\Upsilon_m = 0$ ) and directly frequency- or phase-modulated analog signals onto telemetry subcarriers, respectively, providing waveforms whose frequency content was extracted in real-time by spectral-domain ground-station equipment (GSE). To maximize the modulation index, and hence the signal-to-noise ratio (SNR) of the telemetry channel, it was necessary to ensure that the data maintained nearly

constant amplitude by using rapid automatic gain control (AGC) [*Shawhan et al.*, 1981, p.546], as shown in Figure 1.20(a); to help in the recovery of the relative amplitude, the control voltage of the AGC servo was periodically digitized and transmitted as well [*Crook et al.*, 1969, p.127]. Although variants of this protocol were developed subsequently,<sup>53</sup> the core strategy of utilizing AGC to separately transmit the amplitude and frequency content of the wideband signal, thereby circumventing back-end dynamic range limitations, persisted even as telemetry rates improved and magnetic tape storage materialized [*Florida*, 1969, p.872]. In fact, compressing the dynamic range through AGC proved valuable even with the advent of on-board samplers and digital storage, on account of their low bit-widths [*Scarf and Gurnett*, 1977, p.303]. However, accompanying increases in ADC speed enabled a new class of hybrid SFR-WBR systems, also dubbed radio receivers, an example of which is presented in Figure 1.20(b). First introduced on IMP 8 and extended by ISEE-1, this solution precedes the filter and AGC with a mixer and frequency synthesizer (LO) capable of heterodyning higher-frequency signals into the transmittable baseband, thereby covering the full bandwidth of interest [*Gurnett et al.*, 1978, p.228].

Heavily entrenched, uni-level AGC schemes persisted even once the prevalence of space-qualified ADCs and telemetry systems featuring fully-digital data formats had rendered the modulation schemes which necessitated their invention obsolete. But, in light of the severe complications AGC poses for both data acquisition (sluggish update rates; inability to prevent saturation for rapid-onset phenomena; and the need for commandable hysteresis thresholds) and analysis (piecewise rescaling of both relative and absolute power levels in diuturnal records; artifacts due to switching relays; amplifier nonlinearities; a limited scaling range; and difficulties in interpreting relative amplitude using a single AGC level based on broadband amplitude across bands with several spectral features), a wideband receiver capable of capturing the full dynamic range without the AGC of Figure 1.20 remains highly desirable. Similarly, eliminating

---

<sup>53</sup>In addition to AGC, early WBRs adopted a variety of creative and unique means for decoupling and independently measuring the wave characteristics, including: FM-modulating(AM-modulating) telemetry subcarriers with an averaged(clipped) version of the analog signal, representing its envelope(frequency) content [*Rorden et al.*, 1966]; counting the rate at which the signal crosses a stepped threshold, similar to a ramp-comparison ADC [*Scarf et al.*, 1968]; and using RMS amplitude detectors to coarsely monitor high-frequency bands [*Gurnett*, 1974].

the need for a heterodyne front-end as in Figure 1.20(b) better approximates the goal of acquiring the entirety of the time-domain waveform, with the desired bandwidth and dynamic range, as a single, continuous data stream.

### 1.2.2 Target Receiver

The transition toward smaller, lighter, and lower power spacecraft, batches of which can perform interferometric measurements necessary for the pressing scientific objectives explicated at the outset of this chapter, is exemplified by the recent Cluster [Pedersen et al., 1997] and THEMIS [Angelopoulos, 2008] missions. As evidenced by the opposing mass/power and telemetry trends of Table 1.2, the facilities offered by such satellites no longer favor payloads that combine the three low-rate, front-end architectures to mimic the function of a single, ideal plasma wave receiver. Given that mass, volume, and power limitations of these spacecraft preclude instruments comprised of more than one receiver, the wideband architecture is the obvious choice for such systems, despite its vestigial reliance on AGC and heterodyning to encompass the full signal space of Figure 1.13.

However, by leveraging the improvements in their digital back-ends, not only the vast and continued increases in  $\Upsilon_m$  and  $\Upsilon_t$ , tabulated above, but also the accompanying advent of sophisticated, embedded processing algorithms for frequency tracking, phase cross-correlation, spectral estimation, and data compression,<sup>54</sup> these satellites can now support a modern genre of wideband receiver that overcomes both

---

<sup>54</sup>If the data from a particular instrument are being stored at a much faster rate than can be telemetered (i.e.,  $\Upsilon_m/\Upsilon_t \gg 1$ ), it can only be operated during a small fraction of each orbit. To improve this duty cycle, modern receivers are increasingly leveraging the availability of powerful, radiation-hardened processing units to perform in-flight reduction of the stored data, effectively converting  $\Upsilon_t$  to  $\Upsilon_r$  where  $\Upsilon_r/\Upsilon_t \leq 1$ . Such signal processing strategies, which can achieve packing ratios of  $\Upsilon_m/\Upsilon_r$  as high as 30:1 include: determination of the  $\mathbf{k}$  vector [S-300 Experimenters, 1979, p.323], as well as mode and polarization [Morioka et al., 1990; Shawhan et al., 1981, p.543,p.444–446] through the use of on-board correlators; GSE extraction of plasma parameters from on-board amplitude measurements to inform collection schedules [Lindqvist et al., 1994; Reznikov and Shkliar, 1982]; lossy data compression implemented in both hardware [Markas, 1993; Woolliscroft et al., 1993] and software [Koga et al., 1992]; triggering algorithms that telemeter only a scientifically interesting subset of the data volume [Harvey et al., 2001]; and, most sophisticated, on-board spectrogram production using Fast Fourier Transforms (FFTs) [Bougeret et al., 1995; Ergun et al., 2001; Parrot et al., 2006; Stone et al., 1992, p.296,p.238–245,p.80–82,p.445–446].

of the aforementioned drawbacks and approaches the performance of the ideal receiver by capturing the entirety of the signal space simultaneously.<sup>55</sup>

A target wideband receiver, of the form shown in Figure 1.22, senses electric fields over the full extent in frequency and power, with 12-bit resolution,<sup>56</sup> by acquiring the entirety of the time-domain voltage waveform in a single, continuous data stream with the desired bandwidth and dynamic range, as depicted in Figure 1.21. But, to do so without AGC or heterodyning, it requires a new type of analog front-end consisting of a high-impedance, low-noise amplifier (LNA) to interface with the dipole antenna, and a vigorous anti-aliasing filter (AAF) to ensure faithful analog-to-digital conversion.

In addition to the scientific specifications imposed by the broad frequency and power coverage of Figure 1.21, numerical values for which are annotated on Figure 1.22,<sup>57</sup> such a front-end must also satisfy the payload requirements imposed by any satellite system.<sup>58</sup> Chief among these is radiation hardness, the specifications for which in terms of both total dose and single event tolerance—namely, maintaining performance beyond 100 krad(Si) without latchup—are defined and motivated in Chapter 2. Additionally, low mass and minimal power dissipation are especially critical insofar as these valuable commodities impact development and launch costs, as well as mission lifetime.

Frequently, the mass of an instrument is dominated by:<sup>59</sup> the power supply

---

<sup>55</sup>The primogenitor of this genre was the Freja WAVE experiment [Holback *et al.*, 1994], though the more recent examples aboard FAST [Ergun *et al.*, 2001], DEMETER [Berthelier *et al.*, 2006], and THEMIS [Bonnell *et al.*, 2008] benefit from modern spacecraft resources to achieve performance more closely allied with that of the target receiver.

<sup>56</sup>In addition to the novel analog front-end demonstrated herein, the target receiver utilizes a high-speed, high-resolution, radiation-hardened ADC heretofore unavailable. Adducing [Wang, 2009], contemporary efforts demonstrate the feasibility of such converters and permit the specifications of the cited device to be assumed by the system design that follows, unless otherwise stated. For example, the input range of the Wang [2009] ADC dictates that the peak-to-peak voltage ( $V_{PP}$ ) of the differential signal at the output of the front-end ASIC not exceed  $1 V_{PP}$ .

<sup>57</sup>The subtle but crucial distinction between the 90-dB SFDR cited in Figure 1.22 and the 90-dB dynamic range introduced previously vis-à-vis Figure 1.13 lies in the demands of the former on circuit linearity and is examined in great detail in Section 3.1.2.

<sup>58</sup>Naturally, all the receiver components, not just the front-end ASIC, are subject to these satellite-driven requirements.

<sup>59</sup>When considering receiver specifications for mass, volume, and power, only the contributions from the electronics are germane to the design of the analog front-end circuitry. Hence, despite their

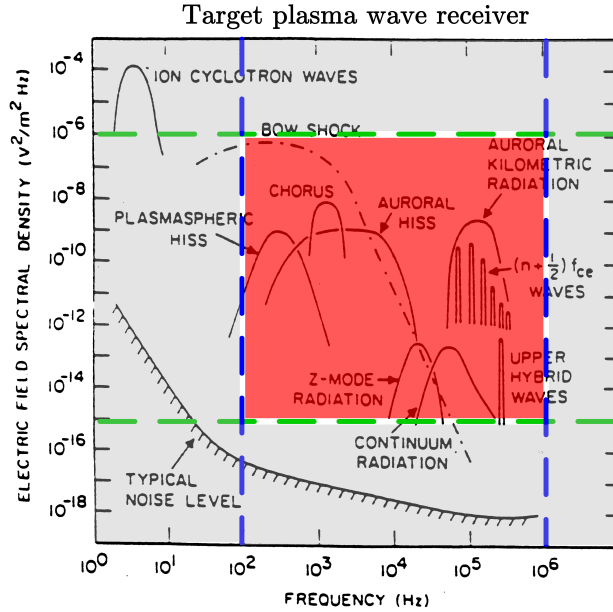


Figure 1.21: Signal space captured by target receiver. All signals within the dark red box are acquired simultaneously. Modified from [Gurnett, 1998, p.123].

regulation circuitry, whose weight is proportional to its power-handling capacity; the quantity of discrete components in the design, which impacts the size of the printed circuit boards (PCBs) and strength of the mechanical enclosure; and the thickness of shielding necessary to keep the accumulated radiation exposure below the rated limits of the components. Previous instruments have addressed these factors by: employing individual, high-efficiency DC-DC switching regulators for each constituent receiver [Häusler *et al.*, 1985]; integrating select portions of the signal path into ASICs, rather than using discrete operational amplifiers (opamps) [Hashimoto *et al.*, 1997]; and, where possible, using radiation-hardened commercial, off-the-shelf (COTS) components that allow for minimal shielding [Bonnell *et al.*, 2008, p.10]. However, to-date no solution minimizes mass on all three fronts, resulting in a range of 0.5–14 kg for wave instrument payloads (cf.  $M_{\text{pwi}}$  in Table 1.2). In contrast, by meeting the front-end performance requirements of the proposed wideband receiver

---

often predominant role, the sensors, including the electric field antennas and magnetometers, as well as the host spacecraft computer and telemetry, have been omitted from these calculations.



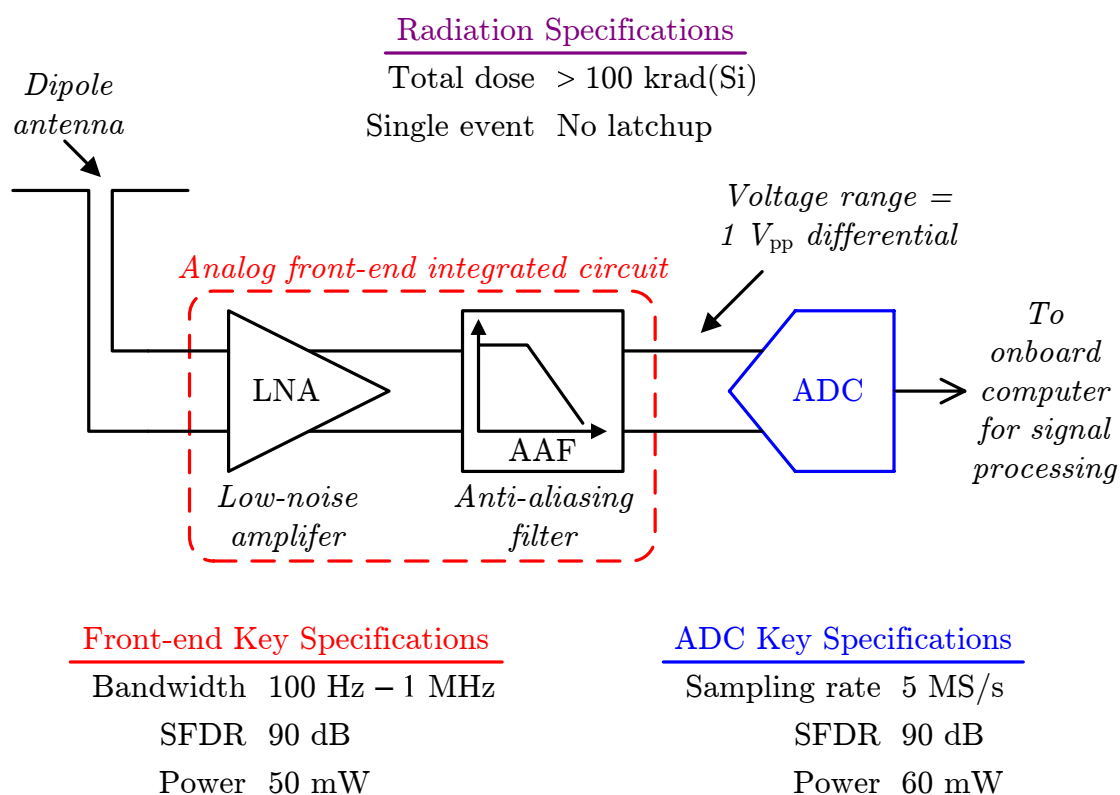


Figure 1.22: Architecture of target wideband receiver annotated with component specifications derived from scientific and satellite requirements presented in this chapter.

with a single, monolithic ASIC that is intrinsically radiation-hardened so as to maintain said performance for at least one year of a standard radiation-belt orbit (cf. Section 2.3.1), SVEPRE permits a dramatic improvement: an instrument that features 100 mg/channel.<sup>60</sup>

Turning to power dissipation and adducing Table 1.2, complete plasma wave instruments, composed of one or more receivers each with one or more channels, consume a total of 0.04–30 W. Within this range, a survey of representatives suggests that the various receiver architectures are allocated on the order of: 1.6–2.0 W/channel (SFR) [Häusler *et al.*, 1985]; 0.12–2.5 W/channel (MSA) [Bell and Helliwell, 1978; Häusler *et al.*, 1985; Scarf, 1985]; and 0.9–1.85 W/channel (WBR) [Gurnett *et al.*, 1997; Häusler *et al.*, 1985]. Although the dearth of detailed power budgets in the literature inhibits a precise estimate of the fraction expended by the analog front-end in each case, the low-frequency analog signal conditioning shared by the receivers in the FAST instrument suite offers a recent example [Ergun *et al.*, 2001]. The analog power is divided amongst the front-end components with 28.4 mW per differential amplifier and 10.8 mW per 6-pole Butterworth filter.<sup>61</sup> Thus, a reasonable power budget for the single-channel target receiver of Figure 1.22, which is fully differential and therefore requires twice the number of filter components, allocates a maximum of 50 mW to the front-end ASIC. The 200-mW/channel power consumption of an example plasma wave instrument composed of five such wideband channels, including the necessary reference generation and a field-programmable gate array (FPGA) for data processing, as derived in Table 1.3,<sup>62</sup> compares favorably with

---

<sup>60</sup>Regardless of the number of possible sensor inputs for a particular receiver, all per-channel quantities for normalized comparisons apply to a single analog or digital output data stream; in the latter case, the total number of channels for given receiver,  $N_{\text{ch}}$ , describes the number of such streams that can be simultaneously acquired in parallel, such that the data rate per channel is  $\Upsilon_{\text{a}}/N_{\text{ch}}$ .

<sup>61</sup>These quantities have been inferred from Table IV of [Ergun *et al.*, 2001, p.88] under the assumptions that: there are a total of 9 (8 survey + 1 burst) CS5016 ADCs, at a cost of 150 mW each [Cirrus Logic, Inc., CS5016]; there are a total of 21 (7 survey + 14 burst) differential amplifiers to supply the maximum number of simultaneous sensor difference voltages; the power dissipation of the 6-pole Butterworth filter simply scales as the ratio of poles from the 7.2-mW cited for the 4-pole Bessel filters.

<sup>62</sup>The power budget in Table 1.3 is merely an estimate accounting for functional blocks that directly support the integration of the target receiver into the channels of a complete instrument.

Functional block	Power/unit (mW)	Power/channel (mW)
Front-end	50	50
ADC buffer	40	40
ADC	60	60
FPGA	80	40
Auxiliary <sup>a</sup>	100	20
Total	1000	200

<sup>a</sup> Includes local supply conditioning, reference generation circuitry, and housekeeping FPGA

Table 1.3: Estimated power budget for example five-channel receiver using SVEPRE. Assumes sharing of auxiliary circuitry amongst all five channels with one control FPGA per channel pair. Unit powers map to available components with requisite performance.

that of any one of the canonical receiver architectures, let alone the combination thereof necessary to obtain comparable signal-handling performance.

## 1.3 Organization

To describe the design of SVEPRE, an ASIC that satisfies the analog-front end requirements dictated by the wideband plasma wave receiver in Figure 1.22, from the derivation of its specifications, to the novel facets of its architecture and circuit implementation, to the confirmation of its performance obtained via the fabrication

---

Unit powers given for the ADC input buffer (whose inclusion is recommended, but optional depending on the selected ADC), FPGA (which, with modern capabilities and of moderate size, presumably can support two channels operating at their nominal rate), and auxiliary circuitry (shared across five channels) reflect construction with presently available, radiation-hardened components. The tabulation does not include power dissipated in the instrument backbone by: the general purpose processor responsible for the command and control of the channels, as well as storing and telemetering their data in cooperation with the host spacecraft computer (also omitted); additional processors for in-flight management of data products and volume; or, switching regulators that step down the spacecraft power bus (typically,  $\pm 28$  V) to levels compatible with the instrument's integrated electronics (typically,  $\pm 5$  V). In light of this restricted scope and approximate nature, the resulting 200-mW is best interpreted as the incremental cost of adding one channel with the stated architecture to an existing instrument.

and measurement of a test chip, this dissertation is organized into seven chapters as follows.

Chapter 1, the present chapter, motivates this research by introducing the fundamentals of space plasma science and instrumentation at its foundation. The scientific framework summarizes both the geography of the Earth's upper atmosphere, highlighting the magnetosphere and its radiation belts which are home to the electromagnetic phenomena of interest, and the elementary plasma physics which govern these phenomena, with emphasis on the unresolved dynamics of wave-particle interactions. A survey of past instruments details their shortcomings in translating the science-driven requirements into hardware for plasma wave measurements and proposes to surpass their performance with a novel receiver architecture contingent upon the development of the analog front-end ASIC recounted in the remaining chapters.

To engender an appreciation for the relevant specifications, Chapter 2 reviews the basic radiation effects to which the target device will be subjected while on orbit through the Van Allen belt. The exposure concomitant with such an orbit, considered in terms of its total dose and single event ramifications, both gradually degrades the performance of the underlying transistors, through ionizing and non-ionizing damage, and suddenly, often catastrophically, interferes with the circuit operation, causing transients and latchup. Rather than resort to shielding or custom manufacturing processes, radiation-hardness-by-design is introduced as the preferred means to mitigate these adverse consequences.

In addition to those imposed by the radiation environment, the precision requirements dictated by the scientific mission objectives present a suite of challenges explicated in Chapter 3, which defines the relevant metrics for programmability, linearity, noise, and impedance. Taken together with the specifications introduced in this chapter, the requirements of Chapter 1 and Chapter 2 translate into a set of technical specifications that inspire the overarching philosophy behind the architecture of the front-end. The second half of this chapter frames the discussion in the subsequent two by highlighting the roles of process choice and feedback in this design concept.

Detailed discussions of the front-end constituent blocks are offered in Chapter 4 and Chapter 5, which cover the design of the LNA and AAF, respectively. In both cases, the novel use of active and passive feedback loops proves critical to meeting the proposed specifications. Through the judicious design of bipolar sub-circuits, the careful implementation of fully differential current-mode signal processing, and the development of custom layout structures, the LNA and AAF designs achieve the exacting programmability, linearity, noise, and impedance requirements laid out in Chapter 3 in the face of the radiation-induced degradations introduced in Chapter 2.

To confirm the efficacy of the techniques presented in Chapters 3–5, Chapter 6 presents measured results of the baseline and radiation performance of the prototype obtained using a single, automated test setup, which is also reported in this chapter. Direct comparison between the baseline characterization and that from a series of radiation exposures using four different sources verifies that the desired levels of performance can be achieved over the specified dose and identifies the performance-limiting aspects of the design.

Chapter 7 concludes this work by summarizing its key contributions and suggesting possible directions for future efforts to extend the research presented herein.

A significant portion of the material in this work is organized into a series of appendices. Indexed according to the order in which they are referenced by the main text, these appendices fall into one of three content categories. For the inquisitive reader, Appendices A, C, and F summarize background material on plasma physics, radiological physics, and filter theory, respectively. By synthesizing canonical treatments into a unified framework—complete with consistent notation used throughout this text—these supplements corroborate and/or augment the arguments of the main text in Chapters 1, 2, and 5, respectively.

The largest appendix family contains stand-alone encapsulations of novel material developed in the course of this research. In an original endeavor, Appendix B surveys a sizable fraction of the plasma wave receiver instruments published since 1959, extracting and tabulating the properties of their antennas and electronics. To arrive at a noise specification for the LNA, Appendix D derives the thermal and short noise limits of an electric dipole immersed in a magnetoplasma. Together, these efforts

inform the SVEPRE specifications established in Chapter 3. Recounting a rewarding collaboration with engineers from National Semiconductor Corporation, Appendix E describes the design, fabrication and testing of several novel gate-controlled lateral pnp (GCLPNP) transistors. The insipid performance of these prototypes inspired the invention of the circuit design (rather than process) techniques in Chapter 4 and Chapter 5 to alleviate the burdens of a non-complimentary bipolar technology. Finally, Appendix G and Appendix H elucidate the details of auxiliary chip- and board-level circuits, respectively. Although subordinate to the core innovations of this research, these peripheral elements are nevertheless instrumental in enabling the function and characterization of the ASIC, as alluded to in Chapters 4–6.

The final subset comprises Appendices I, J, and K, which document the conditions of the total-dose, single-event, and burn-in testing, respectively, to which the fabricated front-end chips were subjected. Each description of experimental setups, procedures, and analyses underpins the corresponding measurement results presented in Chapter 6.

## 1.4 Contributions

In the context of the target receiver described in this chapter, the contributions of this research are enumerated below.

- Design, implementation, and testing of the first fully-integrated analog front-end for satellite-based, wideband plasma wave receivers
- Derivation of the performance requirements for such a circuit based on a survey of existent designs and novel formulations of the prerequisites for advancing the latest generation of wideband receivers toward more comprehensive study of radiation-belt wave-particle dynamics
- Development of a programmable-gain, low-noise amplifier for electric field measurements from 100 Hz to 4 MHz that achieve 90-dB SFDR while consuming less than 2 mW

- Devising a novel transconductor with a  $36\times$  tuning range that enables programmable anti-aliasing filtering with 90-dB third harmonic suppression and power-efficient field trimming
- Demonstration of radiation-hardness-by-design techniques that allow these elements to be fabricated in a commercial  $0.25\text{-}\mu\text{m}$  SiGe BiCMOS manufacturing process, yet maintain performance beyond 100 krad(Si) total dose and remain free of latchup through an LET of  $\sim 100\text{ MeV-cm}^2/\text{mg}$





## Chapter 2

# Radiation Effects

The intrinsic ability to maintain its high performance in spite of the deleterious effects of the radiation-belt environment on its constituent transistors marks a primary advantage of the SVEPRE ASIC, as explained in Section 1.2.2. Deriving from incident particles which deposit energy during their interaction with integrated circuit materials, primarily silicon (Si) and silicon dioxide (SiO<sub>2</sub>), radiation-induced circuit damage was first revealed by the failure of the Telstar 1 communication satellite following the Starfish Prime high-altitude nuclear detonation (cf. Footnote 1 of Chapter 1).<sup>1</sup> However, apart from both the prompt dose and the long-term enhancement in the radiation-belt populations that characterize a so-called hostile radiation environment [*Tribble*, 2003, p.163–165],<sup>2</sup> spacecraft electronics are constantly exposed to three naturally occurring forms of radiation with similarly harmful potential:

**Cosmic rays:** Possessing the highest energies, but lowest fluxes, cosmic rays are further sub-categorized according their source. Primary or galactic cosmic rays

---

<sup>1</sup>Since Explorer I (and, later, Explorer III), were searching for cosmic electromagnetic radiation when such trapped, highly energetic particles were discovered, these were ambiguously granted the designation of *radiation* in keeping with the ‘radiation belt’ moniker [*Tascione*, 1994, p.51]. In context of this work, the term radiation encompasses both energetic particles and electromagnetic energy, in the form of photons, placing particular emphasis on their interaction with matter in the form of conductors, semiconductors, and metals.

<sup>2</sup>For a complete description of the environment produced by a nuclear detonation, including the hostile radiation component, the reader is directed to Chapter 4 of [*Messenger and Ash*, 1992].

(GCRs), released by exploding stars outside the solar system, are composed of protons and heavy ions (85%  $H^+$ , 14%  $He^{2+}$ , 1% heavier nuclei), with energies from 0.1–1 GeV. Although extremely penetrating, due their high energies, they comprise a small fraction of the total dose observed in any orbit, due to low fluxes which vary spatially with the location of the source relative to the geomagnetic field and temporally with the solar cycle [*Holmes-Siedle and Adams, 2002*; *Tascione, 1994*; *Tribble, 2003*, p.138–139,p.19,p.161]. Solar cosmic rays (SCRs), are similar in composition to GCRs, but their ions possess slightly lower energies and lower atomic weights that reflect the distribution of solar material [*Holmes-Siedle and Adams, 2002*, p.23]. The final class, terrestrial cosmic rays (TCRs), which consist primarily of secondary neutrons produced by the interaction between GCRs and the atmosphere near the Earth’s surface, are not relevant at spacecraft altitudes.

**Coronal mass ejections:** The most intermittent but potentially most destructive instances of extraterrestrial radiation are coronal mass ejections (CMEs). Consisting predominantly of the protons released during the same solar particle events (SPEs) responsible for SCRs [*Tribble, 2003*, p.161–162], these are correlated with the solar cycle, but can generate a “thousandfold increase in the radiation dose over a short period of time” [*Tascione, 1994*, p.139]. Considerable variation in the duration, flux, energies, and constituents of CMEs can result in doses ranging from insignificant to lethal, with ‘anomalously large’ events (< 1% incidence) representing the most threatening portion of the statistical ensemble, given the significant spacecraft damage reported from examples in August 1972 and October 1989 [*Holmes-Siedle and Adams, 2002*, p.26].

**Trapped radiation:** At much lower energies and higher fluxes than either cosmic rays or CMEs, the trapped particles of the Van Allen belt (cf. Section 1.1.1) form the third element of the natural space environment. The same geomagnetic field which traps the energetic protons(electrons) in the inner(outer) zone of the belt by deflecting incident particles through the Lorentz force, affords some degree of magnetic shielding from incident GCRs, SCRs, and CMEs. Although

“the degree of protection will depend on altitude and inclination of the orbit,” [Holmes-Siedle and Adams, 2002, p.25] with high altitude polar orbits offering the least isolation, this geomagnetic shielding, combined with their low flux, limits the effective contribution of GCRs to 5-10% of the total dose observed in any orbit [Tascione, 1994, p.139]. Since the radiation related to GCRs and CMEs is negligible in all but rare and extreme cases, the remainder of this chapter concentrates largely on the effects of lower energy, higher flux radiation characteristic of the Van Allen belt.

To appreciate the imminent discussion, as well as the considerations of manufacturing process, chip layout, and radiation testing in subsequent Chapters, a working knowledge of the physics that govern this radiation is beneficial. A primer on the salient underpinnings, including the radiological definitions needed to quantify it and the mechanisms of both its ionizing and non-ionizing solid-state interactions, is provided in Appendix C.

Mitigating the depredations of these underlying interactions as regards the electrical properties of the transistors that comprise the front-end analog circuitry is central to this work. Such effects reflect the impact of radiation-induced variations in physical quantities introduced in Appendix C—such as the number densities of oxide trapped charge ( $N_{ot}$ ) and interface traps ( $N_{it}$ ), minority-carrier lifetimes ( $\tau_n$  or  $\tau_p$ ) and bulk resistivity ( $\rho_n$  or  $\rho_p$ )—on MOSFET parameters—such as threshold voltage ( $V_{th}$ ), transconductance ( $g_m$ ), and leakage current ( $I_L$ )—and BJT parameters—such as base current ( $I_b$ ), common-emitter current gain ( $\beta$ ), base resistance ( $R_b$ ), and emitter resistance ( $R_e$ ).

Traditionally, these effects are grouped into two broad categories based on the time scales over which they evolve: Section 2.1 addresses total dose effects (TDEs), which manifest as a gradual degradation of device properties due to the damage accumulated from prolonged exposure; Section 2.2 covers single event effects (SEEs), which are marked by an almost instantaneous change in the operation of a circuit due the impact of a single ionizing particle. With these effects cataloged for both MOS and bipolar transistors, thereby framing the challenges posed in the design of a

BiCMOS front-end ASIC,<sup>3</sup> Section 2.3 advocates the use of radiation-hardening-by-design, rather than traditional mitigation methods, to reduce, if not eliminate, the impact of these effects.

## 2.1 Total Dose Effects

Differences between MOSFETs and BJTs in terms of their operating principles (field-effect vs junction-based), carrier type (majority vs minority), and current flow (surface vs bulk) govern the relative sensitivity of their parameters to long-term illumination by the two classes of radiation discussed in Section C.2 and Section C.3. In modern MOS technologies, TDEs are almost exclusively the result of ionizing damage to SiO<sub>2</sub> (via TID) [Messenger and Ash, 1992, p.307], with displacement damage, in either the oxide or bulk [Holmes-Siedle and Adams, 2002, p.133], considered inconsequential [Messenger and Ash, 1992, p.262]. Conversely, integrated BJTs are susceptible to damage from both TID and total displacement dose (TDD), but compared to MOSFETs, are much more tolerant of the former than the latter [Messenger and Ash, 1992, p.333]. In light of this distinction, Section 2.1.1 concentrates on the impact of TID for MOSFETs while Section 2.1.2 predominately highlights TDD effects on BJTs.

### 2.1.1 MOS Transistors

Degradation of  $V_{th}$ ,  $g_m$ , and  $I_L$  in modern MOSFETs subject to TID exposure is a direct consequence of the build-up of  $\Delta N_{ot}$  and  $\Delta N_{it}$  and, as such, reflects the dependencies of these quantities on fabrication quality, transistor geometry, oxide electric field (as imposed by the applied gate bias), temperature, dose rate ( $dD/dt$ ), and annealing conditions [Dressendorfer, 1989a, p.256–257], as discussed in Sections C.2.4 and Sections C.2.6, respectively.<sup>4</sup> Where relevant, the influence of

---

<sup>3</sup>With an emphasis on only those effects from each class that are of concern for SVEPRE, Section 2.1 and Section 2.2 offer suggested references for more comprehensive treatment rather than enumerating the complete array of deleterious consequences in each category.

<sup>4</sup>Although a rigorous treatment should also account for the effect of the border traps described in Section C.2.5, via  $\Delta N_{bt}$ , theory to support the experimental evidence that discriminates their

these  $\Delta N_{\text{ot}}$  and  $\Delta N_{\text{it}}$  relationships on the observed behavior of corresponding MOS parameters is noted in the sub-sections below.

### 2.1.1.1 Threshold Voltage

The most pronounced TID effect in MOSFETs is a non-monotonic,  $dD/dt$ -sensitive, shift in  $V_{\text{th}}$  with dose whose recovery is difficult to predict. This shift,  $\Delta V_{\text{th}}$ , from a pre-irradiation value of  $V_{\text{tho}}$  is the sum of contributions from  $\Delta N_{\text{ot}}$  and  $\Delta N_{\text{it}}$ , denoted  $\Delta V_{\text{ot}}$  and  $\Delta V_{\text{it}}$ , respectively, according to [Srou and McGarrity, 1988, p.1450]:

$$\Delta V_{\text{th}} = V_{\text{th}} - V_{\text{tho}} = \Delta V_{\text{ot}} + \Delta V_{\text{it}} \quad (2.1)$$

Decomposed in the  $I_{\text{D}}\text{-}V_{\text{GS}}$  characteristic of an idealized nMOS device according to Figure 2.1, these two effects are handled separately below.

#### $\Delta V_{\text{ot}}$ Contribution

The trapping of holes in the oxide near the interface constitutes a source of fixed, positive charge  $\Delta Q_{\text{ot}} = Q\Delta N_{\text{ot}}$ , whose field acts to deplete(accumulate) the native p-type(n-type) surface of an nMOS(pMOS) transistor body, making it easier(more difficult) to turn on. In this regard, the  $\Delta N_{\text{ot}}$  electric field apes that of an applied positive potential leading to the negative lateral translation in the  $I_{\text{D}}\text{-}V_{\text{GS}}$  curve in Figure 2.1(b) [Holmes-Siedle and Adams, 2002, p.137]. More formally, its effect can be interpreted by treating the gate oxide as the dielectric of an nMOS(pMOS) capacitor,<sup>5</sup> wherein positive charge on the gate terminal induces a negative image charge in the channel, such that the latter moves closer to inversion(accumulation) [Holmes-Siedle

---

impact from that of  $\Delta N_{\text{it}}$  is less robust [Oldham, 1999]. Fortunately, their effects (apart from increased noise) are strongly correlated with those of  $\Delta N_{\text{it}}$  (albeit on slower time scales), so that simply omitting  $\Delta N_{\text{bt}}$  introduces only a small error in all such cases [Holmes-Siedle and Adams, 2002, p.179].

<sup>5</sup>Indeed, if the effects of  $\Delta N_{\text{it}}$  are ignored, it can be shown that  $\Delta V_{\text{ot}} = \Delta V_{\text{FB}}$ , where the latter is the flatband voltage—the voltage at which the surface potential goes to zero [Messenger and Ash, 1992, p.291]—for an identically processed capacitor [Holmes-Siedle and Adams, 2002, p.137]. The method of inferring  $\Delta V_{\text{th}}$  from the  $\Delta V_{\text{FB}}$  of an identically processed capacitor is widely accepted, with the shifting and stretching of its  $C\text{-}V$  curve analogous to that of the  $I_{\text{D}}\text{-}V_{\text{GS}}$  curve in Figure 2.1 [Dressendorfer, 1989a, p.259–261].

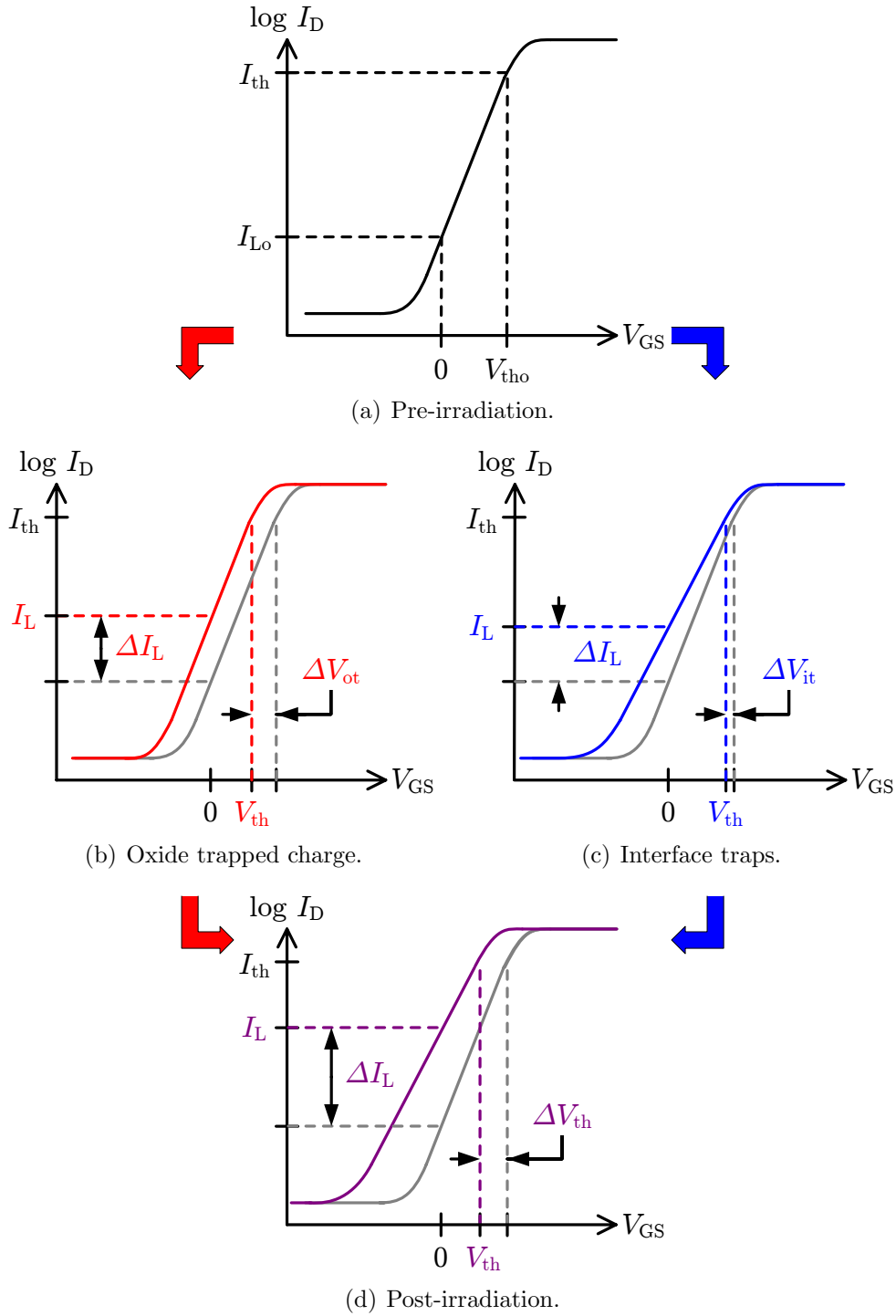


Figure 2.1: Decomposition of  $I_D$ - $V_{GS}$  curve distortions into  $\Delta V_{ot}$  and  $\Delta V_{it}$  effects for a representative nMOSFET. Extent of damage is exaggerated for clarity.

and Adams, 2002, p.137]. Indeed, the conversion from  $\Delta Q_{\text{ot}}$  to  $\Delta V_{\text{ot}}$  is given simply by the reciprocal of areal gate capacitance  $C_{\text{ox}} = t_{\text{ox}}/\epsilon_{\text{ox}}$ , such that:

$$\Delta V_{\text{ot}} = \frac{t_{\text{ox}}}{\epsilon_{\text{ox}}} \Delta Q_{\text{ot}} = -Q \frac{t_{\text{ox}}}{\epsilon_{\text{ox}}} \Delta N_{\text{ot}} \quad (2.2)$$

With the help of (C.17) and (C.18), (2.2) can be expanded to explicitly demonstrate the dependence of  $\Delta V_{\text{ot}}$  on the incident particle energy ( $E_i$ ) and the local oxide field ( $E_{\text{ox}}$ ) as

$$\begin{aligned} \Delta V_{\text{ot}} &= -Q \frac{t_{\text{ox}}^2}{\epsilon_{\text{ox}}} \mathcal{F}_y \mathcal{F}_t K_g D \\ &= -Q \frac{t_{\text{ox}}^2}{\epsilon_{\text{ox}}} \mathcal{F}_y(E_{\text{ox}}, E_i) K_g(E_i) D(E_i) \int_{\Delta x}^{t_{\text{ox}}} \sigma_{\text{pt}}(E_{\text{ox}}) N_{\text{pt}}(x) dx \end{aligned} \quad (2.3)$$

Note that, in contrast to (C.17), the integral for the trapping fraction now begins a distance  $\Delta x$  from the interface in order to describe the steady-state  $\Delta V_{\text{ot}}$  by accounting for the electron tunneling that anneals the deep traps within the first 5–20 nm of the oxide (cf. Figure C.10).<sup>6</sup> This integral can be generalized to handle the  $x$ -dependence of not only  $N_{\text{pt}}$ , but also generation ( $K_g$ ) and recombination ( $\mathcal{F}_y$ ) by introducing  $p(x)$  to denote the non-uniform trapped hole concentration through the oxide such that (2.3) reduces to

$$\begin{aligned} \Delta V_{\text{ot}} &= -Q \frac{t_{\text{ox}}}{\epsilon_{\text{ox}}} \int_{\Delta x}^{t_{\text{ox}}} \mathcal{F}_y(x, E_{\text{ox}}, E_i) K_g(x, E_i) D(E_i) \sigma_{\text{pt}}(E_{\text{ox}}) N_{\text{pt}}(x) x dx \\ &= -\frac{Q}{C_{\text{ox}}} \int_{\Delta x}^{t_{\text{ox}}} p(x, E_{\text{ox}}, E_i) x dx \end{aligned} \quad (2.4)$$

---

<sup>6</sup>It is well known that, on account of the exponential distribution of  $N_{\text{pt}}$  (cf. Footnote 24 of Appendix C),  $\Delta N_{\text{ot}}$  approximately occupies a thin sheet at a mean distance  $x_t$  from the interface [Messenger and Ash, 1992, p.308], [Holmes-Siedle and Adams, 2002, p.142]. Invoking this result allows the integral in (2.3) to degenerate to  $\sigma_{\text{pt}} N_{\text{pt}}(x_t)$ , and yields an expression for  $\Delta V_{\text{ot}} \propto t_{\text{ox}}^2$ . This quadratic relationship is commonly used to justify the intrinsic radiation tolerance of scaled CMOS technologies [McLean et al., 1989, p.152], though its applicability is questionable once  $t_{\text{ox}}$  becomes comparable to the  $\Delta N_{\text{ot}}$  sheet thickness [Holmes-Siedle and Adams, 2002, p.139]. If, instead, for a thick oxide  $N_{\text{pt}}$  is treated as uniform over the range  $\Delta x$  to  $t_{\text{ox}}$ , (2.3) reduces to an expression for  $\Delta V_{\text{ot}} \propto t_{\text{ox}}^3$  [Messenger and Ash, 1992, p.308], which only bolsters the argument.

Recall from solid-state physics that the midgap voltage  $V_{\text{mg}}$  is defined as the first moment of the oxide charge density;<sup>7</sup> (2.4) describes that same moment integral, implying  $\Delta V_{\text{ot}} \approx \Delta V_{\text{mg}}$  [Messinger and Ash, 1992, p.315]. This relationship allows  $\Delta V_{\text{ot}}$  to be determined directly by measuring the change in  $V_{\text{mg}}$  under radiation, provided  $\Delta N_{\text{it}}$  can be ignored so that the total oxide charge density is given by just  $p(x)$ . Historically, neglect of  $\Delta N_{\text{it}}$  has been justified by the fact that interface traps above midgap are acceptors while those below midgap are donors, so that all are neutral when the surface Fermi level is at midgap [Messinger and Ash, 1992, p.316]. However, the asymmetry of  $D_{\text{it}}$  described in Section C.2.6 reveals that not all interface traps possess zero charge at  $V_{\text{mg}}$ ,<sup>8</sup> so this approach can introduce errors in  $\Delta V_{\text{ot}}$  on the order of a few percent [Oldham and McLean, 2003, p.493].

Nevertheless, such measurements of  $\Delta V_{\text{ot}}$  confirm that it increases significantly with positive gate bias, since  $E_{\text{ox}} > 0$  caused the holes to be trapped near the Si-SiO<sub>2</sub> interface, rather than the gate electrode, increasing the charge moment of (2.4) [Dressendorfer, 1989a, p.263]. For this reason, the  $\Delta V_{\text{ot}}$  contribution to the threshold voltage shift for pMOS devices,  $\Delta V_{\text{thp}}$ , is about an order of magnitude less than that for nMOS devices,  $\Delta V_{\text{thn}}$ , when both are biased on during irradiation [Messinger and Ash, 1992, p.308]. In addition,  $E_{\text{ox}}$  influences  $\Delta V_{\text{ot}}$  through the conflicting field dependencies of  $\mathcal{F}_y$  and  $\sigma_{\text{pt}}$ . Specifically, the stronger the gate field, the farther newly formed  $e^-$  and  $h^+$  are separated, leading to less recombination under the geminate model ( $r_t \ll r_p$ ) and larger  $\mathcal{F}_y$  [Holmes-Siedle and Adams, 2002, p.146]; in contrast, it has been shown [Holmes-Siedle and Adams, 2002, p.146] that  $\sigma_{\text{pt}} \propto E_{\text{ox}}^{-1/2}$  [Dressendorfer, 1989a, p.264]. The net effect of  $E_{\text{ox}}$  via  $\Delta x$ ,  $\mathcal{F}_y$ , and  $\sigma_{\text{pt}}$  of (2.4) is that  $\Delta V_{\text{ot}}$  does not simply increase monotonically with larger  $V_G$ . However, as shown in Figure 2.3(a), since the peak is at or above normal operating voltages (1–2 MV/cm [Winokur, 1989, p.223]), the worst-case bias condition for the build up of  $\Delta V_{\text{ot}}$  in nMOS(pMOS) devices occurs when they are biased on(off) during irradiation

<sup>7</sup>The midgap voltage,  $V_{\text{mg}}$ , is defined as the gate voltage that must be applied to render the Fermi level at the surface equal to the energy level at the middle of the Si bandgap (i.e.,  $E_F = E_{\text{mg}}$ ) [Messinger and Ash, 1992, p.315].

<sup>8</sup>As discussed in Footnote 34 of Appendix C, the amphoteric energy levels of the  $P_{\text{b0}}$  center are indeed centered around midgap, but those of the  $P_{\text{b1}}$  center are not. Although not nearly as numerous, the latter shift the effective  $D_{\text{it}}$  toward the conduction band [McLean et al., 1989, p.493].



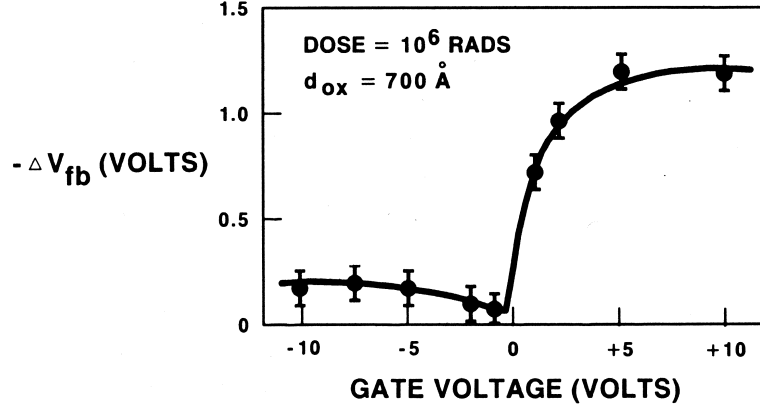


Figure 2.2: Dependence of  $\Delta V_{th}$  on static gate bias during irradiation for an n-type MOS capacitor.  $\Delta V_{thp}$  of an identically processed pMOS transistor can be inferred from  $\Delta V_{FB}$ . Reproduced *in toto* from [Dressendorfer, 1989a, p.262]

[Dressendorfer, 1989a, 264–267], as evidenced in Figure 2.2.

Although the strong increase in  $\Delta V_{th}$  for  $V_G > 0$  is well ascribed to the field-dependence of underlying parameters in (2.4), the equation is less successful in capturing the effects of dose and dose-rate. For example, while it predicts linear growth of  $\Delta V_{ot}$  with  $D(E_i)$ , this dependence only holds over low to moderate doses; at higher doses,  $\Delta V_{ot}$  saturates [Holmes-Siedle and Adams, 2002, p.152] as the number of filled traps approaches maximum capacity [Dressendorfer, 1989a, p.263]. The build up of trapped holds not only leads to more  $e^-h^+$  recombination centers, but creates a space-charge field that counteracts the applied bias thereby reducing the net internal field in the critical region of the oxide that controls  $N_{ot}$  growth through drift [Boesch et al., 1986].<sup>9</sup> The integral in (2.4) also masks the dependence of  $\Delta V_{ot}$  on  $dD/dt$ —at lower dose rates ( $< 1$  rad/s), the reduction of  $\Delta N_{ot}$  via tunnel annealing (cf. Section C.2.4) has more time to proceed, leading to less positive voltage shift than at higher rates (100 rad/s) [Winokur et al., 1986].

### $\Delta V_{it}$ Contribution

Since the corresponding variations in  $\Delta N_{it}$  with  $E_{ox}$ ,  $D(E_i)$  and  $dD/dt$  are quite

<sup>9</sup>This space charge region is believed to be responsible for the ELDRS effect described in Section 2.1.2.3.

opposite those of  $\Delta N_{\text{ot}}$  described thus far, and since the interface traps are only neutral at  $V_G = V_{\text{mg}}$ , an understanding of  $\Delta V_{\text{th}}$  behavior for all bias conditions requires a closer treatment of  $\Delta V_{\text{it}}$ . Recall from Section C.2.6 that  $P_{\text{b}}$  centers are amphoteric, with their occupancy governed by their position relative to  $E_{\text{F}}$  at the Si surface such that when an nMOS(pMOS) device is biased with  $V_G = V_{\text{th}}$  so that  $E_{\text{F}}$  is near the conduction(valence) band, most of the acceptor(donor) levels are filled by electrons(holes) and acquire a net negative(positive) charge [Messenger and Ash, 1992, p.300]. For both transistor types, the polarity of this interface trapped charge,  $\Delta Q_{\text{it}} = Q \Delta N_{\text{it}}$ , inhibits inversion and, since the number of filled traps scales with  $V_G$  through its exponential relationship to  $E_{\text{F}}$ , this leads to distortion of the logarithmic  $I_{\text{D}}-V_{\text{GS}}$  (or  $C-V$ ) curve as depicted in Figure 2.1(c), rather than simple translation [Holmes-Siedle and Adams, 2002, p.137]([Messenger and Ash, 1992, p.324]). This ‘stretching-out’ of the sub-threshold slope is characteristic of  $\Delta N_{\text{it}}$  build-up [Holmes-Siedle and Adams, 2002, p.259] and not only pushes out the  $I_{\text{inv}}$  crossing point at which  $V_{\text{th}}$  is defined, but reduces the switching speed for reaching strong inversion [Winokur, 1989, p.212].<sup>10</sup>

Although representing this nonlinear distortion through an analytical expression for  $\Delta V_{\text{it}}$  in terms of  $\Delta N_{\text{it}}$ , akin to (2.2) for  $\Delta V_{\text{ot}}$  in terms of  $\Delta N_{\text{ot}}$ , is beyond the scope of this examination, the analogous dependencies of  $\Delta V_{\text{it}}$  on  $E_{\text{ox}}$ ,  $D$ , and  $dD/dt$  merit qualitative treatment. All reflect the kinematics of radiation-induced interface trap formation, described in Section C.2.6—a two-step process in which hydrogen-passivated surface defects are activated through the transport of trapped holes and hydrogen ions. Since these carriers only drift to the surface under the influence of positive  $E_{\text{ox}}$ ,  $V_G > 0$  represents the worst-case bias for  $\Delta N_{\text{it}}$  formation, just as for the case of  $\Delta N_{\text{ot}}$  [Dressendorfer, 1989a, p.264];<sup>11</sup> the similarities are highlighted by the

<sup>10</sup>Astute observers may note that  $\Delta N_{\text{it}}$  reduces not only the sub-threshold slope, but also the slope in the saturation region (i.e., the transconductance). Although both effects can be treated as manifestations of a drop in carrier mobility, such an approach is reserved for addressing the latter in the next section, where it is more intuitively satisfying. Here, the focus is on  $\Delta V_{\text{th}}$  effects to emphasize the analogy with  $\Delta N_{\text{ot}}$ .

<sup>11</sup>For both  $\Delta N_{\text{ot}}$  and  $\Delta N_{\text{it}}$ ,  $V_G > 0$  only reflects the worst-case static bias conditions. Data suggest that the densities of these trapped charge populations can be smaller or larger, respectively, when transistors are dynamically biased or operated under nominal loads during irradiation [Holmes-Siedle and Adams, 2002; Winokur, 1989, p.149–150, p.224–225]. However, for analog circuits, in

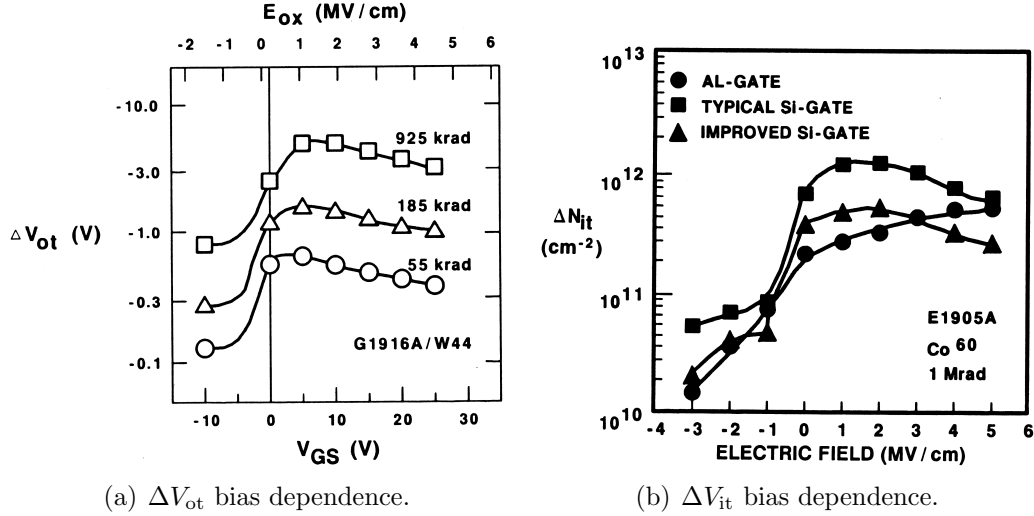


Figure 2.3: Comparison of  $\Delta V_{ot}$  and  $\Delta V_{it}$  gate-bias dependencies. In both cases, field-assisted transport of holes and ions toward the Si surface when  $E_{ox} > 0$  yields larger voltage shifts, peaking at 1–2 MeV/cm. Reproduced *in toto* from [Dressendorfer, 1989a, p.264–265]

plots of  $\Delta N_{ot}$  and  $\Delta N_{it}$  in Figure 2.3(a) and Figure 2.3(b), respectively. For  $V_G < 0$ , there is a negligible increase in density [Winokur, 1989, p.222].

Contrary to their congruent rise with  $E_{ox}$ , the differing responses of  $\Delta N_{ot}$  and  $\Delta N_{it}$  to changing dose conditions lead to opposing behaviors of  $\Delta V_{ot}$  and  $\Delta V_{it}$ . Fundamentally, the slow buildup of both trap densities is influenced by the time-varying  $\langle \tau_H \rangle$  associated with the dispersive, CTRW hole transport mechanism described in Section C.2.3. However, the growth rate is much slower for  $N_{it}$ , since hole transport only represents the first step—field-assisted  $H^+$  oxygen-hopping transport is the second, rate-limiting process [McLean, 1980]. This delayed build-up of interface traps leads to higher concentrations for low dose rates,<sup>12</sup> in opposition to the trend of  $\Delta N_{ot}$  [Dressendorfer, 1989a, p.288], which anneals given the additional time. From

which MOSFETs are not cycled on and off during normal operation but, rather, held in varying degrees of inversion at all times, only consideration of static biasing is appropriate.

<sup>12</sup>This is not at odds with the claims of Section C.2.6 because it has been shown that the increase in measured  $\Delta N_{it}$  at lower dose rates is not a ‘true’ dose rate effect, but rather one of formation time. That is, if the same dose is delivered at two samples at two different rates, but the measurements of both are made at the same time (i.e., after the slower exposure is complete),  $\Delta N_{it}$  will be identical [Winokur, 1989, 221–222].

their accrual over extended periods, negligible annealing at room temperature, and lack of any saturation mechanism with increased dose [McLean and Oldham, 1987, p.37–38], it follows that interface traps become dominant as the MOSFET is subject to higher total doses with their concomitant longer exposures.

This phenomenon is evidenced by Figure 2.4, which exemplifies the well-known ‘rebound’ [Schwank et al., 1984] or ‘super recovery’ [Johnston, 1984] effect for nMOS devices. For a given dose rate,  $\Delta N_{ot}$  form more rapidly than  $\Delta N_{it}$ , such that initially the first term of (2.1) dominates  $\Delta V_{th}$ , causing it to trend negative. With time,<sup>13</sup> as the oxide trapped charge anneals (once the exposure concludes) or its density saturates (if the exposure persists), the delayed accumulation of  $\Delta N_{it}$  can eventually result in  $\Delta V_{it}$  becoming dominant, such that the slope of  $\Delta V_{th}$  changes sign and, potentially,  $V_{th} > V_{tho}$  [Messenger and Ash, 1992, p.298–299]. Note that pMOS devices, for which both  $\Delta V_{ot}$  and  $\Delta V_{it}$  are negative, experience a monotonic decrease in  $\Delta V_{th}$  with dose, becoming increasingly difficult to invert; that is, they are not susceptible to rebound [Dressendorfer, 1989a, p.265].

Since the dynamics of nMOS rebound and the final state of  $V_{th}$  relative to  $V_{tho}$  are sensitive to the competing influences of  $\Delta N_{ot}$  and  $\Delta N_{it}$ , the non-monotonicity of  $\Delta V_{thn}$  with dose poses a threat to circuit performance in a radiation environment that is specific to the details of the transistor fabrication, particularly the quality of their oxides and interfaces.<sup>14</sup> Thus, prior to the circuit design in this work, it was necessary to characterize the devices of the target manufacturing process in order to assess the severity of radiation-induced  $\Delta V_{th}$ . The results for representative pairs of nMOS and pMOS transistors irradiated up to 1 Mrad(Si) TID using a <sup>60</sup>Co chamber (cf. Section I.1.1) are presented in Figure 2.5 and Figure 2.6, respectively.<sup>15</sup>

<sup>13</sup>Rebound is often treated as post-irradiation effect (PIE) [Messenger and Ash, 1992, p.279], but since it only depends on relative formation times and saturation limits of  $\Delta N_{ot}$  and  $\Delta N_{it}$ , it can also arise during a continuous, low dose-rate exposure, as in Figure 2.4. For this reason, its classification as merely a time-dependent effect [Holmes-Siedle and Adams, 2002, p.170] is preferred.

<sup>14</sup>Electronics for both the Ulysses and Galileo spacecraft (cf. Table B.1) experienced failures during integration tests that were attributed to rebound [Holmes-Siedle and Adams, 2002, p.175].

<sup>15</sup>These data were measured by Everett King at The Aerospace Corporation using an HP4155A semiconductor parameter analyzer. The test vehicle (MK832A), graciously provided by National Semiconductor Corporation, was fabricated in their BiCMOS8i process and contained several common-centroid, differential pairs of low-voltage nMOS (Quad H43) and pMOS (Quad H46)

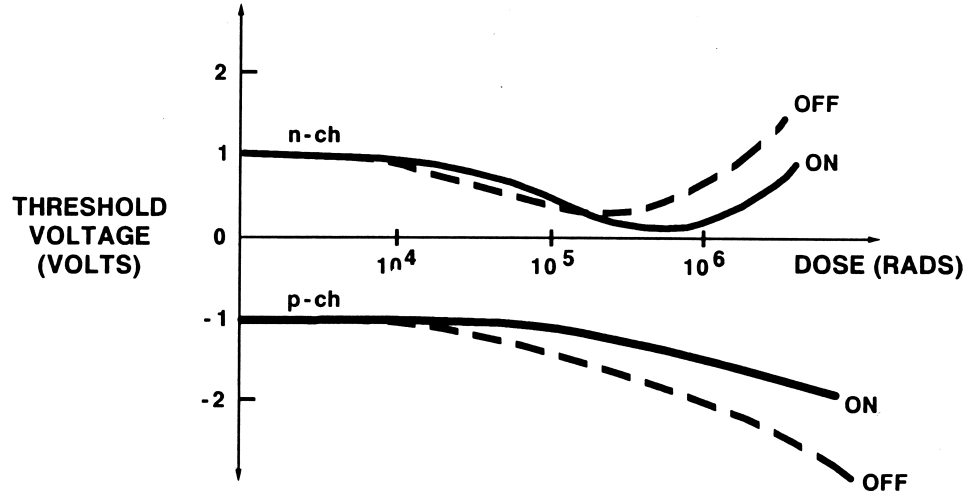
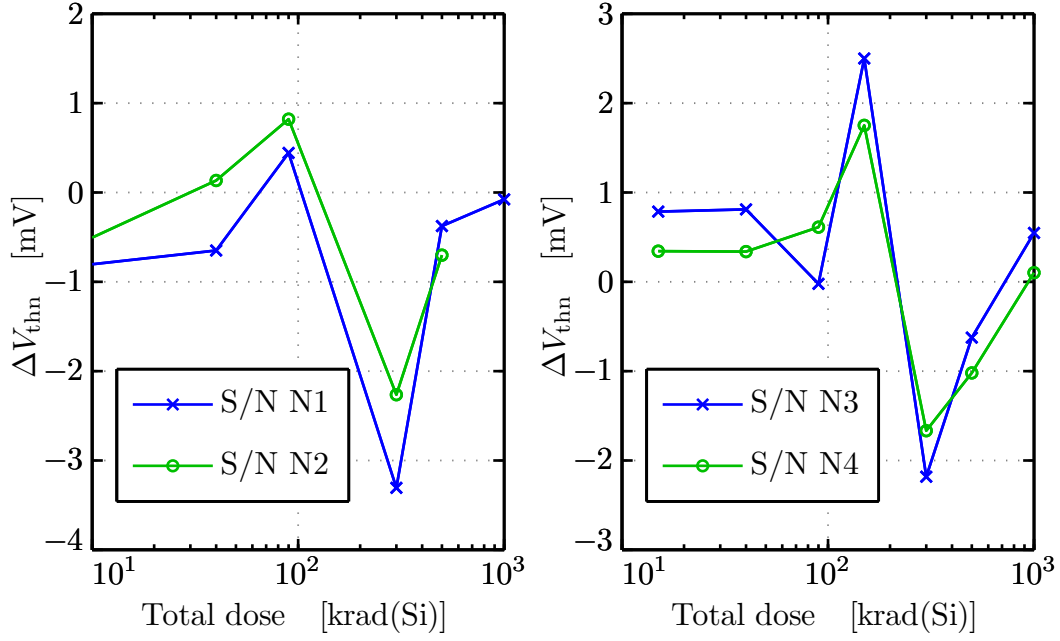


Figure 2.4: Dose dependence of  $\Delta V_{\text{thn}}$  and  $\Delta V_{\text{thp}}$  highlighting rebound of former with sufficient time for  $\Delta N_{\text{it}}$  ( $\Delta N_{\text{ot}}$ ) formation (saturation). Reproduced *in toto* from [Dressendorfer, 1989a, p.265]

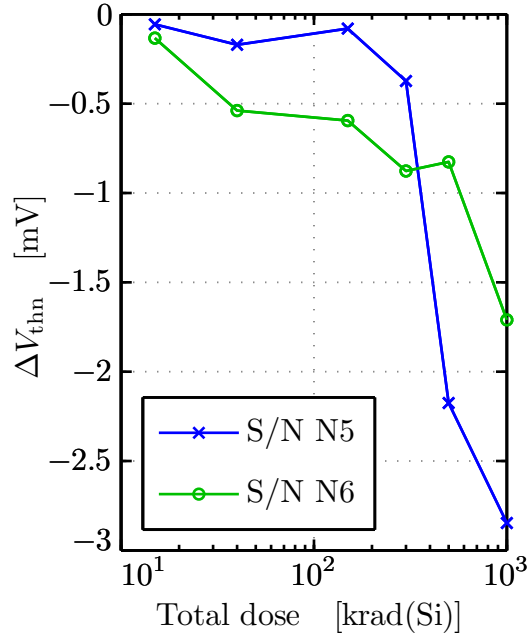
The two nMOS pairs in Figure 2.5(a), N1/N2 and N3/N4, are irradiated under worst-case bias conditions for  $N_{\text{ot}}$  and  $N_{\text{it}}$  (i.e.,  $V_{\text{GS}} = +2.5$  V) and thus exhibit rebound between 300–500 krad(Si). Although the gate oxide is sufficiently thin that net variation in  $V_{\text{thn}}$  is  $\sim 1\%$ , the susceptibility to both  $N_{\text{ot}}$  and  $N_{\text{it}}$  is clearly evident. Compared to the classic case (cf. Figure 2.4), the rise in  $\Delta V_{\text{thn}}$  prior to its  $\Delta N_{\text{ot}}$ -induced decline is postulated to reflect a prompt component of  $N_{\text{it}}$  [Winokur, 1989, p.215] whose effect supercedes that of  $N_{\text{ot}}$  initially because the latter is not significant below 100 krad(Si) for this  $t_{\text{ox}}$ . Biased with  $V_{\text{GS}} = V_{\text{DS}} = 0$ , so as to eliminate  $E_{\text{ox}}$ , the pair in Figure 2.5(b) shows higher tolerance, as expected: to offset a longer  $\Delta x$ , higher doses are required to achieve a charge moment for  $\Delta Q_{\text{ot}}$  that induces significant decline of  $\Delta V_{\text{thn}}$ ; and, in the absence of a positive oxide field,  $\Delta N_{\text{it}}$  formation is negligible, eliminating rebound. Comparing these results to  $\Delta V_{\text{thp}}$  in Figure 2.6 it is significant that the latter is nearly monotonic in its radiation-induced decline. Despite a drop in  $\Delta V_{\text{thp}}$  of nearly 1% at 1 Mrad(Si),<sup>16</sup> the predictability of

devices. Those depicted here, with gate widths(lengths) of  $34.88 \mu\text{m}$  ( $0.24 \mu\text{m}$ ) best match the typical sizings used in the front-end circuitry.

<sup>16</sup>The introduction of an unexplained offset between the pre-irradiation measurement of  $V_{\text{thpo}}$  and subsequent measurements at each dose step has translated the curves of Figure 2.6 such that



(a) Worst-case bias.



(b) Zero-bias.

Figure 2.5: Measured  $\Delta V_{thn}$  of representative nMOS pairs sized at 34.88/0.24. All are irradiated with  $V_S = V_D = V_B = 0$  V but  $V_G$  of (a) N1–N4 is worst-case (+2.5 V) while that of (b) N5/N6 is 0 V. Markers indicate measured data points.

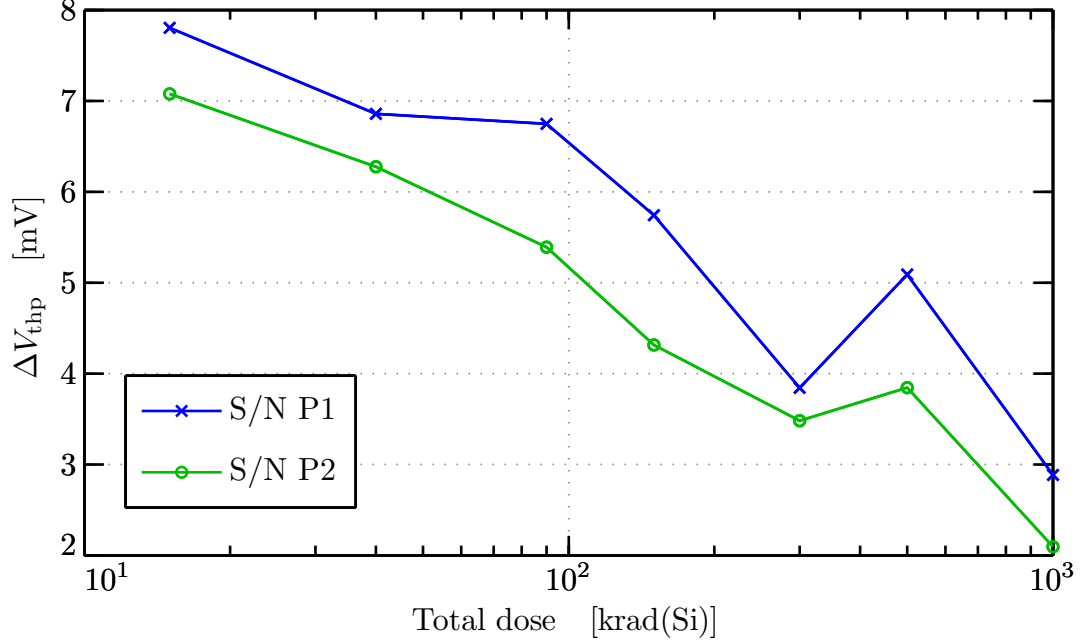


Figure 2.6: Measured  $\Delta V_{\text{thp}}$  of pMOS pair from target process under zero-bias ( $V_{\text{GS}} = 0$  V). Both P1 (in blue) and P2 (in green) are representatively sized at 34.88/0.24 and irradiated with all terminals grounded. Differences are measured with respect to pre-irradiation  $V_{\text{thp}}$  of  $-561$  mV and  $-569$  mV, respectively. Markers indicated measured data points.

its degradation curve compared to the nMOS rebound under worst-case conditions proves advantageous in designing robust reference networks (cf. Section G.2.2.2).

### 2.1.1.2 Transconductance

Section C.3.5 introduces the notion that vacancy-related acceptor defects in bulk Si can serve as additional centers for Coulomb scattering once activated. A similar phenomena takes place at the surface, where the additional impurities take the form of charged interface traps,  $\Delta Q_{\text{it}}$ , that scatter majority carriers in the channel, reducing

---

$\Delta V_{\text{thp}} > 0$ . Nevertheless, as is appropriate, the error grows more negative with dose, as in Figure 2.4, since by definition  $V_{\text{thp}} < 0$ .

their effective mobility.<sup>17</sup> For an nMOSFET,<sup>18</sup> this is can be represented by an empirical relationship between the effective mobility and  $\Delta N_{it}$  analogous to (C.30) [Winokur, 1989, p.213],

$$\mu_n = \frac{\mu_{no}}{1 + \alpha_\mu \Delta N_{it}} \quad (2.5)$$

in which the initial mobility,  $\mu_{no}$ , is inversely proportional to the radiation-induced interface trap density through a fitting parameter,  $\alpha_\mu$ .<sup>19</sup> Although known to be independent of  $\Delta N_{ot}$  [Dressendorfer, 1989a, p.271], this mobility degradation is subject to the same  $\Delta N_{it}$  dependences ascribed to  $\Delta V_{th}$  in the preceding sub-section, including a steeper decline for both  $E_{ox} > 0$ , and higher, low-rate doses.

In addition to the flattening of the sub-threshold slope discussed previously, this mobility degradation manifests in a reduction of the slope of the  $I_D$ - $V_{GS}$  curve in the saturation region (cf. Figure 2.1). From first principles, this slope, representing the voltage-to-current gain of a saturated MOSFET, is defined, in the long-channel limit, as the transconductance,  $g_m$ , according to [Pierret, 1990, p.82–83]:

$$g_m = \frac{\partial I_{DS}}{\partial V_{GS}} = \mu C_{ox} \frac{W}{L} (V_{GS} - V_{th}) \quad (2.6)$$

Through this proportionality,  $g_m$ -degradation directly reflects the dose-dependence of (2.5), provided that the effect of  $\Delta V_{th}$  is obviated by taking the maximum value of the slope of the  $I_D$ - $V_{GS}$  curve,  $\max\{g_m\}$ . Invoking (C.19), the explicit dependence of

---

<sup>17</sup>Compared to the bulk mobility described in (C.31), which accounts for both lattice and ionized-impurity scattering, the effective mobility of MOS carriers in the channel is lowered by the effects of collisions with the Si surface. Rather than replacing the  $\mu_{ni}$  term, this actually introduces a third term ( $\mu_{ns}$ ) into (C.31) which is weighted by  $E_{ox}$ , being more significant as stronger fields attract more carriers to the surface. Henceforth, references to  $\mu_n$  or  $\mu_p$  in MOS context shall refer to this effective mobility, despite having omitted a quantitative description of the  $\mu_{ns}$  term heretofore [Pierret, 1990, p.70–73].

<sup>18</sup>Since the polarity of  $\Delta N_{it}$  matches that of the majority carriers in both nMOS and pMOS devices, (2.5) can be generalized to describe the mobility dependence of each, but is merely presented in nMOS form for simplicity.

<sup>19</sup>A typical value of  $\alpha_\mu$  that has been used for a wide variety of experimental conditions is  $8 \pm 2 \times 10^{-13} \text{ cm}^{-2}$  [Winokur, 1989, p.213].



$g_m$  on dose through  $N_{it}$  is:

$$\max\{g_m\} = \max\left\{\frac{\mu_o C_{ox}}{1 + \alpha_\mu K_i t_{ox}^n D^{2/3}} \frac{W}{L} (V_{GS} - V_{th})\right\} \quad (2.7)$$

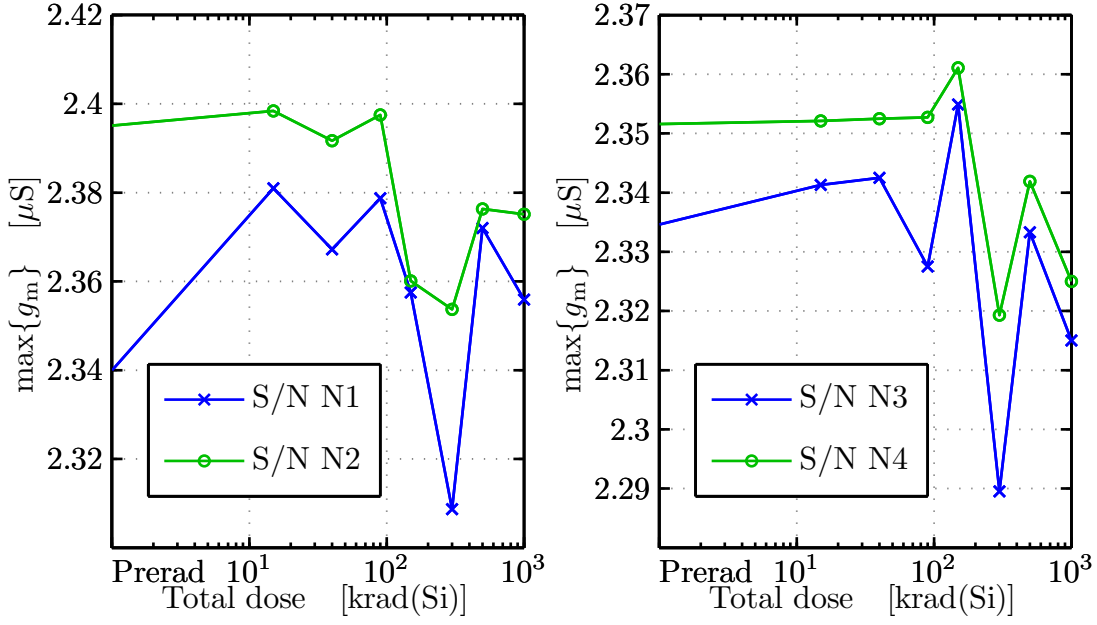
Given its evident dependence on both the thickness ( $t_{ox}$ ) and quality ( $\alpha_\mu$ ,  $K_i$ ,  $\mu_o$ ) of the gate oxide, this quantity has been measured for the aforementioned devices as part of the characterization of the target manufacturing process (cf. Footnote 15), with the results depicted in Figure 2.7 and Figure 2.8.

For the nMOS devices under worst-case bias in Figure 2.7(a), the variations of  $g_m$  with dose are quite small, but also non-monotonic, violating the relationship in (2.7). The undulations, in particular the increases above 300 krad(Si), invoke the character of Figure 2.5 and suggest the influence of  $\Delta N_{ot}$ . Although typically a second-order effect [Dressendorfer, 1989a, p.271], positive charge trapped in the thicker spacer oxides over the lightly-doped drain (LDD) regions of an nMOS transistor can play a role in  $g_m$ -degradation [Holmes-Siedle and Adams, 2002, p.185]. By increasing the surface doping at the edges of the channel, such charge effectively extends the source and drain regions, thereby shortening the channel and increasing  $g_m$  through decreasing  $L$  in (2.6) [Hughes and Benedetto, 2003; King et al., 2000].<sup>20</sup> In the absence of the positive oxide field required to increase the  $\Delta N_{ot}$  yield and charge moment, the nMOS pair in Figure 2.7(b), biased with  $V_{GS} = 0$ , exhibits the steady decline predicted by the general form of (2.7).

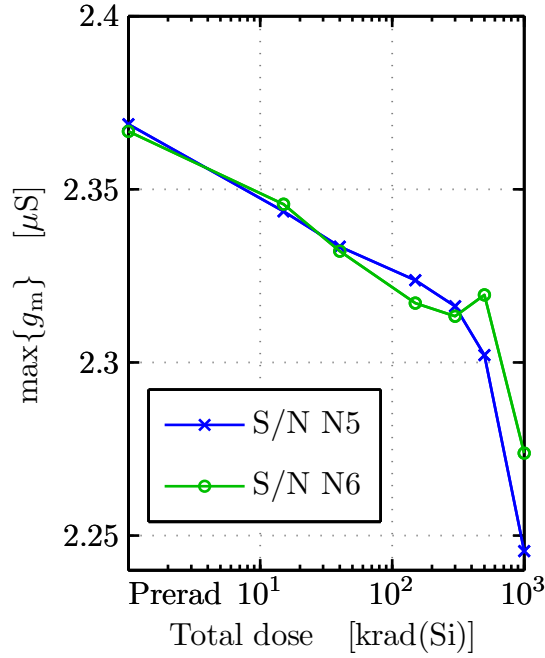
Although the absolute degree of gain loss in Figure 2.7(a) is small, this near-monotonicity of Figure 2.7(b) is more desirable, reflecting well-understood physical mechanisms and permitting the design of circuits which can take advantage of the expected trend (e.g., Section G.2.2.2). However, since it is not possible to operate nMOS devices with  $V_{GS}=0$  in most analog contexts, the alternative is to consider the behavior of the pMOS pair in Figure 2.8. Aside from the 1-Mrad(Si) dose step, where trapped charge in the spacer oxide may become sufficient to widen the channel and further depress  $g_m$ , the responses of both devices closely match the fit line for (2.7).

---

<sup>20</sup>That  $\Delta N_{ot}$  results in a mounting slope of the  $g_m$ -curve at high dose, regardless of the underlying mechanism, is notably opposite to the trend of  $\Delta V_{th}$ , as is the fact that  $\Delta N_{it}$  leads to a drop in  $g_m$  under low dose conditions.



(a) Worst-case bias.



(b) Zero-bias.

Figure 2.7: Measured  $g_m$ -degradation of nMOS pairs from target process whose  $\Delta V_{\text{thn}}$  is described in Figure 2.5. Again, (a) N1-N4 are irradiated with  $V_G = 2.5$  V and (b) N5/N6 with  $V_G = 0$  V. Markers indicate measured data points.

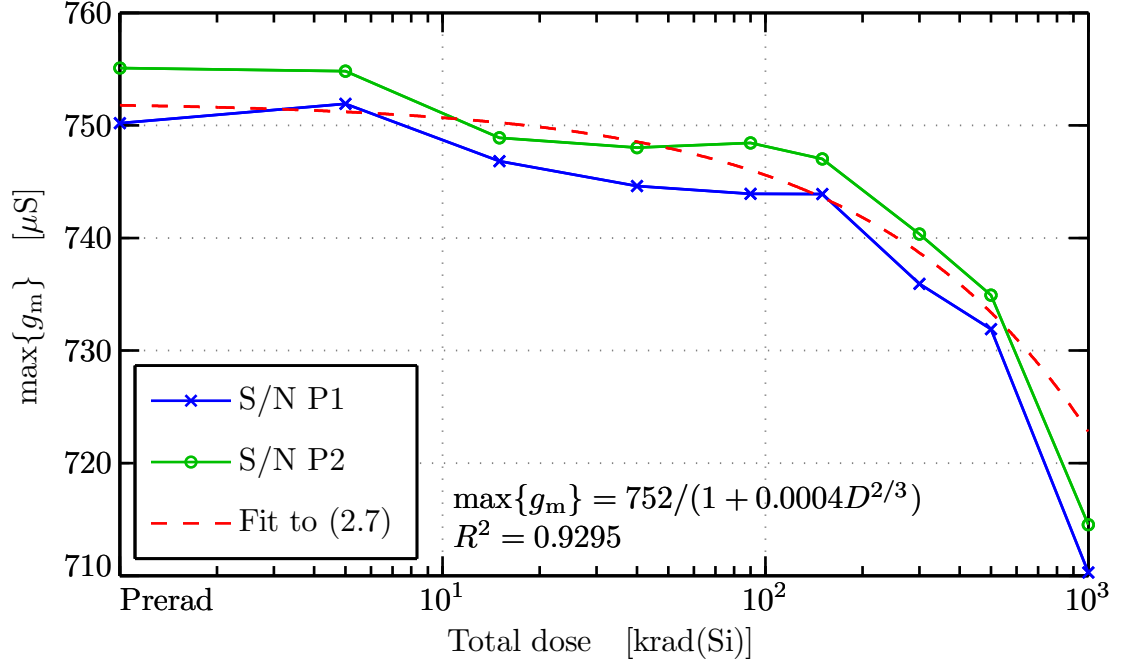


Figure 2.8: Measured  $g_m$ -degradation of pMOS pair from target process under zero-bias ( $V_{GS}=0$  V). Below 1 Mrad(Si), the average behavior of  $\max\{g_m\}$  for devices P1 (in blue) and P2 (in green), whose  $\Delta V_{thp}$  is described in Figure 2.6, is fit to (2.7) (in red). Markers indicate measured data points.

Despite an average drop in  $\max\{g_m\}$  of -5.35% at 1 Mrad(Si), the robust monotonicity of these devices proves a valuable tool in limiting the worst-case power dissipation of the front-end.

### 2.1.1.3 Leakage Current

Although  $\Delta N_{it}$  buildup increases  $I_D$  for  $V_{GS} < V_{th}$  through its effect on the subthreshold slope of Figure 2.4, as cited previously, a more significant rise in the off-state current through the MOSFET, dubbed the leakage current  $I_L$  [Messinger and Ash, 1992, p.330] occurs when positive oxide trapped charges accumulate not in the thin  $\text{SiO}_2$  film beneath the polysilicon gate, but in the much thicker field oxides used for isolation between devices [Holmes-Siedle and Adams, 2002, p.160]. In such cases the component of  $I_L$  due to  $\Delta N_{it}$ -induced slope changes (dubbed subthreshold

leakage and denoted  $I_{\text{sub}}$ ) is dwarfed by charge flowing in one of two parasitic paths,<sup>21</sup> depicted in Figure 2.9 [Dressendorfer, 1989a, p.273]: an intra-device connection from source to drain beneath the field oxide that defines the gate width; or, an inter-device path beneath the field oxide that separates the source/drain diffusions of neighboring MOSFETs or well taps. In either case, this radiation-induced shunt current,  $I_{\text{fox}}$ , is carried through what can be modeled as a field-oxide transistor (FOXFET) [Holmes-Siedle and Adams, 2002, p.480], in which  $\Delta N_{\text{ot}}$  is responsible for  $\Delta V_{\text{th}}$  variations through the same mechanisms as in the main device.

Such FOXFET  $\Delta V_{\text{th}}$ -modulation is more severe than in standard transistors because field oxides are typically much thicker and of much lower quality, not being controlled by the same process tolerances. The former property significantly increases  $V_{\text{th}}$  through the  $t_{\text{ox}}^2$  dependence of (2.3) whereas the latter increases the density of  $E'$  precursors and thus  $\mathcal{F}_t$  [Osborn et al., 1998].<sup>22</sup> As shown in Figure 2.10, these large shifts in FOXFET  $V_{\text{th}}$  can result in an increase of several orders of magnitude in  $I_{\text{fox}}$  (and, thus, the overall  $I_L$ ) at doses as low as 60 krad(Si).

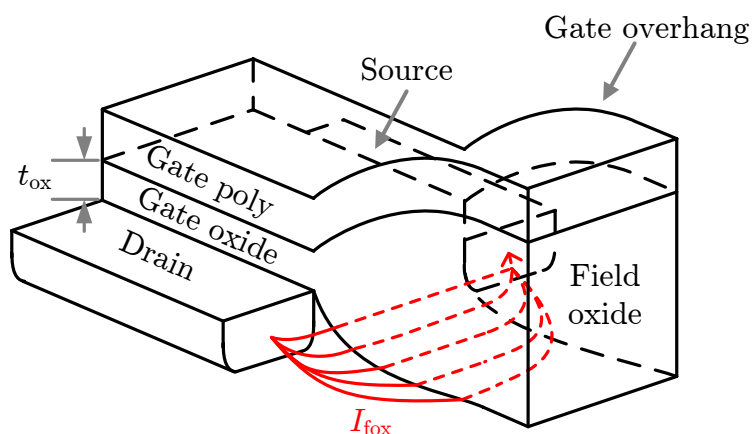
In modern commercial CMOS and BiCMOS technologies, including that employed here, standard field oxide isolation structures, such as the so-called bird's beak of Figure 2.9(a) that differentiates the local oxidation of silicon (LOCOS) technique [Hastings, 2006, p.49], are often replaced by shallow or deep trench isolations (STI or DTI, respectively).<sup>23</sup> These nearly vertical grooves (cf. Figure 2.11), approximately

---

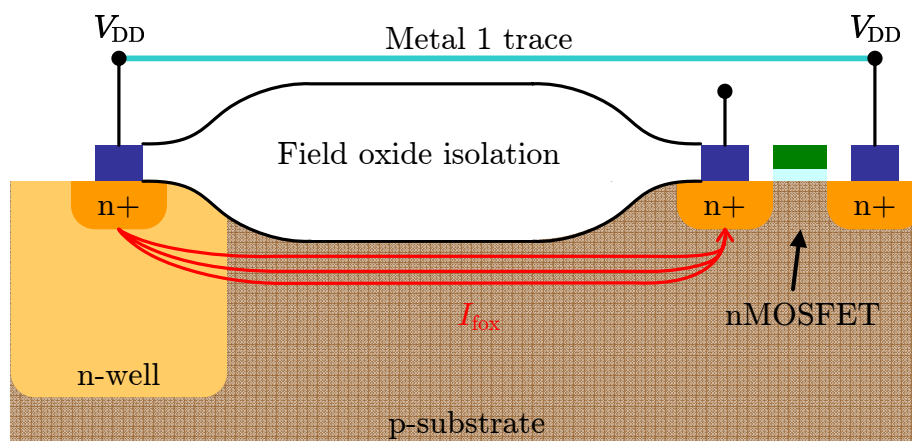
<sup>21</sup>Junction leakage from the source/drain terminals into the bulk constitutes a third leakage path, but is much more significant for bipolar devices, so its treatment is left to Section 2.1.2.2. A fourth type of leakage, ambiguously denoted as radiation-induced leakage current (RILC), can become significant for thin-gate devices ( $t_{\text{ox}} < 10$  nm) in which carriers are able tunnel directly from gate to substrate with assistance from radiation-induced oxide traps [Oldham and McLean, 2003, p.495]. Whereas these  $I_G$  increases can be significant for precision analog circuit operation [Larcher et al., 1999], such effects prove negligible in this design.

<sup>22</sup>Poor Si-SiO<sub>2</sub> interface quality also results in more  $P_b$  precursors and thus larger  $\Delta N_{\text{it}}$  in the FOXFET. Although, in theory, this effect is beneficial in countering the drop in threshold voltage through rebound, and has indeed been intentionally employed in radiation-hardened processes, the longer time scales for interface trap formation, especially in light of the limiting  $H^+$  transport through less ordered field oxides, render such methods unreliable.

<sup>23</sup>For commercial foundries, the motivations for transitioning from LOCOS to STI, or other dielectric isolation methods, are unrelated to radiation hardening *per se* and include: increased speed, through the elimination of junction-isolation capacitances; higher densities resulting from less lateral diffusion; and compatibility with other process steps, in light of the ease of planarization [Hastings, 2006, p.110]. However, in some instances, they can possess advantages for radiation-hardening as



(a) Intra-device (edge) leakage.



(b) Inter-device (isolation) leakage.

Figure 2.9: MOSFET leakage paths in LOCOS-isolated technology.  $I_{fox}$  is conducted through a FOXFET formed by: (a) the source/drain diffusions of the main device and the thick field oxide beneath the gate overhang (overhead view); (b) a metal supply line over the thick field oxide isolating an n-well tap from a neighboring nMOS source/drain diffusion (cut-away view). Drawing dimensions are exaggerated for clarity. After [Dressendorfer, 1989a, p.273].

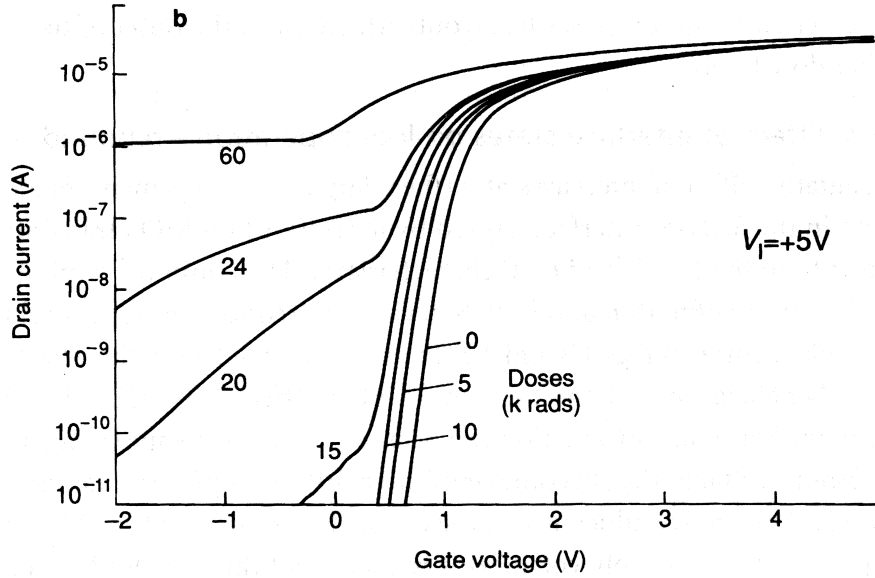


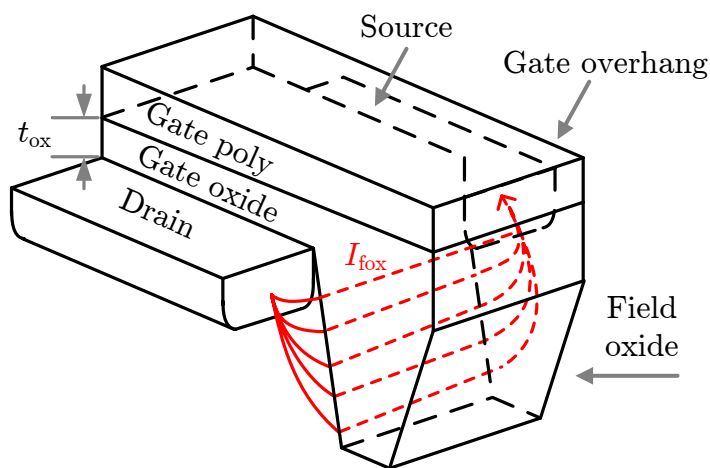
Figure 2.10: Observed TID-induced leakage for LOCOS isolation. Though it only accounts for  $I_{\text{fox}}$  leakage along the path of Figure 2.9(a), data for an nMOSFET ( $t_{\text{ox}} = 50$  nm) biased at  $V_{\text{GS}} = 5$  V during irradiation exhibit a significant increase above 20 krad(Si). Reproduced *in toto* from [Holmes-Siedle and Adams, 2002, p.161].

0.5  $\mu\text{m}$  deep, are ion-etched and their walls thermally oxidized before being completely filled via  $\text{SiO}_2$  deposition [Plummer et al., 2000, p.57–60]. Capable of offering smaller charge collection volumes than traditional LOCOS [Holmes-Siedle and Adams, 2002, p.184], such techniques still involve a sensitive Si-SiO<sub>2</sub> interface that can suffer from charge trapping and thus edge leakage along the path in Figure 2.11(a) [Niu et al., 1999]. In addition, there remains a shunt path akin to that of Figure 2.9(b) which allows charge to flow between the source/drain and neighboring n-type diffusions, albeit only by passing under the trench [Shaneyfelt et al., 1998, p.2584].

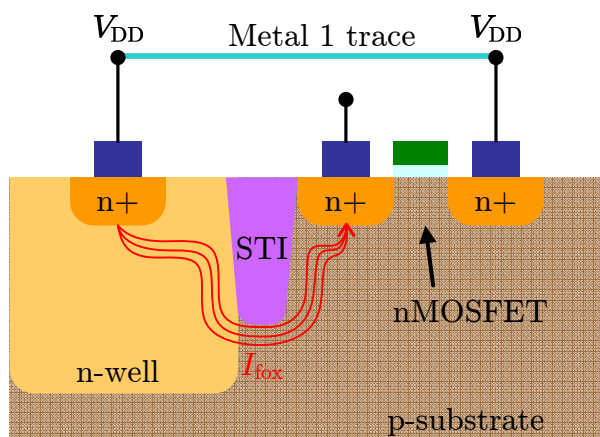
Having merely rotated the problematic plane by 90°, it has been shown that, barring sophisticated process modifications [Brady et al., 1999], nMOS devices using STI can demonstrate just as much leakage as those isolated with LOCOS, as evidenced by juxtaposing Figure 2.12 with Figure 2.10 [Shaneyfelt et al., 1998, p.2584]. For, a SiGe BiCMOS technology comparable to the one employed here, sidewall leakage

---

well, including reduced leakage [Shaneyfelt et al., 1998] and latchup tolerance [Holmes-Siedle and Adams, 2002, p.184].



(a) Intra-device (edge) leakage.



(b) Inter-device (isolation) leakage.

Figure 2.11: MOSFET leakage paths in shallow-trench-isolated technology.  $I_{\text{fox}}$  is conducted: (a) between the source/drain diffusions of the main device along the sidewall of the field-oxide-filled trench beneath the gate overhang (overhead view); (b) along the lateral and bottom perimeter of the trench isolating an n-well tap from a neighboring nMOS source/drain diffusion (cut-away view). Drawing dimensions are exaggerated for clarity. After [Shaneyfelt *et al.*, 1998, p.2585].

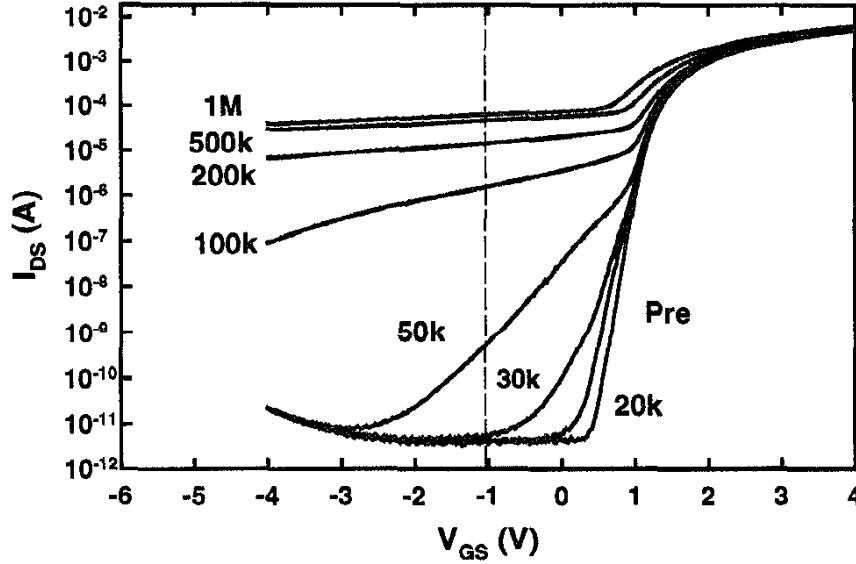


Figure 2.12: Observed TID-induced leakage for shallow-trench isolation. Though only accounting for  $I_{\text{fox}}$  leakage along the path of Figure 2.11(a), these data, obtained by illuminating a 20/0.75 nMOSFET biased at  $V_{\text{GS}} = 5$  V with 10-keV X-rays at 167 rad(SiO<sub>2</sub>)/s, exhibit a significant increase above 50 krad(Si), rendering STI only about  $2.5\times$  better than LOCOS (cf. Figure 2.10). Reproduced *in toto* from [Shaneyfelt *et al.*, 1998, p.2586].

along the face of the trench, with the FOXFET  $\Delta N_{\text{ot}}$  exhibiting a strong dependence on the field produced by  $V_G$  during irradiation, has been reported [Niu *et al.*, 1999]. However, for STI just as for LOCOS [Oldham *et al.*, 1987], processes-specific properties of the field oxide such as its thickness and quality render it “basically impossible to predict the response of such an oxide, without studying the particular oxide in question,” [Oldham and McLean, 2003, p.495]. To that end,  $I_L$  measurements of representative nMOS transistors from the target manufacturing process were conducted using a  $^{60}\text{Co}$  source to reach TID levels up to 2 Mrad(Si).<sup>24</sup> Reported in [Wang, 2009], these confirm the rise in off-state current, and are both quantitatively

<sup>24</sup>In place of the MK832A test vehicle described previously, a custom set of test structures were included on the SVADC-1 die fabricated by Stanford University in National Semiconductor Corporation’s BiCMOS8iED process (cf. [Wang, 2009] for greater detail) to facilitate these measurements, all of which were conducted through a collaboration between engineers from Stanford and The Aerospace Corporation. There is believed to be little difference between the MOS structures and the dielectric isolation used on both chips.



and qualitatively comparable to Figure 2.12, with  $I_L$  growing by about 3(6) orders of magnitude at 100 krad(Si)(1 Mrad(Si)).

#### 2.1.1.4 Noise

Recall from Section C.2.5 that oxide traps in the form of  $E'$  centers that occur within 2–3 nm of the Si-SiO<sub>2</sub> interface are known as borders traps and can exchange carriers with the bulk over a wide range of time scales encompassing those of both slow  $N_{ot}$  ( $> 1$  s) and fast  $N_{it}$  ( $< 1$  s) sites [Fleetwood et al., 1994b, p.1953]. After two decades of research, it is now believed that these defects, arising from oxygen-vacancy precursors, are responsible for flicker, or  $1/f$  noise, in MOSFETs, which is characterized by an increasing spectral density with decreasing frequency [Fleetwood et al., 2002]. Just as for the CTRW transport model (cf. Section C.2.3), this inverse frequency dependence arises from considering a random process with a trapping time  $\delta$ , given by a distribution,  $P(\delta)$ , that possesses not one but a wide range of characteristic time-constants. If, once again, that broad distribution can be represented by  $P(\delta) \propto \delta^{-1}$  for  $\delta_1 \leq \delta \leq \delta_2$ , then its power spectral density (PSD, in V<sup>2</sup>/Hz) is known to obey [Xiong et al., 2002, p.2718]:

$$S(\omega) \propto \int_{\delta_1}^{\delta_2} \frac{\delta}{1 + \delta^2 \omega^2} P(\omega) d\delta \propto \omega^{-1} \quad \text{for } \omega_2 \leq \omega \leq \omega_1 \quad (2.8)$$

For a MOSFET biased in the linear regime ( $V_{DS} < V_{GS} - V_{th}$ ) at room-temperature, experimental data largely conform to a semi-empirical model which captures that proportionality through two constants,  $K_F$  and  $\alpha_F$ , as [Scofield et al., 1989, p.1949]

$$S_v(f) = \frac{K_F}{f^{\alpha_F}} \left( \frac{V_{DS}}{V_{GS} - V_{th}} \right)^2 \quad (2.9)$$

where  $S_v(f)$  is the power spectral density of the noise voltage referred to the drain. The exponent  $\alpha_F$ , typically in the range 0.75–1.10 [Meisenheimer and Fleetwood, 1990, p.1697], accounts for deviations from ‘true’  $1/f$  noise,<sup>25</sup> whereas the coefficient

---

<sup>25</sup>The result in (2.8) only holds provided that the corresponding distribution of activation energies over the range  $E_1 \leq E \leq E_2$ , being related to  $\delta$  by  $\delta = \delta_o e^{-E/kT}$ , is constant. In reality, there is a

$K_F$  can be interpreted as the normalized drain voltage PSD, independent of the bias voltages in the parenthetical term [*Messenger and Ash*, 1992, p.701].

Assuming that the requisite underlying random process is, in fact, the action of border traps capturing carriers near the surface, giving rise to stochastic fluctuations in the carrier number density [*Fleetwood et al.*, 1994b, p.1954],<sup>26</sup> and assuming that the areal border traps energy density,  $D_{bt}$ , is uniformly distributed in space (within 2–6 nm of the oxide) [*Fleetwood et al.*, 1994b, p.1956] and in energy (within a few  $kT$  of  $E_F$  at the surface) [*Fleetwood et al.*, 2002, p.2675],<sup>27</sup> then it has been shown by *Scofield et al.* [1989] that  $K_F$  is approximately proportional to  $D_{bt}$  [*Meisenheimer and Fleetwood*, 1990, p.1696] according to

$$K_F = D_{bt} \frac{q^2 kT}{C_{ox}^2 WL} \ln^{-1} \frac{\delta_2}{\delta_1} \quad (2.10)$$

To confirm this causative relationship with  $D_{bt}$ , *Meisenheimer and Fleetwood* [1990] and others [*Fleetwood et al.*, 1994b, 2002; *Xiong et al.*, 2002] showed that the radiation-induced change in  $K_F$ ,  $\Delta K_F$ , is proportional to  $\Delta N_{ot}$ , but shows no correlation with  $\Delta N_{it}$  below 10 kHz [*Meisenheimer and Fleetwood*, 1990, p.1700]; if interface traps are not relevant, and if border traps are the only oxide traps capable of exchange charge with the bulk, then by deduction,  $N_{bt}$  must be responsible for the  $1/f$  noise. Assuming that, prior to irradiation  $N_{bt} \propto N_{ot}$ , since they share common

---

temperature-dependent distribution of activation energies for the  $E'$  centers,  $P(E_o)$ . But, as long as  $P(E_o)$  is slowly varying with  $kT$  around  $E_F$ , then (2.9) holds with  $\alpha_F$  in the stated range [*Xiong et al.*, 2002, p.2719].

<sup>26</sup>In practice,  $1/f$  noise also reflects random variations in the mobility of channel carriers as a result of scattering off interfacial traps [*Fleetwood et al.*, 1994b, p.1654], but the dominance of number fluctuation is presumed dominant in this model [*Fleetwood et al.*, 2002, p.2675].

<sup>27</sup>Such conditions on border trap locations and energies, which are required for an analytical solution, may seem overly restrictive and unphysical. This is because the model in question assumes that carrier trapping takes the form of thermally activated tunneling, which would only occur with the required frequency profile for moderate activation energies. However, the actual trapping mechanism involves a conformational change in the  $E'$  center once it has captured an electron. This so-called network relaxation raises the trap energy level from below  $E_F$ , which favored  $e^-$  capture, to above it, which favors emission. Thus,  $E_o$  (cf. Footnote 25) and  $\delta$  actually represent the energy and time, respectively, that are required for thermal reconfiguration of the defect, not the tunneling in and out of the trap, since the former process is rate-limiting in terms of the  $1/f$  dynamic [*Fleetwood et al.*, 2002, p.2678]. Nevertheless, (2.10) succeeds in describing the observed behavior.

oxygen-defect precursors, and further assuming that the cross-section for the capture of an electron by a border trap is the same as that for the capture of a hole by an oxide trap, then from (C.17),  $D_{\text{bt}} \simeq \mathcal{F}_t / E_g \sigma_{\text{pt}}$ . Combining this with (2.9) and (2.10) gives [Scofield *et al.*, 1989, p.1950]:

$$S_v(f) = \frac{1}{f^{\alpha_F}} \frac{q^2 kT}{C_{\text{ox}}^2 W L E_g} \frac{\mathcal{F}_t}{\sigma_{\text{pt}}} \left( \frac{V_{\text{DS}}}{V_{\text{GS}} - V_{\text{th}}} \right)^2 \ln^{-1} \frac{\delta_2}{\delta_1} \quad (2.11)$$

The dose dependence of  $1/f$  noise is contained in three terms of (2.11): it increases due to radiation-induced  $\Delta N_{\text{bt}}$  via the trapping fraction  $\mathcal{F}_t$ ; it varies inversely with the  $\Delta V_{\text{th}}$  variations described previously, which can be positive or negative depending on device type and dose; and assuming constant current, it increases as  $V_{\text{ds}}$  grows to compensate for mobility degradation [Fleetwood *et al.*, 1994b, p.1959]. The net effect of the first influence is represented in Figure 2.13, which demonstrates that for an nMOSFET  $\Delta N_{\text{bt}}$  leads to nearly an order of magnitude increase in  $S_v(f)$  at 500 krad(Si).

To better anticipate the radiation susceptibility of  $S_v(f)$  for transistors in the target process, Figure 2.14 shows data obtained by Anelli *et al.* [2001] for variations of  $K_F$  (which they call  $K_a$ ) in a 0.25- $\mu\text{m}$  CMOS technology irradiated up to 100 Mrad(Si). At 54 Mrad(Si), the pMOS(nMOS) devices show an  $1.6 \times (3.5 \times)$  increase in  $1/f$  noise, which is representative of both the  $1.5 \times - 5 \times$  range associated with modern oxide thicknesses and the tendency for pMOS degradation to be slightly more pronounced. Additionally,  $K_F$  for the pMOS device is nearly an order of magnitude lower than for the nMOS, as is expected since the oxide tunneling barrier for holes is higher than that for electrons [Anelli *et al.*, 2001, p.365] and it does not benefit from annealing, since hole traps are not effectively neutralized unless negative bias is employed [Fleetwood *et al.*, 1994b, p.1961].<sup>28</sup> Finally, though not pictured, Anelli *et al.* [2001] reports only negligible variation in MOSFET thermal noise as a function of TID, justifying the exclusive consideration of  $K_F$  in this work.

---

<sup>28</sup>During an anneal, negative(positive) bias attracts holes(electrons) to the border traps, and expels electrons(holes) filling the traps so that there are less available to extract holes(electrons) from the pMOS(nMOS) channel current, reducing its noise.

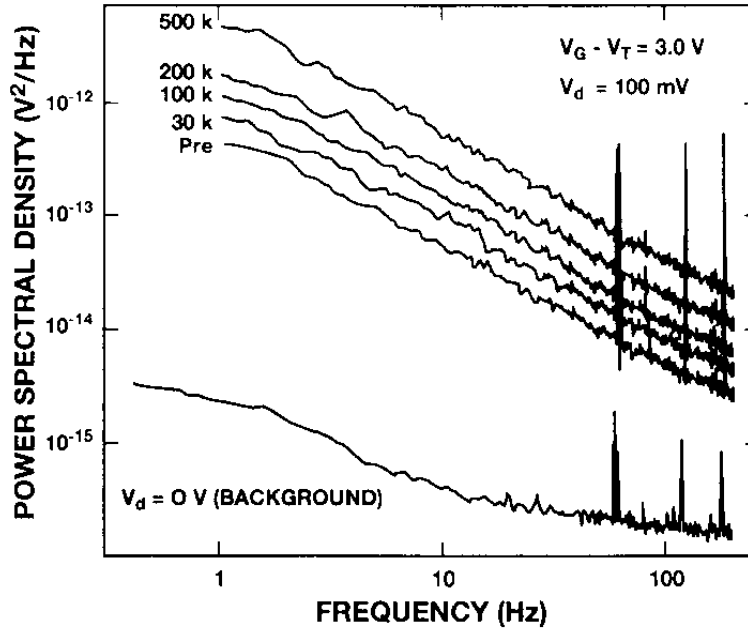


Figure 2.13: Dose dependence of  $1/f$  noise PSD for an nMOS transistor ( $W/L=16/3$ ) with a moderately radiation-hardened oxide when irradiated with  $^{60}\text{Co}$ . To isolate the effect of  $\Delta N_{\text{bt}}$ ,  $V_{\text{DS}}$  and the overdrive voltage ( $V_{\text{GS}}-V_{\text{th}}$ ) were held constant across all steps. Reproduced *in toto* from [Fleetwood *et al.*, 1994b, p.1959]

## 2.1.2 Bipolar Transistors

Although modern bipolar technologies have the potential to be fairly robust to the effects of total dose irradiation [Holmes-Siedle and Adams, 2002, p.240],<sup>29</sup> in practice they are subject to gain, leakage, and noise degradation mechanisms whose severities are determined by process subtleties that typically receive little attention from manufacturers and thus vary widely within and between foundries [Messenger and Ash, 1992, p.333]. The quality of the as-processed Si(SiO<sub>2</sub>) not only controls the initial concentrations of bulk(oxide and interface) trapping sites responsible for minority and majority effects (cf. Section C.3.4 and Section C.3.5), but influences the

<sup>29</sup>The distinction between modern, integrated BJTs and their discrete forerunners is pronounced. The latter, which were discovered *ex post facto* to be responsible for the Telstar failure described in Footnote 1 of Chapter 1 [Pease, 2003, p.539], are much more susceptible on account of their larger charge collection volumes and the secondary radiation produced by photo-ionization of their packaging [Holmes-Siedle and Adams, 2002, p.227].

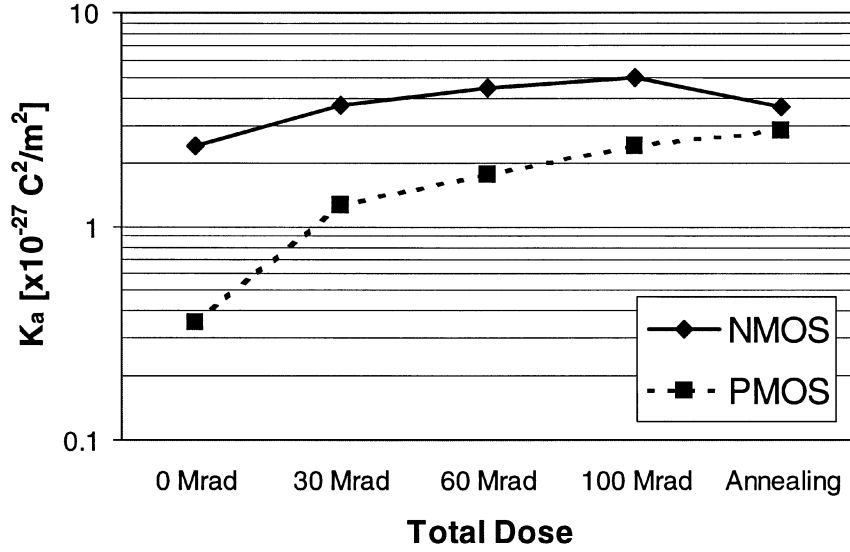


Figure 2.14: Dose dependence of  $K_F$  in a 0.25- $\mu\text{m}$  CMOS technology with  $t_{\text{ox}} = 5.5$  nm. Two pairs of large nMOS and pMOS devices ( $W/L = 2000/0.5$  and  $W/L = 2000/0.78$ ) were irradiated using 10-keV X-rays then annealed, both under worst-case bias conditions at room temperature. Reproduced *in toto* from [Anelli *et al.*, 2001, p.367]

amount of TDD(TID) damage accumulated. Such process sensitivities dictated that the npn BJTs in the target manufacturing process be subject to irradiation in order to characterize their TDEs.<sup>30</sup> In light of these results, which are described below, the succeeding discussion applies to n-type minority carriers, unless otherwise noted.

### 2.1.2.1 Beta Degradation

The primary TDE observed in BJTs is degradation of their common-emitter current gain,  $\beta$ ,<sup>31</sup> with dose as a result of both ionizing and non-ionizing mechanisms. To

<sup>30</sup>As explained in Section 3.2.1, the target technology is non-complementary, offering only an inferior substrate pnp. Without an initial intent to use this transistor in the front-end design, it was, regrettably, not characterized. However, the impact of its presumed total dose response is addressed in Section 6.4.3, in light of expectations derived from the general pnp behaviors described in this section.

<sup>31</sup>Throughout this document, bipolar current gain refers to the common-emitter current gain,  $I_c/I_b$ , which is a function of injection level,  $V_{\text{BE}}$ , and frequency, and denoted by the symbol  $\beta$ , rather than the classic  $h_{\text{FE}}$ . For further clarification on variations of this definition, consult Section E.1

separate these effects, the reciprocal of the gain can be represented as [*Messenger and Ash, 1992*, p.228]:

$$\frac{1}{\beta} = \frac{1}{\beta_{\text{br}}} + \frac{1}{\beta_{\text{sr}}} + \frac{1}{\beta_{\text{ee}}} \quad (2.12)$$

where the three addends are known as the bulk (or volume) recombination term ( $\beta_{\text{br}}$ ), the surface recombination term ( $\beta_{\text{sr}}$ ), and the emitter efficiency term ( $\beta_{\text{ee}}$ ), respectively. The last of these is the primary determinant of the initial gain,  $\beta_o$ , and is responsible for its quadratic temperature dependence, but can be considered a constant under radiation [*Messenger and Ash, 1992*, p.228].

### $\Delta\beta_{\text{sr}}$ Contribution

For ionizing radiation in the form of radiation-belt protons and electrons, the second term becomes dominant, since it reflects the increase in  $N_{\text{ot}}$  and  $N_{\text{it}}$  with TID [*Messenger and Ash, 1992*, p.228]. To see this explicitly,  $\beta_{\text{sr}}$ , which is simply the ratio of the emitter current,  $I_e$ , to the fraction of the base current that results from carrier trajectories which lead to recombination at the surface,  $I_s$ , can be expressed as [*Messenger and Ash, 1992*, p.334]:

$$\frac{1}{\beta_{\text{sr}}} = \frac{I_s}{I_e} = \frac{A_s W_b}{A_e D_n} S_n \quad (2.13)$$

where  $A_s$  is the surface area for the surface recombination,  $D_n$  is the diffusion constant for minority carriers ( $e^-$ ) in the base, and  $S_n$  is the surface recombination velocity.<sup>32</sup> Next, consider the influence of  $\Delta N_{\text{ot}}$  and  $\Delta N_{\text{it}}$  on each of these three quantities, in reverse order.

The surface recombination velocity,  $S_n$ ,<sup>33</sup> can be interpreted as the reciprocal analog of  $\tau_n$  for recombination of minority carriers taking place at the Si surface,

<sup>32</sup>The remaining terms in (2.13) are considered constants under radiation, as they reflect geometric properties, namely the emitter area ( $A_e$ ) and base width ( $W_b$ ).

<sup>33</sup>Comparing (C.24) and (2.14) through dimensional analysis, recombination at the surface is defined by a velocity,  $S$ , rather than a time constant, such as  $\tau$ , because the density of recombination sites,  $N_s$ , is areal, not volumetric like  $N_t$ .  $S_n$  can be interpreted as the tendency of carriers in the base that drift toward the surface to recombine there, rather than in the bulk and ranges from 0 (no surface current, hence no surface recombination) to  $v_T$  (surface recombination with unit probability, hence maximum surface current) [*Messenger and Ash, 1992*, p.47].

rather than the bulk, and is defined as [Messenger and Ash, 1992, p.47]:

$$S_n = N_s \sigma_n v_T \quad (2.14)$$

where  $N_s$  is the areal density of surface recombination sites, and  $\sigma_n$  and  $v_T$  are capture cross-section and thermal velocity of the minority carriers, respectively. At the surface, those recombination centers,  $N_s$ , are interface traps,  $N_{it}$ , as opposed to bulk recombination centers,  $N_t$ , such as the divacancy and vacancy-donor defects that govern  $\tau_n$ . Thus, (2.14) can be re-written to explicitly reflect its proportionality to  $D_{it}$  [Messenger and Ash, 1992, p.325]:

$$S_n = \frac{\pi v_T kT}{2\sqrt{\sigma_n \sigma_p}} D_{it} \quad (2.15)$$

Given that the cross-sections do not vary appreciably with dose, (2.15) implies that, under radiation,<sup>34</sup>  $\Delta S_n \propto \Delta N_{it}$  [Pease, 2003, p.540].

$\Delta N_{it}$  is also responsible for a drop in the diffusion constant at the surface,  $\Delta D_n$ , since the latter is proportional to mobility through Einstein's relation:  $\Delta D_n = \frac{kT}{q} \Delta \mu_n$ . The mobility degradation described by (2.5) suggests that at high doses  $\Delta D_n \propto 1/\Delta N_{it}$ .

Finally, radiation-induced changes in the surface area available for base recombination,  $\Delta A_s$ , depend not on  $\Delta N_{it}$  but  $\Delta N_{ot}$ , since the latter result in surface potential variations that, in turn, affect the extent of the emitter-base (E-B) and collector-base (C-B) depletion regions [Messenger and Ash, 1992, p.333]. Furthermore, the modified surface potential impacts the number of occupied interface traps by shifting the local Fermi level [Pease, 2003, p.540]. This, in turn, modifies  $D_{it}$  and can further enhance  $\Delta S_n$  through their proportionality in (2.15) [Srouf and McGarrity, 1988, p.1449].

These complex dependencies of  $\Delta S_n$ ,  $\Delta D_n$ , and  $\Delta A_s$  on  $\Delta N_{it}$  and  $\Delta N_{ot}$  render it impossible, at present, to arrive at a theoretical expression for the dose dependence of  $\Delta \beta_{sr}$  via (2.13), despite having captured  $\Delta N_{ot}(D)$  and  $\Delta N_{it}(D)$  in (C.18) and (C.19), respectively [Messenger and Ash, 1992, p.339]. The quest to predict  $\Delta \beta_{sr}(D)$

---

<sup>34</sup>This relationship only holds for low doses. Above 10 Mrad(Si),  $S_n$  begins to saturate [Messenger and Ash, 1992, p.337] whereas, according to Section C.2.6,  $\Delta N_{it}$  does not saturate with dose.

is further hampered by the fact that such surface effects are highly process-dependent, depending in particular on the oxide growth steps [*Holmes-Siedle and Adams, 2002*, p.222]. Unlike the gate oxide responsible for  $\Delta N_{\text{ot}}$  in MOSFETs, the oxide in question for BJTs is simply a thermally grown passivation layer used to seal the underlying E-B and C-B junctions; it is typically much thicker [*Holmes-Siedle and Adams, 2002*, p.205] and not as well controlled [*Messenger and Ash, 1992*, p.345], leading to more charge accumulation and manufacturing variability [*Pease, 2003*, p.541].

Nevertheless, it is possible to extract trends in the general behavior of  $\Delta\beta_{\text{sr}}(D)$ , which are typically expressed in terms of its reciprocal,  $\Delta\beta_{\text{sr}}^{-1}$ . First, it has been empirically determined that in many cases  $\Delta\beta_{\text{sr}}^{-1}$  exhibits an inverse power-law dependence on dose such that

$$\Delta\beta_{\text{sr}}^{-1} \propto D^n \quad (2.16)$$

where  $0.5 \leq n \leq 1$  [*Messenger and Ash, 1992*, p.339]. Since the polarity of  $\Delta N_{\text{ot}}$  for npn(pnp) devices favors(hinders) surface recombination [*Schmidt et al., 1996*], increasing(decreasing)  $I_{\text{s}}$ ,  $n$  tends toward the upper(lower) end of the range, and may even be super-linear [*Pease, 2003*, p.546]. However, for lateral and substrate pnp transistors, whose geometries favor more surface conduction than their vertical counterparts,<sup>35</sup> TID sensitivity can be extremely high, as shown in Figure 2.15, causing failures at just 10 krad(Si) [*Messenger and Ash, 1992*, p.345]. Note that the nonlinear  $\beta_{\text{sr}}$ -degradation of (2.16) usually occurs at lower doses than that of  $\beta_{\text{br}}$  [*Holmes-Siedle and Adams, 2002*, p.208].

Secondly, returning to (2.13), it can be shown that because  $I_{\text{s}}$  and  $I_{\text{e}}$  are both proportional to powers of  $e^{V_{\text{be}}/nV_{\text{T}}}$ ,  $1/\beta_{\text{sr}} \propto 1/\sqrt{I_{\text{e}}}$ , or, in turn [*Messenger and Ash, 1992*, p.336],

$$\Delta\beta_{\text{sr}}^{-1} \propto \frac{1}{\sqrt{I_{\text{e}}}} \quad (2.17)$$

implying that gain degradation is greater at lower emitter currents. This simply reflects the fact that, for low-level injection, more of the minority carriers are

---

<sup>35</sup>The geometries of these devices are presented briefly in Section 3.2.1.4 and Section 3.2.1.3. For the purposes of this section, the prevalence of surface recombination in a substrate pnp, which features vertical structure, derives from the non-idealities of its emitter diffusion, which is somewhat shallow and has a high perimeter-to-area ratio.



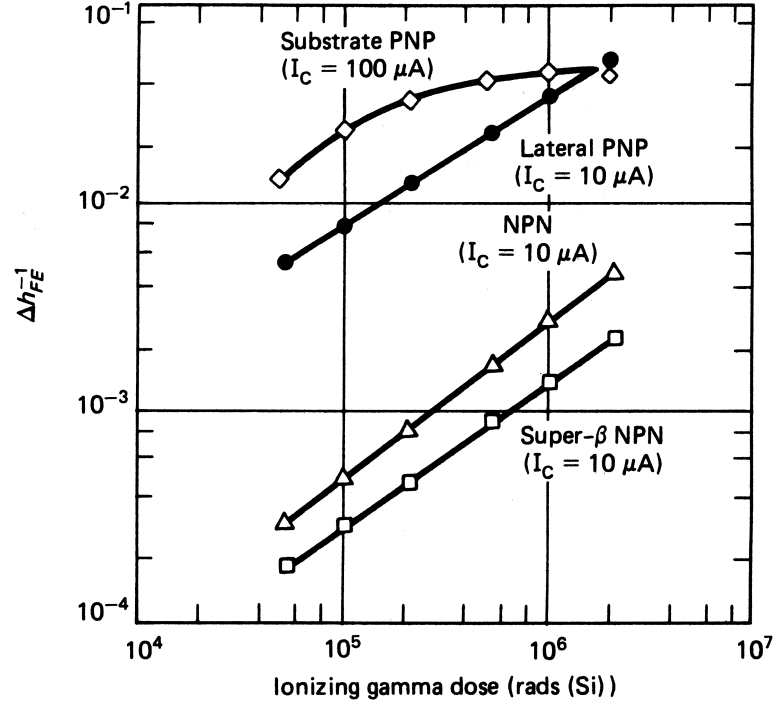


Figure 2.15: Beta degradation of npn, substrate pnp, and lateral pnp transistors. Plotted in terms of  $\Delta h_{fe}^{-1}$  (or  $\Delta \beta^{-1}$ ), the sensitivities of the surface-conducting pnp classes are nearly an order of magnitude higher than those of their npn counterparts. Reproduced *in toto* from [Messenger and Ash, 1992, p.345]

transported near the surface, increasing the importance of field-assisted recombination there [Holmes-Siedle and Adams, 2002, p.223]; the lower absolute value of  $\beta_{sr}$  for low currents means  $\Delta \beta_{sr}^{-1}$  is larger and  $1/\beta_{sr}$  dominates (2.12). At the other extreme, high-level injection conditions lead to an increase of  $W_b$  in (2.13) through the Kirk effect, also lowering  $\beta_{sr}$  and increasing  $\Delta \beta_{sr}^{-1}$  [Messenger and Ash, 1992, p.340]. Thus, the minimum  $\beta_{sr}$ -degradation occurs for devices which are biased at the operating point corresponding to maximum pre-irradiation  $\beta$  [Messenger and Ash, 1992, p.339].

To assess the TID vulnerability of the passivation oxides employed in the target manufacturing process, given the uniqueness cited previously, a series of representative npn BJTs from the aforementioned test vehicle (cf. Footnote 15) were exposed to  $^{60}\text{Co}$   $\gamma$ -rays in steps up to 1 Mrad(Si).<sup>36</sup> The canonical  $\beta$ -vs- $V_{BE}$  curves at each step

<sup>36</sup>The relevant section of the MK832A chip (Quad J04) contained seven distinct npn bipolar

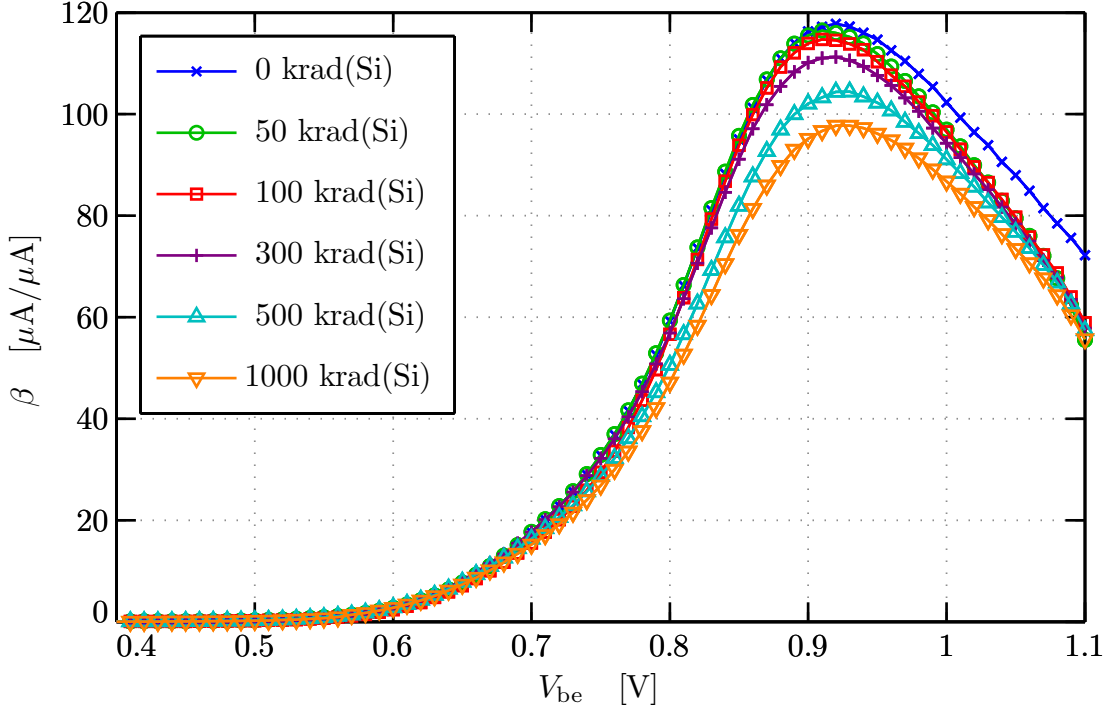


Figure 2.16: Measured  $\beta$ -degradation of representative npn BJT from target process. At 1 Mrad(Si), the peak  $\beta$  of a device with  $A_e = 0.4 \times 0.7 \mu\text{m}^2$  exhibits  $\sim -18\%$  degradation (irradiation bias:  $V_{CE} = 2.5 \text{ V}$ ). Exacerbated high-level injection effects are evidenced by variation of  $\beta$  for  $V_{be} > 1 \text{ V}$ . Markers indicated measured data points.

are plotted in Figure 2.16 for a device whose emitter area ( $0.4 \times 0.7 \mu\text{m}^2$ ) reflects the predominant size employed in the LNA. As expected, the pre-irradiation curve suffers from reduced gain at both low and high injection levels, resulting in a peak near  $V_{BE} = 0.9 \text{ V}$ . Figure 2.17 plots this peak  $\beta$  as a function of dose, along with a fit to (2.16) that yields  $n = 0.918$ , which is consistent with npn theory. In addition, it attests that devices biased at peak  $\beta$ , so as to obtain minimum  $\Delta\beta_{sr}^{-1}$ , experience  $\beta_{sr}$ -degradation of nearly  $-18\%$  at 1 Mrad(Si).

---

transistors of varying size (no shared terminals), six of which were laid out in a CBE configuration, with emitter lengths ranging from  $0.4\text{--}20 \mu\text{m}$ . The seventh, a rotated BEC device, was not considered in this work. For the remainder, irradiation bias conditions consisted of grounding all active pins except collectors, such that  $V_{CE} = 2.5 \text{ V}$ .

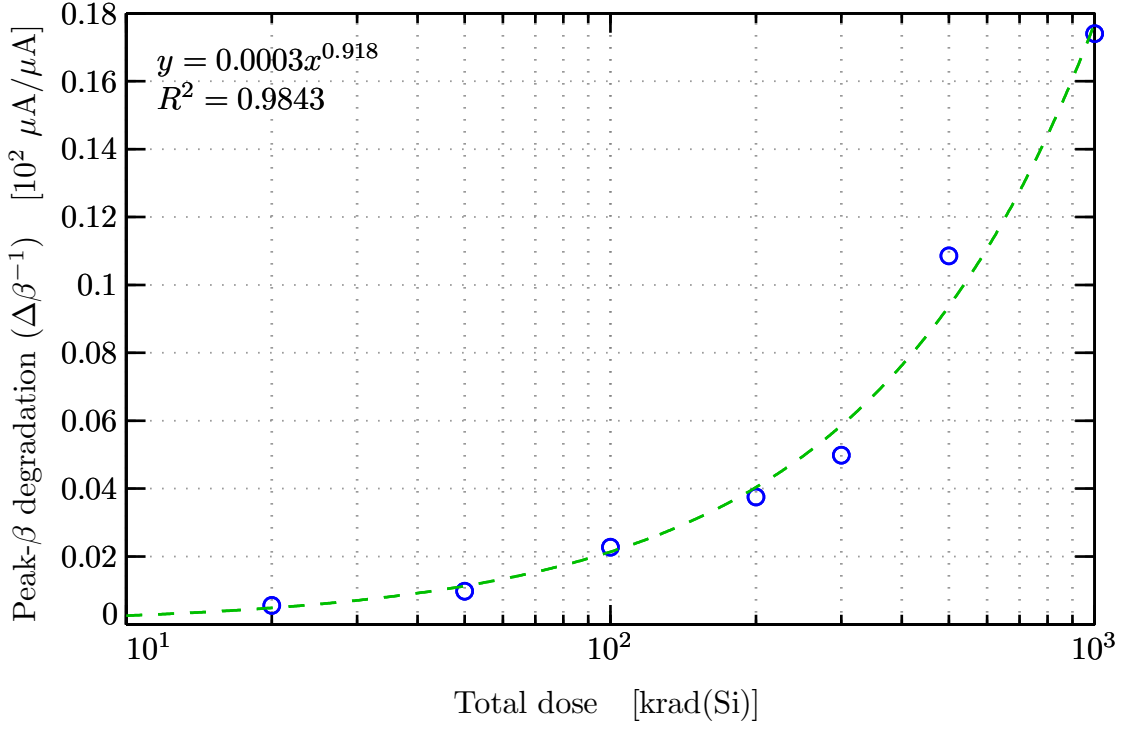


Figure 2.17: Measured degradation of peak  $\beta$  fit to (2.16). Data points (in blue) correspond to maxima of curves in Figure 2.16 (as well as those of additional dose steps omitted for clarity). A power-law exponent of  $n=0.918$  conforms to the accepted range and yields a good fit (in green) since  $\beta$  is dominated by  $\beta_{\text{sr}}$  for  $^{60}\text{Co}$  radiation.

### $\Delta\beta_{\text{br}}$ Contribution

Turning now to the first term of (2.12),  $1/\beta_{\text{br}}$  accounts for the recombination of minority carries in the bulk, primarily in the neutral base, neutral emitter, and the E-B depletion region [Pease, 2003; Srour and McGarrity, 1988, p.1449, p.544] and dominates  $1/\beta$  for TDD exposures [Messenger and Ash, 1992, p.228]. The displacement damage produced by non-ionization radiation decreases the bulk minority-carrier lifetime (cf. Section C.3.4) and this, in turn, directly reduces  $\beta_{\text{br}}$ , defined as Messenger and Ash [1992][p.334]:

$$\frac{1}{\beta_{\text{br}}} = \frac{W_{\text{b}}^2}{2D_{\text{n}}} \frac{1}{\tau_{\text{n}}} \quad (2.18)$$

Unlike (2.13) for  $\beta_{\text{sr}}$ , here  $D_{\text{n}}$  and  $W_{\text{b}}$  in the bulk are unaffected by displacement damage, so  $\beta_{\text{br}}$  admits to a more formal expression of its radiation dependence—it follows directly from (C.3.4):

$$\Delta\beta_{\text{br}}^{-1} = \frac{1}{\beta_{\text{br}}} - \frac{1}{\beta_{\text{bro}}} = \frac{\phi_{\text{D}}}{K_{\tau}\omega_{\text{T}}} \quad (2.19)$$

This is known as the Messenger-Spratt equation [[Messenger, 1973](#)] and expresses the  $\beta_{\text{br}}$ -degradation in terms of the TDD fluence  $\phi_{\text{D}}$ , and the damage factor  $K_{\tau}$ , along with the unity gain frequency of the BJT,  $\omega_{\text{T}}$ . The damage factor is identical to that of  $\Delta\tau_{\text{n}}$ , which in general is larger than that of  $\Delta\tau_{\text{p}}$  (cf. Footnote 45 of Appendix C) by a factor of three,<sup>37</sup> suggesting that npn BJTs are less sensitive to  $\beta_{\text{br}}$ -degradation than their pnp counterparts [[Holmes-Siedle and Adams, 2002](#), p.212].

Whether caused by increased  $S_{\text{n}}$  or decreased  $\tau_{\text{n}}$ , the degradations of  $\beta_{\text{sr}}$  and  $\beta_{\text{br}}$ , respectively, fundamentally reflect a radiation-induced increase in minority carrier recombination. Just as during nominal operation, the corresponding majority carriers that take part in this process are provided by the base current,  $I_{\text{b}}$ . Thus, for moderate degradation levels, the net  $\Delta\beta^{-1}$  is reflected in a corresponding  $\Delta I_{\text{b}} \simeq \Delta\beta^{-1}$  with  $I_{\text{C}}$  approximately constant [[Messenger and Ash, 1992](#), p.339]. Historically, this effect is confirmed by representing data such as that of Figure 2.16 with a Gummel plot [[Pease, 2003](#), p.540], in which  $I_{\text{B}}$  and  $I_{\text{C}}$  are plotted logarithmically against  $V_{\text{BE}}$ . The result, depicted in Figure 2.18, indicates that for a given  $V_{\text{BE}}$ ,  $I_{\text{C}}$  changes negligibly after a 1-Mrad(Si) exposure.<sup>38</sup> Over the range of  $V_{\text{BE}}$  corresponding to peak  $\beta$  (namely,  $0.8\text{V} \leq V_{\text{BE}} \leq 1\text{V}$ ) in which the transistor is biased to minimize  $\Delta\beta_{\text{sr}}^{-1}$  as recommended above, the recombination terms of (2.12) dominate and the post-irradiation  $I_{\text{B}}$  markedly increases. In addition, the sub- $V_{\text{T}}$  base current exhibits a measurable increase at 1 Mrad(Si) indicative of the leakage phenomena described next.

<sup>37</sup>Typical values of  $K_{\tau}$  for an npn transistor at an injection level of  $10^{-3}$  are:  $5 \times 10^5 - 7 \times 10^5$  s/cm<sup>2</sup>, for 1-MeV neutrons (standard to which all other particles are usually referenced);  $3 \times 10^4 - 1 \times 10^5$  s/cm<sup>2</sup> for 20-MeV protons; and  $2.5 \times 10^7 - 3 \times 10^8$  s/cm<sup>2</sup>, for 3-MeV electrons [[Messenger and Ash, 1992](#), p.739].

<sup>38</sup>Rather than being constant, as assumed above, the  $1/\beta_{\text{ee}}$  term of (2.12) is shrinking as the neutral emitter surface resistivity and the effective  $W_{\text{b}}$  decrease in response to variations of the surface potential for  $V_{\text{BE}} > 0.8$  V, as reflected by the slight increase in  $I_{\text{C}}$

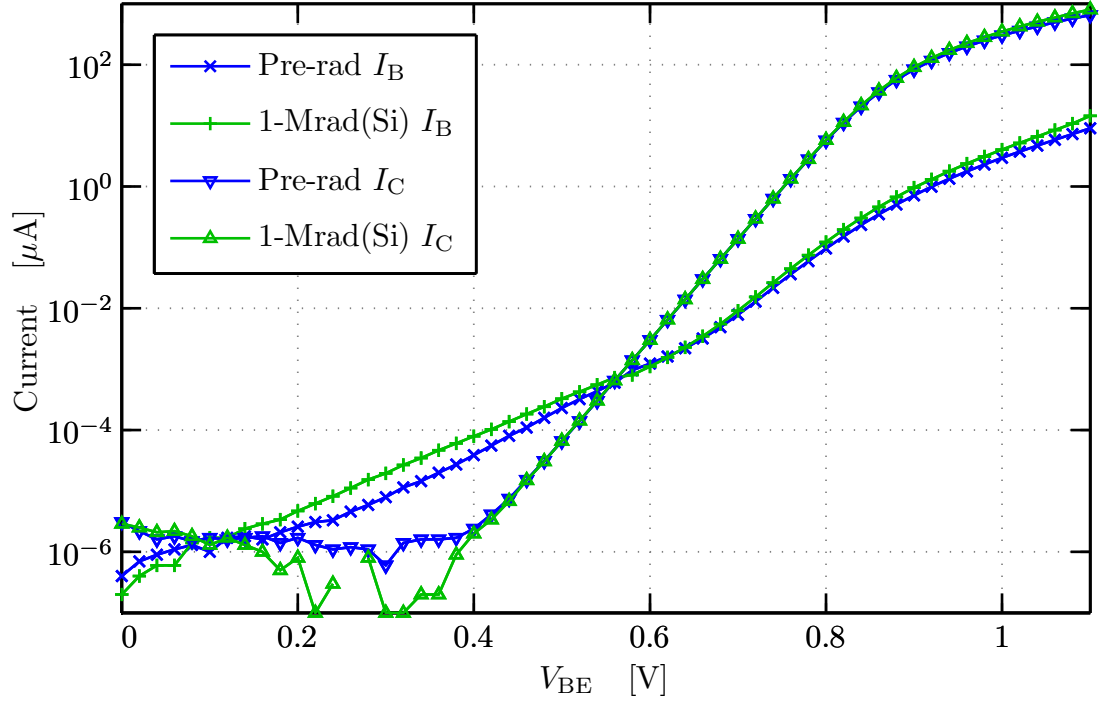


Figure 2.18: Gummel plot corresponding to measured  $\beta$ -degradation at extremes of Figure 2.16. For clarity, markers indicating measured data points are down-sampled by two and those below 100 fA are omitted entirely.

### 2.1.2.2 Leakage Current

Much as for MOSFETs (cf. Section 2.1.1.3), ionizing radiation can activate multiple leakage paths in bipolar designs through the introduction of positive  $\Delta N_{ot}$  in isolation structures composed of thick field oxide [Pease, 2003, p.544]. Figure 2.20 depicts two paths, analogous to those of Figure 2.9, for the case of recessed field oxide (ROX) isolation [Messenger and Ash, 1992, p.348]: an intra-device channel between emitter and collector that forms along the ROX sidewall when  $\Delta N_{ot}$  inverts the base doping; and an inter-device path between the  $n^+$  buried layers of adjacent npn transistors that is formed when the surface of the  $p^+$  guardband beneath the ROX, which would otherwise act as a channel stop, is inverted, forming a conductive channel [Pease et al., 1983].

To mitigate the latter effect, modern bipolar and BiCMOS technologies employ

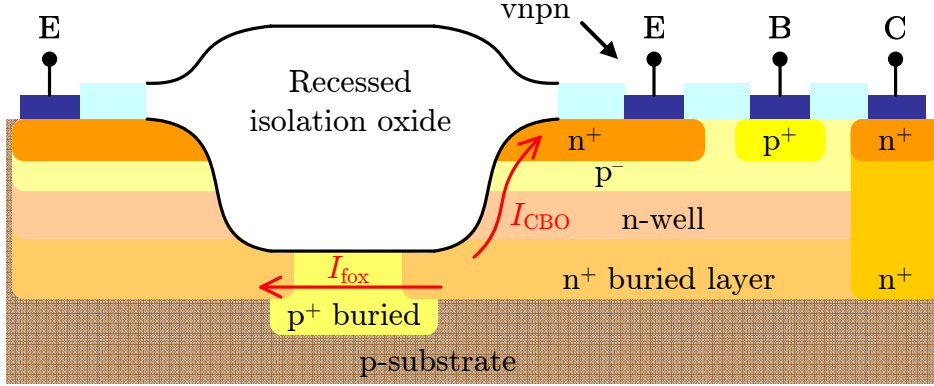


Figure 2.19: Cut-away of BJT leakage paths in ROX-isolated technology. Positive charge trapped in the recessed field oxide can invert both its sidewall, permitting leakage from collector to emitter, and its bottom surface, allowing leakage between the buried layers of neighboring vertical npn (vnpn) BJTs. Drawing dimensions are exaggerated for clarity. After [Pease *et al.*, 2001, p.544].

a deep trench isolation (DTI) scheme, similar to the STI method of Figure 2.11, in which a narrow but deep groove (5–6  $\mu\text{m}$  in some cases [Enlow *et al.*, 1989, p.2415]) is etched vertically between the buried layers of neighboring devices and a thin liner oxide is grown before it is filed via the deposition of undoped polysilicon [Hastings, 2006, p.61]. Although the polysilicon is typically left floating [Enlow *et al.*, 1989, p.2415], this structure, once again, constitutes a vertical, parasitic FOXFET, which is subject to hole trapping and thus inversion of the p-type substrate, resulting in the leakage paths shown in Figure 2.20. Even with the inclusion of the  $p^+$  channel stop beneath the trench, as was done for ROX to increase the threshold voltage of the FOXFET, the negative  $\Delta V_{\text{th}}$ , corresponding to the  $\Delta N_{\text{ot}}$  of Figure 2.21, can be severe enough to permit leakage beneath the DTI.

Furthermore, the DTI technique fails to eliminate the shunt current from collector-to-base,  $I_{\text{CBO}}$ , along the path in Figure 2.20, whose increase is limned in Figure 2.22. In addition to this sidewall current,  $I_{\text{CBO}}$  may also contain a component of leakage current along the surface, should the base doping at the interface be inverted due to excessive  $N_{\text{ot}}$  build-up in the passivation oxide [Holmes-Siedle and Adams, 2002, p.224]. Taken together, these paths can increase the net  $I_{\text{CBO}}$  by an order of

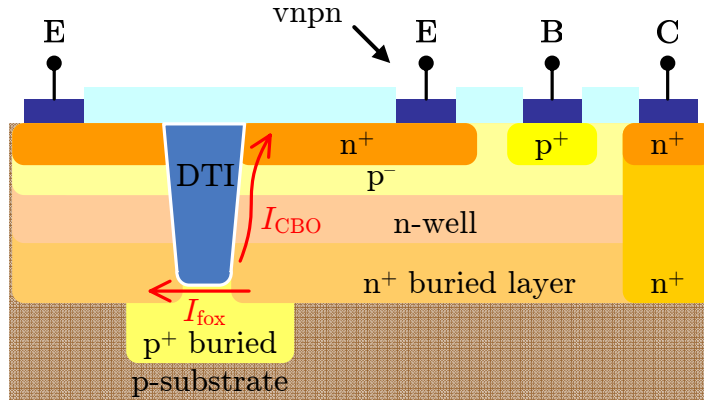


Figure 2.20: Cut-away of BJT leakage paths in DTI-isolated technology. Positive charge trapped in the trench oxide can invert both its sidewall, permitting leakage from collector to emitter, and its bottom surface, allowing leakage between the buried layers of neighboring vertical npn (vnpn) BJTs. Drawing dimensions are exaggerated for clarity. After [Enlow *et al.*, 1989, p.2416].

magnitude at 200 krad(Si), as shown in Figure 2.23.

### 2.1.2.3 Dose-Rate Effects

Thus far, the discussion of BJT TDEs has neglected the impact of dose rate on the decrease(increase) in gain(leakage), when in fact this has been the subject of much research in recent years [Pease, 2003, p.545]. Specifically, it has been shown [Pease *et al.*, 1983], that there exists a ‘true’ dose rate effect for integrated BJTs, not simply a time-dependent effect, in which  $\Delta I_b$  degradation can be 2–50 times worse at low dose-rates (1.1–13.12 rad/s) than at high ones (243.6–300 rad/s) [Enlow *et al.*, 1991; Nowlin *et al.*, 1992, p.1349–1350, p.2033]. The most widely accepted explanation of this enhancement of low-dose-rate sensitivity (ELDRS) effect [Pease, 2003, p.545] hinges on the ramifications of so-called space-charge [Fleetwood *et al.*, 1994a], positive trapped charge in SiO<sub>2</sub> that can only ‘hang around’ long enough to mitigate further damage at high dose rates [Holmes-Siedle and Adams, 2002, p.237–238]. More formally, the oxygen-vacancy precursors to the E’ centers depicted in Figure C.8, metastable complexes known as E’<sub>s</sub> centers [Pease, 2003, p.545], exist throughout the oxide, providing shallow hole traps far from the surface. Since the

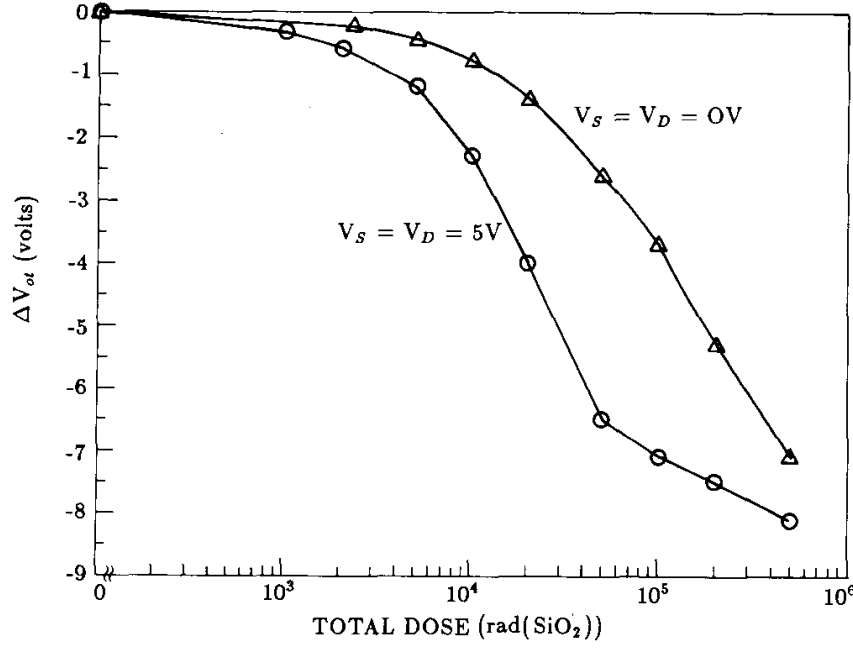


Figure 2.21: Measured  $\Delta V_{ot}$  of DTI FOXFET with floating polysilicon. Irradiation bias conditions for adjacent source/drain regions are indicated to demonstrate bias-dependence of  $\Delta V_{ot}$  which dominates leakage character, exceeding  $\Delta V_{it}$  by an order of magnitude. Reproduced *in toto* from [Enlow *et al.*, 1989, p.2419].

time scale for such a site to either release its hole (anneal) or reconfigure into a more stable, deep trap (typically, the E' center in Figure C.9, also known as E'<sub>γ</sub>) is on the order of seconds to hours [Fleetwood *et al.*, 1994a, p.1879], there is a period during which this space-charge can mitigate the buildup of both  $\Delta N_{ot}$  and  $\Delta N_{it}$  near the interface [Pease, 2003, p.545].

The local electric field generated by this space-charge, in conjunction with that of any established  $\Delta N_{ot}$ , deters the further accumulation of  $\Delta N_{ot}$  through two methods, represented graphically in Figure 2.24. By counteracting the local potential gradient in the region above (in red) that otherwise drives both the separation of  $e^-$  and  $h^+$  and the downward drift of the latter [Fleetwood *et al.*, 1994a, p.1879], it reduces the charge yield,  $\mathcal{F}_y$ , and retards the transport of holes to the Si-SiO<sub>2</sub> interface. This is the same effect responsible for the  $\Delta V_{ot}$  saturation discussed in Section 2.1.1.1. Secondly, the larger effective field between the space-charge and the bulk Si encourages those holes



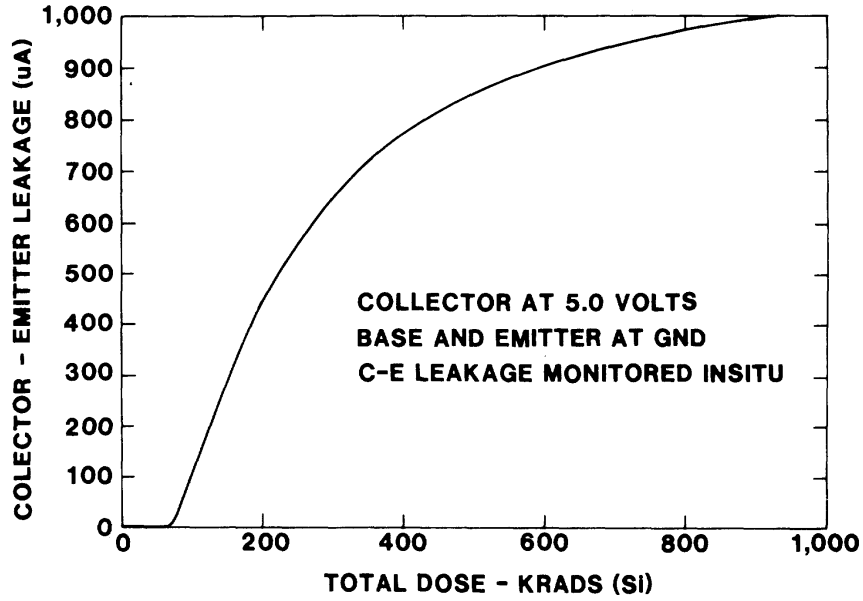


Figure 2.22: Radiation-induced collector-emitter sidewall leakage current for a representative ROX technology. Similar behavior is present along DTI sidewall, although the relative contribution of this path to the total  $I_{CBO}$  may vary. Reproduced *in toto* from [Pease *et al.*, 1983, p.4221].

that are transported to the surface to be trapped even closer to it, where they can more readily be neutralized (in border traps) or annealed (in deep traps) by tunneling electrons [Fleetwood *et al.*, 1994a, p.1879]. Both effects, of course, are only significant if the ambient applied field is small [Fleetwood *et al.*, 1994a, p.1879], which is the case for BJTs, as opposed to MOSFETS, because there is no intended gate above the passivation oxide.

The local field associated with this space-charge retards not only the transport of holes to the surface, but  $H^+$  as well and, in so doing, reduces the buildup of  $\Delta N_{it}$ , which are created through the ion-transport discussed in Section C.2.6 [Witczak *et al.*, 1998, p.2246]. Since holes have much greater oxide mobility than protons, they can accumulate in a space-charge layer that is sufficient to significantly alter subsequent  $H^+$  transport by forming an electrostatic barrier which prevents the latter from reaching the interface and reacting to form  $\Delta N_{it}$  [Rashkeev *et al.*, 2002, p.2650].

Such lessening of  $\Delta N_{ot}$  and  $\Delta N_{it}$  is pronounced at high dose rates, because it

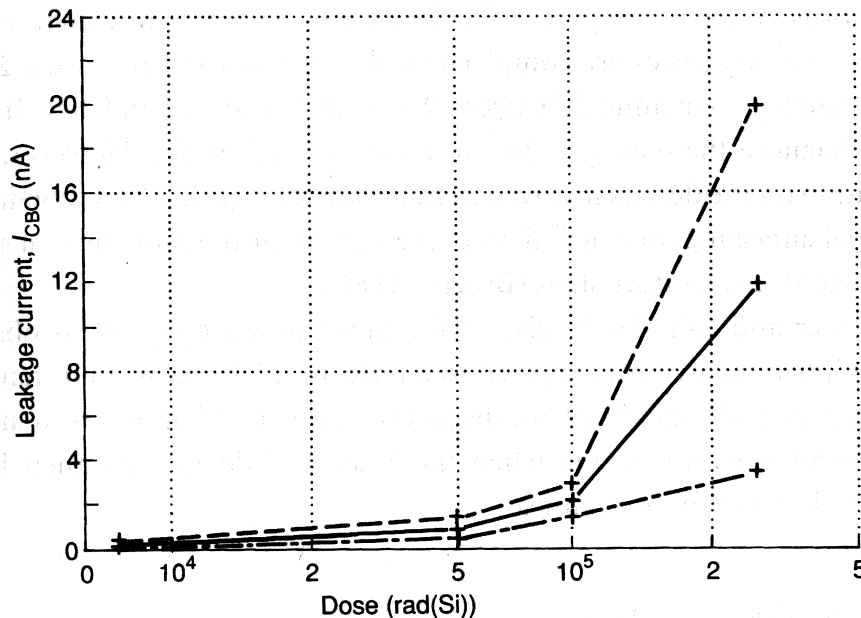


Figure 2.23: Radiation-induced collector-base leakage current for three specimens from the same batch of small-signal BJTs. Device-to-device variability and size of increase in leakage current are noteworthy. Reproduced *in toto* from [Holmes-Siedle and Adams, 2002, p.225].

depends on a high concentration of  $E'_g$  centers to provide the space-charge. At low dose rates, these metastable centers have time to anneal or reconfigure, resulting in the detrapping and/or transport of their holes and, consequently, the absence of any space-charge [Pease, 2003, p.545].<sup>39</sup> Although space-charge limitations begin to abate below 50 rad/s [MIL-STD-883G, 2006, Sect. 3.13], the cut-off for worst-case ELDRS is typically taken to be 10 mrad/s [Holmes-Siedle and Adams, 2002; Pease, 2003, p.178, p.546].

Although elevated temperatures can be used to accelerate space-charge decay and thereby allow for higher dose-rates during part qualification, ELDRS still necessitates onerous test conditions and protracted exposures [MIL-STD-883G, 2006, Sect. 3.13.3]. Furthermore, it is inadvisable to extrapolate results from one manufacturing

<sup>39</sup>Since the time afforded by lower doses allows for the space-charge to disperse before it can impede any ensuing charge trapping, as it does for high-dose-rate exposures, some authors prefer the term suppressed high-dose-rate sensitivity (SHDRS) to describe this space-charge-limited phenomenon [Holmes-Siedle and Adams, 2002, p.178].

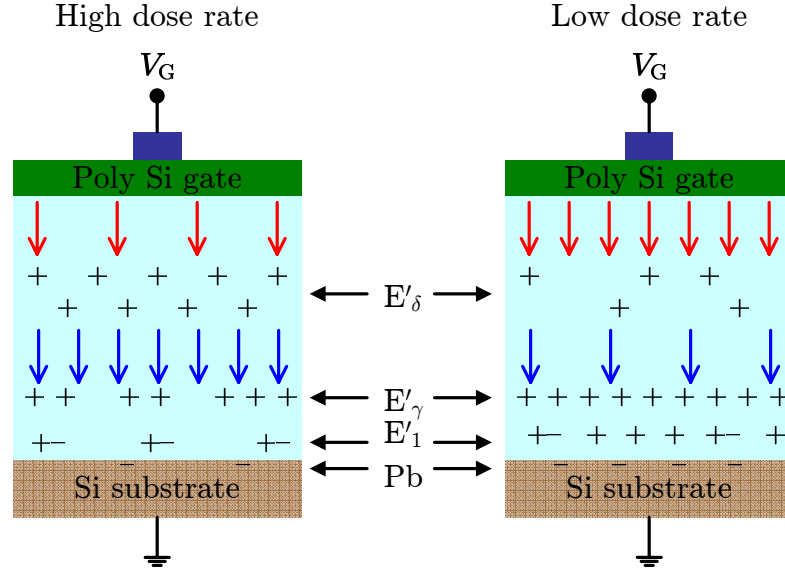


Figure 2.24: Illustration of space-charge fields responsible for ELDRS. When delocalized  $E'_\delta$  centers do not have time to reconfigure, the effective field above(below) them, shown in red(blue) is lessened(enhanced), such that  $\mathcal{F}_y$ ,  $\mathcal{F}_t$ , and transport drift(trap distance from interface and annealing time) are reduced. After [Fleetwood *et al.*, 1994a, p.1878].

process to another, since damage can vary drastically with passivation quality, measured in terms of oxygen-vacancy density [Shaneyfelt *et al.*, 2002, p.3171]; ELDRS is only eliminated in the case of parts without passivation [Pease, 2003, p.547]. Even mitigated by only the minimal shielding provided by micro-satellites, the radiation-belt environment whose fluxes are presented in Section 2.3.1, is not sufficiently hostile that the front-end is exposed to dose rates  $\geq 1$  rad/s. However, since it is simply impractical to adopt the anticipated 3 mrad(Si)/s rate for testing, no ELDRS data was obtained for the sample transistors characterized above. As this rate lies below the putative onset of worst-case ELDRS, aforementioned levels of  $\beta$  degradation and leakage are treated as lower bounds during the design.

## 2.2 Single-Event Effects

As opposed to TDEs, single-event effects are marked by an almost instantaneous change in the operation of a circuit due to the impact of a single ionizing particle. Depicted in Figure 2.25, such an incident particle generates a dense track of  $e^- - h^+$  pairs as it passes through the Si substrate [Srouer and McGarrity, 1988, p.1458] according to the mechanisms described in Section C.2.1. SEEs are typically only significant for protons and heavy ions of sufficient LET that the columnar model of Section C.2.2 describes the recombination along the track [Oldham, 2003, p.14].<sup>40</sup> The effects in question result when the remaining yield of electrons and holes are then collected by nearby reversed biased p-n junctions through drift, diffusion, or funneling [Srouer and McGarrity, 1988, p.1458].<sup>41</sup>

These three mechanisms, and the relative importance of their contributions to this collected charge,  $Q_{\text{col}}$ , as a function of time following the strike, are nicely summarized in Figure 2.26. Carriers generated within the collecting junction, are swept out of the depletion region by the equilibrium built-in potential of the junction in times on the order of 1–10 ps [Srouer and McGarrity, 1988, p.1458], leading to the prompt drift component,  $Q_{\text{D}}$ . Meanwhile, carriers farther down the track, or from tracks distant from the collecting junction, can only be collected once they arrive at the junction via diffusion [Messenger and Ash, 1992, p.453]. This component of the collected charge,  $Q_{\text{DF}}$ , is delayed on account of the slower transport (on the order of several minority

---

<sup>40</sup>Protons often produce SEE effects through indirect ionization since, for Van Allen belt energies, they, like electrons, possess insufficient LET and range [Srouer and McGarrity, 1988, p.1458]. Although direct proton SEEs are becoming more prevalent as feature sizes decrease [Messenger and Ash, 1992, p.438], generally it is the recoil nuclei produced during their inelastic nuclear collisions with the lattice that participate in direct ionization via scattering [Buchner and McMorro, 2005, p.8]. In effect, these spallation products act like incident cosmic ray heavy ions [Messenger and Ash, 1992, p.438], possessing the requisite energies ( $\gg 10$  MeV), mass ( $Z \gg 2$ ), linear stopping power ( $\gg 1$  MeV/ $\mu\text{m}$ ) [Messenger and Ash, 1992, p.424], and LET ( $\mathcal{L} > 40$  MeV-cm<sup>2</sup>/mg) to initiate SEEs [Messenger and Ash, 1992, p.427].

<sup>41</sup>That analysis of SEEs is only concerned with charge collected in the substrate, rather than the oxide, follows directly from the large ratio between the yields in these two materials, as discussed in Section C.2. Specifically, the initial radius of the ionizing track is larger in the bulk Si and the Debye length is smaller, both of which result in less recombination [Oldham, 2003, p.19]. Additionally, the oxide is so much thinner that there are many fewer charges generated *ab initio* [Oldham, 2003, p.19]. Since SEE vulnerability is proportional to  $|Q_{\text{col}}|$ , charge collection in the substrate is paramount.

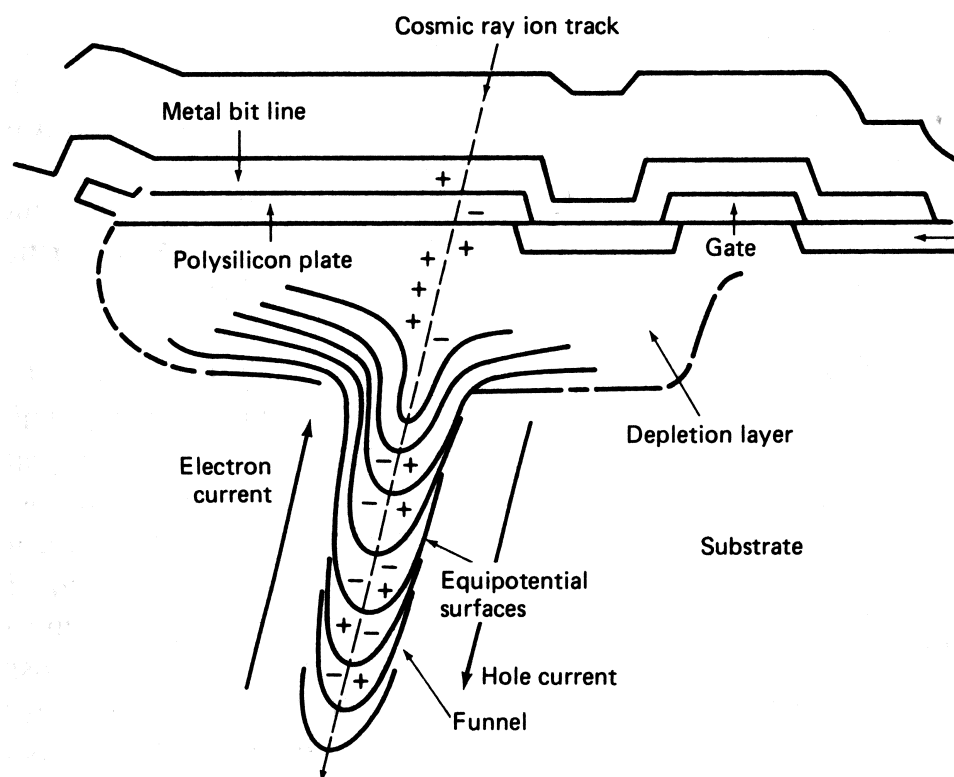


Figure 2.25: Funnel formation by charge track of heavy ion strike. Passing through bulk silicon, a high-LET, ionizing particle distorts the equilibrium junction potentials, collapsing the depletion regions, as shown here in the case of an MOS SRAM cell. Reproduced *in toto* from [Messenger and Ash, 1992, p.453].

carrier lifetimes, or 10-100 ns [Srouf and McGarrity, 1988, p.1458]) and attenuated due to lower yield (with more recombination in the absence of the built-in electric field reducing efficiency [Buchner and McMorrow, 2005, p.10]).

However, perhaps the most important collection phenomenon is the significant increase in the prompt component ( $Q_F + Q_D$ ) over that predicted from the built-in potential alone (i.e.,  $Q_F \gg Q_D$ ) as a result of an enhanced depletion region or funnel [Srouf and McGarrity, 1988, p.1459]—a local field gradient that forces electrons generated along the track to flow back up into the depletion region. A funnel is produced when the ionizing track temporarily distorts the equipotential surfaces of the junction, resulting in the series of nested protrusions that extend down the track deep into the bulk in Figure 2.25 [Messenger and Ash, 1992, p.453]. According to the

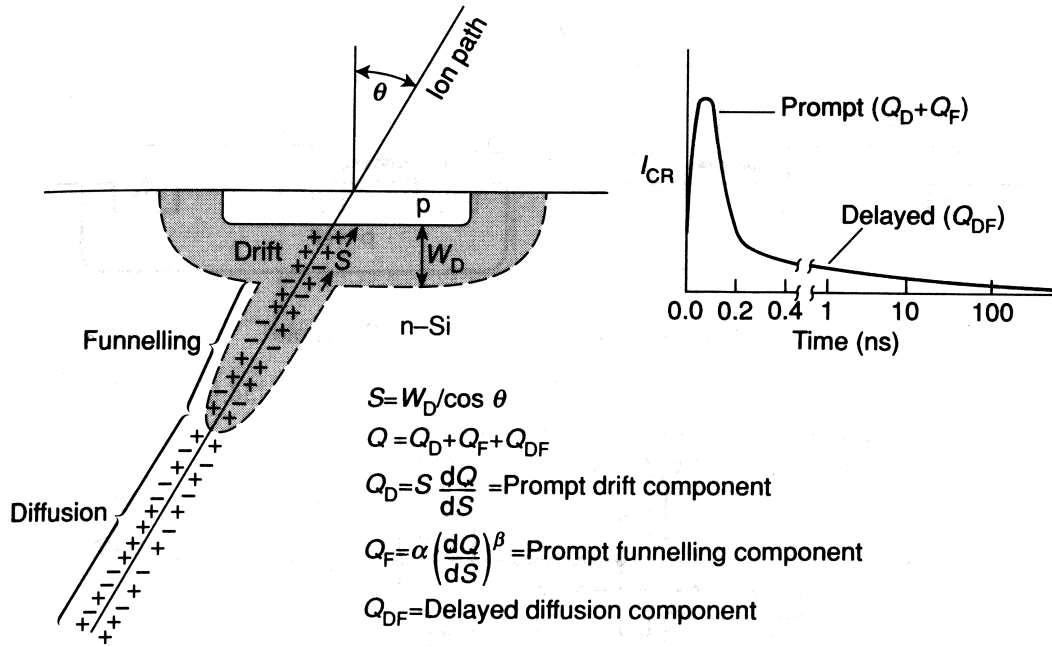


Figure 2.26: Charge track, collection mechanisms, and the resulting current pulse associated with an ion striking a p-n junction. The effective junction width seen by the ion,  $S$ , is a function of incident angle  $\theta$ , increasing in path length for oblique incidence. Reproduced *in toto* from [Holmes-Siedle and Adams, 2002, p.107].

model of McLean and Oldham [1982], the steps in funnel formation are [Messenger and Ash, 1992, p.454], [Oldham, 2003, p.20]:

- On impact, the track forms a filament of plasma that shorts the junction to the bulk, collapsing its equilibrium field.
- Within picoseconds, current flow along the 'wire' dissipates enough energy that the plasma trail comes into thermal equilibrium with the bulk (thermalizes), but still possesses sufficient density that the junction is saturated.
- This high carrier concentration dissipates through ambipolar diffusion, causing the column to expand radially from an initial size of  $\sim 0.1 \mu\text{m}$  and, in the process, the funnel length grows as the junction equipotential lines extend deeper due to the high spreading resistance [Messenger, 1982, p.2024].

- Finally, once the plasma density approaches the background doping levels, the depletion region is reestablished and the funnel interrupted.

The total contribution of funneling to the prompt charge collection is proportional to both the initial ‘wire’ charge density and the effective funnel length, with the latter being longer in p-type substrates (about three times the width of the depletion layer [Messinger and Ash, 1992, p.465]) since  $\tau_n > \tau_p$  [Messinger and Ash, 1992, p.455].

The above description of charge collection applies to an ion strike affecting a single p-n junction. But, for strikes which cross multiple junctions, such as the drain, well, and substrate of a pMOS device [Hauser et al., 1985, p.4121] or the emitter, base and collector of a vertical npn BJT [Knudson and Campbell, 1987, p.1246], the charge collection processes do not proceed independently. Whether the physics of a multi-junction strike, depicted in Figure 2.27 for the case of a vnpn BJT, is conceptualized in terms of the overlap of the two funnel regions or simply as a low-ohmic connection between two like-doped regions [Hauser et al., 1985, p.4115], its effect is to screen out the junction potentials such that charge collection is governed by the relative bias of the two regions [Lacoe, 2003, p.11], and its upshot is to enhance the amount of charge that would otherwise be collected by either junction by as much as a factor of 10(3) for the upper(lower) junction [Knudson et al., 1986, p.1564]. This multiplicative effect, occurring during the early stages charge collection, can result in  $Q_{\text{col}}$  exceeding the charge deposited [Lacoe, 2003, p.9]. By effectively creating a short between device terminals for a brief interval after impact,<sup>42</sup> this so-called ion shunt effect [Oldham, 2003, p.24] for high density tracks results in current pulses whose polarities depend on terminal bias and can be opposite to those induced during collection via drift in reverse-biased junctions [Hauser et al., 1985, p.4120].

Regardless of the collection mechanism, the energy deposited by the collected charge can have either permanent or transitory repercussions on devices and circuits. The most destructive form of potentially permanent damage, known as latchup, occurs at the device level and is discussed in Section 2.2.1, whereas a class of temporary

---

<sup>42</sup>To create a low-impedance connection between proximate diffusion-isolated regions, the track density must exceed not only their background doping densities, but also those of all the interposed layers [Hauser et al., 1985, p.4115]. In practice, this is not difficult for lightly-doped (non-epi) substrates or non-retrograde wells.

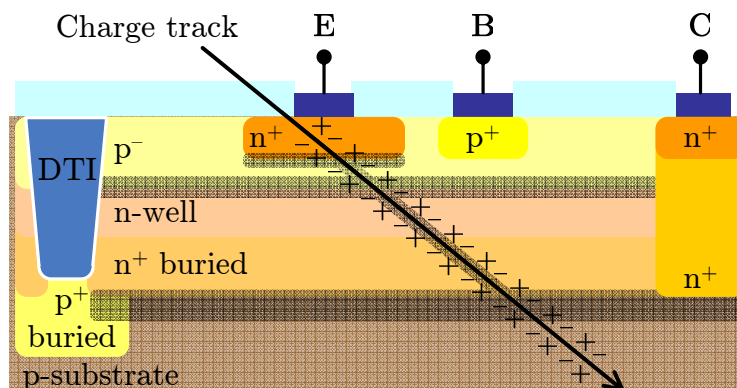


Figure 2.27: Illustration of multi-junction strike for charge track traversing vnpn. After [Hauser *et al.*, 1985, p.4115].

SEEs which pertain to analog circuits, known as single-event transients (SETs) are the subject of Section 2.2.2.

### 2.2.1 Single-Event Latchup

Not unique to radiation environments [Troutman, 1986, p.24–33],<sup>43</sup> latchup is an integrated-circuit condition caused by a parasitic positive feedback loop that, once enabled, is self-sustaining such that its current increases until it effectively shorts the supply to ground, which can permanently damage the chip.<sup>44</sup> Common in CMOS layouts, such as that shown in Figure 2.28(a), the p-n-p-n structure responsible for

<sup>43</sup>Latchup is a concern of the commercial semiconductor industry, not simply the space community [Oldham, 2003, p.36], and has been since its origin [Sexton, 2003, p.603]. The great deal of attention paid to latchup by the former [Johnston, 1996] stems from the host of possible triggering mechanisms outside the SEL context, including: power supply sequencing; overshoot or undershoot on input, output, or supply pins; junction avalanching at high currents; and electrostatic discharge (ESD) events, [Voldman, 2007, p.29–36]

<sup>44</sup>Latchup is certainly not the only means by which single-event ionizing radiation can immutably alter device operation. However, alternatives such as single-event burnout (SEB—thermal runaway from the avalanche breakdown caused by a heavy ion that activates a substrate BJT feedback loop), or single-event snapback (SESB—a regenerative, high-current feedback mechanism like latchup that occurs in a three-layer structures, such as the parasitic BJT that exists between a MOSFET source and drain), and single-event gate rupture (SEGR—when a single ion destroys the MOS gate dielectric through localized heating, rendering a hard short from gate to substrate) are most commonly observed in power transistors. For a thorough introduction to these subjects, consider [Oldham, 2003] and [Sexton, 2003].



latchup can occur anywhere that adjacent diffusions form a pair of parasitic BJTs (lateral npn Qn and vertical pnp Qp) coupled in a loop that is redrawn for clarity in Figure 2.28(b).<sup>45</sup>

A simplified representation of the nonlinear  $I$ - $V$  curve that characterizes this four-layer structure is presented in Figure 2.29 with reference to the terminals of the adjacent schematic. At the extremes are two stable states:<sup>46</sup> the high-impedance regime in Region I, known as the *blocking* or *off* state, is bounded by the switching point,  $(V_s, I_s)$ , [Troutman, 1986, p.11] below which all the p-n junctions are reverse-biased [Sexton, 2003, p.603] and the current scales linearly with voltage [Oldham, 2003, p.35]; and the *latched* or *on* state [Troutman, 1986, p.11], corresponds to Region III, where the junctions are saturated, yielding low-impedance for all voltages that exceed the hold point at  $(V_h, I_h)$ . Between these two lies a metastable region with negative differential resistance (Region II) through which the structure can transition.

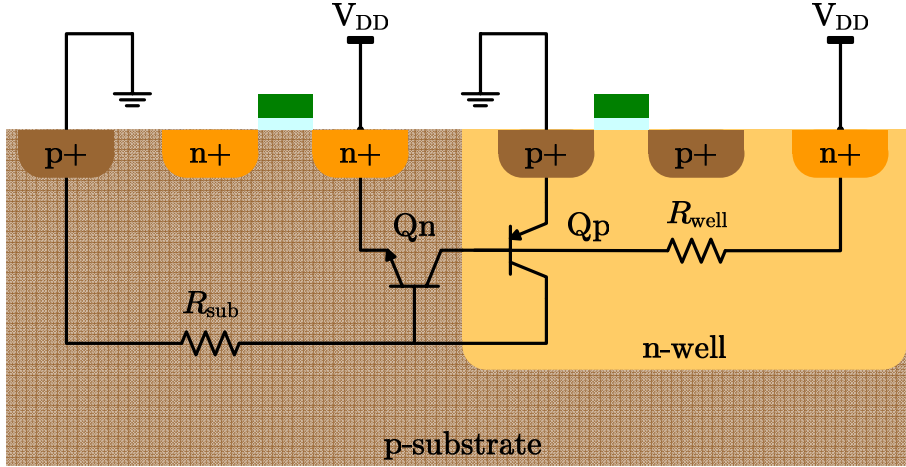
Traditionally, the necessary conditions for latchup are defined as those which guarantee operation in the latched state, and are threefold [Holmes-Siedle and Adams, 2002; Kerns, 1989, p.109, p.554]:

- The product of the transistor gains,  $\beta_n\beta_p$ , must exceed unity.
- The E-B junctions of both Qn and Qp must be forward-biased long enough that  $I \geq I_h$ .
- The biasing and power supply circuitry must be capable of supplying current at or above  $I_h$  in order to maintain the latched condition.

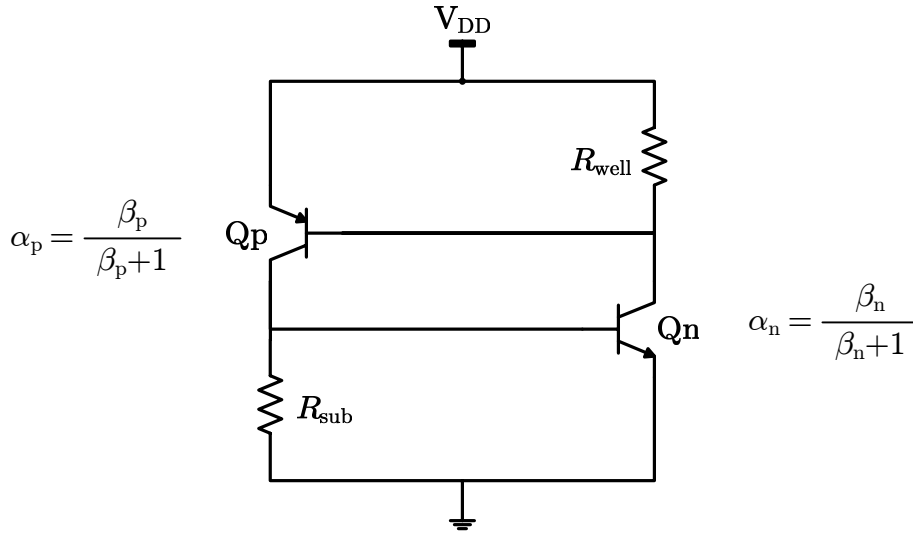
The first condition describes feedback that forces a structure in operating Region II to settled in the latched, rather than blocking, state. A direct outcome of the second condition is that the whole of the charge collection curve in Figure 2.26 is

<sup>45</sup>When created intentionally, such a structure is commonly referred to as a silicon-controlled rectifier (SCR) or thyristor [Holmes-Siedle and Adams, 2002, p.109].

<sup>46</sup>The terminology describing the partitions of Figure 2.29 is poorly standardized, with  $(V_s, I_s)$  known alternately as the *switching point*, *critical point* [Troutman, 1986, p.12], or *break-over point* [Oldham, 2003, p.35] and  $(V_h, I_h)$  variously dubbed the *hold point* or *threshold point* [Troutman, 1986, p.12]. In this work, the naming conventions of [Troutman, 1986] are employed exclusively.



(a) Silicon cross-section.



(b) Equivalent circuit.

Figure 2.28: Example of potential SEL structure in CMOS layout. The adjacent pMOS and nMOS device effectively form a parasitic bipolar feedback loop containing a vertical pnp (Qp) and lateral npn (Qn) with emitter shunt resistors (Rsub and Rwell).

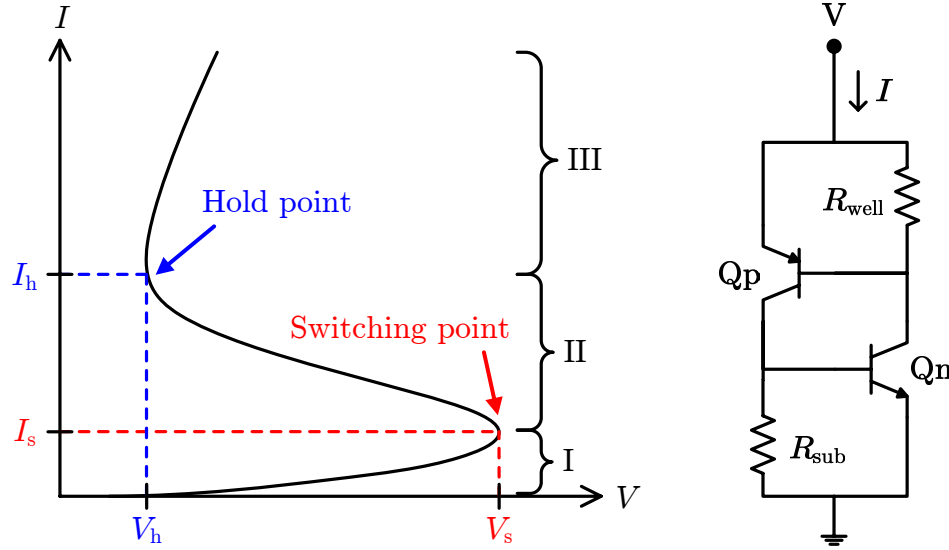


Figure 2.29: Illustrative  $I$ - $V$  characteristic of SEL-prone p-n-p-n structure in Figure 2.28(a) with blocking/off (I), negative-resistance (II), and latched/on (III) regions indicated. At the right, Figure 2.28(b) is re-annotated with terminal quantities. After [Sexton, 2003, p.604].

significant, so latchup can be initiated on long time scales ( $\sim 20$  ns) and by charges from deep within the bulk ( $> 100 \mu\text{m}$ ) [Sexton, 2003, p.607]. The satisfaction of all three conditions enables the p-n-p-n structure to carry such high currents (up to the limits of the power supply [Kerns, 1989, p.554]) as to cause catastrophic failure in the form of thermal overstressing of devices and metalization [Oldham, 2003, p.35], device burnout [Messenger and Ash, 1992, p.385], and electromigration failures [Sexton, 2003, p.607]. These consequences can be avoided, and normal operation restored, if  $V$  is reduced below  $V_h$  in a timely fashion, typically by cycling the power supply [Holmes-Siedle and Adams, 2002, p.385]. However, there exists evidence that latent damage responsible for reducing long-term device reliability can persist [Oldham, 2003, p.35].

Thus, for a robust design it is not sufficient to merely prevent the structure from entering the latched state, or quickly interrupting its power once there. Instead, in a ‘healthy’ technology, “no parasitic PNPN device ever leaves the blocking state” [Troutman, 1986, p.198]. This more conservative approach modifies the above latchup

conditions as follows [[Troutman, 1986](#), p.24]:

- The loop gain of the p-n-p-n feedback loop must exceed unity.
- The E-B junctions of both Qn and Qp must be forward-biased long enough that  $I \geq I_s$ .
- The biasing and power supply circuitry must be capable of supplying current at or above  $I_s(I_h)$  in order to leave the blocking state(maintain the latched condition).

Latchup avoidance strives to violate one or more of these conditions. For instance, system-level techniques can be used to sense incipient latchup and cycle the power before the second condition is attained.<sup>47</sup> Similarly, as CMOS scaling trends reduce supply voltages below 1-V, there comes a point at which it is impossible to satisfy  $V > V_h$ , as implied by the last condition [[Lacoe, 2003](#), p.112], [[Sexton, 2003](#), p.607], [[Oldham, 2003](#), p.37]. But, to develop a package-agnostic ASIC in a 2.5-V BiCMOS process (cf. Section 3.2.1), the radiation-hardness-by-design techniques developed in this work are aimed at the first requirement, because the loop gain can be modified through careful circuit design and layout.

In anticipation of presenting these techniques, and considering the simplified, lumped-element circuit in Figure 2.28(b), the necessary condition on the loop gain to ensure that it remains below unity, avoiding latchup, is given by [[Troutman, 1986](#), p.62]:

$$\alpha'_{AC,n} + \alpha'_{AC,p} < 1 \quad (2.20)$$

where  $\alpha'_{AC,n}$  and  $\alpha'_{AC,p}$  are the effective common-base forward current gains of Qn and Qp, respectively, that correspond to small-signal modeling. As opposed to the standard versions of these small-signal gains, which are defined as partial derivatives of the time-varying terminal currents rather than ratios of their DC values, according

---

<sup>47</sup>Consider the example of the Maxwell 7809 latchup-protected 16-bit ADC [[Maxwell Technologies, 7809LP](#)], which is merely a Burr-Brown ADC7809 die packaged with additional circuitry to sense excess supply current and promptly cycle the power [[Maxwell Technologies, 2005](#), p.14–15].

to [Troutman, 1986, p.62]:<sup>48</sup>

$$\alpha_{AC,n} = \frac{\beta_{AC,n}}{1 + \beta_{AC,n}} = \frac{\partial I_{cn}}{\partial I_{en}} \quad (2.21a)$$

$$\alpha_{AC,p} = \frac{\beta_{AC,p}}{1 + \beta_{AC,p}} = \frac{\partial I_{cp}}{\partial I_{ep}} \quad (2.21b)$$

the primed quantities in (2.20) are effective gains in that they account for the degeneration due to the current dividers at each terminal formed by the emitter bypass resistors  $R_{sub}$  and  $R_{well}$ ,<sup>49</sup> and the small-signal emitter resistances  $r_{en}$  and  $r_{ep}$ ,<sup>50</sup> such that [Troutman, 1986, p.72]

$$\alpha'_{AC,n} = \frac{\alpha_{AC,n}}{1 + \frac{r_{en}}{R_{sub}}} \approx \frac{\alpha_{AC,n}}{1 + \frac{V_T}{I_{en} R_{sub}}} \quad (2.22a)$$

$$\alpha'_{AC,p} = \frac{\alpha_{AC,p}}{1 + \frac{r_{ep}}{R_{well}}} \approx \frac{\alpha_{AC,p}}{1 + \frac{V_T}{I_{ep} R_{well}}} \quad (2.22b)$$

From (2.22), it is clear that the presence of the distributed substrate and well resistances, conveniently but somewhat naively lumped into  $R_{sub}$  and  $R_{well}$ , respectively, increases latchup tolerance with greater effectiveness as they shrink [Voldman, 2007, p.130]. Similarly, reducing the gains of the parasitic transistors,  $\alpha_{AC,n}$  and  $\alpha_{AC,p}$ , through so-called gain spoiling or gain decoupling [Troutman, 1986, p.174], reduces latchup sensitivity. Finally, low-level injection effects (cf. Section E.1.2.1) suppress  $\alpha'_n$  and  $\alpha'_p$  at low emitter currents which, in the case of SEL, are determined by the charge injected from an ionizing track, multiplied up through transistor action;

<sup>48</sup>The distinction between  $\alpha$  and  $\alpha_{AC}$  is analogous to that between  $\beta$  and  $\beta_{AC}$ , as described in Section E.1.

<sup>49</sup>In this formulation, it is assumed that when the parasitic base ( $R_{bn}$ ,  $R_{bp}$ ) and emitter ( $R_{en}$ ,  $R_{ep}$ ) resistances associated with the terminals of Qn and Qp are referred to their emitters, the resulting  $R'_{en} = R_{en} + R_{bn}/(\beta_n + 1)$  and  $R'_{ep} = R_{ep} + R_{bp}/(\beta_p + 1)$  are much smaller than the differential resistance seen looking into their emitters; that is,  $R'_{en} \ll r_{en}$  and  $R'_{ep} \ll r_{ep}$  [Voldman, 2007, p.150].

<sup>50</sup>In the absence of high-level injection effects, the BJT emitter current can be treated as exponentially dependent on  $V_{be}$ , so the small-signal emitter resistances defined as  $r_{en} = \partial V_{ben} / \partial I_{en}$  and  $r_{ep} = \partial V_{bep} / \partial I_{ep}$  can be well approximated by  $r_{en} \simeq V_T / I_{en}$  and  $r_{ep} \simeq V_T / I_{ep}$  [Troutman, 1986, p.64].

so, techniques for reducing the various contributions to the initial  $Q_{\text{col}}$  described in Section 2.2 directly reduce the likelihood of latchup.

### 2.2.2 Single-Event Transients

Whereas ‘hard’ errors, such as latchup, describe physical damage to one (or a pair) of individual transistors, the transient phenomena at the crux of this section result when charge collection by one or more transistors (through drift, diffusion, funneling or shunt mechanisms) perturbs operation at the circuit level [Messenger and Ash, 1992, p.396]. Given the assortment of acronyms used to describe single-event effects (e.g., [Oldham, 2003, p.11]), the terminology surrounding these temporary disturbances produced by the passage of single ion, known as single-event transients, is neither straightforward nor well standardized. Historically, digital SETs (DSETs) have received greater attention [Buchner and Baze, 2001] because they are the predecessors of single-event upsets (SEUs), the latter consisting of the state change (or ‘bit-flip’) that occurs once a sufficiently large DSET is latched into memory [Buchner and Baze, 2001, p.3]. Such ‘soft’ errors, which inflict no permanent damage [Oldham, 2003, p.11], are easily characterized by the loss of a single, dimensionless bit of information [Turflinger, 1996, p.594] that occurs once  $Q_{\text{col}}$  exceeds the critical charge,  $Q_{\text{crit}}$ , necessary to invert a binary value [Messenger and Ash, 1992, p.419].

In contrast, seminal work by Koga *et al.* [1993] confirmed the existence of SETs in analog circuits (ASETs) which tend to be circuit-specific and, thus, elusive. While formal definitions range from “a single particle-induced phenomenon that requires additional dimensions (or attributes) beyond its existence to be adequately defined” [Turflinger, 1996, p.594] to “any temporary voltage [or current] disturbance that occurs in an [analog] integrated circuit (IC) following the passage of an ionizing particle” [Buchner and McMorro, 2005, p.2], an ASET can perhaps best be understood informally as a ‘glitch’ in an analog signal being processed. To be designated as an ASET, such a pulse must exceed a threshold that, unlike  $Q_{\text{crit}}$  for DSETs, can vary from part to part and must be qualified with polarity, duration, and voltage information [Koga *et al.*, 1993, p.1840]. Although efforts have been made

to frame ASET sensitivity in terms of a corresponding  $Q_{\text{crit}}$  [Pease et al., 2001],<sup>51</sup> its value remains “somewhat arbitrary” [Buchner and McMorrow, 2005, p.14], so “nearly all data collected is evaluated on the basis of the voltage amplitude of the SEE-induced pulse” [Turflinger, 1996, p.596] and a threshold,  $V_{\text{thresh}}$ , with the aforementioned qualifications.

An example of such a pulse and pulse-height discrimination threshold are shown in Figure 2.30. The modeled and laser-induced pulse shapes are characteristic of ASETs, which effectively stimulate the impulse response of a critical node, often modeled with a single-pole response; hence, the rapid, often slew-limited, rise followed by exponential decay [Turflinger, 1996, p.594]. Counting the number of pulses which exceed  $V_{\text{thresh}}$  generates an ‘upset’ distribution,  $N_u$ , which can then be quantified using two parameters standard in SEU analysis [Holmes-Siedle and Adams, 2002; Turflinger and Davey, 1990, p.1832, p.107]: saturated cross-section ( $\sigma_{\text{sat}}$ ) and threshold LET ( $\mathcal{L}_{\text{th}}$ ). Both are obtain by plotting the rationalized upset cross-section,  $\sigma_u$ , defined by [Turflinger and Davey, 1990, p.1832]:

$$\sigma_u = \frac{N_u}{R\phi_I} \quad (2.23)$$

as a function of  $\mathcal{L}$ , using the rationalization factor  $R$  to normalize for one or more of the implicit qualifications;  $\phi_I$  is the ionizing radiation fluence.

The ideal shape of such an SEU curve for is contrasted with the actual forms for SEUs and ASETs in the cartoon representation of Figure 2.31. As the LET of the incident particle increases, the SEU curve reaches a point at which every ion deposits sufficient charge that  $Q_{\text{col}} > Q_{\text{crit}}$ , so each causes an upset. The limiting value of  $\sigma_u$  is

---

<sup>51</sup>Theoretically,  $Q_{\text{crit}}$  for analog circuits can simply be obtained from the product of the nodal capacitance and requisite voltage excursion at the critical junction,  $Q_{\text{crit}} = C_{\text{node}}(V_{\text{crit}} - V_o)$ . Of course, it is difficult to identify this node *a priori* [Pease et al., 2001, p.1971] and  $V_{\text{crit}}$  remains application- or system-specific [Buchner and McMorrow, 2005, p.13]. In contrast,  $Q_{\text{crit}}$  can be extracted from experimental data, as the product of the collection depth and incident LET when a pulse exceeds  $V_{\text{thresh}}$ , but this requires an estimate of the collection depth for the critical junction [Buchner and McMorrow, 2005, p.14]. A third approach, using a pulsed laser whose photon energy corresponds to a specific amount of deposited charge (e.g., 1 pC per 2 pJ [Pease et al., 2001, p.1967]), still requires assumptions on collection depth to yield an effective  $Q_{\text{crit}}$ , but has demonstrated greater promise [Pease et al., 2001].

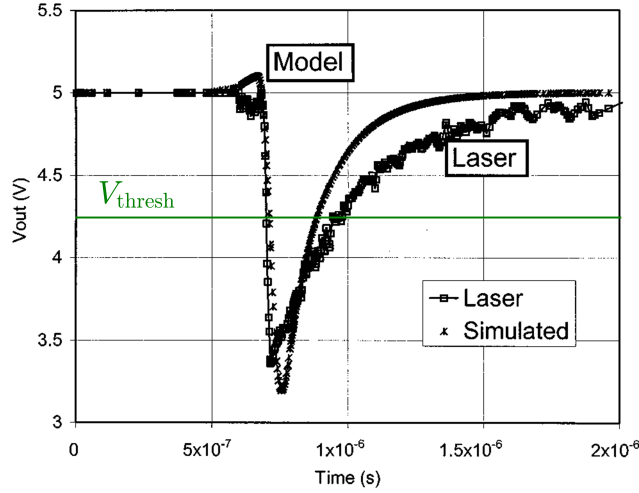


Figure 2.30: Representative ASET measured(modeled) for the LM111 comparator with an input offset of 20 mV(10 mV). For the  $V_{\text{thresh}}$  shown, a laser illuminating the input device (Q1) is sufficient to generate an ASET, so it can be inferred that  $V_{\text{crit}} \geq 20$ . Modified from [Pease *et al.*, 2001, p.1971].

$\sigma_{\text{sat}}$ , which has units of normalized area and thus describes the sensitive fraction of the die surface [Turflinger and Davey, 1990, p.1833]. The LET at which  $\sigma_{\text{lim}} = 0.9\sigma_{\text{sat}}$  is defined as  $\mathcal{L}_{\text{th}}$ , giving rise to a single coordinate that describes the SEU curve,  $(\mathcal{L}_{\text{th}}, \sigma_{\text{lim}})$  [Turflinger and Davey, 1990, p.1833], which is typically a Weibull fit to the data points [Baumeister, 2003, p.35].

However, the behavior of the ASET curve defies such a fit, demonstrating a much more gradual rise and, in many cases, not saturating [Turflinger, 1996, p.599]. The former property can be attributed to upsets in the bias circuitry, which have much slower time constants and thus require larger LET to reach  $V_{\text{crit}}$  for a given pulse duration [Turflinger, 1996, p.595], or to the aggregate behavior of multiple critical nodes, each with its own  $V_{\text{crit}}$  [Buchner and McMorrow, 2005, p.23]. The lack of saturation may reflect the diffusion of a portion of the charge from large but distant strikes to the critical junction(s) [Petersen *et al.*, 1992, p.1585]. Despite the inferior description of the underlying ASET phenomena that is afforded by a characterization using  $V_{\text{thresh}}$ ,  $\sigma_{\text{sat}}$ , and  $\mathcal{L}_{\text{th}}$ , it remains the *de facto* standard for analog circuits and,



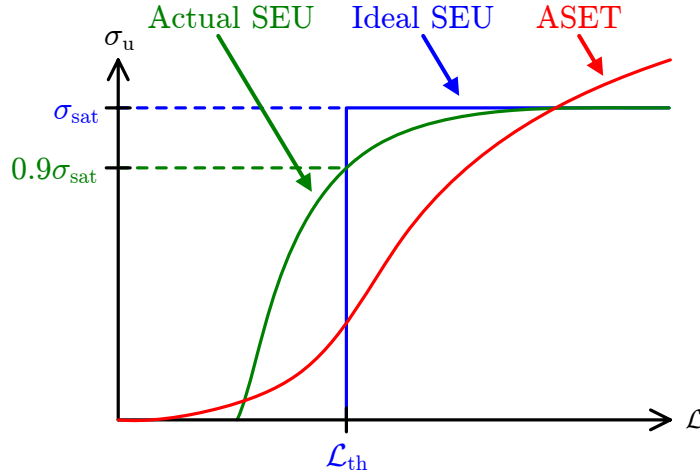


Figure 2.31: Ideal cross-sections for SEUs and ASETs as a function of LET. Whereas the step-function(Weibull) response for ideal(actual) SEUs can be described by a single coordinate,  $(\mathcal{L}_{\text{th}}, \sigma_{\text{sat}})$ , the ASET curve rises gradually and typically does not saturate. After [Buchner and McMorrow, 2005, p.23].

on that count, is employed herein.<sup>52</sup>

To foreshadow the SEE characterization of SVEPRE, Figure 2.32 presents cross-section curves for the OP-42 operational amplifier at various  $V_{\text{thresh}}$  levels, each corresponding to a minimum amplitude of the output transient. For the smallest transients,  $\mathcal{L}_{\text{th}}$  approaches 1 MeV-cm<sup>2</sup>/mg, which is easily attained by heavy ions in space, explaining observed ASETs for protons as low as 30 MeV [Buchner and McMorrow, 2005, p.5]. By depositing charge near individual transistors, it has been found [Koga et al., 1993] that the sensitivity to low- $V_{\text{crit}}$  ASETs in this and, in fact, most amplifiers is governed by devices in the first stage, whose low bias currents and high gains [Johnston et al., 2000, p.2633] produce large voltage pulses in response to the current injected by  $Q_{\text{crit}}$ ; these are then amplified by subsequent stages [Turflinger, 1996, p.599]. At least in the case of Figure 2.32, the part returned to normal operation after each transient [Buchner and McMorrow, 2005, p.4]; for more a sensitive circuit, ASETs can lead to serious malfunctions, such as causing it

<sup>52</sup>More sophisticated methods that derive upset thresholds in both amplitude and duration for operational amplifiers [Adell et al., 2000; Savage et al., 2004], and that divide code upsets into small(noise) and large(offset) errors for ADCs [Turflinger and Davey, 1990; Turflinger et al., 1994] are gaining acceptance, but neither is appropriate for the front-end ASIC.

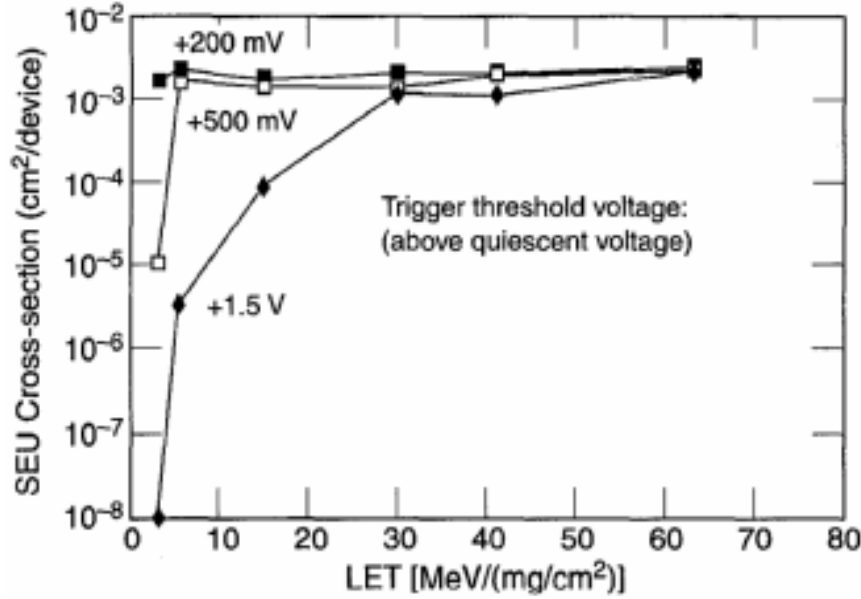


Figure 2.32: Measured ASET cross-sections for OP-15. As demonstrated by [Koga et al. \[1993\]](#), increasing in the trigger level that defines upset raises  $\mathcal{L}_{th}$  but, in all cases,  $\sigma_{sat}$  approaches  $\sim 3.5 \times 10^{-3} \text{ cm}^2$  for this part (total area:  $2.44 \times 10^{-2} \text{ cm}^2$ ). Reproduced *in toto* from [[Buchner and McMorow, 2005](#), p.26].

to oscillate, saturate, or even reset.<sup>53</sup>

In that vein, it should be noted that as opposed to latchup, whose deleterious effect is clear, the detriment of ASETs in a particular analog element depends upon how that block functions within the overall system which, in turn, guides the choice of  $V_{thresh}$ . In some cases, such glitches may simply be treated as noise [[Buchner and McMorow, 2005](#), p.3]. When high-bandwidth operational amplifiers are used with global feedback, large glitches in any one stage can have little overall impact since they are severely attenuated by the closed-loop bandwidth [[Turflinger, 1996](#), p.595]. For mixed-signal systems, only those ASETs which arrive at the downstream ADC with sufficient size and duration to corrupt one or more samples are observed [[Buchner and McMorow, 2005](#), p.3]. Such considerations guide the SET specifications set forth in

<sup>53</sup>Such anomalous changes in instrument state as a result of ASETs, particularly resets caused by ions striking operational amplifiers and comparators, have afflicted several previous satellites, including TOPEX/Posiden (1992), MAP (2001), TDRS, Cassini, SOHO, and TERRA [[Buchner and McMorow, 2005](#), p.1–2].

the discussion of the front-end architecture (cf. Section 2.3.1).

## 2.3 Radiation Hardening

The discipline concerned with mitigating the incidence and ramifications of the TID and SEE effects described in Section 2.1 and Section 2.2 by leveraging the current understanding of the underlying physical mechanisms presented in Appendix C is known as radiation hardening. Of military origins [*Holmes-Siedle and Adams, 2002*, p.474], this term spawned the use of the generic adjectives ‘rad-hard’ and ‘rad-soft’ (or, often, just ‘hard’ and ‘soft’) to refer to electronics of relatively high and low radiation tolerance, respectively.<sup>54</sup> Section 2.3.1 quantifies the required level of radiation-hardness for the front-end ASIC in terms of the dose and LET of a representa

### 2.3.1 Van Allen Belt Fluxes

The energy spectra of the trapped proton and electron populations in the inner and outer zones of the Van Allen belt are provided in Section 1.1.1, along with their corresponding fluxes as a function of altitude. Using the standard NASA AP8 and AE8 models for these quantities [*Stassinopoulos and Raymond, 1988*, p.1426],<sup>55</sup> it is possible to generate an estimated dose profile for a given radiation-belt orbit [*Holmes-Siedle and Adams, 2002*, p.561]; results for several possibilities are shown in Figure 2.33.

In order to derive the specifications for this work, consider the parameters of a representative host satellite for the target receiver: a 5.3-hr elliptical, mid-inclination, medium Earth orbit (MEO) of 6,000 km by 12,000 km with a 1-year mission lifetime

---

<sup>54</sup>Since there exists no universal or precise definition of these designations [*Holmes-Siedle and Adams, 2002*, 131–132], references hereafter to the TID- or SEE-hardness of a design should be interpreted as relative to the target dose or LET levels specified in Section 2.3.1 unless otherwise stated.

<sup>55</sup>Incorporating data from 55 instruments, comprising 1630 channel-months, AP8 and AE8 are considered the best available models for computing electron and proton doses, respectively, for radiation-belt orbits [*Barth et al., 2003*, p.470], despite the fact that all these data were taken before 1980, introducing sometimes significant inaccuracies [*Holmes-Siedle and Adams, 2002*, p.28].

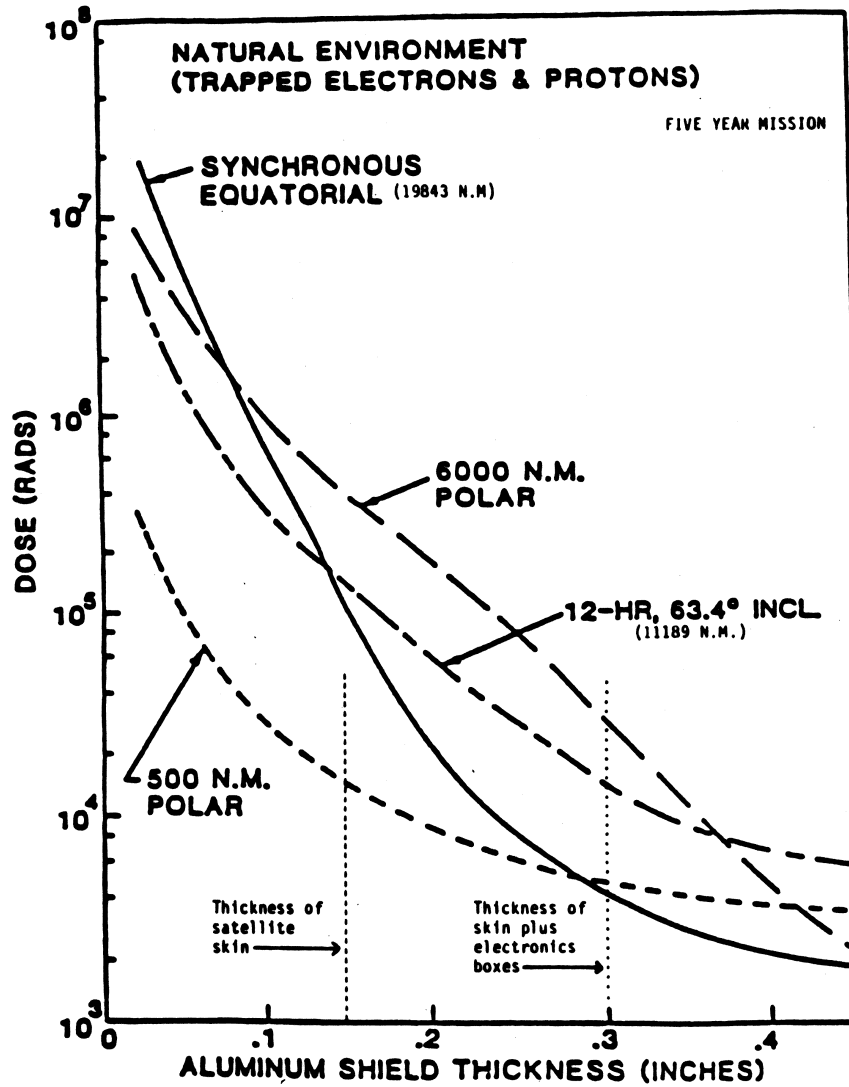


Figure 2.33: 5-year accumulated dose for various radiation-belt orbits, as computed from NASA AP-8 and AE-8 models of trapped protons and electrons, respectively. Reproduced *in toto* from [Tascione, 1994, p.142].

[*Spanjers et al.*, 2006, p.2–3].<sup>56</sup> A reasonable estimate of the 5-yr accumulated dose for this orbit is provided by the ‘6000 N.M. polar’ curve in Figure 2.33; the benefits of more geomagnetic shielding at this altitude are roughly offset by higher fluxes over the poles, thereby approximating the proposed orbit. As delineated by the dotted vertical lines, the average dose rate experienced by the ASIC ranges between 10–100 krad(Si)/yr depending upon the shielding thickness. This is consistent with the set of conservative CRRESRAD-based [*Gussenhoven et al.*, 1996] predictions offered by *Spanjers et al.* [2006] and facilitates a quantitative determination of those hardening approaches in the next section that are applicable to this work.

Though it accounts for the total energy contributed by ionizing and non-ionizing radiation, Figure 2.33 only provides an estimate of the required total-dose tolerance. A complete radiation specification must also incorporate SEE data on the heavy ion flux as function of LET, an example of which is afforded by Figure 2.34. This plot assumes 3.7-mm Al shielding (cf. Section 2.3.2.1) and is based on the CREME96 model set [*Tylka et al.*, 1997], though it pertains to a more pessimistic orbit than Figure 2.33. In the case of a digital circuit with known  $\sigma_u(\mathcal{L})$ , such a curve allows for a determination of the SEU upset rate [*Turflinger and Davey*, 1990, p.1833],  $R_{\text{SEU}}$ , by inverting (2.23), normalizing for time, and integrating its product with  $\sigma_u(\mathcal{L})$  over all  $\mathcal{L}_{\text{max}} > \mathcal{L} > \mathcal{L}_{\text{th}}$  such that [*Petersen et al.*, 1992, p.1579]

$$R_{\text{SEU}} = \int_{\mathcal{L}_{\text{th}}}^{\mathcal{L}_{\text{max}}} \sigma_u(\mathcal{L}) \Phi(\mathcal{L}) d\mathcal{L} \quad (2.24)$$

However, for SEL and ASETs—the events to which the analog front-end is most susceptible—existence is more important than upset rate. Thus, proper operation is defined in terms of the maximum expected LET,  $\mathcal{L}_{\text{max}}$ , for incident particles below which both SEL and any detrimental or long-lived ASETs should be absent; that is,  $\mathcal{L}_{\text{th}} > \mathcal{L}_{\text{max}}$  for SEL and ASETs, collapsing (2.24) to zero. According to Figure 2.34,  $\mathcal{L}_{\text{max}} \simeq 100 \text{ MeV-cm}^2/\text{mg}$  corresponds to those particles whose integral,

---

<sup>56</sup>Incidentally, the Telstar satellite whose failure has been repeatedly cited in previous footnotes also orbited in MEO.

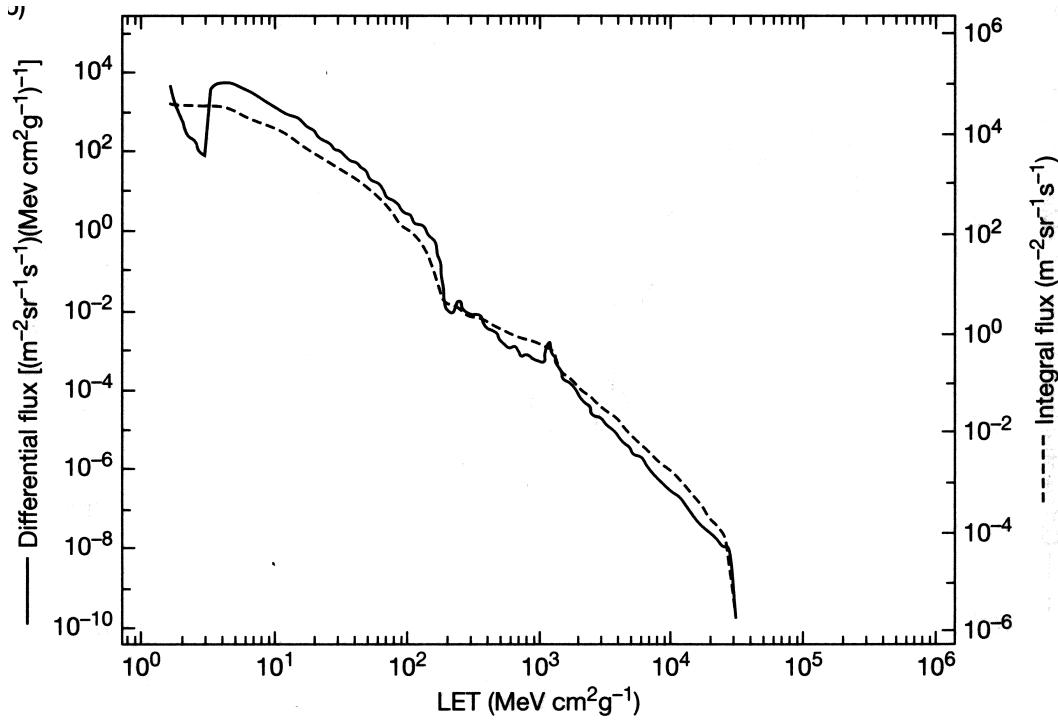


Figure 2.34: Orbit-averaged LET spectrum for circular, geosynchronous orbit of 20182 x 20182 km, 55°. Omnidirectional integral flux for a given LET is obtained by integrating the value on left-hand axis over the full acceptance angle ( $4\pi$  steradians). Reproduced *in toto* from [Holmes-Siedle and Adams, 2002, p.566]

omnidirectional flux exceeds  $\sim \pi \times 10^{-7} \text{ cm}^{-2}\text{s}^{-1}$  and thus are encountered at least once per year. This choice of  $\mathcal{L}_{\text{max}}$  is also consistent with conventional best practices for component selection [Tribble, 2003, p.190], which confer the designation of single event ‘immunity’ on those parts for which  $\mathcal{L}_{\text{th}} > 100 \text{ MeV-cm}^2/\text{mg}$  [Voldman, 2007, p.43].<sup>57</sup>

<sup>57</sup>Since “the maximum LET in space is essentially 30 MeV-cm<sup>2</sup>/mg” [Petersen et al., 1992, p.1590], there is only  $\sim 5\%$  chance of a particle trajectory that is sufficient to produce an effective 100 MeV-cm<sup>2</sup>/mg event. Indeed, “for all practical purposes, the LET distribution of cosmic rays can be truncated at about 100 MeV-cm<sup>2</sup>/mg or less” [Koga, 1996, p.662]. See Section J.2.1.2 for a more thorough treatment of effective LET.

### 2.3.2 Mitigation Strategies

Spurred by military concerns over nuclear weapons and space, the interest in radiation-hardening of satellite electronics has deep roots [*Hughes and Benedetto*, 2003, p.501–504], from which the most salient conclusion is that “there is no ‘magic ingredient’” [*Kerns et al.*, 1988, p.1471]. Instead, “radiation hardness is determined by complex interrelationships among technology, design, and fabrication procedures” [*Hughes and Benedetto*, 2003, p.500]. In light of the specifications derived above, the succeeding sections summarize the principles of three basic strategies for radiation hardening—shielding, process, and design—emphasizing why the latter is most appropriate for this work.

#### 2.3.2.1 Shielding

Perhaps the most obvious approach to limiting the radiation-induced degradation or upset of the ASIC is simply to limit its total exposure [*Rasmussen*, 1988, p.1532]. With the orbit-driven TID and SEE levels mandated by the scientific objectives in Section 1.1.3, the most expedient method of avoidance is to employ shielding [*Tribble*, 2003, p.172]. Although a thorough review of its dependencies on particle type and energy, not to mention the atomic properties of the shielding material, are beyond the scope of this section,<sup>58</sup> shielding is tangentially referenced in Section C.1.1, where it is noted that the high- $Z$  materials, such as lead, can be useful for absorbing low-energy protons and ions, but are less effective against: electrons, which have greater range for the same energy and for which bremsstrahlung is proportional to  $Z^2$ ; neutrons, which lose more momentum per collision in low- $Z$  materials; and photons, which are attenuated but never completely stopped and for which Compton scattering is independent of  $Z$ . These three particle types are best shielded by low- $Z$  materials, such as aluminum, whose lower mass is also preferable [*Rasmussen*, 1988, p.1533].<sup>59</sup>

---

<sup>58</sup>For a more complete yet accessible treatment, the reader is directed to Chapter 11 of [*Holmes-Siedle and Adams*, 2002].

<sup>59</sup>To clarify, electrons themselves are, like protons, best absorbed by high- $Z$  materials, so lead (Pb) acts as a better shield, per unit thickness than aluminum (Al). Only once the deeply penetrating Bremsstrahlung X-rays produced by their back-scatter are considered does the more gradual deceleration of Al become attractive [*Holmes-Siedle and Adams*, 2002, p.389]. Neither material

Given that the Van Allen belt is dominated by protons and electrons, shielding with either aluminum or lead may be employed, with efficacy of the former for a typical orbit at these altitudes captured in Figure 2.33. To reduce total dose levels to 10 krad(Si)/yr, for which most COTS components are suited [Tribble, 2003, p.191], would require a thickness of  $\sim 8$  mm [Spanjers *et al.*, 2006, p.7]. Given its higher density, the corresponding thickness for Pb is only  $\sim 2$  mm, as evidenced by Figure 2.35, but since the miniaturized satellites for which the target receiver is intended (cf. Section 1.2.2) cannot even accommodate 5 mm of Al, on account of their low mass requirements, Pb is out of the question. In fact, for the most prominent member of the picosatellite family, the CubeSat, the thickness of the Al side panels can be no greater than 1/8 inches (3.175 mm) in order to satisfy the 1-kg total mass requirement [Heidt *et al.*, 2000, p.7].

Thus, to enable a target receiver compatible with next-generation satellites and whose mass/channel is commensurate with if not superior to those listed Table B.6, it is conservatively assumed that no more than 3 mm of Al shielding is provided by the spacecraft body. In Figure 2.33, this corresponds to the line denoting the thickness of the satellite skin,<sup>60</sup> implying that the front-end must maintain performance up to at least 100 krad(Si) to survive for one year in a standard Van Allen belt orbit [Rasmussen, 1988, p.1530]. Note that this amount of shielding affords little in the way of SEE protection [Kerns *et al.*, 1988, p.1476], as the high-energy spectrum of the offending particles is hardly slowed [Rasmussen, 1988, p.1533].

---

is especially useful for photon radiation: for 1-MeV photons, there is a 94%(93%) transmission rate through 3.7(0.1) mm of Al(Pb) [Holmes-Siedle and Adams, 2002, p.402]. But, given this lack of dependence on mass-thickness (density times thickness), the lighter material is preferred. Luckily, X-rays and  $\gamma$ -rays are not a primary concern in the radiation belts, with only their secondary production due to Bremsstrahlung and nuclear spallation relevant. Finally, in light of the huge mass that would be required for materials of sufficiently low density (e.g., water), neutron shielding is largely impractical in space [Rasmussen, 1988, p.1533]; but, again, neutron events are comparatively rare outside the homosphere.

<sup>60</sup>As opposed to satellites in production at the time Figure 2.33 was generated, picosatellites as presently conceived accept bare circuit boards without electronics boxes for each instrument.



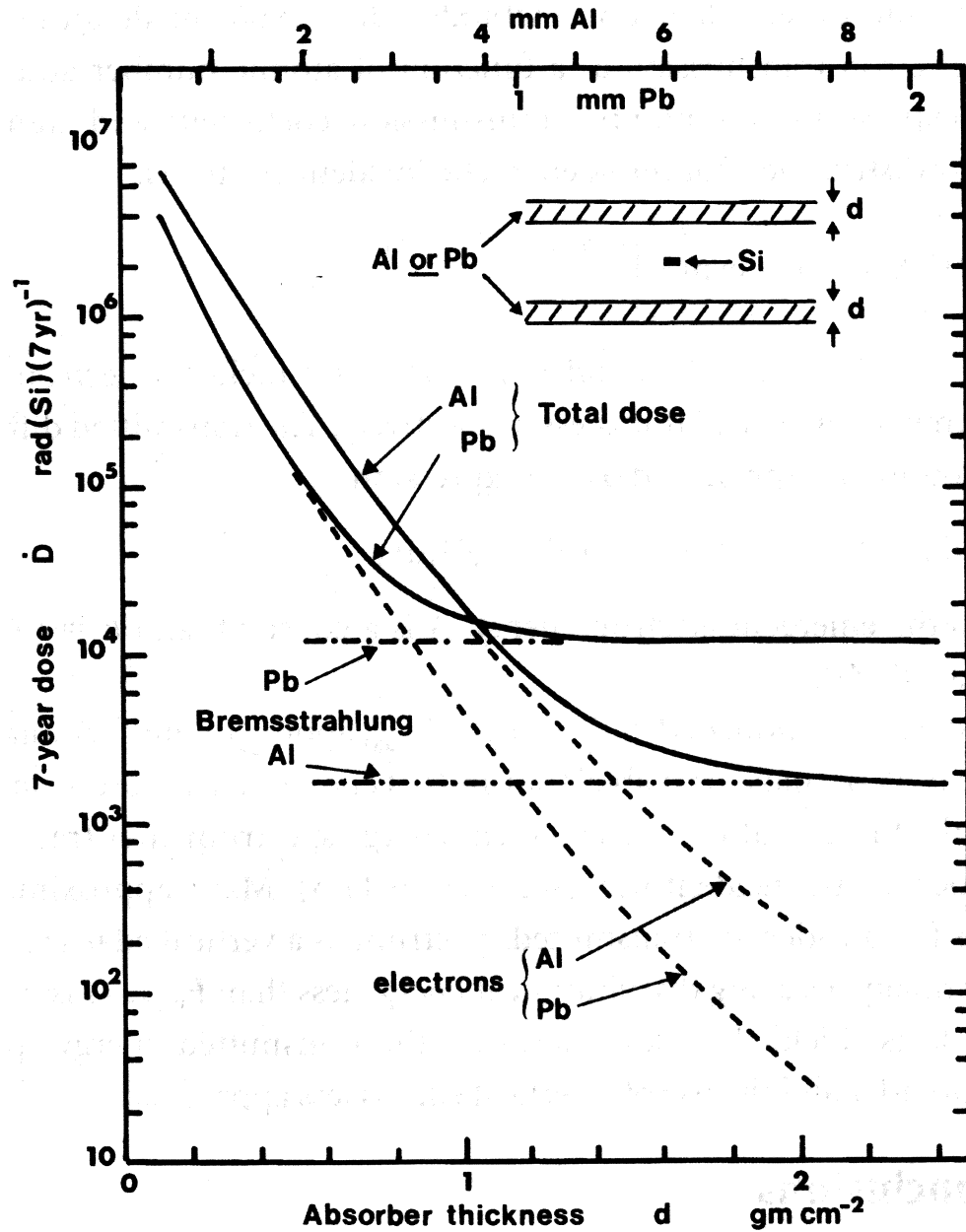


Figure 2.35: Dose-depth curves for Al and Pb shielding over a 7-year geostationary orbit (35,786 x 35,786 km). Although the input fluxes assume an older NASA model for electrons only (AEI-7), and although the lead curve is considered provisional, the relative absorption efficiencies and Bremsstrahlung production of the two materials are indicative of their merits. Reproduced *in toto* from [Holmes-Siedle and Adams, 2002, p.415]

### 2.3.2.2 Radiation-Hardened Process

As evident from the critical roles of oxide constitution and quality (e.g., impurities, defects), interface cleanliness, dielectric structure, and bulk lattice regularity in the physics of Appendix C [*Hughes and Benedetto*, 2003, p.501], the manufacturing process used to fabricate the silicon die is the primary factor in determining its radiation tolerance [*Holmes-Siedle and Adams*, 2002, p.475]. To that end, there has been much effort to develop specialized, radiation-hardened manufacturing processes tailored to mitigate the effects of radiation on their transistors [*Hughes and Benedetto*, 2003; *Lacoe et al.*, 2000, p.512, p.2334].<sup>61</sup> Exemplars of these rad-hard processes assure circuits that can withstand up to 1 Mrad(Si) total dose [*Hughes and Benedetto*, 2003, p.513] and remain free of latchup for LETs in excess of 150 MeV-cm<sup>2</sup>/mg [*Tribble*, 2003, p.191], without the need for any specialized design or layout techniques.

Although the litany of steps unique to a representative radiation-hardened process is too vast to cover here,<sup>62</sup> and is often deemed proprietary or classified by the foundry [*Hughes and Benedetto*, 2003; *Oldham*, 2003, p.496, p.510], it may include: using polysilicon gate material in place of aluminum [*Hughes and Benedetto*, 2003, p.507] (cf. Figure 2.3(b)); limiting the use of siliciding materials due to dose enhancement [*Hughes and Benedetto*, 2003, p.508]; employing Si<sub>3</sub>N<sub>4</sub> as a dielectric to block lateral diffusion [*Hughes and Benedetto*, 2003, p.508]; eliminating impurities such as hydrogen and nitrogen which degrade hardness [*Hughes and Benedetto*, 2003, p.508]; modifying the oxide growth procedure to lessen the accumulation of Si at the interface and reduce the number of defects [*Hughes and Benedetto*, 2003, p.509]; carefully

---

<sup>61</sup>The dichotomy to be carried forward in this section pits rad-hard processes, which are developed and qualified for the production of military-grade, radiation-hardened components against standard commercial manufacturing processes, in which no attention has been paid to intentionally improving radiation tolerance. The literature occasionally distinguishes these two classes, henceforth referred to simply as rad-hard and commercial, based on levels of TID and SEE tolerance, and introduces a third, the rad-tolerant process, in between [*Lacoe et al.*, 2000, p.2338]. But, since the lines of demarcation between these three in terms of TID (2–10, 20–50, >200 krad(Si)) and SEU (5, 20, 80–150 MeV-cm<sup>2</sup>/mg) are somewhat arbitrary, subsequent arguments pertain only to the two extremes [*Tribble*, 2003, p.191].

<sup>62</sup>For a thorough discussion of the guidelines that apply to radiation-hardened manufacturing processes, the reader is once again directed to the excellent text of Ma and Dressendorfer, specifically [*Dressendorfer*, 1989b].

controlling the polishing and implants associated with STI structures to prevent leakage [Brady *et al.*, 1999; Shaneyfelt *et al.*, 1998, p.1838]; properly engineering passivation layers to eliminate ELDRS [Shaneyfelt *et al.*, 2002]; introducing pull-backs and increased sidewall doping densities to prevent leakage under recessed and junction isolations [Pease *et al.*, 1983]; and optimizing the temperatures and conditions of oxide growth to minimize border-traps, reducing  $1/f$  noise [Fleetwood *et al.*, 1994b, p.1961].

On account of the costs associated with implementing these additional and often non-standard modifications [Holmes-Siedle and Adams, 2002, p.475], not the mention the limited market [Holmes-Siedle and Adams, 2002, p.475] and low production volumes [Hughes and Benedetto, 2003, p.513] for rad-hard components, such radiation-hardened processes tend to be expensive to retain (by a factor of  $10\times-1000\times$  [Hughes and Benedetto, 2003; Rasmussen, 1988, p.1534,p.513]), scare enough to make access difficult [Hughes and Benedetto, 2003; Kerns *et al.*, 1988, p.513,p.1471], and several generations behind in performance [Holmes-Siedle and Adams, 2002; Rasmussen, 1988, p.475,p.1527] and feature size [Lacoe *et al.*, 2000; Rasmussen, 1988, p.2334,p.1534] when compared to state-of-the-art commercial equivalents.

### 2.3.2.3 Advanced Commercial Process

However, in some instances, trends in commercial manufacturing lines driven by industry demand for increased performance, reduced cost, and higher operating speeds, have also proven beneficial to the radiation-hardness of these processes [Holmes-Siedle and Adams, 2002; Lacoe *et al.*, 2000, p.485,p.2341]. In particular, the evolution of CMOS scaling, the maturity of silicon-on-insulator (SOI) technologies, and the ascension of heterojunction bipolar transistors (HBTs) have all yielded ancillary improvements in rad-tolerance that make them attractive alternatives to authentic rad-hard processes.

**Scaled CMOS:** Perhaps the most significant of these, on account of the inexorable advance of Moore's law, is CMOS technology scaling, which has, among other

geometric changes, lead to the shrinking of  $t_{\text{ox}}$  below 10 nm and the adoption of trench isolation. According to the  $t_{\text{ox}}^2$  dependence of (2.3), the former would be expected to quadratically reduce  $\Delta V_{\text{ot}}$  by affording less volume for the collection and trapping of oxide charge. But, in fact, the effect can be orders of magnitude more pronounced below 10 nm [Benedetto *et al.*, 1985, p.3919] (cf. Footnote 6). At that point  $t_{\text{ox}}$  approaches the depth at which electron tunneling from both interfaces is capable of completely compensating positive oxide trap charge [Hughes and Benedetto, 2003, p.504],<sup>63</sup> meaning “mainstream commercial oxides are now thin enough that radiation-induced  $\Delta V_{\text{th}}$  has essentially vanished” [Oldham and McLean, 2003, p.494]. Similarly, since  $1/f$  noise, both pre- and post-irradiation, is a function of  $\Delta N_{\text{bt}}$ , it too scales down as  $t_{\text{ox}}^2$  through the  $1/C_{\text{ox}}^2$  dependence of (2.11) [Fleetwood *et al.*, 1994b, p.2681].

Though significant, these radiation benefits from the inherent TID hardness of thin oxides in deep submicron technologies are offset by the LOCOS-like vulnerability to leakage that has been demonstrated by STI (cf. Section 2.1.1.3) and by gate leakage via tunneling from the bulk (cf. Footnote 21) [Larcher *et al.*, 1999]. Additionally, MOSFETs whose linear dimensions scale down by a factor of  $k$ , exhibit increasing SEE susceptibility [Fleetwood *et al.*, 2000, p.22] because: the scaling of  $Q_{\text{crit}}$ , depicted in Figure 2.36, is faster than that of  $Q_{\text{col}}$  ( $k^{-2}$  versus  $k^{-5/6}$  [Messenger and Ash, 1992, p.468–469]); the likelihood of upsetting multiple neighboring devices increases with their density [Johnston, 1998, p.1346]; and faster circuit speeds allow shorter DSETs to propagate and be captured by latches [Fleetwood *et al.*, 2000, p.22]. Although SEL is influenced by enough factors as to defy generalities [Johnston, 1998, p.1352], trends toward slight increases in well resistivity and the evidence of latchup even in thin epitaxial substrates is not promising [Johnston, 1998, p.1347]. However, the use of trench isolation, which spoils the parasitic transistor gains by extending the lateral minority carrier path [Voldman, 2007, p.276], and the reduction in supply voltage, which may eventually drop below the holding point [Johnston, 1996, p.519], can greatly increase SEL tolerance.

---

<sup>63</sup>Current models place the limit of neutralization via electron tunneling at around 6 nm [Holmes-Siedle and Adams, 2002, p.143]; assuming it proceeds from both gate and bulk interfaces,  $\Delta N_{\text{ot}}$  in a 12-nm oxide could be completely denuded.

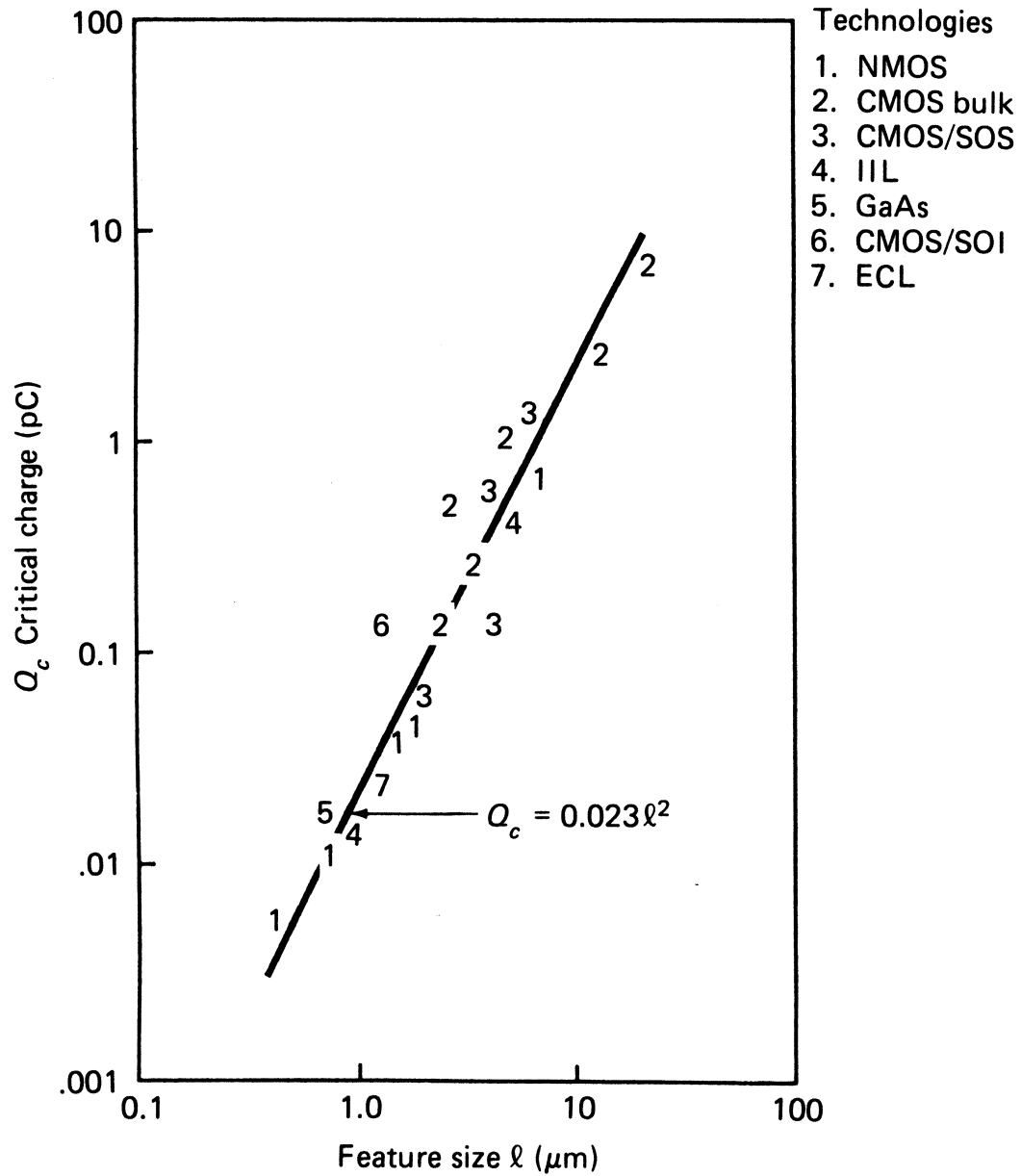


Figure 2.36: Scaling of SEU  $Q_{\text{crit}}$  with feature size. Although the semiconductor material has little impact,  $Q_{\text{crit}}$  varies as  $k^{-2}$  with feature size across technologies, just as for the constant-field scaling of CMOS technology. Reproduced *in toto* from [Messenger and Ash, 1992, p.468]

**Silicon-on-Insulator:** The corresponding advantages and disadvantages of SOI technologies are nearly the inverse of those of scaled CMOS. The use of a buried oxide and thin epitaxial substrate reduces the volume for charge collection in the body of the transistor [Dodd *et al.*, 2001, p.1870] by as much as two orders of magnitude [Schwank *et al.*, 2003, p.522], and drastically truncates funnel depths [Kerns *et al.*, 1988, p.1486], lowering  $Q_{\text{col}}$  and improving SEE tolerance by  $10\times-100\times$  [Kerns *et al.*, 1988, p.1486].<sup>64</sup> Furthermore, these elements eliminate the p-n-p-n structure [Sexton, 2003, p.604], preventing SEL [Kerns, 1989; Kerns *et al.*, 1988, p.1483,p.558] though not SESB (cf. Footnote 44) [Schwank *et al.*, 2003; Sexton, 2003, p.618,p.531].

However, an SOI MOSFET effectively possesses a floating body regulated a back-gate formed by the buried oxide and substrate terminal (cf. Figure 2.37).<sup>65</sup> Just like the standard gate oxide, this buried oxide is susceptible to  $\Delta N_{\text{ot}}$  and  $\Delta N_{\text{it}}$ , and, in fact, exhibits nearly  $\mathcal{F}_t \simeq 1$  [Schwank *et al.*, 2003, p.526] so it is dominated by space-charge effects even in the presence of substrate bias [Oldham and McLean, 2003, p.492].<sup>66</sup> This introduces the possibility of the back-channel opening for large back-gate  $\Delta V_{\text{th}}$  [Dressendorfer, 1989b, p.342], which in turn reduces  $g_{\text{m}}$ , increases  $I_{\text{sub}}$  [Dressendorfer, 1989a, p.275], and even increases  $\Delta V_{\text{th}}$  of the main device [Schwank *et al.*, 2003, p.535]. Thus, the insulator and epitaxial layer are directly responsible for the increased(decreased) SEE(TID) tolerance of SOI technologies [Dressendorfer, 1989b, p.341].

**Heterojunction Bipolar Transistors:** Recently, there has been a great deal of research into the inherent robustness stemming from the smaller features sizes,

---

<sup>64</sup>Although its  $Q_{\text{col}}$  is much smaller, a form of bipolar amplification can occur when the body of an SOI transistor is left floating. This effectively amplifies the charge collected in the body(base) by injecting a much larger amount from the source(emitter) and can result in an effective  $Q_{\text{col}}$  that exceeds  $Q_{\text{crit}}$  [Schwank *et al.*, 2003, p.529].

<sup>65</sup>Any charge that accumulates in the floating body, such as from radiation-induced drain leakage, cannot escape, producing  $\Delta V_{\text{th}}$  through the kink-effect. This and other phenomena related to trapped charge in the epitaxial layer render it a key weakness in the TID radiation response unless properly grounded [Dressendorfer, 1989b, p.278].

<sup>66</sup>A common technique for mitigating hole buildup at the back-channel interface is the application of the appropriate bias to the substrate during irradiation so as to electrostatically prohibit their transport [Dressendorfer, 1989b, p.343].

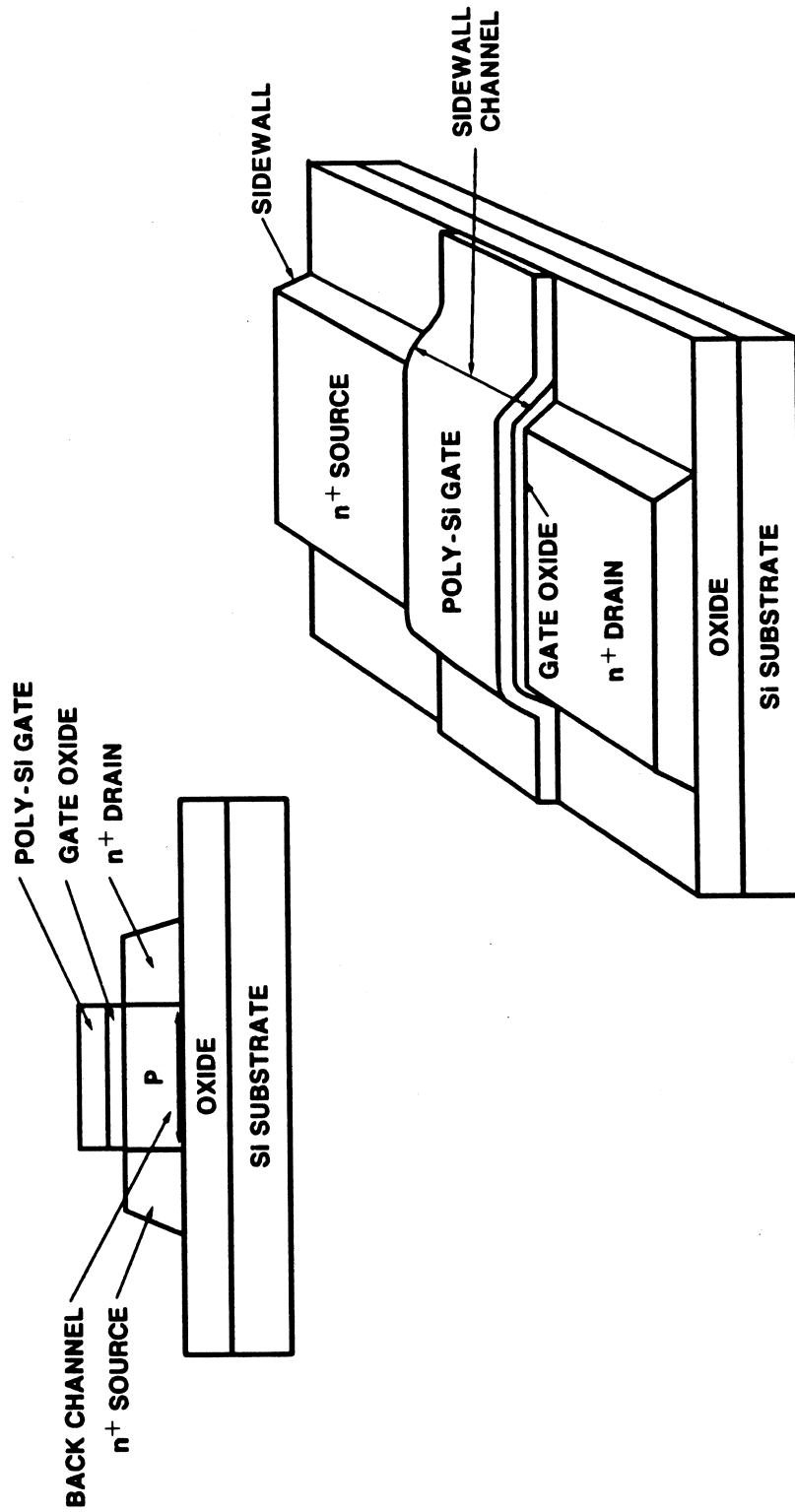


Figure 2.37: Illustration of SOI device construction, including leakage paths. Charge trapping in the buried oxide(gate overhang) can initiate the formation of a sneak path that conducts  $I_{\text{sub}}(I_{\text{fox}})$  through the back(sidewall) channel depicted in the left(right) panel. Reproduced *in toto* from [Dressendorfer, 1989a, p.276].

dielectric isolation techniques, and doping profiles associated with the silicon-germanium (SiGe) npn HBTs offered in modern BiCMOS processes [Cressler, 2005]. Although the bandgap engineering that incorporates germanium into the graded intrinsic base to either increase the barrier to back-injection of (majority) holes into the emitter or create a built-in field that sweeps (minority) electrons more swiftly through the base, or both [Hastings, 2006, p.356], is key to improving the baseline performance of these transistors,<sup>67</sup> one of which is depicted in Figure 2.38 along with its nominal band structure, the radiation-hardness derives from the concomitant increase in the doping profiles and decrease in size [Cressler, 2005, p.1576].

Specifically, it has been shown by researchers at Georgia Tech [Cressler *et al.*, 2002] that high base doping masks displacement damage under most conditions [Zhang *et al.*, 2002, p.3212], rendering moderate TID effects due to electric fields in the narrow E-B spacer oxide [Cressler *et al.*, 2002, p.3203] responsible for observed  $\beta$ -degradation of no more than 30% at 1 Mrad(Si) [Cressler, 2005, p.1574]. Indeed, nearly identical behaviors, in particular the dominance of TID over TDD and the  $< 30\%$   $\beta$ -degradation, were confirmed for the HBTs of the target process (cf. Figure 2.16). Additionally, since the dimensions of the E-B spacer and STI oxides are sufficiently narrow, neither the space charge effects associated with ELDRS [Banerjee *et al.*, 1999] nor the border traps responsible for  $1/f$  noise [Jin *et al.*, 2001] participate materially in TID degradation. With the appropriate thinness of trench isolation [Cressler *et al.*, 2002, p.3207], no discernable collector-base leakage was observed up to 300 krad(Si) [van Vonn *et al.*, 1999, p.416].

The results of SEE testing are less impressive, as might be expected given the small dimensions befitting total dose robustness. In particular, unexplained but high

---

<sup>67</sup>In modern integrated npn BJTs, the component of the base current due to the injection of holes into the emitter usually dominates that due to recombination in determining  $\beta_o$  [Gray *et al.*, 2001, p.12]. So, reducing the former (thereby improving emitter injection efficiency represented by the last term of (2.12)) is more effective. If increased speed trumps gain, this improved  $\beta_{ee}$  can be traded for lower  $r_b$  since a taller back-injection barrier permits increased base doping for the same  $I_b$  [Gray *et al.*, 2001, p.152]. Coupled with a reduction in  $\tau_n$  (increase in  $f_T$ ) due to the drift field of a graded base doping profile, this high-speed capacity of HBTs makes them attractive to RF designers, as mentioned in Section 3.2.1.



levels of charge collection associated with DTI have resulted in  $\mathcal{L}_{\text{th}}$  below 10 MeV-cm<sup>2</sup>/mg for SEUs [Reed *et al.*, 2003], and no ASET data has yet been published. However, compared with the trade-offs cited in the above commercial options, the utility of npn HBTs for this low-noise, high-precision, analog application in a hostile radiation environment is undeniable.

#### 2.3.2.4 Radiation-Hardening-By-Design

In light of the drawbacks of rad-hard processes, the SiGe BiCMOS technology used in this work is manufactured in a commercial process. As with the commercial options listed in Section 2.3.2.3, particularly HBTs, this approach affords several advantages but, in lieu of having transistors that are inherently robust to the effects of both TID and SEE radiation at the levels specified in Section 2.3.1, requires a suite of radiation-hardness-by-design (RHBD) techniques aimed at compensating for the associated shortcomings without incurring the additional mass of with shielding. With the industry-wide “strong emphasis on using unhardened commercial technology as much as possible” [Oldham and McLean, 2003, p.491], the notion of fortifying a soft process through RHBD is common and, indeed, there exists a wealth of literature on the broad range of possible options.<sup>68</sup> In the context of this dissertation, RHBD is construed under the definition of Lacoe [Lacoe, 2003, p.34]:

Hardness-by-design is an approach to producing radiation hardened components and systems using innovative design and layout techniques at the transistor level, the component level and the system level to assure performance and radiation-hardness requirements are met. The fabrication of HBD components is at commercial microelectronics foundries using standard commercial processes and process flow.

Although akin to the IBM SiGe HBT process described in Section 2.3.2.3, and thus somewhat tolerant *a priori*, the BiCMOS8 process generously provided by

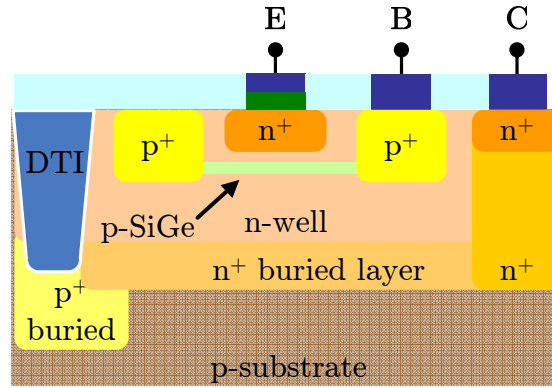
---

<sup>68</sup>A nice review paper, [Kerns *et al.*, 1988] provides a survey of such techniques as applied to various types of commercial processes and is a recommended starting point, whereas Chapter 5 of [Lacoe, 2003] offers a specific look at a few of the most prevalent modern MOS RHBD techniques.

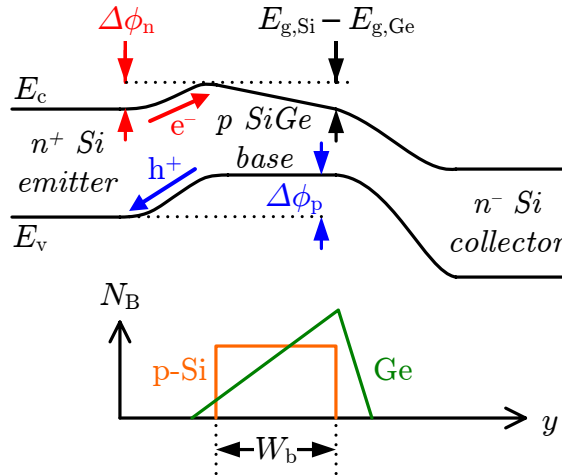
National Semiconductor Corporation offers a few unique challenges to be addressed by such RHBD. First, although it has been established that an epitaxial substrate is valuable in preventing latchup [Johnston, 1998; Kerns *et al.*, 1988, p.1347,p.1486] since the underlying charge collection scales with thickness [Dodd *et al.*, 2001, p.1870], BiCMOS8 is built atop a bulk p-type wafer. Thus, even though an epi substrate is not sufficient to eliminate latchup [Johnston, 1998; Kerns, 1989, p.558,p.1347], the challenge is greater when working with non-epi processes, which are known to be vulnerable [Kerns *et al.*, 1988, p.1476].

Secondly, as it occupies the 0.25- $\mu\text{m}$  technology node, BiCMOS8 is disqualified from the realm of deep submicron and its associated total dose benefits. As such, the effects of trapped charge in the gate and passivation oxides of the MOS and bipolar transistors, respectively, are non-negligible. Indeed, it discovered through both TDD and TID testing that ionizing radiation is of paramount importance to the hardness of the front-end ASIC.

Last is “the well-documented problem [when] using commercial foundries that the intrinsic hardness can change dramatically with no apparent cause” [Hughes and Benedetto, 2003, p.513]. With cautionary tales of a fivefold reduction in hardness due to ‘process updates’ in wide circulation [Hughes and Benedetto, 2003, p.513], it is necessary to first characterize the target process for TID degradation, as was demonstrated in Section 2.1. This establishes the baseline levels of degradation to be overcome through RHBD, the efficacy of which is confirmed by the absence of their impact on the total-dose and single-event responses of SVEPRE (cf. Chapter 6). In that vein, the remainder of this dissertation is concerned with the novel design techniques employed in order to obtain the desired baseline performance for the front-end as well as the RHBD techniques used to preserve this behavior in the face of the radiation effects outlined in this chapter.



(a) Layout cross-section.



(b) Band-digram and base doping.

Figure 2.38: Example layout and band structure of SiGe HBT. The cross-sectional layout view in (a) is not to scale, but includes the E-B oxide spacer between the base and polysilicon emitter. Due to the introduction of Ge, the band diagram in (b) exhibits a larger valence band potential barrier, preventing hole back-injection. The graded Ge profile in (b) produces a built-in base field that reduces electron transit time. After [Cressler, 2005, p.1561–1563]



# Chapter 3

## Architecture

Although the architecture of the front-end ASIC depicted in Figure 1.22 could hardly be simpler, consisting of just two blocks, this decomposition belies the existence of several system-wide considerations that guide the design of its composite LNA and AAF. The requirements of Chapter 1, originating both from the science of plasma waves (namely, the frequency and power ranges of their electric field components) and the demands of the target spacecraft (videlicet, its available power, mass, and antennas), along with the deleterious radiation effects described in Chapter 2 (of both the total dose and single-event varieties), translate into performance specifications for the underlying amplifier and filter. The derivation of these component specifications is one of the key contributions of this research and its upshot justifies the pursuit of a custom solution in the form of SVEPRE.

The primary role of the LNA, as addressed in more detail in Chapter 4, is to translate the potential induced at the terminals of a cylindrical dipole antenna into the voltage range required by the subsequent circuitry without distortion. The first step, accurately sensing that electromotive force (emf) over a wide bandwidth and dynamic range, dictates limitations on the input impedance and input-referred noise of the amplifier whereas the second, the amplification phase itself, hinges upon a gain throughout all LNA stages which is both highly linear and easily tailored to the scientific concerns of the mission.

For the AAF, whose objective is to aggressively attenuate out-of-band interferers,

thereby avoiding aliasing artifacts in the final data samples, it is shown in Chapter 5 that this LNA gain is both a boon to the noise performance and a hindrance to the linearity. Plus, just as the antenna considerations drive the LNA specifications at the input to the chip, the limitations of and variability amongst the ADC and digital back-end of the host spacecraft, constrain the maximum filter bandwidth and attenuation.

As punctuated by the preceding pair of paragraphs, common themes run through both the LNA and AAF specifications derived from the requirements of Chapter 1, each of which presents a challenge that must be met in the face of the TDEs and SEEs of Chapter 2. Section 3.1 categorizes the four most prominent of these: programmability, linearity, noise, and input-impedance. Each is treated in a separate section that determines the numerical value(s) of the appropriate performance metrics for the given component, thereby completing the set of specifications which SVEPRE is designed to satisfy. To achieve these, two high-level design choices that permeate front-end architecture are then outlined in Section 3.2.

## 3.1 Component Specifications

In deriving the set of four component specifications below—some of which apply with equal import to both the LNA and AAF, others to just one—the order of the subsections ranges from the former to the latter. Specifically, the flexibility of the chip and the spectral purity of its overall output are contingent on both the LNA and AAF achieving the wide range of programmability and low levels of harmonic distortion described in Section 3.1.1 and Section 3.1.2, respectively. As a consequence of the Friis noise formula,<sup>1</sup> the noise performance of the LNA is more critical than that of the AAF, so the treatment of the two components in Section 3.1.3 is weighted accordingly. Finally, the high input impedance of the LNA alone is responsible for

---

<sup>1</sup>This noise formula is distinct from the Friis transmission formula employed in the design of antennas for communication links [Stutzman and Thiele, 1998, p.79]. Although originally defined in terms of noise factor [van der Ziel, 1986, p.36–38], the Friis noise formula can be adapted so as to relate the input-referred noise PSD ( $S_{in}(f)$ ) for a signal chain composed of  $K$  stages to the gains ( $A_1, A_2, A_3 \dots A_K$ ) and noise contributions from each of the stages as referred to their own inputs

the antenna coupling promoted in Section 3.1.4.

### 3.1.1 Programmability

The overarching front-end specification is programmability,<sup>2</sup> which describes the ability to command it into different modes during the course of an orbit or mission as befits various scientific objectives. Such flexibility allows the target receiver to be adapted to an array of measurement environments, as is obviously required of any scientific instrument. But, this is especially critical for the advanced investigations proposed at the outset of Chapter 1 that treat the radiation belts as a laboratory in which to perform experiments whose outcomes cannot accurately be predicted *ab initio*. Even when the in-flight configuration is known in advance, the diversity of orbits and system resources featured by the satellites of Table 1.2 demands that SVEPRE possess the capacity to accommodate a variety of wave amplitudes and  $\Upsilon_a$  to find applicability for a broad range of missions.

Whether used pre-launch, in-flight, or both, programmability is paramount amongst the component specifications of this section because it increases the complexity of each, since performance must be maintained throughout the programmable range. That is, SVEPRE must not only satisfy the requirements for linearity, noise,

---

( $S_1, S_2, S_3 \dots S_K$ ) via:

$$\begin{aligned} S_{\text{in}}(f) &= S_1(f) + \frac{S_2(f)}{A_1(f)} + \frac{S_3(f)}{A_1(f) A_2(f)} + \dots \\ &= \sum_{k=1}^K \frac{S_k(f)}{\prod_{j=1}^{k-1} A_j(f)} \end{aligned}$$

Since the contributions from downstream stages ( $k > 1$ ) are mitigated by the preceding stage gains, the first stage, in this case the LNA, should be the dominant source of noise in any well-design communication system [*van der Ziel, 1986, p.34*].

<sup>2</sup>In this document, *programmability* refers to hardware which has a finite and often small number of discrete modes whose operation is mutually exclusive. Each mode is distinguished by a unique set of values for one or more variable parameters (e.g., gain). This is contrasted with the continuous adjustment of circuit properties through an infinite set of analog values spanning a bounded range. Such a procedure is known as *trimming*(*tuning*) when the allowable resolution of the sweep is high(low) but the range narrow(broad).

and power dissipation under both baseline and irradiated conditions, but also across the space of programmable operating modes.

This latter condition implies internal signals with a wide range of amplitudes and frequencies. But, in contrast to the front-ends of the WBRs of Table B.6, SVEPRE does not require multiple frequency divisions or gain settings on account of its wide bandwidth and dynamic range specifications. Instead, as explained in Section 3.1.1.1 and Section 3.1.1.2, respectively, the selection of available modes for the LNA gain and AAF bandwidth is aimed at enhancing the utility of the receiver instrument.

### 3.1.1.1 LNA Gain

Given the 90-dB target SFDR specified in Figure 1.22, which covers the full power range of the signals in Figure 1.21, it would seem at first blush that the gain of the LNA,  $G_p$ , need not be programmable. Indeed, whereas the WBR front-ends of the instruments in Table B.6 employ a VGA with up to 16 gain steps to cover a programmable range of up to 90 dB, often regulated by an AGC loop, this is only necessary to accommodate the limited dynamic range of downstream elements in their signal path (cf. Section 1.2.1.3).

However, there are two system-level motivations for programmable  $G_p$  that arise from subtleties in the representation of the phenomena of interest in Figure 1.13. The first is that at any given point in the orbit, not all the depicted wave phenomena are present simultaneously: Z-mode radiation, upper-hybrid resonance (UHR) noise, and hiss bands of different phenomenological origin are all located at different latitudes throughout the plasmasphere; whistler-mode chorus is pronounced in the trough near the plasmopause; and auroral kilometric radiation (AKR), electron cyclotron waves at the half-harmonics of  $\omega_{ce}$ , type III solar radio bursts, and continuum radiation have only been observed beyond the plasmopause [Lemaire and Gringauz, 1998, p.105–107].<sup>3</sup> Thus, the availability of additional gain settings allows the experimenter to

---

<sup>3</sup>This localization does not obviate the need for the large  $DR_I$  of the target receiver. As described in Section 3.1.2, previous WBRs with large  $DR_T$  but much smaller  $DR_I$  may not have sufficiently linear dynamic range to observe the weaker signatures of phenomena that have propagated to the satellite from distant source regions. The uncertainty about the presence of such low-energy plasma waves in the radiation belts is, in fact, one of the motivations for further experimentation.



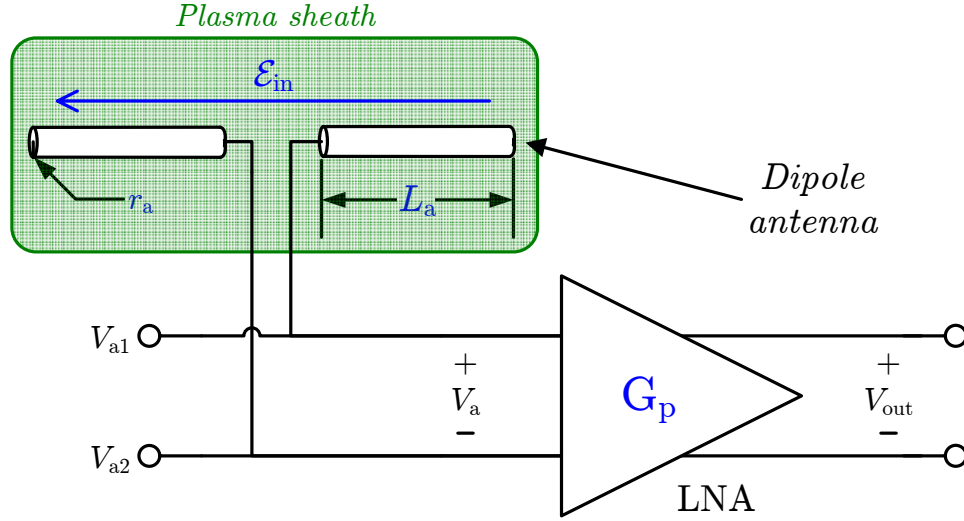


Figure 3.1: Relationship of LNA input to induced dipole emf. The maximum  $V_{out}$ , as dictated by the ADC, necessitates programmable  $G_p$  for the range of expected  $E_{in}$  and  $L_a$ .

concentrate the instrument sensitivity on either local, high-power or distant, low-power signals, should the other class be absent.

Secondly, as depicted in Figure 3.1, the input to the LNA,  $V_a$  is the emf induced between the terminals of the receiving dipole antenna by the electric fields whose spectral densities are plotted in Figure 1.13 (cf. Footnote 23 of Chapter 1). For a given wave electric field,  $\mathbf{E}_{in}$ , whose component in the direction of the dipole axis is  $E_L(l)$ , the potential  $V_{ax}$  (for  $x=1,2$ ) of each of the long, identical dipole elements of length  $L_a$  and radius  $r_a$  is just the mean of the potential along its length, given by [Meyer-Vernet and Perche, 1989, p.2405]:

$$V_{ax} = -\frac{1}{L_a} \int_0^{L_a} l E_L(l) \, dl \quad (3.1)$$

Often, it is convenient to introduce in place of this integral a normalized quantity describing the distance between point charges in an equivalent dipole moment that would generate the same potential. This effective length,  $L_{eff}$ , is given by [Gurnett,

1998, p.124]

$$L_{\text{eff}} = \frac{V_a}{E_L(l)} = \begin{cases} L_a & , \text{ dipole} \\ 2L_a & , \text{ double-probe} \end{cases} \quad (3.2)$$

where the piecewise bifurcation results when  $k_L$ —the component of the wave vector for  $\mathbf{E}_L(l)$ <sup>4</sup>—satisfies  $k_L L_a \ll 1$ . Intuitively, (3.2) reflects the fact that for a dipole much shorter than a wavelength ( $k_L L_a \ll 1$ ),<sup>5</sup>  $\mathbf{E}_L$ , and thus the charge distribution, is approximately uniform across each element, so that the mean of (3.1) lies at  $L_a/2$ ; the pair of such arms effectively mimics an ideal dipole whose charges are thus separated by  $L_{\text{eff}} = L_a$ . By contrast, the charges accumulated on the spheres at the ends of the double probe, which are a faithful approximation to the charges of an ideal dipole for sufficiently large  $L_a/r_a$  ratio, are separated by its full tip-to-tip length,  $L_{\text{tt}} = 2L_a = L_{\text{eff}}$  (cf. Footnote 13 of Appendix B).

According to Table B.3, previous satellites of all classes have flown dipoles with  $0.16 \text{ m} \leq L_{\text{TT}} \leq 500 \text{ m}$ , resulting in a wide range of  $V_a$  for a given  $\mathbf{E}_{\text{in}}$ . Yet, as shown in Figure 3.1, an LNA compatible with all such antennas must translate these assorted  $V_a$  into the voltage range of the subsequent circuitry, which is limited to a maximum of  $1 \text{ V}_{\text{PP}}$  by the ADC (cf. Figure 1.22) such that:

$$V_{\text{out}} = (G_p L_{\text{eff}}) E_L \leq \pm 1 \text{ V}_{\text{PP}} \quad (3.3)$$

Thus, to accommodate the bulk of the entries in Table B.3,<sup>6</sup> with  $6 \text{ m} \leq L_{\text{TT}} \leq 100 \text{ m}$

---

<sup>4</sup>As is addressed in Section 3.1.4, the effective lengths in the piecewise specification of (3.2) hold both with and without the presence of a plasma sheath. For  $f \gg f_{\text{pe}}$ , the antennas simply behave as short dipoles in free space, provided  $k_L L \ll 1$ . In the presence of the sheath, the plasma coupling can be treated as uniform for  $f \ll f_{\text{pe}}$ , so the moment of the charge distribution is still at the middle(end) of each dipole(double-probe) element [Gurnett, 1998, p.127].

<sup>5</sup>If the antenna is long compared to the wavelengths of interest ( $kL \gg 1$ ) then periodic variations in the potential over the length of the antenna reduce the average in (3.1), diminishing the antenna's response to such high-frequency waves. This effect can be expressed either by modifying  $L_{\text{eff}}$  or by explicitly indicating the dependence on direction. A short dipole, like those considered in this work, provides maximum response to fields along its axis, since  $k_L L_a \ll 1$  is satisfied by the fact that  $k_L \leq k$  for all angles. However, a long dipole favors waves incident at an angle perpendicular to the axis of the dipole, for which  $k_L \ll k$  so that while  $kL_a \gg 1$ ,  $k_L L_a \ll 1$  [Meyer-Vernet and Perche, 1989, p.2405]. Thus, these results also hold for long dipoles nearly orthogonal to  $\mathbf{E}_{\text{in}}$ .

<sup>6</sup>Since 1974, no WBR has been flown with dipoles shorter than the floor of this range ( $L_{\text{TT}} \geq 6$

and thus effective lengths ranging from 3 to 50 meters,  $G_p$  must be programmable between 0–24 dB in order to keep the parenthesized term in (3.3) constant.<sup>7</sup>

### 3.1.1.2 AAF Bandwidth

Although modern satellites of sufficient scale can offer copious amounts of system resources discussed in Section 1.2.2, such as telemetry, power, data storage, and high-speed clocking, the growing class of miniaturized satellites remains limited in one or more of these regards. For example, with less surface area(volume) for solar panels(batteries), microsatellites typically offer lower telemetry rates ( $\Upsilon_t$ ) and supply less power than their large-scale counterparts.<sup>8</sup> Both spacecraft genre are also hampered to a degree by the need to share clocking and memory amongst their various instrument payloads. So, the resources required for high-speed sampling, including a fast, low-jitter clock and sufficient solid-state buffers, are rare (cf. Table B.1).<sup>9</sup>

To reduce the demand for the four types of aforementioned resources, all of which pertain to the digital back-end, it is desirable to offer the option of down-clocking this portion of the system. Down-clocking can either be part of the baseline design, in which case the overall back-end is simply designed to run at a maximum sampling rate lower than that achievable by some of its components, or an option to be selected in flight, as often distinguishes an instrument’s burst and survey modes (e.g., the  $64\times$  difference in sampling rate between the survey and burst modes of the FAST WBR documented in Table B.6).

In the latter case, unlike FAST, which uses dedicated ADCs with different sampling rates to support survey and burst mode [Ergun *et al.*, 2001, p.71–73], or the Polar HFWR, which produces the bandwidth divisions in Table B.6 by decimating

---

m). SVEPRE remains compatible with outliers beyond the upper end, such as the long  $E_x$  ( $E_x$  and  $E_y$ ) dipole(s) on DE1(IMAGE), with the use of an external attenuator.

<sup>7</sup>This argument only justifies the need for a 24-dB gain range; it does not explicitly justify starting at 0 dB. The absolute endpoints of the gain range are justified by the dynamic range considerations in Footnote 37.

<sup>8</sup>Adducing Table 1.2, observe that the daughter satellites of the THEMIS(CLUSTER) mission feature approximately an order of magnitude less  $P_{\text{tot}}(\Upsilon_t)$  than the Polar(FAST) spacecraft.

<sup>9</sup>One of the pioneers in this regard is the DEMETER spacecraft, which is uses an X-band telemetry system ( $\Upsilon_t = 16.8$  Mbps) and 8 Gb of on-board flash memory to support a burst mode  $\Upsilon_a$  of 1.6 Mbps [Cussac *et al.*, 2006, p.414].

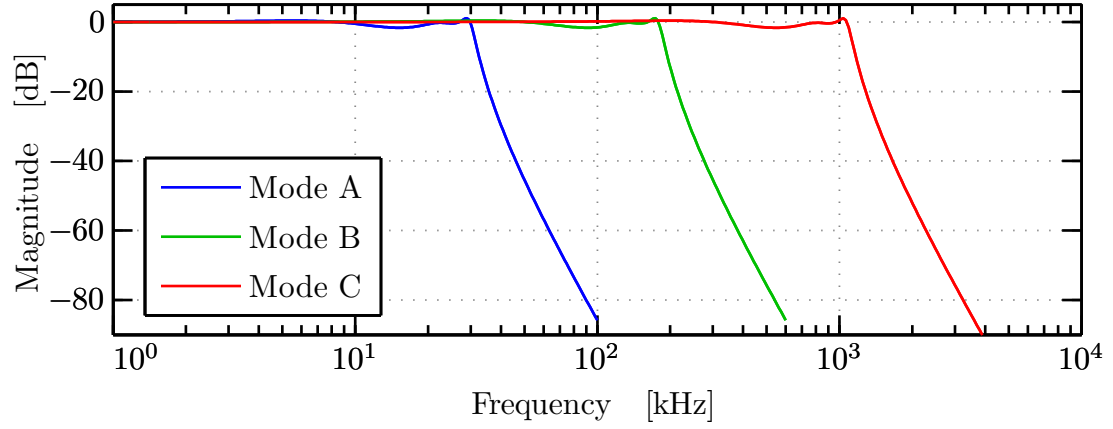
the output of a constant-rate ADC, the full power benefit of down-clocking is only achieved by operating the digital portions of each hardware channel at a lower master clock rate. For the target receiver, such in-flight down-clocking would constitute merely dividing the clock supplied to the ADC and FPGA, reducing their power dissipation proportionally, according to the rule of the thumb for digital logic.<sup>10</sup> The drawback to this approach is that the reduced sampling rate requires a corresponding drop in the cut-off frequency of the AAF to avoid aliasing. Rather than implement this analog circuit as a programmable block, FAST opts to replicate it, creating separate AAFs for each ADC, while Polar performs the necessary filtering in the digital domain after sampling.

To render the target receiver capable of extracting the full power savings associated with in-flight down-clocking, as well as enable its use by classes of satellite whose resources only support lower  $\Upsilon_a$ , the bandwidth of the SVEPRE AAF is programmable. It can be set to one of three modes, hereafter dubbed, in order of increasing bandwidth, Mode A, Mode B, and Mode C, whose passband edges,  $f_{pa}$ ,  $f_{pb}$ , and  $f_{pc}$  correspond to scientifically relevant boundaries. The passbands of the target responses for each are depicted in Figure 3.2.

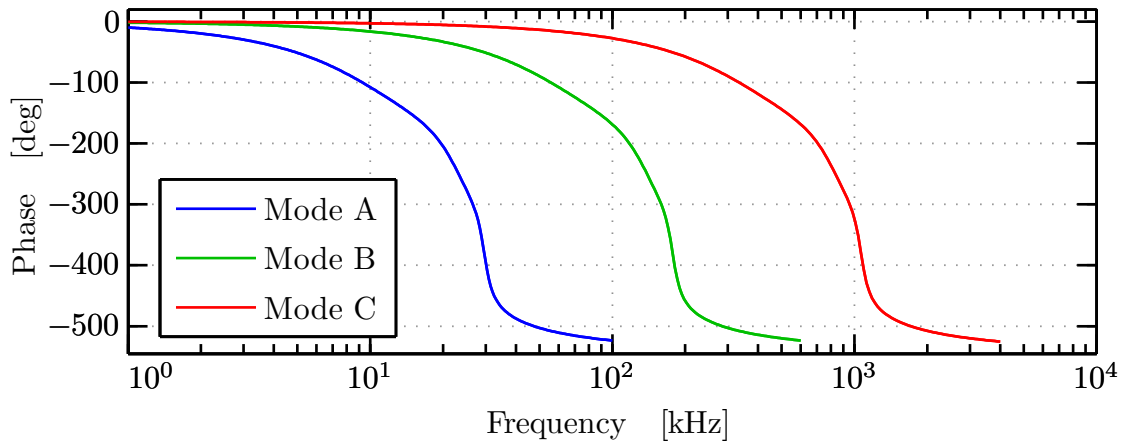
To capture the entirety of the signal space in Figure 1.21, including high-frequency phenomena such as type III solar radio bursts above 100 kHz [Ergun *et al.*, 1998; Reiner *et al.*, 1998], as well as afford the ability to extract plasma parameters from knowledge of  $f_{pe}$  at radiation-belt  $N_e$  levels,<sup>11</sup> Mode C has a bandwidth of  $f_{pc} = 1080$  kHz, supporting the maximum ADC sampling rate (5 MS/s). At the opposite extreme, Mode A features a passband cut-off of just  $f_{pa} = 30$  kHz so as to still capture the whistler mode waves of Figure 1.11 that participate in resonant wave particle interactions (cf. Section A.3) while minimizing demand for spacecraft resources. Logarithmically spaced between these two lies the Mode B cut-off ( $f_{pb} = 180$  kHz) which is both conveniently located from a design standpoint, being a factor of 6

<sup>10</sup>This relationship does not strictly hold for ADCs in general nor that of [Wang, 2009] in particular, but is appropriate for any digital logic therein, as well as all of the subsequent data processors.

<sup>11</sup>According to (1.2),  $f_{pe} = 1$  MHz for  $N_e \simeq 1.2 \times 10^4 \text{ cm}^{-3}$ , which is the average electron density at the inner edge of plasmasphere (cf. Section A.1.2); thus,  $f_{pc}$  exceeds the maximum  $f_{pe}$  observed in the radiation belts.



(a) Magnitude response.



(b) Phase response.

Figure 3.2: AAF Bode plot for each bandwidth mode. The nominal passband cut-offs of  $f_{pa} = 30$  kHz,  $f_{pb} = 180$  kHz, and  $f_{pc} = 1080$  kHz support 150 kHz, 850 kHz, and 5 MHz sampling rates, respectively.

lower(higher) than  $f_{\text{pa}}(f_{\text{pc}})$ , and sufficient to capture all the wave modes native to the plasmasphere (except UHR noise) according to Figure 1.12.<sup>12</sup>

### 3.1.2 Linearity

Since the electromagnetic waves of interest propagate through the magnetosphere, sometimes great distances and often along the geomagnetic field lines, their (potentially faint) reception at points removed from the source region is limited only by changes in the plasma conditions along the path (e.g., the plasmopause as discussed in Section A.1.2) and the minimum signal detectable by the receiver. In contrast to the low instantaneous dynamic range ( $\text{DR}_I$ ) of most of the WBRs in Table B.6, the large  $\text{DR}_I$  of the target receiver permits the simultaneous reception of strong local phenomena and in the presence of weaker, propagated ones.<sup>13</sup> Using the inset spectrogram of Figure 1.14 as an example, note that both strong (red) chorus bursts and weaker (green) hiss bands are present simultaneously, so a  $\text{DR}_I$  of just 50 dB would be insufficient.

However, to clearly discriminate both signals in such a case, instantaneous dynamic range is not the most salient metric. Instead, as explained below, a measure of the distortion lines introduced by the nonlinearities of the receiver front-end is paramount to the spectral analysis of plasma waves, in which spectrograms such as that of Figure 1.14 are the primary means of compactly representing their evolution in time, frequency, and power.<sup>14</sup> In fact, such spectral analysis is so fundamental that for  $\Upsilon_t$ -constrained spacecraft, it is often sufficient to merely telemeter a

---

<sup>12</sup>This choice of  $f_{\text{pb}}$  also enables SVEPRE to interface with legacy terrestrial receivers at Stanford, which support lower resolution sampling at a rate of 333 kS/s.

<sup>13</sup>Recall from Section 1.2.1.1 that the instantaneous dynamic range ( $\text{DR}_I$ ) of a plasma wave receiver is the maximum dynamic range achievable at any single gain setting. In contrast, the total dynamic range ( $\text{DR}_T$ ), which accounts for the extremes in signal size that the receiver is capable of measuring when all allowable gain settings are considered in aggregate, is not pertinent to such measurements of simultaneous wave events, since the duration of their overlap is routinely too short to permit gain stepping. For the WBRs of Table B.6 that feature AGC loops, cycle times range from 86–500 ms, whereas chorus waves only last on the order of 0.1–1 s [Inan *et al.*, 1983].

<sup>14</sup>Indeed, for signals whose electric field spectral densities span 90 dB, it would hardly be practical to distinguish the simultaneous phenomena at the opposite extremes of this range using the time domain record of the measured voltage.

compressed spectrogram image in lieu of the full time-domain data set [Gurnett, 1998, p.135]. By performing Fast Fourier Transforms (FFTs)<sup>15</sup> on successive, potentially overlapping segments of the data record that have been appropriately windowed to prevent frequency smearing (cf. Section 6.2.2.4) and, optionally, averaging the resulting magnitudes of these spectra across multiple such records, the essential spectral character of the wave phenomena can be extracted via signal processing and condensed into a more suitable telemetric format. Whether created aboard the satellite or by GSE during post-processing, such spectrograms are the key data product generated by the target receiver, so its fidelity is best specified using a frequency-domain metric known as spurious-free dynamic range (SFDR).

### 3.1.2.1 Spurious-Free Dynamic Range

In its simplest form, a spectrogram column is just the power density spectrum of the signal produced by the front-end,  $y(t)$ , which can be approximated by the squared-magnitude,  $|Y(f)|^2$ , of the single-sided spectrum,  $Y(f)$ ,<sup>16</sup> that results from the  $N$ -point FFT.<sup>17</sup> Figure 3.3 depicts the case of a single-tone sinusoidal input,  $x(t) = \mathcal{X}_o \sin(2\pi f_o t)$ , that has passed through a generic front-end. In addition to the anticipated peak at  $f_o$ —the fundamental—the spectrum<sup>18</sup> exhibits coherent energy at integer multiples of  $f_o$  known as harmonics,<sup>19</sup> as well as a background noise floor

<sup>15</sup>The details of the Fast Fourier Transform, a commonly employed algorithm for computing the discrete Fourier transform (DFT), are beyond the scope of this work. For an introduction, the reader is recommended to Chapter 9 of Oppenheim et al. [1999, p.629–692].

<sup>16</sup>Without the separate in-phase and quadrature channels found in some SFRs (e.g., IMAGE [Reinisch et al., 2000, p.338]), SVEPRE only generates a real-valued output signal that, by definition, produces a spectrum which is conjugate symmetric about the Nyquist frequency [Oppenheim et al., 1999, p.576]. Thus, only the positive frequencies need be considered.

<sup>17</sup>In practice, since  $y(t)$  is a stationary random signal that does not conform to the Fourier theory encompassing its deterministic counterparts, such as ideal sinusoids, its power density spectrum must be analyzed using spectral estimation techniques, rather than a straightforward DFT. One such method, the periodogram analysis discussed further in Section 6.2.2.4, employs a discrete Fourier transformation (DFT) of the samples of  $y(t)$  ( $y[n]$ ), that, for convenience, is approximated here by the use of the squared-magnitude of the continuous-time Fourier transform of  $y(t)$ ,  $Y(f)$ , rather than the DFT.

<sup>18</sup>For brevity, subsequent references to the signal *spectrum* indicate its power density spectrum, unless otherwise noted.

<sup>19</sup>As per the standard practice, the harmonic at  $2f_o$  is known as the second harmonic, that at  $3f_o$  as the third, and so forth. So, though not typically referred to as such, the fundamental itself would

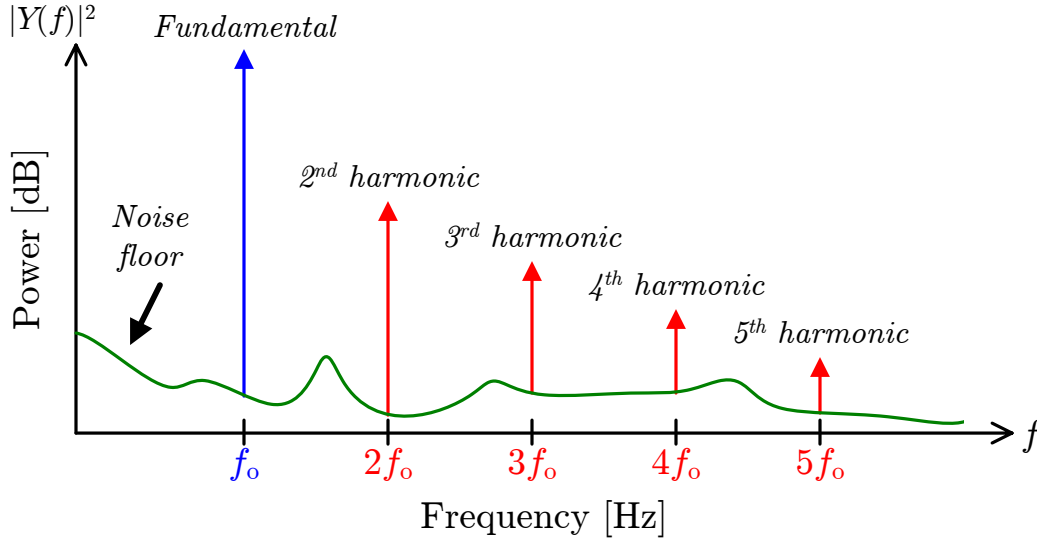


Figure 3.3: Spectral elements utilized in definitions of noise and linearity metrics. The ideal output spectrum contains only the fundamental (in blue), but environmental and circuit nonidealities generate both coherent (in red) and incoherent (in green) power in the real spectrum.

due to random processes. These ancillary elements constitute front-end non-idealities that can be characterized with a variety of metrics.<sup>20</sup>

Perhaps the most common of these is the signal-to-noise ratio (SNR),<sup>21</sup> defined as the ratio (in dB) of the power of the fundamental ( $P_{\text{fund}}$ ) to that of the noise floor ( $P_{\text{noise}}$ ), with the latter integrated over the noise bandwidth of the system,<sup>22</sup> and the

---

be the first harmonic.

<sup>20</sup>Borrowing from the field of ADC testing, this document adheres to the metric terminology of [IEEE Std 1241-2000, 2001], except as noted, since the front-end output is eventually processed in the digital domain to produce spectrograms in any real system.

<sup>21</sup>Alternatively, this may be known as the signal-to-nonharmonic-noise ratio (SNHR) [IEEE Std 1241-2000, 2001, p.13]

<sup>22</sup>The noise bandwidth is simply the bandwidth of an ideal brick-wall filter that possesses the same peak value and total noise power (i.e., area under its magnitude response curve) as the frequency response of the actual system [Lee, 1998, p.246]. For the purposes of this section only, it can be optimistically approximated by the AAF passband cut-off ( $f_p$ ) in a given mode. It is formally specified in Section 6.2.3.3.



cumulative power of the harmonic spurs ( $P_{\text{harm}}$ ) ignored:<sup>23</sup>

$$\text{SNR} = 10\log_{10}\left(\frac{P_{\text{fund}}}{P_{\text{noise}}}\right) \quad (3.4)$$

Associating the power of the harmonics with that of the fundamental from which they are derived, SNR only treats as extrinsic any noise contributions to the spectrum which cause it to deviate from the ideal (scilicet, having all energy concentrated at  $f_o$ ).<sup>24</sup> Although  $P_{\text{noise}}$  indeed limits the ability to resolve small signals (cf. Section 3.1.3.1), this delineation is not appropriate for the spectral analysis of plasma waves for two reasons.

First, the harmonics that result from front-end nonlinearities are equally problematic, as they can easily be mistaken for or interfere with natural harmonics that may be present, as in the case of cyclotron resonance captured by (A.33) or the half-harmonics of  $\omega_{ce}$  depicted in Figure 1.13. Instead, to capture the impact of both  $P_{\text{harm}}$  and  $P_{\text{noise}}$ , the signal-to-noise-and-distortion ratio (SNDR),

$$\text{SNDR} = 10\log_{10}\left(\frac{P_{\text{fund}}}{P_{\text{noise}} + P_{\text{harm}}}\right) \quad (3.5)$$

is commonly invoked.<sup>25</sup> As  $\mathcal{X}_o$  increases, the numerator of (3.5) increases until the amplitude of  $x(t)$  exceeds that which the front-end is capable of processing. The

---

<sup>23</sup>The complementary metric which omits  $P_{\text{noise}}$  in favor of  $P_{\text{harm}}$ , is the total harmonic distortion (THD) which gives the ratio (in dB relative to the fundamental, or dBc) of the quadrature sum of the powers of each of the  $k$  harmonics,  $P_{\text{harm},k}$ , to the power of the fundamental:

$$\text{THD} = 10\log_{10}\left(\sum_k \frac{P_{\text{harm},k}}{P_{\text{fund}}}\right)$$

where  $k$  can index through all available harmonics at frequencies  $kf_o$ , but is formally restricted to the range  $k=2, 3, \dots, 10$  unless otherwise noted [IEEE Std 1241-2000, 2001, p.47].

<sup>24</sup>Although noise from random processes is just one such contributor, along with others such as coherent interferers and intermodulation products [IEEE Std 1241-2000, 2001, p.51], it is the only one pertinent to case of a single-tone input under consideration.

<sup>25</sup>When measured in the time domain as the ratio of the RMS power of the fundamental (represented by a sinusoidal least-squares fit) to the RMS power of the remaining signal content (the so-called total noise), the equivalent quantity is abbreviated as SINAD [IEEE Std 1241-2000, 2001, p.12]. The frequency-domain computation is carried out here in accordance with the theme of spectral analysis.

maximum of (3.5) over this range is the formal definition of what has heretofore been deemed the instantaneous dynamic range:

$$DR_I = \max_{\mathcal{X}_o} \{ \text{SNDR} \} \quad (3.6)$$

Although it accounts for the presence of both undesired harmonics and random noise,  $DR_I$  fails to accurately describe the analytical capability of the front-end for a second reason, depicted in Figure 3.4. In this limiting case, the target receiver and, in fact any RF front-end [Lee, 1998, p.295], must remain linear while capturing strong wave phenomena in the presence of weak ones. For an ideal receiver, as shown in Figure 3.4(a) it is still possible to resolve both the strong tone at  $f_o$  and a second signal of interest (at  $f_1$ ) which is 90-dB weaker. But, if an actual receiver introduces energy both in the noise floor (in green) and at the harmonics (in blue), such that the latter dominates the former and produces a second harmonic just 75 dB below the fundamental, as in Figure 3.4(b), the signals at  $f_1$  and  $f_2$  become indistinguishable from the receiver's own distortion.

Whether these harmonics, generated by nonlinearities of the front-end circuitry, overlap with the weak natural phenomena or merely reside elsewhere in the spectrum, the strongest of them sets the level, relative the fundamental, below which it becomes impossible to discriminate between natural signals and receiver distortion. This power distance from the fundamental to either the largest harmonic, located at  $f_{\text{harm}}$  ( $3f_o$ , in the case shown) or to the peak of the noise floor, located at  $f_{\text{noise}}$  (should it exceed the strongest harmonic), defines the SFDR, in dB, as:

$$\text{SFDR} = 10 \log_{10} \left( \frac{|Y(f_o)|^2}{\max\{|Y(f_{\text{harm}})|^2, |Y(f_{\text{noise}})|^2\}} \right) \quad (3.7)$$

Since SFDR varies with  $\mathcal{X}_o$ , its subsequent specification should be interpreted as a maximum over the signal range, just as for  $DR_I$  in (3.6), unless the input amplitude is explicitly stated. As it is the primary measure of receiver nonlinearity in this work,<sup>26</sup>

---

<sup>26</sup>References hereafter to the linearity of a circuit, are presumed to be in the sense of its maximum SFDR unless otherwise stated.

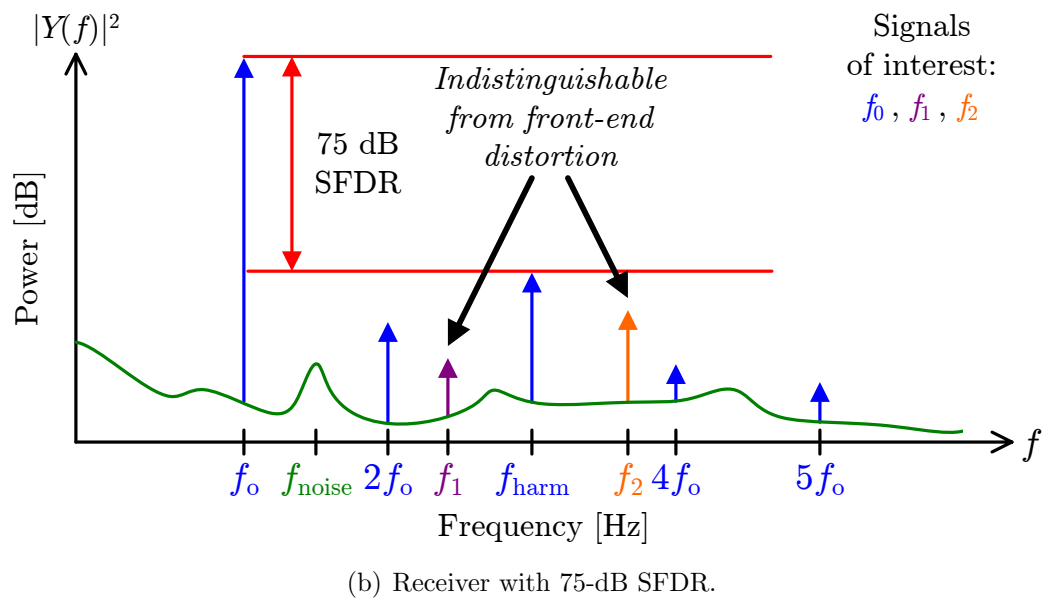
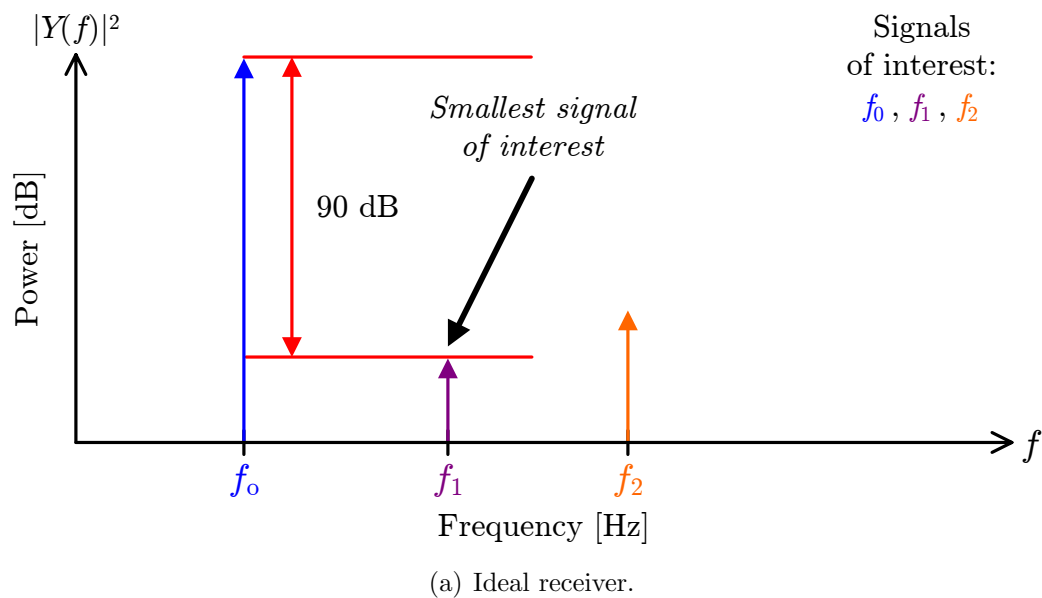


Figure 3.4: Impact of SFDR on signal discrimination in output power spectrum. Signals 90 dB below the fundamental can be resolved by (a) an ideal receiver, but are not visible in the output spectrum of (b) a receiver with just 75-dB SFDR.

a brief discourse on the other subtleties of interpreting, computing, and achieving high SFDR follows.

### 3.1.2.2 Spot Noise

Assessing the SFDR of SVEPRE requires the injection of a single, spectrally pure sinusoid of the form of  $x(t)$  and comparing various peaks in the output power spectrum according to (3.7).<sup>27</sup> Note that as opposed to SNR and SNDR, which consider the total integrated power of the unwanted components, SFDR only measures the localized, or spot power, at specific frequencies ( $f_o$ ,  $f_{\text{harm}}$ ,  $f_{\text{noise}}$ ). When the power spectrum is obtained using an  $N$ -point FFT of samples obtained at a rate of  $f_s$ , as explained in Section 6.2.2.4, each of these corresponds to a frequency bin of finite width  $\Delta f = f_s/N$  and it is critical that this width be specified in order to properly assess linearity via SFDR.

To see why, assume without loss of generality that total power  $P_{\text{noise}}$  exhibits only the circuit noise power,  $P_{\text{no}}$ , which can be modeled by a single output-referred source that is white (i.e., frequency independent) over the full noise bandwidth [Motchenbacher and Fitchen, 1973, p.39]. Then, the peak of the noise floor is simply

$$|Y(f_{\text{noise}})|^2 = \frac{P_{\text{no}}}{N} \quad (3.8)$$

In the absence of harmonic distortion, whereby (3.8) dominates the denominator of (3.7), a longer FFT would effectively improve the SFDR for the same underlying analog circuitry by reducing the per-bin noise. A similar result holds for the coherent signals in (3.7): they have some finite bandwidth,<sup>28</sup> the power at the extremes of which

---

<sup>27</sup>Assuring the purity of the input tone is of critical importance, since the SFDR should only describe the harmonics generated by the nonlinearities of the front-end circuitry, not those injected from the signal source. Techniques for addressing this problem are presented in Section 6.2.2 and Section H.1.3.

<sup>28</sup>From Figure 1.13, it is clear that the noise-like plasma wave signals of interest can, in fact, be very broadband. The astute reader may question, then, the preceding justification of SFDR which contrasted the narrow-band representations of the signals in Figure 3.3 against the broadband noise floor when, in reality, the former are noise-like in character. But, as shown in Section 3.1.3.1, it is possible to represent such phenomena with sine wave equivalents for purposes of testing SFDR and deriving specifications that achieve the desired spectral discrimination [Scarf et al., 1980, p.38].

is erroneously omitted from calculations at  $f_o$  and  $f_{\text{harm}}$  as  $\Delta f$  becomes sufficiently small with increasing  $N$ .

Thus, in all that follows, regardless of the AAF mode (read sampling rate), the 90-dB SFDR required of the SVEPRE front-end is specified for a bin width of 1 Hz, in keeping with the normalization conventionally employed in the noise specifications of operational amplifiers [Motchenbacher and Fitchen, 1973, p.15] and RF circuit blocks [Lee, 1998, p.245] noise specifications in general, and the electric field spectral densities of Figure 1.21 in particular.

### 3.1.2.3 Large Signal Behavior

One of the primary challenges in designing for high SFDR is that, unlike other measures of linearity, which simply extrapolate from the behavior of the composite transistors at low signal levels, SFDR manifests large-signal transistor behavior. For example, the third-order intercept point (IP3) commonly used to assess the degree of intermodulation distortion in RF amplifiers is not actually measured at the power level for which the third-order intermodulation products are equal in size to the fundamental [Lee, 1998, p.301]. Instead, it assumes the nonlinear behavior is sufficiently weak that it can be approximated by extracting the low-order coefficients of the underlying polynomial at a set of three input amplitudes well below the input-referred IP3 (IIP3) [Lee, 1998, p.297–300]. However, extrapolating out to the IIP3 from these amplitudes neglects the impact of not only higher-order polynomial terms in the case of strong distortion, but compression of the fundamental as the input signal approaches its maximum size.<sup>29</sup>

In contrast to those quantified by low-level linearity measures, high-SFDR circuits must account for the extent of transistor nonlinearities at the full scale signal level (1 V<sub>PP</sub>). To illustrate this, Figure 3.5 and Figure 3.6 present the large-signal characteristics of two classes of transistors from the chosen manufacturing process: the standard  $I_D$ -vs- $V_{DS}$  curves for a pMOSFET and, for a pair of npn BJTs, the

---

<sup>29</sup>Indeed, the IIP3 is often specified in conjunction with the  $-1$ -dB compression point, since these two linearity measures describe distinct regimes of the signal space, with the latter corresponding to distortion at high signal levels [Lee, 1998, p.301]. Here, both roles are played by SFDR, which is measured (or simulated) at the full signal power.

$\beta$ -vs- $V_{BE}$  profiles. The linearity of circuits whose dynamic range is limited by  $P_{\text{noise}}$  rather than  $P_{\text{harm}}$  is sufficient to assume that transistors from both classes operate in a narrow region around a quiescent point, indicated by gray dots in Figure 3.5(a) and Figure 3.6(a), where their behavior can be approximated by a linearized small-signal model. However, using the BJTs of Figure 3.6 as an example, this linearization is only good to 10% for a 10 mV signal [Gray *et al.*, 2001, p.28]; clearly, such a model is not accurate enough for the full-scale range of the target receiver.

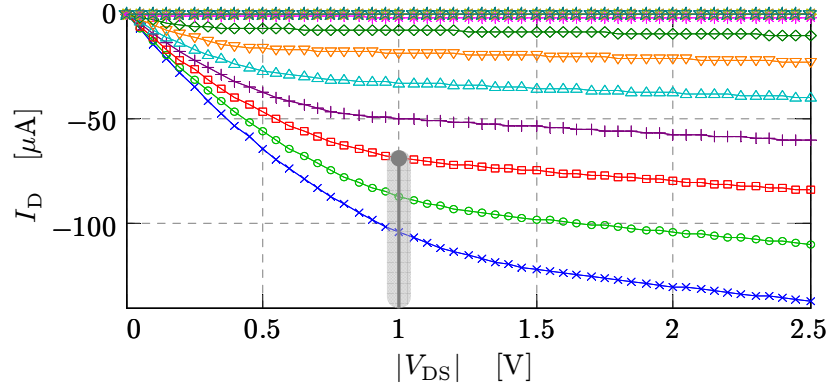
If, as in the case of IIP3, transistor nonlinearities are merely extrapolated from a moderate operating regime corresponding to voltage swings of  $0.1 V_{PP}$ , as in Figure 3.5(b) and Figure 3.6(b), the second and third order coefficients of the resulting polynomials would be relatively small, since the MOS(BJT) response resembles that of an oblique(horizontal) line over that interval.

Instead, to achieve 90-dB SFDR for signals that occupy the wider range of Figure 3.5(c) and Figure 3.6(c), the design of SVEPRE must grapple with the full, inherently nonlinear, large-signal behaviors of the transistor classes. The design principles of Chapter 4 and Chapter 5 that address this challenge can be sufficiently appreciated by representing the nonlinear behaviors of Figure 3.5(c) and Figure 3.6(c) using the simple, first-order constitutive relations for MOSFETs<sup>30</sup> [Sze and Ng, 2007, p.305–306]

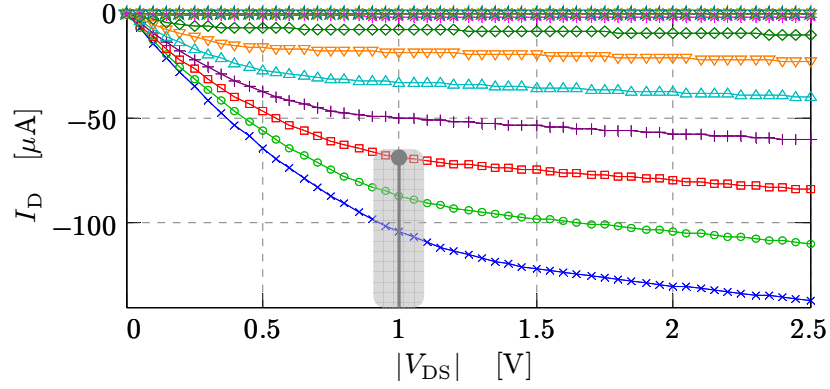
$$I_D = \begin{cases} \mu_p C_{ox} \frac{W}{L} \left[ (V_{gs} - V_{th}) V_{ds} - \frac{V_{ds}^2}{2} \right] & , \text{ for } V_{ds} < V_{ds,sat} \\ \frac{1}{2} \mu_p C_{ox} \frac{W}{L} (V_{gs} - V_{th})^2 (1 + \lambda V_{ds}) & , \text{ for } V_{ds} \geq V_{ds,sat} \end{cases} \quad (3.9)$$

---

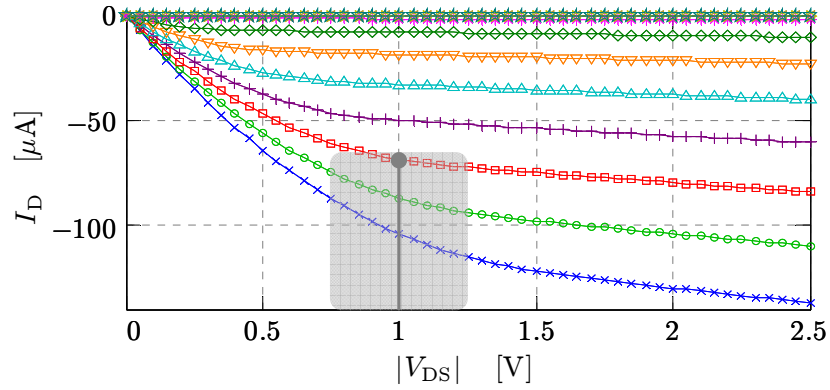
<sup>30</sup>The polarities of all voltages in (3.9) are inherited from the analogous expression that describes the n-type MOSFET. However, a pMOS description is more apropos for the remainder of this text in light of the device litany in Section 3.2.1. Thus, all voltages and currents in (3.9) (including  $V_{th}$ ) are treated as positive quantities by implicitly taking their absolute values.



(a) Small-signal regime.

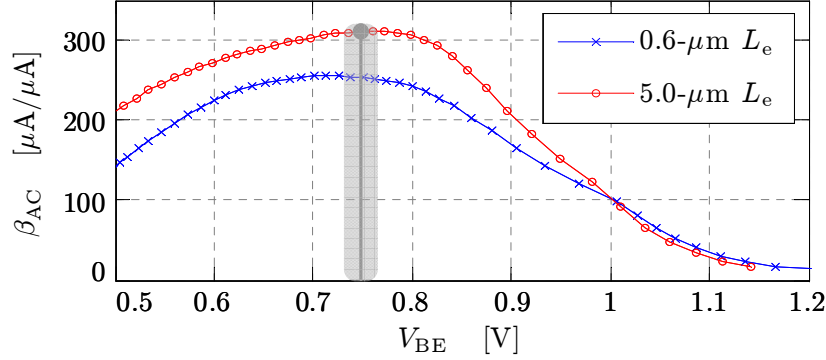


(b) Medium-signal regime.

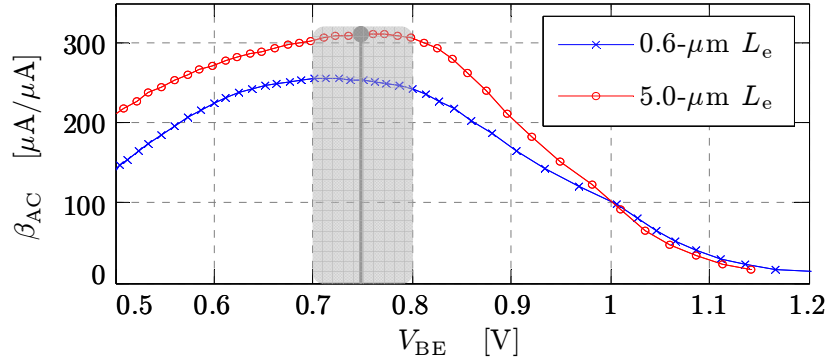


(c) Large-signal regime.

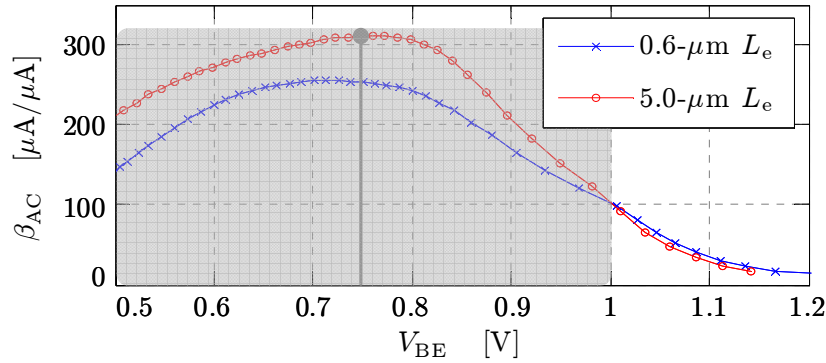
Figure 3.5: Comparison of nonlinear MOSFET behavior. For a 0.5/0.25 pMOS device from the target technology, simulated  $I_D$ -vs- $|V_{DS}|$  curves for  $|V_{GS}|$  swept from 0–2.5  $\text{V}$  in 25  $\text{mV}$  steps indicate increasingly nonlinear behavior for (a) small-signal (b) 0.1  $\text{V}_{PP}$  and (c) 1  $\text{V}_{PP}$  signal swings about the quiescent point (gray dot).



(a) Small-signal regime.



(b) Medium-signal regime.



(c) Large-signal regime.

Figure 3.6: Comparison of nonlinear BJT behavior for various signal swings. For both small ( $W_e = 0.25 \mu\text{m}$ ,  $L_e = 0.6 \mu\text{m}$ ) and large ( $W_e = 0.25 \mu\text{m}$ ,  $L_e = 5 \mu\text{m}$ ) npn devices from the target technology, simulated  $\beta_{\text{DC}}$ -vs- $V_{\text{BE}}$  curves indicate that accurate behavioral models become increasingly nonlinear for (a) small-signal (b)  $0.1 \text{ V}_{\text{PP}}$  and (c)  $1 \text{ V}_{\text{PP}}$  signal swings about the quiescent point (gray dot).



and BJTs<sup>31</sup> [*Gray et al.*, 2001, p.11–16]

$$I_c = I_S e^{V_{be}/nV_T} \left( 1 + \frac{V_{cb}}{V_A} \right) \quad (3.10a)$$

$$\beta = \frac{I_c}{I_b} \quad (3.10b)$$

respectively. Although (3.9) and (3.10) omit significant nonidealities (such as pMOS transconductance limiting with velocity saturation and the reduced  $\beta$  associated with low- and high-level injection in BJTs), they capture the primary nodal-voltage dependences in need of linearization and, as such, are cited extensively hereafter for design intuition.

### 3.1.3 Noise

In the example of Figure 3.4, it was presumed that  $Y(f_{\text{harm}})$  dominated the denominator of (3.7), so that the noise floor,  $Y(f_{\text{noise}})$ , need not be explicitly represented. But, ensuring this is the case requires that contributions to  $P_{\text{noise}}$  be carefully determined. In addition to establishing the linearity limits for large input signals, this reduction of  $P_{\text{noise}}$  is also critical at the other extreme of the dynamic range: it establishes the minimum detectable signal (MDS).<sup>32</sup> In pursuing a specification for the maximum  $Y(f_{\text{noise}})$  that can be tolerated, three contributions must be considered: wave phenomena outside the capture window of

---

<sup>31</sup>The polarity of (3.10) corresponds to an npn BJT. To within sign, corresponding pnp formulas are identical, but are of less utility herein according to the assessment of Section 3.2.1. In the npn case, the reverse saturation current  $I_S$  is given by

$$I_S = \frac{qD_n A_e n_i^2}{W_b N_A}$$

where  $D_n$  is the electron diffusion constant in the base,  $W_b$  and  $N_A$  are the width and doping of the base,  $A_e$  is the cross-sectional area of the emitter, and  $n_i$  is the intrinsic carrier concentration in Si ( $9.65 \times 10^9 \text{ cm}^{-3}$ ).

<sup>32</sup>Although the terms *sensitivity* and *minimum detectable signal* are closely related in radio contexts [*Krauss et al.*, 1980, p.267], the former is also used in feedback theory to describe the dependence of circuit properties on loop parameters. To reduce ambiguity, then, the latter is employed in this section.

Figure 1.13, which are considered undesirable; thermal and shot noise associated with the interaction between charge carriers and a dipole antenna immersed in a magnetoplasma; and thermal and flicker noise generated by the front-end circuitry. Each of these is examined in turn below, where a nominal dipole antenna of  $L_{\text{TT}} = 20$  m ( $L_{\text{eff}} = 10$  m) and  $r_a = 10$  cm has been assumed, as its length approximates the median of the representatives in Table B.3 (22 m) and is viable for deployment by satellites and microsatellites alike.<sup>33</sup>

### 3.1.3.1 Minimum Detectable Signal

Returning to the signal space defined in Figure 1.13, recall that the 90-dB difference between the electric field spectral densities of the strongest ( $|W_{\text{max}}(f)|^2$ ) and weakest ( $|W_{\text{min}}(f)|^2$ ) noise-like signals of interest ( $10^{-6}$  V<sup>2</sup>/m<sup>2</sup>/Hz and  $10^{-15}$  V<sup>2</sup>/m<sup>2</sup>/Hz for bow shock and upper-hybrid waves, respectively) gives rise to the SFDR specification in Section 1.2.2. Additionally, the absence of relevant phenomena below  $W_{\text{min}}(f)$  establishes this quantity as the minimum detectable signal which, in turn, translates into a circuit design requirement: the maximum allowable level of the noise floor  $Y(f_{\text{noise}})$ .

The steps for performing this conversion from plasma wave electric field density,  $|W_{\text{min}}(f)|^2$ , to SVEPRE output noise floor,  $Y(f_{\text{noise}})$ , determining the input referred noise PSD  $X(f_{\text{noise}})$  along the way, are outlined in Figure 3.7. Given a 20-m dipole, the bow shock and UHR result in PSDs at the LNA input of

$$|X_{\text{max}}(f)|^2 = |W_{\text{max}}(f)|^2 L_{\text{eff}}^2 = 10^{-4} \text{ V}^2/\text{Hz} \quad (3.11a)$$

$$|X_{\text{min}}(f)|^2 = |W_{\text{min}}(f)|^2 L_{\text{eff}}^2 = 10^{-13} \text{ V}^2/\text{Hz} \quad (3.11b)$$

In order to resolve the MDS, (3.11b) implies that the input-referred LNA noise floor,  $X(f_{\text{noise}})$  be

$$|X(f_{\text{noise}})| \leq \sqrt{|X_{\text{min}}(f)|^2} = 316 \text{ nV}/\sqrt{\text{Hz}} \quad (3.12)$$

To propagate this value through the LNA and arrive at  $Y(f_{\text{noise}})$ —and, by extension,

---

<sup>33</sup>In subsequent descriptions of the nominal, or any, dipole as being  $x$  m long,  $x$  is value of  $L_{\text{TT}}$ .

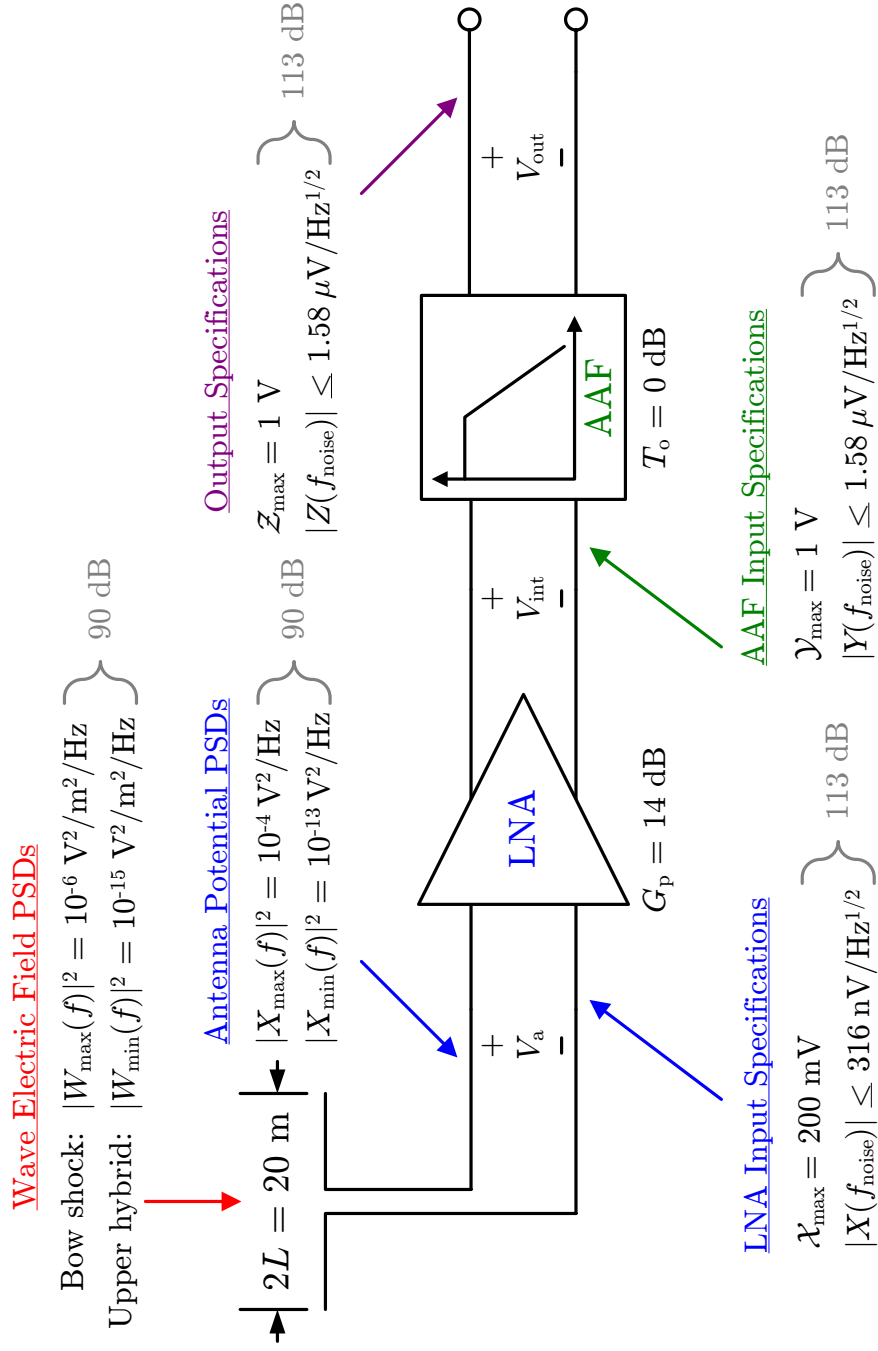


Figure 3.7: Dynamic range specifications for front-end signal path presuming a fully differential signal path and nominal antenna. See text for additional assumptions on signal bandwidth and block gains.

$Z(f_{\text{noise}})$ , since the AAF is presumed here to possess unit gain—the nominal  $G_p$  must be determined.<sup>34</sup> Assuming that the bandwidth of  $X_{\text{max}}(f)$ ,  $\Delta f_{\text{max}}$ , can be conservatively estimated on the logarithmic frequency scale of Figure 1.13 by the location of the peak bow shock power, at 200 Hz, the amplitude of a coherent sinusoid  $x_{\text{max}}(t) = \mathcal{X}_{\text{max}} \sin(\omega t)$  with the same total power as  $|X_{\text{max}}(f)|^2$  in (3.11a) would be<sup>35</sup>

$$\mathcal{X}_{\text{max}} = \sqrt{2\Delta f_{\text{max}} |X_{\text{max}}(f)|^2} = 200 \text{ mV} \quad (3.13)$$

To leverage the resolution of the subsequent ADC, the LNA should amplify this signal so as to occupy the full-scale range of 1 V<sub>PP</sub>. However, as the original specifications for the part of [Wang, 2009] called for a 2 iV<sub>PP</sub> input range, an additional factor of 2 is sought.<sup>36</sup> Thus, the nominal gain of the LNA in this work,  $G_{\text{po}}$ , is established at 14 dB.<sup>37</sup>

This gain translates the input requirements of the LNA—namely, a maximum equivalent sinusoidal signal of 0.2 V<sub>PP</sub> and a noise floor of 316 nV/ $\sqrt{\text{Hz}}$ —into the corresponding AAF specifications:

$$\mathcal{Y}_{\text{max}} = G_{\text{po}} \mathcal{X}_{\text{max}} = 1 \text{ V} \quad (3.14)$$

$$Y(f_{\text{noise}}) = G_{\text{po}} X(f_{\text{noise}}) = 1.58 \text{ } \mu\text{V}/\sqrt{\text{Hz}} \quad (3.15)$$

where  $\mathcal{Y}_{\text{max}}$  is the amplitude of a coherent sinusoid,  $y_{\text{max}}(t) = \mathcal{Y}_{\text{max}} \sin(\omega t)$ , equivalent to the maximum expected electric field density at the AAF input. Examining (3.15),

---

<sup>34</sup>Recall that Section 3.1.1.1 only motivates a programmable range of 24 dB, not the absolute gain.

<sup>35</sup>Published results of equivalent sine wave sensitivities typically account for the total power of broadband plasmas waves by integrating over the actual system bandwidth, rather than the full wave bandwidth ( $\Delta f_{\text{max}}$ ) used here assuming an all-pass signal path. The former method reduces the result of (3.13) by a factor of 1/2 [Scarf *et al.*, 1980, p.38] to 1/4 [Gurnett *et al.*, 1997, p.205]. But, to prevent saturating the front-end, (3.13) is purposely formulated to provide a conservative assessment of maximum expected signal.

<sup>36</sup>In a receiver system that adopts the 1 mV<sub>PP</sub> maximum signal swing, excess  $G_{\text{po}}$  can be traded for a smaller antenna or, alternatively, a more symmetric programming range.

<sup>37</sup>As this corresponds to a 20-m dipole, the programmable gain necessary to achieve compatibility with the extremes of antenna family identified in Section 3.1.1.1 must span 0 dB ( $L_{\text{TT}} = 100 \text{ m}$ ) to 24 dB ( $L_{\text{TT}} = 6.3 \text{ m}$ ).

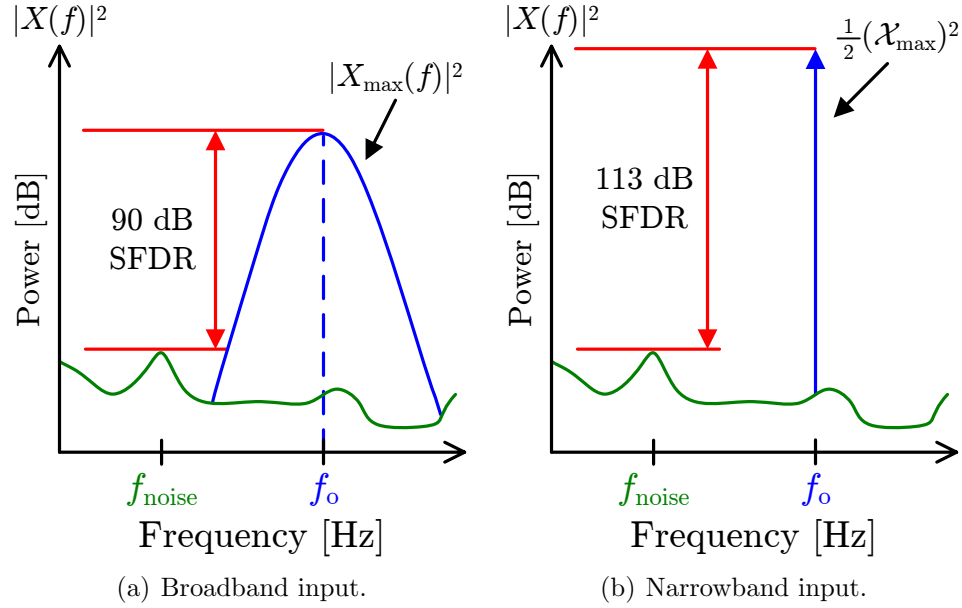


Figure 3.8: Illustration of noise floor for sine wave equivalents of broadband inputs. As opposed to the narrowband case of Figure 3.4, when  $P_{\text{harm}} = 0$  the SFDR is lower for (a) broadband inputs than (b) their sine wave equivalents. The former, observed in flight, set the 90-dB specification; the latter are employed for laboratory characterization.

it is noteworthy that, according to the treatment in Section 3.1.2.1, an SFDR of 90 dB for  $|Y(f_o)|$  of  $2^{-1/2} \text{ V}/\sqrt{\text{Hz}}$  only requires  $Y(f_{\text{noise}}) \leq 23 \mu\text{V}/\sqrt{\text{Hz}}$ . But, since the MDS is determined relative to the noise-like wave phenomena, whose spectral densities are broader and weaker than the equivalent sinusoids used in testing, the noise floor must actually be nearly an order of magnitude lower. This point is illustrated in Figure 3.8 for the simple case of  $P_{\text{harm}} = 0$ . Although the 90-dB SFDR specification is derived by comparing broadband signals against the noise floor in a spot sense, as in Figure 3.8(a), laboratory measurements such as those of Chapter 6, which are obtained using sinusoids of equivalent power, exhibit a much larger spot ratio, as depicted in Figure 3.8(b). This lower noise floor renders the limiting harmonics visible, but cannot itself be properly used to assess the SFDR.

Thus, although the SFDR metric defined in (3.7) would traditionally be sufficient to specify both the requisite harmonic suppression and noise floor, using equivalent

sine waves to test the front-end in place of the broadband plasma phenomena decouples these two quantities. For such inputs, the harmonics must still be suppressed by 90 dB, in order to satisfy (3.7) both for coherent and incoherent waves, but the noise floor must satisfy (3.15) in order to resolve the MDS when it is noise-like in character, requiring a level 113 dB below the fundamental.

### 3.1.3.2 Antenna Noise in Plasmas

In any receiver system, noise generated by the receiver itself should not exceed the MDS. The primary contributions to the noise of plasma wave receivers are that generated by the dipole antenna immersed in the cold plasma of the magnetosphere, discussed here,<sup>38</sup> and that of the integrated electronics, as presented in Section 3.1.3.3.

Uncertainties in the random interactions of the antenna with the electrons and ions of the plasma give rise to two classes of noise: thermal noise (otherwise known as Johnson-Nyquist noise [Lee, 1998, p.244]) and shot noise. It is extremely difficult to obtain accurate analytic expressions that describe the PSDs of these noise phenomena,  $S_T(f)$  and  $S_S(f)$ , respectively, under all conditions. However, in practice, a series of approximations and limiting cases can be employed to arrive at unified model that is sufficient for this work, as is carried out in Appendix D. Assuming familiarity with the background and terminology therein, this section focuses specifically on the low-frequency regime in which these contributions are shown to reach their maxima.

It is well known that any conductor immersed in a plasma is enveloped by an electrostatic plasma sheath [Bittencourt, 1995, p.279–288], whose formation governs the noise of the dipole in the regime where  $f \ll f_{pe}$ . The sheath can be composed of either electrons emitted by the conductor through photo-stimulation under ultraviolet

---

<sup>38</sup>The case of a transmitting antenna is quite distinct. The large potentials driving the antenna result in sufficient energization of the near-field plasma as to merit its treatment using a warm, rather than cold, plasma approximation (cf. Section 1.1.3.1). Additionally, if these potentials exceed the ambient plasma potential, the sheath region becomes highly nonlinear, invalidating the linearization of the fluid theory equations typically used to describe it [Chevalier, 2007, p.12]. Indeed, the sheath structure is sufficiently complicated that kinetic or fluid simulations are the only practical means of properly modeling such cases, with a recent example of the latter provided by the excellent work of Chevalier [2007]. Thankfully, for receive antennas, the linearized cold plasma [Chevalier, 2007, p.4] and electrostatic sheath models [Chevalier, 2007, p.9] leveraged in Appendix D are sufficient.

radiation (photoelectric sheath) or of relatively immobile ions in the plasma (positive ion sheath). The sheath assumes one character or the other depending on the floating potential of the probe,  $V_o$ , and the plasma electron density,  $N_e$ , according to Langmuir theory [Gurnett, 1998, p.126].<sup>39</sup> For a Maxwellian plasma, this formulation dictates that the antenna-plasma coupling is dominated by the resistance and capacitance of the sheath given in (D.9) and (D.13) and restated here for convenience as:

$$R_S = \begin{cases} 2 \frac{kT_e}{q} \frac{1}{I_{\text{pho}} + I_i} & , \text{ positive ion} \\ -2 \frac{kT_{\text{ph}}}{q} \frac{1}{I_{\text{eo}} + I_i} & , \text{ photoelectric} \end{cases} \quad (3.16)$$

$$C_S = \frac{\pi \epsilon_0 L_a}{\ln(D_o/r_a)} \quad (3.17)$$

Through carefully accounting for  $R_S$  in the final computation of the antenna impedance,  $Z_a$ , (cf. Section D.1.2.3) it not only determines the total noise in the low frequency regime, but the maximum expected over the full antenna bandwidth.

To illustrate this, Figure 3.9 presents predictions of the unified model in Appendix D for the total antenna noise PSD,  $S_a(f)$ , at altitudes corresponding to the generally accepted centers of the inner ( $L = 2$ ) and outer ( $L = 4$ ) belt (cf. Section 1.1.1). For each altitude, Table 3.1 summarizes the computed properties.<sup>40</sup> With the exception of the resonance near  $f_{\text{pe}}$ , in both cases, the noise in the low-frequency regime, which is governed by  $R_S$ ,<sup>41</sup> exceeds that above  $f_{\text{pe}}$ , where the

<sup>39</sup>It is this Langmuir theory, which describes the equilibrium voltage and current distributions along a plasma-immersed conductor, that motivates the extraction of plasma parameters from the eponymous probes described in Footnote 9 of Appendix B. Its application to this work is more fully articulated in Section D.1.1.

<sup>40</sup>To complement these outputs, a complete list of the corresponding simulation inputs is provided in Table D.1.4.

<sup>41</sup>The fact that the antenna noise represented by  $R_S$  is inversely proportional to its surface area (cf. via the currents in (3.16) given by (D.4)) while the induced signal voltage is directly proportional to its effective length (cf. (3.2)) presents that rare engineering decision with regard to maximizing SNR in which there is no trade-off: longer is always better [Gurnett, 1998, p.129]. The only constraints are that the antenna remain electrically short (scilicet,  $L_a < \lambda$  so that  $\Delta V = (L_{\text{eff}} \Delta E) \text{sinc}(L_a/\lambda) \simeq L_{\text{eff}} \Delta E$  [Mozer, 1973, p.305]), which is not difficult at VLF frequencies, and, perhaps more challenging, that it be possible to reliably deploy it. Indeed, the spin-stabilization

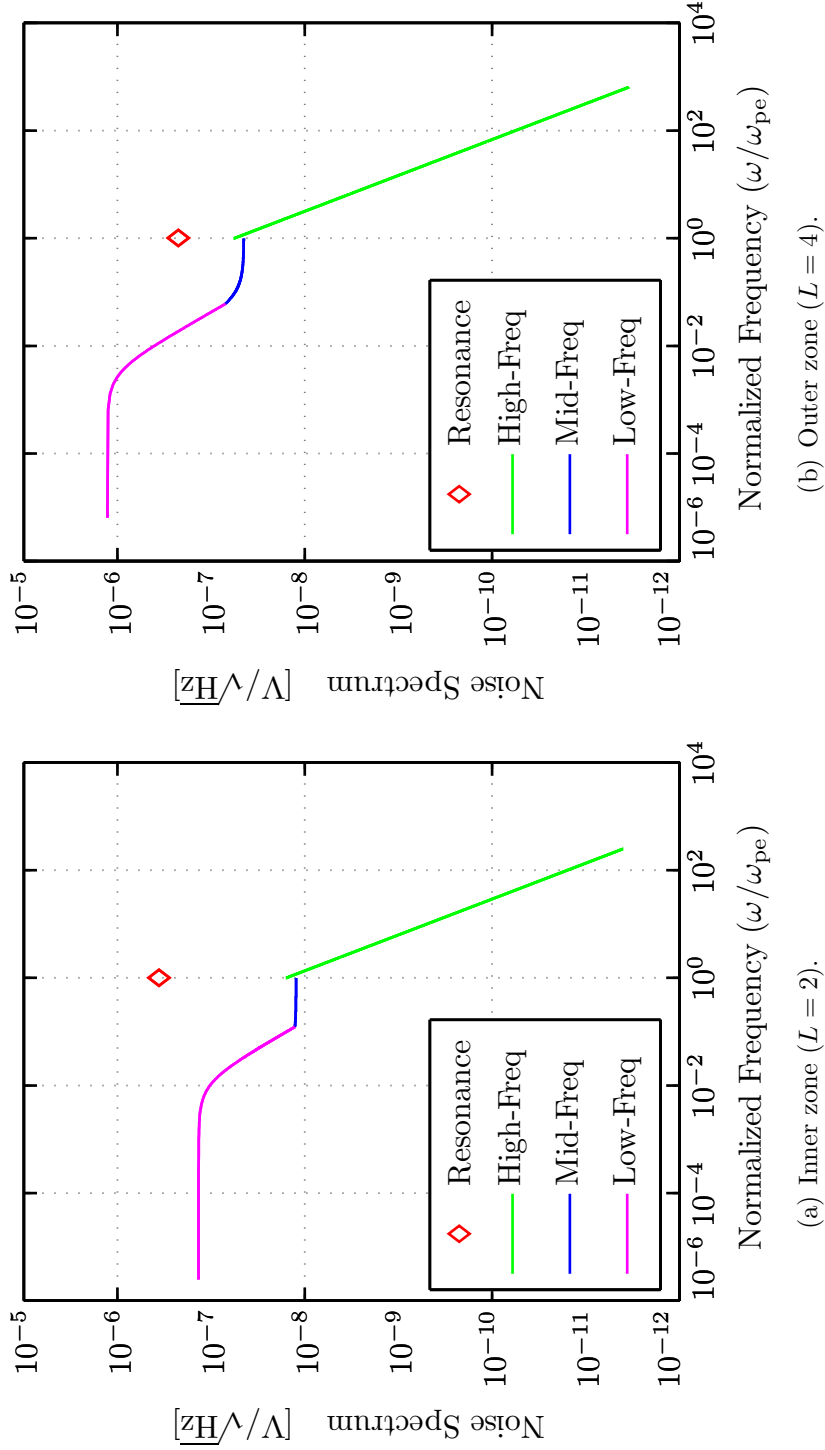


Figure 3.9: Simulated noise of nominal dipole antenna. Fed the typical plasma conditions in Table D.1.4 for (a)  $L = 2$  and (b)  $L = 4$ , the unified model of Appendix D yields a piecewise approximation to the total antenna noise that is limited at low frequencies by the shot noise of its positive ion sheath (assuming  $I_{ph}$  is negligible).



Property	Symbol	Inner zone	Outer zone	Units
Equilibrium sheath				
Type		Ion	Ion	
Floating potential	$V_0$	-0.607	-3.19	V
Sheath impedance				
Resistance	$R_S$	167	2980	k $\Omega$
Capacitance	$C_S$	205	104	pF
Transition	$f_S$	4.64	0.516	kHz
Radiation impedance				
Resistance	$R_r$	1.40	3.62	k $\Omega$
Capacitance	$C_r$	863	134	pF
Total noise				
Low-frequency	$S_a(0)$	0.136	1.28	$\mu\text{V}/\sqrt{\text{Hz}}$

Table 3.1: Antenna properties predicted by unified noise model of Appendix D, corresponding to results in Figure 3.9.

dipole impedance becomes largely reactive, approaching its free-space capacitance:

$$C_A = \frac{\pi \epsilon_0 L_a}{\ln(L_a/r_a) - 1} \quad (3.18)$$

The maximum antenna shot noise ( $\sim 100 \text{ nV}/\sqrt{\text{Hz}}$  in the  $L=2$  case) places an upper bound on the input-referred noise of the front-end electronics in order to provide sufficient spectral fidelity to sense both the antenna thermal noise and MDS [Sentman, 1982, p.1456]. For the  $L=4$  case, the low-frequency noise of  $\sim 1.25 \mu\text{V}/\sqrt{\text{Hz}}$  exceeds the MDS. However, the larger MDS emf and lower shot noise of a longer antenna, coupled with a proportionately smaller LNA gain, would afford the desired dynamic range at this altitude. Specifically, the target SFDR is recovered for  $L_{\text{TT}}=51 \text{ m}$  and  $G_p=6 \text{ dB}$ , illustrating once again the importance of programmable gain.

of the satellites in Table 1.2 is often needed to provide the centrifugal force necessary to maintain the rigidity of the long dipoles listed in Table B.3. Although the design of deployment mechanisms and stacers for such long antennas is quite sophisticated (e.g., [Bonnell et al., 2008]), a simple conception of each as a pair of wires unfurled and maintained in an extended configuration by the rotation of the satellite suffices for this discussion.

### 3.1.3.3 Circuit Noise

Assuming, as in the case of nominal dipole at inner belt altitudes, that the antenna noise remains below the MDS, the second major contribution to receiver noise, that of the electronics to which Section 3.1.3.2 alludes at its outset, should not exceed their difference.<sup>42</sup> Using classical theory for a 2-port network driven by a noisy source [van der Ziel, 1986, p.32], the total noise of SVEPRE can be modeled according to Figure 3.10(b) with a pair of input-referred sources that allow the circuit blocks themselves to be considered noiseless:  $e_n$  is the equivalent input-referred RMS short-circuit noise voltage, which generates the same noise current in a shorted output as the front-end itself when its input port is shorted;<sup>43</sup>  $i_n$  is the equivalent input-referred RMS open-circuit noise current, which generates the same output noise as the front-end itself when its input(output) port is open-circuited(shorted).

These sources are related to the noise currents  $i_{in}$  and  $i_{out}$  associated with the input and output admittances,  $Y_{in}$  and  $Y_{out}$  in the somewhat more intuitive model of Figure 3.10(a) by [van der Ziel, 1986, p.29]

$$e_n^2 = e_{out}^2 = \frac{i_{out}^2}{|Y_F|^2} \quad (3.19)$$

$$i_n^2 = i_{in}^2 + |Y_{in}|^2 e_{out}^2 \quad (3.20)$$

where  $Y_F$  is the forward transconductance gain of the system. Were it not for the second term of (3.20),  $e_n(i_n)$  would be independent of  $i_n(e_n)$ , simply representing the noise generated by the equivalent impedance at input(output) port. Since the correlation through  $Y_{in}$  is quite weak for SVEPRE, given the high LNA input impedance (cf. Section 3.1.4),  $e_n$  and  $i_n$  may be treated as uncorrelated in the following.

Combining the noise sources of Figure 3.10(b) in terms of voltage, thereby

---

<sup>42</sup>Presumably, the noise of contributions of the antenna and electronics are uncorrelated, so their noise powers simply add in quadrature.

<sup>43</sup>Since noise is presumed small enough to conform to a small signal model, the shorting(open-circuiting) of ports is performed in an incremental sense, such as can be achieved by a large capacitor(inductor)[Laker and Sansen, 1994, p.143].

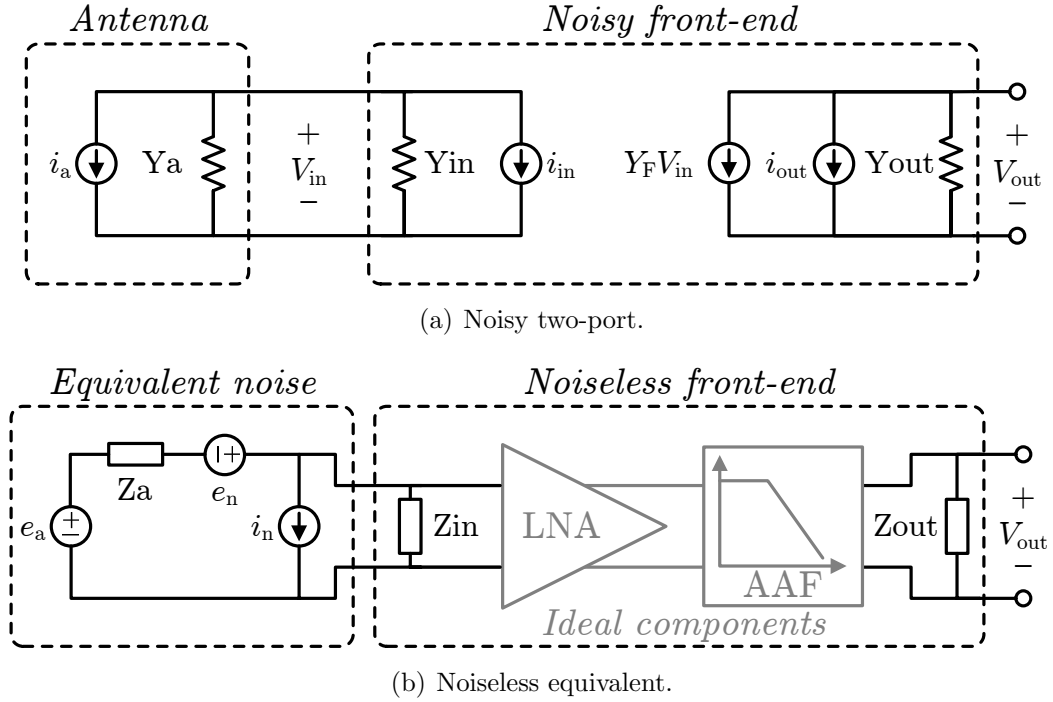


Figure 3.10: Front-end equivalent noise model. Equivalent to (a) the generalized model of the front-end as a two-port with noisy admittances and forward admittance  $Y_F$  is (b) one which the noise contributors, including the antenna, are extracted to the input port, leaving a port noiseless two-port whose impedances are represented explicitly so that the LNA and AAF blocks can be treated as ideal.

converting from port admittances to impedances, as

$$e_r^2 = e_a^2 + e_n^2 + i_n^2 |Z_a|^2 \quad (3.21)$$

reveals the relative contributions of the antenna and circuit noise to the equivalent receiver noise  $e_r$ .<sup>44</sup> Since the total input-referred noise must remain below the MDS, (3.21) can be combined with the results of Figure 3.9(a) and (3.12) to yield an input

<sup>44</sup>As is traditionally the case, the effect of  $Z_{in}$  is omitted from (3.21) because  $e_r$  represents the noisy portion of an equivalent source of impedance  $Z_a$ , the division of which with an arbitrary LNA input impedance can then be handled identically to that of the signal portion of the self-same source—by constructing a voltage divider between  $Z_a$  and  $Z_{in}$ . Furthermore, as discussed in Section 3.1.4, the goal of  $Z_{in} \gg Z_a$  is to maximize voltage gain, which renders  $Z_a$  dominant over  $Z_{in}$  in their parallel combination as seen by  $i_n$ .

noise specification for SVEPRE:

$$\frac{e_n^2 + i_n^2 |Z_a|^2}{\Delta f} \leq |X(f_{\text{noise}})|^2 - \frac{e_a^2}{\Delta f}$$

$$S_{\text{in}}(f) \leq 9 \times 10^{-14} \text{ V}^2/\text{Hz} \quad (3.22)$$

Since, the MDS is specified as a PSD, the SVEPRE noise specification is not on the total power over the noise bandwidth, but on the spot quantity  $S_{\text{in}}(f)$ , a PSD that equates to 300 nV/ $\sqrt{\text{Hz}}$ .<sup>45</sup>

This specification must be met over the full system bandwidth, but is especially challenging at the lower end, near 100 Hz, on account of  $1/f$  noise, which results in increased noise spectral density at low frequencies (i.e., a ‘pink’ spectrum) due to the broad range of time constants associated with the network relaxation that governs the random trapping and de-trapping of channel carriers by near-interfacial (‘border’) oxide traps.<sup>46</sup>

---

<sup>45</sup>An RF designer might question why the noise specification for SVEPRE, and particularly for the LNA, would be an input-referred PSD rather than the more familiar metric of noise figure (NF). The reason is the high-impedance input of an electric-field plasma wave receiver. According to its canonical definition for a 2-port network [Lee, 1998, p.258], the circuit of Figure 3.10(b) would have a noise figure of:

$$\text{NF} = 10 \log_{10} \left( 1 + \frac{e_n^2 + i_n^2 |Z_a|^2}{e_a^2} \right)$$

However, for the case of low  $i_n$ , this expression is trivially minimized whenever,  $Z_a$  is large enough that  $e_a$  trumps  $e_n$ . Since the impedance of a dipole in a magnetoplasma can vary drastically with the plasma parameters and wave frequency (cf. Section D.1.3), routinely achieving resistances in the  $10^6$ – $10^8$  range when sheath effects dominate (cf. Section B.1.2), the receiver NF can artificially appear quite low as a consequence of the high source impedance.

Thus, as opposed to the narrowband LNAs of RF systems, in which the assumption of standardized 50- $\Omega$  port impedances justifies the prevalence of NF specifications [Laker and Sansen, 1994, p.146] (which often omit the source impedance [National Semiconductor Corp., AN104, p.2]), the high input (and expected antenna) impedance of SVEPRE renders it akin to an operational amplifier, whose noise is universally and more accurately captured by  $e_n$  and  $i_n$  [Lee, 1998, p.265]. Adopting a specification on  $S_{\text{in}}(f)$  rather than NF heeds the adamantly issued advice of opamp manufacturers: “Don’t be fooled into believing that low NF means low noise *per se*!” [National Semiconductor Corp., AN104, p.4].

<sup>46</sup>The physical origins and TID dependence of this phenomenon are discussed in Section 2.1.1.4.

**BJT Flicker Noise** For bipolar transistors, the relevant traps lie in the E-B spacer oxide; since only the B-E junction is forward biased during forward-biased operation, flicker noise is associated with the base current [Lee, 1998, p.255]. The total base current noise, analogous to the  $i_{\text{in}}$  source of Figure 3.10(a), is then given by [Laker and Sansen, 1994, p.142–143]

$$i_{\text{in}}^2 = \underbrace{2qI_B\Delta f}_{\text{Shot}} + \underbrace{\frac{K_F I_B}{W_e L_e} \frac{\Delta f}{f^{\alpha_F}}}_{\text{Flicker}} \quad (3.23)$$

where the shot noise term reflects the uncertainty with which discrete charge quanta, in the form of majority carriers, hop the potential barrier of the forward-biased E-B junction [Lee, 1998, p.251].<sup>47</sup> The same phenomena occurs at the reversed-biased C-B junction, giving rise to a representation for  $i_{\text{out}}$  as

$$i_{\text{out}}^2 = \underbrace{2qI_C\Delta f}_{\text{Shot}} \quad (3.24)$$

For assessing circuit performance, it proves convenient to apply the transformations of (3.19) and (3.20) to the results in (3.23) and (3.24), such that:<sup>48</sup>

$$e_n^2 = \frac{i_{\text{out}}^2}{|Y_F|^2} = \frac{2kT}{g_m} \Delta f \quad (3.25)$$

$$i_n^2 = 2qI_B \left( 1 + \frac{\beta_{\text{DC}}}{\beta^2} \right) + \frac{K_F I_B}{W_e L_e} \frac{\Delta f}{f^{\alpha_F}} \quad (3.26)$$

Note that the shot noise portion of (3.23) is white on account of the random arrival times of each charge packet [Lee, 1998, p.251]. So,  $1/f$  noise begins to dominate the

<sup>47</sup>The physical interpretation and analytical derivation of this phenomenon are discussed in Section D.1.2.2.

<sup>48</sup>For low impedance sources or high bias currents ( $I_C > V_T/2R_b$ ), the total BJT noise can be dominated by the thermal noise of the incremental resistor that accounts for lateral resistance of the (predominantly intrinsic) base region,  $R_b$  [Lee, 1998, p.266]. Since the high impedance of the dipole antenna and low LNA bias currents render this point moot, the corresponding term,  $4kTR_b$ , has been omitted from (3.25).

$i_n$  spectrum below the frequency at which the two terms of (3.26) are equal:

$$f_K = \left( \frac{K_f}{2qW_e L_e (1 + \beta_{DC}/\beta^2)} \right)^{\alpha_F} \quad (3.27)$$

This is known as the corner frequency and, for BJTs, ranges from 10–100 Hz [Lee, 1998, p.254], meaning a flat noise spectrum is to be expected over most of the bandwidth of interest. But, given that the large dipole  $Z_a$  places a premium on low  $i_n$ , the potential for bipolar  $1/f$  to degrade the noise floor near 100 Hz prompts a consideration of alternative devices.

**MOS Flicker Noise** Compared to bipolar devices, such noise is much more pronounced for MOSFETs [Babcock *et al.*, 2001; Lee, 1998, p.254], whose surface conduction is more strongly affected by oxide traps. Operating where  $V_{DS} > V_{DS,sat}$ ,<sup>49</sup> the drain current noise of a MOSFET, akin to its  $i_{out}$ , is given by

$$i_{out}^2 = \underbrace{4kT\gamma_d g_{do} \Delta f}_{\text{Thermal}} + \underbrace{\frac{K_F g_m^2}{C_{ox}^2 W L} \frac{\Delta f}{f^{\alpha_F}}}_{\text{Flicker}} \quad (3.28)$$

where  $g_{do}$  is the conductance measured at the drain when  $V_{DS}=0$ . The thermal noise term is modulated by the parameter  $\gamma_d$  to account for the fact that the drain-source conductance,  $g_{ds}$ , is not fixed, as for a passive element, but varies with  $V_{DS}$ .<sup>50</sup> From

<sup>49</sup>The flicker noise term of (3.28), pertaining to the saturation region of operation, should be contrasted against that of (2.11) for linear region.

<sup>50</sup>Specifically, for low-field geometries,  $\gamma_d$  is defined as:

$$\gamma_d = \frac{1}{g_{do} L I_D} \int_0^{V_{DS}} g_L^2(V) dV$$

where  $g_L(V)$  is the unit-length channel conductivity as a function of its potential,  $V(x)$ , which in turn is a function of distance from the source,  $x$ , such that  $I_D = g(V) dV(x) = g_L(V) dV(x) / dx$ . The zero-bias, unit-length conductance is constant across the channel so  $g_L(0) = g_{Lo} = g_{do} L$  [van der Ziel, 1986, p.75] but, in strong inversion, it can be shown [van der Ziel, 1986, p.77] that  $g_L(V) = \mu W C_{ox} (V_{GS} - V_{th} - V)$ . Thus, the above integral reveals that [van der Ziel, 1986, p.78]

$$\gamma_d = \frac{1 - \zeta + \frac{1}{2}\zeta^2}{1 - \frac{1}{2}\zeta}$$

(3.28) the corner frequency can be deduced as

$$f_K = \left( \frac{K_f}{4kT\gamma_d C_{ox}^2} \frac{g_m^2}{g_{do}} \frac{W}{L} \right)^{\alpha_F} \quad (3.29)$$

Although  $f_K$  is a weak function of bias,<sup>51</sup> for a given process  $K_f$ ,  $\alpha_f$ , and  $C_{ox}$  are fixed, so the designer is primarily limited to using larger devices in an effort to reduce flicker noise.

Although the MOS gate terminal cannot generate flicker noise in the absence of DC current,  $i_{in}$  contains two noise terms: the shot noise of any gate leakage current,  $I_G$  [*Laker and Sansen*, 1994, p.86]; and the capacitive coupling of the noisy channel potential through  $C_{gs}$  [*Lee*, 1998, p.249]. These two contributions, the latter of which originates from the same essential randomness as  $i_{out}$  and is therefore correlated with  $e_n$ , are formulated as

$$i_{in}^2 = \underbrace{2qI_G\Delta f}_{\text{Shot}} + \underbrace{4kT\delta_g g_g \Delta f}_{\text{Thermal}} \quad (3.30)$$

where  $g_g = \omega^2 C_{gs}^2 / 5g_{do}$  and, for long channel devices,  $\delta_g = 2\gamma_d$  [*van der Ziel*, 1986, p.89].

According to (3.19) and (3.20), (3.28) and (3.30) can be synthesized using  $Y_{in} \simeq$

---

such that  $\gamma_d$  varies from unity at  $V_{DS} = 0$  to  $2/3$  in strong inversion, as a function of  $\zeta = V_{DS} / (V_{GS} - V_{th})$ .

In weak inversion, the corresponding expression for  $\gamma_d$  only ranges from unity ( $\zeta = 0$ ) to  $1/2$  (saturation), which justifies the preference for weak inversion in many low noise applications. However, since the saturated drain current in weak inversion exhibits the same exponential voltage dependence as a bipolar device [*van der Ziel*, 1986, p.86–88], since this maximum improvement in thermal noise is just 25%, and since the  $1/f$  noise dominates (3.28) for nearly the entire bandwidth of interest, this design favors the use of actual BJTs, offering comparable thermal noise along with much less flicker noise.

Finally, though the low-field assumptions underlying the above expressions are sufficient for the critical MOSFETs in this work, which feature  $L > 1 \mu\text{m}$ , the saturated value of  $\gamma_d$  can be much larger than  $2/3$  for short-channel devices, with values of 2–3 typical but by no means maximal [*Lee*, 1998, p.248].

<sup>51</sup>Just as described in Footnote 50 for  $S_v(f)$ , the improvement in  $f_K$  garnered by operating weak inversion is not large enough to render MOS performance comparable to that of BJTs. Assuming operation in the saturation region with a fixed value of  $g_m$  set by stage gain requirements, the ratio  $\alpha_{sat} = \gamma_{d,sat} g_{do} / g_{m,sat}$  approaches  $2/3$  for strong inversion (where  $g_{do} = g_{m,sat}$ ), and approximately  $(1 + C_d / C_{ox}) / 2$  for weak inversion [*van der Ziel*, 1986, p.86]. For identically sized devices, substituting  $\alpha_{sat}$  into (3.29) yields only  $\sim 20\%$  increase in  $f_K$  for weak inversion over strong, assuming a ratio of depletion capacitance ( $C_d$ ) to  $C_{ox}$  of  $\sim 1/8$ .

$j\omega C_{\text{gs}}$  to completely specify  $e_n$  and  $i_n$  as

$$e_n^2 = e_{\text{nd}}^2 = 4kT\gamma_d \frac{g_{\text{do}}}{g_m^2} \Delta f + \frac{K_F}{C_{\text{ox}}^2 WL} \frac{\Delta f}{f^{\alpha_F}} \quad (3.31)$$

$$i_n^2 = \omega^2 C_{\text{gs}}^2 \left( e_{\text{nd}}^2 + \frac{4}{5} kT \delta_g g_{\text{do}}^{-1} \right) \Delta f + 2qI_G \Delta f \quad (3.32)$$

Since both terms in the parentheses of (3.32) are roughly proportional to  $g_m^{-1}$ , the leading coefficient indicates that they can be neglected at the frequencies of interest, which are well below the MOSFET unity gain frequency,  $\omega_T$  (i.e.,  $\omega \ll g_m/C_{\text{gs}}$ ) [Lee, 1998, p.249];<sup>52</sup> similarly, the shot noise term for  $t_{\text{ox}} > 5$  nm is typically quite small [Laker and Sansen, 1994, p.86]. Thus, on the whole, the MOSFET may be treated as possessing only voltage noise,  $e_n$ , with  $i_n$  sufficiently small as to make it as an excellent candidate for reducing satisfying (3.22) in the presence of large  $Z_a$ .

Unfortunately, since the target bandwidth of the system lies far below the realm of RF design for which many modern CMOS processes are intended, the  $1/f$  corner given by (3.29) can exceed 1 MHz [Razavi, 2001, p.217], rendering MOSFETs impractical for this application. As evidence, consider the  $S_{v,\text{in}}(f)$  simulations of variously sized pMOS transistors from the target BiCMOS technology in Figure 3.11. Despite the fact that pMOS flavors typically offer  $10\times$ – $50\times$  lower  $K_F$  than their nMOS counterparts [Laker and Sansen, 1994, p.84], and even if the entire front-end noise was dominated by just that of a single pMOSFET (which is clearly unrealistic since  $G_p$  can be programmed to 0 dB) a device at least eight times the minimum size is required to satisfy the criterion of (3.22) at 100 Hz. This  $8\times$  area penalty incurred by a single transistor translates to a complete, differential LNA that consumes at least  $4\times$  more real estate than allotted by the AAF layout constraints (cf. Section 6.1.1.1). Furthermore, the area penalty concomitant with deploying such prodigious sizing throughout the front-end is amplified by the margin needed to accommodate the  $2\times$ – $3\times$  increase in  $K_F$  with TID (cf. Section 2.1.1.4).

In summary, it has been shown that in order to sense the minimum detectable

---

<sup>52</sup>This approximation, where has been assumed  $\omega_T \simeq g_m/C_{\text{gs}}$ , begets the earlier contention that the gate and drain noise can be considered uncorrelated over the VLF–HF spectral range in question.



signal (defined in Section 3.1.3.1) in the presence of the thermal and shot noise of the nominal dipole antenna (derived in Section 3.1.3.2), the input-referred noise of the front-end, which is dominated by that of the LNA, must satisfy (3.22). Given the flicker noise of the available bipolar and MOS devices just discussed, this can be achieved by only using MOSFETs sparingly in the most sensitive sections of the design, being limited to large-area pMOS sized with sufficient total dose margin. Instead, bipolar devices—specifically npns, which exhibit lower flicker noise than their pnp brethren [Deen *et al.*, 1998]—are leveraged extensively throughout the SVEPRE circuitry.<sup>53</sup>

### 3.1.4 Input Impedance

Whereas programmability, linearity, and noise requirements translate into specifications for both the LNA and AAF, the final key specification, that of high input impedance, pertains only to the former. To appreciate its necessity, consider the comprehensive impedance model of the antenna-LNA coupling in Figure 3.12. Between the antenna impedance,  $Z_a$ , represented by the generalized model of Figure D.2 and the input impedance of the LNA, represented by  $Z_{in} = R_{in} \parallel C_{in}$

---

<sup>53</sup>Omitted from this comparison of low-noise transistors are two excellent candidates: junction field-effect transistors (JFETs) (or the related metal-semiconductor field-effect transistors, MESFETs) and heterojunction field-effect transistors such as high-electron mobility transistors (HEMTs). The former are frequently used in place of MOSFETs low-noise applications [Laker and Sansen, 1994, p.74], including plasma wave receiver front-ends [Harvey *et al.*, 1995; Stone *et al.*, 1992, p.591,294], since their  $K_F$  can be nearly an order of magnitude smaller than that of an identically sized pMOSFET [Laker and Sansen, 1994, p.84]. However, since they are nonstandard in conventional processes, their availability undermines their consideration for this work [Laker and Sansen, 1994, p.161].

Similarly, GaAs and InP HEMTs, which are capable of outstanding noise performance [Chincarini *et al.*, 2006] due to bandgap engineering akin to that of SiGe HBTs that confines current flow to thin, impurity-free (i.e., non-doped or intrinsic) and, therefore, less noisy layers, are widely found in cryogenic [Duh *et al.*, 1988] and high-frequency [Rosenbaum *et al.*, 1993] applications. However, the exotic semiconductors involved are also incompatible with most commercial manufacturing lines. Furthermore, while initial studies suggest promising total dose performance [McMorrow *et al.*, 1994, p.2055], with displacement damage from fast neutrons the primary exception [Papastamatiou *et al.*, 1997, p.364], troubling SEU susceptibility is motivating a wave of active research into measurement techniques [McMorrow *et al.*, 2007] and models [McMorrow *et al.*, 1994] aimed at better understanding charge collection in these multilayer structures and eventually extending their application to deep space astronomy beyond the LNAs presently leveraged by terrestrial receivers [Pospieszalski, 2005].

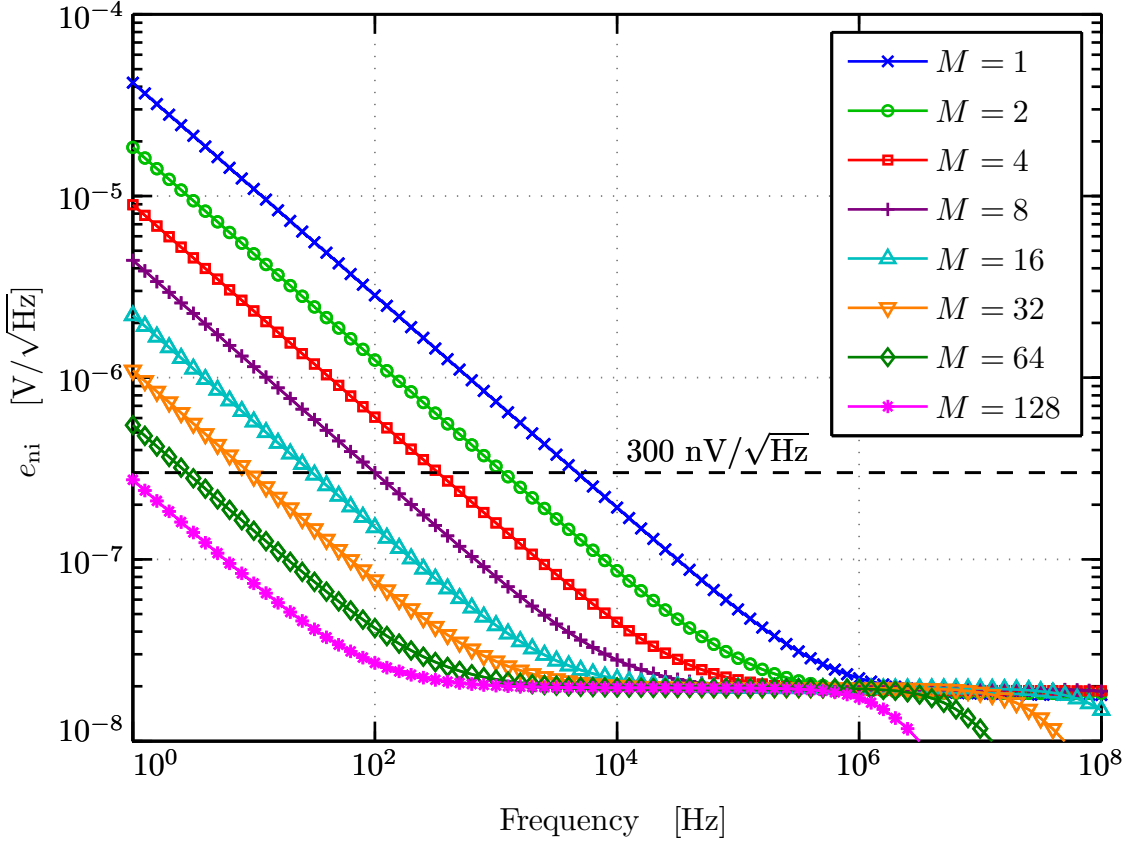


Figure 3.11: Simulated flicker noise of pMOSFETs in target technology, plotting the square-root of (3.31) for a family of devices whose linear dimensions are scaled by  $M$  from a base size of 0.5/0.25 ( $M=1$ ) demonstrates  $f_K \simeq 1$  MHz.

are blocks that account for the array of stray and coupling impedances encountered in a deployable system. Their interpretation in Section 3.1.4.1 informs the general matching strategy explicated in Section 3.1.4.2 as well as its application to the LNA in this work as per Section 3.1.4.3.

#### 3.1.4.1 Antenna-LNA Interface

The base impedances,  $R_{\text{base}}$  and  $C_{\text{base}}$  of Figure 3.12 represent current paths between the antenna itself and the spacecraft housing, with the latter particularly important, as the proximity of a large metal structure can generate sufficient capacitance to distort the symmetric dipole radiation pattern. Similarly, the

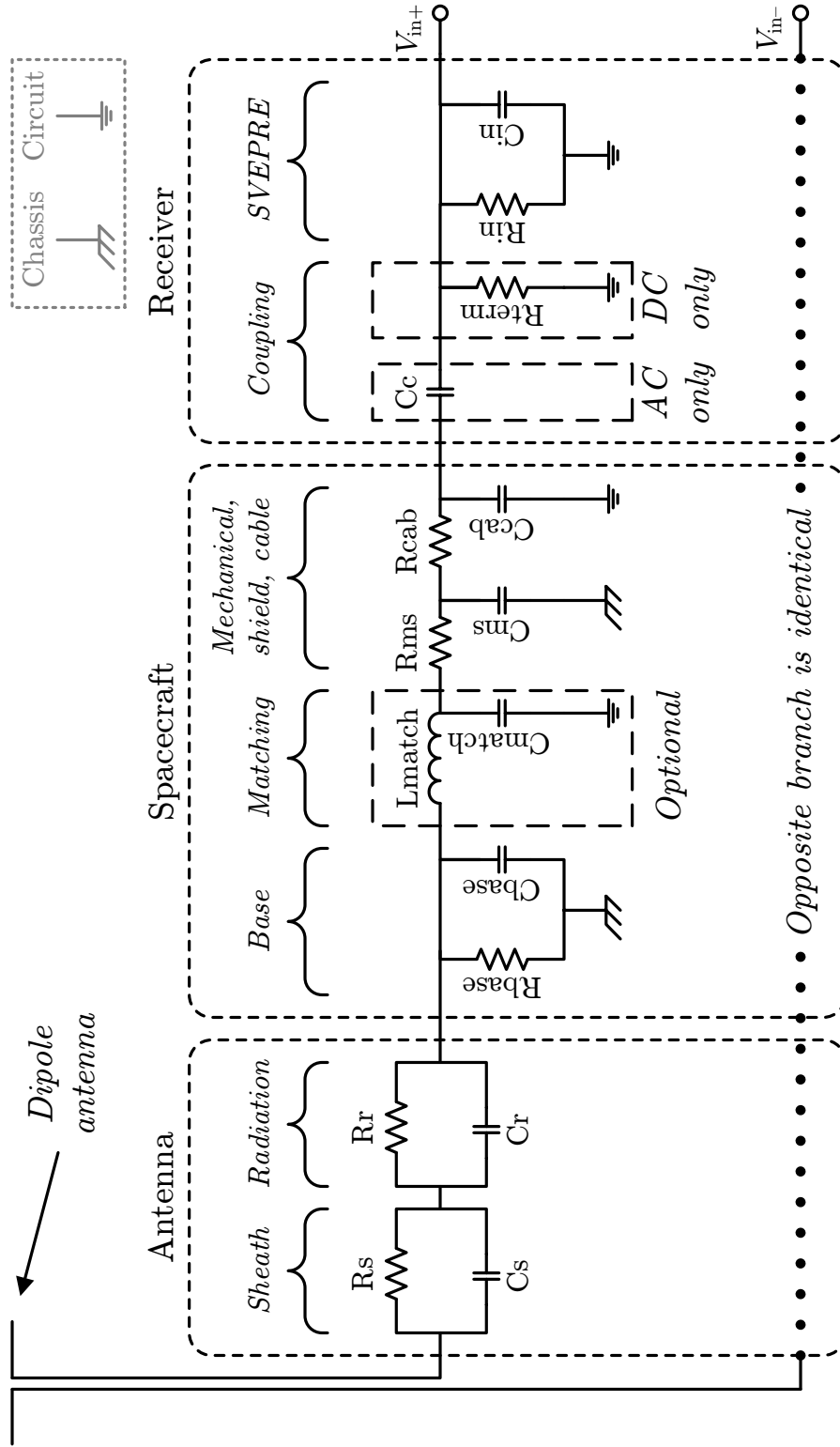


Figure 3.12: Single-sided impedance model for antenna-LNA coupling. The impedance of each component depicted is half that of the differential value with corresponding moniker (e.g., the value of  $R_{in}$  is  $R_{in}/2$ ). For noise analysis, the chassis and circuit grounds are treated separately, though they are considered equivalent for the impedance calculations in this section.

mechanical structures that support the antenna and its cabling (e.g., the mounting booms, stacers, cable harness, and overshield) contribute impedances subsumed by the lumped elements  $R_{ms}$  and  $C_{ms}$ , while the coaxial cable connecting the antenna back to the main electronics unit also exhibits distributed resistance and capacitance lumped into  $R_{cab}$  and  $C_{cab}$ . In the absence of matching circuitry (discussed momentarily), all stray contributions save  $R_{base}$  can be aggregated into a single resistor and capacitor

$$R_{stray} = R_{ms} + R_{cab} \quad (3.33)$$

$$C_{stray} = C_{base} + C_{ms} + C_{cab} \quad (3.34)$$

as depicted in the simplified model of Figure 3.13(a). For the target receiver, the impedances at either end of this chain are sufficiently large that it can be assumed  $C_{coup} \rightarrow \infty$  and  $R_{stray} \rightarrow 0$ , enabling reduction to the fully differential representation of Figure 3.13(b) with its associated definitions.

Opposite antenna coupling mechanisms distinguish DC and wave receivers, with the latter benefiting from an AC coupling capacitor ( $C_c$ ) that both isolates the electronics from the large (kilovolt) floating potentials to which the spacecraft body can charge [Tribble, 2003, p.129–143] and the spin-induced modulation of low-frequency fields (cf. Footnote 42 of Chapter 1). Although more prevalent in DC receivers, both classes may use a large ( $> 10 \text{ M}\Omega$ ) termination resistor,  $R_{term}$ , to bleed off excess charge accumulated on the antenna and provide a measure of protection against transient electrostatic discharge (ESD). For the target receiver, both elements are presumed to be present but sufficiently large as to be neglected relative to other contributors over the signal bandwidth.

Finally, the optional matching network introduced by  $L_{match}$  and  $C_{match}$  is intended to optimize power transfer from the antenna to the LNA by satisfying the canonical conjugate matching relation [Lee, 1998, p.94]. However, as discussed in the next section, the conjugate matching ubiquitous in narrowband systems is of limited utility for plasma wave receivers.

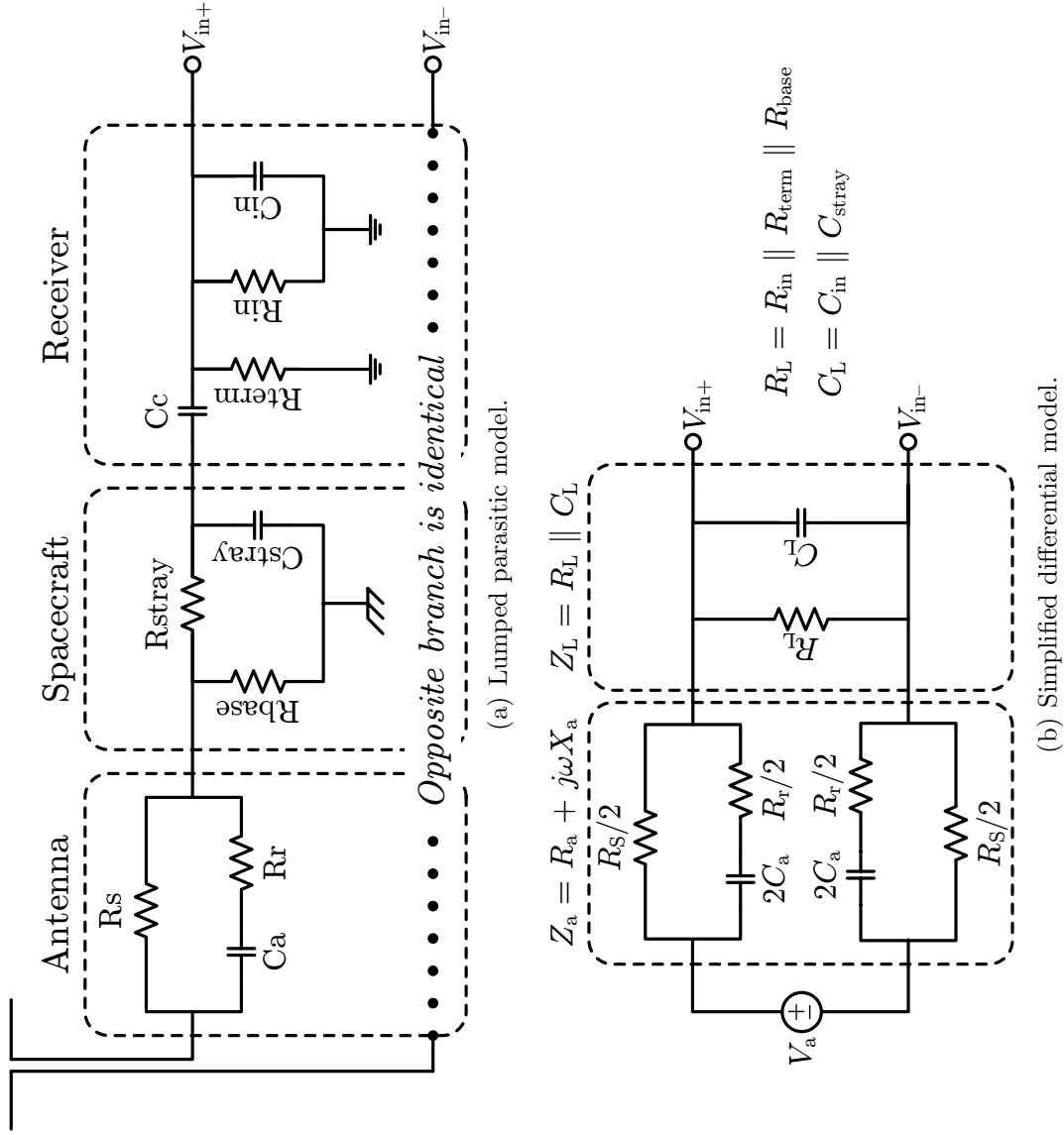


Figure 3.13: Impedance models attained through reduction of Figure 3.12. First (a) omitting matching and lumping stray parasitics, then (b) neglecting  $C_c$  and  $R_{\text{stray}}$  relative to the small  $C_a$  ( $C_L$ ) and large  $R_a$  ( $R_L$ ) of the source (load), yields a simplified differential model of the antenna-LNA coupling.

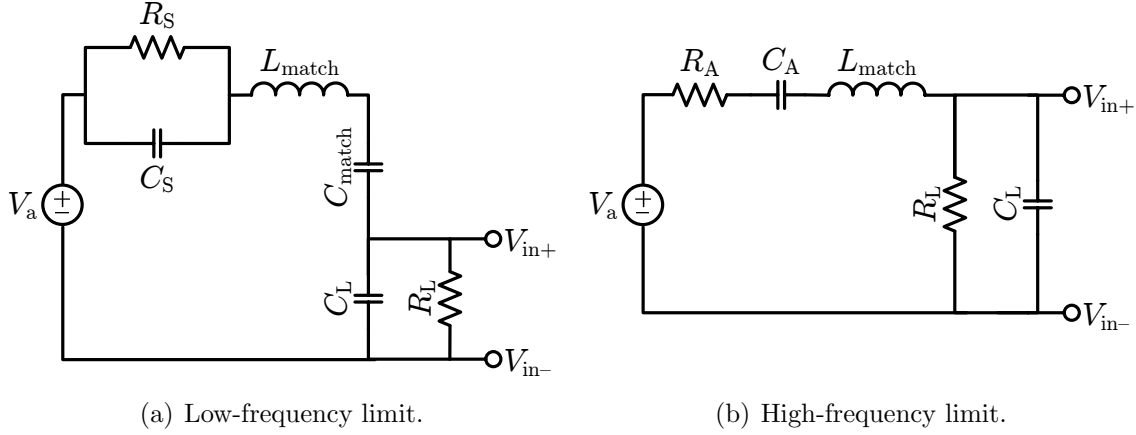


Figure 3.14: Antenna impedance matching at the frequency range extremes. Networks for conjugate matching of  $Z_a$  in (a) the low-frequency limit, when  $Z_r$  goes to zero, and (b) the high-frequency limit, when it behaves as though in free space, can only succeed over a narrow range of frequencies and/or plasma conditions.

### 3.1.4.2 Ideal Voltmeter Operation

Although theoretically desirable, as a practical matter conjugate matching networks are relegated to either discretely tunable adaptive implementations [Reinisch et al., 2000, p.334] or rare instances when plasma parameters vary little over the orbital track. To appreciate these constraints, consider the extremes of the antenna impedance derived in Section D.1.3 and represented by the  $Z_a \simeq Z_S$  and  $Z_a \simeq Z_A$  elements in the low- and high-frequency regimes depicted in Figure 3.14(a) and Figure 3.14(b), respectively.

When the sheath is dominant (cf. Figure 3.14(a)), the antenna contains both a large resistive and moderate capacitive component which can be matched with the tapped-capacitor network composed of  $L_{\text{match}}$  and  $C_{\text{match}}$ , but only over a narrow bandwidth at one frequency [Krauss et al., 1980, p.47]. Even if successful in resonating out  $C_S$ , such a network cannot transform  $R_{\text{in}}$  such that it equals  $R_S$  at all times, since the latter is highly sensitivity to plasma conditions and can vary by orders of magnitude depending on the orbit [Gurnett, 1998, p.127]. Similarly, though it is not difficult to design a series inductance to resonate with the antenna when approaches its free-space reactance well above  $f_p$  [Reinisch et al., 2000, p.334], as in Figure 3.14(b),

any corresponding matching of  $R_L$  to  $R_A$ , which falls off as  $1/f^3$ , is ephemeral at best. Thus, while acknowledging conjugate matching as the ideal, most electric-field wave receivers opt instead to simply maximize  $Z_{in}$  so as optimize voltage transfer by emulating the operation of an ideal voltmeter [*Gurnett, 1998*, p.125].

Pursuing this ideal voltmeter condition, the target receiver omits the matching network and, with reference to the resulting, simplified impedance chain of Figure 3.13(b), demands sufficiently large  $Z_{in}$  of SVEPRE that at all frequencies of interest  $|Z_L(\omega)| \gg |Z_a(\omega)|$ . Consider again the extremes of  $Z_a$  in Figure 3.14. In the presence of the sheath,  $Z_S$  alternates from being primarily resistive below its transition frequency ( $\omega_S = 1/R_S C_S$ ) to primarily capacitive above it. Forcing both types of voltage dividers

$$\frac{V_{in}(\omega)}{V_a(\omega)} = \begin{cases} \frac{R_L}{R_L + R_S} & , \text{ for } \omega < \omega_S \\ \frac{C_S}{C_L + C_S} & , \text{ for } \omega > \omega_S \end{cases} \quad (3.35)$$

toward unity requires that  $R_L \gg R_S$  and  $C_L \ll C_S$ . Similarly, the capacitive divider formed well above the plasma frequency as

$$\frac{V_{in}(\omega)}{V_a(\omega)} = \frac{C_A}{C_L + C_A} \quad , \quad \text{for } \omega \gg \omega_{pe} \quad (3.36)$$

dictates that  $C_L \ll C_A$ , which is somewhat more stringent than the preceding condition on  $C_L$  (cf. Section D.1.3.2) for most altitudes [*Gurnett, 1998*, p.125].

### 3.1.4.3 LNA Input Impedance

In order to satisfy these conditions on  $Z_L$ , the mechanical design of the receiver should minimize the parasitic contributions in Figure 3.13(a), particularly  $C_{stray}$ . But, the implication most germane to the design of the LNA is that its input resistance(capacitance) be as large(small) as possible.

First, consider the range of sheath resistances encountered by previous receivers

(cf. Table B.3),<sup>54</sup> which range approximately from 1 M $\Omega$ –10 G $\Omega$ . Although it may strictly violate the ideal voltmeter condition of (3.35) for the lowest densities observed beyond the plasmopause ( $1\text{--}10^3\text{ cm}^{-3}$  [Gurnett, 1998, p.128]), specifying  $R_{\text{in}}$  for the LNA near the upper end of this range, at 1 G $\Omega$ : is consistent with the generally accepted range for dipoles [Gurnett, 1998, p.128], including all  $R_{\text{L}}$  values reported in Table B.3;<sup>55</sup> ensures  $R_{\text{in}}$  exceeds the reported values of  $R_{\text{term}}$  for wave receivers, which range from 100 M $\Omega$  (for the RAR preamplifiers of Ulysses [Stone et al., 1992, p.294]) to 400 M $\Omega$  (for OGO 5 [Crook et al., 1969, p.124]), and therefore is not the limiting component in determining  $R_{\text{L}}$  for terminated configurations; and maintains more than a three-(two-) order of magnitude ratio with the simulated  $R_{\text{S}}=167\text{ k}\Omega(2.98\text{ M}\Omega)$  of the nominal 20-m dipole simulated in Figure 3.9(a)(Figure 3.9(b)) at  $L=2(L=4)$ , resulting in absolute voltage measurement error less than 0.02%(0.3%).

A precise specification for  $C_{\text{in}}$  is of far less necessity, since its role is always subservient to that of  $C_{\text{stray}}$  in determining  $C_{\text{L}}$  according to Figure 3.13(b). Specifically, with reference to the contributors in (3.34), the LNA input is shunted by:  $C_{\text{cab}}$  ranging from 13 pF (for STEREO [Bale et al., 2008, p.541]) to 102 pF (for OGO 5 [Crook et al., 1969, p.124]);  $C_{\text{ms}}$  on the order of 51 pF (for the Cassini  $E_{\text{v}}$  antenna [Gurnett et al., 2004, p.442]); and  $C_{\text{base}}$  of about 32 pF (for STEREO [Bale et al., 2008, p.541]). Consequently, for a total  $C_{\text{stray}}$  between 45 pF (for STEREO [Bale et al., 2008, p.541]) and 116 pF (for the Cassini  $E_{\text{u}}$  antenna [Gurnett et al., 2004, p.442–443]) the LNA input capacitance can range from 7.5 pF (for THEMIS [Bonnell et al., 2008, p.312]) to 34 pF (for the Cassini  $E_{\text{u}}$  antenna [Gurnett et al., 2004, p.442–443]) without drastically altering  $C_{\text{L}}$ .<sup>56</sup>

<sup>54</sup>Although the  $R_{\text{S}}$  values in Table B.3 are for double-probe antennas, dipoles of similar length possess even lower values (cf. Section D.1.1.3), as evidenced by the 750 k $\Omega$ –2 M $\Omega$  sheath resistances reported for dipoles aboard STEREO [Bale et al., 2008, p.532] and Aureol 3 [Berthelier et al., 1982, p.648]. Thus, designing for  $R_{\text{S}}$  of the double-sphere sheath is undoubtedly conservative.

<sup>55</sup>Dipole load resistances need not be as accurate as those of their double-sphere counterparts whose ability to extract plasma parameters is critically dependent upon the absolute accuracy of their DC field measurements.

<sup>56</sup>Whether the increase in  $C_{\text{L}}$  due to  $C_{\text{in}}$  is deemed acceptable depends upon both  $C_{\text{A}}$  and  $C_{\text{c}}$ . When dictated by the former, as has been assumed thus far, these  $C_{\text{in}}$  values can only be tolerated, given the cited  $C_{\text{stray}}$ , when  $C_{\text{A}}$  is much larger than that of the nominal antenna, as for IMAGE where it reaches 533 pF [Reinisch et al., 2000, p.333], or when the ideal voltmeter condition can be violated, as for Cassini where the ratio of (3.36) is  $\sim \frac{1}{2}$ . Likewise,  $C_{\text{c}}$ , which has been assumed



However, since the nominal dipole presents just  $C_A = 60$  pF and since designs such as FAST have demonstrated that driving the antenna shield to the probe potential can minimize  $C_{\text{stray}}$  and permit  $C_L$  to benefit from  $C_{\text{in}}$  as low as 1 pF [Ergun *et al.*, 2001, p.74–75], this is the value chosen as the specification for the SVEPRE LNA.<sup>57</sup>

### 3.1.5 Specification Summary

Table 3.2 updates the SVEPRE scientific- and satellite-driven specifications annotated on Figure 1.22 to include those derived from the radiation requirements of Chapter 2 and the system-to-component flow-down presented in this chapter.

For a nominal 20-m dipole antenna and digital back-end of sufficient acquisition rate ( $\Upsilon_a$ ), the front-end is capable of processing signals from 100 Hz to 1 MHz at the nominal LNA  $G_p$  and AAF  $f_p$ . However, both parameters are programmable to afford compatibility with satellites offering variegated antenna lengths, power constraints, and data-handling resources. To permit the discrimination of simultaneous plasma wave phenomena whose disparate spectral densities stretch from bow shock waves to the MDS, both the LNA and AAF must suppress harmonic distortion by 90 dB and  $S_{\text{in}}(f)$  of the former must not exceed  $300 \text{ nV}/\sqrt{\text{Hz}}$ ,<sup>58</sup> even down to 100 Hz, where it is  $1/f$ -noise limited. Ideal voltmeter operation requires that the front-end input impedance far exceed that of the dipole antenna over the measurement bandwidth, which translates to a differential LNA input impedance of  $1 \text{ G}\Omega$  in parallel with 1 pF.<sup>59</sup> Finally, all the aforementioned specifications should be met up to at least

---

effectively infinite but can be chosen as low as 22 pF (on Geotail, where it introduces a nearly  $-6$  dB loss due the capacitive divider with  $C_L$  [Matsumoto *et al.*, 1994, p.64]), is quite large for the instruments whose  $C_L$  are cited above, ranging from 100 pF (for STEREO [Bale *et al.*, 2008, p.533]) to  $0.1 \text{ }\mu\text{F}$  (for OGO5 [Crook *et al.*, 1969, p.124]).

<sup>57</sup>Indeed, being the lowest reported value in the literature,  $C_L = 1$  pF represents the state-of-the-art.

<sup>58</sup>Recall that the mitigation of downstream noise via the Friis equation (cf. Footnote 1) dictates that the AAF noise power is attenuated by 14 dB at the nominal gain, rendering the noise of the LNA dominant. For  $G_p = 0$  dB, this is no longer the case; but, the derivation in Section 3.1.3.1 presumes a corresponding increase in the antenna length under such conditions. Therefore, as long as  $e_r$  is dominated by the LNA  $S_{\text{in}}(f)$  at the nominal gain setting, the noise floor at all gain settings is low enough to resolve the MDS.

<sup>59</sup>Port impedances for SVEPRE are always specified as differential, despite the factor-of-2 ambiguity for those from which their specifications are derived in Section 3.1.4.3 (cf. Footnote 7

Property	Symbol	Limit	Specification		Units
			LNA	AAF	
Science requirements					
Passband					
Voltage gain	$G_p$		0–24	0	dB
Lower edge		at most	100	100	Hz
Upper edge	$f_p$	at least	4		MHz
	$f_{pa}$	Mode A		30	kHz
	$f_{pb}$	Mode B		180	kHz
	$f_{pc}$	Mode C		1080	kHz
Linearity					
SFDR (1 Hz/bin)		at least		90	dB
Input range					
Differential signal	$V_{in}$	up to	1	1	$V_{PP}$
Input-referred noise	$e_n$	at most	300	1580	$nV/\sqrt{Hz}$
Satellite requirements					
Input impedance					
Resistive	$R_{in}$	at least	1	n/a	$G\Omega$
Reactive	$C_{in}$	at most	1	n/a	pF
Power dissipation					
Static + dynamic	$P_{tot}$	at most		50	mW
Radiation					
Total dose		at least		100	krad(Si)
No latchup		up to		100	MeV-cm <sup>2</sup> /mg

Table 3.2: Summary of target specifications for SVEPRE front-end.

100 krad(Si) total dose and the part should be free of latchup for equivalent LETs in the range of 100 MeV-cm<sup>2</sup>/mg.

## 3.2 System-Level Strategies

In light of the performance targets in Table 3.2, this section reviews a pair of high-level approaches whose ramifications permeate the circuit designs of Chapter 4 and Chapter 5. The first, presented in Section 3.2.1 is to employ a commercial, SiGe BiCMOS manufacturing process which offers the desired array of transistors at the expense of their being intrinsically rad-hard. The second, discussed in Section 3.2.2, is the liberal application of local, active, non-linear feedback within each component in order to both attain and maintain the desired high-precision operation.

### 3.2.1 Manufacturing Process

As demonstrated in Section 3.1.3.3, design of an LNA with the requisite low-frequency noise characteristics is exceedingly difficult using only pMOSFETs, on account of their  $1/f$  noise.<sup>60</sup> The most expedient route to obtaining junction-based transistors, whose (primarily) bulk current flow is less susceptible to surface effects, is through the use of a BiCMOS technology (cf. Footnote 53), since SiGe HBTs are prevalent in modern RF design [Gray *et al.*, 2001, p.152].

As explained in Section 2.3.2.2, a hardened process for manufacturing such devices with intrinsic radiation tolerance is attended by a series of pragmatic drawbacks, many of which can be addressed by selecting a commercial manufacturing process and applying RHBD principles to mitigate its radiation vulnerabilities. The technology in this work is manufactured in BiCMOS8—a commercial 0.25- $\mu$ m SiGe process graciously provided by National Semiconductor Corporation. Over the course of the research, versions of the front-end ASIC were fabricated in successively more

---

of Appendix D).

<sup>60</sup>To say nothing of the fact that without employing complementary nMOS transistors, whose flicker noise is even more pronounced, the space of possible amplifier topologies is small indeed.

sophisticated variants of this process as they became available.<sup>61</sup>

For example, SVEPRE-1 was built in BiCMOS8iED, which introduces:

- introduces dual gate oxide, high-voltage (3.3 V) MOSFETs and varactors
- metal-insulator-metal (MIM) capacitors with high-K dielectrics
- unsalicided base polysilicon resistors

SVEPRE-3 utilized BiCMOS8B+, which:

- scales the npn base width ( $W_b$ ) to match the minimum CMOS gate length ( $L_m = 0.25 \mu\text{m}$ )
- spawns a class of high-voltage (3.3 V) npn devices
- offers highly linear metal comb capacitors
- re-implements the unsalicided polysilicon resistor options

For completeness, an inventory documenting the manufacturing of each of the SVEPRE-versions (denoted with integer revision numbers) and their precursors, including the target process variant for each, is tabulated in Table 3.3.

In all cases, BiCMOS8 begins with a non-epitaxial p-type Si wafer, constructing CMOS devices that correspond to those of a single-well, 1P5M, 0.25- $\mu\text{m}$  technology with shallow oxide trench isolation, and npn SiGe HBTs that are base doped using a sacrificial emitter and isolated with deep polysilicon trenches. However, because npn transistors are inherently faster than their pnp counterparts by at least a factor of 3, since  $\tau_n < \tau_p$  [*Hastings*, 2006, p.351], and because SiGe processes are traditionally optimized for RF performance (cf. Footnote 67 of Chapter 2), the bipolar side of BiCMOS8 is non-complementary, offering only an inferior substrate pnp. Rather than

---

<sup>61</sup>An even earlier version of this process, BiCMOS8iE, was provided to support preliminary design and radiation evaluation. Although it produced the MK832A test chip whose results are presented in Section 2.1.1 (cf. Footnote 15), no versions of SVEPRE were fabricated in this issuance. The upgrades that accompanied BiCMOS8iED (noted above) did not pertain directly to features employed by this design; it is believed that processing steps surrounding the construction of the npn and low-voltage CMOS devices were unaffected.

Identification		Submission		Fabrication		
Part ID	Die ID	Released	Contents	Completed	BiCMOS <sup>a</sup> Shuttle run	Lot-Wafer# Qty.
SVELNA-1	PARXAV1	10/02/03	LNA	01/16/04	i, R1.2 Callisto 8	V00422FF-5 20
SVEAAF-1	PARXAV2	12/04/03	AAF	06/24/04	i, R1.2 Callisto 9	V00442MT-25 20
SVEPRE-0	PARXAV3	04/09/04	LNA/AAF	09/15/04	iED, R0.14 Callisto 11	469732425-3 20
SVEPRE-1	PARXAV5	08/12/04	LNA/AAF	01/25/05	iED, R0.15 Callisto 13	V00516KQ-10 20
SVETST-1	BO69315	03/08/06	Breakout stage	06/20/06	B+, R0.25 Europa 3	V00643ME-11 56 V00643ME-13 56
SVETST-2	WIPERAV1	03/08/06	LNA/AAF migration	06/20/06	B+, R0.25 Europa 3	V00643ME-11 56 V00643ME-13 55
SVEPRE-2	WIPERAV2	03/08/06	LNA/AAF	06/20/06	B+, R0.25 Europa 3	V00643ME-11 55 V00643ME-13 56
SVEPRE-3	WIPERAV3	09/08/06	LNA/AAF	12/20/06	B+, R1.0 Europa 5	V00718NFG-20 60
SVETST-3	BO73416	01/26/07	Breakout	04/12/07	B+, R1.0 Europa 6	V00737FCD-4 94
SVEPRE-4	WIPERAV4	01/26/07	LNA/AAF	04/12/07	B+, R1.0 Europa 6	V00737FCD-4 47

<sup>a</sup> Variants of BiCMOS8 process are identified in collateral as [*version, release*].

Table 3.3: Catalog of tapeouts associated with SVEPRE.

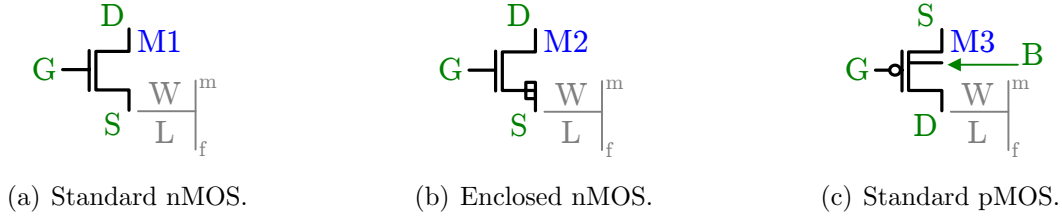


Figure 3.15: MOSFET schematic symbols. Body terminal is only explicit for standard pMOS since each is fabricated in its own tub; lacking p-type tubs, all nMOSFETs share the common substrate as their body. See Section 5.6.2.1 for a description of the enclosed-terminal layout variation.

secure a fully complementary bipolar technology, it is advantageous to retain access to the CMOS devices because they are beneficial in certain sections of the design and, moreover, support the eventual integration of the receiver back-end, specifically the ADC of [Wang, 2009] shown in Figure 1.22, as part of a single-chip solution. Instead, the lack of suitable pnp alternatives [Hastings, 2006, p.90] is ameliorated through the painstaking and frequently novel incorporation of substitutes from amongst the available devices reviewed forthwith.

### 3.2.1.1 CMOS

This design only uses the low-voltage class of CMOS transistors, which are intended to operate from a +2.5 V supply (maximum +2.75 V). The lack of twin tubs allows the nMOS devices to be symbolized as in Figure 3.15(a): the absence of a body contact is unambiguous because all such transistors share the bulk substrate as their common body. It is accepted practice to use an enclosed-geometry nMOS layout when the radiation-induced leakage described in Section 2.1.1.3 is of concern. The symbol for this nMOS variation, which is described in greater detail in Section 5.6.2.1, introduces a box on the enclosed terminal, as shown in Figure 3.15(b).<sup>62</sup>

In contrast, pMOS devices, which are not subject to  $I_{\text{fox}}$  enhancement, only assume

<sup>62</sup>For the enclosed terminal nMOSFET, the annotated width and length values describe the drawn dimensions. As discussed in Section 5.6.2.1, these differ from the effective  $W$  and  $L$  used in modeling device behavior as a consequence of current paths at the corners of the nonstandard geometry [Nowlin et al., 2005].

a single layout. However, as each is fabricated in its own n-type tub, they require individual body contacts, as in the symbol of Figure 3.15(c). For all MOS transistors, the sizing notation of Figure 3.15 is employed in subsequent schematics: the ratio to the left of the vertical bar is that of gate width,  $W$ , (in  $\mu\text{m}$ ) to gate length,  $L$  (in  $\mu\text{m}$ ), while the unitless superscript(subscript) to the right is the number of separate devices(fingers) with these dimensions that are connected in parallel to achieve the final device size.

### 3.2.1.2 Vertical npn

This design only uses the low-voltage class of npn transistors, for which the presence of SiC results in a breakdown voltage ( $V_{\text{ceo}}$ ) of +3 V. Unlike the BSIM3v3 MOS transistor models, which are scalable over a continuous range of gate widths ( $0.58\ \mu\text{m}$ – $20\ \mu\text{m}$ ) and lengths ( $0.24\ \mu\text{m}$ – $20\ \mu\text{m}$ ), vertical bipolar inter-company (VBIC) models are only provided for a finite set of discrete vnpn sizes. Since the members of this set fluctuate unpredictably with each release of a new process variant, the design of SVEPRE conservatively restrains itself to only those npn sizes identified in Table 3.4. Out of the dozen (or so) published models, these offer a compromise between performance (specifically, minimal injection-level effects and high peak  $\beta$ ) and availability (being among the most stable between process releases).

The  $\beta$  peak of the smaller devices, NL1d25x0d6, occurs at a lower  $V_{\text{BE}}$ , corresponding to the  $L_{\text{e}}=0.6\ \mu\text{m}$  curve of Figure 3.6 and rendering it the appropriate geometry for low-bias transistors. The larger size, NL2d25x5d0, offers better current handling capacity—not only does its gain peak at higher  $V_{\text{BE}}$ , but with two base stripes, it is less susceptible to high-level injection effects such as emitter crowding and collector current spreading [*Laker and Sansen, 1994*, p.130–132]. In addition, symmetric base current paths halve both the extrinsic and intrinsic components of  $R_{\text{b}}$ , with the latter eliminated all together at high current densities [*Laker and Sansen, 1994*, p.124]. The corresponding schematic symbols for each device are shown in Figure 3.16.

Property	Symbol	NL1d25x0d6	NL2d25x5d0
Device type			
Style	nnp	Vertical	Vertical
Breakdown	$V_{\text{ceo}}$	+3 V	+3 V
Peak gain			
Current gain	$\beta_{\text{DC}}$	307	329
Bias current	$I_{\text{C}}$	1.9 $\mu\text{A}$	52 $\mu\text{A}$
Base resistance			
Intrinsic	$R_{\text{b}}$	485 $\Omega$	100 $\Omega$
Extrinsic	$R_{\text{B}}$	95 $\Omega$	25 $\Omega$
Base geometry			
Contacts		1	2
Stripes/island		1	2
Emitter geometry			
Stripes/island		1	1
Width	$W_{\text{e}}$	0.25 $\mu\text{m}$	0.25 $\mu\text{m}$
Length	$L_{\text{e}}$	0.6 $\mu\text{m}$	5.0 $\mu\text{m}$
Area	$A_{\text{e}}$	0.15 $\mu\text{m}^2$	1.25 $\mu\text{m}^2$
Island layout		C-E-B	C-B-E-B

Table 3.4: Comparison of NL1d25x0d6 and NL2d5x5d0 BJTs from BiCMOS8. Only these npn devices are used in the SVEPRE design.

### 3.2.1.3 Substrate npn

The substrate npn offered by BiCMOS technologies in general, and BiCMOS8 in particular, is known to exhibit markedly worse performance than its vertical npn counterpart [Johnston *et al.*, 2000, p.2628] and to be of limited utility to designers [Laker and Sansen, 1994, p.139], as summarized by the comparison in Table 3.2.1.3. It does offer a few advantages over its lateral counterpart (cf. Section 3.2.1.4), including: vertical current flow, which supports a larger emitter cross-sectional area [Gray *et al.*, 2001, p.112] and less  $1/f$  noise; and low base doping to offset its larger  $W_{\text{b}}$ , [Laker and Sansen, 1994, p.134]. However, these are largely outweighed by dominance of recombination (primarily  $\beta_{\text{br}}$ ) over emitter injection ( $\beta_{\text{ee}}$ ) in determining the base



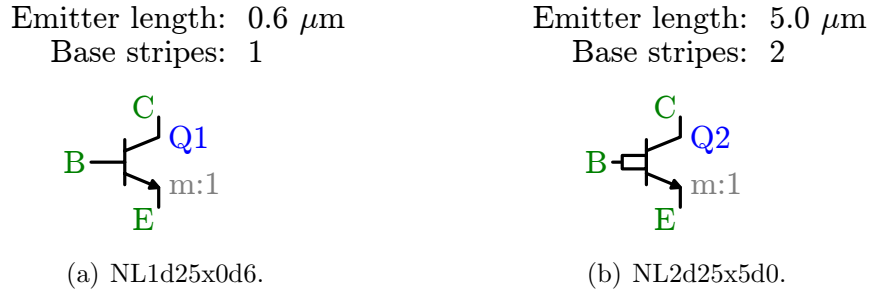


Figure 3.16: npn BJT schematic symbols. See Table 3.4 for a complete comparison of device properties for the two sizes shown.

current. The short  $\tau_p$  of this recombination, though somewhat mitigated by low base doping, is problematic since the wider base implies longer transit times (and lower  $f_T$ ). Plus, the low base doping increases  $R_b$ . The upshot is a slower device with lower gain and a large area penalty—in BiCMOS8, the lone substrate pnp model yields a peak  $\beta < 4$  for an emitter area of 2  $\mu\text{m}$  by 2  $\mu\text{m}$ .<sup>63</sup>

But, most troubling for the design of LNA and AAF is the lack of versatility [Hastings, 2006, p.89]. Since its collector is formed by the common Si bulk, a substrate pnp can only be used as a buffer in emitter follower configurations [Gray *et al.*, 2001; Laker and Sansen, 1994, p.139,p.112]. Without the ability to provide amplification, or to serve as a load for an npn configuration, not to mention its susceptibility to  $\beta$ -degradation under TID exposure (cf. Figure 2.15), the substrate pnp is used sparingly in this work.

#### 3.2.1.4 Lateral pnp

Although BiCMOS8 offers no lateral counterpart to the substrate pnp, such devices are commonly available in CMOS or BiCMOS technologies, as they offer designers more flexibility and can achieve respectable gains even when formed from only MOS layers [Hastings, 2006, p.344]. However, they often perform even more poorly than vertical pnps because, in addition to the same transport inefficiency (i.e., recombination) that dominates their  $\beta$ , they suffer from both surface recombination

<sup>63</sup>When necessary, the standard pnp schematic symbol unambiguously represents this substrate pnp, as it is the only available variant.

Property	Symbol	Vertical npn	Lateral pnp	Substrate pnp	Units
Peak gain					
Current gain	$\beta_{DC}$	300	50	10	
Bias current	$I_C$	5–5000	1–20	1–50	$\mu A$
Small-signal resistance					
Base	$r_b$	400	200	100	$\Omega$
Collector <sup>a</sup>	$r_c$	100	20	50	$\Omega$
Performance limits					
Unity-gain frequency	$f_T$	> 50	< 0.5	< 0.5	GHz
Early voltage	$V_A$	120	80	100	V
Collector connectivity		Available	Available	Grounded	

<sup>a</sup> Collector resistance in saturation, where it modulates C-E conductivity, not forward-active.

Table 3.5: Select performance comparison of bipolar geometries. Each column describes a composite device synthesized from values for typical transistors of that class whose emitter areas range from 2–16  $\mu m^2$  [Gray *et al.*, 2001; Hastings, 2006, p.106–115,p.123–125].

and the presence of an always-on vertical parasitic pnp [Laker and Sansen, 1994, p.137]. Only in MOS technologies featuring narrow feature sizes, thin epitaxial layers, deep source/drain diffusions, and retrograde wells (whose peak doping concentration is near the bottom rather than the surface [Hastings, 2006, p.177]) can the shunt current of the latter be negated, achieving values of  $\beta < 10$  [Laker and Sansen, 1994, p.138].

However, lateral pnp performance can be substantially improved when leveraging bipolar layers, whose deeper junctions offer a larger lateral cross-section and whose  $n^+$  buried layer creates a built-in field that repels minority carriers back to the surface where they are collected by the lateral device, spoiling the gain of its parasitic vertical pnp counterpart [Hastings, 2006, p.316].

Even higher gains are possible by combining MOS and BJT elements into a variation of the standard lateral pnp topology known as gate-controlled lateral pnp (GCLPNP) [Vittoz, 1983]. Motivated by this potential, as well as evidence

of inherent radiation-hardness, a collaboration between engineers at Stanford and National Semiconductor Corporation in the early stages of this research produced a prototype lateral pnp (LPNP), as described in Appendix E, whose layout is illustrated in Figure 3.17.<sup>64</sup> Unfortunately, gains of the early prototypes (cf. Section E.3.2) were not promising enough for National to pursue the inclusion of a GCLPNP as a viable process option, leaving only the aforementioned and limited ( $\beta > 10$ ) substrate pnp.

### 3.2.2 Feedback

Although the application of negative feedback in achieving the goals of Section 3.1 is by no means revolutionary in concept, its role in this work is sufficiently crucial and its manifestation non-standard enough as to invite conceptual treatment at the system level in order to frame subsequent circuit-level discussions. After all, for an active plant whose forward path gain is linear and can be represented in the Laplace domain by  $a(s)$ , as in the so-labeled block of Figure 3.18, the only intrinsic value of encircling it with a negative feedback loop through a linear element of gain  $f(s)$  is desensitivity of the closed-loop gain,  $G(s)$  [Lee, 1998, p.391], as represented by the elementary application of Mason’s gain rule [Mason, 1953]:

$$G(s) = \frac{V_{\text{out}}(s)}{V_{\text{in}}(s)} = \frac{a(s)}{1 + a(s)f(s)} \quad (3.37)$$

The well-known expression of (3.37) indicates that circumscribing the active forward path with a negative feedback loop of sufficiently large loop gain  $L(s) = a(s)f(s) \gg 1$  desensitizes  $G(s)$  to variations in the forward path because  $a(s)$  drops out in the approximation:

$$G(s) = \frac{a(s)}{1 + L(s)} \simeq \frac{1}{f(s)} \quad (3.38)$$

In the absence of the desensitivity embodied by (3.38),  $G(s)$  would be subject to the

---

<sup>64</sup>In particular, the prodigious contributions of engineers Monir El-Diwany and James Shibley with National Semiconductor Corporation are gratefully acknowledged.



Figure 3.17: Cross-section of second-generation prototype GCLPNP layout, corresponding to version #2B of Figure E.13(b). See Section E.3.1 for construction details and Section E.3.2 for measured performance.

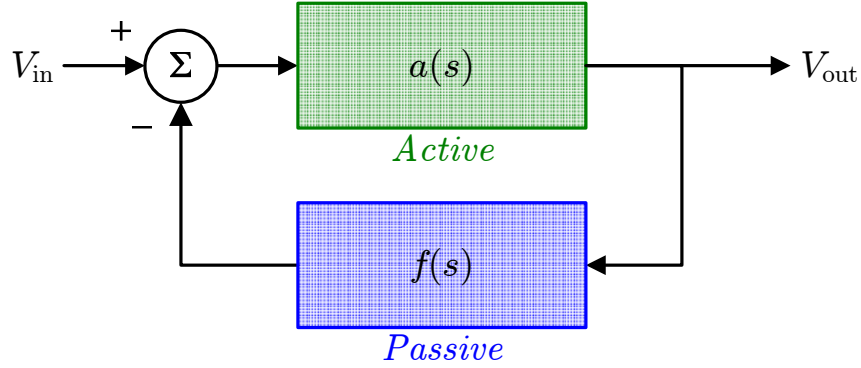


Figure 3.18: Block diagram of canonical negative feedback system, employing the convention that  $f(s)$  is positive, so the sign of  $L(s)$  is formally embedded into nodal subtraction with the indicated polarities.

nonlinearities and radiation susceptibilities of the transistors that comprise  $a(s)$ ; so, the intrinsic benefits of feedback directly address the corresponding specifications of Table 3.2; namely, SFDR and total-dose hardness.

However, when leveraging feedback to achieve the remaining component specifications of Section 3.1, this fundamental behavior is necessary, not sufficient—implementation is just as crucial. Specifically, the remainder of this section explains how the design of SVEPRE manages three trade-offs associated with more subtle complications of feedback realizations.

### 3.2.2.1 Global versus Local

First, consider the LNA implementation. To obtain the desired desensitivity, it is tempting to simply replace the  $a(s)$  block of Figure 3.18 with the LNA itself and employ a switched resistor network to provide variable-gain feedback that exhibits the assumed linearity of  $f(s)$ . Depicted in Figure 3.19(a) for the simple case of two gain steps corresponding to feedback resistors  $R_1$  and  $R_2$ , for which  $f(s) = G_{r1}$  and  $f(s) = G_{r2}$ , respectively, and assuming large loop gain in both modes, such that  $1/G_{r1} < 1/G_{r2} \ll G_p$ , the overall  $G(s)$  for this topology would indeed be largely

independent of  $G_p(s)$  and its attendant vagaries since, at low frequencies,

$$G(s) = \frac{G_p(s)}{1 + G_p(s) G_r(s)} = \begin{cases} G_1(s) = \frac{1}{G_{r1}(s)} & , \text{ for } R = R_1 \\ G_2(s) = \frac{1}{G_{r2}(s)} & , \text{ for } R = R_2 \end{cases} \quad (3.39)$$

However, such global feedback, in which the overall LNA output is fed back to its input, suffers from a fixed gain-bandwidth product, whereby an increase in  $G(s)$  from  $G_1$  to  $G_2$  is accompanied by a corresponding decrease in the closed-loop  $-3$ -dB bandwidth from  $s_1$  to  $s_2$ , as in Figure 3.19(b) because, to first-order,  $G_1 s_1 = G_2 s_2$ .

For the SVEPRE LNA, which must maintain the full 1-MHz bandwidth over the entire range of programmable gain, this is unacceptable. So, to break the gain-bandwidth trade-off, global feedback is eschewed in favor of judiciously applied local feedback, targeting only those transistors within the LNA which are especially in need of its benefits while allowing the overall LNA to operate open-loop. Figure 3.20 descends into the LNA to offer a generic representation of this local feedback.

### 3.2.2.2 Passive versus Active

Thus far, the only restriction placed on  $f(s)$  is that it be linear. However, Figure 3.20 implements  $f(s)$  with a resistor network since, typically, passive elements are used in order to obtain the maximum desensitivity. To see why, rather than simply allowing  $L(s) \rightarrow \infty$  as in (3.38), quantify the sensitivity of  $G(s)$  to variations in  $a(s)$  and  $f(s)$  by taking partial derivatives of (3.37) with respect to each and normalizing to a fractional basis [Lee, 1998, p.391]:

$$\frac{\partial G(s) / G(s)}{\partial a(s) / a(s)} = \frac{1}{1 + L(s)} \quad (3.40a)$$

$$\frac{\partial G(s) / G(s)}{\partial f(s) / f(s)} = -\frac{L(s)}{1 + L(s)} \quad (3.40b)$$

Whereas negative feedback with large loop gain attenuates fractional errors in  $a(s)$  by  $(1 + L(s))^{-1}$  before they are manifest as fractional errors in  $G(s)$ , there is no such

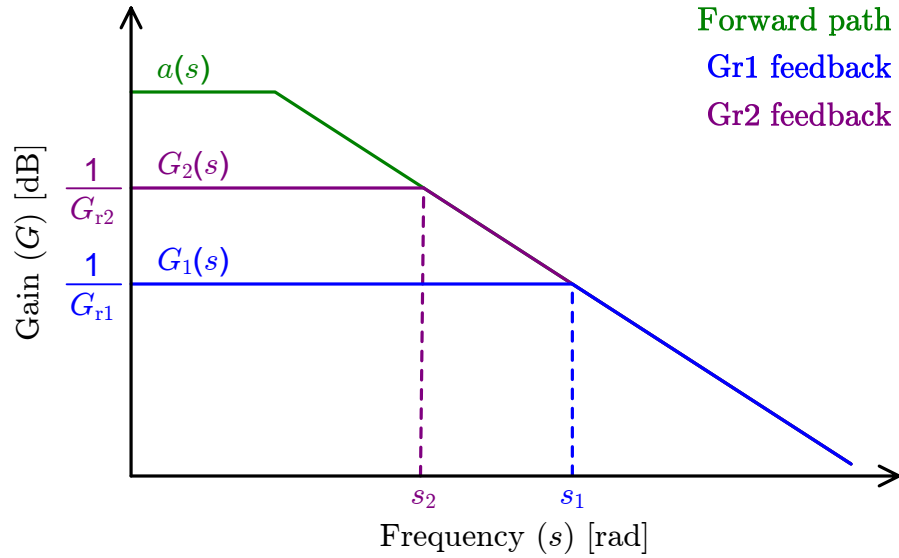
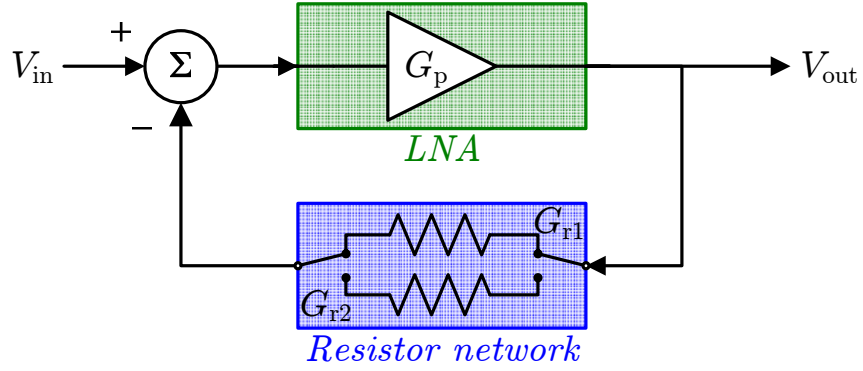


Figure 3.19: Use of global feedback to desensitize LNA. For each of the selectable feedback resistors in (a),  $R_1$  and  $R_2$ , with corresponding feedback functions  $G_{r1}$  and  $G_{r2}$ , the corresponding closed loop gains  $G_1(s)$  and  $G_2(s)$  are depicted in (b) for the case of  $a(s)$  with finite gain-bandwidth product.

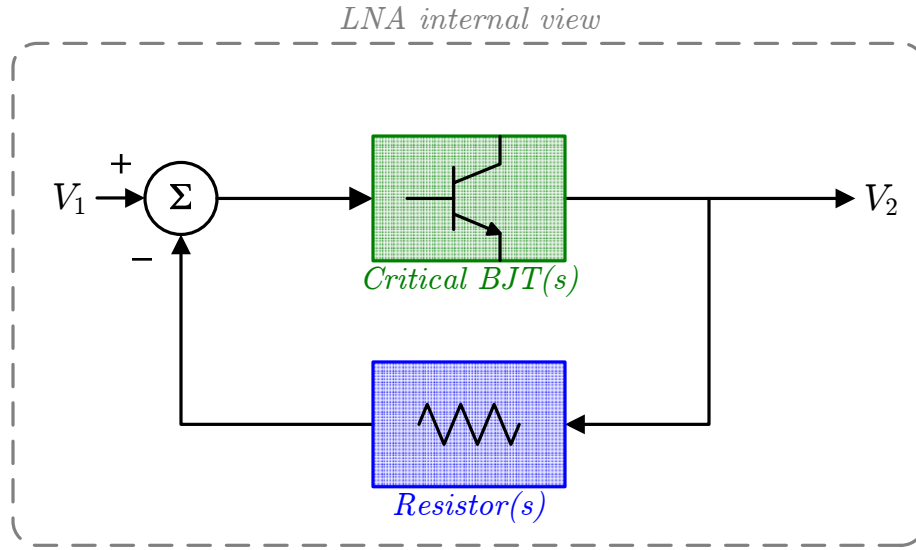


Figure 3.20: Block diagram of passive local feedback within LNA. The BJTs in the nonlinear forward path between nodes 1 and 2 are represented by a single npn just as the passive feedback from node 2 to node 1, provided by a resistive network, is symbolized by a single resistor.

benefit for  $f(s)$ , since the expression in (3.40b) approaches unity. Thus, improving linear operation and radiation tolerance through negative feedback demands that, unlike  $a(s)$ ,  $f(s)$  be implemented from the most linear and rad-hard elements available—passives. Owing to their wide bandwidth and manufacturability, the preferred passive elements are resistors [Lee, 1998, p.392].

Presume the linearity and hardness of the available resistors satisfies the SFDR and TID specifications that the transistors themselves do not.<sup>65</sup> Then, attaining the corresponding component specifications in Table 3.2 via local passive feedback loops like that of Figure 3.20 depends on ensuring sufficient loop gain for all possible  $a(s)$  and  $f(s)$  so that, given an expected magnitude of  $\partial a(s)/a(s)$ , the error described by  $\epsilon_G = \partial G(s)/G(s)$  in (3.40a) is acceptable. However, this error in  $G(s)$ , which represents the measurement uncertainty due to  $\partial a(s)$ , itself varies with respect to the

<sup>65</sup>Without having previously presented data on these properties, this assumption is examined in greater detail in Section 5.5.1.2. For now, it suffices that IC technologies merely offer no better alternative along these axes of performance than resistors and capacitors: if these cannot meet the linearity and radiation specifications, there is little hope for an integrated solution.



forward path gain according to [Mossawir *et al.*, 2006, p.3440]:

$$\frac{\partial \epsilon_G}{\partial a(s)} = -\frac{2f}{(1 + L(s))^3} \simeq -\frac{2}{a(s) L^2(s)} \quad (3.41)$$

So, any drop in loop gain increases not only the absolute value of the instrument's measurement error, but also its drift over the part lifetime.

Maintaining high enough  $L(s)$  to limit the magnitude and drift of the closed-loop gain error described by (3.40a) and (3.41) under all conditions is complicated by the large variations of both  $a(s)$  and  $f(s)$ . The gains of the transistors encapsulated by the forward path block of Figure 3.20 have already been shown to vary by more than 50% as a function of signal size (cf. Figure 3.5 and Figure 3.6), and nearly 20% with TID damage (cf. Figure 2.16). Furthermore, LNA programmability necessitates that a subset of the local feedback resistors be realized as switched networks, as in the global case of Figure 3.19(a), since these resistors dictate the gains of each local loop—at least one of which must be variable—according to (3.38).<sup>66</sup>  $L(s)$  then varies with these resistors as  $G_p$  is tuned over a 24-dB range, increasing the size(drift) of the closed-loop gain error by a factor of approximately 16(256).

Extracting enough desensitivity from passive local feedback loops so that the magnitude and drift of the errors in their closed-loop gain meet the design objectives requires so a large a loop transmission that the single-loop feedback of Figure 3.20 proves inadequate. Instead, as described below, the SVEPRE architecture deploys auxiliary active local feedback to limit  $\partial a(s)/a(s)$ , thereby compensating for those instances in which  $L(s)$  is flagging.

### 3.2.2.3 Linear versus Nonlinear

Active local feedback is required for the most susceptible transistors of the LNA and AAF because resistor-based loops cannot ensure enough loop gain to permit the approximation in (3.38) for all signal sizes, programming modes, and irradiation conditions. However, the derivation of the exact relationship in (3.38) was predicated

---

<sup>66</sup>A similar argument holds for the AAF, but its complexity justifies the preference for the simpler example of the LNA here.

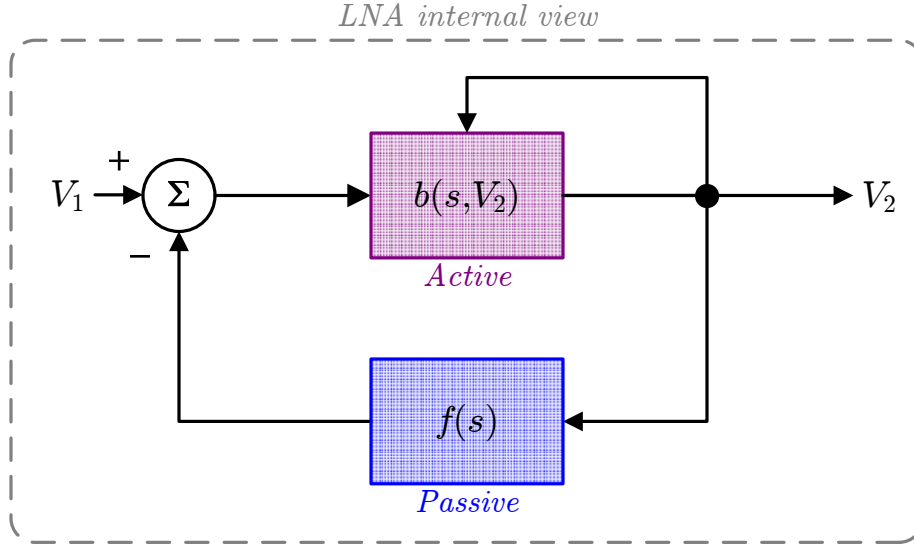


Figure 3.21: Block diagram of nonlinear negative feedback system, in which the forward path gain,  $b(s, V_2)$ , is a function of the output voltage,  $V_2$ , in contrast to the linear gain  $a(s)$  of Figure 3.18.

on the fact that  $a(s)$  in Figure 3.18 is linear. It, too, is not appropriate for the case of local feedback, where  $a(s)$  can consist of individual transistors whose large signal behavior is highly nonlinear. So, the salient model for local feedback, shown in Figure 3.21, replaces  $a(s)$  with a nonlinear block  $b(s, V_2)$  whose gain is now a function of its output and yields

$$G(s) = \frac{V_2(s)}{V_1(s)} = \frac{b(s, V_2)}{1 + b(s, V_2) f(s)} \quad (3.42)$$

To recover the desensitivity afforded by passive local feedback without the need for exorbitant  $L(s)$ , an active feedback loop can be inserted according to either Figure 3.22(a) or Figure 3.22(b). In both cases the  $b^{-1}(s, V_2)$  block is designed and connected so that its non-linearities approximately cancel those of  $b(s, V_2)$ ,<sup>67</sup> resulting in an effective forward-path gain  $a'(s, V_2)$  limned in Figure 3.23 that, despite a weak

<sup>67</sup>Ideally, of course,  $b^{-1}(s, V_2)$  would be precisely the inverse of  $b(s, V_2)$ , as the notation suggests. But, at the levels of precision in this work, complete cancellation is untenable; instead, though every effort is made to neutralize the nonlinearities of  $b(s, V_2)$ , some residual error remains in  $a'(s, V_2)$ .

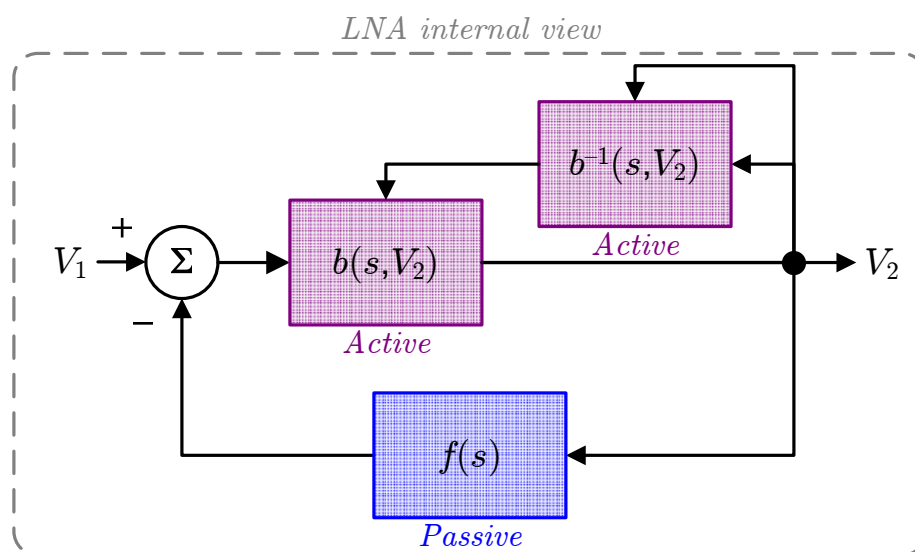
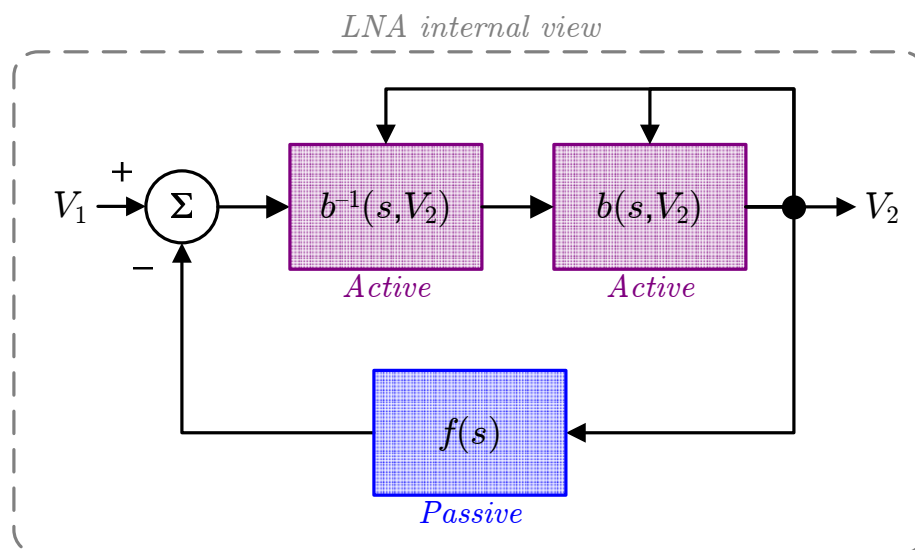


Figure 3.22: Recovery of desensitivity through active feedback loops. Injecting an additional feedback signal through nonlinear block  $b^{-1}(s, V_2)$  so as to (a) predistort the input to  $b(s, V_2)$  or (b) attenuate the nonlinear feedback to  $b(s, V_2)$  results in the linearized forward path of Figure 3.23.

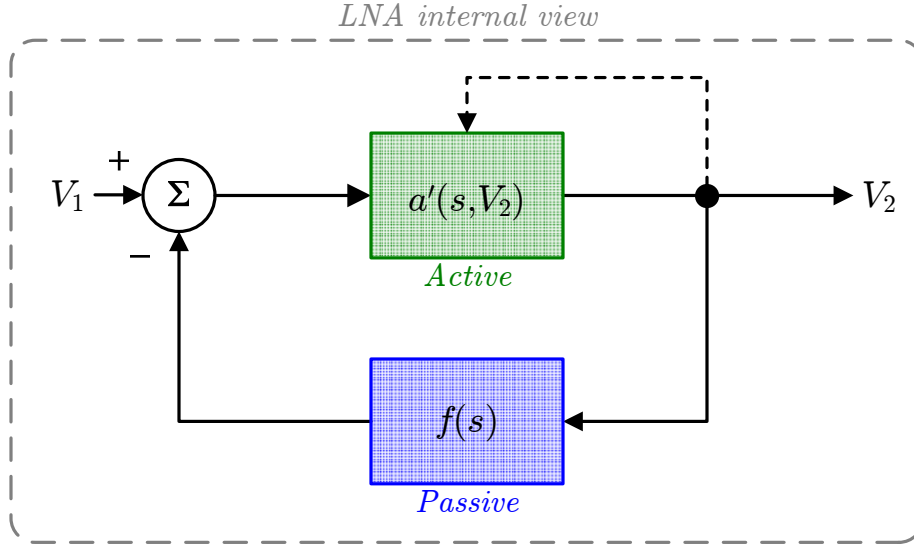


Figure 3.23: Equivalent representation of linearization via techniques in Figure 3.22. The resulting forward path  $a'(s, V_2)$  is nearly linear, exhibiting only a weak dependence on  $V_2$  (dotted line).

$V_2$  dependence, is so robust to variation that compared to the ideal linear plant,

$$\frac{\partial a'(s, V_2)}{a'(s, V_2)} < \frac{\partial a(s)}{a(s)} \quad (3.43)$$

Thus, (3.40a) and (3.41) can tolerate lower  $L(s)$  under a variety of operational modes and achieve the same closed-loop error  $\epsilon_G$ .

So, to realize the desensitivity customarily afforded by global, passive, linear feedback networks to the degree necessitated by the exacting linearity specifications of Table 3.2 over the full set of programming and radiation conditions given therein, a series of local, active, nonlinear feedback loops are deployed throughout the designs of the next two chapters.

# Chapter 4

## LNA Design

To most circuit designers, an LNA is a tuned, narrowband amplifier whose noise and impedance matching are optimized for communication standards. The history of such circuits for use in microwave engineering is fascinating [*Okwit*, 1984] and has progressed from large, cryogenically-cooled amplifiers used in satellite GSE, to microwave/millimeter-wave ICs (MMICs) utilizing HEMTs (cf. Footnote 53 of Chapter 3) [*Whelehan*, 2002]. But, in this work, the term is admittedly misappropriated to describe the first block of the SVEPRE analog front-end which, though occupying the expected position in the signal path—immediately following the antenna—is subject to a distinct set of specifications. Enumerated in Section 3.1, these include broadband operation over four decades in frequency, noise suppression down to 100 Hz, programmable gain, and high input impedance. This chapter explains how such performance is achieved under baseline conditions and preserved in the radiation-belt environment through the design of a custom, integrated LNA for a wideband plasma wave receiver.

One approach would be to classify the design techniques according to the performance metrics they seek to achieve. Aside from being pedantic, such an organization belies the interdependencies between design choices that affect competing objectives and obfuscates the core philosophy of this work—an approach wherein the inherent gain of active elements (read transistors) is consistently and systematically eschewed in favor of performing voltage-to-current conversion

exclusively through passive means, as detailed in Section 4.2.1. Instead, the LNA design is presented through three conceptual lens of increasingly narrow focus: first, Section 4.1 describes the top-level architecture inherited from the legacy of bipolar instrumentation amplifiers; Section 4.2 moves into the transistor-level implementation of this architecture, emphasizing those elements crucial to the performance goals of Table 3.2; finally, the layout of the circuit fabricated on SVEPRE-3 is analyzed in Section 4.3, with emphasis on the hardness-by-design techniques employed.

## 4.1 Architecture

The use of feedback to improve the operation of wide-bandwidth, low-noise amplifiers like that under investigation is an idea that stretches back to at least the vacuum tube era [Weighton, 1955]. But, given that npn BJTs and resistors are the elements of BiCMOS8 whose properties—specifically, noise and linearity, respectively—best suit this application, a better source of historical inspiration is the monolithic instrumentation amplifier (inamp).

First introduced in 1971 [Krabbe, 1971], when many high-performance IC technologies only offered complementary BJTs and resistors, an integrated inamp possesses the same distinguishing characteristics as its more familiar discrete, three-opamp counterpart, depicted in Figure 4.1 [Kitchin and Counts, 2006, p.2-2]. Specifically, it features a balanced,<sup>1</sup> high-impedance differential input which is isolated from the single resistor used to program its variable gain ( $R_d$ ). Coupled with precision gain, low input-bias current, a high common-mode rejection ratio (CMRR), and closed-loop operation via internal local feedback that obviates the need for an external

---

<sup>1</sup>It proves beneficial to clearly distinguish the terms *balanced* and *differential* since they are commonly used as synonyms, though they denote distinct ideas in this text. A single-ended system defines each input/output as simply the potential of (or current on) a single conductor with respect to the system ground. A differential system uses two wires for each input/output and is concerned with the difference between the potentials of (or currents on) these lines. A balanced system also uses two wires for every input/output but, when referenced to system ground, the potentials of (or currents on) the two wires are equal in magnitude and opposite in sign. Thus, whereas the output of a balanced system may be taken differentially (between the two wires), it is imperative that the single-ended potential of each wire (with respect to ground) be clearly defined and (nominally) symmetric.

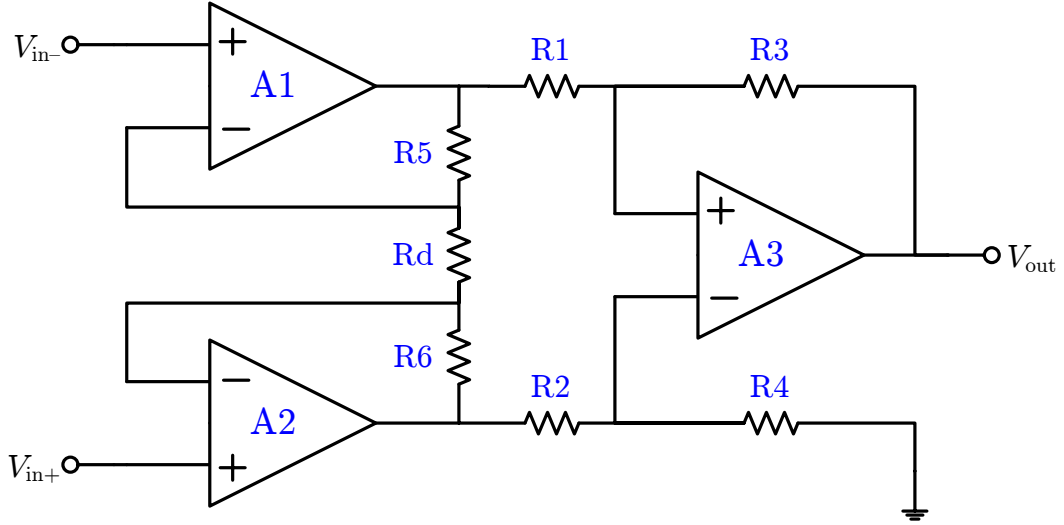


Figure 4.1: Classic, discrete inamp built from three opamps. In addition to the higher area and power consumption of this implementation, its use of discrete opamps restricts the output to single-ended referencing (shown here relative to ground). For perfect resistor matching, a half-circuit analysis reveals that  $R_d$  programs the gain according to  $G_p = (1 + 2R_5/R_d)(R_3/R_1)$ . After [Kitchin and Counts, 2006, p.2-2].

resistor network to provide global feedback [Kitchin and Counts, 2006, p.1–8], these properties render the inamp a preferred choice for interfacing with the analog sensors at the inputs of precision instrumentation in general and the target plasma wave receiver in particular.

Thus, aside from its performing a differential-to-single-ended conversion, the architecture of the monolithic bipolar inamp of Brokaw and Timko [1975] provides an excellent template for understanding that of the LNA in this work. Consideration of the former in Section 4.1.1 provides background and motivation for the modifications found in the SVEPRE LNA and described in Section 4.1.2.

#### 4.1.1 Canonical Inamp

A simplified schematic of the canonical inamp architecture of Brokaw and Timko [1975] is presented in Figure 4.2. It consists of two emitter follower stages, each enclosed with both passive feedback, in the form of degeneration resistors  $R_d$  and  $R_l$ ,

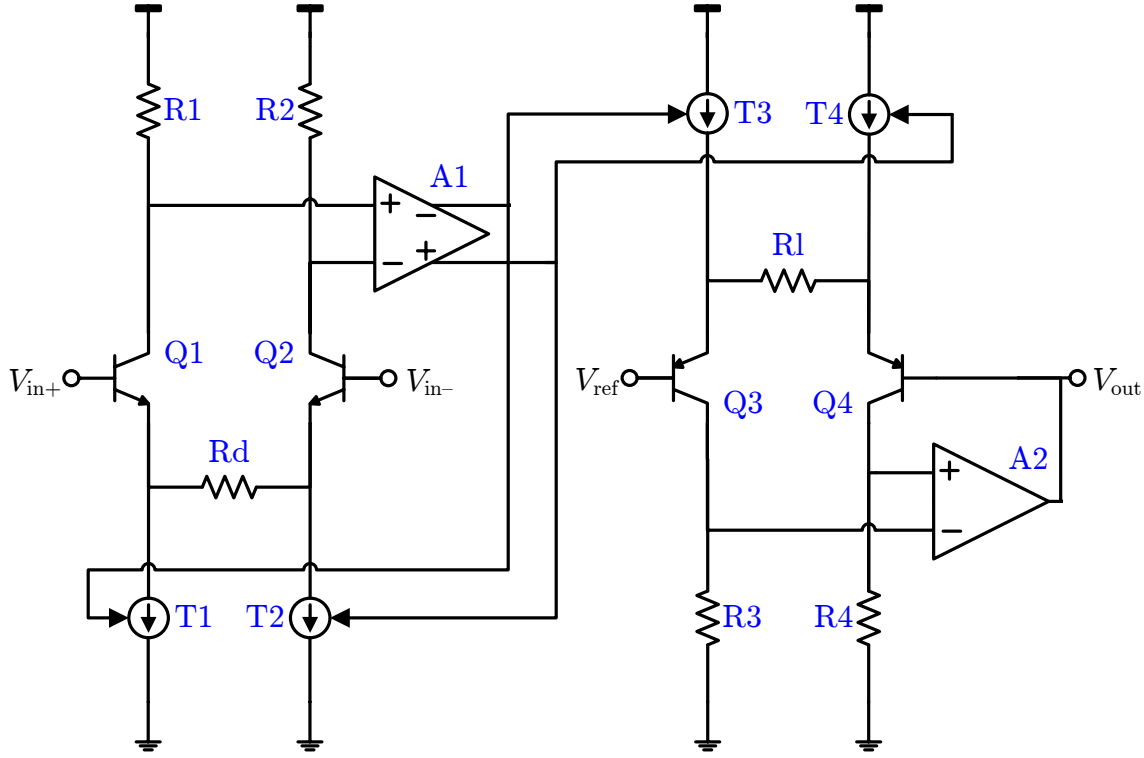


Figure 4.2: Simplified inamp architecture of *Brokaw and Timko* [1975, p.418]. Note that A1(A2) is a differential(single-ended) transconductance(voltage) amplifier.

and active feedback, via amplifiers A1 and A2. The former is fully differential and drives a pair of tracking differential tail currents sources, one in each active loop, for which  $i_{t1} = i_{t3}$  and  $i_{t2} = i_{t4}$ .<sup>2</sup>

Ideally, these loops produce a differential output,  $V_{out}$ ,<sup>3</sup> that is linearly related to

<sup>2</sup>The lower-case variables  $i_{t1}-i_{t4}$  represent only the portions of the currents through these sources that result from A1 and A2. Therefore, the stated equalities do not imply that the total currents,  $I_{tx} = I_{Tx} + i_{tx}$  for  $x = 1, 2, 3, 4$ , are matched between stages. A more through discussion of this point appears in Section 4.1.2.2.

<sup>3</sup>By convention, named nodal voltages in the remainder of this document should be considered differential unless otherwise noted and are defined in terms of their single-ended composites; for example,  $V_{out} = V_{out+} - V_{out-}$ , where  $V_{out+}$  ( $V_{out-}$ ) is the voltage of the output node on the positive(negative) branch of the circuit. The corresponding common-mode component of the pair of branch potentials is  $\bar{V}_{out} = \frac{1}{2} (V_{out+} + V_{out-})$ .

Although offsets that arise in practice are considered as necessary,  $V_{out+}$  and  $V_{out-}$  are ideally balanced as well. So, unless otherwise noted, the branch potentials are related to the differential



its input,  $V_{\text{in}}$ , by the ratio of two resistors:

$$G_{\text{p}} = \frac{V_{\text{out}}}{V_{\text{in}}} = \frac{R_{\text{l}}}{R_{\text{d}}} \quad (4.1)$$

By implementing these resistors off chip, the user is afforded the ability to easily program the gain within the constraints set by the maximum outputs of current sources T1–T4. Notably, through the use of discrete resistors (coupled with analog multiplexers or relays) or potentiometers (controlled manually or digitally) to implement  $R_{\text{d}}$  and  $R_{\text{l}}$ , this programming method permits arbitrary step sizes, rendering an inamp-inspired LNA suitable for WBR applications that require any or all of the VGA step resolutions previously flown (cf. Table B.6).

#### 4.1.1.1 Qualitative Operation

For the sake of intuition, a qualitative description of the idealized operation of the inamp in Figure 4.2 is now provided. Operating as emitter followers, transistors Q1 and Q2 level-shift the differential input signal so that it appears across  $R_{\text{d}}$ . This produces a differential current through  $R_{\text{d}}$  that, in the absence of the active feedback, would simply be conducted to the collectors of Q1 and Q2 and converted into a differential output voltage by their loads. However, the action of A1, in attempting to equalize its inputs, instead imbalances  $I_{\text{T1}}$  and  $I_{\text{T2}}$  so as to provide this current instead. Thus, the Stage 1 collector currents remain fixed.

By applying the same corrections to the tail current sources of the second stage ( $I_{\text{T3}}$  and  $I_{\text{T4}}$ ), A1 effectively translates the differential current from one stage to the next. To ensure that this current flows only through  $R_{\text{l}}$ , the loop containing amplifier A2 attempts to fix the collector currents of Q3 and Q4. In so doing, it succeeds in

---

( $V_{\text{out}}$ ) and common-mode ( $\bar{V}_{\text{out}}$ ) constructions by:

$$V_{\text{out}+} = \bar{V}_{\text{out}} + \frac{V_{\text{out}}}{2}$$

$$V_{\text{out}-} = \bar{V}_{\text{out}} - \frac{V_{\text{out}}}{2}$$

Logically, this convention also applies to branch currents.

converting all the Stage 1 current back into a voltage across  $R_l$  so that the relationship between the voltages across the two resistors is given by (4.1). The constant collector current of Q3 ensures that its emitter voltage is static, fixed one diode drop below the reference driving its base ( $V_{\text{ref}}$ ). Thus, the fluctuations in the voltage across  $R_l$  appear at the emitter of Q4 and are then level-shifted to its base, forming the overall, single-ended output,  $V_{\text{out}}$ .

#### 4.1.1.2 Quantitative Operation

A more rigorous interpretation of the roles of A1 and A2 considers their feedback loops using the formalisms of Section 3.2.2. To develop the required correspondence, deconstruct Stage 1 as in Figure 4.3 to yield the degenerated differential pair formed by Q1, Q2, and  $R_d$  that would exist in the absence of A1.<sup>4</sup> Although load resistors  $R_1$  and  $R_2$  have been transplanted as well, the operation of this block can be considered in terms of an output current,  $I_{\text{out}}$ .

#### Degenerated Differential Pair

Invoking the large-signal descriptions of Q1 and Q2 given by (3.10) (letting  $V_A \rightarrow \infty$ ), the differential-mode and common-mode output currents for this plant, taken from

---

<sup>4</sup>Ignoring the A2 feedback loop incurs no loss of generality, since it is trivial to show that the results of this section apply equally well to the second stage, provided input nodal voltages and output branch currents are interchanged and the direction of signal flow is reversed in all graphs.

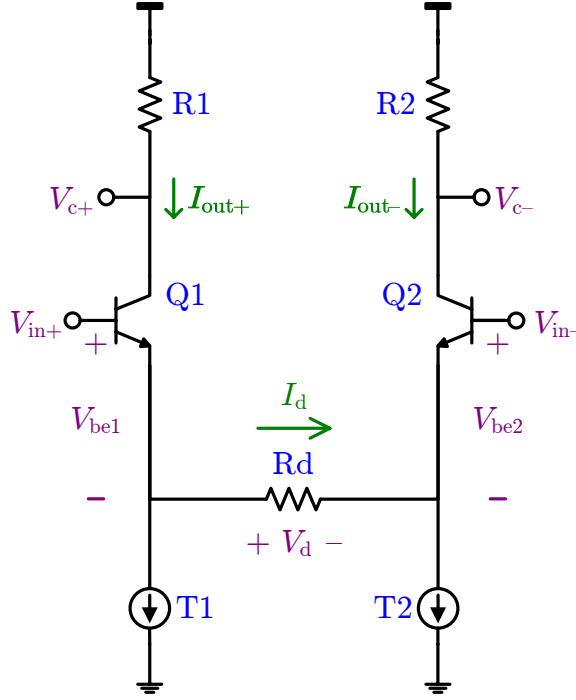


Figure 4.3: Degenerated differential pair extracted from first stage of Figure 4.2. Treated as a transconductance stage, the output of the Q1/Q2 pair is the difference of their collector currents.

their collectors, can be expressed as:<sup>5</sup>

$$I_{\text{out}} = (\alpha_1 I_{T1} - \alpha_2 I_{T2}) + \frac{2nV_T \bar{\alpha}}{R_d} \ln \left( \frac{A_{e1} W_{b2}}{A_{e2} W_{b1}} \right) - \frac{4nV_T \bar{\alpha}}{R_d} \tanh^{-1} \left( \frac{I_{\text{out}}}{2\bar{I}_{\text{out}}} \right) + \frac{2\bar{\alpha}}{R_d} V_{\text{in}} \quad (4.2a)$$

$$\bar{I}_{\text{out}} = (\alpha_1 I_{T1} + \alpha_2 I_{T2}) + \frac{nV_T \Delta \alpha}{R_d} \ln \left( \frac{A_{e1} W_{b2}}{A_{e2} W_{b1}} \right) - \frac{2nV_T \Delta \alpha}{R_d} \tanh^{-1} \left( \frac{I_{\text{out}}}{2\bar{I}_{\text{out}}} \right) + \frac{\Delta \alpha}{R_d} V_{\text{in}} \quad (4.2b)$$

<sup>5</sup>Although the lengthy derivation of these expressions is omitted, it suffices to identify its origin as the application of the translinear principle explained in Section 5.4.2.1 to the loop formed by  $V_{be1}$ ,  $V_{be2}$ , and  $V_d$ . Since the first two quantities are exponentially related to the output currents by (3.10), differencing these voltages produces logarithms of the current ratios; hence the  $\tanh^{-1}$  term, since

$$\tanh^{-1}(x) = \frac{1}{2} \frac{1+x}{1-x}$$

for  $|x| < 1$ .

Since no matching between Q1 and Q2 has been assumed in these expressions, save that  $n_1 = n_2 = n$ , the common-base current gains of Q1 and Q2, defined by  $\alpha = \beta/(1 + \beta)$ , are related through:

$$\Delta\alpha = \alpha_1 - \alpha_2 \quad (4.3a)$$

$$\bar{\alpha} = \frac{\alpha_1 + \alpha_2}{2} \quad (4.3b)$$

The first two terms of (4.2) account for mismatch between the tail current sources T1 and T2 and the drawn geometries of the npns. If, for the moment, both pairs of devices are assumed to be perfectly matched ( $I_{T1} = I_{T2}$ ,  $A_{e1} = A_{e2}$ ,  $W_{b1} = W_{b2}$ ),<sup>6</sup> the resulting simplifications give:

$$I_{\text{out}} = \underbrace{\Delta\alpha I_T + \bar{\alpha}}_{\beta \text{ nonlinearity}} \left[ 1 - \underbrace{\frac{2nV_T}{V_{\text{in}}} \tanh^{-1}\left(\frac{I_{\text{out}}}{2\bar{I}_{\text{out}}}\right)}_{\Delta V_{\text{be}} \text{ nonlinearity}} \right] \frac{2V_{\text{in}}}{R_d} \quad (4.4a)$$

$$\bar{I}_{\text{out}} = \underbrace{2\bar{\alpha} I_T + \Delta\alpha}_{\beta \text{ nonlinearity}} \left[ 1 - \underbrace{\frac{2nV_T}{V_{\text{in}}} \tanh^{-1}\left(\frac{I_{\text{out}}}{2\bar{I}_{\text{out}}}\right)}_{\Delta V_{\text{be}} \text{ nonlinearity}} \right] \frac{V_{\text{in}}}{R_d} \quad (4.4b)$$

which highlights two sources of nonlinearity:

**$V_{\text{be}}$  nonlinearities:** The inverse hyperbolic tangent term arises from the exponential in the constitutive relation of (3.10a), which captures the fundamental BJT nonlinearity. It produces an  $I_{\text{out}}$ -dependent error between the input signal and the level-shifted version appearing across  $R_d$  that is captured by the difference in the base-emitter voltages of Q1 and Q2,  $\Delta V_{\text{be}}$ . Although this error term can typically be neglected for small signals and large bias currents, where  $I_{\text{out}} \ll$

---

<sup>6</sup>Ensuring that the tail current sources(transistor geometries) are, in reality, well-matched is the subject of Section 4.2.4(Section 4.3.1.1).

$2\bar{I}_{\text{out}}$ , neither of these conditions applies to this LNA: when  $G_p = 0$  dB, the first-stage currents can be as large as those at the output; and low-power operation demands minimizing  $I_T \simeq \bar{I}_{\text{out}}$ .

**$\beta$  nonlinearities:** The nonlinearity introduced by the terms of (4.4) that contain those of (4.3) is not directly apparent, but can be inferred from Figure 3.6. Since  $\beta$  is a function of operating point (cf. Section E.1.2), both  $\Delta\alpha$  and  $\bar{\alpha}$  exhibit weak but non-negligible dependence on  $I_{\text{out}}$  and  $\bar{I}_{\text{out}}$ . Indeed, the distortion of such non-constant  $\beta$  effects is a recurring theme in this work, where large variations in  $I_{\text{out}}$  (or, equivalently,  $V_{\text{in}}$ ) do not allow the gain to be treated as signal independent.

### Linearization via A1

Introducing the A1 loop around the degenerated differential pair of Figure 4.3 shrinks both types of nonlinear terms in (4.4). To see this, first recall that, by definition, the  $\Delta\alpha(\bar{\alpha})$  term represents mismatch(finite  $\beta$ ) error in the common-base current gain applied to the resistor current as it passes through Q1 and Q2. Since the A1 loop varies the tail current sources of Q1–Q4, it only copies their emitter currents from Stage 1 to Stage 2, thereby circumventing this common-base path and taking the output of the first stage directly from Rd. Redefining the output of the differential pair to be the single-ended resistor current  $I_d$ , (4.2a) reduces to

$$I_d = \frac{nV_T}{R_d} \ln\left(\frac{A_{e1}W_{b2}}{A_{e2}W_{b1}}\right) + \left[1 - \frac{2nV_T}{V_{\text{in}}} \tanh^{-1}\left(\frac{I_{\text{out}}}{2\bar{I}_{\text{out}}}\right)\right] \frac{V_{\text{in}}}{R_d} \quad (4.5)$$

Furthermore, in keeping the collector currents of Q1 and Q2 approximately equal and constant, the A1 loop suppresses the signal dependency of the argument of the inverse hyperbolic tangent,  $\varepsilon_{\text{swing}} = I_{\text{out}}/2\bar{I}_{\text{out}}$ , leaving

$$I_d = \frac{nV_T}{R_d} \ln\left(\frac{A_{e1}W_{b2}}{A_{e2}W_{b1}}\right) + \left[1 - \frac{2nV_T}{V_{\text{in}}} \tanh^{-1}\left(\frac{I_d}{A_1\bar{V}_c}\right)\right] \frac{V_{\text{in}}}{R_d} \quad (4.6)$$

Although the range of  $I_d$  in (4.6) is on par with that of  $I_{\text{out}}$  in (4.4a), the denominator

of  $\varepsilon_{\text{swing}}$  has been amplified by  $\frac{1}{2}A_1\overline{R}_c$ , where  $\overline{R}_c$  is the average value of R1 and R2, the collector load resistors responsible for setting the common-mode input voltage of A1 at  $\overline{V}_c = \overline{I}_{\text{out}}\overline{R}_c$ . Thus, the effective swing,  $\varepsilon'_{\text{swing}} = V_{\text{in1}}/2\overline{V}_c$ , is much smaller, depending only on the fraction of  $\overline{V}_c$  occupied by the swings of  $I_d$  when referred to the input of A1 as  $V_{\text{in1}}$ .

### Feedback Interpretation

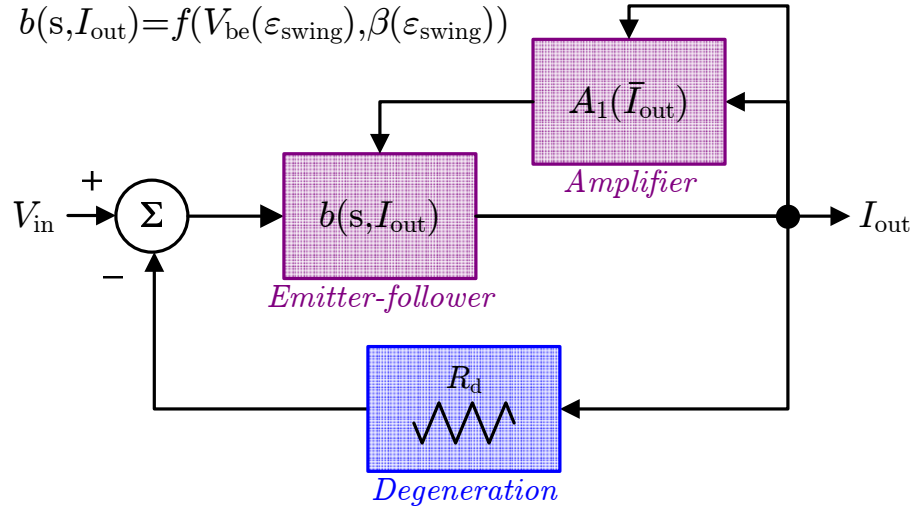
The above derivation corresponds to the graphical representation of passive-loop and active-loop feedback in Figure 3.21, which has been customized for Stage 1 in Figure 4.4. Given the  $\Delta V_{\text{be}}$  and  $\beta$  nonlinearities in (4.4), the transfer function from input voltage  $V_{\text{in}}$  to collector current  $I_{\text{out}}$  for the forward path through Figure 4.3 is embodied by the nonlinear block of Figure 4.4(a) whose gain is represented as  $b(s, I_{\text{out}})$ . The inclusion of A1, which interrupts the nonlinear feedback by suppressing the  $\varepsilon_{\text{swing}}$ -dependence of the terms in (4.4), yields a much more linear  $G(s)$ , given by (4.6) and depicted in Figure 4.4(b), which still depends on  $a'(s, I_d)$ .

For large enough loop gain,<sup>7</sup>  $L(s) \simeq \frac{1}{2}A_1\overline{R}_c \gg \varepsilon_{\text{swing}}$ , the effective swing, indicated by the dashed path of Figure 4.4(b), is attenuated such that it becomes permissible to linearize (4.6) around a Taylor series expansion of the  $\tanh^{-1}$  term and, if drawn geometries are again perfectly matched, obtain  $a'(s, I_d) \rightarrow a'(s)$ , so that:

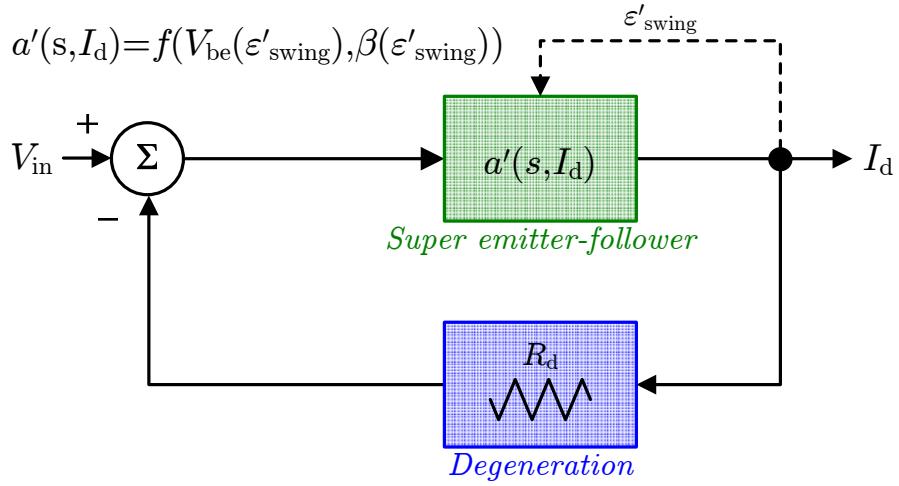
$$\frac{I_d}{V_{\text{in}}} \simeq \frac{1}{R_d + \frac{2nV_T}{A_1\overline{V}_c}} \quad (4.7)$$

When the active-loop gain is even larger, such that its product with that of the passive loop well exceeds unity (i.e.,  $L(s) \gg (\overline{g}_m R_d)^{-1}$ , where  $\overline{g}_m$  is the average npn transconductance), the systematic error in  $a'(s)$  is eliminated and (4.7) reduces to the desired linear gain of simply  $G(s) = 1/R_d$ .

<sup>7</sup>The quantity which appears in the  $\tanh^{-1}$  argument of (4.6),  $\frac{1}{2}A_1\overline{R}_c$ , is actually the loop gain for the case of a non-degenerated pair; but, conceptually, the loop gain arguments espoused here remain valid. The full  $L(s)$  for the small-signal model of Figure 4.2 is presented in Section 4.2.2.3.



(a) Attenuation of nonlinear feedback.



(b) Equivalent linearized network.

Figure 4.4: Flow graph representation of first stage of Figure 4.2 with (a) explicit identification of active ( $A_1$ ) and passive ( $R_d$ ) loops as well as (b) an equivalent network whose linearized forward path  $a'(s, I_d)$  is identified as the super emitter-follower of Section 4.2.2.1.

### 4.1.1.3 Shortcomings

To realize this drastic reduction in the effects of  $\Delta V_{be}$  and  $\beta$  nonlinearities, the classical inamp architecture adopts several tactics at odds with the SVEPRE specifications. Most obvious is its single-ended output, which is incompatible with the fully differential signal path of the target receiver in Figure 1.22.

Secondly, since the overall voltage gain results from inter-stage current-mode signaling, its linearity depends primarily on accurate current handling. In copying currents from  $R_d$  to  $R_l$ , A1 and the current sources it steers must be: high-gain, to minimize errors through high  $L(s)$ ; precise, so as to only transfer the imbalances resulting from the input signal; and closely matched, both between circuit halves and between the two stages, to avoid harmonic distortion.

Finally, as it requires multiple active feedback loops and large bias currents, the power demands of the canonical inamp can be excessive, approaching 60 mW for that of [Brokaw and Timko, 1975, p.422], which surpasses the entire SVEPRE budget. Simply reducing the power rails to those of a modern process, from  $\pm 12$  V to  $\pm 2.5$  V, cannot recover the desired savings, because bipolar circuits, whose DC levels are predicated on diode drops that do not scale, consume headroom voraciously.

To address each of these issues, modifications to the architecture of Figure 4.2 are proposed in the next section.

## 4.1.2 Modified Architecture

A simplified representation of the SVEPRE LNA architecture is presented in Figure 4.5 and should be juxtaposed with that of Figure 4.2 to emphasize the modifications required by this application. Preserving the essential character and operation of the canonical inamp, this topology extends its performance to the meet linearity and radiation requirements, resolving the shortcomings of Section 4.1.1.3 as explained below.



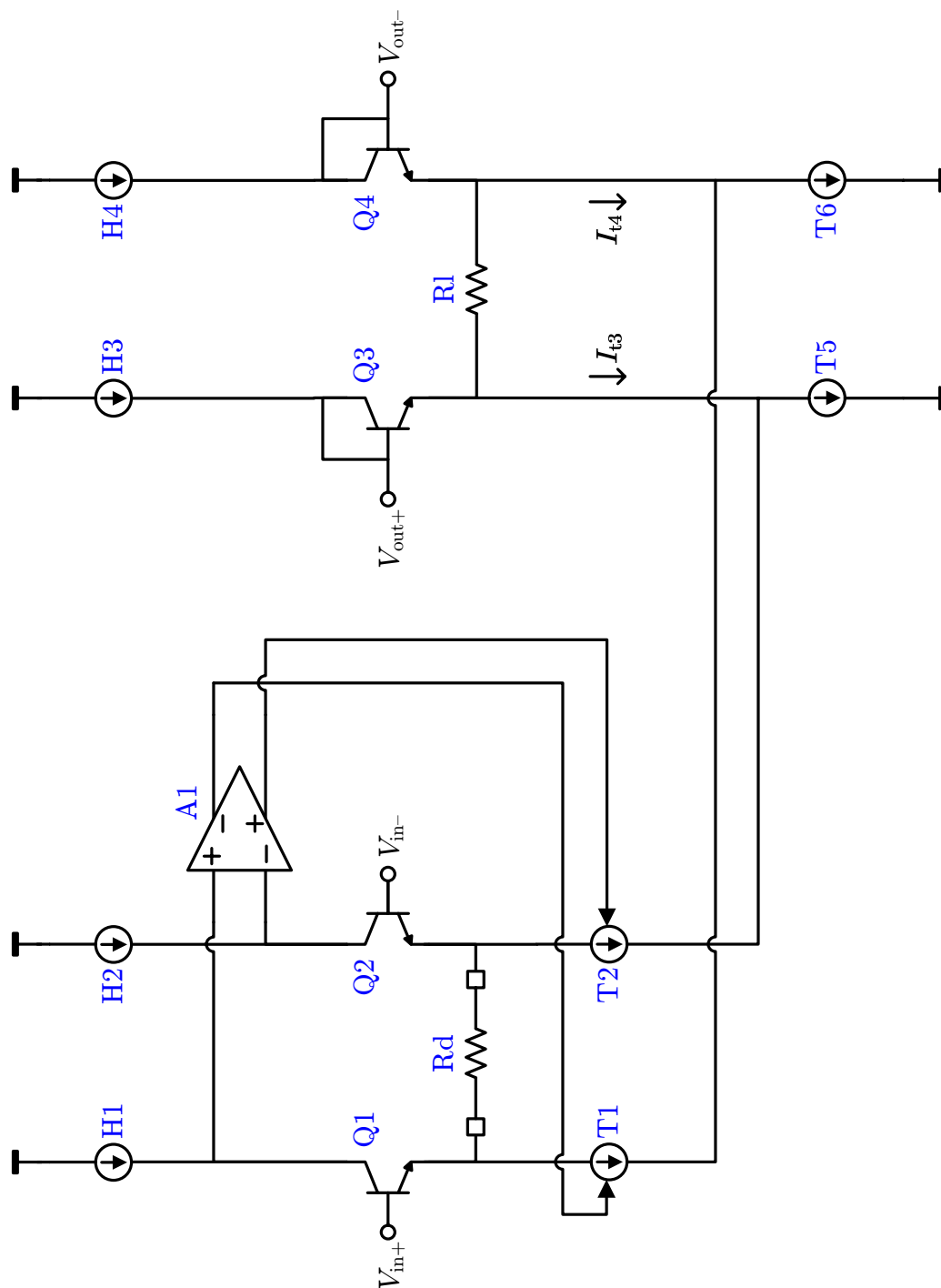


Figure 4.5: Simplified schematic of LNA architecture, highlighting its differential npn output stage, elimination of amplifier A2, inter-stage current steering, and off-chip implementation of Rd (boxes indicate bond pads). Compare with Figure 4.2.

### 4.1.2.1 Differential Output

The fully differential signal path of the target receiver provides a balanced load to the dipole antenna, tolerates a wide input signal range, and rejects common-mode noise that is both conducted from the plasma and power supply bus and radiated by the host spacecraft and surrounding electronics [Razavi, 2001, p.100–103]. In exchange for its improved noise and signal-handling, a fully differential amplifier requires a means of establishing the common-mode level at all nodes, ensuring they remain balanced and reliably biased in the desired operating region (cf. Footnote 1). So, despite the accepted advantages of a fully differential architecture, most inamps perform a differential-to-single-ended conversion at their output in order to reduce back-end complexity at the expense of dynamic range and common-mode rejection [Gray *et al.*, 2001, p.293–299].

In contrast, the LNA of Figure 4.5 directly transmits the differential signal across Rl to its output through the  $V_{be}$  level-shifts of Q3 and Q4. This not only retains the advantages of a differential amplifier, but halves the number of active feedback loops required, reducing power consumption.<sup>8</sup> But, to preserve these gains, the circuitry now responsible for setting the output common-mode level,  $\bar{V}_{out}$ , cannot take the form of traditional common-mode feedback (CMFB)—otherwise, the power of A2 would simply be offset by that of the CMFB amplifier. Furthermore, having omitted the A2 loop, the level-shifted  $V_{out}$  is sensitive to those  $V_{be}$  nonlinearities of Q3 and Q4 ascribed to Q1 and Q2 in Section 4.1.1.2. Thus, a feedforward means of compensating for this distortion is necessary; the replacement of the collector resistors of Q3 and Q4 with current sources H3 and H4 is one element of this mechanism. The full technique for canceling the  $V_{be}$  distortions and setting the output common-mode level of the second stage is embedded in its implementation, as addressed in Section 4.2.3.

---

<sup>8</sup>This reduction is not simply a factor of two, as might be expected. Typically, as it provides the LNA output drive capability, A2 exhibits higher bias currents and more stages than A1. In particular, whereas A1 is an operational transconductance amplifier, or OTA, with correspondingly high output impedance, that of A2 must be low enough to source drive current to the AAF input. Thus, its output buffer stage typically consumes a significant fraction of the total power, be it static or dynamic (e.g., Class AB or D). Although such drive currents are still required in its absence, eliminating all but one of the branches in which they flow by excising in the core of A2 and its bias network can result in an order of magnitude power savings.

#### 4.1.2.2 Current Steering

Easing the requirement for matched, tracking current sources T1–T4 in Figure 4.2, the architecture of Figure 4.5 leverages folding to establish the desired relationship between T1(T2) and T3(T4). Previously, the tracking provided by the multiple outputs of A1 ensured that a signal-induced change  $i_{t1}(i_{t2})$  from the DC value of T1(T2), namely  $I_{T1}(I_{T2})$ , would be mimicked at T3(T4) as  $i_{t3}(i_{t4})$  such that even if  $I_{T1} \neq I_{T3}$  ( $I_{T1} \neq I_{T3}$ ), it was assured  $i_{t1} = i_{t3}$  ( $i_{t2} = i_{t4}$ ). Provided that T5 and T6 are ideal static sources, meaning  $i_{t5} = i_{t6} = 0$ , the connectivity of Figure 4.5 which dictates that

$$I_{t3} = I_{T5} - I_{t2} = I_{T5} + I_{t1} \quad (4.8a)$$

$$I_{t4} = I_{T6} - I_{t1} = I_{T6} + I_{t2} \quad (4.8b)$$

perfectly copies the signal current between stages, as evident by equating the signal-dependent components on both sides of (4.8). Any DC mismatch between T5 and T6 appears as an offset in the output current, whereas non-zero  $i_{t5}$  and  $i_{t6}$  corrupt the linearity of  $G_p$ .

Replacing the need for tracking differential current sources with requirements on the matching and output resistance of static sources is not novel; indeed, it was proposed by *Brokaw and Timko* [1975]. However, their realization was aided by the ability to implement Q3 and Q4 as vertical pnp transistors, whose full bias current could be provided by returning the currents of T1 and T2 to their emitters rather than ground. In contrast, armed only with npn BJTs, the architecture of Figure 4.5 incurs a polarity inversion that must be absorbed by the novel inclusion of T5 and T6 to provide the static emitter bias currents of Q3 and Q4. Thus, an additional matching requirement is imposed on current sources T1 and T2: they must track T5 and T6. The implications of this new qualification are examined in Section 4.2.4.2.

### 4.1.2.3 Gain Programming

In the part developed by *Brokaw and Timko* [1975], neither  $R_d$  nor  $R_l$  is implemented on chip. Instead, connections are made available to the user via two pairs of package pins so that off-chip components of the desired value may be employed. However, it is strictly necessary, and in many cases preferable, to require only a single external component. So, the question naturally arises as to which resistor should be integrated. In Figure 4.5,  $R_l$  is implemented on chip to ensure stability and obtain the desired bandwidth over the range of  $G_p$  settings. These benefits bear further examination.

Bringing a signal from the core of the LNA out to an external resistor (or vice versa) incurs a host of parasitic capacitances associated with: on-chip connections from the transistors to the pad frame (long metal lines and the pads themselves), from the pads to the package lead frame (bond wires and the pins themselves) and from the package to the PCB (solder pads); and off-chip parasitics, including board-level stray capacitance between copper traces or socket leads and the ground layer.<sup>9</sup> A lumped model of these contributions is provided in Figure 4.6, where the total,  $C_{\text{ext}}$ , given by

$$C_{\text{ext}} = C_{\text{line}} + C_{\text{pad}} + C_{\text{wire}} + C_{\text{pin}} + C_{\text{trace}} \quad (4.9)$$

can easily exceed 10 pF. Determination of which LNA nodes are robust enough to such parasitics as to be exported off chip to accommodate external gain setting resistors must account for two implications:

**Stability:** In its original incarnation (cf. Figure 4.2), the active feedback loops of the inamp ensure that the impedances seen by  $R_d$  and  $R_l$  at the emitters of both degenerated differential pairs are low.<sup>10</sup> Indeed, one of the primary advantages

---

<sup>9</sup>As a very rough rule-of-thumb, a 25-mil wide copper trace opposite a ground layer on a PCB of typical thickness contributes  $\sim 2$  pF/in over short distances. For long distances,  $\sim 10$  pF/in is more realistic. Similarly, the capacitance between two plane layers straddling a 25-mil-thick FR4 dielectric, such as power and ground, is  $\sim 100$  pF/in<sup>2</sup>.

<sup>10</sup>As chronicled in Section 4.2.2.2, the active loops provide series-shunt feedback around the standard emitter follower that reduces its output resistance by the loop gain,  $\frac{1}{2}A_1\overline{R}_c$ , yielding an approximate small-signal effective differential output resistance (as seen by  $R_d$ ) of:

$$r_{\text{out}1} \simeq \frac{4}{g_{m1,2}A_1\overline{R}_c}$$

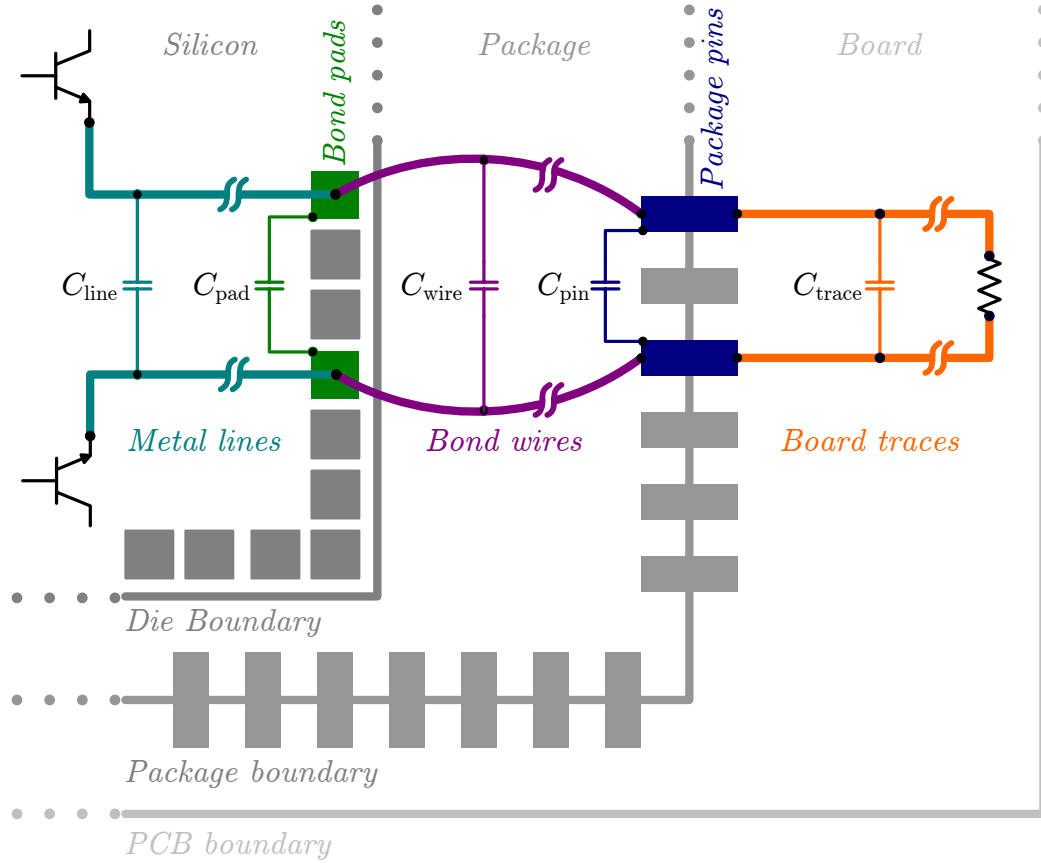


Figure 4.6: Simple, lumped model of parasitic capacitances incurred across off-chip resistor. Each differential capacitor accounts for both direct cross-coupling and the series combination of the single-ended, ground-terminated capacitances for each node. By no means comprehensive, this model merely illustrates the primary contributors.

of the monolithic inamp over that of Figure 4.1 is its bandwidth, as there are no high-impedance nodes in the signal path. However, a potential problem with these negative feedback loops is maintaining stability when the emitter load is largely capacitive [Gray et al., 2001, p.215]. Intuitively, this can be perceived by noting that the dominate pole of  $L(s)$  lies at the input of A1. Although this amplifier sees a relatively low impedance looking into the emitters of Q1 and Q2, any stray capacitance across  $R_d$ , which can be lumped into an element  $C_d$ , lowers the non-dominant pole there, potentially consuming the available phase

margin.<sup>11</sup>

**Bandwidth:** Omitting the A2 feedback loop in Figure 4.5 obviates the risk of its instability, but produces a much higher nodal resistance across  $R_l$  for two reasons. The first is obvious—the output resistance of the Q3/Q4 follower is no longer attenuated by the loop gain. Even more acute is the increased resistance that results from the use of head current sources H3 and H4 in series with diode connected Q3 and Q4 level-shifters. If their output impedances are given by  $r_{oh3}, r_{oh4} \gg r_{o3}, r_{o4}$ , then the effective small-signal resistance seen by a capacitor across  $R_l$ , to be denoted  $C_l$ , is

$$r_{out2} \simeq 2 \left( r_{oh3,4} + \frac{1}{g_{m3,4}} \right) \quad (4.10)$$

which, for all but extremely high bias currents, is much larger than  $R_l$  itself. Thus, the dominant pole of the LNA is given approximately by

$$p_0 = \frac{1}{(R_l \parallel r_{out2}) C_l} \simeq \frac{1}{R_l C_l} \quad (4.11)$$

If  $R_d(R_l)$  is implemented off-chip, the large  $C_{ext}$  incurred across it can destabilize the input loop (reduce the LNA bandwidth). Although neither choice is ideal, many pragmatic concerns favor integrating  $R_l$ . The amount of overdesign required to preserve at least 1-MHz bandwidth for both an indeterminate  $C_l$  and a wide range of  $R_l$  in the course of gain programming is impractical given the limited power budget. With ability to dictate both these quantities to a high degree of accuracy in silicon,<sup>12</sup> the bandwidth of the LNA can be ensured across all gain settings.

Furthermore, by fixing  $R_l$ , the range of corresponding  $R_d$  that produces  $0 \text{ dB} < G_p < 24 \text{ dB}$  can be set low enough so as not to violate the phase margin built into the

---

<sup>11</sup>The same argument holds for the loop in Figure 4.2 comprising Q3, Q4, A2 and  $R_l$ , though its full consideration has been neglected according to the justifications of Footnote 4.

<sup>12</sup>Typically, absolute tolerances for on-chip resistors are no better than 20%. Thus, a degree of margin is built into the chosen  $R_l$  so as to ensure that the target bandwidth is satisfied. For  $C_l$ , which is realized by metal comb capacitors, the absolute value is even more tightly controlled, with only a few percent uncertainty; but, again, allowances for its variation are absorbed into the target  $C_l$  value.

A1 loop, which is further bolstered through careful choice of  $A_1$  and  $\overline{R}_c$  as described in Section 4.2.2.

Finally, if the small-signal resistance seen by  $R_d$  and attenuated through the shunt action of A1 loop is represented by  $r_{\text{out1}}$  (cf. Footnote 10), then placing  $R_d$  off chip, such that  $C_d = C_{\text{ext}}$  and invoking (4.1) and (4.11) produces a first-order model of the LNA frequency response

$$G_p(s) = \frac{Z_l}{Z_d} \simeq G_{\text{po}} \frac{1 + s/z_0}{1 + s/p_0} \quad (4.12)$$

in which the DC gain,  $G_{\text{po}} = R_l/R_d$ , is modified by a high-frequency zero at

$$z_0 = \frac{1}{(R_d \parallel r_{\text{out1}}) C_{\text{ext}}} \simeq \frac{1}{r_{\text{out1}} C_{\text{ext}}} \quad (4.13)$$

Since the LNA requires no global feedback, the reduction of this zero with excess  $C_{\text{ext}}$  is not nearly as detrimental as for  $p_0$ , but it may cause peaking in the magnitude response and an increase in noise bandwidth. Through careful layout of both SVEPRE and those PCBs for which it is intended, it is shown in Section 6.3.2 that even these effects are thwarted for  $C_{\text{ext}} \leq 10$  pF.

## 4.2 Implementation

Even with the architectural advantages afforded by the topology of Figure 4.5, additional techniques are required in the transistor-level implementation of the LNA to meet the full suite of demanding specifications. Proceeding through the inamp in the direction of signal flow, key representatives are highlighted in the remaining subdivisions of this section and their (not always direct) impact on the requirements of Table 3.2 teased out.

### 4.2.1 General Philosophy

Before delving into schematics, an example of the interplay between the architectural ideals and the implementation realities that motivate the aforementioned techniques is

instructive. To wit, consider the LNA linearity and total-dose hardness specifications of Table 3.2. A circuit which achieves the relation of (4.1) succeeds in satisfying both criteria, since the LNA gain is then independent of the large signal nonlinearities (cf. Section 3.1.2.3) and TDEs (cf. Section 2.1) of the underlying transistors, depending only on passive elements—resistors—which are substantially better on both counts.

However, the derivation of (4.1) (or even the approximation to it in (4.7)) is contingent on the ideality of blocks such as operational transconductance amplifier (OTA) A1 which are, themselves, susceptible to these shortcomings in practice. Thus, it is paramount in the construction of the OTA that the impact of these nonidealities is minimized. For example, OTAs that rely heavily on the fundamental amplification properties of their constituent transistors typically violate the conditions behind the derivation of (4.1), as is best demonstrated by presenting a pair of possible implementations.

#### 4.2.1.1 Single-Stage OTA

Consider the case of a common-emitter amplifier in Figure 4.7(a), operating in the large-signal regime where  $V_{be} = v_{in} + V_{BE}$  and  $I_c = i_{out} + I_C$ .<sup>13</sup> The gain-determining relationship, which can be derived from (3.10) as<sup>14</sup>

$$i_{out} = I_{H1} (e^{v_{in}/nV_T} - 1) \quad (4.14)$$

holds over several decades, seemingly making the npn BJT more apropos for amplification subject to the large-signal linearity requirements of this application than its MOS counterparts. However, the output current is directly proportional to  $I_C$  which, in unloaded configuration shown, is provided by current source H1 such that  $I_C = I_{H1}$ . Thus, the nonidealities of an H1 implementation are critical: any signal dependence (i.e., nonlinearity) associated with its finite output resistance,  $R_{o1}$ ,

<sup>13</sup>Note that contrary to conventional notation,  $v_{in}$  and  $i_{out}$  are not small-signal quantities. They merely represent the time-varying components of the base-emitter voltage and collector current, respectively, isolated from the corresponding DC components, as in Section 4.1.2.2

<sup>14</sup>Once again, the Early voltage is assumed infinite in this example as it is not central to and, in fact, only intensifies, the unwanted behavior in question.



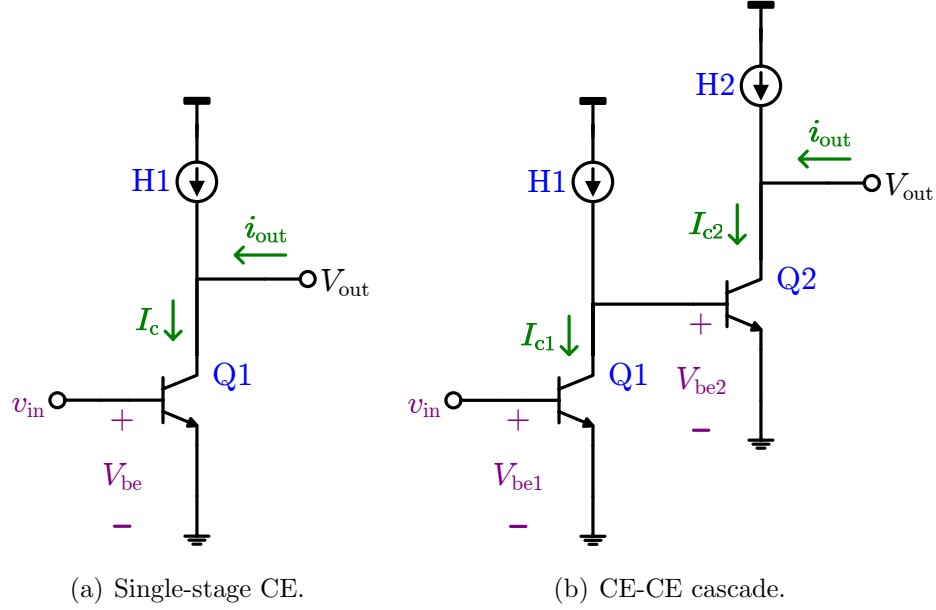


Figure 4.7: Potential single-stage and multi-stage OTA implementations. The gain and linearity of (a) a common-emitter (CE) are highly sensitive to  $H1$  while those of (b) a CE-CE cascade exhibit additional dependencies on device  $\beta_{a2}$  and  $H1$ - $H2$  mismatch.

or drop in  $I_{H1}$  due to radiation-induced  $g_m$  and  $\beta$  degradation directly impacts the gain, since  $A_1 = i_{out}/v_{in} \propto I_{H1}$ .

To assess the SFDR implications of these same issues, consider operation of the CE implementation of  $A_1$  at sinusoidal-steady state. Truncating the Taylor series expansion of the exponential in (4.14) for a sinusoidal input of the form  $v_{in} = v_i \cos(\omega_o t)$ , yields the ratio of the magnitude of the third harmonic to the fundamental, which typically dictates the overall SFDR in any well-designed differential system derived from the half-circuit of Figure 4.7(a), as

$$\frac{|Y(3\omega_o)|}{|Y(\omega_o)|} \simeq \frac{1}{24} \ln^2 \left( 1 + \frac{i_{out}}{I_{H1}} \right) \quad (4.15)$$

where it has been assumed that, although not small, the signal component of the output current satisfies  $i_c \ll 16I_C$ . From (4.15) it is clear that the linearity of the CE amplifier depends on both the static and signal-dependent portions of its output

current.<sup>15</sup> The former dependency is even stronger than in (4.14); in the limit of small signals ( $i_{\text{out}} \ll I_C$ ), the SFDR deduced from (4.15) is proportional to  $I_{\text{H1}}^2$ . Thus, it has been shown that the total-dose degradation and finite output impedance of any H1 realization violates the assumption of the large, perfectly linear  $A_1$  behind the derivation of (4.1).

#### 4.2.1.2 Multi-stage OTA

But, even postulating access to ideal current sources, the A1 implementation is not immune to these effects. Particularly vulnerable are more sophisticated, multistage realizations that provide large  $A_1$  and the concomitant benefits of high loop gain. The simple CE cascade of Figure 4.7(b) is exemplary of the typical interface between successive stages in a such an amplifier, for which the  $\beta$ -dependencies of gain and linearity are crucial. By analogy to (4.14), the large-signal AC gain relationship from  $v_{\text{in}}$  to  $i_{\text{out}}$ , which is now found at the collector of Q2, is

$$i_{\text{out}} = I_{\text{H1}} (\beta_2 - M_2) (e^{v_{\text{in}}/nV_T} - 1) \quad (4.16)$$

where  $\beta_2$  is the large-signal CE gain of Q2,<sup>16</sup> and in the unloaded configuration shown,  $I_{\text{C2}} = I_{\text{H2}} = M_2 I_{\text{H1}}$ . Even if current sources H1 and H2 are ideal, (4.16) indicates that the overall gain remains sensitive to TDEs insofar as they reduce  $\beta_2$  and degrade current source matching via  $M_2$ .

Additionally, since  $A_1 \propto \beta_2$ , the non-constant  $\beta$  effects exemplified in Figure 3.6

---

<sup>15</sup>It is hardly enlightening that the SFDR depends on signal size. Thus, only the ramifications of changes in the static bias current merit attention.

<sup>16</sup>A point of clarification regarding the scope of  $\beta_2$ : As defined in (3.10b),  $\beta$  is the ratio of the total current in the collector to that in the base. This quantity is contrasted with the  $\beta_{\text{DC}}$  and  $\beta_{\text{AC}}$  defined in (E.1) and (E.2), which pertain only to the static and small-signal regimes respectively. The ratio of the large signal currents,  $i_c/i_b$ , is not represented by any of these variants, so (4.16) is not simply (4.14) scaled by some ‘beta’ of Q2.

If, as an exercise, this ratio were to be computed in terms of defined betas and dubbed  $\beta_{\text{ls}}$ , the result would be

$$\beta_{\text{ls}} = \frac{i_c}{i_b} = \beta + \frac{I_B}{i_b} (\beta - \beta_{\text{DC}})$$

For  $\beta$  that is constant as a function of frequency,  $\beta_{\text{ls}}$  reduces to  $\beta$ , but otherwise depends on the relative strength of the AC and DC signal components, rendering it less than useful in (4.16) and (4.17).

translate directly to gain nonlinearities. Substituting (4.16) into (4.15) confirms that the SFDR of A1 depends strongly on both  $\beta_2$  and  $M_2$  according to

$$\frac{|Y(3\omega_o)|}{|Y(\omega_o)|} \simeq \frac{1}{24} \ln^2 \left( 1 + \frac{i_{\text{out}}}{I_{\text{H1}} (\beta_2 - M_2)} \right) \quad (4.17)$$

with these dependences becoming quadratic for small  $i_{\text{out}}$ . Thus, details of the circuit implementation, particularly the matching and output resistance of the current sources and the interstage loading effects of finite, nonlinear  $\beta$ , all of which are dose dependent, must be resolved if the resulting  $A_1$  is to satisfy the assumptions behind (4.1).

#### 4.2.1.3 Extrapolation

Since A1 ultimately appears in the first stage feedback loop, the constraints on the hardness and linearity of  $A_1$  are substantially ameliorated compared to those of the forward path elements. But, the latter are subject to the same concerns regarding current source construction and interstage loading, so the principles of the preceding examples can be extended to encapsulate the general design philosophy applied to all the transconductance elements of SVEPRE.

Specifically, wherever a highly linear, radiation-tolerant transconductance (or transimpedance) is required, the inherent gain of BJTs is abandon, and they are operated purely as voltage-mode devices, thereby escaping the intrinsic nonlinearities represented by the  $\beta_2$  and exponential terms of (4.16). Similarly, MOSFETs are employed purely as current-mode elements, wherein their ideal current gain from source to drain is leveraged to provide lossless summing operations. This effectively cedes all  $V$ -to- $I$  and  $I$ -to- $V$  conversions to the most linear and radiation-tolerant elements available—resistors—just as intended in (4.1).

Although transistor amplification is barred from residing in the forward path, it remains crucial to establish the governing feedback exemplified by A1. But, since the final expression for the LNA gain contains none of the small-signal parameters of the many active elements it employs, the power consumed by these transistors can be minimized, providing just simple level shifts in the forward path and enough  $L(s)$

to enact  $a'(s)$ . In fact, it is shown in Section 6.3.2.4 that even as the LNA gain is programmed from 0 dB to 24 dB, its power remains constant.

## 4.2.2 First Stage

The simplified schematic of the first stage of the LNA in Figure 4.8 highlights the implementation of the Q1-Q2-Rd-A1 loop by means of hybrid super emitter-followers with embedded level shifters. Using pMOS devices to fold the current from the first stage to the second, as opposed to the lateral pnps used by *Brokaw and Timko* [1975] offers several advantages. Among them, by not siphoning signal-dependent base current away from the collectors of Q1 and Q2, it preserves the linearity of their level shift better than a Darlington pair with less supply current or headroom required. Indeed, consumption of these resources is significantly less than in the A1 input stage of the canonical example, where attenuating the required input current presents the most intricate design challenge. This is especially crucial since the LNA is conservatively designed to handle double the required full-scale input swing ( $2 V_{PP}$  differential), affording sufficient design margin that linearity does not suffer at the extremes.

The next sections cite key details in the design of both the hybrid super emitter followers that comprise A1 and the series-shunt loop in which they are enclosed.

### 4.2.2.1 Super Emitter-Follower

Returning to the forward path represented by the degenerated differential pair of Figure 4.3, recall that resistive emitter degeneration of a standard differential pair through the addition of  $R_d$  constitutes a form of passive series-series feedback that greatly expands the range over which it behaves linearly [*Gray et al.*, 2001, p.587–591]. Adducing the simulated results in Figure 4.9,<sup>17</sup> this degeneration produces the classic hyperbolic tangent of (4.4) which exchanges reduced gain for an operating range governed, in the ideal limit, by an argument proportional to  $V_{in}/I_T R_d$  rather

---

<sup>17</sup>Perfect matching of Q1 and Q2 is assumed in the simulations of Figure 4.9 and Figure 4.10, such that  $\Delta\alpha=0$ ,  $\bar{\alpha}=\alpha$ ,  $A_{e1}=A_{e2}$ , and  $W_{b1}=W_{b2}$ .

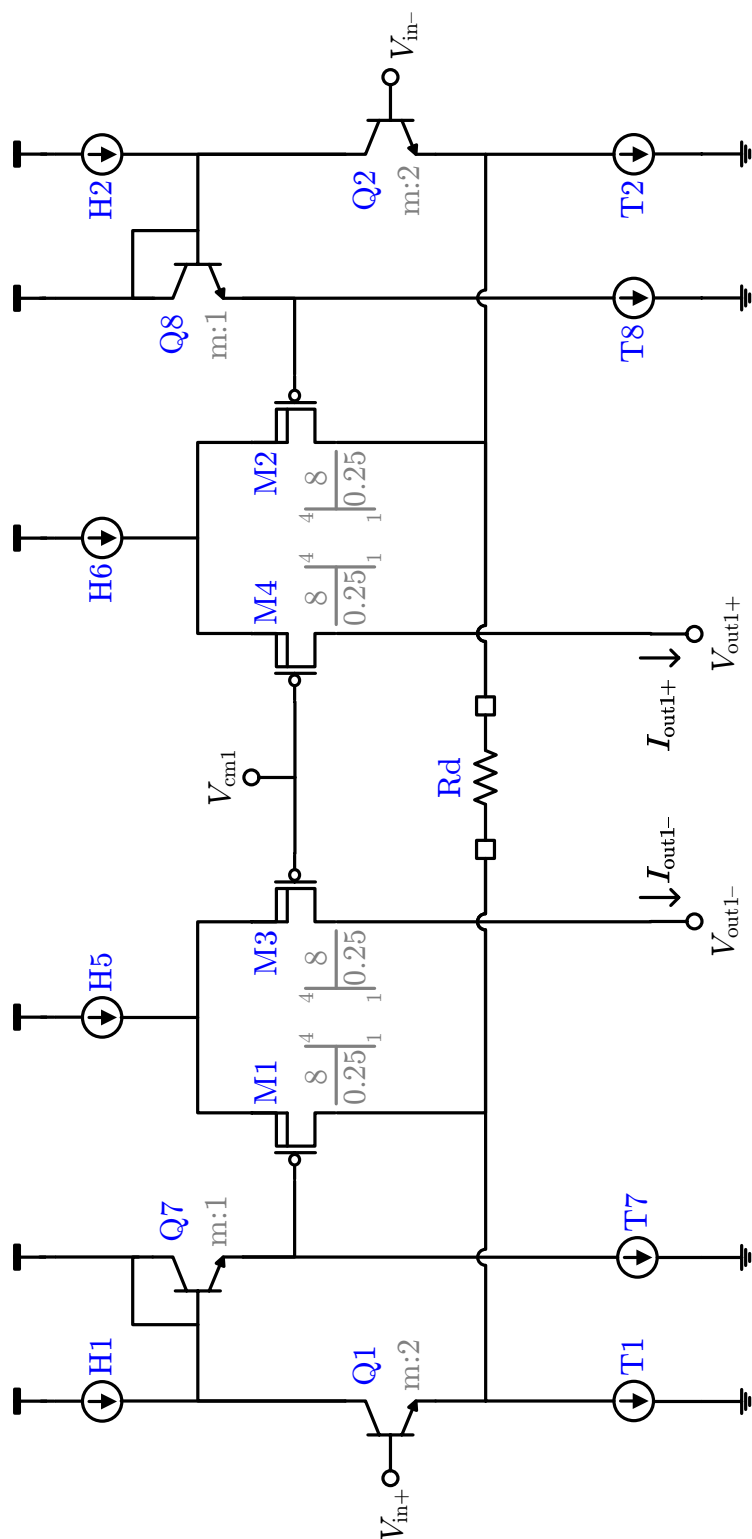


Figure 4.8: Implementation of first stage of Figure 4.5. For simplicity, all current sources are represented as ideal; their implementation details are presented in Section 4.2.4.

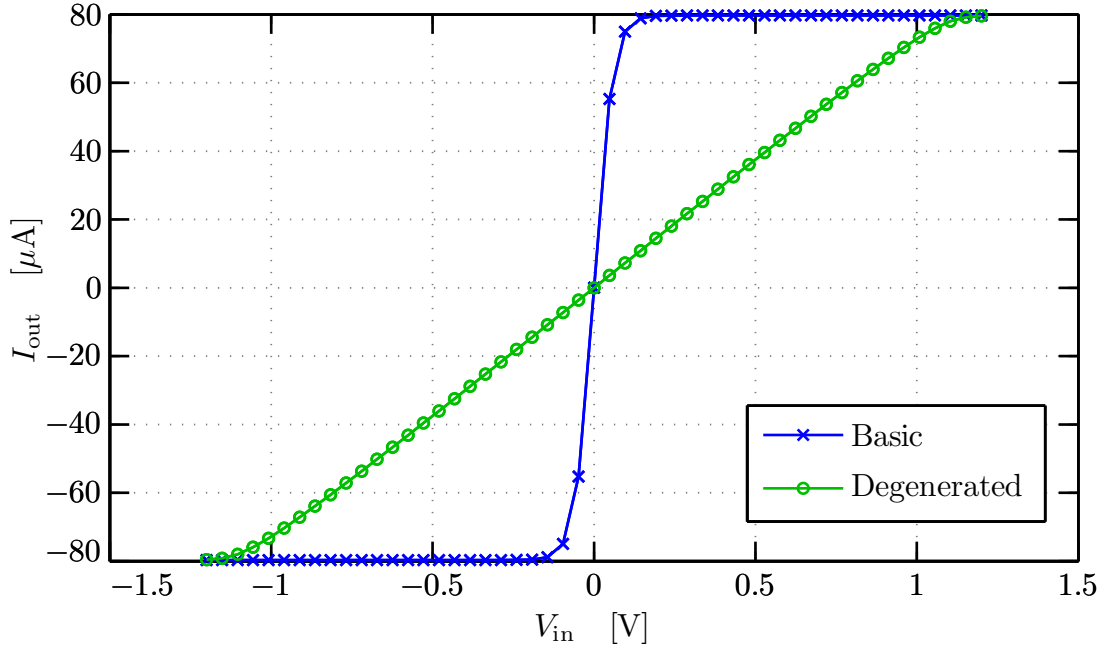


Figure 4.9: Simulated transfer function of degenerated differential pair in Figure 4.3 (in green) compared against that of basic differential pair (in blue). The wider unsaturated region of the former follows from the increased denominator of the argument of the hyperbolic tangent in (4.4).

than  $V_{\text{in}}/V_T$ . The larger the denominator of the former is advantageous since the curve begins to saturate when this argument exceeds unity.

In this application, the product  $V_d = I_T R_d$  is dictated by power dissipation constraints on  $I_T$  and the range of  $R_d$  required for programmable  $G_p$  given the  $R_l$  dictated by bandwidth requirements; together, these yield a range of 0.25–4 V. So, at a given gain setting,  $V_d$  is only a factor of four larger than the maximum input signal size, which means that the excursions of the latter can intrude into the nonlinear regions at the extremes of the transfer function in Figure 4.9. Gain distortion in these regions afflicts inputs well below 1 V because even the middle portion of the transfer function—which appears to be a straight line—is subject to nonlinearities that are accentuated when the transconductance,  $G_m = dI_{\text{out}}/dV_{\text{in}}$  is plotted as in Figure 4.10. Although the gain remains flat over more of the input range than in the basic case, it is not sufficiently independent of the input to achieve the desired SFDR

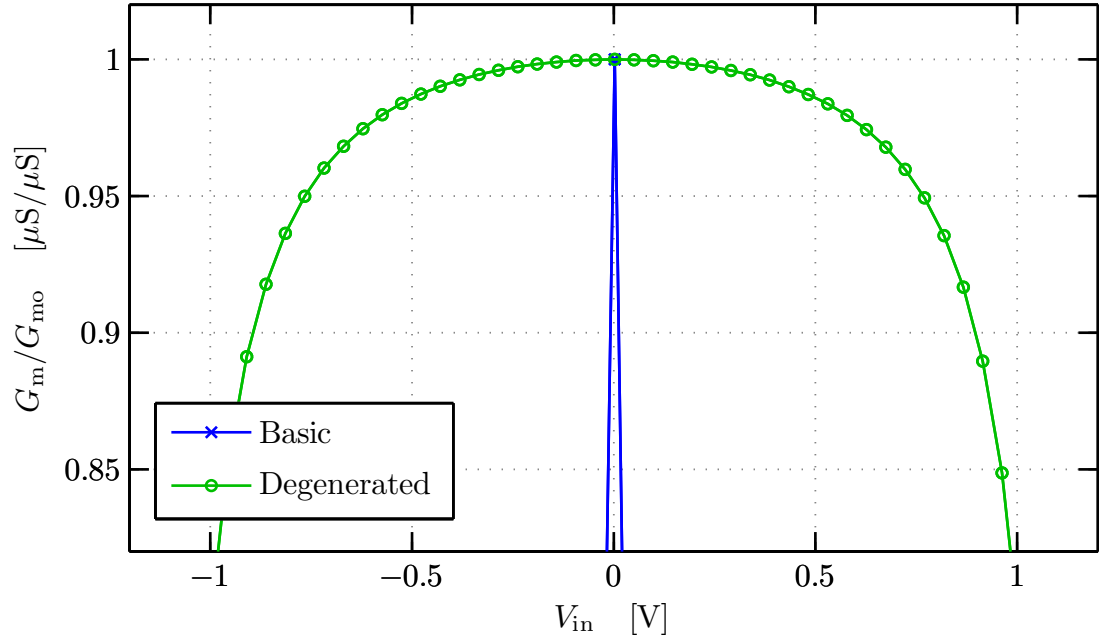


Figure 4.10: Transconductance gains corresponding to slopes of curves in Figure 4.9. Despite its transfer function appearing linear out 1 V, even the gain of the degenerated differential pair (in green) is not sufficiently flat over the full input range to achieve 90-dB SFDR.

of 90 dB at full-scale, even with degeneration.

The roll-off of the gain in Figure 4.10 is the manifestation of the  $\beta$  and  $\Delta V_{be}$  nonlinearities in the second term of (4.4). As noted in Section 4.1.1.2, these can be minimized by connecting A1 so as to take the output current across  $R_d$  and fix  $I_{c1}$  and  $I_{c2}$ , respectively. This is precisely the role played by Q5 and Q6 in the modification of Figure 4.3 shown in Figure 4.11. These devices handle all the signal-dependent current through  $R_d$ , thereby keeping the collector currents of Q1 and Q2 fixed. Converting Q1 and Q2 into so-called super emitter-followers [Gray *et al.*, 2001, p.213], this topology yields a transconductance, now measured at the emitters of Q5 and Q6, which is much flatter over a much wider range, as shown in Figure 4.12 and described by the second addend of (4.6).

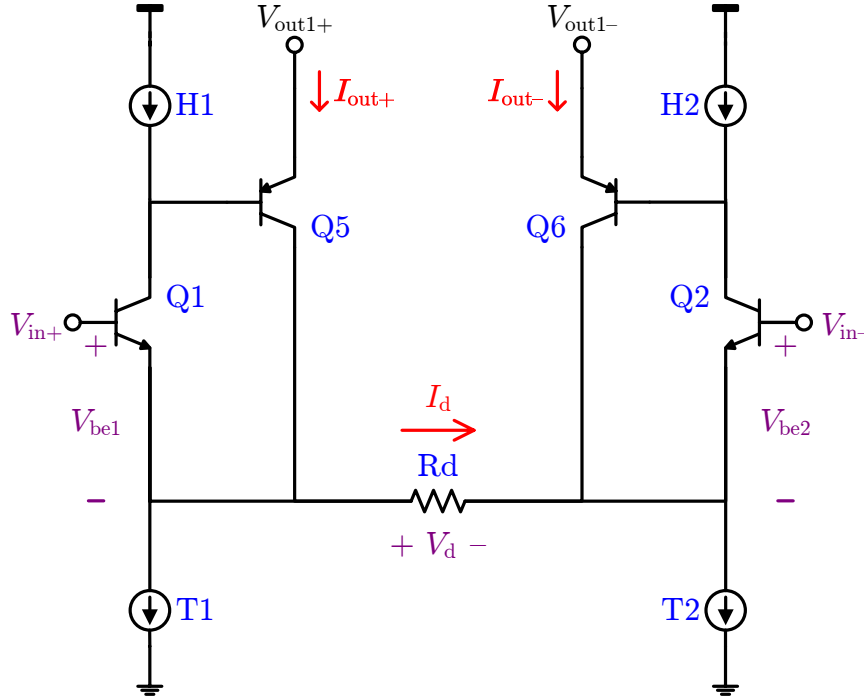


Figure 4.11: Conversion of Figure 4.3 into super emitter-follower. Taking the output current from the emitters of Q5/Q6 allows  $I_d$  to be extracted directly from  $R_d$ , keeping  $I_{c1}$  and  $I_{c2}$  (nearly) constant.

#### 4.2.2.2 Hybrid Super Emitter-Follower

However, this A1 implementation, poses two problems. The most obvious is that Q5/Q6 cannot be implemented with the available substrate pnps, since their collectors are differentially opposed. But, even if a polarity inversion were achieved through the use of an npn equivalent topology, a more serious limitation is the base current of these feedback transistors. Recall that the derivation of (4.6) assumed an idealized A1 that drew no input current. On the contrary, the signal-dependent base currents of Q5/Q6 subtract from the collector currents of Q1 and Q2, and since these increase with dose through the surface and bulk recombination mechanisms of Section 2.1.2.1, they cannot be neglected. Thus, a non-standard implementation of the super emitter-follower is necessary to preserve linearity under radiation.

The solution shown in Figure 4.8 replaces Q5 and Q6 with pMOS differential



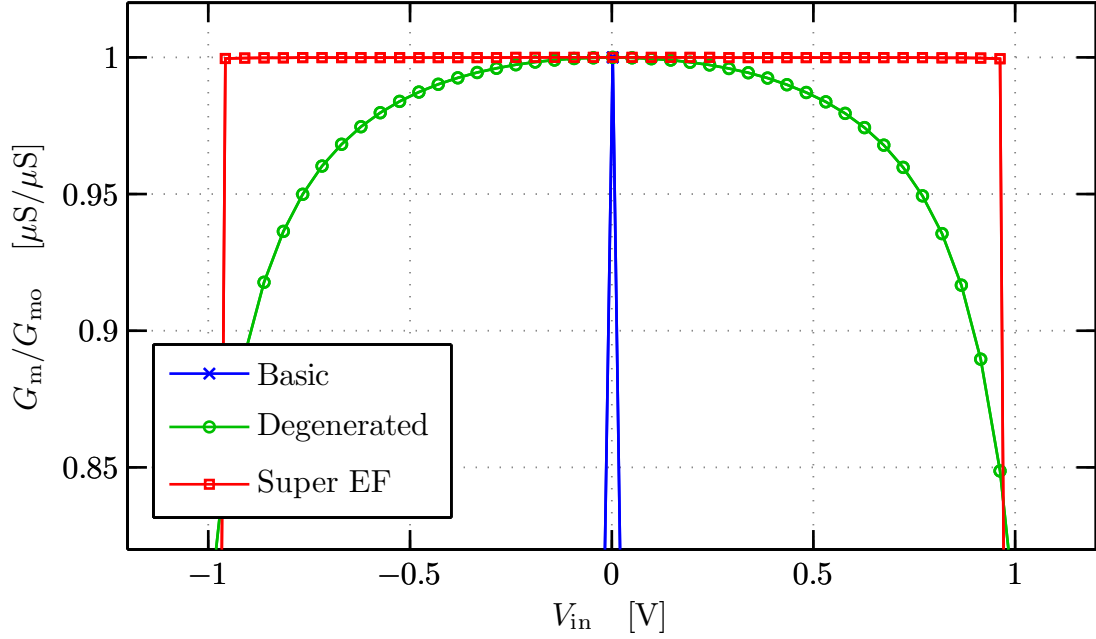


Figure 4.12: Transconductance gain of super emitter-follower compared to those of Figure 4.10. Inclusion of Q5 and Q6 in Figure 4.11 drastically improves the gain linearity (in red).

pairs M1–M4, which affords several advantages, provided they are sized carefully to satisfy flicker noise requirements. Chief among these is the fact that M1/M2 siphon no signal-dependent currents away from the collectors of Q1/Q2, thereby preserving the linearity of their level shifts and validating the description in (4.6). Additionally, by arranging these pMOS devices as differential pairs, the current from the first stage can be folded into the second with no  $g_m$ -dependent losses. As described in Section 4.2.1.3, pMOS current steering leverages the fact that all source current must arrive at the drain (i.e., the ‘base’ current is zero).

Two additional features of the final A1 implementation in Figure 4.8 bear special mention. First, the use of level-shifting devices Q7/Q8 is necessary to maintain sufficient headroom for sources H5/H6 with an input common-mode level of 1.75 V.<sup>18</sup> Since their emitter current is fixed, base currents  $I_{b7}$  and  $I_{b8}$  do not introduce any signal-dependence into  $I_{c1}$  and  $I_{c2}$ , preserving the aforementioned pMOS benefits.

<sup>18</sup>Assume that nominally  $V_{cb1,2} = 0$ .

Any  $\beta_{7,8}$ -degradation introduces a small, fixed drop in the LNA input currents ( $I_{b1}$  and  $I_{b2}$ ).

Secondly, the use of pMOS current sources H1 and H2 (cf. Section 4.2.4.2) in place of collector resistors R1 and R2 drastically increases  $L(s)$  via  $\bar{R}_c$ . Although their currents are small ( $I_{H1,2} = 2.5 \mu\text{A}$ ) so as to limit the input bias current of each LNA terminal to just 10 nA, their large output resistance allows the linearization that produces (4.7) to hold even though the maximum  $\varepsilon_{\text{swing}} \gg 1$ , with  $I_d$  reaching  $8I_{H1,2}$  for full-scale inputs.

### 4.2.2.3 Series-Shunt Loop

Thus far, the assessment of the hybrid super emitter-follower implementation has addressed its impact on large-signal LNA properties governed by the nonlinear characteristic of (4.2); namely, gain and linearity. To obtain design insight into how this choice impacts two additional specifications, namely input impedance and noise, its frequency response can be assessed in the linearized small-signal domain using two-port feedback theory.<sup>19</sup>

The effect of introducing A1 around the degenerated differential emitter follower in Figure 4.5 is to improve its performance as a voltage amplifier through series-shunt feedback.<sup>20</sup> The appropriate block diagram for such a system is given in Figure 4.13. But, as in the presence of an emitter resistor, the super emitter-follower is a degenerative case that conforms poorly to this model, since the sensing of the output voltage takes place at an intermediate node, namely the collector of Q1.<sup>21</sup> Such degenerative single-stage feedback is best handled by just considering small-signal model directly [Gray *et al.*, 2001, p.589].

<sup>19</sup>For a thorough review of basic two-port feedback theory, including the effects of loading by the feedback network, the reader is recommended to Chapter 8 of either [Gray *et al.*, 2001] or [Razavi, 2001].

<sup>20</sup>This configuration is known as ‘series-shunt’ because the feedback network is connected in *series* with the input port of the plant, returning a voltage, and *shunts* the output port, sensing the voltage there. For this reason, it is also known as ‘voltage-voltage’ feedback [Razavi, 2001, p.258].

<sup>21</sup>In the case of an emitter resistor, the degenerative condition, which gives rise to the name of the technique—emitter degeneration—arises because the sense and return paths connect to the same port (i.e., the emitter).

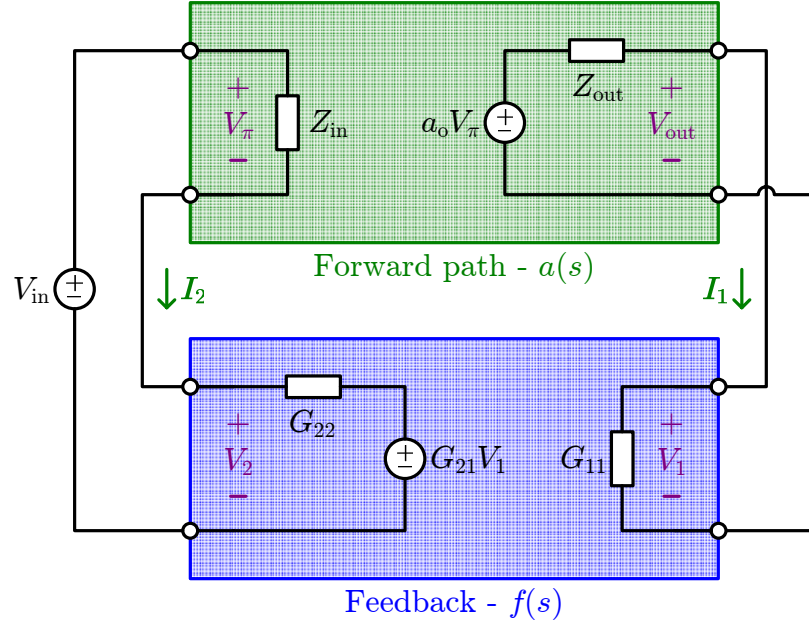


Figure 4.13: Block diagram of canonical series-shunt feedback, as pertains to the active loop of LNA input stage depicted in Figure 4.8. It is typically assumed that the reverse conductance of the feedback block,  $G_{12}$  is negligible. After [Gray *et al.*, 2001, p.580].

The differential half-circuit in Figure 4.14(a) is comprised of the Q1-M1-M3 portion of the A1 loop in Figure 4.8, wherein the output resistance of M3 is assumed sufficiently large that its drain load can be neglected. In this case, the transconductance of M3 simply degenerates M1, resulting in the simplified model of Figure 4.14(b) in which the latter is replaced by an equivalent M2, featuring

$$g_{m2} = \frac{g_{m1}}{1 + g_{m1}r_F} \quad (4.18a)$$

$$r_{o2} = r_{o1} (1 + g_{m1}r_F) \quad (4.18b)$$

$$Z_{\pi2} = Z_{\pi1} (1 + g_{m1}r_F) \quad (4.18c)$$

The effects of the M1 degeneration are encapsulated by the degenerate loop gain  $1 + g_{m1}r_F$ , where  $r_F = r_{H5} \parallel 1/g_{m3}$ .

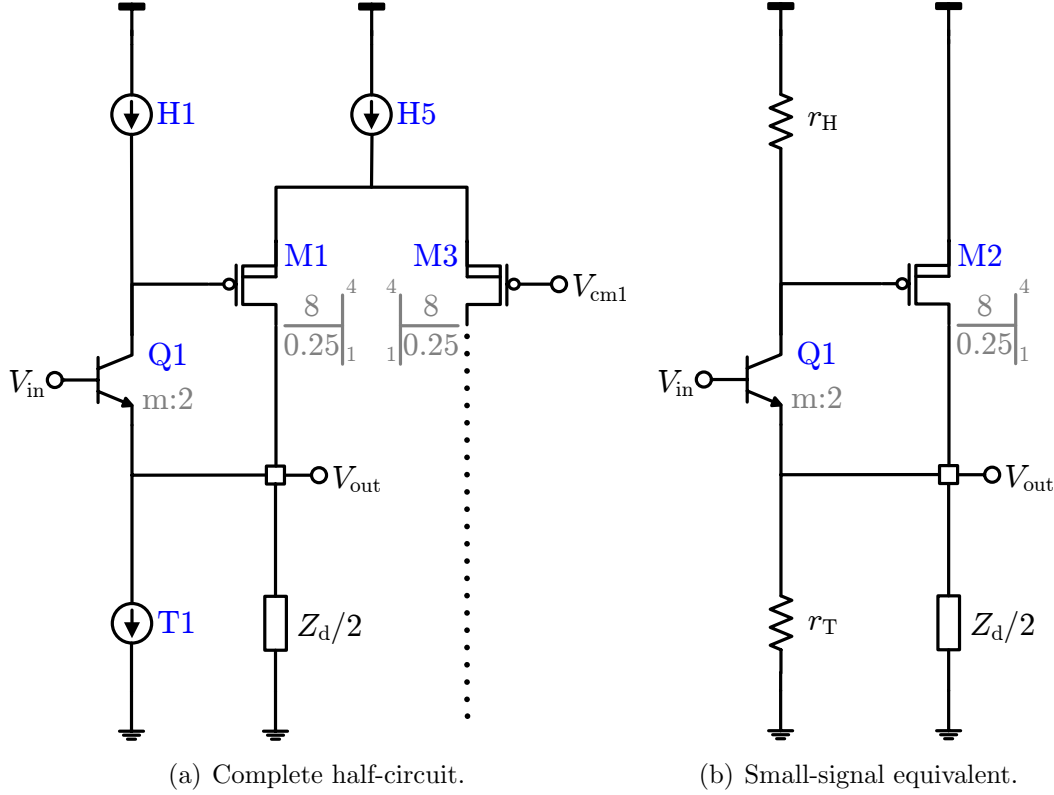


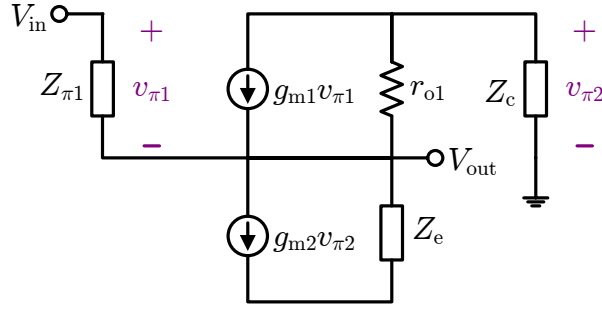
Figure 4.14: Half-circuit of Figure 4.8 (positive side). From (a) the complete half-circuit it is possible to derive (b) a small-signal equivalent in which all current sources are replaced by their output resistances and  $M2$  encapsulates the degeneration of  $M1$  by  $M3$  and  $H5$  (cf. (4.18)).

### Loop Gain

From the small-signal model of Figure 4.14(b), which has been reduced to the form of Figure 4.15, it can be shown that the loop gain afforded by the hybrid super emitter-follower implementation for the case of  $g_{m1}r_{o1} \gg 1$  is approximately

$$L(s) \simeq g_{m2}Z_c \frac{g_{m1}}{g_{m1} + (Y_{\pi 1} + Y_e) \left(1 + \frac{Z_c}{r_{o1}}\right)} \quad (4.19)$$

The leading coefficient should be familiar: it is half the differential  $L(s)$  derived previously, where  $\frac{1}{2}A_1 = g_{m2}$  and  $\bar{R}_c = Z_c$ . Breaking the loop at the gate of  $M1$ ,



$$Z_c = r_H \parallel Z_{\pi 2}$$

$$Z_e = r_{o2} \parallel r_T \parallel Z_d/2$$

Figure 4.15: Small-signal circuit derived from Figure 4.14(b). Given large input and output impedances, this low-frequency incarnation, neglecting BJT small-signal capacitances such as  $C_\mu$  and  $C_\pi$  is appropriate. However,  $C_{gs2}$  is subsumed in  $Z_{\pi 2}$ .

(4.19) is simply the product of the gains of the common-source amplifier M2 and common-base amplifier Q1, where the fraction in (4.19) discounts for the portion of the former's current diverted into  $Z_e$  before reaching the latter. Compared to the  $L(s)$  of Section 4.1.1.2, derived for ideal conditions in which the signal current in  $R_d$  is negligible compared to the Q1/Q2 bias, the fractional part of (4.19) produces a loop gain one-tenth the ideal since this resistor is small ( $\sim 10 \text{ k}\Omega$ ) at the nominal gain. However, sufficient DC loop gain ( $\sim 80 \text{ dB}$  at nominal  $G_p$ ) is maintained by the large  $g_{m2}$  and  $Y_{\pi 2}$  of M1 and the high  $r_H$  realized by the head current sources of Section 4.2.4.2.

### Loop Stability

Consideration of (4.19) for various  $G_p$  reveals that whereas the DC loop gain indeed decreases with  $R_d$  (via  $Y_e$ ), the bandwidth of the loop does not since the dominant pole, which is contributed by  $Z_c$ , lies at

$$p_0 \simeq \frac{1}{r_h \parallel \left(1 + \frac{g_{m1}R_d}{2}\right) r_{o1} \parallel Z_{\pi 2}} \simeq 100 \text{ kHz} \quad (4.20)$$

So, the linearity and input impedance benefits of A1 persist over the bandwidth of interest. However, excessive  $C_{\text{ext}}$  or increased  $R_d$  can decrease the non-dominant pole in the denominator of (4.19), eroding phase margin, since its location can be approximated by  $z_o$  of (4.13) and given formally by considering the output impedance seen by these components with  $g_{m1}r_{o1} \gg 1$  and  $g_{m2}Z_c \gg 1$ :<sup>22</sup>

$$Z_{\text{out}1} \simeq 2 \left( r_T \parallel r_{o2} \parallel Z_{\pi1} \parallel \frac{1}{g_{m2}Z_c} \frac{r_{o1} + Z_c}{g_{m1}r_{o1}} \right) \quad (4.21)$$

Since  $L(s)$  is so large, the final term of (4.21) dominates, yielding an output resistance on the order of ohms that can tolerate  $C_{\text{ext}}$  up to 30 pF for the worst-case gain  $G_p = 0$ .

### Input Impedance

The small-signal model of Figure 4.15, also yields insight into the input impedance, which is plotted in Figure 4.16 for various  $R_d$  and can be derived for high loop gain (i.e.,  $g_{m2}Z_c \gg 1$ ) as:

$$Z_{\text{in}} \simeq 2 \left( Z_{\pi1} + Z_e \frac{r_{o1} + Z_c + \beta_1 r_{o1} g_{m2} Z_c}{r_{o1} + Z_c + Z_e g_{m2} Z_c} \right) \quad (4.22)$$

Since the behavior of  $|Z_{\text{in}}(f)|$  cleaves closely to the model  $Z_{\text{in}} = R_{\text{in}} \parallel C_{\text{in}}$  (except near 30 MHz, due to simulation artifacts), the gain-dependent variations of these parameters, 18.3 G $\Omega$ –4.79 G $\Omega$  and 4.24–14.1 fF, respectively, are easily extracted and seen to satisfy the ideal voltmeter operation sought, even for gains beyond the recommended operating range (scilicet, 28 dB).<sup>23</sup> The cumulative amplification of

<sup>22</sup>This result neglects the influence of the source resistance, which are larger than in most applications. Strictly speaking, its contribution cannot be directly added in series with  $Z_{\pi1}$ , since it also changes the effective  $g_{m1}$ . However, since this effective  $g_{m1}$  is still amplified by  $L(s)$ , the change to the last term of (4.21) is negligible and such accounting can be employed without materially affect the pole location.

<sup>23</sup>Intuition suggests that if the A1 loop succeeds in keeping  $I_{c1,2}$  and thus  $V_{be1,2}$  constant, then  $r_{\pi1,2}$  and  $C_{\pi1,2}$  do not see any change in the voltage across them. This is the basis for the increased input impedance and results in the latter being obviated such that  $C_{\text{in}}$  is actually dominated by  $C_{\mu1,2}$ . But, even these are each less than 10 fF and with Miller multiplication thwarted by A1, which keeps the collector voltages of Q1 and Q2 nearly constant, yield an effective  $C_{\text{in}}$  so small that practically speaking, the LNA input capacitance is set by the choice of packaging and the fastidiousness of the board layout, the stray parasitics associated with which may be desried in

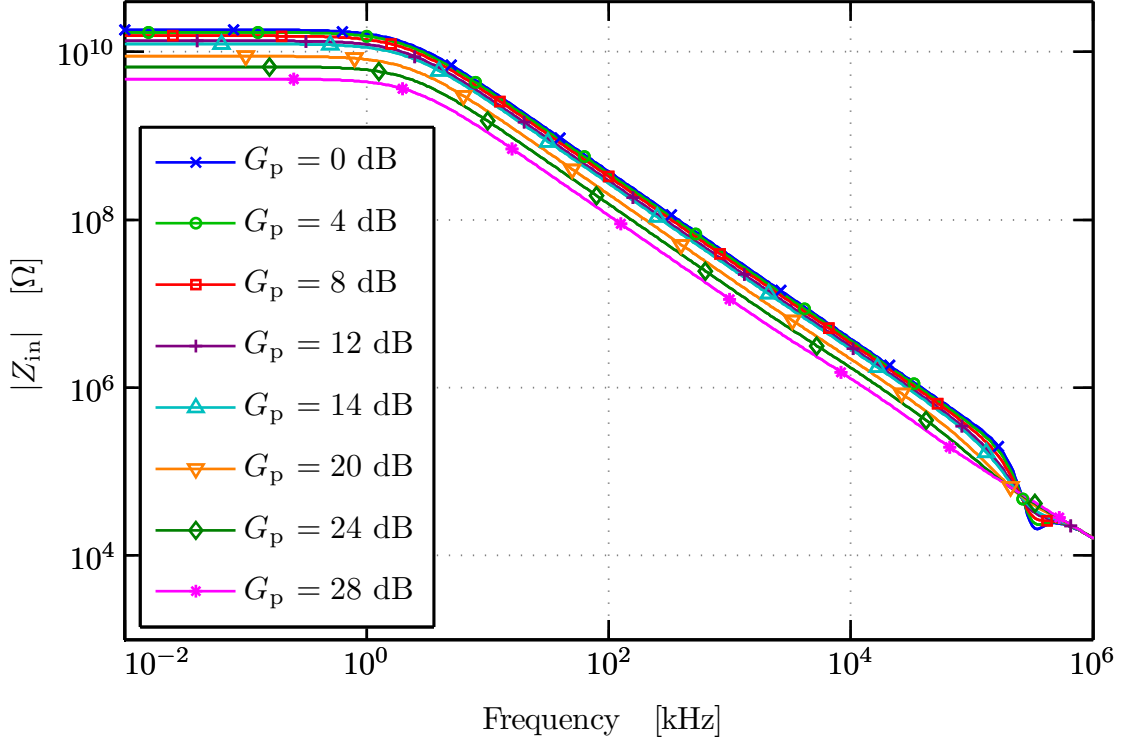


Figure 4.16: Simulated magnitude of LNA input impedance for various gain settings from 0 dB to 28 dB (beyond range). Despite the gain-dependence as  $|Z_{in}|$  decreases(increases) along with the loop gain as  $R_d$  decreases(increases) at higher(lower) gain settings, its absolute value far exceeds the specifications.

the intrinsic  $Z_{\pi 1}$  by factors of  $(1 + g_{m1}Z_e)$  and  $(1 + g_{m2}Z_c)$  as a result of connecting in series with the input terminal the emitter degeneration and A1 loops, respectively, is so great that (4.22) is limited only by the finite  $I_b$  required by  $\beta_1$  and hence, at low gains, approaches the theoretical maximum of  $Z_{\pi 1}(1 + g_{m1}r_{o1})$  [Gray *et al.*, 2001, p.200].

### 4.2.3 Second Stage

The currents folded by the pMOS differential pairs in the first stage of the LNA are fed to the second stage depicted in Figure 4.17. The distinguishing feature of this stage is the elimination of feedback amplifier A2 to reduce power consumption, avoid

---

Figure 4.6.

common-mode instabilities, and generate a fully differential output.

Incited by the inevitable trade-offs are two complications. First, the amplified signal across  $R_l$ , which can reach  $2 V_{PP}$  (including healthy design margin), must be faithfully reproduced at a low-impedance output node capable of driving the pnp AAF inputs.<sup>24</sup> As it is a voltage-mode signal, this operation, though it need have no gain, cannot employ MOSFETs in the signal path. Secondly, in contrast to the first stage, where A1 provided both differential and common-mode feedback, with the latter responsible for keeping the collectors of Q1 and Q2 at  $V_{cmi} = 1.75$  V, the absence of A2 leaves unclaimed the task of establishing a firm common-mode level to which the AAF input swing can be pegged. The following sections describe how the design of the second stage output buffers and load, respectively, compensate for these deficiencies.

#### 4.2.3.1 Output Buffer

Diode-connecting transistors Q3 and Q4 unequivocally establishes the common-mode level at their collectors without the need for feedback via A2. In addition, it presents a high output impedance to currents from the previous stage—approximately,  $2(r_{h3,4} + 1/g_{m3,4})$ —inducing them to flow through  $R_l$  and  $C_l$ , as desired. However, their  $V_{be}$ -shift is only constant so long as H3/H4 have infinite output impedance and Q5/Q6 draw no base current. Since neither is strictly true, additional measures are necessary to prevent nonlinearities from seeping into  $V_{out}$ .

The first technique, the deployment of high-impedance, low-headroom pMOS current sources to drive Q3/Q4, is taken up in greater detail in Section 4.2.4.2. Here, it suffices to note that both properties reflect a concern for the linearity specifications. Since the collectors of Q3/Q4 are biased at a common-mode level of 1.75 V (cf. Section 4.2.3.2), full-scale signal swing reduces the headroom of H3/H4 down to just

---

<sup>24</sup>Unlike A1, which is an OTA, A2 is a voltage buffer that drives the bases of Q3 and Q4 as well as any output load. The same low output impedance and high slew rate are required of the modified second stage because, unlike many CMOS designs, which only drive capacitive loads and can use OTAs exclusively, the SVEPRE AAF described in Chapter 5 uses pnp inputs that present a decidedly finite, and relatively low, resistive load that must be driven without distortion over the full-scale output range.



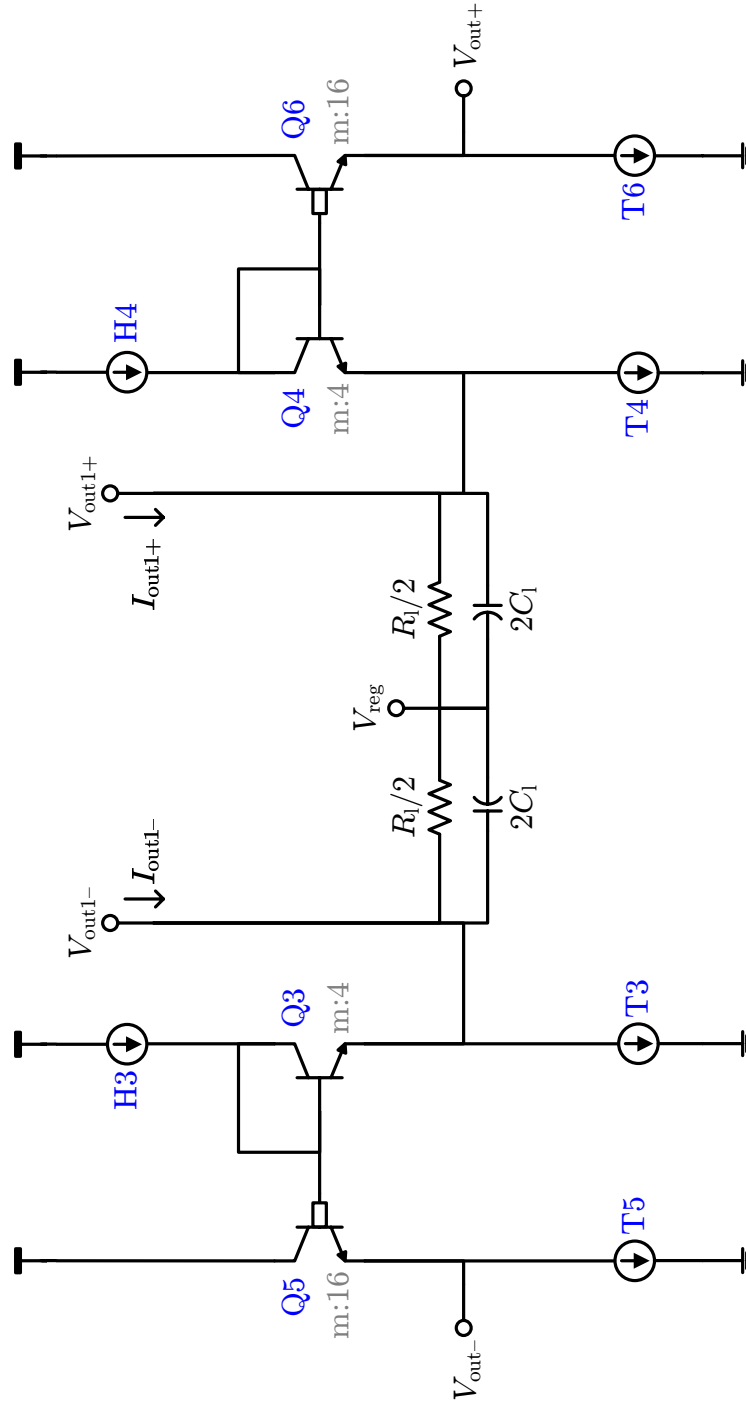


Figure 4.17: Implementation of second stage of Figure 4.5. For simplicity, all current sources are represented as ideal; their implementation details are presented in Section 4.2.4.

250 mV. This certainly cannot support a standard cascade stack and threatens to push the devices into triode, changing the drain current as a function of output signal size. The challenge of maintaining high output resistance with so little headroom is tempered by the fact that linearity typically improves with higher bias currents, since signal fluctuations span a comparatively smaller range. Free of the input bias current specifications by which Q1/Q2 was constrained, there is no need to minimize the base currents of Q3/Q4. With higher collector current bias, signal-dependent changes in  $I_{H3,4}$  are proportionately smaller, which keeps the argument of the hyperbolic tangent that defines  $V_{be3,4}$  small.

To compensate for the residual nonlinearity in the signal at collectors of Q3/Q4, it is buffered by simple, Class A followers Q5/Q6. Not only does such a driver offer higher linearity than its push-pull and Class AB counterparts [Lee, 1998, p.246], but it corrects for  $V_{be}$  nonlinearities of the Q3/Q4 level shift since it shifts the signal back down through a complementary  $V_{be}$ . Mathematically,<sup>25</sup> the net offset through the Q3–Q6 buffer excised in Figure 4.18 is:

$$V_{out} - V_{in} \simeq nV_T \left[ \ln\left(\frac{A_{e4}A_{e5}}{A_{e3}A_{e6}}\right) + \ln\left(\frac{W_{b3}W_{b6}}{W_{b4}W_{b5}}\right) + \ln\left(\frac{I_{H3}}{I_{H4}}\right) + \ln\left(\frac{\alpha_3\alpha_6}{\alpha_4\alpha_5}\right) - 2\sinh\left(\frac{I_{out}}{2I_{out}}\right) \right] \quad (4.23)$$

The first two terms of (4.23) depend on transistor matching (cf. Section 4.3.1.1); the third on current source matching (cf. Section 4.2.4.2). The fourth suffers from non-constant  $\beta$  but only mildly so since: for large absolute  $\beta_x$ ,  $\alpha_x$  is largely independent of bias; and, provided Q3–Q6 are biased near peak  $\beta$ , the quasi-symmetric character of the curves in Figure 3.6 causes any increases(decreases) of  $\alpha_3(\alpha_4)$  in the numerator(denominator) to be largely canceled by those of  $\alpha_5(\alpha_6)$  in the denominator(numerator).

Therefore, the final term of (4.23) is the primary source of nonlinearity in the

---

<sup>25</sup>Those familiar with the translinear principle will observe that its application to Figure 4.18 trivially yields (4.23) under the assumption of balanced output currents. However, this alternative interpretation is reserved for the transconductor described in Section 5.4.2, since the principle is formally introduced in Section 5.4.2.1.

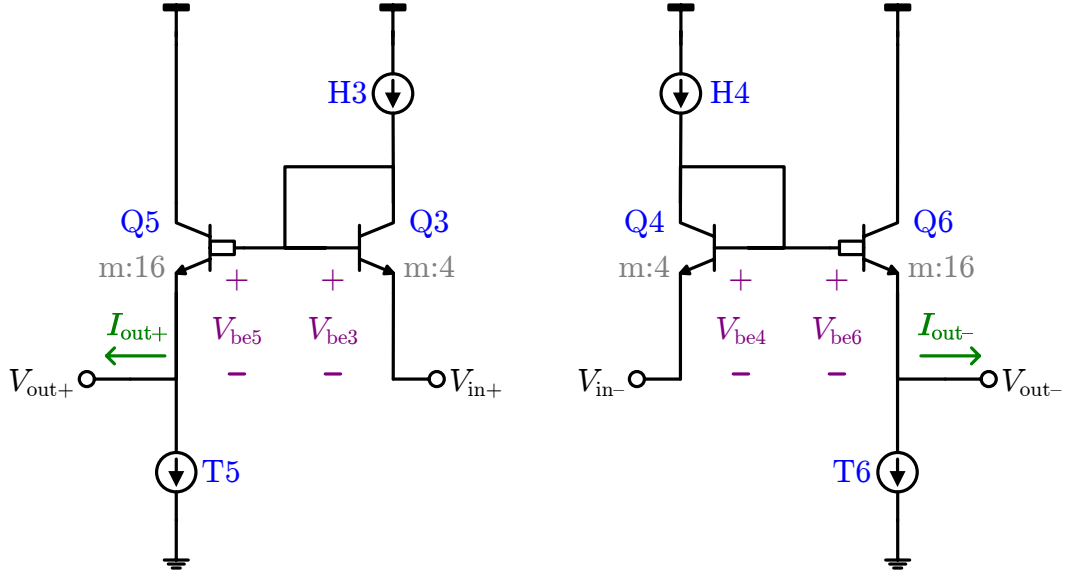


Figure 4.18: Output buffer chain extracted from Figure 4.17. For low output swings, the nonlinear up-shift of  $V_{in}$  through  $V_{be3,4}$  is canceled by the down-shift through  $V_{be5,6}$ .

output buffers. To minimize it, the bias currents of Q5/Q6 are set much larger than those than those of Q3/Q4 ( $160\ \mu\text{A}$  versus  $5\ \mu\text{A}$ ), subject only to the constraint that  $I_{H3,4} \gg \bar{I}_{out}/(\beta_{5,6} + 1)$ , which was used in deriving (4.23). This also lends the LNA a higher slew rate, which is useful for driving the large loads of the test equipment, up to a single-ended maximum of  $6.4\ \text{pF}$  ( $21\ \text{pF}$ ) for a  $1\ \text{V}$  ( $1.2\ \text{V}$ ) sinusoid at  $4\ \text{MHz}$  ( $1\ \text{MHz}$ ). Additionally, since the argument of the hyperbolic tangent is inversely proportional to the size of the LNA load, the input impedance of the transconductors in the first stage of the AAF is enhanced to ensure  $I_{out}/\bar{I}_{out} < 10^3$ .

#### 4.2.3.2 Load Impedance

The diode-connection of Q3/Q4 accommodates a simple, feed-forward, common-mode network free of the load-dependent stability concerns and greater power dissipation that attend a traditional sense-and-return scheme. The common-mode output level is established by driving the midpoint of Rl with an on-chip voltage regulator (cf. Section G.2.1). By employing the same voltage regulator to bias other elements of

the circuit, thereby amortizing its power dissipation, this approach achieves a net savings over a dedicated CMFB amplifier. Additionally, to the extent that paired currents sources on the lateral(vertical) halves of the LNA are well matched, the drive current required at this feed-point is low and its noise is attenuated by the CMRR. The lone drawback of splitting RI is the need to match both segments; this topic is addressed in Section 4.3.1.2.<sup>26</sup>

#### 4.2.4 Current Sources

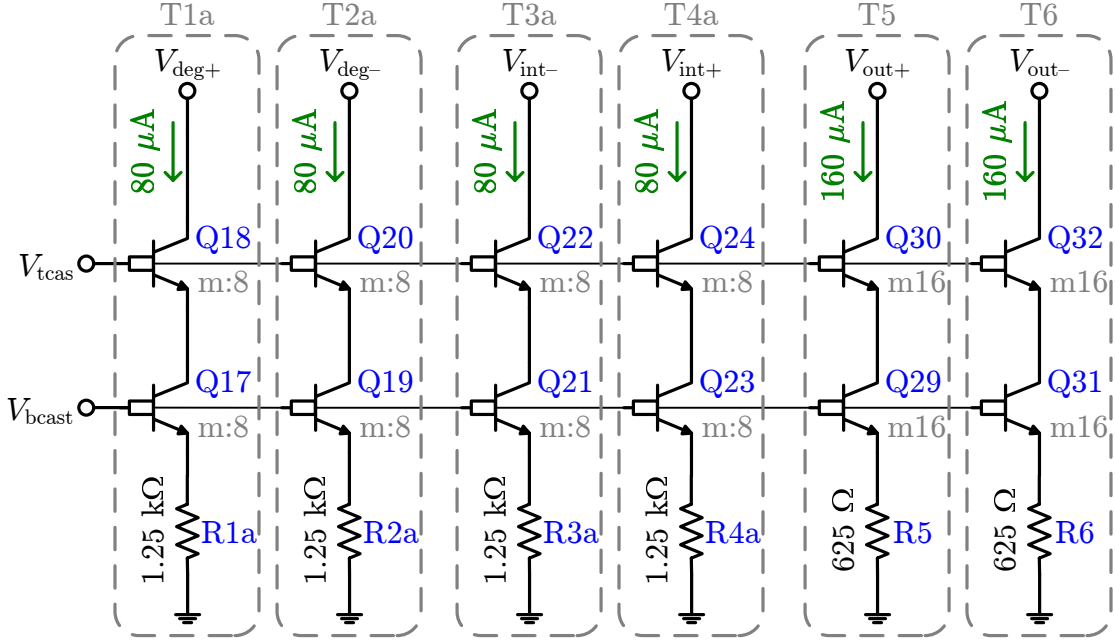
Many of the gain expressions in the preceding circuit analysis require that either the tail (bottom-rail) or head (top-rail) current sources being steered through the current-mode networks are well-matched between the two halves of the circuit and possess high output impedance in order to achieve high linearity and low offset. In addition, the common-mode levels of nodes fed by both tail and head sources depend on the matching between these two networks to achieve high dynamic range. Thus, a brief review of these networks and their biasing follows.

##### 4.2.4.1 Tail Current Sources

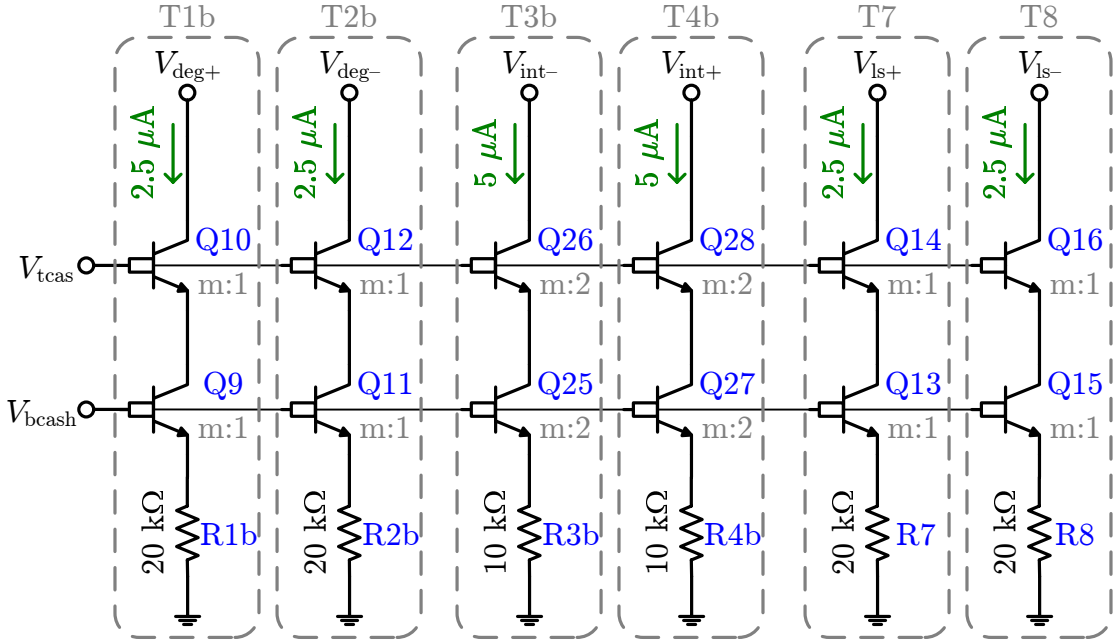
To improve matching, reduce noise, and increase output resistance [Bilotti and Mariani, 1975], the tail current sources are resistively degenerated with  $V_{\text{deg}} \simeq 100 \text{ mV}$  ( $V_{\text{deg}} \simeq 50 \text{ mV}$ ) for the high(low) current branches shown in Figure 4.19(a)(Figure 4.19(b)) and identified by the moniker of their bias voltage, bcast(bcash). Apart from minimally intruding on the limited headroom available to the main signal path, these values are shown to yield the desired level of current matching according to the simulations of Figure 4.20. Since the noise of these slave branches is differential mode, the degeneration resistors are implemented with  $p^+$  diffusion (RPD), which offers an order-of-magnitude lower  $K_F$ . However, their low sheet resistance and

---

<sup>26</sup>As depicted in Figure 4.17, CI is also implemented as two differential halves, but their matching is less crucial to both the DC bias point and the linearity of the differential gain. Although every effort is made to reduce their lithographic mismatch through conservative layout techniques (cf. Section 5.6.1.2), the effects of any phase mismatch above 10 kHz can easily be absorbed into the front-end transfer function since their capacitance does not vary with dose.



(a) High-density (bcast) branches.



(b) Low-density (bcash) branches.

Figure 4.19: Implementation of LNA tail current sources. Both the (a) high-density (bcast) branches, with a current density of  $8 \mu\text{A}/\mu\text{m}^2$ , and the (b) low-density (bcash) branches, at  $2 \mu\text{A}/\mu\text{m}^2$ , are degenerated and cascoded.

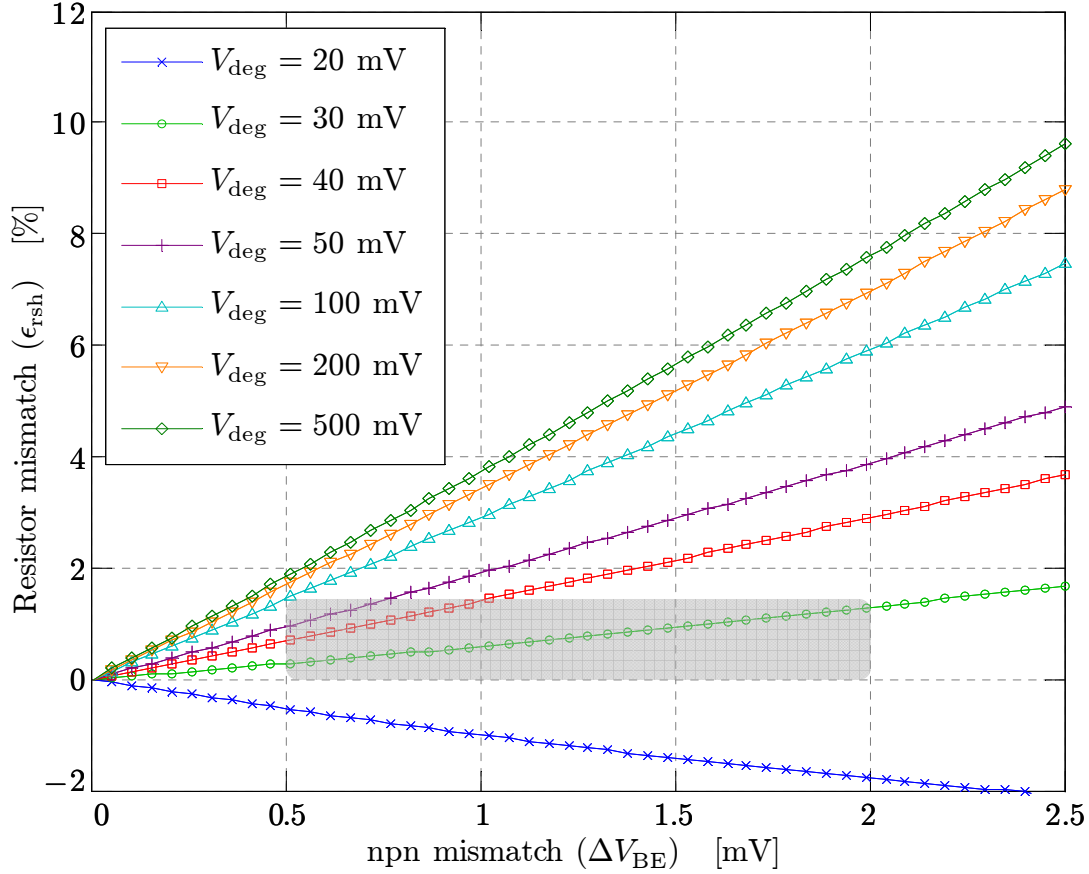


Figure 4.20: Mismatch of current sources in Figure 4.19 as a function of  $V_{\text{deg}}$ . For each  $V_{\text{deg}}$ , degeneration only improves matching when the region defined by the distributions of underlying npn mismatch ( $\Delta V_{\text{be}}$ ) and percent resistor mismatch ( $\epsilon_{\text{rsh}}$ ) lies beneath the corresponding line. For the provided 1- $\sigma$  process tolerances (gray box), the minimum  $V_{\text{deg}}$  of 100 mV improves matching by  $\sim 3x$ ; a more aggressive  $V_{\text{deg}}=50$  mV by  $\sim 1.7x$ .

susceptibility to voltage modulation (cf. Section 4.3.1.2) result in a large layout penalty.

### Construction

Given signal swings of up to 1 V at the nodes they feed, the output resistance of these sources cannot be increased by a simple cascode. However, a low-voltage cascode [Razavi, 2001, p.143–145] that ensures at least  $V_{ce} = 200$  mV for both devices, in conjunction with the degeneration, yields a small-signal output resistance that, in the case of T1b, is given by:

$$r_{T1} \simeq r_{o10} [1 + g_{m10} (1 + g_{m9} R_{1b}) r_{o9}] \simeq \beta_{10} r_{o10} \quad (4.24)$$

As for the input resistance of (4.22), the last approximation of (4.24) represents the theoretical limit approached when the effective emitter resistor seen by Q10 is so large that changes in its base current are the dominant contribution to its output resistance. For T1b(T1a), which is of the low(high) current variety, (4.24) yields an approximate output resistance of 26 G $\Omega$ (850 M $\Omega$ ).

To allow this result to hold for output voltages below 500 mV would require that Q18 and Q20 carry lower current densities, reducing their  $V_{BE}$ . However, the allowable multiplication factor for these devices is constrained by the fact that, through the success of the A1 loop and output buffers, the nonlinear junction capacitance ( $C_\mu$ ) of the cascade devices is actually the limiting factor in terms of linearity. To highlight this, simulated large-signal harmonics for the LNA with  $C_\mu = 0$  in all tail source cascades are compared against the actual performance in Figure 4.21. Thus, headroom is traded for linearity in SVEPRE-3 by using the minimum allowable  $m$ -factors for the tail current sources.<sup>27</sup>

---

<sup>27</sup>For matching, it is preferred that  $m > 1$ . The exception is for the low current network, where the need to divide down the current in the master branch with minimum area demands unity sizing of the slaves.

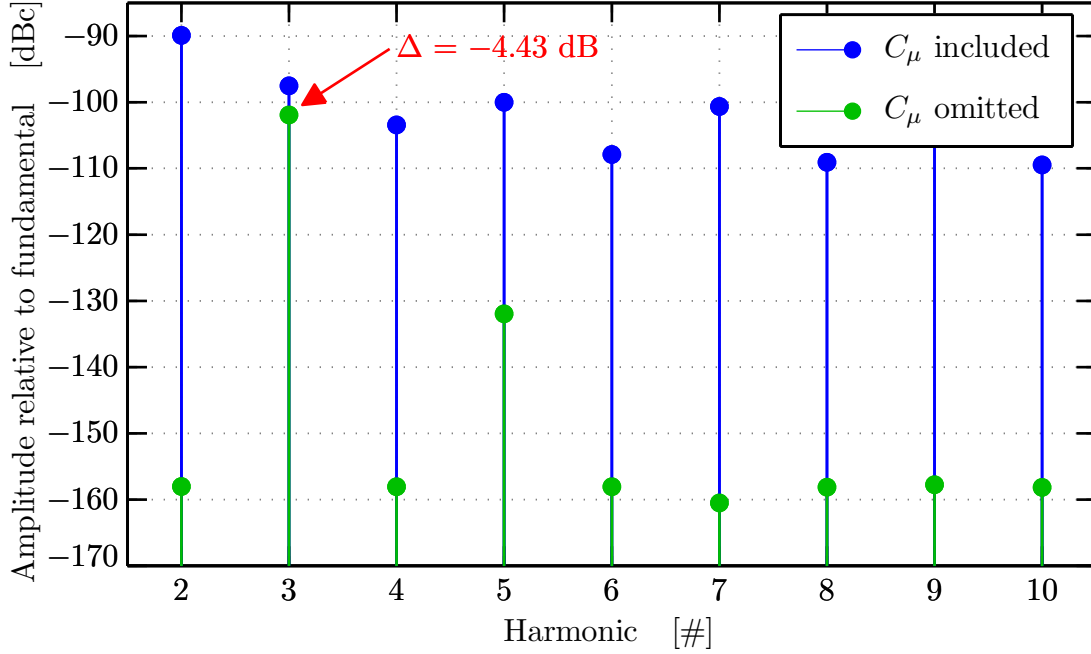


Figure 4.21: Dependence of LNA linearity on tail current source  $C_\mu$  for a 100-kHz input sinusoid at 0.1 V<sub>PP</sub>. When the condition  $C_\mu=0$  is imposed on the NL2d25x5d0 devices that comprise the tail current sources of Figure 4.19, the output harmonics (in green) is considerably reduced over that of the actual case (in blue), with the 3<sup>rd</sup> harmonic exhibiting a minimum improvement of  $\sim 4$  dB and dropping below -100 dBc.

## Biasing

Voltages  $V_{\text{tcas}}$ ,  $V_{\text{bcast}}$ , and  $V_{\text{bcash}}$  are generated from the chip master reference voltages  $V_{\text{tmst}}$  and  $V_{\text{bmst}}$  (cf. Section 5.6.1.1) by means of the bias network in Figure 4.22. The low-voltage cascode bias,  $V_{\text{tcas}}$ , is provided by means of a novel buffer that derives the headroom for the bottom rail devices from resistor stack Rmst1–Rmst3.<sup>28</sup> With RdropB sized so that  $V_{\text{CE47}}$  tracks that of all the cascode slave devices,<sup>29</sup> current

<sup>28</sup>Despite the differing temperature coefficients for these RPDs and the target npns, this method suffices for the operation of SVEPRE since the presence of heaters aboard the target satellite systems alleviates concerns over temperature drift. For applications demanding greater thermal stability, further analysis is advised.

<sup>29</sup>Q42 and Q45 count as such slaves, though their  $V_{\text{CE}}$  is also set by drop resistors Rdrop1 and Rdrop2, respectively, rather than the  $V_{\text{BE}}$  of signal path devices. All drop resistors are sized conservatively, so that  $\pm 20\%$  variations in their absolute values do not push Q42, Q45, or Q47 into saturation.



copying accuracy rests on whether its base voltage can be precisely transmitted to the slaves in spite of  $I_B R_b$  drops.

To do so,  $V_{\text{tcas}}$  is taken not from the base of Q47 but from the base of beta helper Q48 via emitter follower Q49. By ratioing the sizes of Q49 and Q48 such that the current densities of these devices are equal, their  $V_{\text{BE}}$  drops match and  $V_{\text{tcas}}$  tracks the base voltage of Q47 while offering a low impedance to the slave base terminals. Although equality cannot be perfectly maintained, since  $I_{\text{E49}}$  contains base currents from both the low ( $I_B|_{\text{low}}$ ) and high ( $I_B|_{\text{high}}$ ) current branches, each of which has a different current density, it can be approximated by:

$$\begin{aligned}
 I_{\text{E49}} &= I_{\text{B42}} + I_{\text{B45}} \\
 &\quad + 2I_{\text{B10}} + 2I_{\text{B14}} + 2I_{\text{B18}} + 2I_{\text{B22}} + 2I_{\text{B26}} + 2I_{\text{B30}} \\
 &\quad + 2I_{\text{B34}} + I_{\text{B38}} + I_{\text{B40}} \\
 &= 34.5I_B|_{\text{high}} + 35I_B|_{\text{low}} \\
 &\simeq 35I_B|_{\text{high}}
 \end{aligned} \tag{4.25}$$

#### 4.2.4.2 Head Current Sources

Just as for the tail currents sources of Figure 4.19, the cascoded pMOS current sources hanging from the top rail come in both high and low current varieties, depicted in Figure 4.23(a) and Figure 4.23(b), respectively. Their currents are mirrored from biasing branches whose npn lower sections are slaves of those in Figure 4.22. Since both the tail and head currents sources are derived from the same master bias branches, their currents track one another as the properties of these master devices vary with dose and processing, improving common-mode offset.

#### High-Current Branches

Requirements on headroom and output resistance of the high-current mirrors based on  $V_{\text{bcast}}$ , namely M17–M20, are not particularly stringent, since their outputs are tied to the coupled sources of the M1/M3 and M2/M4 differential pairs; benefiting from

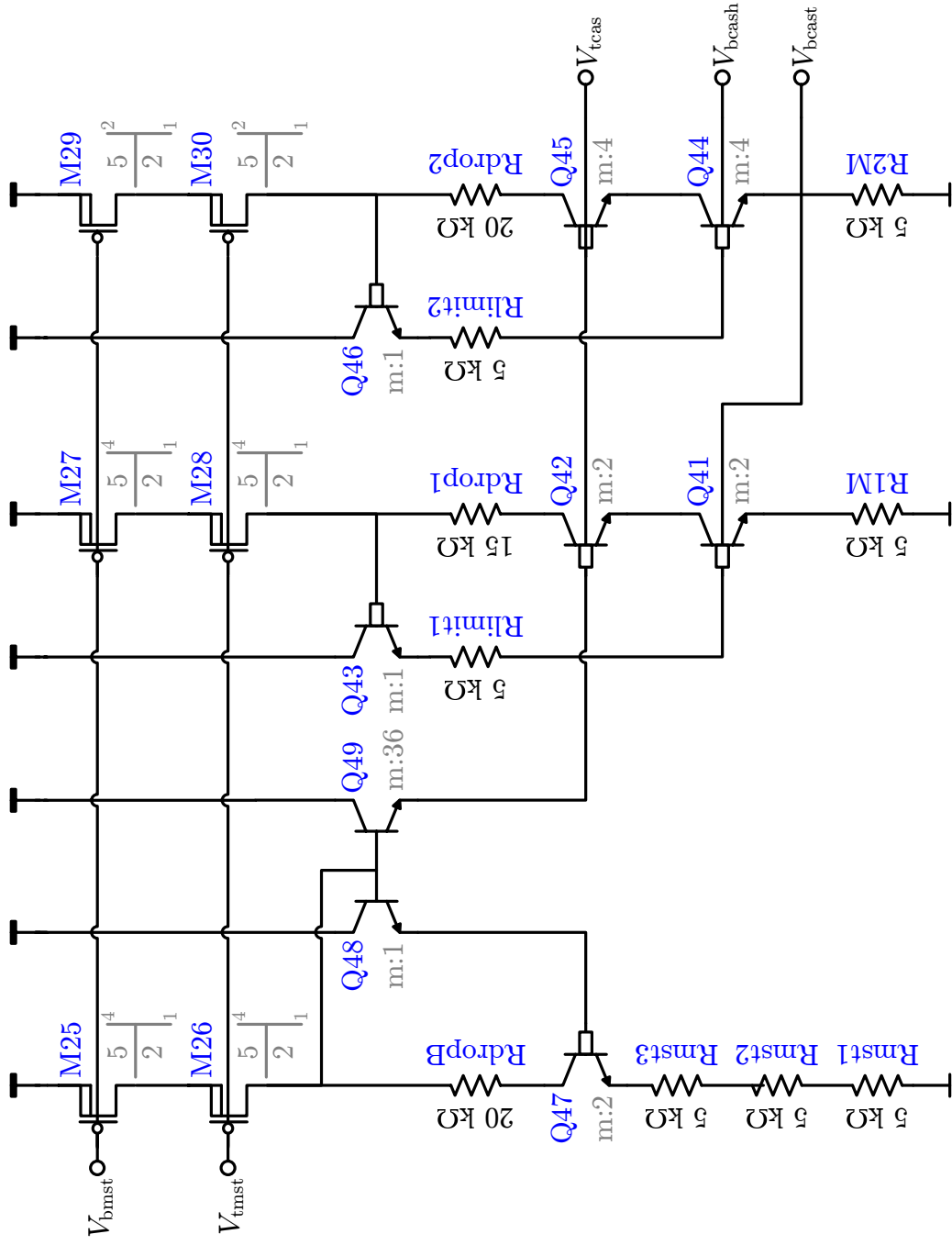
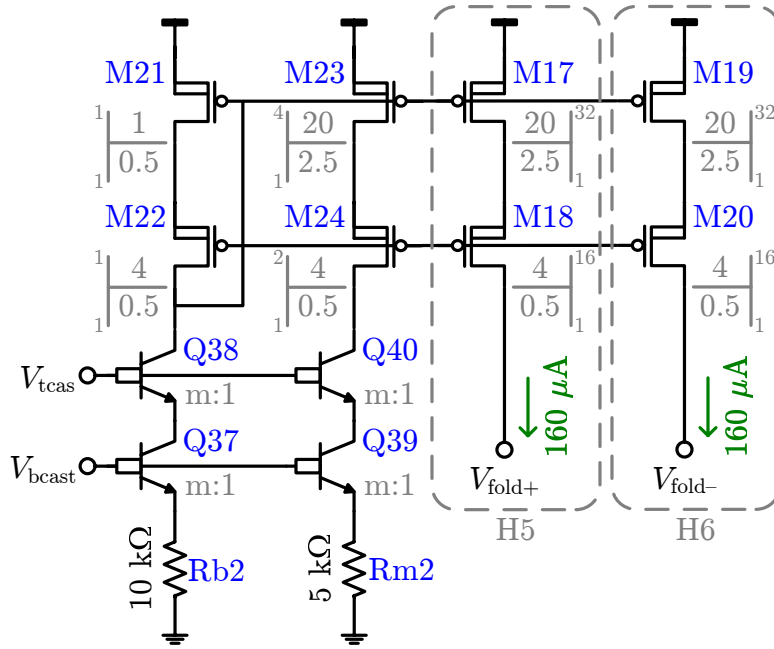
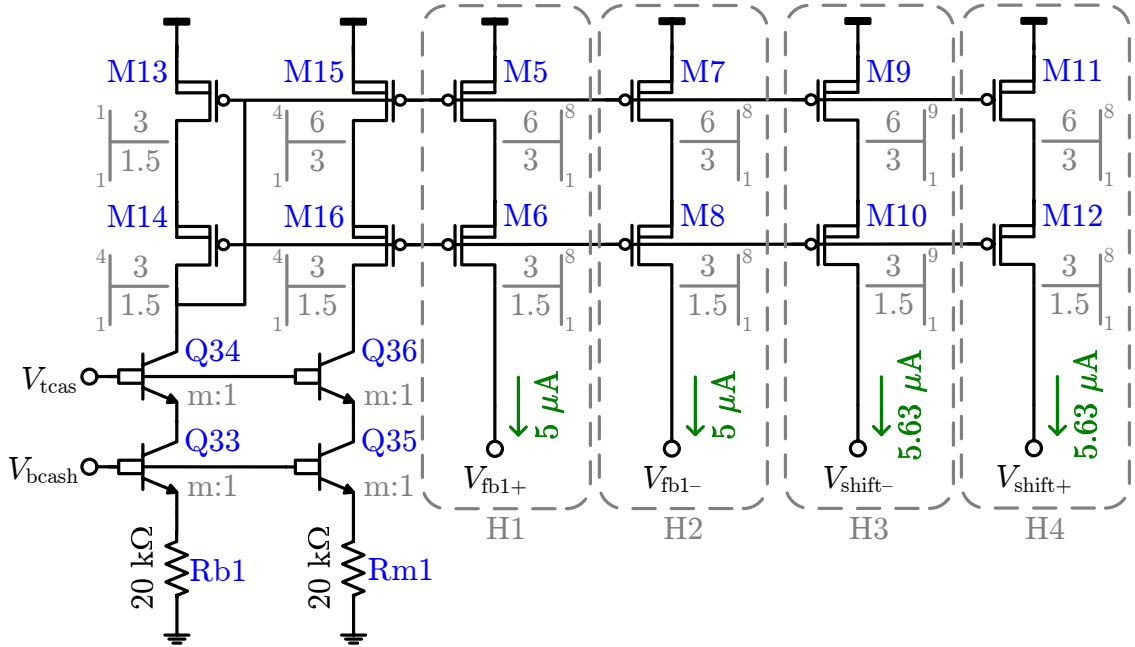


Figure 4.22: Implementation of bias network for Figure 4.5. This circuit the bias voltages in Figure 4.8 and Figure 4.17 from master reference voltages  $V_{bmst}$  and  $V_{tmst}$ .



(a) High-density (bcast) branches.



(b) Low-density (bcash) branches.

Figure 4.23: Implementation of head tail current sources. BJT current densities for the (a) bcast and (b) bcash branches are identical to Figure 4.19, but translate to  $0.1 \mu A/\mu m^2$  and  $0.035 \mu A/\mu m^2$ , respectively, in the cascoded pMOS branches.

common-mode symmetry, these nodes remain within  $750 \pm 100$  mV of the supply over the full input range. Thus both the top-rail and cascode devices are allotted more than 300 mV of headroom, yielding a saturation depth  $V_{ds} - V_{dsat} \geq 150$  mV with enough margin to tolerate  $\Delta V_{th}$  given the large areas of M17/M19 described below.

Since their flicker noise current combines directly with that of Rd and Rl in a differential fashion, these devices are the dominant source of low-frequency noise. If the cascode devices are assumed noiseless, then for the power of the current generated in Rd by a 100-Hz MDS at worst-case  $G_p$  to surpass that of the total uncertainty in the folding currents at  $V_{fold+}$  and  $V_{fold-}$ , the gate lengths of M17 and M19 must satisfy

$$L_{17,19} \geq \sqrt{\frac{2K'_F I_D R_d^2}{C_{ox} f |X_{min}(f)|^2}} \bigg|_{f=100 \text{ Hz}} = 1.27 \text{ } \mu\text{m} \quad (4.26)$$

where the flicker noise term of (3.28) has been employed, using the relationship that  $K'_F = 2\mu_p K_F$ .<sup>30</sup> To provide margin against the  $\sim 2\times$  increases described in Section 2.1.1.4, to accommodate the antenna noise derived in Section 3.1.3.2, and to account for the contributions of M18 and M20,  $L_{17,19}$  is set to twice the minimum value in (4.26). The corresponding width necessary to achieve the 150-mV saturation depth under these  $1/f$  noise constraints is rather larger—640  $\mu\text{m}$ —as a consequence.

### Low-Current Branches

Given the voltage-mode operation of Q1–Q4, the headroom versus noise trade-offs for the low-current branches of Figure 4.23(b) are the opposite of those for M17–M20. In particular, as noted in Section 4.2.3.1, H3/H4, which are implemented by M9–M12, are exposed to the full output voltage swing and, consequently, must provide high output resistance at low headroom to preserve linearity. With a minimum headroom of just 300 mV, H3/H4 are implemented as pMOS low-voltage cascades analogous

---

<sup>30</sup>  $K'_F$  is the flicker coefficient specified in the HSPICE noise model, which uses an alternative formulation of the  $1/f$  term in (3.28) [Avant! Corporation, 1998, p.15-105]:

$$i_{out}^2 = \frac{K'_F I_d^{\alpha_F}}{C_{ox} L^2} \frac{\Delta f}{f^{\epsilon_F}}$$

to the npn tail sources in Section 4.2.4.1, but without degeneration. Omitting the degeneration resistors for headroom necessitates long channel lengths for M9/M11 to preserve output resistance.<sup>31</sup> For  $L_{9,11} = 3 \mu\text{m}$ , the effective output resistance of H3 is approximately,<sup>32</sup>

$$r_{\text{H3}} \simeq r_{10} g_{\text{m10}} r_{\text{o9}} \simeq 250 \text{ M}\Omega \quad (4.27)$$

which is sufficient to keep the signal-dependent error (i.e., nonlinearity) in the  $V_{\text{be3}}$  level shift,  $\Delta V_{\text{be3}}$ , as derived from (4.14), below the signal level at the full-scale output swing by

$$\frac{\Delta V_{\text{be3}}}{\max\{V_{\text{out}}\}} = -n V_{\text{T}} \ln \left( 1 + \frac{\frac{V_{\text{out}+}}{r_{\text{H3}}}}{\frac{V_{\text{out}}}{R_1} + I_{\text{H3}}} \right) \simeq -108 \text{ dB} \quad (4.28)$$

### Biasing

Unlike the Rmst stack used to bias low-voltage cascodes in Section 4.2.4.1, the gate bias for cascode devices M6/M8/M10/M12 is derived from a triode pMOSFET, M13, to ensure that it tracks  $\Delta V_{\text{thp}}$ . Such tracking is critical to ensuring that M10 and M12 remain saturated with only 300 mV of total headroom available to H3/H4 since their threshold voltages increase with dose according to Figure 2.6. Matching its length ( $1.5 \mu\text{m}$ ) to that of the devices it should track, M13 is made wide enough to keep both M9/M11 and M10/M12 50 mV deep into saturation for a full-scale output swing.

## 4.3 Layout

Careful layout is crucial to achieving both the LNA linearity and radiation specifications. In terms of the former, first-order differential circuit analysis assumes that the parameters of paired transistors and resistors on opposing halves of the circuit are

---

<sup>31</sup>When compared to the tail npn sources, omitting degeneration is not as devastating to the output resistance as it might first appear, because the lower  $g_{\text{m}}/I_{\text{d}}$  efficiency of MOSFETs renders degeneration less effective for the same  $V_{\text{deg}}$ .

<sup>32</sup>The input resistance of a MOSFET is, at all but quantum current levels, infinite. Without the equivalent of base current, (4.27) is not subject the same fundamental limitations as (4.24). If chip area were of no concern,  $r_{\text{H3,4}}$  could approach infinity [Gray *et al.*, 2001, p.202].

identical. In that case, the coefficients of the generalized polynomial representations of the transfer functions through the positive and negative halves are also identical, such that:

$$V_{\text{out}+} = G_{\text{po}} + G_{\text{p1}} V_{\text{in}+} + G_{\text{p2}} V_{\text{in}+}^2 + G_{\text{p3}} V_{\text{in}+}^3 + \dots \quad (4.29\text{a})$$

$$V_{\text{out}-} = G_{\text{po}} + G_{\text{p1}} V_{\text{in}-} + G_{\text{p2}} V_{\text{in}-}^2 + G_{\text{p3}} V_{\text{in}-}^3 + \dots \quad (4.29\text{b})$$

For balanced inputs (cf. Footnote 3), the subtraction of these expressions produces a differential output containing only odd-order terms. Thus, the even-order linearity in the output relies on the degree to which a pair of devices can be made to resemble each other. Although this matching is ultimately a function of the manufacturing tolerances for the chosen process, such limits are only approached through a custom layout featuring the appropriate techniques.

The radiation tolerance of analog circuits is also known to be a strong function of their layout [*Hughes and Benedetto, 2003*, p.510]. Fortuitously, the same layout techniques sedulously applied to reduce device mismatch in differential systems, such as spatial locality, common-centroid arrays, and dummy devices [*Hastings, 2006*, p.523–528], also prove effective in regulating the severity of both TDEs and SEEs. This convergence stems from uncertainties in device behavior that are fundamental to both manufacturing and radiation environments. In both cases, deterministic but microscopic (and in some cases quantum mechanical) physical interactions favor similar stochastic descriptions of the macroscopic quantities of interest.

Section 4.3.1 and Section 4.3.2 demonstrate methods for reducing the variance of distributions describing device mismatch and the likelihood of radiation-induced damage, respectively.

### 4.3.1 Matching

Mismatch between the dimensions(doping) of a pair of devices result from the tolerances of the lithography(diffusion or implantation) used to define their lateral dimensions(bulk profile) [*Hastings, 2006*, p.511-521]. The goal of layout techniques

that improve matching is to enhance the uniformity of these processes across an array of two or more effective devices by establishing isotropic conditions for their execution. Although the importance of these two classes of manufacturing steps varies across device types and parameters, in general transistors(resistors) are more sensitive to doping(etching) variability, so this emphasis is reflected in the summaries below.

#### 4.3.1.1 Transistors

Primary sources of transistor mismatch are often divided into two classes: those whose variations occurs on spatial scales smaller than the transistor dimensions, including distributions in the concentrations of bulk dopants (be they introduced through ion implantation or diffusion), fluctuations of mobility, and processing-induced  $V_{\text{ot}}$  [Pelgrom *et al.*, 1989, p.1434]; and those which exhibit long-range correlation distances, such as die stresses that govern bulk resistivity, temperature fluctuations due to localized heating, and variations in oxide thickness [Hastings, 2006, p.521–523]. It has been shown that each class contributes a term to the following general description of the variance of a transistor parameter,  $\Delta P$  between a pair of nominally identical devices of width  $W$ , length  $L$ , and center-to-center spacing  $\Delta d$  [Pelgrom *et al.*, 1989, p.1434]:

$$\sigma^2\{\Delta P\} = \frac{k_{1P}^2}{WL} + k_{2P}^2(\Delta d)^2 \quad (4.30)$$

The first term of (4.30), incorporating empirical fitting parameter  $k_{1P}^2$ , indicates that  $\Delta P$  is reduced for larger devices, over which the local fluctuations tend to cancel and relative to whose dimensions the absolute tolerances of etching and implantation are less significant. The term proportional to  $k_{2P}^2$  captures the reduced statistical fluctuation for pairs of devices whose centers are in close proximity, since this condition limits the impact of long-range nonuniformities.

As particular example, consider the manifestation of (4.30) in the following expressions for threshold voltage mismatch ( $\Delta V_{\text{th}}$ ) and transconductance mismatch ( $\Delta g_m$ ) of a pair of MOSFETs, which has been shown to hold quite well experimentally

[[Lakshmikumar et al., 1986](#); [Pelgrom et al., 1989](#), p.1061, p.1435]:

$$\sigma^2\{\Delta V_{\text{tho}}\} = \frac{k_{1V_{\text{tho}}}^2}{WL} + k_{2V_{\text{tho}}}^2(\Delta d)^2 \quad (4.31a)$$

$$\frac{\sigma^2\{\Delta g_{\text{mo}}\}}{g_{\text{mo}}^2} = \frac{k_{1g_{\text{mo}}}^2}{WL} + k_{2g_{\text{mo}}}^2(\Delta d)^2 \quad (4.31b)$$

These expressions confirm that in order to reduce the variance of the absolute(percent) difference the  $V_{\text{th}}(g_{\text{m}})$  of a MOSFET pair, they should be built as large and as close together as possible. The former is constrained by the circuit design requirements,<sup>33</sup> but the latter can be addressed through layout techniques that drive the effective  $\Delta d$  to zero.

### Basic Common-Centroid Arrays

Over the spatial scales occupied by device pairs of reasonable size, the most commonly encountered nonuniformities with long-range correlation can be modeled as linear gradients [[Hastings, 2006](#), p.523].<sup>34</sup> A standard technique for minimizing the effects of these gradients on device matching is the use of a common-centroid array [[Hastings, 2006](#), p. 277-281]. Consider two devices, A and B, each divided into  $N$  sub-units that are connected in parallel. For even  $N$ , the simple ( $N = 2$ ) two-dimensional examples in Figure 4.24(a) demonstrate how distributing the sub-units such that the A and B constellations share a common geometric centroid can completely cancel one- or two-dimensional linear doping gradients. For every A-unit at one end of the gradient, whose properties are skewed to that extreme, there is a complementary unit

---

<sup>33</sup>The requirements of a given design also dictate which of (4.31a) or (4.31b) is more critical to performance. A differential pair at the input of an amplifier is most sensitive to  $\Delta V_{\text{GS}}$ -mismatch, so clearly (4.31a) is crucial because  $\Delta V_{\text{th}}$  contributes directly to  $V_{\text{GS}}$  in all cases. But, in addition, a large  $\Delta g_{\text{m}}$  contributes non-trivial error to  $V_{\text{GS}}$  when reflecting (even perfectly matched) drain bias currents to the input. So, when pursuing voltage-matching, bias conditions that favor large  $g_{\text{m}}$ , including low overdrive for a given current, can mitigate the effect of errors from (4.31b). On the other hand, in current mirrors where  $I_{\text{D}}$ -mismatch is paramount, the impact of (4.31b) is unadulterated, but that of (4.31a) can be attenuated by using large enough overdrive that, relative to  $V_{\text{GS}}$ ,  $\Delta V_{\text{th}}$  is insignificant [[Hastings, 2006](#), p.512].

<sup>34</sup>Even those effects whose gradients are nonlinear can often be treated as linear over such short distances and benefit from the same layout techniques [[Hastings, 2006](#), p.523].



opposite it (through the centroid) that is affected inversely. When their properties are averaged, all such units form a description of the composite A device that maps to the arrangement's center-of-mass. Since this coincides with the centroid of B,  $\Delta d \rightarrow 0$  and the effects of the gradient on the two devices become indistinguishable.

To maximize its effectiveness, the common-centroid array should not only seek to minimize the systematic  $\Delta d$  between the centroids of A and B, but obey the following rules [*Hastings*, 2006, p.525]:

- The spacing between units should be minimized, keeping the array as compact as possible so that nonlinear gradients appear roughly linear and the residual error from this approximation (which depends on powers of  $\Delta d$ ) is kept small.
- The array should be symmetric both dimensions, with symmetry in the second dimension resulting ideally from the construction of a 2-D array but, barring that, from the inherent symmetry of the unit device construction.
- The orientations of the units should be mirrored about the axes of symmetry to preserve chirality, which influences the profiles of tilted implants [*Plummer et al.*, 2000, p.458].
- The degree of dispersion should be as high as possible (e.g., ABABBABA is preferable to AABBBBAA), as this higher dispersion is more effective for any nonlinear components of the gradient.

According to these stipulations, of the 2-D examples in Figure 4.24(b), the arrangement on the right side is preferred and, thus, adopted for transistor arrays throughout SVEPRE.

In particular, all matched devices in the LNA are laid out according to these conventions, with an especially involved example illustrated by the low-current, degenerated npn tail current sources in Figure 4.25. In exchange for the gradient immunity conferred, the common-centroid configuration increases wiring complexity [*Hastings*, 2006, p.527], especially when, as in this case, the symmetry of the latter is also maintained. Using higher metal layers to accomplish symmetric wiring of a common-centroid array incurs the large parasitic resistance of the interlayer vias.

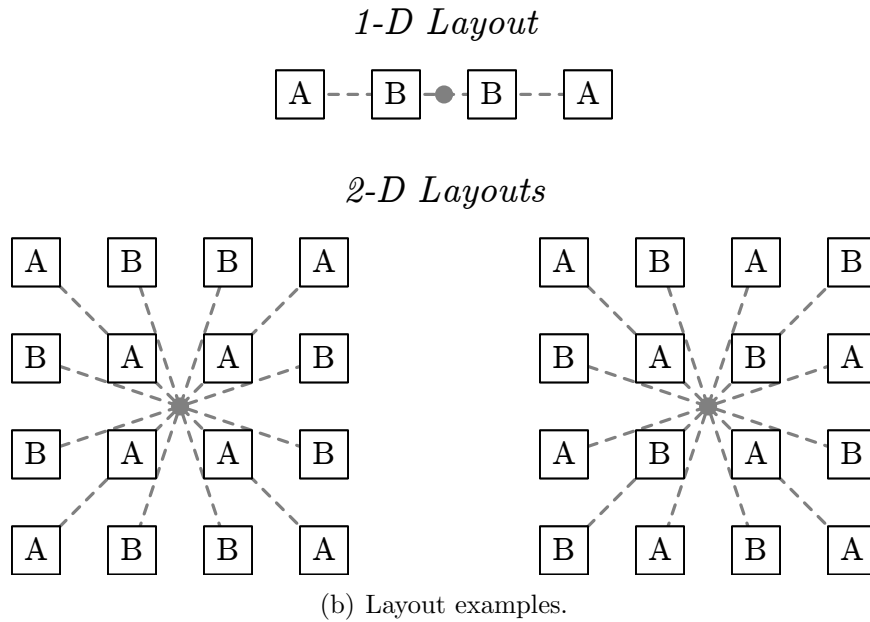
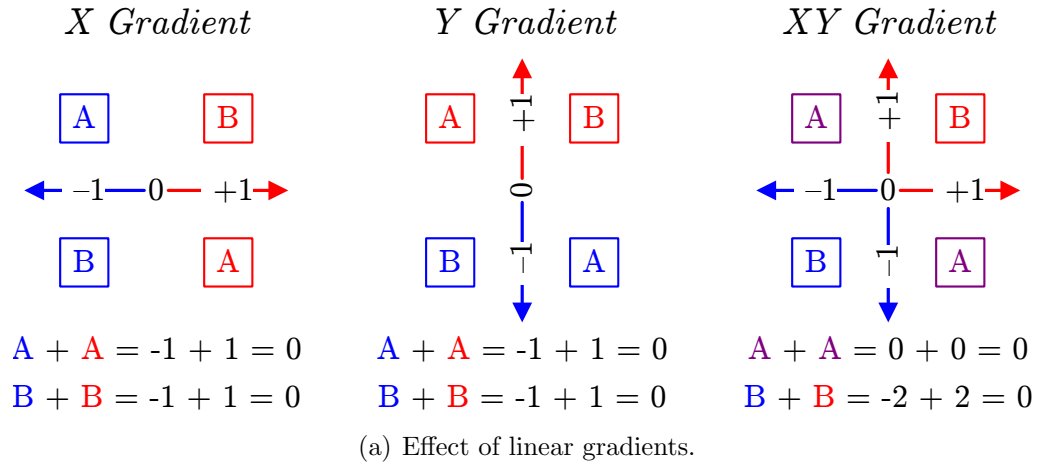


Figure 4.24: Principles and layouts of common-centroid arrays. Manufacturing variations in device properties that obey (a) linear gradients (represented by incremental scalar values  $-1$ ,  $0$ ,  $+1$ ) can be canceled between pairs whose sub-units are (b) laid out with a common centroid.

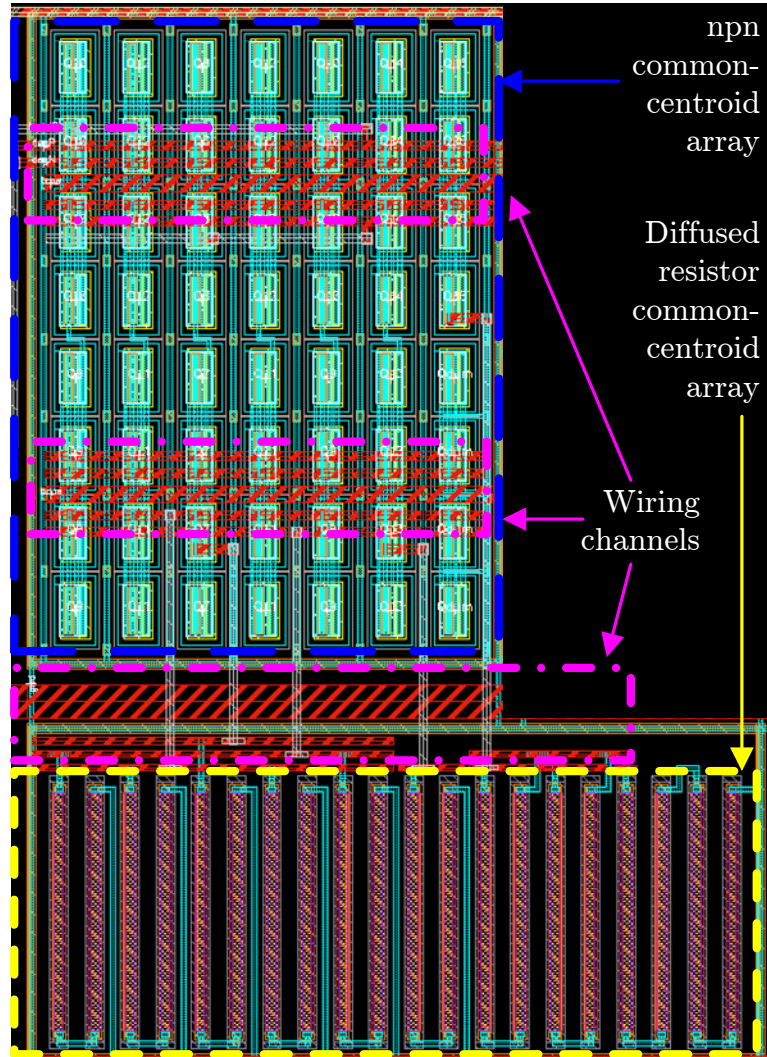


Figure 4.25: Example of npn and resistor common-centroid layouts evidencing the area penalty associated with: the common-centroid arrays themselves; the channels for symmetric wiring (in red); and the substrate-tap rings enclosing each array (cf. Section 4.3.2.1).

In the case of these current mirrors, where base current drops are a primary source of inaccuracy, via resistance reduces the currents of the slaves relative to the masters, even when symmetry preserves matching between the slaves, introducing common-mode offsets. To combat this effect, multiple vias are deployed, particularly on lines carrying sensitive bias voltages, at the cost of increased die area. The resultant structure of Figure 4.25 is representative of the area penalty and wiring symmetry imposed on common-centroid arrays throughout the remaining LNA layout.

#### 4.3.1.2 Resistors

The patterning of resistors incurs irregularities that pertain to both their periphery and area [Hastings, 2006, p.257]. As for transistors, these can be captured by an expression akin to (4.30), in which their effect on sheet resistance is independent of segment length such that the variance relative to the nominal resistance  $R_o$  is

$$\frac{\sigma^2\{\Delta R_o\}}{R_o^2} = \frac{k_{1R}^2}{W^2 R_o^3} + k_{2R}^2 (\Delta d)^2 \quad (4.32)$$

under the assumption of equal width [Hastings, 2006, p.259]. The second term of (4.32) again benefits from the common-centroid techniques introduced in Section 4.3.1.1. However, the geometric term, pertaining to local-scale effects, is highly sensitive to the resistor construction.

**Polysilicon Resistors:** When high resistance is paramount and the noise contributions are common-mode, as is the case for the drop resistors of Figure 4.22, the LNA layout conserves area through the use of unalicated polysilicon (poly) resistors, as exemplified in Figure 4.26. Matching of poly resistors is highly dependent on edge effects associated with lithographic resolution and the sensitivity of etch rates to the density of the surrounding poly. To preserve identical densities along the perimeters of all the segments, grounded dummy segments are placed at ends of this, and all, poly resistor arrays in the LNA layout. Using widths greater than the lithographic minimum at the expense of greater area reduces the dependence on diffraction.

Additionally, the high sheet resistance of the Rdrop resistors renders them

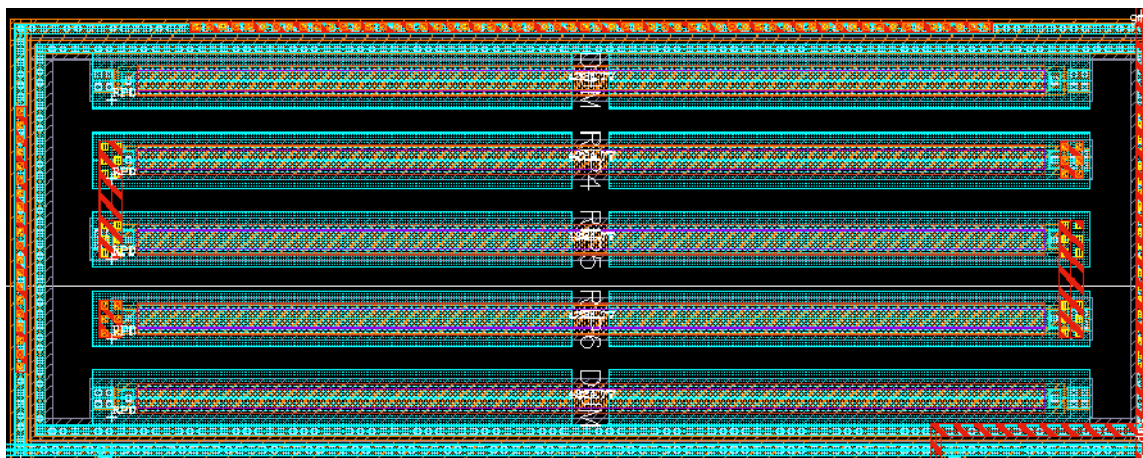


Figure 4.26: Example layout of polysilicon resistor array evidencing the use of: dummy segments at top and bottom of the array to preserve etch rates; Metal 1 split field-plates (in blue) atop all segments; non-minimum widths to minimize impact of diffractive lithographic effects; and concentric guard and substrate-tap rings of SEL prevention (cf. Section 4.3.2.1).

vulnerable to electrostatic fields generated by overhead traces and trapped oxide charges. Capacitive coupling of the former can modulate the conductivity of the resistive layer by attracting(repelling) carriers to(from) its surface, whereas the latter lead to long-term drifts in value due to charge spreading and dielectric polarization [Hastings, 2006, p.292–293]. To minimize these effects, signals are not routed over such resistor arrays unless absolutely necessary. When this is unfeasible, a split field-plate above each segment shields it from conductivity modulation and the noise of the overhead traces [Hastings, 2006, p.294].<sup>35</sup> The cleaving of the plate balances any voltage nonlinearities that would otherwise be induced along its length, since the conductivity modulation and dielectric polarization governed by the plate electric field on one half of the segment are opposed on the other half [Victory et al., 1998, p.1453].

**Diffused Resistors:** For the diffused resistors used extensively in the core of the LNA on account of their low  $K_F$ , the geometric component of mismatch suffers from

<sup>35</sup>The grounded n-type well beneath the segments provides complementary isolation below, shielding them from capacitively coupled substrate noise.

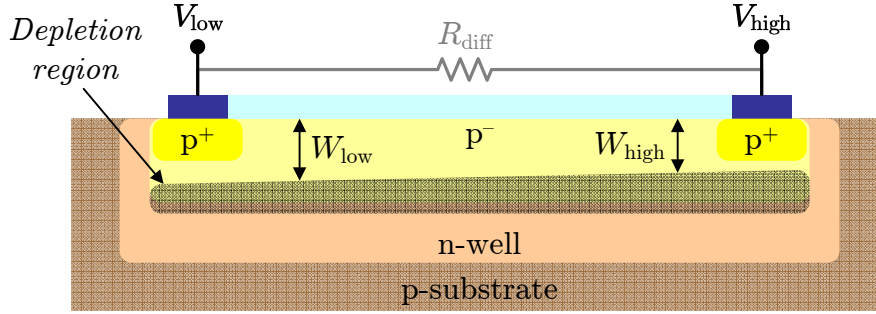


Figure 4.27: Illustration of voltage modulation for p-type diffused resistor. The larger reverse bias of the diffusion-tank junction under  $V_{\text{high}}$  increases its penetration into the p-type diffusion, constricting the path for current flow. After [Hastings, 2006, p.195].

voltage modulation of the tank in which the resistor resides [Hastings, 2006, p.195]. As depicted in Figure 4.27, the depletion region between the resistor and tank at the high-voltage terminal is wider than that at the low-voltage terminal, pinching it at the former end (videlicet,  $W_{\text{high}} < W_{\text{low}}$ ) and increasing its net resistance,  $R_{\text{diff}}$ .

To combat this effect, the voltage drops across corresponding segments of matched diffusion resistors must be identical and should be minimized relative to their tanks. This is accomplished through the layout example of R1 and R2 in Figure 4.28. By placing each segment in its own tank which is tied off to the positive end of that resistor, the diffusion-to-tank voltage is zero at the positive end, and never exceeds the fraction of  $V_{\text{deg}}$  dropped across the segment ( $V_{\text{deg}}/4$  in this case).

### 4.3.2 Radiation Tolerance

The device-level TDEs resulting from the physical mechanisms described in Section C.2 and Section C.3 are primarily a function of MOS and BJT construction, particular their Si and SiO<sub>2</sub> quality, which are beyond the control of the layout designer. However, the spatial proximity recommended for precise matching also reaps rewards in the context of total-dose irradiation. By increasing the similarity of the dose environments of matched pairs, it couples their degradation profiles and limits radiation-induced increases in harmonic distortion.



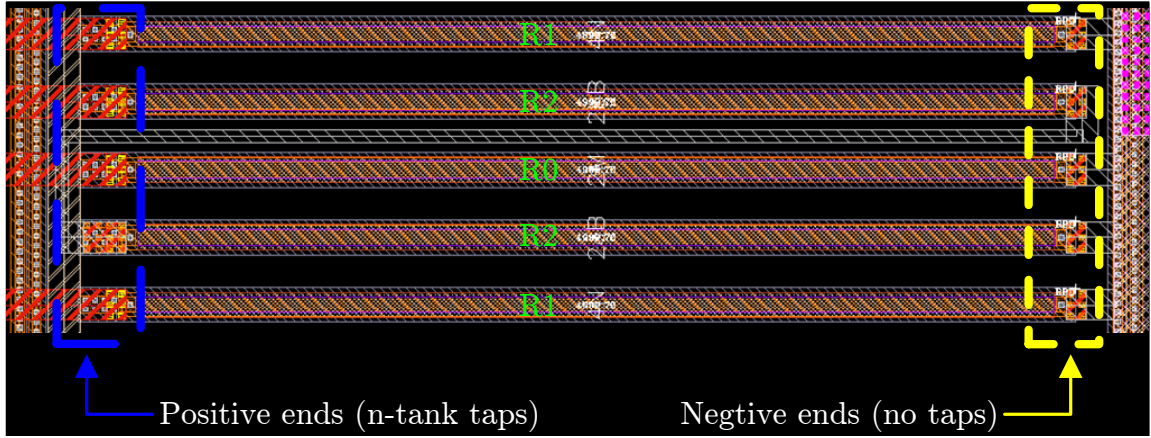


Figure 4.28: Example layout of diffused resistor array consisting of resistors R1 and R2 which are multiples of and matched to R0 (center segment). On the left, the positive end of each resistor segment is tied to the n-type tank beneath it (gray outline) to prevent voltage modulation.

In contrast, since SEEs, in particular ASETs, manifest at the level of circuit operation, the designer has the opportunity to enhance tolerance of these phenomena through a layout that is aware of the most sensitive devices and upset mechanisms. Thus, the LNA layout incorporates techniques aimed at reducing its sensitivity to both SEL and ASETs.

#### 4.3.2.1 SEL Prevention

As described in Section 2.2.1, SEL can be interpreted as the action of a positive feedback loop comprised of two parasitic, complementary BJTs. Of the conditions that prevent this structure from leaving the blocking state, the most fundamental is keeping its loop gain below unity, as expressed in (2.20). The two generally accepted layout precautions aimed at shrinking  $\alpha'_n$  and  $\alpha'_p$  can be intuited from (2.22): reducing the numerators by spoiling the gains of parasitic BJTs, namely  $\alpha_n$  and  $\alpha_p$  defined in (2.21); and increasing the denominators by scaling down emitter shunt resistors  $R_{well}$  and  $R_{sub}$ . Both are addressed by the LNA layout practices exemplified in Figure 4.29 for the case of input pair Q1/Q2.

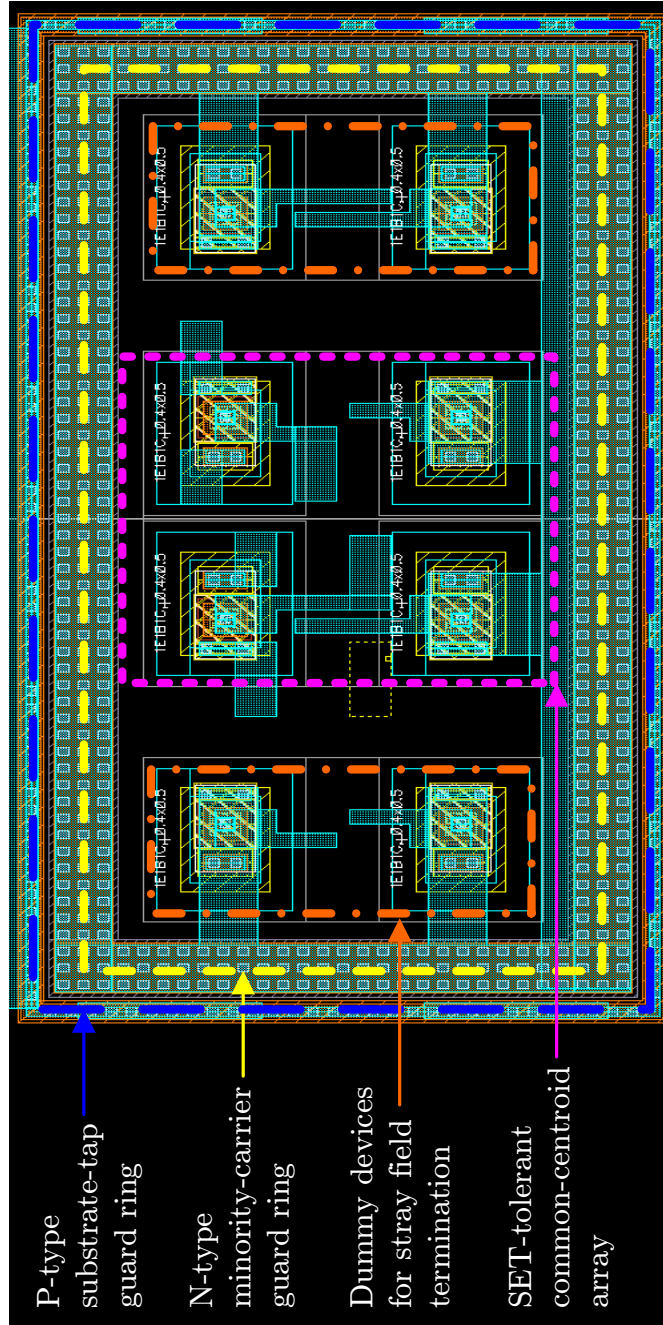


Figure 4.29: Examples of RHBD layout techniques applied to Q1/Q2. Both rings described in Section 4.3.2.1 and the SET-tolerant array ordering of Section 4.3.2.2 are identified.



**Guard rings:** Gain spoiling is the preferred method of SEL hardening, since the rudiments of latchup lie in the action of minority carriers. Enhancing their recombination rate or siphoning them away from the collectors of the thyristor structure renders the loop gain insufficient to activate both BJTs, even if  $R_{sub}$  and  $R_{well}$  are infinitely large. Furthermore, even when the condition of (2.20) is satisfied, the injection of undesired minority-carriers can still lead to SETs or more serious circuit malfunctions should they be collected by sensitive nodes [*Hastings, 2006*, p.171]. Thus, the first line of SEL defense in the LNA layout is the inclusion of minority-carrier guard rings around all sensitive device arrays.

A minority-carrier guard ring consists of a wide depletion region interposed between the suspected emitter and all neighboring collectors with latchup potential. Its goal is to sweep all the unwanted carriers out to the supply before they can initiate the bipolar action at the heart of the feedback loop, thereby slashing  $\alpha$ . To enhance its collection efficiency, the guard ring—or, more specifically, the collecting depletion region—should be as deep and wide as possible and its connection to the appropriate supply low-resistance.

In light of these requirements the innermost ring of Figure 4.29, an annular n-well lined with  $n^+$  contacts to the +2.5 V supply and a continuous metalization strip, serves as an effective collector for minority electrons injected into the substrate near Q1/Q2. The CMOS n-well layer is preferred over the source/drain diffusion layers, since its depth captures a greater fraction of the lateral current flow, whereas the width of  $\sim 1 \mu\text{m}$ , being several times the minimum, provides a broader surface for collecting those carriers which attempt to pass along the bottom of the depletion region. Additionally, lateral dispersion limits diffusion depth for minimum feature sizes, so a ring 2–3 times the minimum width affords the maximum possible junction depth [*Hastings, 2006*, p.173].

**Substrate-tap rings:** The minority-carrier guard ring is nested within a second enclosure designed to minimize the sheet resistances between the well(substrate) and the supply(ground) [*Troutman, 1986*, p.165–172]. This  $p^+$  path need only be of minimum width, as it is concerned with supplying the majority carriers necessary

to facilitate recombination in the base of the lateral npn and preventing substrate debiasing. The substrate-tap ring circumscribes the minority-carrier guard ring,<sup>36</sup> rather than the other way around, because the later is responsible for reducing  $\tau_n$ , so its efficacy is more pronounced when it is proximal to the edge of the sensitive junction(s).

Although not conferring absolute immunity to SEL at arbitrary LET, as no guard ring(substrate-tap ring) can offer 100% collection efficiency(0- $\Omega$  resistance), these nested rings inhibit the thyristor feedback loop by reducing the transistor gains(parasitic resistances) by several orders of magnitude [Troutman, 1986, p.167]. Thus, despite the attendant area penalty [Baumeister, 2003, p.40], they are liberally deployed through the LNA layout, with at least one encircling each homogenous array of either MOSFETs or BJTs, and with the most sensitive devices—those that are connected to the pad frame, experience the full input voltage, or operate at high bias currents—circumscribed by both.

#### 4.3.2.2 ASET Suppression

Given the low MDS to which it must respond and without *a priori* knowledge of  $Q_{\text{crit}}$  for the design presented in this chapter, it is conservatively assumed that the desired operation of the LNA requires  $Q_{\text{crit}} = 0$ ; that is, any charge collected at a node is sufficient to generate an ASET. Under such circumstances, it can be inferred from Section 2.2 that a layout which diligently tailors the electric fields of the junctions that play a prominent role in charge collection via drift, funneling, and, particularly, the ion shunt effect, exhibits a lower upset rate and  $\sigma_{\text{sat}}$ . Augmenting the common-centroid principles of Section 4.3.1.1 with one additional rule, the LNA layout demonstrates a means of rejecting ASETs by increasing the likelihood that they appear as

---

<sup>36</sup>The intricacies of guard ring design and operation are unknown to many circuit designers. As such, it is common for an annular substrate connection to be dubbed a guard ring. The ambiguity of this designation can lead to the application of incorrect design criteria—for example, wasting area on substrate-tap ring that is many times the minimum width. Thus, rather than the terms *minority-carrier guard ring* and *majority-carrier guard ring* employed by Troutman [1986], this section opts for the distinctions of *minority-carrier guard ring* (or, simply, *guard ring* if not fully qualified) and *substrate-tap ring*.

common-mode disturbances.

Consider the two-dimensional common-centroid layouts of a representative pMOS differential pair (Ma/Mb) in Figure 4.30. Although all variations cancel the effects of an arbitrary one- or two-dimensional gradient, the choice of terminal orientation affects the polarity of the transients induced by the deposited charge. In the situation depicted, a hypothetical strike occurs at the center of each array (location Y), when the signal being processed by the differential pair is driving the drain of Ma(Mb) high(low). The field lines of Configuration #1 tend to funnel the negative(positive) charge from the central track toward Ma(Mb). The resulting output transients on the two halves of the circuit are of opposite polarity and, consequently, not differentially canceled. Configuration #2 is somewhat better, with fields of half the strength, while Configuration #3 is optimal, since there is no preferred drift direction.

Repeating this analysis at locations X and Z reveals that, in terms of the expected value of the transients resulting from a randomly located strike, the configurations are ranked in ascending order of preferences as #1, #3, #2. However, since the upset rate is independent of  $Q_{\text{col}}$ , given the high dynamic range, Configuration #1 is preferable because its field structure only induces differential ASETs in one-third of the cases.

Thus, to minimize the ASET probability (read rate), the LNA adopts such terminal orientations, where possible, to produce SET-tolerant common-centroid arrays in which free charge does not preferentially drift toward one half of the circuit. Note that the presence of the neighboring dummies Mc–Mf at fixed (here, ground) potential is a prerequisite for this and similar arguments concerning uniform field terminations, so they are also deployed liberally. Once again, the penalty for localization of the signal-dependent electric fields is one of chip area.

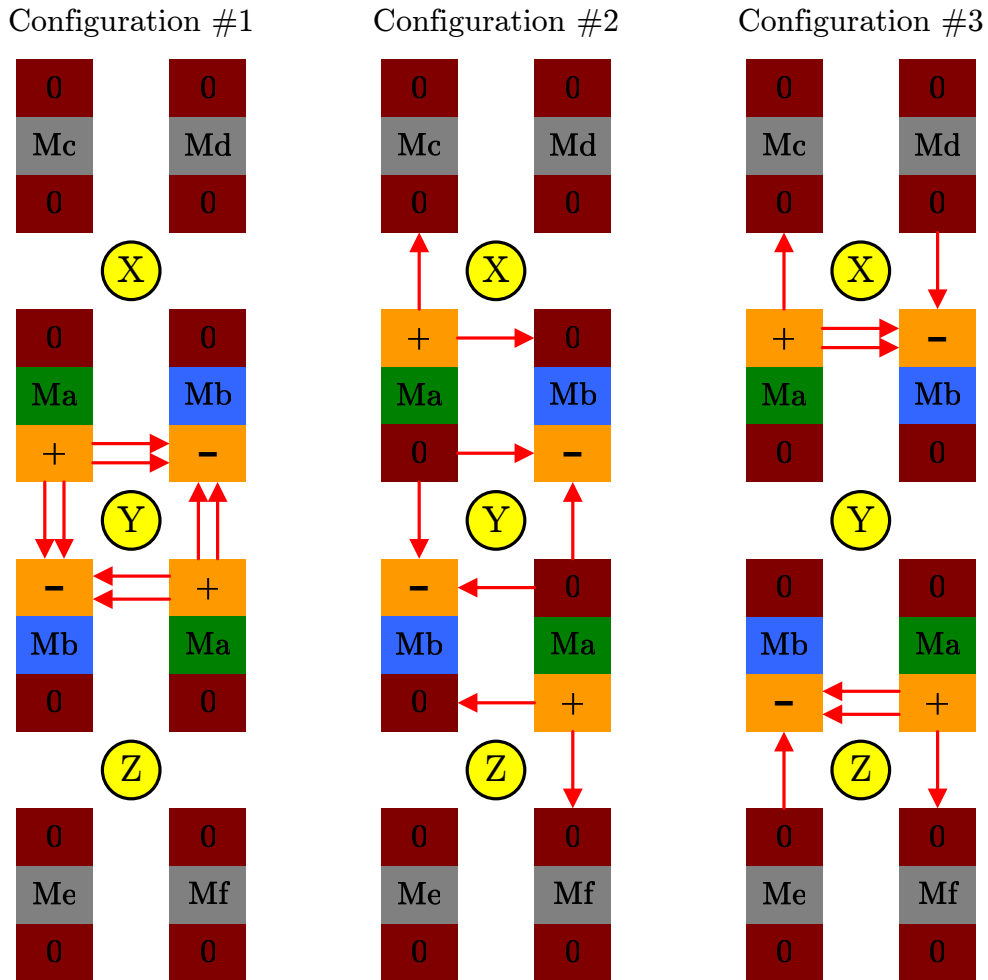


Figure 4.30: Possible common centroid arrays, including SET-tolerant configuration. For Configuration #1—the SET-tolerant variation—only strikes at node Y induce differential transients.

# Chapter 5

## AAF Design

The AAF is foremost charged with producing a spectrum in which the fraction of the LNA output in the bandwidth of interest, known as its passband, is faithfully replicated, while any undesirable interferers that could be irrevocably aliased into and thereby corrupt the passband during the sampling operation of the ADC are simultaneously purged from the region known as the stopband. To maximize the usable bandwidth of the receiver, the interval between the adjacent edge frequencies of the passband ( $\omega_p$ ) and stopband ( $\omega_r$ ), known as the transition band, would ideally be infinitesimal, as depicted in Figure 5.1(a) for the attenuation characteristic of a brick-wall low-pass filter with transfer function  $T(\omega)$  and cut-off frequency  $\omega_c$ . Any actual filter possesses a finite attenuation rate, characterized by the slope, or roll-off rate, of its magnitude response in the transition band,

$$r_\alpha(\omega) = \frac{d|T(\omega)|}{d\omega} \quad , \quad \text{for } \omega_p \leq \omega \leq \omega_r \quad (5.1)$$

which is usually expressed in dB/dec in accordance with logarithmic scale of Figure 5.1(b).

The frequencies that define the edges of the transition band map to corresponding limits on the maximum passband attenuation,  $A_{\max}$ , and minimum stopband

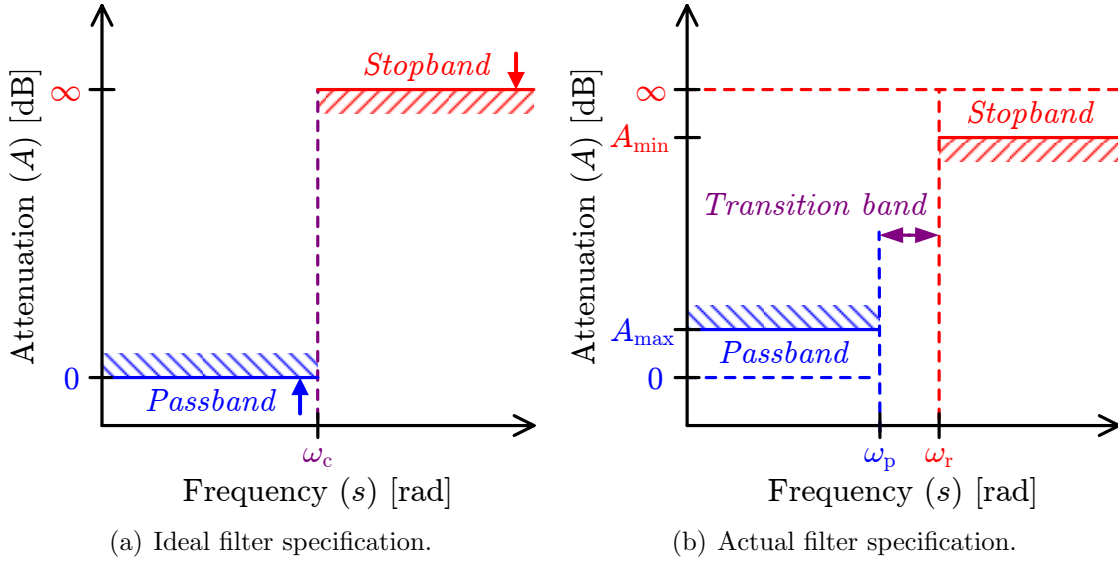


Figure 5.1: Ideal and actual low-pass filter specifications. Traditionally, the filter attenuation  $A(\omega)$ , which is the inverse of its transfer function  $T(\omega)$ , is the specified quantity. After [Sedra and Brackett, 1978, p.81].

attenuation,  $A_{\min}$  formally defined (in dB) as:<sup>1</sup>

$$A_{\max} = -20\log_{10}(|T(\omega_p)|) \quad (5.2a)$$

$$A_{\min} = -20\log_{10}(|T(\omega_r)|) \quad (5.2b)$$

In order to minimize the discrepancy between the cases of Figure 5.1, the AAF roll-off rate is designed such that in a worst-case scenario, consisting of a full-scale but unwanted signal just outside the passband, the aliased interferer lies beneath the resolution of the amplitude quantization to follow. For an  $N$ -bit ADC sampling at  $\omega_s$ , this conservative approach dictates that  $\omega_r$  be defined by

$$A_{\max} - A_{\min} = 20\log_{10}(2^{-N}) \quad (5.3)$$

or, in the case of a unity-gain passband,  $A_{\min} = 20\log_{10}(2^N)$ .

Applied to the simplified depiction of Figure 5.2, in which aliasing causes the

<sup>1</sup>By convention, attenuation denoted by  $A_x$  is a positive quantity in decibels.

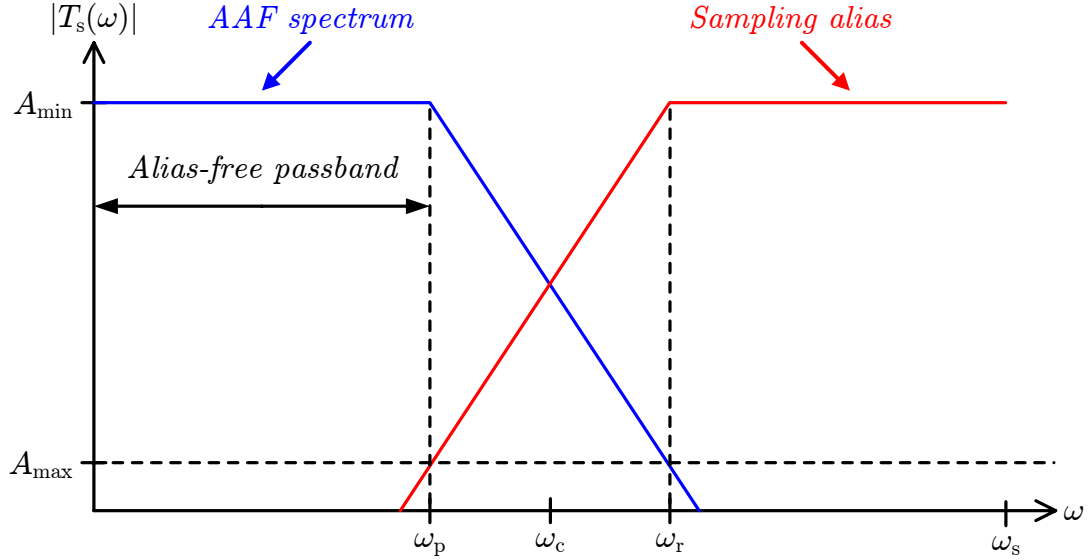


Figure 5.2: AAF roll-off necessary to avoid spectral aliasing in the sampled AAF transfer function. For this limiting case, the condition ensuring that aliases of full-scale interferers at or above  $\omega_r$  are suppressed below  $A_{\max}$  can be obtained by inspection:  $\omega_s = \omega_p + \omega_r$ .

baseband AAF output (in blue) to be replicated as spectral islands (in red) at integer multiples of  $\omega_s$  when the former is sampled to produce  $T_s(\omega)$ , (5.3) dictates that a full-scale interferer in tail of the aliased island below  $\omega_p$  is confined to the ADC noise for any  $\omega_s \geq \omega_p + \omega_r$ . However, the choice of the equality in this expression yields the minimum  $\omega_s$ , thereby easing the requirements on the ADC at the expense of the logarithmic roll-off rate, then given by

$$r_\alpha(\omega) = \frac{|T(\omega_r)|}{\omega_r} \frac{\omega_p}{|T(\omega_p)|} = \frac{20 \log_{10}(2^{-N})}{\log_{10}(2M_s - 1)} \quad (5.4)$$

where  $M_s = \omega_s / 2\omega_p$  is the ADC oversampling ratio.

For a 16-bit ADC,<sup>2</sup> the numerator of (5.4) demands better than 96-dB attenuation

<sup>2</sup>The ADC of [Wang, 2009] has an effective-number-of-bits (ENOB) below 12, but satisfies the same 90-dB SFDR specification as SVEPRE. Thus, by the spectral arguments of Section 3.1.2.1, the attenuation of a coherent tone must exceed 90-dB for it to be suppressed beneath the largest distortion product in the spectrum. Choosing a minimum stopband attenuation of 96 dB ensures compatibility with true high-resolution ADCs whose SFDR is comparable to their SNR—a class that includes several rad-hard alternatives ranging from 14-bit (92-dB SFDR) [Analog Devices, Inc.,

at  $\omega_r$  and, in the target receiver of Figure 1.22, where the maximum sampling frequency of the chosen ADC is fixed at 5 MS/s, the oversampling ratio at the maximum AAF bandwidth ( $f_p = 1.08$  MHz) is just  $\sim 2.3$ . Thus, to attenuate the maximum expected interfere below 16-bit resolution while requiring minimum speed from the ADC, the AAF must achieve an aggressive  $r_\alpha$  of  $\sim -50$  dB/octave.

Although it is challenging, many of the archetypal filter classes can realize such aggressive anti-aliasing. In terms of power and linearity, passive filters are an attractive choice. But, though prominent in terrestrial receivers, at VLF frequencies these are too large to be practically integrated, as they require inductors on the order of millihenries. Increasing in popularity with the ascension of high-speed MOS technologies, switched capacitor (SC) filters [Gregorian and Temes, 1986; Moschytz, 1984] are much more amenable to monolithic realizations. Although their reliance on MOS switches presents no noise penalties, since flicker noise only afflicts MOSFETs carrying DC current [Gray et al., 2001, p.753], the linearity of a triode-region MOSFET is not sufficient over the full input range ( $1 V_{PP}$ ). Remedying this distortion by bootstrapping the switch  $V_{GS}$  can yield excellent SFDR in ADC track-and-hold stages [Abo and Gray, 1999], but such schemes are too power hungry to be practical when applied to every switch in a high-order filter. Furthermore, to achieve 90-dB dynamic range with minimal pre-filtering,<sup>3</sup> a SC filter requires a low-jitter clock at a frequency of at least  $100f_p$  [Azuma et al., 2002]. Such high-precision, high-frequency oscillators that are also radiation-hardened are extraordinarily expensive, if they can be found at all.<sup>4</sup>

Thus, the SVEPRE AAF is constructed as an active, integrated, continuous-time (ICT) filter. Although such filters typically overcome manufacturing tolerances

---

AD6644] to 16-bit (93-dB SFDR) [Linear Technology, LT1761] converters.

<sup>3</sup>In addition to a more sophisticated and less SEE-tolerant layout, a SC AAF, being a sampled-data circuit, needs its own anti-aliasing filter.

<sup>4</sup>An on-chip oscillator alleviates the procurement problem, but for timing and noise compatibility at the system level, must support synchronization with a master reference clock provided by the instrument or spacecraft. Thus, the cost and availability constraints are either pushed up the system hierarchy, or a divider and phase-locked loop must be integrated into the front-end ASIC. Although these additional elements, whose discrete circuitry is more susceptible to SEEs, can be hardened by design, the net increase in complexity and power dissipation may offset any benefit to integrating the front-end at all.



by means of expensive laser trimming to accurately set the cut-off frequency [Abdelmoneum *et al.*, 2004; Langford *et al.*, 1998] and digital linearity calibration for high fidelity [Durham *et al.*, 1992; Wunderlich *et al.*, 1999], the ICT discussed in this chapter is both field-trimmable and requires no external linearity calibration.

In an attempt to represent the interwoven threads of circuit design by a linear yarn, these and other of the AAF features are presented top-down: Section 5.1 employs the theory of Appendix F to provide a mathematical specification of the filter response and general block diagram; Section 5.2 through Section 5.4 descend into the hierarchical architecture, ultimately arriving at the most unique building block—the transconductor; Section 5.5 explores the transistor-level implementation of the novel, programmable transconductor, emphasizing those elements crucial to the performance goals of Table 3.2; finally, the layout techniques used to improve the matching and radiation susceptibility of the SVEPRE-3 AAF are enumerated in Section 5.6.

## 5.1 Filter Architecture

As opposed to the two-stage LNA architecture (cf. Section 4.1), whose flatness exemplifies the axiom that LNA operation is predicated on the careful configuration of only a small nucleus of transistors, the increased complexity and part count of the AAF are managed via several levels of hierarchy. The architecture of each tier strives to not only achieve the aforementioned dual aims of the AAF—a distortion-free passband and a steep roll-off rate—but to preserve these characteristics over the range of operating conditions associated with device mismatch (cf. Section 4.3.1), radiation effects (cf. Chapter 2), and bandwidth programming (cf. Section 3.1.1.2).

This section begins with the overall architecture of the AAF, prefacing subsequent descriptions of its biquadratic stages, active integrators and, finally, tunable transconductors. Establishing the architecture of the AAF begins with selecting the filter approximation—here, Type I Chebyshev—and deriving a mathematical model of the ideal filter of lowest order that achieves the desired  $r_\alpha$  at the nominal  $\omega_p$  of Mode B (180 kHz). Denoted  $\omega_{pb}$ , this frequency serve as the passband edge for the

general descriptions of the filter in the remainder of this chapter, as the Mode A (Mode C) cut-off,  $\omega_{\text{pa}}(\omega_{\text{pc}})$ , is obtained simply by scaling down(up) the poles/zero locations of the middle mode by a factor of six. Through choice of a sufficiently flexible filter architecture, the mapping of the ideal approximation into stages of hardware is, to within the component value scaling, identical for all modes.

### 5.1.1 Filter Approximation

From the set of available options in Section F.1.3, the SVEPRE-3 AAF adopts the Type I Chebyshev approximation, further described in Section 5.1.2, for two key reasons. First, although the accurate measurement of the delay between events is fundamental to the scientific data analysis, linear phase in the passband is not strictly necessary. Rather, it has been shown that the group delay need only vary smoothly over the passband [*Hashimoto et al.*, 1997, p.281]. Thus, in the trade-off between passband phase and roll-off rate, the latter is substantially more important because nonlinear phase in the passband can be corrected in post-processing through the acquisition of a de-embedding data set during periodic instrument characterization; aliasing cannot be undone. The primacy of  $r_\alpha$ , outlined at the start of the Chapter, demotes those approximations with the good phase response but poor  $r_\alpha$ , namely the Butterworth and Bessel designs.

Secondly, since the flatness of both delay and gain in the passband are routinely compensated through instrument calibration, the use of transmission zeros ( $z_i^T$ ) to obtain a flat passband at the cost of limited high-frequency attenuation, as in the Type II Chebyshev and Cauer approximations, is unnecessary. Rather than ensure deep (theoretically, infinitely attenuating) nulls at the  $N$  loss poles ( $p_i^K$ ) of the Type II Chebyshev and Cauer  $K_n(s)$ , but allow the attenuation in the remainder of the stopband, including  $\omega > \omega_{\text{zN}}^T$ , to approach  $A_{\text{min}}$ —and likely exceed it, since the locations of the loss poles cannot be infinitely precise in any practical realization—the SVEPRE AAF opts for the monotonic (and theoretically unbounded) attenuation of the Type I Chebyshev approximation. In fact, since there potentially exist a large number of interferers above the VLF bandwidth of interest, the monotonic and

unbounded roll-off of an all-pole approximation best embodies the conservative anti-aliasing philosophy of the target receiver which, through its high  $r_\alpha$  and  $A_{\min}$ , aims to attenuate the strongest of these to levels below 16-bit resolution.

### 5.1.2 Ideal Response

For a given ADC resolution,<sup>5</sup>  $A_{\min}$  is defined in terms of  $A_{\max}$  by (5.3), and  $\omega_r$  is defined in terms of  $A_{\min}$  by (5.2b). Thus, the free parameter in the AAF design is  $A_{\max}$  or, alternatively, the ripple parameter  $\epsilon$  since, according to Section F.1.3.2

$$A_{\max} = 10\log_{10}(1 + \epsilon^2) \quad (5.5)$$

Recall that passband flatness is less critical here than in many applications, so more than the commonly cited 0.1–0.5 dB of ripple for video applications in the same bandwidth [*Willingham et al.*, 1993, p.1234] can be tolerated. But, to specify the exact value of  $\epsilon$  for the Type I Chebyshev, it is necessary to appreciate its dependence on the filter order by revisiting the definition of  $A_{\min}$  from (5.2b) and substituting (F.3), (F.13), (F.14), and (F.24) such that:

$$A_{\min} - 20\log_{10}(C_N(\tilde{\omega}_r)) \simeq 20\log_{10}(\epsilon) \quad (5.6)$$

where it is assumed that  $\epsilon^2 C_N(\tilde{\omega}_r) \gg 1$ . Iterative simulations of (5.6) over  $N$  confirm that  $\epsilon \simeq 0.56$  is the minimum ripple for which a 6<sup>th</sup>-order Type I Chebyshev can provide the desired  $r_\alpha$ . Since a preliminary estimate of the required capacitor sizes for  $\omega_{\text{pb}}$  limits a reasonable implementation to  $N \leq 6$  (cf. Section 5.6.1.2), this  $\epsilon$  is used in (5.5) to arrive at an  $A_{\max}$  of 1.2 dB, a compromise that minimizes the filter order for reasonable ripple.

A Bode plot of the ideal 6<sup>th</sup>-order Type I Chebyshev with 1.2-dB ripple is provided in Figure 5.3. Its panels emphasize the unbounded stopband attenuation of the all-pole design, the oscillations of  $C_6(\tilde{\omega})$  between 0 and  $(1 + \epsilon^2)^{-1} = 0.76$  near  $\omega_{\text{pb}}$ , and

---

<sup>5</sup>Or, as explained in Footnote 2, an effective resolution equal to the SFDR for coherent interferers, as is provided by the ADC of the target receiver.

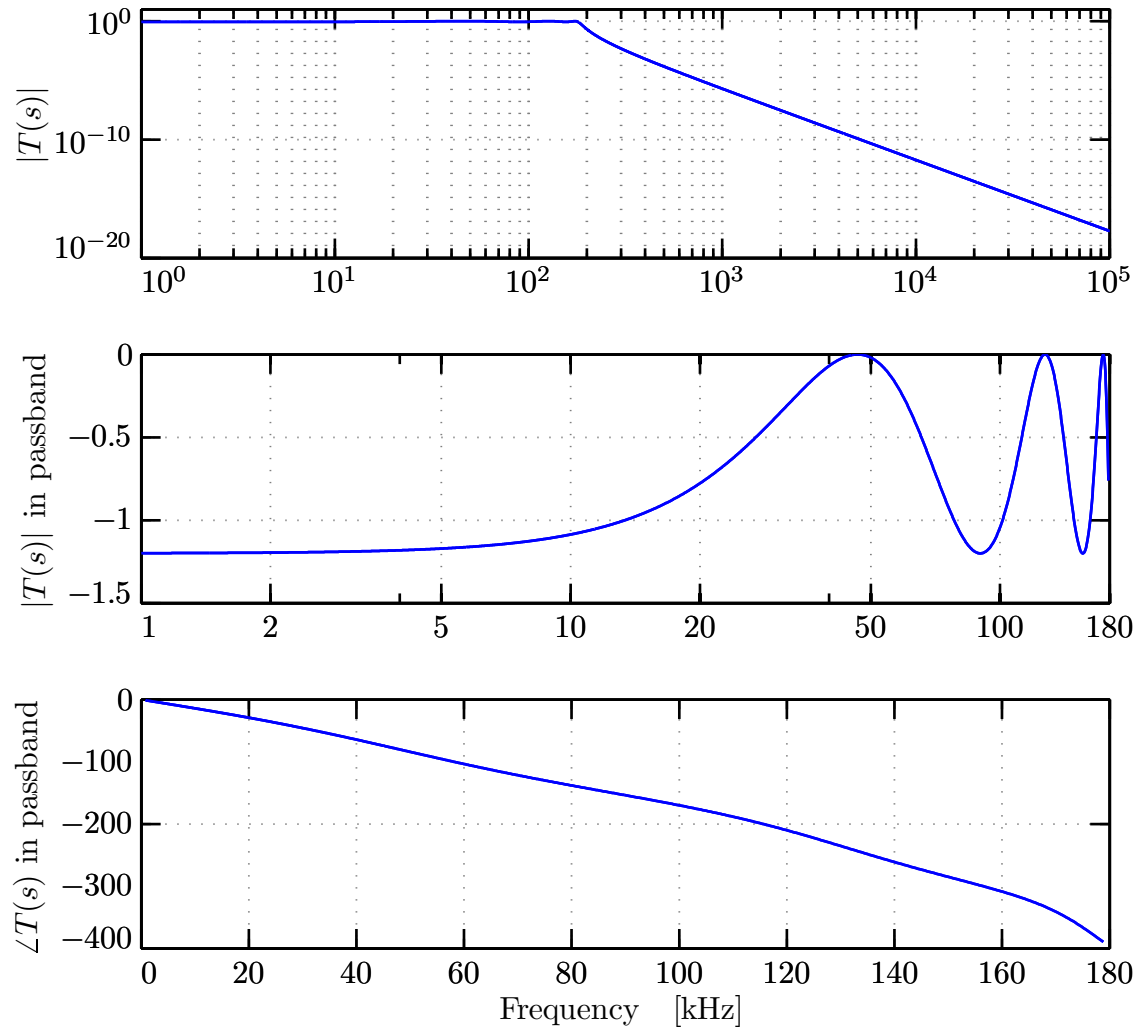


Figure 5.3: Bode response of ideal AAF design for Mode B. Top panel: Complete magnitude response. Middle panel: Zoom of passband magnitude highlighting ripple near  $f_{pb}$ . Bottom panel: Passband phase on linear scale evidencing deviations near  $f_{pb}$ . Responses for other modes are simply scaled accordingly.

Mode	$H(s)$ Coefficients <sup>a</sup>		Poles	Properties	
Stage 1					
	a	b	$u_{1,2}^K$ or $p_{1,2}^T$	$f_{o1}$	$Q_{o1}$
	[rad]	[rad <sup>2</sup> ]	[kHz]	[kHz]	
A	8.18×10 <sup>4</sup>	4.17×10 <sup>9</sup>	−6.51 ± $j$ 7.96	10.3	0.790
B	4.91×10 <sup>5</sup>	1.50×10 <sup>11</sup>	−39.1 ± $j$ 47.7	61.7	0.790
C	2.95×10 <sup>6</sup>	5.41×10 <sup>12</sup>	−234 ± $j$ 286	370	0.790
Stage 2					
	c	d	$u_{3,4}^K$ or $p_{3,4}^T$	$f_{o2}$	$Q_{o2}$
	[rad]	[rad <sup>2</sup> ]	[kHz]	[kHz]	
A	5.99×10 <sup>4</sup>	1.96×10 <sup>10</sup>	−4.77 ± $j$ 21.7	22.3	2.33
B	3.59×10 <sup>5</sup>	7.04×10 <sup>11</sup>	−28.6 ± $j$ 130	134	2.33
C	2.16×10 <sup>6</sup>	2.53×10 <sup>13</sup>	−172 ± $j$ 783	801	2.33
Stage 3					
	e	f	$u_{5,6}^K$ or $p_{5,6}^T$	$f_{o3}$	$Q_{o3}$
	[rad]	[rad <sup>2</sup> ]	[kHz]	[kHz]	
A	2.19×10 <sup>4</sup>	3.49×10 <sup>10</sup>	−1.75 ± $j$ 29.7	29.8	8.53
B	1.32×10 <sup>5</sup>	1.26×10 <sup>12</sup>	−10.5 ± $j$ 178	179	8.53
C	7.89×10 <sup>5</sup>	4.53×10 <sup>13</sup>	−62.8 ± $j$ 1069	1071	8.53

<sup>a</sup> According to definition in (5.7).

Table 5.1: Pole locations for stages of 6<sup>th</sup>-order Type I Chebyshev low-pass AAF in each mode.

the smooth phase response through the passband, whose deviation from linearity is primarily confined to  $f > 100$  kHz. Using (F.24) with  $N = 6$  in (F.13), the overall  $T(s)$  can be derived as:

$$T(s) = \frac{T_o}{(s^2 + as + b)(s^2 + cs + d)(s^2 + es + f)} \quad (5.7)$$

where  $T_o^{-1}$  is the monic normalizing constant for  $H(s)$ , whose positive, real coefficients  $a$ – $e$  and corresponding roots of negative unity ( $u_i^K$ ) are summarized in Table 5.1. Plotting the latter on the complex plane as in Figure 5.4 reveals that the major axis

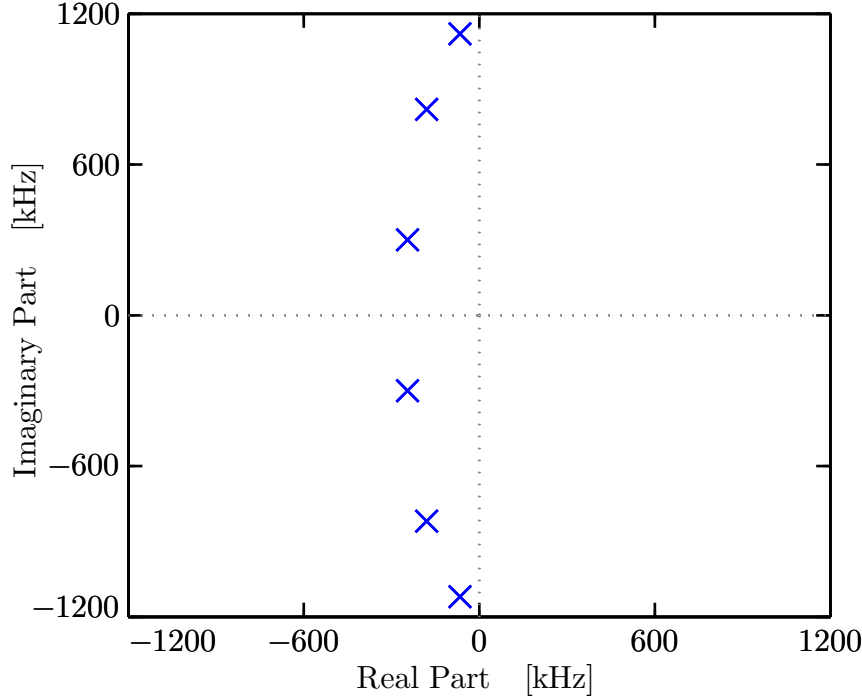


Figure 5.4: Pole/zero plot of ideal AAF design for Mode B. The absence of zeros and orientation of the major axis are characteristic of the Type I Chebyshev low-pass filter described by (F.24). Responses for other modes are simply scaled accordingly.

of the ellipse in (F.26) is parallel to the imaginary axis, so the pole  $Q$  factors of this design are relatively high,<sup>6</sup> especially for the innermost pair ( $\sim 8.5$ ). In Section 5.2 and Section 5.3, it is demonstrated that these high- $Q$  poles dictate the possible stage architectures and constrain the performance of their integrators.

### 5.1.3 Cascade Topology

The cascade architecture of the AAF shown in Figure 5.5 realizes the poles of (5.7) by grouping them into three biquadratic stages. As opposed to popular doubly-terminated ladder networks,<sup>7</sup> whose interconnectivity spreads the responsibility for

<sup>6</sup>This orientation of the ellipse is characteristic of the Type I Chebyshev. The pole constellation of the Type II variant is rotated by  $90^\circ$  due to the reciprocal relationship of (F.27). Thus, a heretofore neglected advantage of the latter implementation is poles of lower  $Q$ .

<sup>7</sup>Although spawned from the passive LC networks of the same arrangement, ladder networks are designed with active components that simulate the required inductance to facilitate on-chip

$\omega_{pi}^T$ -determination amongst all its components and thereby achieves a power gain that is minimally sensitive to component variations [*Sedra and Brackett, 1978*, p.276], the isolation between these stages renders each responsible for a particular pole pair, as shown. This eases the component tolerances of and the reduces power dissipation in the low- $Q$  stages, since, unlike a ladder topology, they are not subject to the same constraints as stages whose high selectivity demands less uncertainty. Furthermore, the reductionist approach of the cascade architecture offers more flexible adjustment of the frequency response than a ladder,<sup>8</sup> which repeatedly proved useful when it became necessary to switch filter approximations over the course of this research.<sup>9</sup>

When faced with implementing a higher order filter through a cascade of several biquadratic stages, the question immediately arises as to how to factor the poles and zeros amongst the stages so that they contain at most two of each.<sup>10</sup> For the chosen Type I Chebyshev, the absence of transmission zeros renders this pole/zero pairing moot. However, the tripartite division of (5.7) still requires algorithms for partitioning its gain and pole pairs, both of which are driven by dynamic range considerations.

### 5.1.3.1 Pole Distribution

Assuming an even  $N^{\text{th}}$ -order filter, there are  $(N/2)!$  ways to order the cascade of biquadratic stages. Although it does not change the overall transfer function, the stage order is critical because it affects the maximum dynamic range.

Specifically, the optimum arrangement keeps the passband as flat as possible at each point in the cascade, since the dynamic range is maximized when the maximum(minimum) signal level observed through the filter is minimized(maximized).

---

integration. It is this latter incarnation to which the cascade in question is rightly contrasted.

<sup>8</sup>The resonances of the ladder arms map directly to the loss poles, making it easy for the designer to relocate the transmission zeros as desired [*Sedra and Brackett, 1978*, p.276]; but, the natural modes arise from interactions amongst all branches.

<sup>9</sup>On multiple occasions,  $M_s$  of the ADC in the target receiver was reduced, requiring steeper  $r_\alpha$ . Often, the poles could be relocated by scaling the appropriate components in each stage. However, when these increases exceeded the roll-off limitations for the chosen order of the approximation, they necessitated that a new approximation be implemented in the same number of stages; thus, the AAF morphed from Bessel to Butterworth to Type I Chebyshev. For efficiently accommodating both classes of modification, the choice of a cascade architecture proved sagacious.

<sup>10</sup>Naturally, there are  $(N/2)!$  ways to distribute each set for any transfer function of even order  $N$ .

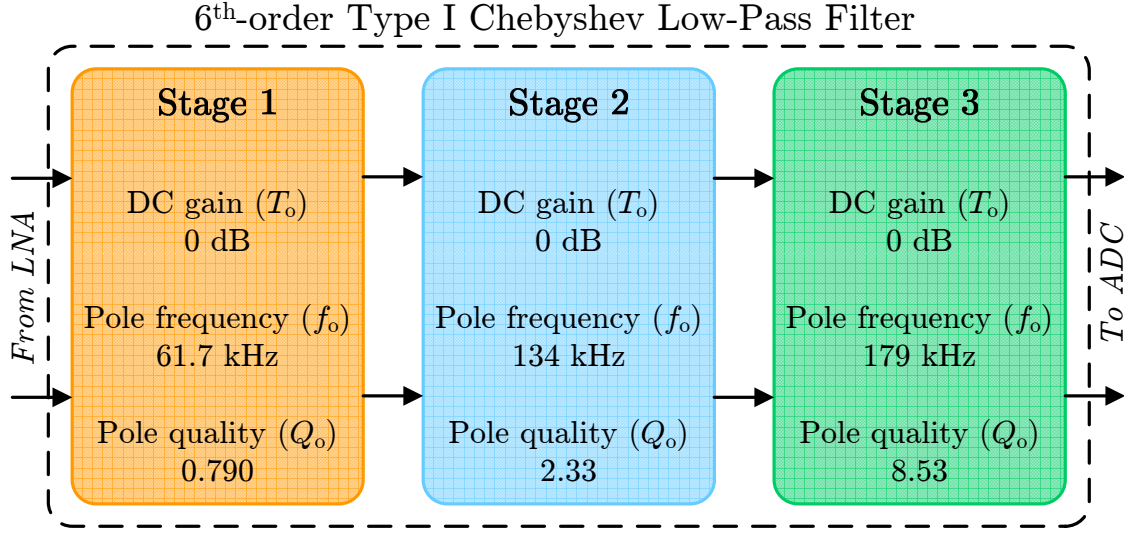


Figure 5.5: Three-stage cascaded filter architecture. The ordering of the stages, each of which implements an all-pole biquadratic transfer function of the form of (5.9), and the distribution of the pole pairs of Table 5.1 amongst them (shown for Mode B), maximize the overall dynamic range.

Although an optimization tool can be employed [Halfin, 1970], a popular and effective *ad hoc* solution advocates ordering the stages according to increasing  $Q$  [Schaumann and van Valkenburg, 2001, p.235–237] so that the flattest stage comes first, then the next flattest, and so on. The peaking in the gain does not occur until the end of the cascade, where it has the least effect on the dynamic range of other stages. This strategy is practiced in the ordering of Figure 5.5.

### 5.1.3.2 Gain Assignment

When faced with implementing a higher order filter like that of (5.7) as a cascade of several biquadratic stages, the question immediately arises as to how to factor the overall gain constant,  $T_o$ , into a product of constants for each biquadratic term. In fact, there are an infinite number of ways to distribute the gain over the stages so as to still achieve the same cumulative value.

To maximize the dynamic range, each stage should process the maximum possible signal but, at the same time, the voltage swing at all internal nodes throughout



the cascade should remain equal, since the dynamic range is maximized when the maximum(minimum) signal level observed through the filter is minimized(maximized) [Schaumann and van Valkenburg, 2001, p.238–239]. To that end, the signal level at the output of each filter stage, including the first, should reach, but never exceed, the maximum allowed. In the case of Figure 5.5 each stage sees the same maximized signal level, equal to the full-scale input, because they each feature 0-dB gain.

## 5.2 Stage Architecture

In general, each of the stages in Figure 5.5 has a transfer function  $T_i(s)$  for  $i=1, 2, 3$ , in which, both  $B_i(s)$  and  $A_i(s)$  are quadratic, such that:

$$T_i(s) = \frac{B_i(s)}{A_i(s)} = T_{oi} \frac{b_2 s^2 + s(\omega_n/Q_n) + \omega_n^2}{s^2 + s(\omega_o/Q_o) + \omega_o^2} \quad (5.8)$$

where the natural frequency and quality factor of the poles(zeros) are denoted by  $\omega_o(\omega_n)$  and  $Q_o(Q_n)$ , respectively.<sup>11</sup> Classically, there exists a panoply of active networks capable of realizing such a biquadratic transfer function, known colloquially as *biquads*. Although the absence of transmission zeros in (5.7) permits its realization with a cascade of second-order  $T_i(s)$  that result from simplifying  $B_i(s)$  in (5.8) such that  $s \rightarrow 0$  and  $\omega_n^2 \rightarrow \omega_o^2$ , or

$$T_i(s) = \frac{B_i(s)}{A_i(s)} = T_{oi} \frac{\omega_o^2}{s^2 + s(\omega_o/Q_o) + \omega_o^2} \quad (5.9)$$

such degenerate stage transfer functions are merely a special case of the more general biquads described below.

---

<sup>11</sup>In some texts,  $Q_o$  is alternative represented by through the damping factor  $\zeta$ , defined as

$$\zeta = \frac{1}{2Q_o} = \sin \theta_o$$

where  $\theta_o$  is the counter-clockwise angle between the pole location and the  $j\omega$ -axis, as defined in Footnote 19 of Appendix F.

### 5.2.1 Single-Ended Biquads

By way of introduction to the space of possible biquad architectures for realizing Stages 1–3 of Figure 5.5, this section describes classic representatives of the established single- and multi-amplifier genres, noting the trade-offs in terms of power, area, and sensitivity that drive the use of the former in power-conscious but prosaic applications and the latter in this work. Admittedly, this survey adopts blanket generalizations of the biquad genres and is by no means comprehensive;<sup>12</sup> but, its insights remain valid for subsequent analyses of implementation nonidealities.

#### 5.2.1.1 Sallen-Key

Archetype for a class of single-amplifier biquads, the Sallen-Key topology of Figure 5.6 consumes less area and power than the multiple-amplifier implementations to follow. However, its high sensitivity to both the properties of its lone opamp and the precise realization of its passive component values renders it unsuitable given the desired robustness. The biquadratic transfer function for Sallen-Key topology of Figure 5.6(a) using an opamp of gain  $A_1(s)$  is:

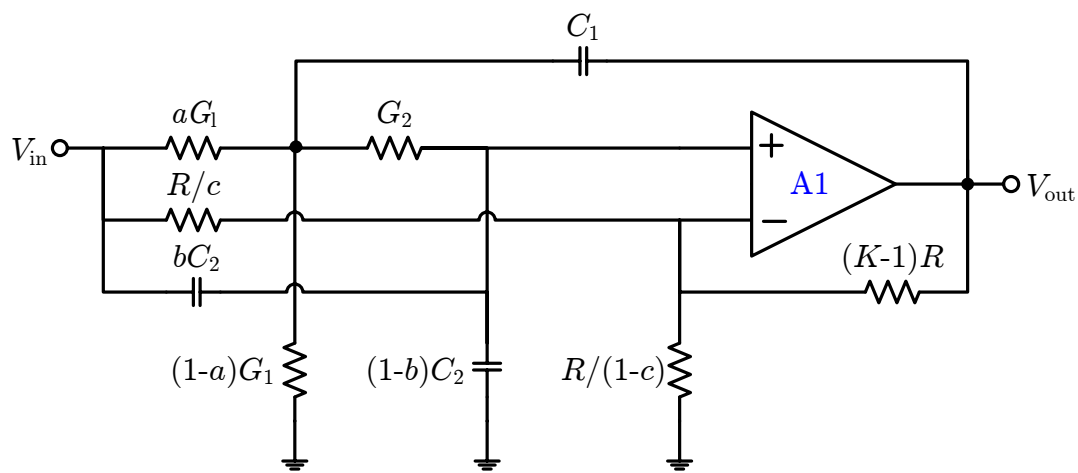
$$T_{SK2}(s) = -\frac{K}{1 + K/A_1(s)} \frac{s^2 [C_1 C_2 (d - b)] + s [C_2 (G_1 + G_2) (d - b) + d G_2 C_1] + (d - a) G_1 G_2}{s^2 [C_1 C_2] + s \left[ C_2 (G_1 + G_2) + G_2 C_1 \left( 1 - \frac{K}{1 + K/A_1(s)} \right) \right] + G_1 G_2} \quad (5.10)$$

where  $d = c(K - 1)/K$ .

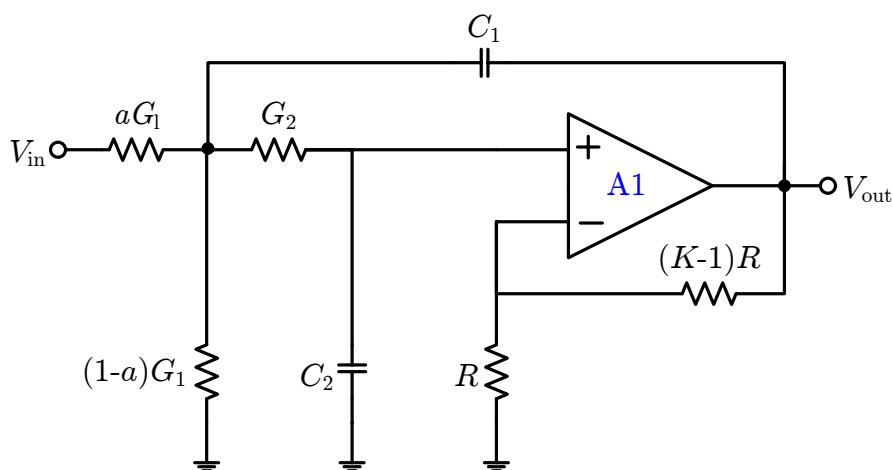
To assess the impact of passive component mismatch, let the opamp be ideal ( $A_1(s) \rightarrow \infty$ ) and, since the Type I Chebyshev AAF specified in Table 5.1 maps to the

---

<sup>12</sup>Chapter 9 of [*Sedra and Brackett, 1978*, p.479–587] is suggested for those interested in a thorough and well-structured analysis of the biquads prevalent in modern ICT filters.



(a) Full biquadratic stage.



(b) All-pole stage.

Figure 5.6: Single-ended Sallen-Key biquads. Using just a single amplifier,  $A_1$ , both (a) a full biquadratic and (b) an all-pole transfer function, corresponding to (5.10) and (5.11), respectively, are realized. After [Sedra and Brackett, 1978, p.516–524].

all-pole Sallen-Key topology of Figure 5.6(b), let  $c=b=0$ ,<sup>13</sup> such that (5.10) becomes:

$$T_{\text{SK1}}(s) = aK \frac{G_1 G_2}{s^2 [C_1 C_2] + s [C_2 (G_1 + G_2) + G_2 C_1 (1 - K)] + G_1 G_2} \quad (5.11)$$

Since this topology actually afford more degrees of freedom than are needed to specify the parameters in the general all-pole formula of (5.9), it is convenient to place some restrictions on the allowable component values, thereby simplifying (5.11). If  $C_1=C_2=C$  and  $G_1=G_2=G$ , then it becomes

$$T_{\text{SK1}}(s) = aK \frac{G^2}{s^2 C^2 + sGC(3 - K) + G^2} \quad (5.12)$$

It is readily apparent from (5.12) that the key parameters of (5.9) are:

$$\omega_o^2 = \frac{G}{C} \quad (5.13a)$$

$$Q_o = \frac{1}{3 - K} \quad (5.13b)$$

$$T_o = aK \quad (5.13c)$$

The undesired sensitivity to component values is then evident by using (5.13b) and (5.13c) to express the percent change of  $Q_o$  and  $T_o$  relative to percent changes in the matching parameter  $K$ , such that

$$\frac{\Delta Q_o / Q_o}{\Delta K / K} \simeq 3Q_o - 1 \quad (5.14a)$$

$$\frac{\Delta T_o / T_o}{\Delta K / K} \simeq 1 \quad (5.14b)$$

---

<sup>13</sup>These choices of  $b$  and  $c$  eliminate the feed-forward capacitor and resistor between the input and the virtual ground nodes of the opamp. Since the natural modes of the filter describe its response with the input grounded, and since these two components add in parallel with their complementary  $(1-b)$  and  $(1-c)$  partners under such conditions, their removal has no impact on the denominator of (5.11), leaving it identical to that of (5.10). Indeed, any feedforward method for introducing arbitrary transmission zeros can be interpreted as partitioning components that lie between the opamp inputs and ground, and feeding the latter terminal of one of the parallel partitions from the input instead [Schaumann and van Valkenburg, 2001, p.211].

Equation (5.14b) is not especially interesting, but (5.14a) reveals that, though acceptable for the first two stages, the sensitivity of the high  $Q_o$  in Stage 3 yields an  $\sim 25\%$  error in selectivity for just a 1% change in the matching of the resistors at the inverting terminal of A1. This amplification of the component sensitivity by a factor of  $(3Q_o - 1)$ , when coupled with the matching tolerances of modern silicon processes, eliminates the Sallen-Key topology from consideration for high- $Q$  AAF realizations [*Schaumann and van Valkenburg, 2001*, p.165].<sup>14</sup>

### 5.2.1.2 Tow-Thomas

Classic multi-amplifier biquads such as the Tow-Thomas topology depicted in Figure 5.7 obviously require more power and area, in this case using three opamps to realize the second-order transfer function of (5.8) (though A3 merely provides an inversion since  $G_6 \equiv G_5$ ). The trade-off is a state-variable design that simultaneously affords access to multiple filter outputs, as well as the advantage of orthogonal tuning, in which the parameters of (5.8) have a one-to-one correspondence with circuit components, so the size of each can be determined successively rather than iteratively. While boasting low passive sensitivities for  $\omega_o$  and  $Q_o$ , low-frequency active sensitivities for  $\omega_o(Q_o)$  that are at(near) the theoretical minimum, and an element spread no larger than  $Q$  [*Sedra and Brackett, 1978*, p.559], the key shortcoming of this topology is its  $Q$ -enhancement, which is the effective increase

---

<sup>14</sup>Even if sufficient matching could be obtained through the use of exacting layout techniques and/or the use of precision off-chip component arrays, single-amplifier biquads such as the Sallen-Key require very high-speed (and, thus, high-power) opamps to realize high- $Q$  stages. Using the simplest possible model for an opamp with finite gain-bandwidth  $\omega_t$ —that of an integrator (cf. Section 3.1.1) for which  $A_1(s) = \omega_t/s$ —it can be shown that the natural frequency and  $Q$  obtained with actual opamps,  $\omega_{or}$  and  $Q_{or}$ , are related to the ideal values by:

$$\frac{\omega_{or}}{\omega_o} = \frac{1}{\sqrt{1 + \epsilon_{sk}}} \simeq 1 - \frac{\epsilon_{sk}}{2}$$

$$\frac{Q_{or}}{Q_o} = \sqrt{1 + \epsilon_{sk}} \simeq 1 + \frac{\epsilon_{sk}}{2}$$

where  $\epsilon_{sk} = (\omega_o/\omega_t)K^2$ . According to these expressions, a minimum-speed opamp, for which a designer's rule-of-thumb dictates that  $\omega_t = 10\omega_o$ , would produce errors of approximately  $-40\%(+40\%)$  in the radial distance( $\theta_o$ ) of the poles in Stage 3 [*Schaumann and van Valkenburg, 2001*, p.166].

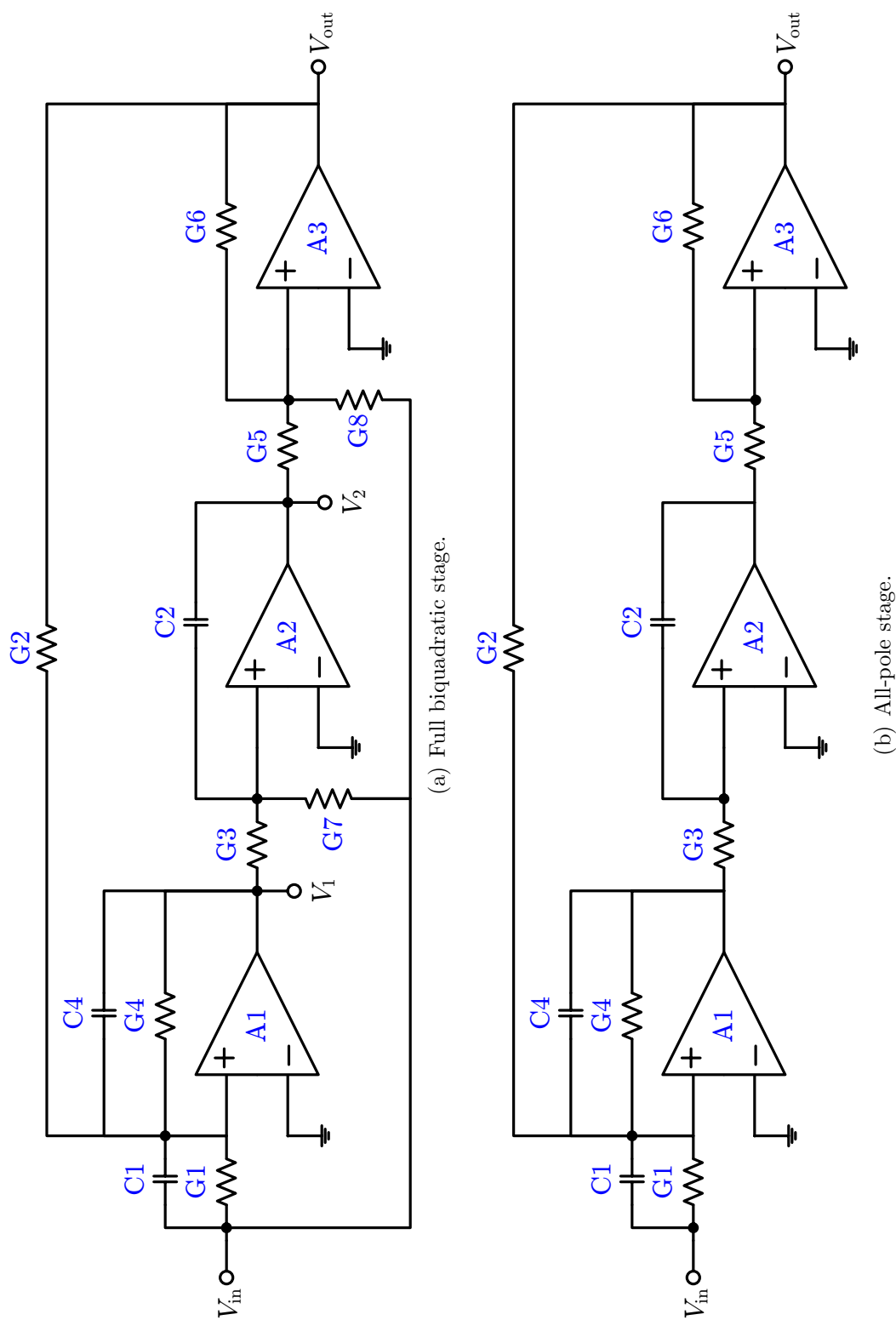


Figure 5.7: Single-ended Tow-Thomas biquads. With three amplifiers, both (a) a full biquadratic (at  $V_1$ ) and (b) an all-pole transfer function (at  $V_{out}$ ), corresponding to (5.15) and (5.16), respectively, are realized.

in  $Q$  when going from design to implementation due to the excess phase contributed by each of the finite-bandwidth amplifiers in the dual-integrator loop.

Before addressing such active sensitivities, first consider the passive sensitivities obtained by deriving the full biquadratic transfer function for the circuit of Figure 5.7(a) assuming  $A_x(s) \rightarrow \infty$  for  $x = 1, 2, 3$ :

$$T_{\text{TT2}}(s) = \frac{V_1}{V_{\text{in}}} = -\frac{s^2 (C_1 C_2) + s \left( G_1 C_2 - \frac{G_8}{G_6} G_2 C_2 \right) + G_2 G_7}{s^2 (C_2 C_4) + s (G_4 C_2) + G_2 G_3} \quad (5.15)$$

Note that the overall output is taken at the output of A1, rather than A3, in order to obtain the best match to (5.8) with minimal dependence on component matching. However, since transmission zeros are not required for the Type I Chebyshev, it suffices for the remainder of this section to consider only the transfer function to the output of A3 in Figure 5.7(b), for which the corresponding state variable has an all-pole response:

$$T_{\text{TT1}}(s) = \frac{V_{\text{out}}}{V_{\text{in}}} = -\frac{G_1 G_3}{s^2 (C_2 C_4) + s (G_4 C_2) + G_2 G_3} \quad (5.16)$$

The relationship between the terms of (5.16) and those of the generalized second-order system in (5.9) can be obtained by inspection:

$$\omega_o^2 = \frac{G_2 G_3}{C_2 C_4} \quad (5.17a)$$

$$Q_o = \frac{\sqrt{G_2 G_3 C_2 C_4}}{G_4 C_2} \quad (5.17b)$$

$$T_o = \frac{G_1}{G_2} \quad (5.17c)$$

The orthogonal tuning is evident—the DC gain( $Q$ ) can be adjusted independently from  $\omega_o$  through changing the value of  $G_1(G_4)$ . Retaining only these two degrees of freedom by assigning to all capacitors(resistors) a value of  $C(R)$  except  $G_1 = kG$ , and

$G_4 = G/q$ , (5.16) and (5.17) reduce to

$$T_{\text{TT1}}(s) = -\frac{kG^2}{s^2C^2 + s\frac{GC}{q} + G^2} \quad (5.18)$$

and

$$\omega_o^2 = \frac{G}{C} \quad (5.19a)$$

$$Q_o = q \quad (5.19b)$$

$$T_o = -k \quad (5.19c)$$

In contrast to the Sallen-Key  $Q$ -sensitivity of (5.14a), the sensitivity of (5.19a) to the mismatch between R4 and the remaining resistors ( $K = 1 - q$ ) depends inversely on  $Q$  according to

$$\frac{\Delta Q_o/Q_o}{\Delta K/K} \simeq 1 - \frac{1}{Q_o} \quad (5.20)$$

which favors the use of the Tow-Thomas architecture for Stage 3.

Although the aforementioned  $Q$ -enhancement for finite-bandwidth opamps can be investigated through a derivation of (5.15) or (5.16) that includes the responses of A1–A3, the proliferation of opamps and the loop complexity of the Tow-Thomas topology produces an expression that, unlike (5.10), is of little intuitive utility. Instead, assume for the moment that the effects of opamp nonidealities, which are handled through a methodology described in Section 5.3, are benign enough to permit further exploration of this architecture.

### 5.2.2 Canonical 2<sup>nd</sup>-Order Section

To eliminate one opamp from the Tow-Thomas biquad, observe that the inversion performed by A3 is trivially accomplished with differential circuitry by simply swapping the positive and negative signal lines. If, in addition, the order of the integrators in Figure 5.7(a) is reversed, so that the lossy integrator comprised of A1



follows the lossless integrator comprised of A2,<sup>15</sup> the result, illustrated in Figure 5.8, is known as a canonical 2<sup>nd</sup>-order section (CSOS) [*Schaumann, 1993*, p.9]. Presuming the availability of fully differential opamps A1 and A2 with infinite bandwidth, the CSOS of Figure 5.8(a) realizes a biquadratic transfer function

$$T_{\text{CS2}}(s) = \frac{V_{\text{out}}}{V_{\text{in}}} = -\frac{s^2 (C_2 C_3) + s G_3 (C_1 - C_5) + G_1 G_3}{s^2 (C_2 C_4) + s (G_4 C_2) + G_2 G_3} \quad (5.21)$$

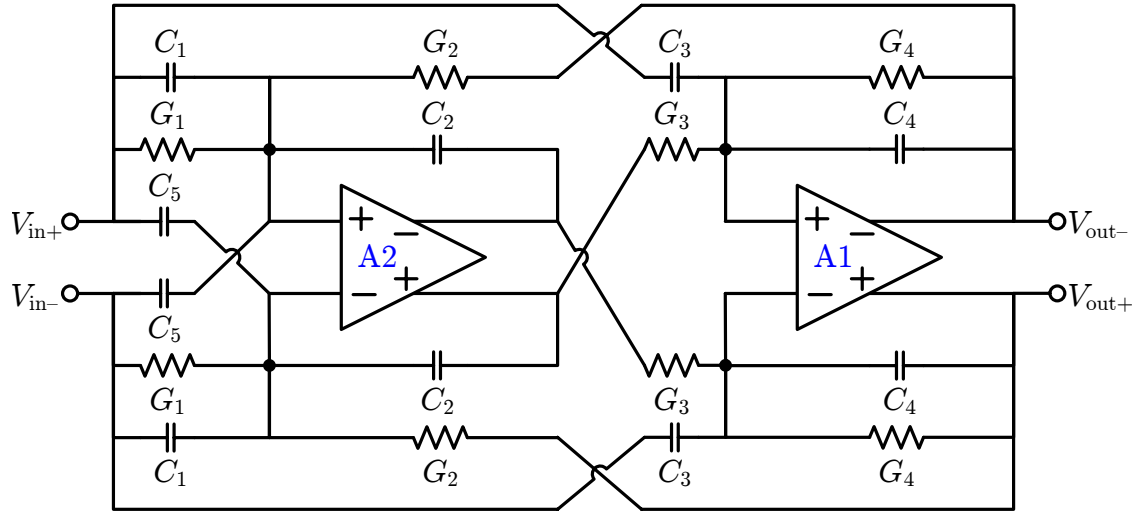
that is practically identical to (5.15).

Based on the Tow-Thomas topology from which it is derived, this may seem somewhat surprising, since it should no longer be possible to introduce feedforward transmission zeros, as in Figure 5.7(a), without a third summing node at which to inject the input (via G8) once A3 has been removed. However, by reversing the order of the lossy and lossless integrators, so that the output of A1, at which (5.15) is measured, becomes the overall output at which (5.21) is measured, and by introducing two new capacitors (C3 and C5) to inject the input into the virtual grounds that remain, an equivalent effect is produced. Using capacitors C3 and C5 as the feedforward elements and driving them with signals of opposite polarity injects currents at the virtual grounds of A1 and A2 that have the correct phase so as to experience the same loop transmission observed when injecting a portion of the input into the virtual grounds of A2 and A3 in Figure 5.7(a) using G7 and G8. However, it is also because of this extra phase that the order of the integrators must be swapped; otherwise, though the overall transfer function would remain biquadratic, orthogonal tuning would no longer be available since the same components would control multiple coefficients in both the numerator and denominator of  $T_{\text{CS2}}(s)$ .

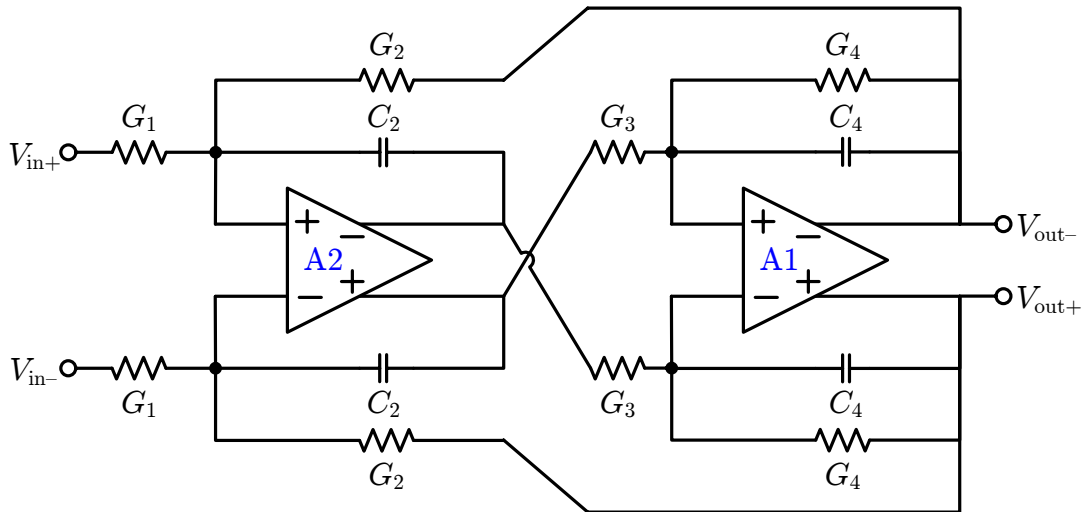
Removing C1, C3, and C5 to produce the all-pole transfer function required for the AAF approximation of (5.7) obviates these differences between the feedforward methods of the CSOS and Tow-Thomas so, not surprisingly, the resulting  $T_{\text{CS1}}(s)$  for Figure 5.8(b) is identical to that of  $T_{\text{TT1}}(s)$  in (5.16). Thus, although sacrificing the full complement of state variable outputs, the differential CSOS affords the benefits

---

<sup>15</sup>Although the amplifier indexing is preserved from Figure 5.7, such that A1(A2) still serves as the basis of a lossy(lossless) integrator, the associated passive components have been renumbered in Figure 5.8.



(a) Full biquadratic stage.



(b) All-pole stage.

Figure 5.8: Differential canonical 2<sup>nd</sup>-order section. By using two fully differential amplifiers, both (a) a full biquadratic and (b) an all-pole transfer function, corresponding to (5.21) and (5.16), respectively, are realized. After [Sedra and Brackett, 1978, p.81].

which attend the single-ended Tow-Thomas biquad, namely orthogonal tuning and sensitivities of  $\omega_o$  and  $Q_o$  to both passive component values and amplifier DC gains that are near theoretical limits, but with one fewer opamp.

In order to perform both the coarse programming and fine trimming of the cut-off frequency electrically, it is clear from the poles of (5.18):

$$p^T = -\frac{G}{2qC} \left( -1 \pm \sqrt{1 - 4q^2} \right) \quad (5.22)$$

that either the unit capacitance ( $C$ ) or unit conductance ( $G$ ) must be variable. In much of the literature, the approach taken is to implement each capacitor as a matrix of parallel elements that can be switched in or out to produce the effective size desired [Durham *et al.*, 1992, p.652–654]. However, as discussed at the outset of this chapter vis-à-vis SC filters, the non-linearity of MOS switches renders them ill-suited to the large signal swing of the AAF. Thus, Section 5.3 focuses primarily on integrator architectures that incorporate variable conductances.

### 5.3 Integrator Architecture

The chosen CSOS stage architecture in Figure 5.8(b) simply depicts the feedback of G2 wrapped around a forward-path containing two active-RC integrators that have been broken out in Figure 5.9: a lossless Miller integrator composed of A2, G1, and C2; and a lossy Miller integrator composed of A1, G3, G4, and C4. Whereas the ideal transfer functions for these circuit implementations

$$T_{M2}(s) = -\frac{G_1}{sC_2} \quad (5.23)$$

$$T_{M1}(s) = -\frac{G_3}{G_4 + sC_4} \quad (5.24)$$

are designed to identically replicate the mathematical description of the filter, these expressions can be drastically perturbed by nonidealities such as the dissipative loss of passive components and the parasitic poles and zeros of active components. Using

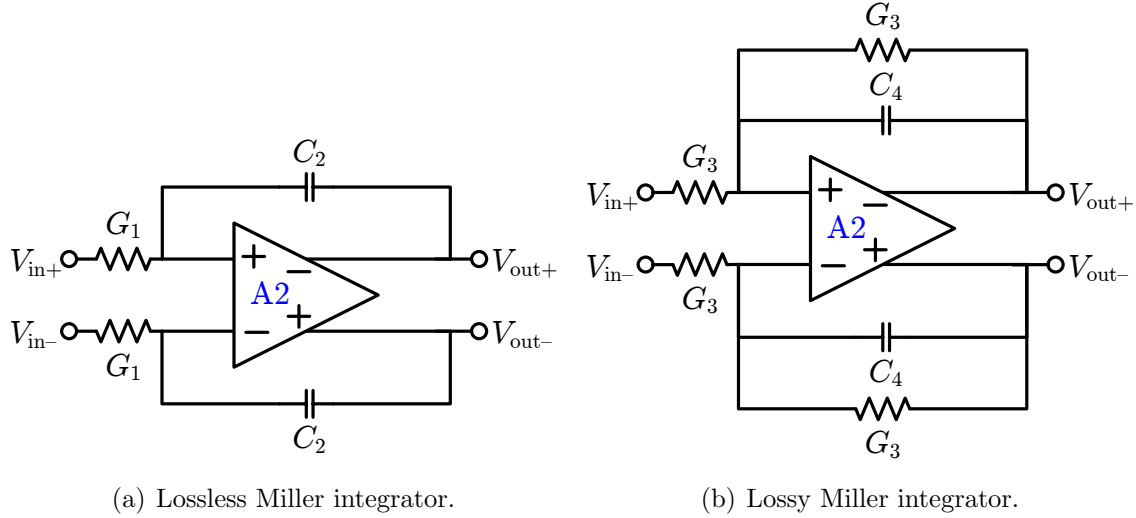


Figure 5.9: Breakout of differential Miller integrators that comprise canonical 2<sup>nd</sup> order section. Component values correspond to those of CSOS in Figure 5.8(b).

the loss metrics of Section F.2, this section evaluates several integrator architectures that seek to minimize the impact of these nonidealities, determining how faithfully they adhere to (5.23) and (5.24), and eventually identifying the hybrid  $G_m$ -C-opamp integrator architecture as most suitable for the AAF stages.

### 5.3.1 Active Integrators

Although efforts to develop low-dissipation integrators have sought to remove the opamp altogether, thereby ameliorating the excess phase in the loop, such transconductance-capacitance ( $G_m$ -C) integrators, lacking feedback, are highly sensitive to parasitic capacitances at the transconductor outputs as well as to variations in the gains of the active transconductors themselves. Thus, for ICTs that require robustness and precision while offering the ability to tuning their frequency response electronically, the two most common integrator topologies employ opamp feedback at the expense of greater excess phase,  $\Delta\phi(\omega)$  [Durham et al., 1992, p.656].

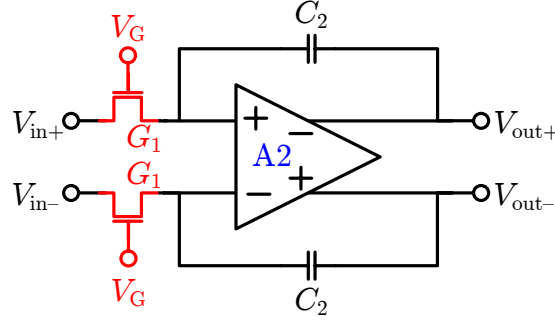


Figure 5.10: Differential, lossless MOSFET-C integrator. Gate bias  $V_G$  tunes the triode drain-source conductance of all nMOSFETs in unison.

### 5.3.1.1 MOS-C-Opamp

Figure 5.10 depicts one such approach, in which the resistors of Figure 5.9(a) are replaced with nMOS transistors operating in the triode region. By tuning the gate overdrive of these elements, their channel resistance can be adjusted, as necessary, to set the pole locations via the unit conductance term in (5.22). Although quite popular [*Banu and Tsividis, 1985; van Bezooijen et al., 1991; van der Plas, 1991*], this so-called MOSFET-C-Opamp integrator suffers from a triumvirate of drawbacks that preclude its employ here.

First, since they carry DC current, triode MOSFETs exhibit flicker noise given by (2.11). As this noisy drain current  $i_{\text{out}}^2$  adds directly to the signal current at the virtual ground nodes, the  $1/f$ -noise of the MOS ‘resistances’ can only be assuaged through making them extremely large, as noted in Section 3.1.3.3. With a minimum of 24 resistors required for three CSOS biquads with the structure of Figure 5.8(b), and at least 25% more mandated for approximations with  $Q > 1$  (as in Stages 2 and 3), the area penalty incurred in reducing the MOS  $f_K$  to  $\sim 100$  Hz is acute.

Secondly, the  $36\times$  programmable range of  $f_p$  specified in Section 3.1.1.2 is far beyond the tuning that can be achieved via nMOS gate voltages. Assuming  $V_{\text{thn}} \simeq 500$  mV, and forgoing any charge pumping to bootstrap the gates, the maximum gate overdrive is only 750 mV since one end of the resistor is always a virtual ground. The corresponding minimum overdrive for the prescribed tuning range,  $\sim 21$  mV, is well below  $V_{\text{ds}}$  at a maximum input signal of  $\sim 500$  mV, making it impossible to maintain

triode operation.

Even for a tuning range narrow enough that  $V_{\text{dsat}} > V_{\text{ds}}$  holds over the entire input signal swing, the traversal of the triode region in Figure 3.5 over the breadth of that swing is so delocalized as to violate the conditions under which MOSFET-C-Opamp operation has been shown to be linear. Whereas *Banu and Tsividis* [1983, p.644–646] argue that switch distortion is differentially canceled, since it only consists of even-order terms arising from the  $V_{\text{ds}}^2$  addend in the first-order, long-channel triode region description of (3.9), such a simplistic equation does not hold over the breadth of triode region encompassed by the large AAF signal swing, especially near the saturation/triode transition. Compounded by mismatch, the breakdown of the triode model for 1-V signals limits practical distortion ratios to  $\sim 60$  dB [*Voorman*, 1993, p.33].

Finally, radiation-induced  $\Delta V_{\text{it}}$  and  $\Delta V_{\text{ot}}$  compound these noise and biasing problems. Without modifying the architecture through additional feedback loops, the unadulterated MOS total-dose degradation can corrupt  $\omega_o$  and  $Q_o$  through nonuniformities in the unit  $G_{\text{mo}}$  that arise from the mismatched  $\Delta V_{\text{th}}$  profiles of unequally biased elements in the two biquad integrators (cf. Section 2.1.1.1). Additionally, the AAF dynamic range suffers as flicker noise levels, already higher in nMOS than pMOS devices, rise with TID (cf. Section 2.1.1.4).

### 5.3.1.2 $G_{\text{m}}$ -C-Opamp

Expending additional power through the use of an active feedback loop that secures linear transconductance via a passive element, as in the first stage of the LNA, the shortcomings of the MOSFET-C-Opamp integrator are largely addressed by the  $G_{\text{m}}$ -C-Opamp integrator of Figure 5.11 [*Georgantas et al.*, 1993, p.1260]. Each pair of triode nMOS elements is replaced with a fully differential active transconductor which, using techniques akin to those of Section 4.2.2, can provide a low-noise, highly linear voltage-to-current conversion that is robust to the effects of radiation. Again, multiple feedback loops desensitize this gain to the nonlinearities and radiation susceptibilities of the composite transistors for which nMOS are eschewed in favor of the lower noise offered by npn BJTs and pMOSFETs. By incorporating a linear current amplifier into

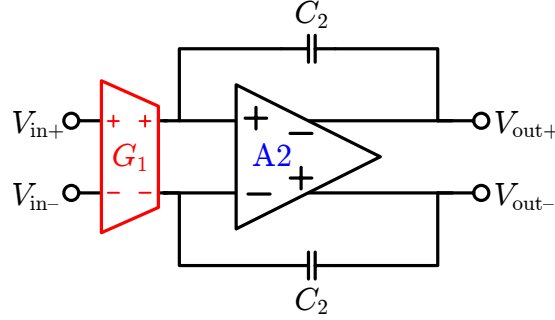


Figure 5.11: Differential, lossless  $G_m$ -C integrator. To produce the same currents on each half of the integrator as the resistors in Figure 5.9(a) while seeing the full  $V_{in}$ , rather than just  $V_{in+}$  or  $V_{in-}$ , the transconductor possesses a single-ended conductance of  $G_1/2$ . Thus, as shown, its differential transconductance is  $G_{m1} = G_1$ . Consult Figure 5.13(a) for transconductor polarity conventions.

each transconductor, its gain can be electronically tuned over a much wider range than a triode nMOSFET. Although its construction is optimized for the power efficiency of this tuning, the static power dissipation of the  $G_m$ -C-opamp integrator necessarily surpasses that of the alternative in Figure 5.10, whose triode elements require minimal bias current and only enough dynamic power to drive their  $C_{gs}$  during tuning.

In addition to its linear, tunable conductance the integrator of Figure 5.11 provides suppression of the opamp noise (specifically,  $e_n$ ) which is superior to the that of its MOSFET-C-Opamp counterpart on account of unilateralization. Consider the noise transfer functions of the two integrators,  $E_{mos}(s)$  and  $E_{gm}(s)$ , when the feedback factors are determined by breaking the loops at the non-inverting opamp input terminals of Figure 5.10 and Figure 5.11 and the finite output resistance of G1 is denoted  $r_{o1}$ :

$$E_{mos}(s) = \frac{V_{out}}{e_n} = A_2(s) \frac{1 + s/p_1}{1 + (s/p_1)(1 + A_2(s))} \quad (5.25)$$

$$E_{gm}(s) = \frac{V_{out}}{e_n} = A_2(s) \frac{1 + s/p'_1}{1 + (s/p'_1)(1 + A_2(s))} \quad (5.26)$$

where  $p_1 = G_1/C_2 = G_{m1}/C_2$  and  $p'_1 = 1/r_{o1}C_2$ , provided  $G_{m1} = G_1$  to permit fair comparison. Since the product  $G_{m1}r_{o1} > 10^2$  in all modes of the AAF transconductors,

(5.26) approximates its theoretical minimum (unity) over a much broader segment of the passband than (5.25) because the unilateralization of Figure 5.11 moves  $p'_1$  much closer to the origin than  $p_1$ .

Whereas the higher output impedance of the transconductor in the circuit of Figure 5.11 drives the feedback factor, and thus  $E(s)$ , closer to unity, the input signal sees the transconductance gain  $G_{m1}$  rather than  $1/r_{o1}$ , so the closed-loop gain of the two integrators remains the same. Thus, the input-referred noise contribution of  $e_n$  in the  $G_m$ -C-Opamp integrator is reduced from that of the MOSFET-C-Opamp integrator by a factor of  $G_{m1}r_{o1}$ , as seen by contrasting:<sup>16</sup>

$$e_{ni,mos}(s) = e_n(s) \frac{E_{mos}(s)}{T_{int}(s)} = -e_n(s) \left(1 + \frac{s}{p_1}\right) \quad (5.27)$$

$$e_{ni,gm}(s) = e_n(s) \frac{E_{gm}(s)}{T_{int}(s)} = -e_n(s) \left(1 + \frac{s}{p'_1}\right) \left(\frac{1}{G_{m1}r_{o1}}\right) \quad (5.28)$$

Although their input-referred noise profiles converge above  $p_1$  to the same minimum value, the  $G_m$ -C-Opamp integrator shapes the low-frequency noise so as to extend this minimum well below the integrator pole, thereby improving its passband SNR.

As depicted in Figure 5.12 this benefit is accrued for opamps with both white ( $e_n(s) = e_{no}$ ) and pink ( $e_n(\sqrt{s}) = e_{no}/s$ ) input noise voltages, so the  $G_m$ -C-Opamp integrators in this work can employ standard MOS opamp designs that feature high input impedance, thereby minimizing nonlinearities associated with signal-dependent

---

<sup>16</sup>To arrive at the ratio of transfer functions used to input-refer  $e_n$  in (5.27) and (5.28), observe that since they reflect the same natural modes, the denominators of the noise ( $E(s)$ ) and signal ( $T(s)$ ) transfer functions are the same:  $1 + L(s)$ . Thus,  $E(s)/T(s)$  is simply the ratio of the forward path gain experienced by the noise to that seen by the input signal. The former is evident by inspection ( $A_2(s)$ ) whereas the latter can be derived by realizing that for  $A_2(s) \rightarrow \infty$ , the ideal transfer function,  $T_\infty(s) = -1/sRC$ , is equivalent to  $a(s)/L_\infty(s)$ , so

$$a(s) = T_\infty(s) L_\infty(s) = A_2(s) \frac{T_\infty(s)}{E_\infty(s)}$$

where the ideal noise transfer function  $E_\infty(s)$  is, by definition, the reciprocal of the feedback factor  $F(s)$ , so

$$\frac{E(s)}{T(s)} = \frac{A_2(s)}{a(s)} = \frac{E_\infty(s)}{T_\infty(s)} = \frac{1}{T_\infty(s) F(s)}$$

Noise shaping accompanies any feedback configuration for which  $T_\infty(s) \neq F^{-1}(s)$ .



input bias current in BJT opamps. Merging the ideal coupling of MOS opamps with largely bipolar transconductors of high linearity and wide programmability enables the development of a hybrid  $G_m$ -C-Opamp integrator explored next.

### 5.3.2 Hybrid $G_m$ -C-Opamp

In light of the many benefits of  $G_m$ -C-Opamp integrators, the final AAF stage topology of Figure 5.13(b) discards the active-RC integrators in the canonical second-order section, replacing each pair of passive resistors indexed  $j = 1, 2, 3, 4$  in Figure 5.8(b) with a differential transconductor whose gain,  $G_{mj}$ , and polarity are defined by the conventions of Figure 5.13(a). To inform the construction of these transconductances, their impact on the performance of the integrators is examined from several perspectives.

#### 5.3.2.1 Element Sizing

In each stage, the  $G_{mj}$  of the two integrators are chosen so that the CSOS transfer function given by (5.18) yields those poles of (5.7) assigned to that stage in Table 5.1. Since an infinite set of  $G$ ,  $C$ ,  $k$ , and  $q$  can produce this mapping, the following constraints are imposed in order to arrive at the final values given in Table 5.2 for Mode B:

**Capacitor area:** Since noise limits the smallest transconductance  $G_{mj}$  that can be realized, and since the pole frequency is governed by the  $G/C$  ratio of (5.19a), the capacitors should be as large as possible within layout area limitations. To conform to the total die size of SVEPRE-2 given the areal density of the metal comb capacitors in BiCMOS8B+, no single capacitor can exceed 23 pF.

**Capacitor matching:** Contrary to (5.18), it is revealed below that additional degrees of freedom are required to meet transconductor sizing constraints, so all capacitors in a stage need not be equal. However, the size of each is an integer multiple of a unit-sized  $C_o$  so that the capacitors of each stage can be laid out

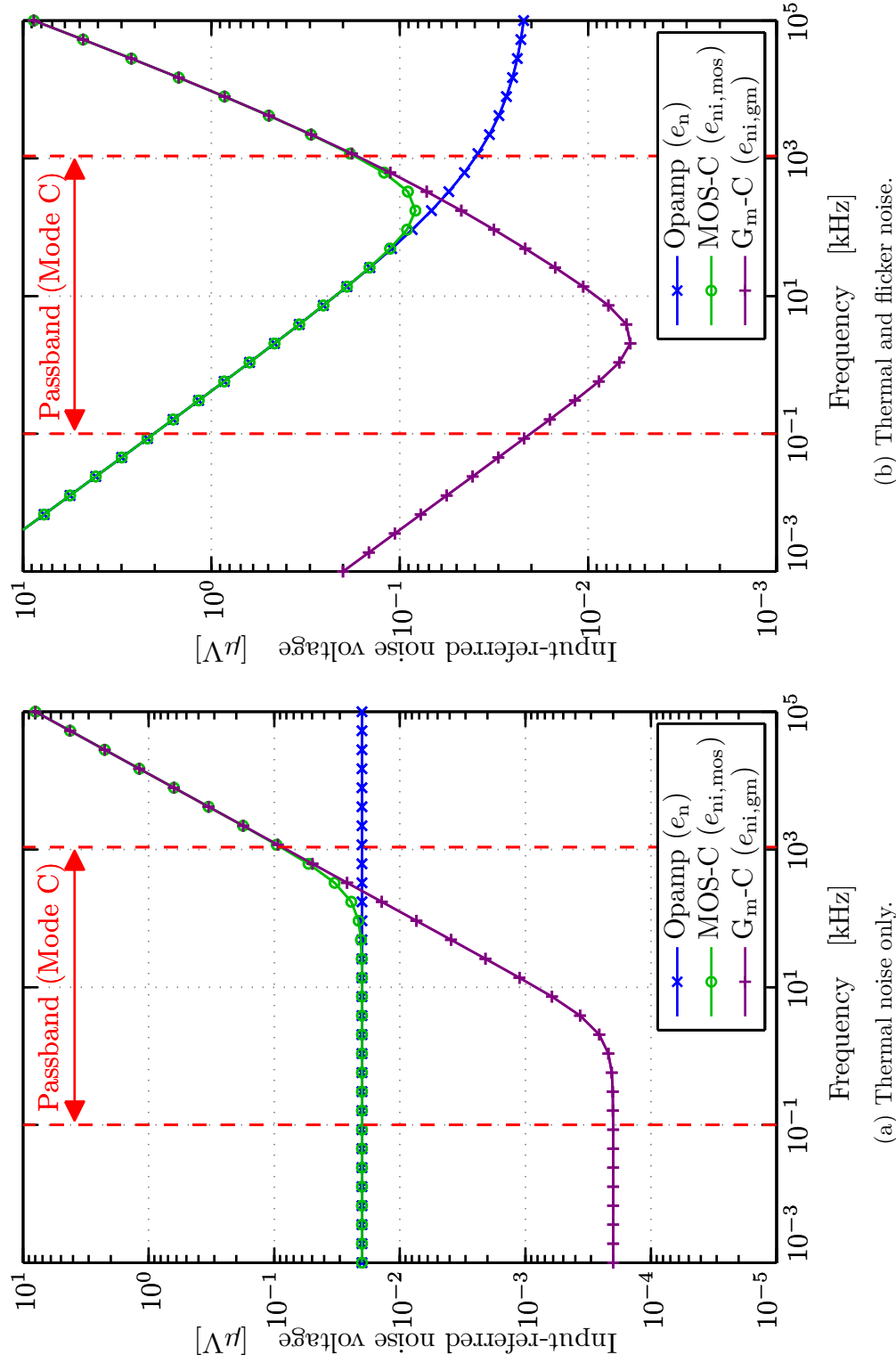
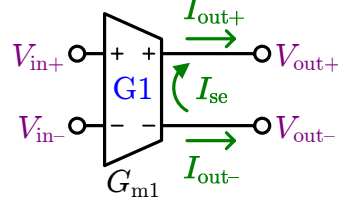
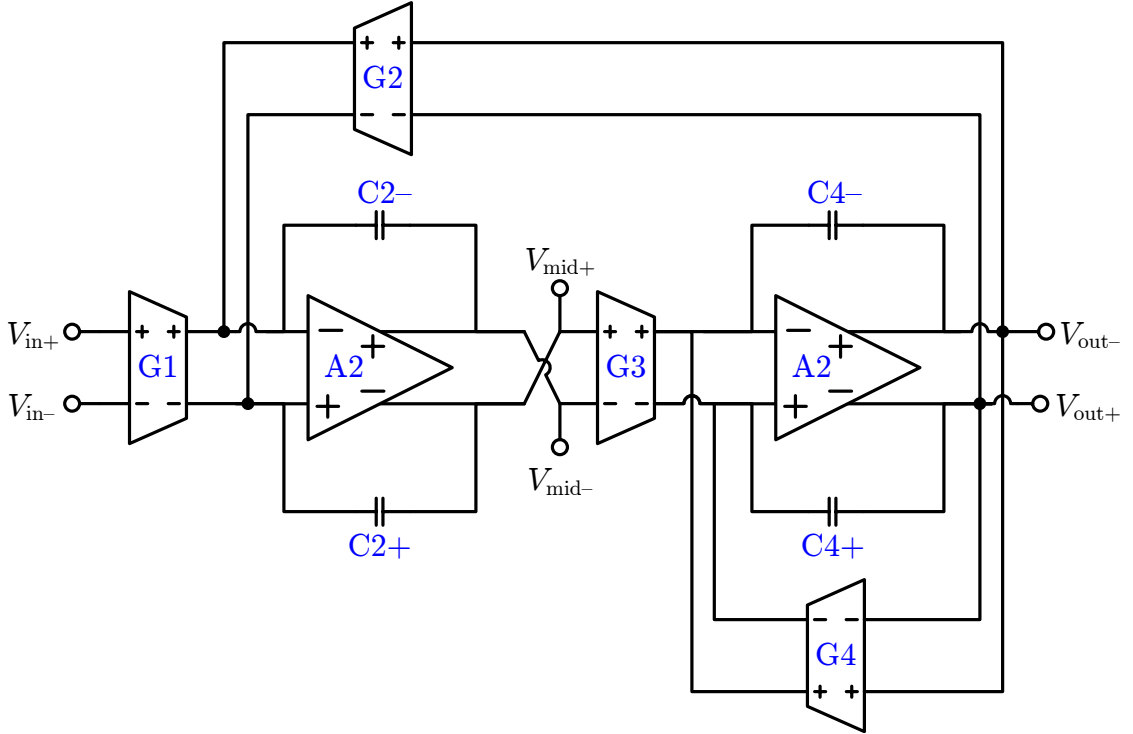


Figure 5.12: Shaping of opamp noise by integrator architectures when the input-referred noise voltage of the opamp is dominated by (a) thermal or (b) flicker noise. The simulations employ the Mode C time constant of the lossless integrator in Stage 3 (cf. Table 5.2) and assume flicker noise corresponding to the  $m=1$  curve in Figure 3.11.



$$G_{m1} = \frac{I_{out+} - I_{out-}}{V_{in+} - V_{in-}} = \frac{2I_{se}}{V_{in}}$$

(a) Transconductor polarity.



(b) AAF stage architecture.

Figure 5.13: Stage architecture that employs the hybrid  $G_m$ -C-Opamp integrators. According to (a) the polarity conventions for the hybrid transconductors in this work,  $V_{in} > 0$  generates  $I_{out}$  through a differential load,  $Z_{load}$ , such that  $V_{out} = I_{se}Z_{load} > 0$ , as for a differential voltage amplifier. This convention determines the polarity of (b) the differential AAF stages, which are composed of integrators derived from Figure 5.11.

in identical common-centroid arrays wherein etch effects are regulated so as to alleviate mismatch.

**Transconductor area:** As shown in Section 5.6, the transconductor layout uses large devices(generous spacing) to lessen the impact(probability) of flicker noise(latchup). Together with the area consumed by the capacitors, the size of transconductors can broach the area limits established by SVEPRE-2 unless the number of transconductors per stage is less than eight.

**Transconductor matching:** Given the large swath of die real estate consumed by the capacitors, it is difficult to maintain tight matching of the transconductors over their corresponding large spatial extent. The best approach is to construct each transconductor from one or more unit cells, each of identical composition and value  $G_{mo}$ , laid out in a common-centroid array and connected in parallel. In other words,  $k$  and  $q$  should be whole-number ratios. Since the total number of transconductors-per-stage is also limited, this requirement translates into a limited  $G_{mj}$ -spread.

**Gain assignment:** The gain assignment prescribed in Section 5.1.3 translates into two ratio constraints on transconductor values. First, to maximize dynamic range, each stage must have 0-dB gain. From (5.19c), this demand implies  $k = 1$ . Although it ensures that the signal at the output of each stage utilizes the full dynamic range, the  $k$ -condition does not prevent the signals at the internal nodes of each stage, in particular the output of opamp A2,  $V_{mid}$  in Figure 5.13(b), from saturating. This is especially likely in high- $Q$  stages where the selectivity of the lossless integrator can be high. At DC, saturation of the internal nodes can be avoided by recalling that  $V_{mid}$  is related to the overall stage output  $V_{out}$  through the reciprocal gain of the lossy integrator:

$$\frac{V_{mid}(s)}{V_{out}(s)} = -\frac{G_4}{G_3} \left( 1 + s \frac{C_4}{G_4} \right) \quad (5.29)$$

By keeping  $G_3 \geq G_4$  in each stage, the internal nodes are assured not to saturate

at DC.<sup>17</sup>

**Stage priority:** The iterative algorithm used to select component sizings according to the above constraints weights the error between the desired and actual coefficients of each stage in proportion its  $Q_o$ . Since the high- $Q$  stages are most sensitive to pole placement, the final sizings seek to minimize errors in the Stage 3 coefficients at the expense of those in Stage 1, resulting in the largest discrepancy for  $a$ .

Synthesizing the component values under these constraints prevents the coefficients of Table 5.1 from being satisfied with the necessary precision unless additional degrees of freedom are re-introduced in (5.18). Thus, though  $k = 1$ , as required for the gain assignment, the stage capacitors and transconductances of (5.16) are otherwise allowed to assume arbitrary integer ratios.<sup>18</sup>

### 5.3.2.2 Ideal Components

Residual discrepancies between the actual and desired loss function coefficients in Table 5.2 that result from the area constraints and discretization of component values are evident when the so-called realizable response is compared with the ideal response characterized by Figure 5.3 and Figure 5.4. If, aside from lacking infinitely precise values, the components of Figure 5.13(b) are otherwise ideal, then Figure 5.14 and

<sup>17</sup>The zero in (5.29) suggests that even if  $G_3 \geq G_4$ , there are frequencies above DC at which the internal node can still saturate if  $V_{out}$  has not rolled-off from its maximum value. Heuristically, it is apparent that  $C_2$  governs the latter phenomenon, since the increase in its current above the pole of the lossless integrator is balanced by a reduction in the output voltage to satisfy KCL at the input to A2. For the limited  $G_m$ -spread in this design, the peaking above DC associated with the C4 zero can also be prevented with the additional constraint that  $C_2 \geq C_4$ . Imposed on the first two AAF stages, unfortunately this inequality cannot be satisfied by the poles of Stage 3, on account of their high  $Q_o$  and the limited  $G_m$ -spread. But, placing them in Stage 3 provides adequate saturation margin since, near its  $\omega_o$ , the input to this stage is already be attenuated below the filter maximum by the preceding two stages because  $\omega_{o1} < \omega_{o2} < \omega_{o3}$ .

<sup>18</sup>An exception must be made in the case of Stage 3, where  $G_{m4} = 0.5G_{mo}$ , in order to provide the necessary  $Q_o$  for Chebyshev pole placement. The layout of this sub-unit transconductor, whose presence arose from the need to modify the AAF transfer function late in the design cycle on account of unforeseen instrument-level exigencies, is accommodated through techniques adumbrated in Section 5.6.1.3.

		Components					Transfer Function		
		Transconductors			Capacitors		$H(s)$ Coefficients <sup>a</sup>		
		ID	Cells <sup>b</sup> [#]	Size [ $\mu$ S]	ID	Cells <sup>c</sup> [#]	Size [pF]	Name	Ideal <sup>d</sup> Actual
Stage 1	G1	1	5	C2+	6	19.02	$a$	$4.91 \times 10^5$	$5.26 \times 10^5$
	G2	1	5	C2−	6	19.02	$b$	$1.50 \times 10^{11}$	$1.38 \times 10^{11}$
	G3	2	10	C4+	6	19.02			
	G4	2	10	C4−	6	19.02			
Stage 2	G1	2	10	C2+	5	15.85	$c$	$3.59 \times 10^5$	$3.94 \times 10^5$
	G2	2	10	C2−	5	15.85	$d$	$7.04 \times 10^{11}$	$7.46 \times 10^{11}$
	G3	3	15	C4+	4	12.68			
	G4	1	5	C4−	4	12.68			
Stage 3	G1	2	10	C2+	2	6.34	$e$	$1.32 \times 10^5$	$1.31 \times 10^5$
	G2	2	10	C2−	2	6.34	$f$	$1.26 \times 10^{12}$	$1.24 \times 10^{12}$
	G3	3	15	C4+	6	19.02			
	G4	0.5	2.5	C4−	6	19.02			

<sup>a</sup> According to definition in (5.7).

<sup>b</sup> Transconductor sizes are relative to a unit value of  $G_{\text{mo}} = 5\mu\text{S}$  (Mode B).

<sup>c</sup> Capacitor sizes are relative to a unit value of  $C_o = 3.17$  pF (Mode B).

<sup>d</sup> Ideal  $H(s)$  coefficients are taken from Table 5.1 (Mode B).

Table 5.2: Transconductor and capacitor sizes for stage of Figure 5.13(b) in Mode B. Discretized to their corresponding unit cells sizes, these values cannot precisely realize the ideal  $H(s)$  coefficients of Table 5.1.

Figure 5.15 demonstrate the performance of the iterative algorithm responsible for the sizings of Table 5.2.

Of note are two minor differences between the ideal and realizable transfer functions. The most significant ramification of unit-cell-based sizing is the error in coefficient  $a$  of Stage 1, which produces a  $-13\%$  drop in the  $f_{\text{pb}}$  of the stage. This additional attenuation provides some margin for the necessary  $r_\alpha$  and is acceptable because the overall  $f_{\text{pb}}$  of the realizable filter remains within 2% of the ideal.

The excess 1-dB of peaking near  $f_{\text{pb}}$  results from a slight increase(decrease) in the  $\omega_o$  of Stage 2(Stage 3); together, these conspire to nearly eliminate  $v_2^T$ . This peak surpasses 0 dB because, in contrast to the ideal case of  $T_{\text{CS1}}(s)$ , the granularity of the unit transconductors does not permit a reduction in DC gain to offset the ripple

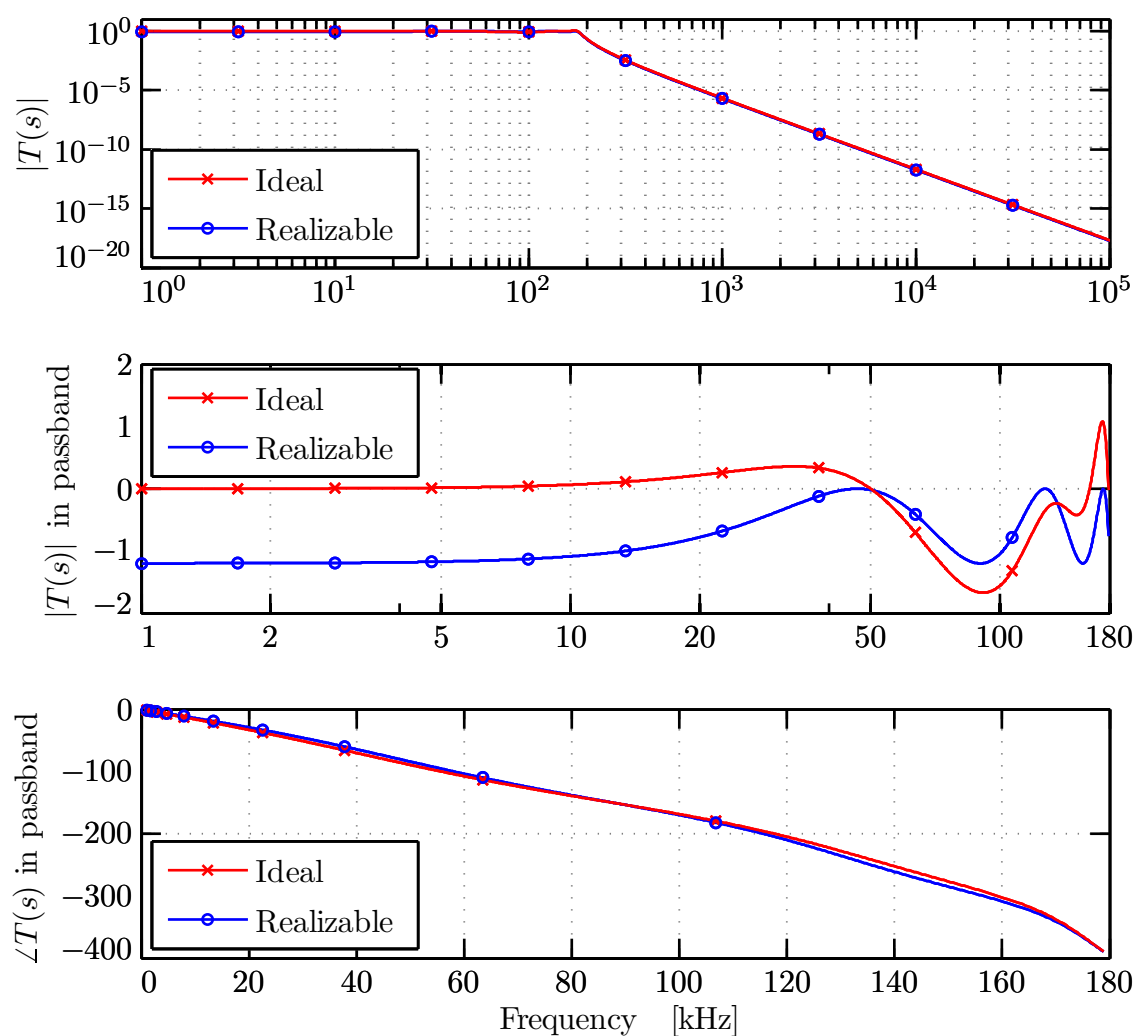


Figure 5.14: Bode response of realizable AAF design for Mode B. Panels correspond to those of Figure 5.3, with the response for the discretized components values of the realizable design in Table 5.2 overlaid. Responses for other modes are simply scaled accordingly.

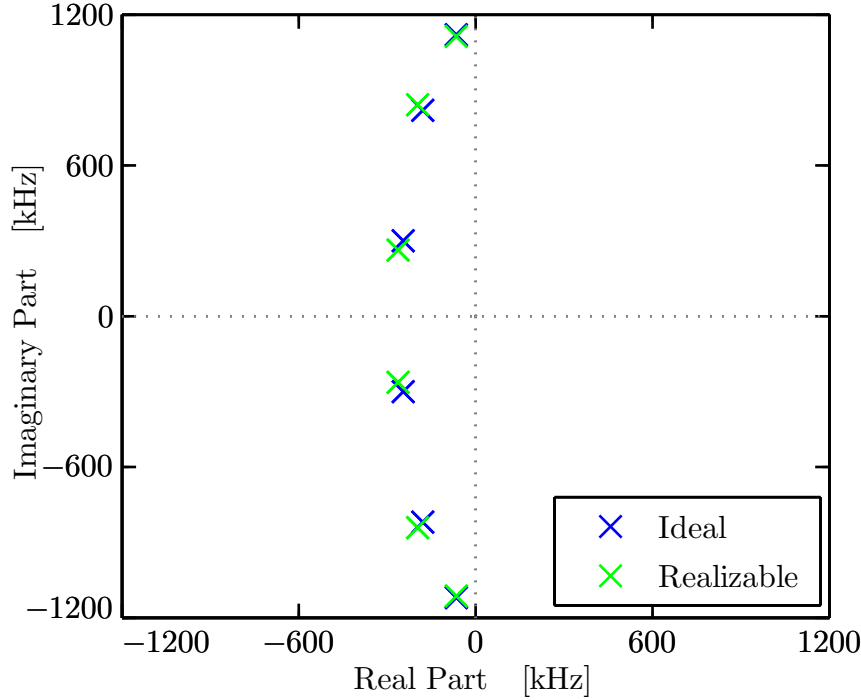


Figure 5.15: Pole/zero plot of realizable AAF design for Mode B. Overlaid with that of the ideal filter (cf. Figure 5.4), the highest- $Q$  poles of the diagram for the realizable design in Table 5.2 exhibit minimum error in accordance with the stage-priority constraint of Section 5.3.2.1. Responses for other modes are simply scaled accordingly.

of  $A_{\max} = -1.2$  dB. Rather than substantially increase the AAF complexity, a simple adjustment of  $G_p$ , whose precision can be arbitrarily small, should be employed if saturation of the ADC is observed.

### 5.3.2.3 Non-Ideal Components, $\alpha$ -error

Figure 5.14 and Figure 5.15 only account for warping of  $T(s)$  due to the nominal component values that can be realized on-chip. Its character is also be affected by the implementation of each of the components in Figure 5.13(b),<sup>19</sup> particularly the

<sup>19</sup>Despite the treatment of Section F.2, which utilizes opamp gain and bandwidth as vehicles for assessing the ideality of an active integrator, the opamp designed for the SVEPRE AAF offers sufficient gain ( $A_o > 80$  dB) and bandwidth ( $\omega_t > 100$  MHz) that the transconductors, of which there are also twice as many, provide the dominant loss terms in (F.34).



transconductors which, in addition to affording the functionality outlined at the start of Section 5.3.1.2, must meet excess phase requirements, since they are active elements whose poles contribute additional terms to the dissipation,  $d_{\text{int}}$ , and time-constant,  $\tau_{\text{int}}$ , of the overall integrator.

Through a network sensitivity analysis that is beyond the scope of this work [*Sedra and Brackett, 1978*, p.362–378] it can be shown that the effect of transconductor excess phase on  $T_i(s)$  is most acute near  $\omega_o$ , where the group delay peaks and results in deviations from the desired attenuation ( $\alpha$ ) and phase lag ( $\phi$ ) of the loss function denoted  $\Delta\alpha$  and  $\Delta\phi$  and approximated by:

$$\Delta\alpha(\omega_o) \simeq d_{\text{int}} \frac{\partial\phi(\omega_o)}{\partial\omega} \quad (5.30a)$$

$$\Delta\phi(\omega_o) \simeq -d_{\text{int}} \frac{\partial\alpha(\omega_o)}{\partial\omega} \quad (5.30b)$$

in the case of uniform dissipation.<sup>20</sup> Since the AAF prioritizes attenuation over passband phase (cf. Section 5.1.1), (5.30a) can be reformulated to explicitly relate the drop in  $\alpha$  to the integrator excess phase using (F.41) as

$$\Delta\alpha(\omega_o) \simeq -\omega_o \tan(\Delta\phi(\omega_o)) \delta(\omega_o) \quad (5.31)$$

where the group delay, expressed as  $\delta(\omega_o)$  (cf. Footnote 8 of Appendix F), and  $\omega_o$  are determined by the form of  $T_i(s)$ .

Figure 5.16 plots (5.31) for each of the stages. It demonstrates that although sizing priorities cause the ideal and realizable curves to deviate most for the first two stages, the reduced group delay of the realized loss functions actually render their  $\Delta\alpha$  less sensitive to transconductor  $\Delta\phi(s)$ . However, to meet a given attenuation error—such as that indicated by the  $\Delta\alpha = 2$  dB line—the excess phase of the transconductors in Stage 3 must be nearly four times less than those in Stage 2, on account of the higher  $Q_o$ . As shown in Figure 6.19(c), attenuation errors near the passband edge in the

<sup>20</sup>Since each of the transconductors is composed of  $x$  unit cells, the variance of the error distribution of beyond/below the average dissipation of the ensemble,  $d_{\text{int}}$ , is narrow enough at  $\pm(2x)^{-1}$ , that each is characterized by the mean  $d_{\text{int}}$  in this analysis.

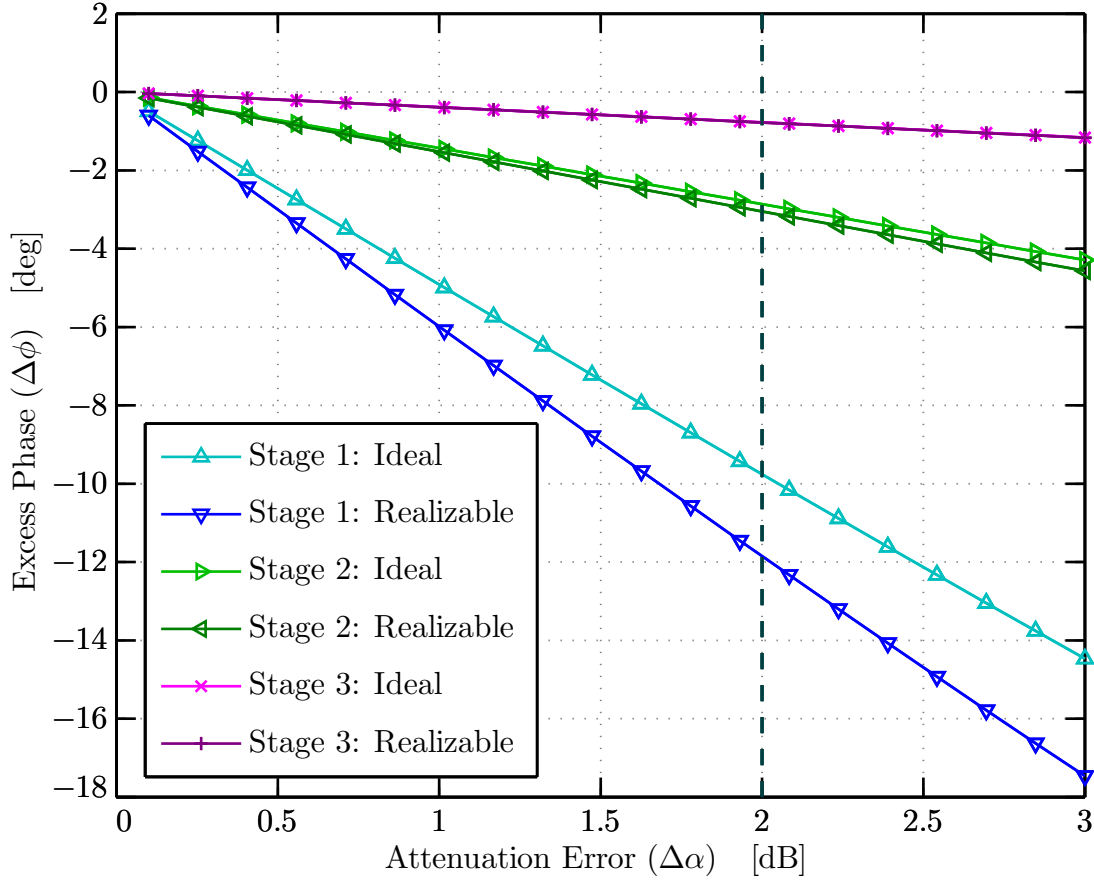
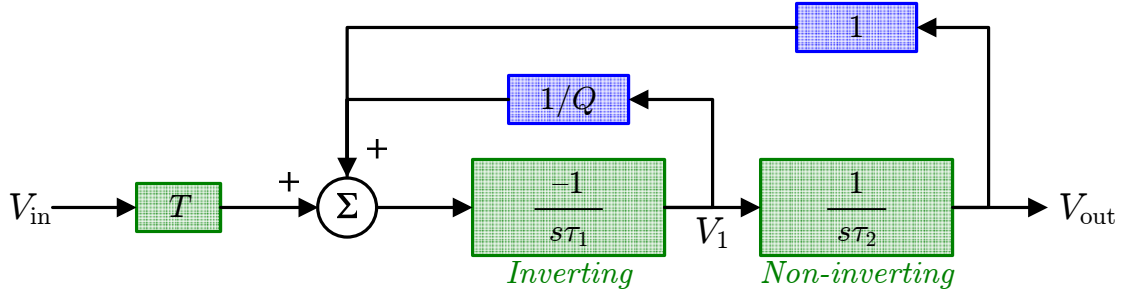


Figure 5.16: Excess phase versus attenuation error for each AAF stage in Mode B. For a reference error of 2 dB (dotted line), the allowable  $\Delta\phi$  of the ideal(realizable) implementation ranges from  $9.76^\circ(11.8^\circ)$  for Stage 1 to  $0.775^\circ(0.778^\circ)$  for Stage 3. Responses for other modes are identical since  $\omega_o$  and  $\delta(\omega_o)$  in (5.31) scale inversely.

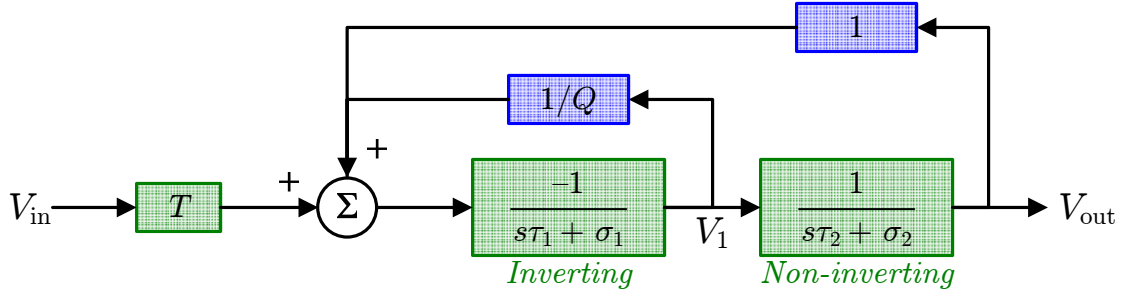
measured  $T(s)$  stem directly from the  $\Delta\phi(s)$ -sensitivity of  $T_3(s)$ .

#### 5.3.2.4 Non-Ideal Components, $Q$ -enhancement

Excess transconductor phase is also responsible for the undesired  $Q$ -enhancement attributed to the Tow-Thomas biquad in Section 5.2.1.2. For the general biquadratic stage, depicted in Figure 5.17(a) and implemented as a two-integrator loop built from the cascade of an inverting and non-inverting integrator, of which the Tow-Thomas topologies is representative, it can be shown that when considering the integrators



(a) All-pole biquad with ideal integrators.



(b) All-pole biquad with non-ideal integrators.

Figure 5.17: Generic biquads based on a two-integrator loop with one inverting and one non-inverting integrator. The generic all-pole transfer function in the case of (a) ideal integrators conforms to (5.9). But, the behavior of (b) actual, lossy integrators corresponds to (5.32).

to have non-ideal transfer functions of the form of (F.34), as in Figure 5.17(b), rather than the ideal, lossless forms of Figure 5.17(a), the transfer function to  $V_1$  (corresponding to  $V_{\text{out}}$  of the CSOS) becomes

$$T_i(s) = \frac{V_1(s)}{V_{\text{in}}(s)} = -T_{\text{or}} \frac{\omega_{\text{or}}/Q_{\text{or}}}{s^2 + s(\omega_{\text{or}}/Q_{\text{or}}) + \omega_{\text{or}}^2} \quad (5.32)$$

where the subscripts on  $\omega_{\text{or}}$ ,  $Q_{\text{or}}$ , and  $T_{\text{or}}$  denote the values of these parameters once the circuit is realized with non-ideal opamps and transconductors. Obviously, (5.32) is in contrast to the ideal formulation of the biquadratic equation given in (5.9) though

the parameters of the two can be related through<sup>21</sup>

$$\omega_{\text{or}} = \omega_o \sqrt{1 + \sigma_1 \sigma_2 + \sigma_2 / Q_o} \quad (5.33a)$$

$$Q_{\text{or}} = Q_o \frac{\omega_{\text{or}}}{\omega_o} \frac{1}{1 + Q_o (\sigma_1 + \sigma_2 \tau_1 / \tau_2)} \quad (5.33b)$$

$$T_{\text{or}} \simeq T_o \frac{1}{1 + Q_o (\sigma_1 + \sigma_2 \tau_1 / \tau_2)} \quad (5.33c)$$

As long as  $Q_o$  is fairly high, the deviation of  $\omega_{\text{or}}$  is small because it is proportional to the product of the losses of the individual integrators,  $\sigma_1$  and  $\sigma_2$ . However, in the case of  $Q_{\text{or}}$  (and  $T_{\text{or}}$ ), the errors defined by the ratios  $Q_{\text{or}}/Q_o$  (and  $T_{\text{or}}/T_o$ ) can be much more significant because, assuming that  $\omega_{\text{or}} \simeq \omega_o$ :

$$\frac{Q_{\text{or}}}{Q_o} \simeq \frac{T_{\text{or}}}{T_o} = \frac{1}{1 + Q_o (\sigma_1 + \sigma_2 \tau_1 / \tau_2)} \quad (5.34)$$

Whenever the parenthetical term in (5.34) is negative, the integrator exhibits  $Q$ -enhancement: the increase over the nominal  $Q_o$  due to the finite bandwidth of its active constituents. Although the denominator of (5.34) depends on the weighted sum of the losses of each opamp, in many cases the two integrators in the loop are set to have the same integration constant, so it is simply the sum of their losses that determines the denominator.

For Figure 5.13(b), assuming that  $\tau_1 = \tau_2$ , and that, as for (5.31), the effect of  $\Delta\phi(\omega)$  is strongest at the natural frequency  $\omega_o$ , the loss terms in (5.34) can be expressed in terms of the excess phase of the  $G_m$ -C-Opamp integrators via (F.41):

$$\left. \frac{Q_{\text{or}}}{Q_o} \right|_{\omega=\omega_o} = \frac{1}{1 - 2Q_o \tan(\Delta\phi(\omega_o))} \quad (5.35)$$

Typically, this condition is less stringent than that of (5.31), but in Stage 3, where the effect is magnified by high  $Q_o$ , transconductors with an excess phase of just  $1^\circ$  enhance the realized  $Q_{\text{or}}$  by more than 40%.

---

<sup>21</sup>In terms of the blocks in Figure 5.17,  $\omega_o = 1/\tau_1 \tau_2$ ,  $Q_o = Q \omega_o \tau_1$ , and  $T_o = TQ$ .

## 5.4 Transconductor Architecture

Since the transconductors in the  $G_m$ -C-Opamp stage integrators ultimately determine the programmability, linearity, radiation-hardness, and noise performance of the overall AAF (as specified in Chapter 3), the crux of the AAF is the invention of a BiCMOS transconductor that satisfies these requirements, along with the low excess phase required for a well-behaved magnitude response near  $f_p$ . The literature is rife with a host of linearized transconductors that depend on either bipolar or MOS amplification.<sup>22</sup> A few examples are briefly summarized in Section 5.4.1 to emphasize the ubiquitous limitations of transistor-based  $G_m$  realizations using feedforward paths before the two-stage architecture of the feedback transconductor in this work, which is predicated on passive voltage-to-current conversion and active current gain, is introduced in Section 5.4.2.

### 5.4.1 Feedforward Transconductors

Seeking to linearize the large-signal behavior of MOS and bipolar transistors summarized by (3.9) and (3.10), single-ended(differential) transconductors commonly use dynamic biasing of one(a pair of) such device(s) at their core to keep it(them) in the correct region of operation regardless of input swing and adjust its(their) transconductance for tuning purposes. Weaknesses of the examples in this section, for which both the input and tuning ranges are limited by the extent to which the bias networks are able to maintain sufficient linearity, inspire the development of a novel solution in Section 5.4.2.

#### 5.4.1.1 Triode MOS

Much as for the MOSFET-C-Opamp integrator in Section 5.3.1.1, the difficulty in relying on the variable resistance of a triode-region MOS device described by

---

<sup>22</sup>In addition to reviewing the operation of and literature on the MOSFET-C-Opamp and  $G_m$ -C-Opamp integrators of Section 5.3.1, [Voorman, 1993] is a worthwhile entrée into the space of such transconductors.

corresponding case of (3.9) to provide a transconductance of the form

$$G_{\text{mo}}|_{\text{linear}} = \frac{\partial I_d}{\partial V_{\text{gs}}} = \mu_n C_{\text{ox}} \frac{W}{L} V_{\text{ds}} \quad (5.36)$$

stems from contrast between the narrow range over which (5.36) holds (namely  $V_{\text{ds}} < V_{\text{ds,sat}}$ ), and the wide input signal swing, which modulates  $V_{\text{ds,sat}}$  proportionally.

To ensure  $V_{\text{ds}}$  is sufficiently low regardless of output current (thereby achieving high  $R_{\text{out}}$ ), the scheme of Figure 5.18(a) [Ali *et al.*, 1993; Castello *et al.*, 1990; Lee, 1998; Pennock, 1985] uses a bipolar EF loop that forces it to track  $R_{\text{lin}} I_{\text{H3}}$ . Unfortunately,  $V_{\text{be1,2}}$  does not remain constant, nor match  $V_{\text{be3}}$ , since the collector currents of Q1 and Q2 are also the output currents. The behavior is reminiscent of (4.4a), but even more detrimental, since  $\Delta V_{\text{be}}$  directly modulates  $G_{\text{mo}}$  through the  $V_{\text{ds}}$  term of (5.36), rather than sublinearly (via a hyperbolic tangent) as in the first stage of the LNA (cf. Section 4.1.1.2).

Full-CMOS incarnations like that of Figure 5.18(b) can employ feedback amplifiers [De Lima and Dualibe, 1999] in place of npn followers to fix  $V_{\text{ds1,2}}$ . But, the excess phase of such transconductors, augmented by that of their internal feedback loops, is routinely higher. Furthermore, all triode-MOS transconductors suffer from  $1/f$  noise, body-effect distortions, and nonlinearity introduced by high-overdrive mobility degradations for large input voltages.

#### 5.4.1.2 Saturated MOS

Since the saturation region of MOS operation can span a wider range than its linear counterpart for reasonable levels of inversion, as in Figure 3.5, the familiar square-law description of saturated behavior is the basis for many MOS transconductors. Perhaps none is more renown than that of Nauta [1992], reproduced in Figure 5.19(a), whose popularity derives from being constructed only of inverters available in any standard CMOS library. If the first set of inverters is well-matched, the voltage-to-current conversion they perform is linear as long as they remain in strong inversion. The cross-coupled inverters between the output lines set the common-mode voltage and offer tunable negative resistance that can increase the DC gain of the transconductor.

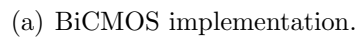


Figure 5.18: Popular differential transconductors based on triode MOS operation. Either (a) a loop of npn EFs (after [Ali *et al.*, 1993, p.43]) or (b) a CMOS feedback amplifier (after [De Lima and Dualibe, 1999, p.642]) ensures M1/M2 remain biased in triode region.

Lacking any internal nodes whose poles could introduce excess phase, the Nauta transconductor trades high bandwidth for high  $1/f$  noise and power supply sensitivity; the former resulting from directly adding all MOS currents to the outputs, the latter from using  $V_{DD}$  to tune the  $G_m$  value [Lee, 1998, p.33–34].

Degenerating each element of the input inverters in Figure 5.19(a) with a MOSFET of opposite polarity yields a linear transconductance element that also operates with both transistors saturated [Park and Schaumann, 1986]. Shown in Figure 5.19(b) for the case of the M1/M2 inverter, wherein the degeneration of M1 and M2 (now dubbed M1a and M2a) takes the form of triode MOSFETs M1b and M2b, the linearity improvement of this configuration over the standard inverter has motivated its vast deployment [Czarnul and Fujii, 1990; Park and Schaumann, 1988; Szczepański et al., 1993], yet its square-law cancellations only remains valid for  $V_{thp} < V_{in} < V_{thn}$  even though it requires additional headroom [Schaumann, 1989, p.185].

### 5.4.1.3 Cross-Coupled Pair

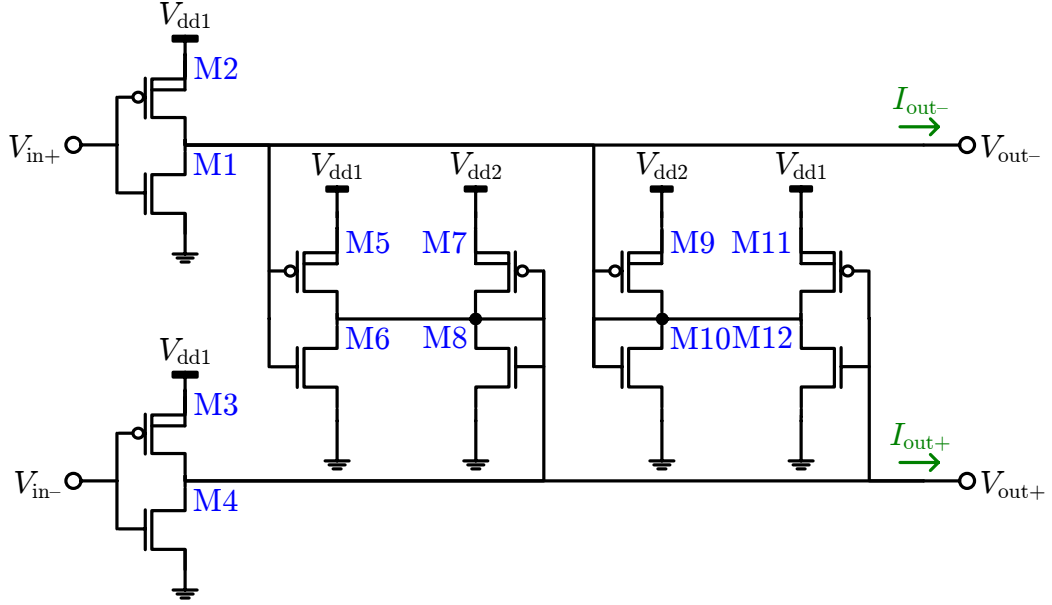
Rather than the degeneration applied to Figure 4.3, both bipolar and MOS differential pairs working as transconductors can be linearized through the addition of a cross-coupled pair, as shown in Figure 5.20(a) for the case of emitter cross-coupling.<sup>23</sup> If the emitter areas of the outer devices ( $A_1 = A_2 = A_{outer}$ ) and inner devices ( $A_3 = A_4 = A_{inner}$ ) are related by a ratio  $M_A = A_{inner}/A_{outer}$  rather than all being equal, the circuit is equivalent to two paralleled differential pairs Q1/Q4 and Q2/Q3 whose left and right elements are related by area ratios  $1:M_A$  and  $M_A:1$ , respectively. Theoretically, complete cancellation of odd-order distortion products occurs when  $M_A = 2 + \sqrt{3}$ , but only over an input range limited to  $\sim 2V_T$ . In practice, third-harmonic distortion rarely exceeds 70 dB [Voorman, 1993, p.32].

In contrast to emitter cross-coupling, a linearized result is also obtained if the drains of the nMOS pairs in Figure 5.20(b) are cross-coupled, provided the shared source of the inner pair is related to that of the outer pair by a constant  $V_A$ . As for the

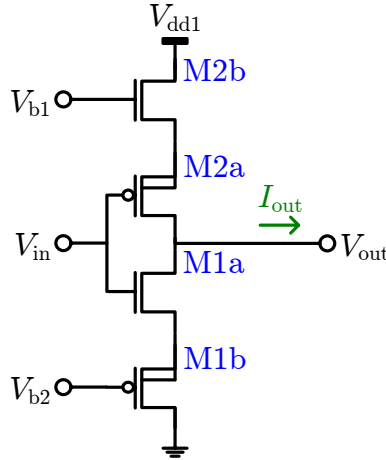
---

<sup>23</sup>The analogous source-coupled MOSFET implementation is at work in the transconductor of Nedungadi and Viswanathan [1984].



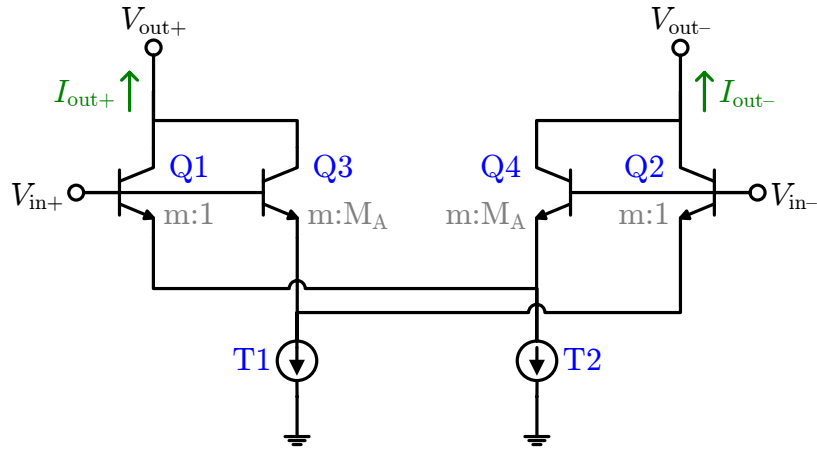


(a) Inverter-based transconductor.

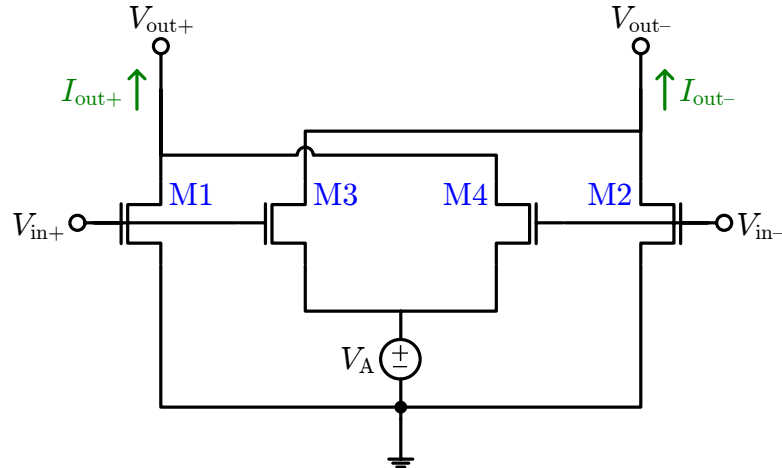


(b) Linearized inverter.

Figure 5.19: Popular transconductors based on saturated MOS operation. The gain(output resistance, and thus, excess phase) of (a) the *Nauta* [1992] transconductor can be tuned via  $V_{dd1}$  ( $V_{dd2}$ ), which supplies the input(cross-coupled output) inverters. To linearize the gain, the input inverters (e.g., M1/M2) can be replaced with a (b) version in which each element is degenerated by a triode MOS of opposite polarity (after [*Park and Schaumann*, 1986, p.1133]).



(a) Emitter cross-coupling.



(b) Drain cross-coupling.

Figure 5.20: Popular transconductors based on cross-coupled differential pairs. In (a) the bipolar case, emitter cross-coupling creates pairs Q1/Q4 and Q2/Q3 within which the device areas are mismatched. In (b) the MOS case, drain cross-coupling must be accompanied by a fixed voltage difference between the shared sources of the M1/M2 and M3/M4 pairs (after [Szczepański *et al.*, 1993, p.259]).

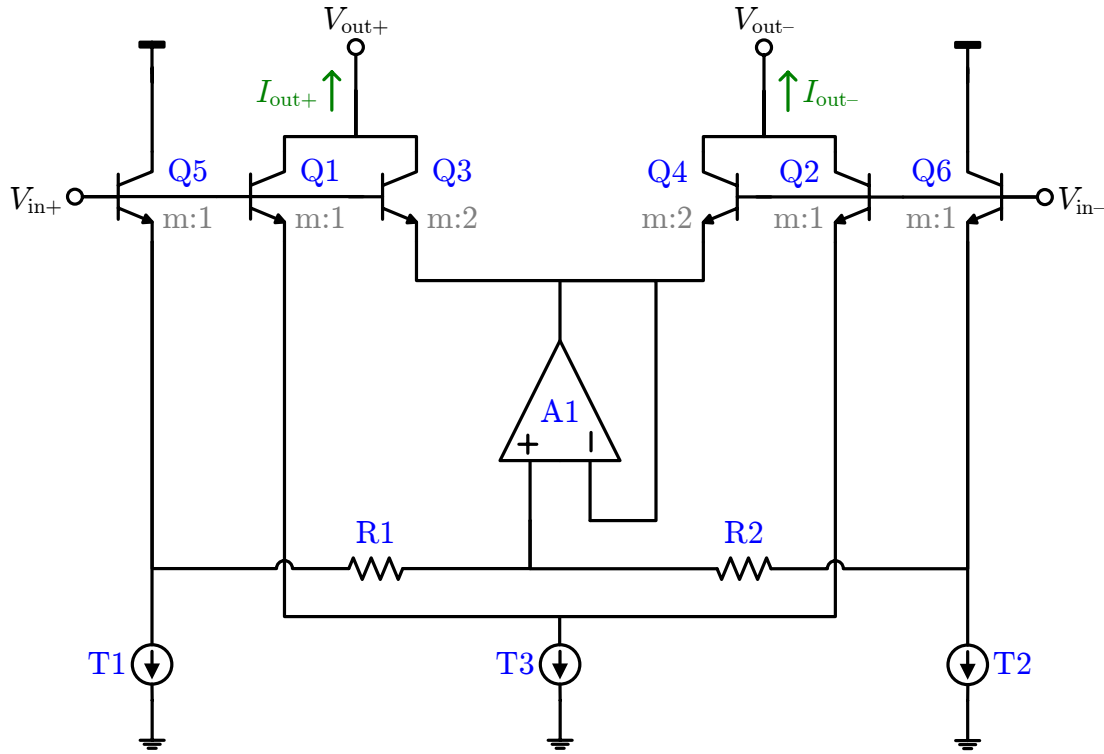
transconductors in Section 5.4.1.2, this configuration relies on cancellation of higher-order terms in the square-law formulation of saturated MOS operation to produce a  $G_m \propto V_A$ . In addition to requiring long-channel devices, any actual design must incorporate supplemental corrections to account for body effect distortions. Plus, the cancellations break down if  $V_{in} > 2|V_A + V_{thn}|$  since both pairs must be kept on [Szczepański *et al.*, 1993].

A variation that melds the fixed source potential of the inner pair of Figure 5.20(b) with the intra-pair area ratios of Figure 5.20(a) is the common-mode siphon implemented alternatively by Figure 5.21(a) and Figure 5.21(b) for the bipolar case. In the former schematic, an inner short-tailed pair with twice the emitter area is connected in parallel with the outer long-tailed pair. But, the shared emitter of the inner pair is driven with the common-mode input voltage, effectively eliminating third-order distortion [Wilson, 1992]. Alternatively, the emitter cross-coupling of Figure 5.20(a) can be preserved and the bases of the equal-sized inner pair driven to the common-mode input voltage, as in Figure 5.21(b) [Voorman *et al.*, 1983]. Both approaches are less sensitive to bias than Figure 5.20(b), just relying on the precision of  $M_A$ , but the transfer function of the latter approach only improves upon that of a standard differential pair by doubling the domain of its tanh, and, similarly, the former exhibits no better than 60 dB THD for  $V_{in} = 2V_T$  [Wilson, 1992].

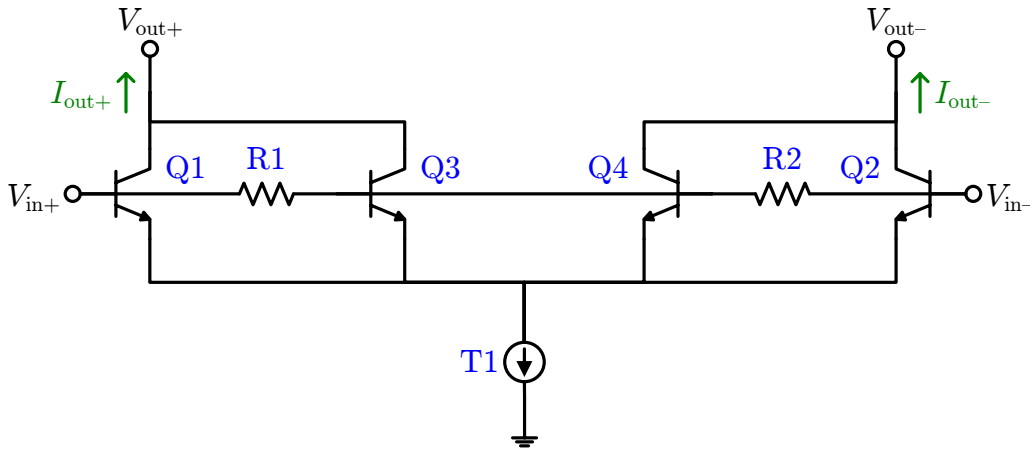
#### 5.4.1.4 Hyperbolic Compensation

With their flicker noise jeopardizing dynamic range and with the limited scope of the triode and square-law models restricting the tuning and input ranges over which they are linear, MOS transconductors are avoided in this design. However, the cross-coupling and common-mode siphons of Figure 5.20 and Figure 5.21 suggest that analog computation using the hyperbolic functions that attend bipolar differential pairs might allow for the cancellation of odd-order distortion over the several decades of input voltage and tuning current for which (3.10) is valid.

**Sinh Compensation:** After all, the differential collector current through Q1 and Q2 of Figure 5.21(a) obeys the standard differential pair formulation obtained from



(a) Emitter-driven CM siphon.



(b) Base-drive CM siphon.

Figure 5.21: Transconductor linearization using common-mode input voltage. In lieu of cross-coupling the inner pair as in Figure 5.20, their (a) emitters (after [Wilson, 1992, p.390]) or (b) bases (after [Voorman *et al.*, 1983, p.188]) can be driven by the common-mode input voltage, computed using resistor divider  $R1/R2$  and, in the former case, (unity-gain) buffered by  $A1$ .

(4.2a) with  $R_d \rightarrow 0$ , as:

$$I_a = I_{c1} - I_{c2} = \frac{1}{\alpha} (2\alpha_1\alpha_2 I_{T3} + \Delta\alpha I_a) \tanh\left(\frac{V_{in} + V_{os1,2}}{2nV_T}\right) \quad (5.37)$$

where the effect of area mismatch is defined as an offset voltage  $V_{os}$  such that

$$V_{os1,2} = nV_T \ln\left(\frac{A_{e1}}{A_{e2}}\right) \quad (5.38)$$

The corresponding relation for the output currents of Q3 and Q4 with  $V_{e3,4} = V_A$  is

$$I_b = I_{c3} - I_{c4} = 2\sqrt{A_{e3}A_{e4}} I_{So} e^{(\bar{V}_{in} - V_A)/nV_T} \sinh\left(\frac{V_{in} + V_{os3,4}}{2nV_T}\right) \quad (5.39)$$

If the intra-pair mismatch is ignored, then the total  $I_{out}$  is

$$I_{out} = I_a + I_b = \alpha_{1,2} I_{T3} \tanh\left(\frac{V_{in}}{2nV_T}\right) + 2A_{e3,4} I_{So} e^{(\bar{V}_{in} - V_A)/nV_T} \sinh\left(\frac{V_{in}}{2nV_T}\right) \quad (5.40)$$

Since the EF formed by Q5/Q6 ensures that Q1–Q4 have the same  $V_{BE}$ , (5.40) reduces to an expression in terms of  $\tilde{V}_{in} = V_{in}/2nV_T$  and  $I_C = I_S e^{V_{BE}/nV_T}$ , namely

$$I_{out} = I_C \tanh(\tilde{V}_{in}) + 2I_C \sinh(\tilde{V}_{in}) \quad (5.41)$$

as long as  $A_{3,4} = 2A_{1,2}$ . Through a Taylor expansion of the hyperbolic functions in (5.41), it can be seen that the  $\sinh$  exactly cancels the  $\tilde{V}_{in}^3$  contribution from  $\tanh$ :

$$\begin{aligned} I_a &= I_C \tanh(\tilde{V}_{in}) = I_C \left( \tilde{V}_{in} - \frac{1}{3} \tilde{V}_{in}^3 + \frac{2}{15} \tilde{V}_{in}^5 - \frac{17}{315} \tilde{V}_{in}^7 + \dots \right) \\ + I_b &= 2I_C \sinh(\tilde{V}_{in}) = I_C \left( 2\tilde{V}_{in} + \frac{1}{3} \tilde{V}_{in}^3 + \frac{1}{60} \tilde{V}_{in}^5 + \frac{1}{2520} \tilde{V}_{in}^7 + \dots \right) \end{aligned} \quad (5.42)$$

---


$$I_{out} = 3I_C \left( \tilde{V}_{in} + \frac{1}{20} \tilde{V}_{in}^5 - \frac{1}{56} \tilde{V}_{in}^7 + \dots \right)$$

Even if the intra- and inter-device matching is imperfect, this  $\sinh$ -compensation significantly reduces the coefficients of all odd harmonics.

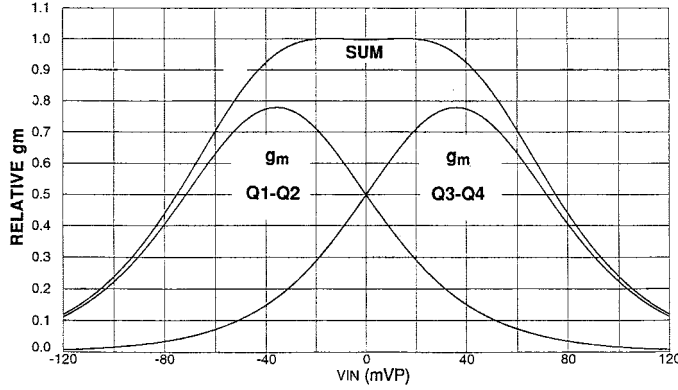


Figure 5.22: Example of multi-tanh principle with two pairs. With the lateral translation of their individual tanh responses controlled by  $M_A$ , the flatness of the combined response, which is linear over a wider input range, is maximized when,  $M_A = 2 + \sqrt{3}$ , as shown. After [Gilbert, 1998, p.7].

**Multi-Tanh Compensation:** However, extending the effect beyond  $\tilde{V}_{in} \leq 1$  requires a different hyperbolic operation. Recall that in the circuit of Figure 5.20(a) Q1/Q4 (Q3/Q2) constitutes a differential pair within which the elements have an area ratio of  $1:M_A(M_A:1)$ . According to (5.38), this ratio can be interpreted as an offset voltage that shifts its tanh-shaped  $G_m$ - $V$  curve along the  $V_{in}$  axis by  $-V_{os}(V_{os})$ . The result, depicted in Figure 5.22 is an example of the ‘multi-tanh’ principle proposed by Gilbert [1998]—a piecewise approximation that affords linearity over a wider range of inputs than a single differential pair.<sup>24</sup> By placing additional pairs with equally-spaced  $V_{os}$  in parallel with those of Figure 5.20(a), the effect can be extended to further broaden the linear operating range. Unfortunately, 25 such pairs are required to suppress third-harmonic distortion by 100 dB [Gilbert, 1998, p.6].

<sup>24</sup>It can be shown that maximizing the linearity of the aggregate transconductance curve in Figure 5.22 by forcing its first and second derivatives to zero requires [Gilbert, 1998, p.7]

$$V_{os} = 2V_T \sinh^{-1} \left( \frac{1}{\sqrt{2}} \right)$$

Using (5.38), this flatness condition translates into the aforementioned (and, at the time, unsubstantiated) choice of  $M_A = 2 + \sqrt{3}$  in Figure 5.20(a). Maintenance of this area ratio among additional pairs preserves linearity as the input range is extended.

### 5.4.2 Two-Stage Unit Cell

The architecture of the unit-transconductors in the AAF capitalizes on the hyperbolic mathematics of Section 5.4.1.4, made possible through the use of npn transistors, to provide even more exacting regularization of nonlinearities. To do so, it adopts a prevalent scheme that partitions the responsibilities of the transconductor into the two-stage topology of Figure 5.23 [Ali *et al.*, 1993, p.43], wherein each stage implements another of Gilbert’s principles.

Stage 1 performs a highly linear conversion of the differential input voltage to an intermediate current with a fixed gain  $G_{\text{tll}}$ . Although this operations sounds familiar, as it is identical to that taking place in the first stage of the LNA (cf. Section 4.2.2), the implementation described in Section 5.5.1 cannot employ super emitter followers for headroom reasons. The second stage acts as a variable-gain amplifier whose output current is related to the intermediate current by a gain  $G_{\text{ggc}}$  that is both programmable and trimmable: it can be coarsely programmed to values of 1/6 (Mode A), 1 (Mode B), and 6 (Mode C), then finely trimmed by means of a single off-chip resistor.

Before presenting the implementation of these stages, the underlying Gilbert principles are succinctly reviewed.

#### 5.4.2.1 Translinear Principle

In the context of the example in Figure 5.24(a) the translinear principle first postulated by Gilbert [1968] can be paraphrased thusly: when traversing a loop consisting of an even number of bipolar  $V_{\text{be}}$ -drops, the product of the currents through the elements whose drops are oriented counterclockwise (Q1 and Q3) is proportional to the product of the currents through the clockwise elements (Q2 and Q4), with the constant of proportionality being the ratio of the products of the saturation currents of the former to the latter. Stated mathematically,

$$\frac{I_{\text{c1}}I_{\text{c3}}}{I_{\text{c2}}I_{\text{c4}}} = \frac{A_{\text{e1}}A_{\text{e3}}}{A_{\text{e2}}A_{\text{e4}}} = \gamma_{\text{A}} \quad (5.43)$$

Note that differences in the emitter areas of the nominally matched devices, which are proportional to their  $I_{\text{S}}$ , have no impact as long as mutual equality of the area

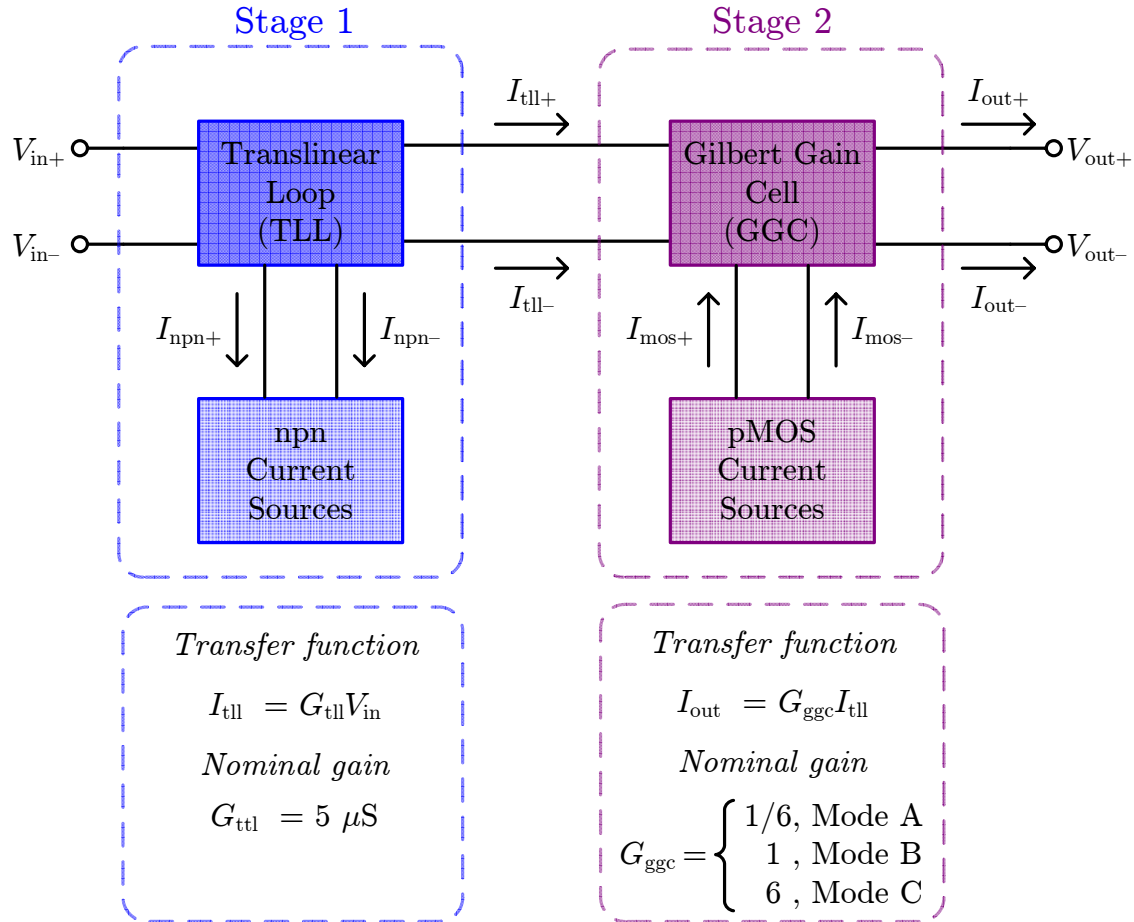


Figure 5.23: Two-stage architecture of unit transconductor. Ideality of the fixed(variable) gain of the first(second) stage,  $G_{tll}(G_{ggc})$ , is achieved through a translinear loop(Gilbert gain cell) such that the transconductor linearity(noise) is limited only by the quality of its npn(pMOS) current sources.



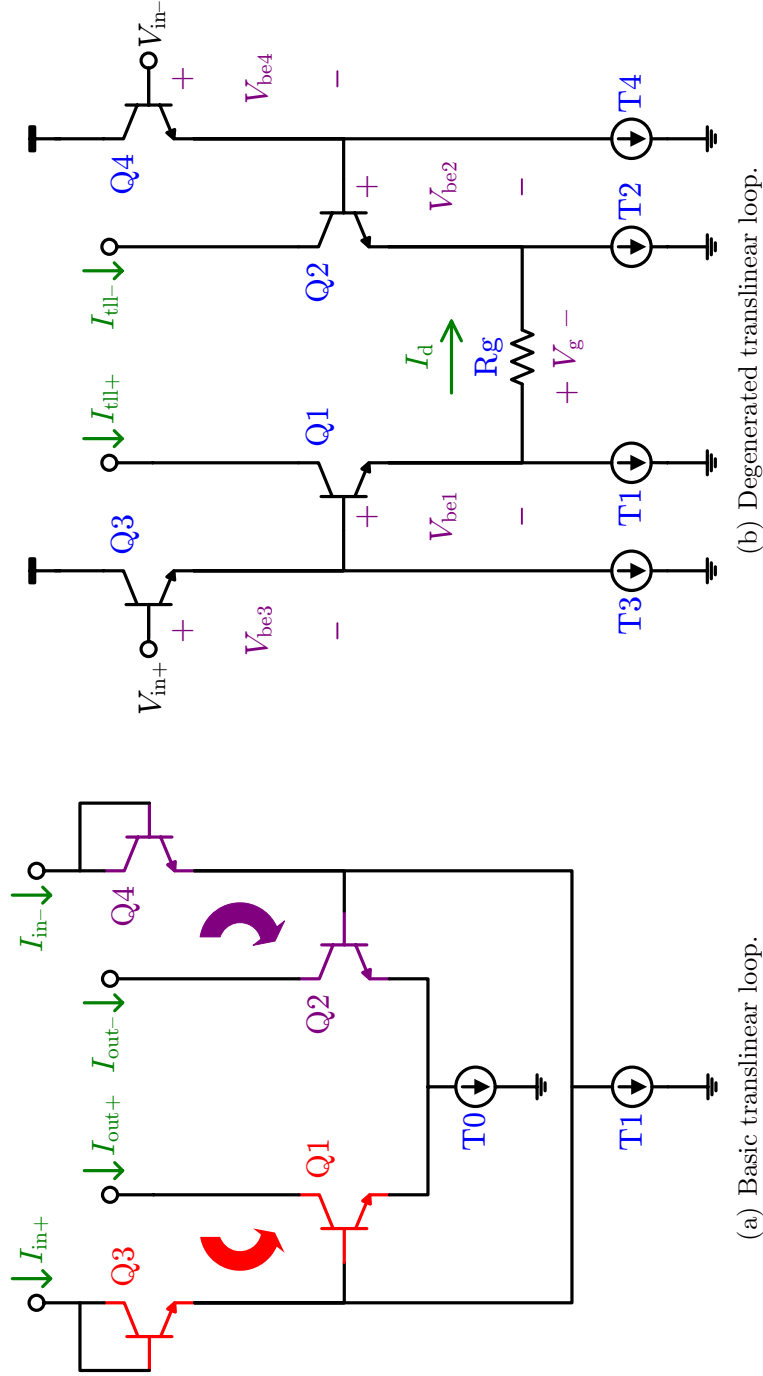


Figure 5.24: Translinear loop examples. The simplest translinear loop contains (a) only counter-oriented pairs of bipolar  $V_{be}$  drops. If these precisely cancel one another, KCL around the loop demands that the drop across (b) a degeneration resistor inserted in the loop,  $V_g$ , be identical to the driving voltage,  $V_{in}$ .

products in the numerator and denominator of (5.43) is maintained.

The relationship in (5.43) follows directly from the loop KCL in which each  $V_{be}$  is proportional to the logarithm of the corresponding  $I_c$  via (3.10a). Foreshadowing its role in the Stage 1 of the transconductor, consider the effect of adding a single resistor,  $R_g$ , into the translinear loop (TLL) of Figure 5.24(a), and driving the configuration in Figure 5.24(b) with an input voltage at the bases of Q1/Q2. Using (5.43), the difference between  $V_{in}$  and  $V_g$  can be obtained by inspection:

$$V_{err} = V_{in} - V_g = nV_T \ln \left( \frac{I_{c1} I_{c3}}{I_{c2} I_{c4}} \right) - nV_T \ln(\gamma_A) \quad (5.44)$$

Although the effects of mismatch merit much discussion in Section 5.4.2.2, assume for the remainder of this section that nominally identical devices are matched in area ( $\gamma_A = 1$ ). Then, (5.44) suggests that the resistor voltage is identical to the input voltage as long as the ratios of the collector currents in outer pair is the reciprocal of that in the inner pair, or

$$\frac{I_{c1}}{I_{c4}} = \frac{I_{c2}}{I_{c3}} \quad (5.45)$$

The ideal current mirror of gain  $K$  in Figure 5.25 attempts to satisfy (5.45), eliminating level-shifting errors by forcing the emitter currents of Q1/Q2 to track the collector currents of Q4/Q3 [Chung *et al.*, 1992]. But, since (5.45) is a ratio of collector currents, this technique only works under two additional assumptions that are revisited in Section 5.5.1:  $\alpha_1 = \alpha_2 = 1$  and  $\alpha_3 = \alpha_4 = 1$ . Permitting the validity of all the assumptions in this paragraph, the description of Figure 5.25 by (5.44):

$$V'_{err} = nV_T \ln \left( \frac{\alpha_3 \beta_2 \left( K\beta_1 + \frac{I_{tll+}}{I_{tll-}} \right)}{\alpha_4 \beta_1 \left( K\beta_2 + \frac{I_{tll-}}{I_{tll+}} \right)} \right) - nV_T \ln(\gamma_A) \quad (5.46)$$

reduces to  $V'_{err} = 0$ .

Just as when converting Q1/Q2 into super emitter followers, constructing this mirroring translinear loop around them constitutes active feedback within a series-series loop containing  $R_g$ . Equating the degenerated differential pair comprised of

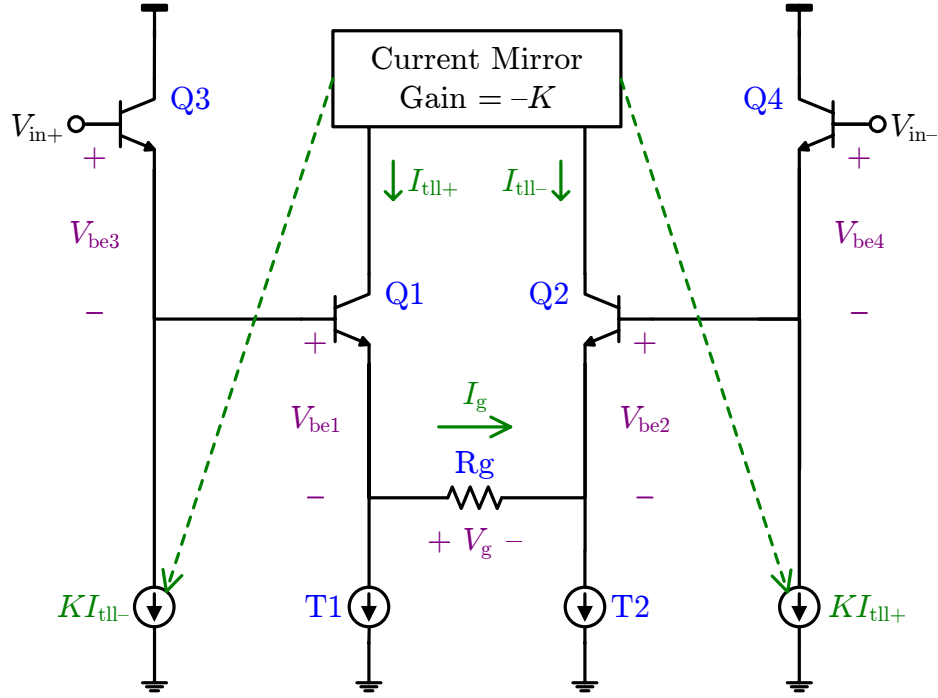


Figure 5.25: Degenerated TLL with feedback linearization via current mirrors. To ensure cancellation of the  $V_{be}$  drops around the TLL, the current mirror returns the collector currents of the inner pair to the emitters of the input pair with negative gain,  $-K$ . After [Chung *et al.*, 1992].

Q1, Q2, and  $R_g$  to that of Figure 4.3, the action of Q3/Q4 and the current mirror can be interpreted as predistorting  $V_{in}$  so that the  $\Delta V_{be}$  nonlinearities of Q1/Q2 are canceled and the transconductance of the block is given by just  $2R_g^{-1}$ .

For this reason, a translinear loop is the basis of the first stage implementation presented in Section 5.5.1. The generalized feedback diagram of Figure 5.26 shows that, unlike Figure 4.4, the predistorting block of Stage 1,  $b^{-1}(s, I_{tll})$ , is in the forward path a lá Figure 3.22(a) and receives its nonlinear feedback from  $I_{tll}$  through the same branch as does  $b(s, I_{tll})$  via the ideal current mirror.

#### 5.4.2.2 Gilbert Gain Cell

The Gilbert gain cell (GGC) in the simplified schematic of Figure 5.27 is an application of the translinear principle to the design of a current amplifier rather

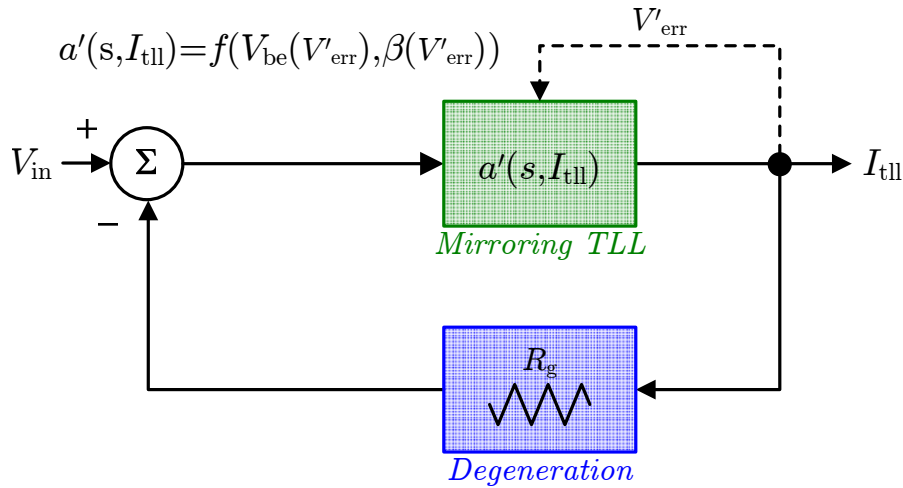
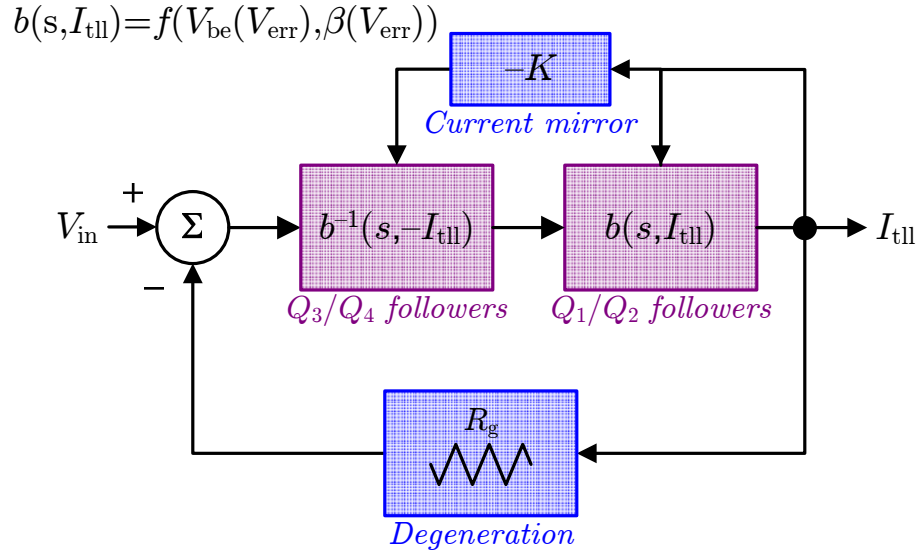


Figure 5.26: Flow graph representation of first stage of Figure 5.23 with (a) explicit identification of active (Q3/Q4) and passive ( $R_g$ ) loops around the Q1/Q2 followers as well as (b) an equivalent network whose linearized forward path  $a'(s, I_{tll})$  is identified as the mirroring translinear loop of Figure 5.25.

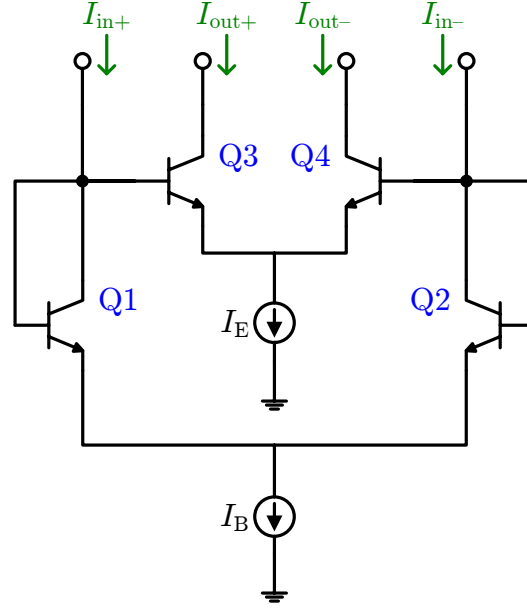


Figure 5.27: Simplified schematic of canonical Gilbert gain cell. As compared to Figure 5.24(a), the inverted structure of the translinear loop confers independence from finite  $\beta$  effects. After [Gilbert, 1968].

than a transconductor [Gilbert, 1968]. In this inverted form it is assumed that the input currents, taken at the collectors of Q1/Q2 and the output currents, taken at the collectors of Q3/Q4, are perfectly balanced, in which case (5.43) gives the gain for ideal, perfectly matched transistors as

$$G_{\text{ggc}} = \frac{I_{\text{out}}}{I_{\text{in}}} = \frac{I_E}{I_B} \quad (5.47)$$

The gain is simply the ratio of the tail current sources, so programming it is trivial. However, this perfectly linear gain is subject to both odd- and even-order distortion when certain underlying assumptions of (5.47) are violated by pragmatic non-idealities.

**Odd-Order Distortion:** Embodying inescapable differences that arise from manufactured doping(dimensions) of the device diffusions(metalization and contacts), cubic

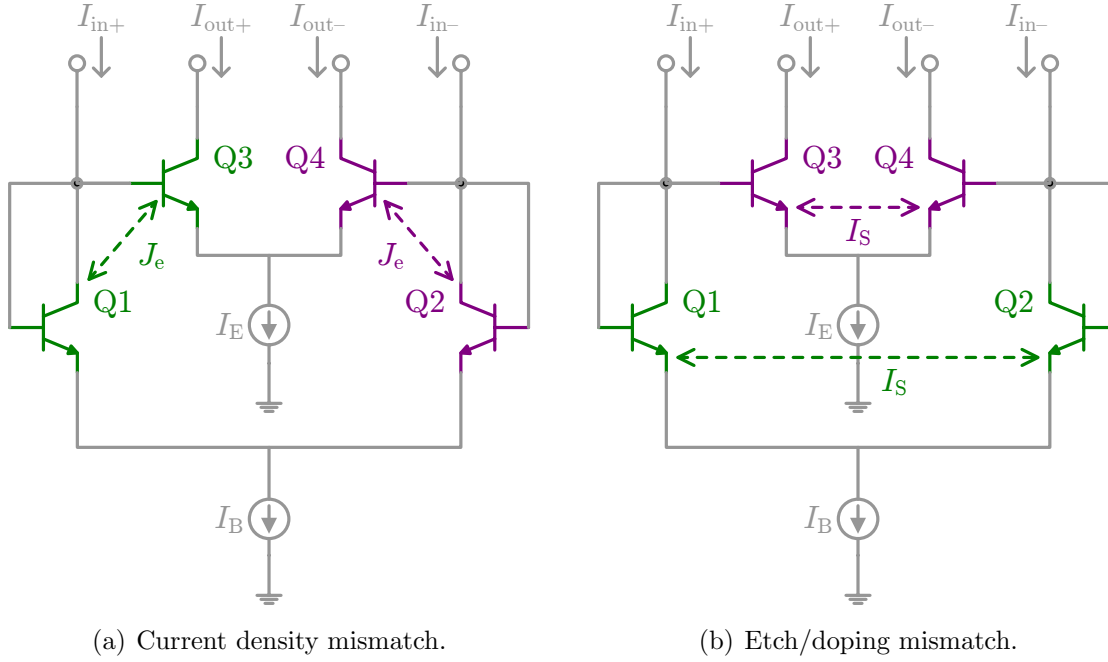


Figure 5.28: Illustration of GGC asymmetries responsible for distortion. The mismatch of  $J_e(I_S, \beta)$  between devices on the same(opposite) half of the differential GGC, as depicted in panel (a)(panel (b)), is responsible for odd(even) harmonics in the spectrum.

terms are introduced into (5.47) by the net effect of resistive parasitics whenever:<sup>25</sup>

$$\begin{aligned} J_{e1,2} &\neq J_{e1,2} \\ \frac{I_{e1,2}}{A_{e1,2}} &\neq \frac{I_{e3,4}}{A_{e3,4}} \end{aligned} \quad (5.48)$$

So, as illustrated in Figure 5.28(a), odd-order distortion arises when the emitter current densities of the devices on the same half of the circuit do not match. [Gilbert, 1968, p.355].

<sup>25</sup>Lumping all the cited parasitics into an equivalent emitter resistor for each npn simplifies the derivation of (5.48), which presumes that the equivalent resistor embodies only parasitics that scale with emitter area [Gilbert, 1968, p.355].

**Even-Order Distortion:** Conversely, even-order distortion, as in any differential circuit, is the byproduct of deviations in the properties of transistors on one half of the circuit relative to their nominally identical counterparts on the other (cf. Figure 5.28(b)). Such lateral asymmetry negates two of the assumptions behind (5.46) and (5.47). The most egregious violation occurs when manufacturing tolerances that govern base doping and etching produce

$$\gamma_A = \frac{I_{S1}I_{S4}}{I_{S2}I_{S3}} \neq 1 \quad (5.49)$$

As in (5.38), this area mismatch can be represented by an offset voltage in the translinear loop,  $V_{os}$ , which imbalances the output currents so as to produce a second-harmonic in (5.47) [Gilbert, 1968, p.355].

Compared to Figure 5.24(a), the TLL of Figure 5.27 is classically said to be independent of the transistor betas, which would certainly benefit this application. However, this ‘independence’ only pertains to the absolute value of  $\beta$ , not  $\beta$ -mismatch between the two circuit halves in response to the opposite polarity of the output currents they carry. Thus, when the signal dependent  $\beta$ -mismatch of Section 3.1.2.3 gives rise to

$$\begin{aligned} \beta_1 &\neq \beta_2 \\ \beta_3 &\neq \beta_4 \end{aligned} \quad (5.50)$$

further second-order distortion is observed. Although, it is difficult to analytically capture the effects of (5.48), (5.49), and (5.50) on (5.47), as was done for the TLL in (5.46), they are demonstrated by simulation in Section 5.5.2.1 and Section 5.5.2.2.

## 5.5 Implementation

The architectural advantages afforded by the chosen filter, stage, and integrator topologies shift the burden of the weighty AAF specifications principally onto the unit transconductor of Figure 5.23, making its implementation critical. Thus, Section 5.5.1(Section 5.5.2) offers a review of the transistor-level techniques which mitigate the nonidealities of the TLL(GGC) in Stage 1(Stage 2) described by

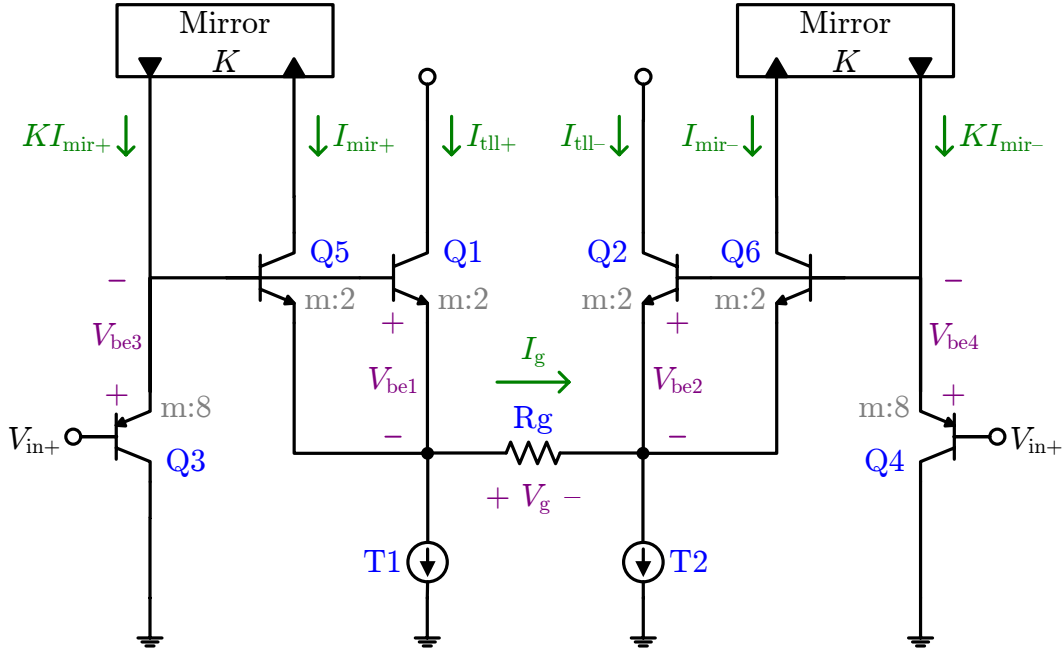


Figure 5.29: Simplified schematic of first stage of Figure 5.23. The roles of Q1–Q4 are unchanged from Figure 5.25, but implementing Q3/Q4 with substrate pnps requires separate mirrors (idealized for now, as are fixed tail current sources T1/T2) fed by a replica of  $I_{tll}$  provided by Q5/Q6 and denoted  $I_{mir}$ .

((5.46)((5.48) through (5.50)) while minimizing excess phase so that the overall AAF meets the requirements of Table 3.2.

### 5.5.1 First Stage

The TLL of Figure 5.25 is the basis for the first stage of the transconductor. Implementing Q1/Q2 and the current mirror so that the predistortion conceptually diagrammed in Figure 5.26 is sufficiently precise dictates several modifications to the work of *Chung and Cha* [1990], captured by the simplified schematic of the novel realization in Figure 5.29.

Since the input to the second stage,  $I_{tll}$ , is provided by the output currents of degenerated pair Q1/Q2, it cannot serve as the input to the current mirror. Instead, as in [*Chung and Cha*, 1990], the collectors of Q1/Q2 are evenly split, resulting in



replicas Q5/Q6 that carry half of the intermediate current.<sup>26</sup> However, *Chung and Cha* [1990] do not address the matching ramifications of this split-collector pair, which are more severe than those of the separate current sources T1 and T2 or the individual segments of composite resistor  $R_g$  that together accommodate the low  $G_{tll}$  associated with VLF frequencies. Section 5.5.1.2 provides evidentiary statistical analysis demonstrating the impact of these mismatch sources on second-harmonic distortion.

The most significant departure from Figure 5.25 is that npn followers Q3/Q4 have been replaced with substrate pnp input devices. The polarity inversion is necessary because a margin-adjusted input swing of  $2\text{ eV}_{PP}$  exceeds the headroom available to T1 and T2 if its translated to  $R_g$  by the  $2V_{BE}$  level-shift of the reference design.<sup>27</sup> But, through swapping the terms in the denominators of (5.45), the pnp conversion changes the sign of the gain through the current mirror, yielding positive feedback.<sup>28</sup> This combination of two established linearization techniques—predistortion and positive feedback [*Lee*, 1998, p.326]—so as to obey the translinear principle while preserving stability is the subject of Section 5.5.1.1.

---

<sup>26</sup>To compensate for the dividing its current amongst two paths, the size of  $R_g$  is doubled. In the ideal case, when (5.46) goes to zero, the transconductance of the loop is simply

$$G_{tll} = \frac{I_{tll}}{V_{in}} = \frac{\left(\bar{I}_{tll} + \frac{V_g}{2R_g}\right) - \left(\bar{I}_{tll} - \frac{V_g}{2R_g}\right)}{V_{in}} = \frac{1}{R_g}$$

So, for the target  $G_{tll}$  of  $5\text{ }\mu\text{S}$  (in Mode B),  $R_g = 200\text{ k}\Omega$ .

<sup>27</sup>It is straightforward to appreciate how severely the headroom in the bipolar portion of the signal path is constrained when every differential node in the AAF design must support a  $1\text{ V}_{PP}$  signal swing. Consider the DC bias points of any two such nodes, A and B, linked by a cascade of two emitter followers so that  $V_A - V_B = 2V_{BE} \simeq 1.5\text{ V}$ . Even when the former is biased at its maximum value  $\max\{V_A\} = V_{DD} - 500\text{ mV} = 2\text{ V}$ , the corresponding bias of node B  $\max\{V_A\} - 2V_{BE} = 500\text{ mV}$  is so low that there is zero available headroom for its tail current source in the presence of a  $\pm 500\text{ mV}$  signal swing. By contradiction, then, this proves that any two nodes carrying signal voltage can be offset by no more than one npn  $V_{BE}$ .

<sup>28</sup>Intuitively, since  $V_{be3}$  now provides the predistortion for  $V_{be1}$ , an increase in one must be offset by an increase in the other and, thus, their currents are in phase.

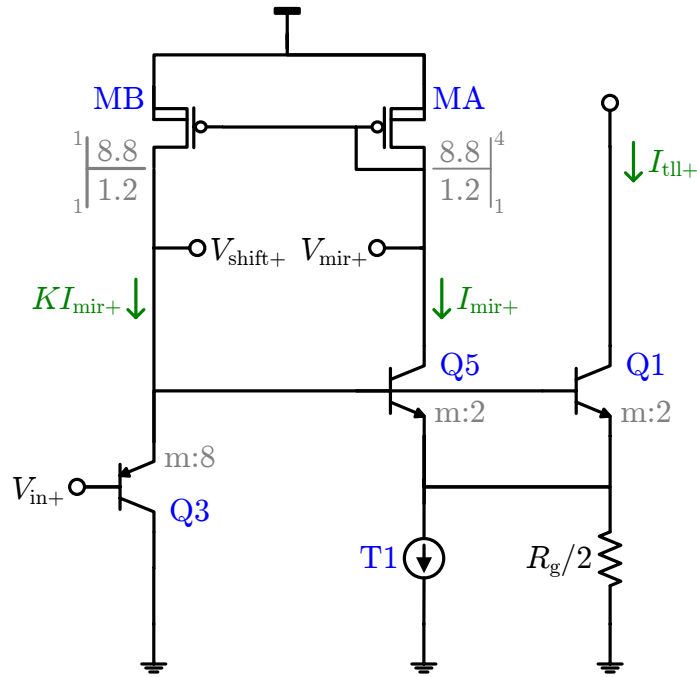


Figure 5.30: Positive feedback loop formed by pMOS mirror on left half of Figure 5.29. The sizes of MA and MB yield  $K = 1/4$ . For the half-circuit, the midpoint of  $R_g$  is grounded.

### 5.5.1.1 Positive Feedback

In the absence of lateral pnps, Q3/Q4 of Figure 5.29 are constructed with substrate pnps and the current mirror is necessarily formed from a pair of pMOS devices denoted MA/MB in the full schematic for the positive feedback loop on the left half of the transconductor in Figure 5.30. For convenience, the lengths of the pMOS mirror devices are equal, so that its gain ratio  $K = W_B/W_A$ .

**Stability Analysis:** To determine the appropriate value of  $K$ , the stability of the positive feedback loop would seem a natural starting point. Ignoring small-signal output resistance and breaking the loop at the base of Q5, gives the DC small-signal

loop gain as:<sup>29</sup>

$$L(0) = \frac{g_{m5} g_{mB}}{g_{m3} g_{mA}} \frac{\alpha_3}{1 + g_{m5} R_g} \quad (5.51)$$

To make the dependence on  $K$  explicit, express the small-signal parameters in terms of large-signal quantities using the square-law relationship of (3.9) and account for the finite base current of Q5 as:

$$L(0) = \frac{\beta_5 K \epsilon_K}{\beta_5 K \epsilon_K - 1} \frac{1}{1 + \frac{\bar{I}_{tll} R_g}{n V_T}} \quad (5.52)$$

where  $\epsilon_K$  describes the error in  $K$  due to pMOS nonidealities as:

$$\epsilon_K = \frac{(\lambda_B V_{mir}) (V_{mir} - V_{thB})}{(\lambda_A V_{shift}) (V_{mir} - V_{thA})} \quad (5.53)$$

The first term of (5.52) is driven toward unity by ensuring that Q5 is biased near its peak  $\beta$  and choosing  $L_{A,B}$  as large as possible to mitigate the Early effect. Despite radiation-induced degradation of  $\beta_5$  and  $\Delta V_{thp}$ , the sizings of Figure 5.30 allow sufficient margin that this condition holds over a wide range. As a result, the loop gain in (5.52) does not depend on  $K$ . Furthermore, because Q5 is degenerated such that the product  $\bar{I}_{tll} R_g$  controls the linearity of its output current, this quantity is necessarily large compared to  $V_T$  (i.e.,  $\bar{I}_{tll} R_g \simeq 4V_T$ ). So, the nominal  $L(0)$  is comfortably below unity and the loop is unconditionally stable as long as all devices remain in the desired operating regions.

**Bias Currents:** With loop stability inherent in the architecture of Figure 5.30, the choice of  $K$  is a trade-off between the linearity of  $G_{tll}$  and the input bias current of the transconductor. For the former, (5.46) advocates that  $\beta_{1,2} K \gg |I_{tll+}/I_{tll-}|$ , but since  $\bar{I}_{tll} \simeq 10I_{tll}$ , values of  $K$  as low as 1/4 satisfy this inequality such that  $\max\{V'_{err}/V_{in}\} \leq -90$  dB, even with the anticipated  $\beta$ -degradation. Thus, to reduce

---

<sup>29</sup>Since the two loop nodes are both low impedance, one seeing the diode connection of MA and the other the diode connection of Q5 (whose input is grounded during the calculation of loop transmission), the effect of small-signal capacitances is negligible. Simulations confirm that  $\max\{L(s)\} = L(0)$  since the zero associated with  $C_{gdB}$  is preceded by the dominant pole.

the base current of Q3, which is the input bias current of the overall transconductor, and to limit power dissipation, the final design favors  $K = 1/4$ . The corresponding input bias current of  $\sim 600$  nA is still quite large, due to the low  $\beta$  of the substrate pnp and increases with multiple unit cells in parallel, which explains why the LNA output stage requires low-impedance followers (cf. Section 4.2.3.1).

### 5.5.1.2 Linearization

Despite employing translinearity in the form of this stable, low-current, positive feedback loop to mollify transistor nonlinearities, residual distortion mandates a series of additional modifications to Figure 5.29 in order to achieve the target SFDR. Incorporated into the complete schematic of the first stage in Figure 5.31, such second-order corrections include heterogeneous resistors, neutralization capacitors, and split-collector matching.

### Heterogeneous Resistors

In the general philosophy of Section 4.2.1, it is assumed that transferring responsibility for  $V$ -to- $I$  conversion from the inherent transconductance of transistors to on-chip resistors such as  $R_g$  garners a net linearity improvement. But, the latter are not perfectly linear either; for a given voltage across it,  $V_R$ , a resistor of nominal value  $R_o$  exhibits a non-linear resistance  $R(V_R)$  that conforms to

$$\frac{R(V_R)}{R_o} = 1 + K_{r1}V_R + K_{r2}V_R^2 \quad (5.54)$$

so its current can be expressed in a polynomial expansion of the form (4.29):

$$I(V_R) = G_o (V_R - K_{r1}V_R^2 - K_{r2}V_R^3) \quad (5.55)$$

where the resistors are presumed linear enough to validate the approximation  $(1 + x + x^2)^{-1} \simeq 1 - x - x^2$ . The differential signal path addresses the quadratic term of (5.55), leaving the residual cubic to limit the overall distortion, depending on the size of  $K_{r2}$ . Indeed, none of the BiCMCOS8 resistors offer sufficiently low coefficients to

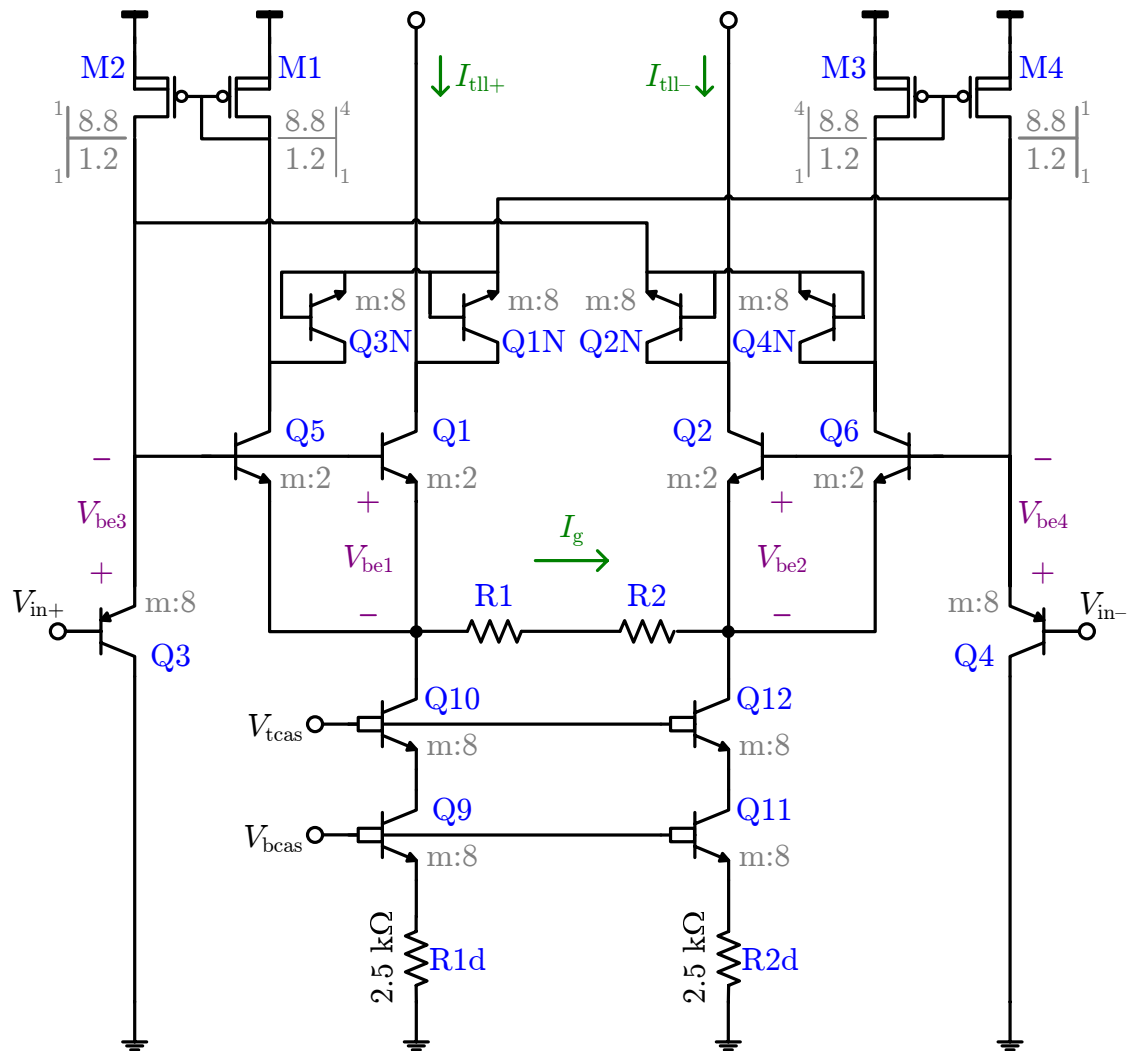


Figure 5.31: Full schematic of first stage of Figure 5.23, including degenerated and cascoded tail current sources (Q9–Q12), neutralization capacitors (Q1N–Q4N) and heterogeneous load resistors (R1/R2). The roles of Q1–Q4 are unchanged from Figure 5.25.

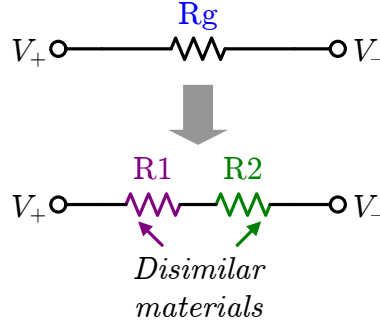


Figure 5.32: Heterogeneous implementation of  $R_g$  consisting of both unsalicyded polysilicon and n+ diffusion segments, depicted in purple and green and lumped into  $R_1$  and  $R_2$ , respectively.

satisfy the 90-dB requirement on the third-order products of  $R_g$ , even if implemented as a set of series-connected segments.<sup>30</sup>

However, an examination of the voltage coefficients for various resistive layers reveals variation in their signs, suggesting a solution. If  $R_g$  is divided into two series segments,  $R_1$  and  $R_2$  in Figure 5.32, of nominal sizes  $R_{o1} + R_{o2} = R_o$ , which are constructed from different materials so that coefficients of the former(latter) are denoted  $K_{r11}$  and  $K_{r21}$  ( $K_{r12}$  and  $K_{r22}$ ), then the effective coefficients of  $R_g$  are

$$K_{r1} = G_o^2 (K_{r11} R_{o1}^2 + K_{r12} R_{o2}^2) \quad (5.56a)$$

$$K_{r2} = G_o^3 (K_{r21} R_{o1}^3 + K_{r22} R_{o2}^3) \quad (5.56b)$$

Ideally, there would exist resistors with coefficients such that

$$\frac{R_{o2}}{R_{o1}} = \left| \frac{K_{r21}}{K_{r22}} \right| = \left| \frac{K_{r11}}{K_{r12}} \right|^{3/2}, \quad \text{where } \frac{K_{r21}}{K_{r22}}, \frac{K_{r11}}{K_{r12}} < 0 \quad (5.57)$$

<sup>30</sup>Of course, in the limit as the number of segments ( $M$ ) approaches infinity, it becomes possible to implement any resistance with sufficiently high linearity because the nonlinear contributions scale down quickly as the  $V_R$  across each segment drops. But, for practical  $M$ , it can be shown that the coefficients of the BiCMOS8 resistors prevent  $R_g$  from being constructed homogeneously. In contrast, the nonlinearity of the resistor primitive classes does not threaten the performance of the LNA because  $R_d$  is smaller than  $R_g$  (by at least  $4\times$ ) and occurs only once, rather than in every transconductor, so  $M$  can be much larger for the same total die area.

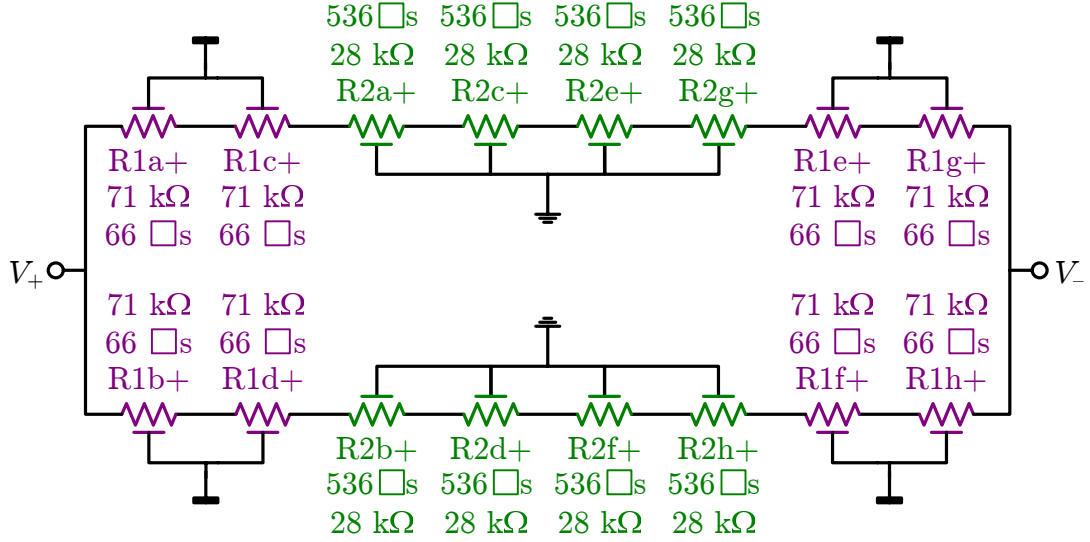


Figure 5.33: Complete decomposition of heterogenous  $R_g$ . To ensure symmetric loading, the high-resistance polysilicon segments (in purple), each shielded beneath by an n-well at supply potential, reside on the outside where they buffer the degeneration nodes from the  $n^+$ -diffusion segments (in green), whose junctions to the grounded substrate present larger parasitic capacitances. Two parallel branches of twice the target  $R_g$  improve matching to G4 of Stage 3 (cf. Footnote 18).

which would drive both  $K_{r1}$  and  $K_{r2}$  to zero; but such circumstances do not attend the BiCMOS8 library. Yet, the cubic term is of utmost importance, so by choosing those resistors whose coefficients come closest to satisfying (5.57) and sizing them such that

$$\frac{R_{o2}}{R_{o1}} = \sqrt[3]{\frac{K_{r21}}{K_{r22}}} \quad (5.58)$$

(5.56a) is minimized and (5.56b) driven to zero. To this end, each half of the  $R_g$  layout of places 264 squares of N+ diffusion in series with 2144 squares of unsalicyded polysilicon, as shown in Figure 5.33.

### Neutralization capacitors

Even with a heterogeneous implementation of  $R_g$ , the dominant odd-order harmonic of the overall transconductor at  $3f_o$  would remain greater than 90 dBc without neutralization to counteract the nonlinear junction capacitances of Q1/Q2, which also

afflict the degenerated tail current sources in the LNA input stage (cf. Section 4.2.4.1). Here, the reversed-biased, signal dependent  $C\mu$  varactors siphon off a signal-dependent portion of the base currents of Q1 and Q2 because their base terminals experience the full input swing while their collector voltages are approximately constant. To cancel this current before it degrades TLL linearity, neutralization capacitors, implemented by the junction  $C\mu$  of Q1N-Q4N are cross-connected from the bases of Q1/Q5 to the collectors of Q2/Q6 and vice versa and sized empirically so as to provide the largest improvement in SFDR when accounting for parasitic capacitors in addition to  $C\mu$ , including the collector-to-bulk capacitance,  $C_{sub}$ . This methodology produces Q1N-Q4N at four times the size of the main devices.

In Figure 5.34, the simulated spectrum of the TLL in Figure 5.31 confirms that for a full-scale input, with ideal matching, the chosen  $K$  and  $\bar{I}_{tll}$  enable the TLL to offer a  $\sim 21$ -dB improvement in the SFDR compared to a standard degenerated pair. Since subsequent operations introduce additional distortion, the third harmonic of  $\sim 140$  dB—at an optimization point that balances the limiting contributions of the  $R_g$  and Q1N-Q4N—is not simply a luxury.

### Split Collector Matching

In terms of even-order distortion, it is notable that the the split-collector configuration of Q1/Q2 and Q5/Q6 shifts the burden of output current matching from T1 and T2 to these device pairs themselves. First, consider the standard deviation of the output current of the basic degenerated differential pair of Figure 4.3,  $I_{out}$ , when tail current sources T1 and T2 are implemented as shown in Figure 4.19.  $\sigma\{I_{out}\}$  depends critically on the mismatch between T1 and T2 according to

$$\sigma\{I_{out}\} = \bar{I}_{out} \frac{\sqrt{\sigma^2\{\epsilon_{vbe}\} + \sigma^2\{\epsilon_{rsh}\}}}{1 - \frac{\sigma^2\{\epsilon_{rsh}\}}{4}} \quad (5.59)$$

where  $\sigma\{\epsilon_{vbe}\}(\sigma\{\epsilon_{rsh}\})$  is the standard deviation of the normalized percent error in the base-emitter voltage(sheet resistance) of the npn transistors(diffusion resistors)



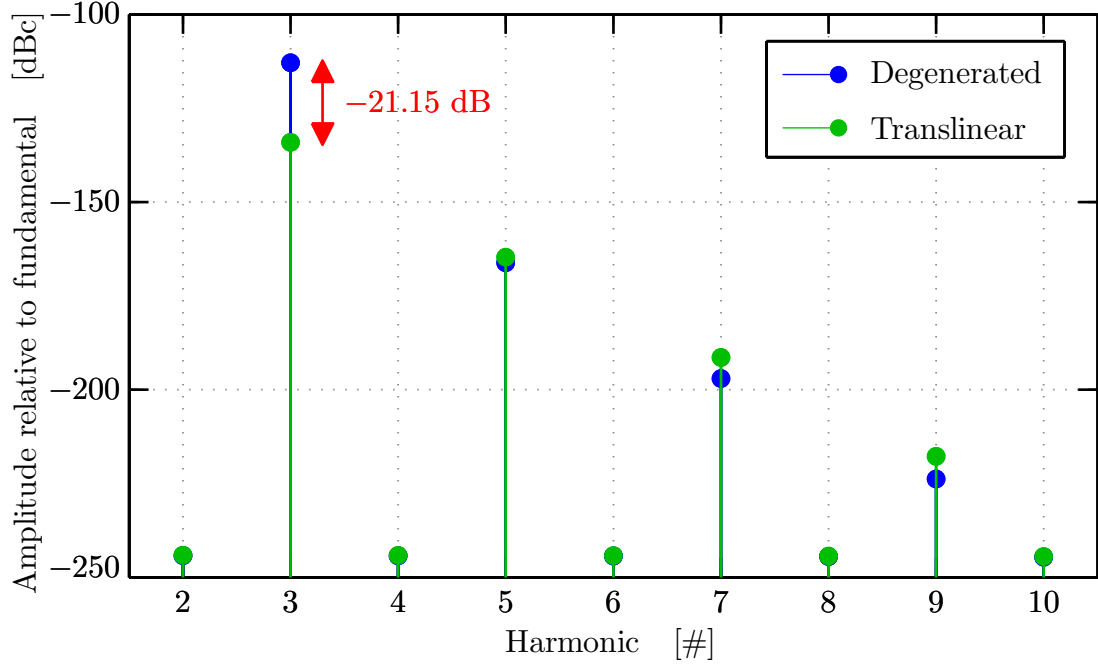


Figure 5.34: Harmonics of  $I_g$  for linearized first-stage TLL with a 100-kHz input sinusoid at 1 V<sub>PP</sub>. In the simulated spectrum for the complete circuit in Figure 5.31 (in green), with  $k=1/4$  and  $\bar{I}_{\text{tll}}=20\ \mu\text{A}$ , the third harmonic is reduced by 21.15 dB from that of a differential pair with degeneration alone (in blue).

that comprise these sources.<sup>31</sup>

In contrast,  $\sigma\{I_{\text{tll}}\}$  depends primarily on the uncertainty with which the tail current on one side, say T1, is divided between Q1 and Q5. It is the randomness of this partitioning, which reflects the correlated, area-dependent  $V_{\text{be}}$ -mismatch between Q1 and Q5,  $\sigma\{\Delta V_{\text{BE}}(A_e)\}$ , that when added in quadrature with the uncorrelated equivalent for Q2/Q6 determines the mismatch between the output current generated

<sup>31</sup>Normalized percent error accounts for the amount of voltage dropped across the degeneration resistor in each tail source,  $V_{\text{Rd}}$ , by defining

$$\epsilon_{\text{vbe}} = \frac{V_{\text{BE1}} - V_{\text{BE2}}}{V_{\text{Rd}}} \quad \text{and} \quad \epsilon_{\text{rsh}} = \frac{R_{\text{sh1}} - R_{\text{sh2}}}{R_{\text{sho}}}$$

The fact that the denominator of  $\epsilon_{\text{vbe}}$  consists of  $V_{\text{Rd}}$  rather than  $V_{\text{BEo}}$  encapsulates the key benefit of the degenerated topology: for sufficiently large  $V_{\text{Rd}}$ , the value of the output current depends more on the voltage across the resistor than on the  $V_{\text{BEo}}$  of the cascode devices. So, as long as  $V_{\text{Rd}} > V_{\text{BEo}}$ , the effective percent error that matters in (5.59), namely  $\epsilon_{\text{vbe}}$ , is lower than simply the raw percent error of the npn  $V_{\text{BE}}$ -mismatch,  $\Delta V_{\text{BE}}/V_{\text{BEo}}$ .

by the two sides as

$$\sigma\{I_{\text{tll}}\} = \bar{I}_{\text{tll}} \frac{\sigma\{\Delta V_{\text{BE}}(A_e)\}}{\sqrt{2}V_T} \quad (5.60)$$

Thus, to reduce even-order distortion at the output of the first stage, the matching of Q1 to Q5 (and Q2 to Q6) is tightened by implementing each with multiple devices in parallel, laid out in a compact common-centroid array. In contrast, the degeneration and symmetric layout of T1 and T2 are not as critical as for the tail current sources in the first stage of the LNA, only producing a second-order effect (i.e., a product of small errors) through  $\bar{I}_{\text{tll}}$  in (5.60).

### 5.5.2 Second Stage

The intermediate current at the output of the first stage is folded from the collectors of Q1/Q2 into the second stage by means of fixed pMOS mirrors. Since their flicker noise adds directly to the signal currents, these must be sized exceedingly large (115/9.6) and their channel lengths made as long as possible to increase their output resistance. However, the effect of the latter on the overall linearity can be mitigated by keeping their drain voltages constant.

This is accomplished as one of several modifications to the standard GGC of Figure 5.27 when incorporating it into the core of the second stage, a simplified version of which is depicted along with the folding mirrors M5/M6 in Figure 5.35. To fix the common-mode level at the drains of M5/M6, a standard CMFB could have been concocted. But, as in the case of the LNA output stage, its power dissipation and stability problems are avoided by a more expedient method. To this end, the GGC tail current source for  $I_B$  has been eliminated and the shared emitter of Q1/Q2 instead biased with the same on-chip regulator that supplies the common-mode level to R1 in the LNA. It can be shown that the use of the translinear principle in the derivation of (5.47) only requires that the collector currents of its input pair, not their emitter currents, be balanced. As long the  $I_{\text{tll}}$  provided by the first stage is symmetric around  $\bar{I}_{\text{tll}} = I_B$ , the tail current source becomes extraneous.<sup>32</sup>

---

<sup>32</sup>Furthermore, to within the signal-dependent base current errors of the inner GGC pair, the current that the regulator must source/sink hardly varies with the input signal. However, it must

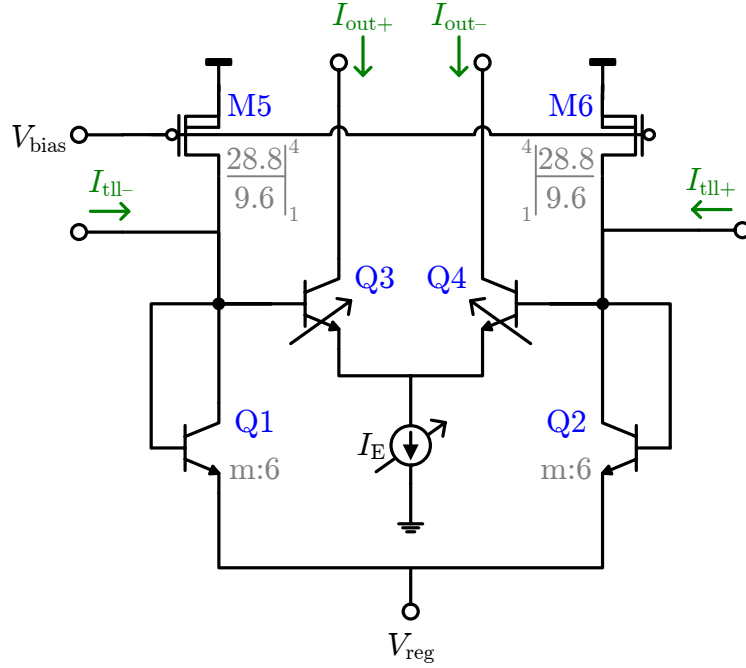


Figure 5.35: Simplified schematic of second stage of Figure 5.23. The roles of Q1–Q4 are unchanged from Figure 5.28, but: the  $I_B$  tail source is replaced by a regulated bias voltage ( $V_{\text{reg}}$ ) that sets the input common-mode level; and  $I_E$  and  $A_{e3,4}$  vary in order to tune the stage gain. Head current sources M5/M6 fold  $I_{\text{tll}}$  into the GGC.

If the tail current of the TLL provides  $I_B$ , theoretically it can be adjusted to change the GGC gain via (5.47). However, Section 5.5.1.1 and Section 5.5.1.2 reveal that its value is paramount for establishing both stability, via the second term of (5.52), and linearity, via the  $I_{\text{tll}}$  ratio in (5.46). In addition, changes in  $I_B$  must flow throughout the whole of the transconductor, whereas increasing  $G_m$  by increasing  $I_E$  provides power-efficient tuning, since the larger bias currents are confined to the minimum number of branches—just those of the two GGC output devices, Q3/Q4. Thus, it is preferable to program and trim the gain of the second stage current amplifier via  $I_E$ .<sup>33</sup> Section 5.5.2.1 and Section 5.5.2.2 describe techniques

sink the entirety of  $I_B$  from each transconductor, suggesting that tuning is best accomplished by varying  $I_E$ .

<sup>33</sup>It is the headroom requirement of the  $I_E$  source that prohibits the use of super emitter followers in the first stage: the drain voltages of M1–M4 in the super emitter-follower of Figure 4.11 are near 1 V but, even if the  $I_E$  source is not degenerated, it must be cascoded for good common-mode rejection, requiring  $>200$  mV of headroom.

Mode		GGC Inner Pair					Tail Current Sources						
ID	$C$	S1 [Pos.]	S2 [Pos.]	S3 [Pos.]	S4 [Pos.]	$A_e$ [ $\mu\text{m}^2$ ]	S1a [Pos.]	S2a [Pos.]	S3a [Pos.]	S4a [Pos.]	S5a [Pos.]	S6a [Pos.]	$I_E$ [ $\mu\text{A}$ ]
A	00	Off	Off	On	On	0.15	On	Off	Off	Off	On	On	6.67
B	01	On	Off	Off	On	0.95	On	On	On	Off	Off	Off	40.0
C	11	On	On	Off	Off	5.40	On	On	On	Off	Off	Off	240

Table 5.3: Configuration of nMOS GGC switches in each AAF mode. Those in the inner pair maintain current density whereas those in the tail current sources program GGC gain.

for enhancing the linearity of additional modifications required for this purpose.

### 5.5.2.1 Odd-Order Distortion

As the overall transconductance scales with  $I_E$ , the size of Q3/Q4 must scale accordingly, to maintain equality in (5.48) lest odd-order distortion increase. To that end, each of these transistors is divided into a series of devices of incrementally larger area, which can be activate/deactivated via switches between their shared emitters, as indicated in Figure 5.36. By synchronizing switches S1 and S2, governed by the 2-bit control word  $C[0:1]$  (where  $C[0]$  is the LSB) with the discrete values of  $I_E$  in each bandwidth mode,  $I_{EA}$ ,  $I_{EB}$ , and  $I_{EC}$ , the effective area of the inner GGC pair scales accordingly, leaving the current density unchanged. For the npn sizings shown in Figure 5.36 and a nominal  $I_E$  in Mode B of  $40 \mu\text{A}$ , the patterns of Table 5.3 ensure that

$$\frac{I_{e3,4}}{A_{e3,4}} = \underbrace{\frac{3.32\mu\text{A}}{0.15\mu\text{m}^2}}_{\text{Mode A}} = \underbrace{\frac{20.0\mu\text{A}}{0.90\mu\text{m}^2}}_{\text{Mode B}} = \underbrace{\frac{120\mu\text{A}}{5.40\mu\text{m}^2}}_{\text{Mode C}} = \frac{I_{e1,2}}{A_{e1,2}} \quad (5.61)$$

Straightforward in theory, in practice several considerations attend the design of switches S1 and S2. In the full-blown schematic of Figure 5.37, they are implemented with nMOS devices S1 and S2 and accompanied by complementary switches S3 and S4, which connect the shared emitters to a static reference when the corresponding device pair is deactivated so that all its terminals are at (approximately) the same voltage. This choice of biasing limits TID effects by minimizing  $\Delta N_{\text{ot}}$  and  $\Delta N_{\text{it}}$  and

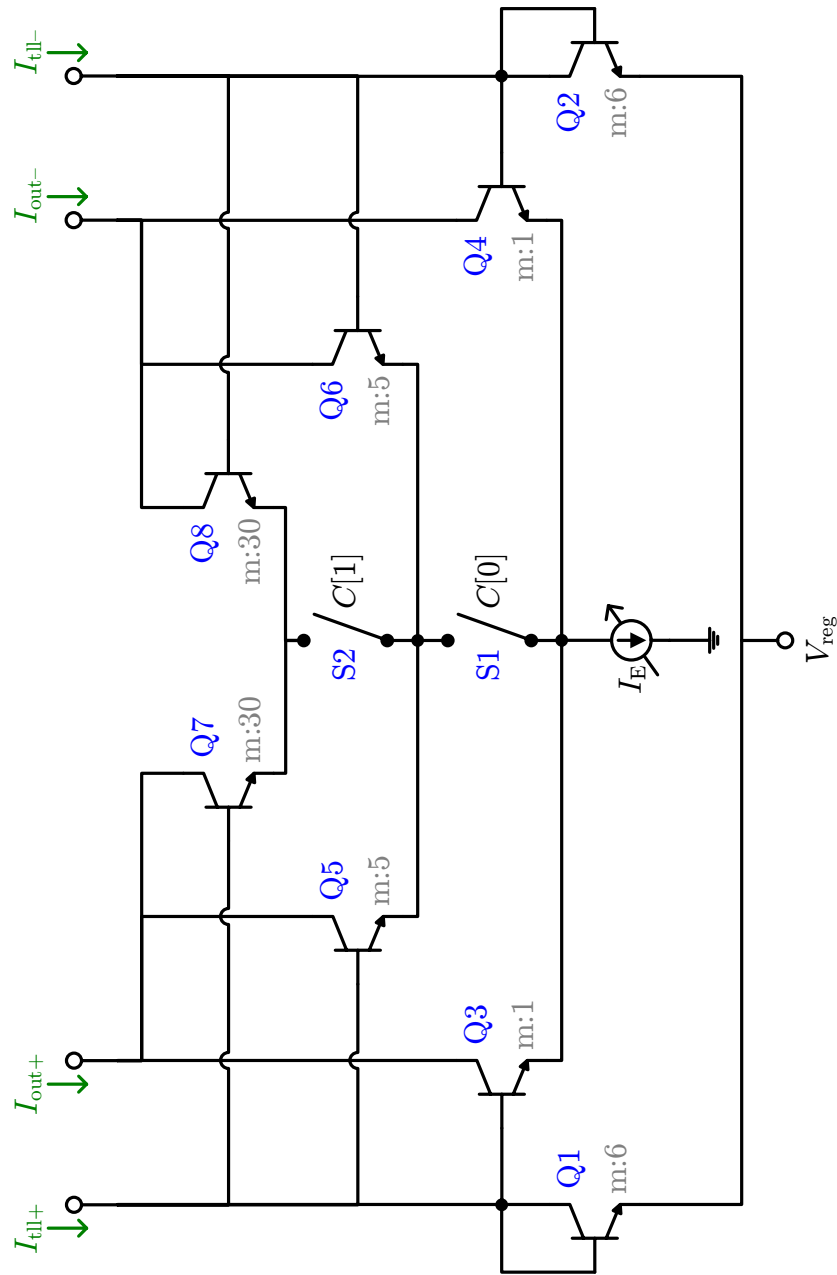


Figure 5.36: Simplified schematic of current density matching technique in GGC. Variable-sized inner pair Q3/Q4 of Figure 5.35 is explicitly decomposed into Q3–Q8. Switches are annotated with value of  $C[0:1]$  control word that activates (read closes) them to affect area scaling in denominator of (5.61) in each mode.

the very presence of S3 and S4 prevents the shared emitters of inactive pairs from otherwise floating, which would render them vulnerable to SEEs.

Deployment of nMOS devices in the signal path has previously been eschewed on account of noise, nonlinearity, and radiation softness. By placing the switches at the shared emitter of each pair, not only are such switch noise and nonlinearities relegated to the common-mode path,<sup>34</sup> but the output impedance of the transconductor remains constant across all modes. To prevent the leakage adumbrated in Section 2.1.1.3, the layout of the switches adopts an enclosed geometry described in Section 5.6.2.1.

Although pMOS switches would have alleviated this problem altogether, the lower on-resistance of nMOS transistors is critical to the TLL principle. So, whereas S3 and S4 carry little current, and can therefore be of minimum size, the substantial tail currents flowing through S1 and S2 when they are active demand that they: possess a high  $W/L$  with minimum length; and are  $I_E$ -scaled so as to ensure  $< 1$  mV drop at the highest current densities (Mode C). Thus, S1 and S2 consume  $\sim 78\%$  of the total GGC switch area.

### 5.5.2.2 Even-Order Distortion

The statistical methods with which the mismatch of bipolar transistors is conventionally characterized subsume the doping and etching uncertainties responsible for the conditions of (5.49) and (5.50) into an effective  $\Delta V_{BE} = V_{BEa} - V_{BEb}$  for a pair of side-by-side transistors Qa and Qb without surrounding dummies. When each transistor is composed of  $m$  paralleled instances, the standard deviation of the effective  $\Delta V_{BE}$ , which represents the mean junction voltage when the same  $V_B$  and  $V_E$  are applied to the entire set, is given by the ensemble average rule applied to an equation of the form of (4.30) [Pitman, 1993, p.146]:

$$\sigma^2\{\Delta V_{BE}(A_e)\} = \frac{\frac{k_{1VBE}^2}{A_e} + k_{2VBE}^2(\Delta d)^2}{\sqrt{m}} \quad (5.62)$$

---

<sup>34</sup>As opposed to the MOS switches of a SC filter, the switches in the tail current source of the GGC retain their state throughout normal operation. As such, the active switches carry DC current which is, as detailed in Section 3.1.3.3, subject to the variability described by their drain flicker noise.

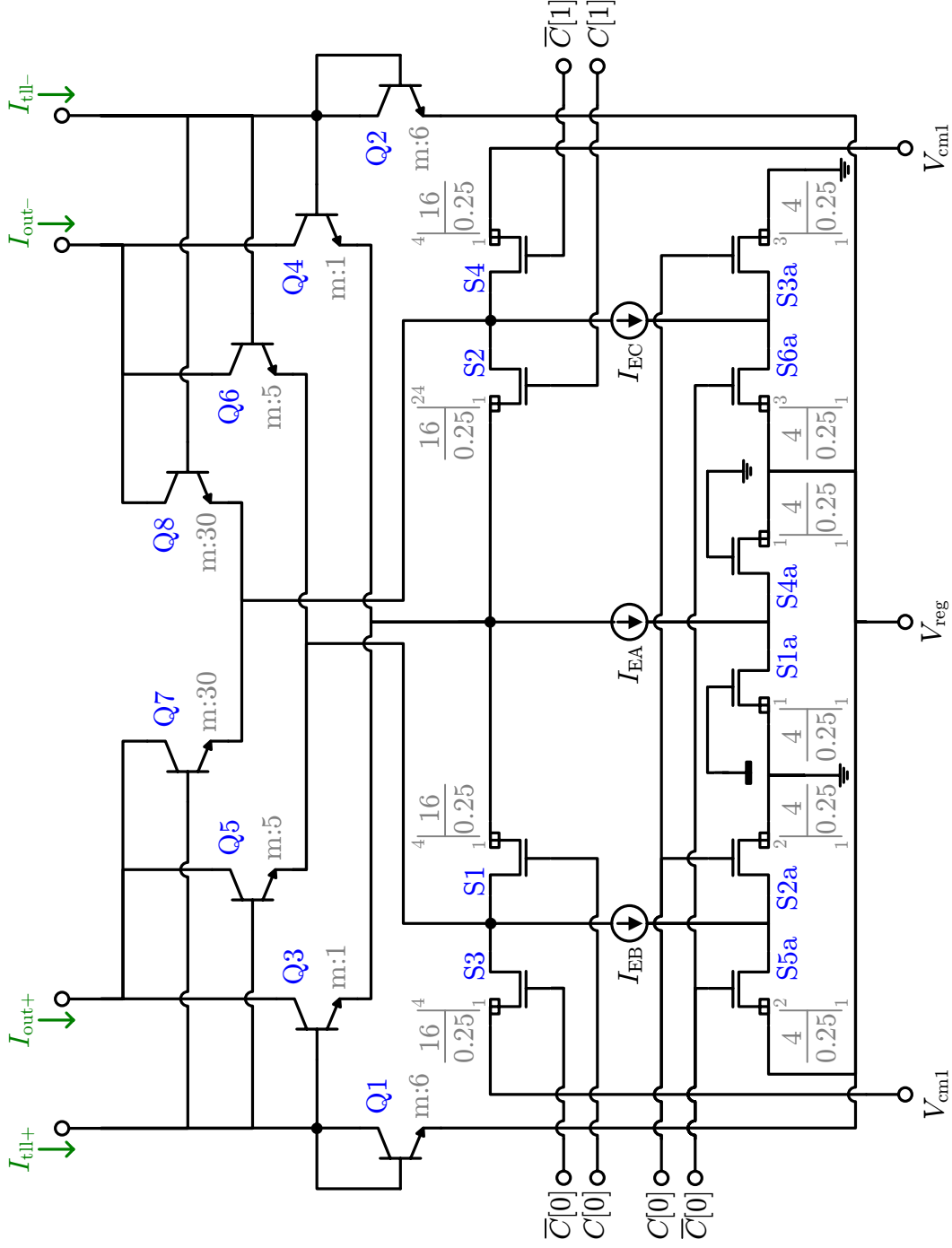


Figure 5.37: SPDT implementation of GGC current-density-matching switches. S1 and S2 of Figure 5.36 are each implemented with a pair of enclosed-source nMOSFETs, becoming S1/S3 and S2/S4. Each branch of the programmable  $I_E$  source also employs SPDT ground-interrupt switches.

where  $A_e$  is the nominal area of each instance and  $\Delta d$  is the drawn separation between the centers of each complementary pair.

For the BiCMOS8B+ technology, the offset term of the resulting affine function dominates (5.62) and is so large that, even for the  $m > 1$  of Q1/Q2 and Q5–Q8 in Figure 5.36, (5.49) introduces a non-negligible  $V_{os}$  into the TLL. To combat this inherent mismatch, degeneration resistors are inserted in the emitters of both the inner and outer pair devices, as shown in Figure 5.38. These are sized so that in the overall response, which takes the form of (5.59), the mismatch of the resistors ( $\sigma\{\epsilon_{rsh}\}$ ), which through careful layout (cf. Section 4.3.1.2) can be made quite small, dominates that of the transistor  $\Delta V_{BE}$  ( $\sigma\{V_{BE}\}$ ). Specifically, each is scaled in proportion to the current density of its corresponding npn, indexed by  $x = 1, 2, \dots, 8$ , such that

$$V_{Rdx} = I_{Ex} R_{dx} = 100 \text{ mV} > V_T \quad (5.63)$$

This level of static  $V_{Rdx}$  renders the normalized  $\sigma\{\epsilon_{vbe}\}$  negligible, but the dynamic drop is not large enough to limit the output current swing.

To confirm the efficacy of this technique, Figure 5.39 presents histograms from 50 Monte Carlo simulations comparing the levels of the second and third harmonic relative to the fundamental both with and without the degeneration resistors. As intended, the mean of the second harmonic drops by nearly 24 dB with degeneration because their series-series feedback attenuates the impact of the intrinsic npn  $\Delta V_{BE}$  mismatch. Additionally, the level of the third harmonic, through already within specification, is also slightly improved by this technique because the discrete resistors, which are sized to precisely mimic the emitter area scaling, dominate the equivalent emitter resistances used to capture intrinsic parasitics, not all of which scale with  $A_e$ . The current density matching prescribed by (5.48) for low odd-order distortion assumes ohmic resistances that behave like the former (cf. Footnote 25).

### 5.5.3 Common-Mode Feedback

The final component of the transconductor is a set of loads at its output which reclaim the common-mode component of the output current ( $\bar{I}_{out}$ ) so that only the



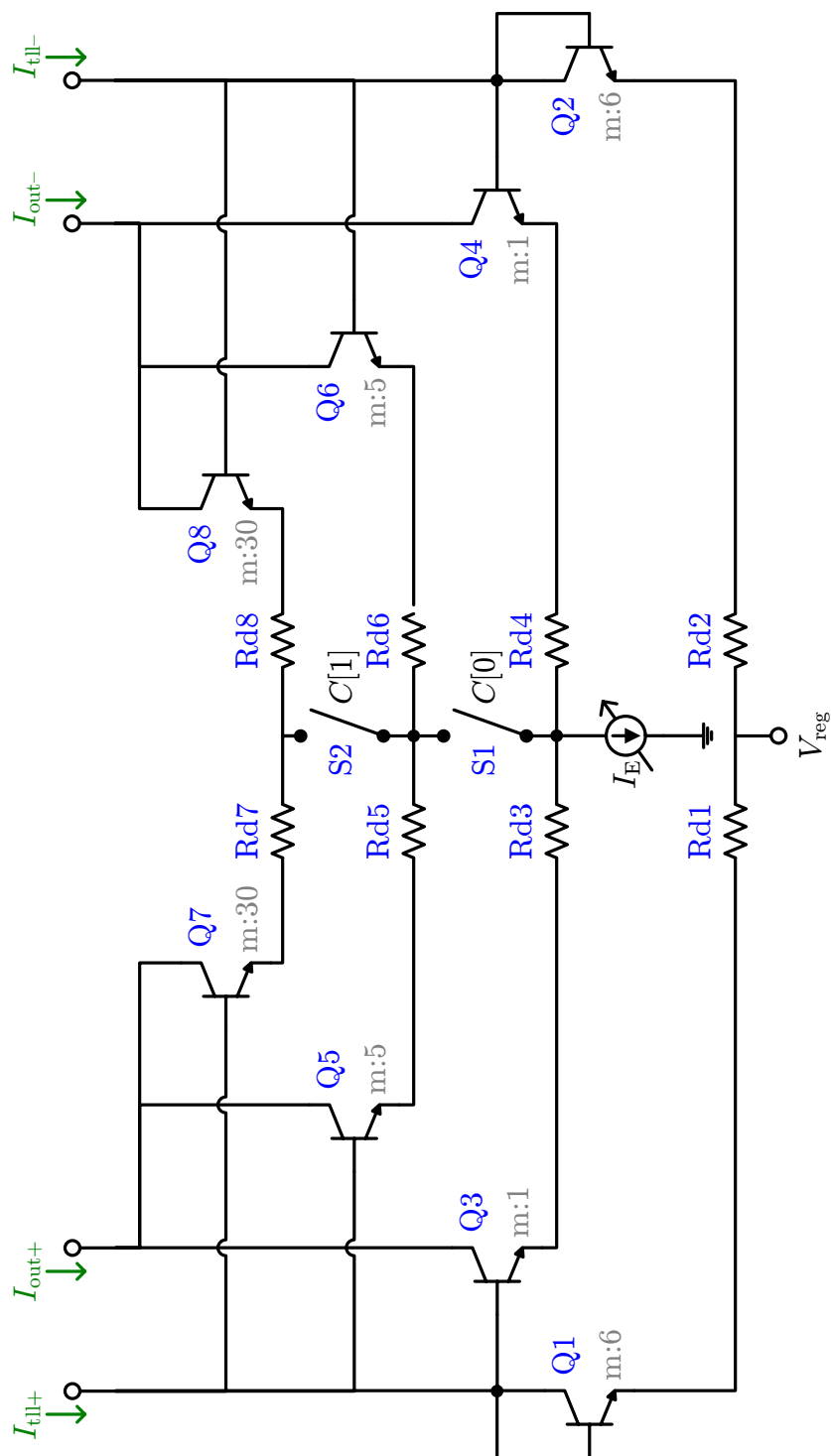


Figure 5.38: Linearized GGC with resistive degeneration. For simplicity, current-density-matching switches are represented as in Figure 5.36. The degeneration resistors are scaled according to (5.63) to provide  $\sim 100$  mV drops in each emitter.

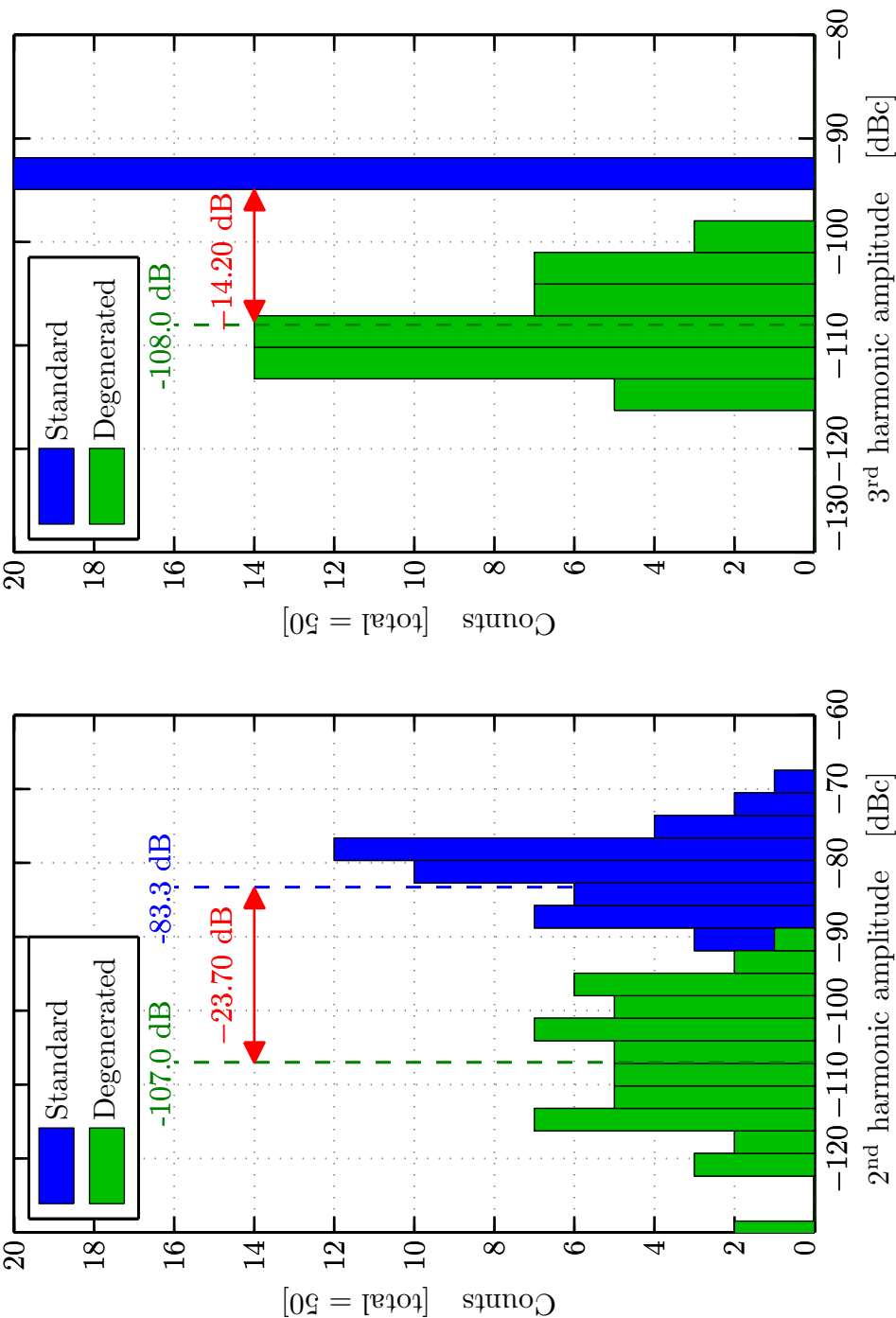


Figure 5.39: Monte Carlo analysis of improved GGC mismatch with degeneration in Mode B. For the same input sinusoid as in Figure 5.34 (100 kHz, 1 V<sub>PP</sub>), the mean of the second(third) harmonic amplitude distribution observed at the transistor output, indicated by a dashed line, drops by over 23 dB(14 dB) when GGC degeneration resistors are employed. Similar improvements are garnered in Modes A and C (not pictured).

differential component,  $I_{\text{out}}$ , is exported. Since the high output resistance of the transconductor is critical to opamp noise suppression in the  $G_m$ -C-Opamp integrator (cf. Section 5.3.1.2), the common-mode loads should be active, low-noise, and capable of sufficiently regulating the common-mode output voltage of the transconductor so that the common-mode input voltage of the subsequent opamp is well-defined. Furthermore, since the bias current in the GGC output stage scales with  $f_p$ , the load currents must be switched in step with  $I_E$  in each mode.

A conceptual representation of the load circuit is portrayed in Figure 5.40. As the only true sense-and-return CMFB loop in the front-end, the stability and power consumption of such a network, heretofore avoided, must be optimized through careful design. With regard to the area and power penalty, the following observation about the biquad in Figure 5.8 is seminal: each unit transconductor feeds the input nodes of an opamp.

Thus, the circuit within the green box of Figure 5.40—the CMFB amplifier—need only be instantiated once per opamp; each occurrence is shared by all transconductors driving a given opamp input. The elements in the blue box—the CMFB loads—source the common-mode current for a single transconductor, so their multiplicity exhibits a one-to-one correspondence with the number of transconductors driving a given opamp input. Section 5.5.3.1 examines the design of the CMFB amplifier whereas Section 5.5.3.2 describes the saturated pMOS transistors that provide the active loads.

### 5.5.3.1 Shared Amplifier

To conform with the common-centroid array in which the transconductors themselves are arranged (cf. Section 5.6.1.3), it is advantageous to divide the CMFB amplifier in half. Together, the two circuits in Figure 5.41 comprise the single CMFB amplifier A1 whose output,  $V_{\text{cntclm}+}$ , is the mirror voltage that drives the gates of the loads in Figure 5.40.

Since the mirrored current must match  $I_E$  in each mode to set  $\bar{V}_{\text{out}}$  accurately, the tail source that originates  $I_{\text{CM}}$  is divided into three parallel branches so as to mimic the tripartite implementation of the  $I_E$  source in Figure 5.37. The polarity

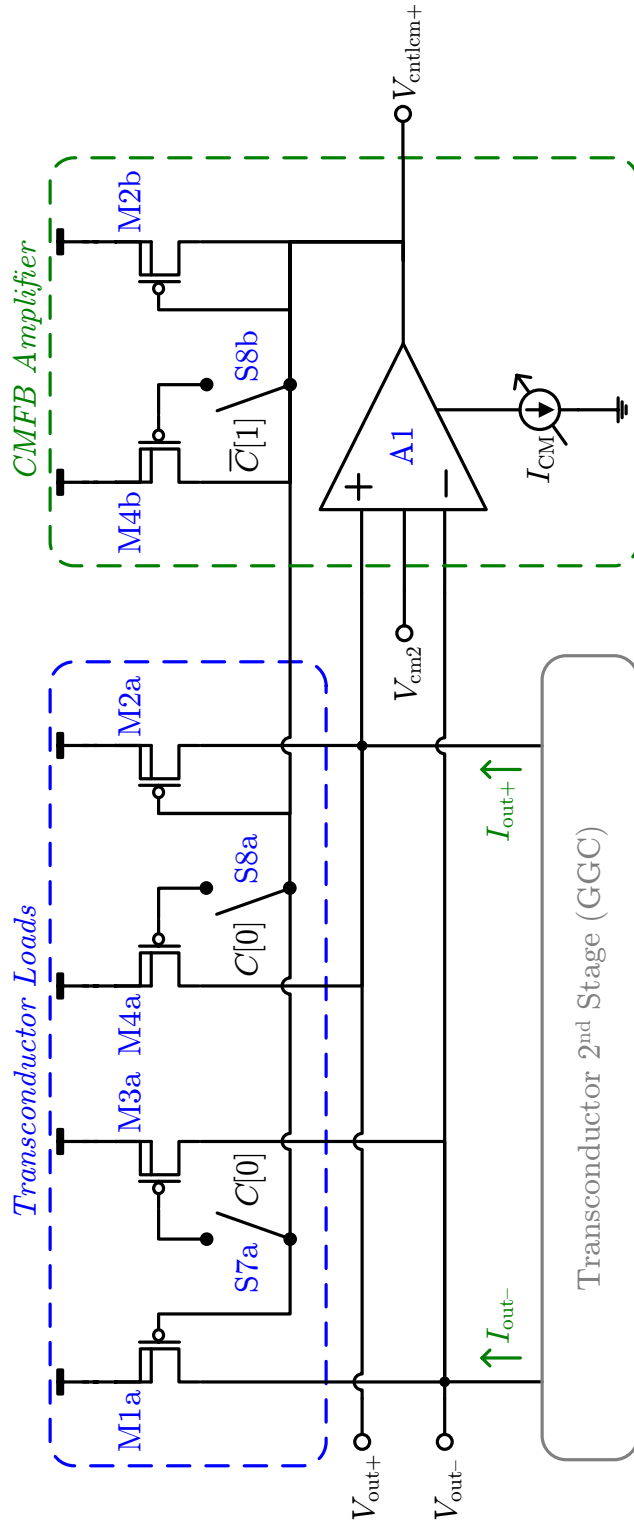


Figure 5.40: Simplified schematic of transconductor CMFB network. Not simply a differential amplifier, here A1 differences the common-mode reference  $V_{cm2}$  from the average of its inverting and non-inverting inputs and steers its bias current,  $I_{CM}$ , (which tracks mode-based variations of  $I_E$  in Figure 5.35) into current-mirror masters M2b/M4b accordingly.



Figure 5.41: Implementation of CMFB amplifier in Figure 5.40. It is partitioned into ‘A’ and ‘B’ halves across which the  $I_E$  sources are asymmetrically distributed. Although the amplifier is fully differential, its load is not:  $V_{\text{cntlcm-}}$  is only used for neutralization (cf. Section 5.5.3.2).

Mode		pMOS Loads					Neutralization			
ID	$C$	S7a [Pos.]	S8a [Pos.]	S9a [Pos.]	S10a [Pos.]	$I_E$ [ $\mu A$ ]	S11a [Pos.]	S12a [Pos.]	S13a [Pos.]	S14a [Pos.]
A	00	Off	Off	On	On	6.66	Off	Off	On	On
B	01	On	On	Off	Off	40.0	On	On	Off	Off
C	11	On	On	Off	Off	240	On	On	Off	Off

Table 5.4: Configuration of pMOS load switches in each AAF mode (cf. Figure 5.44). Their operation matches the load current, which is mirrored from the bias current set by switches in the CMFB amplifier (cf. Table 5.5), to the GGC  $I_E$ .

Mode		Tail Current Sources						pMOS Load Mirrors				
ID	$C$	S1b [Pos.]	S2b [Pos.]	S3b [Pos.]	S4b [Pos.]	S5b [Pos.]	S6b [Pos.]	$I_{CM}$ [ $\mu A$ ]	S7b [Pos.]	S8b [Pos.]	S9b [Pos.]	S10b [Pos.]
A	00	On	On	On	Off	Off	Off	40.0	On	On	Off	Off
B	01	On	On	On	Off	Off	Off	40.0	On	On	Off	Off
C	11	On	Off	Off	Off	On	On	40.0	Off	Off	On	On

Table 5.5: Configuration of CMFB amplifier switches in each AAF mode (cf. Figure 5.41). The mirror switches work with those in the pMOS loads (cf. Table 5.4) to scale the  $I_{CM}$  set by the tail source switches so as to match the GGC  $I_E$ .

of nMOS switches S1b–S6b, which govern  $I_{CM}$ , and pMOS switches S7a–S10a(S7b–S10b) in the loads(CMFB amplifier), which govern the slave(master) devices of the CM current mirror, are assigned such that the bias current of the CMFB amplifier in each mode is constant (cf. Table 5.4 and Table 5.5). That way, even when the GGC in the core is running at the highest  $I_E$  (Mode C), the CMFB amplifier is biased at a lower current (that of Mode B), which is then amplified through the mirror ratio of the pMOS loads, saving power.

Although constant bias current certainly helps, the stability of the CMFB loop is not strictly mode-agnostic; Mode C, in which both the capacitive load on the M1a–M4a pairs and their transconductance are maximal, presents a worst-case stability scenario for this power-conscious biasing scheme. In this mode, Figure 5.40 simplifies to Figure 5.42, with the help of Figure 5.41, isolating the elements necessary for a small-signal stability analysis. Assuming perfect matching and omitting the ‘a’ and

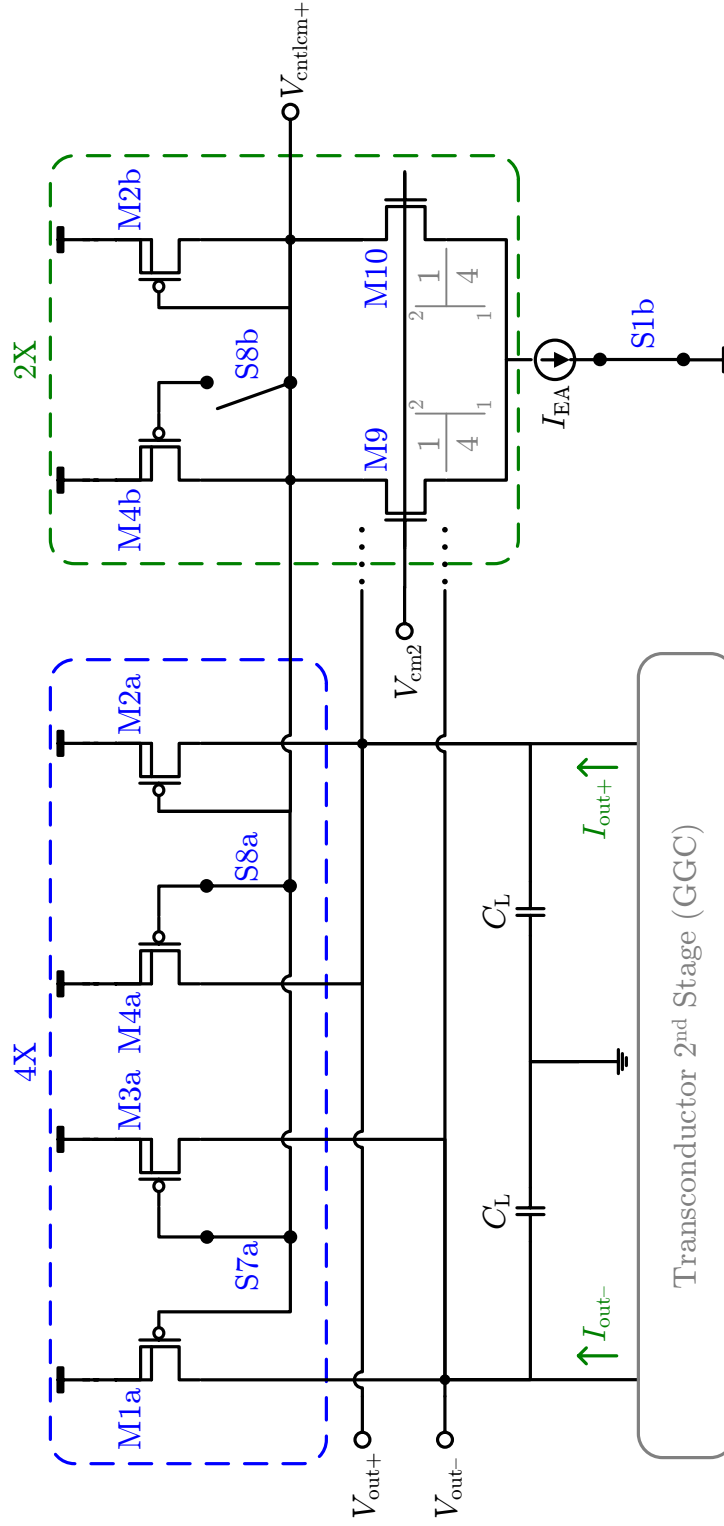


Figure 5.42: Common-mode feedback loop for worst-case stability, in which a single opamp is loaded by four transconductors in Mode C. The loop is completed through the M7/M8 inputs of Figure 5.41, which constitute an inversion omitted for clarity.

‘b’ designators for simplicity, the loop gain is approximately

$$L(s) \simeq \frac{2g_{m9}}{2g_{m2} + sC_{\text{cntlcm}}} \frac{4(g_{m1} + g_{m3})}{4(g_{o1} + g_{o3} + g_{\text{ggc}}) + sC_{\text{outn}}} \quad (5.64)$$

Using (5.64) to express the DC gain as well as the dominant ( $p_0$ ) and non-dominant ( $p_1$ ) poles of the loop gain in terms of the device transconductances and capacitances yields

$$L(0) \simeq \frac{g_{m9}(g_{m1} + g_{m3})}{g_{m2}(g_{o1} + g_{o3} + g_{\text{ggc}})} \quad (5.65a)$$

$$p_0 \simeq 4 \frac{g_{o1} + g_{o3} + g_{\text{ggc}}}{C_{\text{outn}}} \simeq \frac{g_{o1} + g_{o3} + g_{\text{ggc}}}{C_{\text{db1}} + C_{\text{db3}} + C_{\text{ggc}}C_L/4} \quad (5.65b)$$

$$p_1 \simeq \frac{g_{m2}}{C_{\text{cntlcm}}} \simeq \frac{g_{m2}}{C_{\text{gs2}} + 2(C_{\text{gs1}} + C_{\text{gs3}} + C'_{\text{gd1}} + C'_{\text{gd3}})} \quad (5.65c)$$

where the contributions to  $C_{\text{outn}}$  include the common-mode output capacitance of the GGC (and  $C_{\text{ggc}}$ ) and a lumped element representing any extrinsic common-mode load capacitance ( $C_L$ ). The contributions to  $C_{\text{cntlcm}}$  include the gate-to-drain capacitances of the loads, subject to Miller multiplication and, hence, primed in (5.65c). It is evident that the load sizing is critical to phase margin, as higher  $g_{m1,2,3}$  increases  $p_1$  without changing  $L(0)$ , whereas larger  $C_{\text{gs1,2,3}}$  and  $C_{\text{gd1,3}}$  reduce  $p_1$ . But, CMFB loop stability is just one of several complications in the load design that are presented in the next Section.

### 5.5.3.2 pMOS Loads

Over the full tuning range of  $I_E$ , the pMOS load devices in Figure 5.43 must be properly sized so as to: keep the total output noise below that of the GGC; remain saturated even in Mode C, when their overdrive is highest; ensure stability of the CMFB loop whose gain(non-dominant pole) is set by their output resistance(gate capacitance); and provide high output resistance, to accurately realize the GGC  $G_m$  and unilateralize opamp noise. These aims must be met under two constraints imposed by the transconductors: the maximum area of the loads is driven by the



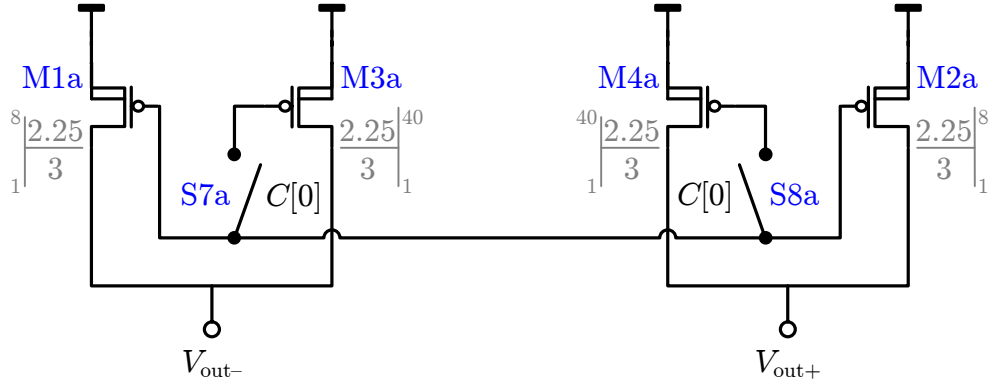


Figure 5.43: Transconductor loads of Figure 5.40 with simplified switching. Final sizes of M1a–M4a shown.

need for them to reside within the area allotted to each unit transconductor; and their fixed bias current levels in each mode are set by the  $I_B(I_E)$  of the first(second) stage.

First consider headroom. Increasing the load widths reduces their overdrive, improving the  $V_{out}$  swing and avoiding triode operation. But, it also destabilizes  $L(s)$  since, according to (5.65),  $L(0)$  and  $p_0$  are unchanged,<sup>35</sup> but  $p_1$  drops because  $g_m \propto \sqrt{W}$  whereas  $C_{gs} \propto W$ . To counteract this effect, the gate length should be scaled inversely with  $W$ . Such area-constrained sizing is not only more compatible with layout restrictions, but keeps the gate capacitances fixed while increasing  $g_m(g_o)$  thereby improving loop stability through simultaneously increasing(decreasing)  $p_1(L(0))$ .

However, reduction of  $L$  cannot be carried out arbitrarily far because a weaker  $L(s)$  degrades the precision of the CMFB and, for fixed drain currents, the flicker noise power is proportional to  $1/L^2$  (cf. Footnote 30 of Chapter 4). Thus, in the final design, the pMOS loads are based on a unit size of 18/3, which provides plenty of margin over the minimum required to remain in saturation ( $\min\{W/L\}=3.5$ ) at the expense of moderate flicker noise.

At these sizes, the loop stability depends on  $C_L$  not only through its effect on  $p_0$

<sup>35</sup>The GGC contribution to  $C_{out}$  dominates that of  $C_{db1}$  and  $C_{db2}$ . Plus,  $g_{o1}$  and  $g_{o3}$  increase slightly with larger  $W$ , so there is little net effect on  $p_0$ .

in (5.65b) but through a more insidious avenue: the Miller multiplication of  $C'_{\text{gd1}}$  and  $C'_{\text{gd3}}$  in (5.65c). Specifically, it can be shown that the effective admittance of these terms depends on  $C_L$  via

$$C'_{\text{gd1},3} = C_{\text{gd1},3} \left( 1 + \frac{g_{\text{m1},3}}{g_{\text{o1},3}} \right) \left( \frac{1 + s \frac{C_L}{g_{\text{o1},3} + g_{\text{m1},3}}}{1 + s \frac{C_L + C_{\text{gd1},3}}{g_{\text{o1},3}}} \right) \quad (5.66)$$

Due to the denominator, larger(smaller)  $C_L$  attenuates(enhances) the Miller gain, thereby increasing(decreasing)  $p_1$  and improving(degrading) loop phase margin.

Since the load capacitance seen at the inputs of the opamp varies with the number of unit-transconductors in the integrator, and since the corresponding metal lines cover a lot of die real estate, such sensitivity of the CMFB loop to  $C_L$  is perilous. To remedy it, neutralization devices M11/M12 are cross-coupled between the output nodes of each transconductor. Visible in the full schematic of Figure 5.44, these are only weakly accumulated, so the predominant cancellation comes via their overlap capacitances.<sup>36</sup> In the absence of a channel, such parasitics do not match the  $C_{\text{gd}}$  of saturated M1a–M4a, so the sizing of M11/M12 is iteratively optimized to yield maximum loop phase margin in Mode C. But, even though theory dictates that stability is only of concern in Mode C, switches S11a–S14a, which along with S7a–S10a are shown in Figure 5.44 to contain pMOS devices immune to radiation-induced leakage, also activate the neutralization in Mode B as a precaution against excessive TID degradation.

## 5.6 Layout

Many of the same techniques discussed in Section 4.3 are at play in the layout of the AAF. In particular, matching of transistors and resistors is pursued through compact, well-dispersed, common-centroid interdigitation and symmetric wiring, at

---

<sup>36</sup>The gates of M11/M12 are tied to the output nodes and their sources/drains to the control lines. This orientation prevents stray noise injection and allows the neutralization capacitors, as well as the pMOS switches that govern them, to share a common well, conserving area.

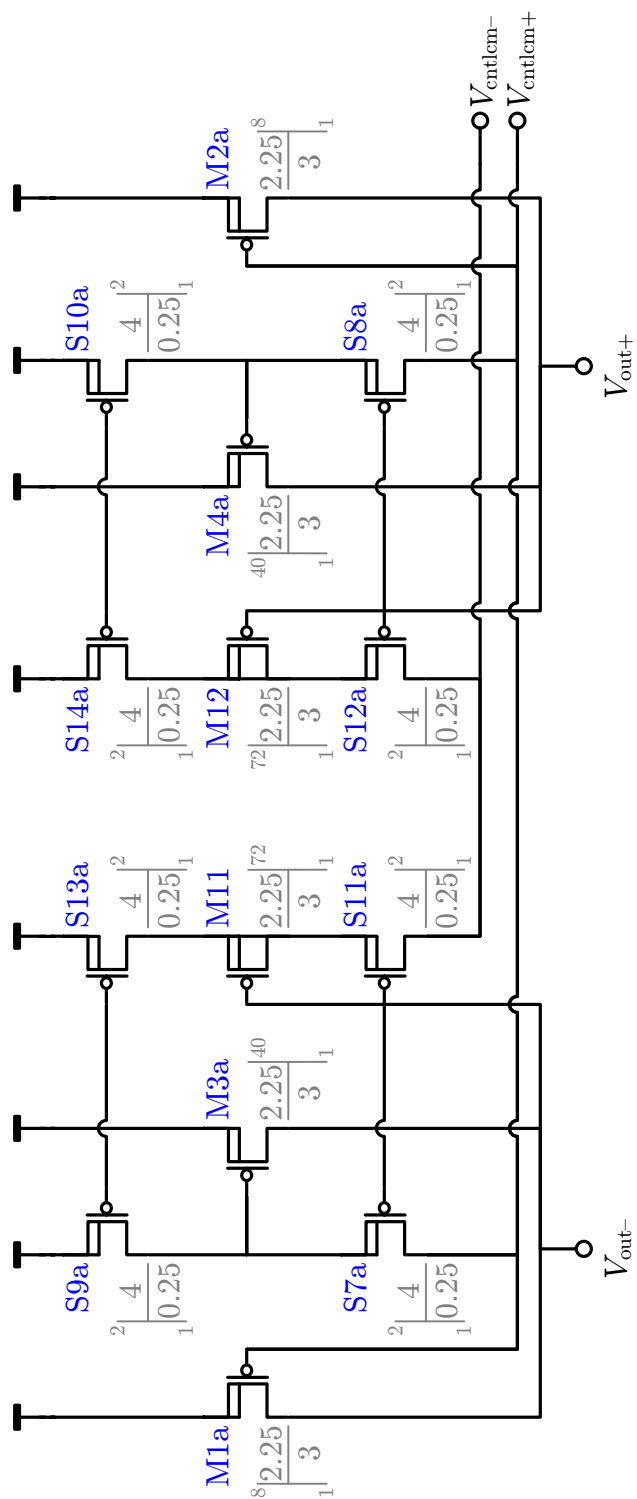


Figure 5.44: Complete transconductor loads of Figure 5.40, including SPDT switching via S7a–S10a and Mode C neutralization capacitors implemented by weakly accumulated M11/M12 and their associated switches, S11a–S14a.

the expense of burgeoning area. Likewise, both minority- and majority-carrier guard rings are liberally employed, particularly because the presence of nMOS devices in both the transconductor CMFB amplifier and opamp introduce the potential for an p-n-p-n structure like that of Figure 2.28(a) to form. Extending these techniques to the AAF involves additional protections to account for the increased mismatch over its sprawling extent, which are detailed in Section 5.6.1, and the introduction of switches, the TID-induced leakage of which (cf. Figure 2.12) is remedied through non-standard geometries described in Section 5.6.2.

### 5.6.1 Matching

Whereas Section 4.3.1 demonstrates techniques for reducing mismatch between the devices that comprise the LNA, namely transistors and resistors, the additional levels of hierarchy in the AAF require the matching of more abstract blocks, particularly the transconductor and capacitor unit elements. In addition, since the area consumed by the AAF is over forty times that of the LNA, the routing distances of critical signals cannot be neglected. Solutions for each of these challenges are provided in the remainder of this section.

#### 5.6.1.1 Reference Distribution

The sources of  $I_B$  and  $I_E$  in each transconductor should be slaved to a pair of master reference currents distributed cleanly and accurately across the chip so that when tuning  $f_p$ , all the transconductance terms in (5.16) scale by the same factor. Ideally, each transconductor would receive these references on a dedicated pair of lines that transmit them in current-mode to alleviate losses associated with mismatch in the resistive wiring parasitics. However, since such lines cannot be shared by multiple unit-transconductors, the size of the wiring for unit-specific referencing is unwieldy.

Instead, as depicted in Figure 5.45, these references—along with the lone reference that supplies all static currents in the front-end,  $I_O$ —are buffered in triplicate as they enter the chip symmetrically and shipped in current-mode to reference generators in each cell. These local generators are responsible for converting  $I_B(I_E)$  into a pair of

voltage-mode signals,  $V_{\text{bmstb}}$  and  $V_{\text{tmstb}}$  ( $V_{\text{bmste}}$  and  $V_{\text{tmste}}$ ) that are then distributed to all transconductors in the stage. The cascaded filter architecture decouples the AAF poles so that interstage  $G_{\text{m}}$ -mismatch is less deleterious.

For each reference current, this pair of voltages bias a top-rail pMOS cascoded current mirror, the masters of which lie in the reference generator, depicted in Figure 5.46, whereas a set of slaves resides in each transconductor. Although the use of pMOS devices eliminates mismatch from voltage drops along these four lines, the long distances between the masters and slaves ( $\Delta d$  in (4.30)) implies that their  $V_{\text{thp}}$  are unlikely to match. To minimize this effect, an identical layout cell is used for the masters and slaves—it is merely duplicated as necessary to affect a mirror ratio that reduces the current flowing in all reference branches to (nominally)  $10\ \mu\text{A}$  so as to conserve power. As is evident in Chapter 6, the achieved pole locations of the final AAF confirm the efficacy of this reference distribution technique.

#### 5.6.1.2 Comb Capacitors

The AAF capacitors enumerated in Table 5.2 are constructed from a unit-sized comb capacitor in metal layers 1 through 4 that, as is clear from the views in Figure 5.47, relies on lateral, rather than vertical, flux between one-dimensionally interdigitated metal lines to realize linear capacitance of moderate density [Samavati *et al.*, 1998].<sup>37</sup> Since only the lateral dimension is well-controlled in any manufacturing process [Hastings, 2006, p.245], such construction minimizes oxide growth and etch effects that would otherwise degrade the matching between capacitors in each stage of the filter [Shyu *et al.*, 1984, p.949].<sup>38</sup>

Errors associated with oxide growth, which affects both the thickness and

---

<sup>37</sup>Compared to a capacitor constructed from joining the source and drain of an MOS transistor [McCreary, 1981], metal comb capacitors offer enhanced linearity at the expense of lower densities.

<sup>38</sup>Although BiCMOS8B+ also offers a comb capacitor with two-dimensional interdigitation, which leverages vertical flux to obtain higher densities, the manufacturer offers no circuit model of this element. A first-order model of its capacitance obtained from a (Poisson) field solver indicates that its wider pitch and use of Metal 5 in place of Metal 1 result in an area savings of only  $\sim 20\%$ , rather than the anticipated factor of two. Despite the large filter capacitors required, the higher matching accuracy and available circuit model of the lateral-flux comb outweigh this modest size reduction in the construction of a high-fidelity filter.

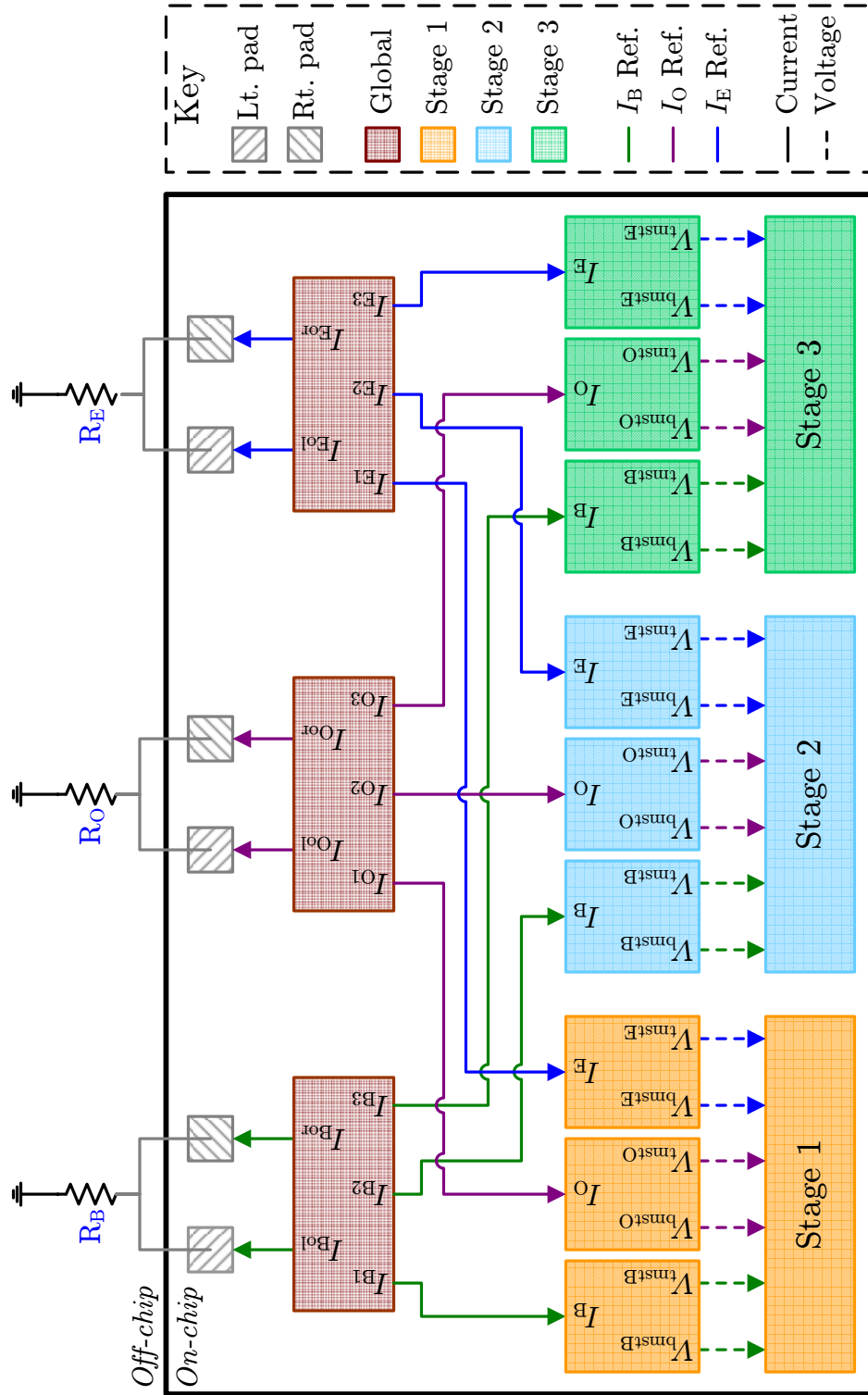


Figure 5.45: Block diagram of reference shipping techniques. Each reference current ( $I_B$ ,  $I_E$ ,  $I_O$ ) is derived from an off-chip resistor wired in parallel to opposing pads on the left and right sides of the chip. Matched currents are then shipped from global generators near the padframe to local  $V$ -to- $I$  buffers in each stage.

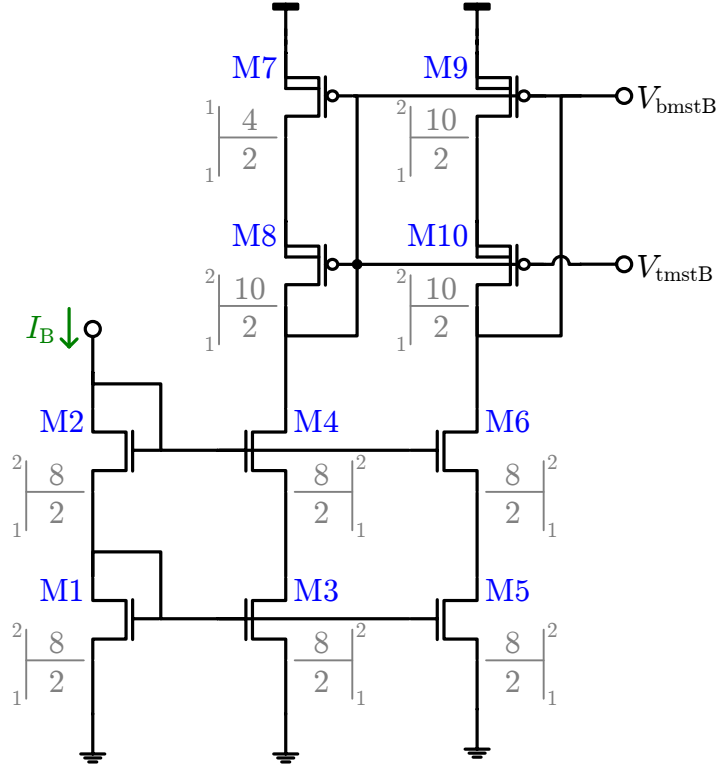


Figure 5.46: Schematic of local reference generators for  $I_B$  and  $V_{bmstB}/V_{tmstB}$  in each stage of Figure 5.45. Identical circuitry also generates  $V_{bmstO}/V_{tmstO}$  ( $V_{bmstO}/V_{tmstO}$ ) from  $I_O(I_E)$ .

permittivity of the dielectric, and etch rates, which act along its edges to define the lateral dimensions of the capacitor, can be described by an equation of the form of (4.30) because both processes exhibit local(global) variations whose autocorrelation is narrow(wide) in  $\Delta d$ , corresponding to a white(pink) noise spectrum over high(low) spatial frequencies [Shyu *et al.*, 1984, p.949]. But, in most processes global effects dominate. So, it is advantageous to construct each of the large filter capacitors from an array of unit elements and accept smaller area in the first term of (4.30) in an effort to minimize  $\Delta d$  in the second term, or eliminate it altogether through the use of common-centroid arrays.

An example—the array comprising the matched capacitors in the lossless integrator of Stage 1—is shown in Figure 5.48. To match the horizontal pitch of the stage, each unit capacitor (3.17 pF) is rectangular at  $248 \mu\text{m} \times 35 \mu\text{m}$  rather

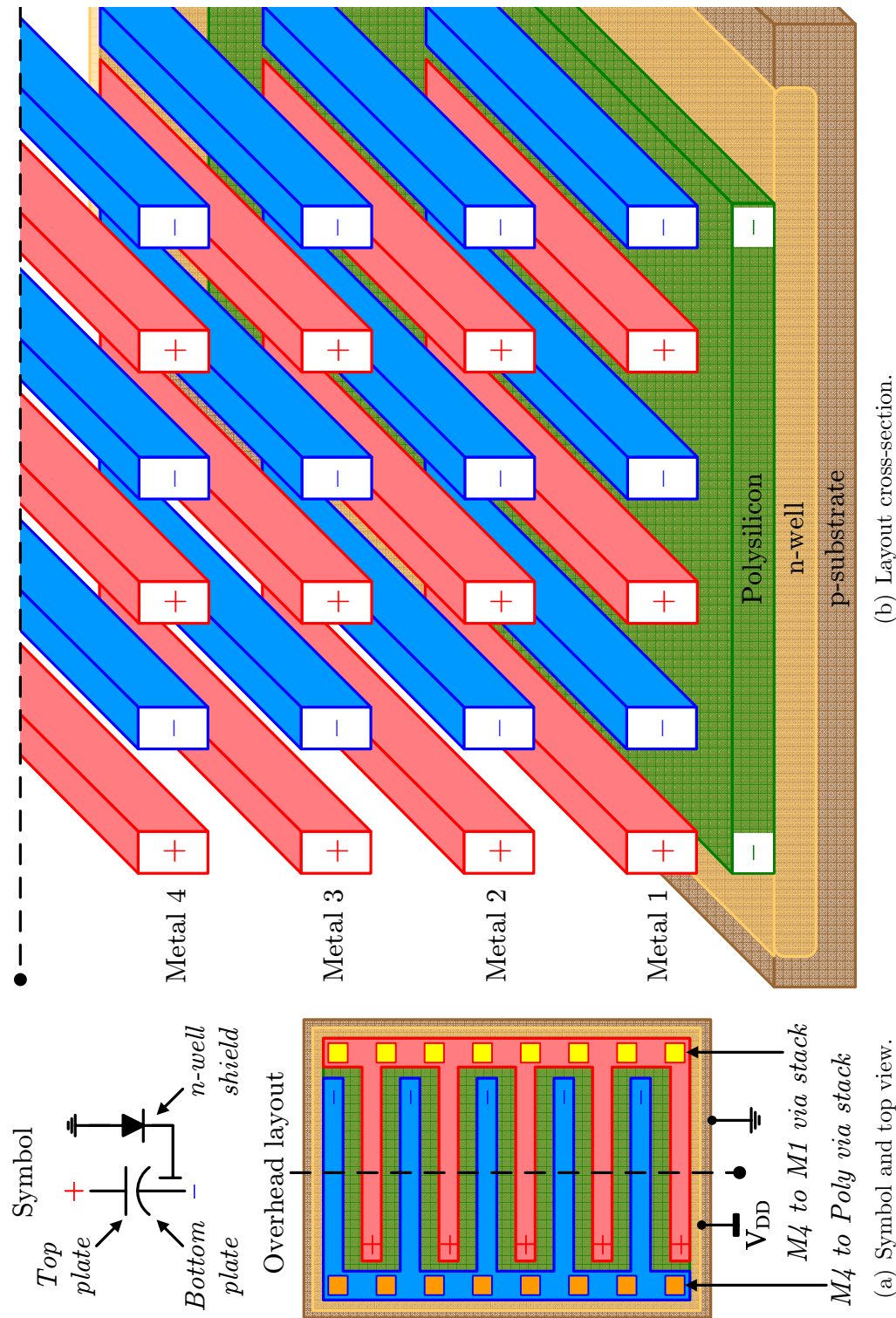
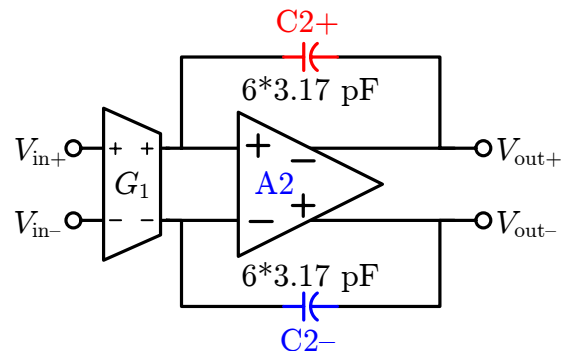
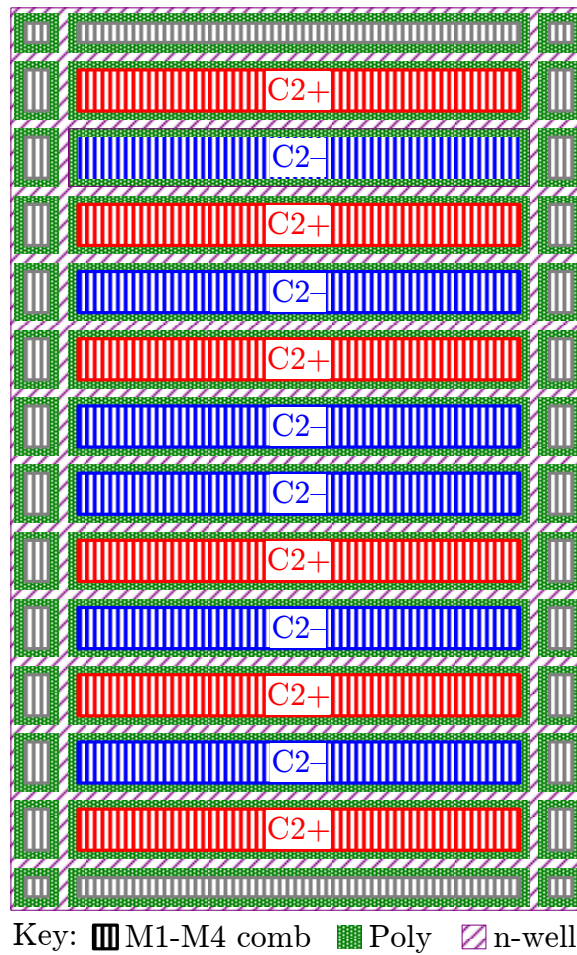


Figure 5.47: SVEPRE metal comb capacitor. Both (a) top and (b) cross-sectional layout views depict the polysilicon and n-well shields in its symbol, as well as its lateral interdigitation pattern. Dimensions exaggerated for clarity.





(a) Schematic highlighting Stage 1 comb cap pair.



(b) Layout of Stage 1 comb caps.

Figure 5.48: Example layout of metal comb capacitor array that realizes matched capacitors in Stage 1 with value  $C_2$ . Dummy capacitors shown in gray.

than square at  $50\ \mu\text{m} \times 50\ \mu\text{m}$  as in the optimal case [*Shyu et al.*, 1984, p.952]. In light of the non-minimum perimeter-to-area ratio of the rectangular geometry [*Hastings*, 2006, p.301], edge effects are addressed through the use of dummy metal stacks around the perimeter of the array. Along with the dual protection of both a supply-driven n-well that extends well beyond the edges of the array and a polysilicon shield connected to the bottom plate, these dummies complete a suite of electrostatic shielding mechanisms aimed at reducing: stray fringing fields that limit capacitor accuracy; destabilizing coupling to nearby signal lines; and noise injection from the substrate. In lieu of a top-metal field plate to complete the electrostatic seal, signal lines and metal fill are completely excluded from the regions over these capacitors.

### 5.6.1.3 Transconductor Array

Not only are common-centroid arrays that follow the rules of Section 4.3.1.1 used to implement each set of matched transistors within the unit transconductor layout, but within each stage, the unit cells themselves can be arranged in such a fashion so as to minimize those gradients with long correlation distance.

The transconductors come in four flavors, tabulated in Table 5.6. Versions A and B each contain one half of the CMFB amplifier corresponding to Figure 5.41(a) and Figure 5.41(b), respectively. Along with version C, which need not have any CMFB circuitry as long as there is one A cell and one B cell connected to the same opamp input, these exhibit the default value  $G_{\text{mo}} = 5\ \mu\text{S}$ . The fourth variety only appears in Stage 3, where Table 5.2 indicates that  $G_{\text{mo}} = 2.5\ \mu\text{S}$  is required (cf. Footnote 18).

Denoting each unit cell with the number of the aggregate transconductor it implements (see Table 5.2) and the version letter of its layout (see Table 5.6), Figure 5.49, Figure 5.50 and Figure 5.51 present block diagrams of each stage featuring its dense, achiral common-centroid transconductor array. In addition, these indicate the placement of: the stage-specific  $I_{\text{B}}$  and  $I_{\text{E}}$  reference generators described in Section 5.6.1.1, denoted GR1 and GR2, which each contain copies of the on-chip regulator; the opamps A1 and A2, denoted OP1 and OP2; the stage-specific  $I_{\text{O}}$  reference generators for the opamps, denoted OR1 and OR2, which also contain buffers for the digital signal C[0:1]; and the capacitor arrays exemplified by

Properties				Instances per stage		
ID	CMFB?	$G_{\text{mo}}^{\text{a}}$ [ $\mu\text{S}$ ]	$R_{\text{g}}$ [ $\text{k}\Omega$ ]	Stage 1 [#]	Stage 2 [#]	Stage 3 [#]
A	Yes	5	200	2	2	2
B	Yes	5	200	2	2	2
C	No	5	200	2	4	3
D	No	2.5	400	0	0	1

<sup>a</sup> Unit value of  $G_{\text{mo}} = 5\mu\text{S}$  for Mode B is assumed.

Table 5.6: Layout variations of unit transconductor cell. CMFB circuitry is only present in flavors A and B, one of which must consequently be present in each integrator.

Figure 5.48.

## 5.6.2 Radiation Tolerance

The techniques described in Section 4.3.2 in the context of mitigating transistor-level TDEs and SEEs in the layout of the LNA are germane to and pervasive throughout the AAF layout as well. In particular, frequent guard rings and substrate-tap rings isolate the common-centroid arrays representing each set of matched transistors from one another. However, the presence of nMOS switches in the core of the transconductor to affect bandwidth programming introduces a heretofore unresolved sensitivity to the  $I_{\text{L}}$  effects described in Section 2.1.1.3. A widely known MOS layout geometry that confers immunity to TID-induced leakage, the enclosed-terminal device, is described in Section 5.6.2.1, whereas Section 5.6.2.2 examines additional steps aimed at mitigating ASETs.

### 5.6.2.1 Switch Leakage

As noted in Section 2.1.1.3,  $I_{\text{fox}}$  is predominantly responsible for the increased  $I_{\text{L}}$  exhibited by MOSFETs under total-dose irradiation. Since, in a standard layout, FOXFET current flows between the source and drain near the edge shown in

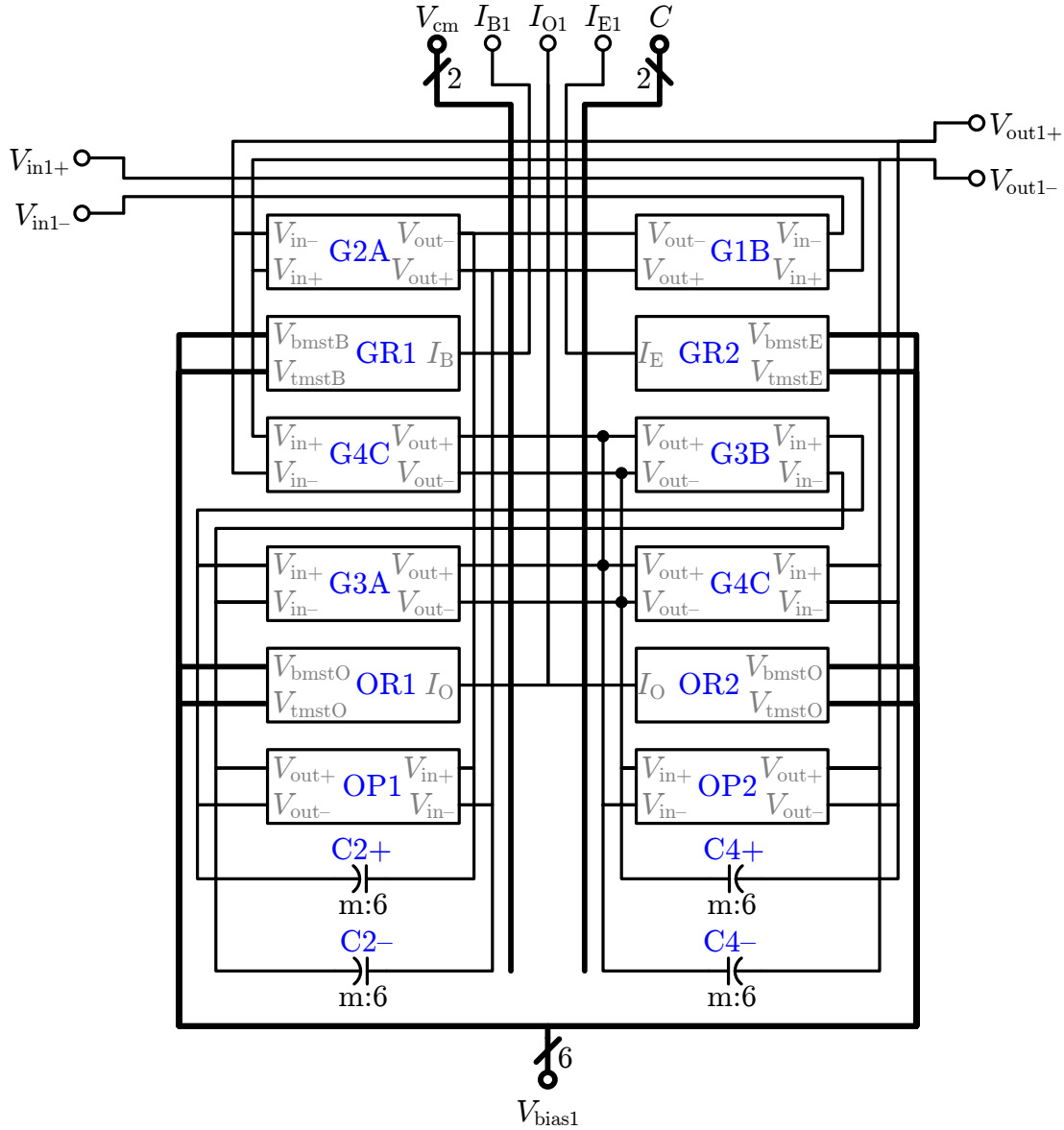


Figure 5.49: Block diagram of Stage 1 layout that implements Figure 5.13(b) architecture with unit-cell elements whose multiplicities are given in Table 5.2. For clarity: local bias voltages derived from  $I_{O,B,E}$ —namely  $V_{bmstO,B,E}$  and  $V_{tmstO,B,E}$ —are grouped into a single bus ( $V_{bias1}$ ), as are  $V_{cm1}$  and  $V_{cm2}$  ( $V_{cm}$ ); and signals internal to the stage, including those of CMFB amplifier and voltage regulator, are omitted.

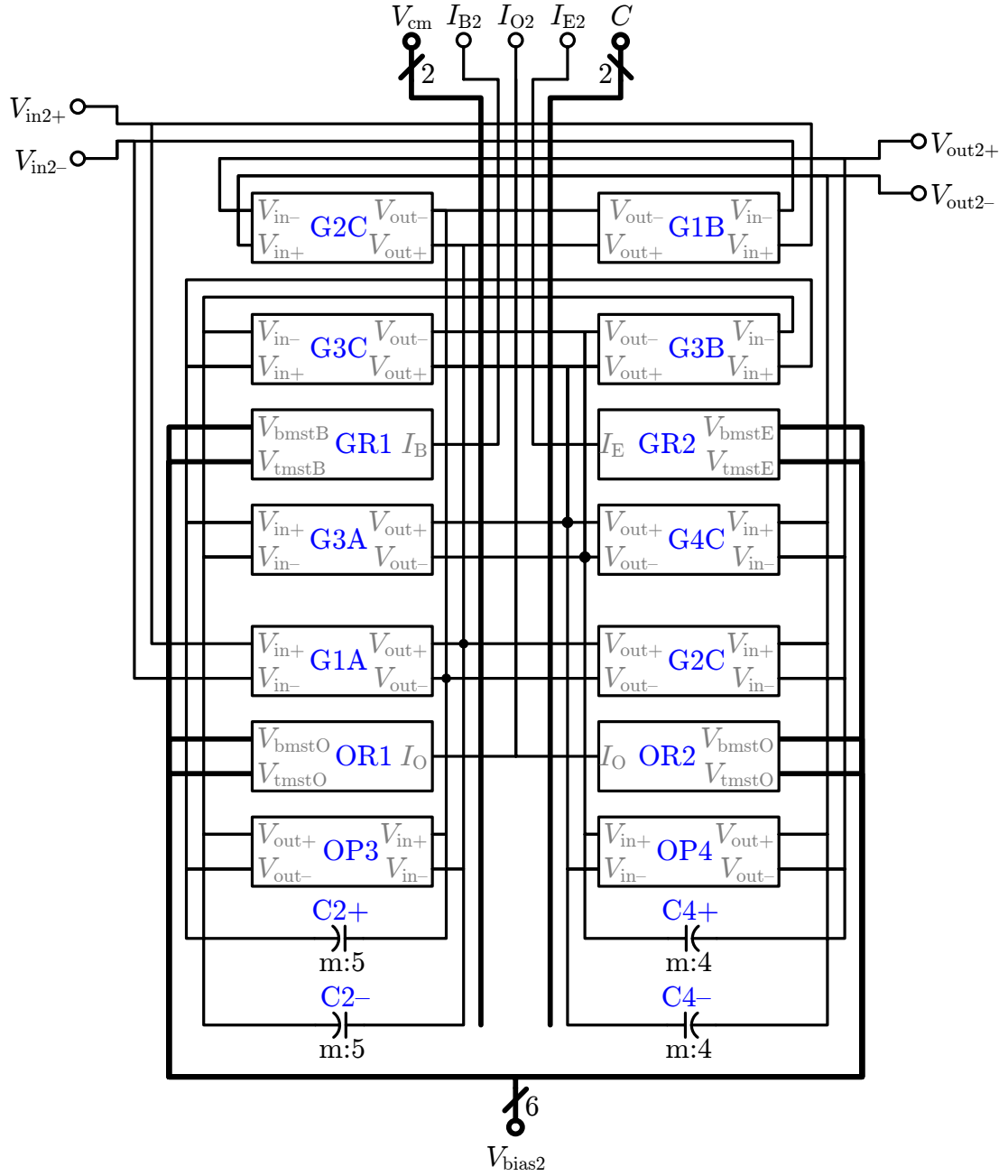


Figure 5.50: Block diagram of Stage 2 layout that implements Figure 5.13(b) architecture with unit-cell elements whose multiplicities are given in Table 5.2. For clarity: local bias voltages derived from  $I_{O,B,E}$ —namely  $V_{\text{bmst}O,B,E}$  and  $V_{\text{tmst}O,B,E}$ —are grouped into a single bus ( $V_{\text{bias}2}$ ), as are  $V_{\text{cm}1}$  and  $V_{\text{cm}2}$  ( $V_{\text{cm}}$ ); and signals internal to the stage, including those of CMFB amplifier and voltage regulator, are omitted.

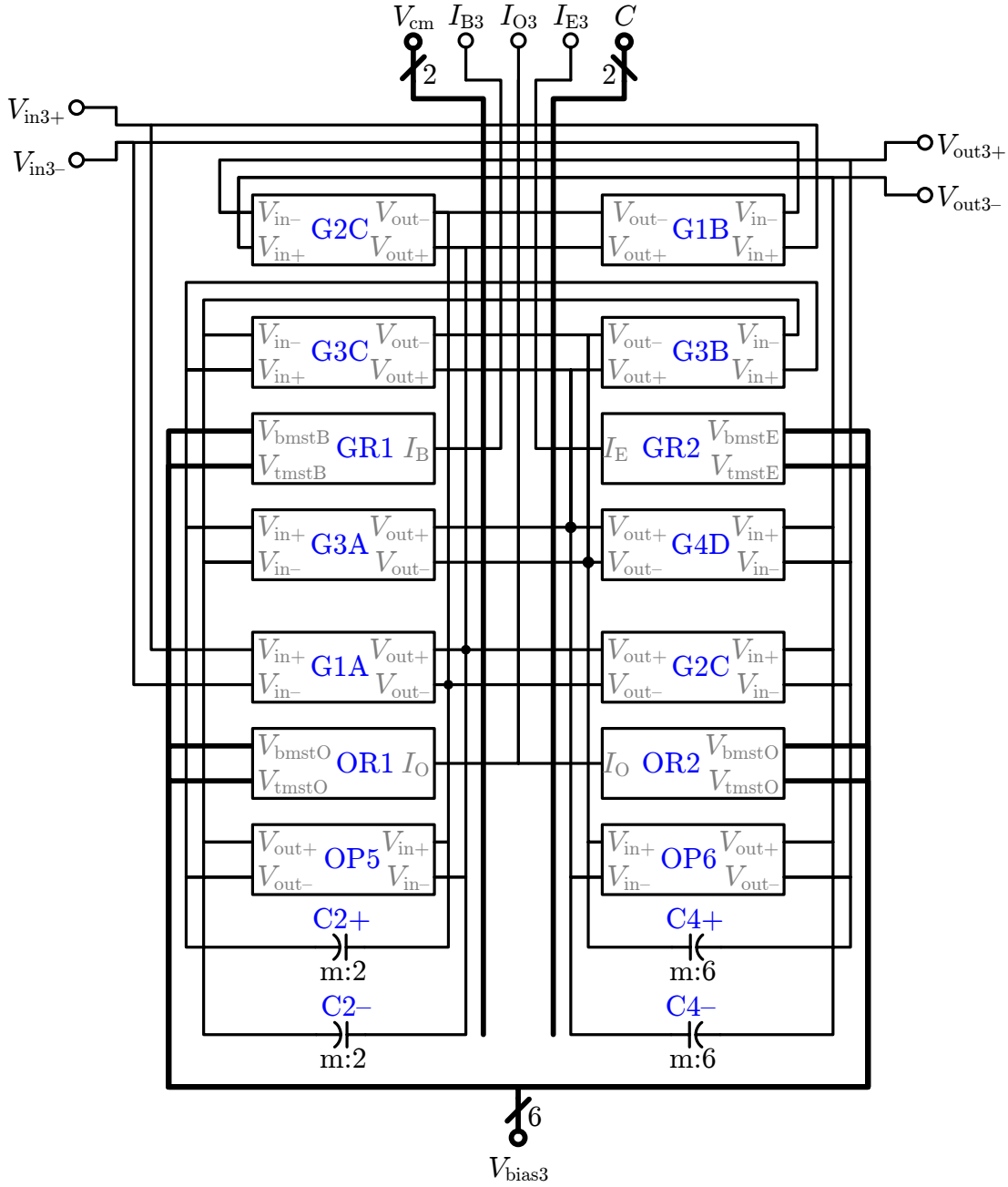


Figure 5.51: Block diagram of Stage 3 layout that implements Figure 5.13(b) architecture with unit-cell elements whose multiplicities are given in Table 5.2. For clarity: local bias voltages derived from  $I_{O,B,E}$ —namely  $V_{bmstO,B,E}$  and  $V_{tmstO,B,E}$ —are grouped into a single bus ( $V_{bias3}$ ), as are  $V_{cm1}$  and  $V_{cm2}$  ( $V_{cm}$ ); and signals internal to the stage, including those of CMFB amplifier and voltage regulator, are omitted.

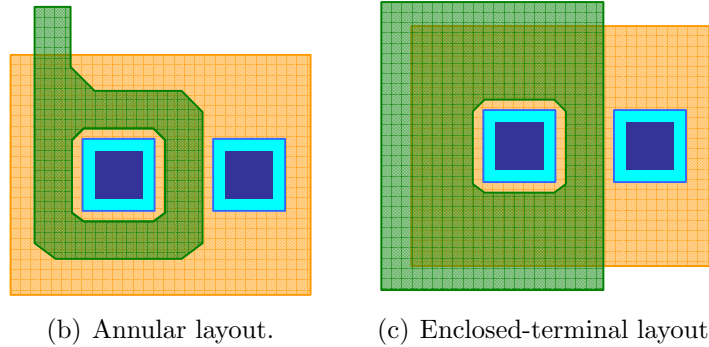
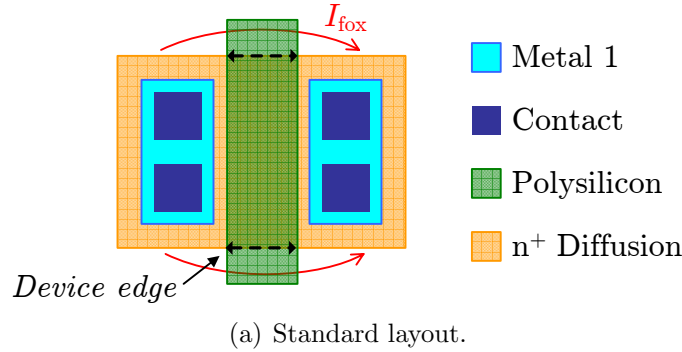


Figure 5.52: Examples of low-leakage nMOS transistor layouts. As compared to (a) the standard layout, both the (b) annular and (c) enclosed-terminal variations mitigate the flow of  $I_{fox}$  along the device edge by interposing thin gate oxide along all such paths. After [Wang, 2009, p.199].

Figure 5.52(a), where the thin oxide beneath the polysilicon gate abuts the field-oxide of the isolation structure (be it LOCOS, STI, etc.),<sup>39</sup> the literature is rich with alternative transistor layouts that doctor this edge to varying degrees [Alexander, 1996; Anelli, 2000; Giraldo, 1998; Nowlin et al., 2004].

**Annular Layout:** Of oldest lineage,<sup>40</sup> the axially symmetric nMOS layout in

<sup>39</sup>In LOCOS technologies, a distinction is often made between  $I_{edge}$ , which flows in the 'edge' transistor adjacent to the main device and is defined by the non-uniform region of field oxide in the bird's beak, and  $I_{fox}$ , which flows in parallel but through the FOXFET further from the main device where the field oxide thickness is maximum [Lacoe, 2003, p.64–65]. For compatibility with the trench isolation schemes of BiCMOS8 (cf. Section 2.1.1.3), this discussion merges the two currents into  $I_{fox}$ , defined as any current flowing beneath field oxide adjacent to the main device. Of course, most of  $I_{fox}$  flows along the device edge.

<sup>40</sup>Applications for annular transistors predate the interest in radiation-hardened electronics, arising from a desire to increase MOS speeds by reducing drain (output) capacitance,  $C_{gd}$ , which

Figure 5.52(b), known alternately as an annular, re-entrant, closed-geometry, or enclosed-layout transistor (ELT) [Lacoe, 2003, p.79], eliminates the problematic edge altogether, ensuring that no field oxide abuts the gate [Snoeyys *et al.*, 2002]. However, at this extreme of leakage suppression there are extreme costs,<sup>41</sup> in that the annular geometry: incurs a substantial area penalty [Lacoe, 2003, p.80], owing to restrictions on its minimum size in order to satisfy design rules [Anelli, 2000, p.105]; presents an extremely asymmetric channel conductance depending on whether the source or drain terminal is enclosed [Anelli *et al.*, 1999, p.1693]; encounters a fundamental mismatch limit unobserved in standard layouts, even for arbitrarily large sizing [Anelli *et al.*, 1999, p.113–132]; and exhibits larger net  $C_g$  and  $C_{sb}$  than a standard layout [Alexander, 1996, p.18].

**Enclosed-Terminal Layout:** A more recently developed geometry [Nowlin *et al.*, 2004], the enclosed-terminal layout shown in Figure 5.52(c), departs much less wildly from the standard in Figure 5.52(a). Ringing a single terminal of the basic nMOS,<sup>42</sup> it does not completely eliminate the edge, but ensures that any current flowing through it must first pass under the thin gate oxide. As noted in Section 2.1.1.3, this oxide accumulates much less  $\Delta N_{ot}$  than the field oxides, so the flow of  $I_{fox}$  is be choked down to the level of  $I_{sub}$ . Insofar as the latter is small, the net drain-to-source leakage can be reduced by several orders of magnitude [Nowlin *et al.*, 2005, p.2498]. Compared to the annular device, this leakage suppression is attended by fewer nonidealities since the enclosed-structure, more closely resembling a standard two-edged layout, is: less asymmetric, accompanied by less parasitic capacitance, and more easily

---

is often Miller multiplied (cf. Section 5.5.3.2). Since this capacitance arises along the perimeter of the polysilicon gate and drain diffusion, and since the circle has the smallest perimeter-to-area of any two-dimensional geometry, the annular transistor offers the lowest  $C_{gd}$ -per-unit-width of any structure. The speed improvement is not without drawbacks, as  $C_{gs}$  increases substantially [Hastings, 2006, p.462–463].

<sup>41</sup>At the opposing extreme, and not considered here, is the so-called dog-bone geometry [Alexander, 1996, p.18]. Least intrusive in terms of modifying the behavior of the main transistor, this approach simply widens the polysilicon overhang to increase(decrease) the effective length(strength) of the FOXFET gate, which reduces, but does not completely eliminate,  $I_{fox}$ .

<sup>42</sup>In many applications, including digital logic, the nMOS source terminal is grounded so it can more readily accommodate the increased capacitance associated with being ringing in polysilicon.



modeled.<sup>43</sup>

For these reasons, each of the nMOS switches in the GGC adopt the enclosed-source layout of Figure 5.52(c). The dissertation of Wang [2009, p.198–204], who constructed the devices used in this work, provides a brief but insightful review of the specifics of the enclosed geometry. Of note for conforming to sound and well-established design practices are the use of minimum polysilicon dimensions required for manufacturability and the chamfering of the corners along the inner perimeter of the gate, since sharp elbows can intensify the local electric field, degrading reliability [Hastings, 2006, p.462]. Generating results nearly identical to those of [Nowlin *et al.*, 2005, p.2498], which are reproduced in Figure 5.53 for reference, Wang [2009] has conducted radiation testing of representative samples up to 2 Mrad(Si) and validated that the  $I_L$  of these enclosed-source nMOS devices is nearly six orders of magnitude lower than those adopting the standard BiCMOS layout.

### 5.6.2.2 SEE Prevention

The presence of both nMOS and pMOS transistors in the blocks of the AAF are cause for SEL concern. Thus, in addition to the gain-spoiling guard rings and frequent substrate tapping employed in the LNA, the AAF layout also enforces large separations between banks of the two MOS flavors. In fact, the area penalties that accompany the linearized transconductor design are a boon to this cause—with each unit transconductor occupying approximately  $300\ \mu\text{m} \times 300\ \mu\text{m}$  there is ample room to separate the MOSFET arrays so as to increase(decrease) the effective  $W_b(\beta)$  of the parasitic bipolars in Figure 2.28.

**SPDT Switching:** Likewise, the AAF extends the ASET precautions of the LNA beyond the SET-tolerant common-centroid arrays of Figure 4.30 (which remain a

---

<sup>43</sup>The ease of modeling is critically important when abnormal layout geometries are employed, since the models provided to the circuit designer by the foundry only apply to transistors drawn in standard fashion [Wang, 2009, p.199]. Although models for the effective  $W/L$  of both the annular [Giraldo, 1998] and enclosed-terminal [Nowlin *et al.*, 2005] variations have been developed, each requires empirical fitting parameters. Through judicious placement, all non-standard device layouts are confined to the common-mode path so as to alleviate the impact of such modeling uncertainties on the performance of the front-end.

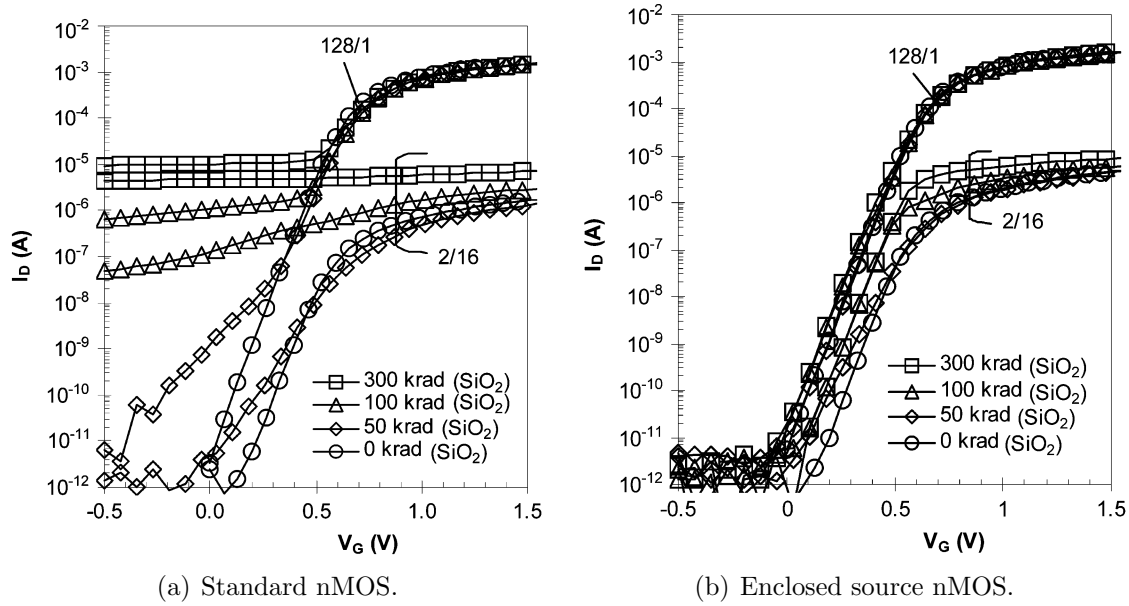
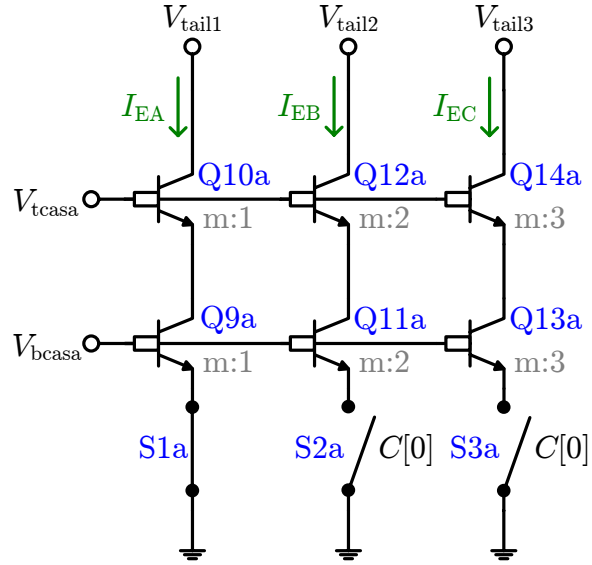


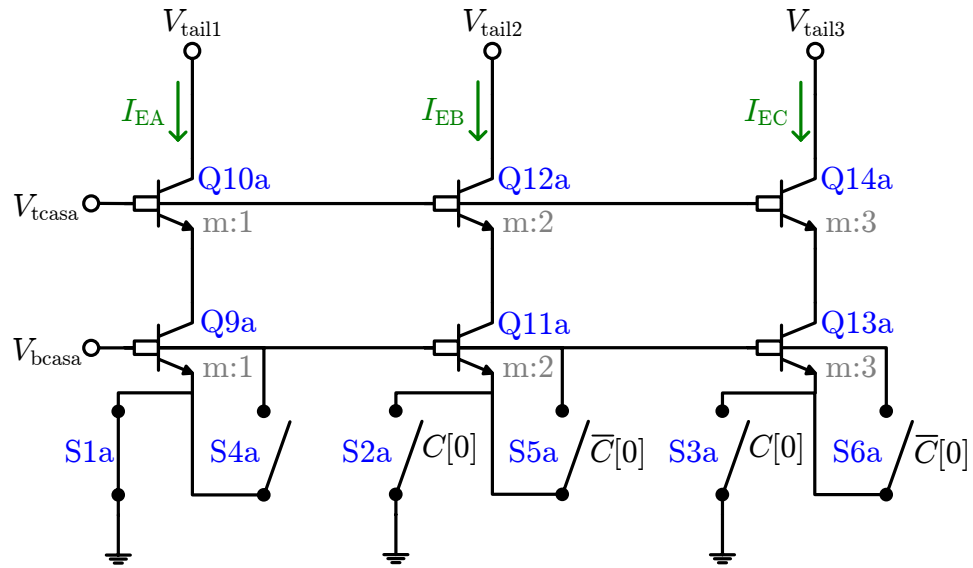
Figure 5.53: Measured leakage suppression of enclosed-source nMOS. For both large (128/1) and small (2/16) devices, the  $I_D$ - $V_{GS}$  curves reveal six orders of magnitude more  $I_L$  at 300 krad(Si) for (a) standard nMOS layouts than (b) their enclosed-source counterparts. Reproduced *in toto* from [Nowlin *et al.*, 2005, p.2498].

fixture in the signal path layout) to account for the presence of digital switches. Contrasting the switch configurations of Figure 5.54, the use of a single nMOS switch in Figure 5.54(a) to disconnect one branch of the GGC  $I_E$  current source leaves the emitter of Q11a or Q13a floating. Floating nodes, which possess no DC return path, can accumulate enough charge from an ion track that their associated junctions temporarily activate, drawing unwanted current and glitching the shared bias line. To limit ASETs, it is imperative that, regardless of the bandwidth mode, no floating node are permitted within the transconductor.

Thus, both the nMOS switches in the GGC and the pMOS switches in the CMFB and its loads, are constructed as complementary pairs, like that of Figure 5.54(b). By ensuring that every switched node is driven by a low-impedance source both when active and inactive, this technique amounts to using single-pole, double-throw (SPDT) switches in all instances.



(a) SPST switching.



(b) SPDT switching.

Figure 5.54: GGC ground-interrupt switching strategies. As opposed to (a) the SPST switching of the simplified schematic in Figure 5.36, the actual GGC employs (b) the SPDT switching implemented in Figure 5.37 to suppress ASET sensitivity. Final sizing of npn tail current sources for  $I_{EA}$ ,  $I_{EB}$ , and  $I_{EC}$  is shown.

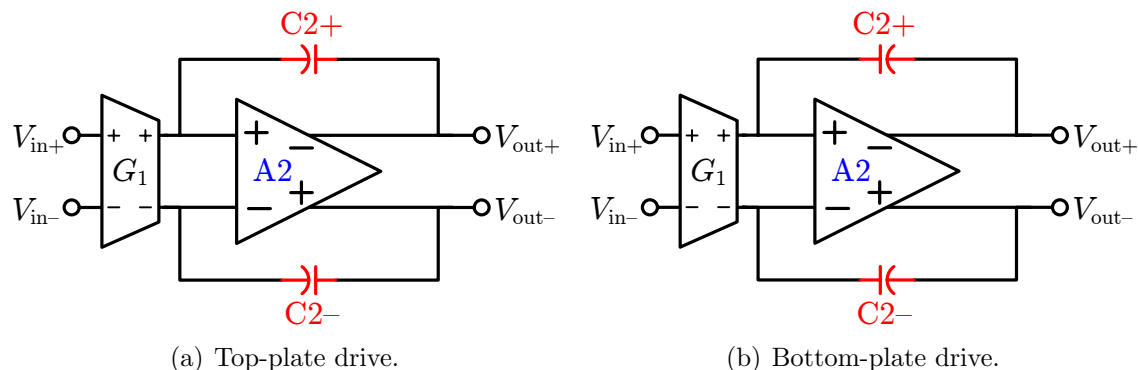


Figure 5.55:  $G_m$ -C-opamp capacitor drive strategies. Although (a) top-plate drive improves closed-loop bandwidth, (b) bottom-plate drive benefits stability SEE robustness.

**Bottom-Plate Drive:** The assiduous pruning of floating nodes extends to the orientation of the feedback capacitors in each integrator. On account of the polysilicon and n-well shielding at work, each metal comb capacitor possesses a relatively large bottom plate parasitic ( $\sim 40\%$  of the nominal parallel-plate capacitance). Examining the two possible capacitor orientations in the simplified  $G_m$ -C-Opamp integrators of Figure 5.55, it is clear that the bottom-plate node in Figure 5.55(a) sees only high impedance return paths, including the output(input) impedance of the transconductor(opamp) and the feedback capacitor itself.

The opposite case, shown in Figure 5.55(b), whose attendant stability benefits are well known to most analog designers [Graeme, 1997, p.21–28], offers improved ASET performance as well. Driving the bottom-plate capacitance with the low opamp output impedance is a superior means of limiting charge collection and, by extension, the potential for undesirable transients at that node.

# Chapter 6

## Measured Results

To confirm that the architectural, design, and layout techniques of Chapter 4 and Chapter 5, shown to satisfy those target metrics amenable to full-chip simulation, achieve all specifications of Table 3.2 in the final silicon, the LNA and AAF aboard the fabricated SVEPRE ASIC are subject to an array of performance measurements. Both for experiments conducted in the absence of radiation, which evaluate baseline performance of the part, and those performed during or after irradiation, which assess its radiation susceptibility, the LNA and AAF are characterized individually, in keeping with the segmentation of the aforementioned chapters.<sup>1</sup> In fact, their development schedules dictated that the appraisal of the LNA and AAF be temporally disjoint as well. As such, all LNA(AAF) data presented in this chapter are obtained from SVEPRE-1(SVEPRE-3) die,<sup>2</sup> and though both circuits reside on every die,<sup>3</sup> the post-irradiation performance of each section of the chip is characterized for a subset of the full suite of radiation sources in the interest of time.

Prior to the analysis of these data, Section 6.1 briefly catalogs the equipment

---

<sup>1</sup>Since the LNA and AAF share the same die, this isolation is obviously incomplete. However, the presence of distinct input, output, and supply pins allows their signal paths to be decoupled and the elements individually powered, restricting their interaction to the shared silicon substrate and common bias voltages.

<sup>2</sup>Refer to Section 3.2.1 and Table 3.3 for a complete inventory of the SVEPRE versions, including their manufacturing schedules, fabrication shuttles, and constituents.

<sup>3</sup>Whereas the AAF approximation and pole locations evolved from SVEPRE-1 to SVEPRE-3 (cf. Footnote 9 of Chapter 5), the design of the LNA is identical.

utilized for their acquisition in both the baseline and radiation environments.<sup>4</sup> Section 6.2 then offers an extensive review of the common experimental procedures and configurations from which both baseline and radiation measurements were obtained; to promote accord between the data sets where possible, differences between their experimental setups are assiduously minimized,<sup>5</sup> thereby justifying their preemptory discussion. The background of these sections then informs the organization, presentation, and interpretation of the baseline(radiation) results summarized in Section 6.3(Section 6.4). Finally, Section 6.5 encapsulates the results of reliability tests conducted on the lot of SVEPRE-3 parts qualified for flight.

## 6.1 Experimental Setup

A complex, configurable, and highly automated experimental setup is necessary to accurately quantify the high-fidelity operation of the SVEPRE constituents to the precision of the specifications in Table 3.2 across the full range of programmable modes and radiation conditions. This section examines the elements of a custom setup developed in this vein, decomposing them as follows: in the course of testing, a given version of SVEPRE, denoted as the device-under-test (DUT) and detailed in Section 6.1.1, is housed by one of the three custom PCBs described in Section 6.1.2, which interfaces with selected instrumentation from amongst the litany in Section 6.1.3.

### 6.1.1 Devices Under Test

To track the instances of SVEPRE throughout testing, each of the individual SVEPRE-1 and SVEPRE-3 die are serialized, as are the ultimate DUTs into which they are packaged.<sup>6</sup> Since both the die layouts and DUT packaging are performance

---

<sup>4</sup>Properties of terrestrial radiation sources peculiar to the latter category of test environment, with emphasis on those offered at facilities visited for this research, are covered in Appendix I and Appendix J.

<sup>5</sup>Configurational customizations unique to radiation testing appear in Section 6.4.

<sup>6</sup>Die serial numbers—only used internally—are specific to each of the die identifiers in Table 3.3, whereas the set of serial numbers assigned to each part, such as those of SVEPRE-3 tracked during

critical, features that impact the forthcoming results are addressed in Section 6.1.1.1 and Section 6.1.1.2, respectively, with an emphasis on those of SVEPRE-3, the final version intended for flight.

#### 6.1.1.1 Die Layout

A lot of 60 SVEPRE-3 die were generously fabricated by National Semiconductor Corporation in their BiCMOS8B+ SiGe manufacturing process through their University Collaboration Program. The CMOS side is equivalent to a 0.25- $\mu\text{m}$ , 1P5M,<sup>7</sup> single-well technology, constructed on a non-epitaxial substrate and using shallow-trenches for interdevice isolation (cf. Section 2.1.1.3). The npn BJTs, whose bases are 0.25  $\mu\text{m}$  wide and doped using sacrificial emitters, are isolated using deep polysilicon trenches (cf. Section 2.1.2.2). Additional process details are documented in Section 3.2.1.

Figure 6.1 provides a photomicrograph of the fabricated SVEPRE-3 chip, measuring 3.16 mm by 3.19 mm. Although the total chip area is 10.1 mm<sup>2</sup>, much of that is allocated to the mandated pad frame,<sup>8</sup> so that the active area is only 5.5 mm<sup>2</sup>, of which the AAF, occupying 5.375 mm<sup>2</sup>, consumes the majority. The stacks of unit transconductors (297  $\mu\text{m}$  x 286  $\mu\text{m}$ ), opamps (297  $\mu\text{m}$  x 187  $\mu\text{m}$ ), and unit capacitors (248  $\mu\text{m}$  x 35  $\mu\text{m}$ ) within each of its stages, which are sequentially arrayed side-by-side, align so as to facilitate wiring and ensure that each group incurs common die stresses and gradients. With two less unit transconductors necessary in Stage 1 (cf. Table 5.6), the area available in the upper left-hand corner of the die is more than sufficient to accommodate the LNA, which consumes just 0.125 mm<sup>2</sup>. By keeping the LNA as close as possible to corresponding I/O and bias pads in that corner, this placement minimizes the distance traveled by sensitive LNA signals, improving its

---

burn-in testing and enumerated in Table K.7, are used to uniquely distinguish DUTs.

<sup>7</sup>Although Metal 5 is the top metal, pad stacks include an additional layer of so-called bump metal which is unpassivated to permit bonding. The remainder of bump metal in the layout serves only as metal fill to satisfy coverage rules and is not electrically connected.

<sup>8</sup>To qualify for fabrication, layouts must satisfy the manufacturer's design rules for latchup prevention that dictate the minimum spacing between I/O circuitry (whose junctions directly contact the pad frame) and core circuitry, so as to prevent transients from triggering latchup in the latter. As a consequence, a wide moat of metal-fill snakes is observed encircling the core of Figure 6.1 and swelling the total die area.



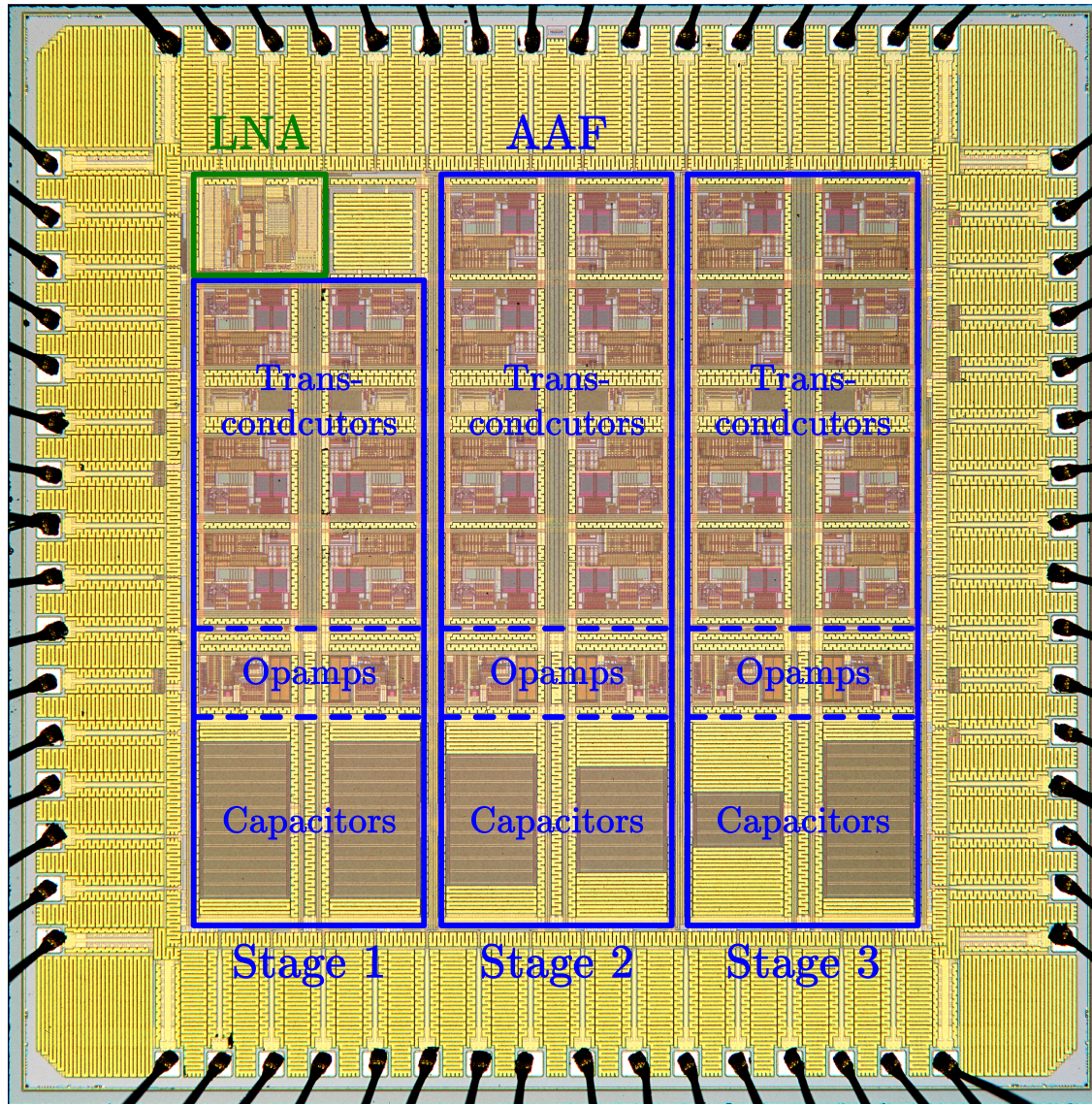


Figure 6.1: Photomicrograph of fabricated SVEPRE-3 chip, including bond wire connections. Locations of the LNA(AAF) components are highlighted in green(blue). Actual dimensions: 3.16 mm by 3.19 mm.



input impedance and noise performance.<sup>9</sup>

As in the ring that separates the core from the pad frame (cf. Footnote 8) and in many smaller regions throughout the core, the fallow area to the right of the LNA is populated with metal, polysilicon, and diffusion fill structures in order to satisfy coverage rules that ensure the planarity of density-dependent polishing steps responsible for dielectric layer thicknesses [*Hastings*, 2006, p.521]. All told, the active regions of the remainder of the die contain approximately 3100 MOSFETs, 1325 vn timer BJT, 45 substrate pn timer, 4400 resistors, and 2600 capacitors.<sup>10</sup>

### 6.1.1.2 Packaging

For characterization, the SVEPRE die are bonded into ceramic, 68-pin, J-leaded chip carriers (J-LDCC) whose pin counts accommodate valuable test points in addition to the primary signals required for operation. The standard pinout for this package is provided in Figure 6.2, where the naming conventions of preceding schematics (particularly, Figure 5.45) are augmented with use of prefixes ‘L’, ‘A’, and ‘E’ to denote the signals associated with the LNA, AAF,<sup>11</sup> and ESD circuitry, and ‘C’ for the package cavity.<sup>12</sup> Note the multiplicity of supply and ground pins, whose symmetric arrangement properly terminates the on-chip power grids so as to minimize their resistance, thereby improving headroom, chip reliability, and latchup tolerance. To prevent large, noisy AAF return currents from corrupting the LNA, all returns of the latter use a separate metalization (LGND) which only connects to that of the AAF (AGND) at a single point on the board (by way of a lone via to the ground plane).

Although the accompanying gold-plated Kovar lids feature a solder-compatible

---

<sup>9</sup>For both the LNA and AAF, the parasitics of differential connections to the pads are balanced by imposing equal path lengths for the positive and negative lines as well as shielding each pair with neighboring ground lines in the same metal layers.

<sup>10</sup>For the passive components, each of the individual unit elements in the array corresponding to a single logical instance is tallied separately; hence, compared to the active devices, their counts are deceptively large.

<sup>11</sup>The numeric suffixes of input and output signals without prefixes correspond to the indices of the opamps at the heart of the filter stages in Figure 5.49 through Figure 5.51. These signals are used for debugging purposes only.

<sup>12</sup>The connections to the package cavity are required to safely ground the chip substrate. See Footnote 14 for further details.

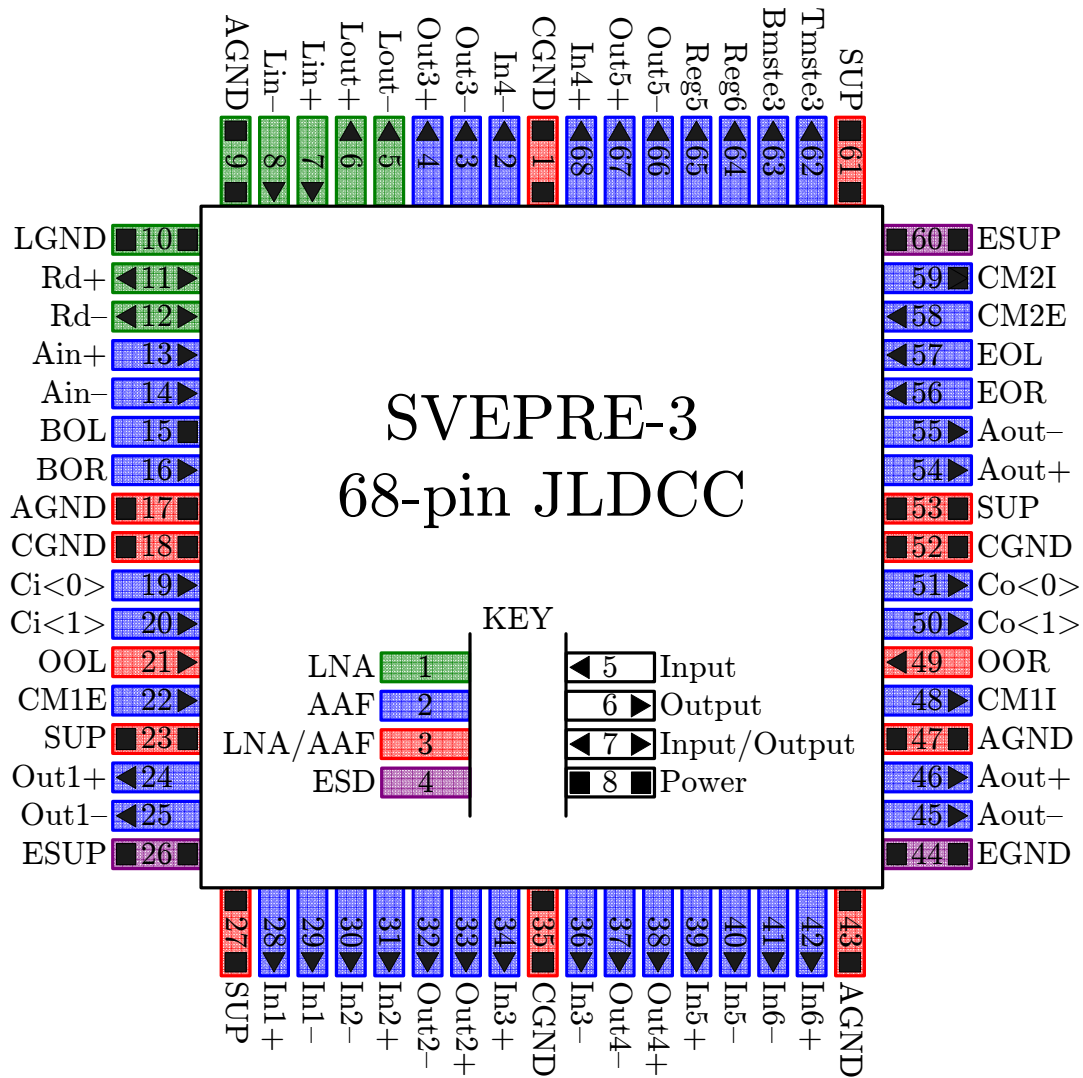


Figure 6.2: Full pinout of SVEPRE in 68-pin JLDCC package. Static signals identified in all capital letters. Indexed input and output pins refer to AAF integrator opamps.

Package				Dimensions					Parts
Type		Pins		Package			Cavity		Used
Style	Material	Qty.	Pitch	Wid.	Len.	Hght.	Wid.	Len.	Qty.
SOIC	Ceramic	28	0.050	0.293	0.705	0.057	0.170	0.283	13
J-LDCC	Ceramic	44	0.050	0.650	0.650	0.065	0.250	0.250	42
J-LDCC	Ceramic	68	0.050	0.950	0.950	0.080	0.400	0.400	4

Table 6.1: Flight packaging options for SVEPRE-3 and complete parts inventory (as of 04 December 2009). All dimensions in inches unless otherwise noted.

seal-ring, permitting these packages to be hermetically sealed for flight, the DUT lids are impermanently affixed such that they can be removed during radiation testing, eliminating undesired backscatter. In the same vein, a through-hole zero insertion force (ZIF) socket with a matching cut-out in its spring-loaded clamshell lid is employed on the characterization and radiation bias boards (cf. Section 6.1.2) to facilitate the repeated installation (and removal) of these surface-mount parts with minimal stress to the components and board but without impeding an applied radiation beam, when present.<sup>13</sup>

Since many of the signals in Figure 6.2 are purely for debugging purposes, it proves desirable to employ more compact packaging for the SVEPRE flight units, saving valuable PCB real estate on the instrument. For the missions outlined in Chapter 7.2, SVEPRE-3 has been made available in an array of ceramic package sizes, with as few as 28 pins. Although the corresponding pinout diagrams are omitted, Table 6.1 summarizes their dimensions. In all cases, the die are affixed to the gold-plated cavity of the package with conductive (usually, silver load) epoxy,<sup>14</sup> and bonded to its lead

<sup>13</sup>The integrity of the mating between the package leads and socket contacts requires the use of 40-mil thick nylon 6,6 shim, since the socket is designed for a plastic (PLCC) package. Despite its discoloration and loss of tensile strength when exposed to TID radiation [*Holmes-Siedle and Adams, 2002*, p.374–375], this thin, low-Z shim does not materially enhance the dose received by the underlying die.

<sup>14</sup>This electrical connection to the silicon substrate demands that the cavity floor be firmly driven to ground potential in order to limit noise coupling and the potential for latchup. For this reason, the pinout of Figure 6.2 features four dedicated cavity ground pins (CGND). Internal to the package, these are bonded directly to the cavity floor and, externally, should via directly to the PCB ground plane.

frame using 1- $\mu$ m diameter gold wire. For the 68-pin package, the maximum bond wire length is less than 4 mm.<sup>15</sup>

### 6.1.2 Circuit Boards

All out-of-beam measurements of DUT performance are conducted via a PCB custom designed so as to be easily configured in support of each of the first four test benches in Section 6.2. From amongst the complexities inherent in accurately measuring the full suite of the associated metrics over the range of DUT programming modes, the key features of this characterization board are emphasized in Section 6.1.2.1. Separate and decidedly simpler PCBs house one or more DUTs whilst they are irradiated and baked, with Section 6.1.2.2 and Section 6.1.2.3 describing the adaptations of these boards that ensure proper bias is maintained in the radiation and burn-in environments, respectively. Unless otherwise noted, all the SVEPRE PCBs consist of FR4 dielectric stacked between copper traces (1-oz weight) with a minimum pitch and width of 8 mils.

#### 6.1.2.1 Characterization Board

A block diagram of the characterization PCB is pictured in Figure 6.3. Measuring 8 inches wide by 13.8 inches long (and 0.062 inches thick), it uses four routing layers, the inner two of which are poured as split ground and power planes to isolate the noise of the digital and analog supply domains while providing low impedance paths to each supply source and shielding the top and bottom routing layers from one another at the expense of additional trace capacitances. Although provisions exist for joining the analog (GndA) and digital (GndC) ground planes (cf. Figure 6.3) near the perimeter of the board,<sup>16</sup> this option was never enabled, as it injects clock noise

---

<sup>15</sup>The pad pitch of the SVEPRE die is set by the tolerances of the bonding equipment, which require at least 150  $\mu$ m; thus, the pads of Figure 6.1 are 3-mil square with 3-mil spacing.

<sup>16</sup>Ideally, the single-point ground for the entire board is provided by the bench chassis from(to) which all the test equipment is powered(grounded). In that case, joining GndA and GndC creates a ground loop that includes the master power supply and clock generator (among other instruments), each of which provides a connection to Earth ground via the outer conductor of its SMA cable, which is tied to its chassis internally. However, a jumper between the shield of each on-board SMA

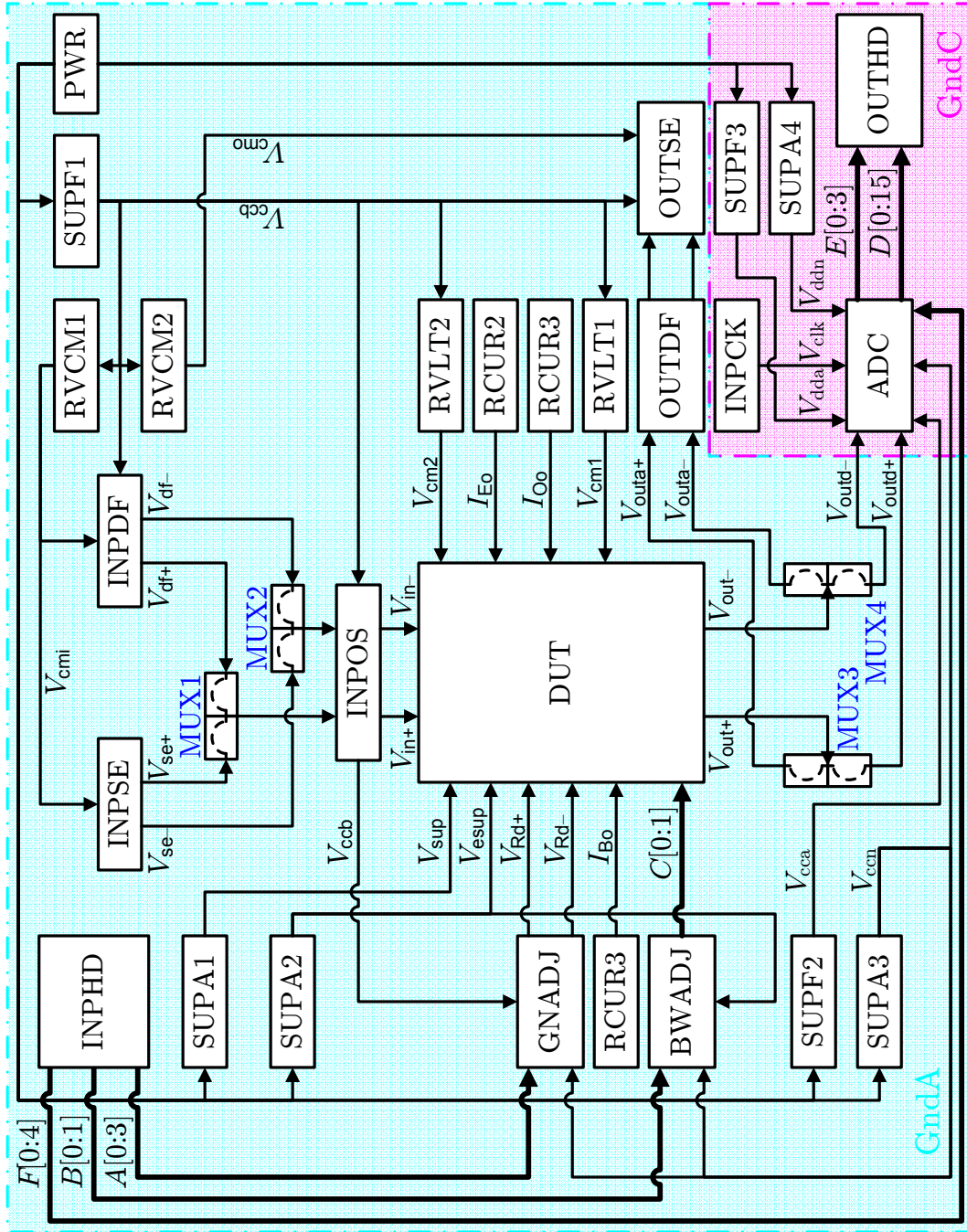


Figure 6.3: Block diagram of characterization PCB. Extent of analog(digital) ground plane, GndA(GndC), is shown in light blue(purple).

into the sensitive analog circuitry.

Highly configurable, the characterization PCB architecture allows many aspects of the DUT itself, as well as its interfaces with the instrumentation of Section 6.1.3, to be adapted during testing. For each of the blocks, design features germane to this configurability are detailed in Appendix H.

### 6.1.2.2 Radiation Bias Board

As indicated by the bias dependences of Section 2.1.1 and Section 2.1.2, the applicability of terrestrial radiation testing to in-flight performance is dubious unless the part is biased during the former exactly as during its planned operation. This requires that the DUT be mounted in a radiation bias PCB that can exercise its functionality during the tests.<sup>17</sup> Although for many sources, the radiation beam is relatively narrow,<sup>18</sup> the entire PCB upon which the DUT is mounted during irradiation is subject to some exposure. Thus, it is good practice to preclude the radiation bias PCB from containing any active components whose radiation response may be conflated with that of the DUT.<sup>19</sup>

To that end, the radiation bias PCB is simply a version of the characterization PCB assembled only from passive components and the minimum number at that.<sup>20</sup> In particular, it presumes the availability of bench-top power supplies that can provide

---

connector and the appropriate ground plane (implied if not pictured hereafter) permits the former to be left floating relative to the board, making it possible to avoid this loop when the planes are joined.

<sup>17</sup>The level of operation depends on the type of testing. As discussed in Section 6.2.5.3, the part need only process signals during SEE tests; static bias is sufficient for TID testing.

<sup>18</sup>For example, as described in Section I.2.1, the LBNL proton beam measures just 2.5 inches in diameter.

<sup>19</sup>Theoretically, qualified components whose radiation hardness exceeds the expected test levels should not pose any complication. But, in practice, such parts are often very expensive and their transient responses are rarely reported (cf. Section 2.3.2.2). Meanwhile, COTS components can easily fail at even low dose levels [Johnston, 1998, p.1345–1348]. Eliminating all active elements is a more affordable and robust approach.

<sup>20</sup>For LNA <sup>60</sup>Co TID testing, an alternate bias PCB was designed and assembled by Mark A. Turpin of The Aerospace Corporation. Supporting the simultaneous exposure of up to nine DUTs, each with its own open-frame, lateral-force, thru-hole socket, it features similar passive signal conditioning but, unlike the characterization PCB, is designed to fit snugly within the Pb-Al box used to prevent backscatter in the Aerospace <sup>60</sup>Co chamber (cf. Section I.1.1.3).

+10 V, +2.5 V, +1 V, and +1.75 V thru the external connectors of PWR, SUPA, RVLT, and RVCM, respectively. As such, only the passive filters in the paths of each (as described in Section H.2) are populated. Similarly, gain and bandwidth control are performed by analog potentiometers and the input signal is processed through the passive signal path of either Figure H.2(a) or Figure H.3.

### 6.1.2.3 Burn-In Bias Board

Requirements for the PCB on which the SVEPRE DUTs are housed during burn-in testing (cf. Appendix K) are similar to those for radiation testing,<sup>21</sup> with the ease of omitting an input signal balanced by the complication that the entire lot must be baked simultaneously. Thus, Bob Bumala of Lockheed Martin Corporation designed a variation of the radiation bias PCB with lateral-force sockets for 50 parts, each deriving its voltage(current) references from a global(local) resistor network. To prevent the failure of any instance from affecting the rest, individual connections to the master input common-mode reference and power supplies are each ‘fused’ with 10- $\Omega$ , 0.1-W series resistor. In the event of a malfunction that shorts one of these connections to ground, the resistor would melt, creating an open circuit and sparing the remaining devices any damage.

### 6.1.3 Instrumentation

The complete collection of instruments required for the testing described in this chapter,<sup>22</sup> and their connectivity to the characterization PCB, is diagrammed in Figure 6.4.<sup>23</sup> Instrument control and data acquisition are managed by a Windows

---

<sup>21</sup>Just as COTS active components can fail under radiation (cf. Footnote 19), many are not rated to tolerate the temperatures of the burn-in cycle described in Section K.2.1. Plus, rather than illuminating only the DUT with a narrow beam, the entire PCB is placed in the thermal chamber; so, the DUT and all ancillary components experience the same thermal stress. Given these failure risks, active parts are not tolerated on the burn-in bias PCB.

<sup>22</sup>The lone exception is the use of a Textronix TDS3054B(LeCroy WP960XL) digitizing oscilloscope in place of the PC NIDAQ card during heavy-ion(pulsed-laser) SEE testing, as depicted in Figure 6.12(b).

<sup>23</sup>For clarity, MUX1–MUX4 of Figure 6.3 are represented as a DPDT switches, as are the DUT selection switches within the DUT block.

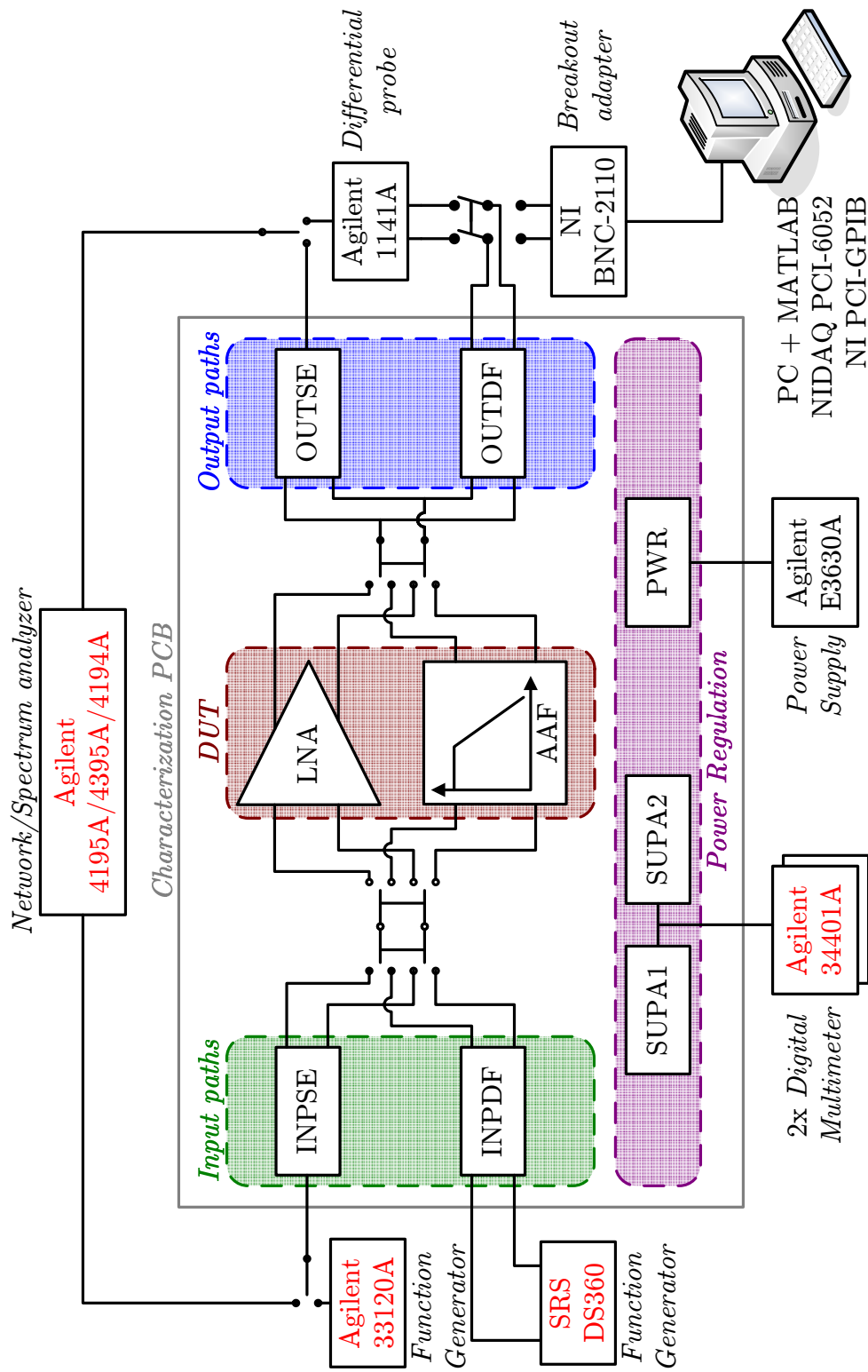


Figure 6.4: Block diagram of instrument connectivity for characterization PCB. Instruments shown in red are automated via GPIB. Switches are merely conceptual; on-board multiplexing is performed via headers.



PC outfitted with a National Instruments PCI GPIB controller card and a 333 kS/s, 16-bit data acquisition card (National Instruments PCI-6052E)—hereafter, NIDAQ card—to carry out these respective tasks. Automation and coordination of these events, as well as all data analysis, is delegated to a hierarchy of custom scripts running under version 7.0.4 of the MATLAB environment.<sup>24</sup> As for the hardware, since the instrument settings and signal routing options depend upon the metric under examination, such configurations are documented alongside the corresponding test bench in Section 6.2.

## 6.2 Test Benches

The choice of DUT, PCB, and test equipment, together with the configuration of each and the requisite piece of custom acquisition-and-analysis code to conduct the experiment itself, constitutes a test bench, the five of which outlined in this section are sufficient to evaluate all the specifications of interest during both baseline and radiation testing. In addition to the state of the setup—both the connectivity of the instrumentation and the configuration of all hardware options<sup>25</sup>—each test bench defines a set of experimental procedures for measuring the associated metrics. These steps are largely automated by a bench-specific MATLAB application decomposed into two modules: one, configured via a graphical user interface (GUI), is responsible for real-time data acquisition;<sup>26</sup> the second is run offline via the interactive command line interface to post-process and analyze these data.<sup>27</sup> Both the acquisition and analysis modules are parameterized by version-controlled configuration files and generate extensive run logs to ensure thorough documentation of the test bench

---

<sup>24</sup>In addition to assuring repeatability and minimizing the prospects for operator error, the automation of the test bench is critical given the time constraints imposed on TID and SEE radiation testing by the annealing criteria dictated in *MIL-STD-883G* [2006] and the limited availability of beam time (cf. Section 6.4.1).

<sup>25</sup>Within this section, headings identifying the elements of each test bench use shorthand denoting the former as *instrumentation* and the latter as *configuration*.

<sup>26</sup>This task requires installation of the following MATLAB options: Data Acquisition Toolbox (DQT), version 2.5.1 and Instrument Control Toolbox (ICT), version 2.2.

<sup>27</sup>These tasks require installation of the following MATLAB options: Signal Processing Toolbox (SPT), version 6.2.1 and Curve Fitting Toolbox (CFT) Toolbox, version 1.1.2.

settings and procedures, respectively, for future reference. These facets of the test benches are summarized below as a prelude to the presentation of the corresponding measurements in the remainder of the chapter.

## 6.2.1 Frequency Response

The operation of the frequency response (FR) test bench, which evaluates the gain and bandwidth of the LNA(AAF) in each of its programming modes using the instrument configuration of Figure 6.5(a)(Figure 6.5(b)), is described by the following settings and procedures.

### 6.2.1.1 Instrumentation

An Agilent 4395A(4194A) network/spectrum analyzer(gain/phase analyzer) acquires the frequency response of the LNA(AAF).<sup>28</sup> Featuring only single-ended 50  $\Omega$  ports, it dictates the configuration of the input and output paths shown in Figure 6.5(a) and Figure 6.5(b). Within INPSE, the active path of Figure H.2(b) is employed since achieving frequency-independent termination is paramount over linearity for this test. This choice also prevents the low-frequency roll-off of X1 in INPDF from corrupting the Bode plots.

Ideally, both the LNA and AAF would utilize OUTSE to perform the differential-to-single-ended conversation required by the network analyzer. However, when AC-coupled(DC-coupled) to the LNA, even with C3–C5 of Figure H.5(a) omitted, the effective input capacitance(common-mode input range) of A1 and the traces leading to it exceed the drive capability(output common-mode range) of the LNA, which is designed for the high input impedance(1.75-V  $V_{\text{cmi}}$ ) of the AAF.<sup>29</sup> Thus, the

---

<sup>28</sup>During LNA TID testing, a 4195A was used in place of the 4395A employed for baseline measurements since only the former was available at the testing facilities. The differences between the two are irrelevant to this work; both require an Agilent 87512A transmission/reflection test set to for power splitting. However, due to a catastrophic failure of the RF source in the 4395A after the completion of the LNA measurements, the transition to an available 4194A was adopted for all AAF characterization. Although primarily used for impedance (especially  $C$ - $V$ ) measurements, its standard measurement unit is capable of reporting the  $S$ -parameters sought.

<sup>29</sup>The common-mode range incompatibilities can be resolved, and DC-coupling of the LNA to OUTSE employed, if A1 is powered off standard  $\pm 5$ -V rails. However, the  $-5$ -V supply was excised

distinction between the measurement configuration of the LNA in Figure 6.5(a) and that of the AAF in Figure 6.5(b): the former depicts the use of a high-impedance differential probe (Agilent 1141A) with a differential input capacitance of just 7 pF to sense the LNA output right at the socket.<sup>30</sup>

Prior to each set of DUT frequency response measurements, two calibration procedures are applied using the setup in Figure 6.6. First, a full two-port calibration of the network analyzer is performed with the standards from a 50-Ω N-type Agilent 87512A calibration kit. Secondly, as depicted in Figure 6.6, the DUT is placed in bypass mode (cf. Section H.1.1) so that the frequency response of the channel sans SVEPRE can be acquired. Since both the DUT and the output termination, be it the Agilent 1141A (in Figure 6.6(a)) or OUTSE (in Figure 6.6(b)), present a high impedance to INPSE, the loading of the latter in bypass mode is comparable to that during DUT measurements. Thus, the calibration data acquired in this step capture effects related to all circuitry in the signal path except the DUT itself, which are then de-embedded from the final results in the procedure of Section 6.2.1.4.

### 6.2.1.2 Configuration

For input coupling, the FR test bench uses the single-ended-to-differential conversion of the active INSPE path in Figure H.2(b), with the output of the network analyzer coupled via J1 (J2 is floating). The shields of both connectors are grounded. The output of the LNA is sensed by OUTDF, in which only polystyrene capacitors C2, C4, and C6 are populated (cf. Figure H.5(a)). The output of the AAF is AC-coupled to OUTSE via C1 and C2 of Figure H.5(b) by configuring MUX1–MUX4 accordingly. The network analyzer settings for each of the AAF modes (A, B and C) and the LNA (which is hereafter given a default identifier of Mode D), are shown in Table 6.2.

---

from the prototype PCB design for expediency.

<sup>30</sup>Not shown in Figure 6.5(a) is the Agilent 1142A probe supply required to operate the Agilent 1141A. Besides providing control and power, its 50-Ω output impedance is specifically designed to match that of the Agilent 419XA test port, rendering its presence, though not depicted, mandatory.

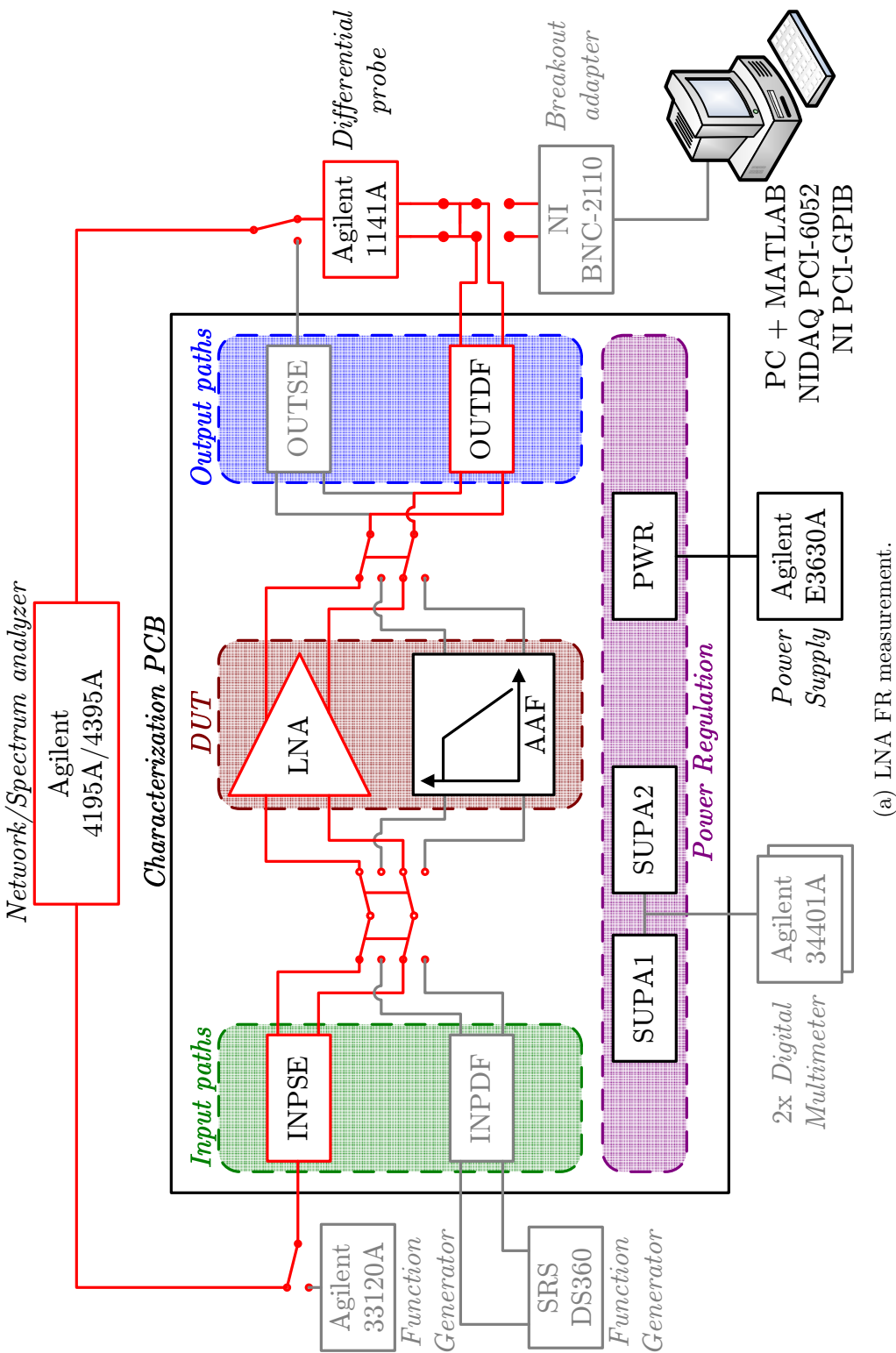


Figure 6.5: (a) Block diagram of instrument connectivity for frequency response measurements of LNA. Required elements on(off) the signal path are highlighted in (red)(black). Active INPSE path in use.

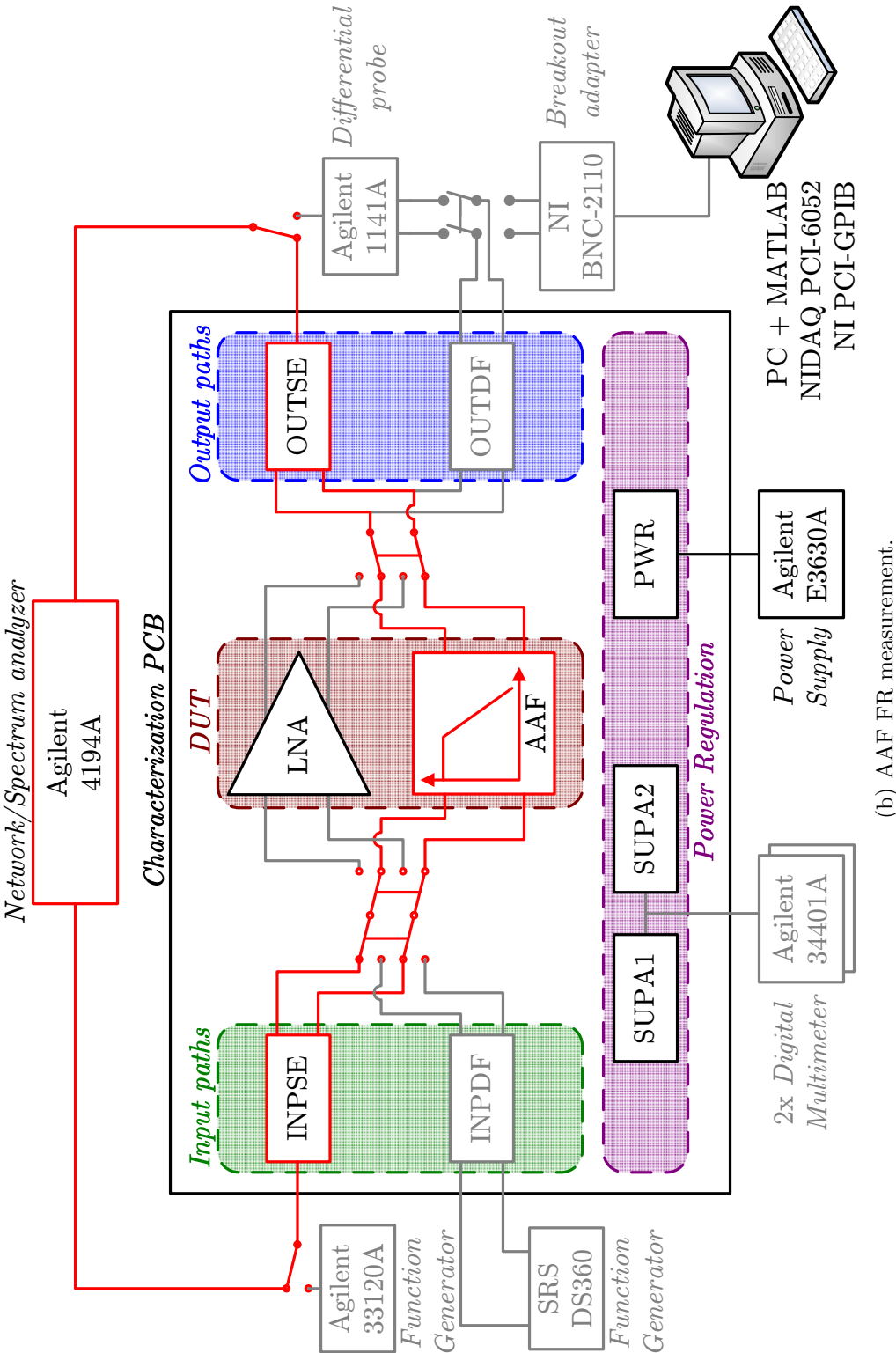


Figure 6.5: (b) Block diagram of instrument connectivity for frequency response measurements of AAF. Required elements on(off) the signal path are highlighted in (red)(black). Active INPSE path in use.

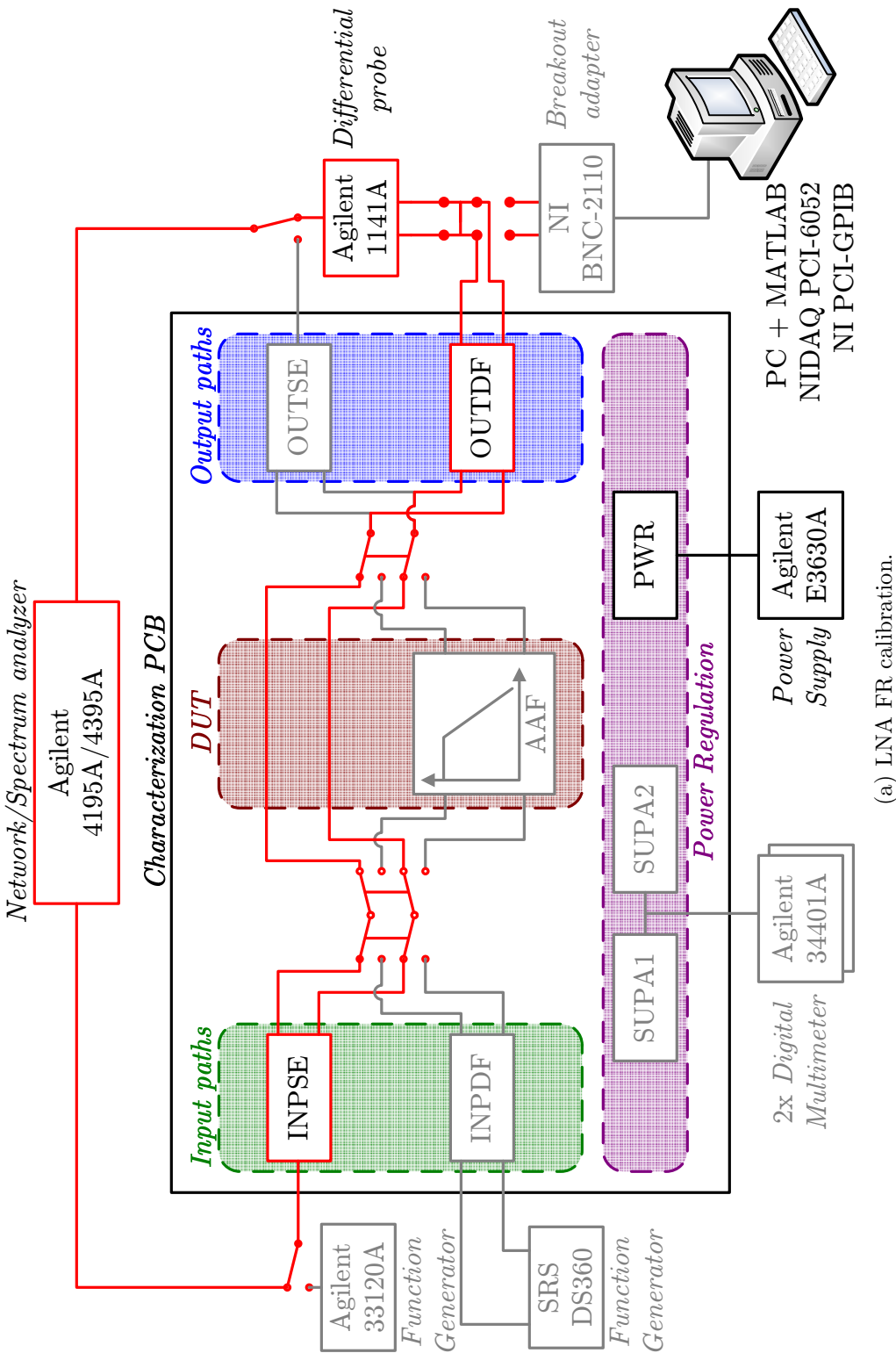


Figure 6.6: (a) Block diagram of instrument connectivity for frequency response calibration of LNA. Required elements on(off) the signal path are highlighted in (red)(black). Active INPSE path in use.

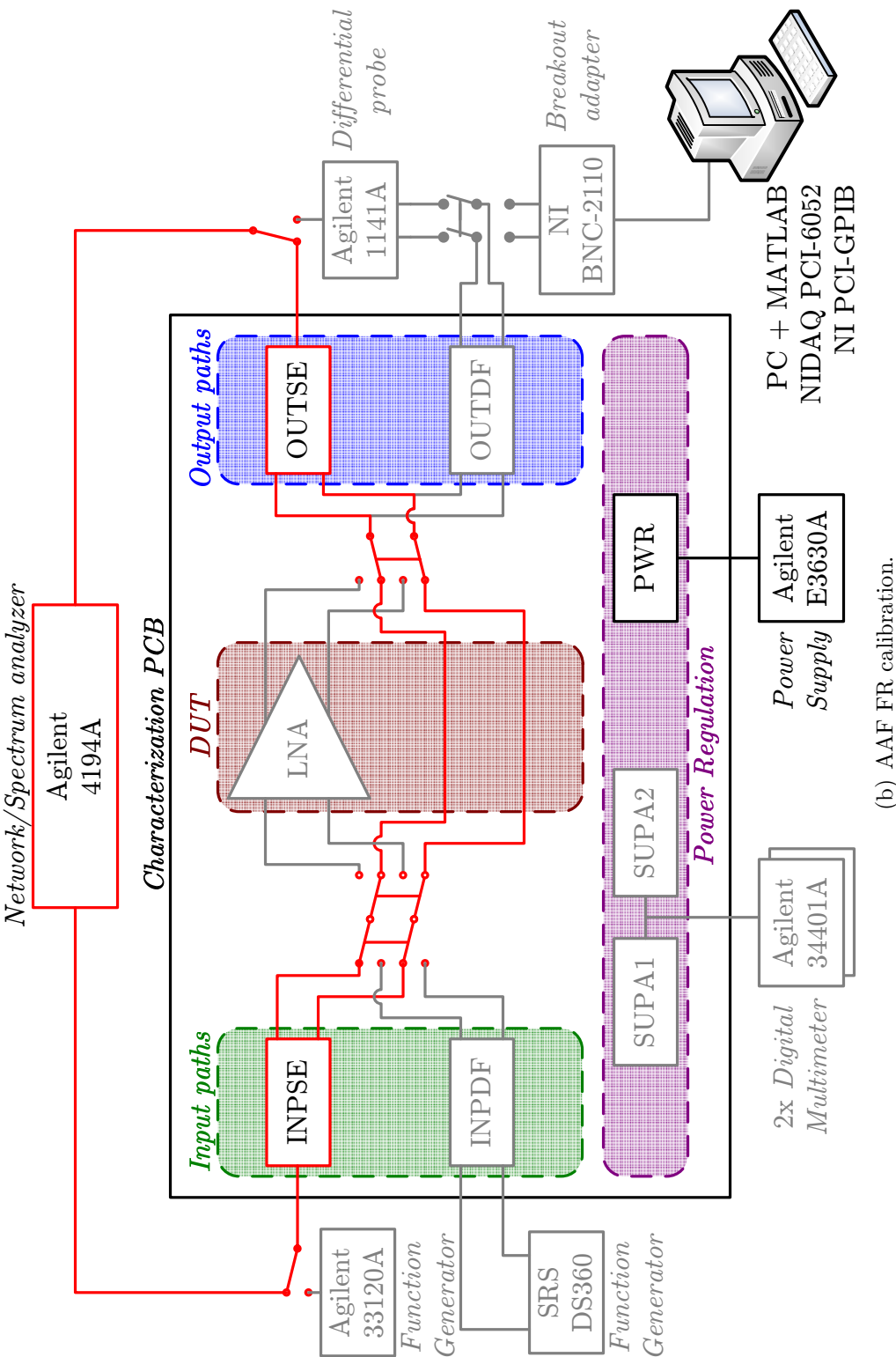


Figure 6.6: (b) Block diagram of instrument connectivity for frequency response calibration of AAF. Required elements on(off) the signal path are highlighted in (red)(black). Active INPSE path in use.

DUT settings		Agilent 419XA settings					
Device	Mode	$f_{\text{start}}^{\text{a}}$ [Hz]	$f_{\text{stop}}^{\text{a}}$ [kHz]	$P_{\text{RF}}^{\text{b}}$ [dBm]	IF BW <sup>c</sup> [Hz]	Avg. <sup>c</sup> [#]	Time <sup>d</sup> [sec]
AAF	A	100	100	-10	200	2	24
	B	100	600	-10	200	2	24
	C	100	4000	-10	200	2	24
LNA	D	100	10000	-10	200	2	24

<sup>a</sup> Linear, 401-point sweep performed over each decade of range ( $f_{\text{stop}}/f_{\text{start}}$ )

<sup>b</sup> Power delivered at RF port does not account for 11.6 dB insertion loss to 50- $\Omega$  test port of Agilent 87512A transmission/reflection test set

<sup>c</sup> Reduced IF bandwidth and multiple-acquisition averaging attenuate noise

<sup>d</sup> Aggregate sweep time over all decades, including averaging

Table 6.2: Network analyzer settings for FR test bench. Variation between Agilent models listed in Figure 6.4 is negligible.

### 6.2.1.3 Acquisition

Following two-port calibration, the DUT bypass mode is enabled and the MATLAB acquisition module acquires the calibration data set via the network analyzer (cf. Figure 6.6). These steps are conducted once for the LNA, but repeated for each AAF bandwidth mode, since their acquisition bandwidths vary. The resulting transfer functions, derived from the complex  $S_{21}$  parameter and denoted  $T_{\text{cal}}^{\text{A}}(s)$ ,  $T_{\text{cal}}^{\text{B}}(s)$ , and  $T_{\text{cal}}^{\text{C}}(s)$  for the three AAF modes, and  $T_{\text{cal}}^{\text{D}}(s)$  for the LNA, are gathered at the outset of each experiment. Subsequently, multiple measurements of each DUT are performed by routing the signal path through either the LNA—yielding  $T_{\text{meas}}^{\text{D}}(s)$ —or the AAF—yielding mode-specific  $T_{\text{meas}}^{\text{A}}(s)$ ,  $T_{\text{meas}}^{\text{B}}(s)$ , and  $T_{\text{meas}}^{\text{C}}(s)$ .

Since the memory depth of the network analyzer limits a single sweep to only 401 frequencies, resolution in the critical low-frequency regime is enhanced by conducting separate linear sweeps for each of the five decades of interest (between 100 Hz and 10 MHz) and stitching their samples together to arrive at each  $T_{\text{cal}}(s)$  and  $T_{\text{meas}}(s)$ , rather than covering the full bandwidth with a single logarithmic sweep.<sup>31</sup>

<sup>31</sup>Only transfer functions  $T^{\text{C}}(s)$  and  $T^{\text{D}}(s)$  cover the full five decades. Although they too begin at 100 Hz, the sweep extents for the lower bandwidth AAF modes, Mode A and Mode B, need only cover three and four decades, respectively, as shown in Table 6.2, resulting in shorter data records.



#### 6.2.1.4 Analysis

To isolate the response of the DUT, the PCB and other setup parasitics are de-embedded by taking the complex difference between each measured transfer function and the corresponding calibration transfer function as

$$T_{\text{dmbd}}(s) = T_{\text{meas}}(s) - T_{\text{cal}}(s) \quad (6.1)$$

Next, a 3-tap(15-tap) median filter is applied to  $|T_{\text{dmbd}}(s)|(\angle T_{\text{dmbd}}(s))$  to remove impulsive, single-sample(multi-sample) noise that can safely be attributed to extrinsic processes. Properties of  $T_{\text{dmbd}}(s)$ , such as  $G_p$ ,  $f_p$ , and  $r_\alpha$  are then computed during post-processing, rather than using the measurement functions of the network analyzer. In this way, the DC gain is estimated by the average value of  $|T_{\text{dmbd}}(s)|$  over the entire passband, rather than as one or an average of the noisy values near 100 Hz.

### 6.2.2 Linearity

The operation of the linearity (LN) test bench, which evaluates the SFDR of the DUT in each of its programming modes using the instrument configuration of Figure 6.7, is described by the following settings and procedures.

#### 6.2.2.1 Instrumentation

To measure the SFDR of the LNA or AAF, it is necessary to both generate a spectrally pure sinusoidal input tone and sample the time-domain output with sufficient linearity so that non-fundamental tones in the resulting spectrum are rightly attributed to the DUT. The former task is accomplished by an SRS DS360 ultra-low distortion function generator capable of producing a balanced sinusoid with typical THD below 100 dB for frequencies up to 40 kHz.<sup>32</sup> As described in Section 6.2.2.2, its output is processed through by a minimal set of devices in INPDF so as not degrade this performance.

---

<sup>32</sup>To generate input tones in excess of 50 kHz, the output of the less linear Agilent 33120A (limited to 45-dB SFDR above 100 kHz) is aggressively bandpass filtered to remove undesired harmonics. This strategy has proven successful in laboratory testing, but was not implemented as part of the SVEPRE characterization suite due to time restrictions imposed by the radiation schedule.

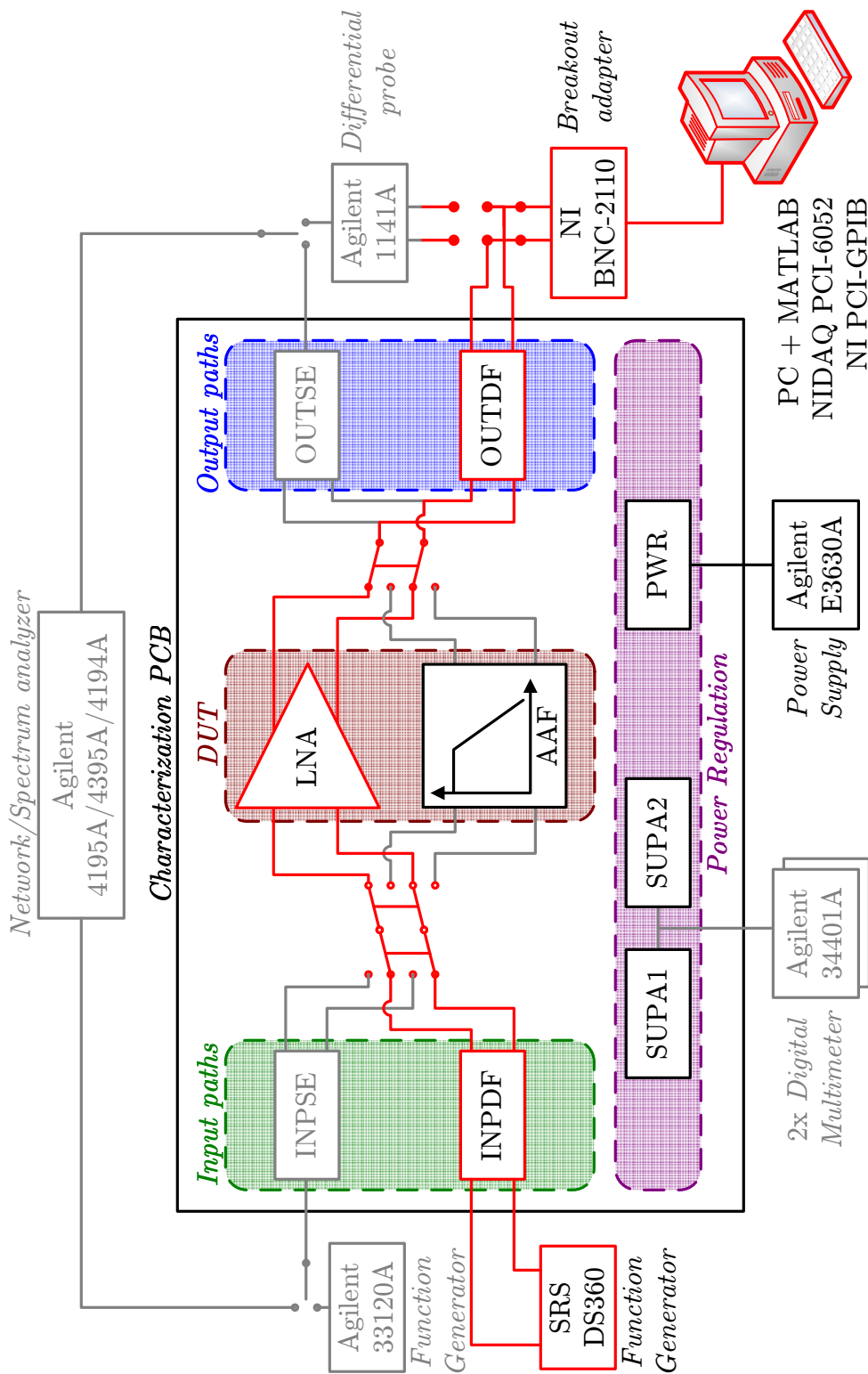


Figure 6.7: Block diagram of instrument connectivity for linearity measurements of LNA. Except for signal routing at DUT, instrument connectivity is identical for AAF. Required elements on(off) the signal path are highlighted in (red)(black).

For data acquisition, the 16-bit sampler of the NIDAQ card is configured for differential input and connected to OUTDF,<sup>33</sup> which is devoid of all passive load elements.<sup>34</sup> Custom, twisted-pair cables cleanly convey the signal from the PCB to the BNC-2110 breakout box, which provides BNC connections to each of the NIDAQ card input channels.<sup>35</sup> The resulting instrument connectivity is depicted in Figure 6.7 for the case of the LNA as DUT; arrangements for the AAF can be easily inferred (subject to the caveat of Footnote 33).

### 6.2.2.2 Configuration

The LN test bench directly couples the output of the SRS DS360 to INPDF path in Figure H.3 via J5 and J6, whose shields are driven to  $V_{\text{cmi}}$  by configuring MUX1 and MUX2 accordingly (i.e., to the right as drawn). With the LNA(AAF) as DUT, common-mode choke L1 on the shields of J5/J6 is bypassed(enabled) since the return currents are relatively small(large). In contrast, balun B1 is enabled(bypassed) during linearity testing since the LNA(AAF) is highly(less) sensitive to imbalances in the differential input noise and impedance. Finally, since the smaller(larger) input power levels used in LNA(AAF) testing render its even-order distortion more(less) sensitive to the absolute difference between R5 and R6,<sup>36</sup> these are each set to 25  $\Omega$ (150  $\Omega$ ) while the differential output impedance of the DS360 is programmed to 50  $\Omega$ (300  $\Omega$ ), preserving the proper impedance matching.<sup>37</sup> These INPDF customizations are

---

<sup>33</sup>The spectra presented in Section 6.3.3 are sampled with the NIDAQ card connected to the output of the first AAF stage (pins Out2+ and Out2– of Figure 6.2) for reasons described in that section.

<sup>34</sup>Between eliminating all resistors and capacitors in Figure H.5(a) and using the differential input capability of the NIDAQ card, extrinsic sources of imbalance (read even-order) distortion are minimized. Unfortunately, the BNC-2110 offers only a coaxial interface, so there remains some residual imbalance between the impedances on the inner (positive) and outer (negative) signal lines.

<sup>35</sup>Setting each analog input channel of the BNC-2110 to accept ground-referenced signals, even though the DUT outputs are referenced to a non-zero common-mode level, prevents these line from otherwise being unbalancing when their BNC shields are grounded through and  $RC$  load.

<sup>36</sup>The input offset current of the DUT is of commensurate—if not greater—importance. Since this quantity is approximately half as large for the LNA as for the AAF, whereas the difference in their input signal ranges is nominally a factor of five, its effect on the input-referred offset voltage, and hence even-order distortion, is also more pronounced for the LNA.

<sup>37</sup>Eliminating any uncertainty as to the amplitude of the input tone—as this parameter is critical to determining the maximum SFDR—R3 and R4 are replaced with 0- $\Omega$  resistors in the LN test

INPDF settings			DUT settings	
Element	Identifier	Units	LNA	AAF
SMA shield	MUX1/MUX2	V	$V_{\text{cmi}}$	$V_{\text{cmi}}$
CM choke	L1	n/a	Bypass	Enable
Balun	B1	n/a	Enable	Bypass
Filter-R GndA return	H5	n/a	Disable	Disable
Filter-C GndA return	H6	n/a	Enable	Enable
Series termination	R3/R4	$\Omega$	0	0
Parallel termination	R5/R6	$\Omega$	25	150

Table 6.3: INPDF settings for LN test bench. All instance identifiers refer to Figure H.3.

summarized in Table 6.3. In all cases, the current of the filter capacitors is returned to GndA via H6 so as to keep the  $V_{\text{cmi}}$  line clean.

The interface between the DUT output at OUTDF and the NIDAQ card in Figure 6.7 is bridged by a pair of custom hydra cables (cf. Section 6.2.2.1): one measuring the overall differential output and one, in the case of the AAF only, measuring the output of Stage 1.<sup>38</sup> These are sequentially sampled by adjacent NI PCI-6052E channels which minimizes cabling discrepancies at the expense of potential crosstalk. By properly grounding the BNC-2110 unit to GndA (via its AIGND terminal) and specifying a conservative inter-channel sample skew delay (as this is of little consequence to the spectral measurements), this crosstalk proves negligible.

### 6.2.2.3 Acquisition

To determine the maximum SFDR of the LNA(AAF) for a given fundamental frequency (cf. Section 3.1.2.1), the SRS DS360 issues a single tone whose differential amplitude is swept between 50 mV<sub>PP</sub>(40 mV<sub>PP</sub>) and 250 mV<sub>PP</sub>(1.2 V<sub>PP</sub>) in 100 mV steps. This amplitude sweep is then repeated for an array of fundamental frequencies between 1 kHz and 40 kHz. Only results for the 1 kHz, 5 kHz, and 10 kHz tones are presented herein, as their harmonics lie within the passband of both the LNA

bench, avoiding the 6-dB attenuation otherwise introduced by the R3–R6 voltage divider.

<sup>38</sup>As mentioned in Footnote 33, the need for this second connection is explained in Section 6.3.3.

and AAF in all programming modes.<sup>39</sup> For each point in the amplitude-frequency space of input tones so defined, each NIDAQ channel acquires ten seconds of data at a sampling rate of 100 kHz. The total acquisition time required to uniformly sample the two-dimensional input space in this fashion varies slightly with the processor and hard drive activity of the PC, but is approximately 3(4) minutes for each LNA(AAF) mode.

#### 6.2.2.4 Analysis

Spectral estimation techniques are applied to the finite, time-domain data from the LN test bench in order to infer the underlying PSD, from which the SFDR is measured as described in Section 3.1.2.1.<sup>40</sup> For the continuous-time signal  $z(t)$  (using the notation of Figure 3.7), the power density spectrum,  $S_{zz}(\omega)$ , is defined as the continuous-time Fourier transform (CTFT) of its autocorrelation,  $R_{zz}(t)$ , such that [Oppenheim et al., 1999, p.68–70]:

$$\begin{aligned} S_{zz}(\omega) &= \mathfrak{F}_{\text{CT}}\{R_{zz}(t)\} \\ &= \int_{-\infty}^{\infty} \left( \int_{-\infty}^{\infty} z(\tau) z(\tau - t) d\tau \right) e^{-j\omega t} dt = Z(j\omega) Z^*(j\omega) \quad (6.2) \\ &= |Z(j\omega)|^2 \end{aligned}$$

Once  $z(t)$  is sampled at a rate  $f_s = 1/T$  by the NIDAQ card, generating  $z[n]$ , the power density spectrum of the sequence,  $S_{zz}(\tilde{\omega})$ , is found by replacing the CTFT of

---

<sup>39</sup>The upper bound of low-frequency linearity testing is also severely constrained by the performance of both the SRS DS360 and the NI PCI-6052E. The former only maintains 100-dB THD for fundamental frequencies below 40 kHz, whereas the latter features a maximum sampling rate of 333 kS/s. These limitations collude such that the injection(capture) of undesired(relevant), extrinsic(intrinsic) distortion products is found to preclude accurate measurements for tones above 10 kHz.

As described in Section H.1.3 and Section H.3.3, the characterization PCB enables 100-kHz linearity testing through its input filtering options and the presence of an on-board ADC. However, the radiation schedule prevented the necessary reconfiguration and additional acquisition time required to carry out the high-frequency linearity testing (cf. Footnote 32).

<sup>40</sup>Spectral estimation is commonly employed in statistical signal processing for the purpose of estimating the power spectral density of a random signal from a finite sequence of time-domain samples [Oppenheim et al., 1999, p.730–731].

(6.2) with the DTFT of the autocorrelation sequence  $R_{zz}[n]$ , such that:<sup>41</sup>

$$S_{zz}(\tilde{\omega}) = \mathfrak{F}_{\text{DT}}\{R_{zz}[n]\} = \frac{1}{T} \left| Z\left(\frac{j\tilde{\omega}}{T}\right) \right|^2 \quad (6.3)$$

where, akin to Section F.1.3, here  $\tilde{\omega} = \omega T$  normalizes the continuous frequency variable  $\omega = 2\pi f$  to  $f_s$ . Thus, it is straightforward to arrive at  $S_{xx}(\omega)$  once  $S_{xx}(\tilde{\omega})$  is known, since the combination of (6.2) and (6.3) expresses the former in terms of the latter as:

$$S_{zz}(\omega) = T S_{zz}(\tilde{\omega})|_{\tilde{\omega}=\omega T} \quad (6.4)$$

However, the DTFT of  $R_{zz}[n]$  required to compute  $S_{zz}(\tilde{\omega})$  is not readily determined since: the  $N$ -point DFT of  $R_{zz}[n]$  performed in MATLAB only yields samples at frequencies  $\tilde{\omega} = 2\pi k/N$ ; and, rather than being infinite in extent like the continuous-time  $z(t)$  it represents,  $z[n]$  is finite, possessing only  $L$  samples and, in turn, its  $R_{zz}[n]$  has length  $2L-1$ . To infer the power density spectrum of the whole signal from just a finite subset  $L$  of its samples in  $z[n]$  necessarily introduces some error, especially for small  $L$ .<sup>42</sup> So, the goal of the spectral estimation is to generate an estimate of  $S_{zz}(\tilde{\omega})$  (and, indirectly through (6.4) an estimate of  $S_{zz}(\omega)$ ), denoted  $S'_{zz}(\tilde{\omega})$ .

Broadly speaking, all spectral estimators rely on an intermediate quantity derived from either the sequence  $z[n]$  or its DFT  $Z[k]$  that determines the accuracy of their  $S'_{zz}(\tilde{\omega})$ . This work employs estimators of the latter class whose frequency-domain methods trade computational efficiency for accuracy, which is tolerable given the relatively long sequences and high SNR of the data. Within this category, the methods

---

<sup>41</sup>Implicit in the derivation of (6.3) is the following relationship between the CTFT of a signal  $x(t)$  and the DTFT of the sequence  $x[n]$  formed by sampling it at  $f_s$ :

$$\mathfrak{F}_{\text{DT}}\{x[n]\}|_{\tilde{\omega}=\omega T} = \frac{1}{T} \mathfrak{F}_{\text{CT}}\{x(t)|_{t=nT}\}$$

The leading coefficient on the right-hand side results from the indicated change of variables.

<sup>42</sup>An inference of the properties of the underlying random process (e.g., its mean or variance) from those of a finite-length sampled segment (e.g., the sample mean or and sample variance) necessarily assumes the ergodicity of the former (e.g., mean-ergodic or mean-square ergodic) to allow this error to approach zero in the limit of  $L \rightarrow \infty$ . In such cases, it is also common, though by no means necessary, to presume the process is stationary, so that the convergent values are time-independent. Both assumptions are invoked here when pursuing of unbiased estimator in the presence of natural noise sources (cf. Footnote 45).

can further be subdivided as parametric or non-parametric. The former assumes  $z[n]$  results from a hypothetical, stationary, linear, time-invariant (LTI) process that can be described parametrically and then explicitly estimates the model parameters that can be used by the estimators to find the resulting  $S'_{zz}(\tilde{\omega})$ . Non-parametric methods, which assume no such model and instead derive an intermediate quantity directly from  $Z[k]$  that is operated upon by an estimator to arrive at  $S'_{xx}(\tilde{\omega})$ , suffice for this analysis.

The non-parametric spectral estimator most germane to the measurement of SFDR is a PSD estimator based on a Welch-averaged, modified periodogram.<sup>43</sup> Since the ordinary periodogram defined by [Schuster \[1898\]](#) for the N-point DFT,<sup>44</sup> as

$$Q_{zz}[\tilde{\omega}_k] = \frac{1}{L} |Z[k]|^2 \quad (6.5)$$

with  $k=0, 1, \dots, N-1$  yields neither unbiased nor consistent estimate of  $S_{xx}(\tilde{\omega})$ ,<sup>45</sup> the chosen estimator addresses each shortcoming with a corresponding modification to (6.5).

First, since the bias of  $Q_{zz}[\tilde{\omega}_k]$  results from the abrupt truncation of the sequence  $z[n]$  at a length of  $L$ , each one-second interval of the sequence is multiplied by a windowing function,  $w[n]$ , producing  $v[n] = w[n] z[n]$  and limiting spectral leakage in the subsequent FFT operation on  $v[n]$ .<sup>46</sup> For this work, a 4-term, N-point cosine

---

<sup>43</sup>The popular magnitude-squared spectrum (MSS) estimator is recommended for use only with abruptly truncated (i.e., non-windowed) discrete-time sequences, since the absolute values of its samples, which correspond to the integrated signal power in each frequency bin of width  $2\pi/L$ , are easily corrupted by the shape and height of the main window lobe. An MSS based on a modified periodogram eliminates dependence on the height of the main lobe, but lobe width violates the MSS assumption that the signal varies little between over the  $N/L$  samples bracketing each bin.

<sup>44</sup>[Schuster \[1898\]](#) defines the periodogram in terms of the DTFT, rather than the DFT, but the sampled formulation of the periodogram in (6.5) is conceptually equivalent and is simply be referred to as the *periodogram* hereafter.

<sup>45</sup>An unbiased estimator is one whose mean approaches the actual quantity as the number of samples increases. A consistent estimator is one whose variance approaches zero as the number of samples approaches infinity [[Oppenheim et al., 1999](#), p.731].

<sup>46</sup>Any finite,  $L$ -length sequence  $x[n]$  can be viewed as the result of multiplying the infinite series corresponding to samples of  $x(t)$  by a rectangular window of length  $L$ . In the frequency domain, this is expressed as the convolution of the true power density spectrum of  $x(t)$  with the square of the sinc function, which is the DTFT of the rectangular window. For a pure tone, this convolution tends to smear the power of the tone over all the sidelobes of the sinc, resulting in ‘leakage’ of the

window with continuous third-derivative, derived by [Nuttall, 1981, p.88] as:

$$w[n] = \frac{1}{N} \sum_{k=0}^3 (-1)^k a_k \cos\left(2\pi \frac{kn}{N}\right) \quad (6.6a)$$

with

$$a_0 = 0.338946, \quad a_1 = 0.481973, \quad a_3 = 0.161054, \quad a_4 = 0.018027 \quad (6.6b)$$

offers a combination of side-lobe suppression (82.67 dB), side-lobe decay rate (30 dB/octave), and main lobe width ( $\sim 4$  samples at FWHM) that facilitates harmonic discrimination at 90-dB SFDR levels. To account for the fact that multiplication with  $w[n]$  changes the average power of  $v[n]$  relative to that of  $z[n]$ , the periodogram of (6.5) is modified,<sup>47</sup> normalizing it by the average power of the window such that

$$Q_{vv}[\tilde{\omega}_k] = \frac{1}{UL} |V[k]|^2 \quad (6.7)$$

where  $U$  is the total power of the window computed in the time domain and divided by the number of samples to arrive at the power/sample as

$$U = \frac{1}{L} \sum_{n=0}^{L-1} |w[n]|^2 \quad (6.8)$$

When employed by the PSD estimator in place of (6.5) the modified periodogram  $Q_{vv}[\tilde{\omega}_k]$  is shown to yield asymptotically an unbiased estimate of  $S_{xx}(\tilde{\omega})$ , as desired

---

tone into adjacent bins and potentially obscuring signals present there.

By gradually forcing the finite-length time-domain sequence to zero at its extremes, multiplication by an appropriate window artificially enforces periodicity with the sequence length, ensuring that at least the longest wavelength matches the DFT bin width. Note that the preceding discussion of leakage depends in no way on the use of the DFT—leakage is simply a property of using a finite-length sequence and tends to disappear as  $L \rightarrow \infty$  because the sinc functions in the frequency-domain approach Dirac delta functions. However, if it is the case that all wavelengths of the discrete signal divide the window evenly, then the DFT would artificially suppress all spectral leakage [Oppenheim *et al.*, 1999, p.698–703].

<sup>47</sup>Intuitively, this need is evident from the fact that the window naturally attenuates the signal samples near the edges of the sequence. To negate this effect, the power of the window is normalized out, so that it is not added into the final periodogram of  $v[n]$ .



[[Oppenheim et al., 1999](#), p.734].

The modified periodogram of (6.7) that incorporates an effectively unit-power smoothing window can eliminate the bias of a  $S_{xx}(\tilde{\omega})$  based upon it, but still suffers from the fact that, like the standard periodogram of (6.5), it does not yield a consistent estimator because its variance does not tend to zero as  $L \rightarrow \infty$ . To suppress edge effects of the convolution operation responsible for this variability,<sup>48</sup> the Welch method performs averaging that reduces the sample-to-sample variation of  $Q_{vv}[\tilde{\omega}_k]$ , smoothing the resulting periodogram [[Welch, 1967](#)]. Specifically, it divides the sequence  $z[n]$  of length  $L$  into a series of smaller segments, each of length  $R$ , that may or may not overlap. Each segment is then windowed and a modified periodogram computed in accordance with (6.7). The resulting  $Q_{vv}[\tilde{\omega}_k]$  for all such segments are then averaged to arrive at the Welch-smoothed periodogram.

Decomposing  $z[n]$  into ten one-second-long, half-overlapping sections,<sup>49</sup> performing  $2^{17}$ -point, zero-padded FFTs on each section,<sup>50</sup> obtaining a modified periodogram from each FFT according to (6.7),<sup>51</sup> and averaging the magnitudes of these ten  $Q_{vv}[\tilde{\omega}_k]$  yields an estimate of  $S_{zz}(\tilde{\omega})$  that possesses both the desired  $\sim 1$ -Hz bin width (cf. Section 3.1.2.2) and, by performing a quadrature summation of the samples within the main lobe of the window,<sup>52</sup> an accurate measure of the power in each coherent

---

<sup>48</sup>This large variability is due to the estimation process itself; namely, in the underlying time-domain autocorrelation of (6.2), the samples at the ends of  $R_{zz}[n]$  are produced by the shifting-and-addition of only a few samples of  $z[n]$ , whereas those in the center of  $R_{zz}[n]$  contain contributions from all the input samples [[Oppenheim et al., 1999](#), p.736].

<sup>49</sup>Half-overlap spacing, in which each section shares the first(last) half of its samples with those of the preceding(succeeding) section, represents a near-optimal choice and can be shown to offer a factor-of-two improvement in the consistency of the PSD estimator [[Welch, 1967](#), p.72]. Greater overlap only reduces the independence of the segments and, hence, the benefit to the variance of ensemble averaging [[Oppenheim et al., 1999](#), p.738].

<sup>50</sup>By providing more samples of  $S_{zz}(\omega)$  in the final estimate,  $S'_{zz}(\tilde{\omega}_k)$ , zero-padding avoids misleading ‘picket-fence’ artifacts that can occur if the window nulls fall on the harmonics of interest [[Oppenheim et al., 1999](#), p.708]. It also ensures that  $N$  is a power of two, improving the computational efficiency of the FFT. These benefits outweigh the bin width of 0.76 Hz/bin that accompanies rounding  $N$  to the nearest power of two, despite its being slightly less than the target of 1 Hz/bin (cf. Section 3.1.2.2).

<sup>51</sup>This modification comprises the window-normalizing coefficient obtained from substituting (6.6a) into (6.8).

<sup>52</sup>Computing the power of each harmonic consists of determining the width of the corresponding spectral peak relative to the local noise floor, then integrating both the signal and estimated noise power over that bandwidth, before subtracting the latter from the former to arrive at  $P(f_{\text{harm}})$ .

signal. For a spectral estimated with these characteristics, it is trivial to ratio the power of the largest harmonic to the fundamental and arrive at the SFDR according to (3.7).<sup>53</sup>

### 6.2.3 Noise

The operation of the noise (NS) test bench, which evaluates the input-referred noise of the DUT in each of its programming modes using the instrument configuration of Figure 6.8, is described by the following settings and procedures.

#### 6.2.3.1 Instrumentation

The noise measurement procedure described in Section 6.2.3.3 is predicated on the existence of a source whose noise spectral density is known. With a noise bandwidth of 10 MHz, the Agilent 33120A provides white (Gaussian) noise of variable total power.<sup>54</sup> Using the passive path of INPSE (cf. Figure H.2(a)) to minimize additional noise,<sup>55</sup> this source is connected as shown in Figure 6.8 for the case of the LNA as DUT. Designed to exhibit low  $e_n$ , and with its contribution demoted through Friis' equation (cf. Footnote 1 of Chapter 3), OUTSE is able to convert the noisy LNA output to a 50- $\Omega$  impedance compatible with the Agilent 4395A, operating in its spectrum analyzer mode,<sup>56</sup> despite containing active circuitry.

<sup>53</sup>Note that in the results of Section 6.3.3, the power of the 2<sup>nd</sup> and 3<sup>rd</sup> relative to the fundamental are explicitly computed in lieu of identifying the SFDR alone.

<sup>54</sup>The spectral density of noise provided by the Agilent 33120A is not exactly white; the imperfections that attend its direct digital synthesis (DDS) of arbitrary waveforms, including low-frequency spurs at -74-dBc levels, are documented in [*Agilent Technologies, Inc., 33120A Manual*, p.276-286]. However, the Gaussian approximation is sufficient for this work since the  $S_{si}(f)$  calibration described in Section 6.2.3.3 accounts for any undulations with frequency.

<sup>55</sup>Naturally, ambient noise can still be coupled in through a variety of sources in the passive INPSE path, especially through the magnetic flux of X1 and B1. Short of access to an electrically and magnetically quiet test facility, this effect is unavoidable; the ramifications of the associated errors are addressed in Section 6.2.3.4.

<sup>56</sup>Preference for the shielding afforded by coaxial cables during sensitive noise measurements, as well as the comparatively higher noise of the Agilent 1141A probe, also promote the choice of output path through OUTSE.

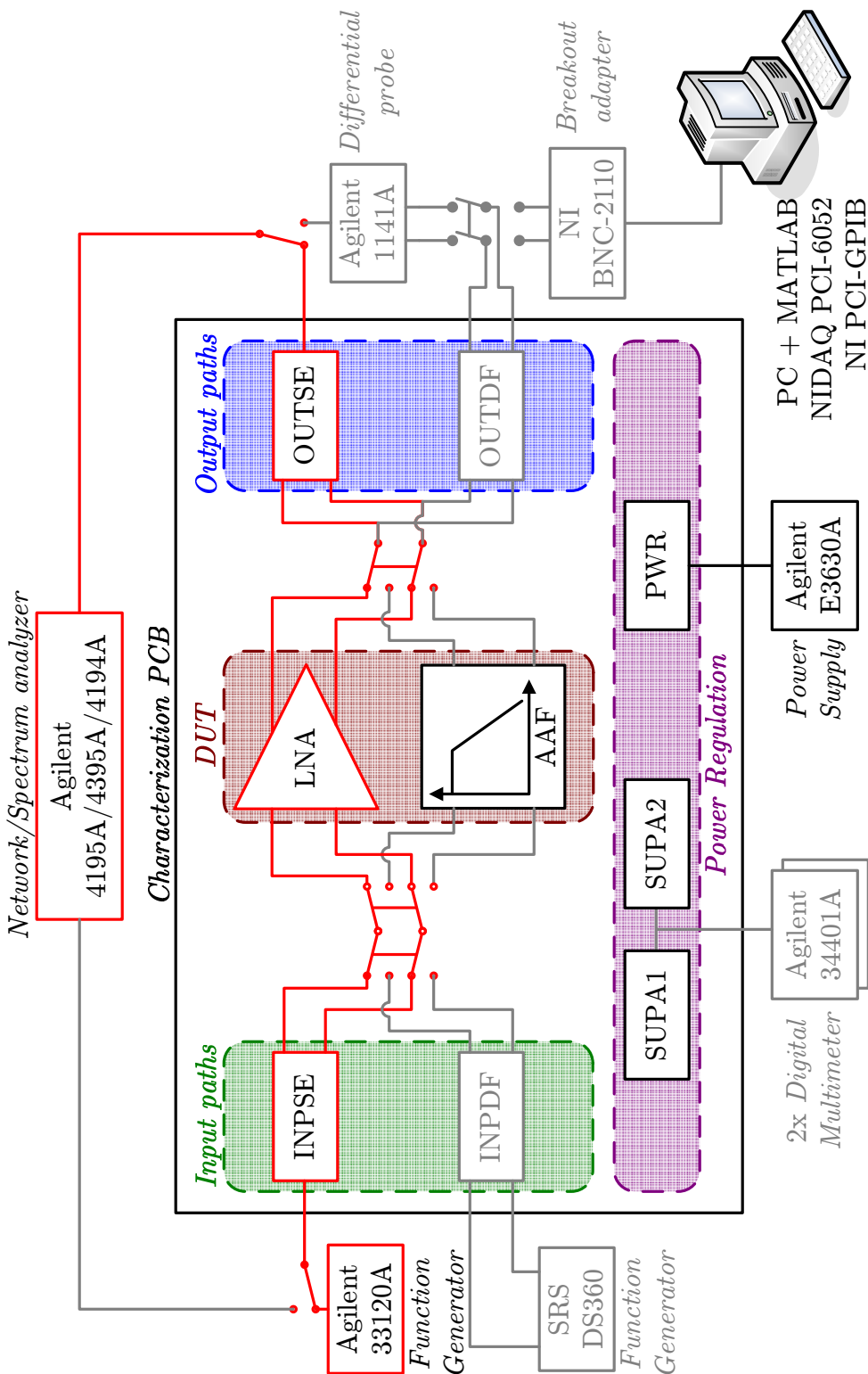


Figure 6.8: Block diagram of instrument connectivity for noise measurements of LNA. Except for signal routing at DUT, instrument connectivity is identical for AAF. Required elements on(off) the signal path are highlighted in (red)(black). Passive INPSE path in use.

### 6.2.3.2 Configuration

For input coupling, the NS test bench uses the single-ended-to-differential conversion of the passive INSPE path in Figure H.2(a), with the output of the Agilent 33120A function generator coupled via J5, whose shield is grounded. Filters F1–F3 and B1 are all bypassed, sparing the input any additional filtering. R1 is removed, so that the function generator sees a  $50\text{-}\Omega$  termination.

The output of the DUT is DC-coupled to OUTSE by configuring MUX1–MUX4 of Figure H.5(b) accordingly. A1 is programmed for 0-dB gain and C3–C5 are removed to, once again, prevent slimming of the noise bandwidth.

The Agilent 33120A features a 10-MHz noise bandwidth and the ability to generate white noise with programmable output power (into a  $50\text{-}\Omega$  load) between  $-30$  dBm and  $+10$  dBm [*Agilent Technologies, Inc., 33120A Manual*, p.59].<sup>57</sup> To sense these levels with a dynamic range of just 70 dB, the spectrum analyzer is configured with an internal attenuation of 20 dB on its test port. Just as for the FR test bench (cf. Section 6.2.1.3), its frequency resolution is improved by conducting linear sweeps over the five decades from 100 Hz to 1 MHz, with the resolution bandwidth and averaging specified in Table 6.5.

### 6.2.3.3 Acquisition

A simple model of the noise through the signal path of Figure 6.8 is depicted in Figure 6.9, which highlights the following contributors:

- $S_{\text{si}}(f)$ : PSD of noise injected at DUT input by known source.
- $S_{\text{ai}}(f)$ : PSD of noise injected into DUT by ambient environment, including flux pick-up via coils of X1 in INPSE.
- $S_{\text{di}}(f)$ : Equivalent input-referred noise PSD of DUT, which is assumed to be an ideal, noiseless block of gain  $G_{\text{p}}$ .

---

<sup>57</sup>As described in Section 6.2.3.3, an attenuator is placed in series with the output of the function generator to achieve noise powers low enough for LNA testing.

Decades		Agilent 4195A settings			
ID	$f_{\text{start}}^{\text{a}}$ [Hz]	$f_{\text{stop}}^{\text{a}}$ [kHz]	RBW <sup>b</sup> [Hz]	Avg. <sup>c</sup> [#]	Time <sup>d</sup> [sec]
0	$10^1$	$10^2$	1	$2^4$	5.481
1	$10^2$	$10^3$	3	$2^5$	1.388
2	$10^3$	$10^4$	10	$2^4$	2.082
3	$10^4$	$10^5$	30	$2^5$	1.104
4	$10^5$	$10^6$	100	$2^4$	2.343

<sup>a</sup> Linear, 401-point sweep performed over each decade of range ( $f_{\text{stop}}/f_{\text{start}}$ )

<sup>b</sup> Resolution bandwidth (RBW) scales with decade as the effect of  $1/f$  noise depreciates

<sup>c</sup> Averaging selected to reduce variance while equalizing sweep times, except for noisiest decade (ID 0)

<sup>d</sup> Aggregate sweep time over all decades, including averaging

Table 6.4: Spectrum analyzer settings for NS test bench, including resolution bandwidth (RBW) and number of averages (Avg.). Decade ID numbers are used to track data files.

- $S_{\text{co}}(f)$ : Equivalent output-referred noise PSD of all circuitry in the signal path other than the DUT. Although rendering this noise independent of  $G_p$  is only an approximation, the dominant noise contributions are, in fact, in OUTSE, since the active path of INPSE is eschewed.
- $S_{\text{mo}}(f)$ : Noise PSD measured by spectrum analyzer. Due to the limitations of this instrument,  $S_{\text{mo}}(f)$  is constrained to a maximum(minimum) value of  $S_{\text{mf}}(S_{\text{me}})$ .

To isolate  $S_{\text{di}}(f)$ , during each run the known input power of the function generator is swept between  $-50$  dBm and  $+10$  dBm and the spectral content of  $S_{\text{mo}}(f)$  from 100 Hz to 1 MHz is acquired by the spectrum analyzer with 401 points/decade and the settings shown in Table 6.4. The corresponding levels of  $S_{\text{si}}(f)$  are given in Table 6.5, which reveals that for steps A through O, a 20-dB attenuator is placed in series with the function generator output to deliver power levels below  $3.5 \mu\text{V}/\sqrt{\text{Hz}}$  at the DUT input. The remaining contributors of Figure 6.9, which are presumed stationary, are then characterized by the following steps:<sup>58</sup>

<sup>58</sup>The connectivity for Steps 1–3 is simple enough that is not pictured in Figure 6.8.

Powers		Agilent 33120A settings		PCB equivalents		
ID	Panel <sup>a</sup>	Attenuator <sup>b</sup>	Effective	At J5		At DUT
	[dBm]	[dB]	[dBm]	$[\mu\text{V}_{\text{rms}}]$	$[\mu\text{V}/\sqrt{\text{Hz}}]$	$[\mu\text{V}/\sqrt{\text{Hz}}]$
A	−30	20	−50	1.41	0.45	0.03
B	−27	20	−47	2.00	0.63	0.04
C	−24	20	−44	2.82	0.89	0.06
D	−21	20	−41	3.99	1.26	0.08
E	−18	20	−38	5.63	1.78	0.11
F	−15	20	−35	7.95	2.51	0.16
G	−12	20	−32	11.23	3.55	0.22
H	−9	20	−29	15.87	5.02	0.31
I	−6	20	−26	22.41	7.09	0.44
J	−3	20	−23	31.66	10.01	0.62
K	0	20	−20	44.72	14.14	0.88
L	3	20	−17	63.17	19.98	1.24
M	6	20	−14	89.23	28.22	1.76
N	9	20	−11	126.04	39.86	2.48
O	12	20	−8	178.04	56.30	3.51
P	−5	0	−5	251.49	79.53	4.95
Q	−2	0	−2	355.23	112.33	6.99
R	+1	0	+1	501.78	158.68	9.88
S	+4	0	+4	708.79	224.14	13.95
T	+7	0	+7	1001.19	316.60	19.71
U	+10	0	+10	1414.21	447.21	27.84

<sup>a</sup> Power level programmed on front panel

<sup>b</sup> Power level following Mini-Circuits HAT-20 20-dB attenuator (0 if absent)

Table 6.5: Function generator settings for NS test bench, highlighting the transformation of the total noise specified on its panel to the equivalent PSD at the DUT input, accounting for passage through the optional −20-dB attenuator and INPSE circuitry. Power ID numbers are used to track data files.

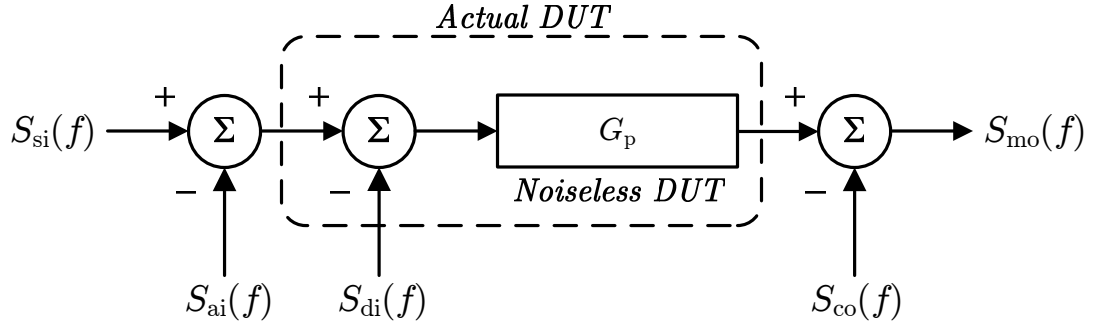


Figure 6.9: Block diagram of simplified noise model for NS test bench signal path. The subscripts ‘i’ and ‘o’ distinguish quantities referred to the input and output of the DUT, respectively.

1.  $S_{me}(f)$  is measured with the spectrum analyzer input floating.
2.  $S_{si}(f)$  is measured by subtracting  $S_{me}(f)$  from a measurement taken with the spectrum analyzer directly connected to the output of the function generator (or attenuator, if applicable).
3.  $S_{ai}(f)$  and  $S_{co}(f)$  are estimated by configuring the DUT in bypass mode and extrapolating the intercept of the  $S_{mo}(f)$ -versus- $S_{si}(f)$  curve at each frequency; this intercept approximates  $S_{co}(f) + G_p S_{ai}(f)$ .
4.  $S_{di}(f)$  is estimated by repeating Step 3 with the DUT in the signal path. The extrapolated intercept that results, after subtracting off that of Step 3, corresponds to the output-referred DUT noise PSD,  $G_p S_{di}(f)$ .

#### 6.2.3.4 Analysis

Given the model of Figure 6.9, consider the noise measured by an ideal spectrum analyzer at a single frequency,  $f_o$ . When the amplitude of the input power,  $S_{si}(f_o)$ , is swept over the course of each run, the expression for  $S_{mo}(f_o)$  is easily identified as affine:

$$S_{mo}(f_o) = \underbrace{G_p}_{\text{Slope}} S_{si}(f_o) + \underbrace{G_p S_{ai}(f_o) + G_p S_{di}(f_o) + S_{co}(f_o)}_{\text{Intercept}} \quad (6.9)$$

where the quantity of interest,  $S_{\text{di}}(f_o)$ , is subsumed into the intercept. However, this simple representation, depicted by plotting  $S_{\text{mo}}(f_o)$  versus  $S_{\text{mo}}(f_o)$  in Figure 6.10(a), assumes  $S_{\text{me}} \rightarrow 0$  and  $S_{\text{mf}} \rightarrow \infty$ ; in practice, the limited ( $\sim 70$  dB) dynamic range of the spectrum analyzer dictates that these lower and upper limits on  $S_{\text{mo}}(f)$  are actually finite, resulting in the single-frequency input-output curve of Figure 6.10(b), whose regions are defined in a piecewise manner by:

$$S_{\text{mo}}(f_o) = \begin{cases} S_{\text{me}}(f_o) & , \text{ cut-off} \\ G_{\text{p}}S_{\text{si}}(f_o) + (G_{\text{p}}S_{\text{ai}}(f_o) + G_{\text{p}}S_{\text{di}}(f_o) + S_{\text{co}}(f_o)) & , \text{ linear} \\ S_{\text{mf}}(f_o) & , \text{ saturation} \end{cases} \quad (6.10)$$

The inflection point along the  $S_{\text{si}}(f_o)$  axis that defines the boundary of the cut-off(saturation) region,  $S_{\text{se}}(f_o)(S_{\text{sf}}(f_o))$  varies with  $f_o$ , since the noise floor(Bode response) of the spectrum analyzer(signal path) increases(rolls-off) at the lower(upper) extreme of the measured bandwidth due to flicker noise(X1 in INPSE).

Nevertheless, punctilious establishment of the  $S_{\text{si}}(f_o)$  sweep range at each  $f_o$  and the use of a 16-tap mean (running average) filter to smooth the  $S_{\text{mo}}(f)$  measured at each sweep step ensure that all three regions of the curve in Figure 6.10(b) are represented. In that case,<sup>59</sup> it is possible to identify the linear region, perform a first-order fit, and extrapolate the intercept of (6.9). Applying this technique at each frequency point for the configurations of Step 3 and 4, and subtracting the resulting intercepts as indicated, yields the desired profile of  $S_{\text{di}}(f)$ .

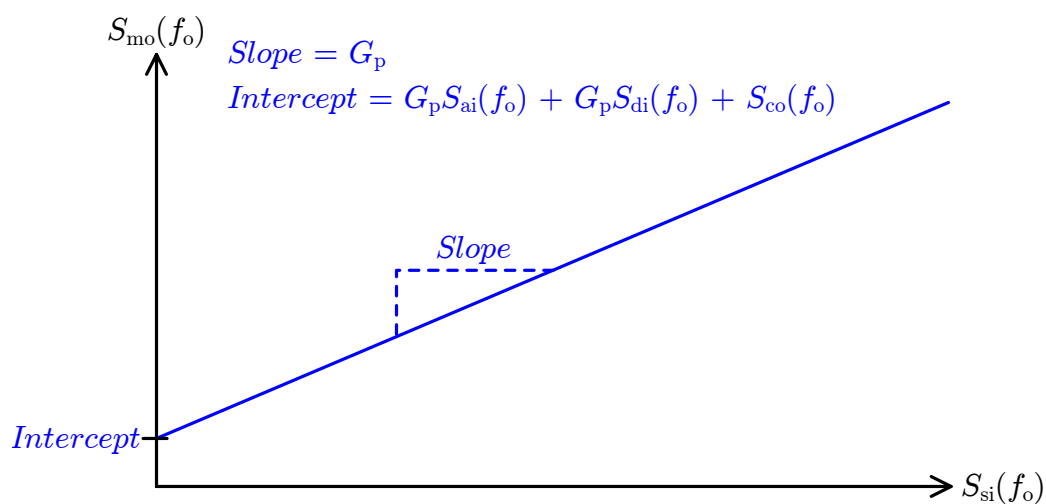
### 6.2.4 Power Dissipation

The operation of the power dissipation (PD) test bench, which evaluates the power consumed by the DUT in each of its programming modes using the instrument

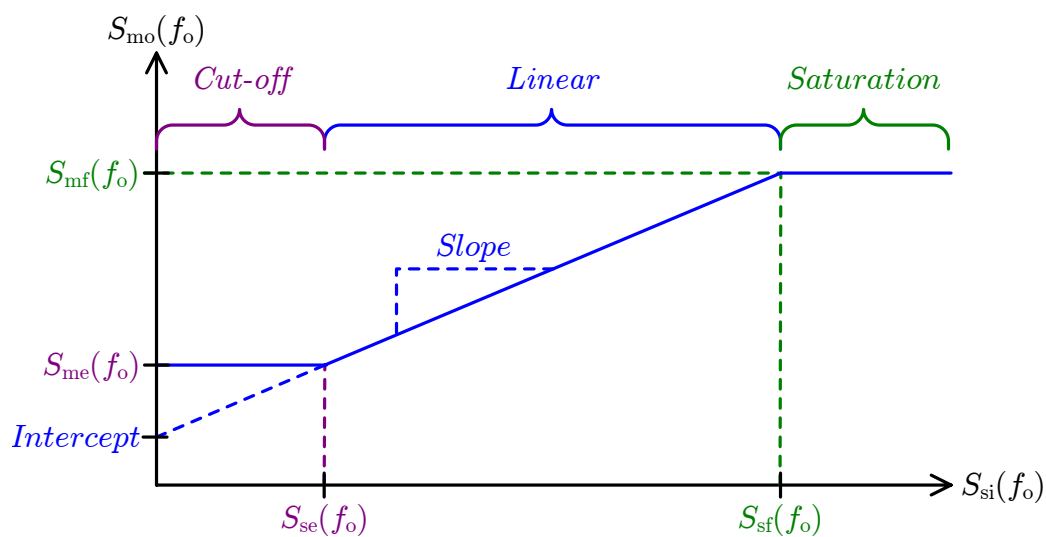
---

<sup>59</sup> The flicker noise of the spectrum analyzer limits the width of the linear region at low frequencies. Hence, the quality of the fit suffers and the variability in the extrapolated intercept between neighboring frequencies increases, manifesting as higher variance of the estimated noise floor below 1 kHz. Similarly, at high frequencies, X1 roll-off muddles the onset of the saturation region, rendering it difficult to properly identify the bounds of the linear region and, as a consequence, the linear fit tends to overestimate the intercept above 800 kHz.





(a) Ideal spectrum analyzer.



(b) Actual spectrum analyzer.

Figure 6.10: Single-frequency ( $f_o$ ) slice of two-dimensional  $S_{mo}(f)$  surface mapped by input frequency and power sweeps for (a) ideal and (b) actual spectrum analyzer dynamic range.

configuration of Figure 6.11, is described by the following settings and procedures.

#### 6.2.4.1 Instrumentation

To measure the average dynamic power dissipation of the SVEPRE components, it is configured as shown in Figure 6.11, with the complete signal path through both the LNA and AAF active. The SRS DS360 provides the chip with a representative sinusoidal input while Agilent 34401A digital multimeters (DMMs) connect to instances of the circuit of Figure H.6 that appear in series with the  $V_{\text{sup}}$  and  $V_{\text{gnd}}$  traces near the socket.<sup>60</sup> To discriminate between the power consumption of the LNA and AAF, the total supply current is compared against that flowing through the LNA ground return.<sup>61</sup> This technique allows both devices to remain active, mimicking signal-dependent power demands observed in the field for an improved estimate.

During baseline(radiation) testing the current is sensed by an ammeter(voltmeter) measuring the current through(voltage across) H1(R1). In both cases, the voltage is also measured across H2. When monitoring for SEL, the DMMs are repeatedly queried over the GPIB bus to provide real-time tracking to the operators (cf. Section 6.2.5.3).

#### 6.2.4.2 Configuration

Input coupling for the PD test bench is relatively inconsequential, as the SRS DS360 only drives INPDF so as to provide a nominal input signal—a 10-kHz, 50-mV/ $\sqrt{\text{Hz}}$  sinusoid that exercises half the full-scale output range—to both the LNA and AAF, which are cascaded to form the complete signal path in Figure 6.11. To that end, the configuration of the INPDF options is identical to that of the LN test bench when

---

<sup>60</sup>Measurements of  $V_{\text{esup}}$  yield negligible current during normal operation, so this supply is only monitored for SEL.

<sup>61</sup>As evident from the pinout of Figure 6.2, rather than drawing from separate supplies, the LNA and AAF, as well as communal on-chip circuitry such as the common-mode voltage regulators, share a single core power network ( $V_{\text{sup}}$ ). But, the LNA return is distinct from that of the AAF for noise purposes (cf. Section 6.1.1.2). Thus, despite being unconventional, it is expedient to simply measure the total return current and that of the LNA separately, subtracting the latter from the former to arrive at the current consumption of the AAF. The power drawn by the communal circuitry is, then, assigned to the AAF, which is appropriate given that this circuitry is replicated within each stage.

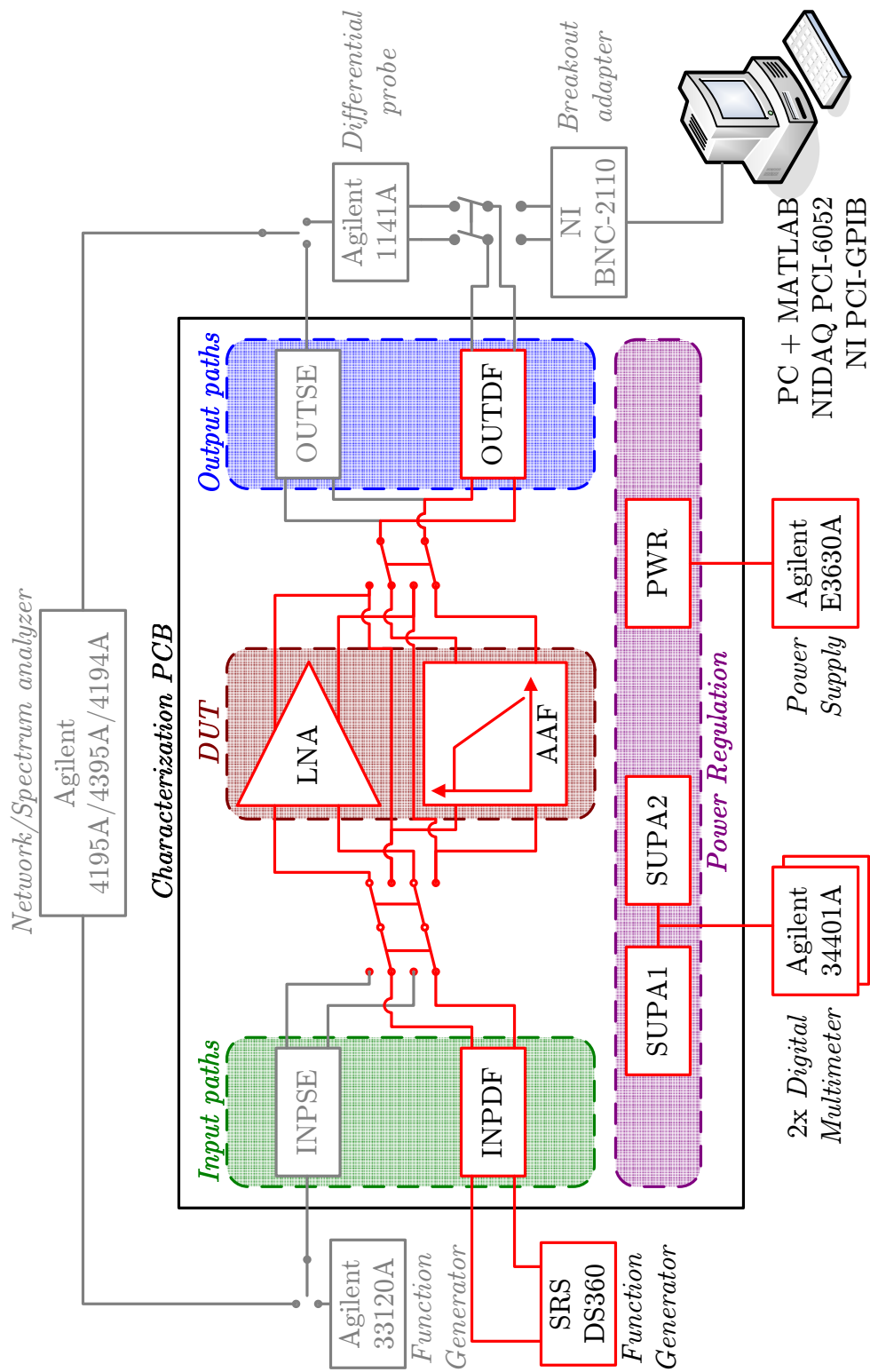


Figure 6.11: Block diagram of instrument connectivity for simultaneous power dissipation measurements of the LNA and AAF. Required elements on(off) the signal path are highlighted in (red)(black).

driving the LNA (cf. Table 6.3). Likewise, the output is terminated in OUTDF, whose configuration matches that of the LN test bench (cf. Section 6.2.2.2) though it need not be directly measured by additional instruments.

### 6.2.4.3 Acquisition

The pair of Agilent 34401A multimeters that sense  $I_{\text{sup}}(V_{\text{sup}})$  and  $I_{\text{lgnd}}(V_{\text{lgnd}})$  using H1(H2) of Figure H.6 are polled in a round-robin fashion at the maximum rate supported by the GPIB interface ( $\sim 42$  Hz aggregate)<sup>62</sup> over the course of a 30-second acquisition duration. Typically, the voltage measurements are performed only twice—at the beginning and end of the record—while current measurements are made continuously.

### 6.2.4.4 Analysis

A simple average of the dynamic power dissipated by the DUT while processing a nominal input tone is obtained by separately multiplying the time-averaged current measurement of each DMM by the initial-plus-final average  $V_{\text{sup}}$  such that:

$$\overline{P}_{\text{total}} = \overline{V}_{\text{sup}} \overline{I}_{\text{sup}} \quad (6.11a)$$

$$\overline{P}_{\text{lina}} = \overline{V}_{\text{sup}} \overline{I}_{\text{lgnd}} \quad (6.11b)$$

With (6.11b) accounting for all the return current of the LNA, the time-averaged power consumption of the AAF is simply the difference of the two expressions in (6.11):  $\overline{P}_{\text{aaf}} = \overline{P}_{\text{total}} - \overline{P}_{\text{lina}}$ .<sup>63</sup>

---

<sup>62</sup>Rather than toggling between the two DMMs, the GPIB controller opts for a more efficient schedule that acquires 20 samples from each instance before commuting them. By reducing the switching overhead, this technique approaches the theoretical maximum rate, achieving 640 samples per 30 seconds or 21.3 Hz per DMM, without completely sacrificing synchronicity.

<sup>63</sup>Although more than accurate enough for this work, this technique counts the base current of the pnp inputs to G1 in Stage 1 of the AAF as part of  $\overline{P}_{\text{lina}}$  and, conversely, subsumes the common-mode currents drawn by the segments of  $R_1$  into  $\overline{P}_{\text{aaf}}$ . Both these quantities are quite small, justifying the neglect of these error terms.

## 6.2.5 Single-Event Effects

For clarity, the operation of the single-event effects (SEE) test bench is conceptualized as the simultaneous, parallel operation of two test benches—one for detecting SEL events, the other for ASETs.<sup>64</sup> Using the configurations of Figure 6.12(a) and Figure 6.12(b), which partition the instrumentation accordingly, these evaluate both the ASET and SEL sensitivity of the DUT in each of its programming modes as described by the following settings and procedures.

### 6.2.5.1 Instrumentation

Utilizing the same input and output processing blocks of the characterization PCB, as is evident in Figure 6.12(a) and Figure 6.12(b), the subsets of the SEE test bench only differ insofar as a digitizing oscilloscope(DMM) scans the DUT outputs(supplies) for SET(SEL) phenomena while the part is irradiated.

### SEL Testing

When apprising SEL sensitivity, it is necessary to periodically sample the supply voltage waveforms, revealing to the experimenter gradual(sudden) variations that presage(identify) latchup so that precautions are taken to protect the DUT from catastrophic damage. To that end, the multiple DMMs depicted in Figure 6.12(a) are polled over GPIB to provide a real-time graphical display of the  $V_{\text{sup}}$  and  $V_{\text{esup}}$  waveforms (e.g., Figure 6.36).<sup>65</sup>

### SET Testing

To monitor SETs during heavy-ion(pulsed-laser) testing, Figure 6.12(b) depicts a

---

<sup>64</sup>Although their compatibility permits the capture of both SEE phenomena when the DUT is exposed to a particular SEE source (cf. Appendix J) and, indeed, both halves of the SEE test bench are typically operated simultaneously, either can be eschewed as desired without compromising the measurements of the other.

<sup>65</sup>The limited memory depth and transfer rates of the digitizing oscilloscopes employed for SET monitoring are not sufficient for the long (>300 s) exposures that characterize SEL experiments. The GPIB polling trades a lower sampling rate and variability in sample-to-sample spacing for arbitrarily long acquisition times.

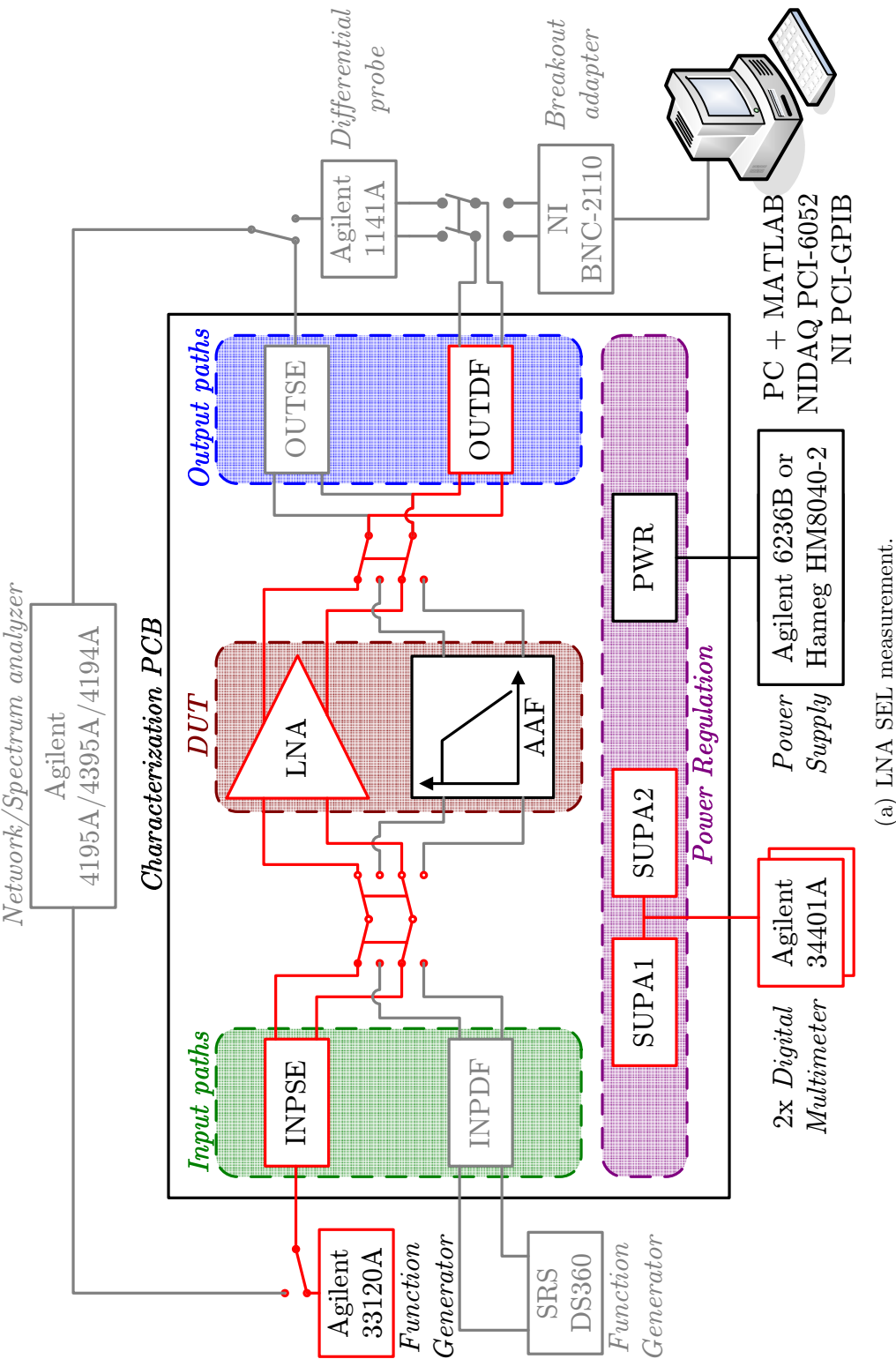


Figure 6.12: Block diagram of instrument connectivity for (a) SEL and (b) SET testing of the LNA. Except for signal routing at DUT, instrument connectivity is identical for AAF. Required elements on(off) the signal path are highlighted in (red)(black).

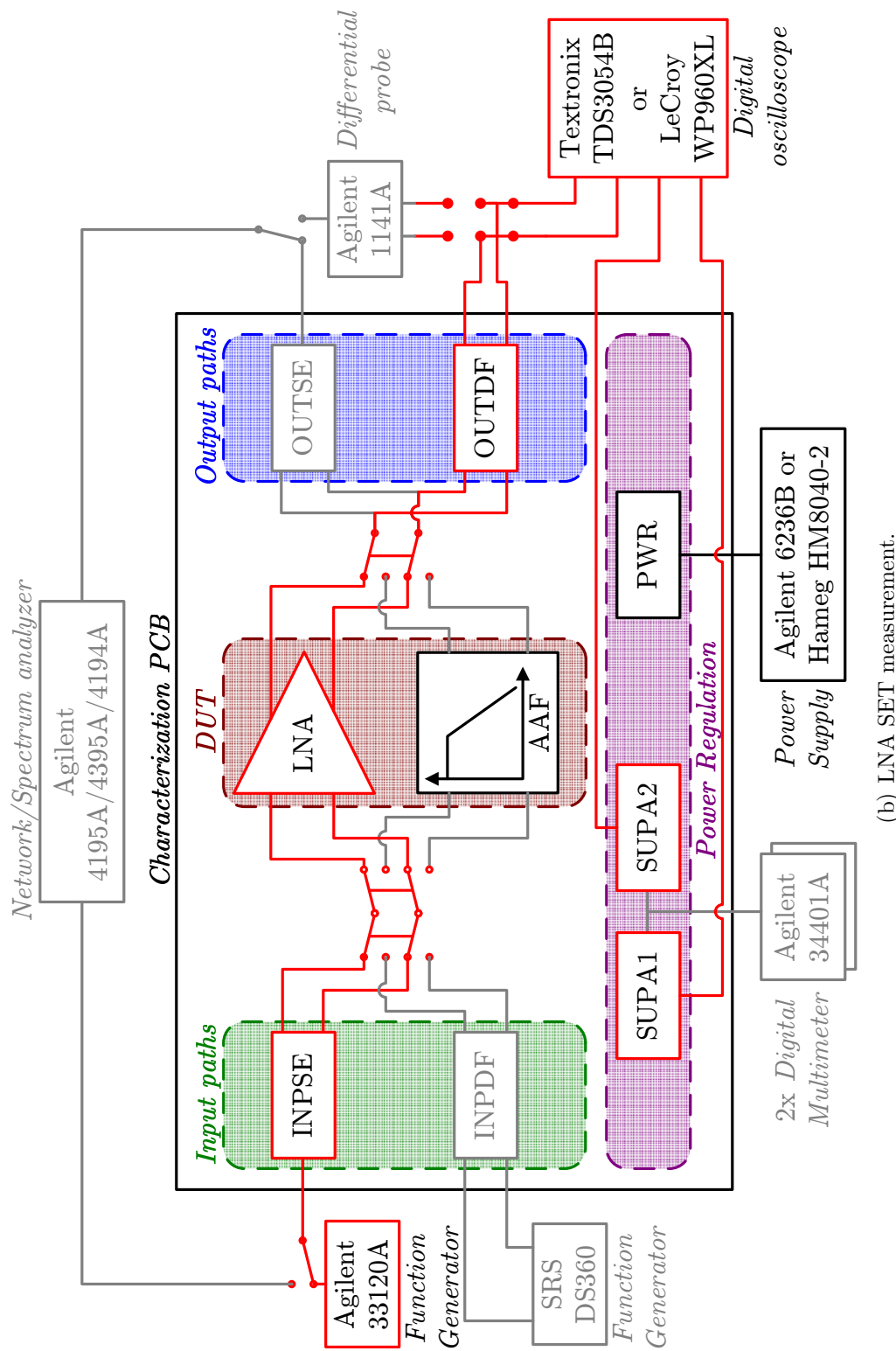


Figure 6.12: Block diagram of instrument connectivity for (a) SEL and (b) SET testing of the LNA (cont.). Except for signal routing at DUT, instrument connectivity is identical for AAF. Required elements on(off) the signal path are highlighted in (red)(black).

variation of Figure 6.8 in which the Agilent E3630A power supply is replaced by an Agilent 6236B(Hameg HM8040-2)<sup>66</sup> and the spectrum analyzer is replaced by a four-channel Textronix TDS3054B(LeCroy WP960XL) oscilloscope.<sup>67</sup> Although the oscilloscope channel allocations vary with the specific device under examination,<sup>68</sup> the depicted configuration allots two channels to the LNA outputs while two probe the supply voltages  $V_{\text{sup}}$  and  $V_{\text{esup}}$  as a precaution.

### 6.2.5.2 Configuration

As shown in Figure 6.12(a) and Figure 6.12(b) both SEL and SET evaluation employ an Agilent 33120A function generator coupled to the DUT via the passive path of INPSE (cf. Figure H.2(a)). The configuration of this signal path is identical to that of the NS test bench (cf. Section 6.2.3) to ensure proper termination of the function generator, whose output impedance remains at 50  $\Omega$ . Similarly, during both SEL and SET testing the DUT output is terminated into OUTDF, with only polystyrene capacitors C2, C4, and C6 populated, as in the case of LNA testing with the FR test bench (cf. Section 6.2.1). These capacitors render the DUT loading independent of the presence of the oscilloscope, such that the DUT performs comparably for both flavors of testing.

### SEL Testing

When monitoring  $V_{\text{sup}}$  and  $V_{\text{lgnd}}$  during pulse-laser SEL testing, the DMMs of Figure 6.12(a) are configured as ammeters, bypassing R1 of Figure H.6 and sensing the supply current directly (cf. Section H.2.1.1).

---

<sup>66</sup>Since its on-board regulation renders the operation of the characterization PCB agnostic to the model of the power supply, alternatives conveniently available at each test facility are readily coopted.

<sup>67</sup>In both cases, the oscilloscope belongs to the associated test facility, so the features of each model reflect the particulars of the test environment. For heavy-ion testing, the TDS3054B (5-GS/s) acquisition module counts events defined by a predetermined trigger criterion, whereas the sampling and storage capabilities of the WP960XL (4-GS/s, 16 MB/channel) permit the synchronous recording of the full input and output waveforms on all four channels.

<sup>68</sup>For example, during laser testing, one channel is dedicated to capturing the timing and duration of the precipitating pulse.



However, for heavy-ion testing, the DMMs serve as voltmeters, measuring the voltage across  $R_1$  at H1, as this technique is least susceptible to ground-loop pickup ( $I * R$  errors) associated with the noise environment (long cable runs) endemic to the test facility. For the supply monitor on  $V_{\text{sup}}(V_{\text{lgnd}})$ , a value of  $1 \Omega$  ( $10 \Omega$ ) for  $R_1$  garners DMM voltage resolution to better than two decimal places under normal operation, wherein  $V_{R1} \simeq 16 \text{ mV}$  ( $V_{R1} \simeq 7 \text{ mV}$ ),<sup>69</sup> yet affords ample dynamic range to capture sharp increases in the supply current that precede and/or accompany SEL events.

### SET Testing

The digital oscilloscope responsible for capturing output waveforms and counting upsets during SET testing is configured according to the particulars of the radiation source (cf. Section J.1.3 and Section J.2.3). As the pulsed-laser scans the SVEPRE-1 die, the scaling and triggering of the LeCroy WP960XL is manually controlled, ensuring accurate capture of the observed waveforms and averaging 2000 points at a sample rate between 25–100 MHz. In contrast, with experimenters barred from the heavy-ion chamber, the Tectronix TDS3054B records both SET events and the corresponding waveforms automatically. As such, its triggering and acquisition settings are summarized in Table 6.6. Notably, when the DUT is receiving sinusoidal(DC) signals, the oscilloscope trigger—and, thus, the criterion for an ASET—identifies each pulse whose width(amplitude) that is narrower(greater) than one half-period of the tone( $V_{\text{cmo}} \pm 30 \text{ mV}$ ).

#### 6.2.5.3 Acquisition

Both SEL and SET data are captured in a series of intervals, known as runs, during each of which the energy of the radiation source and the parameters of input tone and DUT are held constant. For heavy-ion testing, the duration of each run is 300

---

<sup>69</sup>To ensure that the nominal supply voltage of +2.5 V reaches the DUT, regulator SUPA1 is adjusted to compensate for this voltage drop. Since this procedure is only performed in Mode C, decline of  $I_{\text{sup}}$  in the lower AAF bandwidth modes increases  $V_{\text{sup}}$ . But, as this mode-dependent variation amounts to at most 4.5 mV, it has negligible impact on performance. Similarly, the  $V_{R1} \simeq 7 \text{ mV}$  offset of LGND is comfortably tolerated.

TDS3054B settings	Input type		Explanation
	Sinusoid	DC	
Upset triggering			
Mode	Normal		Trigger when all conditions are met; count trigger events
Source	Channel 1		Trigger on $V_{\text{out}+}$ of selected DUT
Coupling	AC	DC	$V_{\text{cmo}}$ of sinusoid exceeds offset constrains for DC coupling
Type	Pulse	Edge	'Pulse' based on waveform characteristics, not absolute threshold
Condition	$<40\mu\text{s}$	$\pm 30\text{ mV}$	Sine: pulses less than half-period; DC: rising-edge crossings
Waveform acquisition			
Mode	Sample		'Peak detect' is too sensitive to narrow noise spikes
Channels	1, 2		All channels captured, but only DUT outputs saved
Resolution	Normal		'Fast trigger' trades speed for fewer samples
# of points	$10^4$		'Fast trigger' yields only 500 points; instead, $f_s = 50\text{ MHz}$

Table 6.6: Digitizing oscilloscope settings for SEE test bench during heavy-ion testing, which permit both upset counting and waveform acquisition.

SEE source		Agilent 33120A settings			
Type	Test	Impedance <sup>a</sup> [ $\Omega$ ]	Frequency [kHz]	Panel <sup>b</sup> [mV <sub>PP</sub> ]	Effective <sup>c</sup> [mV <sub>PP</sub> ]
Pulsed-laser	Sinusoid	50	10	200	25
Heavy-ion	DC <sup>d</sup>	50	0	0	0
	Sinusoid	50	10	250	30
	Sinusoid	50	10	500	60

<sup>a</sup> Expected load impedance for programmed amplitude

<sup>b</sup> Singled-ended amplitude programmed on front panel

<sup>c</sup> Differential amplitude at DUT input terminals

<sup>d</sup> To effect a DC input, the function generator is physically disconnected

Table 6.7: Function generator settings for SEE test bench, including the relationship between the single-ended amplitude on the instrument panel and the effective differential amplitude at the DUT input, accounting for gain and impedance matching through INPSE.

seconds whereas for pulsed-laser testing it varies with beam location.<sup>70</sup> In both cases, the DUT is provided with a nominal input, the details of which are summarized in Table 6.7, but the data collection is unique to the expected phenomena.

## SEL Testing

For pulsed-laser testing, the free-running DMM samples are inspected by the experimenters in real-time so that any latchup event can be noted and interrupted, but are not permanently stored. Instead, as described below, the supply waveforms are recorded by the oscilloscope. Conversely, during heavy-ion testing the DMM samples for each 300-s run are both displayed to the operators in real-time and permanently stored, whereas the oscilloscope channels monitoring these same signals (cf. Figure 6.12(b)) are not saved.<sup>71</sup>

<sup>70</sup>As opposed to the computer-controlled shutter for the heavy-ion beam, the laser shutter is manually controlled; uncertainty in the duration of each run is a direct consequence of the concomitant imprecision.

<sup>71</sup>Limited beam time and the sluggish transfer rate over the eScope interface collude to render the of download waveforms from all four oscilloscope channels on each run impractical. Since the supply voltage exhibited no appreciable variation—let alone sudden transients—throughout the entirety of

## SET Testing

Given the inherent ambiguity in defining analog SETs as compared to their digital counterparts (cf. Section 2.2.2), it is considered good practice to capture both continuous and discrete forms of SET data.

**Waveforms:** The former, consisting of samples of the representative waveforms observed at the DUT output, would ideally embody a single large data set containing a continuous stream of samples taken throughout each run. With time-domain records of all transients, classification according to width, height, rate of occurrence, and other morphologies can be performed in post-processing [*Buchner and McMorro*, 2005, p.25]. However, in the setup of Figure 6.12(b), the limited memory and data transfer rate of the oscilloscope responsible for this operation precludes continuous recording. In fact, since the ASET rate typically exceeds the time required to capture and transmit a single channel buffer, even synoptic recording is impractical, as upsets that occur during the transfer are missed.

As a compromise, then, two sets of waveforms are obtained. The first set contains only the waveform captured at the conclusion of each run, whose transfer obviously does not inhibit further acquisition.<sup>72</sup> The second and more comprehensive set is obtained by qualitative inspection of synoptic results obtained with a free-running beam.<sup>73</sup> During this evaluation, the most representative and unique finds are preserved.

**Cross-Sections:** To compute a cross-section according to (2.23), the complete, time-domain, transient record is distilled into a discrete ‘upset’ distribution,  $N_u$ , by means of a pulse-discrimination threshold (cf. Section 2.2.2). Since the SET sensitivity of the DUT can be data-dependent, Table 6.7 indicates the use of both DC and

---

SEE testing, it proved expedient to omit the data of Channels 3 and 4 from the oscilloscope record, relying only on the coarse sampling of the DMM.

<sup>72</sup>This data set is only collected during heavy-ion testing. Since pulsed-laser exposures are effectively free-running (cf. Footnote 70), there is no need to impose a distinct conclusion. Instead, representative or anomalous waveforms are saved whenever they are observed.

<sup>73</sup>In the case of a free-running beam, the run concludes when the experimenter deems the collected data sufficient representative, or as dictated by ancillary time constraints.

sinusoidal inputs. For the former, which is analogous to the condition of Figure 2.30, a pulse-height threshold,  $V_{\text{thresh}}$ , is the most appropriate criterion whereas, for naturally oscillating outputs, the width of the transient is compared to that of the fundamental frequency, establishing a maximum  $t_{\text{thresh}}$ .<sup>74</sup>

In the DC case, the DUT inputs are fixed at  $V_{\text{cmi}}$  and the oscilloscope trigger level, which is equivalent to  $V_{\text{thresh}}$  (cf. Section 2.2.2), is set at either 30 mV above or below the corresponding  $V_{\text{cmo}}$ .<sup>75</sup> Since only a positively or negatively signed trigger can be enacted during a given run, the DC experiments each consist of two runs whose parameters are identical, save for the trigger sign. For sinusoidal inputs, the oscilloscope pulse trigger, which is equivalent to  $t_{\text{thresh}}$ , is set to 80% of the half-period for the nominal 10-kHz tone (cf. Table 6.7). These two triggering mechanisms are summarized in Table 6.6.

At the conclusion of each run, the oscilloscope reports the total number of triggers, providing  $N_u$  for the computations of Section 6.2.5.4.<sup>76</sup> To reduce the variance of this result, each run is conducted twice in succession and their results averaged, yielding 600 seconds of data for each beam setting.

#### 6.2.5.4 Analysis

Although objective, the detection of both SEL and SET events is largely qualitative; in both cases, the first level of data analysis merely consists of visual observations of the time-domain supply and output waveforms, respectively. However, the

---

<sup>74</sup>Naturally, extremely long ASETs are possible, but a long fundamental period (100  $\mu\text{s}$ ) ensures that the number of such outliers excluded by setting a maximum  $t_{\text{thresh}}$  is small.

<sup>75</sup>This trigger level is determined empirically such that the corresponding error rate for this part yields a statistically significant distribution size within in the allotted beam time. Although “there exists no minimum required data set to characterize an analog circuit” [Turflinger, 1996, p.596], the resulting seven-point  $N_u$  set meets the minimum recommended [Petersen et al., 1992, p.1591]. In addition, this trigger level is comfortably beneath the  $V_{\text{thresh}}$  used in many published amplifier reports (50–100 mV) [Adell et al., 2000; Koga et al., 1993, p.1840,p.2621], rendering the cross-sections of this work comparatively pessimistic.

<sup>76</sup>Due to a bug in the eScope environment, this acquisition count was not transmitted to the operator station along with the final waveform. Thus, the experimenters opened the cave after each run and recorded the on-screen  $N_u$  value. In aggregate, the delays incurred each time the cave is opened—due to the mechanics of displacing a heavy concrete door and, more significantly, the abatement of stray radiation below safe levels inside (cf. Table C.2)—consumes a non-trivial fraction of the total beam time available.

mathematical rigor increases when employing the pulse-discrimination methodology of Section 2.2.2 to define cross-sections and compile statistics on detected ASETs during post-processing of SET data.

### SEL Testing

In contrast to the analyses performed by the other test benches, including the SET portion of this one, SEL analysis runs concurrent with the testing itself to permit stable and potentially catastrophic latchup conditions from persisting unchecked.<sup>77</sup> If latchup occurs, supply currents such as  $I_{\text{lna}}$  and  $I_{\text{esd}}$  would exhibit sharp increases (capped only by the 100-mA current limit of the on-board regulators described in Section H.2.2) as the structure of Figure 2.28 transitions from the blocking to latched state, where it then remains until power is removed. Other metastable variations, encompassing any conditions outside the blocking state, can produce signs of incipient latchup, including gradual rises and or increased variability.

For pulsed-laser evaluations, the operators monitor the DMM for these conditions. During heavy-ion testing, the GUI application polling each DMM generates a running strip chart that is examined at the SEL station for instantaneous and long-run fluctuations in all supply currents.

### SET Testing

As in Section 6.2.5.3, the analytics distinguishing the continuous and discrete data sets merit separate treatment.

**Waveforms:** For the continuous (waveform) data set, consisting of digitized waveforms recorded before and after each run, as well as a set of synoptic observations obtained with a free-running beam, simple statistics of the amplitudes and recovery times of the observed ASETs are computed over the ensemble. Since the statistical

---

<sup>77</sup>Provided no latchup occurs, a more detailed examination of the supply waveforms—which are digitized and stored during both pulsed-laser and heavy-ion testing—can proceed at the conclusion of the testing. In this work, a survey of the strip charts from each experiment seeking signs of incipient latchup uncovered no such anomalies.

significance of these descriptions is diluted by the size of the data records and the infrequency of transients at the extremes of the amplitude and recovery time distributions, the primary upshot of this statistical catalog is to assess the incidence of either catastrophic cases, in which the device malfunctions (e.g., oscillation, saturation, reset), or irrecoverable or prolonged transients which can be sensed by the ADC.<sup>78</sup>

**Cross-Sections:** The discrete data set, consisting of ‘upsets’ counted for various input types and their associated threshold criteria, is used to construct a cross-section curve such as that of Figure 2.31.<sup>79</sup> In so doing, it should be emphasized that such a curve represents not the distribution of  $\sigma_u$  for the most sensitive sections of the circuit but, rather, a distribution of the sensitivities of the various sections themselves [Petersen *et al.*, 1992, p.1578].<sup>80</sup> This interpretation justifies fitting the cross-section versus LET ( $\sigma_u$ -vs- $\mathcal{L}$ ) curve with a so-called integral Weibull distribution—specifically, the cumulative distribution function (CDF) of the Weibull probability distribution, scaled by a constant to fit the asymptotic limit—which is employed in reliability and risk analysis to describe a system whose failure results from that of any one of a population of identical components, each with independent probability of failure [McCormick, 1981, p.42]<sup>81</sup>. The four-parameters of the Weibull model

<sup>78</sup>It is quite rare for an analog circuit to not demonstrate any ASET susceptibility whatsoever. Thus, at moderate to particle/photon energies, transients are not only expected but accepted. Their impact on downstream circuitry determines whether they qualify as ‘upsets’ in the context of the instrument system, as noted in Section 2.2.2.

<sup>79</sup>According to (2.23), both  $N_u$  and  $\phi_R$  (the fluence of ionizing radiation) are required to arrive at  $\sigma_u$ . Since, only the heavy-ion facility permits determination of  $\phi_R$  with acceptable precision (cf. Footnote 70), upset distributions and cross-section curves are not computed for pulsed-laser data. Also, the rationalization constant  $R$  in (2.23) is fixed at unity since the limited number of input conditions undermines meaningful normalization.

<sup>80</sup>For example,  $\mathcal{L}_{th}$  describes only the scenario in which “the most sensitive region [is] hit in it’s most sensitive location and does not represent the entire” chip [Petersen *et al.*, 1992, p.1578].

<sup>81</sup>The success of the Weibull distribution in “a large number of diverse situations,” including SEU analysis for microelectronics, stems from its being appropriate for describing any process whose conditional failure probability as a function of time follows a power-law distribution [McCormick, 1981, p.41–42].

proposed by *Petersen et al.* [1992, p.1586],<sup>82</sup>

$$\sigma_u(\mathcal{L}) = A \begin{cases} 1 - e^{-[(\mathcal{L}-\mathcal{L}_o)/W]^S} & , \quad \mathcal{L} > \mathcal{L}_o \\ 0 & , \quad \mathcal{L} < \mathcal{L}_o \end{cases} \quad (6.12)$$

allow a succinct summary of the SEU response that is compatible with standard rate-prediction tools, such as CREME96 [*Tylka et al.*, 1997, p.2157].

Provided with these inputs and a description of the sensitive volumes of the die, the tool can estimate the upset rate of the part by: breaking the cross-section curve into sections, each corresponding to a sensitive volume with a unique  $Q_{\text{crit}}$ ; integrating each section over its sensitive volume to determine an upset rate using the Weibull parameters to weight the sum of these rates, accounting for the areal fraction governed by each  $Q_{\text{crit}}$ .<sup>83</sup>

---

<sup>82</sup>In the context of SEU analysis, the four free Weibull parameters are known as [*Petersen et al.*, 1992, p.1586]:

$A$  : *Limiting cross-section.* Analogous to  $\sigma_{\text{sat}}$  for the ideal curve of Figure 2.31

$\mathcal{L}_o$  : *Onset threshold.* Analogous to  $\mathcal{L}_{\text{th}}$  for the ideal curve of Figure 2.31

$W$  : *Width parameter.* Controls width of the distribution

$S$  : *Shape parameter.* For specific values, the distribution degenerates to familiar archetypes:

- $S=1$  : Exponential distribution
- $S=4$  : Rayleigh
- $S=4$  : Gaussian
- $S \rightarrow \infty$  : Log-normal

This parameterization is not universal: the presence of the scaling factor  $A$  and the selected symbols vary across disciplines. However, it reflects the conventions of the SEU hardness-assurance community [*Petersen*, 1995; *Tylka et al.*, 1997, p.1995,p.2152].

<sup>83</sup>This algorithm can be implemented using both integral weighting, as described here, or mathematically equivalent differential weighting [*Petersen et al.*, 1992, p.1592–1593]. Regardless, it makes several assumptions about the particle trajectory: its flux is isotropic; its path length is independent of LET; its LET is constant through the sensitive three-dimensional volume in which  $Q_{\text{crit}}$  is deposited; its deposited energy is the simply product of a constant LET and the length of a funnel-adjusted chord through the volume; and the space of all possible chord lengths can be bounded by assuming a rectangular parallelepiped (RPP) shape for the sensitive volume [*Petersen et al.*, 1992, p.1579–1580].



## 6.3 Baseline Performance

Using the test benches of Section 6.2.1 through Section 6.2.4, the baseline performance of the LNA and AAF were measured in a series of tests conducted by the author in the laboratories of the David Packard Building at Stanford University between September 2004 and June 2008. Section 6.3.1 states the general procedures and test conditions applicable to all such measurements, whereas key results for the LNA(AAF),<sup>84</sup> which are obtained at a nominal gain(bandwidth mode) of  $G_p = 14$  dB( $f_p = 180$  kHz) unless otherwise stated, are presented in Section 6.3.2(Section 6.3.3) confirming that the device performance satisfies the corresponding specifications of Table 3.2 in terrestrial operation.

### 6.3.1 Procedure

All testing is conducted at room temperature ( $\sim 28^\circ\text{C}$ ) and nominal supply voltage ( $V_{\text{sup}} = V_{\text{esup}} = +2.5$  V) with the part lidded. Except as noted in Section 6.2.4.1, the LNA output is decoupled from the AAF input such that the two components are separately characterized. For the specific procedures governing operation of the FR, LN, NS, and PD test benches that comprise the baseline characterization described below, refer to Section 6.2.1 through Section 6.2.4.

### 6.3.2 LNA Results

Aside from its input impedance, whose very large(small) resistive(capacitive) component resists accurate measurement with available laboratory instrumentation, and whose magnitude is confirmed in Figure 4.16 to exceed the specified level of  $1\text{ G}\Omega\|1\text{ pF}$ , ranging from  $18.3\text{ G}\Omega\|4.2\text{ fF}$  to  $6.7\text{ G}\Omega\|10.4\text{ fF}$  for  $G_p$  between 0 dB and 24 dB, the LNA performance metrics of Table 3.2 are grouped by test bench as follows.

---

<sup>84</sup>In the interest of brevity, the data presented in Section 6.3.2 and Section 6.3.3 are limited to the most vital measures. The full set of measurements permuting all programming modes of the two DUTs with the four baseline test benches and their configuration options is prodigious—and somewhat unwieldy for a document of this nature.

### 6.3.2.1 Bode Response and Programming

Figure 6.13 depicts the de-embedded magnitude ( $|T_{\text{dmbd}}^{\text{D}}(f)|$ ) and phase ( $\angle T_{\text{dmbd}}^{\text{D}}(f)$ ) of the LNA Bode response as its gain is manually programmed over the full range (0–24 dB) in 2 dB steps.<sup>85</sup> Along with the flatness of the passband,<sup>86</sup> Figure 6.13(a) demonstrates that the overall –3-dB bandwidth,  $f_p$ , remains at 3.91 MHz even for the highest gain setting. This behavior is a direct result of employing local rather than global feedback in the LNA input stage (cf. Section 3.2.2.1) and should be contrasted to the gain-bandwidth limitations of the latter, as depicted in Figure 3.19(b). Hence, it confirms the efficacy of the feedback techniques described in Section 4.2.2 vis-à-vis rendering the entire gain range at full bandwidth.

Recognizing that the 4 MHz specification of  $f_p$  is extremely conservative, since any LNA roll-off above  $f_p$  merely aides in the anti-aliasing of the subsequent filter, the measured LNA bandwidth is ample and its evaluation unencumbered by phase-measurement artifacts above  $f_p$ .<sup>87,88</sup> In fact, when loaded by the AAF rather than the spectrum analyzer, the rise in the non-dominant pole of the LNA (cf. Section 6.4.2.1) compensates for the –2.25% droop in  $f_p$  from its predicted value.

---

<sup>85</sup>At each step the RF output power of the network analyzer is reduced by –2 dB, keeping the LNA output amplitude constant (at 1 V<sub>PP</sub>) so as to improve agreement between the measurement and calibration data sets by using the same internal amplifiers within the network analyzer.

<sup>86</sup>The discontinuities near 100 kHz reflect measurement artifacts in the calibration data set where the boundaries of the decades to either side are stitched together. Since they are not repeatable, as demonstrated by their absence at certain gains (e.g., 16 dB) they are attributed to the physical setup of the FR test bench and the vagaries of the directional coupler responsible for power division at the output of the network analyzer.

<sup>87</sup>Errors in the phase measurements of the Agilent 4395A result in discontinuities near 8 MHz which, like those of the magnitude response described by Footnote 86, are patently unphysical.

<sup>88</sup>The rise of the magnitude response near 10 MHz is an artifact of peaking in the OUTSE inamp, whose unity-gain bandwidth is just 1 MHz. Since only a single calibration data set is obtained (cf. Section 6.2.1.3), the success with which this OUTSE peaking is de-embedded varies at each gain setting as the LNA  $Z_{\text{out}}$  responsible for driving the OUTSE inamp changes along with  $Z_{\text{in}}$ . Similar impedance dependencies are evident at lower gains, particularly  $G_p = 0$  dB, where  $Z_{\text{out}}$  is well below the  $\sim 50 \Omega$  presented to OUTSE by the function generator in bypass mode.

In light of this behavior, later LNA characterization was performed with the Agilent 1141A in the configuration of Figure 6.5(a). But, since OUTSE was in use during the total-dose testing, it is appropriate that it be employed to gather the baseline data for comparison with the results of Section 6.4.2.1.

Examining the relationship between the inverse of the gain-programming resistance,  $R_d$ , and the achieved DC gain for each curve of Figure 6.13(a), Figure 6.14 plots the latter against the former, revealing an excellent linear fit. In fact, with a coefficient of determination ( $R^2$ ) that differs from unity by just -94.1 dB,<sup>89</sup> this regression indicates that the feedback provided by super emitter-followers of the first stage has not only reduced the nonlinearities of (4.4a) to the level of (4.7), but has satisfied the necessary conditions to further reduce the latter to the ideal form of (4.1) in which (to within a constant offset):<sup>90</sup>

$$G_p = \frac{R_l}{R_d} = \frac{46.104 \text{ k}\Omega}{R_d} \quad (6.13)$$

The tight adherence of the LNA programming curve to (6.13) confirms that the proposed circuit accurately realizes the gain as merely a ratio of resistors, rendering it independent of transistor parameters.

### 6.3.2.2 Linearity

Figure 6.15 presents spectral estimates obtained with the LN test bench when the LNA is programmed to a gain of 14 dB and supplied with nearly full-scale tones at 1 kHz and 5 kHz. At both frequencies, the SFDR is better than 90 dB,<sup>91</sup> and, as

---

<sup>89</sup>In this chapter, the goodness of fit for linear regressions of  $M$ -point data sets is assessed using the coefficient of determination, defined in terms of the observation values  $y_i$  and the fit, or modeled values,  $f_i$  as:

$$R^2 = 1 - \frac{\sum_{i=0}^M (y_i - f_i)^2}{\sum_{i=0}^M (y_i - \bar{y})^2}$$

As a ratio of the sum of the squares of the residual fitting errors to the sample variance, the fractional term can be interpreted as a measure of unexplained variance. Thus, as it tends to zero, confidence in the predictive ability of the selected regression model approaches certainty.

<sup>90</sup>Incidentally, the value of  $R_l = 46 \text{ k}\Omega$  inferred from the regression behind (6.13) indicates an absolute resistor tolerance of 8% that lies well within the 20% margin allocated during design. The design of biasing circuits that rely on RPD values (cf. Section 4.2.4) is thereby proven sufficiently conservative.

<sup>91</sup>In calculating the SFDR, the energy associated with 60 Hz pickup and its harmonics, clearly visible at the low-end of the spectrum, has been ignored.

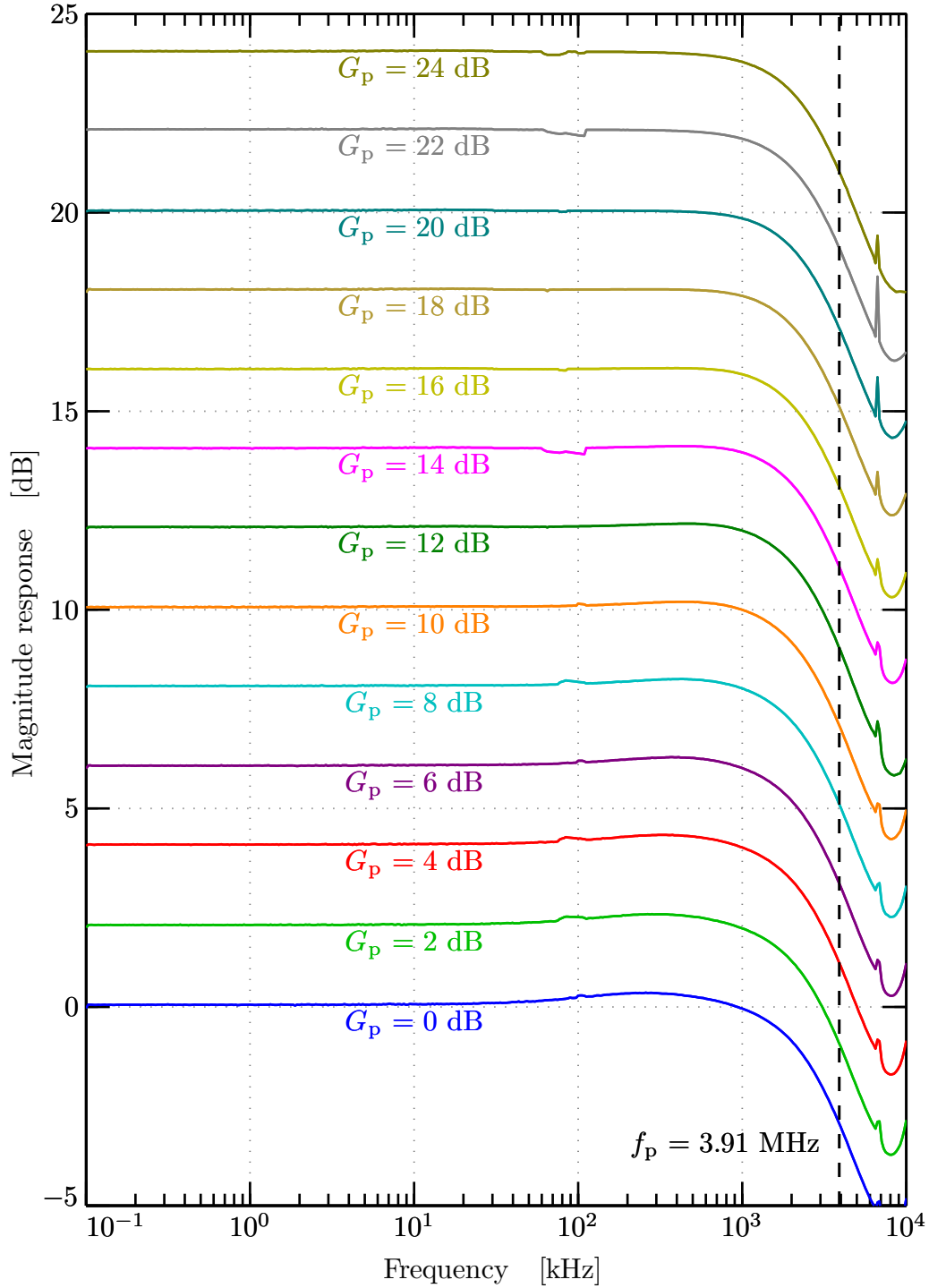
(a) Measured  $|T_{\text{dmbd}}^{\text{D}}(f)|$ .

Figure 6.13: (a) Measured magnitude of LNA Bode response for  $G_p$  programmed from 0 dB to 24 dB in 2 dB steps. Step size chosen arbitrarily.

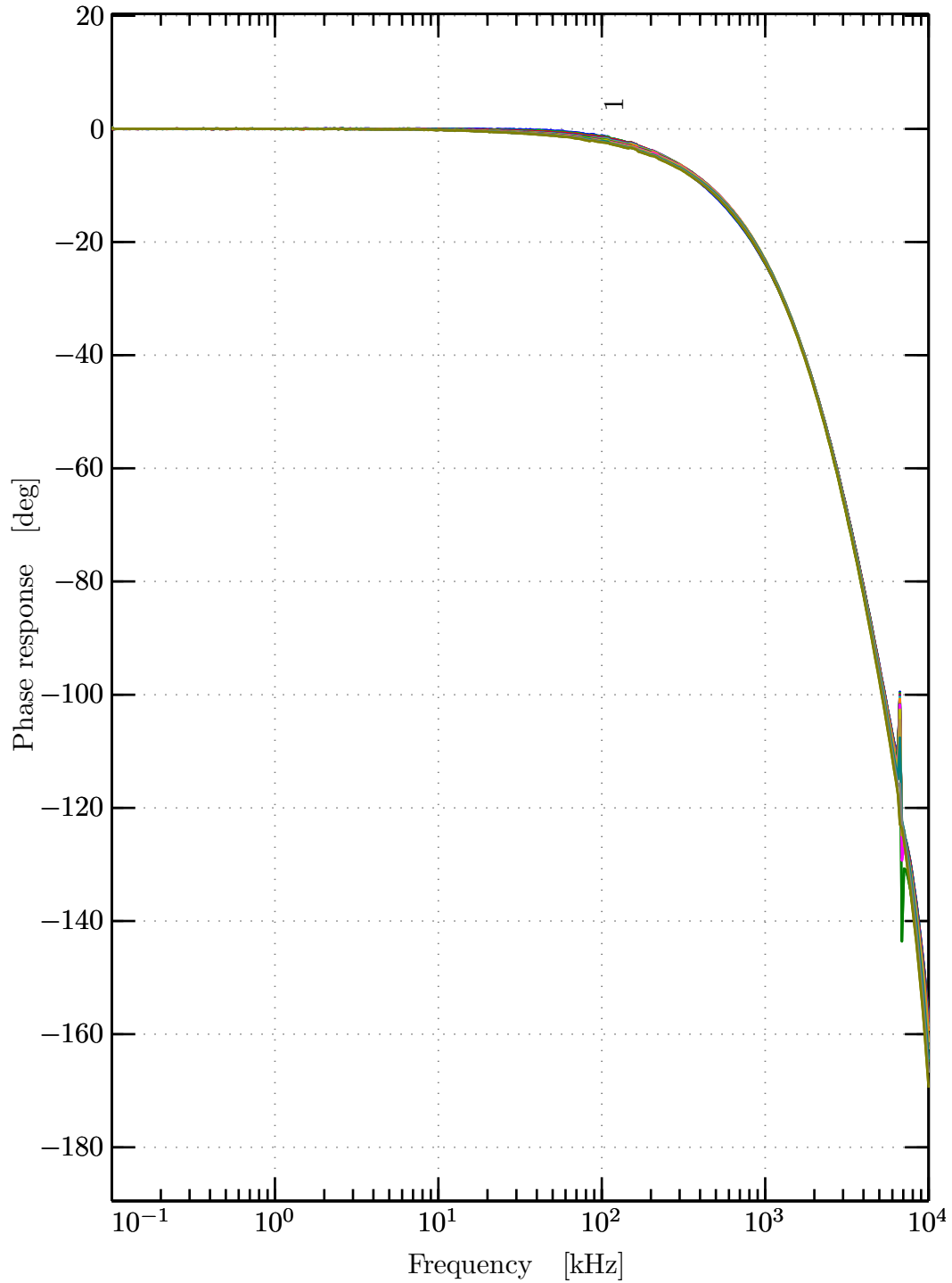
(b) Measured  $\angle T_{\text{dmbd}}^{\text{D}}(f)$ .

Figure 6.13: (b) Measured phase of LNA Bode response for  $G_{\text{p}}$  programmed from 0 dB to 24 dB in 2 dB steps. Consult Figure 6.13(a) for step sizes and color legend.

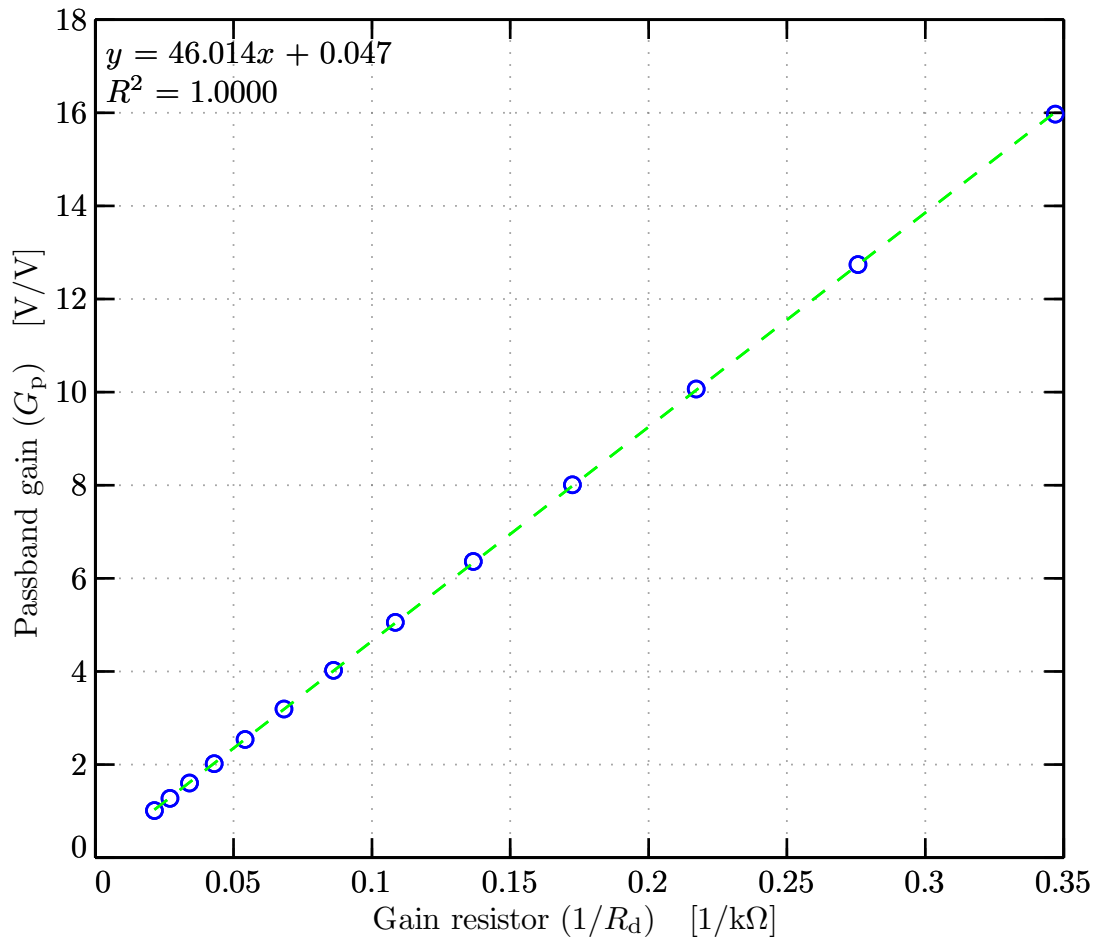


Figure 6.14: Measured LNA gain programming curve. For each of the gain steps in Figure 6.13, the measured  $G_p$  (blue circles) is plotted against the reciprocal of the corresponding measured  $R_d$  and the result fit to a linear regression (green line) in a least-squares sense.

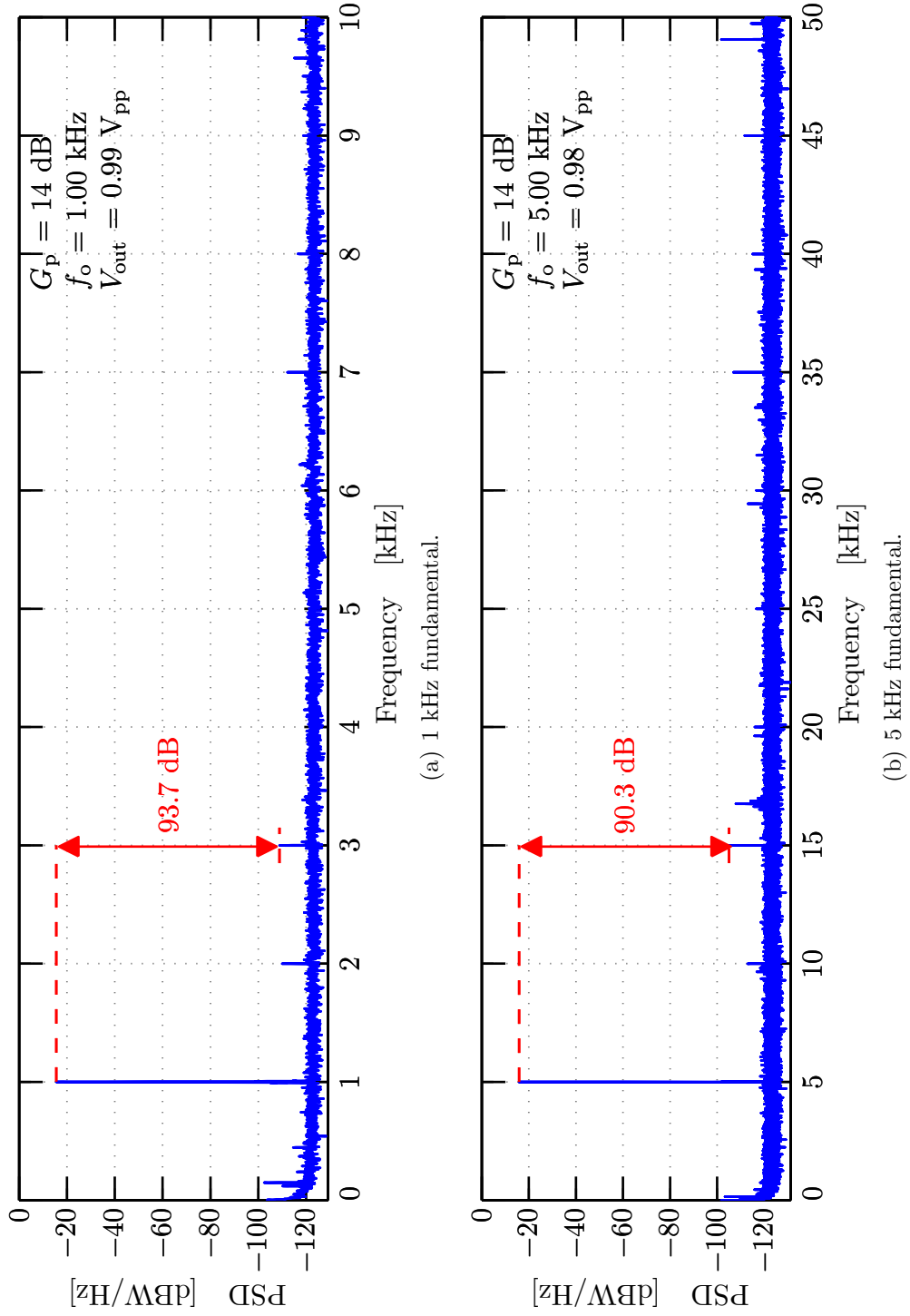


Figure 6.15: Measured LNA output PSD using (a) 1 kHz and (b) 5 kHz input tones. PSD estimator compiled from Welch-averaged,  $2^{17}$ -point modified periodograms (0.76 Hz/bin). Annotated SFDR computed over first ten harmonics.

expected, is dominated by the third harmonic, whose presence is attributed to the CB junction capacitances of the tail current sources (cf. Figure 4.21). Notably, layout techniques to improve matching between the differential halves of the circuit have succeeded in suppressing the 2<sup>nd</sup> harmonic below -100 dBc.<sup>92</sup> In fact, at 0.76 Hz/bin resolution, this distortion is nearly indistinguishable from the variety of environmental tones intermittently present in the laboratory environment.<sup>93</sup>

### 6.3.2.3 Noise

Using the noise measurement techniques of Section 6.2.3, the input-referred noise voltage of the LNA in Figure 6.16 is obtained. Not only is the average of this noise floor—and, therefore the mean of the true  $S_{\text{in}}(f)$ —below the specified equivalent of 300 nV/ $\sqrt{\text{Hz}}$  over the passband, but even its peak value only exceeds this limit on an occasional sample. The two most egregious exceptions are near the extremes: at 100 Hz, the effects of  $1/f$  noise, which are otherwise effectively suppressed throughout, begin to dominate whereas, at 1 MHz, artifacts related to the sparse data set from which the extrapolation is performed cause a rapid, unphysical rise (cf. Footnote 59).

Ignoring the latter for obvious reasons, it is evident that the effective  $f_K$  of the LNA approaches 200 Hz, thereby keeping its low-frequency  $S_{\text{in}}(f)$  flat over the passband, as desired. The minimal observed impact of the 1-MHz flicker corner of the constituent pMOS devices (cf. Figure 3.11) reflects the proper sizing of M1–M4 in Figure 4.8 and the shaping afforded by the large loop gain of (4.19).

### 6.3.2.4 Power Dissipation

The power dissipation of the LNA (not pictured) exhibits negligible variation over the course of the programming performed when generating Figure 6.13, remaining

---

<sup>92</sup>Here, harmonic amplitudes are measured relative to that of the fundamental. Borrowing from RF literature, where the fundamental is known as the carrier frequency, these measurements are in units of dB relative to the carrier, or dBc.

<sup>93</sup>Despite the use of  $\mu$ -metal shielding during much of the testing, such pick-up cannot be completely suppressed. However, variations in the frequency and amplitude of the various coherent interferers present in these spectra reflect the ephemeral character of such signals in the data records and attest to their extrinsic origins.



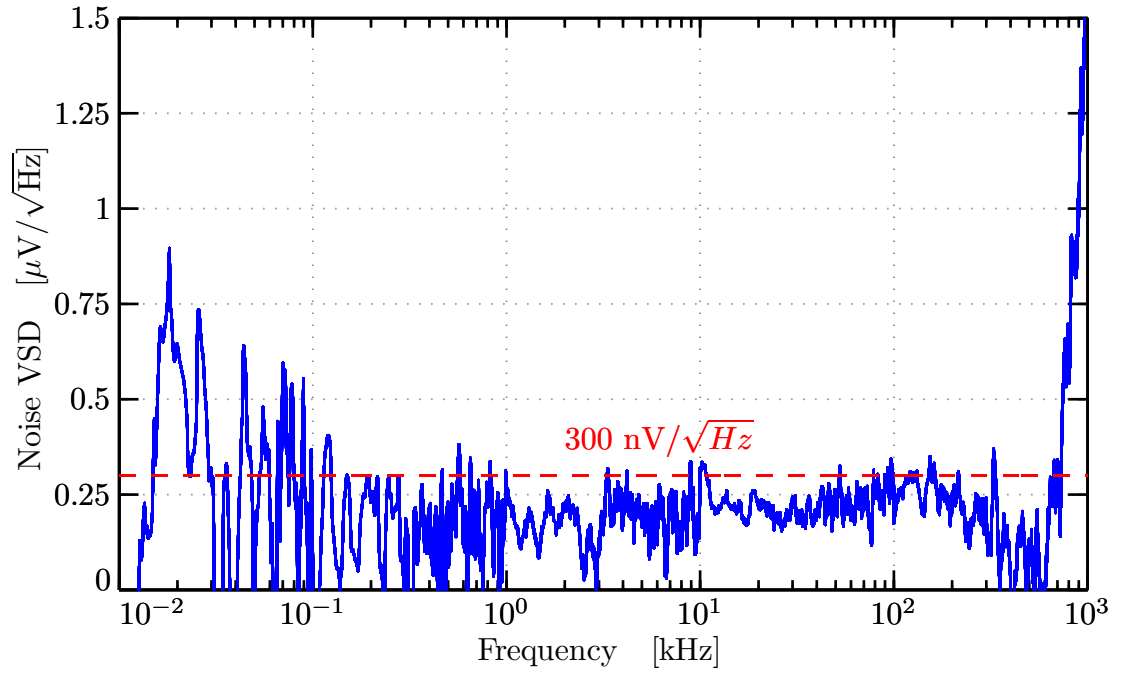


Figure 6.16: Measured LNA input-referred noise, converted to voltage spectral density to facilitate comparison with the specified limit of  $300 \text{ nV}/\sqrt{\text{Hz}}$ . Obtained using methodology of the NS test bench with LNA programmed to  $G_p = 14 \text{ dB}$ .

between 1.783 and 1.785 mW throughout.<sup>94</sup> Not only is this absolute level sufficient for plasma wave receiver applications,<sup>95</sup> its independence from  $G_p$  is attractive for robust but configurable sensor systems in general.

### 6.3.3 AAF Results

In the following, measurements of each of the AAF performance metrics of Table 3.2 are grouped by test bench. The results for all three bandwidth programming modes are included.<sup>96</sup>

#### 6.3.3.1 Bode Response

In Figure 6.17 and Figure 6.18, the Bode response of the AAF is shown to tightly follow that predicted in previous chapters. Along with the magnitude(phase) of  $T_{\text{meas}}(f)$ , measured according to the procedures of Section 6.2.1, the panels of Figure 6.17(Figure 6.18), which portray magnifications of the passband (Subpanel 1) and transition band (Subpanel 2) alongside the full response in each bandwidth mode, include the following data:

##### *Ideal*

Predicted filter approximation using infinitely precise values of the components in (5.16). This trace conveniently echoes that of Figure 5.3, produced via MATLAB simulation with the coefficients of (5.7) from the corresponding column of Table 5.2.

##### *Realizable*

Predicted filter approximation using the discretized component values in Table 5.2, which allow the filter to be realized with unit-cell transconductors and capacitors. This trace conveniently echoes that of Figure 5.14, produced via

---

<sup>94</sup>With no trend to these minor variations, they are presumed to merely reflect thermal fluctuation, measurement error, and other random processes.

<sup>95</sup>Even with the variations of the AAF power dissipation in Figure 6.35, the total remains below the 50 mW limit under all measured conditions.

<sup>96</sup>This luxury is not permissible when the size of the corresponding data sets from each test bench swells over the range of radiation conditions in Section 6.4.3.

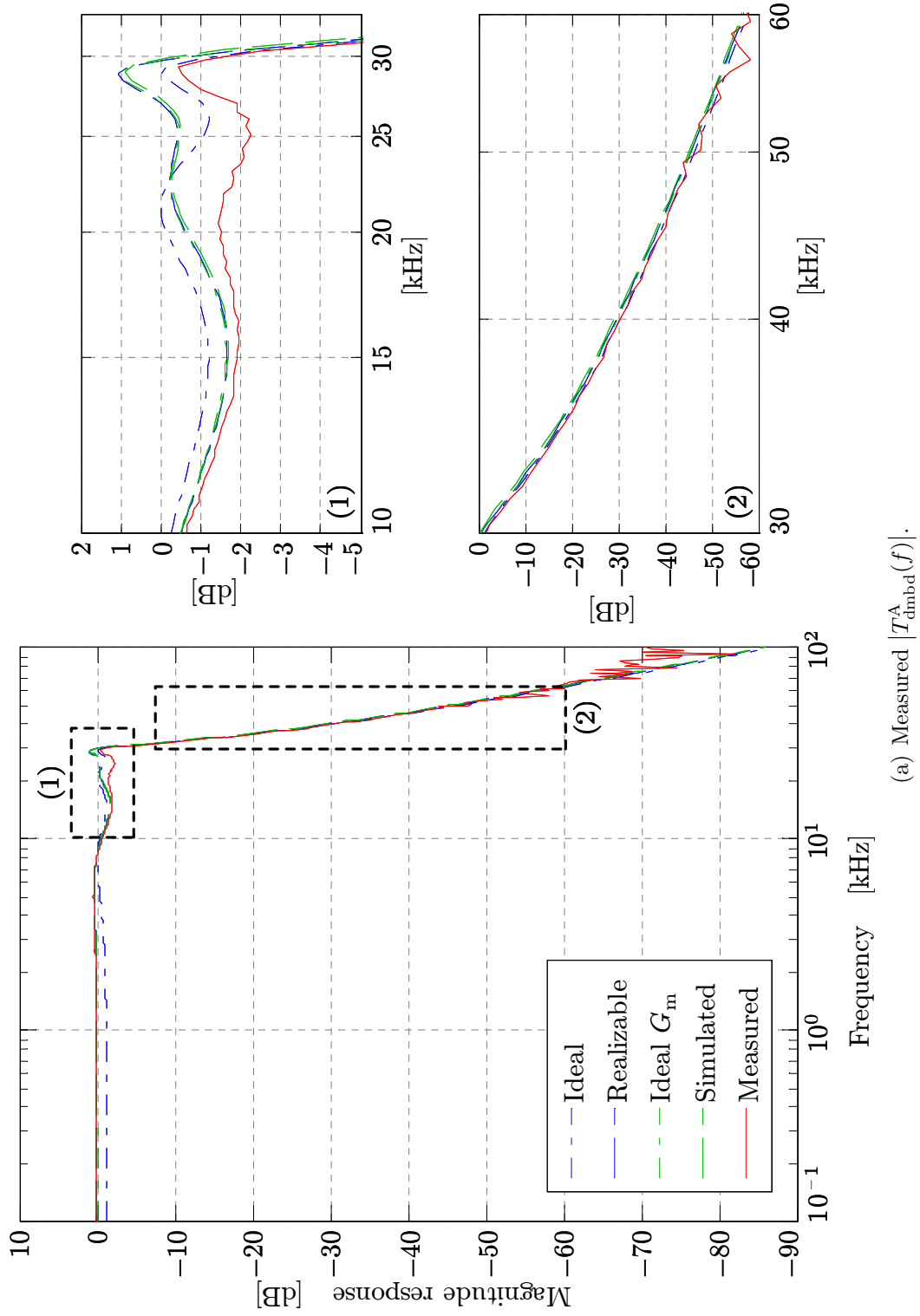


Figure 6.17: (a) Predicted and measured magnitude of AAF Bode response in Mode A. Subpanels magnify passband and transition band. For origins of prediction curves, refer to Section 6.3.3.1.

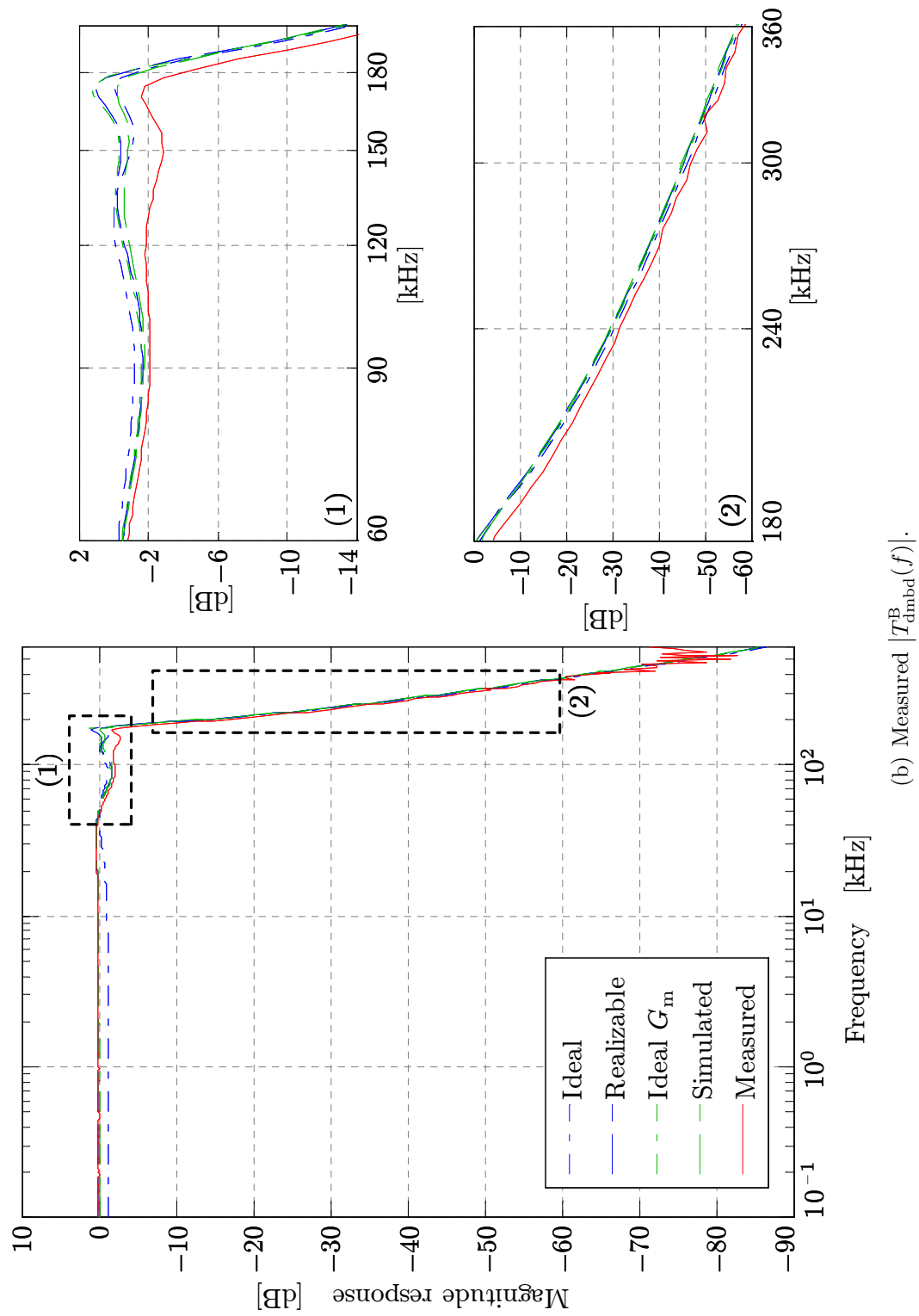


Figure 6.17: (b) Predicted and measured magnitude of AAF Bode response in Mode B. Subpanels magnify passband and transition band. For origins of prediction curves, refer to Section 6.3.3.1.

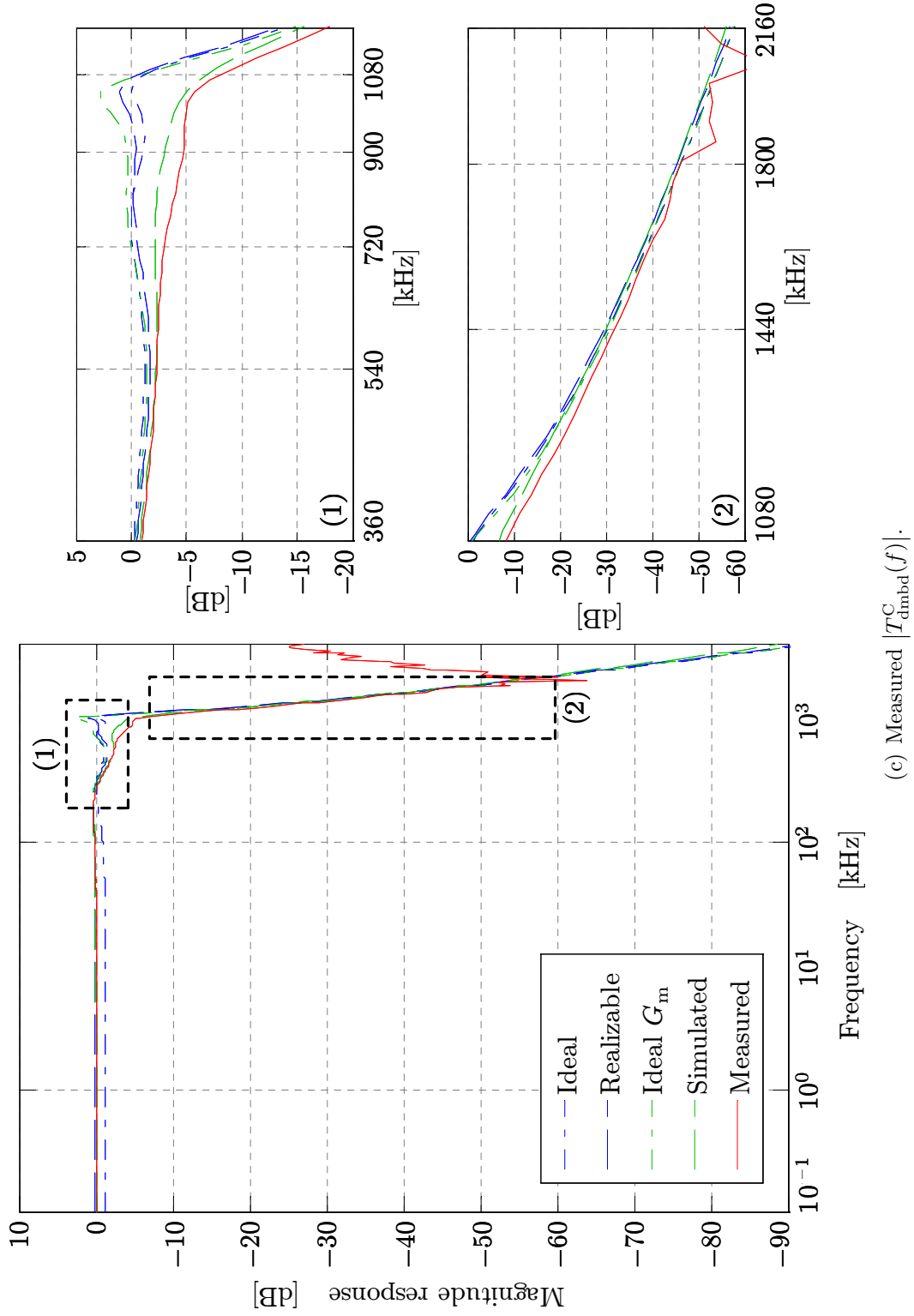


Figure 6.17: (c) Predicted and measured magnitude of AAF Bode response in Mode C. Subpanels magnify passband and transition band. For origins of prediction curves, refer to Section 6.3.3.1.

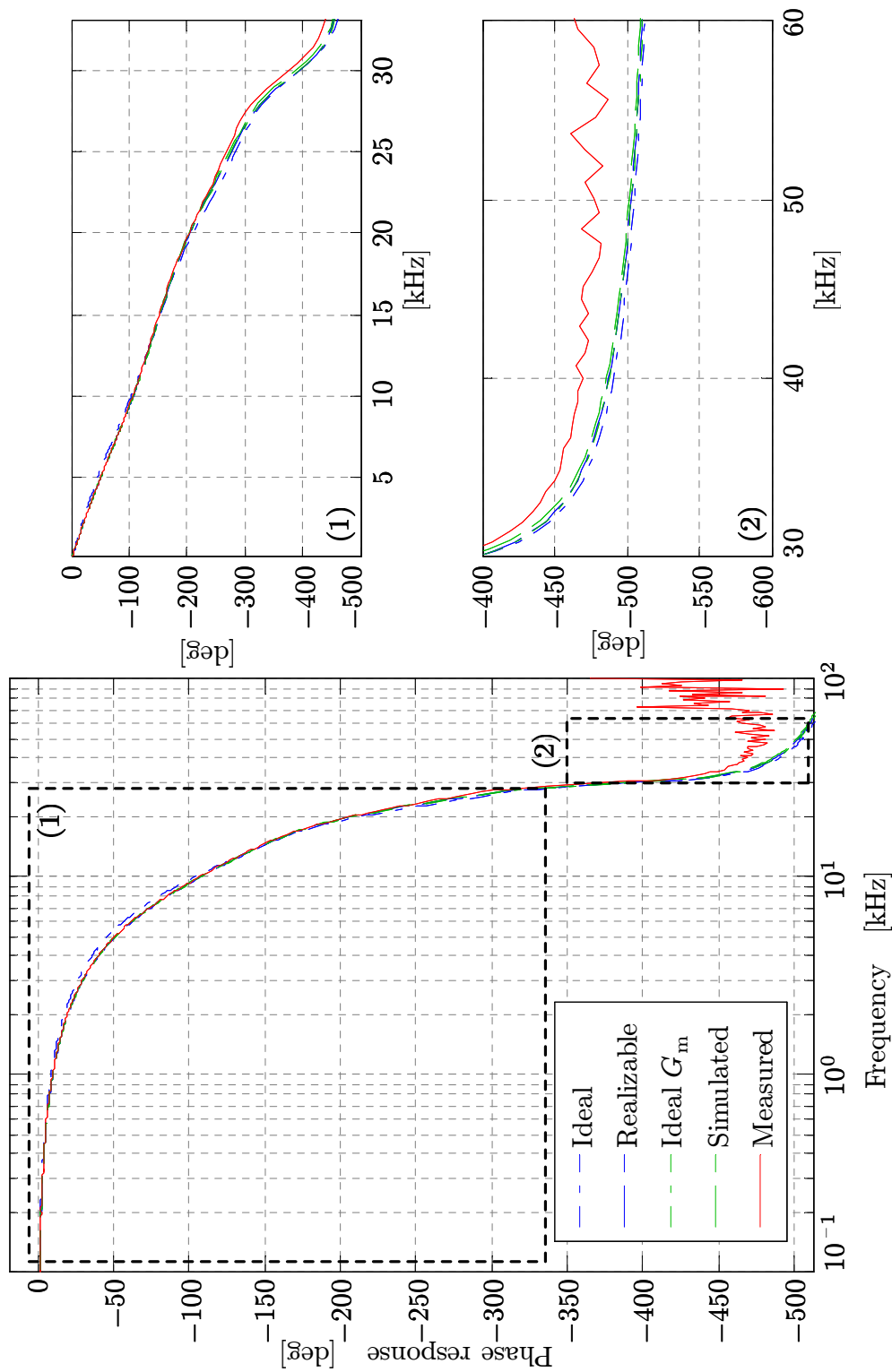
(a) Measured  $\angle T_{\text{dmbd}}^A(f)$ .

Figure 6.18: (a) Predicted and measured phase of AAF Bode response in Mode A. Subpanels magnify passband and transition band. For origins of prediction curves, refer to Section 6.3.3.1.

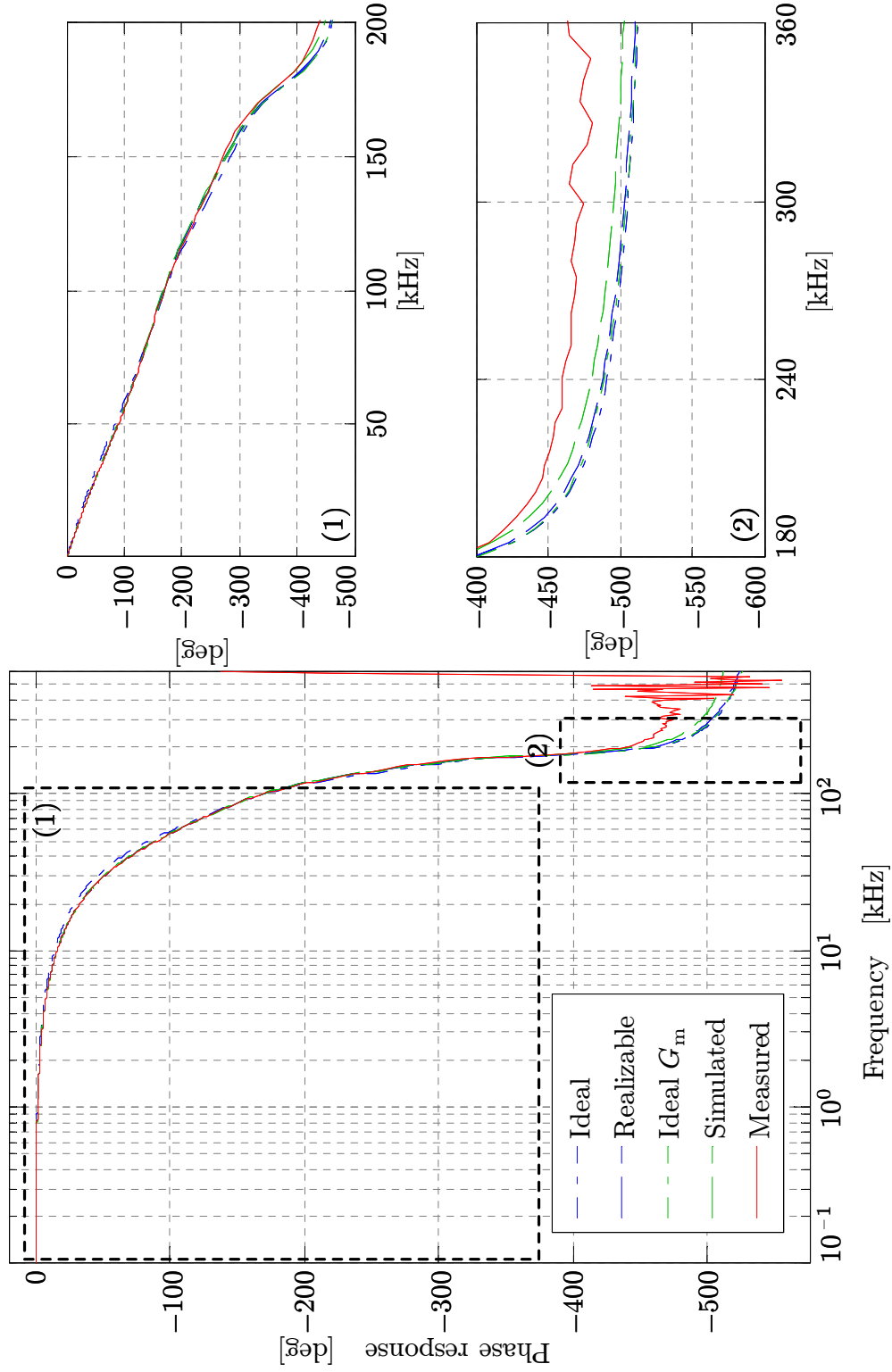
(b) Measured  $\angle T_{\text{dmbd}}^B(f)$ .

Figure 6.18: (b) Predicted and measured phase of AAF Bode response in Mode B. Subpanels magnify passband and transition band. For origins of prediction curves, refer to Section 6.3.3.1.

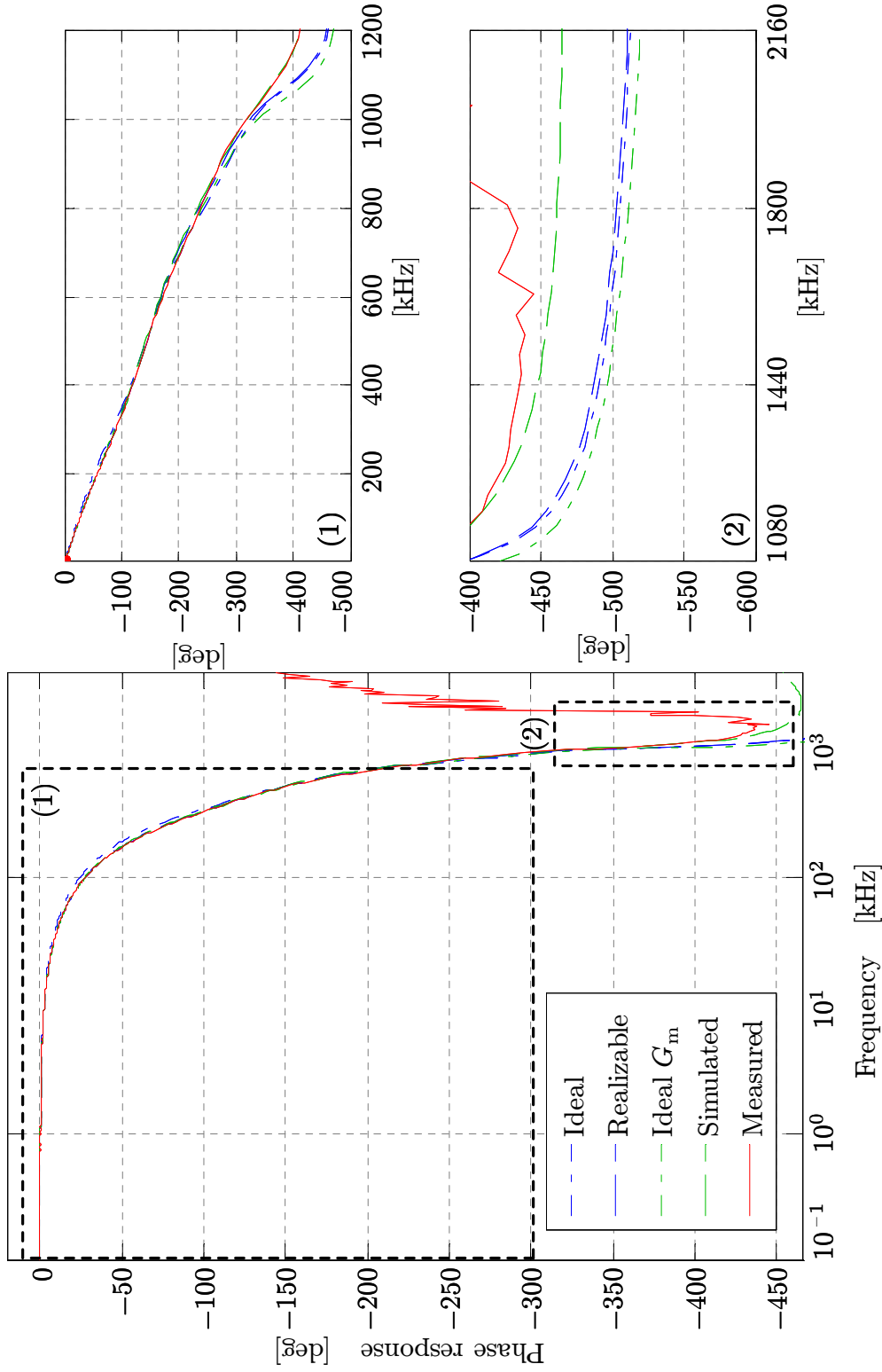
(c) Measured  $\angle T_{\text{dmbd}}^C(f)$ .

Figure 6.18: (c) Predicted and measured phase of AAF Bode response in Mode C. Subpanels magnify passband and transition band. For origins of prediction curves, refer to Section 6.3.3.1.



MATLAB simulation with the coefficients of (5.7) in the corresponding column of Table 5.2.

#### *Ideal $G_m$*

Predicted filter approximation using models of the actual capacitors and opamps but ideal transconductors to implement the stage architecture of Figure 5.13(b). This trace is generated via the SPECTRE circuit simulator with the capacitors and transconductors of each stage sized using the realizable values in Table 5.2.

#### *Simulated*

Predicted filter approximation from a full-chip simulation of SVEPRE-3 using the SPECTRE circuit simulator.

In all three modes, the magnitude response exhibits excellent agreement with the predicted curves. Although the suppressed peaking near the edge of passband evidences the impact of layout and PCB parasitics in all modes,<sup>97</sup> this has no impact on the all-important  $r_\alpha$ , which is shown in the transition band subpanels to closely track the ideal roll-off.<sup>98</sup> Thus, the fabricated AAF provides the expected degree of anti-aliasing.

Peak suppression is most evident in the simulated and measured magnitude responses for Mode C (see Subpanel 1 of Figure 6.17(c)): at high frequencies, the excess phase of the transconductors precludes the high  $Q$  required in Stage 3. To match the realizable peak profile when using ideal transconductors, the bandwidth of the design in Section 5.4, which is currently limited to 12 MHz by the zero formed across  $R_g$ , must be enhanced. However, the existent behavior—as opposed to  $Q$ -enhancement, which threatens stability—can easily be incorporated into the instrument calibration.

---

<sup>97</sup>Particularly influential is the parasitic capacitance incurred at the input and output nodes of each filter opamp, which is enhanced by making these available on test pads for debugging purposes (see the OutX+ and OutX− pins of Figure 6.2).

<sup>98</sup>No special care is taken during testing to tune the filter cut-off frequencies to match those of simulation. Thus, since the Bode responses of Figure 6.17 are not normalized, absolute differences related to the location of the measured  $f_p$  are evident, though not salient. For reference, the measured baseline values of  $f_{pa}$ ,  $f_{pb}$ , and  $f_{pc}$  are 30.53 kHz, 181.56 kHz, and 552.44 kHz, respectively.

Note that the dynamic range of the network analyzer and high-frequency phase errors observed throughout characterization (cf. Footnote 87)<sup>99</sup> render it only possible to confirm  $r_\alpha$  up to 60-dB attenuation. However, the all-pole response of the chosen approximation (cf. Section 5.1.1) guarantees that there are no stopband zeros to comprise  $r_\alpha$  beyond this point, which serves as a proxy for  $f_r$  and is denoted  $f_n$  hereafter.

Despite limited accuracy of the phase measurements in the transition band due to the large drop associated with a 6<sup>th</sup>-order design and the instrument limitations of Footnote 87, Subpanel 1 of Figure 6.18 exhibits strong accord between the linearity of the predicted and measured passband phase in all modes.

### 6.3.3.2 Trimming

In lieu of laser trimming or digital tuning, whose attendant cost and complexity are eschewed, Figure 6.14 demonstrates that in all three modes the AAF cut-off can be accurately trimmed in the field through a single off-chip resistor.<sup>100</sup> Over a range corresponding to  $30 \mu\text{A} \leq I_E \leq 50 \mu\text{A}$ ,<sup>101</sup>  $f_{pa}$ ,  $f_{pb}$ , and  $f_{pc}$  can each be trimmed by  $\pm 25\%$  around their nominal values of Table 3.2, which is more than sufficient to cover  $f_p$ -variations due to process tolerance, temperature, and radiation-induced degradation [Acosta *et al.*, 2009, p.2148].<sup>102</sup>

The traversal of this wide trimming range exhibits a highly linear dependence on  $I_E$ , just as for the programming of  $G_p$  in Figure 6.14, as is evidenced in the analogous regression plots of  $f_{pa}$ ,  $f_{pb}$ , and  $f_{pc}$  versus  $I_E$  in Figure 6.20. Once again, in all modes the near-unity  $R^2$  affirms the precise realization of the ideal trimming relationship, given for the AAF by the gain expression for the GGC in (5.47).<sup>103</sup>

<sup>99</sup>Mirroring the attribution of Bode artifacts in the LNA response to the peaking of OUTSE (cf. Footnote 88), the unphysical rise near the same frequency in the measured magnitude response of Mode C in Figure 6.17(c) should not be confused with the actual AAF performance.

<sup>100</sup>The corresponding phase responses are omitted for brevity, but each demonstrates a similar trend: field-trimming via  $I_E$  produces only a lateral shift, with no material deviation in the shape of the curve. Hence, the phase behavior with trimming is readily inferred from Figure 6.18 by analogy to Figure 6.20.

<sup>101</sup>The corresponding values of the off-chip resistor range from 21.9 k $\Omega$  to 36.4 k $\Omega$ .

<sup>102</sup>The latter of these is minimal, as shown in Section 6.4.3.

<sup>103</sup>That  $R^2$  is lowest in Mode C is unsurprising given the difficulty in accurately measuring  $f_{pc}$  due

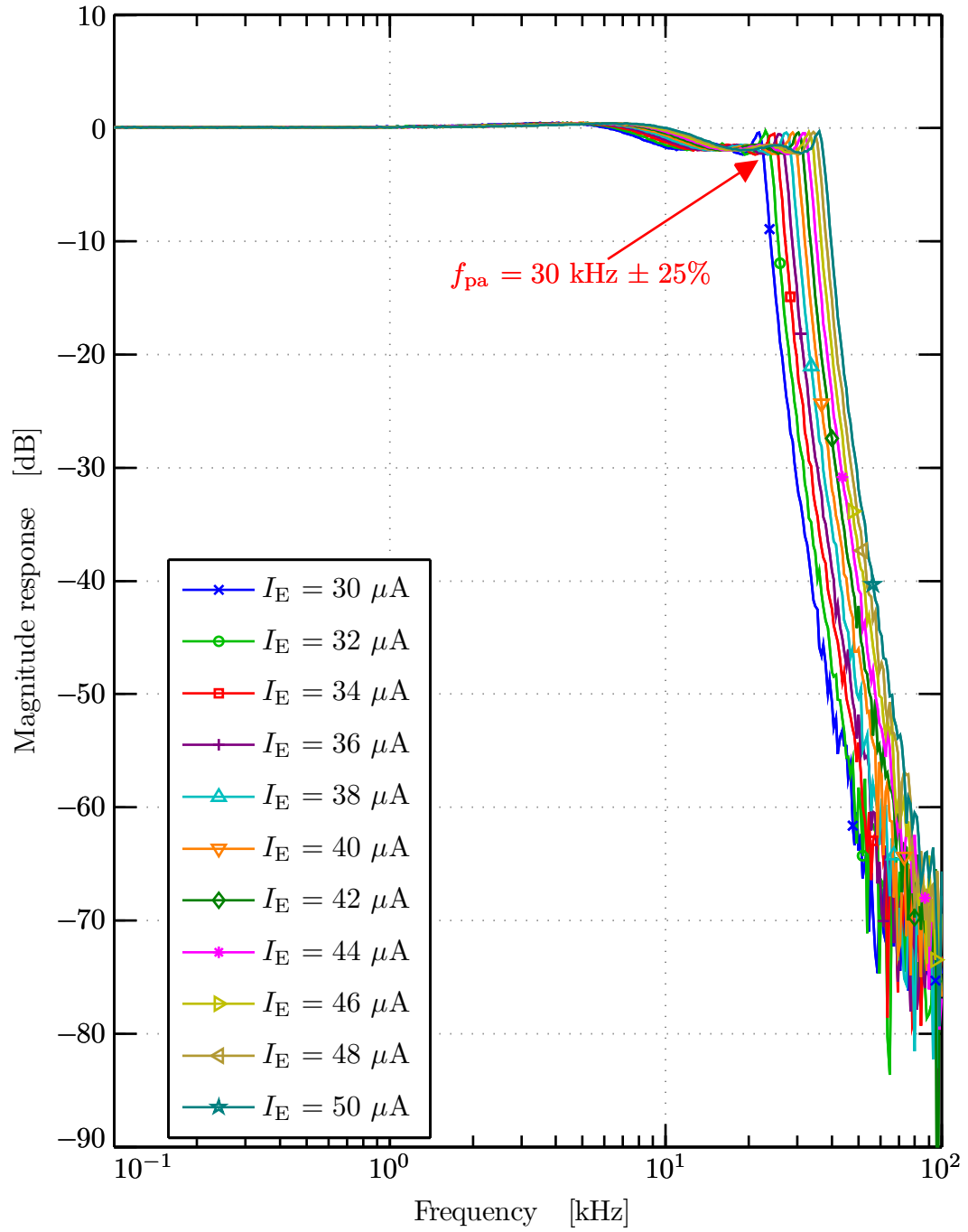
(a) Measured  $|T_{\text{dmbd}}^A(f)|$ .

Figure 6.19: (a) Measured magnitude of AAF Bode response in Mode A when trimmed over  $f_{pa} \pm 25\%$  range via  $I_E$ .

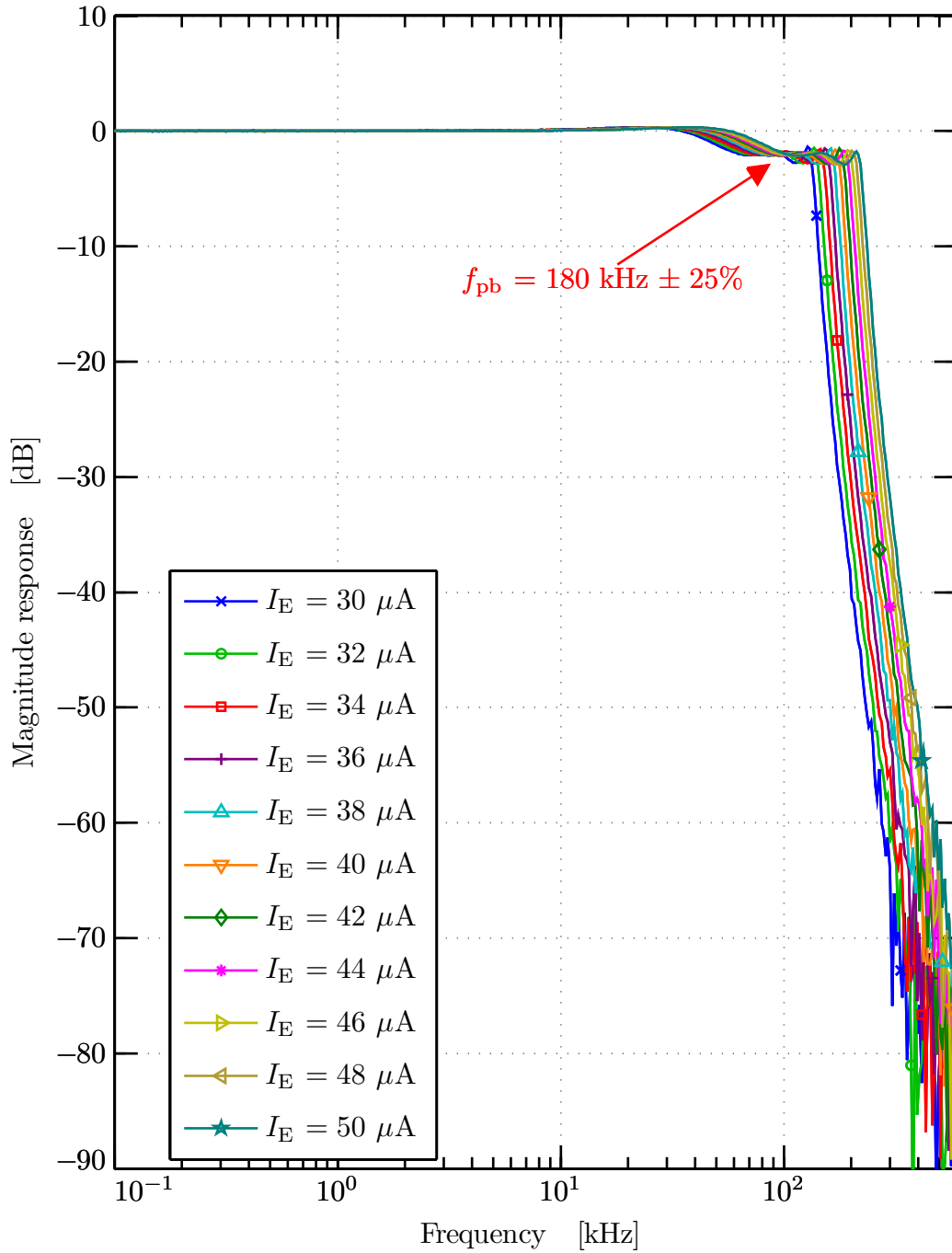
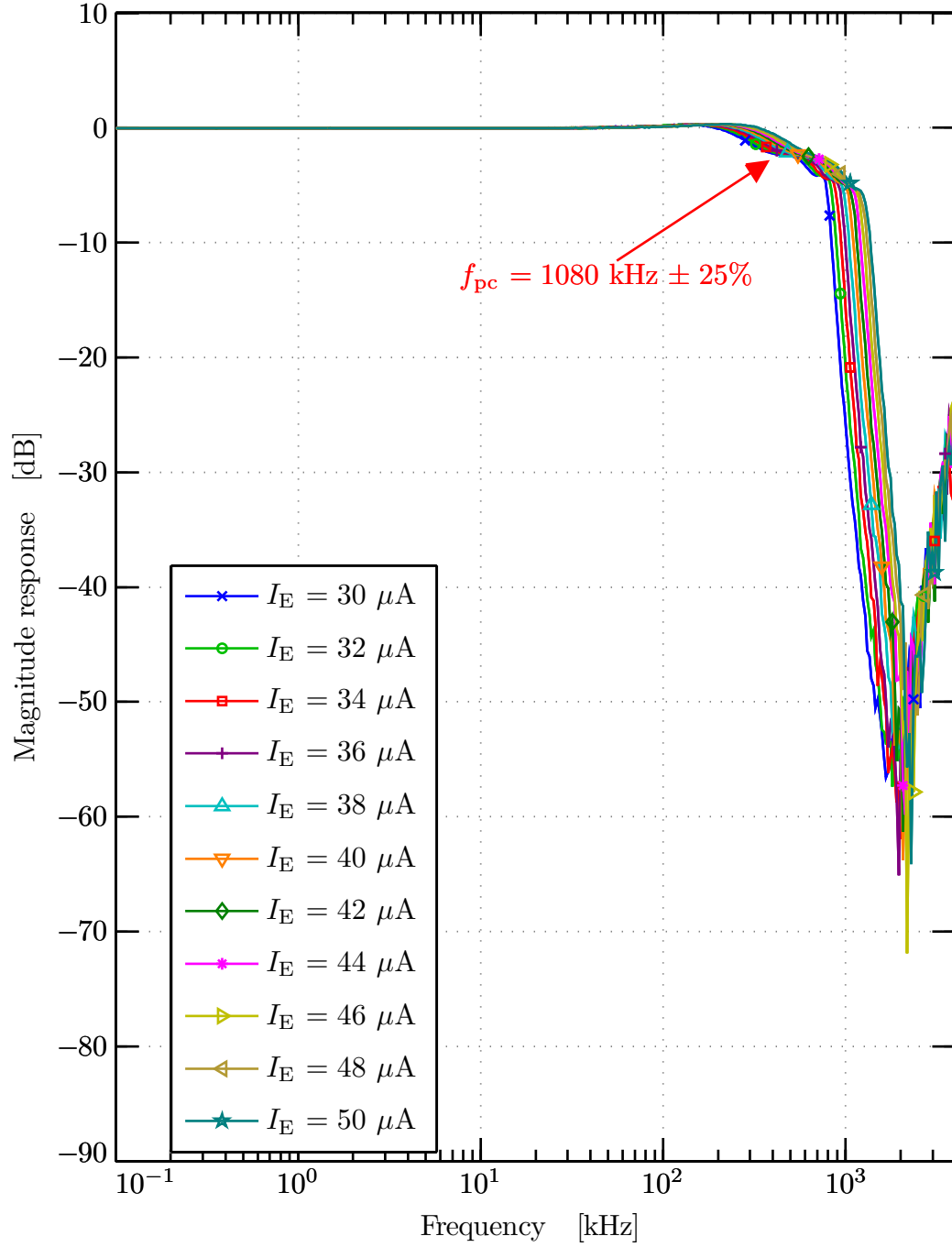
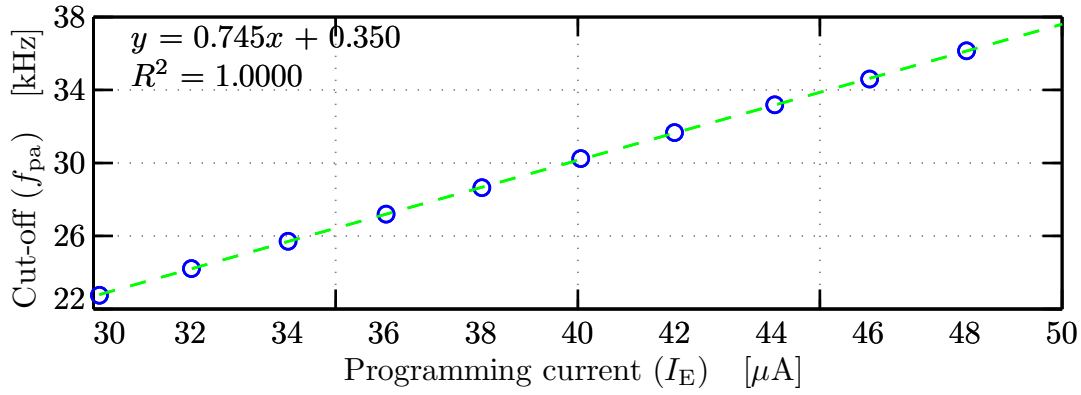
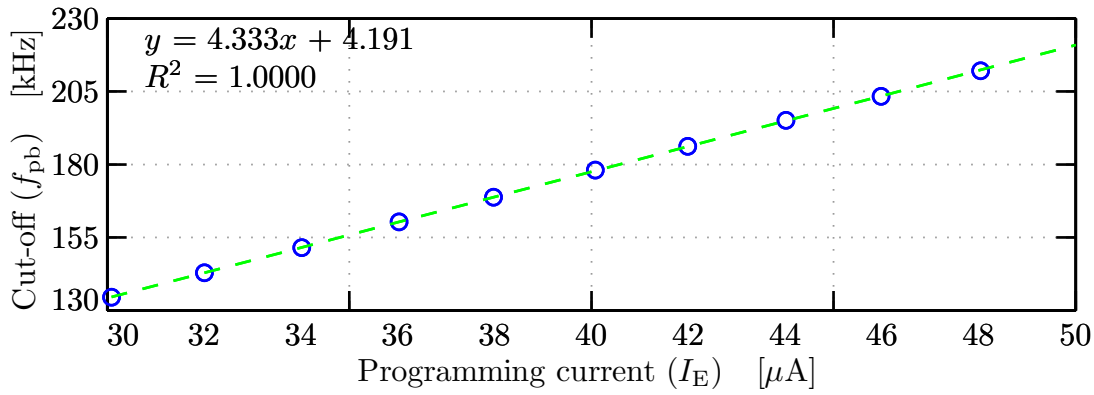
(b) Measured  $|T_{\text{dmbd}}^{\text{B}}(f)|$ .

Figure 6.19: (b) Measured magnitude of AAF Bode response in Mode B when trimmed over  $f_{pb} \pm 25\%$  range via  $I_E$ .

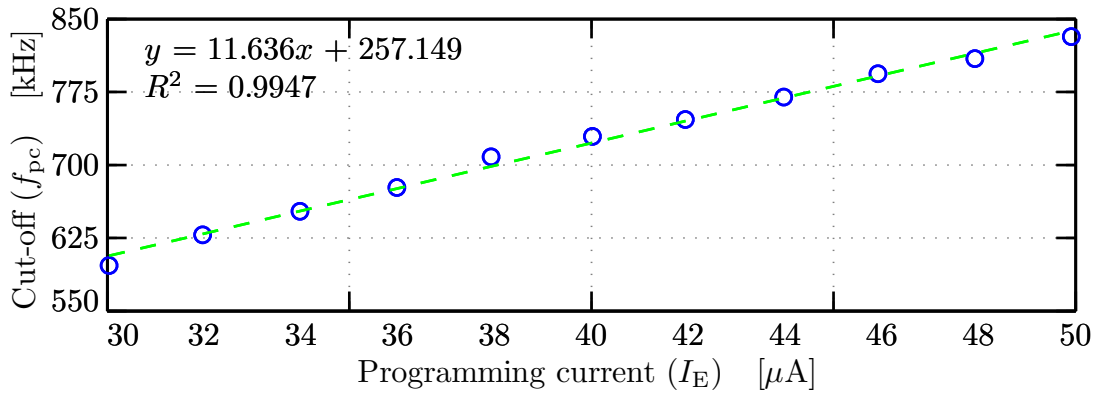
(c) Measured  $|T_{\text{dmbd}}^C(f)|$ .Figure 6.19: (c) Measured magnitude of AAF Bode response in Mode C when trimmed over  $f_{pc} \pm 25\%$  range via  $I_E$ .



(a) Mode A.



(b) Mode B.



(c) Mode C.

Figure 6.20: Measured AAF bandwidth trimming curve for (a) Mode A, (b) Mode B, and (c) Mode C. For each, the measured  $f_p$  (blue circles) is plotted against the corresponding measured  $I_E$  and the result fit to a linear regression (green line) in a least-squares sense.

### 6.3.3.3 Linearity

To assess the linearity of the transconductor, Figure 6.21 and Figure 6.22 present measured spectral estimates at the output of Stage 1 of the AAF for each bandwidth mode using an over-ranging tone at 1 kHz and 10 kHz, respectively.<sup>104,105</sup> In all cases the second harmonic clearly exceeds the third, limiting the SFDR.

This phenomenon reflects the fact that the GGC degeneration resistors described in Section 5.5.2.2 were not included on SVEPRE-3; due to inaccurate modeling of the  $\sigma^2\{\Delta V_{BE}\}$  described by (5.62), the inherent npn mismatch of the process was underestimated during the design phase. Therefore, the transconductors suffer from the even-order distortion that accompanies the  $\Delta V_{BE}$ -mismatch of the GGC halves illustrated in Figure 5.28(b). When aggregated over all the unit transconductors and then accumulated across each stage, the resulting  $V_{os}$  (cf. Equation (5.38)) of the inner (Q3–Q8) and outer (Q1–Q2) GGC pair in Figure 5.36 yields an input-referred offset observed as large as  $\sim 300$  mV in practice.<sup>106</sup> The concomitant imbalance of the overall filter outputs corrupts the spectrum of their signal, leaving the transconductor linearity best assayed at the output of Stage 1.<sup>107</sup>

Upon empirical determination of this severe device mismatch, a version of SVEPRE was fabricated whose transconductors incorporate the GGC degeneration resistors and, thus, benefit from the 24(14)-dB improvement of 2<sup>nd</sup>(3<sup>rd</sup>) harmonic amplitude depicted in the Monte Carlo histograms of Figure 5.39 (cf. Section 7.3). But, for the remainder of this chapter, discussions of transconductor linearity are restricted to the odd-order SFDR as determined by the 3<sup>rd</sup> harmonic and defined by

---

to the high-frequency instrument and PCB limitations described by Footnote 87 and Footnote 88, respectively.

<sup>104</sup>An explanation of the circumstances inhibiting high-frequency linearity testing at 100 kHz, is provided in Footnote 32.

<sup>105</sup>In the case of the 10-kHz tone in Mode A, maximum linearity is observed at an amplitude just below full-scale, as pictured, because the spectrum is infiltrated by large interferers near each harmonic that impair the ability to accurately measure the latter.

<sup>106</sup>For the unity-gain stages of the AAF and the near-unity transconductance ratios within each stage (cf. Table 5.2), the Friis equation does little to mitigate the DC offsets of each transconductor when referred to the overall filter input.

<sup>107</sup>Hereafter, AAF spectral estimates and quantities derived from them are measured in this fashion.

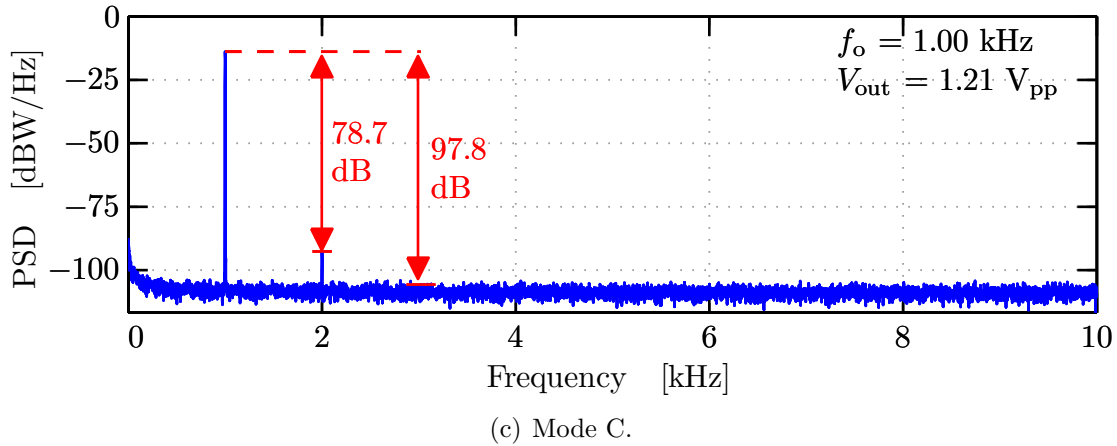
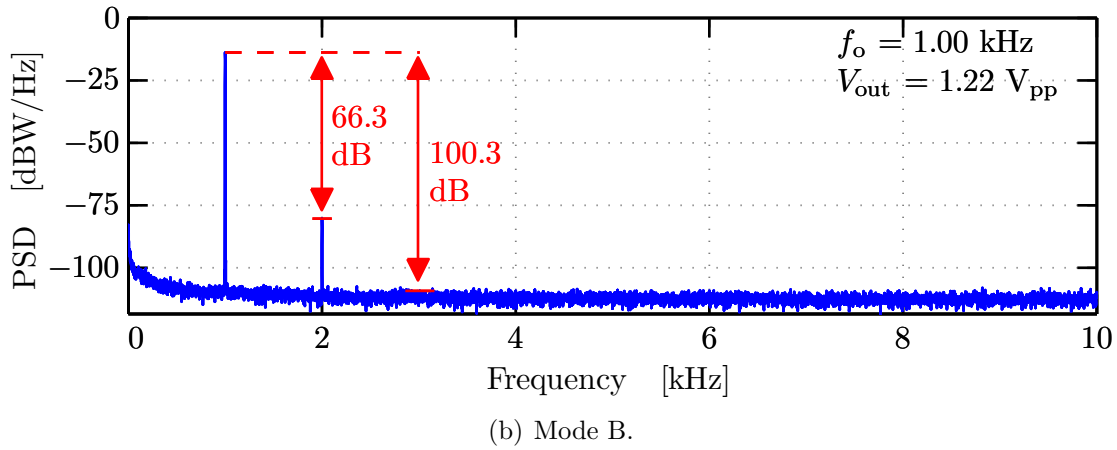
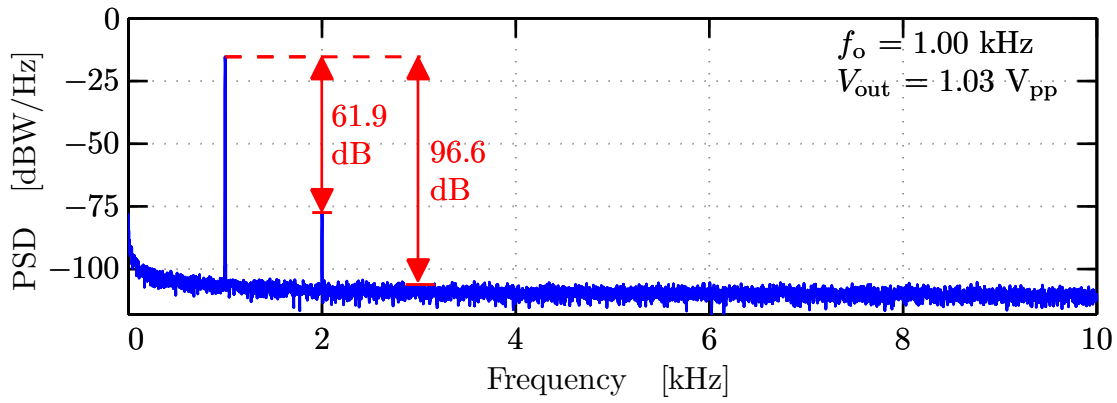
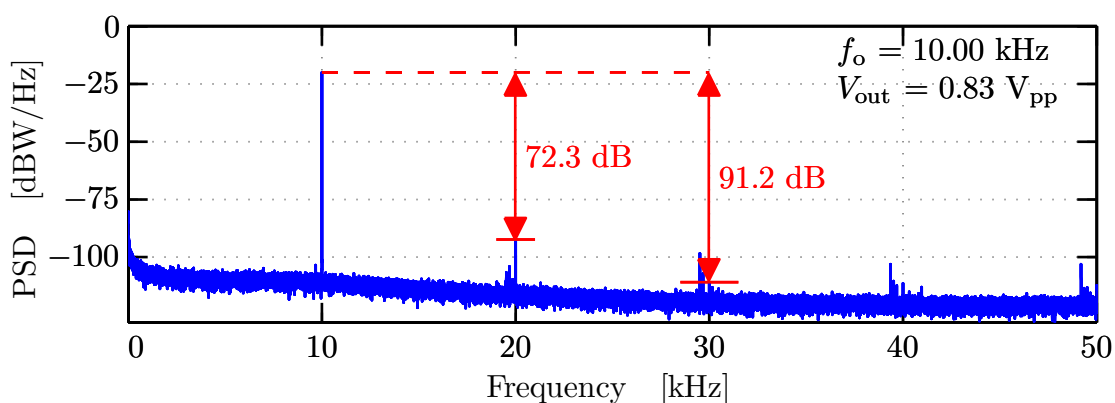
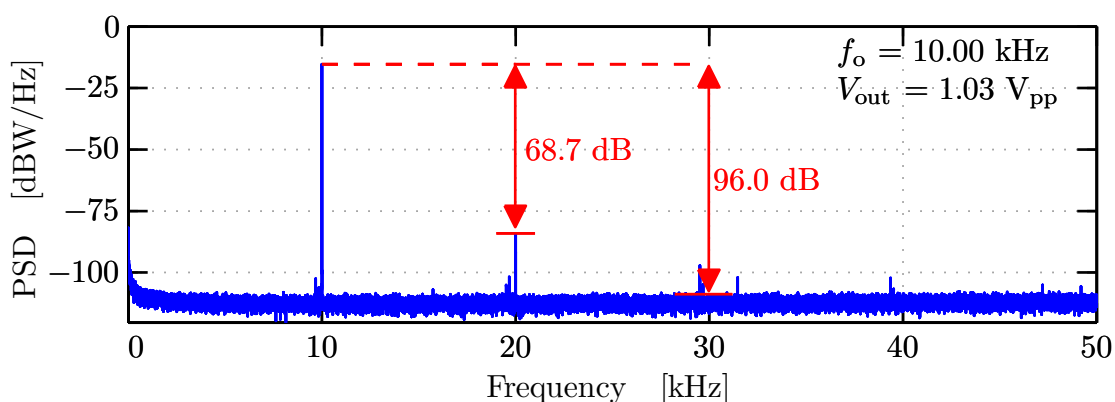


Figure 6.21: Measured AAF Stage 1 PSD for (a) Mode A, (b), Mode B, and (c) Mode C using a 1-kHz input tone. PSD estimator compiled from Welch-averaged,  $2^{17}$ -point modified periodograms (0.76 Hz/bin). Annotated SFDR computed over first ten harmonics.

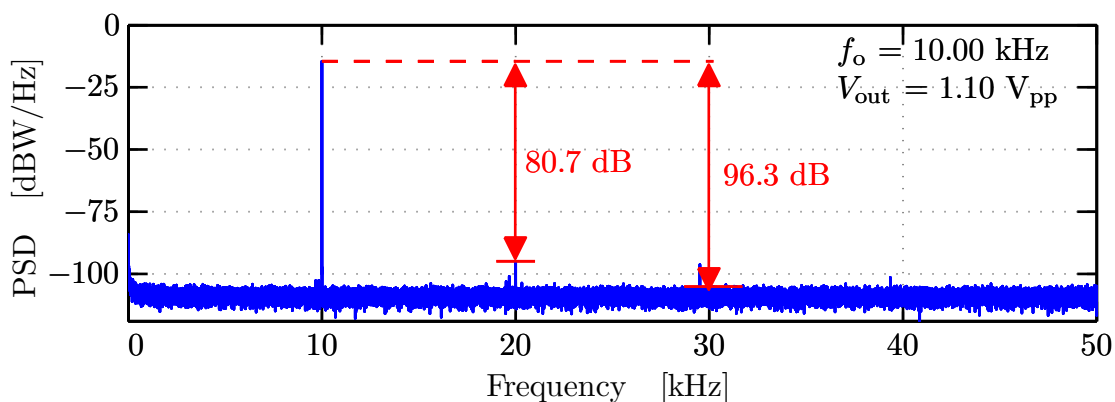




(a) Mode A.



(b) Mode B.



(c) Mode C.

Figure 6.22: Measured AAF Stage 1 PSD for (a) Mode A, (b), Mode B, and (c) Mode C using a 10-kHz input tone. PSD estimator compiled from Welch-averaged,  $2^{17}$ -point modified periodograms (0.76 Hz/bin). Annotated SFDR computed over first five harmonics.

analogy to (3.7) as:

$$\text{SFDR}_3 = 10 \log_{10} \left( \frac{|Y(f_o)|^2}{|Y(3f_o)|^2} \right) \quad (6.14)$$

Accordingly, it is evident that the 3<sup>rd</sup> harmonic remains better than 96 dB below the level of a 1(10) kHz fundamental in all bandwidth modes.<sup>108</sup> Thus, the translinear positive-feedback principles and  $J_e$ -matching exercised in the design of the first and second stage of the transconductor, respectively (cf. Section 5.5.1 and Section 5.5.2), yield the target large-signal, odd-order linearity. Furthermore, when the offset abatement conferred by GGC degeneration resistors is applied to the measured levels of the second-order distortion products in Figure 6.21 and Figure 6.22, these spectra confirm that the 90-dB SFDR specification can be attained.

#### 6.3.3.4 Power Dissipation

The average power dissipation of the AAF (not pictured), is measured at 36.7 mW, 38.8 mW, and 48.1 mW, in Mode A, Mode B, and Mode C, respectively, demonstrating two facets of the power-efficient filter design. First, though the difference between  $f_{pa}$  and  $f_{pc}$  represents a factor of  $36\times$  increase in the filter cut-off, it is accompanied by only a  $1.25\times$  increase in the power consumed. This scaling is a direct result of confining the mode-dependent bias currents to the inner GGC devices, decoupling the bulk of the static power load of the transconductor from the programmed value of its transconductance.

Secondly, for the 6<sup>th</sup>-order Type I Chebyshev approximation implemented on SVEPRE-3, the corresponding power per pole—a common figure-of-merit for integrated filters—ranges from 6–8 mW. This compares very favorably to highly linear ICT filters of the past two decades, whose THD (cf. Footnote 23 of Chapter 3) rarely exceeds 80 dB, despite consuming 4–157 mW/pole [Acosta *et al.*, 2009, p.2156].

Not only does the absolute power dissipation exhibit minimal dependence on the programmed cut-off, but the  $I_E$ -based field-trimming ensures that it does not

---

<sup>108</sup>The presence of non-harmonic spurs near the third-harmonic of Figure 6.22 limit its measured amplitude to just  $-91.2$  dBc. But, as noted in Footnote 105, this case is somewhat anomalous and, even if artificially inflated, this degree of third-order distortion still achieves the 90-dB goal.

scale appreciably with fine-tuning of  $f_p$ . In Figure 6.23, the power efficiency of this field trimming is evident in the normalized linear regression of the average power dissipation ( $\bar{P}_{\text{aaf}}$ ) versus cut-off frequency ( $f_p$ ) for each of the curves in Figure 6.20. With an  $R^2$  value near unity, and slope much less than unity, the fit lines for Mode A, Mode B, and Mode C reveal that a change in  $f_{\text{pa}}$ ,  $f_{\text{pb}}$ , or  $f_{\text{pc}}$  of, say, 10% requires just a  $\sim 1.2\%$ ,  $\sim 1.6\%$ , or  $\sim 4.8\%$  increase in  $\bar{P}_{\text{aaf}}$ . This is formally captured by defining the trimming power efficiency,  $\nu_{\text{trim}}$ , in terms of the relative changes in  $f_p$  and  $\bar{P}_{\text{aaf}}$  normalized with respect to their nominal values ( $f_{\text{po}}$  and  $\bar{P}_{\text{aaf0}}$ ) as

$$\nu_{\text{trim}} = 1 - \frac{\Delta \bar{P}_{\text{aaf}}}{\Delta f_p} \frac{f_{\text{po}}}{\bar{P}_{\text{aaf0}}} \quad (6.15)$$

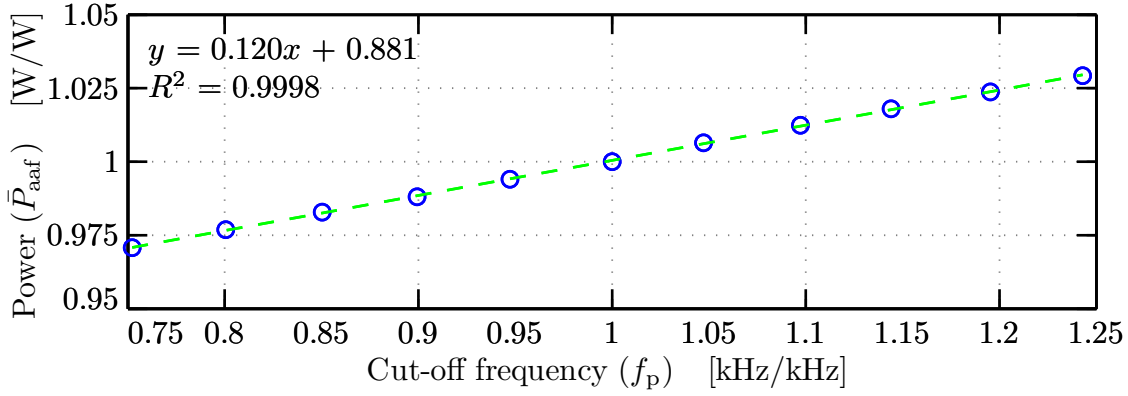
such that the ideal case, in which the slope of the curve in Figure 6.23 is zero and trimming costs no power, corresponds to 100% efficiency.

## 6.4 Radiation Performance

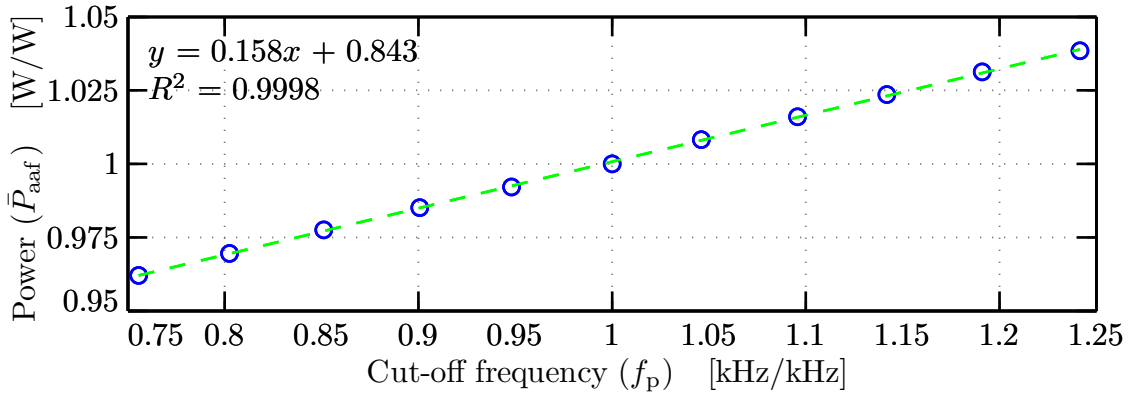
Using the test benches of Section 6.2.1 through Section 6.2.5, the radiation performance of the SVEPRE LNA and AAF were measured in a series of total-dose and single-event tests conducted by the author in collaboration with experimenters from Stanford University, The Aerospace Corporation, and Lawrence Berkeley National Laboratory and summarized in Table 6.8 and Table 6.9 for total-dose and single-event effects, respectively.<sup>109</sup> Section 6.4.1 describes aspects of the experimental procedures unique to each radiation source whereas key results for the LNA(AAF),<sup>110</sup> which are obtained at a nominal gain(bandwidth mode) of  $G_p = 14$  dB( $f_p = 180$  kHz) unless otherwise stated, are presented in Section 6.4.2(Section 6.4.3) confirming that the performance of Section 6.3.2(Section 6.3.3) is maintained in the anticipated radiation

<sup>109</sup>Absent from this compendium are the total-dose device characterizations of the MK832A test vehicle performed by Everett E. King of The Aerospace Corporation on 11 November 2004. These experiments yielded the transistor-level process characterization data presented Section 2.1.1 and Section 2.1.2 (cf. Footnote 15 of Chapter 2). However, as they were conducted in the absence of the author, there is insufficient documentation available to permit their inclusion in Table 6.8.

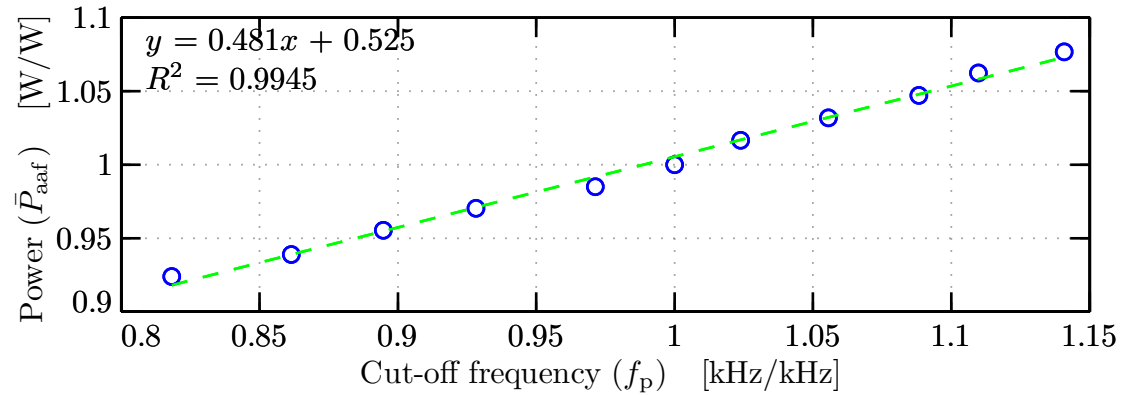
<sup>110</sup>As in Section 6.3, the contents of Section 6.4.2 and Section 6.4.3 are limited to only the most salient quantities and most representative DUT operational modes.



(a) Mode A.



(b) Mode B.



(c) Mode C.

Figure 6.23: Measured power efficiency of AAF trimming for (a) Mode A, (b) Mode B, and (c) Mode C. For each, the measured  $\bar{P}_{\text{aaf}}$  (blue circles), normalized to the nominal bandwidth, is plotted against the normalized  $f_p$  and the result fit to a linear regression (green line) in a least-squares sense.

environment.

### 6.4.1 Procedure

To aid interpretation of the radiation results presented in Section 6.4.2 and Section 6.4.3, Appendix I and Appendix J document the test conditions for the total-dose and single-event sources, respectively. As opposed to the test bench procedures of Section 6.2, which pertain to the DUT, these descriptions address the particulars of the radiation environment and should be consulted to affirm the integrity of the data presented herein.

### 6.4.2 LNA Results

During both  $^{60}\text{Co}$  and 50-MeV proton testing, the LNA on a single (though not the same) instance of SVEPRE-1 was irradiated under nominal bias conditions and a programmed gain of 14 dB. Between dose steps, it was subject to characterization using the test benches of Section 6.2.1 through Section 6.2.4, except for the NS test bench,<sup>111</sup> at a programmed gain of 20 dB.<sup>112</sup> Similarly, while illuminated with both pulsed-laser and heavy-ion sources, the LNA on a single, unique part operated under nominal bias conditions with a gain of 20 dB. Measurements from all radiation environments are grouped by test bench as follows.

#### 6.4.2.1 Bode Response

Variation in the Bode magnitude response of the LNA up to 1 Mrad(Si) total dose from the  $^{60}\text{Co}$   $\gamma$ -ray(50-MeV  $\text{H}^+$ ) source is shown in Figure 6.24(a)(Figure 6.24(b)).<sup>113</sup>

Regardless of the radiation source, the DC gain remains accurate to within

---

<sup>111</sup> Severe ambient noise is ubiquitous at the TID test facilities, rendering it extremely difficult in practice to obtain measurements whose precision is commensurate with, and thus worthy of comparison to, that of Figure 6.16. Consequently, the limited time for device characterization between dose steps was allocated to the more viable test benches.

<sup>112</sup> During proton characterization, the selected value of  $R_d$  produced  $G_p \simeq 19.8$  dB. Although slightly lower than the 20-dB target achieved during  $^{60}\text{Co}$  testing, the difference yields no discernible effect in performance.

<sup>113</sup> Analogous in character, plots of  $\angle T_{\text{de-embed}}^D(f)$  are only omitted for space considerations.

Chip	DUT	Source	Max. dose [krad(Si)]	Dates	Facility	Experimenters
SVEPRE-1	LNA	$^{60}\text{Co}$ $\gamma$ -ray	2000	12–13 Apr. 2006	The Aerospace Corporation, El Segundo, CA	Benjamin J. Mossawir <sup>a</sup> , Steven C. Witczak <sup>b</sup> , James L. Roeder <sup>b</sup> , Jon V. Osborn <sup>b</sup> , Mark A. Turpin <sup>b</sup> , Robert Garrett <sup>b</sup>
SVEPRE-1	LNA	50-MeV protons	2000	9–10 Jun. 2006	88-inch Cyclotron at Lawrence Berkeley National Laboratory (LBNL), Cave 4A	Benjamin J. Mossawir <sup>a</sup> , Steven C. Witczak <sup>b</sup> , Rokutaro Koga <sup>b</sup> , Jeffrey S. George <sup>b</sup> , Michael B. Johnson <sup>c</sup>
SVEPRE-3	AAF	30-MeV protons	300	28 Mar. 2008 – 1 Apr. 2008	88-inch Cyclotron at Lawrence Berkeley National Laboratory (LBNL), Cave 4A	Benjamin J. Mossawir <sup>a</sup> , Rokutaro Koga <sup>b</sup> , Jeffrey S. George <sup>b</sup> , Kirk B. Crawford <sup>b</sup> , Michael B. Johnson <sup>c</sup>

<sup>a</sup> Experimenter is with Stanford University.  
<sup>b</sup> Experimenter is with The Aerospace Corporation.  
<sup>c</sup> Experimenter is with Lawrence Berkeley National Laboratory.

Table 6.8: Total-dose radiation testing performed in support of this dissertation.

Chip	DUT	Source	Max. LET [MeV-cm <sup>2</sup> /mg]	Dates	Facility	Experimenters
SVEPRE-1	LNA	590-nm pulsed laser	> 1000	6-7 Apr. 2006	The Aerospace Corporation, El Segundo, CA	Benjamin J. Mossawir <sup>a</sup> , Stephen D. LaLumondiere <sup>b</sup> , James L. Roeder <sup>b</sup> , Stephanie Brown <sup>b</sup>
	AAF					
SVEPRE-1	LNA	10-MeV/ nucleon heavy ions	58.72	26-27 Sep. 2006	88-inch Cyclotron at Lawrence Berkeley National Laboratory (LBNL), Cave 4B	Benjamin J. Mossawir <sup>a</sup> , Charles C. Wang <sup>a</sup> , Rokutaro Koga <sup>b</sup> , Jeffrey S. George <sup>b</sup> , Van T. Tran <sup>b</sup>

<sup>a</sup> Experimenter is with Stanford University.  
<sup>b</sup> Experimenter is with The Aerospace Corporation.

Table 6.9: Single-event radiation testing performed in support of this dissertation.

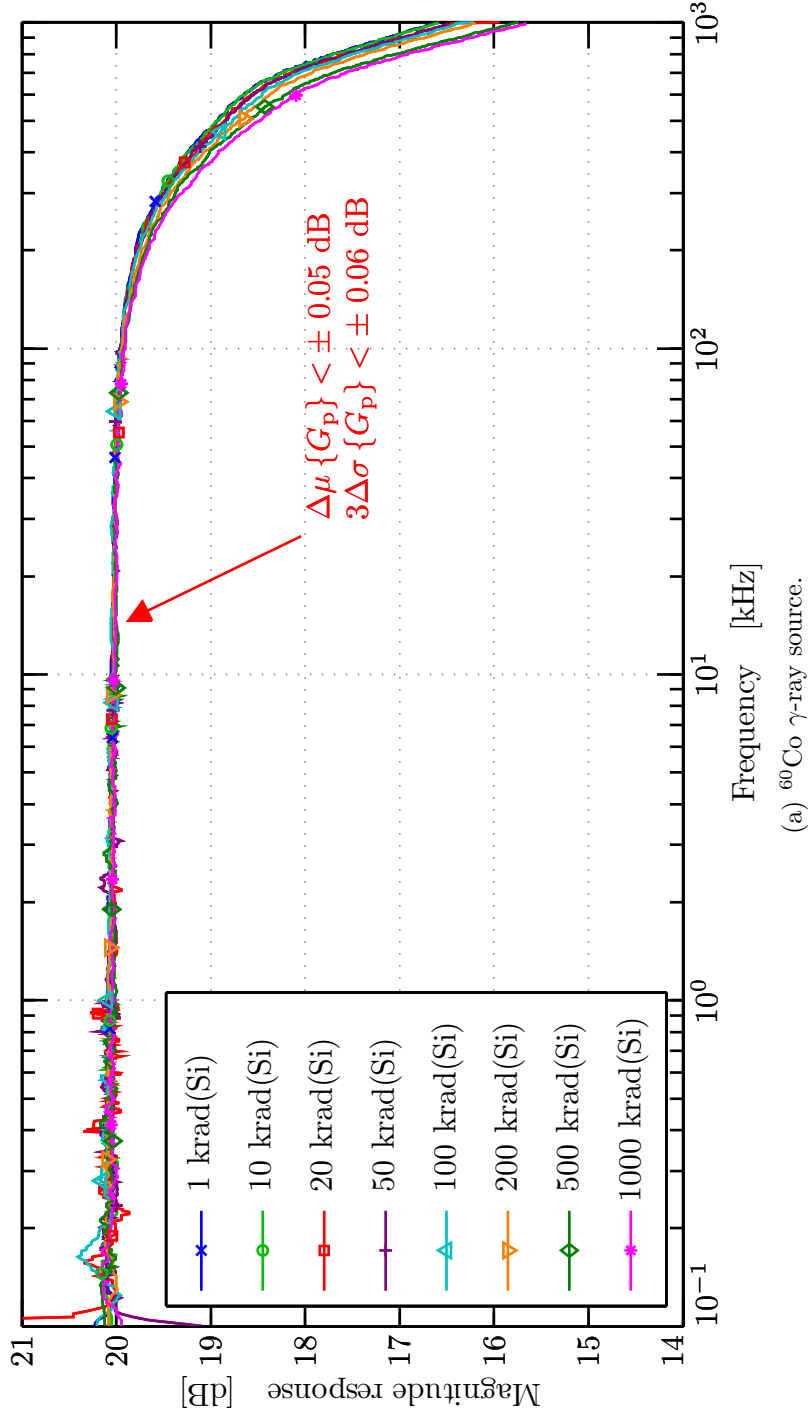


Figure 6.24: (a) Measured magnitude of LNA Bode response ( $|T_{\text{dmbd}}^{\text{D}}(f)|$ ) for  $^{60}\text{Co}$   $\gamma$ -ray TID exposures up to 1 Mrad(Si). To permit comparison, only dose steps in common with Figure 6.24(b) are shown.



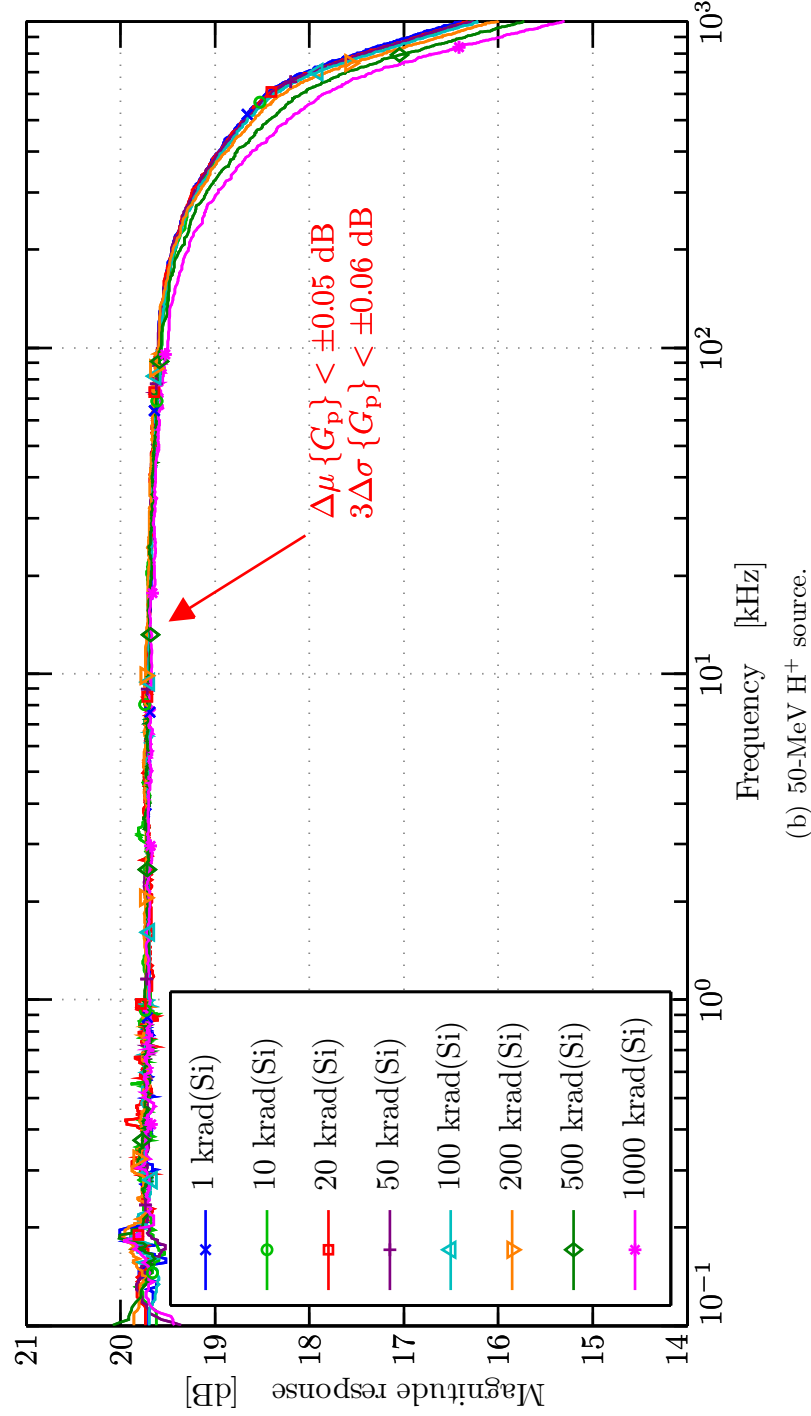


Figure 6.24: (b) Measured magnitude of LNA Bode response ( $|T^D_{\text{dmbd}}(f)|$ ) for 50-MeV  $H^+$  TID exposures up to 1 Mrad(Si). To permit comparison, only dose steps in common with Figure 6.24(a) are shown.

$\pm 0.05$  dB and the flatness of the passband gain, as measured by the  $3\text{-}\sigma$  ripple, is preserved to within  $\pm 0.06$  dB.<sup>114</sup> Additionally, the strong agreement between the data of Figure 6.24(a) and Figure 6.24(b) confirms that the predominant TID damage mechanism consists of oxide damage in the form of  $\Delta N_{\text{ot}}$  and  $\Delta N_{\text{it}}$ . The displacement damage unique to the 50-MeV  $\text{H}^+$  exposure has no measurable effect on the LNA frequency response.<sup>115</sup>

The role of radiation-hardness-by-design (RHBD) techniques in achieving the relative immunity of the passband gain is validated by contrasting this robustness with the sizable bandwidth compression, since the latter reveals that there indeed exist radiation-induced changes in the parameters of both underlying transistor flavors. Specifically, this reduction of the non-dominant pole,  $p_2 = 1/R_o C_L$ , which is governed by the LNA load capacitance,  $C_L$ ,<sup>116</sup> and the effective LNA output resistance,  $R_o$ , can be shown to depend directly on pMOS  $g_m$ -degradation and npn  $\beta$ -degradation via  $R_o$  which is approximated from a small-signal analysis of Figure 4.17 by:

$$R_o = \frac{1}{g_{m5,6}} + \frac{\frac{1}{g_{m3,4}} + \frac{R_l}{2}}{\beta_{5,6} + 1} \simeq \frac{V_T}{I_{C5,6}} + \frac{R_l}{2\beta_{5,6}} \quad (6.16)$$

While directly revealing an increase in output resistance with the drop in  $\beta_{5,6}$ , (6.16) does not directly exhibit the dependence on pMOS  $g_m$ . However, as shown in Section G.2.2.2, the master reference current of the chip,  $I_O$ , is set by a resistive divider containing a pMOS diode and, thus, all bias currents—including  $I_{C5,6}$ —scale with its transconductance.

At 1 Mrad(Si), when this  $g_m$  degrades by  $-5.35\%$  as shown in Figure 2.8,  $I_{C5,6}$  drops accordingly and, coupled with the  $-18\%$  drop in  $\beta_{5,6}$  at this dose (cf.

<sup>114</sup>For explicit depictions of the differences in these properties (and  $-3\text{-dB}$  bandwidth) as a function of dose for both sources, the reader is recommended to [Mossawir *et al.*, 2006].

<sup>115</sup>Since the process characterization data of Chapter 2 were obtained via  $^{60}\text{Co}$  irradiations, this fact affirms that it is sufficient to account only for the reported ionization-induced degradations in the front-end design; parameter shifts are not further enhanced by displacement effects in the proton-rich inner belt.

<sup>116</sup>The large  $C_L$  presented by the Agilent 1141A is the only reason such bandwidth compression is at all visible. As discussed in conjunction with the Bode plots of Section 6.3.2, the actual loading of the AAF would restore the full bandwidth, rendering this effect incidental.

Figure 2.16), (6.16) predicts an increase in  $R_o$  of 15%. Thus, the  $\sim 15\%$  bandwidth compression of Figure 6.13(a) is shown to directly result from the combination of pMOS  $g_m$ -degradation (which reduces  $I_C$  via  $I_O$ ) and npn  $\beta$ -degradation predicted by the characterization data in Section 2.1.1 and Section 2.1.2, respectively.

Given this proof of significant and simultaneous parameter shifts in the underlying transistors, the lack of corresponding change in the passband quantities cited above confirms that the RHBD techniques of Chapter 4 are indeed effective in mitigating the dependence of the LNA gain on its active devices.

#### 6.4.2.2 Linearity

To examine the efficacy of these same techniques in preserving highly linear operation, radiation-induced changes in the SFDR derived from spectral estimates such as those of Figure 6.15 is tracked as a function of dose for both sources in the normalized plots of Figure 6.25.<sup>117</sup> Recall from (4.15) and (4.17) that the SFDR of a typical OTA is a strong function of  $\beta$  and  $I_C$ , leaving it susceptible to the degradations just described in Section 6.4.2.1. Although the patterns of Figure 6.25 are commingled the standard error of the measurement, reflecting uncertainties in both environmental noise and instrument specificity, the lack of any declining trend and the mutual correlation of the data from both sources breed confidence that the harmonic fidelity is uncorrelated with TID up to 1 Mrad(Si) as a result of design efforts to shift the linearity burden to passive elements.

#### 6.4.2.3 Power Dissipation

Finally, the success of the conservative design of the reference current generators in Section G.2.2.2, which ensures that the overall LNA power dissipation does not grow as TID damage accumulates, is borne out by the results of the PD test bench in Figure 6.26. For both  $^{60}\text{Co}$  and 50-MeV  $\text{H}^+$  exposures, the normalized maximum

---

<sup>117</sup>In this figure, fundamental frequencies of 1 kHz and 10 kHz are chosen simply to demonstrate that testing was conducted beyond those frequencies used in Figure 6.15.

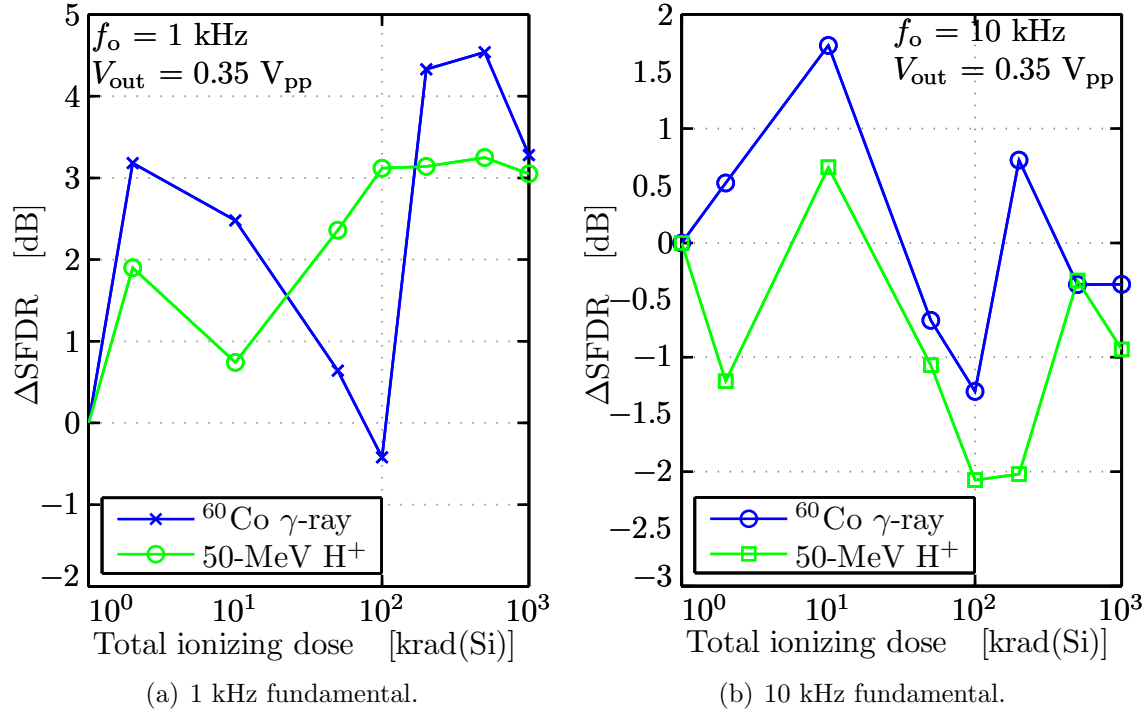


Figure 6.25: Measured change in LNA SFDR for both  $^{60}\text{Co}$   $\gamma$ -ray and 50-MeV  $\text{H}^+$  TID exposures up to 1 Mrad(Si) using a (a) 1 kHz and (b) 10-kHz input tone. Underlying spectral estimates are derived as in Figure 6.15. Deviations normalized to baseline measurements.

power dissipation is actually reduced by an average of  $-3.484\%$  at 1 Mrad(Si),<sup>118</sup> confirming that the LNA current draw does not increase with dose and, thereby, limiting the peak demand on spacecraft resources.

#### 6.4.2.4 Single-Event Transients

In keeping with the conventions of Section 6.2.5.4, the continuous and discrete data sets acquired during the pulsed-laser and heavy-ion testing of the LNA, respectively, are considered separately.

<sup>118</sup>The maximum power dissipation is obtained by utilizing the supply voltage measurements taken at the outset of the PD test bench procedure, before the LNA supply demands are able to relax as the part reaches thermal equilibrium outside the radiation cave.

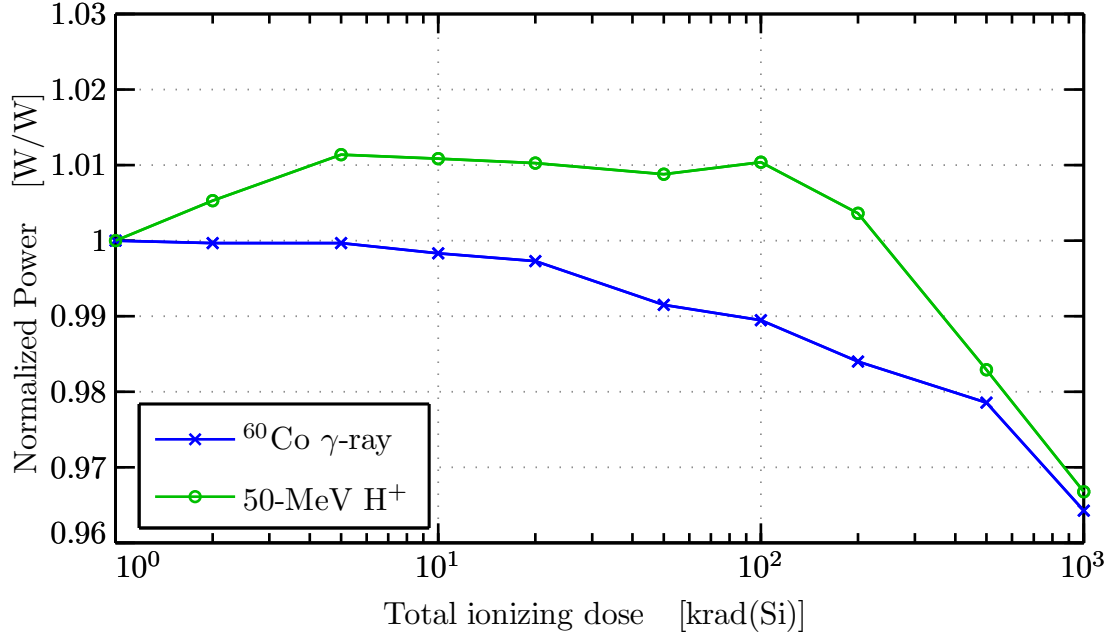


Figure 6.26: Measured change in maximum LNA power dissipation for both  $^{60}\text{Co}$   $\gamma$ -ray and 50-MeV  $\text{H}^+$  TID exposures up to 1 Mrad(Si). Power measured prior to thermal equilibrium and normalized to baseline measurements.

**Waveforms:** Figure 6.27 and Figure 6.28 exhibit representative ASETs observed at the output of the LNA during a pulsed-laser threshold scan at a beam energy of 22.7 pJ corresponding to an equivalent LET of 68.2 MeV-cm<sup>2</sup>/mg. These examples replicate a particularly threatening scenario in that: they illuminate the input pair (Q1/Q2) which are biased and low current densities to improve input impedance and, thus, are most sensitive [Turflinger, 1996, p.599]; the charge is deposited inside the protective guard ring (cf. Figure 6.27(b) and Figure 6.28(b)); and since the device sizes prohibit a fully common-centroid layout, this array does not take advantage of the preferred electric-field symmetries described by Figure 4.30.<sup>119</sup>

The resulting transients in Figure 6.27(c)(Figure 6.28(c)) indeed arise differentially, as stray drift fields sweep some of the deposited charge into Q2(Q1), even though only Q1(Q2) is directly illuminated. Further evidence of the inter-device fields is implied by the trend in this and other low-beam-strength cases (< 57 pJ) that

<sup>119</sup>Based on the results of this section, the layout of the Q1/Q2 array was modified to obey the principles of Figure 4.30 as part of revisions incorporated into SVEPRE-3.

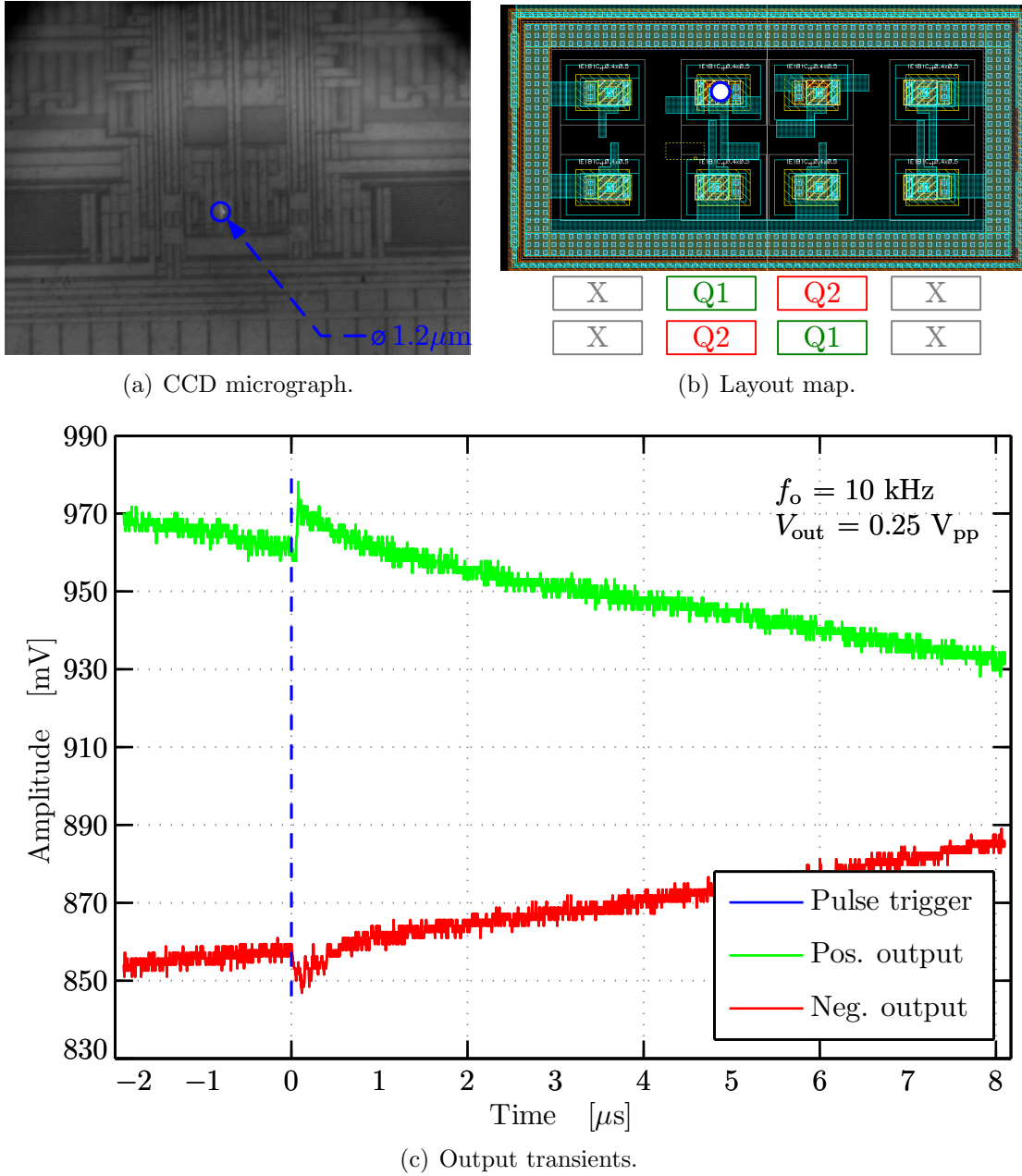


Figure 6.27: Measured output transients for pulsed-laser illumination of Q1. A 22.7-pJ threshold scan of the location identified in the (a) CCD micrograph primarily illuminates Q1, as seen in the (b) layout map, resulting in (c) a +20-mV(−13-mV) ASET on the positive(negative) LNA output shown in green(red).

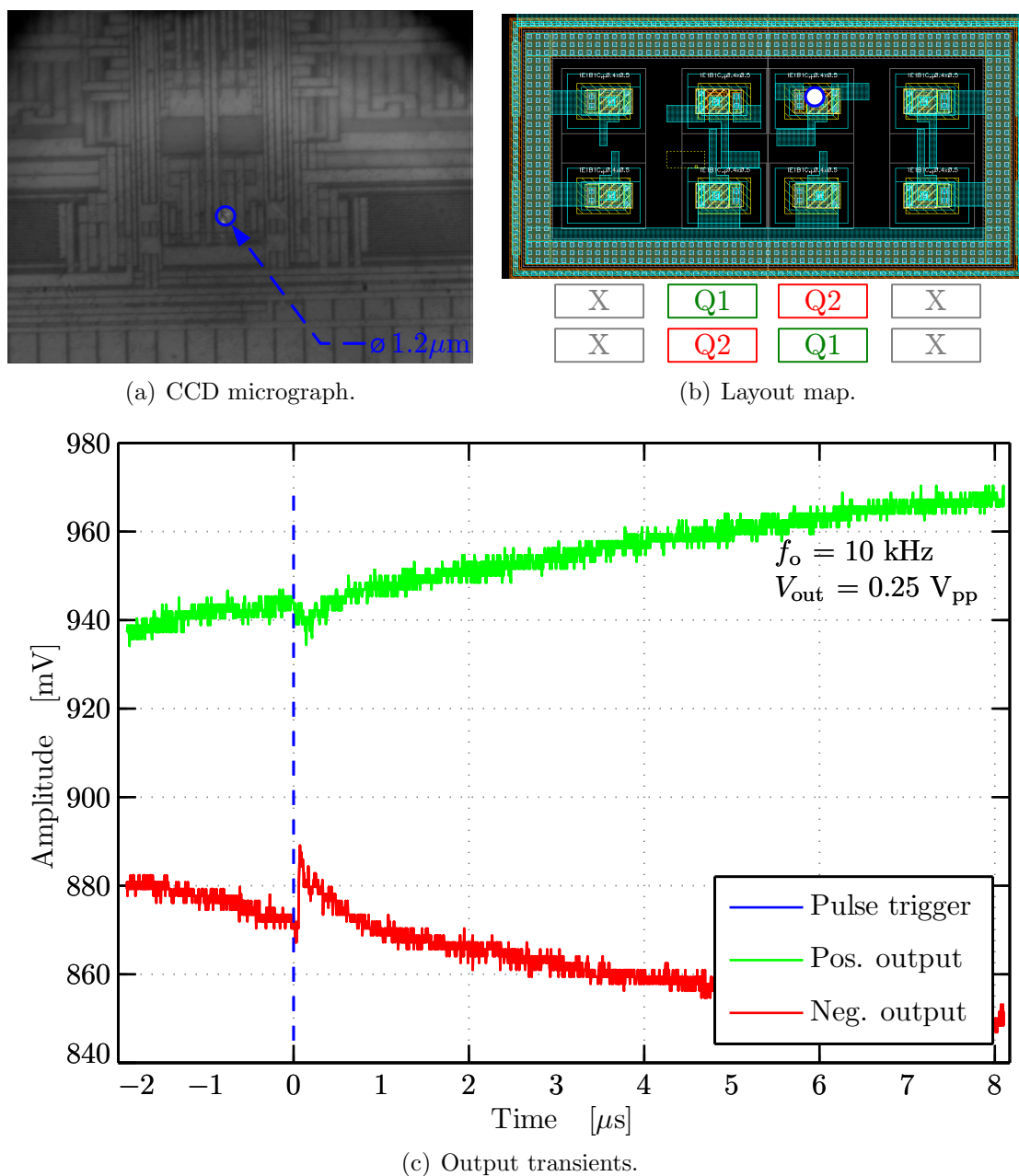


Figure 6.28: Measured output transients for pulsed-laser illumination of Q2. A 22.7-pJ threshold scan of the location identified in the (a) CCD micrograph primarily illuminates Q2, as seen in the (b) layout map, resulting in (c) a  $-10\text{-mV}(+20\text{-mV})$  ASET on the positive(negative) LNA output shown in green(red).

SET property	Scan type	Average	Maximum	Units
Amplitude <sup>a</sup>	Threshold	10–25	40	mV
	High-LET <sup>c</sup>	75–100	400	mV
Recovery time <sup>b</sup>	Threshold	1–1.5	4	$\mu$ s
	High-LET <sup>c</sup>	2–2.5	8	$\mu$ s

<sup>a</sup> Peak amplitude is measured relative to extrapolated sinusoidal value at the corresponding sample time

<sup>b</sup> Recovery time is measured from onset edge to settling within 1%

<sup>c</sup> High-LET scans are those in which beam energy exceeds 57 pJ ( $\sim 170$  MeV-cm<sup>2</sup>/mg)

Table 6.10: Statistical summary of ASETs observed during pulsed-laser testing of LNA.

transient polarities are correlated with the phase of the input signal rather than the target device. That is, the positive-going transient occurs on the side of the circuit where the sinusoid is in its negative half-period.<sup>120</sup> Therefore, differential ASETs should be suppressed when the field terminations of the SET-tolerant common-centroid array described in Section 4.3.2.2 are deployed. An example of this occurs in the head current sources, which adopt such a layout and where illumination of M12 (see Figure 4.23(b)) at a beam energy of 18.1 pJ ( $\sim 54.1$  MeV-cm<sup>2</sup>/mg) generates transients of the same polarity, such that the net differential amplitude is approximately one-sixth what it would be if the transients demonstrated opposite polarity.

Notably, the transient amplitudes were insensitive to increases in beam energy beyond its threshold value. Also, no irrecoverable upsets, oscillations, or saturation were induced. For all arrays scanned, the outputs remained bounded-input, bounded-output (BIBO) stable with exponential recovery times, except for slewing noted at extremely high energies. The statistical characteristics of LNA ASETs observed with the pulsed-laser are summarized in Table 6.10.

<sup>120</sup>Whereas the polarity of the transient is determined by the signal phase, its amplitude is a function of the target device—in Figure 6.27(Figure 6.28), the transient on the positive(negative) LNA output is larger than that on negative(positive) output because Q1(Q2) is more strongly illuminated.



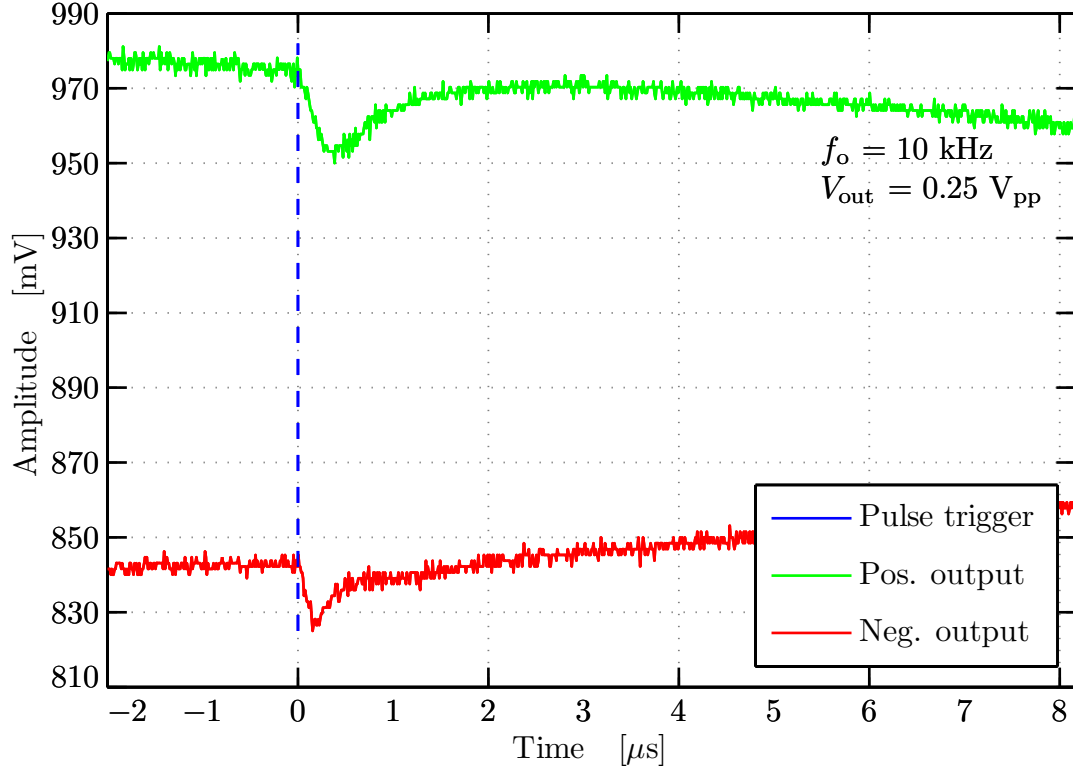
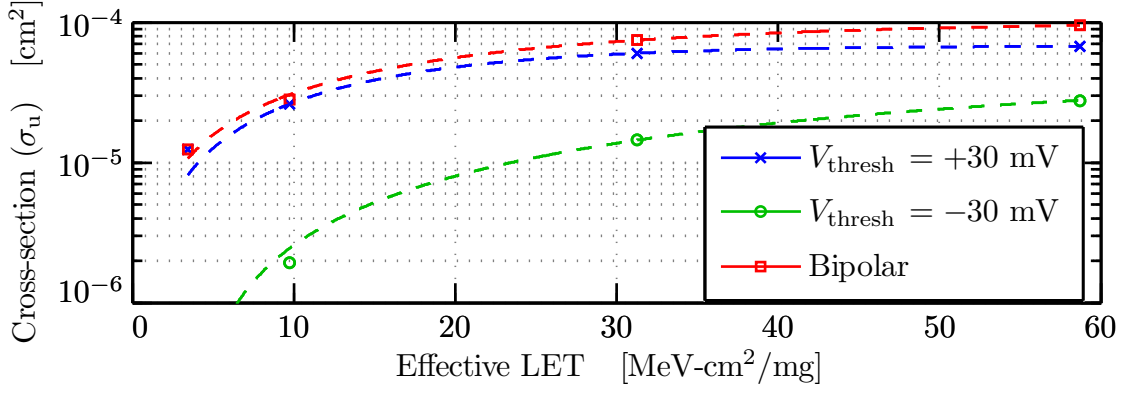


Figure 6.29: Measured output transients for pulsed-laser illumination of M12. A 18.1-pJ threshold scan of the head current source pMOSFET M12 (cf. Figure 4.23(b)) results in a  $-25\text{-mV}$  ( $-18\text{-mV}$ ) ASET on the positive(negative) LNA output shown in green(red).

**Cross-sections:** The upset distributions resulting from illumination of the LNA by the 10 MeV/nucleon heavy-ion cocktail give rise to the marked data points in cross-section curves of Figure 6.30. Since the SEU cross-sections of digital circuits are known to depend on input conditions [Buchner and McMorrow, 2005], the LNA is tested with both a DC input and two sinusoidal inputs. For the former, ‘upsets’ are defined relative to  $V_{\text{thresh}}$ ; for the later, relative to  $t_{\text{thresh}}$ . Since the differential halves of the internal circuitry operate with greater imbalance the larger the signal,  $\sigma_{\text{sat}}$  is largest for the DC case: when the circuit is balanced, the  $Q_{\text{crit}}$  required to create a measurable imbalance is small. For all input conditions shown,  $\sigma_{\text{sat}}$  is approximately an order of magnitude below that of the OP-15 amplifier (cf. Figure 2.32), and the



(a) DC input.

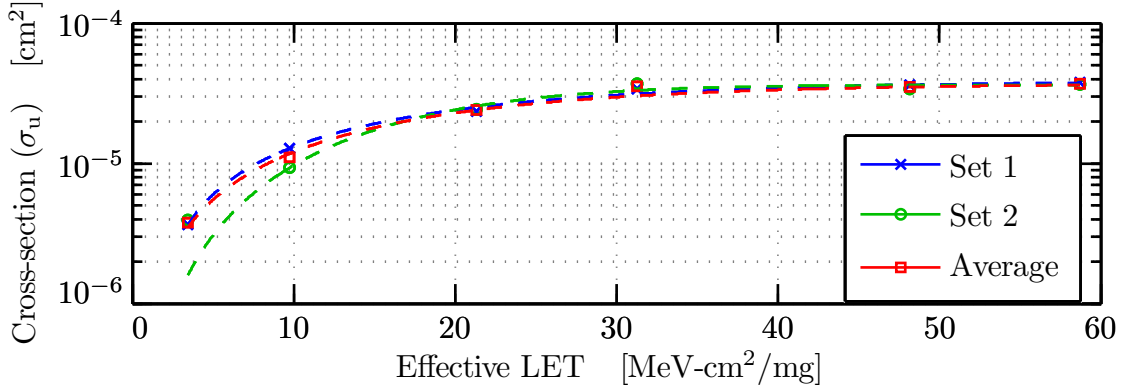
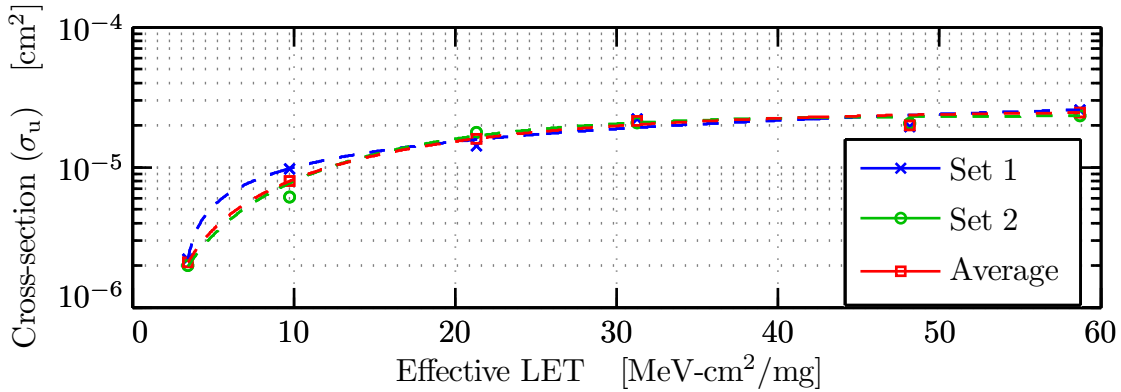
(b) 30  $\text{mV}_{\text{PP}}$  input.(c) 60  $\text{mV}_{\text{PP}}$  input.

Figure 6.30: Measured heavy-ion cross sections for LNA using a (a) DC input and sinusoidal inputs of (b) 30  $\text{mV}_{\text{PP}}$  and (c) 60  $\text{mV}_{\text{PP}}$  amplitude. Markers indicate measured data points. Dashed lines indicate least-squares fits to Weibull distribution of (6.12) (see Table 6.11 for parameters).

Input type		Data set <sup>a</sup>	Weibull parameters			
Type	Amplitude		$A$	$L_o$	$W$	$S$
DC	0 V	+30 mV	$6.812 \times 10^{-5}$	$2.220 \times 10^{-14}$	17.14	1.282
		−30 mV	$4.557 \times 10^{-5}$	3.229	58.07	1.324
		Bipolar	$1.024 \times 10^{-4}$	$6.707 \times 10^{-14}$	24.62	1.121
Sinusoid	30 mV <sub>PP</sub>	Set 1	$3.885 \times 10^{-5}$	0.760	19.86	1.156
		Set 2	$3.635 \times 10^{-5}$	$1.171 \times 10^{-7}$	19.07	1.813
		Average	$3.697 \times 10^{-5}$	$4.152 \times 10^{-8}$	20.53	1.291
Sinusoid	60 mV <sub>PP</sub>	Set 1	$6.864 \times 10^{-5}$	3.101	236.4	0.524
		Set 2	$2.334 \times 10^{-5}$	$2.220 \times 10^{-14}$	18.17	1.463
		Average	$2.550 \times 10^{-5}$	1.027	20.49	1.149

<sup>a</sup> For DC inputs, data sets are delineated by trigger polarity

Table 6.11: Weibull parameters for LNA heavy-ion cross-section fits in Figure 6.30. Refer to (6.12) parameter definitions and Footnote 82 for their interpretation.

sensitive region as a percentage of the total circuit area is nearly identical ( $\sim 8\%$ ).<sup>121</sup>

According to the methodology of Section 6.2.5.4, the cross-sections are fit to the Weibull distribution of (6.12), resulting in the dashed lines of Figure 6.30;<sup>122</sup> the fitting parameters are summarized in Table 6.11. Parameters  $A$  and  $L_o$  are analogous to the  $\sigma_{\text{sat}}$  and  $\mathcal{L}_{\text{th}}$  for each input type (cf. Footnote 82). Thus, when combined with an appropriate model of particle flux,<sup>123</sup> this table can be employed in a differential- or integral-weighted algorithm (cf. Footnote 83) to predict SVEPRE ASET rates for a given orbital ephemeris.

A discussion of SEL results pertaining to the chip as a whole is provided in Section 6.4.3.4.

<sup>121</sup>The maximum value of  $\sigma_{\text{sat}}$  observed “correspond[s] to the expected sensitive area for the entire chip” [Petersen et al., 1992, p.1584].

<sup>122</sup>A robust, nonlinear, least-squares method is employed to perform all of the Weibull fits in Figure 6.30.

<sup>123</sup>Despite its limitations [Barth et al., 2003, p.478], the CREME96 model [Tylka et al., 1997] is a common choice for SEU error-rate calculations and generally accurate for ordinary solar conditions [Petersen et al., 1992, p.1581].

### 6.4.3 AAF Results

During 30-MeV proton testing, the AAF on a single instance of SVEPRE-3 was irradiated under nominal bias conditions and programmed to Mode A. Between dose steps, it was subject to characterization using the test benches of Section 6.2.1 through Section 6.2.4 in all three bandwidth modes.<sup>124</sup> Similarly, while illuminated by a pulsed-laser, the AAF on a single, unique SVEPRE-1 part operated under nominal bias conditions in Mode A. Measurements from both radiation environments are grouped by test bench as follows.

#### 6.4.3.1 Bode Response

Variation in the Bode magnitude response of the AAF for 30-MeV  $H^+$  exposures up to 300 krad(Si) is depicted in Figure 6.31.

In all modes, the location of  $f_p$  remains accurate to within  $\pm 1.45\%$  whereas that of  $f_n$ —the working proxy for  $f_r$ —varies by no more than  $\pm 3.44\%$ . Note that the latter is heavily influenced by phase measurement errors, particularly in Mode C.<sup>125</sup> Nevertheless, the radiation-induced depression of  $r_\alpha$  is minimal—certainly well below the underlying  $-18\%$  and  $-5.35\%$  degradation of npn  $\beta$  and pMOS  $g_m$ , respectively—and disappears altogether at the conclusion of the anneal.

To emphasize this preservation of the filter’s anti-aliasing capability, Figure 6.32 compares the measured  $f_n$  to that of the various predictions in Figure 6.17 across the range of tested doses, revealing that the measured attenuation reaches the  $-60$ -dB level at or below the  $f_n$  predicted by full-chip simulation (or, in the case of Mode C,  $f_m$ , as defined in Footnote 125).<sup>126</sup> Similarly, there are no measurable variations of the passband gain or ripple with dose up to 300 krad(Si). Thus, filter performance is maintained in both the passband and transition band as a result of unit transconductors whose values and bandwidths are insensitive to transistor TID

<sup>124</sup>Adding the rationale of Footnote 111, the NS test bench is also skipped during AAF total-dose characterization.

<sup>125</sup>In particular, the response of Mode C barely reaches  $-60$ -dB attenuation before the OUTSE peaking intercedes. Thus, in Figure 6.32(c), the  $-45$ -dB frequency,  $f_m$ , is substituted for  $f_n$ .

<sup>126</sup>The location of the measured  $f_n$  or  $f_m$  is still subject to the caveat of Footnote 98, which does not guarantee the alignment of  $f_p$  between the measured and predicted responses.

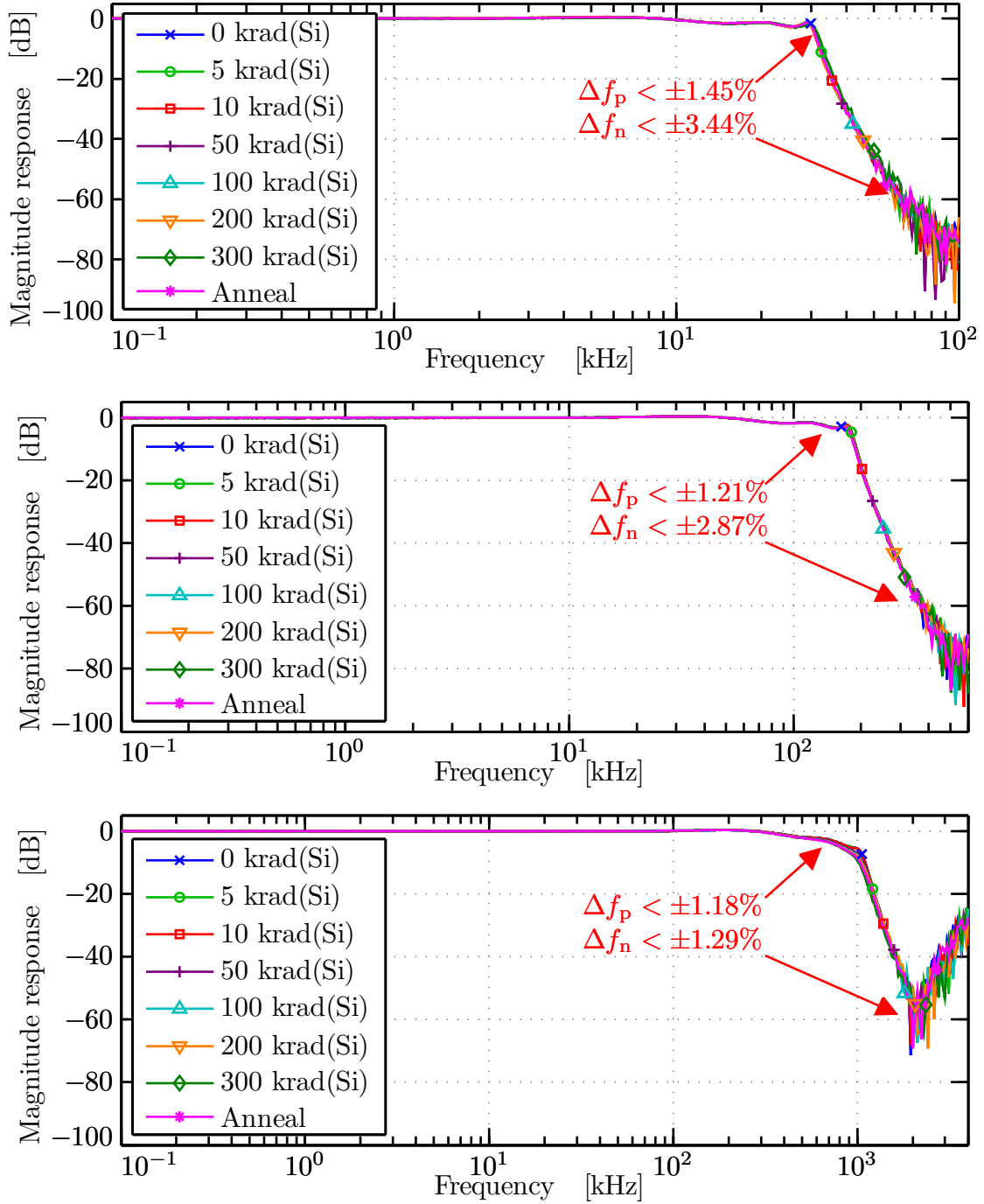


Figure 6.31: Measured magnitude of AAF Bode response in (from top) Mode A, Mode B, and Mode C for 30-MeV  $H^+$  TID exposures up to 300 krad(Si). The final curve reflects performance after a 70-hour unbiased, room-temperature anneal.

degradation.

### 6.4.3.2 Linearity

Considering linearity exactly as in the spectral estimates of Section 6.3.3, the SFDR3 as a function of dose is plotted in Figure 6.33(Figure 6.34) for a 1-kHz(10-kHz) fundamental tone. For the 1-kHz tone, the hardening techniques preserve at least 90-dB suppression of the 3<sup>rd</sup> harmonic throughout the tested range in both Mode B and Mode C, while Mode A satisfies this criterion up to 100 krad(Si). Given that the performance of this mode does not recover during the annealing period, as for the others, the possibility of measurement error exists.<sup>127</sup> This effect is less pronounced at 10 kHz,<sup>128</sup> where the SFDR3 of all three modes is reminiscent of Figure 6.25, exhibiting random fluctuations around the 90 dB without clear trend below 300 krad(Si).

However, the distinct increase in odd-order distortion at the 300 krad(Si) step in all panels of Figure 6.34 supports the conclusion that the current gain of the substrate pnps required for the operation of the positive-feedback TLL drops below unity at that dose. As for the frequency response, the performance rebounds after the 70-hour unbiased anneal at room temperature, so there is no permanent loss of performance.

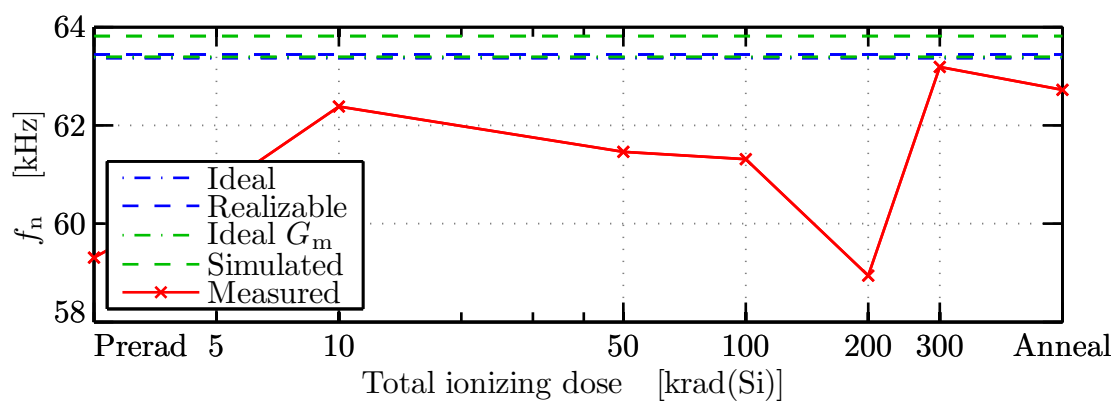
### 6.4.3.3 Power Dissipation

Figure 6.35 summarizes the relationships between the maximum and average  $P_{\text{aaf}}$  for each of the bandwidth modes as a function of total dose. In all modes, the maximum and average power dissipation track one another closely and show no evidence of the increases observed in other parts from this process [Wang, 2009, p.279–281]. As

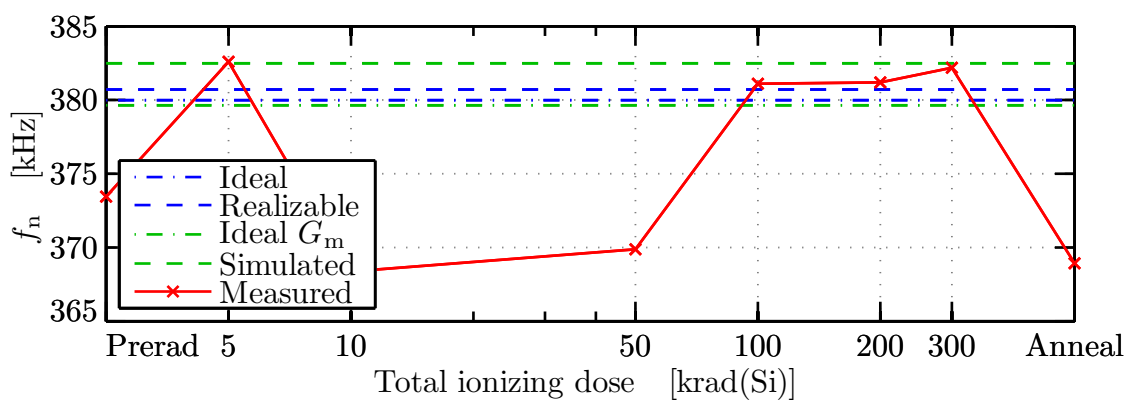
---

<sup>127</sup>The potential for  $J_e$ -mismatch through the attenuation of the current mirrors of Figure 5.40 in this mode also points to a weakening of the CMFB network, though no formal connection has been established due to lack of visibility into the heart of the transconductors within the fabricated AAF.

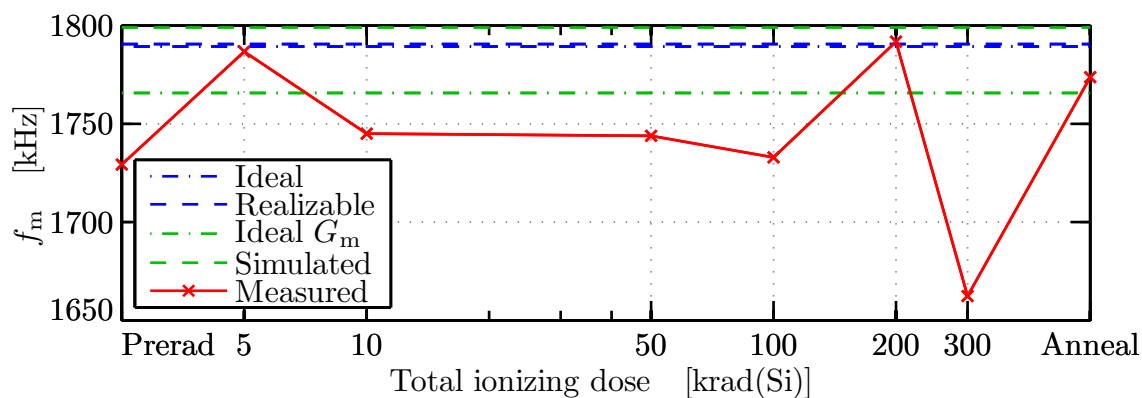
<sup>128</sup>It is tempting to attribute the improved linearity of Mode A at 10 kHz to the higher-order harmonics being filtered by the roll-off above  $f_{\text{pa}}$ ; specifically, Table 5.1 indicates that the two low- $Q$  poles of Stage 1 yield  $f_{o1} = 10$  kHz in Mode A, resulting in  $\sim 26$ -dB attenuation at  $f_{\text{pa}}$ . However, this attenuation only applies to signals at the filter input: as a function of their location within the loop, the transconductors internal to the stage generate distortion that is shaped substantially less, if at all. In any event, provided it reflects only power injected by the DUT, an assessment of the 3<sup>rd</sup> harmonic amplitude—even near  $f_{\text{pa}}$ —remains valid.



(a) Mode A.

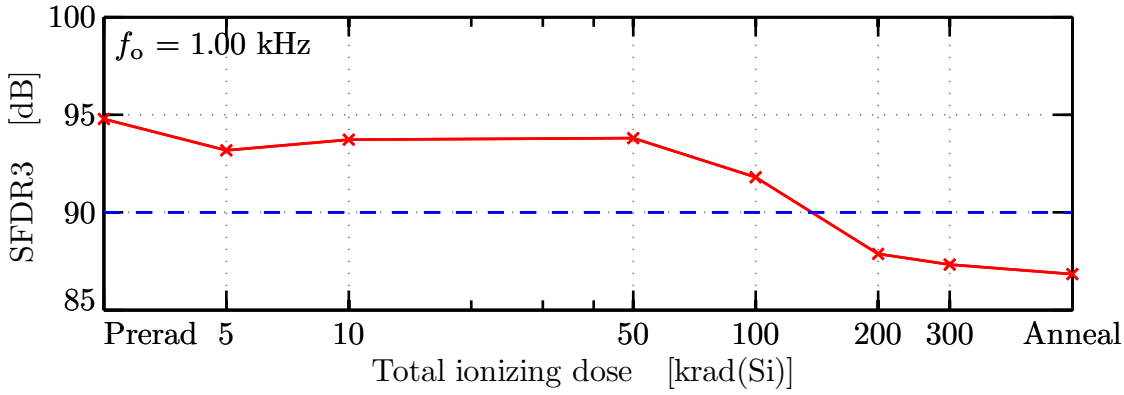


(b) Mode B.

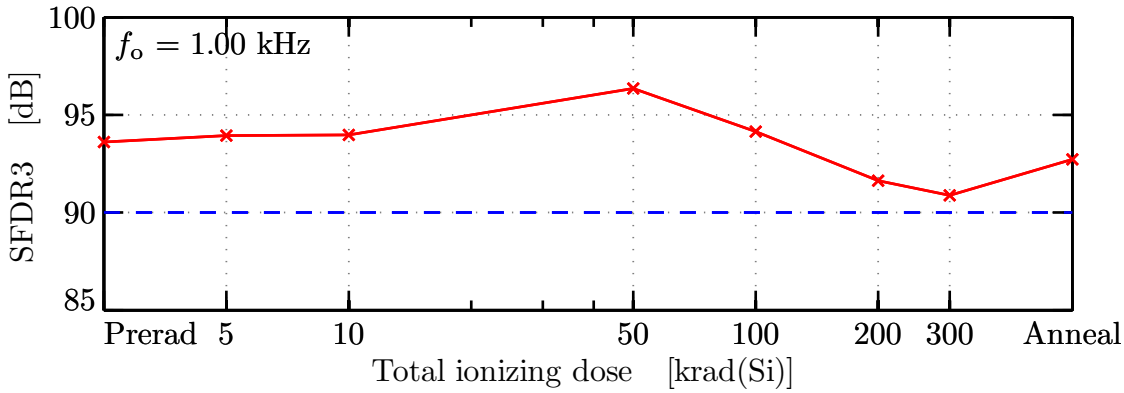


(c) Mode C.

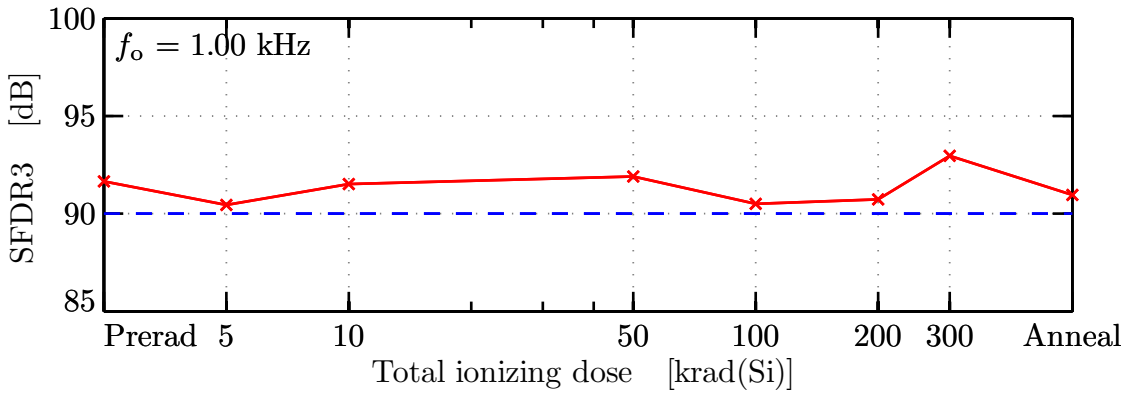
Figure 6.32: Measured AAF attenuation in (a) Mode A, (b) Mode B, and (c) Mode C for 30-MeV  $H^+$  TID exposures up to 300 krad(Si). For each dose step in Figure 6.31 (plus anneal),  $f_n$  or  $f_m$  is extracted as a proxy for  $f_r$  and compared to that of each predictor in Figure 6.17.



(a) Mode A.



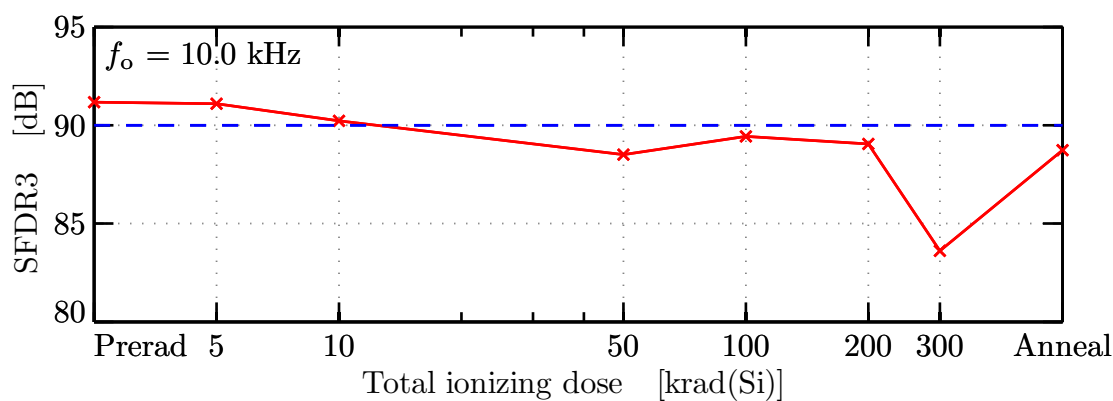
(b) Mode B.



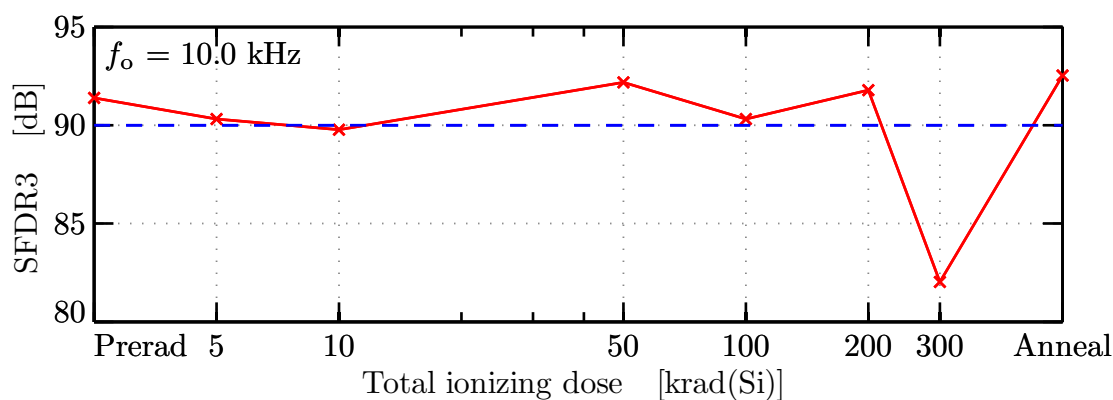
(c) Mode C.

Figure 6.33: Measured AAF Stage 1 SFDR3 in (a) Mode A, (b) Mode B, and (c) Mode C for 30-MeV  $H^+$  TID exposures up to 300 krad(Si) using a 1-kHz input tone. SFDR3 is extracted from PSD estimates computed as in Figure 6.21.

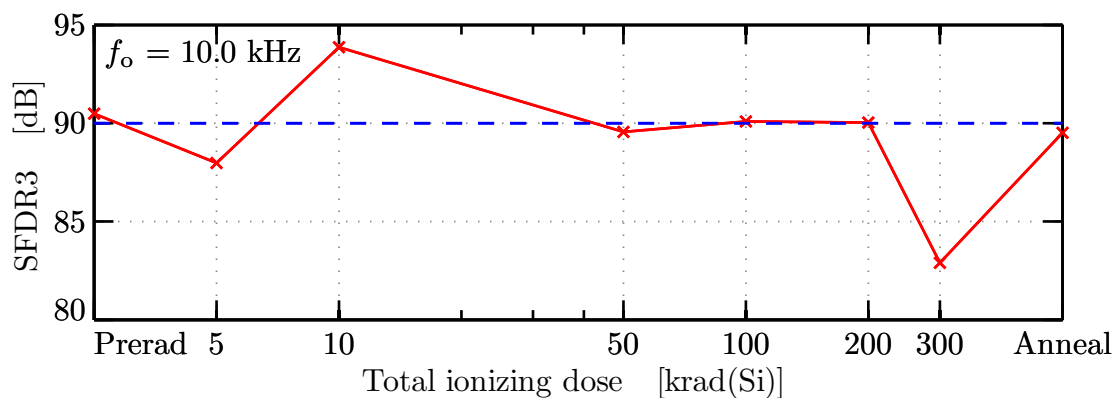




(a) Mode A.



(b) Mode B.



(c) Mode C.

Figure 6.34: Measured AAF Stage 1 SFDR3 in (a) Mode A, (b) Mode B, and (c) Mode C for 30-MeV  $H^+$  TID exposures up to 300 krad(Si) using a 10-kHz input tone. SFDR3 is extracted from PSD estimates computed as in Figure 6.22.

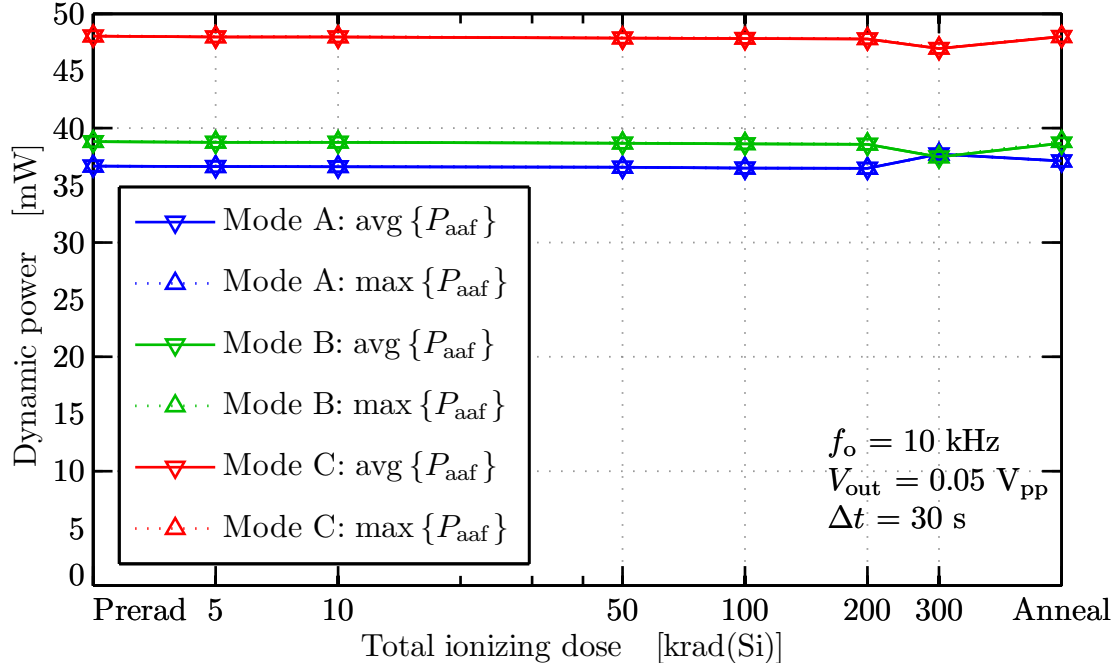


Figure 6.35: Measured maximum and average AAF power dissipation in all modes for 30-MeV  $H^+$  TID exposures up to 300 krad(Si). Maximum measured prior to thermal equilibrium. Average taken over 30-s application of 10 kHz, 50 mV<sub>PP</sub> sinusoid to the SVEPRE-3 signal path.

for the LNA, this robust performance results from the conservative scheme for the generation of three master reference currents— $I_E$ ,  $I_B$ , and  $I_O$ —which is based on the degradation of pMOS  $g_m$  reflected in Figure 2.8 (cf. Section G.2.2.2). As evidenced by the lack of spikes or even gradual increases in the curves of Figure 6.35, this technique proves efficacious for AAF as well.

#### 6.4.3.4 Single-Event Latchup

To determine the latchup susceptibility of the entire SVEPRE chip—LNA and AAF, as well as the associated circuitry of Appendix G, which includes the potentially sensitive ESD structures—the supply currents are monitored during each pulsed-laser and heavy-ion run, producing records such as that of Figure 6.36 which pertains to a

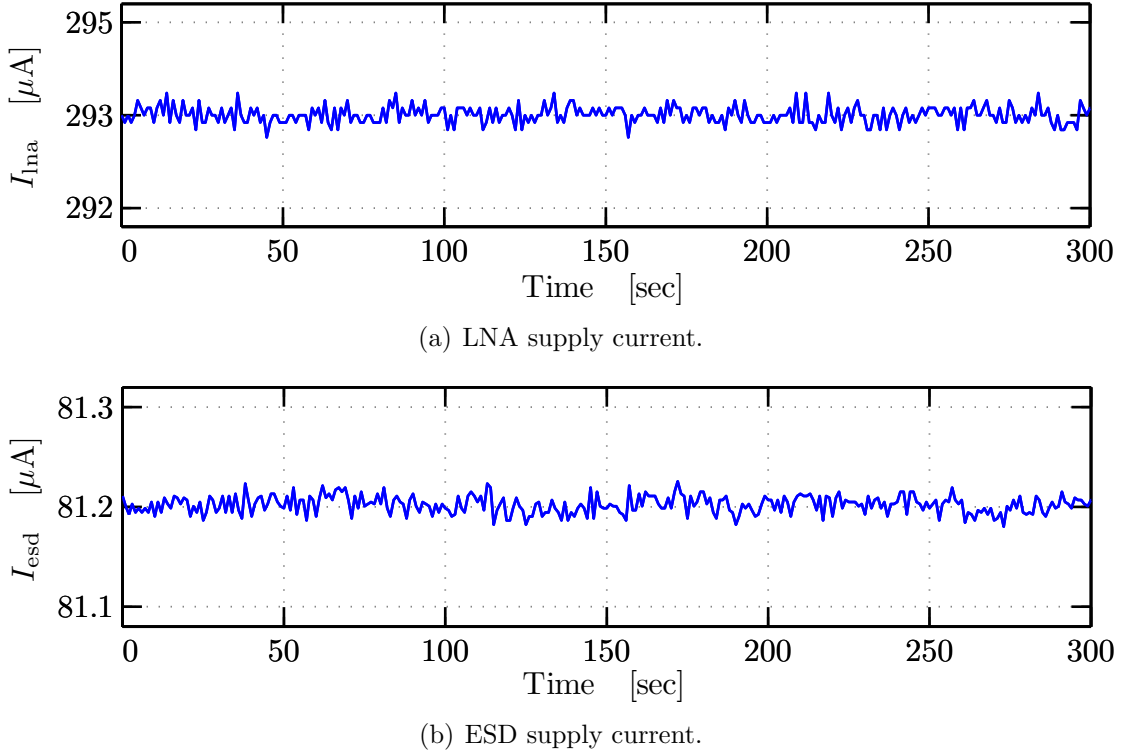


Figure 6.36: Example of measured SVEPRE-1 latchup sensitivity for heavy-ion exposure. Monitoring the (a) LNA and (b) ESD supply current waveforms during a 300-s heavy-ion run at maximum LET (58.72 MeV-cm<sup>2</sup>/mg) yields no indication of latchup or its precursors. Although not pictured, results for  $I_{AAF}$  are analogous.

300-s heavy ion (xenon) run at 58.72 MeV-cm<sup>2</sup>/mg, the highest LET available.<sup>129</sup>

None of the latchup signatures described in Section 6.2.5.3 are observed in the record of Figure 6.36 nor, in fact, during any of the SEE testing conducted. When operating the pulsed-laser up a maximum energy of 1.3 nJ/pulse, reaching equivalent LETs in excess of 100 MeV-cm<sup>2</sup>/mg, and scanning the die with spot sizes up to 700  $\mu\text{m}^2$  whilst it processed a 25-mV<sub>PP</sub> sinusoidal, the supplies remained free of glitches, droop, or oscillations, regardless of die location, beam intensity, or spot size.<sup>130</sup>

<sup>129</sup>In this example,  $I_{aaf}$  is absent, but its behavior conforms to that of the supply currents shown; namely, it did not exhibit any anomalies during the battery of SEE tests.

<sup>130</sup>Again, it should be emphasized that, while highly correlated with particle radiation, equivalent laser LET is qualified by the fact that the laser cannot penetrate regions of the die optically obscured by metalization, leaving the coverage of such testing incomplete. However, in the SVEPRE layout,

Having satisfied the prerequisite of surviving front-side laser illumination, a more comprehensive latchup test of the DUT is typically conducted using heavy ions. In the case of the 10 MeV/nucleon heavy-ion cocktail at LBNL, no latchup was observed for a total fluence of  $2.92 \times 10^7$  particles/cm<sup>2</sup> ( $1.76 \times 10^7$  particles/cm<sup>2</sup>) when the part was bombarded with particles of the highest LET available, namely Xenon, while processing a sinusoidal(DC) input signal.

In summary, under the conditions of these two tests, each of which involved operation at room temperature with nominal supply voltage and a variety of input signals,<sup>131</sup> no latchup was observed, confirming the negligible sensitivity of the SVEPRE layout. A complete summary of the LNA(AAF) baseline and radiation performance demonstrated in this chapter is compiled in Table 7.1 (Table 7.2).

## 6.5 Burn-In Performance

As part of qualification for flight opportunities, a lot of 32 SVEPRE-3 chips were subjected to burn-in testing to screen for early lifetime failures.<sup>132</sup> The purpose of burn-in testing is to identify those devices in the population whose time-to-failure is far shorter than the ensemble average on account of inherent defects or manufacturing tolerances. To do so, the testing employs isothermal baking to “stress microcircuits at or above maximum rated operating conditions which reveal[s] time and stress dependent failure modes” [*MIL-STD-883G*, 2006, Method 1015.9, Sect. 1]. Eliminating these marginal instances from the flight component inventory enhances

---

the most sensitive core and ESD devices are devoid of metal fill (for matching reasons). So, this method allows the potentially vulnerable regions to be exposed to higher equivalent LETs than otherwise achievable at the available particle facilities.

<sup>131</sup>Elevated supply voltage and temperature increase the likelihood of latchup, primarily due to the positive and potentially large temperature coefficient of  $R_{\text{well}}$  [*Johnston*, 1996, p.511]. However, the nominal test conditions are deemed sufficient to qualify the part for missions of interest (cf. Footnote 28 of Chapter 4).

<sup>132</sup>In addition to burn-in, the chips underwent vibration and shake tests to evaluate the mechanical integrity of their bonding and packaging. Although the details are omitted here, being ancillary to their electronic design, it is noteworthy that all units qualified under the guidelines of Military Standard 810G, Environmental Engineering Considerations and Laboratory Tests for these high-reliability tests, including random and sinusoidal vibration and shock spectrum [*MIL-STD-810G*, 2008, Method 513.6–516.6].

the overall reliability of the population, increasing mission longevity.

Burn-in testing is conducted in collaboration with the Lockheed Martin Advanced Technology Center in Palo Alto, CA and conforms to the edicts of the applicable Military Standard [*MIL-STD-883G*, 2006, Method 1015.9]. A comprehensive exegesis of the experimental conditions and results is provided in Appendix K, the salient points of which are included below.

### 6.5.1 Procedure

As in the PD test bench, the complete signal path through both the LNA and AAF is assessed during burn-in testing.<sup>133</sup> Using a suite of modified test benches corresponding to those of Section 6.2.1 through Section 6.2.4, the SVEPRE-3 lot is first characterized in terms of its frequency response, gain compression, SFDR, and power dissipation. Next, the chips are placed in a thermal chamber for a minimum of 160 continuous hours while held at a constant temperature of 125°C and operating under nominal bias.<sup>134</sup> At the conclusion of the bake,<sup>135</sup> each device is re-evaluated using the identical characterization procedures and the results compared with the preceding data to ascertain which devices remained functional and best retained their performance.

### 6.5.2 Results

No part failures were observed during burn-in, with all components remaining functional. Furthermore, performance degradation along the axes noted in Section 6.5.1

---

<sup>133</sup>The output of the LNA, which is programmed to a nominal gain of  $G_p = 23$  dB, is AC-coupled to the input of the AAF, which is programmed to Mode A and trimmed to a nominal bandwidth of  $f_{pa} = 35$  kHz. For further explanation of this configuration, refer to Section K.1.2.

<sup>134</sup>Each part is housed in a lateral-force socket with its input and output terminations, reference current generation, programming voltages/resistances, supply decoupling, and fusing provided locally. All values are nominal except that  $R_d = 19.6$  k $\Omega$  and  $I_E \simeq 47$   $\mu$ A in order to effect to programming described in Footnote 133. Power (+2.5 V) and reference voltages (+1.0 V and +1.75 V) are tapped from a global resistor ladder via 10- $\Omega$  fuses. Consult Figure K.1 for complete details.

<sup>135</sup>The post-burn-in measurements must be concluded within 96 hours of the removal of bias or temperature (whichever is later) in order to avoid a 24-hour re-burn interval [*MIL-STD-883G*, 2006, Method 1019.5, Sect. 3.2].

Fundamental Frequency [kHz]	Power		Gain error		Residue		SFDR	
	$\Delta\mu$ [%]	$\Delta\sigma$ [%]	$\Delta\mu$ [dB]	$\Delta\sigma$ [dB]	$\Delta\mu$ [%]	$\Delta\sigma$ [%]	$\Delta\mu$ [dB]	$\Delta\sigma$ [dB]
$10^{-1}$			0.03	0.02	0.03	-0.18	-0.15	-0.06
$10^0$	0.05	0.43	-0.01	0.00	0.04	-0.19	-0.25	-0.25
$10^1$			-0.01	0.00	0.02	-0.22	-0.01	-0.04
Average	0.05	0.43	0.00	0.01	0.03	-0.20	-0.14	-0.09

Table 6.12: Summary of SVEPRE-3 performance variation during burn-in testing. Columns describe the burn-in-induced change in the mean ( $\Delta\mu$ ) and standard deviation ( $\Delta\sigma$ ) of each metric over the tested population. Consult Section K.2.2 for metric definitions.

was minimal.

Table 6.12 summarizes the changes ( $\Delta$ ) in the ensemble mean and ensemble standard deviation of the power dissipation, DC gain error, gain compression residue, and SFDR (each of which is rigorously defined in Section K.2.2) for each of the fundamental frequencies tested. Aggregating the results at all frequencies emphasizes that the cumulative changes in both the mean and spread of performance across the ensemble are negligible. For instance, the change in the mean SFDR is only  $-0.14$  dB and the standard deviation of the SFDR averaged over the population changes by just  $-0.094$  dB, so both the absolute linearity and the spread in fidelity across the lot are practically insensitive to thermal stress at all frequencies measured. Thus, burn-in evaluation confirms the robustness of the SVEPRE-3 design.

# Chapter 7

## Conclusion

The development of the next generation of wideband plasma wave receivers for satellites investigating wave-particle dynamics in the Van Allen belt is contingent upon a new type of analog front-end—an integrated circuit consisting of a highly linear, broadband, low-noise amplifier (LNA) with programmable gain and an aggressive, low-distortion, anti-aliasing filter (AAF) whose bandwidth can be both coarsely programmed and finely trimmed. These elements should faithfully sense the potential induced by the magnetospheric phenomena of interest at the terminals of a long dipole antenna and condition the resulting high-dynamic-range signal to permit subsequent scientific analysis via spectrographic representations in the discrete domain. All the while, the integrity of this signal processing must withstand the deleterious consequences suffered by microelectronics in the near-Earth radiation environment—both the long-term, accumulated damage suffered from prolonged total dose exposure and the instantaneous but potentially catastrophic repercussions of single particle impacts.

This dissertation describes the design, implementation and testing of SVEPRE—the first fully-integrated analog front-end for such satellite-based, wideband plasma wave receivers. While uncovering no comparable solutions with flight heritage, a comprehensive and heretofore unavailable survey of plasma wave receivers—flown past and present—identifies the mass and power required of such a front-end for the resulting instrument to be compatible with both medium-scale and miniaturized host

satellites.

An assessment of the total dose effects of both ionizing and non-ionizing radiation on the degradation of MOS and bipolar transistors, as well as their potential to engender single-event latchup and transients, confirms that the benefits of fabrication with a commercial manufacturing process can best be retained through the use of radiation-hardness-by-design techniques to mitigate these undesirable ramifications. This conclusion is supported through total-dose characterizations of representative transistors from the target technology: a 0.25- $\mu\text{m}$  SiGe BiCMOS technology fabricated on a non-epitaxial substrate whose CMOS(bipolar) transistors are isolated by shallow(deep) trenches filled with silicon dioxide(polysilicon).

By next distilling the scientific requirements for adaptability, dynamic range, spectral analysis, and absolute accuracy into a set of circuit specifications for the LNA and AAF, this work extends previous design efforts by proffering several novel derivations, particularly with regard to: the range of programmability necessary for a single front-end to be integrated with the majority of electric-field antennas and digital back-ends presently in use; the preeminence of spurious-free dynamic range (SFDR) in assessing the spot and large-signal linearity of incoherent signals; and the relative contributions from the noise of a dipole antenna in a magnetospheric plasma and from MOSFET flicker noise in attaining high dynamic range from 100 Hz to 1 MHz.

To satisfy these satellite-, radiation-, and science-driven requirements, a three-tiered strategy is employed in the SVEPRE design. At the architectural level, feedback provided by both linear, passive components and nonlinear, active elements is nested locally within both the LNA and AAF so as to ultimately render their overall performance independent of the nonlinearities and radiation susceptibilities of the underlying transistors over the full range of programmable operation. Judicious typing, sizing, balancing, and biasing of the transistor-level implementations of the feedback loops, and their plants, attempts to maximize desensitivity subject to power and area constraints. Finally, to mitigate fabrication nonidealities, the custom layout of the final chip is liberally infused with latchup-prevention, transient-tolerance, and differential-matching structures.



For the LNA, this approach is realized by a modified, fully-differential instrumentation amplifier wherein super hybrid emitter-followers comprising a loop of npn and pMOS devices in the first stage achieves high input impedance, low noise, and a highly linear gain that is programmed by means of a single off-chip resistor. A low-power, wide-bandwidth output stage complements this input stage but leverages feed-forward principles to reduce overhead and improve stability. Together, these techniques produce an LNA with 0–24 dB programmable gain that is capable of electric-field measurements from 100 Hz to 4 MHz with better than 96.9-dB(90.3-dB) peak SFDR at 1 kHz(5 kHz) while consuming just 1.78 mW.

The AAF implements a 6<sup>th</sup>-order Type I Chebyshev low-pass transfer function using a cascade of three canonical second-order sections. At the heart of each fully differential, biquadratic stage are  $G_m$ -C-Opamp integrators featuring a novel transconductor that harnesses the aforementioned principles to attain a  $36\times$  tuning range without sacrificing third-harmonic suppression of at least 96.6 dB(91.2 dB) at 1 kHz(10 kHz). To attain this combination of tunability and fidelity, the first stage of the transconductor incorporates innovative positive feedback into a customary translinear loop to perform a highly linear, fixed-gain, voltage-to-current conversion, whereas the second stage—a linearized Gilbert gain cell with unique scalability and common-mode biasing—amplifies that current. By economizing the power required for these two steps, the power consumed by the overall filter: equates to just 6–8 mW/pole; varies by only  $1.25\times$  over the full tuning range; and exhibits an efficiency of up to 88% as the cut-off frequency is trimmed via a single off-chip resistor.

Radiation testing of SVEPRE samples with both  $^{60}\text{Co}$  and high-energy proton sources verifies that despite the degradation of their radiation-soft transistors, the LNA and AAF maintain performance up to at least 100 krad(Si) total-dose and remain functional up to 1000 krad(Si) and 300 krad(Si), respectively, as a result of the design hardening techniques employed. In addition, no evidence of latchup or irrecoverable transients are observed during multiple rounds of single-event testing with heavy-ion LETs up to 58.72 MeV-cm<sup>2</sup>/mg and pulsed-laser equivalent LETs in excess of 100 MeV-cm<sup>2</sup>/mg. Finally, the flight worthiness of SVEPRE is confirmed through burn-in, vibration, and shock screening.

## 7.1 Performance Summary

Permitting direct comparison with the specifications put forth in Table 3.2, the measured performance of the SVEPRE LNA and AAF are summarized in Table 7.1 and Table 7.2, respectively.<sup>1</sup> Apart from the second-harmonic linearity of the AAF, which is compromised by the omission of the GGC degeneration resistors described in Section 5.5.2.2, these devices achieve the stated requirements for baseline operation and, over the full sets of programmable gain and bandwidth, maintain their performance up to 100 krad(Si) total dose and remain free of latchup up to  $\sim 100 \text{ MeV-cm}^2/\text{mg}$ .

Additionally, it has been shown that the LNA(AAF) remains functional up to a total accumulated dose of 1000 krad(Si)(300 krad(Si)) from 50-MeV(30-MeV) protons. Deviations in the measured gain, bandwidth, linearity, and power dissipation of both devices between the specified total-dose target and these operational limits is gradual and benign, bespeaking their utility for applications in even more hostile radiation environments where absolute fidelity is not as essential as prolonged functionality.

Furthermore, since no latchup or catastrophic single-event transients were observed up to the highest LET tested with both pulsed-laser ( $100 \text{ MeV-cm}^2/\text{mg}$ ) and heavy-ion ( $58.72 \text{ MeV-cm}^2/\text{mg}$ ) stimulation, the designs exhibit robustness to single-particle phenomena at energy levels anticipated in near-Earth space.

All 32 devices in a lot subject to 160-hour burn-in at  $125^\circ\text{C}$  remained functional and exhibited only minor variations in gain, linearity, and power dissipation.

---

<sup>1</sup>These capabilities also compare very favorably with the instruments of Table B.6, though a lack of comprehensive data on their front-end designs undermines line-by-line juxtaposition. It suffices to recognize that, without the need for logarithmic compression or automatic gain control, the dynamic range and bandwidth of the SVEPRE front-end surpasses that of all (let alone any one) of the paths within all but one of these WBRs.

Property		Measured performance	
Technology		0.25- $\mu\text{m}$ SiGe BiCMOS, 1P5M	
Supply voltage		+2.5 V	
Output range		1.0 V <sub>PP</sub> differential	
Chip area		10.0 mm <sup>2</sup> (5.5 mm <sup>2</sup> core)	
LNA area		0.125 mm <sup>2</sup>	
Gain range <sup>a</sup>		0–24 dB ( $R^2=1.0000$ )	
Input-referred noise <sup>b</sup>		190 nV/ $\sqrt{\text{Hz}}$	
Input impedance <sup>c</sup>			
$G_p=0$ dB		18.3 G $\Omega$ $\parallel$ 4.24 fF	
$G_p=24$ dB		6.66 G $\Omega$ $\parallel$ 10.4 fF	
Total dose <sup>d</sup>	0 krad(Si)	$\Delta$ @ 100 krad(Si)	$\Delta$ @ 1 Mrad(Si)
DC gain	20.0 dB	+0.03 dB	−0.02 dB
−3 dB bandwidth	3.91 MHz	−5.2%	−1.53%
SFDR <sup>e</sup>			
$f_o=1$ kHz	96.9 dB	−1.27 dB	−0.71 dB
$f_o=5$ kHz	90.3 dB	−2.07 dB	−0.93 dB
Power consumption	1.78 mW	+1.04%	−3.26%
Single event	Heavy ion (10 MeV/nuc.)	Pulsed laser (590-nm)	
No latchup	up to 58.72 MeV-cm <sup>2</sup> /mg	up to $\sim 100$ MeV-cm <sup>2</sup> /mg	
Transients <sup>f</sup>		No oscillation/saturation	
Amplitude <sup>g</sup>		10–25 [40] mV	
Recovery time <sup>g</sup>		1–1.5 [4] $\mu\text{S}$	
Sat. cross-section <sup>h</sup>	See Figure 6.30		
$V_{\text{in}}=0$ V <sub>DC</sub> <sup>i</sup>	$1.02 \times 10^{-4}$ cm <sup>2</sup>		
$V_{\text{in}}=30$ V <sub>amp</sub> <sup>j</sup>	$3.70 \times 10^{-5}$ cm <sup>2</sup>		
$V_{\text{in}}=60$ V <sub>amp</sub> <sup>j</sup>	$2.55 \times 10^{-5}$ cm <sup>2</sup>		

<sup>a</sup> Programming coefficient of determination measured for linear fit to  $R_d^{-1}$  over 0–28 dB

<sup>b</sup> Average over measurement bandwidth of 100 Hz to 800 kHz

<sup>c</sup> Obtained from full-chip AC simulations; does not include bonding and packaging

<sup>d</sup> Tested using <sup>60</sup>Co and 50-MeV H<sup>+</sup>; worst-case deviation ( $\Delta$ ) given at each dose

<sup>e</sup> Assessed from 100 Hz to  $5f_o$  with resolution bandwidth of 0.76 Hz/bin

<sup>f</sup> Results for threshold scans (<57 pJ) given; for high-LET scans, see Table 6.10

<sup>g</sup> Range corresponds to typical-case averages; quantity in brackets is maximum observed

<sup>h</sup> Saturated cross-sections ( $\sigma_{\text{sat}}$ ) from Weibull fits; See Table 6.11 for remaining parameters

<sup>i</sup> Total  $\sigma_{\text{sat}}$  for DC input (given in V<sub>DC</sub>) where  $V_{\text{thresh}} = \pm 30$  mV

<sup>j</sup> Averaged  $\sigma_{\text{sat}}$  for sinusoidal input (given in V<sub>amp</sub>) where  $t_{\text{thresh}} = 40$   $\mu\text{S}$

Table 7.1: Summary of measured SVEPRE LNA performance.

Property	Measured performance								
Technology	0.25- $\mu\text{m}$ SiGe BiCMOS, 1P5M								
Supply voltage	+2.5 V								
Output range	1.0 $V_{\text{PP}}$ differential								
Chip area	10.0 $\text{mm}^2$ (5.5 $\text{mm}^2$ core)								
AAF area	5.375 $\text{mm}^2$								
Bandwidth mode	Mode A			Mode B			Mode C		
Passband cut-off	$f_{\text{pa}} = 30$ kHz			$f_{\text{pb}} = 180$ kHz			$f_{\text{pc}} = 1080$ kHz		
Trimming range	$\pm 25\%$			$\pm 25\%$			$\pm 25\%$		
Linearity <sup>a</sup>	$R^2 = 1.0000$			$R^2 = 1.0000$			$R^2 = 0.9947$		
Efficiency <sup>b</sup>	88.0%			84.2%			51.9%		
Total dose <sup>c</sup> [krad(Si)]	0	100	300	0	100	300	0	100	300
Passband gain [dB]	+0.06	+0.09	−0.07	−0.14	−0.11	−0.08	−0.16	−0.14	−0.07
Roll-off freq. <sup>d</sup> [kHz]									
$f_{\text{m}}$ @ −45 dB	49.0	48.9	50.7	296	291	291	1730	1730	1660
$f_{\text{n}}$ @ −60 dB <sup>e</sup>	59.3	61.3	63.2	373	381	382			
SFDR3 <sup>fg</sup> [dB]									
$f_{\text{o}} = 1$ kHz	96.6	94.3	87.3	100.3	95.5	93.5	97.8	92.7	93.0
$f_{\text{o}} = 10$ kHz	91.2	89.4	83.6	96.0	90.6	82.9	96.3	90.5	83.8
Power <sup>h</sup> [mW]	36.7	36.5	37.7	38.8	38.7	37.5	48.1	47.9	47.0
Single event	Heavy ion (10-MeV)					Pulsed laser (590-nm)			
No latchup	up to 58.72 MeV-cm <sup>2</sup> /mg					up to ~100 MeV-cm <sup>2</sup> /mg			

<sup>a</sup> Trimming coefficient of determination measured for linear fit to  $I_{\text{E}}$  over indicated range<sup>b</sup> Power efficiency as defined by (6.15) is measured from linear regression over full range<sup>c</sup> Tested using 30-MeV  $\text{H}^+$ ; 0 krad(Si)—Baseline; 100 krad(Si)—Specified limit; 1 Mrad(Si)—Highest functional dose<sup>d</sup> Roll-off is relative to actual, not nominal,  $f_{\text{p}}$  location. See Footnote 98 of Chapter 6 for values<sup>e</sup> Measurement nonidealities corrupt  $f_{\text{n}}$  determination in Mode C; See Footnote 125 of Chapter 6<sup>f</sup> Accounts for 3<sup>rd</sup> harmonic distortion; Measured at Stage 1 output according to (6.14)<sup>g</sup> Assessed from 100 Hz to  $5f_{\text{o}}$  with resolution bandwidth of 0.76 Hz/bin<sup>h</sup> Average power consumption measured over 30-s interval with 10-kHz, 50 mV<sub>PP</sub> input tone

Table 7.2: Summary of measured SVEPRE AAF performance.

## 7.2 Mission Opportunities

On the basis of these characteristics, the SVEPRE front-end is presently slated for deployment on the following missions:<sup>2</sup>

### *Sprite-Sat*

Launched by Tohoku University on January 23, 2009 and nicknamed Raijin, the Sprite-Sat satellite is presently carrying a single-channel VLF plasma wave receiver with a SVEPRE front-end.

### *DSX*

The Air Force Research Laboratory's Demonstration and Science eXperiments (DSX) satellite (scheduled launch: 2012) will carry the Wave Induced Precipitation of Energetic Electrons (WIPER) instrument (scheduled delivery: 2009) whose BroadBand Receiver (BBR) contains five channels that leverage the SVEPRE front-end to process signals from both electric and magnetic field antennas.<sup>3</sup>

### *Firefly*

A collaboration between NASA and Siena College on a CubeSat nanosatellite, the Firefly mission (scheduled launch: 2012) will use SVEPRE for the front-end of a two-channel, electric-field receiver.

In addition, it should be evident that the SVEPRE front-end and the techniques used in its design are applicable whenever high-fidelity, broadband, radiation-hardened amplification and filtering are required.

## 7.3 Suggestions For Future Research

The first and most obvious direction for future research on this topic encompasses extended characterization of the proposed design. As noted in Section 6.2.2, the LN

---

<sup>2</sup>All dates are current as of December 1, 2009.

<sup>3</sup>On the B-field channels, SVEPRE is fed by the integrated preamplifiers of the magnetometer search coils, which are responsible for the impedance matching.

test bench is designed and verified to evaluate the SVEPRE SFDR at 100 kHz,<sup>4</sup> but such high-frequency measurements were prohibited by the constraints of the radiation test schedule. Carrying out these measurements in both baseline and total-dose radiation environments is a straightforward exercise and will confirm the simulated efficacy of the proposed linearization techniques for the both the LNA and AAF at the upper end of the plasma wave spectrum. Also, upon its return from fabrication, the latest version of SVEPRE incorporating the previously omitted GGC degeneration resistors to improve matching (cf. Section 6.3.3.3) should be subject to the suite of characterization test benches described in Section 6.2; particularly the LN test bench, in order to verify the improved distortion predicted by Monte Carlo analysis. Finally, to ascertain the specific causes of the total-dose failures observed above 300 krad(Si), further radiation diagnostics may be conducted on the current part inventory.<sup>5</sup>

A broader category of potential investigations centers on extensions to the present design. Perhaps the most straightforward is to eschew the limiting substrate pnp transistors of the AAF by migrating the design to a process that offers complementary bipolar transistors (with vertical pnp devices comparable in gain and radiation-hardness to their npn counterparts) or mature gate-controlled lateral pnps. At the outset of Chapter 5 it is noted that switched-capacitor (SC) filters offer power savings and a degree of inherent anti-aliasing that makes them attractive alternatives to the integrated, continuous-time (ICT) realization pursued here, provided linearity and radiation-hardening challenges can be met and a high-precision, high-frequency clock obtained. With SC filters and modulators a continued area of active research for communications applications [*Korotkov et al.*, 2008; *White et al.*, 2009], significant progress on these fronts may well be imminent. The implementation of an automatic tuning scheme for the AAF [*Banu and Tsividis*, 1985] was circumvented in light of

---

<sup>4</sup>A brief description of the LN test bench configuration for 100-kHz sinusoidal input is provided in Section 6.2.2.1 and more detailed enumeration of the associated PCB options attends the treatment of the appropriate blocks in Appendix H.

<sup>5</sup>Given the shortcomings of the SVEPRE-3 layout in terms of design-for-test sensibilities, perhaps a more efficient approach is the fabrication of a radiation test vehicle containing break-outs of the suspected culprits—especially the substrate pnps in the transconductors—with sufficient transparency so that individual circuit blocks can be evaluated in isolation during controlled radiation experiments.

similar reservations regarding the implementation of an on-chip phase-locked loop (PLL) or oscillator.<sup>6</sup> However, an extension of the placement and layout strategies employed for the transconductor switches of Section 5.5, which proved efficacious in single-event testing of SVEPRE, as well as incorporating recent proposals for improving the hardness of digital logic [[Lee, in preparation](#)], may offer opportunities to realize all the elements of such a tuning scheme without sacrificing the robustness of the front-end.

Finally, in keeping with the theme of integration, the next phase in the evolution of satellite-based, wideband, plasma wave receivers is to not only integrate all the analog amplification and filtering, as in the SVEPRE front-end, but the analog-to-digital converter (ADC) as well. To that end, it is postulated that SVEPRE and the ADC of [Wang \[2009\]](#) can be integrated onto the same die to form a mixed-mode, system-on-chip that further leverages the economies of mass and power discussed in Section 1.2.2.<sup>7</sup> Doing so may well demand solutions to the issues of: buffering the ADC input;<sup>8</sup> preventing digital noise from coupling into the sensitive analog circuitry through the substrate [[Xu, 2001](#)]; and reducing the total die area. But, individually, none of these challenges is anticipated to be insurmountable and the collective solution may pave the way for the incorporation of the aforementioned switched-capacitor and automatic-tuning schemes. Indeed, with the eventual goal of also synthesizing the full digital back-end, thereby producing a single-chip, single-channel, wideband plasma wave receiver, the pursuit of large-scale, mixed-signal integration that preserves the demonstrated baseline performance and radiation tolerance of the SVEPRE design is perhaps the most promising tack for future exploration.

---

<sup>6</sup>Specifically, the increased complexity and power dissipation associated with hardening such discrete circuitry against SEEs may neutralize the benefits of their integration.

<sup>7</sup>Notably, the [Wang \[2009\]](#) converter only integrates the analog section of an ADC. As conceived, this joint solution would also incorporate the digital portion presently housed in a rad-hard FPGA so as to reduce the impact of its inclusion on resource-limited or single-channel instruments.

<sup>8</sup>For example, in the WBR model of Section K.1.2, a discrete opamp implementation of a high-speed, gain-of-two buffer precedes the ADC. If it still proves necessary, then the design of this block certainly factors into the set of integration challenges.





# Appendix A

## Space Plasma Physics

This appendix provides an overview of plasma physics in the Earth’s magnetosphere as it pertains to wave-particle interactions. Each section offers a broader context for the topics in a corresponding section of Chapter 1. In so doing, it not only justifies restricting this work to a subset of wave-particle phenomena—the interactions of a particular class of electromagnetic solutions to the wave equation (i.e., electron whistler-mode waves) with particles in a small portion of the magnetosphere (i.e., the radiation belts)—but also provides perspective on the critical role of such interactions in the whole of magnetospheric physics.

Section A.1 outlines the geometry of the near-Earth space environment, particularly the magnetosphere, as it frames the radiation belts described in Section 1.1.1. In Section A.2, the physics that govern particle trapping in the radiation belts is explored through the role of the Earth’s magnetic field (cf. Section 1.1.2) in determining the motions of particles at each point in the magnetosphere. Finally, Section A.3 expounds on the nature of the interactions between the plasma waves of Section 1.1.3 and radiation-belt particles that form the basis of the science for which the target receiver is intended.

## A.1 The Earth's Magnetosphere

Initial efforts to classify the stratification of the Earth's atmosphere as a function of altitude were guided by temperature gradient measurements,<sup>1</sup> giving rise to the nomenclature depicted in Figure A.1: the *troposphere* (so named by Napier Shaw) describes the region in which temperature decreases with altitude, or lapses, up to 10 km; above this, the temperature then increases with altitude, or mounts, throughout the *stratosphere* (Shaw), up to 50 km; the return to a lapsing gradient from 50–80 km was jointly dubbed by Sydney Chapman and Marcel Nicolet as the *mesosphere*; the mounting region above the mesosphere, known as the *thermosphere* (attributed to Chapman), extends upwards from 80 km to 1000 km; and, finally, the term *exosphere* (coined by Nicolet) applies to the uppermost layer, above the thermosphere, from which particles can escape the Earth's atmosphere (not pictured) [[Chapman, 1960](#), p.1-4], [[Nicolet, 1960](#), p.17–22]. By convention, the boundary, or pause, between any two regions is identified with the lower strata, producing the depictions of the *tropopause*, *stratopause*, *mesopause*, and *thermopause*, in ascending order.

Subdivision of the same altitude range according to the average molecular mass of the atmospheric constituents,  $M_m$ , rather than temperature, produces a distinction between the *homosphere* (Nicolet), below 85 km, where the mixing afforded by air turbulence is sufficient to homogenize the molecular composition, and the *heterosphere* (Nicolet), where mass-dependent diffusion and dissociation processes driven by the large temperature gradient dominate, leading to variations in composition with altitude [[Nicolet, 1960](#), p.20]. For slabs over which the temperature and force of gravity can be treated as constant, the air in these regions is modeled as an ideal gas, held in diffusive equilibrium by the balance of density and gravitational ( $g$ ) forces, and each of its constituents exhibits an exponential pressure ( $P$ ) and density ( $N$ ) distribution in altitude ( $h$ ) that obeys

$$\frac{P}{P_0} = \frac{N}{N_0} = e^{-\frac{h}{H}} \quad (\text{A.1})$$

---

<sup>1</sup>With only gradual transitions delineating them, there is some debate about the precise altitude boundaries of the regions described herein; all distances should be considered approximate.

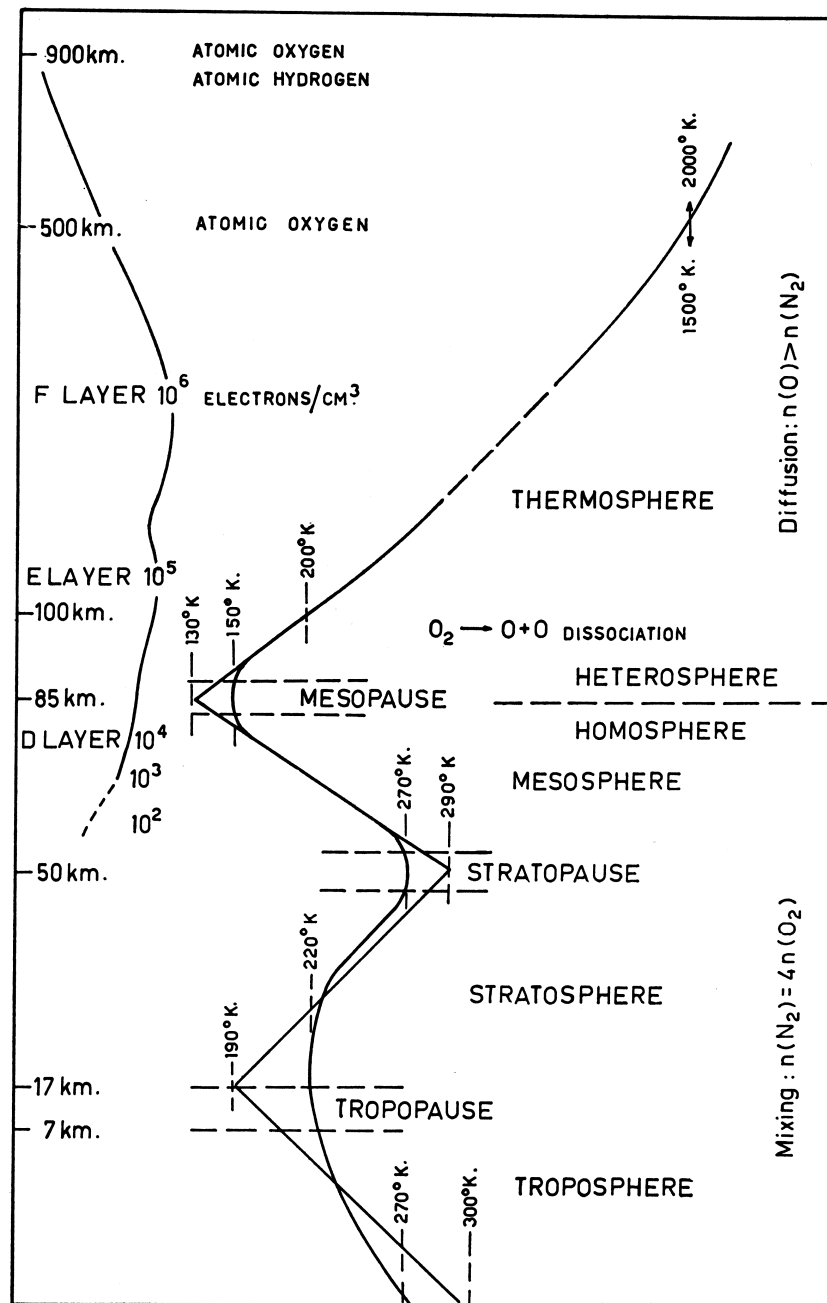


Figure A.1: Nomenclature for strata of the Earth's upper atmosphere. The central curves represent the variation of temperature (abscissa) with altitude (ordinate) whereas the curve in the upper left uses electron density as its abscissa. The taxonomies for delineation according to  $N_e$ ,  $T$ , and  $M_m$  are denoted from left-to-right using all capital letters. Reproduced *in toto* from [Nicolet, 1960, p.18].

where  $H$  is known as the local *scale height* (Chapman) given by  $H = kT/mg$  [Nicolet, 1960, p.19]. At the edge of the homosphere, where the mean mass is uniform,  $H \simeq 6$  km [Bortnik, 2004, p.38].

In the study of solar system plasma physics it is convenient to superimpose upon Figure A.1 a third taxonomy that delineates layers according to the properties of their constituent plasmas and dominant interaction mechanisms. The lowermost of these, identified by Robert Watson-Watt in 1926 as the *ionosphere* [Gardiner, 1969], covers the range from 90–1000 km, lying predominantly in the thermosphere. Here, solar ultraviolet radiation partially ionizes the neutral atmosphere, giving rise to a weakly-ionized but dense, cool plasma,<sup>2</sup> with ion and electron energies typically less than 0.1 eV [Spasojević, 2003, p.5–6]. Above about 1000 km, the ionosphere smoothly transitions into a realm where the neutral collision frequency drops significantly with the exponential rarefaction of the atmosphere in (A.1) [Banks, 1979, p.63]. With only infrequent collisions, the behavior of the strongly and, in its outer reaches, even fully ionized but tenuous plasma in this region is dominated by the terrestrial magnetic field; hence, it is has been termed the *magnetosphere* [Gold, 1959]. Home to a complex, closed set of five large-scale current systems, populated by ionized particles with a wide range of energies, and interlaced with magnetic and electric fields of diverse origin, the magnetosphere can be decomposed into several plasma domains, illustrated in Figure A.2 and summarized below.

### A.1.1 Outer Magnetosphere

A magnetosphere can be understood as the plasma cavity defined by the field lines of a magnetized body when it presents an obstacle to a continuously streaming plasma flow [Roederer, 1979, p.3]; this renders it a feature common to many celestial bodies. In the case of the Earth, whose magnetic field lines would otherwise resemble those of a dipole at such distances (cf. Section 1.1.2.1), the supersonic flow of a hot, collisionless stream of radiation from the sun’s corona, known as the solar wind, impinges upon

---

<sup>2</sup>More formally, these plasma adjectives should be taken to imply the following numerical properties in the context of the ionosphere: *weakly ionized*— $3 \times 10^{-3}$  [Inan and Inan, 2000, p.444]; *dense*— $10^3 \leq N_e \leq 10^6 \text{ cm}^{-3}$  [Banks, 1979, p.83]; and *cool*— $3 \times 10^2 \leq T_e \leq 10^4 \text{ K}$  [Banks, 1979, p.83].

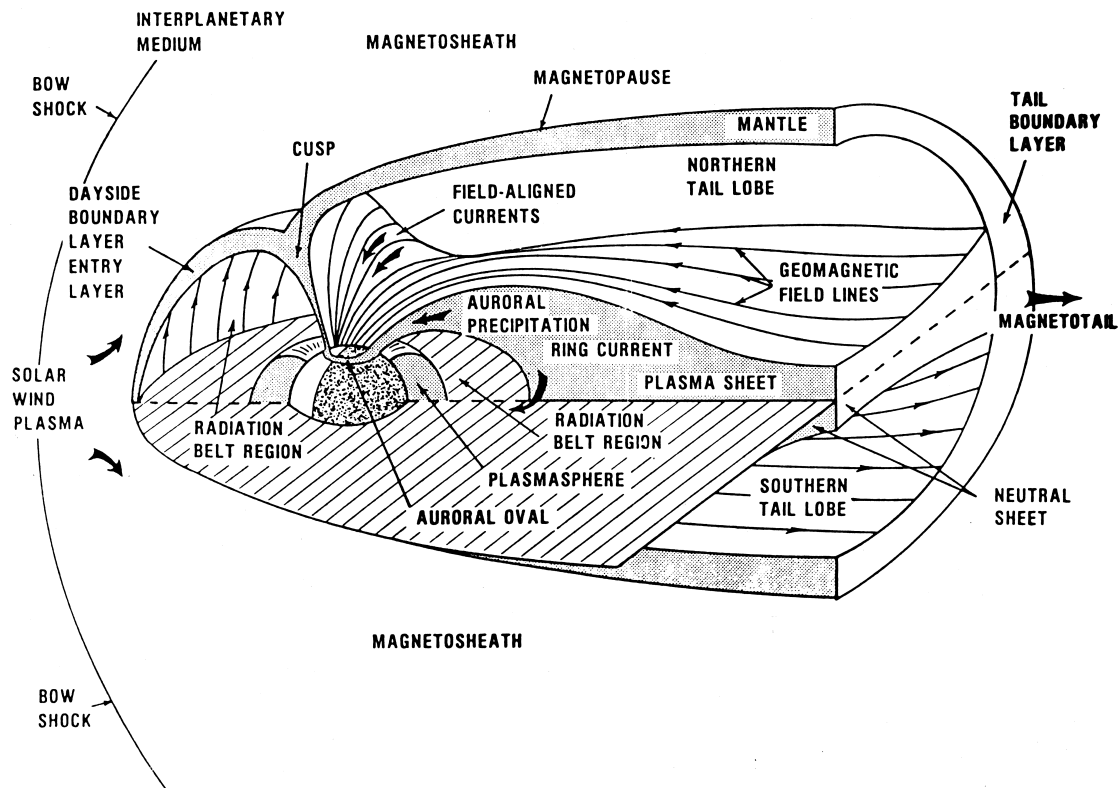


Figure A.2: Artist's rendition of Earth's magnetosphere in cross-section illustrating the radiation belts, described in Section 1.1.1, encircled by several nested plasma layers. Beginning closest to the sun (to the left but not pictured), those detailed in the remainder of this section are the solar wind, bow shock, magnetopause, and plasmasphere. Reproduced *in toto* from [Tascione, 1994, p.58].

this field, and results in the distorted, bullet-like shape of the magnetosphere shown in Figure A.2.

#### A.1.1.1 Solar Wind

The solar wind constitutes a fully ionized plasma, composed primarily of hot protons with average energies of 10 eV [Spasojević, 2003, p.3] that streams away from the sun with a mean velocity of 400–500 km/s [Tascione, 1994, p.31]. Though quite tenuous, with  $N_i \simeq 5 \text{ cm}^{-3}$  at 1 AU [Tribble, 2003, p.19],<sup>3</sup> its impact on the formation of the

<sup>3</sup> 1 AU  $\simeq 1.5 \times 10^8$  km; an Astronomical Unit (AU) is defined as the distance from the Sun to the Earth.

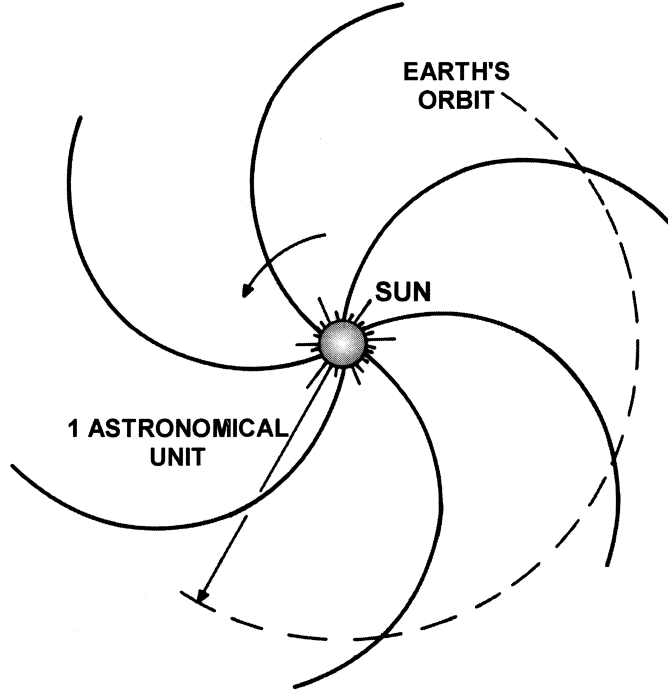


Figure A.3: Two-dimensional projection of Archimedean spiral formed by solar wind as it emanates from the rotating sun at uniform velocity, carrying with it the twisting IMF (Parker spiral). Reproduced *in toto* from [Bittencourt, 1995, p.14].

magnetosphere derives from the fact that the coronal magnetic field is embedded into or ‘frozen-in’ the plasma and carried away from the Sun, along with the Archimedean spiral of corpuscular radiation shown in Figure A.3, forming the interplanetary magnetic field (IMF), which averages 5 nT at 1 AU [Tribble, 2003, p.19].

Obtained from models first reported to much skepticism in 1958 [Parker, 1958], this frozen-in condition derives from treating the solar wind as a perfectly conducting fluid, so that its magnetic Reynolds number,  $R_m = \mu_0 \sigma_0$ , approaches infinity (where  $\mu_0$  and  $\sigma_0$  are the permeability of free space and the fluid electrical conductivity, respectively). Under such conditions, the application of Faraday’s law

$$-\frac{\partial \mathbf{B}}{\partial t} = \nabla \times \mathbf{E} \quad (\text{A.2})$$

and a generalized version of Ohm's law<sup>4</sup> for an infinitely conducting fluid with velocity  $\mathbf{u}$

$$\mathbf{E} = -\mathbf{u} \times \mathbf{B} \quad (\text{A.3})$$

yields the condition that

$$\frac{\partial \mathbf{B}}{\partial t} = \nabla \times (\mathbf{u} \times \mathbf{B}) \quad (\text{A.4})$$

From (A.4) it can be shown that the fluid motion in the direction of the magnetic field is unconstrained, since the cross product goes to zero, whereas the magnetic flux must remain constant through any closed surface of differential area  $d\mathbf{S}$  moving perpendicular to the field [*Bittencourt*, 1995, p.312–315]; or,

$$\frac{\partial}{\partial t} \{\mathbf{B} \cdot d\mathbf{S}\} = 0 \quad (\text{A.5})$$

So, as the solar wind plasma streams transverse to the Sun's magnetic field, constituent particles on a particular field line must remain on it; thus, the solar wind effectively carries the IMF within it.

#### A.1.1.2 Bow Shock

Under most conditions, this solar wind plasma with its embedded IMF cannot efficiently mix with the terrestrial magnetic field, which is similarly frozen into the magnetospheric plasma. Instead, the former is deflected around the latter through a complex interaction that forms a collisionless, magnetohydrodynamic bow shock [*Tascione*, 1994, p.59]. With the frozen-in character of the IMF acting in place of gas-dynamic collisions, this electromagnetic bow shock is somewhat analogous to “the aerodynamic shock found by a blunt object in the supersonic flow of a wind tunnel” [*Tascione*, 1994, p.57]. In both cases, a shock wave is produced because the wind flow is supersonic,<sup>5</sup> meaning no wave in the medium can travel fast enough to convey

<sup>4</sup>As  $\sigma_0$  approaches infinity, the generalized Ohm's law for steady-state ( $\partial/\partial t \rightarrow 0$ ), nearly cold ( $T \rightarrow 0$ ), collisionless ( $\nu \rightarrow 0$ ) plasmas, namely  $\mathbf{J} = \sigma_0(\mathbf{E} + \mathbf{u} \times \mathbf{B})$ , reduces to (A.3).

<sup>5</sup>As opposed to a collisional, thermalized gas, where the mach number reflects the ratio of the fluid velocity to the speed of sound, the term *supersonic* is not terribly appropriate for a collisionless, directed plasma flow. Instead, for the latter case this term should be read as *superalfvénic*, where the Alfvén velocity in (1.13) marks the limit of information transmission in a collisionless plasma,

information about the impending obstacle. In the case of the solar wind, it “converts some of the directed energy of the ions and electrons into thermal motion and reduces the bulk flow velocity to a value below the plasma wave speed” [[Walt, 1994](#), p.2].

### A.1.1.3 Magnetopause

Moving into the narrow region directly behind the bow shock, known as the *magnetosheath*, the subsonic plasma, now compressed and heated, remains turbulent and the fields disordered, until its inward kinetic and plasma pressure balance the outward magnetic and plasma pressure of the magnetosphere [[Walt, 1994](#), p.3]. This surface just behind the shock, akin to a laminar flow boundary [[Tascione, 1994](#), p.57], delineates the IMF from the terrestrial magnetic field and is known as the *magnetopause*. Compressed by the pressure on the sunward side, the magnetopause is located at approximately 8–10  $R_E$ , depending on solar conditions, whereas, on the nightside, tangential drag and other poorly understood processes [[Walt, 1994](#), p.3] result in an indistinct frontier that stretches well beyond the Moon ( $> 60R_E$ ) into the *magnetotail*.

To support the boundary conditions at the border between these two large-scale magnetic fields of distinct origin, the Chapman-Ferraro current system [[Chapman and Ferraro, 1931](#)] flows along the magnetopause, canceling the Earth’s terrestrial field beyond and confining the remaining current systems within. Those additional magnetospheric current systems, which support geomagnetic field arrangements, as well as convert between plasma kinetic energy and electromagnetic field energy, include: the plasma sheet (or cross-tail) current running east-to-west in the magnetotail, which separates the north/south magnetic field lobes from the poles [[Walt, 1994](#), p.3]; the ring current, representing the azimuthal drift of the radiation belts due to the gradients and curvature of the geomagnetic field (cf. Section [A.2.1.2](#)) [[Spasojević, 2003](#), p.7]; and the Birkeland or field-aligned currents, which connect the magnetospheric and ionospheric plasmas (cf. Section [1.1.1.2](#)), playing a role in polar aurora formation [[Birkeland, 1908](#), p.95–105].

---

yielding a solar wind mach number of  $8^+$  [[Tascione, 1994](#), p.39–40].



### A.1.2 Plasmasphere

At the innermost edge of the magnetosphere, with its lower bound provided by the ionosphere, exists the region of highest magnetospheric plasma density, ranging from about  $10^1$ – $10^4$   $\text{cm}^{-3}$  [Tascione, 1994, p.68]. It is populated by electrons and ions injected from the topside ionosphere [Lemaire, 1989], which may be accelerated to average energies near 1 eV by a variety of processes, including Coulomb collisions with suprathermal photoelectrons [Schunk and Watkins, 1979] and interactions with waves generated by the ring current [Gorbachev et al., 1988]. Due to the electric field established by frictional drag, this cold, relatively dense plasma, forming a toroid below  $60^\circ$  geomagnetic latitude,<sup>6</sup> co-rotates with the Earth [Banks, 1979, p.85]. At altitudes where the co-rotational electric field becomes smaller than the convective electric field supporting the cross-tail current ( $\sim 5$   $\mu\text{V}/\text{cm}$  [Schulz and Lanzerotti, 1974, p.6]), plasma densities drop by a factor of 5–10 [Tascione, 1994, p.68]. This sharp, field-aligned density gradient, that on average maps to a circle of  $4R_E$  at the geomagnetic equator,<sup>7</sup> as shown in Figure A.4, forms a boundary beyond which the low density ( $1$ – $10$   $\text{cm}^{-3}$ ) plasma no longer rotates with the angular velocity of the planet, but instead is governed by convection patterns established through interactions with the solar wind [Spasojević, 2003, p.7].

Confirming the pioneering hypotheses of Storey [Storey, 1953] and later Dungey [Dungey, 1954], this boundary and the dense cavity within were independently discovered by Gringauz [Gringauz et al., 1962, p.107] and Carpenter [Carpenter, 1963],<sup>8</sup> termed by the latter as the *plasmopause* and *plasmasphere*, respectively, in keeping with the thermal nomenclature conventions described above [Carpenter, 1966, p.695]. Both are central to the study of resonant wave-particle interactions. Since its abrupt density transition leads to “remarkable differences in wave regimes inside and

---

<sup>6</sup>Henceforth, a coordinate system referenced to the magnetic, as opposed to geographic poles of the Earth, is adopted for all latitude measurements, with the distinction explicitly defined in Section 1.1.2.2.

<sup>7</sup>The difference between the physical equator at which  $R_E$  is defined, and the geomagnetic equator that defines the plane in which the plasmopause dimensions are given, is addressed in Section 1.1.2

<sup>8</sup>For an excellent historical review of the developments surrounding the worldwide participation in the discovery of the plasmasphere, as well as a detailed overview of the associated theoretical and experimental achievements, the reader is referred to [Lemaire and Gringauz, 1998].

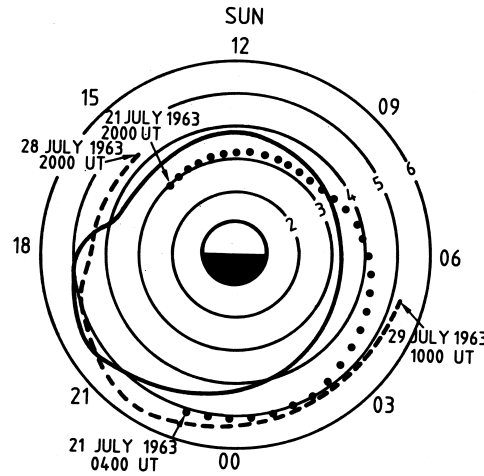


Figure A.4: Average equatorial radius of the plasmapause. The solid line corresponds to moderate levels of geomagnetic activity, whereas the dotted (dashed) lines represent more (less) perturbed conditions. Concentric rings denote  $L$ -shells. Reproduced *in toto* from [Carpenter, 1966, p.698].

outside the plasmapause,” [Lemaire and Gringauz, 1998, p.106] with different wave modes confined to each side, “certain wave-particle interaction effects ... can differ strongly from one side of the plasmapause to the other” [Lemaire and Gringauz, 1998, p.102]. In addition, the plasmasphere, though dense relative to the rest of the magnetosphere, can be mathematically be treated essentially collisionless, so that it acts as “a kind of cavity in which waves are trapped and throughout which they may spread widely,” [Lemaire and Gringauz, 1998, p.98] unencumbered by collisional damping. Such favorable wave conditions are accompanied by an abundant particle population, for within the plasmasphere lie the entire inner zone and the innermost edge of the outer zone of the radiation belts under study in this dissertation (cf. Section 1.1.1); the behavior of this energetic population, which is superimposed on the cold background plasmaspheric plasma just described, is treated next.

## A.2 Particle Trapping

Although Section 1.1.2.1 offers a simple model of the geomagnetic field, which is responsible for the trapping of energetic particles in the radiation belts, the physical

mechanism responsible for this behavior—the Lorentz force—is best examined using the notion of adiabatic invariance. As prologue to the treatment of radiation-belt particle trapping via adiabatic invariance in Section A.2.2, the fundamental components of charged particle motion in this dipole field model are explicated in Section A.2.1.

### A.2.1 Particle Motion

Consider the simple case of a single charged particle of charge  $Q$ , mass  $m$ ,<sup>9</sup> and velocity  $v$  in the presence of a magnetic field,  $\mathbf{B}$ , oriented in the  $\hat{\mathbf{z}}$  direction. A uniform  $\mathbf{B}$  gives rise to pure cyclotron motion, while the nonuniform geomagnetic field introduces additional behaviors, namely drift and bounce motion.

#### A.2.1.1 Cyclotron Motion

In the absence of an electric field ( $\mathbf{E}=0$ ), the Lorentz force,

$$\mathbf{F} = Q (\mathbf{E} + \mathbf{v} \times \mathbf{B}) \quad (\text{A.6})$$

only possesses a component perpendicular to the particle motion,  $\mathbf{v} \times \mathbf{B} = \mathbf{v}_\perp \times \mathbf{B}$ , where  $\mathbf{v}_\perp(\mathbf{v}_\parallel)$  is magnitude of the particle velocity in the  $\hat{\mathbf{x}}\text{-}\hat{\mathbf{y}}$  plane( $\hat{\mathbf{z}}$ -direction), such that  $\mathbf{v} = \mathbf{v}_\parallel + \mathbf{v}_\perp$ . This force can do no work; instead, it is a centripetal force, satisfying Newton’s second law by producing an equilibrium condition in which the particle executes circular motion in the plane perpendicular to  $\mathbf{B}$  with an angular frequency of

$$\omega_c = \frac{|Q|B}{m} \quad (\text{A.7})$$

and a radius of

$$r_c = \frac{mv_\perp}{|Q|B} \quad (\text{A.8})$$

These quantities are known as the cyclotron gyrofrequency (or cyclotron frequency, or Lamor frequency) and gyroradius (or cyclotron radius, or Lamor radius), respectively.

---

<sup>9</sup>Restricting all that follows to the non-relativistic case renders  $m=m_o$ , the particle’s rest mass.

On account of their positive charge and heavier mass, protons rotate much more slowly and in larger,<sup>10</sup> clockwise orbits than counter-clockwise-gyrating electrons.<sup>11</sup> For either carrier, this gyromotion constitutes a current loop that produces its own dipole field with a magnetic dipole moment,  $\boldsymbol{\mu}_m$ , given by analogy to (1.4) as:

$$\boldsymbol{\mu}_m = I\mathbf{S} = \frac{Q\omega_c}{2\pi}\pi r_c^2 \hat{\mathbf{z}} = \frac{mv_\perp^2}{2B} \hat{\mathbf{z}} = \frac{p_\perp^2}{2mB} \hat{\mathbf{z}} \quad (\text{A.9})$$

where  $p_\perp$  represents the perpendicular component of the particle's momentum.

As a consequence of the cross-product in (A.6), this cyclotron motion is simply superimposed upon any initial motion of the particle in the direction of the field, leaving  $\mathbf{v}_\parallel$  unchanged and resulting in a helical trajectory over time. The density of this helix is described by the angle between  $\mathbf{v}$  and  $\mathbf{B}$ , known as the pitch angle  $\alpha_v$ , which is related to the components of  $\mathbf{v}$  through  $\alpha_v = \arctan(v_\perp/v_\parallel)$ .

### A.2.1.2 Drift Motion

In the presence of an additional force  $\mathbf{F}_d$ , the conditions for this uniform circular motion can be violated. The perpendicular component of  $\mathbf{F}_d$  skews the gyroradius at each point in the planar orbit, depending on whether it is working in concert with or in opposition to the  $\mathbf{v} \times \mathbf{B}$  force. The net effect of these contributions is obtained by averaging the sum of both forces over the gyrocircumference,<sup>12</sup> thereby subsuming

---

<sup>10</sup>The larger gyroradius of protons explains why the outer belt consists primarily of electrons: compared to  $r_{ce}$ , the gyroradius for high energy protons is so large that they encounter the homosphere near the poles and are lost to collisions with neutrals [Tascione, 1994, p.54]. By contrast, at inner belt altitudes, given the increased field strength according to (1.7c), the  $r_{ci}$  predicted by (A.8) is small enough to permit stable proton trapping.

<sup>11</sup>This clock-based description assumes a vantage at the field line terminus (cf. Footnote 25 of Chapter 1). Many authors do not take the absolute value of  $Q$  in (A.7) and, instead, use the sign of  $\omega_c$  to describe the sense of rotation, with  $\omega > 0$  implying counter-clockwise rotation, as it typically does for angles in the Cartesian plane. However, this would yield  $\omega_{ce} < 0$ , which is inconsistent with the use of a terminal observation point from which electrons appear to rotate counter-clockwise. Thus, for the stated vantage, this document treats  $\omega_c$  as positive according to (A.7) and imposes the rotational sign convention dictated by problem geometry.

<sup>12</sup>The trajectory that results from the presence of  $\mathbf{F}_d$  traces out a cycloid, not a circle, in the  $\hat{\mathbf{x}}\text{-}\hat{\mathbf{y}}$  plane. But, since  $\mathbf{B}$  and  $\mathbf{F}_d$  are assumed uniform, it is equivalent to integrate over a complete revolution of either. Since the work performed by the conservative force  $\mathbf{F}_d$  must cancel out over the course of one revolution, and since  $\mathbf{B}$  can also do no work, these forces must sum to zero,

the specifics of the cyclotron motion and instead describing the net behavior of the so-called ‘guiding center’ of the orbit [Walt, 1994, p.14]. Such an analysis reveals that the guiding center slowly drifts in the  $\hat{\mathbf{x}}\text{-}\hat{\mathbf{y}}$  plane at a speed  $v_d \ll v$  given by:

$$\mathbf{v}_d = \frac{1}{Q} \frac{\mathbf{F}_d \times \mathbf{B}}{B^2} \quad (\text{A.10})$$

The non-uniformity of Earth’s dipole field introduces two sources of  $\mathbf{F}_d$ , giving rise to two types of longitudinal guiding center drift. The first, known as gradient drift, derives from the  $r^{-3}$  dependence of (1.7a); at a given colatitude, the increase in field strength nearer the Earth constitutes an inwardly directed radial gradient,  $\nabla \mathbf{B}$ , whose corresponding increase in  $\mathbf{v} \times \mathbf{B}$  with  $r$  maps to a force  $\mathbf{F}_{\text{grad}} = -mv_{\perp}^2 \nabla \mathbf{B} / 2B$  such that

$$\mathbf{v}_{\text{grad}} = \frac{mv_{\perp}^2}{2Q} \frac{\mathbf{B} \times \nabla \mathbf{B}}{B^3} \quad (\text{A.11})$$

Conversely, for a particle to continue to gyrate around a given field line as it curves near the poles according to (1.9), it must experience a centrifugal force along  $\hat{\mathbf{R}}_c$ , the direction of the radius of curvature  $R_c$ , that is imposed by the field itself. This force,  $\mathbf{F}_{\text{curv}} = mv_{\parallel}^2 / R_c \hat{\mathbf{R}}_c$ , gives rise to the curvature drift

$$\mathbf{v}_{\text{curv}} = \frac{mv_{\parallel}^2}{QR_c^2} \frac{\mathbf{R}_c \times \nabla \mathbf{B}}{B^2} = \frac{mv_{\parallel}^2}{Q} \frac{\mathbf{B} \times \nabla \mathbf{B}}{B^3} \quad (\text{A.12})$$

The second expression in (A.12), only valid in the absence of any other sources of magnetic fields, formulates the curvature drift as simply drift in response to the gradient observed when traveling latitudinally at a given radius, rather than (A.11), which applies to the gradient observed when traveling radially at a given latitude [Walt, 1994, p.20].

The drifts described by (A.11) and (A.12) are perpendicular to the ambient magnetic field, parallel to one another, and oppositely directed for protons and electrons. When experienced by those particles trapped in the radiation belts,<sup>13</sup>

---

$\mathbf{F}_d + Q(\mathbf{v}_d \times \mathbf{B}) = 0$ , from which (A.10) follows directly; after all, if there were any net force after one gyroperiod, the particle would be accelerated indefinitely [Tribble, 2003, p.123].

<sup>13</sup>Although all trapped particles contribute to some degree [Spasojević, 2003, p.8], the bulk of the

they give rise to an azimuthal current circulating westward around the Earth—the ring current described in Section A.1.1.3 [*Spasojević, 2003*, p.7]. On account of the geometry of the underlying gradients,  $\mathbf{v}_{\text{grad}}(\mathbf{v}_{\text{curv}})$  drift dominates for particles traveling perpendicular(parallel) to the Earth’s field, with correspondingly large(small)  $\alpha_v$ . Given the leading terms of (A.11) and (A.12), protons and electrons with the same kinetic energy in the relevant direction drift at the same speed, even though they have markedly distinct gyroradii, cyclotron frequencies, and thermal velocities [*Tascione, 1994*, p.6].

### A.2.1.3 Bounce Motion

Just as the component of  $\mathbf{F}_d$  perpendicular to the ambient magnetic field controls the azimuthal drift velocity in the above cases, the guiding center of a gyrating particle is also affected by the component of  $\mathbf{F}_d$  parallel to the field, which accelerates the particle according to Newton’s second law, impacting  $\mathbf{v}_{\parallel}$  accordingly. Specifically, it can be shown that wherever magnetic field lines converge, the gradient of increased field strength in that direction, say  $\hat{\mathbf{z}}$ , produces a force in the opposite direction given by [*Walt, 1994*, p.21]:

$$\mathbf{F}_m = -\frac{mv_{\perp}^2}{2B} \frac{\partial B}{\partial z} \hat{\mathbf{z}} = -\mu_m \frac{\partial B}{\partial z} \hat{\mathbf{z}} \quad (\text{A.13})$$

Since it results only from the magnetic field geometry, like its cyclotron and drift counterparts, such a force cannot change the particle energy; instead, as it opposes and thereby reduces  $\mathbf{v}_{\parallel}$ , there must be a corresponding increase in  $\mathbf{v}_{\perp}$  so that  $\mathbf{v}^2 = \mathbf{v}_{\parallel}^2 + \mathbf{v}_{\perp}^2$  is constant. This manifests as an increase in pitch angle and, in the extreme case when the force has decelerated  $\mathbf{v}_{\parallel}$  to zero, converts all the particle’s kinetic energy into perpendicular motion, tipping its pitch angle to  $90^\circ$ . At that point, the particle reverses direction, leading to the description of (A.13) as the mirroring force. Since the convergence of the terrestrial magnetic field at the poles constitutes a gradient capable of such a force, a particle gyrating around a field line with non-zero  $\mathbf{v}_{\parallel}$  at the equator is observed to ‘bounce’ back and forth in latitude, being reflected by this

---

hot plasma comprising the ring current consists of those ions with energies between 1 and 100 keV, for which drift forces due to the steady magnetospheric electric fields are also significant [*Schulz and Lanzerotti, 1974*, p.6].

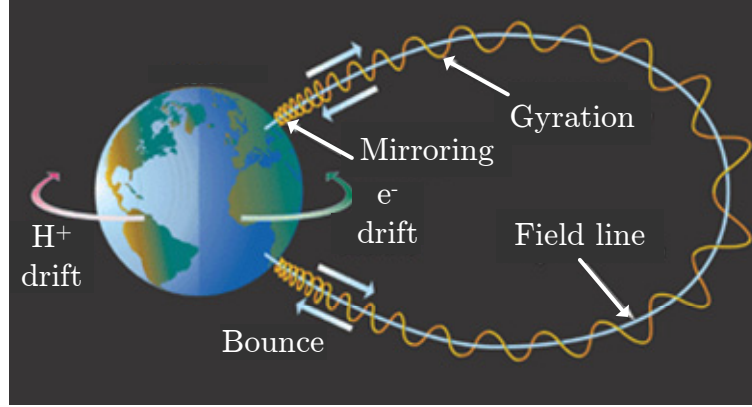


Figure A.5: Three fundamental periodic orbits executed by geomagnetically trapped particles. Depiction of (1) cyclotron (2) bounce and (3) drift orbits is not to scale, nor is rotational sense meaningful except as noted for (3). After [*Jursa, 1985*, p.5-9].

force at its mirror height—that distance from either pole where the field gradient is sufficient to reduce  $v_{\parallel}$  to zero.

Figure A.5 depicts the superposition of all three circular motions described above in a simplified representation of net particle motion in the radiation belts.

### A.2.2 Adiabaticity

In the Earth's magnetic field geometry, each of the three types of conservative particle motion in Figure A.5—gyration, mirroring, and drift—is periodic on a characteristic time scale of order  $10^{-3}$ , 1, and  $10^3$  seconds, respectively, though these vary with the particle energy [*Horne, 2002*, p.808]. In such distinct temporal regimes, these rotational motions are conveniently described through the Hamilton-Jacobi reformulation of classical mechanics, in which the canonical coordinates of phase space, consisting of generalized spatial coordinates  $\mathbf{q}_i$  and their conjugate momenta  $\mathbf{p}_i$ , are transformed into new canonical coordinates, consisting of the action angles  $w_i$  and their generalized angular momenta  $J_i$ , with the latter defined as

$$J_i = \oint \mathbf{p}_i \cdot d\mathbf{q}_i \quad (\text{A.14})$$

where  $d\mathbf{q}_i$  is the differential path length along the  $i^{\text{th}}$  periodic orbit [*Walt, 1994*, p.39]. In these action-angle coordinates, such integrals constitute adiabatic invariants—quantities which remain constant provided that the underlying forces change on time scales(dimensions) much slower(larger) than the frequencies(radii) of the periodic motion [*Schulz and Lanzerotti, 1974*, p.46]. For the triumvirate of charged particle circumvolutions in question, the three integrals corresponding to  $i = 1, 2, 3$  in (A.14) replace the constants associated with three-dimensional rectilinear motion, namely the conservation of the three components of momentum, or of any two and energy [*Schulz and Lanzerotti, 1974*, p.8].

#### A.2.2.1 Adiabatic Invariants

The first adiabatic invariant,  $J_1$ , is obtained from (A.14) by integrating the canonical momentum of a charged particle<sup>14</sup>

$$\mathbf{p} = m\mathbf{v} + Q\mathbf{A} \quad (\text{A.15})$$

over its gyro-orbit, using (A.7), (A.8), and the fact that  $\mathbf{A}$ , the vector magnetic potential, is related to  $\mathbf{B}$  by definition ( $\mathbf{B} \equiv \nabla \times \mathbf{A}$ ). The resulting quantity

$$J_1 = \frac{\pi p_{\perp}^2}{|Q|B} \quad (\text{A.16})$$

must remain constant in the absence of abrupt spatial or temporal variations of the magnetic field [*Schulz and Lanzerotti, 1974*, p.14]. Since any quantity proportional to (A.16) also exhibits this behavior, it is customary to replace  $J_1$  by the particle's magnetic dipole moment,  $\mu_m$ , given by (A.9) so that

$$J_1 \propto \frac{p_{\perp}^2}{2mB} \propto \mu_m = \text{constant} \quad (\text{A.17})$$

---

<sup>14</sup>The second term in (A.15) arises from the presence of the ambient B-field, any time variation of which gives rise, through Faraday's law, to an electric field that asserts force on the particle, thus imparting momentum, even for zero initial velocity.



The second adiabatic invariant, known as the integral invariant, is associated with bounce motion such that when  $d\mathbf{q}_2$  in (A.14) is replaced by the differential length element  $d\mathbf{s}$  along the bounce orbit, which encloses no net magnetic flux, the terms related to  $\mathbf{v}_\perp$  and  $\mathbf{A}$  drop out of the integration of (A.15), leaving

$$J_2 = \oint \mathbf{p}_\parallel \cdot d\mathbf{s} = \text{constant} \quad (\text{A.18})$$

Conversely, the adiabatic invariant associated with drift motion, the third or flux invariant, sees the first term of (A.15) become negligible when integrated over a drift trajectory around the equator, due to the much slower  $v_d$ , leaving

$$J_3 = Q \oint \mathbf{B} \cdot d\mathbf{s} = Q\Phi_m = \text{constant} \quad (\text{A.19})$$

#### A.2.2.2 Adiabatic Motion

For radiation-belt particles, the constancy of each invariant informs the nature of the rotational motion associated with the next highest invariant. Firstly, bounce motion can be interpreted as preservation of the dipole moment since, as seen in (A.13), the mirroring force is directly proportional to  $\mu_m$ ;  $\mathbf{F}_d$  increases the pitch angle in conjunction with  $\partial B/\partial z$  as the field strength increases near the poles, so as to keep  $\mu_m$  fixed despite increasing  $\mathbf{B}$ . In fact, this perspective enables a trivial computation of the mirror height, or the terminus of the bounce motion, in terms of  $\alpha_v$ . From the definition of pitch angle, recall that  $v_\perp = v \sin \alpha_v$ , or  $p_\perp = p \sin \alpha_v$ , where the total momentum,  $p$ , is constant in the absence of electric fields. Substituting this into (A.17) expresses the pitch angle at any point along the field line in terms of its value and that of the magnetic field at the equator, namely  $\alpha_{v_{\text{eq}}}$  and  $B_{\text{eq}}$ :

$$\begin{aligned} \frac{p^2 \sin^2 \alpha_v}{2mB} &= \frac{p^2 \sin^2 \alpha_{v_{\text{eq}}}}{2mB_{\text{eq}}} \\ \therefore \sin^2 \alpha_v &= \frac{B}{B_{\text{eq}}} \sin^2 \alpha_{v_{\text{eq}}} \end{aligned} \quad (\text{A.20})$$

At the mirror point, where the pitch angle goes to  $90^\circ$ , this implies  $B_m = B_{eq} \csc^2 \alpha_{v_{eq}}$ . According to the ideal dipole model in Section 1.1.2.1, specifically (1.7c), this mirror field  $B_m$  occurs at an altitude of  $h_m = r_m - R_E$ , where

$$\sin^2 \alpha_{v_{eq}} = \sqrt{\frac{(r_m/LR_E)^3}{\sqrt{1 + 3(1 - r_m/LR_E)}}} \quad (\text{A.21})$$

If  $h_m$  lies in the homosphere, below  $h_T = r_T - R_E \simeq 85$  km, the particles are subject to collisions which violate the first adiabatic invariant.<sup>15</sup> Giving up momentum in the process, they then precipitate into the ionosphere, rather than mirroring back along the field line, and are said to be lost [Schulz and Lanzerotti, 1974, p.58]. From (A.21), it is clear that the subset of particles at a given  $L$  for which  $h_m \leq h_T$  possesses an equatorial pitch angle  $\alpha_{v_{eq}} \leq \alpha_{v_{blc}}$  where [Lauben et al., 2001]:

$$\sin^2 \alpha_{v_{blc}} = \sqrt{\frac{(r_T/LR_E)^3}{\sqrt{1 + 3(1 - r_T/LR_E)}}} \quad (\text{A.22})$$

These particles are said to be in the bounce loss cone defined by  $\alpha_{v_{blc}}$ , with those at  $\alpha_{v_{eq}} = \alpha_{v_{blc}}$  critically trapped so that any drop in their mirror height through a violation of the first adiabatic invariant causes them to precipitate out of the radiation belts [Bortnik, 2004, p.38].

Next, the integral invariant defines the surface mapped by the drift motion of the particle around the Earth because, at each latitude, there exists only one field line along which  $J_2$  remains constant. This surface is asymmetric due to the compression of field lines on the sunward side: the drift shell must move closer to the Earth on the nightside to encounter higher  $\mathbf{B}$  and thus maintain  $J_2$  over the shorter field lines there [Walt, 1994, p.46]. Additionally, it requires that a particle return to its initial field line, regardless of the distortions it encounters along the path. The lone exception can occur when, during its orbit, the particle adopts a  $J_2$ -conserving field line over the South Atlantic anomaly where  $h_m \leq h_T$  due to the local asymmetry of the Earth's

---

<sup>15</sup>The upper boundary of the homosphere can be treated as a finite limit because  $H$  is sufficiently small compared to the length of the bounce path that the increase in neutral density to a level where  $\nu_n \geq \omega_c/2\pi$  is effectively abrupt.

field relative to the upper atmosphere. Particles which satisfy this condition are said fall into the drift loss cone where  $\alpha_{v_{\text{eq}}} < \alpha_{v_{\text{dlc}}}$ .

Note that together the first two invariants describe the set of field lines at each longitude traced out by a particle in terms of their  $B_{\text{eq}}$  and  $J_2$ , since these quantities are preserved throughout. For an ideal dipole field, such as that described by (1.7c) and (1.9), these define an azimuthally symmetric surface of field lines, or drift shell, with a unique  $L$ , or equatorial crossing altitude. Thus, in the study of geomagnetically trapped radiation, it is convenient to describe a particle's location in terms of an  $L$ -shell. However, the  $L$  value is only a constant when using the offset, tilted, ideal dipole model; in the actual, distorted Earth field, conservation of  $B_{\text{eq}}$  and  $J_2$  throughout a drift orbit requires the particle to follow field lines with slightly different equatorial crossings. Nevertheless, since the  $L$  value along a given field line varies by less than 1% [Tascione, 1994, p.46], it proves sufficient to assume that the magnetic drift shell maps to shell of constant  $L$  at radiation-belt altitudes. In this coordinate system, then, positions on a given  $L$ -shell are equivalent when considering particle bounce and drift motion.

Finally, the flux invariant resolves the specific details of the trajectory followed in response to slow changes in the magnetic field configuration whose causes may include secular variation, solar events, and geomagnetic substorms [Walt, 1994, p.52].

### A.2.2.3 Non-Adiabatic Motion

As emphasized in Section 1.1.1, the composition of the radiation belts is not static, so the motion of its particles cannot be purely adiabatic. After all, “if the invariants were rigorously conserved . . . a trapped particle would remain trapped forever” [Walt, 1994, p.92]. Thus, the source and loss mechanisms that regulate the trapped populations, such as the aforementioned wave-particle interactions, operate by disrupting the conservation of one or more of the adiabatic invariants.<sup>16</sup> This occurs when the underlying assumptions of adiabatic theory regarding the temporal and spatial derivatives of the ambient electromagnetic fields are violated by the presence of wave

---

<sup>16</sup>The exception is the introduction of trapped particles through radioactive decay, including CRAND, wherein the invariant relationships are preserved.

fields that are capable of inducing behavioral changes on those same scales of the corresponding invariant. In the next section, wave participation in such non-adiabatic interactions is cataloged at the level of current understanding.

### A.3 Wave-Particle Interactions

In Section A.2.2.3, it was noted that adiabatic motion of radiation-belt particles constitutes a large-scale, steady-state behavior, deviations from which, in the form of non-adiabatic motion, underlie their non-static nature. Specifically, “geophysically interesting dynamical phenomena related to radiation-belt physics involve the violation of one or more adiabatic invariants” [*Schulz and Lanzerotti, 1974*, p.8]. For each of the generalized angular momenta  $J_i$ , this can occur when disruptive forces act on temporal(spatial) scales shorter(smaller) than characteristic period(radius) of the corresponding rotational motion, over which adiabatic theory only ensures the constancy of the action integral for slowly varying electromagnetic fields. In other words, such forces can finely discriminate amongst particles with the same  $J_i$  according to their orbital phase, given by the canonically conjugate cyclic coordinate  $\mathbf{w}_i$ , thereby preventing them from being treated equivalently.

Instead, under such conditions it becomes necessary to account for these individual phases by considering the entire distribution function,  $f(J, \mathbf{w}, t)$ , akin to that introduced in Section 1.1.3.1 to similarly account for the behavior of the collective plasma. Through a unit Jacobian transform,  $f$  is expressed here in terms of the adiabatic-invariant space, rather than canonical phase space, as in  $f(\mathbf{p}, \mathbf{q}, t)$ , so as to provide a reference frame in which the distribution function only changes when one or more of the invariants is violated, thereby isolating the deviations of interest from the background adiabatic motion [*Walt, 1994*, p.97]. From Liouville’s theorem, a force which is sufficiently coherent so as to selectively organize the set of particles with common invariants around a particular  $\mathbf{w}_i$  must result in corresponding expansion of  $f$  around  $J_i$ , because any local volume of phase space is incompressible [*Schulz and Lanzerotti, 1974*, p.47]. Thus, a spreading in the values of  $J_i$ , and a violation of the corresponding adiabatic invariant, necessarily follows from a deterministic

relationship between the equilibrium  $f$  and a disruptive force that can be described as a function of  $\mathbf{w}_i$ .

In practice, the deterministic character of this broadening of  $J_i$  is obscured by the fact that measurements of both the instantaneous particle population [*Schulz and Lanzerotti, 1974*, p.47] and time-varying fields [*Walt, 1994*, p.93] are inherently phase-averaged due to the finite resolution, in time and space, of any physical instrument. The behavior of the  $f_{\text{avg}}(J, t)$  that results from such inevitable phase mixing, in which the dependence on the cyclic coordinates has been suppressed, thus exhibits “an essential component of randomness [wherein] ... after phase averaging, the various elements of the particle distribution, subject to nonadiabatic forces, usually appear to have walked randomly with respect to the violated invariants” [*Schulz and Lanzerotti, 1974*, p.47]. Given this apparent randomness in  $f_{\text{avg}}$  that results from the loss of the  $\mathbf{w}_i$  information, it is mathematically convenient to employ diffusion theory to frame “the time evolution of a distribution of particles whose trajectories are disturbed by innumerable small, random changes” [*Walt, 1994*, p.93] as diffusion of  $f$  with respect to the adiabatic invariants via Brownian motion in  $J$ -space.<sup>17</sup>

Although somewhat oversimplified, the conventional approach in radiation-belt physics is to offer separate treatments of pitch-angle diffusion, wherein  $J_1$  and/or  $J_2$  are violated, which results in a net loss of trapped particles, and radial diffusion, wherein only  $J_3$  is violated, which can serve as an energization source for new particles [*Schulz and Lanzerotti, 1974*, p.48]. For the purposes at hand, the former provides a sufficient example, as it describes some of the most prominent wave-particle behaviors in the radiation belts.<sup>18</sup>

---

<sup>17</sup>To admit arbitrary coordinate systems, the diffusion formulation conventionally proceeds from the Fokker-Planck equation, which can be formulated in a convenient coordinate system so as to minimize the number of dimensions  $x$  with non-zero diffusion coefficients, given by  $D_{xx} = d/dt(\sigma_{\Delta x}/2)$ . A rigorous presentation of the stochastic mathematics is beyond the scope of this work, but can be found in Chapter 6 of [*Walt, 1994*].

<sup>18</sup>As pertains to the radiation-belt source mechanisms intimated in Section 1.1.1.1, it suffices to observe that inward radial diffusion, which reduces the enclosed flux,  $\Phi_m$ , while preserving  $J_1(J_2)$ , requires an increase in  $p_{\perp}(p_{\parallel})$  in response to the stronger fields(short field lines) at lower altitudes. An exhaustive limning of radial diffusion mechanisms and drivers can be found in Chapter 3 of [*Schulz and Lanzerotti, 1974*].

### A.3.1 Pitch-Angle Diffusion

Occurring on temporal and spatial scales comparable to those of gyration and bounce motion, pitch-angle diffusion allows the assumption of constant  $L$ , since the third invariant is irrelevant [Schulz and Lanzerotti, 1974, p.55]. Thus, the diffusion is best expressed in a coordinate system of comprised of  $J_1$  and  $J_2$ , represented equivalently by equatorial pitch angle ( $\alpha_{\text{veq}}$ ) and total energy ( $E$ ), with  $L$  taking the place of  $J_3$ , using  $f(\alpha_{\text{veq}}, E, L)$  [Walt, 1994, p.101]. Diffusion coefficients for both pitch-angle diffusion ( $D_{\alpha\alpha}$ ) and energy diffusion ( $D_{EE}$ ), also known as range straggling, can then be computed.<sup>19</sup>

Pitch-angle diffusion can arise through many nonadiabatic forces in the radiation belts. One example, critical to the mechanisms underlying the formation of the loss-cones defined by  $\alpha_{\text{vblc}}$  and  $\alpha_{\text{vdlc}}$ , is that of Coulomb collisions between radiation-belt electrons with  $h_{\text{m}} > h_{\text{T}}$  and upper ionospheric neutrals [Schulz and Lanzerotti, 1974, p.48].<sup>20</sup> Only dominant enough to prevent all trapping for  $L < 1.3$ , and with little impact on the electrons'  $E$  or  $L$  (except for electron-electron collisions, whose range straggling is often negligible), the primary implication of such interactions is to cause diffusion in the pitch-angle of the trapped electrons such that for some subset of the population  $\alpha_{\text{veq}} < \alpha_{\text{vblc}}$  or  $\alpha_{\text{veq}} < \alpha_{\text{vdlc}}$ . From (A.22), this corresponds to  $h_{\text{m}} < h_{\text{T}}$ , meaning the electrons in the loss cone then mirror so low as to precipitate (i.e., be permanently removed from the plasmasphere) [Walt, 1994, p.111–112].

However, as discovered during the 1962 Starfish Prime experiment (cf. Footnote 1 of Chapter 1), such collisions are not the dominant source of pitch-angle diffusion at higher  $L$ -shells, where diffusion through resonant wave-particle interactions becomes significant [Walt, 1994, 116–117]. These non-collisional diffusion mechanisms take

<sup>19</sup>For radiation-belt electrons, whose initial distribution tends to be fairly isotropic in  $E$ , it is common to neglect any additional smoothing via energy diffusion [Schulz and Lanzerotti, 1974, p.55].

<sup>20</sup>Due to their greater mass, protons and heavy ions experience little pitch-angle deflection or range straggling as a result of such collisions. Instead, they either give up their energy to free and bound electrons, decelerating in the process, or, if lower in energy, absorb one such electron and are reduced (cf. Section C.2.1.2). Deceleration leads to a systematic, non-diffusive reduction of  $J_1$  and  $J_2$  that necessitates special 'flow' terms in the Fokker-Planck equation. Such terms also appear for electrons, but as cited in the above text, are insignificant compared to diffusion in  $\alpha_{\text{veq}}$  [Schulz and Lanzerotti, 1974, p.48–49].

place when the frequency of a wave-induced perturbation felt by the particle is on the order of either its bounce frequency or gyrofrequency, giving rise to the subdivisions below, corresponding to violation of the second or first adiabatic invariant, respectively.

### A.3.2 Bounce Resonance

For waves with wave-normal angle  $\theta_k < 90^\circ$ , including magnetosonic MHD and electrostatic modes, there can be non-zero wave field components along the field line, namely  $\mathbf{b}_\parallel$  and  $\mathbf{e}_\parallel$ , respectively, whose forces affect only  $\mathbf{p}_\parallel$ . Such parallel forces conserve the first and third invariants, but alter the particle's energy and thereby violate the integral invariant. The change in parallel velocity, and thus pitch angle, is most pronounced for wave frequencies close to the bounce frequency of the particle, which produces a constructive effect, and for particles with  $\alpha_v \simeq 90^\circ$ , which renders the mechanism incapable of scattering particles into the loss cone [*Schulz and Lanzerotti, 1974*, p.62–65]. For the latter reason, bounce resonance has “received considerably less attention” [*Lyons, 1979*, p.142] than cyclotron resonance in the literature, a partiality likewise adopted here.

### A.3.3 Cyclotron Resonance

Involving wave-induced violations of the first adiabatic invariant, cyclotron resonance can occur for a variety of particle  $\alpha_v$  and wave  $\omega$ ; indeed, the breadth of modalities motivates the advanced plasma wave study for which the target receiver is intended. The following sub-sections deal with the normal and anomalous modes from a deterministic perspective, which results in pitch-angle scattering, before offering the diffusive interpretation of the cyclotron interaction between the phase-averaged particle distribution  $f_{\text{avg}}$  and a wave packet with its own distribution in  $\mathbf{k}$  (and thus  $\omega$  for a given propagation mode), giving rise to pitch-angle diffusion.

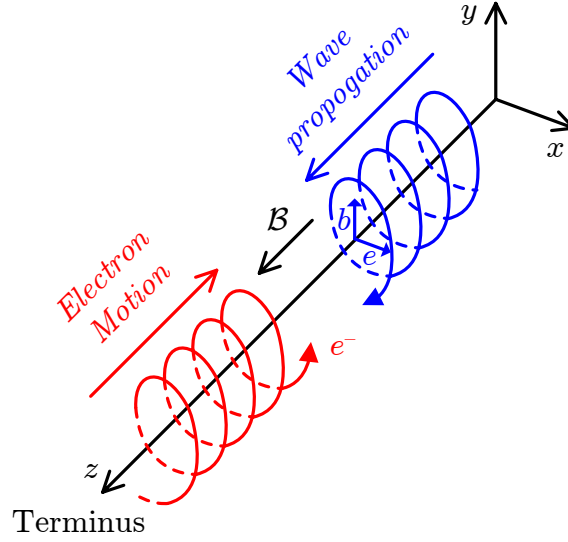


Figure A.6: Geometry of normal-mode electron cyclotron resonance interaction. By convention, handedness is determined with respect to the ambient  $\mathbf{B}$ , not direction of travel, so to an observer in the lower left, the right-handed gyration of the electron position vector(wave electric field vector) is counter-clockwise(clockwise). This rotational opposition is captured by the sign of the Doppler shift in (A.24). After [Walt, 1994, p.119].

### A.3.3.1 Normal Scattering

Consider the underlying deterministic,  $\mathbf{w}$ -aware, Lorentz interaction for the special case of a single trapped electron and a parallel-propagating ( $k_{\perp} = 0$ ) whistler-mode electron cyclotron wave of frequency  $\omega$ , as depicted in Figure A.6. As shown in Figure A.7, invoking the notation of [Walt, 1994], this situation establishes wave electric and magnetic fields,  $\mathbf{e}$  and  $\mathbf{b}$ , that lie in the plane of  $\mathbf{v}_{\perp}$  with a phase difference between  $\mathbf{v}_{\perp}$  and  $\mathbf{b}$  given by

$$\phi = (\omega_{ce} - \omega - k_{\parallel}v_{\parallel})t + \phi_0 \quad (\text{A.23})$$



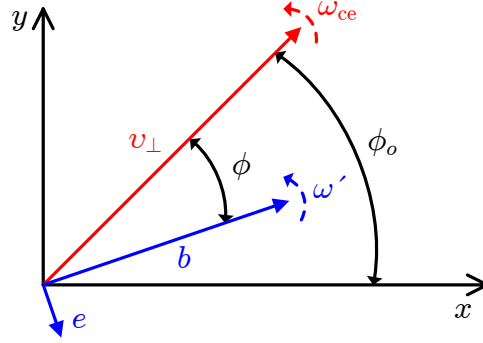


Figure A.7: Phase relationships of wave fields and electron velocity perpendicular to ambient field. As it counterstreams, the electron, whose  $\mathbf{v}_\perp$  vector rotates at  $\omega_{ce}$  in the fixed reference frame, sees the wave magnetic field  $\mathbf{b}$  rotating at  $\omega'$ . In a reference frame moving with the particle, then, the phase difference between these vectors,  $\phi$  is given by (A.23). After [Walt, 1994, p.120].

where  $\phi_o$  is a random initial offset.<sup>21</sup> The first term in (A.23) represents the phase that accumulates between the two vectors over time, due the difference between rate of rotation of the particle ( $\omega_{ce}$ ) and the Doppler-shifted angular frequency at which it perceives the wave field vectors to be rotating, namely

$$\omega' = \omega \left( \frac{v_p}{v_p - v_\parallel} \right) \approx \omega \left( 1 + \frac{v_\parallel}{v_p} \right) = \omega + k_\parallel v_\parallel \quad (\text{A.24})$$

where the approximation comes from noting that  $v_\parallel \ll v_p$  for non-relativistic electrons.<sup>22</sup> It can be shown that the pitch-angle and energy changes which occur over time as  $\mathbf{e}$  and  $\mathbf{b}$  act upon  $\mathbf{v}_\perp$  and  $\mathbf{v}_\parallel$  via the Lorentz force of (A.6) depend

<sup>21</sup>Recall that the particle velocity vector,  $\mathbf{v}$ , with magnitude  $v = |\mathbf{v}|$ , can be further decomposed into its projections perpendicular and parallel to  $\mathbf{B}$ , namely  $\mathbf{v}_\perp$  and  $\mathbf{v}_\parallel$ . Since the magnitudes of these vectors,  $v_\perp$  and  $v_\parallel$ , are always positive,  $v_\parallel$  contains no information about the direction of propagation along  $\mathbf{B}$ . Thus, the sign conventions in (A.23) and its descendants are specific to the geometry of Figure A.6, so  $k_\parallel v_\parallel > 0$  even though  $\mathbf{k}_\parallel \cdot \mathbf{v}_\parallel < 0$ . However, they remain valid for the case of a particle traveling with the wave, in the  $+\hat{\mathbf{z}}$  direction, by assuming  $v_\parallel < 0$ . For the remainder of this section, it is also useful to note that  $\omega > 0$ ,  $v_p > 0$ , and  $\omega_{ce} > 0$  according to the scalar polarity conventions in use.

<sup>22</sup>For whistler-mode interactions with non-relativistic electrons, it is typically assumed that  $v \gg v_p$  [Walt, 1994, p.120], since, as shown in Figure 1.11, such modes have  $n \leq 10$ . However, for particles outside the loss cone, the component of in the direction of the magnetic field is typically small enough that  $v_\parallel \ll v$ .

critically upon  $\phi$  through [Walt, 1994, p.121]:

$$\frac{dE}{dt} = ebv_p v_\perp \sin \phi \quad (\text{A.25a})$$

$$\frac{d\alpha_v}{dt} = \frac{eb}{m} \left( 1 + \frac{v_p \cos \alpha_v}{v} \right) \sin \phi \quad (\text{A.25b})$$

In the general case when  $\omega_{ce}$  and  $\omega$  are uncorrelated, the angular difference between  $\mathbf{v}_\perp$  and  $\mathbf{b}$  varies constantly with time, so that the average of  $\sin \phi$  and thus of (A.25a) and (A.25b) goes to zero, resulting in no net difference. But, if  $\omega + k_\parallel v_\parallel = \omega_{ce}$ , then  $\mathbf{v}_\perp$  and  $\mathbf{b}$  rotate together such that  $\phi$  is constant (i.e., first term of (A.23) goes to zero) and the net force on the particle over the course of the interaction is non-zero. This case, in which  $\omega$  is Doppler-shifted up to  $\omega_{ce}$  to align the wave and particle oscillations in phase yielding  $\sin \phi = \sin \phi_o$ , constitutes a resonance condition wherein the particle and wave can exchange momentum so long as they occupy the same helical trajectory [Walt, 1994, p.122].

Determining the net momentum exchange in one such interaction, represented by  $\Delta\alpha_v$  and  $\Delta E$ , requires an estimate of that resonance duration,  $\Delta t$ . It can be shown that this depends upon the interplay between the length of the wave and its bandwidth. Namely, a wave of infinite duration, whose spectrum is represented by a Dirac delta, can only resonant with a particles of precise energy, related to  $p_\parallel = m(\omega_{ce} - \omega)/k$ , and then falls out of resonance as soon as the particle has accumulated an infinitesimal  $\Delta\alpha_v$  and  $\Delta E$  [Walt, 1994, p.122]. But, any finite wave possesses infinite bandwidth and therefore is capable of interacting with a broader range of energies, albeit over a shorter period of time. As suspected in light of the Heisenberg uncertainty principle [Schulz and Lanzerotti, 1974, p.62], the product of the interaction interval  $\Delta t$  and the wave bandwidth  $\Delta\omega$  is a constant that depends upon the wave group velocity,  $v_g$ , according to [Walt, 1994, p.123]:

$$\Delta\omega\Delta t = \frac{\pi}{1 + \frac{v_\parallel}{v_g}} \quad (\text{A.26})$$

Given the resulting  $\Delta\alpha_v$  and  $\Delta E$  from an exchange of duration  $\Delta t$ , it is clear that

the particle momentum is not conserved, but rather is transformed from  $p_\perp$  to  $p_\parallel$  (or vice versa) through a non-conservative process in which the wave gains (or loses) energy [*Schulz and Lanzerotti, 1974*, p.69]. This point can easily be obscured since, as noted above, it is common to consider only pitch-angle diffusion for electrons while ignoring energy diffusion on account of the large ratio between the fractional changes of  $\alpha_v$  and  $E$  given, according to (A.25a)–(A.26), by [*Walt, 1994*, p.125]

$$\frac{\Delta E}{E} \approx \frac{2\alpha_v \sin \alpha_v}{v/v_p} \frac{\Delta \alpha_v}{\alpha_v} \quad (\text{A.27})$$

When considering whistler-mode waves for which, as assumed previously,  $v \gg v_p$ , (A.27) indeed suggests that  $D_{EE}$  can be ignored relative to  $D_{\alpha\alpha}$ . However, the loss of particle energy during the conversion from  $p_\perp$  to  $p_\parallel$  reemerges when considering the reference frame moving with the wave, in which  $\mathbf{e}$  goes to zero and thus there can be no net force exerted on the particle [*Tsurutani and Lakhina, 1997*, p.499]. In that case, energy must be conserved according to [*Walt, 1994*, p.126]

$$\begin{aligned} \frac{dE}{dt} &= \frac{d}{dt} \left[ \frac{1}{2} m \left( v_\perp^2 + (v_\parallel + v_p)^2 \right) \right] = 0 \\ \therefore \frac{1}{2} m v_\perp^2 + \frac{1}{2} m (v_\parallel + v_p)^2 &= \text{constant} \end{aligned} \quad (\text{A.28})$$

which maps out a trajectory in velocity space (Figure A.8), that can be contrasted with the circle that would result from the  $\Delta E \rightarrow 0$  approximation in the particle reference frame in order to emphasize the energy exchange that accompanies the particle diffusion. Namely, as particles diffuse to lower(higher) pitch angles, marked by greater  $v_\parallel(v_\perp)$ , they lose(gain) energy that is transferred to the wave, resulting in its amplification(damping) [*Schulz and Lanzerotti, 1974*, p.68]. The circumstance considered thus far, in which the wave velocity is Doppler-shifted up to exactly match the cyclotron frequency, is the first-order ( $l=1$ ), normal-mode ( $k_\parallel v_\parallel > 0$ ) of a more general electron cyclotron resonance condition for which [*Schulz and Lanzerotti, 1974*, p.69]

$$\omega + k_\parallel v_\parallel = l\omega_{ce} \quad \text{for } l = +1, +2, \dots \quad (\text{A.29})$$

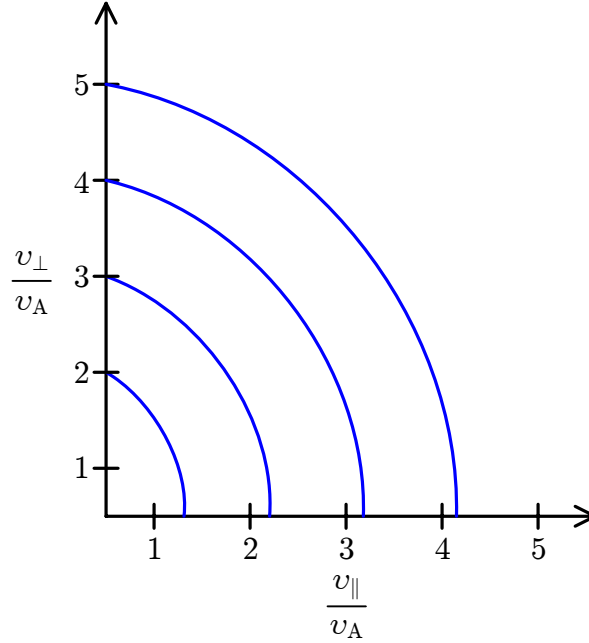


Figure A.8: Particle momentum trajectories in normalized velocity space due to cyclotron-resonant wave interactions for various initial energies. These represent first-quadrant portions of the circles defined by (A.28), which are centered at  $-v_p$  on the x-axis. Tracing any representative confirms that particle energy decreases with decreasing pitch angle. After [Schulz and Lanzerotti, 1974, p.68].

The case in point, normal mode resonance, most commonly occurs near the equator, where the minimum in ambient field (minimum  $\omega_{ce}$ ) minimizes the particle energy (minimum  $v_{\parallel}$ ) necessary for resonance with a particular wave frequency according to (A.29).<sup>23</sup> Additionally, since the slope of  $\mathbf{B}_0$  is nearly constant at the equator (cf. Figure 1.7), quantities in (A.29) that depend on  $\mathbf{B}$ , including  $\omega_{ce}$  (via (A.7)) and  $v_{\parallel}$  (via (A.16) and the conservation of energy) do not change appreciably over large distances, maximizing the extent of the resonant interaction region. In contrast to bounce resonance, normal mode cyclotron resonance preferentially impacts particles with small pitch angles (large  $v_{\parallel}$ ), which accommodate lower wave frequencies [Schulz and Lanzerotti, 1974, p.70]. For these reasons, such “wave-particle interactions will

<sup>23</sup>As noted previously, radiation-belt fluxes are larger for particles of lower energy. So, at the geomagnetic equator there are more particles with the minimum required resonant energy than at any other latitude [Tsurutani and Lakhina, 1997, p.496].

be most intense at the equator” [*Tsurutani and Lakhina, 1997*, p.496].

### A.3.3.2 Anomalous Scattering

For  $\mathbf{k}_{\parallel} \cdot \mathbf{v}_{\parallel} > 0$ , meaning the particle and wave stream in the same direction along the field line, (A.29) admits an ‘anomalous’ resonance mode in which the wave frequency is Doppler-shifted down to  $\omega_{ce}$  as the particle overtakes it.<sup>24</sup> This mode is ‘anomalous’ because the wave polarization appears reversed to the overtaking particle, so in order for the perceived wave vector to ultimately appear stationary, the wave must initially begin with polarization opposite to that of the particle [*Tsurutani and Lakhina, 1997*, p.497]. Thus, electrons in this mode interact with left-handed waves, for which the sign of  $\omega'$  in (A.24) flips such that (A.29) becomes<sup>25</sup>

$$-\omega + k_{\parallel}v_{\parallel} = l\omega_{ce} \quad \text{for } l = +1, +2, \dots \quad (\text{A.30})$$

Requiring much higher energy particles, anomalous resonance typically occurs only for relativistic electrons, increasing their pitch angle and damping the wave in the process [*Schulz and Lanzerotti, 1974*, p.72].

### A.3.3.3 Electrons versus Ions

The above electron-centric discussion pertains equivalently to positive ions as well, leading to versions of (A.29) and (A.30) in which  $\omega_{ce} \rightarrow \omega_{ci}$ , but  $l < 0$ . For normal mode resonance, ion solutions require waves with left-handed angular rotation, which negates all the terms on the left-hand side of (A.29) (as was done for the electron anomalous mode), such that it reduces to

$$-\omega - k_{\parallel}v_{\parallel} = l\omega_{ci} \quad \text{for } l = -1, -2, \dots \quad (\text{A.31})$$

---

<sup>24</sup>For electrons, the right-hand side of (A.29) is always positive, so the anomalous mode necessitates that  $k_{\parallel}v_{\parallel} > \omega$ , or  $v_{\parallel} > v_p$ , which results in the particle outstripping the wave.

<sup>25</sup>Recall that all scalar quantities in (A.29)–(A.33) are treated as positive. So, the signs of (A.29) must be manipulated for the anomalous-mode geometry to arrive at (A.30) as follows: first, negate the left-hand side of the former to reflect a counter-clockwise  $\omega'$ ; then, invert the sign of the second term on the left-hand side to account for the counter-streaming geometry here, according to whose vector representation  $\mathbf{k}_{\parallel} \cdot \mathbf{v}_{\parallel} > 0$ .

Similarly, (A.30) can be adapted to the case when ions ( $l < 0$ ) experience an anomalous resonance while overtaking ( $\mathbf{k}_{\parallel} \cdot \mathbf{v}_{\parallel} > 0$ ) right-handed waves ( $\omega' > 0$ ),

$$\omega - k_{\parallel} v_{\parallel} = l \omega_{\text{ci}} \quad \text{for } l = -1, -2, \dots \quad (\text{A.32})$$

Combining (A.29) through (A.32) yields a general resonance condition applicable to both particle types (through a generic  $\omega_c$ ) and streaming orientations,

$$\pm \omega + k_{\parallel} v_{\parallel} = l \omega_c \quad \text{for } l = +1, +2, \dots \quad (\text{A.33})$$

in which all scalars are positive, with the leading plus(minus) sign pertinent to the directionality and speed relationships of the normal(anomalous) mode. The cyclotron harmonic modes ( $l > 1$ ) behave similarly to the parallel propagation case heretofore explicated, and are primarily responsible for wave damping, but are only manifest for oblique waves ( $k_{\perp} \neq 0$ ) whose elliptical polarization and anisotropic phase velocity project a  $k_{\parallel}$  capable of a sufficiently large Doppler-shift [*Schulz and Lanzerotti, 1974*, p.72], [*Walt, 1994*, p.130].<sup>26</sup>

Due to the inverse mass dependence in (A.25b), the ion cyclotron resonances captured in (A.31) and (A.32) result in much less  $\Delta\alpha_v$  than their electron counterparts for waves of nominal power spectral density. Without sufficient energy for pitch-angle scattering, interactions with these left-handed ion cyclotron waves “are probably not important for equatorially mirroring protons” [*Lyons, 1979*, p.151]. Since, “pitch-angle diffusion is not known to play an important role in establishing the observed flux profile of outer-zone protons” [*Schulz and Lanzerotti, 1974*, p.193], the corresponding

---

<sup>26</sup>The special case of  $l=0$  ( $v_{\parallel} = v_p$ ) is known as the Landau resonance and results in a particle’s energy ( $p_{\parallel}$ ) diffusion in response to an  $e_{\parallel}$  that appears nearly constant. Predominantly associated with  $\theta_k \simeq 90^\circ$ , since such waves transmit most of their energy in  $e_{\parallel}$ , and independent of the phase relationships in the perpendicular plane, it permits the acceleration(deceleration) of the particle when the  $e_{\parallel}$  oscillations are nearly synchronized with(against) the particle velocity [*Lyons, 1979*, p.143]. Particles whose  $v_{\parallel}$  is slightly below(above)  $v_p$  are accelerated(decelerated) until they are in resonance, damping(amplifying) the wave by gaining (losing) energy from(to) it. The classic analogy for the first case is that of a slow-moving surfer gaining enough energy to be accelerated to the speed of underlying wave [*Bortnik, 2004*, p.46–47]. For any point  $v_p$  in a Maxwellian particle energy distribution, there are always more particles with  $v < v_p$ , so Landau damping dominates over growth, making it the most common loss process in a collisionless plasma [*Tsurutani and Lakhina, 1997*, p.491].

ion cyclotron waves are not germane to this study.

#### A.3.3.4 Scattering versus Diffusion

The deterministic interaction between an electron and a single-frequency wave can be extended to that of a phase-averaged particle distribution and an incoherent wave packet spread over a band of  $k_{\parallel}$  (and thus  $\omega$ ) through diffusion theory.<sup>27</sup> Such an approach, which constitutes stochastic pitch-angle diffusion rather than deterministic pitch-angle scattering, explains the wave-particle interactions between distributions of trapped electrons and broadband whistler-mode waves such as hiss and chorus (rather than the narrowband whistlers treated above) [*Lyons, 1979*, p.146]. In particular, such encounters drive a non-Maxwellian  $f_{\text{avg}}$  that is anisotropic with respect to  $\alpha_{v_{\text{eq}}}$ , due to an empty loss cone, toward an equilibrium pitch-angle distribution such that the free energy released as  $p_{\perp}$  is converted to  $p_{\parallel}$  according to Figure A.8 leads to wave growth [*Schulz and Lanzerotti, 1974*, p.68–69].

The link between wave growth(damping) and the diffusion of particles into(away from) the loss cone, as evidenced by their concomitant precipitation(trapping), is fundamental to regulation of the radiation-belt fluxes [*Kennel and Petscheck, 1966*] and lies at the heart of this research.

---

<sup>27</sup>The required mathematics are beyond the scope of this text, but are artfully derived by *Walt* [1994, p.122–128].





# Appendix B

## Plasma Wave Instruments

This appendix offers a survey of the plasma wave instruments aboard the satellites listed in Table 1.2, with particular emphasis on the plasma wave receivers carried therein. Enumerating their relevant properties, such as bandwidth, dynamic range, gain, power dissipation, and sampling rate, teases out trends in the historical evolution of their capabilities that both motivate the establishment of and provide context for the specifications of the target wideband receiver summarized in Figure 1.22. In addition to aggregating and cataloging the published performance of these instruments, the attendant benefits of which are many, this Appendix contains a selected bibliography of that literature to facilitate the continued evaluation of this inventory by future researchers.

By no means exhaustive in covering nearly half a decade worth of astronautic endeavors by researchers around the world, the limited scope of this survey merits some preliminary remarks. As plasma wave receivers provide information valuable to a variety of space experimentation and communication missions, they are nearly ubiquitous aboard spacecraft deployed for such purposes. However, for the geophysical research at issue here, it suffices to consider only satellites intended for exploration of naturally occurring magnetospheric wave phenomena between the extremely low frequency (ELF) and high frequency (HF) bands, covering 3 Hz to 3 MHz. Secondly, in accordance with the goal of advancing the measurement of plasma wave AC electric fields in this research (cf. Section 1.2), the litanies in Section B.1

omit antennas and electronics only capable of sensing magnetic fields.<sup>1</sup> Finally, for practical reasons, only instruments with sufficient published matter in English-language journals are cited, a choice which biases the results toward larger projects of American origin.

Section B.1 registers the properties of the various flown examples of the three canonical plasma wave receiver architectures; not only their electronic components, but also their dipole antennas, with the latter assisting in the interpretation of the former. The references from which the data in this section is culled are keyed to the bibliography in Section B.2.<sup>2</sup>

## B.1 Hardware Surveys

Each of the sections below tabulates the properties of a specific hardware component pertaining to previous plasma wave receivers.<sup>3</sup> In Section B.1.1, a companion to Table 1.2 extends the description of each of the satellites in question, identifying the relevant instrument payloads and providing an index into the bibliography of Section B.2 corresponding to each instrument. To inform the discussion of antenna impedance in Section 3.1.4, the parameters of the electric dipole antennas for representative satellites, including the expected impedance matching between their sheaths and preamplifiers, is included in Section B.1.2. Finally, the key specifications of the receiver electronics for each instrument are documented in the subdivisions of Section B.1.3.

---

<sup>1</sup>This especially restricts which of the satellite antennas are documented in Section B.1.2. Since it is common to fly both electric and magnetic field sensors, many of the satellites in Table 1.2 also contain the latter in the form of air-core loops and search-coil magnetometers whose details have been omitted. However, for reference, [*Ficklin et al.*, 1965; *Rorden et al.*, 1966] and [*Gurnett et al.*, 1978; *S-300 Experimenters*, 1979], respectively, describe the construction and performance of those with the most heritage.

<sup>2</sup>Since it is incompatible with that used in the main bibliography of the dissertation, the citation convention adopted in Section B.1.1 demands that the bibliography in Section B.2 duplicate some entries from the former.

<sup>3</sup>As noted in Section 1.2.2, modern satellites rely heavily on software for in-flight processing, identification, reduction, compression, and encoding of large data volumes. Although references to these critical receiver components are noted in Table B.1 where applicable, their treatment in any depth is not relevant to the analog front-end of the target receiver.

### B.1.1 Instruments

Although Table 1.2 describes the orbital, mechanical, and telemetric properties of the satellites to be considered here, space does not permit it to fully identify each entry, nor its constituent instrumentation; thus, Table B.1 augments its columns. For each satellite from Table 1.2,<sup>4</sup> it provides the full name as well as the sobriquet common in the literature, if any. In the absence of an international naming standard, confusion may remain; to alleviate this, the identifier assigned to each spacecraft by the North American Aerospace Defense Command (NORAD), dubbed the NORAD ID and denoted *NID*, is also included. Where applicable, references that address aspects of the spacecraft construction, orbit, and mission objectives required to populate associated tables in this dissertation are provided in the *Ref.* column.

Each satellite carries one or more plasma wave instruments that may, in turn, contain one or more wave receivers; each such receiver consists of one more antenna systems and associated electronics packages that are subsequently explicated in Section B.1.2 and Section B.1.3, respectively. To map the entries of the tables in these Sections to their host spacecraft, Table B.1 defines an abbreviated moniker for each wave instrument.<sup>5,6</sup> In addition, it lists the name and institution (be it educational, industrial, or governmental) of the principal investigator responsible for its development.<sup>7</sup> This information can not only aid in further searches for literature on a particular instrument but, when coupled with the name (in the *Lineage* column) of the satellite whose wave instrument is the most recent forerunner of that in question, can also assist in tracing the heritage of modern cognates to the target

---

<sup>4</sup>One entry, OGO 6, has been omitted as result of insufficient documentation. However, it is well-represented by the remaining polar OGO satellites (OGO 2 and OGO 4).

<sup>5</sup>In an exception to the practices enacted throughout the rest of this document, these abbreviations and those of the host institutions (cf. Footnote 7) are not explicitly defined. But, since the full names of the instruments are irrelevant to the tabulation of their performance, these acronyms can simply be treated as atomic identifiers.

<sup>6</sup>The complexity of more recent payloads has necessitated individual names for the receivers comprising each instrument, which proves useful given the receiver classification system at work here. Such receiver designators are provided in the table notes, since the main entry pertains only to the collective instrument.

<sup>7</sup>The convention for rendering institution names assumes familiarity with the key players, particularly universities in the United States and England. For foreign participants, the abbreviated country of origin provides a clue as to decoding the acronym which is not defined here.

receiver. The final column indicates recommended references for each instrument from the selected bibliography.

Satellites				Wave Instruments				
Name	Sobriquet	NID	Ref.	Name	Institution	Investigator	Lineage	Ref.
Vanguard 3		00020	[18; 19]					[19]
Alouette 1		00424	[33]	VLF				[6; 33]
Injun 3	Injun-2B	00504	[92; 93]	VLF	U Iowa	D. Gurnett	Injun 1	[44; 93]
OGO 1	OGO-A	00879		VLF	Stanford	R. Helliwell		[29; 58; 103]
OGO 2	OGO-C	01620		VLF	Stanford	R. Helliwell	OGO 1	[31; 59]
				VLF-2	Dartmouth	M. Morgan		[78; 89]
OGO 3	OGO-B	02195		VLF	Stanford	R. Helliwell	OGO 1	[32; 58]
Ariel 3		02773		FFSS	U Sheffield	T. Kasier		[15; 120]
OGO 4	OGO-D	02895		VLF	Stanford	R. Helliwell	OGO 2	[59; 105]
				VLF-2	Dartmouth	M. Morgan		[78; 89]
Pioneer 8	Pioneer-C	03066		PWD	TRW	F. Scarf		[107]
OGO 5	OGO-E	03138		PWD	TRW	G. Crook	Pionr. 8	[22; 69]
Injun 5	Injun-C	03338		VLF	U Iowa	D. Gurnett	Injun 3	[21; 46]
Pioneer 9	Pioneer-D	03533		EFD	TRW	F. Scarf	Pionr. 8	[109; 110]
ISIS 1	ISIS-A	03669		VLF	Can. DC	R. Barrington	Alouette	[33]
				Iowa	U Iowa	D. Gurnett		[39; 48]
IMP 6	IMP-I	05043		Minn	U Minn.	P. Kellogg		
				NASA	GSFC	T. Aggson		

Satellites				Wave Instruments				
Name	Sobriquet	NID	Ref.	Name	Institution	Investigator	Lineage	Ref.
ISIS 2	ISIS-B	05104		VLF	Can. DC	R. Barrington	ISIS 1	[33]
S <sup>3</sup> A	Explr. 45	05598	[82]	Iowa	U Iowa	D. Gurnett	IMP 6	[2; 86]
Ariel 4		05675		VLF-ELF MBN	U Sheffield Cambridge	T. Kaiser F. Smith	Ariel 3	[14; 114] [118]
Pioneer 10	Pioneer-F	05860		VLF-2	Dartmouth	T. Laaspere	OGO 2	
IMP 8	IMP-J	06893	[72]	Iowa	U Iowa	D. Gurnett	IMP 6	[37; 77]
Hawkeye 1		07325		ELF/VLF	U Iowa	D. Gurnett	IMP 8	[39; 47; 73; 77]
Helios 1	Helios-A	07567		SWPW FFSA	U Iowa U Minn.	D. Gurnett P. Kellog	IMP 6 IMP 6	[38]
Intercomsos 14		08471		ELF/VLF	Cze. AS	P. Triska		[63; 80]
Helios 2	Helios-A	07567		SWPW FFSA	U Iowa U Minn.	D. Gurnett P. Kellog	IMP 6 IMP 6	[38]
S3-3	S74-2	09007		ELF/VLF AC/DC	Aerospace Berkeley	H. Koons F. Mozer		[20; 87; 88; 90]
GEOS 1	GEOS-1	07931	[75]	S-300 <sup>a</sup>	Dan. SRI	E. Ungstrup		[67; 104]
Voyager 1	Mariner A	10321		PWS	U Iowa	D. Gurnett	ISEE 2	[111]
Voyager 2	Mariner B	10271		PWS	U Iowa	D. Gurnett	ISEE 2	[111]

Satellites				Wave Instruments				
Name	Sobriquet	NID	Ref.	Name	Institution	Investigator	Lineage	Ref.
ISEE 1	ISEE-A	10422	[94; 95]	Waves	U Iowa	D. Gurnett	IMP 6	[47]
				HEM VLF	Stanford	R. Helliwell	OGO 1	[7; 27]
ISEE 2	ISEE-B	10423	[34; 95]	Waves	U Iowa	D. Gurnett	ISEE 1	[47]
Pioneer	Venus Orbiter	10911		OEFD	TRW	R. Strangeway	Pionr. 8	[112]
GEOS 2	GEOS-2	10981	[75]	S-300 <sup>a</sup>	Dan. SRI	E. Ungstrup		[67; 104]
ISEE 3	ISEE-C	11004	[95; 117]	Waves	TRW	E. Greenstadt	ISEE 1	[108]
DE 1	DE-A	12624	[17; 60; 61]	PWT <sup>b</sup>	U Iowa	D. Gurnett	ISEE 1	[41; 113]
DE 2	DE-B	12625	[17; 60; 61]	VEFI	GSFC	N. Maynard		[85]
Aureol 3	ARCAD-3	12848	[70]	TBF-ONCH <sup>c</sup>	CRNS	J. Berthelier	GEOS 1	[9; 102]
CCE	AMPTE	15199	[26]	PWE	TRW	F. Scarf	PVO	[106]
IRM	AMPTE	15200	[56]	HF SFR1	U Iowa	D. Gurnett		[55]
				ELF/VLF	U Iowa	D. Gurnett	Helios 1	[55]
				WBR	U Iowa	D. Gurnett	DE 1	[55]
				VLF/MF	Aerospace	H. Koons	S3-3	[55]
UKS	AMPTE	15201	[119]	HF SFR2	Max-Planck	B. Häusler		[55]
				SFA	U Sheffield	L. Woolliscroft		[25]

Satellites			Wave Instruments					
Name	Sobriquet	NID	Ref.	Name	Institution	Investigator	Lineage	Ref.
Akebono	EXOS-D	19822	[97]	PWS	Tohoku U	H. Oya	ISEE 1	[96]
				VLF <sup>d</sup>	Kyoyo U	I. Kimura		[54; 57; 71]
Galileo		20298	[66]	PWS	U Iowa	D. Gurnett	DE 1	[43]
CRRES		20712	[65; 116]	PWE	U Iowa	R. Anderson	ISEE 1	[3]
				ELFWA	Aerospace	H. Koons		[76]
Ulysses	ISPM	20842	[121]	URAP <sup>e</sup>	GSFC	R. MacDowall		[115]
Geotail	GEOTAIL	22049	[91]	PWT <sup>f</sup>	Kyoto U	H. Matsumoto	ISEE 1	[84]
Freja		22161	[83]	WAVE	Swe. ISP	B. Holback		[62; 81]
Wind	WIND	23333	[51]	WAVES <sup>g</sup>	Meuden	J. Bougeret	Ulysses	[13]
Interball 1	Tail probe	23632	[122]	OPERA	Ricerche	E. Amata		[1; 10; 74]
Polar	POLAR	23802	[51]	PWT <sup>h</sup>	U Iowa	D. Gurnett	<sup>h</sup>	[45; 52]
FAST		24285	[100]	Fields <sup>i</sup>	Berkeley	C. Carlson		[30]
Interball 2	Auroral probe	24293	[122]	IESP	IZMIRAN	V. Chmyrev		[99]
				NVK-	IZMIRAN	O. Molchanov		[79; 99]
				ONCH				
				MEMO	Ricerche	F. Lefeuvre		[79]
				POLRAD	CNRS	J. Hanasz		[50]



Satellites				Wave Instruments				
Name	Sobriquet	NID	Ref.	Name	Institution	Investigator	Lineage	Ref.
Cassini		25008	[64]	RPWS <sup>j</sup>	U Iowa	D. Gurnett	j	[42]
IMAGE		26113	[16; 35]	ANR	U Mass.	B. Reinisch	Wind	[36; 101]
Cluster	Cluster 2	26463	[98]	WBD	U Iowa	D. Gurnett	Polar	[40]
				EFW	Swe. ISP	G. Gustafsson		[49]
DEMETER		28368	[24]	ICE	CETP	J. Berthelier	FAST	[8]
STEREO		29510	[28; 68]	SWAVES <sup>k</sup>	Meudon	J. Berthelier	<sup>k</sup>	[5; 12]
THEMIS		30580	[4; 53]	EFI	Berkeley	F. Mozer	Cluster	[11; 23]

<sup>a</sup> The S-300 receivers include: ELF, Filter Bank, and SFA

<sup>b</sup> PWI is comprised of the following receivers: LFC, LWR, SFC, and WBR

<sup>c</sup> The TBF-ONCH receivers include: FB, FBF, and FBS

<sup>d</sup> VLF is comprised of the following receivers: ELF, MCA, and WBA

<sup>e</sup> The URAP receivers include: FES, PFR, and RAR

<sup>f</sup> PWI is comprised of the following receivers: MCA, SFA, and WFC

<sup>g</sup> WAVES is subdivided into WAVES1 (comprised of RAD1, RAD2, and TNR) and WAVES2 (including TDS)

<sup>h</sup> The PWI receivers include: MCA and SFR (inherited from ISEE 1), LFWR (from DE 1), WBR (from Galileo) and HFWR

<sup>i</sup> The Fields receivers include: BBF, HSBM, PWT, SFA, and a WBR with Survey and Burst modes

<sup>j</sup> The RPWS receivers include: MFR and WBR (inherited from Galileo), HFR (from Wind), and 5WFR

<sup>k</sup> The SWAVES receivers include: HFR and TDS (inherited from Wind), and LFR (from FAST)

Table B.1: Wave instruments payloads of satellites in Table 1.2.

### B.1.2 Antennas

Typically, each of the receivers that comprise the wave instruments in Table B.1 can be connected to one or more of the spacecraft antennas via a wide analog multiplexer (e.g., [Gurnett *et al.*, 1995, p.607]). For measurements of the wave electric field, the preferred antenna selection is a long cylindrical monopole or dipole,<sup>8</sup> rather than a Langmuir probe,<sup>9</sup> on account of the lower noise and higher, more reliable gain associated with such a structure.

To appreciate these advantages, recall from Section D.1.3 that in the low-frequency limit ( $f \ll f_{pe}$ ) the differential impedance,  $Z_a(\omega)$ , of an electrically short cylindrical dipole antenna of arm length  $L_a$  and radius  $r_a$  is dominated by that of its sheath, whereas well above the plasma frequency it reverts to an almost purely capacitive impedance, as in free space; or, distilling (3.16) through (3.18) for convenience:

$$Z_a(\omega) = \begin{cases} \frac{R_S}{1 + j\omega R_S C_S} & , \quad f \ll f_{pe} \\ \frac{1}{j\omega C_A} & , \quad f \gg f_{pe} \end{cases} \quad (\text{B.1})$$

As physical intuition would suggest, these same expressions hold for a spherical double-probe. Additionally, since the sheath resistance is inversely proportional to surface area for both antennas (cf. Section D.1.1.3), their geometry only discriminates them according to the values of the sheath ( $C_S$ ) and free-space ( $C_A$ ) capacitances in (B.1), whose definitions in Table B.2 have been culled from Section D.1.1 and

---

<sup>8</sup>Although many satellites use single-ended amplifiers to measure the potential of individual antenna elements (including Ulysses, Cassini, and STEREO), such examples do not truly constitute monopoles because the spacecraft itself, acting as a finite ground plane, serves as the second element to which each potential is referenced [Gurnett, 1998, p.123]. True monopoles [Scarf *et al.*, 1968] have not been flown in recent years since, unlike their differential counterparts, they are directly couple noise generated by the spacecraft itself into the measured signal [Gurnett, 1998, p.123].

<sup>9</sup>A spherical double-probe or Langmuir probe, consisting of two metal spheres mounted at the opposing ends of a long boom, is more commonly deployed for DC electric field measurements. By measuring the potential difference between the spheres as a result of their bias voltage and the accompanying currents exchanged with the surrounding plasma, the probe can be used to determine the density, temperature, and potential of the plasma; the latter, relative to charge at infinite distance, describes the DC or slowly varying component of ambient electric field. For theoretical background on this technique as well as an example of its application on DE 2, the reader is recommended to [Mozer, 1973] and [Maynard *et al.*, 1981], respectively.

Capacitance	Cylindrical dipole	Spherical double-probe
Sheath	$\frac{\pi\epsilon_0 L_a}{\ln(\lambda_D/r_a)}$	$2\pi\epsilon_0 r_a \left(1 + \frac{r_a}{\lambda_D}\right)$
Free-space	$\frac{\pi\epsilon_0 L_a}{\ln(L_a/r_a) - 1}$	$2\pi\epsilon_0 r_a$

Table B.2: Limiting capacitances for dipole and double-probe antennas.

[[Gurnett, 1998](#), p.126].<sup>10</sup> When comparing the columns, recognize that capacitances of the spherical double-probe depend only on the radius of the spheres ( $2 \text{ cm} \leq r_a \leq 10 \text{ cm}$ ) not their separation ( $0.6 \text{ m} \leq L_a \leq 130 \text{ m}$ ). On account of their filamentary character, with  $L_a/r_a$  ratios on the order of  $10^4$ – $10^5$  for average lengths ( $3 \text{ m} \leq L_a \leq 100 \text{ m}$ ) and radii ( $1 \text{ mm} \leq r_a \leq 10 \text{ mm}$ ), dipoles thus tend to exhibit much larger  $C_A$  and  $C_S$ .

From this pronounced discrepancy, three distinct advantages of the dipole antenna emerge. First, recall from Section 3.1.4.2 that for ideal voltmeter operation, the net load impedance,  $Z_L(\omega)$ , must remain much larger than  $Z_a$  at all frequencies. The larger capacitance of the dipole can thereby tolerate larger  $C_{\text{stray}}$  and  $C_{\text{in}}$  [[Gurnett, 1998](#), p.125].<sup>11</sup> Secondly, for representatives of the two antenna types whose total surface areas are comparable, the higher  $C_S$  of the dipole results in a lower transition frequency; that is, its impedance is capacitive over more of the low-frequency regime.<sup>12</sup>

<sup>10</sup>Here the generic Debye length  $\lambda_D$  can represent either that of a photoelectric or positive-ion sheath, depending on the antenna floating potential. In either case, steady-state assumptions allow it to serve as the equilibrium sheath radius in the low frequency limit.

<sup>11</sup>As discussed in Section 3.1.4.1, The capacitive portion of  $Z_L(\omega)$  is typically dominated not by that of the amplifier input transistors ( $C_{\text{in}}$ ) but by contributions from the stray capacitance between the antenna element and the spacecraft body ( $C_{\text{base}}$ ) and that of the mechanics connecting it to the receiver ( $C_{\text{ms}}$ ), particularly the capacitance per unit length of the coaxial cable ( $C_c$ ). Since the parameters of these elements are either difficult to estimate or highly constrained by aeronautical mechanics, the eased  $C_{\text{stray}}$  requirements of a high-capacitance dipole are especially appreciated by system designers.

<sup>12</sup>In light of higher transition frequency of Langmuir probes, the astute reader might question their predominant application to low-frequency and DC plasma measurements, as noted in Footnote 42 of Chapter 1. The seeming inconsistency is resolved with the realization that for such applications, it is common to adaptively bias the antenna with a DC current that increases the influx of plasma carriers, thereby decreasing  $R_S$  (cf. (D.9) of Section D.1.1.3), often by several orders of magnitude, as from  $\sim 1 \text{ G}\Omega$  to  $\sim 10 \text{ M}\Omega$  in the work of [Bonnell et al. \[2008\]](#). Although this actually increases

Since its larger capacitance is only beneficial to the gain of the input voltage divider when the latter is dominated by reactance, the lower transition frequency of the dipole translates to high gain over a wider swath of the signal bandwidth. The tendency for  $C_S$  to dominate  $R_S$  over the most of the low-frequency regime offers an additional advantage for the dipole—since  $R_S$  can vary substantially with antenna location and orientation, due to plasma current fluctuations, whereas  $C_S$  is less sensitive to plasma parameters than geometry, its  $Z_a(\omega)$  demonstrates less variability relative to  $Z_L(\omega)$ , decoupling its gain from plasma conditions [Gurnett, 1998, p.127]. Finally, the smaller dipole capacitances present a lower impedance to the unwanted currents generated at the LNA input by the thermal and shot noise of both the plasma itself (cf. Section 3.1.3.2) and the electronics (cf. Section 3.1.3.3). This results in an input-referred noise voltage that can be 20–40 dB lower than that of a double-probe [Gurnett, 1998, p.130].

On account of these advantages, long cylindrical dipoles are the de facto standard for differential sensing of voltages induced by wave electric fields. But, occasionally mission constraints dictate the use of monopoles and/or spherical double-probes [Bale et al., 2008, p.533]. Thus, Table B.3 presents the mechanical properties of all three types, particularly their tip-to-tip length,  $L_{TT}$ , and active element diameter,  $d_A$ .<sup>13</sup> as well as the electrical impedances  $Z_A$ ,  $Z_S$ , and  $Z_L$ , where available.<sup>14,15</sup>

---

the transition frequency, it sufficiently reduces  $R_S$  so as to maintain voltmeter operation ( $R_{in} \gg R_S$ ) in the face of fluctuating plasma currents [Mozer et al., 1979].

<sup>13</sup>Note that interpretation of these quantities varies with antenna type: for dipoles,  $L_{TT} = 2L_A \simeq 2L_{eff}$  and  $d_A$  is the filament diameter; for double probes,  $L_{TT} = 2L_A \simeq L_{eff}$  and  $d_A$  is the diameter of the spheres; and, for monopoles,  $L_{TT} = L_A \simeq 2L_{eff}$  and, again,  $d_A$  is the filament diameter.

<sup>14</sup>As per the convention herein, such quantities should be measured differentially; but, such an approach is not universal. Since reported antenna and amplifier impedances rarely specify this property, relative factor-of-2 ambiguities in the values below must be tolerated.

<sup>15</sup>Entries whose  $C_L$  seems suspiciously low reflect instances in which only the contribution from  $C_{in}$ , not  $C_{stray}$ , was reported. This phenomenon accounts for the wide range of values in the final column of the table, though its occurrence is not explicitly denoted here. Instead, Section 3.1.4.3 provides a complete breakdown of  $C_L$  for notable entries.

Satellites		Spherical double-probe						Cylindrical dipole						
Name	Mechanical			Impedances			Mechanical	Impedances			Free-Space			Load
	Axis	$L_{TT}$ [m]	$d_A$ [cm]	$R_S$ [k $\Omega$ ]	$C_S$ [pF]	$R_L$ [M $\Omega$ ]		$C_L$ [pF]	Axis	$L_{TT}$ [m]	$R_A$ [k $\Omega$ ]	$C_A$ [pF]	$R_L$ [M $\Omega$ ]	
Alouette 1								$E_x$	45.7					
								$E_y$	22.8					
OGO 2								E	3			0.2		
OGO 3								$E_{xy}^a$	2.9					
OGO 4								E	3					
								$E_{xy}^a$	2.9					
Pioneer 8								$E_z^b$	0.16		2	300		
OGO 5	$E_q$	0.5	3.01	$10^5-10^8$		800	113							
	$E_r$	0.5	3.01	$10^5-10^8$		800	113							
	$E_s$	0.5	3.01	$10^5-10^8$		800	113							
Injun 5	$E_y$	2.85	20.3	$10^1-10^4$	15-100	20	10							
Pioneer 9								$E_z^b$	0.16					
ISIS 1								$E_x$	18.7					
								$E_y$	73					
IMP 6								$E_x$	53.5 <sup>c</sup>					
								$E_y$	92.5					
								$E_z$	7.7					



Satellites		Spherical double-probe					Cylindrical dipole						
Name	Mechanical		Impedances			Load	Mechanical		Free-Space		Impedances		
	Axis	$L_{TT}$ [m]	$d_A$ [cm]	$R_S$ [k $\Omega$ ]	$C_S$ [pF]		$R_L$ [M $\Omega$ ]	$C_L$ [pF]	Axis	$L_{TT}$ [m]	$R_A$ [k $\Omega$ ]	$C_A$ [pF]	$R_L$ [M $\Omega$ ]
Voyager 1								$E_x$	$10^e$				
Voyager 2								$E_y$	$10^e$				
ISEE 1	$E_u$	73.5	8					$E_x$	$10^e$				
	$E_s$	0.61	10					$E_y$	$10^e$				
ISEE 2	$E_s$	0.61	10					$E_v$	215				
PVO	$E_z^f$	0.76	10.5					$E_x$	30				
GEOS 2	$E_x$	3	10										
	$E_y$	42	8										
	$E_z$	6	10										
ISEE 3	$E_s$	0.61	10					$E_u$	90				
DE 1	$E_s$	0.61	10					$E_x$	200 <sup>f</sup>			$10^3$	91
								$E_z$	9 <sup>f</sup>			$10^3$	91
DE 2								$E_x$	23				
								$E_y$	23				
								$E_z$	23				





Satellites		Spherical double-probe						Cylindrical dipole							
Name		Mechanical		Impedances			Load	Mechanical	Impedances			Load			
		Axis	$L_{TT}$ [m]	$d_A$ [cm]	$R_S$ [k $\Omega$ ]	$C_S$ [pF]			$R_L$ [M $\Omega$ ]	$C_L$ [pF]	Axis		$L_{TT}$ [m]	$R_A$ [k $\Omega$ ]	$C_A$ [pF]
Wind									$E_x$	100					
		$E_x$	4.4						$E_y$	15					
		$E_z$	4.4						$E_z$	12					
Interball 1															
		$E_x$	130	8					2						
		$E_y$	100	8					2						
Polar															
		$E_z$	14	8					2						
		$E_{x1}$	5			$10^3-10^6$	5	$10^5$	1						
FAST		$E_{y1}$	5			$10^3-10^6$	5	$10^5$	1						
		$E_{x2}$	56			$10^3-10^6$	5	$10^5$	1						
		$E_{y2}$	56			$10^3-10^6$	5	$10^5$	1						
		$E_z$	7.7			$10^3-10^6$	5	$10^5$	1						
Interball 2		$E_x$	4.5	8					$E_1$	11					
		$E_y$	25	8					$E_2$	22					
		$E_z$	25	8					$E_3$	22					



Satellites		Spherical double-probe						Cylindrical dipole					
Name	Mechanical		Impedances			Load	Mechanical		Free-Space		Impedances		
	Axis	$L_{TT}$ [m]	$d_A$ [cm]	$R_S$ [k $\Omega$ ]	$C_S$ [pF]		$R_L$ [M $\Omega$ ]	Axis	$L_{TT}$ [m]	$R_A$ [k $\Omega$ ]	$C_A$ [pF]	$R_L$ [M $\Omega$ ]	$C_L$ [pF]
	THEMIS	$E_x$	50	8	$10^4$ – $10^6$	14	$10^6$	$E_z$	7			$10^6$	7.5–9
$E_y$		40	8	$10^4$ – $10^6$	14	$10^6$							

<sup>a</sup> Actually a 2.9-m square loop operated as a monopole for electric field measurements  
<sup>b</sup> Acts as an unbalanced dipole in concert with grounded spacecraft and stub  
<sup>c</sup> Acts as an unbalanced dipole due to unequal lengths of deployed arms (24.4m and 27.6m)  
<sup>d</sup> Acts as a monopole with  $L_{eff} = 8$  m since one arm failed to deploy properly  
<sup>e</sup> V-shaped, rather than collinear, so  $L_{eff} = 7$  m  
<sup>f</sup> Due to insulated sections,  $L_{eff}$  of the 200-m(9-m) dipole is 101.4(5) m at AC, but 171.3(8) m at DC  
<sup>g</sup> Sheath resistance; reflects active current-biasing of antenna elements  
<sup>h</sup> Due to finite ground plane formed by spacecraft body,  $L_{eff} = 25$  m  
<sup>i</sup> Uses 27-pF AC-coupling and 100 M $\Omega$  termination; AC & DC preamplifiers available to both antennas  
<sup>j</sup> Does not account for stray capacitance to spacecraft, which brings  $C_L$  closer to 150 pF  
<sup>k</sup> Ranges from 1.5 M $\Omega$  to 245 k $\Omega$  for  $N_e$  over  $4 \times 10^3$ – $1.2 \times 10^4$  cm<sup>3</sup>  
<sup>l</sup> Actually 3 6-m unbalanced dipoles; since spacecraft is not infinite ground plane  $L_{eff} = 1.5$  m

Table B.3: Properties of electric field antennas and their amplifiers for instruments in Table B.1.

### B.1.3 Electronics

For comparison with the performance of the target wideband receiver depicted in Figure 1.22, this section inventories the key specifications of the analog electronics within each of plasma wave instruments listed in Table B.1. Since these instruments are comprised of one or more receivers that embody the fundamental architectures of Section 1.2.1, the litany is segmented accordingly.<sup>16</sup> However, just as for the preceding subsections, the scope of the subsequent tables in terms of their entries and properties is constrained for practical reasons; scilicet, a finite amount of time to search and space to synopsise the results. Not only is it difficult to obtain a comprehensive description of each instrument's specifications but, given their individuality, the task of assimilating what can be obtained into a unified format is similarly unfeasible. Thus, a few words about the summary conventions and terminology of these tables are in order.

First, contrary to the abridged representations in the coverage maps of Figure 1.15, Figure 1.17, and Figure 1.19, most receivers do treat the entirety of the frequency range as a whole. Instead, this full *bandwidth* (BW) is portioned into a series of *divisions*, within each of which the receivers employ their characteristic strategies (e.g., an instrument might contain two MSAs, one covering 1–10 kHz and the other 10–100 kHz, so that the total bandwidth of 1–100 kHz is handled as two separate divisions, perhaps with different frequency resolution). For a particular instrument, then, each receiver of a given type occupies a single entry in the table, with each row of that entry denoting the specifications for one of its divisions. Whether the outputs of all divisions are sampled serially or simultaneously varies between instruments, but the given sampling rate is the maximum cumulative rate shared across all divisions, unless otherwise stated.

---

<sup>16</sup>Since the tripartite simplification of receiver classes cannot neatly encompass all existent instruments, this codification of a given instrument's subsystems is admittedly arbitrary. It is especially unsuitable for highly flexible or largely digital topologies, where there exists little resemblance between the actual hardware and the functional blocks of the canonical architectures. In such cases, every attempt has been made to perform a best fit between the philosophies of the two regarding the range and resolution trade-offs in frequency, power, and time so as to ultimately classify the former according to its conceptual approach to signal acquisition. This can result in different 'modes' of the same receiver being cataloged under different architectures.

Secondly, the receivers often measure wave quantities besides simply the RMS amplitude, including phase, frequency, maximum amplitude, minimum amplitude, mean amplitude, and especially for WBRs, samples of the voltage waveform. Such variations are indicated on a case-by-case basis so that the measured quantity can be assumed to be RMS amplitude unless noted. Furthermore, as discussed in Section 1.2.1.1, most receivers use logarithmic compression, in either the analog or digital domain [Ergun *et al.*, 2001, p.82], to represent the measured numbers in fewer bits. However, certain exceptions, particularly among the WBRs, capture the voltage waveform on a linear scale, either by modulating it directly onto a telemetry subcarrier or sampling it with a high-rate ADC. Thus, in addition to indicating the measured quantity, the *amplitude* column denotes its *scale* (scl.) as either linear or logarithmic. This column also distinguishes between the instantaneous and total dynamic range (DR<sub>I</sub> and DR<sub>T</sub>, respectively) as defined in Section 1.2.1.1, with the former denoting that achievable at any particular gain setting and the latter the effective span in power afforded by considering all such settings in the aggregate. Both are the quoted maxima over all bandwidth divisions and gain settings of the instrument.

Finally, for each receiver the default *back-end* is assumed to consist of an ADC (and, optionally, a digital compression algorithm) with the *resolution* and *sampling* rate given in the corresponding columns.<sup>17</sup> However, if the conversion resolution is not available, the resolution column is alternately used to encode the storage format as either analog (A) or digital (D).<sup>18</sup> Finally, for early receivers with neither samplers nor on-board storage, the back-end column is used to indicate the modulation scheme, by which the measured quantity was applied to the telemetry subcarrier(s)—amplitude (AM), frequency (FM), or phase (PM).

---

<sup>17</sup>When expressed in number of bits, the resolution includes the effect of any compression and may therefore be less than the number of bits generated by the converter.

<sup>18</sup>Early receivers employed magnetic tapes for storing both analog and digital representations of measured quantities, whereas their modern counterparts rely on solid-state storage that only accommodates the latter format, first deployed aboard FAST [Ergun *et al.*, 2001].

### B.1.3.1 Sweep Frequency Receivers

Table B.4 summarizes the bandwidth, amplitude, and back-end specifications for the divisions of each SWR embedded within the instruments of Table B.1. In addition, it encapsulates the specifics of the frequency sweep in terms of:

- *Steps*: The number of individual frequencies synthesized by the LO.
- *Size*: The distance between frequency steps. For linear(logarithmic) sweeps the step size is given in Hz(%).
- *RBW*: The resolution bandwidth defined as the spectral width centered on each frequency step within which signal power is integrated to arrive at the amplitude measurement.
- *Cycle*: The minimum time required to generate a complete spectrum by performing a sweep through all the frequency steps.

Identification		BW	Frequency steps				Amplitude			Back-end	
Host	Instr.	Span [Hz]	Steps [#]	Size [Hz or %]	RBW [Hz]	Cyc. [s]	Scl.	DR <sub>I</sub> [dB]	DR <sub>T</sub> [dB]	Res. [bits]	Rate [S/s]
OGO 1	VLF	0.2–1.6		5.4 Hz	40			90	90	D	2 <sup>a</sup>
		1.5–12.5	256	43	160	2.3	Log	90	90	D	14 <sup>a</sup>
		12.5–100		344	600			80	80	D	110 <sup>a</sup>
OGO 2	VLF	0.2–1.6		5.4 Hz	40		Log	90	90	D	7 <sup>b</sup>
		1.5–12.5	256	43	160	4.6	Log	90	90	D	28 <sup>b</sup>
		12.5–100		344	600		Log	90	90	D	111 <sup>b</sup>
		14.4–26.3		100	50		<sup>c</sup>	80	80	D	111 <sup>b</sup>
OGO 3	VLF	0.2–1.6		5.4 Hz	40			90	90	D	2 <sup>a</sup>
		1.5–12.5	256	43	160	2.3	Log	90	90	D	14 <sup>a</sup>
		12.5–100		344	600			80	80	D	110 <sup>a</sup>
OGO 4	VLF	0.2–1.6		5.4 Hz	40		Log	90	90	D	7 <sup>b</sup>
		1.5–12.5	256	43	160	4.6	Log	90	90	D	28 <sup>b</sup>
		12.5–100		344	600		Log	90	90	D	111 <sup>b</sup>
		14.4–26.3		100	50		<sup>c</sup>	80	80	D	111 <sup>b</sup>
Ariel 4	MBN	250k–4M			6000	16	Log	90	90	D	10
Helios 1	FFSA	11–309	24	15 %							
		209–6.07k	48	8 %						D	455
		6.4k–205k	96	4 %							

Identification		BW	Frequency steps				Amplitude			Back-end		
Host	Instr.	Span [Hz]	Steps [#]	Size [Hz or %]	RBW [Hz]	Cyc. [s]	Scl.	DR <sub>I</sub> [dB]	DR <sub>T</sub> [dB]	Res. [bits]	Rate [S/s]	
Helios 2	FFSA	11–309	24	15 %						D	455	
		209–6.07k	48	8 %								
		6.4k–205k	96	4 %								
GEOS 1	SFA	150–77k	256	300 Hz	3000	22	Lin <sup>d</sup>			D	1488	
ISEE 1	SFR	100–830						100	100			
		830–6.7k	32	6.5 %		32	Log	100	100			
		6.7k–50k						100	100			
		50k–400k						80	80			
GEOS 2	SFA	150–77k	256	300 Hz	3000	22	Lin <sup>d</sup>			D	1488	
DE 1	SFC	100–800										
		800–6.4k	32	1.0 %		32	Log <sup>e</sup>	70	100	D	4	
		6.4k–50k										
		50k–400k										
IRM	MF	275–2.5k			100					D	4	
		900–9.9k	32		300	1	Log		100			
		9k–99k			3k							



Identification		BW	Frequency steps				Amplitude			Back-end	
Host	Instr.	Span [Hz]	Steps [#]	Size [Hz or %]	RBW [Hz]	C <sub>yc.</sub> [s]	Scl.	DR <sub>I</sub> [dB]	DR <sub>T</sub> [dB]	Res. [bits]	Rate [S/s]
IRM	HF 1	93k–184k	7	10k	24k	2	Log	100	100	D	21
		194k–360k									
		396k–713k									
		799k–1.4M									
		1.6M–2.8M									
	3.2M–5.6M										
IRM	HF 2	10k–156M	64			4	Log	110	110	D	16
UKS	SFA	392–134k	256	512 <sup>f</sup> Hz	515	16	Log	60	72	8	16
Akebono	PWS	20k–5.1M	5100	1000 Hz	100	1	Log			8	1024
Galileo	PWS	5.6–31.1	4	66.7 %	2.75	2.67			110		
		42.1–161k	112	8 %	120	18.7	Log	100	100	8	30
		101k–5.6M	42	10 %	1340	18.7		100	100		
CRRES	PWE	100–800			7	32					
		800–6.4k			56	16					
		6.4k–50k	32	6.7 %	448	8	Log	100	100	8	4
		50k–400k			3600	8					
Ulysses	RAR	1.3k–48.5k	64		750	64					
		52k–940k	12		3000	24	Lin <sup>g</sup>	70	70	D	128
Ulysses	PFR	570–35k	32	14 %	750	0.5	Log <sup>h</sup>	128	128	D	128

Identification		BW	Frequency steps				Amplitude			Back-end	
Host	Instr.	Span [Hz]	Steps [#]	Size [Hz or %]	RBW [Hz]	Cyc. [s]	Scl.	DR <sub>I</sub> [dB]	DR <sub>T</sub> [dB]	Res. [bits]	Rate [S/s]
Geotail	PWI	24–200		1.3 Hz	2.6	64					
		200–1.6k		10.7 Hz	10	64					
		1.6k–12.5k	128	85.4 Hz	85	8	Log	90	120	D	
		12.5k–100k		683 Hz	680	8					
		100k–800k		5470 Hz	5400	8					
Wind	RAD1	20k–1M	64	4000 Hz	3000	24	Log	90		8	8
Wind	RAD2	1M–13.8M	48	50000 Hz	20k	3	Log	90		8	48
Polar	SFR <sup>i</sup>	24–200	64	2.75 Hz	5						
		200–1.6k	64	22 Hz	15.6						
		1.6k–12.5k	64	170 Hz	125	64	Log	100	100	8	
		12.5k–100k	128	684 Hz	1000						
		100k–808k	128	5531 Hz	8000						
FAST	SFA	10k–2M		8 kHz							
		10k–1M	256	4 kHz	15k	0.03	Log	80		8	4096
		10k–500k		2 kHz							
Interball 2	Polrad	4k–491k	120	4096 Hz	2700	6	Log				
		4k–983k	240			12					
Interball 2	MEMO	1–20k	40	500 Hz	800		Log			8	

Identification		BW	Frequency steps			Amplitude			Back-end		
Host	Instr.	Span [Hz]	Steps [#]	Size [Hz or %]	RBW [Hz]	Cyc. [s]	Scl.	DR <sub>I</sub> [dB]	DR <sub>T</sub> [dB]	Res. [bits]	Rate [S/s]
Cassini	MFR	24–180	16	13 %	5.6	16	Log	110	110	8	
		180–1.5k	32	7 %	19.4	16					
		1.5k–12k	32	7 %	139	8					
IMAGE	ANR	3k–3M	142	5 %	312		Log <sup>g</sup>	60	126	12	625
STEREO	HFR	125k–16M	318k	50k Hz	25k		Log <sup>g</sup>		80	12	464k

<sup>a</sup> Sampling rates correspond to 1, 8, and 64 kbps telemetry modes  
<sup>b</sup> Sampling rates correspond to 4, 16, and 64 kbps telemetry modes  
<sup>c</sup> Measures only phase of 100-Hz harmonics  
<sup>d</sup> Measures full-wave amplitude (from 150–3150 Hz) rather than RMS average by using WBR  
<sup>e</sup> Measures RMS amplitude and cross-correlates clipped signals between antenna pairs using XOR gates  
<sup>f</sup> Also offers wideband mode with 3260-Hz RBW  
<sup>g</sup> Measures full-wave amplitude rather than RMS average  
<sup>h</sup> Measures maximum and mean amplitudes rather than RMS average; offers wideband mode with 3-kHz RBW  
<sup>i</sup> Also offers 32-sec/cycle mode with 32 or 64 logarithmically spaced steps ranging in size from 8–3 %

Table B.4: Sweep frequency receivers aboard satellites in Table B.1.

### B.1.3.2 Multichannel Spectrum Analyzers

Table B.5 summarizes the bandwidth, amplitude, and back-end specifications for the divisions of each MSA embedded within the instruments of Table B.1. In addition, it encapsulates the specifics of the frequency channels in terms of:

- *Channels*: The number of parallel filter bands through which the signals within a division are processed.
- *Spacing*: The distance between the center frequencies of the channels. For linearly(logarithmically) spaced channels this is given in kHz(per decade or octave); in the event of non-uniform spacing, there is one entry for each inter-channel distance in ascending channel order.
- *FWHM*: The full-width half-maximum bandwidth of the channel band-pass filters (BPFs) given either in Hz or as a percentage of the center frequency.

Identification		BW	Frequency channels			Amplitude			Back-end	
Host	Instr.	Span [Hz]	Ch. [#]	Spacing [kHz or /base]	FWHM [Hz or %]	Scl.	DR <sub>I</sub> [dB]	DR <sub>T</sub> [dB]	Res. [bits]	Rate [S/s]
Injun 3	VLF	700–8.8k	6	2, 1.6, 1.2, 1.5, 1.8	50 Hz	Log <sup>a</sup>	40	80	4	12
Ariel 3	FFSS	3.2k–1.6k	3	6.4	1k Hz	Log <sup>a,b,c</sup>		75	6	0.36
Pioneer 8	PWD	400–22k	2	21.6	15 %				D	0.14
OGO 5	PWD	560–70k	7	~1 / octave	15 %	Lin		80	D	0.87
Injun 5	VLF	7.5k–105k	6	3, 11.5, 30.5, 17.5, 35	15 %	Log	60	60	D	0.25
Pioneer 9	EFD	400–30k	2	29.6	15 %				D	0.14
IMP 6	Iowa	40–178k	16	4 / decade	15 %	Log <sup>b,c</sup>		100		3.13
S <sup>3</sup> A	Iowa	40–100k	15	4 / decade	15, 30 <sup>g</sup> %	Log		80	D	
Ariel 4	VLF	750–17.8k	6	0.5, 2, 6.4, 6.4, 1.8	1k Hz <sup>f</sup>	<sup>a,b,c</sup>				0.67
IMP 8	Iowa	40–178k	15	4 / decade	15 %	Log <sup>b,c</sup>		100		1.47
Hawkeye	ELF-VLF	20–178k 20–5.62k	16 8	4 / decade	7.5– 30 %	Log <sup>b,c</sup>		100		1.39
Helios 1	SWPW	30–178k	16	4 / decade	8, 10 <sup>i</sup> %	Log <sup>b,d</sup>		100	D	28.4
Helios 2	SWPW	30–178k	16	4 / decade	8, 10 <sup>i</sup> %	Log <sup>b,d</sup>		100	D	28.4
S3-3	ACDC	30–100k	13	4 / decade					D	13

Identification		BW	Frequency channels			Amplitude			Back-end	
Host	Instr.	Span [Hz]	Ch. [#]	Spacing [kHz or /base]	FWHM [Hz or %]	Scl. [dB]	DR <sub>I</sub> [dB]	DR <sub>T</sub> [dB]	Res. [bits]	Rate [S/s]
GEOS 1	Filter bank	200–10k	5							
		630–5k	3	1 / octave	67 %	Log <sup>c</sup>		75	D	5.8
		200–5k	4							
Voy. 1	PWS	10–56.2k	16	4 / decade	15, 30 <sup>h</sup> %	Log	100	140	8	4
Voy. 2	PWS	10–56.2k	16	4 / decade	15, 30 <sup>h</sup> %	Log	100	140	8	4
ISEE 1	HEM	1k–32k	5	1 / octave	67 %	Lin <sup>e</sup>		70	A/D	
ISEE 1	Plasma waves	6–311k	20							
		6–10k	14	4 / decade	15, 30 <sup>g</sup> %	Log		110	8	4
ISEE 2	Waves	6–31.1k	16	4 / decade	15, 30 <sup>g</sup> %	Log		110	8	4
PVO	OEFD	100–30k	4	0.6, 4.7, 24.6	30 %			90	D	4
GEOS 2	Filter bank	200–10k	5							
		630–5k	3	1 / octave	67 %	Log <sup>c</sup>		75	D	5.8
		200–5k	4							
ISEE 3	Plasma waves	20–100k	16							
		20–1k	8	4 / decade	15 %	Log				2
		0–10	3							
DE 1	LFC	1.78k–100k	8	~1 / octave	30 %	Log		100	D	4

Identification		BW	Frequency channels			Amplitude			Back-end	
Host	Instr.	Span [Hz]	Ch. [#]	Spacing [kHz or /base]	FWHM [Hz or %]	Scl.	DR <sub>I</sub> [dB]	DR <sub>T</sub> [dB]	Res. [bits]	Rate [S/s]
DE 2	VEFI	4–1k 1k–512k	8 4	1 / octave 7.4, 30, 280	67 % 120 %	Log <sup>b,c</sup>		60	D	50
Aureol 3	Bank	10–1k	6	3 / decade	~75 %	Log		60	D	50
Aureol 3	TBF- ONCH	500–16k 140–15k	7 5	~1 / octave 0.3, 0.4, 3.7, 10.5	56– 160 %	Log		60	D	50
CCE	PWE	5–178k	5	0.6, 4.6, 24.6, 148	30 %	Log <sup>k</sup>		90	D	8
IRM	SA	31–178k	16	4 / decade	22, 38 <sup>l</sup> %	Log <sup>b,d</sup>		100	D	31.3
Akebono	MCA	3–17.8k	16	4 / decade	30 %	Lin	33	80	8	4
CRRES	PWE	5–10k	14	4 / decade	15, 30 <sup>g</sup> %	Log		110	8	8
Ulysses	FES	100–20k 600–60k	4 3	0.6, 2.2, 7.7 7.7, 22	1 dec	Log <sup>b</sup>	64	96	6	892
Geotail	PWI	6–311k 6–10k	20 14	4 / decade	15, 30 <sup>g</sup> %	Log		110 100	8	4
Wind	TNR	4k–16k 8k–32k 16k–64k 32k–128k 64k–256k	32	16 / octave	9 <sup>l</sup> %	Log <sup>m</sup>	30	100	8	1M





Identification		BW	Frequency channels			Amplitude			Back-end	
Host	Instr.	Span [Hz]	Ch. [#]	Spacing [kHz or /base]	FHWM [Hz or %]	Scl.	DR <sub>I</sub> [dB]	DR <sub>T</sub> [dB]	Res. [bits]	Rate [S/s]
Demeter	ICE	20–17.4k	890		20 Hz	Lin <sup>m</sup>	96	85	6	40k
		10k–3.2M	970		3k Hz		48	42	8	6.7M

<sup>a</sup> Measures minimum amplitude rather than RMS average  
<sup>b</sup> Measures maximum amplitude rather than RMS average  
<sup>c</sup> Measures mean amplitude over 400 ms rather than RMS average  
<sup>d</sup> Measures mean amplitude over 50 ms rather than RMS average  
<sup>e</sup> Records full waveform by sampling amplitude  
<sup>f</sup> FWHM is 500 Hz for channels below 1.25 kHz and 1000 Hz for channels above 3.2 kHz  
<sup>g</sup> FWHM is 15%(30%) for channels above(below) 10 kHz  
<sup>h</sup> FWHM is 15%(30%) for channels above(below) 1 kHz  
<sup>i</sup> FWHM is 8%(10%) for channels above(below) 3 kHz  
<sup>j</sup> FWHM is 38%(22%) for channels above(below) 3 kHz  
<sup>k</sup> Also offers amplitude measurements on linear scale  
<sup>l</sup> Also offers a 16-channel model with 4.4% FWHM filters  
<sup>m</sup> Filtering of sampled linear waveform performed in digital domain, followed by log compression  
<sup>n</sup> Signals between 125 kHz and 16 MHz can be heterodyned into 25-kHz division

Table B.5: Multichannel spectrum analyzers aboard satellites in Table B.1.

### B.1.3.3 Wideband Receivers

Table B.6 summarizes the bandwidth, amplitude, and back-end specifications for the divisions of each WBR embedded within the instruments of Table B.1. In addition, it encapsulates the specifics of their gain settings in terms of:

- *Steps*: The number of gain settings to which the VGA can be programmed. A zero value implies a fixed-gain amplifier.
- *Span*: The minimum and maximum gain settings of the VGA. For a fixed-gain amplifier, only one number is present.
- *Size*: The distance between the gain steps, which are assumed to be uniformly distributed across the span.
- *Cycle*: The update rate for one cycle of the AGC feedback loop (when this information is unavailable,  $n/a$  is noted). An empty entry indicates the absence of AGC, in which case the VGA is presumably commandable from the ground.

Unlike the SFR and MSA, here the quoted back-end acquisition rate is not cumulative, but instead applies to each digital output stream, of which there can be up to one per division.

Identification		BW		Gain range			AGC		Amplitude		Back-end	
Host	Instr.	Span [Hz]	Steps [#]	Span [dB]	Size [dB]	Cyc. [s]	Scl.	DR <sub>I</sub> [dB]	DR <sub>T</sub> [dB]	Res. [bits]	Rate [S/s]	
Alouette 1	VLF	400–10k	16	0–89	3	0.2	Lin	60	89		FM	
Injun 3	VLF	500–7k	1	0–40		0.2	<sup>a</sup>	40	40		FM	
OGO 1	VLF	300–12.5k	0				Log	80	80		FM/AM <sup>b</sup>	
OGO 2	VLF	300–12.5k	0				Log	80	80		FM/AM <sup>b</sup>	
OGO 3	ELF	15–300	0				Log	90	90		FM/AM <sup>b</sup>	
	VLF	300–12.5k						80	80			
OGO 4	ELF	15–300	0				Log	90	90		FM/AM <sup>b</sup>	
	VLF	300–12.5k						80	80			
Pioneer 8	PWD	100–100k	0				<sup>c</sup>			D	0.14	
OGO 5	PWD	1k–22k	> 0			n/a					AM	
Injun 5	VLF	30–650		0–60		0.25	Log	20	80		FM	
		650–10k										
Pioneer 9	PWD	100–100k	0				<sup>c</sup>			D	0.14	
ISIS 1	VLF	50–30k	2	0–80		n/a	Lin		80		AM	
IMP 6	Iowa	10–1k 650–30k	> 0			n/a					AM	
ISIS 2	VLF	50–30k	2	0–80		n/a	Lin		80		AM	
S <sup>3</sup> A	Iowa	100–10k	> 0			n/a	Lin		80		AM	

Identification		BW		Gain range			AGC		Amplitude			Back-end	
Host	Instr.	Span [Hz]	Steps [#]	Span [dB]	Size [dB]	Cyc. [s]	Scl.	DR <sub>I</sub> [dB]	DR <sub>T</sub> [dB]	Res. [bits]	Rate [S/s]		
IMP 8	Iowa	10–1k	> 0			n/a				AM			
Hawkeye 1	ELF	150–10								AM			
	VLF	1k–45k											
Helios 1	FFSA	1–200											
Helios 2	FFSA	1–200											
S3-3	ACDC	0.05–16	2				Lin			8	32		
		0.05–6k											
		0.05–10.5k								FM			
		0.05–18.6k											
GEOS 1	ELF	0–450	4	0–80	20	0.086	Lin	80	D	1488			
Voy. 1	PWS	50–10k	> 0			0.5	Lin		4	28k			
Voy. 2	PWS	50–10k	> 0			0.5	Lin		4	28k			
ISEE 1	Plasma waves	10–1k <sup>d</sup>	> 0			n/a	Log			FM			
		650–10k <sup>d</sup>							AM				
		650–40k <sup>d</sup>							AM				
ISEE 2	Plasma waves	10–1k <sup>d</sup>	> 0			n/a	Log			FM			
		650–10k <sup>d</sup>							AM				
GEOS 2	ELF	0–450	4	0–80	20	0.086	Lin	80	D	1488			

Identification		BW		Gain range			AGC		Amplitude		Back-end	
Host	Instr.	Span [Hz]	Steps [#]	Span [dB]	Size [dB]	Cyc. [s]	Scl.	DR <sub>I</sub> [dB]	DR <sub>T</sub> [dB]	Res. [bits]	Rate [S/s]	
DE 1	LWR	1.5k–3k	7	0–70	10	2	Lin	30	100	AM	AM	
		2.9k–3.3k										
		3k–6k										
		10k–16k										
DE 1	WBR	1–1k <sup>d</sup>	> 0	650–10k <sup>d</sup>	650–40k <sup>d</sup>	n/a	Log	110	FM	AM	AM	
		650–10k <sup>d</sup>										
		650–40k <sup>d</sup>										
Aureol 3	Bank	10–1.5k	4	0–37.3	13.3	0.3	Lin	60	FM			
Aureol 3	TBF	70–16k	2	0–24	24		Log	20	60	AM		
IRM	WBR	5–1k <sup>d</sup>	> 0	650–10k <sup>d</sup>	n/a	Log	110	FM				
		650–10k <sup>d</sup>										
Akebono	WBA	50–7k	4	0–75	25	0.5	Lin	33	80	PM		
Akebono	ELF	0–50	4	0–75	25	0.5	Lin	33	80	8	160	
Akebono		0–100								320		
Galileo	PWS	5–1k <sup>d</sup>	> 0	n/a	Log	24	4	202k				
		50–10k <sup>d</sup>										
		50–80k <sup>d</sup>										

Identification		BW	Gain range			AGC		Amplitude			Back-end	
Host	Instr.	Span [Hz]	Steps [#]	Span [dB]	Size [dB]	Cyc. [s]	Scl.	DR <sub>I</sub> [dB]	DR <sub>T</sub> [dB]	Res. [bits]	Rate [S/s]	
CRRES	ELFW	10–25 10–124	3	0–40	20	n/a	Lin	48	90	D	500	
Geotail	PWI	10–4k 100–4k	3	0–40	20		Log	66	106	8	12k	
Freja	WAVE	0–60	2	0–34	34		Lin	48	82	16	128	
		1–2k								16	4k	
		1–16k								16	32k	
		100k–4M								8	8M	
Wind	TDS	0.3–3.3k 0.3–60k					Log		90	8	7.5k 120k	
Interball 1	OPERA	100–1k	2	0–20	20		Lin		80	8	2k	
Polar	HFWR	20–250 <sup>e</sup>	3	0–30	10	129	Lin	72	102	12	71k	
		20–2k <sup>e</sup>										
		20–16k <sup>e</sup>										
		20–25k										
Polar	LFWR	0.1–25	0				Lin		72	12	100	



Identification		BW	Gain range			AGC	Amplitude			Back-end		
Host	Instr.	Span [Hz]	Steps [#]	Span [dB]	Size [dB]	Cyc. [s]	Scl.	DR <sub>I</sub> [dB]	DR <sub>T</sub> [dB]	Res. [bits]	Rate [S/s]	
Cassini	5WFR	1–26 3–2.5k	4	0–30	10	n/a	Lin	72	102	12	100 7.1K	
	WBR	60–10.5k 800–75k	8	0–70	10	0.1	Lin	48	100	12	27.7k 222k	
Cluster	WBD	25–9.5k <sup>f</sup>	16	0–75	5	0.1	Lin	48	120	8 <sup>g</sup>	220k	
		50–19k <sup>f</sup>						24	100	4 <sup>g</sup>		
		1k–77k <sup>f</sup>						24	100	4 <sup>g</sup>		
Cluster	EFW	0–10	2	0–148		n/a	Lin	96	77 <sup>h</sup>	16	36k	
		0–180										
		0–4k										
		0–32k										
		50–8k										
DEMETER	DC	0–15					Lin	96		16	39	
	ELF	15–1k						96		80	16	2.5k
	VLF	15–17.4k						96		85	16	40k
	HF	10k–3.2M						48		42	8	6.6M



Identification		BW		Gain range			AGC		Amplitude			Back-end	
Host	Instr.	Span	[Hz]	Steps	Span	Size	Cyc.	Scl.	DR <sub>I</sub>	DR <sub>T</sub>	Res.	Rate	
				[#]	[dB]	[dB]	[s]		[dB]	[dB]	[bits]	[S/s]	
STEREO	TDS	500–3k										8k	
		500–13k						Log		80	16	31k	
		500–54k										125k	
		500–109k										250k	
THEMIS	EFI	10–8k		2	0–15.5	15.5		Lin	60	120	16	16k	
		30k–500k						Log	48	70	8	8k	

<sup>a</sup> AGC holds output level constant so that frequency content (versus time) modulates carrier  
<sup>b</sup> Averaged(clipped) signal FM-(AM-)modulates carrier with amplitude(frequency) content  
<sup>c</sup> Counts positive-going crossings of threshold that cycles through 8(16) levels every 1(7.5) minutes  
<sup>d</sup> By heterodyning inputs, span can effectively start from 0, 31.25, 62.5, 125, 500, 1000, or 2000 kHz  
<sup>e</sup> Frequency divisions arise from digital filtering and decimation of signal sampled at full rate  
<sup>f</sup> By heterodyning inputs, span can effectively start from 0, 125, 250, 500 kHz  
<sup>g</sup> Either sampling rate can be applied to any frequency division and achieve attendant DR  
<sup>h</sup> DR limited by noise from sheath photoelectrons, not electronics

Table B.6: Wideband receivers aboard satellites in Table B.1.

## B.2 Selected Bibliography

The following bibliography accompanies Table B.1, providing the numbered references it adduces as sources for the satellite, antenna, and receiver specifications tabulated in this appendix.

# Instrument Bibliography

- [1] Amata, E., Baldetti, P., Bellucci, G., Formisano, V., and Morbidini, A. “The experiment OPERA for the mission Interball”. *Il Nuovo Cimento C*, vol. 13, no. 1, pp. 155–161, February 1990. doi:10.1007/BF02515785.
- [2] Anderson, R. R. and Gurnett, D. A. “Plasma wave observations near the Plasmapause with the S<sup>3</sup>-A satellite”. *Journal of Geophysical Research*, vol. 78, no. 22, pp. 4756–4764, August 1973. doi:10.1029/JA078i022p04756.
- [3] Anderson, R. R., Gurnett, D. A., and Odem, D. L. “CRRES plasma wave experiment”. *Journal of Spacecraft and Rockets*, vol. 29, no. 4, pp. 570–573, July 1992. doi:10.2514/3.25501.
- [4] Angelopoulos, V. “The THEMIS mission”. *Space Science Reviews*, vol. 141, pp. 5–34, December 2008. doi:10.1007/s11214-008-9336-1.
- [5] Bale, S. D., Ullrich, R., Goetz, K., Alster, N., Cecconi, B., Dekkali, M., Lingner, N. R., Macher, W., Manning, R. E., McCauley, J., Monson, S. J., Oswald, T. H., and Pulupa, M. “The electric antennas for the STEREO/WAVES experiment”. *Space Science Reviews*, vol. 136, no. 1–4, pp. 529–547, April 2008. doi:10.1007/s11214-007-9251-x.
- [6] Barrington, R. E. and Belrose, J. S. “Preliminary results from the Very-Low Frequency receiver aboard Canada’s Alouette satellite”. *Nature*, vol. 198, no. 4881, pp. 651–656, May 1963. doi:10.1038/198651a0.

- [7] Bell, T. F. and Helliwell, R. A. “The Stanford University VLF wave injection experiment on the ISEE-A spacecraft”. *IEEE Transactions on Geoscience Electronics*, vol. 16, no. 3, pp. 248–252, July 1978. doi:10.1109/TGE.1978.294556.
- [8] Berthelier, J. J., Godefroy, M., Leblanc, F., Malingre, M., Menvielle, M., Lagoutte, D., Brochot, J. Y., Colin, F., Elie, F., Legendre, C., Zamora, P., Benoist, D., Chapuis, Y., Artru, J., and Pfaff, R. “ICE, the electric field experiment on DEMETER”. *Planetary and Space Science*, vol. 54, no. 5, pp. 456–471, April 2006. doi:10.1016/j.pss.2005.10.016.
- [9] Berthelier, J. J., LeFeuvre, F., Mogilevsky, M. M., Molchanov, O. A., Galperin, Y. I., Karczewski, J. F., Ney, R. ad Gogly, G., Guerin, C., LeVeque, M., Moreau, J.-M., and Sene, F. X. “Measurements of the VLF electric and magnetic components of waves and DC electric field on board the AUREOL-3 spacecraft: the TBF-ONCH experiment”. *Annales de Géophysique*, vol. 38, no. 5, pp. 643–667, 1982.
- [10] Błęcki, J., Gadomski, S., Juchniewicz, J., Korepanov, V., Krawczyk, Z., Savin, S., Słomiński, J., Triska, P., Vojta, J., and Wronowski, R. “SAS wave experiment on board Magion 4”. *Annales de Géophysique*, vol. 15, no. 4, pp. 528–532, May 1997. doi:10.1007/s00585-997-0528-x.
- [11] Bonnell, J. W., Mozer, F. S., Delory, G. T., Hull, A. J., Ergun, R. E., Cully, C. M., Angelopoulos, V., and Harvey, P. R. “The electric field instrument (EFI) for THEMIS”. *Space Science Reviews*, vol. 141, no. 1, pp. 303–341, December 2008. doi:10.1007/s11214-008-9469-2.
- [12] Bougeret, J. L., Goetz, K., Kaiser, M. L., Bale, S. D., Kellogg, P. J., Maksimovic, M., Monge, N., Monson, S. J., Astier, P. L., Davy, S., Dekkali, M., Hinze, J. J., Manning, R. E., Aguilar-Rodriguez, E., Bonnin, X., Briand, C., Cairns, I. H., Cattell, C. A., Cecconi, B., Eastwood, J., Ergun, R. E., Fainberg, J., Hoang, S., Huttunen, K. E. J., Krucker, S., Lecacheux, A., MacDowall, R. J., Macher, W., Mangeney, A., Meetre, C. A., Moussas, X., Nguyen, Q. N., Oswald, T. H., Pulupa, M., Reiner, M. J., Robinson, P. A., Rucker, H., Salem, C., Santolik, O.,

- Silvis, J. M., Ullrich, R., Zarka, P., and Zouganelis, I. "S/WAVES: The radio and plasma wave investigation on the STEREO mission". *Space Science Reviews*, vol. 136, no. 1–4, pp. 487–528, April 2008. doi:10.1007/s11214-007-9298-8.
- [13] Bougeret, J.-L., Kaiser, M. L., Kellogg, P. J., Manning, R., Goetz, K., Monson, S. J., Monge, N., Friel, L., Meetre, C. A., Perche, C., Sitruk, L., and Hoang, S. "Waves: The radio and plasma wave investigation on the Wind spacecraft". *Space Science Reviews*, vol. 71, no. 1–4, pp. 231–263, February 1995. doi:10.1007/BF00751331.
- [14] Bullough, K., Denby, M., Gibbons, W., Hughes, A. R. W., Kaiser, T. R., and Tatnall, A. R. L. "E.l.f./v.l.f. emissions observed on Ariel 4". *Proceedings of the Royal Society of London. Series A, Mathematical and Physical Sciences*, vol. 343, no. 1633, pp. 207–226, April 1975.
- [15] Bullough, K., Hughes, A. R. W., Hudson, T., Dickinson, D., Broomhead, P., and Tomlinson, P. "The Sheffield University v.l.f. experiment on the satellite Ariel 3". *Journal of Physics E: Scientific Instruments*, vol. 1, no. 2, pp. 77–85, February 1968. doi:10.1088/0022-3735/1/2/202.
- [16] Burch, J. L. "IMAGE mission overview". *Space Science Reviews*, vol. 91, no. 1–2, pp. 1–14, January 2000. doi:10.1023/A:1005245323115.
- [17] Burch, J. L. and Hoffman, R. A. "Introduction to the dynamics explorer mission". In *23<sup>rd</sup> AIAA Aerospace Sciences Meeting, Reno, NV, Jan. 14-17, 1985*, AIAA-85-0061, pp. 1–8. Washington, DC: American Institute of Aeronautics and Astronautics, January 1985.
- [18] Cain, J. C., Shapiro, I. R., Stolarik, J. D., and Heppner, J. P. "A note on whistlers observed above the Ionosphere". *Journal of Geophysical Research*, vol. 66, no. 9, pp. 2677–2680, September 1961. doi:10.1029/JZ066i009p02677.
- [19] ———. "Vanguard 3 magnetic-field observations". *Journal of Geophysical Research*, vol. 67, no. 13, pp. 5055–5069, December 1962. doi:10.1029/JZ067i013p05055.

- [20] Cattell, S. A. “S3-3 satellite instrumentation and data”. In *The IMS Source Book: Guide to the International Magnetospheric Study Data Analysis*, C. T. Russell and D. J. Southwood, eds., chap. 1, pp. 91–98. Washington, DC: American Geophysical Union, 1982. ISBN 0-87590-228-6.
- [21] Cauffman, D. P. and Gurnett, D. A. “Satellite measurements of high latitude convection electric fields”. *Space Science Reviews*, vol. 13, no. 3, pp. 369–410, July 1972. doi:10.1007/BF00219164.
- [22] Crook, G. M., Scarf, F. L., Fredricks, R. W., Green, I. M., and Lukas, P. “The OGO-V plasma wave detector: Instrumentation and in-flight operation”. *IEEE Transactions on Geoscience Electronics*, vol. 7, no. 2, pp. 120–135, April 1969. doi:10.1109/TGE.1969.271332.
- [23] Cully, C. M., Ergun, R. E., Stevens, K., Nammari, A., and Westfall, J. “The THEMIS digital fields board”. *Space Science Reviews*, vol. 141, no. 1–4, pp. 343–355, December 2008. doi:10.1007/s11214-008-9417-1.
- [24] Cussac, T., Clair, M.-A., Ultré-Guerard, P., Buisson, F., Lassalle-Balier, G., Ledu, M., Elisabelar, C., Passot, X., and Rey, N. “The demeter microsatellite and ground segment”. *Planetary and Space Science*, vol. 54, no. 5, pp. 413–427, April 2006. doi:10.1016/j.pss.2005.10.013.
- [25] Darbyshire, A. G., Gershuny, E. J., Jones, S. R., Norris, A. J., Thompson, J. A., Whitehurst, G. A., Wilson, G. A., and Woolliscroft, L. J. C. “The UKS wave experiment”. *IEEE Transactions on Geoscience and Remote Sensing*, vol. GE-23, no. 3, pp. 311–314, May 1985. doi:10.1109/TGRS.1985.289533.
- [26] Dassoulas, J., Margolies, D. L., and Peterson, M. R. “The AMPTE CCE spacecraft”. *IEEE Transactions on Geoscience and Remote Sensing*, vol. GE-23, no. 3, pp. 182–191, May 1985. doi:10.1109/TGRS.1985.289512.
- [27] Develco. “VLF wave injection receiver”. Manual 983-761029, Develco, Inc., Sunnyvale, CA, November 1976.

- [28] Driesman, A., Hynes, S., and Cancro, G. “The STEREO observatory”. *Space Science Reviews*, vol. 136, no. 1–4, pp. 17–44, April 2008. doi:10.1007/s11214-007-9286-z.
- [29] Dunckel, N. and Helliwell, R. A. “Whistler-mode emissions on the OGO 1 satellite”. *Journal of Geophysical Research*, vol. 74, no. 26, pp. 6371–6385, December 1969. doi:10.1029/JA074i026p06371.
- [30] Ergun, R. E., Carlson, C. W., Mozer, F. S., Delory, G. T., Temerin, M., McFadden, J. P., Pankow, D., Abiad, R., Harvey, P., Wilkes, R., Primbsch, H., Elphic, R., Strangeway, R., Pfaff, R., and Cattell, C. A. “The FAST satellite fields instrument”. *Space Science Reviews*, vol. 98, no. 1–2, pp. 67–91, August 2001. doi:10.1023/A:1013131708323.
- [31] Ficklin, B. P., Rorden, L. H., Mills, M. E., Stehle, R. H., and Orsak, L. E. “Description and operation of the instruments for the Stanford University/Stanford Research Institute experiment (5002) to be flown on the POGO satellite”. Technical Memorandum 2 L-21858, Stanford Research Institute, Menlo Park, CA, March 1965.
- [32] Ficklin, B. P., Stehle, R. H., Barnes, C., and Mills, M. E. “Instrumentation for the Stanford University/Stanford Research Institute VLF experiment (B-17) on the OGO-3 satellite”. Supplemental Report L-19361, Stanford Research Institute, Menlo Park, CA, May 1967.
- [33] Florida, C. D. “The development of a series of ionospheric satellites”. *Proceedings of the IEEE*, vol. 57, no. 6, pp. 867–875, June 1969.
- [34] Formisano, V. “The International Sun-Earth Explorer Mission - ISEE-2”. In *The IMS Source Book: Guide to the International Magnetospheric Study Data Analysis*, C. T. Russell and D. J. Southwood, eds., chap. 1, pp. 27–36. Washington, DC: American Geophysical Union, 1982. ISBN 0-87590-228-6.
- [35] Fuselier, S. A., Burch, J. L., Lewis, W. S., and Reiff, P. H. “Overview of the

- IMAGE science objectives and mission phases”. *Space Science Reviews*, vol. 91, no. 1–2, pp. 51–66, January 2000. doi:10.1023/A:1005255224024.
- [36] Green, J. L., Benson, R. F., Fung, S. F., Taylor, W. W. L., Boardsen, S. A., Reinisch, B. W., Haines, D. M., Bibl, K., Cheney, G., Galkin, I. A., Huang, X., Myers, S. H., Sales, G. S., Bougeret, J.-L., Manning, R., Meyer-Vernet, N., Moncuquet, M., Carpenter, D. L., Gallagher, D. L., and Reiff, P. H. “Radio plasma imager simulations and measurements”. *Space Science Reviews*, vol. 91, no. 1–2, pp. 361–389, January 2000. doi:10.1023/A:1005256703977.
- [37] Gurnett, D. A. “The Earth as a radio source: Terrestrial kilometric radiation”. *Journal of Geophysical Research*, vol. 79, no. 28, pp. 4227–4238, October 1974. doi:10.1029/JA079i028p04227.
- [38] Gurnett, D. A. and Anderson, R. R. “Plasma wave electric fields in the solar wind - initial results from Helios 1”. *Journal of Geophysical Research*, vol. 82, no. 4, pp. 632–650, February 1977. doi:10.1029/JA082i004p00632.
- [39] Gurnett, D. A. and Frank, L. A. “A region of intense plasma wave turbulence on auroral field lines”. *Journal of Geophysical Research*, vol. 82, no. 7, pp. 1031–1050, March 1977. doi:10.1029/JA082i007p01031.
- [40] Gurnett, D. A., Huff, R. L., and Kirchner, D. L. “The wide-band plasma wave investigation”. *Space Science Reviews*, vol. 79, no. 1–2, pp. 195–208, January 1997. doi:10.1023/A:1004966823678.
- [41] Gurnett, D. A. and Inan, U. S. “Plasma wave observations with the Dynamics Explorer 1 spacecraft”. *Reviews of Geophysics*, vol. 26, no. 2, pp. 285–316, May 1988. doi:10.1029/RG026i002p00285.
- [42] Gurnett, D. A., Kurth, W. S., Kirchner, D. L., Hospodarsky, G. B., Averkamp, T. F., Zarka, P., Lecacheux, A., Manning, R., Roux, A., Canu, P., Cornilleau-Wehrlin, N., Galopeau, P., Meyer, A., Boström, R., Gustafsson, G., Wahlund, J.-E., Åhlen, L., Rucker, H. O., Ladreiter, H. P., Macher, W., Woolliscroft, L. J. C.,



- Alleyne, H., Kaiser, M. L., Desch, M. D., Farrell, W. M., Harvey, C. C., Louarn, P., Kellogg, P. J., Goetz, K., and Pedersen, A. "The Cassini radio and plasma wave investigation". *Space Science Reviews*, vol. 114, no. 1–4, pp. 395–463, September 2004. doi:10.1007/s11214-004-1434-0.
- [43] Gurnett, D. A., Kurth, W. S., Shaw, R. R., Roux, A., Gendrin, R., Kennel, C. F., Scarf, F. L., and Shawhan, S. D. "The Galileo plasma wave investigation". *Space Science Reviews*, vol. 60, no. 1–4, pp. 341–355, May 1992. doi:10.1007/BF00216861.
- [44] Gurnett, D. A. and O'Brien, B. J. "High-latitude geophysical studies with satellite Injun 3. 5, Very Low Frequency electromagnetic radiation". *Journal of Geophysical Research*, vol. 69, no. 1, pp. 65–89, January 1964. doi:10.1029/JZ069i001p00065.
- [45] Gurnett, D. A., Persoon, A. M., Randall, R. F., Odem, D. L., Remington, S. L., Averkamp, T. F., Debowe, M. M., Hospodarsky, G. B., Huff, R. L., Kirchner, D. L., Mitchell, M. A., Pham, B. T., Phillips, J. R., Schintler, W. J., Sheyko, P., and Tomash, D. R. "The Polar plasma wave instrument". *Space Science Reviews*, vol. 71, no. 1–4, pp. 597–622, February 1995. doi:10.1007/BF00751343.
- [46] Gurnett, D. A., Pfeiffer, G. W., Anderson, R. R., Mosier, S. R., and Cauffman, D. P. "Initial observations of VLF electric and magnetic fields with the Injun 5 satellite". *Journal of Geophysical Research–Space Physics*, vol. 74, no. 19, pp. 4631–4648, September 1969. doi:10.1029/JA074i019p04631.
- [47] Gurnett, D. A., Scarf, F. L., Fredricks, R. W., and Smith, E. J. "The ISEE-1 and ISEE-2 plasma wave investigation". *IEEE Transactions on Geoscience Electronics*, vol. 16, no. 3, pp. 225–230, July 1978. doi:10.1109/TGE.1978.294552.
- [48] Gurnett, D. A. and Shaw, R. R. "Electromagnetic radiation trapped in the Magnetosphere above the plasma frequency". *Journal of Geophysical Research*, vol. 78, no. 34, pp. 8236–8249, December 1973. doi:10.1029/JA078i034p08136.

- [49] Gustafsson, G., Bostrom, R., Holback, B., Holmgren, G., Lundgren, A., Stasiewicz, K., Ahlen, L., Mozer, F. S., Pankow, D., Harvey, P., Berg, P., Ulrich, R., Pedersen, A., Schmidt, R., Butler, A., Fransen, A. W. C., Klinge, D., Thomsen, M., Falthammar, C.-G., Lindqvist, P.-A., Christenson, S., Holtet, J., Lybekk, B., Sten, T. A., Tanskanen, P., Lappalainen, K., and Wygant, J. “The electric field and wave experiment for the Cluster mission”. *Space Science Reviews*, vol. 79, no. 1–2, pp. 137–156, January 1997. doi:10.1023/A:1004975108657.
- [50] Hanasz, J., Schreiber, R., de Feraudy, H., Mogilevsky, M. M., and Romantsova, T. V. “Observations of the upper frequency cutoffs of the auroral kilometric radiation”. *Annales de Géophysique*, vol. 16, no. 9, pp. 1097–1104, September 1998. doi:10.1007/s005850050679.
- [51] Harten, R. and Clark, K. “The design features of the GGS Wind and Polar spacecraft”. *Space Science Reviews*, vol. 71, no. 1–4, pp. 23–40, February 1995. doi:10.1007/BF00751324.
- [52] Harvey, P., Mozer, F. S., Pankow, D., Wygant, J., Maynard, N. C., Singer, H., Sullivan, W., Anderson, P. B., Pfaff, R., Aggson, T., Pedersen, A., Fälthammar, C.-G., and Tanskannen, P. “The electric field instrument on the Polar satellite”. *Space Science Reviews*, vol. 71, no. 1–4, pp. 583–596, February 1995. doi:10.1007/BF00751342.
- [53] Harvey, P., Taylor, E., Sterling, R., and Cully, M. “The THEMIS constellation”. *Space Science Reviews*, vol. 141, no. 1–4, pp. 117–152, December 2008. doi:10.1007/s11214-008-9416-2.
- [54] Hashimoto, K., Nagano, I., Yamamoto, M., Okada, T., Kimura, I., Matsumoto, H., and Oki, H. “EXOS-D (AKEBONO) very low frequency plasma wave instruments (VLF)”. *IEEE Transactions on Geoscience and Remote Sensing*, vol. 35, no. 2, pp. 278–286, March 1997. doi:10.1109/36.563267.
- [55] Häusler, B., Anderson, R. R., Gurnett, D. A., Koons, H. C., Holzworth, R. H., Bauer, O. H., Treumann, R., Gnaiger, K., Odem, D., Harbridge, W. B., and Eberl,

- F. "The plasma wave instrument on board the AMPTE IRM satellite". *IEEE Transactions on Geoscience and Remote Sensing*, vol. GE-23, no. 3, pp. 267–273, May 1985. doi:10.1109/TGRS.1985.289526.
- [56] Häusler, B., Melzner, F., Stöcker, J., Valenzuela, A., Bauer, O. H., Parigger, P., Sigritz, K., Schöning, R., Seidenschwang, E., Eberl, F., Kaiser, K.-H., Lieb, W., Merz, B., Pagel, U., Wiezorrek, E., and Genzel, J. P. "The AMPTE IRM spacecraft". *IEEE Transactions on Geoscience and Remote Sensing*, vol. GE-23, no. 3, pp. 192–201, May 1985. doi:10.1109/TGRS.1985.289513.
- [57] Hayakawa, H., Okada, K., Ejiri, M., Kadokura, A., Kohno, Y.-I., Maezawa, K., Machida, S., Matsuoka, A., Mukai, T., Nakamura, M., Nishida, A., Obara, T., Tanaka, Y., Mozer, F. S., Haerendel, G., and Tsuruda, K. "Electric field measurement on the Akebono (EXOS-D) satellite". *Journal of Geomagnetism and Geoelectricity*, vol. 42, no. 4, pp. 371–384, March 1990.
- [58] Helliwell, R. A. and Angerami, J. J. "Final report for experiments A17 (OGO 1) and B17 (OGO 3)". Contractor Report NASA-CR-110716, The Radioscience Laboratory, Stanford University, Stanford, CA, June 1968.
- [59] ———. "Final report for experiments C02 (OGO 2) and D02 (OGO 4)". Contractor Report NASA-CR-110658, The Radioscience Laboratory, Stanford University, Stanford, CA, July 1969.
- [60] Hoffman, R. A., Hogan, G. D., and Maehl, R. C. "Dynamics Explorer spacecraft and ground operations systems". *Space Science Instrumentation*, vol. 5, no. 4, pp. 349–367, December 1981.
- [61] Hoffman, R. A. and Schmerling, E. R. "Dynamics Explorer program: an overview". *Space Science Instrumentation*, vol. 5, no. 4, pp. 345–348, December 1981.
- [62] Holback, B., Jansson, S.-E., Åhlén, L., Lundgren, G., Lyngdal, L., Powell, S., and Meyer, A. "The Freja wave and plasma density experiment". *Space Science Reviews*, vol. 70, no. 3–4, pp. 577–592, November 1994. doi:10.1007/BF00756887.

- [63] Irzhichek, F., Mal'tseva, O. A., Titova, E. E., Triska, P., and Yakhnina, T. A. "Peculiarities of the propagation of VLF choruses in the Magnetosphere". *Geomagnetism and Aeronomy*, vol. 26, no. 6, pp. 842–846, January 1986.
- [64] Jaffe, L. D. and Herrell, L. M. "Cassini/Huygens science instruments, spacecraft, and mission". *Journal of Spacecraft and Rockets*, vol. 34, no. 4, pp. 509–521, July 1997. doi:10.2514/2.3241.
- [65] Johnson, M. H. and Kierein, J. "Combined release and radiation effects satellite (CRRES) - spacecraft and mission". *Journal of Spacecraft and Rockets*, vol. 29, no. 4, pp. 556–563, July 1992. doi:10.2514/3.55641.
- [66] Johnson, T. V., Yeates, C. M., and Young, R. "Space Science Reviews volume on Galileo mission overview". *Space Science Reviews*, vol. 60, no. 1–4, pp. 3–21, May 1992. doi:10.1007/BF00216848.
- [67] Jones, D. "Introduction to the S-300 wave experiment onboard GEOS: For GEOS S-300 experimenters". *Space Science Reviews*, vol. 22, no. 4, pp. 327–332, October 1978. doi:10.1007/BF00210871.
- [68] Kaiser, M. L., Kucera, T. A., Davila, J. M., St. Cyr, O. C., Guhathakurta, M., and Christian, E. "The STEREO mission: An introduction". *Space Science Reviews*, vol. 136, no. 1–4, pp. 5–16, April 2008. doi:10.1007/s11214-007-9277-0.
- [69] Kennel, C. F., Scarf, F. L., Fredricks, R. W., McGehee, J. H., and Coroniti, F. V. "VLF electric field observations in the Magnetosphere". *Journal of Geophysical Research*, vol. 75, no. 31, pp. 6136–6152, November 1970. doi: 10.1029/JA075i031p06136.
- [70] Khmyrov, B. E., Kavelin, S. S., Popel, A. M., Lyssenko, I. N., Polluskov, I. M., Varydin, V. S., Rodin, K. V., and Ovsyanikov, V. V. "The AUREOL-3 satellite". *Annales de Géophysique*, vol. 38, no. 5, pp. 547–555, 1982.
- [71] Kimura, I., Hashimoto, K., Nagano, I., Okada, T., Yamamoto, M., Yoshino, T., Matsumoto, H., Ejiri, M., and Hayashi, K. "VLF observations by the Akebono

- (EXOS-D) satellite". *Journal of Geomagnetism and Geoelectricity*, vol. 42, no. 4, pp. 459–478, March 1990.
- [72] King, J. H. "Availability of IMP-7 and IMP-8 data for the IMS period". In *The IMS Source Book: Guide to the International Magnetospheric Study Data Analysis*, C. T. Russell and D. J. Southwood, eds., chap. 1, pp. 10–20. Washington, DC: American Geophysical Union, 1982. ISBN 0-87590-228-6.
- [73] Kintner, P. M. and Gurnett, D. A. "Observations of ion cyclotron waves within the Plasmasphere by Hawkeye 1". *Journal of Geophysical Research*, vol. 82, no. 16, pp. 2314–2318, June 1977. doi:10.1029/JA082i016p02314.
- [74] Klimov, S., Romanov, S., Amata, E., Błęcki, J., Büchner, J., Juchniewicz, J., Rustenbach, J., Triska, P., Woolliscroft, L. J. C., Savin, S., Afanas'yev, Y., de Angelis, U., Auster, U., Bellucci, G., Best, A., Farnik, F., Formisano, V., Gough, P., Grard, R., Grushin, V., Haerendel, G., Ivchenko, V., Korepanov, V., Lehmann, H., Nikutowski, B., Nozdrachev, M., Orsini, S., Parrot, M., Petrukovich, A., Rauch, J. L., Sauer, K., Skalsky, A., Słominski, J., Trotignon, J. G., Vojta, J., and Wronowski, R. "ASPI experiment: measurements of fields and waves on board the INTERBALL-1 spacecraft". *Annales de Géophysique*, vol. 15, no. 5, pp. 514–527, May 1997. doi:10.1007/s00585-997-0514-3.
- [75] Knott, K. "The availability of GEOS data for IMS research". In *The IMS Source Book: Guide to the International Magnetospheric Study Data Analysis*, C. T. Russell and D. J. Southwood, eds., chap. 1, pp. 43–52. Washington, DC: American Geophysical Union, 1982. ISBN 0-87590-228-6.
- [76] Koons, H. C., Roeder, J. L., and Harbridge, W. B. "Extremely low frequency wave analyzer". *Journal of Spacecraft and Rockets*, vol. 29, no. 4, pp. 606–607, July 1992. doi:10.2514/3.26367.
- [77] Kurth, W. S., Baumbach, M. M., and Gurnett, D. A. "Direction-finding measurements of auroral kilometric radiation". *Journal of Geophysical Research*, vol. 80, no. 19, pp. 2764–2770, July 1975. doi:10.1029/JA080i019p02764.

- [78] Laaspere, T., Morgan, M. G., and Johnson, W. C. “Observations of lower hybrid resonance phenomena on the OGO 2 spacecraft”. *Journal of Geophysical Research–Space Physics*, vol. 74, no. 1, pp. 141–152, January 1969. doi:10.1029/JA074i001p00141.
- [79] Lefeuvre, F., Parrot, M., Rauch, J. L., Poirier, B., Masson, A., and Mogilevsky, M. “Preliminary results from the MEMO multicomponent measurements of waves on-board INTERBALL 2”. *Annales de Géophysique*, vol. 16, no. 9, pp. 1117–1136, September 1998. doi:10.1007/s005850050681.
- [80] Likhter, I. I., Sobolev, I. P., and Vernova, L. V. “Ion-cyclotron noise excitation in the topside ionosphere according to observations at the Intercosmos-14 satellite”. *Journal of Atmospheric and Terrestrial Physics*, vol. 40, no. 9, pp. 1047–1055, September 1978.
- [81] Lindqvist, P.-A., Marklund, G. T., and Blomberg, L. G. “Plasma characteristics determined by the Freja electric field instrument”. *Space Science Reviews*, vol. 70, no. 3–4, pp. 593–602, November 1994. doi:10.1007/BF00756888.
- [82] Longanecker, G. W. and Hoffman, R. A. “S<sup>3</sup>-A spacecraft and experiment description”. *Journal of Geophysical Research*, vol. 78, no. 22, pp. 4711–4717, August 1973. doi:10.1029/JA078i022p04711.
- [83] Lundin, R., Haerendel, G., and Grahn, S. “The Freja science mission”. *Space Science Reviews*, vol. 70, no. 3–4, pp. 405–419, November 1994. doi:10.1007/BF00756879.
- [84] Matsumoto, H., Nagano, I., Anderson, R. R., Kojima, H., Hashimoto, K., Tsutsui, M., Okada, T., Kimura, I., Omura, Y., and Okada, M. “Plasma wave observations with GEOTAIL spacecraft”. *Journal of Geomagnetism and Geoelectricity*, vol. 46, no. 1, pp. 59–95, January 1994.
- [85] Maynard, N. C., Bielecki, E. A., and Burdick, H. F. “Instrumentation for vector electric field measurements from DE-B”. *Space Science Instrumentation*, vol. 5, no. 4, pp. 523–534, December 1981.

- [86] Maynard, N. C. and Cauffman, D. P. "Double floating probe measurements on S<sup>3</sup>-A". *Journal of Geophysical Research*, vol. 78, no. 22, pp. 4745–4750, August 1973. doi:10.1029/JA078i022p04745.
- [87] Mizera, P. F., Fennell, J. F., Croley, Jr., D. R., and Gorney, D. J. "Charged particle distributions and electric field measurements from S3-3". *Journal of Geophysical Research–Space Physics*, vol. 86, no. A9, pp. 7566–7576, September 1981. doi:10.1029/JA086iA09p07566.
- [88] Mizera, P. F., Fennell, J. F., Croley, Jr., D. R., Vampola, A. L., Mozer, F. S., Torbert, R. B., Temerin, M., Lysak, R., Hudson, M., and Cattell, C. A. a. "The aurora inferred from S3-3 particles and fields". *Journal of Geophysical Research–Space Physics*, vol. 86, no. A4, pp. 2329–2339, April 1981. doi: 10.1029/JA086iA04p02329.
- [89] Morgan, M. G. and Laaspere, T. "An experiment to study whistlers and audio-frequency emissions with a receiving system on board the POGO S-50 satellite OGO-C/2 in conjunction with an existing network of ground-based observing stations". Contractor Report NASA-CR-97605, Thayer School of Engineer, Dartmouth College, Hanover, NH, February 1968.
- [90] Mozer, F. S., Cattell, C. A., Temerin, M., Torbert, R. B., von Glinski, S., Woldorff, M., and Wygant, J. "The DC and AC electric field, plasma density, plasma temperature, and field-aligned current experiments on the S3-3 satellite". *Journal of Geophysical Research*, vol. 84, no. A10, pp. 5875–5884, October 1979. doi:10.1029/JA084iA10p05875.
- [91] Nishida, A. "The GEOTAIL mission". *Geophysical Research Letters*, vol. 21, no. 25, pp. 2871–2873, December 1994. doi:10.1029/94GL01223.
- [92] O'Brien, B. J. "High-latitude geophysical studies with satellite Injun 3. 3, precipitation of electrons into the atmosphere". *Journal of Geophysical Research*, vol. 69, no. 1, pp. 13–43, January 1964. doi:10.1029/JZ069i001p00013.

- [93] O'Brien, B. J., Laughlin, C. D., and Gurnett, D. A. "High-latitude geophysical studies with satellite Injun 3. 1, description of the satellite". *Journal of Geophysical Research*, vol. 69, no. 1, pp. 1–12, January 1964. doi:10.1029/JZ069i001p00001.
- [94] Ogilvie, K. W. "Data from ISEE-1 for the IMS period". In *The IMS Source Book: Guide to the International Magnetospheric Study Data Analysis*, C. T. Russell and D. J. Southwood, eds., chap. 1, pp. 21–26. Washington, DC: American Geophysical Union, 1982. ISBN 0-87590-228-6.
- [95] Ogilvie, K. W., Durney, A., and von Rosenvinge, T. T. "Description of experimental investigations and instruments for the ISEE spacecraft". *IEEE Transactions on Geoscience Electronics*, vol. 16, no. 3, pp. 151–153, July 1978. doi:10.1109/TGE.1978.294535.
- [96] Oya, H., Morioka, A., Kobayashi, K., Iizima, M., Ono, T., Miyaoka, H., Okada, T., and Obara, T. "Plasma wave observation and sounder experiments (PWS) using the Akebono EXOS-D satellite—instrumentation and initial results including discovery of the high altitude equatorial plasma turbulence". *Journal of Geomagnetism and Geoelectricity*, vol. 42, no. 4, pp. 411–442, March 1990.
- [97] Oya, H. and Tsuruda, K. "Introduction to the Akebono (EXOS-D) satellite observations". *Journal of Geomagnetism and Geoelectricity*, vol. 42, no. 4, pp. 367–370, March 1990.
- [98] Pedersen, A., Cornilleau-Wehrlin, N., de La Porte, B., Roux, A., Bouabdellah, A., Décréau, P. M. E., Lefeuvre, F., Sene, F. X., Gurnett, D., Huff, R., Gustafsson, G., Holmgren, G., Woolliscroft, L., Alleyne, H. S. C., Thompson, J. A., and Davies, P. H. N. "The wave experiment consortium (WEC)". *Space Science Reviews*, vol. 79, no. 1–2, pp. 93–106, January 1997. doi:10.1023/A:1004927225495.
- [99] Perraut, S., Roux, A., Darrouzet, F., de Villedary, C., Mogilevsky, M., and Lefeuvre, F. "ULF wave measurements onboard the Interball auroral probe".



- Annales de Géophysique*, vol. 16, no. 9, pp. 1105–1116, September 1998. doi:10.1007/s005850050680.
- [100] Pfaff, R., Carlson, C., Watzin, J., Everett, D., and Gruner, T. “An overview of the Fast Auroral SnapshoT (FAST) satellite”. *Space Science Reviews*, vol. 98, no. 1–2, pp. 1–32, August 2001. doi:10.1023/A:1013187826070.
- [101] Reinisch, B. W., Haines, D. M., Bibl, K., Cheney, G., Galkin, I. A., Huang, X., Myers, S. H., Sales, G. S., Benson, R. F., Fung, S. F., Green, J. L., Boardsen, S., Taylor, W. W. L., Bougeret, J.-L., Manning, R., Meyer-Vernet, N., Moncuquet, M., Carpenter, D. L., Gallagher, D. L., and Reiff, P. “The radio plasma imager investigation on the IMAGE spacecraft”. *Space Science Reviews*, vol. 91, no. 1–2, pp. 319–359, January 2000. doi:10.1023/A:1005252602159.
- [102] Reznikov, A. E. and Shkliar, D. R. “Single VLF plane wave characteristics and plasma parameter determination by means of amplitude measurements on board a satellite”. *Annales de Géophysique*, vol. 38, no. 5, pp. 669–673, 1982.
- [103] Rorden, L. H., Orsak, L. E., Ficklin, B. P., and Stehle, R. H. “Instruments for the Stanford University/Stanford Research Institute VLF experiment (4917) on the EOGO satellite”. Supplemental Report NASA-CR-139258, Stanford Research Institute, Menlo Park, CA, May 1966.
- [104] S-300 Experimenters. “Measurements of electric and magnetic wave fields and of cold plasma parameters on-board GEOS-1. Preliminary results”. *Planetary and Space Science*, vol. 27, no. 4, pp. 317–339, April 1979. doi:10.1016/0032-0633(79)90110-7.
- [105] Scarabucci, R. R. “Satellite observations of equatorial phenomena and defocusing of VLF electromagnetic waves”. *Journal of Geophysical Research–Space Physics*, vol. 75, no. 1, pp. 69–84, January 1970. doi:10.1029/JA075i001p00069.
- [106] Scarf, F. L. “The AMPTE/CCE plasma wave investigation”. *IEEE*

- Transactions on Geoscience and Remote Sensing*, vol. 23, no. 3, pp. 250–252, May 1985. doi:10.1109/TGRS.1985.289522.
- [107] Scarf, F. L., Crook, G. M., Green, I. M., and Virobik, P. F. “Initial results of the Pioneer 8 VLF electric field experiment”. *Journal of Geophysical Research–Space Physics*, vol. 73, no. 21, pp. 6665–6686, November 1968. doi:10.1029/JA073i021p06665.
- [108] Scarf, F. L., Fredricks, R. W., Gurnett, D. A., and Smith, E. J. “The ISEE-C plasma wave investigation”. *IEEE Transactions on Geoscience Electronics*, vol. 16, no. 3, pp. 191–195, July 1978. doi:10.1109/TGE.1978.294544.
- [109] Scarf, F. L., Green, I. M., and Burgess, J. S. “The Pioneer 9 electric field experiment: Part 3, radial gradients and storm observations”. *Astrophysics and Space Science*, vol. 20, no. 2, pp. 499–507, February 1973. doi:10.1007/BF00642219.
- [110] Scarf, F. L., Green, I. M., and Crook, G. M. “The Pioneer 9 electric field experiment: Part 1, near Earth observations”. *Cosmic Electrodynamics*, vol. 1, no. 4, pp. 496–512, October 1971.
- [111] Scarf, F. L. and Gurnett, D. A. “A plasma wave investigation for the Voyager mission”. *Space Science Reviews*, vol. 21, no. 3, pp. 289–308, December 1977. doi:10.1007/BF00211543.
- [112] Scarf, F. L., Taylor, W. W. L., and Virobik, P. F. “The Pioneer Venus Orbiter plasma wave investigation”. *IEEE Transactions on Geoscience and Remote Sensing*, vol. GE-18, no. 1, pp. 36–38, January 1980. doi:10.1109/TGRS.1980.350257.
- [113] Shawhan, S. D., Gurnett, D. A., Odem, D. L., Helliwell, R. A., and Park, C. G. “The plasma wave and quasi-static electric field instrument (PWI) for Dynamics Explorer-A”. *Space Science Instrumentation*, vol. 5, no. 4, pp. 535–550, December 1981.

- [114] Singh, U. P. and Singh, D. P. “Intense low latitude VLF emissions observed aboard Ariel 4”. *Journal of Geophysical Research*, vol. 103, no. A9, pp. 20727–20734, September 1998. doi:10.1029/98JA00066.
- [115] Stone, R. G., Bougeret, J. L., Caldwell, J., Canu, P., de Conchy, Y., Cornilleau-Wehrlin, N., Desch, M. D., Fainberg, J., Goetz, K., and Goldstein, M. L. “The unified radio and plasma wave investigation”. *Astronomy and Astrophysics Supplement Series*, vol. 92, no. 2, pp. 291–316, January 1992.
- [116] Vampola, A. L. “Combined release and radiation effects satellite”. *Journal of Spacecraft and Rockets*, vol. 29, no. 4, p. 555, July 1992. doi:10.2514/3.55640.
- [117] von Rosenvinge, T. T. “Data from ISEE-3 for the IMS period”. In *The IMS Source Book: Guide to the International Magnetospheric Study Data Analysis*, C. T. Russell and D. J. Southwood, eds., chap. 1, pp. 1–9. Washington, DC: American Geophysical Union, 1982. ISBN 0-87590-228-6.
- [118] Walsh, D., Hayes, A. P., and Harrison, V. A. W. “Observations of radio frequency noise from Ariel 4”. *Proceedings of the Royal Society of London. Series A, Mathematical and Physical Sciences*, vol. 343, no. 1633, pp. 227–240, April 1975.
- [119] Ward, A. K., Bryant, D. A., Edwards, T., Parker, D. J., O’Hea, A., Patrick, T. J., Sheather, P. H., Barnsdale, K. P., and Cruise, A. M. “The AMPTE UKS spacecraft”. *IEEE Transactions on Geoscience and Remote Sensing*, vol. GE-23, no. 3, pp. 202–211, May 1985. doi:10.1109/TGRS.1985.289514.
- [120] Weighton, D. “A satellite-borne receiver for low-frequency radio astronomy.” *The Radio and Electronic Engineer*, vol. 36, no. 5, pp. 317–323, November 1968.
- [121] Wenzel, K. P., Marsden, R. G., Page, D. E., and Smith, E. J. “The ULYSSES mission”. *Astronomy and Astrophysics Supplement Series*, vol. 92, no. 2, pp. 207–219, January 1992.

- [122] Zelenyi, L. M. and Mularchik, T. M. “The INTERBALL project (sixth issue)”. *Cosmic Research*, vol. 40, no. 4, pp. 318–318, July 2002. doi:10.1023/A:1019886109791.

# Appendix C

## Radiological Physics

This appendix provides an overview of the physical mechanisms by which radiation engenders the transistor-level effects that form the subject of Chapter 2, beginning with the fundamentals of its solid-state interactions. The degree of interaction of energetic particles or photons with matter is a function of their composition, mass, velocity, and incidence rate, not to mention the material properties. In general, as fermions or bosons move through bulk matter in, say, the  $x$ -direction, the energy ( $E$ ) they lose through a variety of mechanisms, including scattering, is said to be deposited in the material at a rate of  $dE/dx$ , in MeV/cm [*Holmes-Siedle and Adams, 2002*, p.61].<sup>1</sup> Quantified as the absorbed dose, the total deposited energy found by integrating  $dE/dx$  over the path through the sample can fuel three basic processes within the target material, delineated by the relationship between the energy of the incident radiation and the strength of the bonding forces in the target atoms.

The weakest of these forces, the electromagnetic force which binds electrons to the nucleus, is subject to disruption by all types of radiation, but particularly charged particles (i.e., protons and electrons) and photons [*Tribble, 2003*, p.167]. In fact, it takes only a few eV (specifically,  $18 \pm 3$  eV in the case of SiO<sub>2</sub> [*Ausman and McLean,*

---

<sup>1</sup>Conventionally,  $-dE/dx$  describes the particle's energy loss per unit path length, known as the linear stopping power. However, it is assumed that all the energy lost by the particle takes part in material interactions, resulting in bond breaking and/or energization of sub-atomic particles near the particle track, as discussed in Section C.1.2.1. Hence,  $dE/dx$  is equal to the energy deposition into the target over the course of the particle trajectory.

1975]) to liberate an electron ( $e^-$ ) and, in its absence, leave behind an electron hole ( $h^+$ ) in the valence band. This formation of an  $e^- - h^+$  pair constitutes ionization damage and requires so little energy (an ionization energy of 17 eV in  $\text{SiO}_2$ )<sup>2</sup> as to render the incident radiation, aptly classified as ionizing radiation, the most common variety.

Disrupting the bonds between atoms in the target matter requires more energy than ionization, since the stronger electromagnetic forces between neighboring nuclei and electron clouds must be overcome in order to displace a lattice atom. However, as opposed to photons, electrons, or low-energy protons, more massive particles such as heavy ions, as well as energetic protons and neutrons [Tribble, 2003, p.167-168], can impart enough energy to create such a displacement by knocking an atom off its lattice site and into an interstitial (I) space, leaving behind a vacancy (V) and forming a Frenkel defect pair (V–I). In contrast to the previous case wherein free carriers are produced, the causative dose is provided by so-called non-ionizing radiation.

The third and least common phenomena, nuclear activation, requires collisions with incident particles of such high mass (or energy) as to overcome the strong nuclear force between the nucleons of a target atom, thereby injecting or removing a baryon and changing the atom's mass number. Being unstable, the resultant atom decays radioactively, rendering the target material 'activated' [Holmes-Siedle and Adams, 2002, p.61]. Since the secondary ionization and displacement damage that result from the dose imparted by the products of this decay are not significant compared to that of the primary dose [Holmes-Siedle and Adams, 2002; Tribble, 2003, p.167,p.101], the underlying physics of induced radioactivity are omitted here.<sup>3</sup> Rather, Section C.2

---

<sup>2</sup>Although the theoretical prediction of the  $e^- - h^+$  pair production energy in  $\text{SiO}_2$  offered by [Ausman and McLean, 1975], namely 18 eV, has been experimentally confirmed is generally cited, more precise measurements reported in [Benedetto and Boesch, 1986] put the value of the ionization energy at  $17 \pm 1$  eV.

<sup>3</sup>Despite its small contribution, nuclear activation is certainly part of the radiation environment in question. Indeed, energetic protons in the inner radiation belt, as well as GCRs [Holmes-Siedle and Adams, 2002, p.101], have sufficient energies to induce radioactivity both in the silicon die itself and the packaging materials, as has been previously demonstrated on a number of spacecraft [Dyer, 1980]. However, as noted in Chapter 2, GCRs are not considered in this treatment on account of their orbit-dependent variability (neither are neutrons, the degree of activation by which is strongly dependent on their spectrum). Furthermore, protons are only a third as efficient as GCRs in inducing radioactivity and can be more easily shielded [Holmes-Siedle and Adams, 2002, p.101]. Whereas the

and Section C.3 summarize the physical ramifications of the ionizing and non-ionizing components of the radiation, respectively, prefaced by the radiological definitions provided for consistency in Section C.1.

## C.1 Dosimetry

The science of measuring the absorbed dose delivered by a particular radiation exposure, known as dosimetry, provides a valuable framework for quantifying the radiation environment in the Van Allen belt, facilitating both the derivation of radiation specifications for SVEPRE and the validation of its performance at terrestrial facilities designed to simulate that environment. Since modern dosimetry reflects convergent evolution through both biological and aerospace lineages (the former as a product of classical science, the latter arising out of space and military applications),<sup>4</sup> it is useful to review the subset of the field that pertains to the ASIC in this work, with emphasis on the forms of radiation and energy deposition germane to latter.

### C.1.1 Radiation Types

As noted at the outset of Chapter 2, the dose absorbed by spacecraft electronics in the radiation belts is dominated by energetic particles. Historically, these were categorized in ascending order of penetrating capability as alpha, beta, and gamma radiation and, though these distinctions prove insufficient in light of modern

---

particle physics behind nuclear decay can be ignored on account of these factors, and whereas the ionizing and non-ionizing dose from its secondary radiation behave identically to that from the inducing radiation, and are therefore covered by Section C.2 and Section C.3, respectively, it should be noted that this radioactivity influences the choice of materials, particles, energies, and exposure times used during radiation testing (cf. Section 6.4.1).

<sup>4</sup>Although historically construed to cover only the interactions between ionizing radiation and organic materials, stemming from its radiobiological origins, dosimetry in this context is expanded to include both non-ionizing radiation and crystalline solids. In addition, aside from the cursory discussions of ion chambers in Section I.1.1.3 and Section I.2.1.2, a discussion of the many dosimetric techniques and dosimeter variations lies outside the scope of this work. For such review, especially as it pertains to radiation testing of ICs, a detailed treatment can be found in Chapters 12–16 of [Attix, 1986] and a comprehensive bibliography in Appendix D of [Holmes-Siedle and Adams, 2002].

understanding, they serve as a useful outline [[Tribble, 2003](#), p.153].

#### C.1.1.1 Alpha Particles

Usually ejected from the decay of nuclei with high mass number, alpha particles are helium nuclei ( $\text{He}^{2+}$ ) capable of strongly ionizing matter on account of their charge state and high energy, typically 5 MeV. A significant component of GCRs, their large mass(charge) results in frequent nuclear(Coulombic) interactions within the target material, yielding low penetration distances, typically 23  $\mu\text{m}$  in Si (at 5-MeV) [[Holmes-Siedle and Adams, 2002](#), p.3] and 70  $\mu\text{m}$  in human skin (at 7.5-MeV) [[Lide, 2008](#), p.16–46].

#### C.1.1.2 Beta Particles

Electrons and their antimatter counterparts (positrons) constitute beta particles, which are much less ionizing and have much deeper penetration ranges than alpha particles since they are significantly smaller (e.g., an energy of just 7-keV is required to penetrate the skin [[Lide, 2008](#), p.16–46] while a 1-MeV electron can travel nearly 1 cm in Al). Although the trapped energetic electrons prevalent through both of the radiation belts are of primary concern, electrons(positrons) can also be emitted during the beta decay of nuclei with excess neutrons(protons), and are often liberated with high velocity as secondary radiation during photonic interactions (cf. Section [C.2.1.1](#)).

On account of their low mass, energetic electrons are the most likely particles to approach relativistic speeds, as occurs above approximately 500 keV [[Tribble, 2003](#), p.173] where there are sometimes dubbed  $\delta$ -rays [[Attix, 1986](#), p.3]. When electrons of such an energy are accelerated or decelerated by the strong electric fields near atomic nuclei of the target material, they frequently must lose additional kinetic energy in order to conserve momentum through the deflection. This results in the emission of photons with a continuum of energies in the X-ray portion of the spectrum, known as Bremsstrahlung or ‘braking radiation.’ Since Bremsstrahlung production is proportional to  $Z^2$  (where  $Z$  is the atomic number of the target material), it subverts the utility of dense shielding materials in the radiation belts by generating deeply



penetrating secondary photons that, as evident in the next section, are often more damaging than the primary beta particles [*Holmes-Siedle and Adams, 2002*, p.395].

### C.1.1.3 Gamma Rays

The most penetrating form of radiation consists of massless, high-energy photons often interchangeably identified as gamma rays ( $\gamma$ -rays) or X-rays.<sup>5</sup> Unaffected by electrostatic forces, a beam of such photons penetrates the target in a straight line until impinging upon a nucleus, where one of three types of interactions may occur, depending upon the photon energy (cf. Section C.2.1.1).

Each of these mechanisms ( $k=1, 2, 3$ ) absorbs a fraction of the number of incident photons  $n_p$  with a probability governed by the effective interaction cross-section for its photon energy threshold,  $\sigma_k$ , and the target number density,  $N$ . The sum of these cross-sections,  $\sum \sigma_k = \sigma_t$ , determines the photon absorption probability  $dn_p/n_p$  at a particular depth,  $x$ , according to [*Tribble, 2003*, p.173]:

$$\frac{dn_p}{n_p} = -N\sigma_t x \quad (\text{C.1})$$

Thus, the beam intensity,  $I_p$ , as a function of target depth  $x$  and surface intensity  $I_{po}$  can be expressed by integrating (C.1) to arrive at

$$I_p = I_{po} e^{-N\sigma_t x} = I_{po} e^{-\mu_m \rho x} \quad (\text{C.2})$$

where  $\rho$  is the target mass density,  $\mu_m = N\sigma_t/\rho = \mu/\rho$  is the so-called mass attenuation coefficient [*Tascione, 1994*, p.11], and  $\mu = N\sigma_t$  is the mean free path—the average

---

<sup>5</sup>The ambiguity between these terms arises from the practical convergence of neighboring segments of the electromagnetic spectrum historically considered distinct. Initially,  $\gamma$ -rays referred to the higher energy band with wavelengths of  $10^{-14}$ – $10^{-11}$  m ( $3 \times 10^{19}$ – $3 \times 10^{22}$  Hz) and energies of at least 0.1 MeV [*Lide, 2008*, p.2–46]. Photons in the somewhat arbitrary keV range [*Tribble, 2003*, p.173], covering  $10^{-11}$ – $10^{-8}$  m ( $3 \times 10^{16}$ – $3 \times 10^{19}$  Hz) were known as X-rays. But, with improved X-ray sources capable of generating ‘hard’ X-rays up to 510 keV, from  $3 \times 10^{-12}$ – $10^{-10}$  m ( $318 \times 10^3$ – $10^{20}$  Hz), and the discovery of ‘soft’  $\gamma$ -ray sources in the same range, the distinction became blurred [*Lide, 2008*, p.10–240]. Thus, the commonly accepted modern definitions distinguish the rays by source, with X-rays resulting from electronic collisions, and  $\gamma$ -rays from nuclear interactions [*Holmes-Siedle and Adams, 2002*, p.3].

distance a photon travels before it first interaction with the target medium [Attix, 1986, p.187]. Note that the beam intensity decays exponentially, but can never be completely shielded by a finite thickness of material [Tribble, 2003, p.175].

#### C.1.1.4 Nucleons and heavy ions

Although they are not products of the radioactive decay described previously, energetic baryons comprise a significant fraction of the trapped population in the Van Allen belt (cf. Section 1.1.1) and are a primary source of both ionizing and non-ionizing radiation hazards. With a mass approximately 1836 times that of an electron [Lide, 2008, p.1], a proton does not have nearly the same penetration range as an electron of the same energy, though it tends to travel in a straight line, rather than deflect through large angles with each bounce, since its momentum is largely retained during both electronic and nuclear collisions [Tribble, 2003, p.171]. This phenomenon is evidenced by the aluminum shielding data presented in Figure C.1, which provides the range for both particles in units of mass thickness that have been normalized to eliminate the material dependence ( $\text{g}/\text{cm}^{-2}$ ).<sup>6</sup> With a range of only tens of microns in Al, a proton comes to rest nearly three orders of magnitude more shallow than

---

<sup>6</sup>As with most radiological quantities, *range* has both a precise definition and a generally accepted meaning. The agreement between these depends upon radiation type and energy. For a large population of charged particles (neutrons are excluded since their low interaction probability invalidates a stochastic treatment [Attix, 1986, p.160]), the *range* is formally defined as the expected value of the total path length traversed until coming to rest (i.e., losing all kinetic energy save that of thermal motion) [Attix, 1986, p.180]; this path can be quite circuitous, especially for electrons. A related term, the *projected range*, considers only the extremes of the path and is defined as the expected value of the farthest depth of penetration in the initial direction [Attix, 1986, p.180]. Due to backscattering, it is possible that the average resting point of the particle is actually shallower than its projected range (again, especially for electrons). For a homogeneous photon beam, the project range computed from the distribution in (C.2) is equivalent to its mean free path,  $\mu$ , which is alternatively known as the relaxation length since it describes the depth at which  $1/e$  of the incident photons are stopped [Attix, 1986, p.187].

In light of these definitions, the distinction between range and projected range can roughly be construed as one of total path length versus ‘crow-flight’ penetration distance. For heavier particles, whose elastic deflections are minor, these two quantities approach one another (with the former only 3% larger for protons [Attix, 1986, p.184]) and are often used interchangeably. For electrons, however, the range typically exceeds the projected range on account of their meandering. Additionally, their larger span of angular displacements results in a broader range of penetration depths, so that the maximum of the penetration depth distribution, the *maximum range*, can far exceed the projected range, leading to so-called range straggling [Holmes-Siedle and Adams, 2002, p.387].

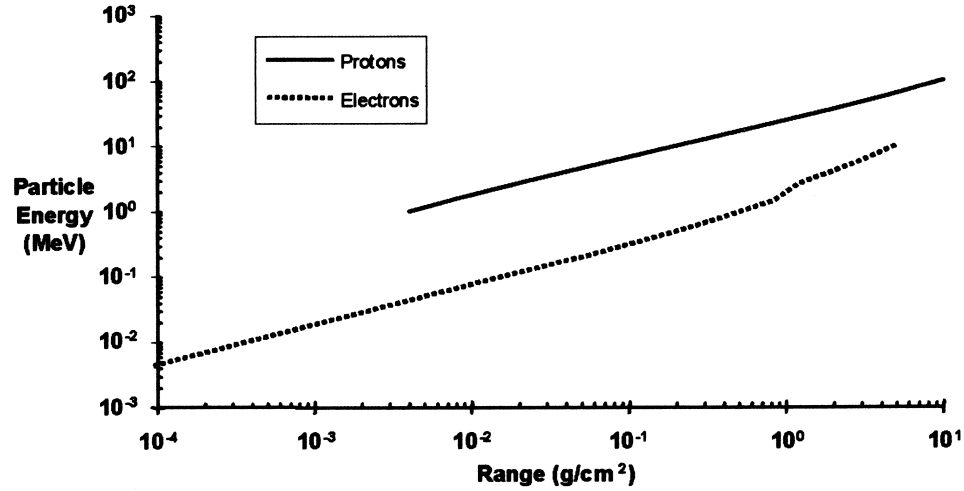


Figure C.1: Range of protons and electrons in aluminum. Normalized units eliminate dependence on  $\rho_{\text{Al}}$ . Reproduced *in toto* from [Tribble, 2003, p.172]

an electron [Holmes-Siedle and Adams, 2002, p.3]. This discrepancy is even more pronounced for heavy ions, which are subject to similar physics.

Lacking electric charge, neutrons are the most penetrating nucleon since they are not subject to electronic interactions. Unlike charged particles and photons, which are readily absorbed by high  $Z$  materials, neutron capture, which results in the release of  $\gamma$ -rays, is most efficient in low-density, hydrogenous materials [Holmes-Siedle and Adams, 2002, p.3], though it depends strongly upon the type of target-specific nuclei involved [Holmes-Siedle and Adams, 2002, p.388]. Atoms such as hydrogen, are preferable because their mass is closest to that of a neutron, thereby maximizing the kinetic energy loss per collision [Messenger and Ash, 1992, p.207]. For thermal ( $< 1$  eV) neutrons, water [Holmes-Siedle and Adams, 2002, p.3] and cadmium [Tribble, 2003, p.176] provide good shielding via a large elastic scattering cross-section, whereas for fast ( $> 100$  keV) neutrons, paraffin [Tribble, 2003, p.176] and iron, which favor inelastic scattering, are commonly employed.

---

In this and all subsequent usages, the term *range* shall actually denote *projected range* and thus is synonymous with mean penetration depth, as is the convention [Holmes-Siedle and Adams, 2002, p.387].

### C.1.2 Radiation Metrics

When a target is illuminated with radiation for a finite period of time, the number of particles that pass through a unit cross-sectional area,  $\phi$ , known as the fluence (in particles/cm<sup>2</sup>), can be calculated by integrating the fluence rate,  $\Phi$ , or flux (in particles/cm<sup>2</sup>/s) over the exposure duration (in s) [*Holmes-Siedle and Adams, 2002*, p.4]. The total energy lost by an incident particle per unit path length traveled in the target,  $-dE/dx$ , is known as the linear stopping power of the material and is given by:<sup>7,8</sup>

$$\mathcal{S} = -\frac{dE}{dx} = N\sigma_{\text{stop}} \quad (\text{C.3})$$

where the stopping cross-section  $\sigma_{\text{stop}}$  (in MeV-cm<sup>2</sup>) gives the probability of removing a given amount of energy from the particle in a given element of cross-sectional area [*Tribble, 2003*, p.171]. Note that, paradoxically, the linear stopping power is typically associated with the target material, even though it describes only the energy lost by the incident particle, not that absorbed.

#### C.1.2.1 Linear Energy Transfer

As discussed at the outset of this appendix, the particle's lost energy fuels three different processes,<sup>9</sup> making the total linear stopping power the sum of: electronic stopping power (due to inelastic collisions with electrons), nuclear stopping power (due to elastic nuclear collisions), and activation stopping power (due to inelastic nuclear collisions that induce radioactivity). Denoting these with the subscripts  $e$ ,  $n$ ,

---

<sup>7</sup>Although *stopping power* typically applies only to charged particle radiation, the generalized notion of stopping power for all particles is invoked here.

<sup>8</sup>See Footnote 1 for further clarification

<sup>9</sup>Often a fourth term, radiative stopping power, is employed to account for Bremsstrahlung and Cherenkov radiation emitted by high-energy electrons during nuclear interactions. For the purposes of this treatment, it is sufficient to lump this behavior into the activation stopping power, since it results in the production of photons through inelastic processes in the vicinity of target nuclei.

and  $a$ , respectively, (C.3) can be expanded as:

$$\begin{aligned}
 \mathcal{S} &= \mathcal{S}_e + \mathcal{S}_n + \mathcal{S}_a \\
 &= -\frac{dE_e}{dx} - \frac{dE_n}{dx} - \frac{dE_a}{dx} \\
 &= N(\sigma_{\text{stop},e} + \sigma_{\text{stop},n} + \sigma_{\text{stop},a})
 \end{aligned} \tag{C.4}$$

Of the energy lost through  $\mathcal{S}_e$ , that which is subsequently deposited in the material is deemed the linear energy transfer (LET). It is represented by  $\mathcal{L}_e$  and quantifies the ionizing component of the incident radiation [Holmes-Siedle and Adams, 2002; Tribble, 2003, p.107,p.177].<sup>10</sup> By analogy,  $\mathcal{L}_n$  captures the linear transfer of non-ionizing energy to the material, dubbed the non-ionizing energy loss (NIEL) [Holmes-Siedle and Adams, 2002; Tribble, 2003, p.72,p.177].<sup>11</sup> In both cases, the lost and deposited energies per unit length can be normalized by the target material density, giving rise to the mass stopping power and mass linear energy transfer, which are identified with an additional  $m$  subscript and related as:

$$\mathcal{L}_{m,e} = -\mathcal{S}_{m,e} = \frac{1}{\rho} \frac{dE_e}{dx} = \frac{N}{\rho} \sigma_{\text{stop},e} = \frac{\mu_e}{\rho} = \mu_{m,e} \tag{C.5a}$$

$$\mathcal{L}_{m,n} = -\mathcal{S}_{m,n} = \frac{1}{\rho} \frac{dE_n}{dx} = \frac{N}{\rho} \sigma_{\text{stop},n} = \frac{\mu_n}{\rho} = \mu_{m,n} \tag{C.5b}$$

Note that in (C.5a) and (C.5b), mass stopping coefficients  $\mu_{m,e}$  and  $\mu_{m,n}$  have been defined by analogy with the mass absorption coefficient for photons,<sup>12</sup>  $\mu_m$  in (C.2),

<sup>10</sup>LET is a measure of localized ionization, so it technically ignores those freed electrons with sufficient kinetic energy to depart from the vicinity of the ionizing track, that is,  $\delta$ -rays with  $E(\delta) \geq E_\Delta$ , for some  $E_\Delta$ . The ionizing energy actually deposited in the material is then given by  $E_e - E(\delta)$ , so that  $\mathcal{L}_e < -\mathcal{S}_e$ . However, as discussed in Footnote 1, it is assumed in this work that  $E_\Delta \rightarrow \infty$ , so that  $\mathcal{L}_e$  and  $-\mathcal{S}_e$  can be considered equivalent, which is akin to equating the LET with the unrestricted, rather than restricted, stopping power [ICRU, 1998, p.11].

<sup>11</sup>The use of the term *loss* is an unfortunate historical artifact, since NIEL describes the deposited energy, and therefore  $\mathcal{L}_n$  is related to  $\mathcal{S}_n$  as  $\mathcal{L}_e$  is to  $\mathcal{S}_e$ . Incidentally, the analogy can be extended to consider the linear transfer of activation energy,  $\mathcal{L}_a$ , but, as justified in the introduction to Section C.1, this term is omitted from further consideration.

<sup>12</sup>Just as for an incident particle, where  $\mathcal{L}$  represents the fraction of the energy lost via  $\mathcal{S}$  that is locally deposited in the target, a similar distinction is made for photons. In that case, the mass energy transfer coefficient  $\mu_{m,\text{tr}} = \mu_{\text{tr}}/\rho$  describes the fraction of the energy lost through attenuation

though they are expressed in units of MeV-cm<sup>2</sup>/mg.<sup>13</sup>

### C.1.2.2 Absorbed Dose

Integrating the total per-particle  $\mathcal{L}$  over the fluence yields the total absorbed dose,  $D$ , according to:

$$D = \int_{\phi} \mathcal{L}_e + \mathcal{L}_n \quad (\text{C.6})$$

Although the SI unit of *gray* (1 Gy = 1 J/kg) has been assigned to this quantity, publications on radiation effects have historically employed the legacy unit of *rad*, which is achieved when 100 ergs have been deposited in a gram of material (1 Rad = 0.01 Gy), so the rad is adopted here as well [*Holmes-Siedle and Adams, 2002; Tribble, 2003*, p.5,p.176]. Furthermore, since the energy transferred by a given particle flux varies with the underlying material, it is common to explicitly state the absorbing material for a given dose, as in rad(Si) and rad(SiO<sub>2</sub>) which be frequently employed below.<sup>14</sup>

Often, the two terms of the integrand in (C.6) are considered separately, such that the total ionizing dose (TID) and total displacement dose (TDD), resulting from the deposition of energy over the course of exposure to ionizing ( $\phi_I$ ) and non-ionizing ( $\phi_D$ ) fluences, respectively, are given by:

$$\text{TID} = \int_{\phi_I} \mathcal{L}_e = \int_{\phi_I} \frac{1}{\rho} \frac{dE_e}{dx} \quad (\text{C.7a})$$

$$\text{TDD} = \int_{\phi_D} \mathcal{L}_n = \int_{\phi_D} \frac{1}{\rho} \frac{dE_n}{dx} \quad (\text{C.7b})$$

It also proves useful to measure the rate at which a given dose is applied to the target,

---

via  $\mu_m$  that is transferred to energetic charged particles (i.e., produces ionization). If those liberated charge carriers go on to participate in secondary Coulomb collisions (cf. Section C.2.1.1), which is the case for all but  $\delta$ -rays,  $\mu_{m,\text{tr}}$  is referred to as the mass energy absorption coefficient,  $\mu_{m,\text{en}} = \mu_{\text{en}}/\rho$  [*Attix, 1986*, p.22–25].

<sup>13</sup>In keeping with the conventions of the literature on radiation effects, which employ these units liberally, LET should be taken to imply density-independent LET throughout this document. Accordingly, the explicit  $m$  subscripts, are hereafter dropped.

<sup>14</sup>If not explicitly stated, one should assume that *rad* implicitly refers to *rad(Si)* throughout this document.

$dD/dt$ , which is known as the dose rate and obtained simply replacing the integration over fluence in (C.6) with one over flux:

$$\frac{dD}{dt} = \int_{\Phi} \mathcal{L}_e + \mathcal{L}_n \quad (\text{C.8})$$

### C.1.2.3 Equivalent Dose

Although LET(NIEL), TID(TDD), and dose rate suffice herein to parameterize the effects of all types ionizing(non-ionizing) radiation on electronic circuits, radiobiologists have observed that radiation effects on organic matter depend not only on the deposited energy but also the particle type.

Initially, this particle-dependent damage factor was captured by assigning to each a so-called quality factor,  $Q_{\phi}$ , that is proportional to its LET; this accounts for the density of ionization along its track, which is critical to the biological response, yet subsumed by the integral of (C.6) [ICRP, 1991c, p.5]. The product  $H_{\phi} = Q_{\phi}D$  defines the equivalent dose,  $H_{\phi}$ , for a particular dose  $D$  comprised of particles with quality  $Q_{\phi}$  [Lide, 2008, p.1–39].

Whereas this  $Q_{\phi}$ -weighted equivalent dose is computed at each point, the biological impact is best assessed by considering the average dose absorbed over an entire tissue. Thus, recent standards adopt the use of unitless radiation weighting factors,  $w_R$ , for each type of radiation. Rather than being derived from  $Q_{\phi}$ , such factors are proportional to a quantity known as the relative biological effectiveness (RBE), which describes the number of grays(rads) of 200-keV photonic radiation that cause the same biological damage as 1 Gy(1 Rad) of the particular radiation type [Tascione, 1994, p.140]. Reflecting differences in the observed tissue damage from an average dose, rather than differences in the ionizing track density at a point, these RBE-derived weighting factors can be used in place of  $Q_{\phi}$  to better represent the equivalent dose to tissue,  $H_T$ , according to [ICRP, 1991c, p.5]:

$$H_T = \sum_k w_{R,k} D_k \quad (\text{C.9})$$

where the sum is performed over all  $k$  types of radiation to which the target is exposed.

Radiation type	Energy $E_i$ [MeV]	Weighting factor $w_R$ [none]
Photons	All	1
$e^-$ , muons	All	1
$H^+$ , charged pions	$> 2$	5
$He^{2+}$ , heavy ions, fission fragments	All	20
Neutrons	$< 0.01$	5
	0.01–0.1	10
	0.1–2	20
	2–20	10
	20	5

Table C.1: Latest radiation weighting factors recommended by International Commission on Radiological Protection (ICRP) (cf. Footnote 15) [*ICRP*, 2007].

Although it is simply a weighted absorbed dose possessing the same fundamental units of J/kg (ergs/g) as  $D$ , the equivalent dose  $H_T$  is expressed in distinct units of Sievert(Roentgen equivalent man), abbreviated Sv(rem), that connote the biological rather than physical aspects of the absorbed dose given in Gy(Rad).

The latest radiation weighting factors, summarized in Table C.1,<sup>15</sup> indicate that particle radiation can be far more harmful than photonic radiation, particularly in the case of neutrons and alpha particles. The harm suffered manifests either as deterministic effects (or tissue reactions), wherein there is enough irreparable cell damage to prevent replication and/or impair tissue function, or stochastic effects, wherein self-repair allows the modified cell to survive and reproduce, but with increased probability of manifesting and/or transmitting a cancer [*Lide*, 2008, p.69]. While the stochastic effects are linear with average dose,<sup>16</sup> hence the proportionality

<sup>15</sup>In the most recent set of ICRP recommendations [*ICRP*, 2007], the neutron  $w_R$  is expressed as a continuous function of energy [*Wrixon*, 2008, p.163], rather than the piecewise approximation used previously [*ICRP*, 1991c, p.7] and invoked here for simplicity.

<sup>16</sup>The dose dependence of stochastic effects can be further quantified by invoking a second level of dose weighting, which arrives at an effective dose for the whole body,  $H_B$ , that is obtained from



Application	Equivalent dose limits	
	Occupational [mSv/yr]	Public [mSv/yr]
Whole body (total effective)	20 <sup>a</sup>	1 <sup>b</sup>
Lens of the eye	150	15
Skin	500	50
Hands and feet	500	n/a

<sup>a</sup> Five year average, with  $\leq 50$  mSv in any one year

<sup>b</sup> Five year average, with higher annual maximum in select circumstances

Table C.2: Latest equivalent dose limits recommended by ICRP for occupational and public settings; radiation workers fall into the former category [ICRP, 1991e, p.46].

of (C.9), deterministic effects are non-linear, exhibiting a threshold dose below which their probability is zero, but above which damage is extensive enough to guarantee cell death/sterility and severity continues to increase with dose [ICRP, 1991a, p.15].

Thus, radiation safety efforts seek to minimize the incidence of stochastic effects, but prevent deterministic effects through the establishment of suitable thresholds [ICRP, 1991b, p.25]; an example of these limits is found in Table C.2. According to Table C.3, about 100 rem causes the immediate onset of radiation sickness [Tascione, 1994, p.140], but the average person experiences just 0.620 rem/yr, with 50% from natural background sources and 48% from medical technologies [NCRP, 2009].

$H_B = \sum_j w_{T,j} H_{T,j}$ , where the summation is carried out over each tissue/organ, whose equivalent dose is scaled by a tissue weighting factor  $w_T$  [ICRP, 1991c, p.6–7]. These  $w_T$ , which are normalized so as to sum to one over all organs, are larger for rapidly reproducing cells, such as gonads and bone marrow (see [ICRP, 1991d, p.68]), where mutations are likely to survive. It is worth noting that both  $w_R$  and  $w_T$  pertain only to the probability of stochastic effects, so  $H_B$  and  $H_T$  are only valid below the deterministic threshold, where the dose-proportionality holds [ICRP, 1991c, p.9]. Nevertheless, the deterministic thresholds themselves can be expressed in terms of  $H_T$  with the recognition that for  $w_R > 1$ , deterministic RBEs are lower than their stochastic counterparts, rendering the cut-offs conservative [ICRP, 1991a, p.15].

Radiation dose		Probable effect in population
$D$ [rad]	$H_B^a$ [rem]	
0–50	0–50	No obvious effects (minor blood changes)
80–120	50–100	5%–10% chance of radiation sickness (nausea and vomiting)
130–170	50–100	25% chance of radiation sickness (nausea and vomiting)
180–220	150–200	50% chance of radiation sickness (nausea and vomiting)
270–330	200–350	~100% chance of radiation sickness 20% chance of death
400–500	350–550	Universal radiation sickness 50% chance of death in 1 month
550–750	550–750	Nausea within 4 hours; few survivors
1000	1000	Nausea within 1–2 hours; no survivors

<sup>a</sup> Total (whole body) effective dose (cf. Footnote 16)

Table C.3: Hazardous effects of radiation doses for sample population, as estimated by [[Tribble, 2003](#), p.187] and [[Tascione, 1994](#), p.141].

## C.2 Ionizing Radiation

Second only to that of organic matter in terms of severity [*Tribble*, 2003, p.179], the susceptibility of electronic materials to ionizing radiation damage merits enough study to permit a thorough understanding of the underlying physics. This section summarizes those principles, focusing almost exclusively on the insulating SiO<sub>2</sub> film at the heart of the MOS transistor, which is exceptionally vulnerable and, thus, critical to the front-end ASIC design.<sup>17</sup> Adapting the organization of [*McLean et al.*, 1989], the following sub-sections address the stages of ionization damage chronologically, from the radiation-induced generation of free carriers to their eventual trapping near the Si-SiO<sub>2</sub> interface, according to the numbering of Figure C.2.

### C.2.1 Generation

In SiO<sub>2</sub>, the energy required for the generation of  $e^- - h^+$  pairs that characterizes ionizing radiation is relatively low, such that it accounts for the majority of  $D$  (i.e.,  $TID \gg TDD$ ) and can be deposited by every type of radiation cataloged in Section C.1.1 [*Holmes-Siedle and Adams*, 2002, p.85]. In fact, assuming an ionization energy of 17 eV (cf. Footnote 2), 1 rad(Si) of TID can generate  $K_g = 8.12 \times 10^{12}$  pairs/cm<sup>3</sup> [*Srouf and McGarrity*, 1988, p.1453]. However, the specific mechanism by which electrons are promoted from the valence band to the conduction band depends upon the type and energy of the incident radiation, making it convenient to delineate between photonic and particle radiation.

#### C.2.1.1 Photonic Mechanisms

The ionizing interactions of light and matter that pertain to primary and, more commonly, secondary radiation via X-rays and  $\gamma$ -rays, vary with both photonic quantum energy  $E_p$  and target  $Z$ . This  $E_p$ - $Z$  space can be subdivided into

---

<sup>17</sup>For a clear and comprehensive treatment of the solid-state physics which govern the TID effects on MOS oxides, the canonical reference texts by *Ma and Dressendorfer* [1989] and *Oldham* [1999] are strongly recommended.

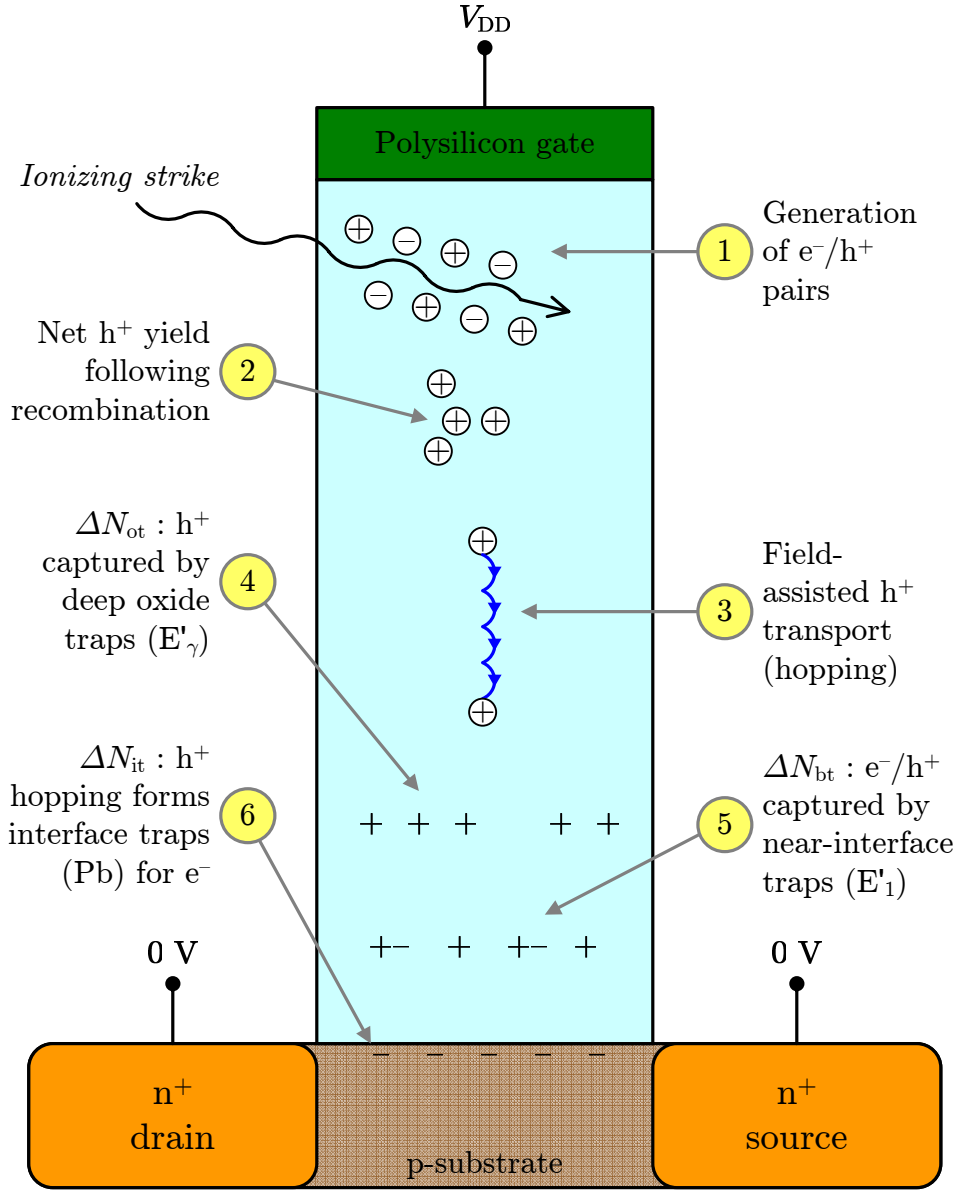


Figure C.2: Key steps in radiation-induced oxide damage, demonstrated for nMOSFET under positive gate bias (dimensions exaggerated for clarity). Section C.2 explains each step in detail. After [McLean *et al.*, 1989, p.89]

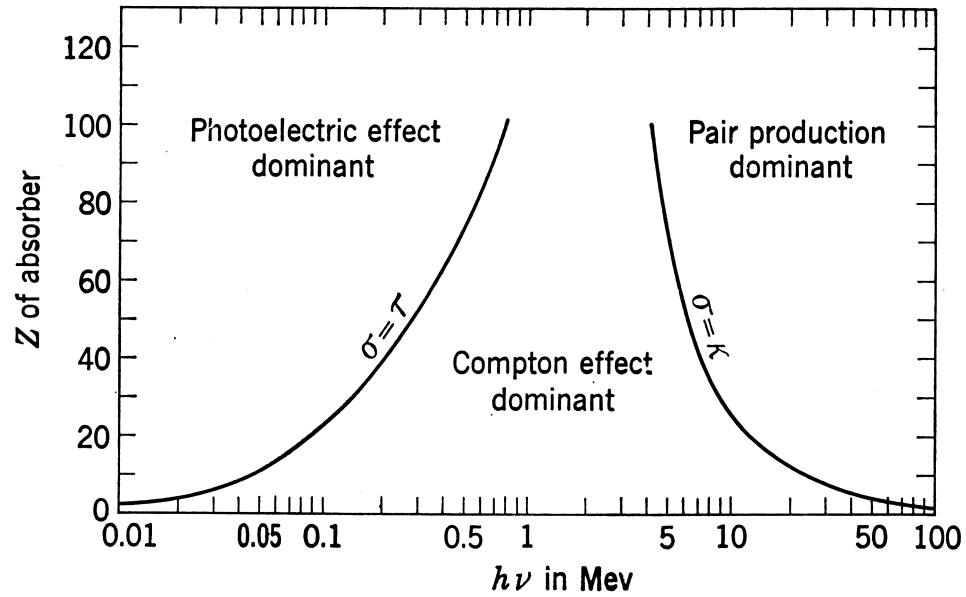


Figure C.3: Relative strength of photoionization mechanisms as a function of photon energy ( $E_p$ ) and target density ( $Z$ ). Along curves, mass transfer coefficients of two processes are equal. Reproduced *in toto* from [Evans, 1955, p.712]

three regions, as shown in Figure C.3,<sup>18</sup> each dominated by a different interaction mechanism, but with the total mass energy transfer coefficient,  $\mu_{m,tr}$ , given by the sum of those for each process.

**Photoelectric Effect:** Soft X-ray ( $< 0.5$  MeV [Tribble, 2003, p.174]) photons participate in the photoelectric effect, whereby they penetrate the innermost electron orbitals (K-shell) of the target atom and free a bound electron [Srouer and McGarrity, 1988, p.1444]. This interaction is more probable for lower energy photons, provided they have enough energy to free a K-shell electron, and for a higher density of target nuclei; below 0.1 MeV, the photoelectric

<sup>18</sup>Although there are many other photon scattering mechanisms, such as photonuclear interactions (namely,  $(\gamma, p)$  and  $(\gamma, n)$  events) [Attix, 1986, p.154] and the Rayleigh scattering responsible for the color of the sky due to its  $1/\lambda^4$  dependence [Tascione, 1994, p.11], these do not produce appreciable, if any, conduction-band electrons and so are not considered here.

contribution to the mass energy transfer coefficient goes as [[Attix, 1986](#), p.140]:

$$\mu_{\text{m,tr}}|_{\text{photo}} = \left( \frac{Z}{E_p} \right)^3 \quad (\text{C.10})$$

The energy of the photon in excess of that required overcome the electron-nucleus bond is transferred to the electron in the form of kinetic energy, such that the former is annihilated—with zero rest-mass, a photon is annihilated once it loses all its energy [[Tascione, 1994](#), p.11]. In a transition that emits a lower wavelength, visible photon,<sup>19</sup> an electron from a higher energy level (L-shell) then drops down to take the place of that now in the conduction band. The optical photon can then carry out a cascade of photoelectric reactions, terminating when photon energies are sufficient to excite outer shell electrons but no longer can liberate those in inner orbitals [[Messenger and Ash, 1992](#), p.269–270].

**Compton Scattering:** Hard X-rays and soft  $\gamma$ -rays with higher energies (0.5–5 MeV [[Tribble, 2003](#), p.174]) can participate in Compton scattering, wherein a free or loosely-bound electron scatters the incident photon off course, leaving it with a fraction of its original momentum that depends upon its energy and angle of incidence [[Tascione, 1994](#), p.11].<sup>20</sup> In this elastic collision, the electron receives additional energy sufficient to eject it from the atom, thereby ionizing it [[Messenger and Ash, 1992](#), p.269–270]. Since the presence of the nucleus is not required to conserve momentum or account for any electron binding energy

---

<sup>19</sup>It is also possible, though far less common, for this to result in the ejection of one or more additional, so-called Auger electrons rather than a fluorescent photon. In this case, the energy released by the de-exciting L-shell electron unbinds (and provides kinetic energy to) an electron from a higher orbital, say M. Electrons from even higher valences recursively drop down to fill the L and M orbital vacancies until the only remaining vacancies are in the outermost shells, where they are neutralized by conduction band electrons [[Attix, 1986](#), p.142–144]. The Auger effect, which only occurs when the energy difference between the initial and final states of the first de-excited electron is sufficient large, is nearly the inverse of the Auger recombination described in Section C.3.4 [[Messenger and Ash, 1992](#), p.:270].

<sup>20</sup>First-order treatments of the Compton effect assume an unbound, stationary electron, which is obviously unphysical given that all atomic electrons are both bound and in motion. But, the approximation proves well-justified [[Attix, 1986](#), p.125].

in this formulation, the mass energy transfer coefficient for the Compton effect is independent of  $Z$  for  $E_p > 0.1$  MeV, following [Attix, 1986, p.132–133]:

$$\mu_{m, \text{tr}}|_{\text{comp}} = \frac{1}{E_p} \quad (\text{C.11})$$

**Pair Production:**  $\gamma$ -rays of the highest energies are also capable of pair production, whereby a photon spontaneously decomposes into an unbound electron-positron pair. Upon its annihilation, the photon's energy is converted into matter in the form of the two beta particles so it must possess at least  $2m_e c^2 = 1.022$  MeV [Tribble, 2003, p.174], with any excess appearing as the kinetic energy of the pair. In order to conserve momentum given that a photon is massless, this pair creation, much as for Bremsstrahlung, must occur in the presence of an atomic nucleus that absorbs a small amount of recoil energy [Messenger and Ash, 1992, p.270];<sup>21</sup> the heavier the nucleus, the more probably the phenomenon [Tascione, 1994, p.11]. This latter fact, along with the sub-linear energy dependence for  $E_p > 1.022$  MeV is reflected in the proportionality of the mass energy transfer coefficient given by [Attix, 1986, p.149–150]:

$$\mu_{m, \text{tr}}|_{\text{pair}} \propto Z \log E_p \quad (\text{C.12})$$

In Si ( $Z = 14$ ) and SiO<sub>2</sub> ( $\langle Z \rangle = 15$ ), the Compton effects dominates for photons between 50 keV and 20 MeV, while the photoelectric effect(pair production) is of primary significance below(above) this range [Srouer and McGarrity, 1988, p.1444], as evidenced in Figure C.3.

### C.2.1.2 Particle Mechanisms

An incident particle can participate in both elastic and inelastic collisions with the target atoms, with charged particles undergoing so many such low-energy collisions

---

<sup>21</sup>Although much less likely, an atomically bound electron can also serve as the third particle necessary for momentum conservation, in which case it acquires enough kinetic energy to be ejected, doubling the degree of ionization [Attix, 1986, p.146].

as to be almost continuously retarded [Attix, 1986, p.160]. Although Rutherford (or Coulomb) scattering, in which energy- and momentum-conserving elastic Coulomb collisions deflect the charged particle, do occur (and are responsible for NIEL as discussed in Section C.3) only inelastic Coulomb collisions, in which kinetic energy drives ionization [Tascione, 1994, p.11], contribute to its LET. Soft(hard) Coulombic interactions occur when an incident particle passes beyond(within) the atomic radius of a target atom and account for roughly half of the total LET because each results in minor(significant) energy loss, but is highly(much less) probable [Attix, 1986, p.161–162]. Collisional ionization predominates for electrons [Holmes-Siedle and Adams, 2002, p.391] but becomes less prevalent for protons, which transfer more momentum to the target atoms as represented by their higher NIEL, and even less significant for heavy ions.

However, these more massive particles also participate in nuclear collisions that, just as for Coulomb collisions, may be either elastic or inelastic [Srouf and McGarrity, 1988, p.1444]. Once again, the elastic scattering process primarily contributes to NIEL (cf. Section C.3), although such nuclear collisions may be of sufficient energy that the atomic recoil produces subsequent ionization [Messenger and Ash, 1992, p.203]. For protons, heavy ions, and neutrons, the latter of which cannot take partake in Coulomb collisions, inelastic nuclear collisions induce ionization through indirect mechanisms, such as: exciting atomic nuclei, which emit ionizing  $\gamma$ -rays when they de-excite [Tribble, 2003, p.176]; and neutron capture or transmutation [Srouf and McGarrity, 1988, p.1444], in which a neutron ( $n$ ) or proton ( $p$ ) is absorbed by a nuclear reaction that converts the target into another element and, in the process, releases either an alpha particle (in the  $(n,\alpha)$  and  $(p,\alpha)$  reactions) or proton (in the  $(n,p)$  and  $(p,p')$  reactions), which then goes on to ionize other atoms [Messenger and Ash, 1992, p.203].

### C.2.2 Recombination

For each ionizing mechanism,  $e^- - h^+$  pairs generated in the  $\text{SiO}_2$  tend to recombine with one another on time scales that depend on both the density of the ionizing track



created by the incident particle and relative mobility of the electron and holes in the oxide. If recombination is to occur in modern oxides, the latter demands that it happen within 1 ps of generation [McLean *et al.*, 1989, p.91], since all the electrons are swept out by any imposed electric field in this interval while the holes, whose mobility is anywhere from  $2 \times 10^5$ – $4 \times 10^{12}$  slower [Hughes *et al.*, 1975, p.2229], remain essentially stationary.

During this short period, the dynamics of the recombination depend upon the density of the ionizing track, which is captured by the ratio of two distances: the mean separation between its  $e^- - h^+$  pairs,  $r_p$ ; and the initial separation between the  $e^-$  and  $h^+$  of a pair once they are thermalized (i.e., reach thermal equilibrium),  $r_t$  [McLean *et al.*, 1989, p.92]. That is, if  $r_t$  is taken to be the characteristic half-width of a presumably Gaussian ionizing column, a high(low) density track is one in which the separation between pairs is so small(large) compared to column width,  $r_p \ll r_t$  ( $r_p \gg r_t$ ) that the Coulomb attraction between the elements of a given pair is negligible(significant), but that between pairs is significant(negligible). For these extremes of low and high density ionizing tracks, recombination is well described by columnar and geminate models, respectively, with a synthesis of the two required for intermediate conditions.

**Columnar model:** For low energy and heavily charged particles, which exhibit high LET, the small ratio of  $r_p/r_t$  suggests a columnar model, first proposed by Jaffé [1913], which treats the ionizing track as a column of cylindrically symmetric electron and hole densities,  $N_n(r, t)$  and  $N_p(r, t)$ , that evolve according to diffusion (with coefficients  $D_n$  and  $D_p$ ), drift (in response to an electric field  $E_x$  normal to the track), and recombination (with probability  $\alpha_R$ ) as [McLean *et al.*, 1989, p.94]:

$$\frac{\partial N_n(r, t)}{\partial t} = \underbrace{D_n \nabla^2 N_n(r, t)}_{\text{Diffusion}} + \underbrace{\mu_n E_x \frac{\partial N_n(r, t)}{\partial x}}_{\text{Drift}} - \underbrace{\alpha_R N_n(r, t) N_p(r, t)}_{\text{Recombination}} \quad (13a)$$

$$\frac{\partial N_p(r, t)}{\partial t} = \underbrace{D_p \nabla^2 N_p(r, t)}_{\text{Diffusion}} - \underbrace{\mu_p E_x \frac{\partial N_p(r, t)}{\partial x}}_{\text{Drift}} - \underbrace{\alpha_R N_n(r, t) N_p(r, t)}_{\text{Recombination}} \quad (13b)$$

Using a column width of 3–4 nm [Oldham and McGarrity, 1981, p.3977], numerical solutions to (C.13) show good agreement for  $\alpha$ -particles incident on SiO<sub>2</sub> [Stapor et al., 1985, p.4400]. In contrast,  $r_t$  for Si approaches 100 nm because charges interact much less effectively with the lattice. This increased charge separation still satisfies the columnar model condition, but combined with a smaller  $\lambda_D$  screening distance, leads to much less Coulomb force and thus recombination in Si than SiO<sub>2</sub> [McLean et al., 1989, p.103].

**Geminate model:** Conversely, energetic particles of low mass can exhibit low enough LET that  $r_p/r_t$  is so large as to allow each  $e^- - h^+$  pair to be considered in isolation. In this geminate scenario, the probability density of an uncombined electron,  $P_n(r, t)$ , still depends on drift and diffusion according to the Smoluchowski equation for Brownian motion [McLean et al., 1989, p.96]:

$$\frac{\partial P_n(r, t)}{\partial t} = \overbrace{D_n \nabla^2 P_n(r, t)}^{\text{Diffusion}} - \underbrace{\mu_n \nabla \cdot (\mathbf{E}_t P_n(r, t))}_{\text{Drift + Recombination}} \quad (\text{C.14})$$

but, the recombination is handled by including the Coulombic attraction between the pair in the total drift field of the second term,  $\mathbf{E}_t$ . This was performed by Onsager [1938] in his analytical solution to (C.14), which is dominated by drift for most field strengths.

### C.2.3 Transport

Following recombination by one of these mechanism, the hole yield described by the fraction  $\mathcal{F}_y$ , constitutes an introduced population of positive free carriers which slowly drift in response to an electric field applied across the oxide. It is shown in Section 2.1.1 that for a MOS device with a radiation-hardened gate oxide under bias,<sup>22</sup> this field-assisted transport dominates the time evolution of its properties in response to ionizing radiation [McLean et al., 1989, p.145–146].

---

<sup>22</sup>In this and subsequent discussions of carrier drift in oxides, it should be assumed that the oxide is subject to positive bias from gate to bulk, corresponding to an nMOS enhancement-mode transistor, unless otherwise noted.

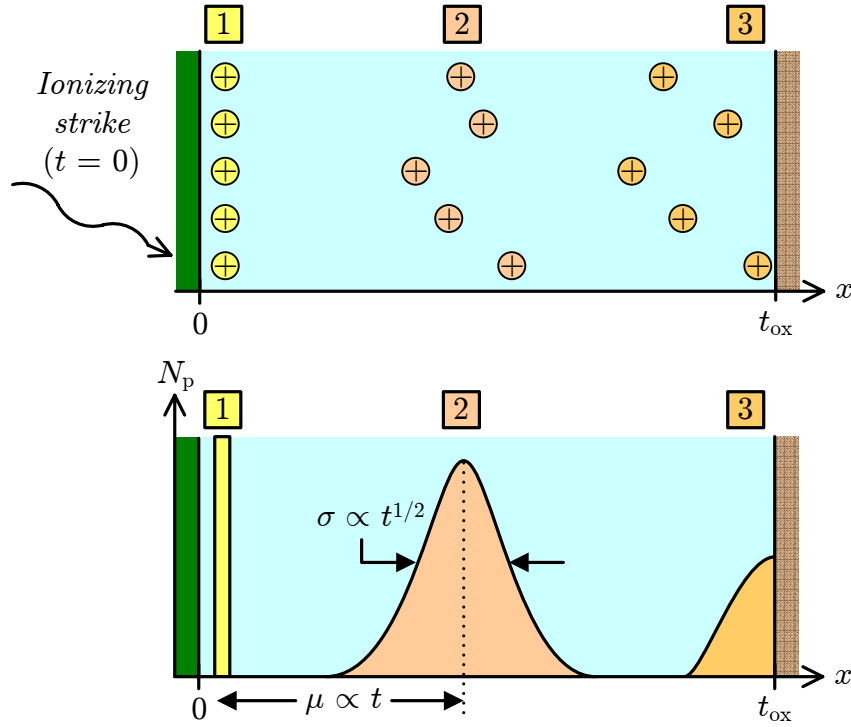


Figure C.4: Under Gaussian transport, the hole distribution retains its shape, with the location of the mean ( $\mu$ ) and its variance ( $\sigma^2$ ) both proportional to  $t$ . After [Pfister and Scher, 1978, p.751]

The conduction is deemed anomalous because, as seen in comparing Figure C.5 to Figure C.4, the evolution of the initial hole distribution  $N_p(x, t)$  is highly dispersive, with its leading edge penetrating very quickly while it widens as its peak moves much more slowly [Pfister and Scher, 1978, p.753]. It has been convincingly shown [McLean et al., 1976a, b] that this broad distribution in the hole transit times,  $\tau_H$ , is well modeled by a generalized continuous-time random walk (CTRW)—a stochastic mechanism for charge transport in amorphous solids that describes each path as a series of random steps separated by a probabilistic time interval  $\delta$  [Pfister and Scher, 1978]. As opposed to a Gaussian model which describes the range of  $\tau_H$  resulting from an exponential distribution of  $\delta$  that possesses a single characteristic time constant  $\tau$ :

$$P(\delta) \propto e^{-\delta/\tau} \quad (\text{C.15})$$

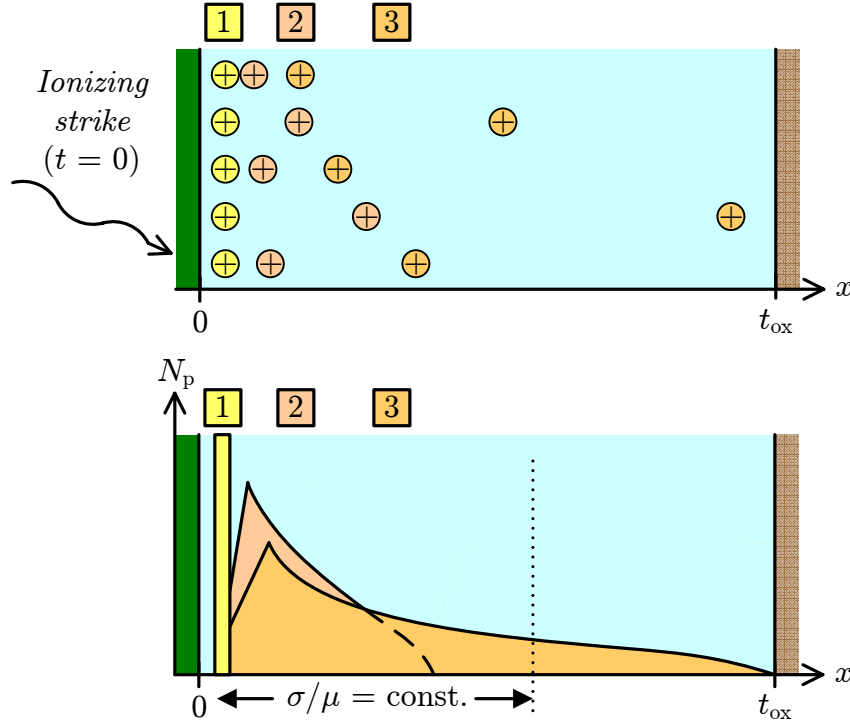


Figure C.5: Non-Gaussian hole transport model. Compared to the Gaussian model in Figure C.4, anomalous conduction via CTRW is marked by its fast leading edge and lagging mean, resulting in a constant ratio of the standard deviation ( $\sigma$ ) to the latter. After [Pfister and Scher, 1978, p.752]

the CTRW model assumes that  $P(\delta)$  is a slowly-varying function that reflects the presence of many types of delay events, each with their own time constant, subsumed into the disorder parameter  $\alpha_\tau$ :

$$P(\delta) \propto \delta^{-(1+\alpha_\tau)} \quad (\text{C.16})$$

Since some carriers transit via a succession of very rapid events, leading to the asymmetric evolution of Figure C.5, the fraction of carriers immobilized by long- $\delta$  events increases nonlinearly with time and the average transit time,  $\langle\tau_H\rangle$ , follows. This time-dependent  $\langle\tau_H\rangle$  yields an effective hole mobility,  $\mu_p$ , that decreases with time (or, alternative, oxide thickness) and is considerably less meaningful than the intrinsic mobility associated with the symmetrically evolving distribution in the Gaussian

transport of Figure C.4, giving rise to the broad range for  $\mu_n/\mu_p$  cited in the preceding Section [McLean *et al.*, 1989, p.118–120].

Trap-mediated (or multiple-trapping) transport and hopping transport are two microscopic processes whose sensitivity to local lattice parameters can give rise to the requisite broad range of event time constants described by (C.16) [McLean *et al.*, 1989, p.118]. The former, depicted in Figure C.6(a), occurs when holes are conducted through valence band states but intermittently waylaid by localized traps with an exponentially distributed continuum of trapping energies [Srouf and McGarrity, 1988, p.1451]. Even small variations in trap energy  $E_t$  can lead to a large spread in emission rates ( $\delta$ ), since the latter depend on thermal activation factors of the form  $e^{-E_t/kT}$  [Curtis and Srouf, 1977, p.3820]. But, evidence suggests that hopping, whereby holes tunnel directly between localized trap sites with overlapping wave functions, as shown in Figure C.6(b), is more consistent with measured observations [McLean *et al.*, 1989, p.135–136]. Specifically, the lack of correlation between  $\tau_H$ -dispersion and variations in either temperature or activation energy implicates structural causes, such as a spatial distribution of intersite hopping distances or of the bond angles that govern orbital overlap [McLean *et al.*, 1989, p.124]. Small fluctuations in these parameters can have a pronounced effect on the transfer integrals that govern hop times ( $\delta$ ) for a variant known as small polaron hopping [Oldham and McLean, 2003, p.486]. As depicted in Figure C.7, this occurs when thermal fluctuations form a coincident state between a trap site occupied by a polaron, or self-trapping hole,<sup>23</sup> and its neighbor, allowing the carrier to tunnel through [McLean *et al.*, 1989, p.125–126].

#### C.2.4 Oxide Traps

The most long-lived radiation effects in MOS oxides arise from the build up of positive charge near the Si-SiO<sub>2</sub> interface, where the transported holes are subject to capture

---

<sup>23</sup>For the purposes of this simplified treatment, a small polaron describes a carrier at either a lattice site or defect (trap) which so strongly polarizes the surrounding lattice that the configuration of lowest free energy involves the deformation of the latter. When this lattice distortion is large enough, the carrier becomes localized, or self-trapped, though the deformation can be conceptualized as following the carrier whilst it is conducted via tunneling. SiO<sub>2</sub> favors polaron formation, and thus such phonon-assisted tunneling, on account of the easily polarized states at the top of the valence band created by the non-bonding 2p orbitals of is oxygen atoms [McLean *et al.*, 1989, p.124–126].

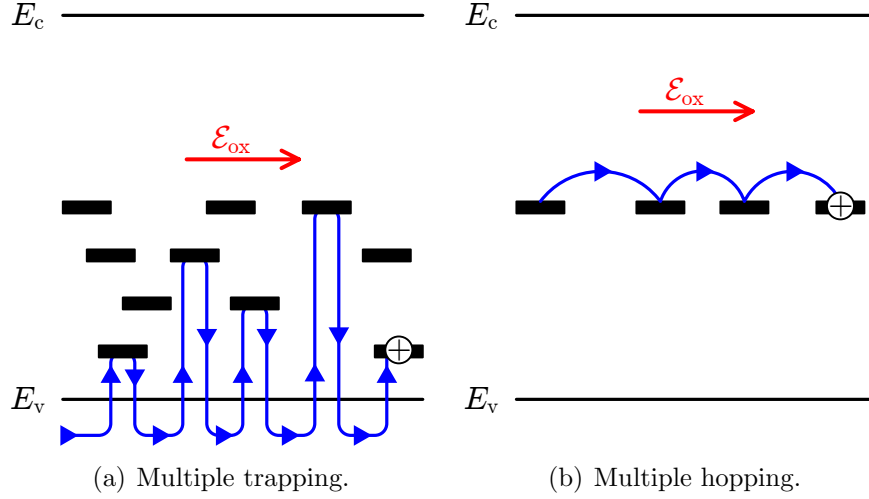


Figure C.6: Comparison of trapping and hopping hole transport models. Left-to-right drift field and distribution of trap levels are arbitrarily chosen, though most efficacious traps for multiple trapping(hopping) lie close to valance band(midgap). After [McLean *et al.*, 1989, p.123]

by deep-trapping sites [McLean *et al.*, 1989, p.149]. The volume distribution of such hole traps,<sup>24</sup>  $N_{\text{pt}}$ , each with a probability of hole capture given by the local field-dependent cross-section  $\sigma_{\text{pt}}(E_{\text{ox}})$ , is responsible for trapping a fraction of the radiation-induced holes,<sup>25</sup>  $\mathcal{F}_t$ , given by [McLean *et al.*, 1989, p.152]:

$$\mathcal{F}_t = \int_0^{t_{\text{ox}}} \sigma_{\text{pt}}(E_{\text{ox}}) N_{\text{pt}} dx \quad (\text{C.17})$$

The radiation tolerance of an oxide can be characterized by its trapping fraction, with the long(short) time scales of trapping(transport) dominating the evolution of the properties of soft(hard) oxides with  $0.2 < \mathcal{F}_t < 0.5$  ( $\mathcal{F}_t < 0.1$ ). Unlike the shallow traps responsible for multiple-trapping and hopping transport, these sites lie deep

<sup>24</sup>The hole trap distribution, beginning at the Si-SiO<sub>2</sub> interface and extending a distance  $\delta x$  into the SiO<sub>2</sub> bulk, where  $\delta x < 20$  nm [Holmes-Siedle and Adams, 2002, p.87], is non-uniform. Since most evidence suggests that in high-quality oxides there is a higher concentration of traps near the surface [McLean *et al.*, 1989, p.155], an exponential distribution of  $N_{\text{pt}}$  is often assumed [McLean *et al.*, 1989, p.160].

<sup>25</sup>The remainder of the holes  $(1 - \mathcal{F}_t)$  reach the interface and cross into the Si substrate, where there are lost to recombination [McLean *et al.*, 1989, p.150].

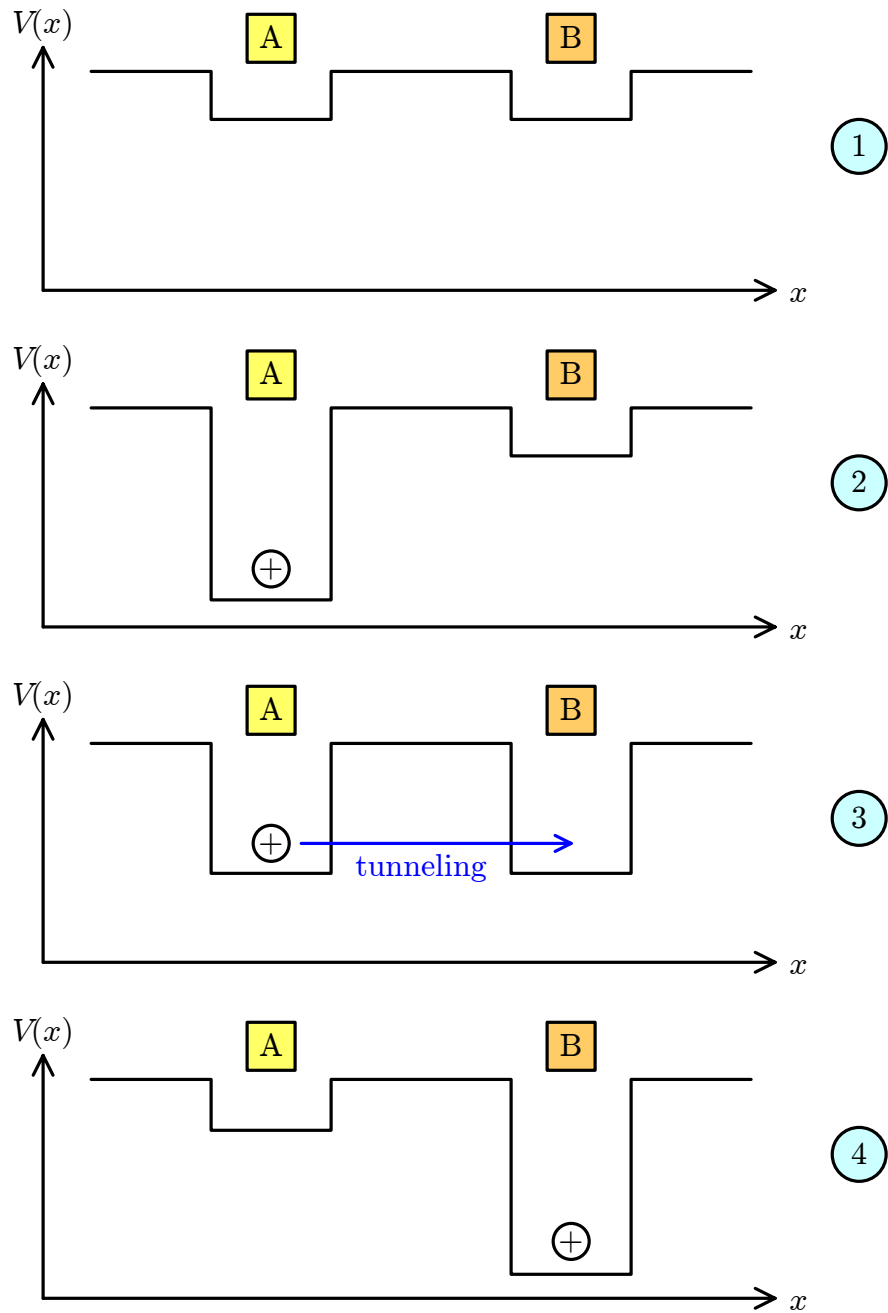


Figure C.7: Transport of self-trapped hole (polaron) via tunneling from A (in 1) to B (in 4). Polaron formed by self-trapped hole in (2) is able to tunnel to neighboring potential well (3) when the two are aligned by thermal fluctuations. The rate of such occurrences is sensitive to orbital separation in space and energy, giving rise to power-law delay statistics. After [McLean *et al.*, 1989, p.123]

enough in the band gap that phonons (thermal lattice vibrations) are unlikely to activate the holes [Holmes-Siedle and Adams, 2002, p.86], which are retained for anywhere from milliseconds to years [McLean et al., 1989, p.158].

Assuming the mechanisms described in Section C.2.1 generate  $K_g$  holes/cm<sup>3</sup> per rad of incident dose and a fraction  $\mathcal{F}_y$  of those escape the recombination mechanisms in Section C.2.2, then for an incident dose  $D$  these deep traps result in an areal density of positive trapped charge,<sup>26</sup>  $\Delta N_{\text{ot}}$ ,<sup>27</sup> that is simply [Srour and McGarrity, 1988, p.1453]:

$$\Delta N_{\text{ot}} = t_{\text{ox}} \mathcal{F}_t \mathcal{F}_y K_g D = \phi_t \mathcal{F}_t \quad (\text{C.18})$$

where it is notable that  $\Delta N_{\text{ot}}$  is proportional to oxide thickness  $t_{\text{ox}}$  (through  $\phi_t$ , the fluence of holes incident on the traps), since the number of pairs generated is proportional to ionizing track length.

### Physical model

At the microscopic level, only a single class of defect centers has been detected in conjunction with these deep hole traps to-date—the E' centers [McLean et al., 1989, p.171]. Depicted graphically in Figure C.8,<sup>28</sup> the precursor to one such E' center is an SiO<sub>2</sub> lattice complex in which the absence of a bridging oxygen results in a pair of trivalently bonded Si atoms, each with a single dangling (i.e., broken covalent) bond in the form of a non-binding sp<sup>3</sup> orbital [Helms, 1988, p.100] that overlap to form a strained Si-Si bond [Oldham and McLean, 2003, p.488].<sup>29</sup>

<sup>26</sup>Of course, as a result of this same D,  $\phi_t$  electrons are incident upon these traps as well, where they can recombine with a trapped hole with probability  $\sigma_R$ . However, such electron trapping is three orders of magnitude less probable, and therefore no net negative charge trapping is typically observed [McLean et al., 1989, p.167].

<sup>27</sup>Whereas  $N_{\text{oto}}$  describes the positive charge arrested by traps intrinsic to the oxide,  $\Delta N_{\text{ot}}$  denotes the additional contribution from radiation-induced oxide traps. Only the latter is dose-dependent and of interest here.

<sup>28</sup>Technically, the term E' center refers to the positively charged defect in Figure C.9 that results when a hole is trapped. Thus, the 'empty' hole trap should be treated as a precursor to the E' center.

<sup>29</sup>Although they all consist of a trivalent Si atom with an unpaired electron, various forms of the E' centers (and their precursors) are typically delineated with subscripts, depending on the surrounding atoms. For the purposes of this section, the most common case of an E'<sub>1</sub> center formed from a simple oxygen vacancy is treated as representative [Feigl et al., 1974]; the version that arises



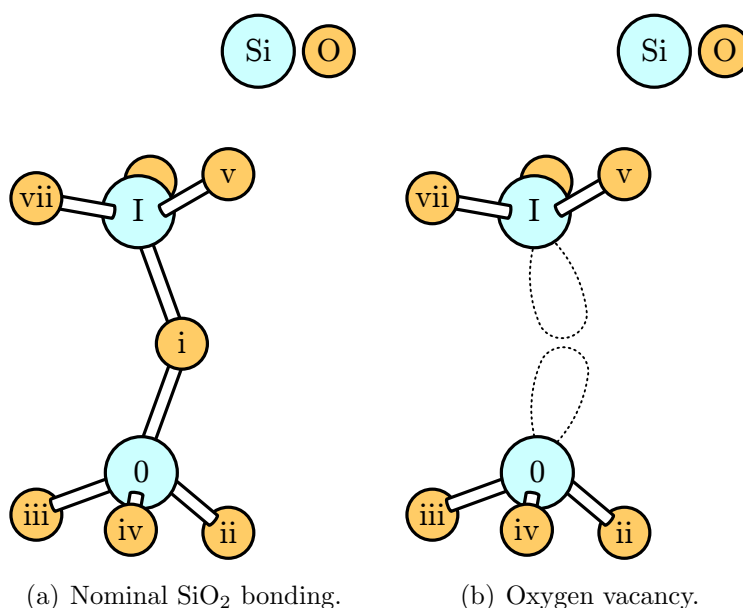


Figure C.8: Precursor to E' center formed by Si-Si orbital overlap in absence of binding oxygen (i). When one atom of this strained bond captures a hole, the positively-charged complex becomes an E' center, as shown in Figure C.9. After [Feigl *et al.*, 1974, p.226]

Such precursors arise in regions that are abnormally rich in Si or where Si-O bonds are subject to high strain; both conditions prevail at the Si-SiO<sub>2</sub> interface, rendering it intrinsically prone to such vacancies [McLean *et al.*, 1989, p.168–169]. Specifically, in order to match the lattice of crystalline silicon to that of amorphous silica,<sup>30</sup> a 0.2–0.3 nm thick layer of non-stoichiometric SiO<sub>x</sub> forms at the boundary [Helms, 1988, p.119]. On either side of this, bonds are strained to permit surface relaxation to the lowest free energy [Helms, 1988, p.93], resulting in to a high density of Si-O-Si bonds whose angles are reduced to match the Si lattice pitch within the first 1–4 nm of SiO<sub>2</sub> [McLean *et al.*, 1989, p.169].

---

from a strained Si-O bond, consisting of a trivalent Si plus non-bridging oxygen, each with a dangling orbital [Revesz, 1971], behaves similarly.

<sup>30</sup>Although lacking the long-range order characteristic of crystalline materials, vitreous (or amorphous) Si exhibits correlation between Si-O-Si bond angles order for clusters of 10–20 atoms [Helms, 1988, p.88]. This close-range order renders the Si-SiO<sub>2</sub> interface subject to traditional models of lattice-matching strain [Holmes-Siedle and Adams, 2002, p.87].

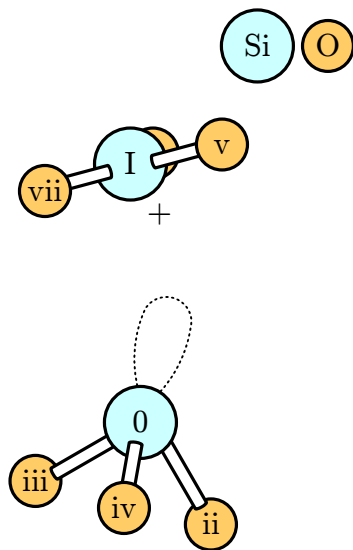


Figure C.9: Molecular representation of  $E'$  center, in which upper Si atom to relax into planar configuration after hole capture. Positive charge of complex is associated with this atom. After [Helms, 1988, p.99]

Often, such structural defects are passivated during fabrication by impurities that occupy the dangling or weakened chemical bonds of Si atoms. In modern silicon fabrication processes, which no longer suffer from the undesirable impurities (e.g., sodium) and the intentional contamination (e.g., gettering) initially responsible for such debilitating defects [McLean *et al.*, 1989, p.149], the primary impurity that remains ubiquitous in thermally grown oxides is hydrogen [Holmes-Siedle and Adams, 2002, p.88]. In such cases, the precursor structure of Figure C.8 will form when either SiH [Zvanut *et al.*, 1993, p.470] or OH [Holmes-Siedle and Adams, 2002, p.91] bonds are severed by ionizing radiation, reversing the passivation.

Whether intrinsically present (as in the bulk  $\text{SiO}_2$ ) or latent until induced by radiation (as is more common near the interface) [Holmes-Siedle and Adams, 2002, p.90], such a precursor can trap an incident hole and become a fixed, positively charged defect known as an  $E'_1$  center through the transformation depicted in Figure C.9. One Si atom absorbs the hole and becomes positively charged, relaxing back into the plane of its oxygen atoms [Helms, 1988, p.100]; the other retains a single unpaired electron, remaining neutral, but its non-binding orbital projects

into the space of the oxygen deficiency [*Holmes-Siedle and Adams, 2002*, p.90] in an abnormally strained tetrahedral configuration [*McLean et al., 1989*, p.170].<sup>31</sup>

## Neutralization

Though the  $E'_1$  center is stable, the holes may eventually be de-trapped through one of two mechanisms, tunneling and thermal annealing, that serve to reduce  $\Delta N_{\text{ot}}$  with time and elevated temperature, respectively [*McLean et al., 1989*, p.158]. The former consists of the quantum tunneling of an  $e^-$  from Si into  $\text{SiO}_2$ , where it recombines with the trapped  $h^+$ , thereby emptying the trap and reducing the vertical extent of  $\Delta N_{\text{ot}}$  at a rate of 0.2 nm per decade of time [*McLean et al., 1989*, p.160]. Tunneling, whose higher activation energies favor annealing of shallower traps at normal operating temperatures, is sensitive to the field in the oxide and, on account of the exponential fall-off of the tunneling probability with distance into  $\text{SiO}_2$ , dominates closer to the interface [*McLean et al., 1989*, p.158].

In contrast, isochronal annealing, which exposes the oxide to a series of progressively higher temperatures each for a fixed duration, can more quickly depopulate the deeper traps, since the activation energy for thermal detrapping the holes is  $\sim 2.25\times$  lower [*McLean et al., 1989*, p.167]. Though operating over different time scales and temperature ranges, both mechanisms achieve the same effect—over time, the traps near the interface are annealed, reducing  $\mathcal{F}_t$  and confining the net, long-term  $\Delta N_{\text{ot}}$  to a sheet of positive trapped charge between 5–20 nm into the  $\text{SiO}_2$ , as depicted in Figure C.10.

### C.2.5 Border Traps

Figure C.10 also illustrates the location of near-interface, or so-called border traps [*Fleetwood, 1992*, p.269], which are formed when an  $e^-$  tunnels into the non-binding orbital of the neutral Si atom in an  $E'_1$  center where it can then: recombine with the hole on the other Si atom, annealing it [*Lelis et al., 1989*, p.1808]; tunnel back

---

<sup>31</sup>This complex can alternately be interpreted as a hole captured by a neutral oxygen vacancy [*Srouf and McGarrity, 1988*, p.1453] or an unpaired electron spin associated with an  $sp^3$  orbital of a trivalent silicon atom [*McLean et al., 1989*, p.170].

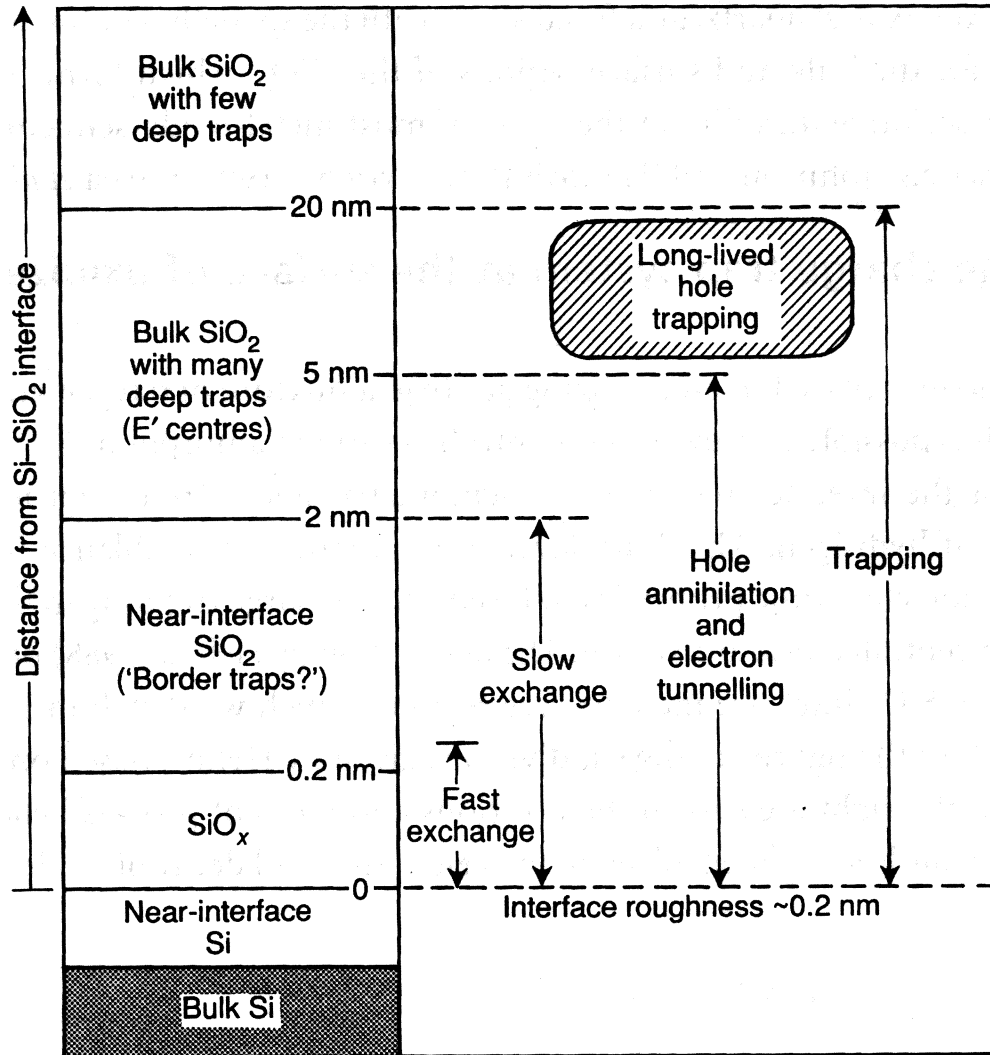


Figure C.10: Illustration of trap locations in Si oxide. Trap depth (in energy) increases with distance from interface. Oxide traps within  $\Delta x \simeq 5$  nm anneal naturally. Near-interfacial and interface traps are discussed subsequently. Reproduced *in toto* from [Holmes-Siedle and Adams, 2002, p.87]

and forth, repeatedly exchanging charge with the Si substrate [*Oldham and McLean, 2003*, p.488]; or, even act as an  $e^-$ -trap to facilitate tunneling of another  $e^-$  from the substrate to deep  $E'$  centers [*Oldham and McLean, 2003*, p.488]. The location of border traps is roughly defined by the distance over which tunneling is capable of completely passivating all trapped charge in a 1 minute interval [*Fleetwood, 1992*, p.269–270]; hole traps beyond this are of the deep type described above. Their name reflects a character that blends the atomic structure of the deep oxide traps ( $E'$  centers) with the charge exchange rates of the interface traps described below [*Holmes-Siedle and Adams, 2002*, p.179]. Like interface traps, they can freely exchange carriers with the Si, but the time scales of that exchange can be much longer for border traps (which can serve as ‘slow’ interface/surface states) than for interface traps (which are always ‘fast’ interface/surface states) [*Deal, 1980*, p.607]. As proves critical in Section 3.1.3.3, the slower time scales of the hole trapping and electron tunneling facilitated by border traps are believed to be responsible for  $1/f$  noise in MOS transistors [*Fleetwood et al., 2002*].

### C.2.6 Interface Traps

In addition to the deep oxide traps and border traps, Figure C.10 illustrates the existence of interfacial traps adjacent to the Si-SiO<sub>2</sub> interface. Although it can be demonstrated that their microscopic structure is similar to that of deep oxide traps, these interface traps are distinguished by three fundamental properties: they reside within or 1–2 atomic bond distances ( $\sim 0.5$  nm) of the Si surface [*Winokur, 1989*, p.194], in the non-stoichiometric layer whose strained labile bonds (primarily, Si-Si) act as precursors [*Winokur, 1989*, p.194]; their distribution in energy,  $D_{it}$ , is continuous throughout the Si bandgap, exhibiting an asymmetric U-shape that reaches a minimum at midgap and monotonically increases in near the band edges [*Winokur, 1989*, p.199–200]; and they are amphoteric, meaning that they permit positive, negative, and neutral charge states, which allows the trapping of either electrons or holes depending on the surface potential [*Srour and McGarrity, 1988*, p.1453].

The first two characteristics lead to the common designation [[Winokur, 1989](#), p.196] of *fast interface states* for these traps.<sup>32</sup> Since carriers tunnel from the Si valance and conduction bands at a rate exponentially and inversely proportional to trap energy depth relative to these bands, the higher density of  $D_{it}$  near the band edges implies that most interface traps exchange charge with the substrate more rapidly than border or deep oxide traps. Amphoterism produces two classes of interface traps whose charge state depends upon the position of the Fermi level in response to applied bias and thus are discriminated with the conventional terminology of Si dopants—donors and acceptors. An acceptor(donor) trap is neutral(positively charged) and paramagnetic(diamagnetic) when above the Fermi level, where it contains one(zero) electron(s), but becomes negatively charged(neutral) and diamagnetic(paramagnetic) when it moves below the Fermi level and increases its charge state to two(one) [[Lenahan and Conley, 1998](#), p.2139–2140]. It is commonly accepted that interface traps located above(below) the Si midgap act as acceptors(donors) [[Winokur, 1989](#), p.197], and that the asymmetry of  $D_{it}$  (namely, demonstrating more traps in the upper half of the bandgap) results from the presence of two microscopic defect centers, each responsible for a donor and acceptor level, but only one having these centered around midgap [[Winokur, 1989](#), p.202].

Although the interface trap density is highly dependent upon manufacturing details and conditions such as temperature and applied field, a generic expression for  $\Delta N_{it}$ , the areal charge density generated by ionizing radiation of dose  $D$  is:<sup>33</sup>

$$\Delta N_{it} = K_i t_{ox}^n D^{2/3} \quad (C.19)$$

---

<sup>32</sup>Despite its prevalence in the literature and the etymological origins of the term *border state* [[Fleetwood, 1992](#), p.269], the label *states* is not used herein to denote near-interfacial trapping sites, such as those in the interface and border regions of Figure C.10. For clarity, and in keeping with the conventions of [Deal \[1980\]](#), these sites are instead be described as interface and border *traps*, respectively, throughout this document.

<sup>33</sup>Though extremely clean, modern fabrication processes cannot produce an Si-SiO<sub>2</sub> interface free of these traps. But, in high-quality oxides, whose as-processed  $N_{it}$ ,  $N_{ito}$ , can range from  $10^9$  [[Winokur, 1989](#), p.194] to  $10^{13}$  [[Oldham and McLean, 2003](#), p.490] cm<sup>-2</sup>, these are typically passivated by hydrogen, as discussed below. So, it suffices here to assume total passivation prior to exposure ( $N_{ito} = 0$ ), such that all post-irradiation interface traps result from radiation-related depassivation and  $N_{it} = \Delta N_{it}$ .

where the proportionality constant,  $K_i$ , can be extrapolated from a 1-Mrad(Si) dose applied to a 100-nm oxide as  $5 \times 10^5$ , though it is sample-specific in general [*Srour and McGarrity, 1988*, p.1454]. Similarly,  $n$ , the exponent for the  $t_{\text{ox}}$  dependence, can range from 0.5–2, although it is generally close to 1 for thick oxides and may increase substantially for  $t_{\text{ox}} < 10$  nm [*Winokur, 1989*, p.229]. The sublinear dose dependence is thought to reflect a splitting of trap energy levels, and thus a reduced number of traps near the band edge, when the density of populated traps rises enough for electrons confined in neighboring sites to repel each other [*Winokur, 1989*, p.219].

However, there is no reported evidence of  $\Delta N_{\text{it}}$  saturating with dose (up to 20 Mrad(Si)) and no dependence on dose rate has been observed [*Winokur, 1989*, p.242]. Although not captured in (C.19),  $\Delta N_{\text{it}}$  is known to increase strongly for positive irradiation biasing of the oxide [*Srour and McGarrity, 1988*, p.1454] and for elevated temperatures, just as is the case for  $\Delta N_{\text{ot}}$ . But, in stark contrast, no annealing of  $N_{\text{it}}$  is observed at room temperature; even at elevated temperatures, where thermal annealing can be significant, the thermal activation energy of 1.4 eV [*Winokur, 1989*, p.226] is greater than that for deep oxide traps ( $< 1.3$  eV) [*Holmes-Siedle and Adams, 2002*, p.167].

### Physical model

Despite these differences in  $D$ ,  $t_{\text{ox}}$ , and annealing dependencies, the microscopic structure of the defects believed responsible for interface traps, a class of trivalent silicon defects known  $P_b$  centers [*Lenahan and Dressendorfer, 1983*], is quite similar to that for deep oxide traps ( $E'$  centers) [*Lenahan and Dressendorfer, 1984*, p.3495]. This congruence is highlighted by Figure C.11, which depicts the  $P_b$  center in its neutral and paramagnetic state,<sup>34</sup> complexed with a conjugate Si atom on the  $\text{SiO}_2$

<sup>34</sup>Just as for the  $E'$  center (cf. Footnote 29), the class of  $P_b$  centers consists of many variations delineated with subscripts; specifically, the  $P_b$  center (cf. Figure C.11) for  $\langle 111 \rangle$  Si, and the  $P_{b0}$  and  $P_{b1}$  centers for  $\langle 100 \rangle$  Si.  $P_b$  and  $P_{b0}$  are essentially identical defects, with the only difference being that the  $P_{b0}$  dangling orbital, since it is always oriented along the  $[111]$  crystallographic direction, is not normal to the surface (i.e., the  $(100)$  plane) [*Lenahan and Conley, 1998*, p.2138]. Although it is known to also be trivalently back-bonded to Si atoms at the interface, the detailed chemical structure of the  $P_{b1}$  defect is undetermined as yet [*Lenahan and Conley, 1998*, p.2139], so it is only distinguished from its counterparts by the asymmetry of its donor and acceptor levels with respect to

side of the interface. The SiO<sub>2</sub> side of this configuration is identical to that of the E' center (cf. Figure C.9), wherein the Si atom participates in three oxygen bonds but is absent its remaining electron such that it exhibits a net positive charge. The P<sub>b</sub> center itself consists only of the substrate Si atom, trivalently back-bonded to Si (not O) atoms, with its dangling orbital (and its unpaired electron spin) projecting orthogonally to the interface [Winokur, 1989, p.233]. Although it has been included to conform with Figure C.9, the positively charged facing Si is not necessary for its formation, so the charge state of the P<sub>b</sub> center is defined strictly by the occupancy of the pictured orbital [Helms, 1988, p.100]. When acting as an e<sup>-</sup> trap, this defect accepts(donates) an electron as it moves below(above) the Fermi level, according to  $P_b + e^- \rightarrow P_b^-$  ( $P_b \rightarrow P_b^+ + e^-$ ), such that its unbonded orbital is full(empty) and the charge state of the now diamagnetic center becomes negative(positive). In the converse case, this amphoteric behavior holds for the trapping of holes by acceptors ( $P_b \rightarrow P_b^- + h^+$ ) and donors ( $P_b + h^+ \rightarrow P_b^+$ ), as well [Lenahan and Dressendorfer, 1984, p.3496].

With an Si-O bond under interfacial strain in the non-stoichiometric layer as the most common precursor (rather than the oxygen vacancy depicted in Figure C.9 and Figure C.11) there are several competing models to describe the formation of the eventual P<sub>b</sub> center depicted above, all of which are initiated by the presence of trapped holes (cf. Section C.2.4). One such model, is based on the injection of electrons from the Si (via tunneling) which can recombine with holes trapped near the interface through a nonstandard mechanism which reduces free energy by inducing a structural change that results in dangling bonds [Winokur, 1989, p.236].

Secondly, and more promising, the bond-strain gradient (BSG) model [Grunthaner *et al.*, 1982] involves a two-step reaction driven by radiation-induced holes and seeks to explain correlations between E' and P<sub>b</sub> formation [Winokur, 1989, p.238]. In the first step, holes are trapped in the near-interfacial, border region (< 3 nm) where, as described in Section C.2.4, there exist many strained Si-O bonds to satisfy lattice matching. The bonds of these precursors are ruptured, forming E' centers (perhaps,

---

midgap [Lenahan *et al.*, 2002]. Since all are formed through similar mechanisms and from identical precursors, it is sufficient to consider the structure of only the P<sub>b</sub> center here.



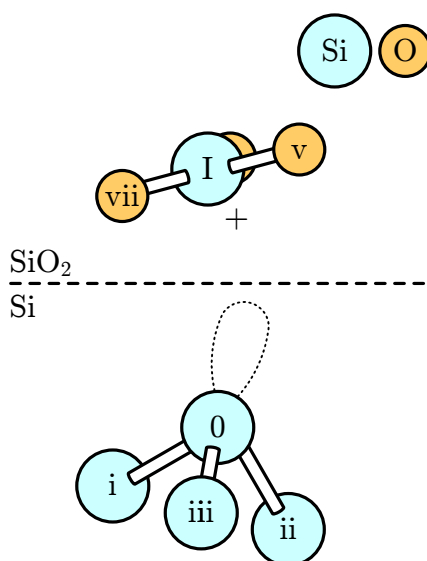


Figure C.11: Molecular representation of  $P_b$  center, which when complexed with  $\text{SiO}_2$  is similar to Figure C.9, though the  $P_b$  comprises only the bulk atom, by definition, shown in it is paramagnetic state. After [Helms, 1988, p.99]

future border traps) and releasing non-bridging oxygen which migrates in the direction of increasing bond strain [Winokur, 1989, p.233] until it arrives at the interface, terminating in the formation of  $P_b$  centers.

Given recent understanding of the subtleties of border traps (cf. Section C.2.5), both these model families, which rely on the conversion of trapped oxide charge into interface traps, are discounted by many [Oldham and McLean, 2003, p.491]. Instead, the most accepted class of models [Oldham and McLean, 2003, p.490] incorporate the aforementioned passivation of dangling Si bonds at the interface by hydrogen introduced during processing.

According to the most recent formulation [McLean, 1980], such surface Si-H complexes serve as precursors to  $P_b$  formation and are dissociated by radiation-induced holes in two steps:

1. Hole transport through small polaron hopping (cf. Section C.2.3) releases enough energy to liberate  $\text{H}^+$  ions from trivalent Si (in Si-H) or strained Si-O (in Si-OH) complexes introduced in the bulk  $\text{SiO}_2$  during fabrication, potentially

creating  $E'$  centers

2. These hydrogen ions, again following a dispersive CTRW transport model but hopping between non-bonding orbitals of neighboring oxygen atoms [*McLean*, 1980, p.1655], migrate to the interface where they react almost instantaneously with passivated Si-H bonds and dimerize, leaving behind a dangling Si bond—an electrically active  $P_b$  center—in a complex reaction [*Brown*, 1985; *Griscom*, 1985].

The broad range of longer time constants associated with the second step governs the extended formation rate of  $\Delta N_{it}$ , which can take  $10^{-2}$ – $10^3$  s after the initiation of exposure to reach its final value [*McLean and Oldham*, 1987, p.26].

## C.3 Non-Ionizing Radiation

Unlike LET, which is most significant in device oxides where carrier concentrations are otherwise low, NIEL is primarily associated with heavy energetic particles impacting the Si bulk and disturbing its otherwise regular lattice; only bulk NIEL is considered in this section. According to the Lindhard model, which applies to the partitioning of  $\mathcal{S}$  in (C.4) for particle radiation [*Srouf and McGarrity*, 1988, p.1445], this  $\mathcal{S}_n$  accounts for a much smaller fraction of the total energy deposited than  $\mathcal{S}_e$ , with approximate  $\mathcal{S}_e/\mathcal{S}_n$  ratios of 318 [*Holmes-Siedle and Adams*, 2002, p.113] and 1000 [*Srouf and McGarrity*, 1988, p.1445] for 1-MeV  $e^-$  and  $H^+$ , respectively. Nevertheless, the resulting displacement damage is critical to the operation of transistors whose current flows in the bulk, rather than along the surface, with even  $2.5 \times 10^{-8} \text{ cm}^{-3}$  such displacements responsible for appreciable degradation in bipolar device parameters [*Messenger and Ash*, 1992, p.200]. Echoing the structure of Section C.2, this section explores the physics of NIEL mechanisms chronologically.

### C.3.1 Generation

Akin to  $e^- - h^+$  production via  $\mathcal{L}_e$ ,  $\mathcal{L}_n$  is primarily responsible for creating a Frenkel defect pair or close pair [*Srouf and McGarrity*, 1988, p.1446] by dislodging an Si

atom from its lattice position, forcing it to squeeze into an interstitial location (I) and leaving behind a vacancy (V). Though they are thermodynamically stable and can exist naturally,<sup>35</sup> these intrinsic defects are mobile and can combine with dopants or impurities to form defect-impurity complexes as well as group together to form extended defects, such as divacancies (V-V), diinterstitials (I-I), or clusters [*Watkins, 1999*, p.125]. Requiring additional binding energy, these complexes are commonly associated with radiation for which  $\mathcal{S}_n$  exceeds simply the energy required to overcome the Si lattice bonds,  $E_d$ ,<sup>36</sup> resulting in a cascade of reactions. Candidates include both elastic particle collisions with either the lattice electron clouds or nuclei and indirect inelastic or photonic mechanisms, as described subsequently.

### C.3.1.1 Photonic Mechanisms

Without momentum of their own, photons can only succeed in displacing a lattice atom through the action of secondary, energetic electrons produced by Compton scattering (cf. Section C.2.1.1) [*Srou and McGarrity, 1988*, p.1445]. Although their low mass clearly renders them less effective than nucleons and heavy ions, these scattered electrons are capable of generating displacement damage, according to the particle mechanisms described below [*Holmes-Siedle and Adams, 2002*, p.71].

### C.3.1.2 Particle Mechanisms

Section C.2.1.2 alluded to the ways in which elastic Coulombic and nuclear collisions, involving either an incident particle or a secondary particle liberated by an inelastic

---

<sup>35</sup>Intrinsic defects are those which can exist in the absence of impurities. An isolated vacancy possess a formation energy of 3.3–4.1 eV and can migrate without thermally activated diffusion [*Watkins, 1999*, p.132], tending to complex with donor dopants in Si [*Holmes-Siedle and Adams, 2002*, p.65]. Similarly, the isolated interstitial, which forms with an energy of 3.3–3.7 eV, is so mobile even at 4.2 K [*Watkins, 1999*, p.136] that it has never been observed directly, only trapped in larger complexes [*Holmes-Siedle and Adams, 2002*, p.64], even though there is ample evidence for its existence [*Watkins, 1999*, p.135]. There also exists a third intrinsic defect, the antisite, which is not of consequence here [*Watkins, 1999*, p.125].

<sup>36</sup>This is known as displacement energy and is alternatively cited as 10 eV [*Holmes-Siedle and Adams, 2002*, p.73], 21 eV [*Srou and McGarrity, 1988*, p.1446], or 25 eV [*Messenger and Ash, 1992*, p.198].

nuclear collision contribute to energy loss via  $\mathcal{S}_n$ . As opposed to the continual slowing-down that occurs for linear electronic stopping power, wherein the particle losses minute amounts of momentum as it participates in  $\sim 10^5$  Coulomb interactions along its track, these elastic collisions occur very infrequently but each dissipate a significant portion of the particle's kinetic energy [Attix, 1986, p.160].

For nuclear collisions, the energy transferred between atoms can be determined through simple mechanics to be [Holmes-Siedle and Adams, 2002, p.73]

$$\Delta E_i = \frac{4A}{(1+A)^2} \sin^2 \frac{\theta_i}{2} E_i \quad (\text{C.20})$$

where  $A$  is the atomic mass number of the target (28 for Si) and  $\theta$  is the angle through which the incident particle of energy  $E_i$  is deflected. Equating  $\Delta E_i$  in (C.20) with  $E_d$  (cf. Footnote 36), the minimum incident energy required to displace an Si lattice atom,  $E_{\min}$ , is

$$E_{\min} = \frac{(1+A)^2}{4A} E_d \approx 150 \text{ eV} \quad (\text{C.21})$$

Although (C.21) applies to a hard-sphere collision between neutral atoms, not every incident particle with  $E_i > E_{\min}$  encounters a lattice atom. This depends upon its interaction probability as captured by its NIEL cross-section,  $\sigma_n$ , which is also a function of  $E_i$ . Thus, the likelihood that an incident species generates displacement, depends upon  $E_i$  through both stochastic ( $\sigma_n(E_i)$ ) and deterministic ( $E_{\min}$ ) factors. So, whereas protons with  $E_i > E_{\min}$  typically initiate displacement-generating collisions [Srou and McGarrity, 1988, p.1445], since they are likely to collide with the lattice as they are buffeted by Coulombic forces, neutrons, which have a much lower  $\sigma_n$ , are unlikely to do so unless  $E_i > 10 \text{ keV}$  [Holmes-Siedle and Adams, 2002, p.73]. Furthermore, because their significant size disadvantage yields such a low  $\sigma_n$ , the likelihood of displacement by electrons is only significant for energies above 125–130 keV [Holmes-Siedle and Adams, 2002; Srou and McGarrity, 1988, p.73,p.1455].

In all such reactions, the first atom encountered by the particle, the so-called primary knock-on atom (PKA) or primary recoil atom, receives the largest fraction

of the momentum [Messenger and Ash, 1992, p.198]. Provided this is sufficient, the PKA then generates additional V–I pairs through a cascade of analogous elastic collisions that terminates once the kinetic energy of the secondary atoms drops below  $E_d$  [Messenger and Ash, 1992, p.200], usually within nanoseconds [Holmes-Siedle and Adams, 2002, p.75]. The end result is the formation of ‘damage tree’ whose terminal subclusters store the bulk of the incident NIEL energy in the form of thermally stable defect clusters [Holmes-Siedle and Adams, 2002, p.67]. From the kinematics of this displacement cascade and the proportionality in (C.20), it can be shown that the density of induced Frenkel pairs is a linear function of the energy of the PKA [Kinchin and Pease, 1955]. Neutrons with  $E_i > 10$  keV tend to yield PKA in the range of  $10^3$ – $10^6$  eV whereas the range is much broader for protons(electrons) which are capable of producing recoils with energies down to  $E_{\min}$  at low(high)  $E_i$  on account of their lower higher(lower)  $\sigma_n$  and participation in Rutherford scattering [Holmes-Siedle and Adams, 2002, p.73].<sup>37</sup>

### C.3.2 Recombination and aggregation

Within microseconds of the displacement tree formation, vacancies and interstitials begin to aggregate into extended defects as well as recombine with one another [Holmes-Siedle and Adams, 2002, p.64]. Just as for ionizing radiation, the degree of this recombination (and aggregation) depends upon the density of pairs along the particle track. By analogy with the columnar(geminate) recombination models for the  $e^- - h^+$  pairs generated by high(low) LET ionizing particles (cf. Section C.2.2), the density of close V–I pairs in the large(small) terminal clusters that result from high-NIEL(low-NIEL) particles leads to more(less) initial recombination and aggregation [Holmes-Siedle and Adams, 2002, p.75–76]:

**Low-energy PKAs:** The low-energy ( $\leq 5$  keV) PKAs generated by low-NIEL electrons, photons, and low-energy protons, have few knock-ons, yielding sparse V and I populations along their damage tracks as noted above [Srouer and

---

<sup>37</sup>For protons, Rutherford scattering tends to dominate the production of low energy recoils ( $\leq 5$  keV) whereas nuclear interactions, which are more efficient, yield recoils with energy in excess of 10 keV. Only the latter process is modeled by (C.20) and (C.21), which ignore Coulombic forces.

*McGarrrity, 1988*, p.1446]. In this case, clusters are small, weak, and/or rare [*Messenger and Ash, 1992*, p.200], and the tendency is for the freshly-formed, isolated defects to migrate away, often over long distances, before appreciable recombination or aggregation can occur [*Holmes-Siedle and Adams, 2002*, p.76]. During this time, the vacancies can serve as efficient traps for minority carriers, reducing recombination lifetimes as described in Section C.3.4 [*Messenger and Ash, 1992*, p.198]. Furthermore, the most probable destination for these vacancies at the conclusion of their long diffusion paths is a defect-impurity complex, rather than an extended defect composed of other vacancies [*Holmes-Siedle and Adams, 2002*, p.74].

**High-energy PKAs:** By contrast, only a few point defects migrate away from the large terminal clusters formed by the surfeit of knock-ons generated by the high-energy ( $\geq 10$  keV) PKAs of particles with high NIEL, such as neutrons, heavy ions, and energetic protons in the MeV range [*Srouf and McGarrrity, 1988*, p.1446]. The remainder either annihilate or aggregate into extended defects, with most dimerizing into V-V and I-I clouds in the latter case [*Holmes-Siedle and Adams, 2002*, p.75]. Such clouds can eventually coalesce into even broader defects, or be released to migrate through the bulk where, being both thermally stable and electrically active, the divacancy is known to be an especially important  $e^- - h^+$  recombination center, reducing mobilities and increasing leakage currents [*Holmes-Siedle and Adams, 2002*, p.64], as discussed in Section 2.1.2.1 and Section 2.1.2.2, respectively.

### C.3.3 Defect Migration

Both vacancies and interstitials are highly mobile in Si, so those that survive initial recombination and aggregation at the site of the terminal clusters tend to rapidly diffuse away from these regions which, especially for high-NIEL radiation, are of high concentration [*Holmes-Siedle and Adams, 2002*, p.75]. The activation energy and, consequently, the mobility of these isolated defects, as well as any dimerized aggregates from the cluster, is a strong function of their charge state [*Srouf and*

[McGarrrity, 1988](#), p.1447]. Like the  $P_b$  center, both the vacancy and divacancy are amphoteric with  $-2$ ,  $-1$ ,  $0$ ,  $+1$ , and  $+2$  allowable electron states the occupancy of which depends upon their location relative to the Fermi level [[Messenger and Ash, 1992](#); [Watkins, 1999](#), p.127–128, p.241]. The singly charged vacancy is particularly mobile at room temperature [[Srour and McGarrrity, 1988](#), p.1447], but since their activation energies are so low, vacancies can also migrate athermally, that is, at temperatures below those required for thermal activation, depending upon the minority carrier levels in the bulk [[Watkins, 1999](#), p.132].

Once the isolated and dimerized defects have migrated to their final location, they often, though not necessarily,<sup>38</sup> become thermally stable by complexing with impurities or donor(acceptor) atoms of the lattice [[Srour and McGarrrity, 1988](#), p.1447], such as oxygen(phosphorous) [[Holmes-Siedle and Adams, 2002](#), p.74]. Regardless of the specific chemical structure, all such complexes perturb the Si lattice so as to permit energy levels within the bandgap. Just as the traps in the various strata of the oxide, as described in Section C.2.4 through Section C.2.6, can temporarily or permanently immobilize carriers in the oxide, these sites provide a mechanism for not only the trapping but also the recombination of the complimentary carrier species in the bulk silicon.<sup>39</sup> In the next two subsections, these phenomena are treated in reverse order, corresponding to their relative import for transistor degradation, assuming an n-type substrate for the simplicity of identifying the majority ( $e^-$ ) and minority ( $h^+$ ) carrier species without loss of generality.

---

<sup>38</sup>In the remaining cases, multivacancy or multiinterstitial complexes are usually observed [[Holmes-Siedle and Adams, 2002](#), p.64].

<sup>39</sup>This distinction is somewhat artificial, since all energy levels within the bandgap can partake in the same fundamental physical interactions (e.g., hole traps in the oxide also facilitate recombination, especially bulk and interface traps). In conventional parlance, a defect site which has a high(low) probability of re-emitting a carrier before facilitating its recombination with one of opposite polarity is deemed a trap(recombination center). Thus, shallow traps, which lie close to one band but have a low probability of capturing a carrier from the opposite band, are much less effective as recombination centers [[Messenger and Ash, 1992](#), p.27]. Conversely, the presence of both carrier species in the semiconducting bulk, albeit in disparate concentrations, yields much shorter carrier lifetimes than in the oxide, which requires quantum tunneling of electrons from below, so the bulk admits treatment of deep trap sites as recombination centers.

### C.3.4 Minority Carrier Trapping

The vacancy itself, along with divacancy and vacancy-impurity complexes, plays a primary role in trapping minority carriers that have sufficient thermal energy to be promoted from the conduction band and mediating their recombination with majority carriers. The increased concentration of these vacancies and their complexes in response to non-ionizing radiation increases the excess carrier recombination rate,  $\Gamma$ , by reducing the mean length of time holes spend in the valance band prior to recombination, known as the minority-carrier lifetime,  $\tau_p$ . These are related through the relationship<sup>40</sup>

$$\Gamma = \frac{N'_p}{\tau_p} \quad (\text{C.22})$$

As would be expected,  $\Gamma$  (usually expressed in  $\text{cm}^{-3}\text{s}^{-1}$ ) increases for higher concentrations of excess holes,  $N'_p$ , and shorter lifetimes, but it is the latter that are affected by vacancy-related defect centers.

The minority-carrier lifetime<sup>41</sup> is governed by two distinct recombination mechanisms, Shockley-Read-Hall (SRH) recombination and Auger recombination, with associated time constants of  $\tau_{\text{SRH}}$  and  $\tau_A$ , respectively, according to [Kerns, 1989, p.496]:

$$\frac{1}{\tau_p} = \frac{1}{\tau_{\text{SRH}}} + \frac{1}{\tau_A} \quad (\text{C.23})$$

**SRH Recombination:** In SRH recombination [Hall, 1952; Shockley and Read, 1952], the energy level,  $E_t$ , introduced by a vacancy-related defect complex near midgap can sequentially trap an electron and hole, from the conduction and valance bands, respectively, thereby facilitating their recombination without the energetically

---

<sup>40</sup>Since both majority and minority excess carriers take part in recombination, it is not immediately obvious that the steady-state recombination rate should depend only on  $\tau_p$ . But, even though the time-constant associated with steady-state recombination, the carrier recombination lifetime,  $\tau_\Gamma$ , is indeed the same for both species, that is,  $\tau_\Gamma = N'_p/\Gamma = N'_n/\Gamma$ , it is not the case that  $\tau_p = \tau_n$ . The difference arises from the dependencies of  $\tau_p$  and  $\tau_n$  on injection level, as is explained in Footnote 42.

<sup>41</sup>It has been suggested [Messenger and Ash, 1992, p.209] that the *carrier recombination lifetime* ( $\tau_\Gamma$ ) be used in place of the more common minority carrier lifetime ( $\tau_p$ ), since the two are synonymous for low level injection. While acknowledging the symmetry of this argument, the latter is employed herein for historical continuity, noting that even Messenger and Ash [1992] do not adopt their own suggestion.



unfavorable need for tunneling across the bandgap [Messenger and Ash, 1992, p.26–27]. This process is most efficient when  $E_t = E_F$ , in which case the lifetime of minority carriers depends inversely on volumetric trap number density,  $N_t$ , the carrier thermal velocity,  $v_T$ , and the capture cross-section at that energy,  $\sigma_{n,p}(E) = \sigma_{n,p}(E_F)$ , according to:<sup>42</sup>

$$\tau_{\text{SRH},p} = \frac{1}{\sigma_p(E_F) v_T N_t} \quad (\text{C.24})$$

Although complete theory is quite complicated [Kerns, 1989, p.495] when accounting for the continuum of possible  $E_t$  rather than just  $E_F$  as in (C.24)

---

<sup>42</sup>This relationship only holds for low-level injection, wherein the excess carrier density  $N'_p = N'_n$ , is much less than the initial majority carrier concentration; for n-type Si, this implies  $N'_p, N'_n, N_{po} \ll N_{no}$ , which explains why  $\Gamma$  is expressed in terms of  $\tau_p$  rather than  $\tau_n$  in (C.22) [Messenger and Ash, 1992, p.41].

From Footnote 40, recall that

$$\Gamma = \frac{N'_p}{\tau_\Gamma}$$

where  $\tau_\Gamma$  is the excess carrier recombination lifetime. By definition, the excess carrier recombination rate,  $\Gamma$ , reflects the difference between the recombination rates in two cases: equilibrium, when the hole concentration,  $N_{po}$ , exhibits a lifetime  $\tau_{po}$ ; and after the introduction of  $N'_p$ , when the total population,  $N_p = N_{po} + N'_p$ , exhibits a lifetime of  $\tau_p$ , such that

$$\Gamma = \frac{N_p}{\tau_p} - \frac{N_{po}}{\tau_{po}}$$

The analogous case holds for the majority carriers:

$$\Gamma = \frac{N_n}{\tau_n} - \frac{N_{no}}{\tau_{no}}$$

However, the key difference is that for holes,  $\sigma_p(E)$  in (C.24) does not change appreciably because the probability of capture is proportional to  $N_n$  and  $N_n = N_{no} + N'_n \simeq N_{no}$ . Thus,  $\tau_p = \tau_{po}$ . Utilizing this fact and equating the first two expressions for  $\Gamma$  gives

$$\tau_\Gamma = \tau_{po}$$

Thus, the steady-state recombination lifetime for *both* types of excess carriers is equal to the equilibrium lifetime for intrinsic *minority* carriers. By contrast, whereas under the low-injection assumption  $N'_n \ll N_{po}$ , it is not necessarily the case that  $N'_p \ll N_{po}$ . So the presence of excess holes can appreciably increase  $N_p$ , increasing the likelihood of electron capture,  $\sigma_p(E)$ , and resulting in  $\tau_n < \tau_{no}$ ; specifically,

$$\tau_n = \frac{\tau_{no}}{1 + \frac{N'_p}{N_{po}}}$$

[*Messenger and Ash, 1992*, p.29], a simplified model with excellent predictive prowess [*Curtis, 1975*] can be obtained by decomposing  $\tau_{\text{SRH}}$  into three time constants ( $\tau_x$  where  $x=1, 2, 3$ ) [*Messenger and Ash, 1992*, p.213],

$$\frac{1}{\tau_{\text{SRH}}} = \frac{1}{\tau_1} + \frac{1}{\tau_2} + \frac{1}{\tau_3} \quad (\text{C.25})$$

each of which employs (C.24) to describe a set of traps that all reside at a single energy level,  $E_x$ , and possess the same capture cross section  $\sigma_x$ . At low-level injection, when  $N'_p$  is much less than the initial doping  $N_{\text{no}}$  [*Holmes-Siedle and Adams, 2002*, p.78], recombination is dominated by  $\tau_1$  since  $E_1$  is deep (read efficient). But, as  $N'_p$  increases the  $E_1$  traps fill up, so the number available drops and  $\tau_{\text{SRH}}$  actually increases until the shallower  $E_2$  traps come into play [*Srouer and McGarrity, 1988*, p.1448]. The  $E_3$  traps, near mid-band, are included for empirical accuracy [*Messenger and Ash, 1992*, p.215].

**Auger Recombination:** Eventually, as  $N'_p$  increases to the point of high-level injection ( $N'_p/N_{\text{no}} \gg 1$ ), the ever-decreasing lifetime predicted by (C.25) causes the second term of (C.23) to dominate. At that point, the recombination rate is limited by Auger recombination,<sup>43</sup> which does not depend on the presence of  $N_t$ , but instead allows for non-radiative, band-to-band tunneling in an indirect bandgap semiconductor such as Si through the inclusion of a third particle to conserve momentum, typically an neighboring  $e^-$  or  $h^+$  [*Messenger and Ash, 1992*, p.44]. In contrast to (C.24), the lifetime depends only on carrier concentration, rather than trap density, since  $\Gamma$  is fixed at  $\Gamma_A$  so that [*Kerns, 1989*, p.496]:

$$\tau_{A,p} = \frac{N'_p}{\Gamma_A} \quad (\text{C.26})$$

---

<sup>43</sup>There also exist radiative means of recombination involving the release of photons or phonons. In the latter case, the momentum and energy released by the recombination event are converted into acoustic waves launch along the crystal lattice. However, such mechanisms submit less readily to modeling [*Messenger and Ash, 1992*, p.25].

Below the Auger limit, radiation-induced increases  $\Delta N_t$  in the form of vacancy-related defects, lead to degradation of  $\tau_p$  that obeys a rate-balance equation of the form<sup>44</sup>

$$\begin{aligned}\frac{1}{\tau_p} &= \frac{1}{\tau_{po}} + \frac{\phi_D}{K_\tau} \\ \therefore \Delta\tau_p^{-1} &= \frac{\phi_D}{K_\tau}\end{aligned}\tag{C.27}$$

where  $\phi_D$  is the incident fluence of NIEL radiation and  $K_\tau$  is an empirically determined parameter known as the damage factor [*Srouer and McGarrity, 1988*, p.1448].<sup>45</sup> Complex dependencies subsumed in the choice of  $K_\tau$ , which is specific to the incident particle type and energy, include: substrate resistivity, initial impurity levels, injection level, and temperature [*Messenger and Ash, 1992*, p.216–221]. However, in all cases there is strong evidence that  $K_\tau$  scales linearly with NIEL, suggesting that despite the differences in generation and recombination, discussed in Section C.3.1 and Section C.3.2, the individuality of different PKAs may become homogenized through random collisional processes [*Holmes-Siedle and Adams, 2002*, [p.74–75].

The reciprocal relationship of (C.3.4), which also has been shown to govern displacement-generated degradation of diffusion lengths and mobility (see Section C.3.5) [*Srouer and McGarrity, 1988*, p.1448], dictates the form of the bipolar gain degradation in Section 2.1.2.1, since the BJT is a minority-carrier device.

### C.3.5 Majority Carrier Trapping

Whereas deep traps acting as recombination centers reduce minority-carrier lifetimes and thus gain in bipolar transistors, shallower trap centers associated with vacancy-impurity complexes immobilize majority carriers, thereby changing the conductivity

<sup>44</sup>If, instead of the minority carrier lifetime, its reciprocal, the minority carrier recombination frequency,  $f_{R,p} = 1/\tau_p$ , were the quantity of interest, this expression would simply state that  $\Delta f_{R,p} \propto \phi_D$ .

<sup>45</sup>Typical values for  $K_\tau$  for a pnp transistor at an injection level of  $10^{-3}$  are:  $2 \times 10^5$ – $4 \times 10^5$  s/cm<sup>2</sup>, for 1-MeV neutrons (standard to which all other particles are usually referenced);  $10^4$ – $5 \times 10^4$  s/cm<sup>2</sup> for 20-MeV protons; and  $3 \times 10^6$ – $5 \times 10^7$  s/cm<sup>2</sup>, for 3-MeV electrons [*Messenger and Ash, 1992*, p.739].

of doped diffusions. Specifically, acceptor traps such as the divacancy (in both  $-1$  and  $-2$  states), donor-vacancy ( $-1$ ), and, to a lesser extent, oxygen-vacancy ( $-1$ ) complexes, retain electrons from the conduction band, thereby depleting it and leading to higher resistivity in a process known as carrier removal [*Messenger and Ash, 1992*, p.241]. If the reaction rate coefficients for the production of the first two defects are denoted  $K_V$  and  $K_{DV}$ , respectively, then the acknowledged relationship governing the majority carrier concentration,  $N_n$ , under the influence of carrier removal is [*Messenger and Ash, 1992*, p.245]:

$$N_n = N_{no} e^{-2\phi_D K_{DV} K_V} \quad (C.28)$$

This decrease from  $N_{no}$  to  $N_n$  as a function of  $\phi_D$  maps directly to an increase in the resistivity of the bulk, n-type Si,  $\rho_n$ , since the latter is defined as  $\rho_n^{-1} = Q\mu_n N_n$ . So, it is not surprising that most commonly invoked formulation for  $\rho_n$  takes the form of [*Messenger and Ash, 1992*, p.242]

$$\rho_n = \rho_{no} e^{\phi_D / k_n} \quad (C.29)$$

where the exponential coefficient  $k_n$  is empirically determined but can be interpreted as the fractional density of trapped electrons according to the relation  $k_n = \frac{1}{2} K_{DV} K_V$  [*Messenger and Ash, 1992*, p.242].

Augmenting this increase with removed  $N_n$ ,  $\rho_n$  also grows, by definition, with NIEL-induced reductions in  $\mu_n$ . Typically, such  $\mu_n(\phi_D)$  variations are small relative to those of  $N_n(\phi_D)$ , but this relative primacy shifts with temperature and initial doping concentrations. When it proves significant, it is possible to factor out the effects of NIEL on the mobility term by fitting  $\mu_n(\phi_D)$  to a familiar rate-balance expression, using a semi-empirical damage coefficient,  $K_\mu$  [*Messenger and Ash, 1992*, p.243].<sup>46</sup>

$$\frac{1}{\mu_n} = \frac{1}{\mu_{no}} + \frac{\phi_D}{K_\mu} \quad (C.30)$$

---

<sup>46</sup>A typical value of  $K_\mu$  for neutron spectra incident upon 2  $\omega$ -cm n-type Si is  $\sim 3 \times 10^{18} (V - s)^{-1}$  [*Messenger and Ash, 1992*, p.243].

This degradation from the unirradiated mobility value,  $\mu_{\text{no}}$ , is caused by divacancy and donor-vacancy complexes that, having trapped electrons, effectively increase the density of Coulombic scatter centers for free carriers in transit. Specifically, if  $\mu_{\text{n}}$  is partitioned into a component due to scattering from phonon-precipitated energy band bending,  $\mu_{\text{nl}}$ , and a component due to Rutherford scattering from ionized dopant impurities,  $\mu_{\text{ni}}$ , according to the Conwell-Weisskopf formula [*Messenger and Ash, 1992*, p.22]:

$$\frac{1}{\mu_{\text{n}}} = \frac{1}{\mu_{\text{nl}}} + \frac{1}{\mu_{\text{ni}}} \quad (\text{C.31})$$

then the effect of NIEL is to increase the total number of impurity scattering centers that contribute to the second term, which is the sum of the densities of ionized donor dopants ( $N_{\text{D}}$ ) and active vacancy-related acceptor traps,  $\Delta N_{\text{n}} = |N_{\text{n}} - N_{\text{no}}|$ , where  $N_{\text{n}}$  is given by (C.28) [*Messenger and Ash, 1992*, p.248].



# Appendix D

## Antenna Noise in a Magnetoplasma

For a plasma wave receiver, the noise introduced by the front-end electronics and, in particular the LNA (cf. Footnote 1 of Chapter 3), should be confined below the combined thermal and shot generated by the receiving dipole.<sup>1</sup> Translating this consideration into a specification for the LNA in Section 3.1.3.2 requires knowledge of the antenna noise levels when operating in the magnetoplasma of the radiation belts. Thus, this appendix examines the theoretical predictions of this noise for electric as well as magnetic antennas and, for the former, proposes a unified model to describe the spectrum of this noise over the entire bandwidth of interest.

It assumes familiarity with: the definitions of the key plasma parameters in Section 1.1, including  $\lambda_D$  and  $f_p$ ; the effect of the geomagnetic field on particle motion described in Section A.2.1, particularly cyclotron motion with gyrofrequency  $f_c$  and gyroradius  $r_c$ ; and the basics of dipole antenna operation presented in Section 3.1.1.1. Leveraging these concepts, Section D.1, which comprises the bulk of this appendix, examines the expected noise for electric field measurements using a cylindrical dipole antenna, with which SVEPRE is intended to operate, as justified in Section B.1.2.

---

<sup>1</sup>This condition assumes that a sufficiently large antenna has been chosen for the mission orbit so as to keep the antenna noise below the minimum detectable signal. If this is not the case, the latter sets the bound for the LNA noise floor.

For completeness, Section D.2 offers an abbreviated but analogous treatment of noise in magnetic field sensors, primarily simple loops and search coils.

Before embarking on the mathematics, a brief notional clarification is in order. As explicated in Section 3.1.3, the primary noise metric in this work is the spot noise power spectral density (PSD), as it directly determines spectrogram quality. In the field of statistical signal processing, this is often represented by  $S_v(f)$ , with the subscript emphasizing that it describes the statistics of an underlying random voltage,  $v_n$ , whose PSD can be expressed in  $V^2/\text{Hz}$  (cf. Footnote 23 of Chapter 1), as is the convention in much of this document. Rather than this analytical description of the stochastic noise process, circuit designers often prefer to work with the measured fluctuation of  $v_n$  in terms of the mean-squared noise voltage,  $E_n = \langle v_n^2 \rangle$ . Having been integrated over the full measurement noise bandwidth  $\Delta f$  (cf. Footnote 22 of Chapter 3), this is not a spectral density, but (a proxy for) total power. However, the two are related through [Motchenbacher and Fitchen, 1973, p.10–11]:

$$S_v(f) = \frac{\langle v_n^2 \rangle}{\Delta f} = \frac{E_n}{\Delta f} \quad (\text{D.1})$$

Since it is shown that the modeling of the antenna noise results from describing its impedance in terms of lumped circuit elements, expediency dictates that the results of this appendix be expressed in terms the equivalent RMS noise voltage,<sup>2</sup> which is derived from  $E_n$  as simply  $e_n = \sqrt{E_n}$ . Notably,  $e_n(E_n)$  converges to the standard deviation(variance) of  $S_v(f)$  over  $\Delta f$  when the expected value of  $v_n^2$  is measured over an infinite duration.

## D.1 Electric Antennas

When minimizing dependencies on plasma parameters and pursuing low-noise applications at the expense of high-frequency performance, the cylindrical dipole

---

<sup>2</sup>On occasion it also proves useful to represent the noise through these circuit elements as a random current  $i_n$ , in which case similar conventions for denoting the PSD  $S_i(f)$ , mean-square noise current,  $I_n = \langle i_n^2 \rangle$ , and RMS noise current,  $i_n = \sqrt{I_n}$  are invoked, with the foremost pair of quantities related though  $\Delta f$  by analogy to (D.1).



antenna (hereafter referred to simply as a *dipole*) is preferred over a spherical double probe for electric field measurements, as discussed in Section B.1.2. Therefore, the following pertains to the long, symmetrical dipole of arm-length  $L_a$  and radius  $r_a$  invoked in Section 3.1.1.1.

Section D.1.1 expands the introduction to sheath effects in Section 3.1.3.2 to include the canonical results of Langmuir theory for dipoles, including the resistance and capacitance of different sheath types. Section D.1.2 then presents an approach to computing the antenna noise contributions over a range of plasma conditions by generalizing such resistances and reactances to describe its impedance. Finally, in Section D.1.3, a four-part piecewise noise model is constructed from the antenna impedance and applied to simulations of the nominal dipole in this work.

### D.1.1 Langmuir Theory

As mentioned in Section 3.1.3.2, the local violation of macroscopic electric neutrality that occurs near a conductor immersed in a plasma is known as a plasma sheath whose behavior, for the purposes of this work, can be well described by the electrostatic probe theory of Langmuir and Mott-Smith [*Langmuir*, 1929; *Mott-Smith and Langmuir*, 1926]. This theory describes the  $V_a$ - $I_a$  curve of a such a conductor in terms of its equilibrium floating potential,  $V_o$ , defined relative to the ambient plasma potential infinitely far away, which can be treated as ground [*Bittencourt*, 1995, p.281]. The sign of  $V_o$  gives rise to two types of sheaths—photoelectric ( $V_o > 0$ ) and positive-ion ( $V_o < 0$ )—whereas the slope of the  $V$ - $I$  curve yields the small-signal probe impedance.

#### D.1.1.1 Antenna Currents

The sign of the floating potential, and thus the sheath character, is determined by the balance between plasma electrons and ions incident upon the conductor and photo-electrons emitted from it under exposure to ultraviolet radiation. From Kirchhoff’s current law (KCL) for charge conservation, this results in the current

balance described by

$$I_a = I_e + I_i + I_{ph} \quad (D.2)$$

where  $I_a$  is the total antenna current,<sup>3</sup>  $I_e$  and  $I_i$  the currents of the incident plasma electrons and ions, respectively, and  $I_{ph}$  the current due to the emission of photoelectrons. The polarity of the terms in (D.2) is defined such that currents on the left(right) side of the equality flow out of(into) the terminals of the antenna, so  $I_e < 0$ .

For a two-component (proton/electron), Maxwellian plasma with respect to which the probe potential ( $V_a$ ) is calculated and only small deviations from equilibrium permitted, the currents on the right side of (D.2) obey Langmuir probe theory [Cauffman and Gurnett, 1972, p.374]. So, for a neutral probe ( $V_a = 0$ ), it can be shown that the current due to a particle,  $I_x$ , where  $x$  is either  $e$ ,  $i$ , or  $ph$ , is a direct function of its impact rate upon the probe,  $\nu_x$ , given by [Meyer-Vernet and Perche, 1989, p.2409]

$$\nu_x = \frac{S}{\sqrt{4\pi}} N_x v_T \quad (D.3)$$

where  $v_T$  is the thermal component of the particle velocity provided by  $kT$ . Observe that (D.3) simply describes the impact rate in terms of the surface area subtended by the probe ( $S$ ), and the number of particles per unit area that pass by it per unit time ( $N_x v_T$ ). For the three current components of (D.2) under neutral conditions, this implies [Fahleson, 1967; Hoegy and Brace, 1961, p.24,p.243]:

$$I_{pho} = S j_{ph} \quad (D.4a)$$

$$I_{eo} = -S N_e q \sqrt{\frac{kT_e}{2\pi m_e}} \quad (D.4b)$$

$$I_{io} = S N_i Q_i \sqrt{\frac{kT_i}{2\pi m_i}} \quad (D.4c)$$

where  $j_{ph}$  is the photoelectron current density, which is often determined empirically.<sup>4</sup>

<sup>3</sup>For an unbiased antenna, this value is zero; otherwise it is simply the value of the applied current, defined as flowing out of the antenna terminals in this convention.

<sup>4</sup>Typical values of  $j_{ph}$  range from  $1.5 \times 10^{-5}$ – $6 \times 10^{-5}$  A<sup>2</sup>/m [Cauffman and Gurnett, 1972, p.375]

As expected, all three composite currents are proportional to the surface area of a single dipole element,  $S_a = 2\pi r_a L_a$ . Intuitively,  $I_{ph}$  also depends upon illumination (going to zero at night), whereas  $I_e$  and  $I_i$  vary instead with plasma conditions.

Although sufficient for a neutral and stationary antenna, these electron(ion) currents must be extended to account for nonzero antenna voltage,  $V_a$  (spacecraft velocity,  $v_s$ ). The former is accomplished by incorporating the Boltzmann factor, which governs the density of plasma constituents in the presence of an applied potential at thermal equilibrium [Bittencourt, 1995, p.181–183]. When  $V_a < 0$ , the Boltzmann factor must be applied to  $I_e$  so that  $N_e$  sheath falls off exponentially near the antenna due to Coulomb repulsion. Conversely, for  $V_a > 0$ , the attraction of photoelectrons leads to a decrease in particle emission, represented by applying the Boltzmann factor to  $I_{ph}$ . Thus, the total electron and photoelectron currents,<sup>5</sup>

---

in the lower ionosphere to  $10^{-4} \text{ A}^2/\text{m}$  [Fahleson, 1967, p.243] in the topside ionosphere, although these even these are only good to an order of magnitude and should be considered approximate.

<sup>5</sup> The absence of a modified version of (D.6) for ions begs the question as to why their contribution is not subject to the Boltzmann factor. The answer lies in the Bohm criterion which is implicit in this formulation of the linearized, positive ion sheath produced by Debye shielding [Bittencourt, 1995, p.287]. The Bohm criterion

$$kT_i < m_i u_{io}^2$$

demand that the plasma ions effectively be considered cold, so that the kinetic energy associated with their drift at the plasma fluid velocity upon entering the sheath ( $u_{io}$ ) exceeds their thermal velocity [Chevalier, 2007, p.75].

In the case of a receiving antenna, a second, related assumption is also necessary if (D.4c) is to remain unmodified by the Boltzmann factor [Bittencourt, 1995, p.285]:

$$kT_i \gg qV_S(r)$$

where  $V_S(r)$  is the sheath potential, ranging from  $V_o$  at the antenna ( $r=0$ ) to zero at large distances away ( $r \rightarrow \infty$ ). Coupled with the Bohm criteria, this assumption that potential energy of the ions is small compared to their thermal velocity, implies  $N_i$  within the sheath is largely unaffected by the electrostatic field, as it is insufficient to counter their directed kinetic energy. In fact, for a Bohm sheath it is common to consider  $N_i \simeq N_{io}$  [Mlodnosky and Garriott, 1963, p.486] since these two approximations yield [Bittencourt, 1995, p.484–485]

$$N_i = \frac{N_{io}}{\sqrt{1 - \frac{2qV_S(r)}{m_i u_{io}^2}}} \simeq N_{io}$$

This expression only breaks down right near the probe, where the field of  $V_S(r) < 0$  is strong enough accelerate the ions.

Incidentally, since this acceleration implies  $u_i > u_{io}$  throughout the sheath, a more restrictive

modified from (D.4a) and (D.4b), are

$$I_{\text{ph}} = \begin{cases} I_{\text{pho}} & , \text{ for } V_{\text{a}} < 0 \\ I_{\text{pho}} e^{-qV_{\text{a}}/kT_{\text{ph}}} & , \text{ for } V_{\text{a}} > 0 \end{cases} \quad (\text{D.5a})$$

$$I_{\text{e}} = \begin{cases} I_{\text{eo}} e^{qV_{\text{a}}/kT_{\text{e}}} & , \text{ for } V_{\text{a}} < 0 \\ I_{\text{eo}} & , \text{ for } V_{\text{a}} > 0 \end{cases} \quad (\text{D.5b})$$

When addressing the motion of the satellite at constant velocity  $v_{\text{s}}$ , the disparity between the masses of ions and electrons dictates that  $(2kT_{\text{i}}/m_{\text{i}})^{1/2} < v_{\text{s}} \ll (2kT_{\text{e}}/m_{\text{e}})^{1/2}$  (cf. Footnote 5) [Cauffman and Gurnett, 1972, p.374]. This relationship results in the dependence of  $I_{\text{i}}$ , but neither  $I_{\text{e}}$  nor  $I_{\text{ph}}$ , on  $v_{\text{s}}$ , as the probe intercepts only the quasi-stationary ions while it flies.<sup>6</sup> To a good approximation, the resulting increase over  $I_{\text{io}}$  formulated by Sagalyn *et al.* [1963, p.205] (which it itself an approximation to the expressions of Hoegy and Brace [1961, p.52–55]) can be represented by restating (D.4c) as [Fahleson, 1967; Mlodnosky and Garriott, 1963, p.487, p.243] as

$$\begin{aligned} I_{\text{i}} &= SN_{\text{i}}Q_{\text{i}}\sqrt{\frac{kT_{\text{i}}}{2\pi m_{\text{i}}} + \frac{v_{\text{s}}^2}{16}} \\ &\simeq \frac{1}{4}SN_{\text{i}}Q_{\text{i}}\left[v_{\text{s}} + \sqrt{\frac{2kT_{\text{i}}}{\pi m_{\text{i}}}}\right] \end{aligned} \quad (\text{D.5c})$$

---

version of the Bohm criteria is often employed, which affirms the discrepancy between the ion thermal and drift velocities and demands the opposite relationship for electrons [Chevalier, 2007, p.75]:

$$m_{\text{e}}u_{\text{e}}^2 \ll kT \ll m_{\text{i}}u_{\text{i}}^2$$

This expression allows the electron inertia to be neglected, rendering  $N_{\text{e}}$  and  $N_{\text{ph}}$  subject to  $V_{\text{a}}$  via the Boltzmann factor in (D.5a) and (D.5b), even though  $|q|V_{\text{S}}(r) \ll kT_{\text{e}}$ .

<sup>6</sup>More formally, the random thermal motion of the electrons is sufficiently large that the intercepted population has no incremental average contribution.

### D.1.1.2 Sheath Character

To unify the preceding discussion across sheath types, assume an unbiased antenna ( $I_a = 0$ ) with constant ion current ( $I_i = I_{io}$ ) for simplicity and first consider the case of a low density plasma illuminated by the sun. When the ambient plasma electron current is not large enough to compensate for the emission of photoelectrons ( $|I_e| < I_{io} + I_{ph}$ ), the latter are attracted to the probe by the resulting positive  $V_o$ , thereby forming a photoelectric sheath whose thickness, according to (1.1), is given by the photoelectron screening distance [Cauffman and Gurnett, 1972, p.376]:

$$\lambda_{Dph} = \sqrt{\frac{kT_{ph}\epsilon_0}{N_{ph}q^2}} \quad (D.6)$$

On the other hand, at high ambient densities and low illumination levels, the photoelectric effect is not sufficient to offset the large incident electron current, so  $|I_e| > I_{io} + I_{ph}$ , and the accumulation of negative charge on the antenna due to  $I_e$  repels further electrons up to a distance of  $\lambda_{De}$  [Cauffman and Gurnett, 1972, p.376]. At this equilibrium, the probe assumes a negative floating potential and the absence of plasma electrons in the surrounding space-charge region screens the probe by leaving behind a positive-ion sheath. In the magnetosphere, the transition from a photoelectric sheath to a positive-ion sheath typically occurs when the density exceeds  $10^2$ – $10^3$   $\text{cm}^{-3}$  [Gurnett, 1998, p.125], so when traversing the plasmasphere on radiation-belt orbits, both forms are encountered.

Using this bifurcated reasoning, the floating potential of the unbiased antenna that results from setting  $I_a = 0$  in (D.2), is [Cauffman and Gurnett, 1972; Fahleson, 1967, p.374, p.243]:

$$V_o = \begin{cases} -\frac{kT_e}{q} \ln\left(\frac{-I_{eo}}{I_i + I_{pho}}\right) & , \text{ for positive ion sheath} \\ \frac{kT_{ph}}{q} \ln\left(\frac{I_{pho}}{-I_i - I_{eo}}\right) & , \text{ for photoelectric sheath} \end{cases} \quad (D.7)$$

### D.1.1.3 Sheath Resistance

When a small differential voltage,  $dV_a$ , is applied to the antenna terminals, there is a corresponding change in the particle current impinging on the antenna that, according to (D.2), changes the total current  $I_a$ . In a small-signal model, where the applied potential is considered a small deviation from the floating potential bias point, that is,  $V_a = V_o + dV_a$ , the current component that changes in phase with the applied voltage can be represented by a differential small signal resistance such that [Mlodnosky and Garriott, 1963, p.485]:

$$R_S = 2 \left. \frac{dV_a}{dI_a} \right|_{V_a=V_o} \quad (\text{D.8})$$

where the factor of two describes the series combination of the small signal resistances of each arm as seen from the differential antenna input (i.e.,  $\Delta V_a = 2dV_a$ ).<sup>7</sup> Equation (D.8) is known as the sheath resistance of an unbiased dipole, and models the power dissipation due to the loss of momentum associate with particle impacts in response to an applied potential. Substituting (D.5) into (D.2) and taking the derivative with respect to  $V_a$ , results in a quantity whose reciprocal in (D.8) gives [Cauffman and Gurnett, 1972, p.376,p.126]:

$$R_S = \begin{cases} 2 \frac{kT_e}{q} \frac{1}{I_i + I_{pho}} & , \text{ for positive ion sheath} \\ -2 \frac{kT_{ph}}{q} \frac{1}{I_i + I_{eo}} & , \text{ for photoelectric sheath} \end{cases} \quad (\text{D.9})$$

### D.1.1.4 Sheath Capacitance

When a small differential voltage is applied to the antenna terminals,  $dV_a$ , there is a resulting change in the sheath radius. For instance, in the case of a positive-ion sheath,

---

<sup>7</sup> In the discussion of antenna impedance throughout this document, all quantities are treated as differential. Since it is common in the literature to simply describe the resistance and capacitance of the individual dipole arms, this is a nonstandard choice. According to this convention, the differential voltage and current of the antenna,  $\Delta V_a$  and  $\Delta I_a$  respectively, are related to those of the individual arms  $V_{a+}$  and  $I_{a+}$  (or  $V_{a-}$  and  $I_{a-}$ ) by  $\Delta V_a = V_{a+} - V_{a-}$  and  $\Delta I_a = I_{a+} - I_{a-}$ , such that  $Z_a = \Delta V_a / \Delta I_a$ .

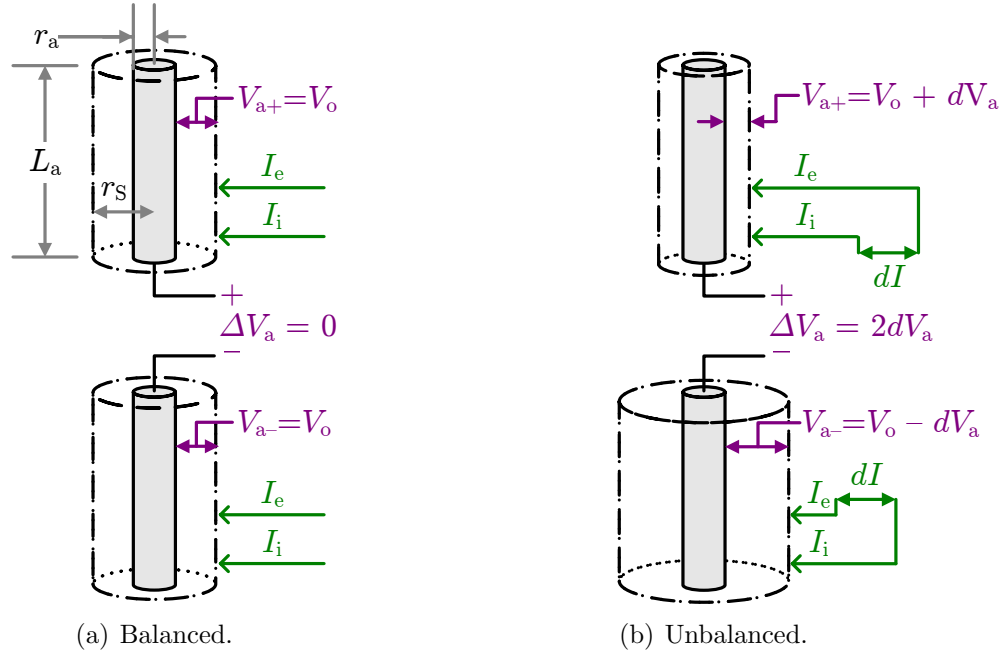


Figure D.1: Bias-dependent geometry of a positive-ion sheath surrounding a dipole antenna. As opposed to (a) the ideal, balanced case in which the sheath is cylindrically symmetric for  $\Delta V_a = 0$ , application of a (b) small positive bias ( $\Delta V_a = 2dV_a$ ) increases(decreases) the electron current to the positive(negative) arm, reducing(expanding) its sheath radius,  $r_s$ . Lengths of current arrows are proportional to magnitude. Dimensions exaggerated for clarity.

the radius around the more positive conductor collapses due to its higher affinity for electrons, while the sheath around the more negative conductor expands [Mlodnosky and Garriott, 1963, p.485–486], as shown in Figure D.1.<sup>8</sup> This expansion(contraction) increases(decreases) the ion space charge in the sheath and since this charge must be neutralized by the charge on the dipole according to Poisson’s equation,<sup>9</sup> there is a corresponding increase(decrease) in the antenna surface charge.

<sup>8</sup>Note that the definition and computation of the sheath radius are rather involved [Mlodnosky and Garriott, 1963, p.488]. So, although it is comparable to  $\lambda_{De}(\lambda_{Dph})$  for the a positive-ion(photoelectric) sheath, as discussed in Section D.1.1.2, it merits further consideration later.

<sup>9</sup> To isolate the sheath impedance, assume that the plasma beyond its radius is connected to an infinitely conducting ground so that no fields are able to penetrate it; by definition, this plasma is at zero potential. This eliminates all contributions of the antenna radiation resistance. It also implies the ion sheath charge is exactly balanced by the charge on the surface of the antenna [Wang, 1970, p.113–115].

In a gross simplification that assumes  $N_e = 0$  and  $N_i = N_{i0}$  within the radius of the sheath,  $r_s$  [*Jastrow and Pearse*, 1957, p.416],<sup>10</sup> its behavior is akin to that of the depletion region between the oppositely doped semiconductors. Thus, the charge balance in this situation can be modeled as a capacitance,  $C_S$ , by analogy with the depletion capacitance of a p-n junction. The reactive nature of this behavior is even more evident for an antenna, since the charge on its surface is  $90^\circ$  out of phase with its potential because  $E_a = -\nabla V_a = \rho_q / \epsilon_0$ , where  $\rho_q$  is the antenna surface charge density, such that the total charge of one element is  $Q_{a+} = Q_{a-} = 2\pi r_a L_a \rho_q$ .

In a small-signal model where, as above,  $V_a = V_o + dV_a$ , this current component that changes in quadrature phase with the applied voltage can be represented by a differential small-signal capacitance such that [*Mlodnosky and Garriott*, 1963, p.485]

$$C_S = \frac{1}{2} \left. \frac{dQ_a}{dV_a} \right|_{V_a=V_o} \quad (\text{D.10})$$

where the factor of one-half describes the series combination of the small-signal capacitances of each arm as seen from the differential input (cf. Footnote 7); (D.10) is the sheath capacitance of an unbiased dipole. By assuming that the sheath edge, located at radius  $r_s$  from the axis of the dipole in a cylindrically symmetric coordinate geometry, is an abrupt boundary between the infinitely conducting plasma and the space charge region, then the charge stored on each dipole arm,  $Q_a$  in (D.10), is [*Mlodnosky and Garriott*, 1963, p.488]

$$Q_a = -N_i Q_i \pi (r_s^2 - r_a^2) L_a \quad (\text{D.11})$$

To then model the relationship between the sheath radius and antenna potential required by (D.10), simply solve Poisson's equation under all the above assumptions to find [*Jastrow and Pearse*, 1957, p.416]:

$$2\epsilon_0 V_a = N_i Q_i \left[ -r_s^2 \ln\left(\frac{r_s}{r_a}\right) + \frac{1}{2} (r_s^2 - r_a^2) \right] \quad (\text{D.12})$$

---

<sup>10</sup>See Footnote 5 for a rudimentary justification of these conditions under the assumptions of a Bohm sheath.



Taking the derivatives of (D.11) and (D.12) with respect to  $r_s$ , evaluating them at  $V_o$ , and substituting into (D.10) gives a general result for the capacitance of the sheath, regardless of its composition,<sup>11</sup> as [*Mlodnosky and Garriott, 1963*, p.488]

$$C_S = \frac{\pi \epsilon_0 L_a}{\ln(r_{S_o}/r_a)} \quad (\text{D.13})$$

where  $r_{S_o}$  is the equilibrium sheath radius obtained from evaluating (D.12) at the floating potential.

Since  $C_S$  appears in parallel with  $R_S$  of (D.9), between the plasma ground and the antenna terminals, the complex, small-signal, differential sheath impedance is simply  $Z_S = R_S \parallel C_S$ . At frequencies above(below)  $\omega_S = 1/2\pi R_S C_S$ , the sheath exhibits a primarily capacitive(resistive) character. Notably,  $R_S$  depends much more heavily on the plasma parameters than  $C_S$  since the latter, as expected, is primarily a function of antenna geometry [*Gurnett, 1998*, p.127].

### D.1.2 Noise Sources

Broadly speaking, the two forms of noise afflict the measured voltage at the antenna terminals,  $\Delta V_a$ —thermal noise and shot noise. This section employs a set of piecewise approximations to render these noise behaviors mathematically tractable, as it is extremely difficult to derive analytical expressions that hold over the wide range of plasma conditions and wave frequencies encountered in the radiation belts.

#### D.1.2.1 Thermal Noise

For calculations of thermal noise, the probe is typically considered to be a grid antenna or filamental dipole whose surface area is negligible [*Meyer-Vernet and Perche, 1989*, p.2407]. When the plasma is homogeneous, stationary, and in thermal equilibrium

---

<sup>11</sup> Although the development in this section proceeded from the assumption of a positive-ion sheath within which  $N_e = 0$  and  $N_i = N_{i_o}$ , a similar assumption can be employed in the photoelectric case [*Gurnett, 1998*, p.126]. Since the resulting  $C_S$  of (D.13) is largely a function of geometry anyway, the only differences arise from the computation of  $r_{S_o}$  via (D.12).

with the probe, it has been shown by [*Meyer-Vernet*, 1979, p.5374] that the mean-squared noise generated at the antenna terminals by the random motion of charges in the plasma,  $e_T^2$ , simply reduces to the Nyquist formula,

$$e_T^2 = 4kT_a \Re\{Z_a\} \Delta f \quad (\text{D.14})$$

where  $T_a$  and  $Z_a$  represent the absolute temperature and overall impedance of the antenna. The strategy in Section D.1.3 is to undertake detailed derivations of  $Z_a$  under various circumstances to allow direct calculation of the thermal noise PSD from (D.14).

#### D.1.2.2 Shot Noise

Shot noise results from the random timing of impacts upon and emission from the surface of the antenna by discrete charge quanta.<sup>12</sup> For each DC current through the antenna,  $I_x$ , the exponential distribution of the time between charge arrivals gives rise to a Poisson process  $h_x$  of standard deviation  $Q$ , so the average impact/emission rate is  $\Gamma_x = I_x/Q$ . Thus, the mean-squared noise current resulting from each such process is

$$i_x^2 = \langle |H_x(f)|^2 \rangle \Gamma_x \Delta f = 2Q^2 \frac{I_x}{Q} \Delta f = 2Q I_x \Delta f \quad (\text{D.15})$$

where the folding that accompanies the use of a single-sided Fourier transform  $H_z(f)$  to determine the average power (read variance) of  $h_x$  results in the factor of two. Assuming an unbiased antenna, the cumulative shot noise from the three currents of

---

<sup>12</sup>To eliminate these impacts, insulated probes are sometimes flown, as on Geotail [*Matsumoto et al.*, 1994, p.64]. Although this approach proves valuable for Langmuir probes, the presence of the cladding can result in both high capacitance and reduced radiation efficiency that are highly undesirable for wave receivers.

(D.5) yields an equivalent mean-squared noise voltage,  $e_s^2$  of

$$e_s^2 = 2qI_x |Z_a|^2 \Delta f$$

$$= \begin{cases} 2qSN_e \sqrt{\frac{kT_e}{2\pi m_e}} e^{qV_o/kT_e} |Z_a|^2 \Delta f & , \text{ for positive ion sheath} \\ 2qSj_{ph} e^{-qV_o/kT_{ph}} |Z_a|^2 \Delta f & , \text{ for photoelectric sheath} \end{cases} \quad (D.16)$$

where  $x$  takes on values of either  $e$  or  $ph$  depending on the sign of the floating potential.

To simplify future computations, an alternative but logically equivalent method for representing shot noise in terms of the sheath resistance is now presented. After all, as described above,  $R_S$  already models the same random process—the exchange of energy at the antenna surface due to the impact or emission of electrons with a Maxwellian distribution of thermal velocities. Thus, the Johnson-Nyquist noise of  $R_S$  is numerically equivalent to the shot noise described by (D.16) according to

$$\begin{aligned} e_T^2|_{R_S} &= \frac{4kT_x}{R_S} |Z_a|^2 \Delta f \\ &= \frac{4kT_x}{2(kT_x/qI_x)} |Z_a|^2 \Delta f \\ &= 2qI_x |Z_a|^2 \Delta f \\ &= e_s^2 \end{aligned} \quad (D.17)$$

### D.1.2.3 Total Noise

Obviously, the total antenna noise must account for both the thermal and shot contributions. If (D.14) is employed to describe the former, then the shot noise can be incorporated using either (D.16) or (D.17). But, in the former case, when adding (D.16) to (D.14), sheath contributions must be ignored when calculating  $\Re\{Z_a\}$  in (D.14) by substituting the modified, sheathless impedance  $Z'_a$ ; this method treats sheath noise as shot type. In the latter case, using the full  $Z_a$  in (D.14), thereby including contributions from  $R_S$ , implicitly handles the addition of (D.17); this method treats sheath noise as thermal. To clarify, it would be redundant to both

include  $R_S$  in the  $\Re\{Z_a\}$  term of (D.14) and add to it (D.16), because the former step already accounts for the sheath noise via the effective thermal noise of (D.17).

Thus, the total noise of the antenna, as represented by mean-square noise voltage  $e_a^2$ , can be computed either in terms of  $Z'_a$ , as

$$e_a^2 = e_T^2 + e_s^2 = \begin{cases} \left( \frac{4kT_e}{R'_a} + 2qI_x \right) |Z_a|^2 \Delta f & , \quad \text{for } Z_a = R_a \parallel jX_a \\ (4kT_e \Re\{Z'_a\} + 2qI_x |Z_a|^2) \Delta f & , \quad \text{for } Z_a = R_a + jX_a \end{cases} \quad (\text{D.18})$$

or in terms of the total antenna impedance  $Z_a$  (which includes  $R_S$ ) as

$$e_a^2 = e_T^2 + e_s^2 = \begin{cases} \frac{4kT_e}{R_a} |Z_a|^2 \Delta f & , \quad \text{for } Z_a = R_a \parallel jX_a \\ 4kT_e \Re\{Z_a\} \Delta f & , \quad \text{for } Z_a = R_a + jX_a \end{cases} \quad (\text{D.19})$$

both of which allow direct computation whether the antenna impedance is derived in terms of a parallel ( $Z_a = R_a \parallel jX_a$ ) or series ( $Z_a = R_a + jX_a$ ) equivalent impedance topology.

### D.1.3 Dipole Impedance

While the impedance of a dipole in free space demonstrates a straightforward dependence on wave frequency,  $f$ , immersion in a thermal plasma drastically alters this result. In particular,  $Z_a$  demonstrates a strong resonance at  $f_p$ , the mathematics of which are quite complex, limited in their generality, and beyond the scope of this appendix. Meanwhile, at frequencies well above or below  $f_p$ , the effective impedance varies from nearly that of an antenna in free space to simply that of the plasma sheath itself. Consequently, the analysis to follow is divided according to broad frequency regions over each of which the impedance is captured by a single model. These are delineated by the relationship of the normalized wave frequency  $f' = \omega'/2\pi = f/f_p$  to unity.

Although the dominant contributions to  $Z_a$  are substantially different across the

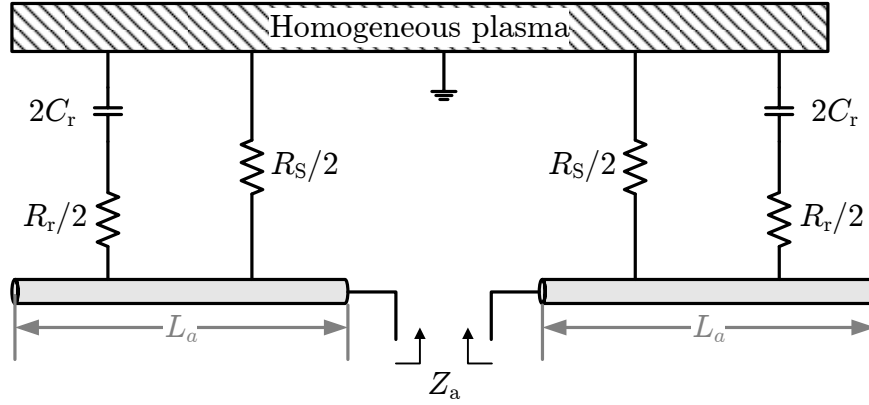


Figure D.2: Generalized model of dipole antenna impedance. In a given frequency regime, the differential antenna impedance,  $Z_a$ , is expressed as a combination of lumped elements representing losses to the sheath ( $R_s$ ) and wave fields ( $R_r$ ,  $C_r$ ) whose relative sizes vary. Although depicted as grounded, distant plasma is not subject to this restriction in all frequency regimes.

frequency range of  $f'$ , a generalized model of the total antenna impedance can be constructed as shown in Figure D.2 [Chevalier, 2007; Meyer-Vernet and Perche, 1989, p.2409]. In addition to sheath effects, this model captures the radiation impedance,  $Z_r$ , in terms of resistance  $R_r$ <sup>13</sup> and capacitance  $C_r$ .<sup>14</sup>

The appearance of  $R_s$  in parallel with  $Z_r$ , rather than in series as proposed by many other authors merits some qualitative comments. Without loss of generality, the series representation of the real and imaginary components of the radiation impedance

<sup>13</sup> Of primary concern here is the portion of the radiation resistance responsible for sensing (and, by reciprocity, exciting) plasma or electroacoustic waves,  $R_{r,pw}$  [Whale, 1963a, p.421]. Indeed, this greatly exceeds the component of  $R_r$  responsible for energy associated with ‘normal’ or electromagnetic waves,  $R_{r,nw}$ , for all cases except  $f' \gg 1$  [Schiff, 1970, p.1489]. To see why, recall that for a short dipole, the free space radiation resistance [Stutzman and Thiele, 1998, p.46]:

$$R_{r,nw}|_{\text{free space}} = 20\pi^2 \left( \frac{2L_a}{\lambda} \right)^2 = 20(kL_a)^2$$

is already quite small since  $kL_a \ll 1$ . But, in a cold, isotropic plasma, this is modified by the relative permittivity,  $K_\epsilon = \sqrt{1 - f'^{-2}}$  [Whale, 1963a, p.416]. Unless  $f' \gg 1$ ,  $R_{r,nw}$  is even smaller than its free space value, vanishing completely when  $f' < 1$ . Thus, in all but Section D.1.3.4,  $R_{r,nw}$  can be ignored, leaving  $R_r = R_{r,pw}$  [Balmain, 1965, p.564].

<sup>14</sup>The designation of  $C_r$  as the radiation capacitance is purely for subscript consistency—clearly the reactive component of its impedance cannot radiate any power. Instead, this element merely subsumes all reactive terms in  $Z_a$  from sheath effects to the free-space capacitance of (3.18).

in terms of  $Z_r = R_r + jX_r$  where  $X_r = -1/\omega C_r$  is standard practice [*Whale, 1963a*, p.415–416].<sup>15</sup>  $R_r$  accounts for the power radiated into the plasma as displacement current in order to satisfy continuity with the antenna conduction current [*Stutzman and Thiele, 1998*, p.8], whereas  $X_r$  represents the energy driving the oscillating charge distribution on the antenna surface; for sinusoidal fluctuations, this charge and its electric field are in phase quadrature with the current, the former being its integral. In the presence of a sheath,  $X_r$  is governed by the neutralizing effect of the shielding charges, as discussed in Section D.1.1.4, so  $C_r$  approaches  $C_s$  under electrostatic conditions ( $f' \rightarrow 0$ ). Meanwhile,  $R_s$  represents an alternate but parallel means of antenna-plasma power transfer due to the momentum exchange from carrier impacts/emissions, as described in Section D.1.1.3, the quantum nature of which is not captured by Maxwell's equations governing  $R_r$ .<sup>16</sup> As such,  $R_s$  and the shot noise it represents should appear in parallel with  $Z_r$  under all conditions [*Meyer-Vernet and Perche, 1989*, p.2409]. Subsequent discussions explain simplifications to this model based upon the relative sizes of its components in the various frequency regimes.<sup>17</sup>

### D.1.3.1 Low-Frequency Regime

At frequencies well below  $f_p$ ,  $f' \ll 1$ , consideration of the dipole impedance centers on the sheath contributions since the coupling to the plasma, and thus the radiation resistance for plasma waves, is dominated by the inhomogeneous sheath region near the antenna, rather than the homogeneous background. That is,  $R_r$  can be neglected

---

<sup>15</sup>The antenna is presumable constructed of good (i.e., perfectly) conducting material, so that Ohmic losses can be ignored [*Stutzman and Thiele, 1998*, p.44].

<sup>16</sup>The neglect of the physical presence of the antenna, which is represented as a current sheet, and the prevention of electron exchange between the plasma and the conductor, imposed by a rigid boundary condition, are well-known limitations of the induced emf method used to calculate  $Z_r$  throughout this section [*Balmain, 1965*, p.565].

<sup>17</sup>Since  $R_s$  appears in parallel with the series combination of  $R_r$  and  $C_r$ , it is very cumbersome to construct the  $Z'_a$  required by (D.18). Ideally, given a fully parallel(series) representation of  $Z_a$  in terms of  $R_{r\parallel}$ ,  $C_{r\parallel}$ , and  $R_{s\parallel}$  ( $R_{rs}$ ,  $C_{rs}$ , and  $R_{ss}$ ), the thermal noise of  $R_s$  could be ignored simply by letting  $R_{s\parallel} \rightarrow \infty$  ( $R_{ss} \rightarrow 0$ ), thereby eliminating its noise contribution without changing the relevant impedance. But, instead of the performing the series-to-parallel transformation to achieve one of these representations, which would only be valid over a narrow frequency range, it is assumed that  $R_r = R_{r\parallel} = R_{rs}$  and  $C_r = C_{r\parallel} = C_{rs}$ .

[*Mlodnosky and Garriott, 1963*, p.486].<sup>18</sup> In addition, the reactive portion of the radiation impedance is presumably dominated by  $C_S$ , since  $\rho_q$  is governed by the thermally driven electrostatic shielding rather than the comparatively small wave fields (cf. Footnote 5), allowing  $C_A$  to be omitted and yielding  $Z_a = R_S \parallel C_S = Z_S$  [*Mlodnosky and Garriott, 1963*, p.486]. Thus,

$$\Re\{Z_a\} = \Re\{Z_S\} = \Re\left\{\frac{R_S}{1 + j\omega R_S C_S}\right\} = \frac{R_S}{1 + \omega^2 R_S^2 C_S^2} \quad (\text{D.20})$$

Correspondingly, with the use of the series form of (D.19), since  $Z'_a$  makes little sense here, the noise seen at the terminals of the antenna is:

$$e_a^2 = \frac{4kT_e R_S}{1 + \omega^2 R_S^2 C_S^2} \quad (\text{D.21})$$

Depending upon the sheath character, the corresponding  $R_S$  from (D.9) should be substituted into (D.21). In only accounting for the shot noise of  $R_S$ , which is effectively due to those particles which reach the antenna, this result ignores noise contributions from the fields induced on the antenna either by particles in the plasma beyond the sheath (which is implicitly assumed to be grounded according to Footnote 9) or by those which enter the sheath but never actually contact the conductors.

### D.1.3.2 Mid-Frequency Regime

For  $f' < 1$ , the imminent onset of the plasma frequency resonance begins to alter the nature of the antenna's resistive component, giving rise to modeling complexities. As a result, this problem has been historically been treated with both the full, Vlasov kinetic theory embodied by (1.10), and with the hydrodynamic fluid

---

<sup>18</sup>In the parlance of Footnote 13, the strong plasma coupling for  $f' \ll 1$  in the low-frequency regime minimizes the effect of  $R_{r,nw}$ , while the dominance of sheath effects within that coupling renders  $R_{r,pw}$  negligible. The presence of a positive-ion sheath is commonly subsumed into an effective relative permittivity  $K'_e = \sqrt{1 - f''^{-2}}$  derived from  $f''$ , which accounts for the lower in electron density (and, thus, lower  $\omega_{pe}$ ) within the sheath [*Whale, 1964*, p.453]. The effect of larger  $K'_e$  is to diminish both  $R_{r,nw} \propto \sqrt{K'}$  and  $R_{r,pw} \propto 1 - K'/\sqrt{K'}$  [*Whale, 1963b*, p.472], relative to  $R_S$ .

approximations such as those encapsulated by the moments of Table 1.1.<sup>19</sup> Typically, the former(latter) has been applied to isotropic(anisotropic) plasmas,<sup>20</sup> with sheath inhomogeneities frequently omitted in both cases. Although cold plasma results can be extended to include finite temperature through the inclusion of a scalar pressure term in the hydrodynamic equations [*Chevalier, 2007*, p.7] (e.g. [*Wang and Bell, 1972*]), the more difficult pursuit of kinetic theory in this regime [*Balmain, 1972*, p.772] is necessary to accurately model the dispersion relation for plasma waves as their periods grow short enough that a cold, thermally equilibrated plasma can no longer be assumed [*Schiff, 1970*, p.1489]. Specifically, the component of  $R_r$  below the plasma frequency due to Landau damping (cf. Footnote 26 of Chapter A) is only apparent when using the dispersion relation of Vlasov kinetic theory in the range  $f' < 1$  [*Kuehl, 1966*, p.975].

In addition to omitting collisions and the ambient magnetic field, as noted above, seeking a rigorous, closed-form derivation using kinetic theory necessitates the approximation of a grid antenna in a homogeneous plasma, effectively neglecting shot impacts and sheath coupling. Although compensation for the former is simple and additive [*Meyer-Vernet and Perche, 1989*, p.2407], it is of little consequence since the resonant behavior overwhelms such second-order, stochastic effects. But, the more difficult inclusion of the sheath reveals substantial deviations from otherwise approximated solutions [*Meyer-Vernet et al., 1978*, p.71]. To begin, both shot noise and sheath effects are neglected. Later, corrections to the impedance expressions address these shortcomings.

The induced emf method for determination of receiving antenna impedance,  $Z_a$

---

<sup>19</sup>Not all hydrodynamic treatments employ the moment method. As an example, *Wang and Bell* [1969] use a spatial Fourier transform of the phasor representations of Maxwell's equations for a linearized hydrodynamic fluid to arrive at full-wave solutions in terms of the 'principal-polarized' modes. Others have employed even more approximations via quasi-electrostatic theory [*Balmain, 1964*, p.605].

<sup>20</sup>For analytical tractability, kinetic formulations for warm (or compressible) plasmas tend to avoid the anisotropy that would result from the presence of magnetic field, whereas hydrodynamic theory is used to treat magnetoplasmas without finite temperature, deemed cold (or incompressible) [*Balmain, 1972*, p.772]. However, there exist notable exceptions, including the use of tensor pressure theory to apply hydrodynamics to warm plasmas by *Meyer and Vernet* [1974] and use of kinetic theory for anisotropic plasmas by *Nakatani and Kuehl* [1976].



[[Balmain, 1965](#), p.565] simply performs the integration of the current density along the antenna,  $\mathbf{J}_a(l)$ , against the field to be measured,  $\mathbf{E}(l, t)$ , as inferred from the Poynting theorem. Once normalized by the squared magnitude of the peak current,  $I_0$ ,<sup>21</sup> this gives [[Schiff, 1970](#), p.1490]

$$Z_r = -\frac{1}{|I_0|^2} \int_{-L_a}^{L_a} \mathbf{E}(l) \cdot \mathbf{J}_a^*(l) \, dl \quad (\text{D.22})$$

or, in Fourier space, [[Schiff, 1970](#), p.1490]

$$Z_r = \frac{1}{(2\pi)^3 |I_0|^2} \int_0^\infty \mathbf{E}(K) \cdot \mathbf{J}_a^*(K) \, dK \quad (\text{D.23})$$

where the asterisk denotes complex conjugate of a phasor quantity.

For an isotropic, Maxwellian plasma, wherein  $f_c \ll f_p$ , and assuming a triangular current distribution along the axis of the antenna for  $|l| < L_a$ ,<sup>22</sup> namely

$$\mathbf{J}_a^*(l) = \frac{I_0}{2\pi r_a} \left[ 1 - \frac{|l|}{L_a} \right] \delta(r - r_a) \hat{\mathbf{l}} \quad (\text{D.24})$$

it can be shown [[Schiff, 1970](#), p.1491] that the antenna impedance for plasma waves reduces to the familiar

$$Z_r = \frac{4j}{\pi^2 \epsilon_0 \omega} \int_0^\infty \frac{F_1(K L_a) J_0^2(K r_a)}{D_L(\omega, K)} \, dK \quad (\text{D.25})$$

where  $J_0$  is the ordinary zero-order Bessel function and the following definitions from

---

<sup>21</sup>The peak current always occurs at the antenna terminals, so  $I_0 = I(0)$ .

<sup>22</sup>Although radiation-belt plasma is neither in thermal equilibrium (being practically collisionless) or isotropic (being magnetized) the assumption of an isotropic plasma with a Maxwellian velocity distribution is typically employed near the plasma frequency because it produces good(better) approximations of the antenna noise(impedance) [[Meyer-Vernet and Perche, 1989](#), p.2407]. The approximation of a triangular current distribution is much less easily justified [[Balmain, 1965](#); [Chevalier, 2007](#), p.565,p.53–54], but its traditional adoption in exchange for restricting the results to short dipoles [[Balmain, 1964](#), p.609] is sufficient for this work, where it is valid since  $r_a \ll \lambda_D$  and  $kL_a \ll 1$  [[Meyer-Vernet and Perche, 1989](#), p.2406].

*Kuehl* [1966, p.972] are adopted for the dipole:<sup>23</sup>

$$F_1(y) = \frac{y\text{Si}(y) - \frac{y}{2}\text{Si}(2y) - 2\sin^4\left(\frac{y}{2}\right)}{y^2} \quad (\text{D.26})$$

$$D_L(\omega, K) = 1 - \frac{1}{2\lambda_{\text{De}}^2 K^2} Z'_p \left( \frac{\omega}{K} \sqrt{\frac{m_e}{2kT_e}} \right) \quad (\text{D.27})$$

By expressing  $\mathbf{E}(K)$  in terms of  $\mathbf{J}_a K(u)$  using the  $D_L(\omega, K)$  to describe the plasma permittivity, the preceding development of (D.25) from the induced emf method and a triangular current distribution was left sufficiently general that it applies to both hydrodynamic and kinetic theory. However, the choice of the latter to express  $D_L(\omega, K)$  in (D.27),<sup>24</sup> reflects the aforementioned preference.

To evaluate the expression for  $Z_r$  in this frequency regime, further assume that the antenna is filamental ( $r_a \ll L_a$  and  $Kr_a \ll 1$ ) and long compared to the Debye length ( $L_a \gg \lambda_{\text{De}}$  and  $KL_a \ll 1$ ). In these limits,  $F_1(y) \simeq \pi/4y$  and  $|D_L| \simeq 1 + (K\lambda_{\text{De}})^{-2}$ , so the resulting antenna resistance and reactance simplify to [*Meyer-Vernet and Perche*, 1989; *Schiff*, 1970, p.2409,p.1492]:

$$R_r = \Re\{Z_r\} = \frac{\sqrt{\pi/2}}{4\epsilon_0\omega_{\text{pe}}L_a} = \frac{1}{4\epsilon_0} \sqrt{\frac{\pi m_e}{2k}} \times \frac{\lambda_{\text{De}}}{L_a} \times \frac{1}{\sqrt{T_e}} \quad (\text{D.28})$$

$$X_r = \Im\{Z_r\} = -\frac{\ln(\lambda_{\text{De}}/r_a)}{\pi\epsilon_0\omega L_a} \quad (\text{D.29})$$

---

<sup>23</sup>In (D.26), the sine integral function has been denoted by

$$\text{Si}(y) = \int_0^y \frac{\sin t}{t} dt$$

and, in (D.27),  $Z'_p$  refers to the longitudinal plasma dispersion function for a Maxwellian distribution, tabulated and defined by *Fried and Conte* [1961, p.1] as having real part proportional to the Hilbert transform of a Gaussian.

<sup>24</sup>For hydrodynamic theory, the dispersion function corresponding to (D.27) would be [*Schiff*, 1970, p.1490]:

$$D_L(\omega, K) = 1 - \frac{1}{(\omega/\omega_{\text{pe}})^2 - 2\lambda_{\text{De}}^2 K^2}$$

From (D.29) it is clear that the capacitive portion of the antenna impedance,

$$C_r = -\frac{1}{\omega X_r} = \frac{\pi\epsilon_0 L_a}{\ln(\lambda_{De}/r_a)} \quad (\text{D.30})$$

is still dominated by the capacitance of the sheath in this regime, though it differs from (D.13) in using a sheath radius of  $\lambda_{De}$  rather than  $r_{So}$ .

From this result, it is typically concluded [*Gurnett, 1998*, p.126] that once a non-zero radiation impedance is introduced, the sheath radius can be approximated simply as the Debye length of the sheath's governing charges, rather than solving (D.12) to determine the actual sheath radius as a function of  $V_a$ . That is, if  $L_a \gg \lambda_{De} \gg r_a$ , which is the case for the radiation-belt altitudes ( $2 \ll L \ll 7$ ) and if the antenna lengths of interest (here,  $L_a = 10$  m) satisfy  $L_a/r_a \geq 100$  (i.e.,  $r_a \leq 10$  cm), then the sheath can be approximated as having uniform thickness across the antenna, with a capacitance equal to that of a coaxially aligned pair of the conductors whose interior is treated as free-space (cf. Section D.1.1.4), so [*Cauffman and Gurnett, 1972*, p.376].<sup>25</sup>

$$C_s = \begin{cases} \frac{\pi\epsilon_0 L_a}{\ln(\lambda_{De}/r_a)} & , \text{ for positive ion sheath} \\ \frac{\pi\epsilon_0 L_a}{\ln(\lambda_{Dph}/r_a)} & , \text{ for photoelectric sheath} \end{cases} \quad (\text{D.31})$$

Using the modified sheath radius of (D.31) and no longer neglecting  $R_r$  as in the low-frequency regime, the equivalent series impedances needed for (D.18) and (D.19)

---

<sup>25</sup>To reconcile (D.31) and (D.13) intuitively, note that once the grounded plasma restriction used to derive the equilibrium capacitance in (D.13) is removed (cf. Footnote 9), such that signals can be radiated into the plasma, only a fraction of the antenna potential is dropped across the sheath. Thus, the potential in response to which the antenna charges redistribute is only a fraction of the potential difference applied to the antenna terminals. This effectively increases the capacitance and results in the smaller sheath radius since, typically,  $\lambda_D < r_{So}$ .

are

$$\Re\{Z'_a\} = \Re\left\{R_r + \frac{1}{j\omega C_r}\right\} = R_r \quad (\text{D.32})$$

$$Z_a = \left(R_r + \frac{1}{j\omega C_r}\right) \parallel R_s = \frac{R_s (1 + j\omega C_r R_r)}{1 + j\omega C_r (R_r + R_s)} \quad (\text{D.33})$$

Employing (D.32) and (D.33) to compute the noise from the series forms of (D.18) and (D.19), respectively, yields:

$$e_a^2 = 4kT_e R_r + 2qI_x R_s^2 \left( \frac{1 + \omega C_r^2 R_r^2}{1 + \omega^2 C_r^2 (R_r + R_s)^2} \right) \Delta f \quad (\text{D.34})$$

$$\begin{aligned} e_a^2 = & 4kT_e R_r \left( \frac{\omega^2 C_r^2 R_s^2}{1 + \omega^2 C_r^2 (R_r + R_s)^2} \right) \\ & + 4kT_e R_s \left( \frac{1 + \omega C_r^2 R_r^2}{1 + \omega^2 C_r^2 (R_r + R_s)^2} \right) \Delta f \end{aligned} \quad (\text{D.35})$$

Notably, invoking the definition of  $R_s$  in (D.9) reveals that the second terms of (D.34) and (D.35) are identical, whereas the disparity between their first terms results from the approximation described in Footnote 17 and vanishes when taking the limit as  $R_s \rightarrow \infty$ .

Proceeding from (D.34) given this equivalence and assuming that  $R_r \ll R_s$  since the radiated power remains small for  $f' < 1$ ,

$$e_a^2 = 4kT_e R_r + 2qI_x \left( \frac{R_s^2}{1 + \omega^2 C_r^2 R_s^2} + \frac{\omega C_r^2 R_r^2 R_s^2}{1 + \omega^2 C_r^2 R_s^2} \right) \Delta f \quad (\text{D.36})$$

Next, to simplify the shot noise (second) term, note that the second fraction within the parenthesis is always be negligible in this frequency regime, as long as  $(R_s C_r)^{-1} \ll$

$\omega \ll (R_r C_r)^{-1}$  [*Meyer-Vernet and Perche*, 1989, p.2409]. Thus, (D.36) reduces to

$$\begin{aligned} e_a^2 &= \frac{\lambda_{De} \sqrt{\pi m_e k T_e}}{\sqrt{2} \epsilon_0 L_a} + \frac{2^{3/2} r_a \sqrt{m_e k T_e} \ln^2(\lambda_{De}/r_a)}{\pi^{3/2} \epsilon_0 L_a} \frac{1}{f'^2} e^{qV_o/kT_e} \Delta f \\ &= \frac{1}{\epsilon_0 L_a} \sqrt{\frac{2m_e k T_e}{\pi}} \left( \frac{\pi \lambda_{De}}{2} + \frac{2r_a \ln^2(\lambda_{De}/r_a)}{\pi f'^2} e^{qV_o/kT_e} \right) \Delta f \end{aligned} \quad (D.37)$$

after substitution of (D.5b), (D.28), and (D.31) for positive ion sheaths.

As promised, (D.37) includes a term to address shot noise that would otherwise have been omitted from the grid antenna derivation (e.g., [*Schiff*, 1970]). But, no attention has yet been paid to the assumption of plasma homogeneity inherent in the Nyquist formulation of the noise. Since the plasma is clearly inhomogeneous in the sheath region surrounding the antenna, it is reasonable to assume that the actual resistance of the antenna at frequencies just below  $f_p$  should be higher than expressed in (D.28) and (D.29).

In fact, *Meyer-Vernet et al.* [1978, p.70] shows that the mid-frequency resistance increases by several orders of magnitude when expressions are modified to account for sheath inhomogeneities. Specifically, when modeled with an abruptness coefficient,  $\alpha_S$ ,<sup>26</sup> rather than as a vacuum sheath as in the formulation of [*Gurnett*, 1998], the real part of the antenna impedance exhibits secondary resonances below  $f_p$  for  $0.8 < f' < 1$ . However, the locations of these peaks depends strongly on the chosen value of  $\alpha_S$ , which is empirical.

Thus, for simplicity, this treatment does not precisely model the noise properties very close to the plasma frequency. Results given in the section can be applied over  $0.8 < f' < 0.95$  assuming  $\alpha_S > 0.5$  with the realization that, while the maximum value of the noise floor is bounded by the expressions in the next section, resonant peaking may occur over the noted interval if, in practice,  $\alpha_S < 0.5$  [*Meyer-Vernet et al.*, 1978, p.71].

---

<sup>26</sup>Intriguingly, this model is logically equivalent to that used to capture the abruptness of graded germanium diffusions in SiGe HBTs [*Hastings*, 2006, p.356].

### D.1.3.3 Resonant Regime

At  $f' \simeq 1$ , the antenna impedance experiences a resonant peak the mathematics surrounding which are exceedingly complex. Since the peak is quite narrow relative the overall bandwidth of interest, approximate results for the maximum responses are sufficient to bound the model in lieu of an analytical expression.

*Meyer-Vernet et al.* [1978] indicates that in this regime, thermal noise dominates and is fundamentally dependent upon the induced antenna potential due to incident plasma waves of wave number

$$k_p = \frac{1}{\lambda_{De}} \sqrt{\frac{f'^2 - 1}{3}} \quad (\text{D.38})$$

provided  $k\lambda_{De} \ll 1$ . For antennas that satisfy  $L_a \gg \lambda_D$  this peak occurs at normalized frequency

$$f'_{\text{peak}} \simeq 1 + 8 \left( \frac{\lambda_{De}}{L_a} \right)^2 \quad (\text{D.39})$$

with a value given by

$$e_T^2 = \frac{0.04}{\epsilon_0} \frac{L_a}{\lambda_{De}} \sqrt{\frac{\pi m_e k T_e}{2}} \Delta f \quad (\text{D.40})$$

### D.1.3.4 High-Frequency Regime

For frequencies exceed the plasma frequency as  $f' \gg 1$ , both the resonant behavior of the antenna and the sheath effects are negligible. In essence, the antenna behaves as though in free space and, consequently, exhibits a primarily capacitive impedance characteristic of short dipoles. Neglecting plasma effects and assuming once again that  $L_a \gg \lambda_{De}$  allows the approximations of  $F_1(y) \simeq \pi/4y$  and  $|D_L| \simeq 1$  in (D.26) and (D.27), respectively, where the latter is obvious since there is no plasma dispersion

[[Schiff, 1970](#), p.1493]. The impedance resulting from these simplifications is

$$R_r = \Re\{Z_r\} = \frac{\omega_p^2}{2\epsilon_0\omega^3 L_a} = \frac{1}{2\epsilon_0} \sqrt{\frac{m_e}{k}} \frac{\lambda_{De}}{L_a} \frac{1}{\sqrt{T_e}} \frac{1}{f^3} \quad (\text{D.41})$$

$$X_r = \Im\{Z_r\} = -\frac{\ln(L_a/r_a) - 1}{\pi\epsilon_0\omega L_a} \quad (\text{D.42})$$

Confirming the qualitative description of this regime as being equivalent to free space,  $X_r$  dominates  $R_r$  with increasing frequency above  $f_p$ , such that the impedance in the limit is given by strictly  $C_r$ , where

$$C_r = -\frac{1}{\omega X_r} = \frac{\pi\epsilon_0 L_a}{\ln(L_a/r_a) - 1} \quad (\text{D.43})$$

matches the well-known definition of  $C_A$  in [\(3.18\)](#).

Since shot effects are irrelevant in his regime,<sup>27</sup> the total noise is given by the thermal behavior

$$e_T^2 = 4kT_e \Re\{Z_a\} = \frac{2\lambda_{De} \sqrt{m_e k T_e}}{\epsilon_0 L_a f^3} \Delta f \quad (\text{D.44})$$

#### D.1.4 Summary

Table [D.1](#) summarizes the impedances and noise levels over each of the frequency regimes described above. Together with the nominal plasma and antenna parameters of Table [D.1.4](#), these model equations serve as the basis of the code for simulating the noise predictions at  $L=2$  and  $L=4$  shown in Figure [3.9](#).

## D.2 Magnetic Antennas

In space science, magnetic field measurements are often performed with one of two designs: simple loop or search coil. As the name implies, the loop design consists of  $N_a$  turns of wire wound into standard geometry (e.g., circle, square, triangle, etc.).

---

<sup>27</sup>The omission of  $R_S$  is justified intuitively from the free-space treatment, as the sheath does not have time to form, so there is no net charge accumulation.

Regime	Range	Effective resistance $R_a = \Re\{Z_A\}$	Effective reactance $X_a = \Im\{Z_A\}$	Total noise PSD (thermal + shot) $S_a(f) = E_n/\Delta f$
Low	$f \ll f_{pe}$	$\frac{R_S}{1 + \omega^2 R_S^2 C_S^2}$	$-\frac{j\omega R_S^2 C_S}{1 + \omega^2 R_S^2 C_S^2}$	$\frac{4kT_e R_S}{1 + \omega^2 R_S^2 C_S^2}$
Mid <sup>a</sup>	$f < f_{pe}$	$R_r + \frac{1}{\omega^2 R_S C_r^2}$	$\frac{\ln(\lambda_{De}/r_a)}{\pi \epsilon_0 \omega L_a}$	$\frac{\sqrt{2m_e k T_e}}{\sqrt{\pi \epsilon_0 L_a}} \left( \frac{\pi \lambda_{De}}{2} + \frac{2r_a \ln^2(\lambda_{De}/r_a)}{\pi f^2} e^{qV_a/kT_e} \right)$
Resonance	$f \simeq f_{pe}$	$0.01 \frac{\sqrt{\pi m_e} L_a}{\sqrt{2kT_e} \lambda_{De} \epsilon_0}$	n/a	$0.04 \frac{\sqrt{\pi m_e k T_e} L_a}{\sqrt{2} \lambda_{De} \epsilon_0}$
High	$f \gg f_{pe}$	$\frac{\omega_{pe}^2}{2\epsilon_0 \omega^3 L_a}$	$\frac{1 - \ln(L_a/r_a)}{\pi \epsilon_0 \omega L_a}$	$\frac{2\lambda_{De} \sqrt{m_e k T_e}}{\epsilon_0 L_a f^3}$

<sup>a</sup> These results correspond to (D.35)-(D.37), reflecting their assumptions of:  $R_r \ll R_S$ ;  $1/R_S C_r \ll \omega \ll 1/R_r C_r$ ; and a positive ion sheath.

Table D.1: Summary of unified noise model for dipole antenna in magnetoplasma. See Section D.1.3.1 through Section D.1.3.4 for corresponding derivations.



Property	Symbol	Inner zone	Outer zone	Units
<i>Antenna parameters</i>				
Dipole				
Length <sup>a</sup>	$L_{\text{TT}}$		20	m
Radius <sup>a</sup>	$r_{\text{a}}$		5	cm
Satellite				
Speed <sup>b</sup>	$v_{\text{s}}$		5	km/s
Altitude	$L$ -shell	2	4	$R_{\text{E}}$
<i>Plasma parameters</i>				
Electrons				
Density <sup>b,c</sup>	$N_{\text{e}}$	$2 \times 10^9$	$3 \times 10^8$	$\text{m}^{-3}$
Temperature <sup>b,d</sup>	$T_{\text{e}}$	$2 \times 10^3$	$1 \times 10^4$	K
Plasma frequency <sup>b,d</sup>	$f_{\text{pe}}$	402	155	kHz
Debye length	$\lambda_{\text{De}}$	6.90	39.8	cm
Protons				
Temperature <sup>b,d</sup>	$T_{\text{e}}$	$2 \times 10^3$	$1 \times 10^4$	K
Photoelectrons <sup>e</sup>				
Density <sup>f</sup>	$N_{\text{ph}}$		$1 \times 10^9$	$\text{m}^{-3}$
Temperature <sup>f</sup>	$T_{\text{ph}}$		$1.8 \times 10^4$	K
Current density <sup>g</sup>	$J_{\text{ph}}$		$2.5 \times 10^{-5}$	A/m <sup>2</sup>

<sup>a</sup> According to [Chevalier \[2007, p.88\]](#).

<sup>b</sup> According to [Wang \[1970, p.110\]](#).

<sup>c</sup> According to [Chevalier \[2007, p.32\]](#).

<sup>d</sup> According to [Chevalier \[2007, p.20\]](#).

<sup>e</sup> In Figure 3.9, nighttime operation assumed ( $I_{\text{ph}}=0$ ).

<sup>f</sup> According to [Cauffman and Gurnett \[1972, p.375\]](#).

<sup>g</sup> According to [Fahleson \[1967, p.243\]](#).

Table D.2: Plasma and antenna parameters invoked by antenna noise simulations of Figure 3.9.

A search coil comprises many turns of wire ( $N_a \gg 100$ ) wrapped around a high-permeability metal core. The  $\mu$ -metal core that concentrates the magnetic flux is often modeled as a long thin ellipsoid of revolution, though in fact it is made from layered rectangles to reduce eddy currents [Gurnett, 1998, p.130]. Both operate on the principle of Faraday's law, converting variations in the magnetic flux,  $\Phi_m$ , into an electromotive force,  $V_{\text{ind}}$  according to

$$V_{\text{ind}} = N_a \frac{d\Phi_m}{dt} = N_a \frac{d \oint \mathbf{B} \cdot d\mathbf{S}}{dt} = \omega N_a B S \quad (\text{D.45})$$

where vectors  $\mathbf{B}$  and  $\mathbf{S}$  are the magnetic field strength and vector surface area of the antenna cross-sectional area. The last equality in (D.45) holds only under sinusoidal steady-state conditions, when the magnetic field strength is constant across and perpendicular to  $\mathbf{S}$ .

### D.2.1 Antenna Basics

A brief review of the basic principles governing the design and operation of both types of magnetic receiving antennas provides prologue to the treatment of the noise properties that are fundamentally limited by such constraints.

#### D.2.1.1 Bandwidth

The primary trade-off between the two magnetic antenna designs is the exchange of high-frequency bandwidth for low-frequency bandwidth. Since the effective field strength inside the search coil is much larger, it presents a substantially larger inductance at its terminals. As evidenced below, this reduces the high-frequency performance of the search coil approximately according to

$$\omega_{\text{LC}} = \frac{1}{\sqrt{L_a C_a}} \quad (\text{D.46})$$

Whereas the loop antenna benefits at high frequency from its lower inductance, the relatively small number of turns results in a correspondingly low resistance that degrades its low-frequency response. Preservation of the antenna as the dominant

noise source in the receiver requires that it equivalent thermal noise exceed that of the LNA, represented by  $R_{\text{in}}$ . Even in the case of low input-impedance preamplifiers, this condition, along with the low resistance of the loop,  $R_{\text{a}}$ , necessitates the use of a transformer to couple the two [Gurnett, 1998, p.131]. Inherently, the shunting effect of the transformer's primary inductance yields diminished signal for frequencies below [Paschal, 1988, p.24].

$$\omega_{\text{t}} = \frac{(R_{\text{a}} + R_{\text{pc}}) \parallel \kappa_{\text{L}} (R_{\text{sc}} + R_{\text{in}})}{L_{\text{a}} + L_{\text{pc}}} \quad , \quad \text{where } \kappa_{\text{L}} = \frac{L_{\text{a}} + L_{\text{pc}}}{\eta^2 L_{\text{pc}}} \quad (\text{D.47})$$

Where the resistance and inductance of the transformer's primary and secondary coils are denoted with the subscripts  $pc$  and  $sc$ , respectively, and  $\eta$  is its turns ratio. Thus, the transformer limits the low-frequency response of the loop antenna, while the high inductance of the  $\mu$ -metal core limits the high-frequency performance of the search coil.

#### D.2.1.2 Impedance

To maintain generality, consider the case of an LNA with arbitrary input impedance that may or may not be preceded by a transformer. Let  $Z_{\text{in}} = R_{\text{in}} + jX_{\text{in}}$  represent the impedance seen looking out from the terminals of the antenna such that, in the case of the loop design, it accounts for the effects of the transformer including the coil impedances and transformer turns ratio.

To evaluate the impedance parameters of the antenna, consider for simplicity that the antenna is constructed of wire with mass density  $\rho_{\text{m}}$ , cross-sectional diameter  $d_{\text{a}}$ , and resistivity  $\rho_{\text{r}}$ , wound in a geometry with  $N_{\text{a}}$  turns, each of length  $s$ . Then, [Inan

and Inan, 2000; Paschal, 1988, p.30–31]:

$$R_a = \frac{2\rho_r N_a s}{\pi d_a^2} \quad (\text{D.48})$$

$$L_a = \begin{cases} 2 \times 10^{-7} N_a^2 s \left[ \ln \left( \frac{s}{d_a \sqrt{N_a}} \right) - c_2 \right] & , \text{ loop} \\ \frac{5\mu N_a^2 s^2}{2\pi (9s/2\pi + 10N_a d_a)} & , \text{ search-coil} \end{cases} \quad (\text{D.49})$$

where  $c_2$  is a numerical constant that depends on the shape of the loop and ranges from 0.815 (circular) to 1.696 (isosceles).

Unfortunately, no reasonable analytical expression exists for calculating the distributed antenna capacitance. The typical procedure is to build the antenna and measure its resonance in order to derive  $C_a$ . Since the input impedance of the LNA is likely to have a large capacitive component, especially if multiplied up by a transformer, the small  $C_a$  is likely to be overwhelmed by  $C_{\text{in}}$ , so there is no need to determine its exact value [Paschal, 1988]. For the purposes of this appendix, assume  $C_a$  can be chosen as necessary to achieve the desired resonance.

## D.2.2 Noise Sources

As opposed to the dipole antenna, immersion in a plasma does not notably affect the noise properties of a reasonably sized magnetic antenna [Gurnett, 1998, p.130]. Thus, the noise referred to it terminals is simply the Nyquist noise generated by the conductor that forms the antenna itself according to (D.14)<sup>28</sup>

$$e_t^2 = 4kT_a R_a \left[ \frac{R_{\text{in}}^2 + X_{\text{in}}^2}{\mathcal{D}(\omega)} \right] \quad (\text{D.50})$$

---

<sup>28</sup>In the presence of a transformer,  $e_n^2$  is understood to represent the noise at the secondary port and the quantities related to  $Z_{\text{in}}$  appropriately scaled by  $\eta$ .

where

$$\begin{aligned} \mathcal{D}(\omega) = & \left( R_{\text{in}} + R_{\text{a}} - \omega R_{\text{a}} C_{\text{a}} X_{\text{in}} - \omega^2 L_{\text{a}} C_{\text{a}} R_{\text{in}} \right)^2 \\ & + \left( X_{\text{in}} + \omega L_{\text{a}} + \omega R_{\text{a}} C_{\text{a}} R_{\text{in}} - \omega^2 L_{\text{a}} C_{\text{a}} X_{\text{in}} \right)^2 \end{aligned}$$

This result only includes the thermal noise generated by the antenna itself, so  $Z_{\text{in}}$  is assumed noiseless. To account for the contribution of the latter, the following should be added to (D.50):

$$e_{\text{t}}^2 = 4kT_{\text{a}} R_{\text{in}} \left[ \frac{R_{\text{a}}^2 + L_{\text{a}}^2}{\mathcal{D}(\omega)} \right] \quad (\text{D.51})$$

Nevertheless, the resonant behavior of the circuit is evident. Although the low-frequency noise level is easily approximated by

$$e_{\text{t}}^2 = 4kT_{\text{a}} (R_{\text{a}} \parallel R_{\text{in}}) \quad (\text{D.52})$$

the noise peaks several orders of magnitude above this level at the frequency cited in (D.46) [Gurnett, 1998, p.133].

To push this resonance out of the band of interest, and thus minimize the in-band thermal noise, the low end of the resonance, marked by the frequency [Gurnett, 1998, p.133]

$$\omega_{\text{RL}} = \frac{\sqrt{R_{\text{in}} R_{\text{a}}}}{L_{\text{a}}} \quad (\text{D.53})$$

should be maximized. However,  $R_{\text{in}}$  is typically small in order to dampen the sharp peaking associated with the resonance. Thus, the designer must manage this trade-off to the benefit of the overall system.

### D.2.3 Summary

To encapsulate the range of magnetic antenna noise levels, a sample loop antenna [Paschal, 1988, p.19] and sample search coil [Gurnett et al., 1995, p.603,613] have been simulated under various temperature conditions, using code based on (D.50) and (D.51). The results, presented in Figure D.3 and Figure D.4 for  $L = 2$  and  $L = 4$ , respectively, highlight the resonance behavior because they assume  $R_{\text{in}} \rightarrow \infty$

and  $X_{\text{in}} \rightarrow 0$ .

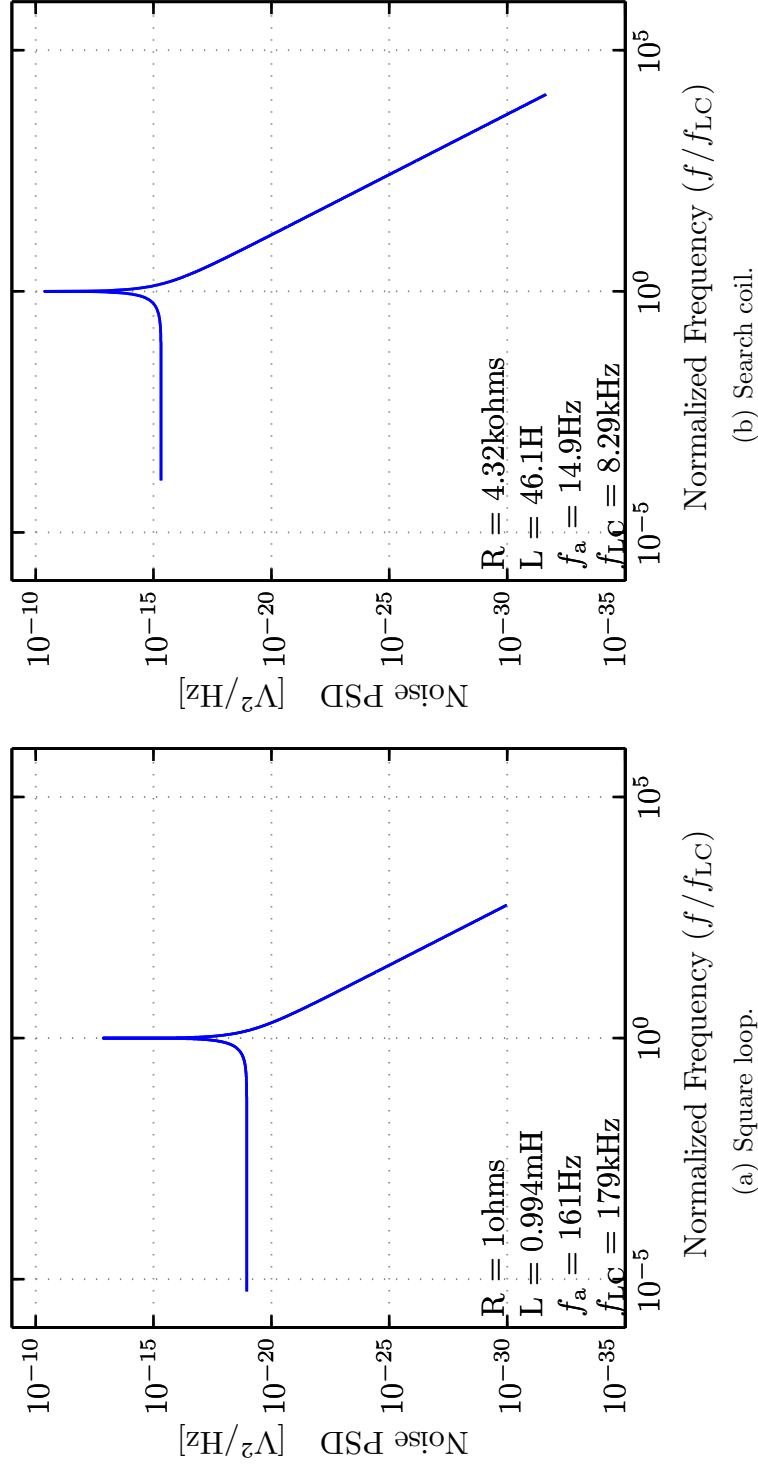


Figure D.3: Simulated noise of magnetic antennas in inner zone ( $L = 2$ ). Fed the typical plasma conditions in Table D.1.4, models of (a) a 56.7-cm square copper loop composed of 21 turns of AWG18 wire (1.02-mm diameter) and (b) a search coil composed of 20,000 turns of AWG40 wire (0.08-mm diameter) both exhibit resonance at  $f_{LC}$ .

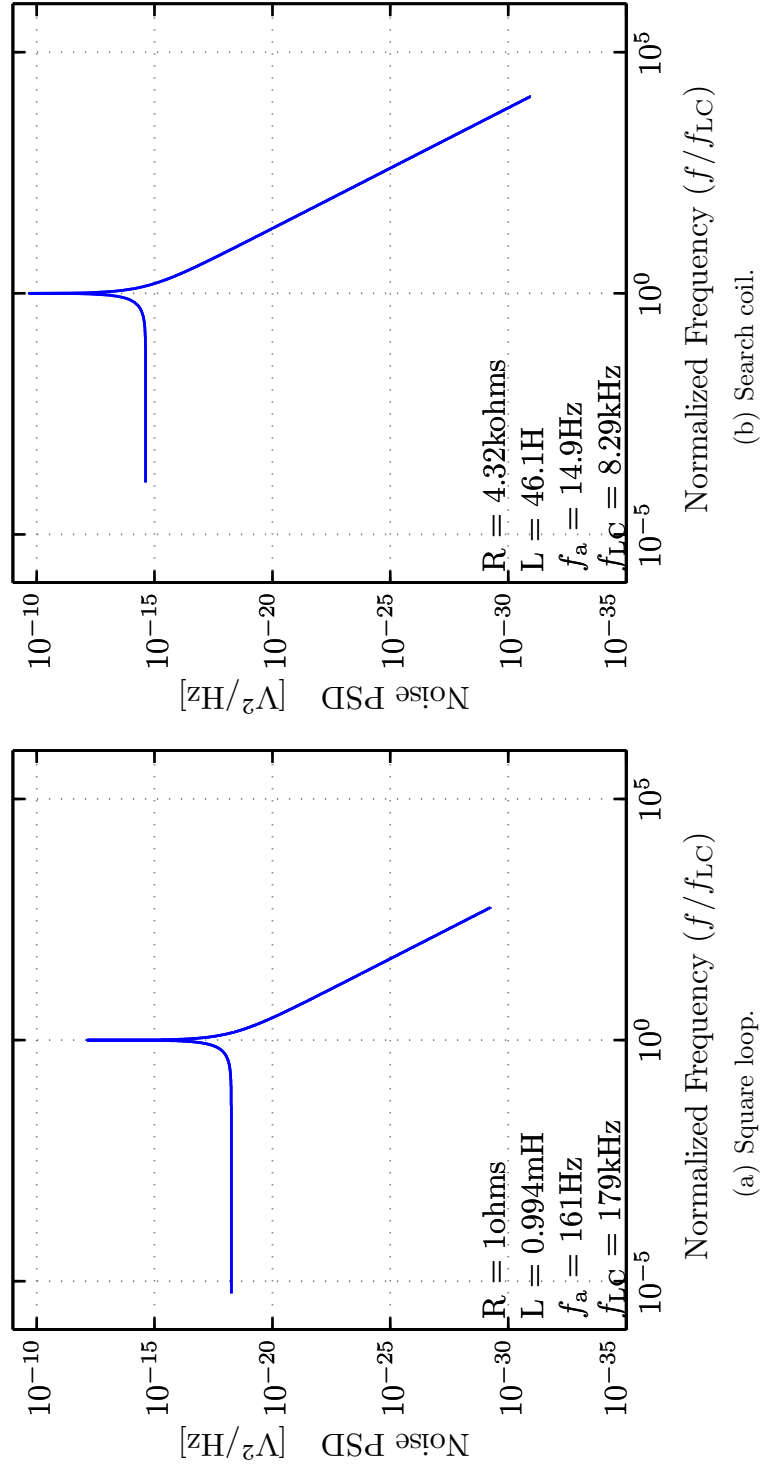


Figure D.4: Simulated noise of magnetic antennas in inner zone ( $L = 4$ ). Fed the typical plasma conditions in Table D.1.4, models of (a) a 56.7-cm square copper loop composed of 21 turns of AWG18 wire (1.02-mm diameter) and (b) a search coil composed of 20,000 turns of AWG40 wire (0.08-mm diameter) both exhibit resonance at  $f_{LC}$ .



# Appendix E

## Gate-Controlled Lateral pnp

This appendix presents an introduction to the design, construction, and fabrication of gate-controlled lateral pnp transistors (GCLPNPs) as demonstrated by efforts to develop a novel version of such a device for the BiCMOS8 SiGe technology provided by National Semiconductor Corporation (NSC). The penury of suitable, complementary alternatives to the high-performance vertical npn BJTs in BiCMOS8, which offers only a low- $\beta$  vertical pnp whose collector is tied to the substrate shared chip-wide as ground, motivated a collaboration between Stanford and NSC engineers Monir El-Diwany and James Shibley to design and build a prototype GCLPNP with better gain. Although progress was made through several generations, the final version was not officially adopted into the NSC process flow, necessitating use of the only option available: the substrate pnp described in Section 3.2.1.3.

Nevertheless, this appendix summarizes the research conducted in this endeavor both for completeness and as a springboard to future work on circumventing the performance limitations imposed by the substrate pnps in the AAF transconductors Section 7.3. Section E.1 provides background on the physical mechanisms underlying the gain of integrated bipolar transistors, with emphasis on lateral topologies, as it represents the primary feature sought in the new GCLPNP. The structure of the canonical GCLPNP and the details of its operation are contained in Section E.2, which emphasizes their attractiveness for both commercial and radiation-tolerant applications. Finally, Section E.3 describes the construction of the novel BiCMOS8

GCLPNP and presents measured results of the performance for a series of fabricated prototypes.

## E.1 Bipolar Gain

To appreciate the design trade-offs that complicate the construction of a GCLPNP whose current-emitter gain,  $\beta$ , surpasses that of the substrate pnp presently available, a review of device physics pertaining to the base and collector currents of the BJT is instructive. In particular, treating  $\beta$  as a constant for a particular device, which suffices in first-order calculations [*Gray et al.*, 2001, p.23], is insufficient for this application, in which signal currents vary over many orders of magnitude.

Consider, for example, the typical curves for  $\beta$ -vs- $I_C$  and  $\log \beta$ -vs- $V_{BE}$  in Figure E.1. Whether as a function of  $I_C$  or  $V_{BE}$ ,  $\beta$  varies logarithmically from its peak for moderate values (denoted by Region II of Figure E.1(a) or  $V_{BET} < V_{BE} < V_{BEK}$  in Figure E.1(b)) to much lower levels in the regions corresponding to low-level (Region I or  $V_{BE} < V_{BET}$ ) and high-level injection (Region III or  $V_{BE} > V_{BEK}$ ). This behavior should be familiar, as it is exhibited in the  $\beta$ -degradation curves for the representative npn transistors in Figure 2.16.

Although Figure E.1(a) demonstrates the operating-point dependence for DC or static conditions, where  $\beta$  is given by [*Laker and Sansen*, 1994, p.105]

$$\beta_{DC} = \frac{I_C}{I_B} \quad (E.1)$$

a similar effect manifests for the incremental version of the gain employed in small-signal analysis, known as  $\beta_{AC}$  or  $h_{fe}$  and given by

$$\beta_{AC} = \frac{\partial I_C}{\partial I_B} = \frac{\beta}{1 - \frac{\partial \beta}{\partial I_C} \frac{I_C}{\beta}} \quad (E.2)$$

as indicated by the dashed curves of Figure E.1(b). The dependence of (E.2) on  $\partial \beta / \partial I_C$ , which is clearly non-zero at the extremes of Figure E.1(b), results in the deviations from the solid curve that only emphasize the importance of avoiding  $\beta_{AC}$

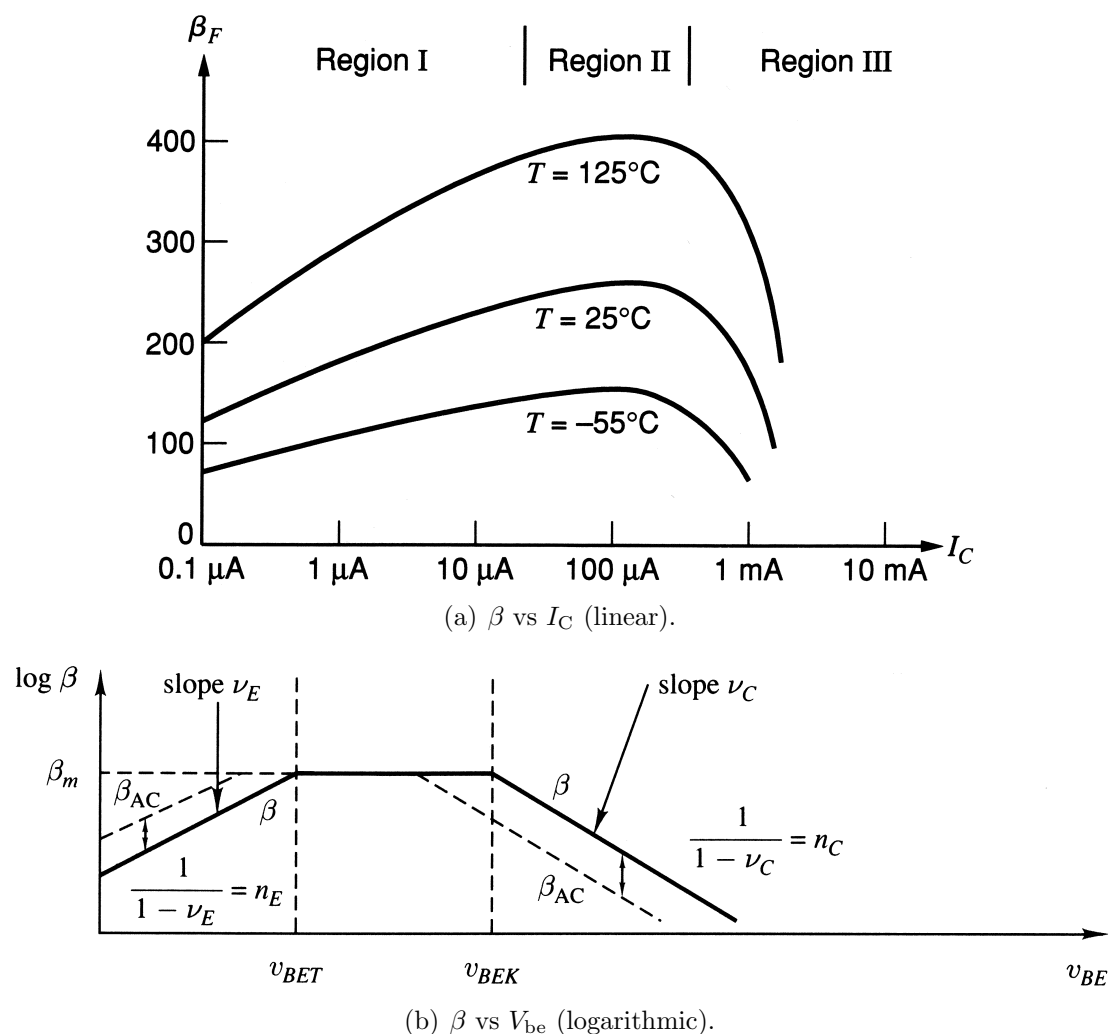


Figure E.1: Typical variation of  $\beta$  with npn bias conditions. A relatively flat peak- $\beta$  regime flanked by regions over which  $\beta$  markedly ebbs is characteristic regardless of whether  $\beta$  is plotted (a) on a linear scale against  $I_C$  or (b) on a logarithmic scale against  $V_{be}$ . Reproduced *in toto* from (a) [Gray et al., 2001, p.24] and (b) [Laker and Sansen, 1994, p.129].

in this design, whose linearity depends on by the dynamic, large signal  $\beta = I_c/I_b$  (cf. Section 3.1.2.3).

Since this sensitivity of a BJT's gain to its operating conditions is a function of its construction, described in Section E.2, dependences on depletion region widths and collector current levels are first examined in Section E.1.1 and Section E.1.2, respectively.

### E.1.1 Base Decomposition

Recall from (2.12) that  $\beta$  can be decomposed according to those components of  $I_b$  that arise from minority-carrier recombination in the base and those that arise from their back-injection into the emitter. More formally, this interpretation partitions the base current,  $I_{b1}$ , for a pnp device as [Gray *et al.*, 2001; Messenger and Ash, 1992, p.12,p.227]<sup>1</sup>

$$I_{b1} = \underbrace{\frac{1}{2} \frac{qW_b P_e h_e N_{pb}}{\tau_p}}_{\text{Bulk recombination}} + \underbrace{qS_p W_b P_e N_{pb}}_{\text{Surface recombination}} + \underbrace{qP_e h_e N_{ne} \sqrt{\frac{D_n}{\tau_n}}}_{\text{Emitter injection}} \quad (\text{E.3})$$

where the lifetimes of the minority carrier holes(electrons) in the base(emitter) are given by  $\tau_p(\tau_n)$ ; and their edge densities at the base(emitter) side of the E-B depletion region are  $N_{pb}(N_{ne})$ ; and (for an annular structure), the cross-sectional area of the E-B junction is represented by the product of the perimeter and height of the emitter diffusion ( $P_e h_e$ ).<sup>2</sup>

When  $I_{b1}$  is dominated by the first two terms, the device is said to be transport-efficiency limited and factors such as base width ( $W_b$ ) and bulk(surface) impurities, which effect  $\tau_p(S_p)$ , are critical to its gain. When the last term dominates (E.3), the device is emitter-injection-efficiency limited, and the emitter's doping profile and

---

<sup>1</sup>To completely define  $\beta_1$  requires the corresponding expression of  $I_{c1}$ :

$$I_{c1} = \frac{qP_e h_e D_p N_{pb}}{W_b}$$

<sup>2</sup>Comparing (E.3) to (2.13), the astute reader will observe that  $A_s = W_b P_e$  and  $A_e = P_e h_e$ .

perimeter-to-area ratio must be large to achieve high gain [*Verdonckt-Vandebroek et al.*, 1991, p.2491–2492].<sup>3</sup> For modern lateral BJTs, base widths are so narrow that the latter condition is most often encountered in practice [*Gray et al.*, 2001, p.12].

#### E.1.1.1 Homogeneous Base

The relative impact of the transport efficiency and injection efficiency terms of (E.3) is best appreciated by relating (E.3) back to (2.12) by computing  $1/\beta_1$  from the ratio of this decomposed  $I_{b1}$  to  $I_{c1}$  (cf. Footnote 1). This yields

$$\begin{aligned} \frac{1}{\beta_{b1}} = \frac{I_{b1}}{I_c} &= \frac{W_b^2}{2\tau_p D_p} + \frac{S_p W_b^2}{h_e D_p} + \frac{D_n W_b N_D}{D_p L_n N_A} \\ &= \frac{\tau_b}{\tau_p} + 2S_p \frac{\tau_b}{h_e} + \frac{L_n \tau_p W_b N_D}{L_p \tau_n L_p N_A} \end{aligned} \quad (\text{E.4})$$

where  $L_p = \sqrt{D_p \tau_p}$  ( $L_n = \sqrt{D_n \tau_n}$ ) is the minority carrier diffusion length in the base(emitter) and  $\tau_b$  is known as the (forward) base transit time, representing the average time holes take to cross from emitter to collector [*Laker and Sansen*, 1994, p.100]. The density of dopant atoms in the base ( $N_D$ ) and emitter ( $N_A$ ) have appeared by assuming that

$$N_D = \frac{N_i^2}{N_{po}} \quad (\text{E.5a})$$

$$N_A \simeq \frac{N_i^2}{N_{no}} \quad (\text{E.5b})$$

Each of the terms of (E.4) corresponds to that in the same position of (2.12), with the first two equivalent to the definitions of (2.18) and (2.13), respectively. Thus, a transport-limited device exhibits  $\beta_{br} < \beta_{ee}$  and/or  $\beta_{sr} < \beta_{ee}$  whereas one limited by injection efficiency has a lower  $\beta_{ee}$ .

---

<sup>3</sup>These two conditions are sometimes captured formally by expressing the transistor common-base gain  $\alpha$  as the product of a base transport factor,  $\alpha_b$  and emitter injection efficiency  $\gamma_e$ , each of which should ideally approach unity, but deviate as a consequence of the design parameters noted [*Gray et al.*, 2001, p.13].

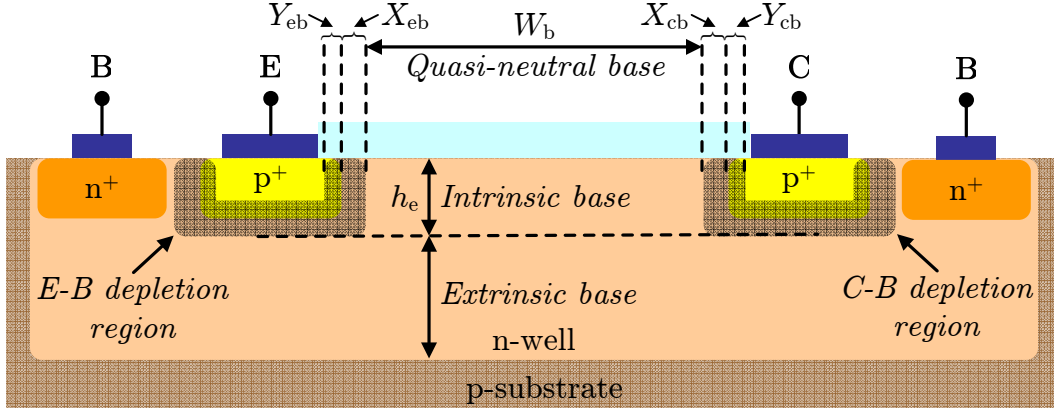


Figure E.2: Decomposition of base regions in lpnp topology. The lateral width of the quasi-neutral base is  $W_b$ , whereas the extent of the E-B(C-B) depletion region in the base is  $X_{eb}(X_{cb})$  and that in the emitter(collector) is  $Y_{eb}(Y_{cb})$ . The depth of the intrinsic base is equal to that of the emitter,  $h_e$ . Dimensions greatly exaggerated for clarity.

#### E.1.1.2 Space-Charge Regions

However, the above decomposition assumes a one-dimensional, homogeneous base, ignoring the effects of two-dimensional base current paths and the depletion regions at its boundaries with the emitter and collector. In fact, as shown in Figure E.2 for the case of a lateral pnp, the actual base can be subdivided into disparate regions: the space-charge regions near the junctions are contrasted with the quasi-neutral base between them; and the intrinsic base, which accounts for lateral current flow no deeper than the junctions themselves is distinct from the extrinsic base, containing paths that emanate from or terminate on the bottoms of the E-B and C-B junctions. The former distinctions are especially important because each of the recombination terms in (E.3) only accounts for SRH recombination in the neutral base. As a result, (E.3) only describes the base current in Region II of Figure E.1(a).

With reference to the Gummel plot of Figure E.3, which corresponds to the  $\beta$  curves in Figure E.1(b), it can be seen that the slope of  $I_b(I_c)$  deviates at low(high) injection levels, giving rise to the observed  $\beta$  variations. Next it is shown how the field-assisted recombination mechanisms in the E-B depletion region not captured by (E.3) explain these behaviors.

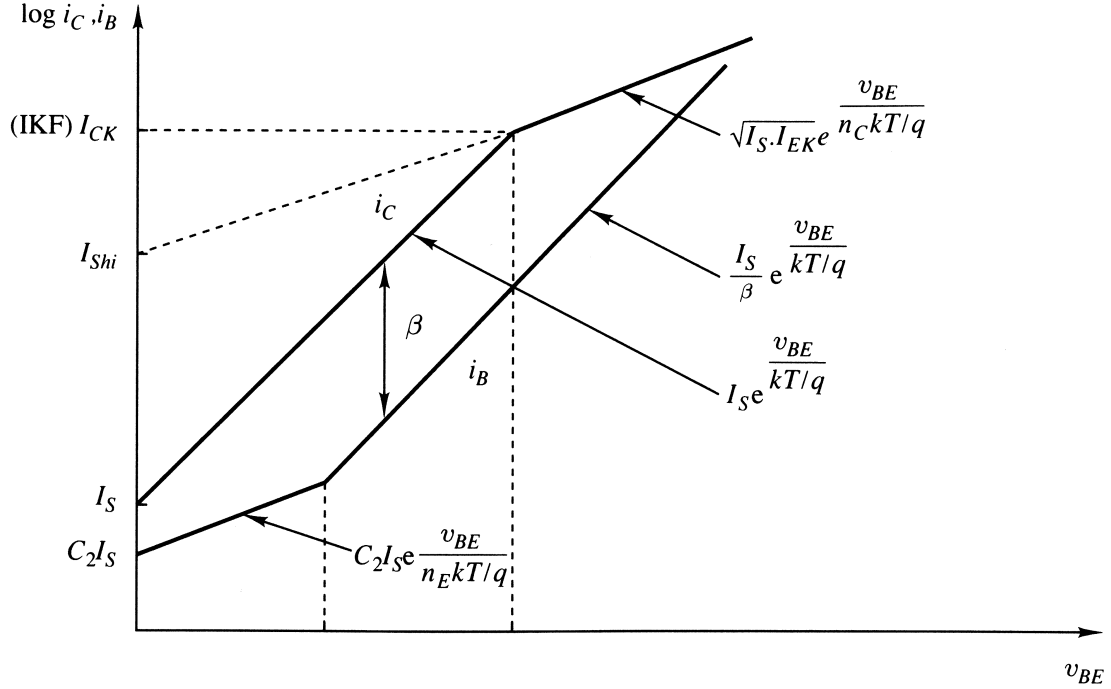


Figure E.3: Gummel curve corresponding to npn  $\beta$  described in Figure E.1(b). The inflection point at which low-level(high-level) injection flattens the slope of the  $I_c(I_b)$  curve corresponds to the lower(upper) edge of the peak- $\beta$  region in Figure E.1(b). Reproduced *in toto* from [Laker and Sansen, 1994, p.129].

## E.1.2 Injection Level

As noted previously,<sup>4</sup> under low-level(high-level) injection conditions, the excess carrier concentration in the BJT base satisfies  $N'_p/N_{no} \ll 1$  ( $N'_p/N_{no} \gg 1$ ). At these extremes, the change in the dominant recombination mechanism(effective base doping) renders (E.3) or its equivalent for  $I_{c1}$  (cf. Footnote 1) incapable of describing the base(collector) current of Figure E.3. Instead, new models are introduced below.

### E.1.2.1 Low-Level Effects

The recombination terms of (E.3) are proportional to the edge density of the minority carriers in the base,  $N_{pb}$ , which under forward active operation can be related to the

<sup>4</sup>For example, in Footnote 42 of Appendix C and Section C.3.4, which also discuss the effects of injection-level on recombination, but without consideration of space-charge phenomena.

equilibrium minority carrier density in the neutral base,  $N_{po}$ , by using the Boltzman factor to approximate a Fermi-Dirac distribution [*Gray et al.*, 2001, p.9]:

$$N_{pb} = N_{po}e^{V_{be}/V_T} \quad (E.6)$$

Although this assumption indeed holds under low-level injection, it is shown next that the resulting exponential dependence of the recombination terms of (E.3), explicitly,

$$I_{b1} = \underbrace{\frac{1}{2} \frac{qW_b P_e h_e N_{po}}{\tau_p} e^{V_{be}/V_T}}_{\text{Bulk recombination}} + \underbrace{qS_p W_b P_e N_{po} e^{V_{be}/V_T}}_{\text{Surface recombination}} + \underbrace{\frac{qP_e h_e N_i^2}{N_A} \sqrt{\frac{D_n}{\tau_n}} e^{V_{be}/V_T}}_{\text{Emitter injection}} \quad (E.7)$$

is dwarfed by those describing recombination in the E-B depletion region.

The relative lack of free carriers and the presence of the drift electric field in the space-charge region violate the assumptions of SRH recombination underpinning (E.7) and instead favor mid-gap recombination that requires additional base current,  $I_{b2}$ , according to [*Laker and Sansen*, 1994, p.103]:

$$I_{b2} = \underbrace{\frac{1}{2} \frac{qW_{eb} P_e h_e N_i}{\tau_{peb}} e^{V_{be}/2V_T}}_{\text{Bulk recombination}} + \underbrace{\frac{1}{2} qS_p W_{eb} P_e N_i e^{V_{be}/2V_T}}_{\text{Surface recombination}} \quad (E.8)$$

where  $W_{eb}$ , the width of the E-B depletion region, has replaced  $W_b$  in (E.3). Further comparison with the corresponding terms of  $I_{b1}$  in (E.7) reveals that in the absence of free carriers, the hole concentration at the emitter edge has been replaced with the square root of the intrinsic carrier density,  $N_i = e^{V_{BE}/V_T}$ , giving rise to an exponential whose smaller power prevents it from falling off as fast as that of (E.6) at low  $V_{BE}$ .<sup>5</sup> Thus, while  $I_{b2}$  is negligible in Region II, it dominates the slope of  $I_b$  at low injection levels in Figure E.3.

---

<sup>5</sup>The halving of the exponential power between (E.7) and (E.8) is often modeled by a variable that accounts for nonidealities which result in small deviations from the ideal factor-of-two [*Laker and Sansen*, 1994, p.105].



### E.1.2.2 High-Level Effects

At high injection levels, when the excess minority carrier concentration in the base rivals that of the majority carriers, additional majority carriers are needed to maintain charge neutrality. In fact, if  $N'_p \simeq N_{no}$  the electron concentration at the E-B edge must double. To prevent these additional electrons from diffusing toward the collector, there must exist an electric field to provide a counterbalancing drift whose orientation repels majority carriers from the collector, while simultaneously attracting minority carriers.<sup>6</sup> This field, whose orientation of acts to increase the total voltage drop across the B-E junction, is provided by an increase in  $V_{BE}$  for the same  $I_c$ . The result is the reduced slope of the  $I_c$  curve in Region III of Figure E.3, which can be shown to be equal to that of  $I_b$  in Region I according to [Laker and Sansen, 1994, p.128]:<sup>7</sup>

$$I_{c2} = \frac{qP_e W_{eb} D_p N_i}{W_b} e^{V_{be}/2V_T} \quad (E.9)$$

## E.2 GCLPNP Basics

The GCLPNP is certainly not a new idea [Vittoz, 1983]. But, benefiting from the advanced capabilities of modern processes, a  $\beta$  in excess of  $10^6$  has been recently reported for such a device [Yan et al., 1997, p.120], making it an attractive alternative to the BiCMOS8 substrate pnp ( $\beta < 10$ ). The extra degree of freedom afford by the gate terminal of the GCLPNP offers yet another benefit: the ability to mitigate TID effects [Barnaby et al., 1999, p.1655]. Before explaining the customizations necessary to implement a variant of this device into the BiCMOS8 flow, this section reviews the fundamentals which must be considered to successfully perform this migration. Section E.2.1 introduces the GCLPNP layout and provides some familiarity with its non-standard features. Then, Section E.2.2 and Section E.2.3 describe how the above baseline and radiation performance can be achieved through the control afforded by

---

<sup>6</sup>Thus, minority carriers injected from the emitter no longer simply diffuse to the collector, as under low-level injection, but drift as well.

<sup>7</sup>This expression omits consideration of other high-level injection effects, such as the Kirk effect, which causes an effect increase in base width to satisfy the space charge relations at the C-B junction [Messenger and Ash, 1992, p.340].

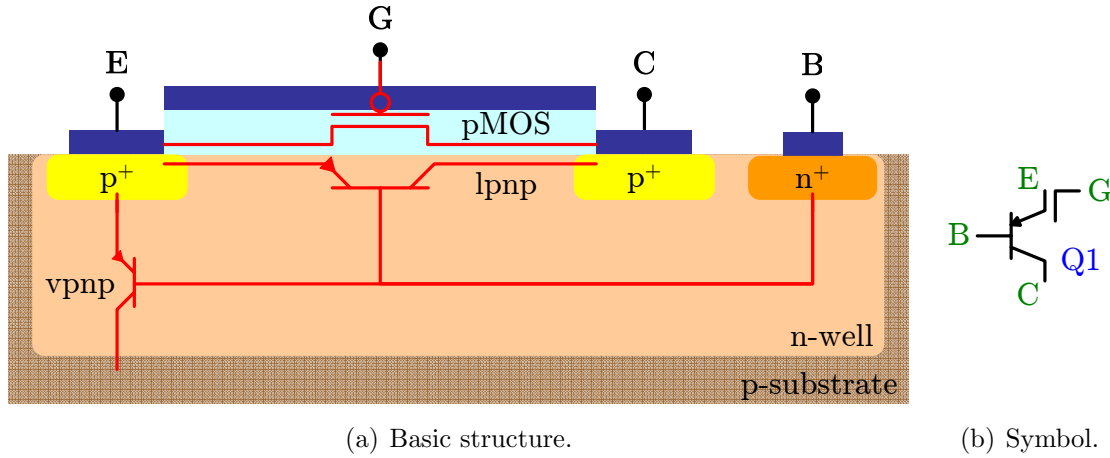


Figure E.4: Structure and circuit symbol of simplified GCLPNP. The simplified GCLPNP (a) structure contains three transistors, including a pMOSFET in parallel with the lpnp whose gate forms the fourth terminal of the (b) non-standard circuit symbol.

pMOS terminals	lpnp terminals
Substrate	Substrate
n-well	Base
Drain	Collector
Source	Emitter
Gate	n/a

Table E.1: Terminal mapping for pMOS and lpnp that comprise GCLPNP.

the presence of the gate terminal.

### E.2.1 Structure

A simplified representation of a GCLPNP is depicted in Figure E.4 along with a non-standard circuit symbol. As indicated by the red transistors, the GCLPNP can be interpreted as a four-terminal device formed by the parallel conduction paths of a standard pMOSFET and its parasitic lateral pnp. The mapping of these terminals into the common nomenclature for the two is given in Table E.1. In addition, Figure E.4 illustrates a sneak path through a parasitic substrate pnp.

Through careful construction rendering the gain of the last device negligible and proper biasing of the gate terminal relative to the well/base (both of which are addressed momentarily), it is permissible to focus the operational description of the device, given in the next section, on its lateral elements alone.

## E.2.2 Operation

Although the diversity of terminal voltage relationships and current paths in Figure E.4 gives rise to many interpretations of its operation, including ones which simply treat it as two heterogeneous devices operating in parallel [Yan *et al.*, 1997, p.119–121], perhaps it is best understood by focusing on the lateral pnp and considering the gate-to-well bias,  $V_{GW}$ , as a means of dynamically altering its doping profile. At the extremes of  $V_{GW}$ , this interpretation gives rise to consideration of the BJT operation with either an accumulated or depleted base.

### E.2.2.1 Accumulated Base

When  $V_{GW} > 0$ , the MOSFET is accumulated, increasing(decreasing) the surface doping of the base(emitter), dubbed  $N_{sb}(N_{se})$ . The resulting quasi-neutral, heavily doped base produces ‘pure’ BJT action [Verdonckt-Vandebroek *et al.*, 1991, p.2487] whose  $\beta$  is governed by competing effects: high  $N_{sb}$  raises the barrier to hole injection from the emitter [Verdonckt-Vandebroek *et al.*, 1991, p.2490] and low  $N_{se}$  increases the space-charge region in the emitter, reducing emitter current by favoring recombination there [Cazenave *et al.*, 1998, p.2580] both of which reduce  $\beta$ ; but, high  $N_{sb}$  also limits recombination in the base depletion region(intrinsic neutral base) by decreasing its width(unbalancing the surface carrier concentrations) [Barnaby *et al.*, 1999, p.1655] and creates a drift field that forces minority carriers away from the surface, where there would otherwise be subject to  $S_n$  [Cazenave *et al.*, 1998, p.2580], all of which improves  $\beta$ . Although the net effect depends on the specifics of device construction, emitter efficiency tends to be more important than base recombination in determining  $\beta$  according to (2.12) so  $V_{GW} > 0$  results in less gain [Yan *et al.*, 1997, p.119].

### E.2.2.2 Depleted Base

Conversely, if the base is depleted by setting  $V_{\text{GW}} < 0$ ,<sup>8</sup> the above effects are effectively reversed.  $\beta$  grows much larger because when the base(emitter) is depleted(accumulated) the barrier for hole(electron) injection into it is lower(higher) [Cazenave *et al.*, 1998, p.2578], even though lower  $N_{\text{sb}}$  increases the recombination component of  $I_{\text{B}}$  by expanding the base space-charge region, permitting carrier flow near the surface, and balancing the extrinsic neutral base carrier ratios [Cazenave *et al.*, 1998, p.2580].<sup>9</sup> Thus, using  $V_{\text{GW}}$  to deplete the lateral pnp base, effectively fostering a parallel sub-threshold conduction path by operating the MOSFET in weak inversion while the BJT conducts, can improve the effective  $\beta$  [Yan *et al.*, 1997, p.120].<sup>10</sup>

## E.2.3 Radiation Tolerance

The use of lateral pnp transistors in which the metalization of the emitter contact is extended over the majority of the exposed n-well, is called field-plating [Hastings, 2006, p.333] and has been known for some time to improve the reliability, matching, and repeatable manufacturing of such devices, especially the stability of their gain [Jones, 1967, p.277], by preventing the unwanted accumulation of surface charge from effectively modifying the base surface doping as discussed above. Since ionizing radiation is an especially pernicious source of such charge (cf. Section C.2.1), it is logical to consider whether use of the gate itself to perform this function might yield

---

<sup>8</sup>This  $V_{\text{GW}}$  condition only results in depletion if  $|V_{\text{GW}}| < |V_{\text{thp}}|$ , which is assumed throughout. Otherwise the MOSFET would be in strong inversion and channel formation would simply dominate the device behavior [Verdonckt-Vandebroek *et al.*, 1991, p.2487].

<sup>9</sup>An extreme case of  $\beta$  enhancement occurs when  $V_{\text{GW}} = 0$  and, in the absence of a threshold implant, the base becomes fully depleted [Cazenave *et al.*, 1998, p.2578]. Under such conditions, it has been shown [Verdonckt-Vandebroek *et al.*, 1991, p.2490] that the disparity in base doping between the depleted intrinsic base at the surface and the extrinsic neutral base beneath produces band-bending akin to a heterojunction, whereby the holes(electrons) flowing into the base(emitter) see a lower potential barrier in, and therefore primarily flow through, the former(latter) region. By appropriately engineering the ratio of the barriers at these separate interfaces, the emitter efficiency can be optimized, just as for HBTs.

<sup>10</sup>However, the lower  $N_{\text{sb}}$  renders this mode of operation more prone to high-level injection effects, so the improved  $\beta$  is not available over as wide a range of  $I_{\text{c}}$  [Cazenave *et al.*, 1998, p.2578].

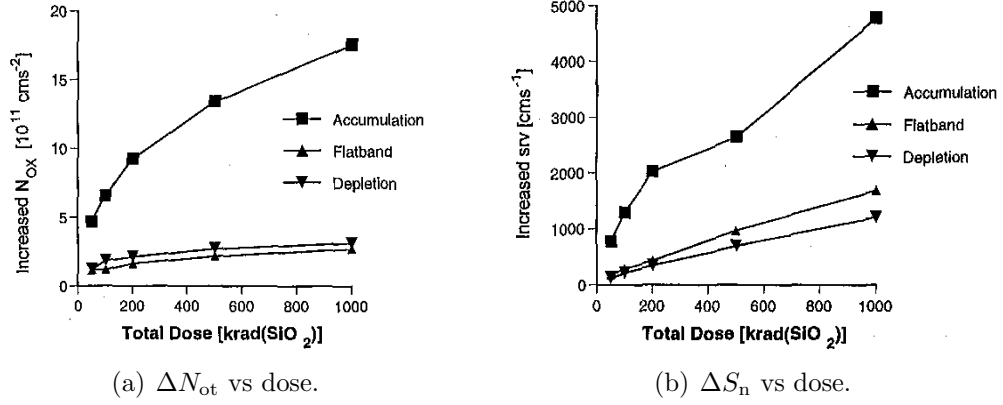


Figure E.5: Measurements of GCLPNP dependence on irradiation bias for an annular device with an emitter diameter of  $1.8 \mu\text{m}$  and  $W_b$  of  $2.6 \mu\text{m}$ . When the well is accumulated during irradiation both (a)  $\Delta N_{\text{ot}}$  (denoted  $N_{\text{ox}}$ ) and (b)  $\Delta S_n$  (denoted  $\text{srv}$ ), which is an indirect measure of  $\Delta N_{\text{it}}$  are substantially higher. Reproduced *in toto* from [Barnaby *et al.*, 1999, p.1656–1657].

improved total-dose hardness for a GCLPNP. Indeed, by dynamically toggling the intrinsic base from depletion during irradiation to accumulation during measurement using the gate bias, both the build-up and subsequent ramifications of  $\Delta N_{\text{ot}}$  and  $\Delta N_{\text{it}}$  can be tailored [Barnaby *et al.*, 1999, p.1657]. Each of these steps is discussed separately below.

### E.2.3.1 Irradiation Bias

During irradiation, as explained in Section 2.1.1.1, a positive  $E_{\text{ox}}$  favors the transport of  $h^+$  and  $H^+$  to the interface, enhancing the formation of  $\Delta N_{\text{ot}}$  and  $\Delta N_{\text{it}}$ ; so, the benefit of using  $V_{\text{GW}} < 0$  during irradiation is evident. Measured results such as those of Figure E.5 confirm this intuition, as both  $\Delta N_{\text{ot}}$  and  $\Delta S_n$ , which is proportional to  $N_{\text{it}}$  via (2.15), are more than five times worse at 1 Mrad(Si) when the devices is biased in accumulation rather than depletion during irradiation.

Even if the preferred depletion biasing is not feasible in an active circuit, the net charge trapping for a GCLPNP is substantially lower than that of a traditional bipolar device because the sensitive oxide volume over the intrinsic base, being constructed of gate rather than field oxide, is substantially thinner [Cazenave *et al.*, 1998, p.2580].

### E.2.3.2 Measurement Bias

Next, consider the  $\beta$ -degradation at the conclusion of an exposure, which depends on  $\Delta N_{ot}$  and  $\Delta N_{it}$  just as for a standard BJT (cf. Section 2.1.2.1). The presence of  $\Delta N_{ot}$  mimics the electric field of accumulation-mode biasing: it increases the surface doping in the neutral intrinsic base, thereby increasing the barrier to the injection of holes from the emitter and lowering the gain, as discussed in Section E.2.2.1. Although it can also reduce the amount of base recombination ( $I_b$ ) by unbalancing the surface carrier concentrations ( $I_{b1}$ ) and reducing the width of the depletion region ( $I_{b2}$ ) [Barnaby *et al.*, 1999, p.1655], the primary effect of  $\Delta N_{ot}$  is thus to reduce the emitter-injected (collector) hole current [Cazenave *et al.*, 1998, p.2580].  $\Delta N_{it}$  also lowers the gain, but does so by increasing both  $I_{b1}$  and  $I_{b2}$  via the higher surface recombination velocity associated with radiation-induced  $P_b$  centers [Barnaby *et al.*, 1999, p.1655].

For a given irradiation bias, the structure of the GCLPNP does not inherently preclude  $\Delta N_{ot}$  and  $\Delta N_{it}$  buildup; however, the choice of measurement bias can enhance or suppress the effects just enumerated. Biasing the device in depletion during measurement renders it most sensitive to TID degradation because: it encourages current flow near the surface, where  $\Delta N_{it}$  are lurking to increase  $I_b$ ; and the presence of  $\Delta N_{ot}$  partially neutralizes the applied field, preventing the full depletion of the surface and limiting the attendant benefits to emitter efficiency (cf. Section E.2.2.2) as compared to pre-irradiation performance at the same  $V_{GW}$  [Cazenave *et al.*, 1998, p.2580]. By contrast, accumulation biasing significantly enhances the robustness to  $N_{it}$  by forcing holes to flower deeper in the base, unbalancing the surface carrier concentrations, and reducing the width of the E-B depletion region [Barnaby *et al.*, 1999, p.1656].

The conclusion that depletion biasing during irradiation limits the formation of  $\Delta N_{ot}$  and  $\Delta N_{it}$  whereas accumulation biasing during the subsequent measurement suppresses their effects on  $\beta$  is summarized by comparing Figure E.5 with Figure E.6. In the latter, the device biased in accumulation mode, which previously incurred the most radiation damage, actually demonstrates the least  $\beta$ -degradation.

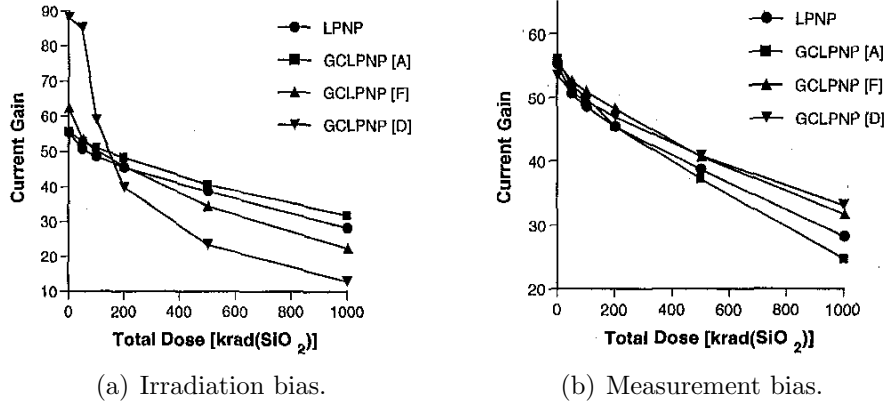


Figure E.6: Dependence of GCLPNP  $\beta$ -degradation on measurement and irradiation bias for an annular device with an emitter diameter of  $1.8 \mu\text{m}$  and  $W_b$  of  $2.6 \mu\text{m}$ . The degradation of peak  $\beta$  is (a) least when biased in depletion during irradiation, but TID damage is (b) best suppressed during measurement by operating the device in accumulation. Reproduced *in toto* from [Barnaby *et al.*, 1999, p.1653–1654].

## E.3 Novel GCLPNP

To realize the impressive gain and radiation tolerance of the GCLPNP in the BiCMOS8 technology, existing layers are repurposed so as to develop a structure closely resembling that of Figure E.4. The final design must satisfy the same suite of design rules as conventional transistors, to ensure manufacturability, while minimizing the onset of low- and high-level injection effects and maximizing both base transport and emitter injection efficiencies in pursuit of large and robust peak  $\beta$ . Section E.3.1 describes two generations of GCLPNP prototypes aimed at satisfying these requirements and Section E.3.2 presents the measured results for each.

### E.3.1 Construction

The general structure of the GCLPNP realization is depicted in Figure E.7 in both bird's-eye and cut-away cross-section along with a conceptual, one-dimensional model. The distance between the emitter and collector diffusions is dubbed the drawn base width,  $W'_b$  which differs from the neutral base width described earlier,  $W_b$  by the equilibrium extents of the E-B and C-B depletion regions into the base,  $X_{eb}$  and  $X_{cb}$ ,

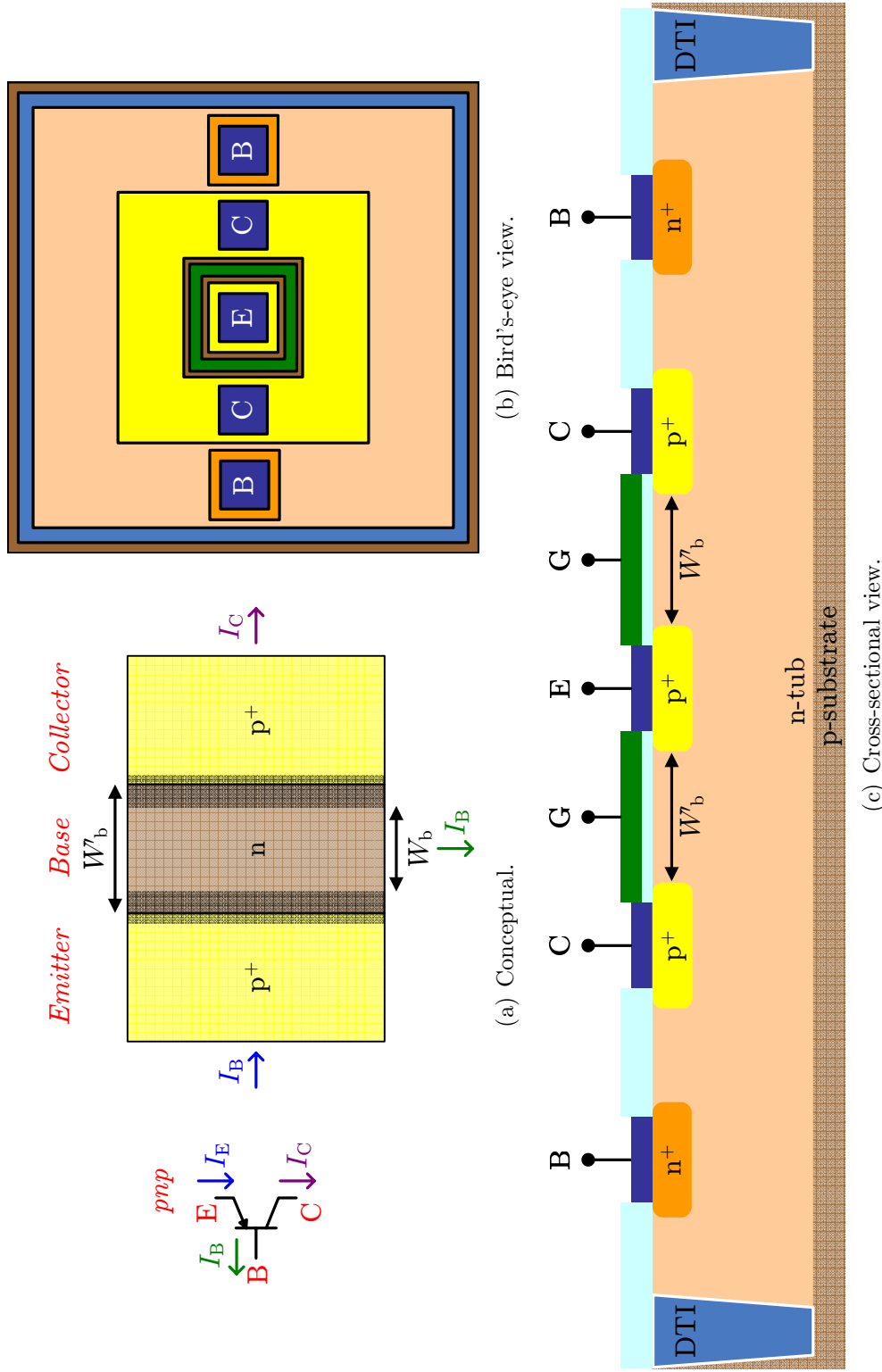


Figure E.7: General structure of GCLPNP progressing from (a) conceptual representation of a lateral pnp transistor to (b) a bird's-eye view of the GCLPNP layout to (c) the cross-sectional cut-away of the GCLPNP structure.



according to

$$W'_b = W_b + X_{eb} + X_{cb} \quad (\text{E.10})$$

Although several variations of this basic layout were proposed, each involved only minor changes to this fundamental structure. Thus, the design goals and implementation details for each of the GCLPNP terminals in the general template of Figure E.7 are examined first, incorporating the preceding identification of those lateral pnp properties responsible for a large, bias-insensitive  $\beta$  that is robust to TID effects.

#### E.3.1.1 Emitter

Figure E.8 highlights the lone emitter stripe in the geometry of the general GCLPNP template. Key features of its design include:

**Aspect ratio:** To limit the gain of parasitic vertical pnp in Figure E.4, by favoring sidewall injection of holes toward the collectors rather than vertical injection toward the substrate, the emitter should have a large perimeter-to-area ( $P_e/A_e$ ) ratio. It has been constructed with the minimum dimensions allowed by the manufacturing rules at  $1.7 \mu\text{m}$  by  $1.7 \mu\text{m}$ .

**Doping:** Since the gain,  $\beta_{b1}$ , of an injection-efficiency limited device is proportional to the emitter doping  $N_A$  according to (E.4), the emitter is implemented using the MOS  $p^+$  source/drain diffusion layer (PPSD), which is more highly doped than the npn base layer. However, for the sake of reducing MOS junction capacitances, this layer is relatively shallow (low  $h_e$ ), which limits the intrinsic base width and reduces the efficiency with which holes are collected by the collectors as opposed to the substrate.

**Ohmic resistance:** Although typically the least important of the contact resistances [Laker and Sansen, 1994, p.126], the emitter resistance,  $r_e$  is minimized by saliciding its contact.<sup>11</sup> However, this must be limited to the the minimum area

---

<sup>11</sup>Saliciding, a common descriptor for the self-aligned siliciding technique, produces low-resistance contacts through a heat-activated reaction between an overlying metal (usually, titanium or

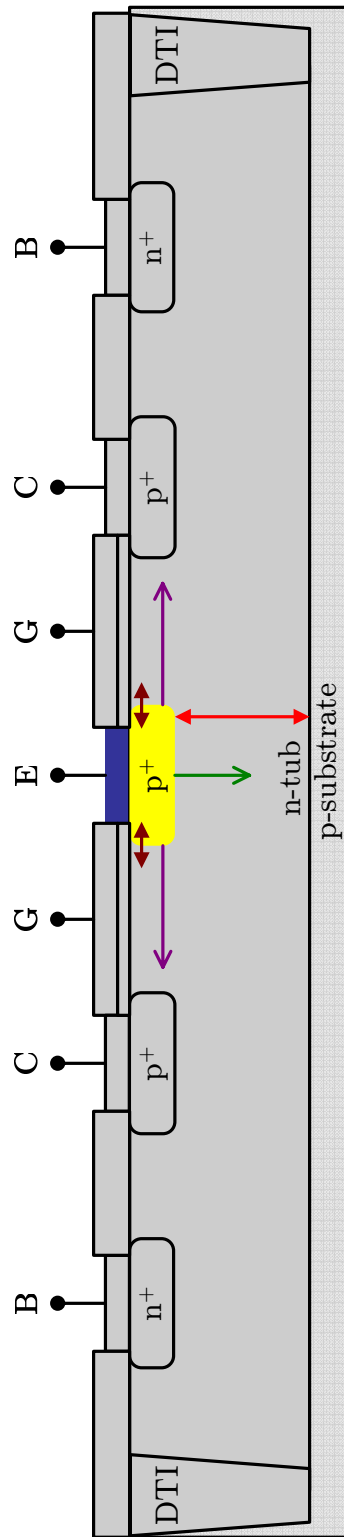


Figure E.8: Breakout of GCLPNP emitter design. The large  $P_e/A_e$  ratio favors(limits) the desired(unwanted) sidewall(vertical) injection toward the collector(substrate) indicated in purple(green). Salicide is excluded from the emitter edges to limit further thinning, as indicated in brown. However, the shallowness of the diffusion, indicated in red, limits injection efficiency.

(0.9  $\mu\text{m}$  by 0.9  $\mu\text{m}$ ), as saliciding the edges would consume silicon and further thin the already shallow diffusion.

### E.3.1.2 Collector

Figure E.9 highlights the collector ring which encircles the emitter of the general GCLPNP template. Obviously, the proximity of the former to the latter determines  $W'_b$  and therefore should be minimized. Further, the collector contact is salicided, just as for the emitter, though sheet resistivity usually dominates the contribution of the ohmic contact to the overall  $r_c$ . Additional key features of the collector design include:

**Aspect ratio:** To maximize its collection efficiency, this ring should be as deep as possible, extended beneath the intrinsic base if possible. However, the lack of a deep p-type diffusion layer in the process flow leaves no choice but to employ the same relatively shallow PPSD layer used to implement the emitter. To compensate, the collector is made somewhat wider than the minimum size (1.33  $\mu\text{m}$ ) in most varieties.

**Doping:** Ideally the collector would be as lightly doped as possible, encouraging the C-B depletion region to extend primary on its side of the junction; that is  $Y_{cb} \gg X_{cb}$ . Such a condition increases both the Early voltage ( $V_A$ ) and punch-through breakdown voltage of the device. Additionally, a lightly doped collector suppresses avalanche breakdown, so that both components of the collector-emitter breakdown voltage ( $V_{eco}$ ) are minimized. Unfortunately, the PPSD layer is much more heavily doped than would be preferred in light of these concerns. Nevertheless, it is chosen because the Ge implant of the npn base layer presents too many complications.

**Lightly doped regions:** To offset the undesirably high doping of the collector

---

tungsten) and the underling silicon or polysilicon. Surface layers of the latter are consumed in the process [Plummer *et al.*, 2000, p.699–700]. To prevent this manufacturing step, many processes offer a salicide exclusion (SALEX) layer to be drawn over polysilicon gates and resistors or source/drain diffusions.

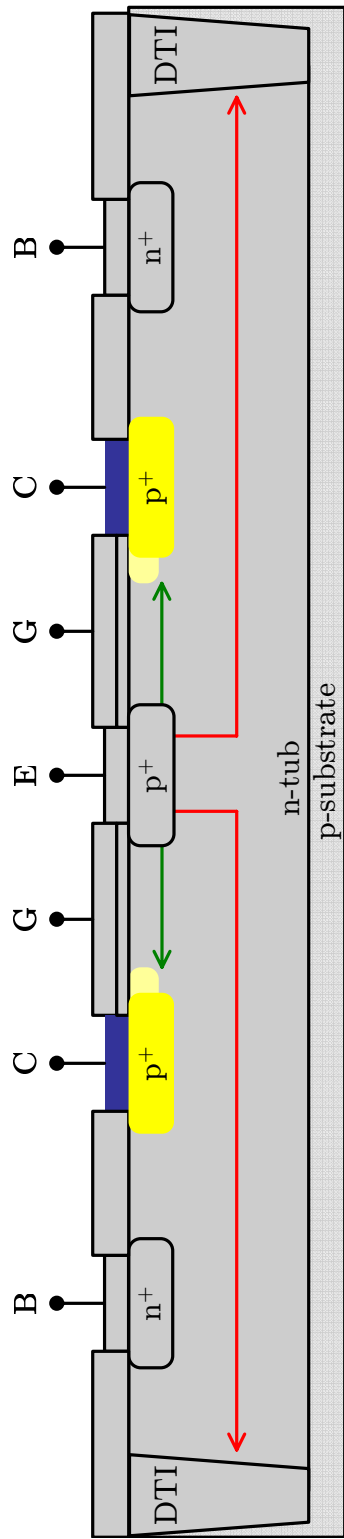


Figure E.9: Breakout of GCLPNP collector design. The shallowness of the diffusion only intercepts a fraction of the minority carriers (in green), allowing others to pass under to the isolation (in red), reducing collection efficiency. The lightly-doped drain extensions reduce  $Y_{cb}$ , thereby reducing the Early voltage ( $V_A$ ) and increasing the breakdown voltage ( $V_{eco}$ ).

lightly-doped p-type diffusions can be implanted near the C-B edge. The increase in  $Y_{cb}$  associated with this layer (PLDD) should improve  $V_A$  and  $V_{eco}$ .

### E.3.1.3 Base

Figure E.10 highlights the definition of the base width by means of the polysilicon gate grown between the collector and emitter, as well as the base contact, which must be the outermost ring if that  $W'_b$  is to be minimized, thereby reducing the numerators of all terms in (E.4). The n-type tub that forms the base itself, is addressed momentarily; here, the key features of the two base structures cited are taken to include:

**Base width:** Using a MOS polysilicon gate to define the drawn base width means  $W'_b$  is only limited by the minimum lithographic feature, in this case  $0.4 \mu\text{m}$ . The sidewall spacers extending  $0.1 \mu\text{m}$  on either side of the gate, a vestige of the MOS design rules, do not increase  $W'_b$ , whose outer edge is set by the collector PLDD implants. Note that while  $W'_b$  defines the intrinsic base width, the effective  $W_b$  depends on the weighted average of all current paths from the emitter to collector, including circuitous routes through the extrinsic base that terminate on the bottom face of the collector implant.

**Base contact:** Leveraging the existence of deep n-type sinker (NSINK) layer, the GCLPNP can reduce the contact resistance to the deepest portion of the base well, which would otherwise result in an unacceptably large  $r_b$ . It also act as a depletion stop, preventing minority carriers from drifting beneath the collector and reaching the neighboring deep-trench isolations (DTI), improving collection efficiency and DIT sidewall leakage.

### E.3.1.4 n-Type Tub

Figure E.11 describes three construction options for the n-type tub that composes the entire base diffusion. According to (E.4) the doping of this region ( $N_D$ ) should be as light as possible in order to limit recombination by increasing  $\tau_p$  (through the cross-section term of (C.24)) and increase injection efficiency. Additionally, the doping profile would ideally mix that of retrograde and non-retrograde wells, so that

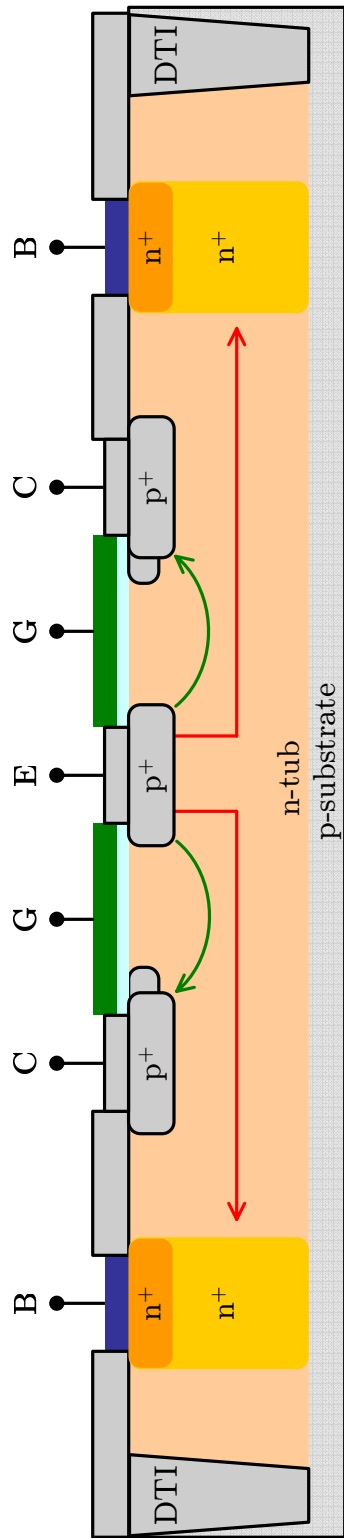


Figure E.10: Breakout of GCLPNP base design. The drawn width  $W'_b$  is determined by the lithographic etching of the MOS gate, although the effective width also incorporates circuitous routes, such as those in green. The deep  $n^+$  sinker provides a depletion stop and prevents those minority carriers that leak beneath the collector (shown in red) from reaching the isolation.

it increases both at the base of the tub and its surface. The former spoils the gain of the parasitic vertical pnp by creating a potential gradient that repels minority carriers upwards (toward to the lateral pnp) and enhances recombination for those that do make it to the junction edge before they reach the substrate. The latter lessens the impact of the second term in (E.4), pertaining to recombination, via a built-in field that forces carriers to flow away from the surface.

The implementations of Figure E.11 embody unique trade-offs between base doping level and profile, summarized as follows:

**pMOS well:** Constructing the GCLPNP tub from the same layer that forms the n-well for a pMOSFET (NWELL) benefits from a non-retrograde profile that reduces the depletion width at the surface and whose built-in field limits current flow there. However, this same field can direct minority carriers too deep, into the extrinsic base where the collection efficiency is lower. Most importantly, though, the NWELL layer is relatively highly doped, and may contain threshold implants that counterdope the surface, increasing  $S_p$  at the expense of a more well controlled  $N_D$ . If the doping is high enough, recombination in the E-B space-charge region may dominate at low-injection levels, exacerbating the impact of this higher  $S_p$ .

**npn collector:** Offering nearly the opposite properties of the previous option, a tub implanted with the doping used for the collector of npn BJTs (NCOLL) is much more lightly doped than with NWELL, but of uniform density as a function of depth, sacrificing the increased surface recombination for better collection efficiency. The lower  $N_D$  also improves injection efficiency according to (E.4), but if too low can incite high-level injection effects at moderate  $I_c$ .

**Buried layer:** A key advantage of GCLPNPs built in BiCMOS technology is access to an  $n^+$  buried layer that is traditionally used as the collector of the vertical npn, but can serve as an excellent means of thwarting the parasitic conduction path of the vertical pnp. The doping asymmetry between this layer (NBL) and the tub itself (especially if the latter is doped with NCOLL), creates an electric field that repels minority carriers from the substrate, favoring their collection

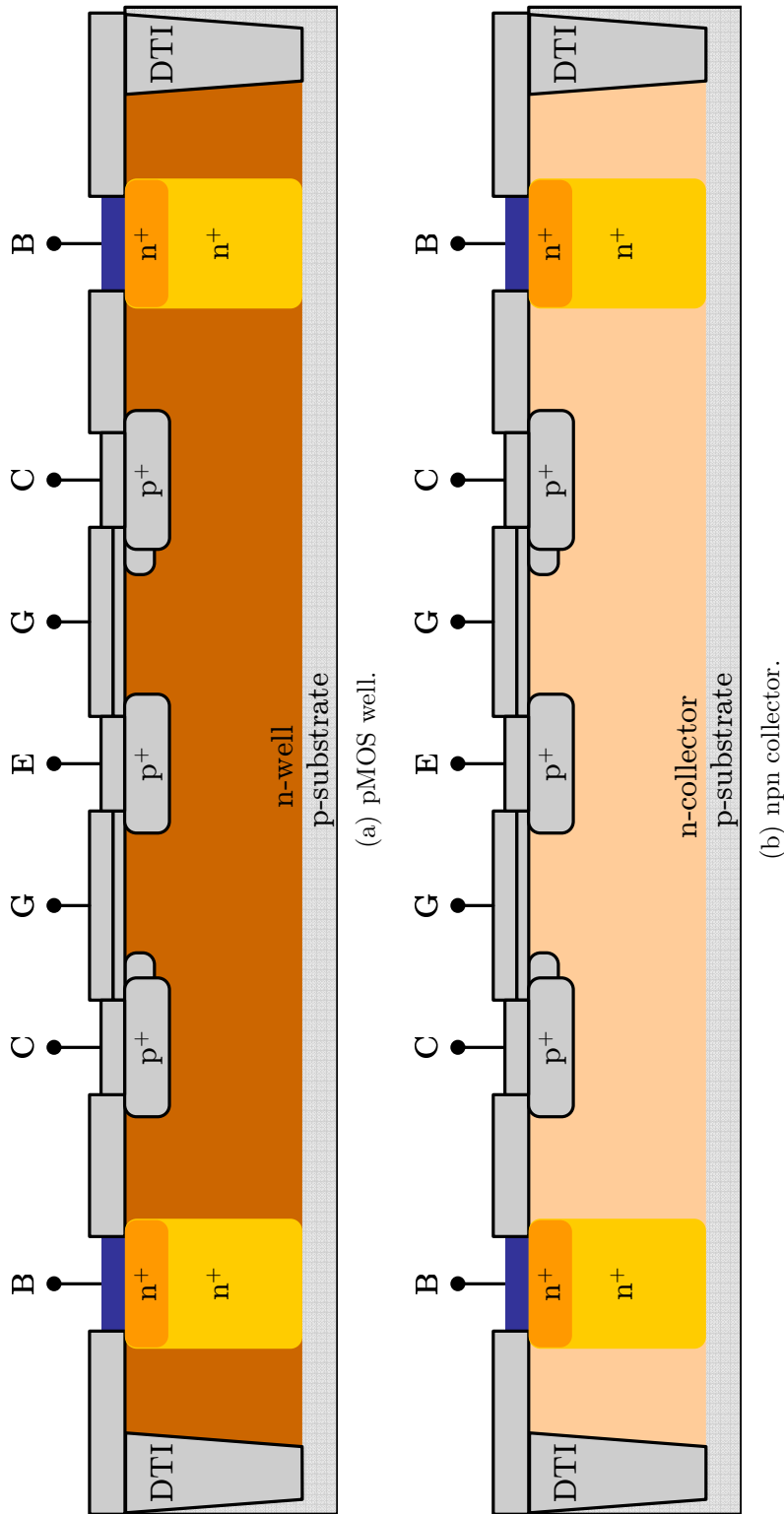


Figure E.11: Breakout of GCLPNP n-tub design. The use of: (a) the pMOS well layer trades a non-retrograde profile for high absolute doping levels; (b) the npn collector layer offers the opposite trade-offs; (c) an n<sup>+</sup> buried layer is advised to spoil the vnp and improve collection efficiency.



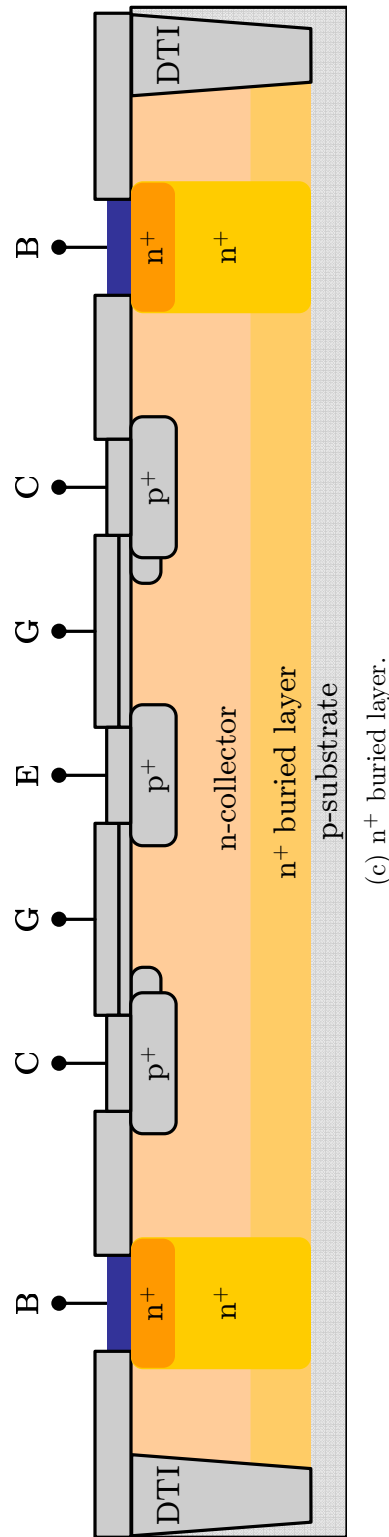


Figure E.11: Breakout of GCLPNP n-tub design (cont.). The use of: (a) the pMOS well layer trades a non-retrograde profile for high absolute doping levels; (b) the npn collector layer offers the opposite trade-offs; (c) an  $n^+$  buried layer is advised to spoil the vnp and improve collection efficiency.

by the GCLPNP and increasing reliability by preventing their injection into the isolation (leakage) or substrate (latchup). The asymmetry also acts a depletion stop, preventing the C-B depletion layer from reaching the substrate and breaking down at high  $V_{ec}$ . Finally, connecting the NBL to the base via NSINK, reduces the extrinsic component of  $r_b$ .

### E.3.1.5 Variations

In the first generation of prototype GCLPNPs, two variations on the topology of Figure E.7 were fabricated. Depicted in Figure E.12, both favored the combination of NCOLL and NBL in an attempt to maximize  $\beta$  at the expense of  $V_A$  and  $V_{ceo}$ . The only difference is the presence(absence) of the PLDD regions at the C-B edge near the surface in the 1A(1B) device set.

For reasons explicated in Section E.3.2, the second generation again encompassed two variants, but both used NWELL in place of NCOLL and omitted the PLDD implants. The flavors designated 2A and 2B, and illustrated in Figure E.13, are distinguished by the use of an NBL layer only in the former.

## E.3.2 Measured Results

A test vehicle containing both generations of GCLPNP devices was fabricated on Callisto 11 along with SVEPRE-0 (cf. Table 3.3). For each version, a triad containing two instances laid out in common-centroid fashion around a single master affords flexible connectivity to assess the performance of either the individual transistors or a current-mirror mirror arrangement. The former approach was taken during characterizations of the first(second) generation devices performed by the author on February 5, 2005(January 30, 2005) in the E. L. Ginzton Applied Physics Laboratories at Stanford University. Using an Agilent 4155C semiconductor parameter analyzer and a probe station,  $I$ - $V$  curves are traced out for all instances of each GCLPNP version by fixing the emitter/source at +2.5 V and sweeping the base current and collector voltage in nested loops for various gate voltages.<sup>12</sup>

---

<sup>12</sup>Although traditionally such characterization treats  $I_B$  and  $I_c$  as negative, since they flow out of the device, this polarity is inverted here to ease bookkeeping; as only pnp devices are being

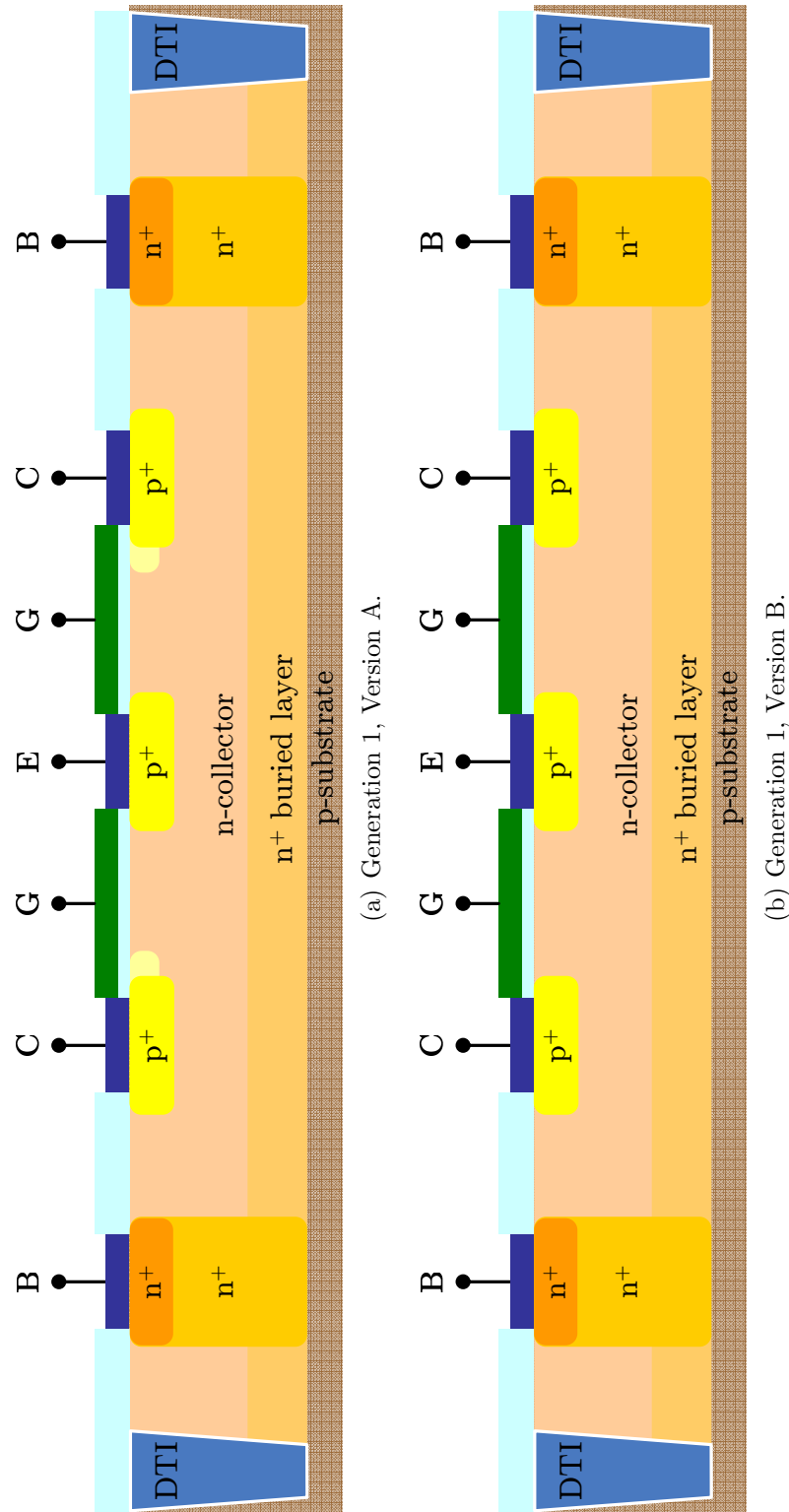


Figure E.12: Design of first-generation GCLPNP devices. In this generation both variants employ tubs with NCOLL and NBL. The only difference is that (a) version 1A uses lightly-doped drain material at the C-B edge, whereas (b) version 1B does not.

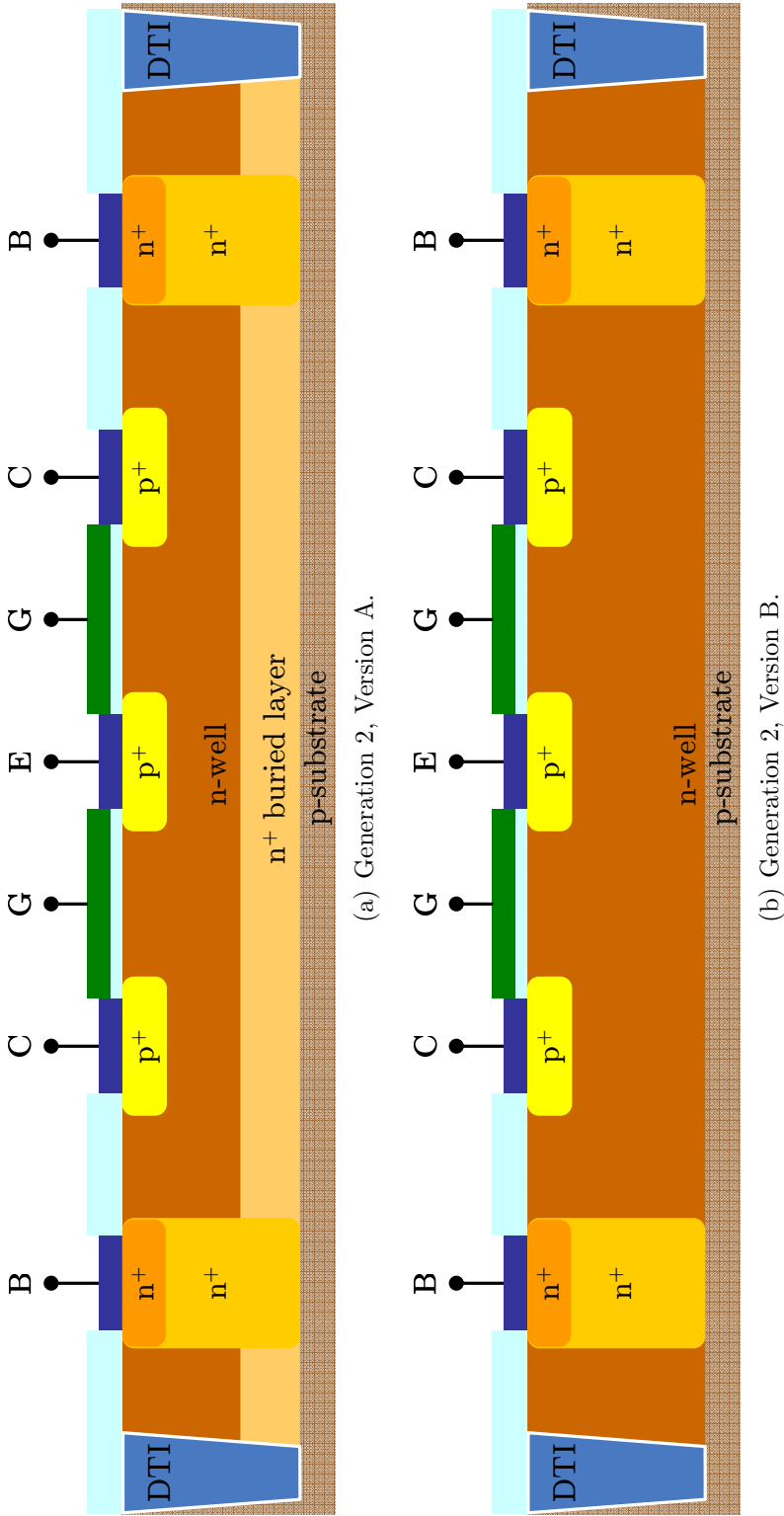


Figure E.13: Design of second-generation GCLPNP devices. In this generation both variants employ NWELL tubs and omit the PLDD implants. The only difference is that (a) version 2A uses an n<sup>+</sup> buried layer, whereas (b) version 2B does not.

The measured results for samples of the two variations in the first generation of GCLPNPs are provided in Figure E.14. For both devices,  $V_G$  is swept from 0 V to 2.5 V in 0.5 V steps. Only the extremes of this range are depicted, along with  $V_G = 1.0$  V and  $V_G = 1.5$  V—bias points intended to deplete the base without turning on the pMOS channel over most of the  $V_{ec}$  sweep. Although the curves of Figure E.14(a) largely exhibit the desired pnp character, two nonidealities are evident:  $\beta$  is a strong function of  $I_b$ , varying from 6-20 at  $V_{ec} = 1$  V; and substantial base-width modulation leads to a low  $V_A$  and thus a steep slope for  $V_{ec} > 0.5$  V. In addition, gummel plots (not shown) reveal an excess of collector current at low  $V_{eb}$  that artificially enhances  $\beta$ , especially for strong accumulation biasing. The performance of both device types is so similar as to conclude that the presence of NLDD is of little consequence.

From additional analysis, it is postulated the presence of NBL actually degraded the  $\beta$  of these devices because the base width of the vertical devices is sufficiently narrow that its field does little to repel minority carriers, which instead rapidly recombine in this highly doped layer. The low Early voltage likely reflects the large  $X_{cb}$  (and  $X_{eb}$ ) that result from the low doping of the NCOLL tub. With such a large fraction of  $W'_b$  consumed by these depletion regions, fractional changes in the latter with bias can be substantially enhanced when translated to  $W_b$ . Finally, the excess collector current at low bias simply reveals that the pMOS device is being activated. It turns out that, since NCOLL lacks a threshold implant, this transistor is behaving as a depletion-mode device that is extremely difficult to turn off, since its threshold is near zero.

All three of these shortcomings are addressed in the second generation of GCLPNPs, which use a more highly doped NWELL base diffusion, with its attendant threshold implant, to reduce  $X_{cb}$  and  $X_{eb}$  and increase  $V_{thp}$ . Additionally, the absence of NBL should improve  $\beta$  if the above inferences are correct. Corresponding results from a representative of this batch are provided in Figure E.15. Here, the absence of NBL in the second variant indeed increases  $\beta$ , as predicted, compared to the first. However, the use of NWELL has reduced the absolute  $\beta$  with little corresponding improvement of  $V_A$ . Instead, it seems that even with the threshold implant, the examined, this introduces no ambiguity.

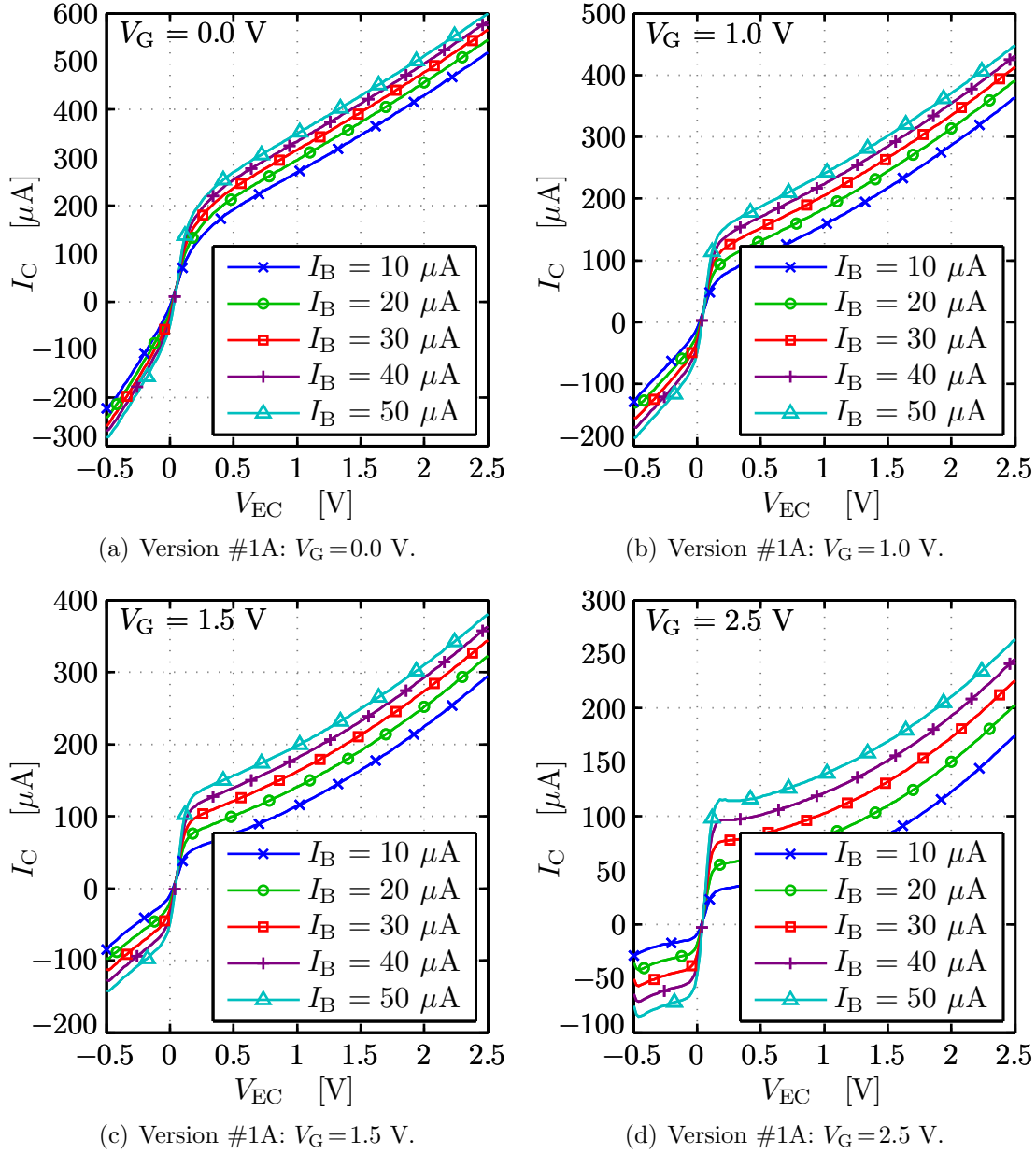


Figure E.14: Measured  $I_C$ -vs- $V_{EC}$  curves for GCLPNP version #1A. With  $V_E = +2.5 \text{ V}$ ,  $V_C$  is swept from 3 V to 0 V in  $-20 \text{ mV}$  steps and  $I_B$  is swept from  $10 \mu\text{A}$  to  $50 \mu\text{A}$  in  $10 \mu\text{A}$  steps for (a)  $V_G = 0 \text{ V}$  (b)  $V_G = 1.0 \text{ V}$ , (c)  $V_G = 1.5 \text{ V}$ , and (d)  $V_G = 2.5 \text{ V}$ . All terminal voltages/currents are compensated for pnp polarity.

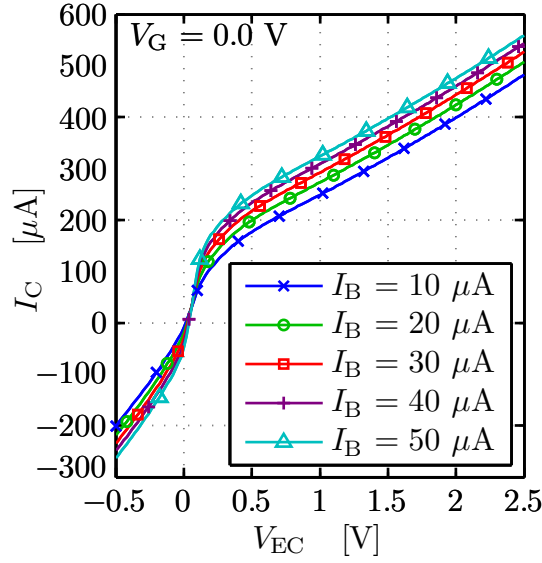
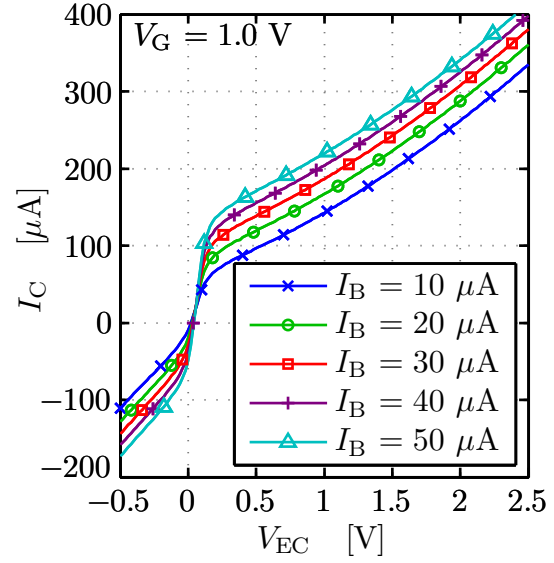
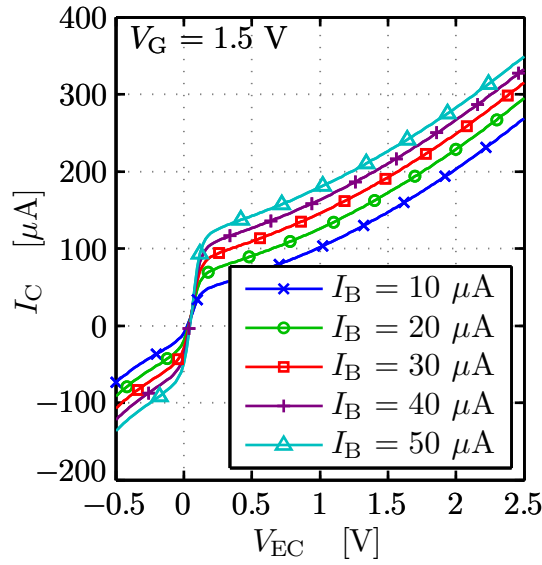
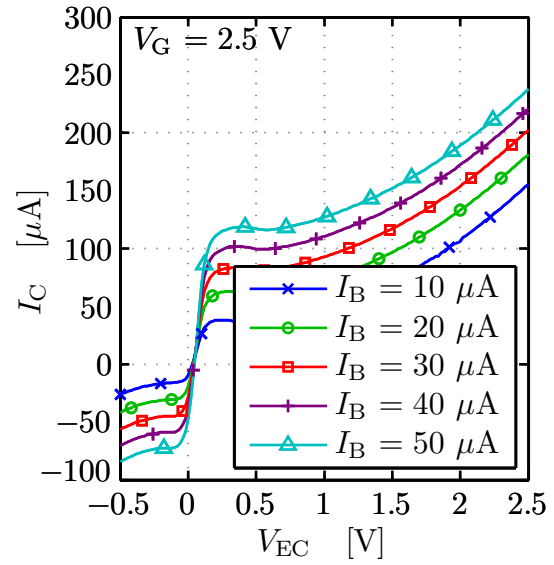
(e) Version #1B:  $V_G = 0.0$  V.(f) Version #1B:  $V_G = 1.0$  V.(g) Version #1B:  $V_G = 1.5$  V.(h) Version #1B:  $V_G = 2.5$  V.

Figure E.14: Measured  $I_C$ -vs- $V_{EC}$  curves for GCLPNP version #1B. With  $V_E = +2.5$  V,  $V_C$  is swept from 3 V to 0 V in  $-20$  mV steps and  $I_B$  is swept from  $10 \mu\text{A}$  to  $50 \mu\text{A}$  in  $10 \mu\text{A}$  steps for (e)  $V_G = 0$  V (f)  $V_G = 1.0$  V, (g)  $V_G = 1.5$  V, and (h)  $V_G = 2.5$  V. All terminal voltages/currents are compensated for pnp polarity.

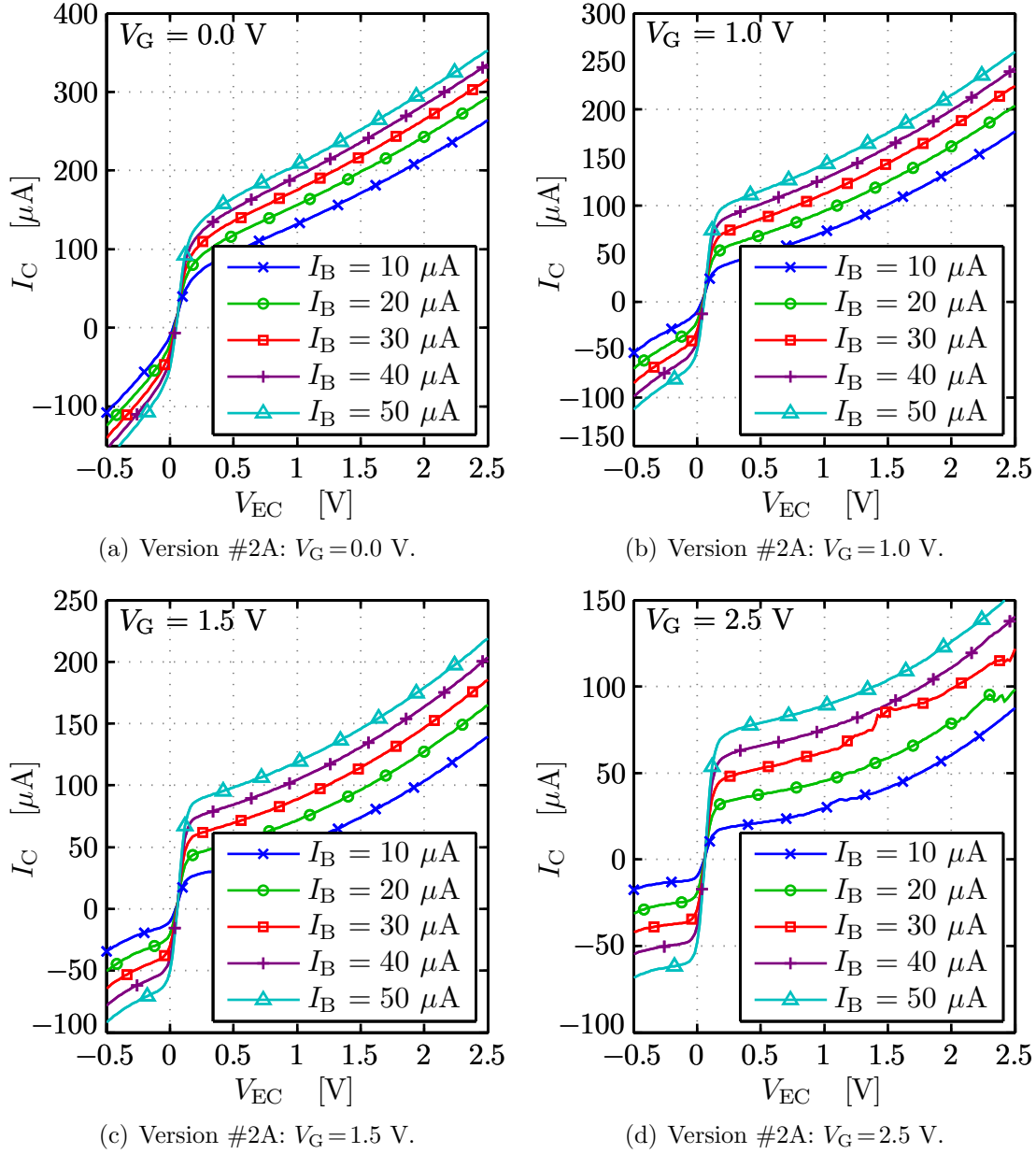


Figure E.15: Measured  $I_C$ -vs- $V_{EC}$  curves for GCLPNP version #2A. With  $V_E = +2.5 \text{ V}$ ,  $V_C$  is swept from 3 V to 0 V in  $-20 \text{ mV}$  steps and  $I_B$  is swept from 10  $\mu\text{A}$  to 50  $\mu\text{A}$  in 10  $\mu\text{A}$  steps for (a)  $V_G = 0 \text{ V}$  (b)  $V_G = 1.0 \text{ V}$ , (c)  $V_G = 1.5 \text{ V}$ , and (d)  $V_G = 2.5 \text{ V}$ . All terminal voltages/currents are compensated for pnp polarity.



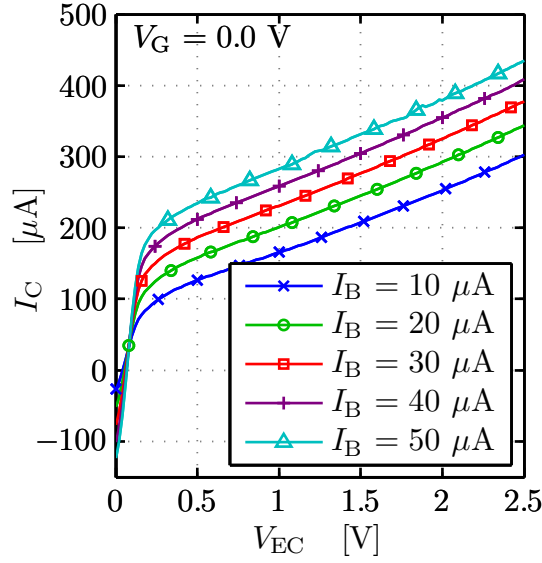
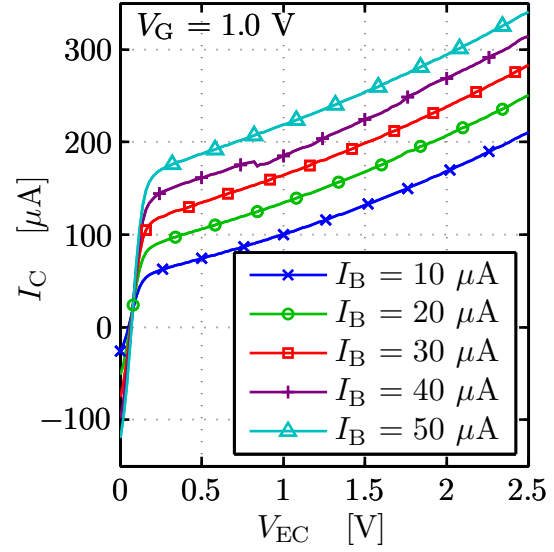
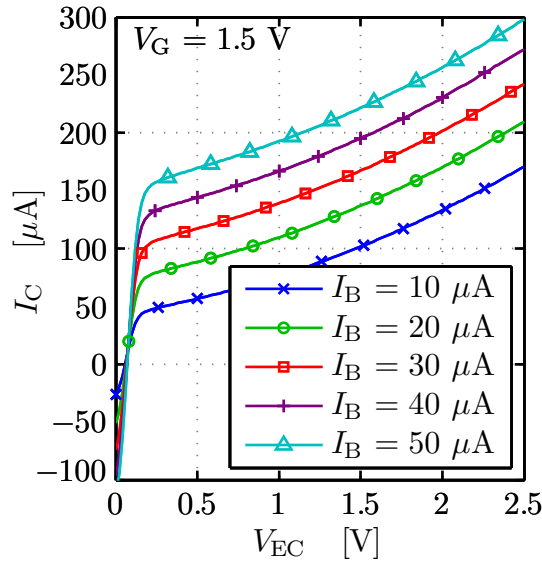
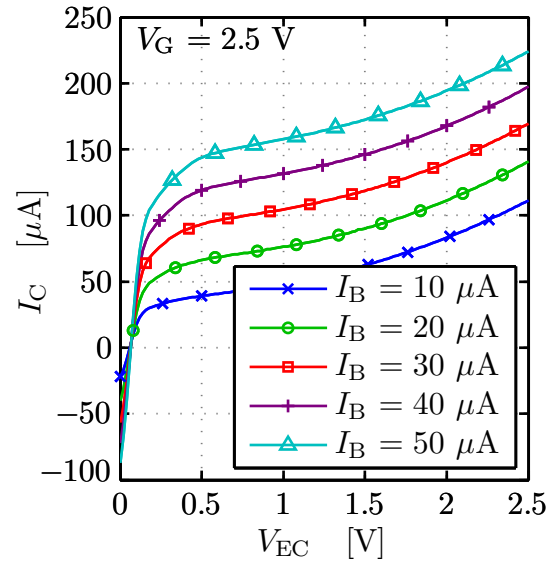
(e) Version #2B:  $V_G = 0.0$  V.(f) Version #2B:  $V_G = 1.0$  V.(g) Version #2B:  $V_G = 1.5$  V.(h) Version #2B:  $V_G = 2.5$  V.

Figure E.15: Measured  $I_C$ -vs- $V_{EC}$  curves for GCLPNP version #2B. With  $V_E = +2.5$  V,  $V_C$  is swept from 3 V to 0 V in  $-20$  mV steps and  $I_B$  is swept from  $10 \mu\text{A}$  to  $50 \mu\text{A}$  in  $10 \mu\text{A}$  steps for (e)  $V_G = 0$  V (f)  $V_G = 1.0$  V, (g)  $V_G = 1.5$  V, and (h)  $V_G = 2.5$  V. All terminal voltages/currents are compensated for pnp polarity.

attempt to bias the base in depletion with  $V_G = 1$  V is still inducing channel formation when the GCLPNP is forward biased, since  $V_{GW} < 0.7$  V.

## E.4 Summary

As a result of low Early voltage and only moderate  $\beta$ , neither generation of GCLPNP achieved the desired performance. Although further investigation into the role of the base doping profile and the unexpected detriment of the buried layer are necessary, Figure E.16 reflects the best operational mode at the present time for a second generation sample without NBL. Rather than deplete the base in an attempt to increase gain, the gate bias has been set to its maximum value,  $V_G = 2.5$  V so as to accumulate the surface and prevent channel formation. In so doing, the undesired source-to-drain leakage of the ‘parasitic’ pMOS at low bias can be suppressed, and the resulting  $I_c$  curves are substantially flatter. Nevertheless, for  $V_{EC} > 1$  V, the low Early voltage is still manifest, resulting in the steep slope. In exchange for channel suppression, this biasing condition reduces  $\beta$ , such that it ranges from  $\sim 3$  at  $I_b = -10$   $\mu$ A to  $\sim 5$  at  $I_b = -50$   $\mu$ A at  $V_{ec} = 1$  V. Although low, such values are practically identical to the gain of the substrate pnp presently offered in BiCMOS8. Thus, if follow-on efforts are able to diagnosis and correct the low Early voltage behavior, a version of the second generation GCLPNP could provide performance comparable to that of the BiCMOS8 substrate pnp with greater utility for circuit designers.<sup>13</sup>

---

<sup>13</sup>There is also the potential for the inherent TID hardness described previously, but no such determination was made for the prototype devices presented here.

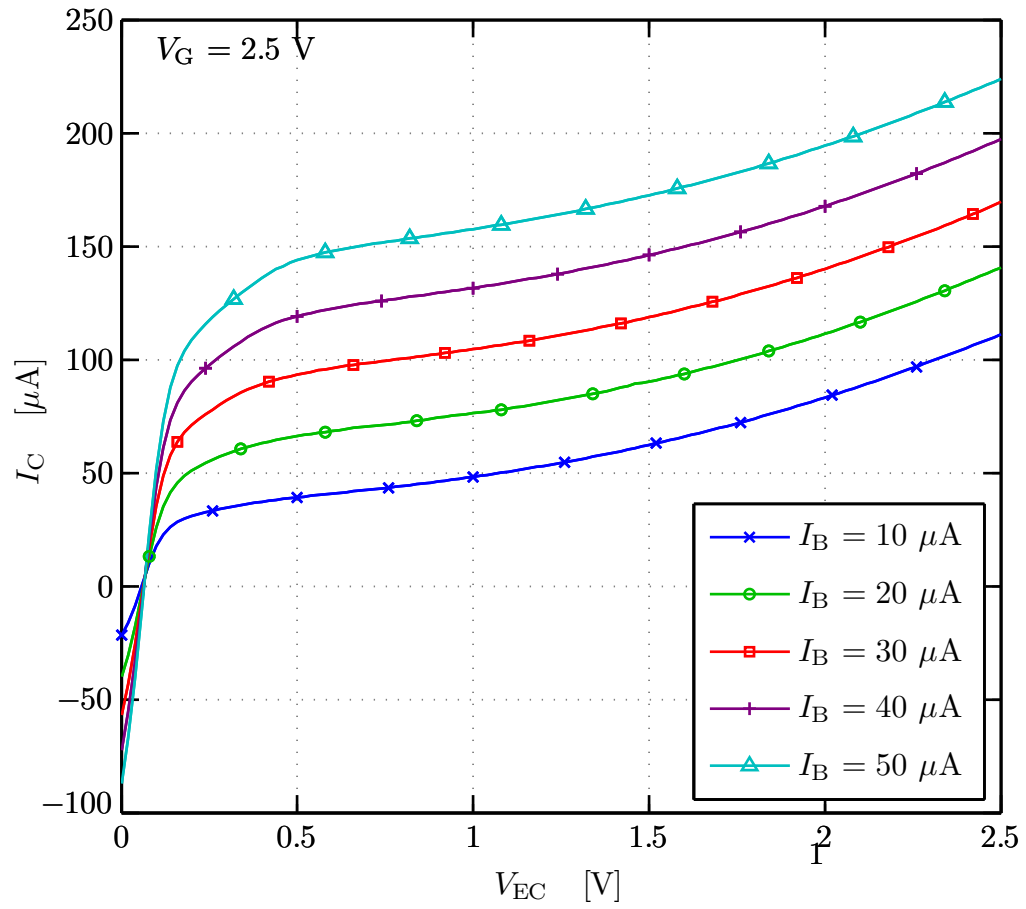


Figure E.16: Measured performance under best operating conditions, corresponding to an accumulated version #2B GCLPNP with  $V_G = +2.5$  V. All other conditions are as in Figure E.15. All terminal voltages/currents are compensated for pnp polarity.



# Appendix F

## Filter Theory

Classically, the problem of filter design is divided into two phases: approximation and realization [Sedra and Brackett, 1978, p.35]. Although Chapter 5 is primarily concerned with the latter, as it describes a physical network that realizes the desired AAF behavior, the first half of this appendix synthesizes the former:<sup>1</sup> Section F.1 provides the analytical framework to evaluate potential approximations in terms of the ideal responses of which they are capable. To then facilitate the realization of a circuit that minimizes the error between its response and this ideal, Section F.2 synthesizes the popular metrics for characterizing non-ideal integrators, such as those employed in the realization of Chapter 5.

### F.1 Filter Descriptions

Using elementary filter theory, this section arrives at a rational representation of the transfer function for target filter. To interpret the behavior of the mathematical model in Section 5.1.1, Section F.1.1 elucidates its relationship to a class of frequency-domain polynomials that offer some intuition.

---

<sup>1</sup>This is distinguished as the approximation phase because its upshot,  $T(s)$ , is necessarily an approximation to the idealized brick-wall filter of Figure 5.1(a). It is also noteworthy that the two phases are rarely ignorant of one another, with iteration required to arrive at a filter approximation that can be realized under constraints beyond just those on frequency response, such as available component values, power budgets, area limitations, and other technological specifications.

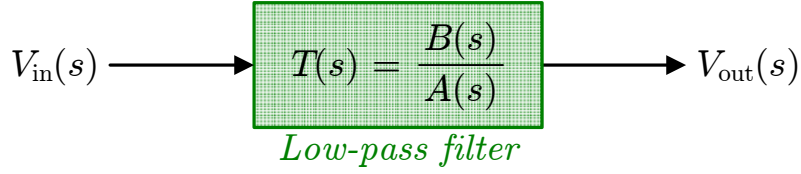


Figure F.1: Simple block diagram defining transfer function,  $T(s)$ , of low-pass filter.

### F.1.1 Filter Polynomials

As when characterizing the feedback systems of Section 3.2.2, the filter block in Figure F.1 is most readily described by the ratio of its output to input in terms of the complex frequency variable  $s = \sigma + j\omega$  in the Laplace domain. For all practical circuit realizations of  $N^{\text{th}}$ -order filters,<sup>2</sup> this relationship, captured by the transfer function  $T(s) = V_{\text{out}}(s) / V_{\text{in}}(s)$ , can be expressed as a rational function of polynomials  $A(s)$  and  $B(s)$ , of degree  $N$  and  $M$  respectively (where  $N \geq M$ ) [Sedra and Brackett, 1978, p.3],<sup>3</sup> such that

$$T(s) = \frac{B(s)}{A(s)} \quad (\text{F.1})$$

The roots of the numerator(denominator) are known as the transmission zeros(poles) and denoted by  $z_i^{\text{T}}(p_j^{\text{T}})$  for  $i=1, 2, \dots M(j=1, 2, \dots N)$ .<sup>4</sup>

Although  $T(s)$  is a real rational function of  $s$  [Schaumann and van Valkenburg, 2001, p.5],<sup>5</sup> in the Fourier domain where  $s=j\omega$ , it constitutes a complex number that can be expressed either in Cartesian or polar coordinates as:

$$T(j\omega) = T(s)|_{s=j\omega} = R(\omega) + jX(\omega) = \rho_{\text{T}}(\omega) e^{j\Theta_{\text{T}}(\omega)} \quad (\text{F.2})$$

where the Cartesian components ( $R(\omega)$  and  $X(\omega)$ ) are related to their polar counterparts ( $\rho_{\text{T}}(\omega)$  and  $\Theta_{\text{T}}(\omega)$ ) through the standard expressions.

<sup>2</sup>The order of the filter is simply the number of homogeneous solutions of  $A(s)$ .

<sup>3</sup>If  $M > N$ , the filter cannot be realized with a finite number of real components [Schaumann and van Valkenburg, 2001, p.6].

<sup>4</sup>It can be inferred that there exist  $N - M$  transmission zeros at infinity.

<sup>5</sup>If the filter is to be implemented with positive-valued circuit elements and avoid oscillation, the coefficients of  $B(s)$  and  $A(s)$  must be real-valued and, in the latter case, all positive (e.g.,  $A(s)$  is strictly a Hurwitz polynomial [Sedra and Brackett, 1978, p.3]) so that the zeros(poles) of  $T(s)$  lie in the closed(open) left-half plane [Schaumann and van Valkenburg, 2001, p.5–6].

To promote a better understanding of the available filter approximations, these representations of the transfer function are often replaced with a class of polynomials enumerated in the remainder of this section that describe the filter in terms of its attenuation.

#### F.1.1.1 Loss Function

Since the  $p_i^T$  represent the natural modes of the system, which is the information most germane to filter design, classical treatments of the subject prefer to work with  $H(s)$ , the reciprocal of  $T(s)$  defined in Fourier space in by analytical continuation of its Laplace transform as

$$H(j\omega) = H(s)|_{s=j\omega} = \frac{1}{T(s)} \Big|_{s=j\omega} = \frac{A(j\omega)}{B(j\omega)} \quad (\text{F.3})$$

Whereas the transfer function,  $T(j\omega)$ , is a measure of signal transmission through the system,  $H(j\omega)$  is known as the loss transfer function, or simply *loss function*. In this context, the roots of  $B(j\omega)$  are alternately called the *loss poles*, but the roots of  $A(\omega)$  are still known as the natural modes, or simply poles, since they are independent of the direction of signal flow through the circuit.

By analogy to (F.2), its also customary to define  $H(j\omega)$  in terms of an exponential in a single complex variable  $\Theta_H$ , such that

$$H(j\omega) = e^{j\Theta_H(\omega)} \quad (\text{F.4})$$

The variable  $\Theta_H$ , known (rather confusingly) as the effective transmission constant [Sedra and Brackett, 1978, p.10], is decomposed according to  $\Theta_H = \alpha(\omega) + j\phi(\omega)$  where the real and imaginary parts are derived from (F.4) as

$$\alpha(\omega) = \ln(|H(j\omega)|) \quad (\text{F.5a})$$

$$\phi(\omega) = \arctan\left(\frac{\Im\{H(j\omega)\}}{\Re\{H(j\omega)\}}\right) \quad (\text{F.5b})$$

By substituting (F.2) and (F.3) into (F.5), it can also be expressed in terms of  $T(j\omega)$ :<sup>6</sup>

$$\alpha(\omega) = -\ln(\rho_T(\omega)) = -\frac{1}{2}\ln(R^2(\omega) + X^2(\omega)) \quad (\text{F.6a})$$

$$\phi(\omega) = -\Theta_T(\omega) = \arctan\left(-\frac{X(\omega)}{R(\omega)}\right) \quad (\text{F.6b})$$

The real part of the transmission constant,  $\alpha(\omega)$ , is known as the attenuation function,<sup>7</sup> while the imaginary part,  $\phi(\omega)$ , is the phase lag.<sup>8</sup> Although these two

---

<sup>6</sup>In the context of filter design,  $\arctan$  is the so-called *atan2* operation—a variation of the standard arctangent ( $\tan^{-1}$ ) that expands its range from  $[-\pi/2, \pi/2]$  to  $(-\pi, \pi]$ , placing the angle in its proper quadrant. For  $R \leq 0$  it dictates that  $+\pi(-\pi)$  be added to the result of  $\tan^{-1}(X/R)$  whenever  $X$  is positive(negative).

<sup>7</sup>The attenuation function  $\alpha(\omega)$  can be related to the more commonly specified measure of attenuation (in dB):

$$A(j\omega) = -20\log(|H(j\omega)|) = 20\log(e^{\alpha(\omega)})$$

by the factor of  $20\log(e) \simeq 8.686$ . Hence the units of  $\alpha(\omega)$  are Nepers (a corruption of the name of the famed Scottish logarithmic mathematician, John Napier) where 1 Neper  $\simeq 8.686$  dB.

<sup>8</sup>Since the phase lag is a transcendental function of the coefficients of  $R(\omega)$  and  $X(\omega)$ , and since it is much more difficult to measure accumulated phase than the change in instantaneous phase,  $\phi(\omega)$  is not a particularly convenient metric for filter designers (though it proves mathematically useful subsequently). Instead of total phase lag, it is preferable to specify and measure the derivative of the phase lag function with respect to instantaneous frequency. By analogy to the reciprocal of its spatial equivalent,  $v_g$  (cf. Footnote 32 of Chapter 1) this derivative is known as the group (or envelope) delay,  $\delta(\omega)$ , and can be expressed as an analytical function of the real and imaginary polynomials of  $T(j\omega)$  using (F.2):

$$\delta(\omega) = \frac{\partial \phi}{\partial \omega} = \frac{\partial}{\partial \omega} \tan^{-1}\left(-\frac{X(\omega)}{R(\omega)}\right) = \frac{1}{\rho_T} \left( -R(\omega) \frac{\partial X(\omega)}{\partial \omega} + X(\omega) \frac{\partial R(\omega)}{\partial \omega} \right)$$

It can be shown through analytic continuation (that is, by substituting  $\omega = s/j$ ) that this expression yields a real rational polynomial  $\delta(s)$  that is analytically integrable, allowing the relationship between  $\phi(s)$  and  $\delta(s)$  to be expressed as

$$\phi(s) = \int_0^s \delta(x) \, dx + \phi(0)$$

Notably, this implies that the area under the group delay curve only depends on the asymptotes of the phase lag function because, letting  $s \rightarrow \infty$ :

$$\int_0^\infty \delta(x) \, dx = \phi(\infty) - \phi(0)$$

In other words, the subtle variations of the phase lag function with frequency do not effect the



parameters can be computed in terms of the real and imaginary parts of  $T(j\omega)$  in (F.6), they fundamentally describe the loss transfer function and as such the negative signs associated with the loss of magnitude (in Nepers) and lag in phase (in radians) are subsumed into their definitions.

### F.1.1.2 Characteristic Polynomials

A quantity of particular interest in filter design, for reasons of mathematical simplicity, is the squared magnitude of the transfer function, obtained by multiplying the transfer function and its conjugate as<sup>9</sup>

$$|T(j\omega)|^2 = T(j\omega) T^*(j\omega) = T(s) T(-s)|_{s=j\omega} \quad (\text{F.7})$$

Notably, since  $T(s)$  contains only real coefficients, (F.7) makes use of the fact that its conjugation only requires negation of the complex variable itself:

$$T^*(j\omega) = T(-j\omega) = T(-s)|_{s=j\omega} \quad (\text{F.8})$$

This rule holds for all the polynomials described in this section.

Just as for  $T(j\omega)$  itself in (F.1), it is always possible to express (F.7) as a ratio of two polynomials whose order matches that of  $|T(j\omega)|^2$ ,<sup>10</sup> such that

$$|T(j\omega)|^2 = \frac{|B(j\omega)|^2}{|A(j\omega)|^2} \quad (\text{F.9})$$

But, since  $|T(j\omega)|^2$  is both real and even [Schaumann and van Valkenburg, 2001, p.255], each term of (F.9) can also be expressed as just a polynomial of  $\omega$  with order

---

accumulated group delay—only the difference between the initial and final value of  $\phi(s)$  matter.

<sup>9</sup>Intuitively, this convenience can be understood in terms of symmetry. Any stable filter has all its poles in the (open) left half of the complex plane. But, an analytical description of their locations would be cleaner if mirrored analogs with positive real part also existed, forming a symmetric constellation about the imaginary axis. Such is the case for the function described by  $T(s)T(-s)$ ; hence, its utility.

<sup>10</sup>The degree of the numerator polynomial goes to  $n$  by explicitly counting the zeros at infinity (cf. Footnote 4).

$n=2N$ . Using the subscript  $n$  to denote the order of each such polynomial,<sup>11</sup> so that the numerator and denominator become  $A_n(\omega)$  and  $B_n(\omega)$ , which are known as the *characteristic polynomials*, (F.9) can alternatively express  $T_n(\omega)$  as

$$T_n(\omega) = |T(j\omega)|^2 = \frac{B_n(\omega)}{A_n(\omega)} \quad (\text{F.10})$$

Without loss of generality, the relationship between these  $n^{\text{th}}$ -order characteristic polynomials and their namesake  $N^{\text{th}}$ -order decompositions in (F.1) can be extracted by considering just  $A_n(\omega)$ . If  $A(s)$  is factored such that  $A(s) = a \prod_{i=1}^N (s + p_i^T)$ , where  $a$  is a real number chosen such that  $A(s)$  is monic,<sup>12</sup> then

$$A_n(\omega) = |A(j\omega)|^2 = a^2 \prod_{i=1}^N (j\omega + p_i^T) (-j\omega + p_i^T) = a^2 \prod_{i=1}^N (\omega^2 + (p_i^T)^2) \quad (\text{F.11})$$

Since the coefficients of  $A(s)$  are real (cf. Footnote 5), its roots,  $p_i^T$ , are either real singletons or conjugate pairs [Sedra and Brackett, 1978, p.3]. They can be squared without first taking their magnitude in (F.11), which reveals that the  $n$  roots of  $A_n(\omega)$  are simply the positive and negative version of each of the roots of  $A(s)$ ; the same is true for  $B_n(\omega)$ :

$$A_n(\omega) = A(\omega^2) \big|_{p_i^T \rightarrow (p_i^T)^2} \quad (\text{F.12a})$$

$$B_n(\omega) = B(\omega^2) \big|_{z_i^T \rightarrow (z_i^T)^2} \quad (\text{F.12b})$$

Typically, a filter approximation only specifies  $A_n(\omega)(B_n(\omega))$  so the underlying  $A_\omega(B_\omega)$  can be chosen such that it contains the  $N$  roots of  $A(\omega^2)(B(\omega^2))$  with negative real part to guarantee stability.

---

<sup>11</sup>The corollary: polynomials without subscripts are of order  $N$ .

<sup>12</sup>Monic representations of the characteristic polynomials, whose leading (i.e., highest-order) terms have unity coefficients, are preferred for identifying the roots when factoring. In addition to simplifying the mathematics, this choice of  $a$  is convenient for the filter implementations being considered, whose most complicated  $A(s)$  is derived from trigonometric or Chebyshev functions of real variables.

### F.1.1.3 Characteristic Function

To express the difference between the presence of a filter with an arbitrary response  $|T(j\omega)|^2$ , and the absence of any filter, in which case  $T(j\omega) = H(j\omega) = 1$ , it also proves convenient to express  $H(s)$  in terms of a polynomial  $K(s)$  known as the *characteristic function* such that

$$|H(j\omega)|^2 = 1 + |K(j\omega)|^2 \quad (\text{F.13})$$

using the same analytical continuation as in (F.7).<sup>13</sup> For an example bandpass filter, this relationship, and the connection to  $\alpha(\omega)$  of (F.5a), is nicely summarized in Figure F.2. From (F.1), (F.3), and (F.13), it can be shown that  $K(s)$  is also a real rational function of  $s$  with the same denominator as  $H(s)$  [Sedra and Brackett, 1978, p.52], so the Fourier representation employed in (F.13) can be expressed more generally as

$$K_n(\omega) = |K(j\omega)|^2 = \epsilon^2 \frac{F_n(\omega)}{B_n(\omega)} \quad (\text{F.14})$$

where  $\epsilon$  is a real number whose extraction renders  $B_n(\omega)$  monic. As for  $A_n(\omega)$  and  $B_n(\omega)$  in (F.12),  $F_n(\omega)$  can also be expressed as a polynomial in  $\omega^2$ , with roots  $z_i^K$  known as reflection zeros.

Combining (F.10), (F.13), and (F.14) yields the central equation of approximation theory, known as the Feldtkeller equation [Sedra and Brackett, 1978, p.54]:

$$A_n(\omega) = B_n(\omega) + \epsilon^2 F_n(\omega) \quad (\text{F.15})$$

Equation (F.15) defines the relationship between the  $n$  roots of  $A_n(s)$  (the poles,  $\pm p^T$ ),  $B_n(s)$  (the loss poles,  $\pm z^T$ ), and the  $F_n(s)$  (the reflection zeros,  $\pm z^K$ ) through  $\epsilon$ , which is dubbed the ripple parameter for reasons made apparent in Section 5.1.1.

---

<sup>13</sup>In addition to encapsulating the deviation of the transfer function from unity, the structure of (F.13) permits the application of rational functions which approximate zero, rather than unity, which are simpler in nature [Sedra and Brackett, 1978, p.51].

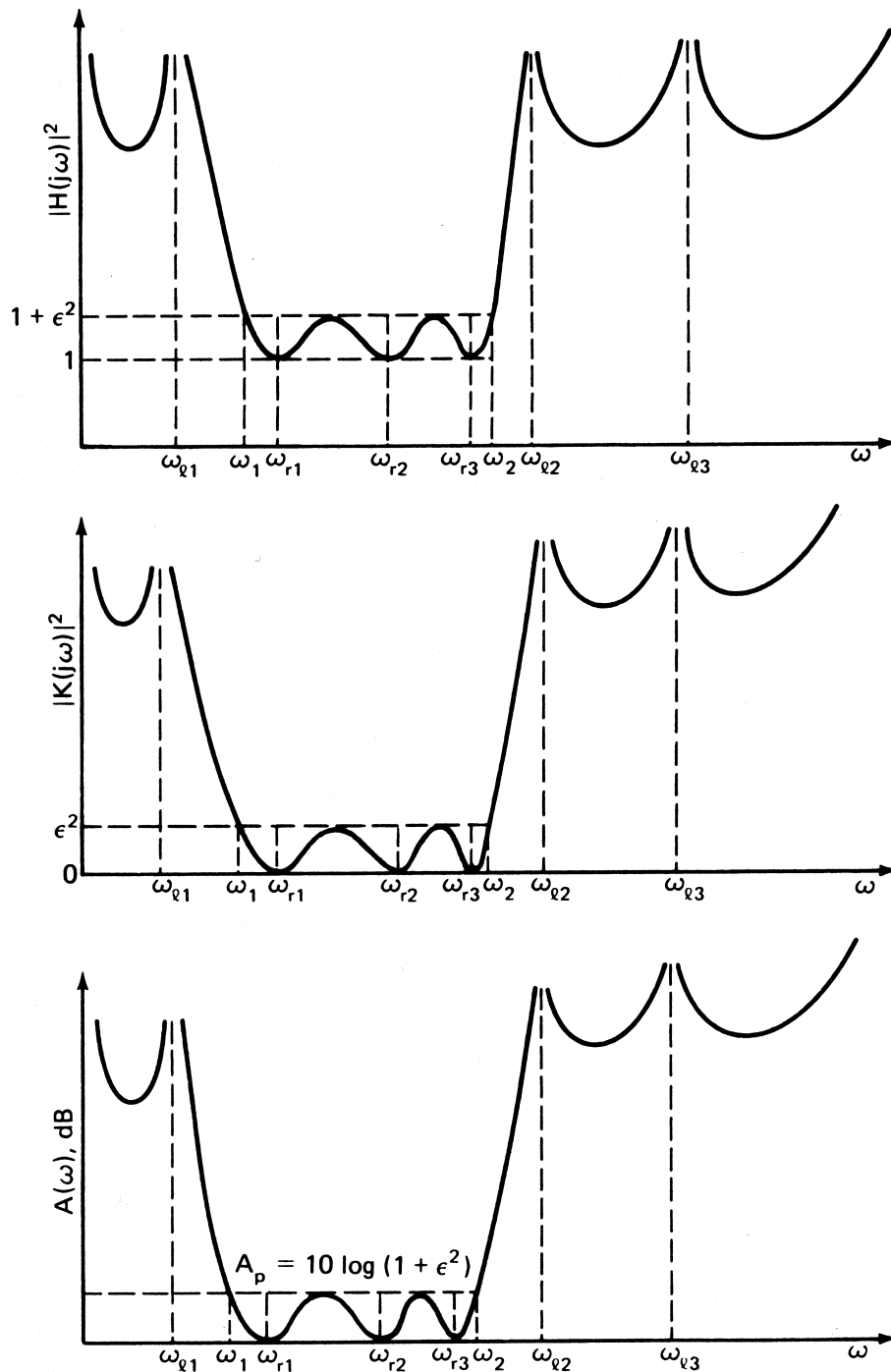


Figure F.2: Relationship between (top)  $H(j\omega)$ , (middle)  $K(j\omega)$ , and (bottom)  $\alpha(\omega)$  (denoted as  $A(\omega)$  here) for an example bandpass filter according to (F.13) and (F.5a). Reproduced *in toto* from [Sedra and Brackett, 1978, p.53].

### F.1.2 Pole-Zero Relationships

According to (F.13), the ideal brick-wall low-pass filter of Figure 5.1(a) possesses a characteristic function given by

$$K_\infty(j\omega) = \begin{cases} 0 & , \text{ for } \omega \leq \omega_c \\ \infty & , \text{ for } \omega > \omega_c \end{cases} \quad (\text{F.16})$$

Intuitively, to best approximate this unity-gain(zero-gain) in the passband(stopband), the reflection zeros(transmission zeros) should be located directly on the  $j\omega$  axis at or below(above)  $\omega_p(\omega_r)$  [Sedra and Brackett, 1978, p.67].

The implications of this approach for the choice of  $K(s)$  arise from a formally expanding (F.14) according to (F.11) for the case when the roots of  $F(s)$  and  $B(s)$  are complex and, consequently, occur as conjugate pairs:<sup>14</sup>

$$K_n(\omega) = |K(j\omega)|^2 = \epsilon^2 \prod_{i=1}^{N/2} \frac{(\omega^2 + (z_i^K)^2)(\omega^2 + (z_i^{K*})^2)}{(\omega^2 + (z_i^T)^2)(\omega^2 + (z_i^{T*})^2)} \quad (\text{F.17})$$

If, to best approximate the ideal filter,  $z_K^i \rightarrow j\omega_K^{zi}$  and  $z_T^i \rightarrow j\omega_T^{zi}$ , then

$$\frac{F^2(\omega)}{B^2(\omega)} = \prod_{i=1}^{N/2} \frac{(\omega^2 - (\omega_{zi}^K)^2)^2}{(\omega^2 - (\omega_{zi}^T)^2)^2} \quad (\text{F.18})$$

So, the conditions that the numerator and denominator of  $K(s)$  have real coefficients and possess only imaginary roots results (via (F.12) and (F.17)–(F.18), respectively) in

$$K_n(\omega) = |K(j\omega)|^2 = K(\omega^2) \Big|_{z_i^K \rightarrow -(\omega_{zi}^K)^2, z_i^T \rightarrow -(\omega_{zi}^T)^2} = K^2(\omega) \quad (\text{F.19})$$

Whether  $K_n(\omega)$  is expressed in terms of  $K(\omega^2)$  (with the appropriate substitutions) or  $K^2(\omega)$ —both prove useful given the  $K(s)$  described in Section F.1.3—the roots of its numerator(denominator),  $F_n(\omega)(B_n(\omega))$ , are the positive and negative

<sup>14</sup>For clarity, assume  $N$  is even. Otherwise, there exists an additional root for each polynomial on the real axis.

versions of the reflection(transmission) zeros, scilicet, the roots of  $F(s)(B(s))$ .

### F.1.2.1 Summary

Consider now the following summary of the relationships between the roots of  $A_n(\omega)$ ,  $B_n(\omega)$ , and  $F_n(\omega)$  as defined by (F.15) and the behavior of the desired  $T_n(s)$ :

**Transmission zeros:** The zeros of  $T_n(\omega)$ , are the loss poles of  $H_n(\omega)$  and  $K_n(\omega)$ , which are related to the transmission zeros (i.e., the roots of  $B(s)$ ) by (F.18) as  $\pm z_i^T$ . Since they are typically placed on the imaginary axis in the stopband, the transmission zeros lie at those frequencies  $\omega_{zi}^T$  where the filter gain is identically zero.

**Reflection zeros:** The zeros of  $K_n(\omega)$  are related to the reflection zeros (i.e., the roots of  $F(s)$ ) by (F.18) as  $\pm z_i^K$ . Since they are typically placed on the imaginary axis in the passband, the reflections zeros lie at those frequencies  $\omega_{zi}^K$  where (F.13) reaches its minimum value (unity) and, thus  $T_n(\omega)$  is maximized (at unity).

**Roots of  $\epsilon^2$ :** Assuming  $K(s)$  is bounded, in which case the maximum value of  $K_n(\omega)$  is  $\epsilon^2$  through the choice of this constant so as to monically normalize it. Then, the loss function  $H_n(s)$  reaches its maximum value of  $1 + \epsilon^2$  whenever  $F_n(s) = B_n(s)$ . These values of  $s$ , denoted  $v_i^K$  are often purely imaginary ( $v_i^K \rightarrow j\omega_{vi}^K$ ) and represent the minima of  $T_n(s)$ . They occur in the passband, where  $B_n(s)$  is roughly constant (since the transmission zeros have not kicked in), at those points between reflection zeros where  $F_n(s)$  is maximum.

**Roots of negative unity:** Literally interpreting (F.13), there should be no poles of  $T_n(\omega)$  on the  $j\omega$ -axis because  $K_n(\omega)$  is always positive. But, by analytical continuation, for which  $\omega \rightarrow s/j$  and by (F.19), for which  $K_n(\omega)$  can be represented as  $K^2(\omega)$ , squaring of the imaginary constant permits negative values of  $K_n(s)$  elsewhere in the complex plane. At points where  $K_n(s) = -1$ , known as negative roots of unity,  $u_i^K$ , the loss function goes to zero—such values of  $s$  are the poles  $p_i^T$ . Although not purely imaginary, these are related to  $F_n(\omega)$

and  $B_n(\omega)$  through analytical continuation of (F.14) as being the points for which  $F_n(s) = \epsilon^{-2} B_n(s)$ .

The relationship of various critical points in the domain of the characteristic function, both along the  $j\omega$ -axis and throughout complex plane, to the corresponding properties of the transfer function, are summarized in Table F.1.

### F.1.3 Filter Approximations

The choice of characteristic function trades off the accuracy of the filter approximation in both magnitude and phase across the full frequency space against the complexity of its realization in terms of component quantity and quality. Over the course of this research, various characteristic functions were considered and/or implemented on SVEPRE prototypes to evaluate the suitability of the architecture for realizing a range of approximations. These are briefly summarized as:

#### F.1.3.1 Butterworth

The Butterworth filter offers a maximally flat passband, meaning as many derivatives of the transfer function are zero at the origin as possible. Consequently, the attenuation increases monotonically from the origin to the edge of the passband, providing linear phase in the absence of zeros there, and beyond. To see this formally, consider the characteristic function for an  $N^{\text{th}}$ -order filter of the form

$$K_n(\omega) = \epsilon^2 \tilde{\omega}^n \quad (\text{F.20})$$

where the frequency variable has been normalized to the passband edge so that  $\tilde{\omega} = \omega/\omega_p$ . Since  $B_n(s) = 1$ , there are no transmission zeros and the gain falls off monotonically through the transition band and stopband after reaching its passband minimum at the lone root of  $\epsilon^2$  at  $\tilde{\omega} = 1$ . The only reflection zero is at the origin, so the loss is initially zero and stays as flat as possible with increasing frequency. By

Characteristic function			Transfer function		Location			
Property	$K_n(s)$	$K_n(\omega)$	Property	$T_n(s)$	$T_n(\omega)$	$s$ -plane	Filter band	
Loss poles	$\pm p_i^K$	$\pm \omega_{pi}^K$	Roots of $B_n(s)$	Transmit. zeros	$\pm z_i^T$	$\pm \omega_{zi}^T$	Imaginary	Stopband
Reflection zeros	$\pm z_i^K$	$\pm \omega_{zi}^K$	Roots of $F_n(s)$	Maxima	$\pm \max_i^T$	Value of unity	Imaginary	Passband
Roots of $\epsilon^2$	$\pm v_i^K$	$\pm \omega_{vi}^K$	$F_n(s) = B_n(s)$	Minima	$\pm \min_i^T$	Value of $(1 + \epsilon^2)$	Complex	Passband
Roots of $-1$	$\pm u_i^K$		$F_n(s) = \epsilon^{-2} B_n(s)$	Poles	$\pm p_i^T$	Roots of $A_n(s)$	Off $j\omega$ -axis	Transition

Table F.1: Summary of relationship between poles, zeros, roots, maxima, and minima of filter polynomials.



expressing (F.20) in the alternate parlance of (F.19), as

$$K(\omega^2) = (\epsilon \tilde{\omega}^N)^2 = (\tilde{\omega}')^2 \quad (\text{F.21})$$

and letting the ripple parameter be subsumed into a normalized frequency  $\tilde{\omega}' = \epsilon^{1/n} \tilde{\omega}$  it is clear that the  $n$  roots of negative unity of (F.21), are equally spaced around a circle of radius  $1(\epsilon^{-1/N})$  in the normalized (raw)  $s$ -plane. Those  $N$  roots in the left-half plane are designated as  $p_i^T$  to ensure the filter is stable.

### F.1.3.2 Type I Chebyshev

The advantage of a Chebyshev filter lies in permitting the passband to exhibit non-monotonic variations, provided they are bounded by a specified  $A_{\max}$ . As seen when comparing Figure 5.1(b) to Figure 5.1(a), allowance of  $A_{\max} > 0$  dB permits deviation from unit gain over the full passband. The Type I Chebyshev low-pass filter possesses equiripple in the passband to most efficiently satisfy the attenuation specification rather than far exceeding it at low frequencies, with a monotonically decaying stopband and moderate group delay.

It requires a  $K_n(\omega)$  that oscillates between 0 and  $\epsilon^2$  over the passband, so that  $H_n(\omega)$  oscillates between 0 and  $20\log(1 + \epsilon^2) = A_{\max}$  dB. Such a function is obtained by scaling a  $K_n(\omega)$  that oscillates repeatedly between  $\pm 1$  for  $\tilde{\omega} < \pm 1$  known as the Chebyshev polynomial of order  $N$ .<sup>15</sup>

$$C_N(\tilde{\omega}) = \cos(N \cos^{-1}(\tilde{\omega})) \quad (\text{F.22})$$

---

<sup>15</sup>It can be shown that (F.22) is indeed a polynomial using trigonometric identities. The result is a recursive definition:

$$C_N(x) = 2xC_{N-1}(x) - C_{N-2}(x)$$

wherein the order of  $N$  determines the initial conditions,  $|C_N(0)|^2$  and  $|C_N(1)|^2$ , according to

$$|C_N(0)|^2 = \begin{cases} 0 & , \text{ for odd } N \\ 1 & , \text{ for even } N \end{cases}$$

and

$$|C_N(1)|^2 = 1$$

Here,  $N$  can be understood as a multiplier to enhance the number of cycles of the output between  $\pm 1$  for each cycle of the input over the same range.

Simply scaling the full Chebyshev polynomial in (F.22) by  $\epsilon$  would allow it to oscillate between the desired limits over the passband, but the description is deficient because the inverse cosine function at its heart is not defined for  $|\tilde{\omega}| \geq 1$ ; beyond the passband, the argument of (F.22) becomes imaginary. However, utilizing Euler's representation of  $\cos(x)$  to derive relationships that hold over the range  $|\tilde{\omega}| \geq 1$  and substituting them into (F.22) gives

$$C_N(\tilde{\omega}) = \cosh(N \cosh^{-1}(\tilde{\omega})) \quad (\text{F.23})$$

Combining (F.23) with (F.22) yields a piecewise Chebyshev function that can serve as  $K_n(\omega)$  when scaled and squared according to (F.19):

$$K_n(\omega) = K^2(\omega) = \epsilon^2 C_N^2(\tilde{\omega}) = \begin{cases} [\epsilon \cos(N \cos^{-1}(\tilde{\omega}))]^2 & , \text{ for } |\tilde{\omega}| < 1 \\ [\epsilon \cosh(N \cosh^{-1}(\tilde{\omega}))]^2 & , \text{ for } |\tilde{\omega}| \geq 1 \end{cases} \quad (\text{F.24})$$

Lacking transmission zeros, analysis of (F.24) focuses on the passband branch, which exhibits maxima(minima) at the reflection zeros(roots of  $\epsilon^2$ ) that occur when (F.22) goes to zero(unity). Such points correspond to

$$\max_i^T = \tilde{\omega}_{zi}^K = \cos\left(\frac{\pi}{2} \frac{2i+1}{N}\right) \quad (\text{F.25a})$$

$$\min_i^T = \tilde{\omega}_{vi}^K = \cos\left(\frac{\pi}{2} \frac{2(i+1)}{N}\right) \quad (\text{F.25b})$$

for

$$i = 1, 2, \dots, \frac{N}{2} \quad , \text{ for even } N$$

$$i = 1, 2, \dots, \frac{N}{2} - 1 \quad , \text{ for odd } N$$

Note that all the reflection zeros lie on the imaginary axis inside the unit circle. In contrast, solving (F.24) for its negative roots of unity and breaking each  $u_i^K$  into

its real and imaginary parts such that  $u_i^K = \tilde{\sigma}_{ui}^K + j\tilde{\omega}_{ui}^K$ , indicates that the  $p_i^T$  lie on an ellipse given by:

$$\left( \frac{\tilde{\sigma}_{ui}^K}{\sinh(a)} \right) + \left( \frac{\tilde{\omega}_{ui}^K}{\cosh(a)} \right) = 1 \quad (\text{F.26})$$

where  $a = N^{-1} \sinh^{-1}(\epsilon^{-1})$ .

### F.1.3.3 Type II Chebyshev

The Type II (or inverse) Chebyshev response combines the maximally flat passband of a Butterworth filter with Chebyshev (or equiripple) behavior in the stopband while offering moderate group delay.<sup>16</sup> The presence of transmission zeros in the stopband increases  $r_\alpha$ , just like the reflection zeros in the Type I response, but the stopband attenuation is no longer monotonic. Exchanging high-frequency attenuation for a flatter passband is attractive in many applications, but comes at a hardware cost associated with implementing the transmission zeros—unlike its Type I analog, the transfer function can no longer be all-pole.

The inverse Chebyshev transfer function is derived from simple transformations of its Type I counterpart: first, subtract the latter from one, to produce a high-pass equivalent. Then, replace  $\tilde{\omega}$  with its reciprocal to reflect the response about the logarithmic frequency axis. It can be shown that these manipulations convert (F.24) into

$$K_n(\omega) = K^2(\omega) = \frac{1}{\epsilon^2 C_N^2\left(\frac{1}{\tilde{\omega}}\right)} \quad (\text{F.27})$$

where  $C_N(x)$  still represents the piecewise  $N^{\text{th}}$ -order Chebyshev polynomial of (F.24) but the mirroring now defines the normalization in terms of the stopband edge:  $\tilde{\omega} = \omega/\omega_r$ .

Since both the argument of  $C_N(x)$  and the overall expression of (F.27) are reciprocated from their counterparts in (F.24), the reflection zeros of the latter are the reciprocals of the transmission zeros of the former. However, when (F.24) and (F.27) are substituted into (F.15), the reciprocation of the overall expressions is moot, so

---

<sup>16</sup>In some cases, the passband of the Type II Chebyshev can be even flatter than that of a Butterworth filter of the same order [*Schaumann and van Valkenburg, 2001*, p.303].

the poles, maxima, and minima of the two transfer functions can be directly mapped from one to the other merely through reciprocation. The upshot is that  $z_i^K$  and  $v_i^K$  lie beyond  $|j1|$  on the imaginary axis, in the stopband along with  $z_i^T$ , while the poles assume residence outside the unit circle at a reciprocal distance from the origin, but with the same azimuthal location, and thus quality factor, as in the Type I case.

#### F.1.3.4 Cauer

The Cauer (or elliptic) filter can be viewed as a combination of the Type I and Type II Chebyshev responses. That is, its transfer function contains complex poles inside the unit circle located around an ellipse to provide equiripple in the passband (as in Type I) as well as transmission zeros along the imaginary axis beyond  $|j1|$  to provide equiripple in the stopband (as in Type II). The use of equiripple in both the passband and stopband provides for best use of the allowable attenuation specifications and thus the lowest possible order for a given transition bandwidth.

Let the poles inside the unit circle match the negative roots of unity for the Type I characteristic function in (F.24). Then the Cauer  $K_n(\omega)$  must possess the same reflection zeros on the imaginary axis,  $\omega_{zi}^K$  given by the roots of the Chebyshev polynomial. Conversely, if the loss poles of the Cauer  $K_n(\omega)$  are set to match those of the Type II characteristic function in (F.27),  $\omega_{pi}^K$ , then they must be given by the reciprocal roots of the Chebyshev polynomial. Using the format of (F.18), these conclusions are encapsulated by expressing the Cauer characteristic function as<sup>17</sup>

$$K_n(\tilde{\omega}) = \epsilon^2 \prod_{i=1}^{N/2} \frac{(\tilde{\omega}^2 - (\tilde{\omega}_{zi}^K)^2)^2}{(\tilde{\omega}^2 - (\tilde{\omega}_{pi}^K)^2)^2} \quad (\text{F.28})$$

But, through (F.24) and (F.27), it has already been shown that the Type I

---

<sup>17</sup>In actuality, the  $T_n(s)$  pole and zero locations that arise from (F.28) are not identical to those of the Type I and Type II Chebyshev approximations. One complication is the presence of non-unitary  $B_n(\omega)$  in (F.27), which changes the negative roots of unity from those of Type I case. Even though  $B_n(\omega)$  is hardly different from unity in the passband, since the transmission zeros of (F.27) lie in the stopband, the  $p_i^T$  are not identical. Secondly, scaling of the geometric mean presented in (F.29) (cf. Footnote 18) is necessary to standardize the normalization of  $\omega_p$  and  $\omega_r$ . Typically, tables must be used to arrive at the exact values of  $p_i^T$  and  $z_i^T$ .

reflection zeros and Type II loss poles are reciprocals of one another, such that

$$\tilde{\omega}_{\text{pi}}^{\text{K}} \tilde{\omega}_{\text{zi}}^{\text{K}} = \tilde{\omega}_{\text{m}}^2 \quad (\text{F.29})$$

where  $\tilde{\omega}_{\text{m}}$  is the geometric mean frequency chosen to lie in between the poles and zeros (in the transition band).<sup>18</sup>

### F.1.3.5 Bessel

Although their analytical formulations do not conform as easily to a description in terms of  $H_n(s)$  and  $K_n(s)$ , Bessel filters are a popular choice for plasma wave receiver AAFs on account for their maximally flat delay and critical damping of their step response [*Ergun et al., 2001*, p.78]. Their approximations are derived somewhat akin to that of a Butterworth filter, but with all derivatives of the group delay, rather than loss function, being set to zero so as to maintain the DC value (of zero) as long as possible [*Schaumann and van Valkenburg, 2001*, p.401–405].

Consider the comparison of pole locations for 3<sup>rd</sup>-order Butterworth, Type I Chebyshev, and Bessel filters in Figure F.3. The quality factor ( $Q$ ) of the Bessel poles is much lower than that of the other approximations owing to their angle with the  $j\omega$ -axis.<sup>19</sup> Since flat delay requires low- $Q$  poles, while steep roll-off requires high  $Q$ , the Bessel  $r_\alpha$  is vastly inferior even to that of a Butterworth approximation [*Schaumann and van Valkenburg, 2001*, p.405].

Although 4-pole Bessel AAFs are the standard in modern WBRs, such as those of FAST [*Ergun et al., 2001*, p.78] and THEMIS [*Bonnell et al., 2008*, p.315], their  $r_\alpha$  is only  $\sim 24$  dB/octave. Without the benefit of higher oversampling ratios that can

<sup>18</sup>Although they are reciprocals,  $\tilde{\omega}_{\text{m}}$  is typically not set to unity because some scaling is needed so that the  $\tilde{\omega} = 1$  is at the edge of the passband, rather than being in the middle of the transition band.

<sup>19</sup>Recall that the  $Q$  of a complex pair of poles  $\sigma \pm j\omega$  is given by  $Q = \sigma^2 + \omega^2 / \sigma$ . So, the angle between the pole location and the imaginary axis,  $\theta = \tan^{-1}(\sigma/\omega)$  is

$$\Theta = \sin^{-1} \left( \frac{1}{2Q} \right)$$

The higher the pole  $Q$ , the closer the pair lies to the imaginary axis—for  $Q > 6$ ,  $\theta < 5^\circ$ .

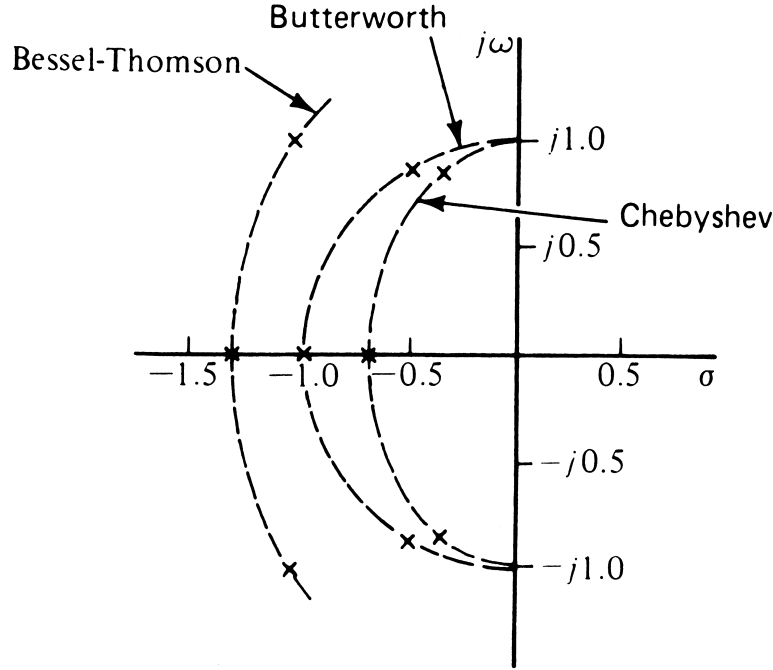


Figure F.3: Relative pole locations of Bessel approximation. For a representative, normalized, 3<sup>rd</sup>-order low-pass filter, the poles of the Bessel approximation (denoted Bessel-Thomson) lie outside the unit circle(ellipse) on which the poles of the Butterworth(Type I Chebyshev) approximation fall. Reproduced *in toto* from [Schaumann and van Valkenburg, 2001, p.409].

tolerate gradual attenuation while maintaining high resolution, the passband of the target receiver would shrink by 75% if a 4<sup>th</sup>-order Bessel AAF were adopted. Since the order of the Bessel filter necessary to preserve the full  $\omega_p$  ( $N \geq 8$ ) is too high for practical integration in silicon at VLF frequencies, such approximations were not considered for the SVEPRE AAF.

## F.2 Integrator Loss Metrics

From a factoring like that of (F.18), the desired  $T(s)$  for each of the filters in Section F.1.3 can be realized as a combination of lossless and lossy integrators that

are ideally represented as

$$T_{\text{lossless}}(s) = \frac{1}{s\tau} \quad (\text{F.30a})$$

$$T_{\text{lossy}}(s) = \frac{1}{s\tau + 1} \quad (\text{F.30b})$$

Whether building such integrators from passive or active components, the non-ideality of their constituent elements has long been a key consideration.

Traditionally, there are three methods of describing the degree to which an actual implementation of an analog integrator deviates from (F.30) due to losses associated with the circuit building blocks. Since each has a direct analog to the parasitic losses of a passive reactance—the simplest integrator/differentiator—Section F.2.1 begins by presenting these fundamentals; Section F.2.2 extends the concepts to active integrators. The most salient metric for filter designers, on account of the ease with which it is both measured and interpreted, excess phase, receives additional attention in Section F.2.3.

Formalizing the relationships between loss, dissipation, integrator  $Q$ , and excess phase provides an analytical structure capable of treating errors from both circuit classes analogously. When applied to analysis of the integrator circuits in Section 5.3, this method identifies the allowable tolerances for such nonidealities in light of the integrator specifications.

### F.2.1 Reactive Losses, Passive

Consider the simplest, ideal integrator: an ideal capacitor whose admittance is given by  $Y(s) = sC$ . Of course, any actual capacitor also exhibits some finite energy loss resulting from leakage across its dielectric, which can be modeled as a parasitic parallel conductance,<sup>20</sup>  $\sigma_C = 1/\rho_C$ , changing its admittance to

$$Y'(s) = sC + \sigma_C \quad (\text{F.31})$$

---

<sup>20</sup>In actuality most real capacitors present a series parasitic resistance, not a parallel one. But, when acting as an integrator, it is the parallel resistance that changes the location of the pole, thus the equivalent mathematical description is formatted accordingly.

Real-valued, since it models shunt power dissipation, the loss term  $\sigma_C$  moves  $Y(s)$  off the imaginary axis, even for pure sinusoidal signals.

### F.2.1.1 Dissipation

In a second interpretation, assume that the size of this resistance is inversely proportional to the value of the capacitor—which is intuitively satisfying since smaller capacitors have thicker dielectrics and thus longer resistive paths for leakage current—so that the parasitic effects of  $\sigma_C$  can be incorporated into the admittance as

$$Y'(s) = sC + \sigma_C = sC + d_C C = (s + d_C) C \quad (\text{F.32})$$

where the  $d_C$  is the reciprocal of the constant of proportionality between the capacitor and  $\rho_C$ . Known as the dissipation factor,  $d_C$  is zero for an ideal capacitor and can be defined analogously for the series parasitic resistance of an inductor (as  $R_p = d_L L$ ), though does not prove as germane to the discussion that follows.

Representing the parasitic loss of the capacitor using its dissipation factor is convenient in that, adducing (F.32), merely substituting  $s \rightarrow s + d_C$  in all the relevant loss functions accurately accounts for the frequency domain effects:<sup>21</sup> it is akin to evaluating the sinusoidal steady-state response along the line  $s = j\omega + d_C$ .

### F.2.1.2 Quality Factor

More commonly, the quality of an ideal inductor or capacitor is quantified by its  $Q$ , or quality-factor, which, just as for the pole- $Q$  (cf. Footnote 19) is defined as the ratio of its nominal reactance(susceptance) to the total parasitic resistance(conductance) when the parasitic impedance(admittance) in question is in series(parallel) with the

---

<sup>21</sup>Provided the dissipation is independent of frequency. When it is not, as discussed just hence, excess phase is a more appropriate metric.



element. Thus, the relationship between  $Q$  and  $d$  is derived from (F.32) as:

$$Q_C = Q_{\text{parallel}} = \frac{\Im\{Y(j\omega)\}}{\Re\{Y(j\omega)\}} = \frac{\omega C}{\sigma_C} = \frac{\omega}{d_C} \quad (\text{F.33a})$$

$$Q_L = Q_{\text{series}} = \frac{\Im\{Z(j\omega)\}}{\Re\{Z(j\omega)\}} = \frac{\omega L}{\rho_L} = \frac{\omega}{d_L} \quad (\text{F.33b})$$

## F.2.2 Reactive Losses, Active

To see how the notions of loss, quality factor, and dissipation can be extended to active integrators—and, in fact, any element—consider the simplest case of the ideal, lossless active-RC integrator defined by (F.30a) and generalize its transfer function such that  $T_{\text{int}}(s) = 1/s\tau$ , where  $\tau$  is the integration constant and  $1/\tau$  the unity-gain frequency. The corresponding loss function,  $H_{\text{int}}(s) = s\tau$  is thus analogous to the admittance of an ideal capacitor of value  $\tau$ .

However, in a non-ideal implementation of this integrator, additional terms appear in the  $H_{\text{int}}(s)$ . For example, it can be shown that if it is built from an amplifier A2 with finite DC gain  $A_{o2}$ , as in Figure 5.9(a), then the non-ideal  $H'_{\text{int}}(s)$  contains a loss term  $\sigma_{\text{int}} = 1/A_{o2}$  such that:

$$H'_{\text{int}}(s) = s\tau + \sigma_{\text{int}} = \left(s + \frac{1}{\tau A_{o2}}\right) \tau = (s + d_{\text{int}}) \tau \quad (\text{F.34})$$

where the rightmost result expresses the dissipation of the integrator as  $d_{\text{int}} = 1/\tau A_{o2}$  by analogy with (F.32). Extending this notion to an integrator with a loss function of arbitrary order  $m$ , it is always possible factor the  $H'_{\text{int}}(s)$  polynomial so that it obeys the general form of (F.34) using a generalized time constant  $\tau_{\text{int}}(s)$  and generalized dissipation factor  $d_{\text{int}}(s)$ :

$$\begin{aligned} H'_{\text{int}}(s) &= a_m s^m + a_{m-1} s^{m-1} + \dots \\ &= \left( \frac{a_m}{a_k} s^{m-k-1} + \frac{a_{m-1}}{a_k} s^{m-k-2} + \dots \right) a_k s^{k-1} \\ &= (s + d_{\text{int}}(s)) \tau_{\text{int}}(s) \end{aligned} \quad (\text{F.35})$$

where  $k$  is the order of the lowest odd power of  $s$  in  $H'_{\text{int}}(s)$ , typically unity.<sup>22</sup>

Leveraging analytical continuation into the Fourier domain to evaluate the cumulative non-ideal effects of various elements in the integrator circuit, the effective integration constant and dissipation in (F.35) become:

$$\tau_{\text{int}} = \frac{\Im\{H'_{\text{int}}(j\omega)\}}{\omega} \quad (\text{F.36a})$$

$$d_{\text{int}} = \frac{\Re\{H'_{\text{int}}(j\omega)\}}{\tau_{\text{int}}} = \omega \frac{\Re\{H'_{\text{int}}(j\omega)\}}{\Im\{H'_{\text{int}}(j\omega)\}} \quad (\text{F.36b})$$

Since all loss terms are subsumed into  $d_{\text{int}}$ , it is also possible to define an effective  $Q_{\text{int}}$  by analogy with (F.33):

$$Q_{\text{int}} = \frac{\Im\{H'_{\text{int}}(j\omega)\}}{\Re\{H'_{\text{int}}(j\omega)\}} = \frac{\omega}{d_{\text{int}}} \quad (\text{F.36c})$$

Each non-ideality, including the DC gain and parasitic poles of A2, results in an additional term in  $H'_{\text{int}}(s)$  of (F.35) that is included in the summation for  $d_{\text{int}}(s)$ . Thus, the non-ideal  $T'_{\text{int}}(s)$  can be derived from its ideal counterpart using  $s \rightarrow s + d_{\text{int}}$ .

### F.2.3 Excess Phase

Unfortunately, for most realistic integrator implementations, it can be extremely cumbersome to compute  $\tau_{\text{int}}$  and  $d_{\text{int}}$  from (F.36), so such a substitution is nontrivial. The difficulty in extending the  $d_{\text{int}}$  or  $Q_{\text{int}}$  model to higher order  $H'_{\text{int}}(s)$  is that both quantities, related through  $Q = \omega/d$  arise from the assumption that  $\sigma_{\text{int}}$  is proportional to  $\tau_{\text{int}}$  but independent of frequency. Another formulation better suited for capturing the losses that vary with frequency is to treat the additional terms in  $H'_{\text{int}}(s)$  as undesired poles and quantify their contribution to phase lag of the signal,  $\phi(\omega)$ , in excess of the  $90^\circ$  that is characteristic of an ideal integrator. This interpretation is especially suited to active integrators in which there is often a one-to-one correspondence between these parasitic poles and the frequency response of the elements in the feedback loop.

---

<sup>22</sup>For unit  $k$ ,  $\tau_{\text{int}}(s) = \tau_{\text{int}}$ , whereas  $d_{\text{int}}(s) = d_{\text{int}}$  for  $m < 2$ .

### F.2.3.1 Lossless Integrator

An elementary example of excess phase computation returns to the generalized lossless integrator of (F.30a) and re-derives the result not for an opamp with finite gain as in (F.34), but one with finite bandwidth, by using the integrator model for the opamp first introduced in Section 5.2.1.1 (cf. Footnote 14 of Chapter 5) in which  $A_2(s) = \omega_t/s$ . The loss function then becomes

$$H''_{\text{int}}(s) = - \left[ s^2 \frac{\tau}{\omega_t} + s \left( \tau + \frac{1}{\omega_t} \right) \right] \quad (\text{F.37})$$

Rather than collecting the second-order term into  $d_{\text{int}}(s)$ , recall the definition of the phase lag function  $\phi(\omega)$  provided in (F.5b). Assuming that  $\omega_t \tau \gg 1$ , which implies that the cut-off frequency associated with the integration constant,  $\omega_o = 1/\tau$ , is much smaller than the opamp gain-bandwidth product and employing the usual analytical continuation to Fourier space, (F.37) becomes

$$H''_{\text{int}}(j\omega) = \frac{\omega^2 \tau}{\omega_t} - j\omega\tau \quad (\text{F.38})$$

which corresponds to a phase lag of

$$\phi(\omega) = \arctan\left(\frac{\Im\{H''_{\text{int}}(j\omega)\}}{\Re\{H''_{\text{int}}(j\omega)\}}\right) \simeq \frac{\pi}{2} + \tan^{-1}\left(\frac{\omega}{\omega_t}\right) \quad (\text{F.39})$$

where final approximation assumes  $\omega \ll \omega_t$ .

Since the excess phase of a first-order integrator,  $\Delta\phi(\omega)$ , is defined as  $\Delta\phi(\omega) = \phi(\omega) - \pi/2$ , the excess phase contribution of the opamp to the lossless integrator is given by

$$\Delta\phi(\omega) = \phi(\omega) - \frac{\pi}{2} = \tan^{-1}\left(\frac{\omega}{\omega_t}\right) \simeq \frac{\omega}{\omega_t} \quad (\text{F.40})$$

where the approximation truncates the Taylor expansion of  $\tan^{-1}(x)$  at  $\tan^{-1}(x) \simeq x$ . The term  $\omega/\omega_t$  resembles the phase contribution in the vicinity of a pole, so the excess phase can be interpreted as the additional lag in the feedback loop due to the single-pole response of the opamp.

Substituting (F.36) into (F.40), the excess phase of (F.40) can alternately be expressed in terms of the integrator dissipation and quality factor, unifying the four loss accounting methods in a single formula:

$$\Delta\phi(\omega) = -\tan^{-1}\left(\frac{d_{\text{int}}}{\omega}\right) = -\tan^{-1}\left(\frac{1}{Q_{\text{int}}}\right) = -\tan^{-1}\left(\sigma_{\text{int}}\frac{\omega_o}{\omega}\right) \quad (\text{F.41})$$

### F.2.3.2 Lossy Integrator

Having shown through the preceding examples that (F.41) has an approximate value of  $\omega/\omega_t$  for the lossless integrator of Figure 5.9(a) it is worth noting for completeness that the same result holds for the lossy integrator of (F.30b). Again using the integrator opamp model for A1, the generalized loss function for the circuit of Figure 5.9(b) is found as

$$H''_{\text{int}}(s) = -\left[s^2\frac{\tau}{\omega_t} + s\tau\left(1 + \frac{1}{\omega_t\tau}\left(1 + \frac{1}{T_o}\right)\right) + \frac{1}{T_o}\right] \quad (\text{F.42})$$

where the finite DC gain is captured by  $T_o = -R_4/R_3$  and the gain-adjusted time constant  $\tau = \tau'/T_o$  is the time constant of an equivalent lossless integrator absent the effect of this DC gain. Provided that the  $\omega_t\tau \gg 1 + 1/T_o$ , which is the case so long as the DC gain is reasonably large, the analytic continuation of (F.42) into Fourier space yields an expression very similar to that of (F.38):

$$H''_{\text{int}}(j\omega) = \left(\frac{\omega^2\tau}{\omega_t} - \frac{1}{T_o}\right) - j\omega\tau \quad (\text{F.43})$$

The loss term  $\sigma_{\text{int}}$  (in parentheses) now contains two components: one due to the fact that this is a lossy integrator ( $1/T_o$ ), and one which results from the opamp gain-bandwidth product ( $\omega^2\tau/\omega_t$ ). Since only the latter embodies opamp nonidealities, the former can be ignored, leaving the loss transfer function(excess phase) identical to that of (F.38)((F.40)) for the lossless case.

# Appendix G

## Auxiliary SVEPRE Circuits

This appendix briefly describes the design, operation, and simulated performance of selected SVEPRE building blocks smaller in scale than the LNA and AAF but nonetheless vital to the overall function of front-end. Intended primarily for reference, rather than exhaustive tableau, the coverage herein supplements that of Chapter 4 and Chapter 5 by highlighting the unique and performance-critical aspects of these auxiliary circuits and establishing connections between their implementations and those of the LNA and AAF.

Rounding out the chronicle of the SVEPRE contents, Section G.1 examines constituents of the AAF heretofore neglected, particularly the operational amplifier (opamp) at the core of each integrator. Section G.2 catalogs circuits at the top of the SVEPRE hierarchy that impact both the LNA and AAF by providing global bias and reference signals. In both sections, transistor-level schematics capture the design principles and simulation results confirm their efficacy, which cannot be directly measured on the fabricated die in the absence of direct access to these embedded elements.

### G.1 AAF Elements

With the novel transconductors extensively limned in Section 5.4 and Section 5.5, and the construction of its metal comb capacitors recounted in Section 5.6.1.2 the

remaining constituents within each biquadratic stage of the AAF (cf. Figure 5.8(b)) are documented in this section. Chief among these, in terms of power consumption, die real estate, and impact on performance are the operational amplifiers (opamps) in the  $G_m$ -C-Opamp integrators of Figure 5.11;<sup>1</sup> Section G.1.1 summarizes key aspects of their design.

### G.1.1 Operational Amplifier

The fully differential integrator opamps must provide high gain and wide bandwidth, while consuming a modicum of supply current. A key distinction from the operational transconductance amplifier (OTA) of a  $G_m$ -C integrator is the need for a low output impedance in order to drive the pnp inputs of each transconductor, as well as any off-chip load at the output of the AAF. To meet these objectives, each opamp adopts the two-stage architecture of Figure G.1.

Stage 1 is a folded cascode amplifier with nMOS inputs whose high output impedance provides all the gain necessary for the opamp. To buffer the signal, Stage 2 implements a pseudo-differential, level-shifting, Class A follower network. As opposed to a traditional opamp, the fully differential signal path requires common-mode feedback (CMFB) to establish the mean voltage  $\bar{V}_{\text{int}}$ , which would otherwise be subject to the vagaries of the matching between top- and bottom-rail sources of the folded cascode. Finally, all three elements are biased from the chip-wide  $I_O$  master reference current using an innovative network akin to that of the LNA. Each of these four elements is elucidated separately below.

#### G.1.1.1 First Stage

The schematic of the folded cascode that implements the first stage of the opamp, including its biasing branches, is shown in Figure G.2. Despite the gain penalty associated with their body-effect sensitivity and the increased flicker noise (cf. Section 3.1.3.3), nMOS input devices M1 and M2 are chosen over pMOS in order

---

<sup>1</sup>For simplicity, all AAF integrator opamps are identical. For especially power-conscious applications, a more aggressive approach optimizes opamp power consumption by scaling the size of the amplifier in each integrator in proportion to the  $Q$  of its stage.

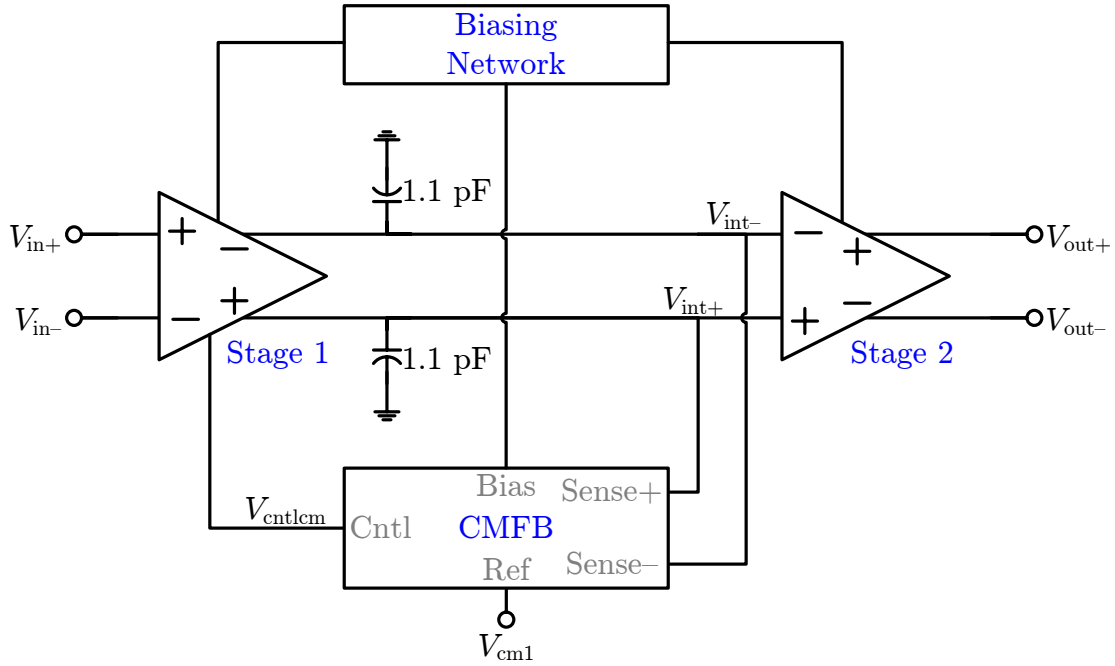


Figure G.1: Simplified schematic of opamp architecture. Stage 1(Stage 2) provides high(unity) gain with high(low) output impedance. The CMFB network ensures  $\bar{V}_{int}$  is firmly specified, whereas the 1.1pF capacitors at this node set the dominant pole location.

to accommodate the input common-mode range set by the 1.75-V  $V_{cmo}$  of the transconductors. Establishing the proper ratio of the static current through this input pair to that of M3/M4, prevents the remainder of the cascode stack (M5–M10) from being starved of current at the extremes of the input swing, speeding their recovery from large ASETs or slewing events. The CMFB control signal returns to the gates of M9a/M10a, which are adjusted until  $\bar{V}_{int}$  reaches the desired level. Note that this signal,  $V_{cntlcm}$ , could have been returned to Q1/Q2 to ensure that the input pair is also governed in the CMFB loop, but this introduces additional phase shifts that undermine loop stability (cf. Section G.1.1.3).

#### G.1.1.2 Second Stage

The second stage of the opamp is responsible for providing low output impedance with  $\sim 0$ -dB gain. The unity-gain voltage buffer of Figure G.3 accomplishes this

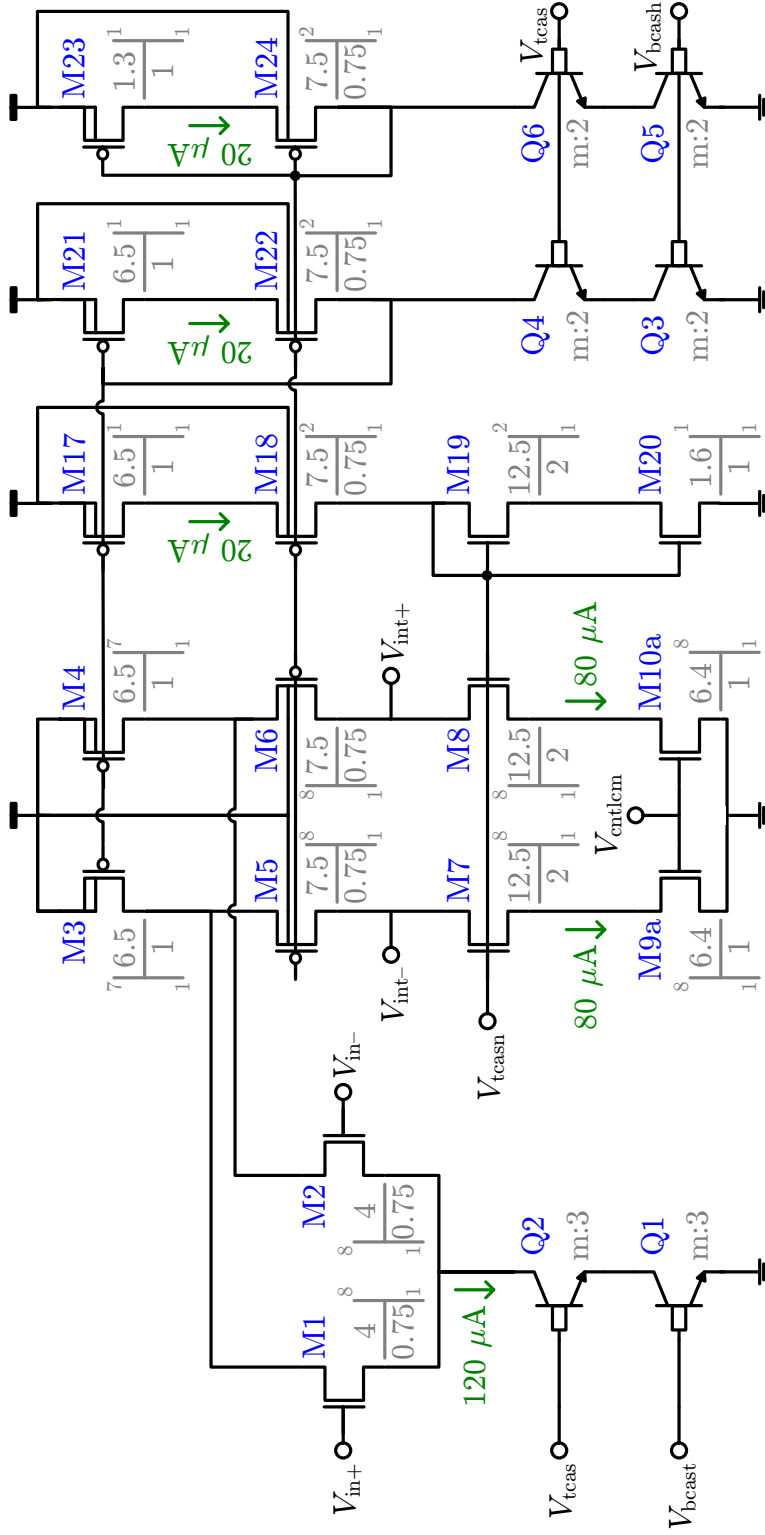


Figure G.2: Schematic of first stage of opamp. The biasing network of Figure G.5 provides  $V_{tcas}$ ,  $V_{bcast}$ , and  $V_{bcash}$ . The CMFB network of Figure G.4 provides  $V_{cntcm}$ . Nominal bias currents annotated in green.



through a pseudo-differential architecture in which the sizing and bias currents of M25/M26(Q7/Q8) match their nominal  $V_{GS}(V_{BE})$  at  $\sim 775$  mV. As consequence, the  $\bar{V}_{int} = 1$  V established by the CMFB network is preserved through the upward(downward) level-shift of the pMOS(npn) followers, producing  $\bar{V}_{out} \simeq 1$  V.<sup>2</sup>

The npn followers Q7/Q8 form a Class A output stage featuring high linearity and slew-rate on account of their large emitter bias currents. In the general case, the opamp slew rate sets the maximum current draw according to [Gray *et al.*, 2001, p.680–691]

$$I_{max} \geq 4\pi f_o V_{amp} C_L \quad (G.1)$$

where  $f_o(V_{amp})$  is the fundamental frequency(amplitude) of the fastest(largest) sinusoid of interest, and  $C_L$  is the differential load capacitance. However, for the special case of the AAF topology, the opamp must only supply as much charge to the feedback capacitors as is driven onto them by the transconductors,<sup>3</sup> plus that for any overall load. Thus,  $I_{max}$  is much smaller than that predicted by (G.1) and, in the worst case of the largest transconductor (G3 of Stage 3), driving the smallest feedback capacitor (C2 of Stage 3), as well as its bottom-plate parasitic in parallel with an instrument/probe, representing a differential load of  $C_L = 7.6$  pF, the maximum current requirement is:

$$I_{max} \geq m_a m_f G_{m3} V_{amp} \left( 1 + \frac{C_L}{C_2} \right) \quad (G.2)$$

where  $m_a = 1.2(m_f = 1.25)$  includes a 20%(25%) margin for amplitude(frequency). The 300  $\mu$ A limit set by (G.2) sets  $I_{E7,8}$  in Figure G.3.

The biasing branches are analogous to those of Figure G.2, but here both pMOS cascode biases,  $V_{bcasp}$  and  $V_{tcasp}$ , are exported to the CMFB network in order to ensure that the tail currents steered by the CMFB amplifier match those flowing in

---

<sup>2</sup>It is notable that the connectivity of Figure G.1 prioritizes the CM level at  $V_{int}$  over that of  $V_{out}$ , since the former is a high impedance node more sensitive to current imbalances. Although the relationship between the two is not guaranteed by feedback, the net level-shift of the second stage can vary without dire consequence to the transconductors on account of healthy design margin for  $\bar{V}_{out}$ .

<sup>3</sup>This argument ignores the current drawn by the transconductor inputs, which is negligible by comparison.

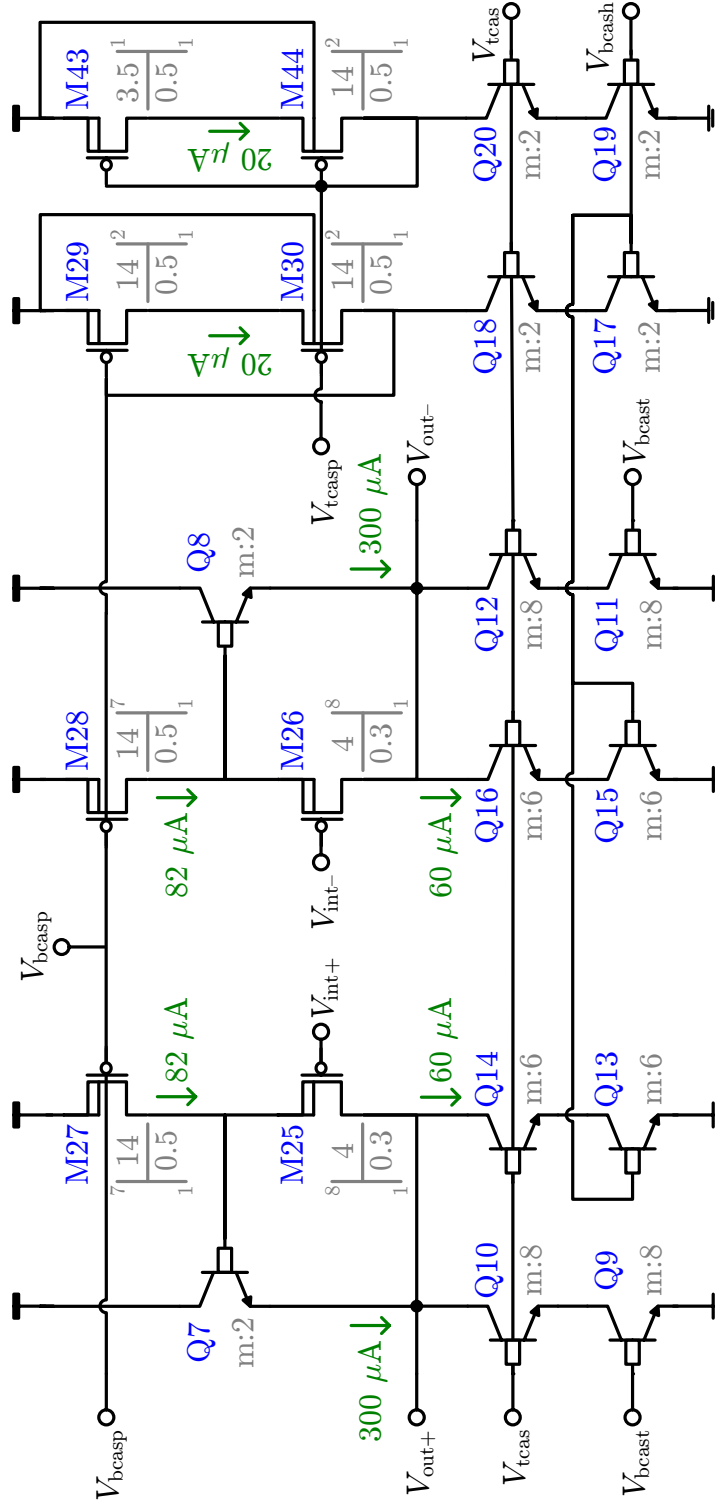


Figure G.3: Schematic of second stage of opamp. The biasing network of Figure G.5 provides  $V_{tcas}$ ,  $V_{bcas}$ , and  $V_{bcas}$ . Nominal bias currents annotated in green.

the cascode stack.<sup>4</sup>

### G.1.1.3 Common-Mode Feedback

The cross-coupled, degenerated differential pairs of Figure G.4 are the heart of the common-mode feedback network in Figure G.1: they sense the common-mode level  $V_{\text{int}}$ , compare it against the specified  $V_{\text{cm1}}$  and mirror the appropriate currents from M9b/M10b to M9a/M10a of Figure G.2 via  $V_{\text{cntlcm}}$  so as to adjust  $\bar{V}_{\text{int}}$  accordingly. Degeneration resistors R1 and R2 are sized at 60 k $\Omega$  so as to expand the operating range of the CMFB network without sacrificing enough gain to degrade its accuracy. To reduce mismatch between the currents flowing in the CMFB amplifier and those it is controlling, M9b/M10b and M15/M16 are laid out in common-centroid with their counterparts in the folded cascode (M9a/M10a and M7/M8) and former are also biased from  $V_{\text{tncas}}$ .<sup>5</sup>

The potential for M9/M10 current mirror errors due to either mismatch between the devices themselves or between the CMFB and folded cascode biasing, presents two significant and conflicting challenges in the design of the CMFB network: ensuring that its gain is sufficient to correct for the expected range of CM imbalances in the folded cascode and preserving stability under worst-case conditions. The former is addressed by ensuring that the gain of CMFB network is within 20 dB of that of the differential signal path.<sup>6</sup> To achieve this condition, M31–M34 are sized and biased so that, even when degenerated, the CMFB loop gain exceeds 65 dB and M9a/M10a carry the full tail current to the folded cascode, not only a fraction as recommended for stability *Gray et al.* [2001, p.822–823].

As for stability, sensing the common-mode level at  $V_{\text{int}}$  rather than  $V_{\text{out}}$  and returning  $V_{\text{cntlcm}}$  to M9a/M10a rather than Q1/Q2 minimizes the number of elements,

---

<sup>4</sup>Naturally, such matching could be even better attained by exporting these signals from first stage. Indeed, the stated approach carries minimal layout impact and, thus, was chosen for expediency rather than performance; a different trade-off should attend future revisions.

<sup>5</sup>Similar considerations apply to M35–M42, but their currents are matched to those of the second stage as described in Footnote 4.

<sup>6</sup>This rule-of-thumb should properly be extended to dictate equality of the differential-mode and common-mode gains in the most conservative of designs. However, this is a stringent and potentially intractable requirement [*Duque-Carrillo*, 1993, p.131–140].

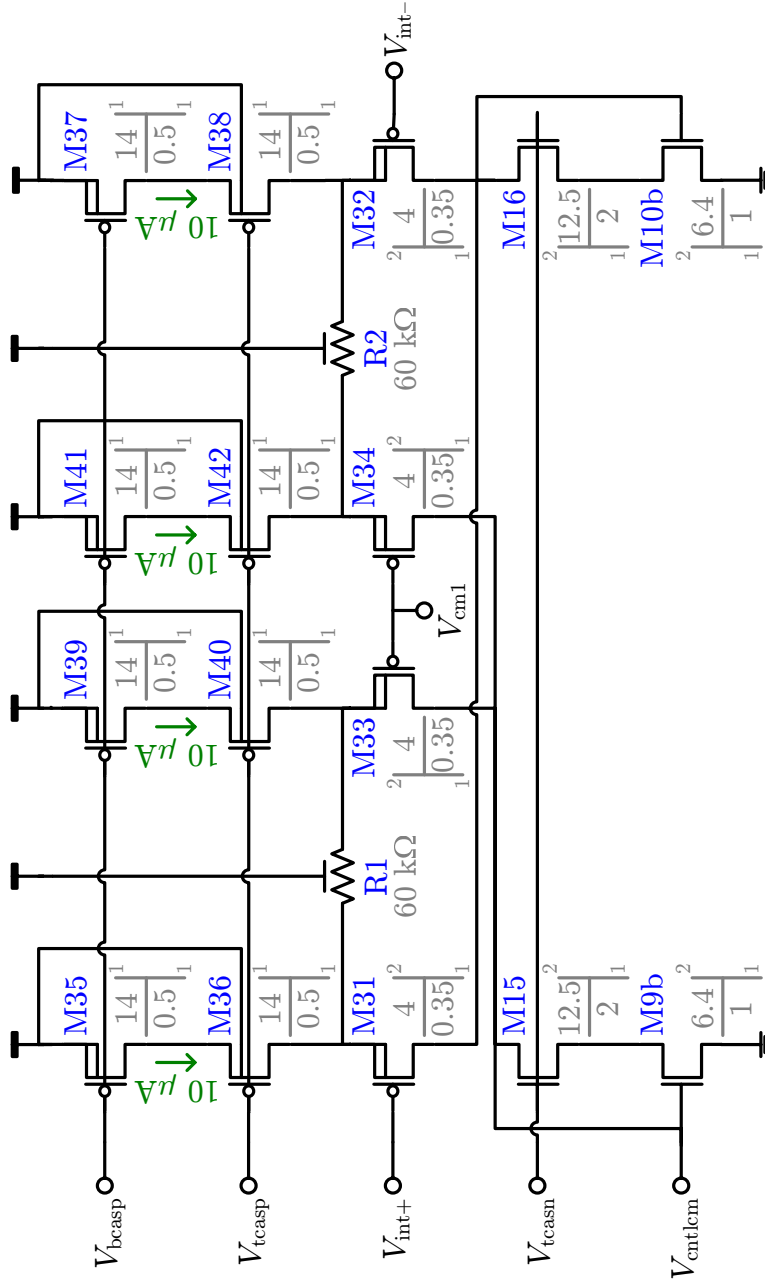


Figure G.4: Schematic of opamp common-mode feedback amplifier. The npn(pMOS) bias voltage(s)  $V_{\text{tcasp}}$  ( $V_{\text{tcasp}}$  and  $V_{\text{tcasp}}$ ) are provided by Stage 1(2) as shown of Figure G.2( Figure G.2). Nominal bias currents annotated in green.

Property	Value	Units
DC loop gain	66.8	dB
−3 dB bandwidth	6.0	kHz
Unity-gain frequency	12.5	MHz
Phase margin	66.3	degrees
Power <sup>a</sup>	99.9	$\mu$ W

<sup>a</sup> Power applies to the CMFB amplifier of Figure G.4 only; biasing not included

Table G.1: Simulated performance of opamp CMFB loop with differential load of 6 pF at  $V_{\text{out}}$ . Gain measured by breaking loop at  $V_{\text{cntlcm}}$ , injecting signal at gates of M9a/M9b, and sensing output at gate of M9b.

and thus non-dominant poles, in the CMFB loop. Intuitively, since this loop possesses the same dominant pole at  $V_{\text{int}}$  as the first stage, matching their gains (to within 20 dB) dictates that additional phase lag in the CMFB path be equal or less than that experienced by signals traveling from  $V_{\text{in}}$  to  $V_{\text{int}}$  in the first stage.

The gain and stability of the CMFB loop are evidenced by the specification summary provided in Table G.1. Validated in simulation by breaking the CMFB loop and injecting a input signal while terminating  $V_{\text{out}}$  in a 6 pF differential load, these properties of opamp CMFB network, together with confirmation of its robustness to process-induced device mismatch, affirm the integrity of the design.

#### G.1.1.4 Biasing

The novel bias network in Figure G.5, which provides the bias voltages for both the low ( $V_{\text{bcash}}$ ) and high ( $V_{\text{bcast}}$ ) current-density tail sources throughout the opamp, as well as cascode voltage  $V_{\text{tcas}}$ , is effectively identical to that of Figure 4.22. Thus, for a complete description of its design and operation, refer to Section 4.2.4.1.

#### G.1.1.5 Summary

The simulated performance of the complete opamp in Figure G.1 is summarized in Table G.2. For a differential capacitive load of 3 pF (6 pF), representing a  $1.5 \times (3 \times)$

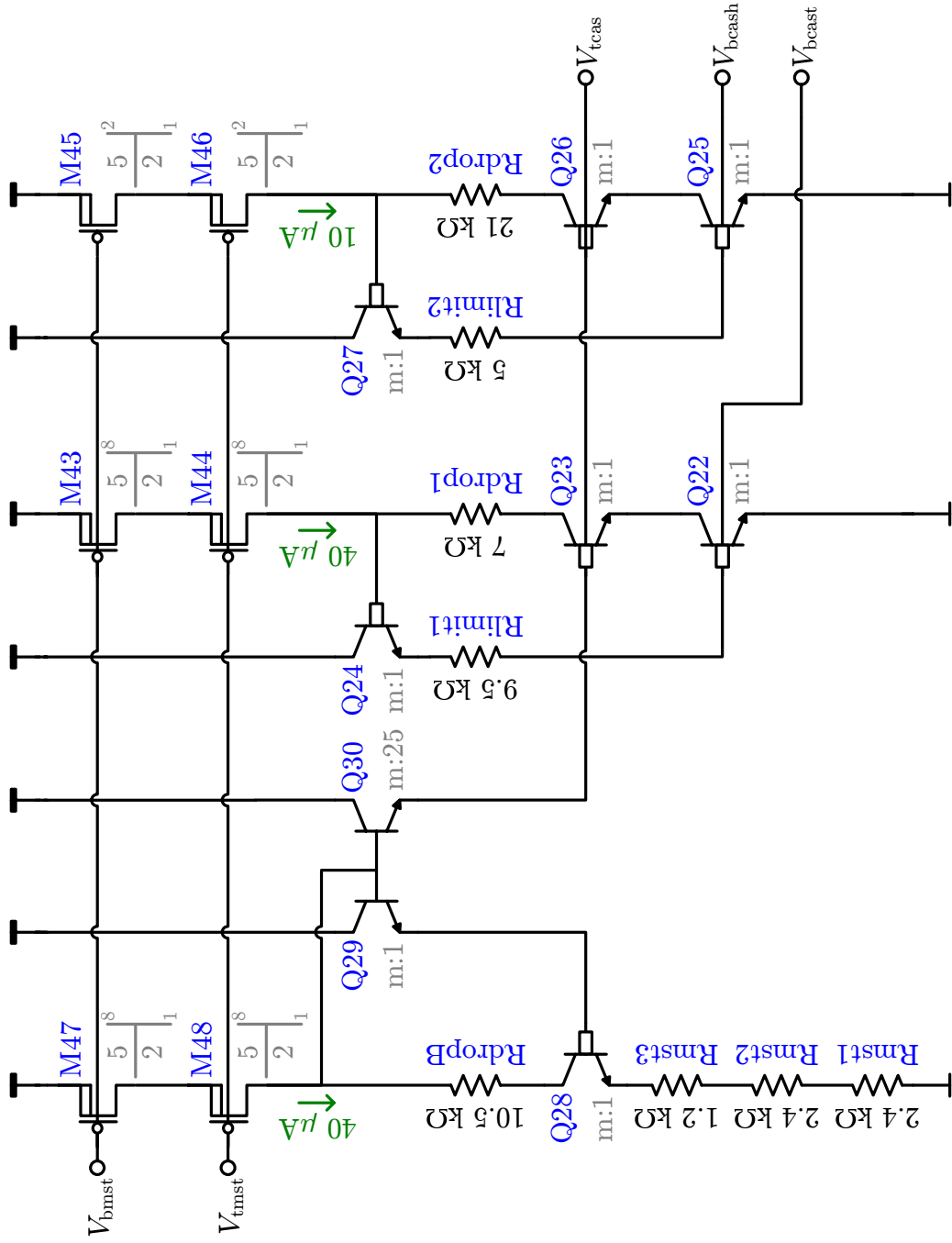


Figure G.5: Schematic of opamp biasing network. Provides  $V_{\text{tcas}}$ ,  $V_{\text{bcash}}$ , and  $V_{\text{bcast}}$  to the opamp stages and CMFB. Compare with that of the LNA in Figure 4.22. Nominal bias currents annotated in green.

Property	Value	Units
DC gain	82.73	dB
−3 dB bandwidth	7.41	kHz
Input capacitance <sup>a</sup>	37.30	fF
Unity-gain frequency <sup>b</sup>		
$C_L = 3$ pF	95.04	MHz
$C_L = 6$ pF	85.22	MHz
Phase margin <sup>b</sup>		
$C_L = 3$ pF	46.38	degrees
$C_L = 6$ pF	34.78	degrees
Input-referred noise		
@100 Hz	487	nV/ $\sqrt{\text{Hz}}$
@13.8 MHz <sup>c</sup>	127	nV/ $\sqrt{\text{Hz}}$
Power dissipation	3.44	mW
Active	2.95	mW
Biasing	492	$\mu\text{W}$

<sup>a</sup> Input capacitance measured incrementally and differentially at  $V_{\text{in}}$

<sup>a</sup> Load capacitance measured differentially at  $V_{\text{out}}$

<sup>c</sup> The minimum of the input-referred noise curve occurs at this frequency

Table G.2: Simulated performance of opamp embedded in AAF integrators. All capacitance measured differentially.

margin over the load imposed by the bottom-plate parasitic of the largest feedback capacitor ( $\sim 4$  pF single-ended),<sup>7</sup> these result exhibit sufficient bandwidth and gain overdesign to accommodate the radiation-induced MOSFET and BJT degradation described in Section 2.1.1 and Section 2.1.2, respectively.

<sup>7</sup>This load excludes the feedback capacitors themselves, which are in series with the opamp outputs when computing the integrator loop gain and therefore do not directly contribute to the non-dominant poles there.

## G.2 System Elements

The novel solutions of at the cores of Chapter 4 and Chapter 5 depend upon global circuitry that, while more conventional in construction, is nevertheless critical to the overall performance of the front-end. A sampling of these system-level elements is offered below. Section G.2.1 describes the voltage regulator responsible for establishing  $V_{\text{reg}}$ —the common-mode bias of both the LNA output stage (via the center-tap of R1 in Figure 4.17) and the transconductor GGC (via the shared emitter of Q1/Q2 in Figure 5.35). Circuits embedded in the pad frame to handle the internal or external generation of master reference voltages ( $V_{\text{cm1}}$  and  $V_{\text{cm1}}$ ) and currents ( $I_{\text{B}}$ ,  $I_{\text{E}}$ ,  $I_{\text{O}}$ ) are described in Section G.2.2.

### G.2.1 Voltage Regulator

To eliminate the power consumption and potential instabilities associated with common-mode feedback networks, the common-mode output(input) voltage of the second stage of the LNA(AAF) is established by a feed-forward mechanism explained in Section 4.2.3.2(Section 5.5.2) that relies on a regulated, on-chip voltage,  $V_{\text{reg}} \simeq 1$  V. Although liberal margin in the design of both components renders their performance insensitive to the absolute value of this voltage to within several hundred millivolts, and although its noise—being common-mode—is of little consequence, any signal-dependence of  $V_{\text{reg}}$  on the load current  $I_{\text{load}}$  can potentially incite distortion through common-mode to differential-mode conversion. Thus, the primary goal in the design of the regulator is to ensure high load regulation, defined as the percent change in the output voltage for a specified change in the load current.

Rather than a single regulator, layout symmetries inspire the use of two identical regulators per AAF stage.<sup>8</sup> Each regulator must sink the tail currents from the outer pair of GGC npn devices from up to four transconductors, for a maximum load of 240  $\mu\text{A}$  at an output of  $\sim 1$  V with load regulation better than 0.01%. The remainder

---

<sup>8</sup>The regulator in Stage 1 is closest to the LNA and provides it with  $V_{\text{reg}}$ . Since the load current sourced/sunk by the LNA is negligible compared to that of the transconductors, this connection does not demand additional performance of that regulator.



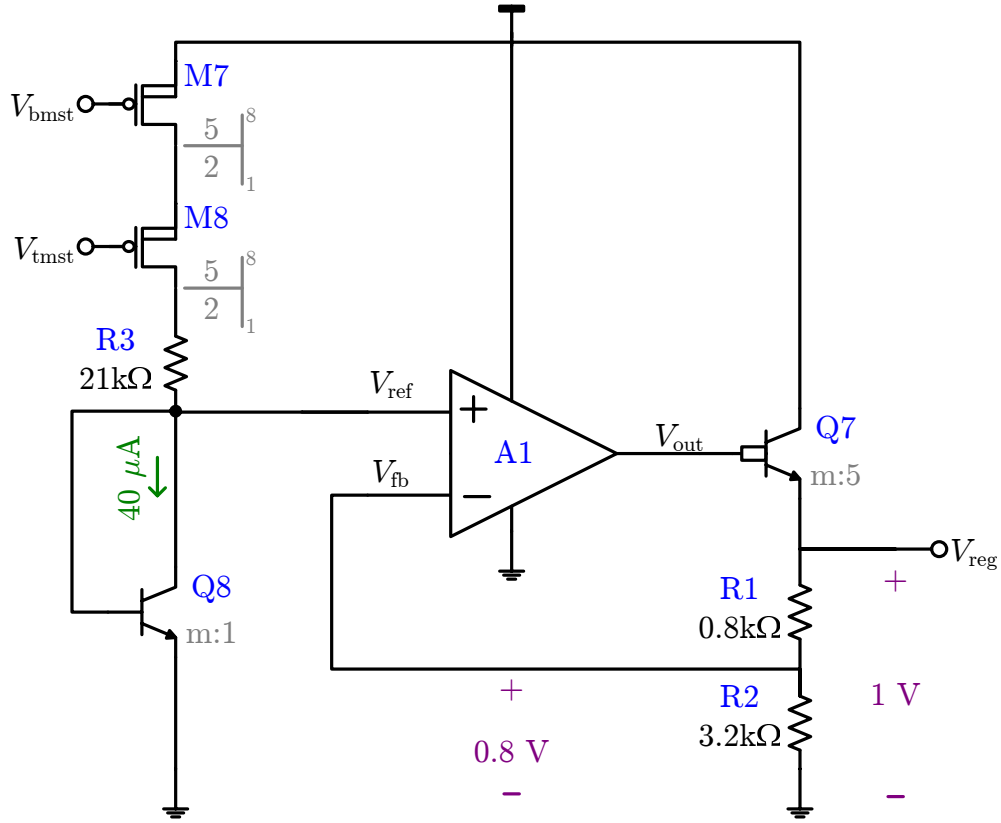


Figure G.6: Simplified schematic of regulator feedback loop. All bias currents are derived from  $I_O$ , via  $V_{bmst}$  and  $V_{tmst}$ . The feedback factor of 0.8 ensures high load regulation and accurate matching. Nominal bias currents annotated in green.

of this section describes the feedback circuit used to achieve these specifications.

### G.2.1.1 Feedback Loop

Each regulator comprises the feedback loop shown in Figure G.6, at the heart of which lies a simple operational amplifier, A1 [Gray *et al.*, 2001, p.594]. The positive input terminal is fed by a reference ladder that establishes a target value of  $V_{ref} = 0.8$  V by driving a single diode-connected npn (Q8) with a  $40\text{-}\mu\text{A}$  current derived from  $I_O$ .<sup>9</sup>

<sup>9</sup>To build a truly stable reference that is insensitive to temperature and the supply voltage from which it is derived requires a more sophisticated approach [Gray *et al.*, 2001, p.596–599]. In particular, since the  $V_{be}$  of Q8 varies according to the classic  $-2$  mV/°C—recall that  $V_{be}$  is complementary to absolute temperature (CTAT), whereas  $\Delta V_{be}$  is proportional to absolute

From the target  $V_{\text{reg}}$  of 1 V, this requires R1 and R2 to establish a feedback factor of 0.8 for  $V_{\text{fb}}$  that is selected for two reasons. First, since a value of 0.8 V is easily derived from an npn  $V_{\text{be}}$ ,  $V_{\text{ref}}$  tracks any TID degradation of the same property in the target GGC devices,<sup>10</sup> preserving the desired headroom in the face of radiation. Secondly, load regulation is inversely proportional to the value of  $V_{\text{ref}}$  via [Gray *et al.*, 2001, p.594]

$$\frac{\Delta V_{\text{reg}}}{V_{\text{reg}}} = \frac{R_o}{A_o V_{\text{ref}}} \frac{\Delta I_{\text{load}}}{I_{\text{load}}} \quad (\text{G.3})$$

where  $A_o(R_o)$  is the DC gain(output resistance) of A1. The larger the feedback factor, the better the load regulation, limited only by the 1 V target for  $V_{\text{reg}}$ . Since the matching of R1 and R2 benefits from a common-centroid-compatible ratio of 1:4, a feedback factor of 0.8 is accurately realized.<sup>11</sup>

The load regulation is simulated by sweeping  $I_{\text{load}}$  from 0  $\mu\text{A}$  to 250  $\mu\text{A}$  and tacking  $V_{\text{reg}}$ . The result, depicted in Figure G.7 confirms better than 0.005% regulation is attained for this choice of feedback factor and the A1 design described in the next section.

### G.2.1.2 Feedback Amplifier

A schematic of the opamp at the heart of each voltage regulator is provided in Figure G.8. The first stage is a simple pMOS-input differential pair, whose tail 40- $\mu\text{A}$  tail current is derived from  $I_O$ . It employs  $\beta$ -helper Q3 to balance the loading of Q4 at the input to the Darlington pair that comprises the second stage. A standard lead network comprised of R3 and C1 compensates the two-stage design by: leveraging the high gain of the Darlington pair to Miller-multiply C1 and thereby effect pole-splitting, shifting the dominant(non-dominant) pole at output of the first(second)

---

temperature (PTAT)—the circuit shown makes no attempt to implement temperature correction. However, like the supply fluctuations which affect M7/M8 just as they do master devices from which they derive their bias current, such temperature shifts are incurred by the GGC outer pairs, so the net headroom available to the tail sources of the inner pair of each transconductor remains practically independent of temperature.

<sup>10</sup>Incidentally, replicating the behavior of the GGC devices motivates the implementation of Q8 with an NLd25x0d6 transistor.

<sup>11</sup>Of course, other layout-friendly ratios such as 1:8 and 1:16 can be employed at the expense of a more elaborate  $V_{\text{ref}}$  generating branch.

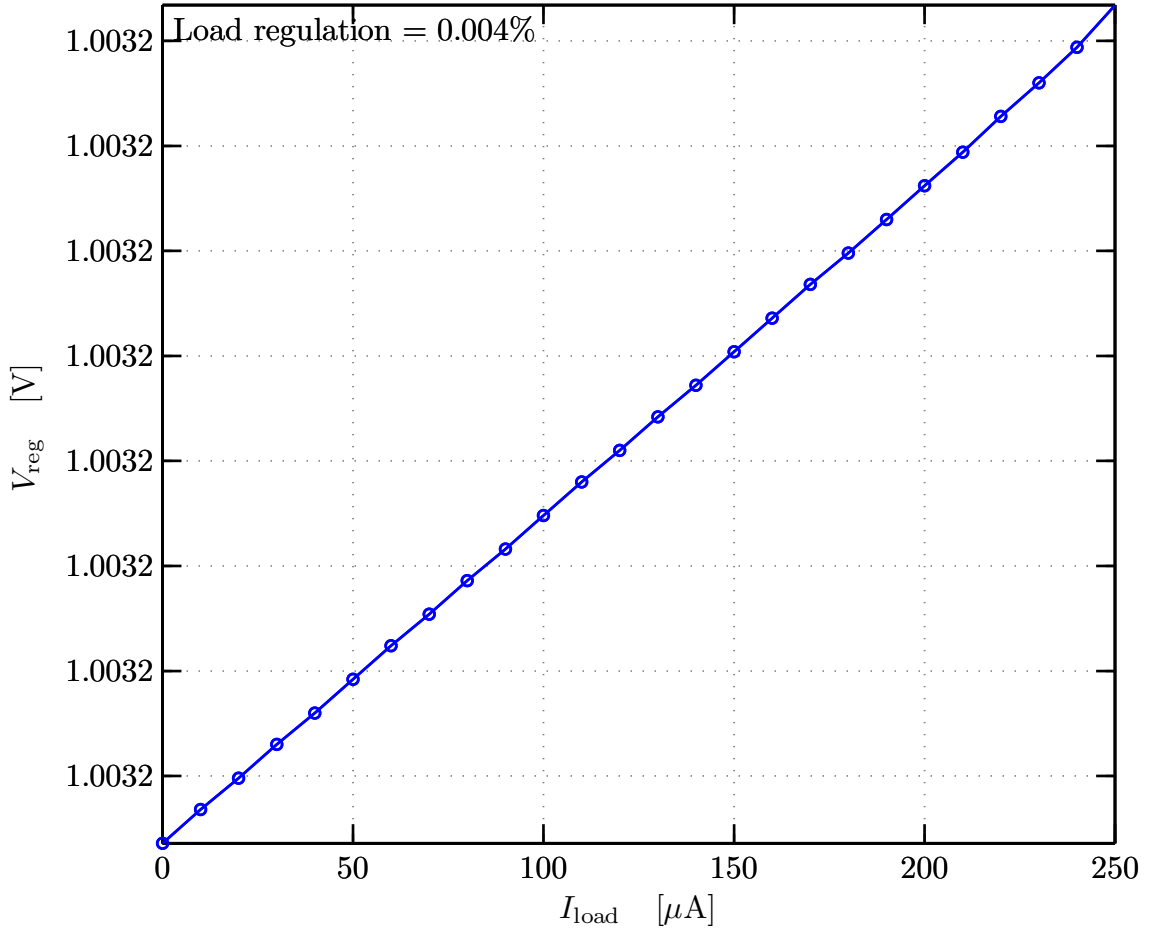
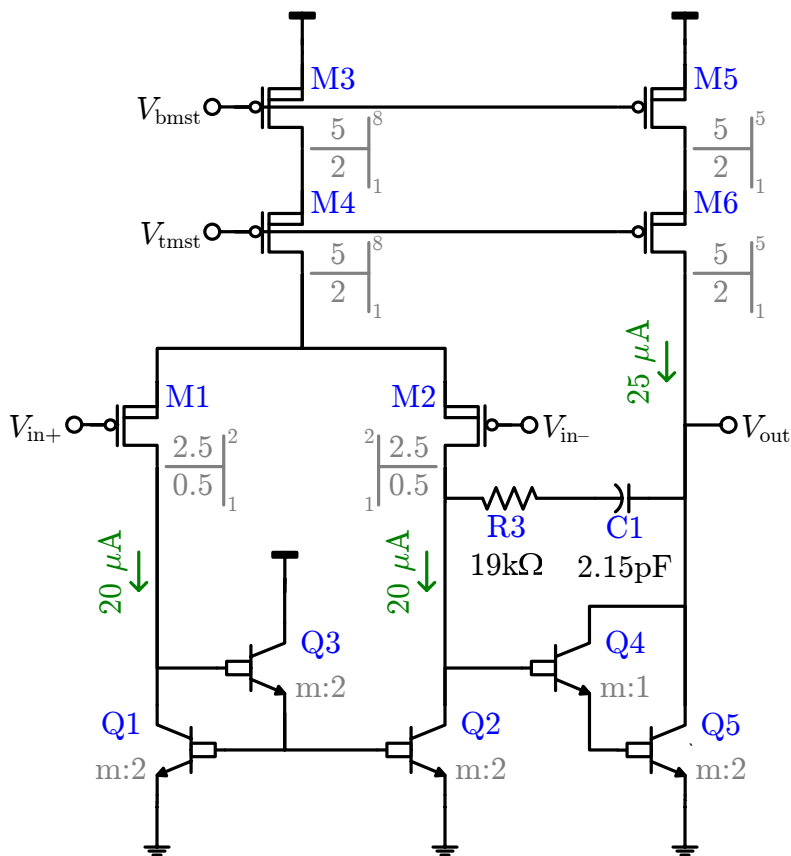


Figure G.7: Simulated load regulation of on-chip voltage regulator. In addition to load regulation to better than 0.01%, the line regulation (not shown) is better than  $-95 \text{ dB}$  ( $-30 \text{ dB}$ ) at  $100 \text{ Hz}$  ( $1 \text{ MHz}$ ). Markers indicated simulated data points.

stage down(up) to  $\sim 100 \text{ Hz}$  ( $\sim 16 \text{ MHz}$ ); and introducing a zero at  $3.9 \text{ MHz}$  that is low-enough relative to the non-dominant pole at  $V_{\text{out}}$  for nearly all of its phase to be contributed prior to the gain-crossover.<sup>12</sup>

The key performance metrics for the regulator amplifier are summarized in Table G.3. When embedded in the feedback loop of Figure G.6, it remains stable while providing gain and output resistance sufficient to achieve the desired load regulation (cf. Figure G.7).

<sup>12</sup>It is important that this zero be well below the non-dominant pole because cancellation is not assured given process tolerances.



### G.2.2 Reference Generators

For ease of use, SVEPRE affords the option to generate the  $V_{\text{cm1}}(V_{\text{cm2}})$ , the reference voltage used to set the common-mode output level of the LNA(transconductors), from either an on-chip reference ladder or a board-level source. In contrast, the three reference currents,  $I_{\text{B}}$ ,  $I_{\text{E}}$ , and  $I_{\text{O}}$  must be established through off-chip elements, but provisions exist to accommodate both discrete resistors and adjustable current sources.

Property	Value	Units
DC gain	99.17	dB
−3 dB bandwidth	97.65	Hz
Unity-gain frequency	10.8	MHz
Phase margin	72.0	degrees
Power <sup>a</sup>	162.5	$\mu$ W

<sup>a</sup> Power applies to the regulation amplifier of Figure G.8 only; biasing not included

Table G.3: Simulated performance of opamp for on-chip regulator with differential load of 10 pF at  $V_{\text{out}}$ . In the absence of the feedback loop,  $V_{\text{out}}$  settles to 1.754 V.

### G.2.2.1 Reference Voltages

As shown in Figure G.9, a 100-k $\Omega$  on-chip resistor ladder in the pad frame, supplied by  $V_{\text{sup}}$ , provides an  $\sim 1$  V reference for  $V_{\text{cm1}}$ .<sup>13</sup> An identical circuit is connected to CM2I and CM2E, except that  $V_{\text{ref}}$  is tapped off between R2 and R3. In both cases, A1, a simple buffer amplifier whose schematic is provided in Figure G.10, provides the drive current for the bias line feeding the core of the chip.<sup>14</sup> Bypass capacitor C1 serves as a local charge reserve to counteract rapid fluctuations in the load on this line.

To activate this internal reference, switch S1(S2) is opened(closed), completing the feedback loop around the A1 buffer and isolating the chip from the board-level source.<sup>15</sup> In some instances, it is preferable to drive one or more SVEPRE instances from a master, on-board reference voltage generator such as that of Section H.2.4, to ensure uniformity and reliability. To that end, switch S1 can be closed so as to

<sup>13</sup>Since symmetric layout practices are applied to the construction of R1, R2, and R3, improving their matching and temperature coefficients, the achieved  $V_{\text{ref}}$  is most sensitive to variations in  $V_{\text{sup}}$  as a result of  $IR$ -drops and temperature fluctuations. However, since both the LNA and AAF design offer margin that tolerates variation of hundreds of millivolts in  $V_{\text{cm1}}$ , this uncompensated ladder need not operate from a regulated supply.

<sup>14</sup>By design, the reference voltage only drives MOS gates and is a common-mode signal that does not limit the speed of the differential path. Hence, A1 need not supply much current.

<sup>15</sup>Switches S1 and S2 are merely conceptual and need not be formally implemented on the PCB.

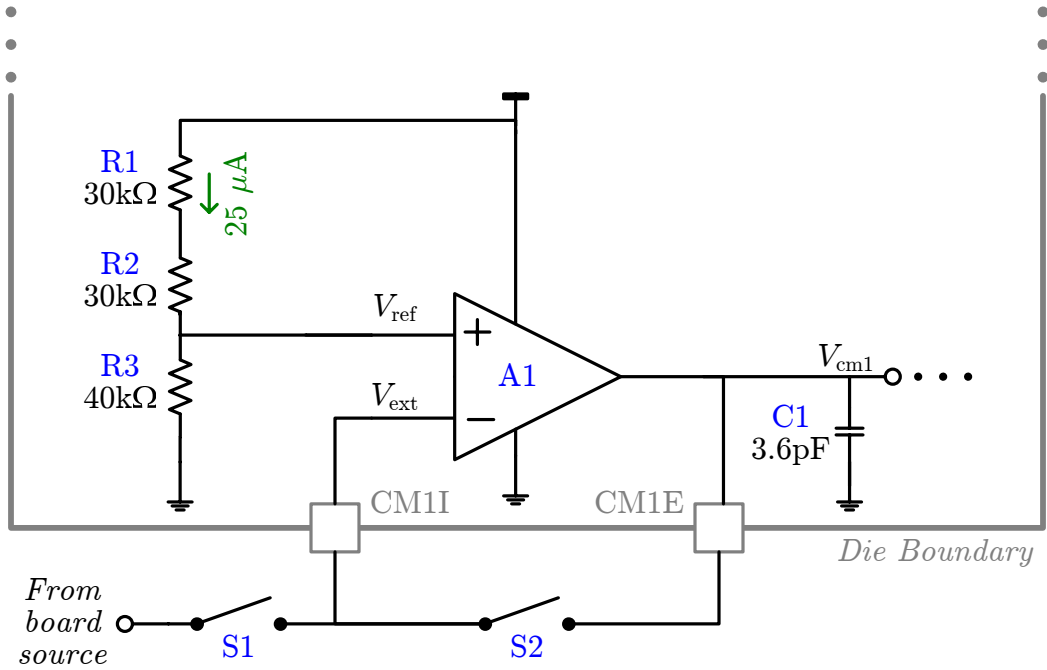


Figure G.9: Diagram of options for reference voltage generation. The on-chip ladder, buffer, and bypass capacitor for  $V_{cm1}$  are depicted; those of  $V_{cm2}$  are identical except that  $V_{ref}$  is tapped off between  $R2$  and  $R3$  ( $\sim 1.75$  V). Switches to route signals at the PCB level are merely conceptual.

directly drive the  $V_{cm1}$  line from this source. For radiation environments where SEEs are of concern, it is recommended that  $S2$  remain closed in this configuration, so as to prevent the  $V_{ext}$  from floating.

### G.2.2.2 Reference Currents

Figure G.11 reveals the implementation of the global reference current generators blocked out in Figure 5.45; shown for the  $I_B$  network, the circuitry for the  $I_E$  and  $I_O$  networks is identical. In all three cases, identical copies of these current mirrors are connected to pins on both the left (BOL, EOL, and OOL) and right (BOR, EOR, and OOR) sides of the pad frame, providing symmetric feed points for the tripartite distribution grids illustrated in Figure 5.45. Terminating only one of the two master mirrors provides a pin voltage of  $V_{bor} \simeq 1.05$  V at the nominal current of  $40 \mu\text{A}$ .

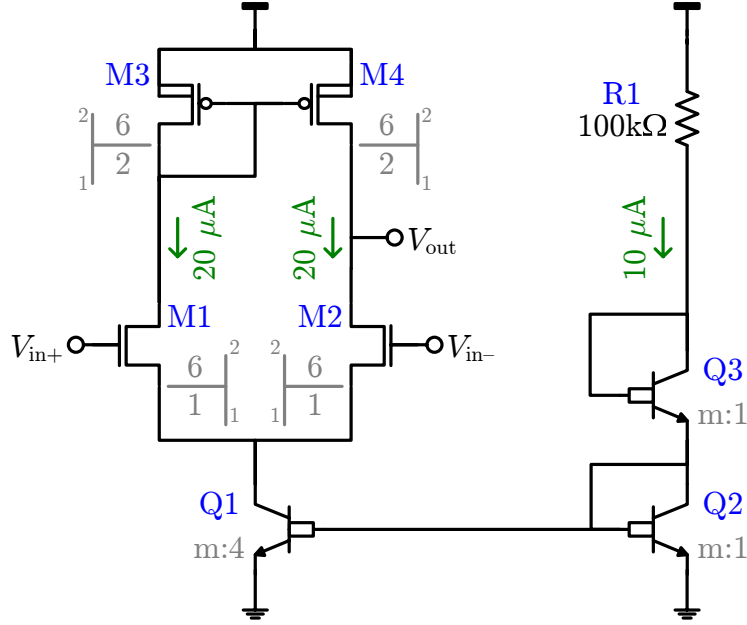


Figure G.10: Schematic of voltage buffer for on-chip references. Co-located in the pad frame with the other elements of Figure G.9, this amplifier is also powered from  $V_{\text{sup}}$ . R1 is comprised of ten segments of a high-resistance polysilicon. Nominal bias currents annotated in green.

To obtain an additional 100 mV of headroom, which may be necessary to operate discrete current sources such as the LM334 [*Linear Technology, LM334*],<sup>16</sup> both pins can be joined to provide a voltage of  $\sim 1.16$  V at  $40 \mu\text{A}$ .

The use of a pMOS, rather than nMOS, diode stack is designed to limit the current consumption of SVEPRE in the face of total dose degradation. For the case of Figure G.11, a small-signal model can be used to assess the dependence of  $I_{\text{Bo}}$  on the radiation-induced degradation of  $g_{\text{m1}}$  and  $g_{\text{m2}}$ , yielding the simple relation [*Mossawir et al., 2006*, p.3442].

$$I_{\text{Bo}} = \frac{V_{\text{sup}}}{\frac{1}{g_{\text{m1}}} + \frac{1}{g_{\text{m2}}} + R_{\text{B}}} \quad (\text{G.4})$$

<sup>16</sup>To supply  $2 \mu\text{A} \leq I_{\text{set}} \leq 100 \mu\text{A}$ , the LM334 only requires 0.8 V headroom. But, to limit noise and current transients, it is recommended that a choke inductor be placed in series with the source. The additional headroom required for the static current through this inductor can exceed 0.2 V, in which case both the left and right pins should be joined.

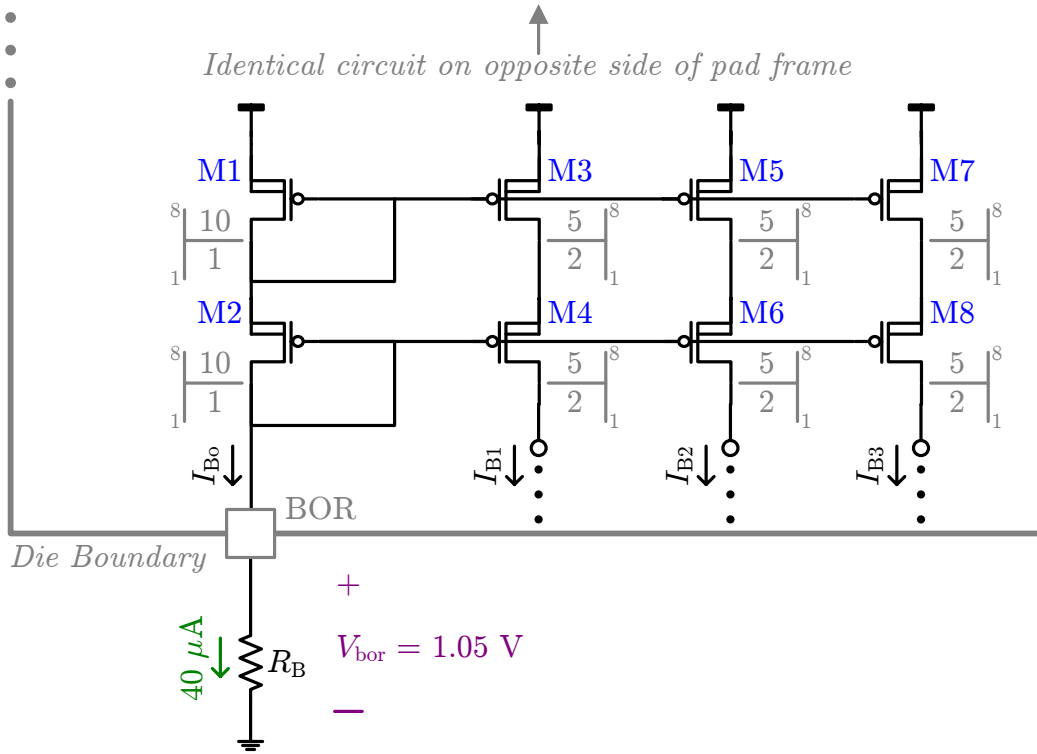


Figure G.11: Schematic of global, on-chip reference current generators. The current mirrors on the right-side of the pad frame (at pin BOR) for  $I_{B0}$  are depicted; those on the left side (pin BOL) are identical, as are the sets for  $I_{E0}$  and  $I_{O0}$  on both sides. Off-chip termination with a discrete resistor sized for  $40\ \mu\text{A}$  is shown, affording  $V_{\text{bor}}$  of 1.05 V(1.16 V) when one(both) pins are joined. Nominal bias currents annotated in green.

Since the nominal voltage at BOR lies near  $V_{\text{sup}}/2$ ,  $I_{B0}$  is seen to roughly scale in proportion to  $g_{m1,2}$ . Thus, implementing M1 and M2 with pMOS devices whose  $g_m$ , as opposed that of to their nMOS counterparts, exhibits a gradual, nearly monotonic decline with total dose up to 1 Mrad(Si) (e.g., contrast Figure 2.8 with Figure 2.7), ensures that the overall power dissipation of the chip does not grow as TID damage accumulates.



# Appendix H

## Characterization Board

This appendix offer details of the characterization printed circuit board (PCB) with which all the reported data on the performance of the SVEPRE front-end ASIC were obtained. Part documentation of its design, assembly, and operation, part guide to its further employ, this appendix both complements the descriptions of each test bench configuration in Section 6.2 and instructs future researchers on the additional capabilities of the PCB (cf. Section 7.3), recommending techniques to realize the demanding measurement precision using the on-board signal conditioning.<sup>1</sup>

The components in the complete block diagram of the characterization PCB in Figure 6.3—which is reproduced below as Figure H.1—can be classified by function into three categories that structure the subsequent explication: Section H.1 describes blocks that are directly responsible for processing the device-under-test (DUT) input and output signals; Section H.2 explores the circuitry for accurately generating static signals such as supply voltages and reference voltages/currents; finally, Section H.3 presents the analog and digital means for effecting control of the adjustable board elements.

---

<sup>1</sup>Although the entire PCB is highly adaptable in order to support a range of measurement options, those facets which are routinely customized as part of the test benches in Section 6.2 are emphasized here.

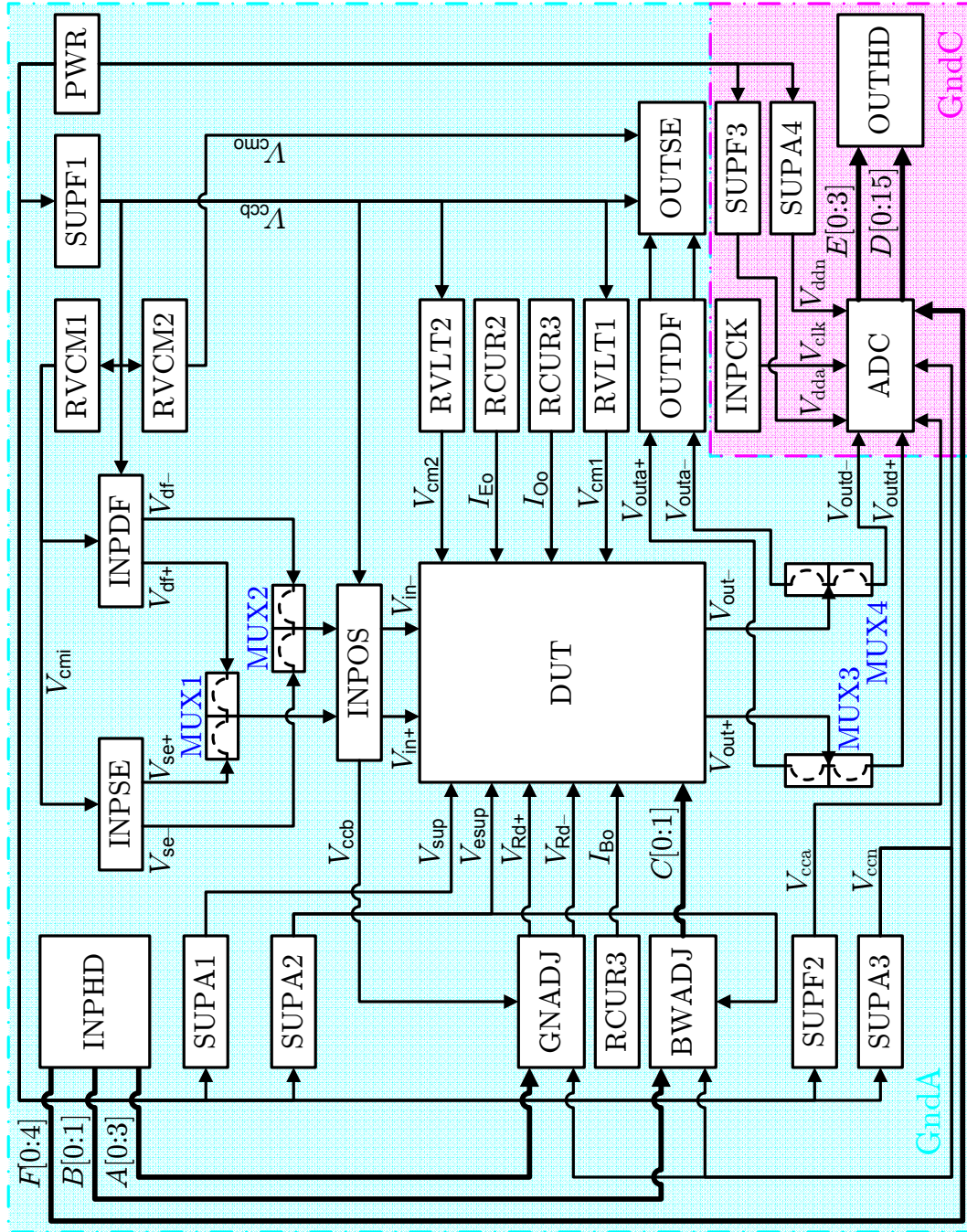


Figure H.1: Block diagram of characterization PCB reproduced from Figure 6.3 for convenience. Extent of analog(digital) ground plane, GndA(GndC), is shown in light blue(purple).

## H.1 Signal Path

The most essential role of the characterization PCB is to provide(extract) input(output) signals to(from) the DUT with sufficient fidelity to permit characterization of its distortion and noise down to  $-90$ -dB levels. The nonlinearities of the laboratory instrumentation and the presence of both coherent and incoherent noise sources in the ambient laboratory environment render these tasks particularly challenging. Preceded by a description of the mounting and multiplexing options for DUT itself in Section H.1.1, the circuits along the input and output paths of the characterization PCB are visited in the order of signal flow through the remainder of this section.

### H.1.1 Device-Under-Test (DUT)

Not pictured within the DUT block of Figure H.1 are multiplexers that allow  $V_{\text{in}}$  ( $V_{\text{out}}$ ) to be routed to(from) the input(output) of either the LNA or AAF. Additionally, these multiplexers can be enabled in bypass mode, whereby the  $V_{\text{in}}$  and  $V_{\text{out}}$  paths are directly connected together, effectively replacing the DUT with a pair of wires. This is critical for de-embedding the parasitics and frequency response of the PCB from the measured performance of the DUT (cf. Section 6.2.1.4).

To mitigate the impact of supply noise on DUT performance, the  $V_{\text{sup}}$ ,  $V_{\text{esup}}$ , and  $V_{\text{lgnd}}$  traces are each bypassed to GndA with 10-nF and 100-nF ceramic (X7R) and 1- $\mu$ F and 10- $\mu$ F tantalum (TANT) chip capacitors directly beneath the corresponding socket leads [Limotyrakis, 2004, p.133].<sup>2</sup> Similarly, the leads carrying  $V_{\text{cm1}}$ ,  $V_{\text{cm2}}$ ,  $I_{\text{Bo}}$ ,  $I_{\text{Eo}}$ , and  $I_{\text{Oo}}$  are each bypassed to GndA with 1- $\mu$ F tantalum capacitors near the socket.

---

<sup>2</sup>In layout, these are ordered such that smaller values are closer to the socket leads, minimizing the parasitic inductance of their connecting traces and increasing the highest self-resonant frequency above which the low-impedance of the bypass is spoiled. High-value tantalum capacitors render low-frequency supply and ground noise common to both lines while moving any lingering supply line resonances down into regions where the on-board opamps possess high PSRR. Their high equivalent series resistance (ESR) and inductance (ESL) is negated by placing them in parallel with ceramic capacitors that continue to provide bypass at higher frequencies. Using multiple sizes of both dielectrics smoothes out the individual self-resonances of any individual capacitor [Analog Devices, Inc., AN257, p.117-118].

### H.1.2 Single-Ended Input (INPSE)

When using single-ended sources (see Section 6.2.1.1 for examples), the INPSE block is responsible for converting the available signal to a balanced, differential format compatible with the LNA and AAF input requirements while preserving its fidelity. The simplified schematics of Figure H.2 accomplish this task through both a passive and an active path within INPSE, the selection of which (via output multiplexers not pictured) depends upon the test bench in operation.

#### H.1.2.1 Passive Path

At the heart of the passive path in Figure H.2(a) is a center-tapped 1:1 transformer (X1) that, when properly terminated through the choice of thru-hole resistors R6 and R7,<sup>3</sup> matches the source impedance so as to transmit the full-scale input signal, centered around an average value of  $V_{\text{cmi}}$ ,<sup>4</sup> from J5 to  $V_{\text{se1}}$ . The choice of transformer is complicated by linearity concerns, since the smaller magnetics of miniature models saturate at relatively low fluxes ( $B_{\text{sat}}$ ) and such distortion is rarely characterized by the manufacturer. Thus, the INPSE floorplan allows real-time selection one of three different X1 transformers: two proven to exhibit high linearity—a Mini-Circuits T1-6T [Vleugels, 2002, p.141] and a Coilcraft TTWB2010L [Limotyrakis, 2004, p.134]—and one stated to offer  $-92$  dB THD—Coilcraft AS8397-B [Coilcraft, Inc., AS8397-B].<sup>5</sup> For frequency response characterization (cf. Section 6.2.1), the best performance accompanies the use of the T1-6T, terminated with  $R_6 = R_7 = R_8 = R_9 =$

<sup>3</sup>In Figure H.2 and subsequent board-level schematics, bubbles on component terminals indicate thru-hole mounting; otherwise, all components are surface mount (SMT). Rather than being permanently soldered, the former are ‘socketed’ using pin receptacles, allowing them to be easily interchanged during testing. Of lower reliability, this assembly technique is used sparingly, but is critical for components (primarily, resistors) whose values either vary between board configurations or cannot be known *a priori*. However, all SMT resistors feature EIA E192 0.1% accuracy, whereas their thru-hole equivalents are good to just 1% (EIA E96).

<sup>4</sup>This common-mode potential is generated on-board by RVC1 (cf. Section H.2.5), and locally decoupled to GndA by ceramic (X7R) capacitor C1 to limit noise.

<sup>5</sup>Offering lower primary inductance to achieve bandwidth in excess of 1 MHz, the AS8397 actually possesses a turns ratio of 1:1.2. Although the on-board termination impedances can be adjusted accordingly, it proves convenient to also evaluate the 1:1 AS8456-A, which occupies the same SMT footprint, but cites only  $-89$  dB THD [Coilcraft, Inc., AS8456-A].

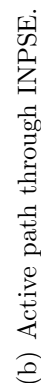
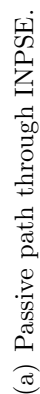


Figure H.2: Schematic of INPSE block, which contains both (a) passive and (b) active paths for accurate single-ended-to-differential conversion.

50  $\Omega$ .<sup>6</sup>

Whereas the transformer provides the differential character, balance is assured through a current balun (B1) on the primary side (Coilcraft T-626), which also suppresses common-mode line noise on the coaxial SMA cable from the signal source [*Mini-Circuits*, AN20-001]. Although not employed in the test benches of Section 6.2, a 100-kHz diplexer (e.g., Allen Avionics DPS00P10S), whose high(low) output is connected to J1(J2) and terminated by R3 and R5(R2 and R4), can precede the balun—by joining J3(J4) to J5—to ensure the source sees a fixed 50- $\Omega$  load at all frequencies, thereby maximizing its linearity for high-frequency, single-tone tests.

The final element of passive input signal conditioning is the option for primary-side(secondary-side) filtering afforded by F1(F2 and F3), which suppresses both out-of-band noise and spurious harmonics associated with the signal source(and transformer) [*Vleugels*, 2002, p.141]. For wideband testing, a primary-side low-pass filter, such as the Coilcraft P7LP (a 7-pole elliptic LC filter) or, for better linearity, the P3LP (a 3-pole Butterworth), proves sufficient whereas, for single-tone, high-frequency measurements, implementing F2 and F3 by a pair of 100-kHz bandpass filters, such as the Allen Avionics BPS00P10S, prevents any exogenous spurs in the input signal spectrum due to transformer nonlinearities.

### H.1.2.2 Active Path

To present a fixed impedance to the signal source, regardless of the DUT configuration or the insertion of filters prior to it, and to buffer its output signal in those cases when it must be driven down long cables before reaching the PCB, active single-ended-to-differential conversion is performed by the AD8138 amplifier (A1) in Figure H.2(b) when J1 is driven while J2 is floating.<sup>7</sup> Resistors R3–R6 are sized so as

---

<sup>6</sup>To alleviate imbalance in the transformer secondary winding, R6–R9 should return to  $V_{\text{cmi}}$  rather than GndA. Testing confirms that the latter connectivity, optionally supported on the PCB, introduces greater distortion.

<sup>7</sup>Also, R1 should be omitted. When feeding both J1 and J2 in its presence, signal routing to/from the AD8138 can be configured to operate it as a fully differential buffer [*Analog Devices, Inc.*, AD8138]. But, this option is not required in practice because the drive capability of the SRS DS360 differential outputs (cf. Section 6.2.2.1) is sufficient over the short cable runs of the LN test bench (cf. Section 6.2.2).

to match: the effective input impedance to that of the source (presumed to be  $50\ \Omega$ ); and the impedances seen by the inverting and non-inverting inputs of the AD8138, preventing imbalances due to its input offset current.<sup>8</sup> Unity-gain is achieved by matching  $R_7/R_8$  to  $R_5/R_6$  (using 0.1% parts). As for the transformer center-taps, the common-mode output voltage is provided by RVCM1.

The load seen by A1 at the output,  $V_{se2}$ , is effectively independent of the DUT due to the isolation afforded by R9 and R10 and the balanced arrangement of C2–C4 [*Linear Technology, LTC2203*]. Additionally, during low-frequency (i.e., Mode A and B) testing, this arrangement provides single-pole noise shaping above 625 kHz.<sup>9</sup> To preserve the spectral purity of the input signal, C2–C4 feature polystyrene (PSTY) dielectrics, rather than traditional ceramics, as is also the case for all signal-path capacitors in INPDF [*Williams, 1993*, p.122].

### H.1.3 Differential Input (INPDF)

For most differential sources, the simple filtering and impedance matching afforded by the INPDF block, whose contents are presented in Figure H.3, is enough to couple signals into the DUT without degrading their spectral purity. In his case, coaxial cables from the positive and negative outputs tie directly to J5/J6. An exception is the case of high-frequency, single-tone testing wherein the input signal drives J1 and J2 with a pair of 100-kHz bandpass filters (e.g., Allen Avionics BPS00P10S) connected between J3/J4 and J5/J6 to eliminate undesired harmonic content, as in

---

<sup>8</sup>With J2 floating and R1 omitted, the resistance seen at J1 is given by [*Linear Technology, LT1994*]:

$$R_{\text{eff}} = R_3 \parallel \left[ R_{5,6} + \left( \frac{R_{5,6} + R_2 \parallel R_4}{2(R_{5,6} + R_2 \parallel R_4) + R_{7,8}} \right) R_{7,8} \right]$$

Setting  $R_{\text{eff}} = R_s$  matches the buffer to a source impedance of  $R_s$ . On the other hand, neutralizing the AD8138 input offset current requires that:

$$R_5 + (R_s \parallel R_3) = R_6 + (R_2 \parallel R_4)$$

Together with the unity-gain requirement,  $R_{7,8} = R_{5,6}$ , these conditions establish the values of R3–R6 for given source and feedback resistor sizes, with the latter kept small ( $510\ \Omega$ ) to prevent the opamp input capacitance from destabilizing the loop.

<sup>9</sup>To ensure that the noise currents do not infiltrate the  $V_{\text{cmi}}$  line, these capacitors return their charge to GndA.

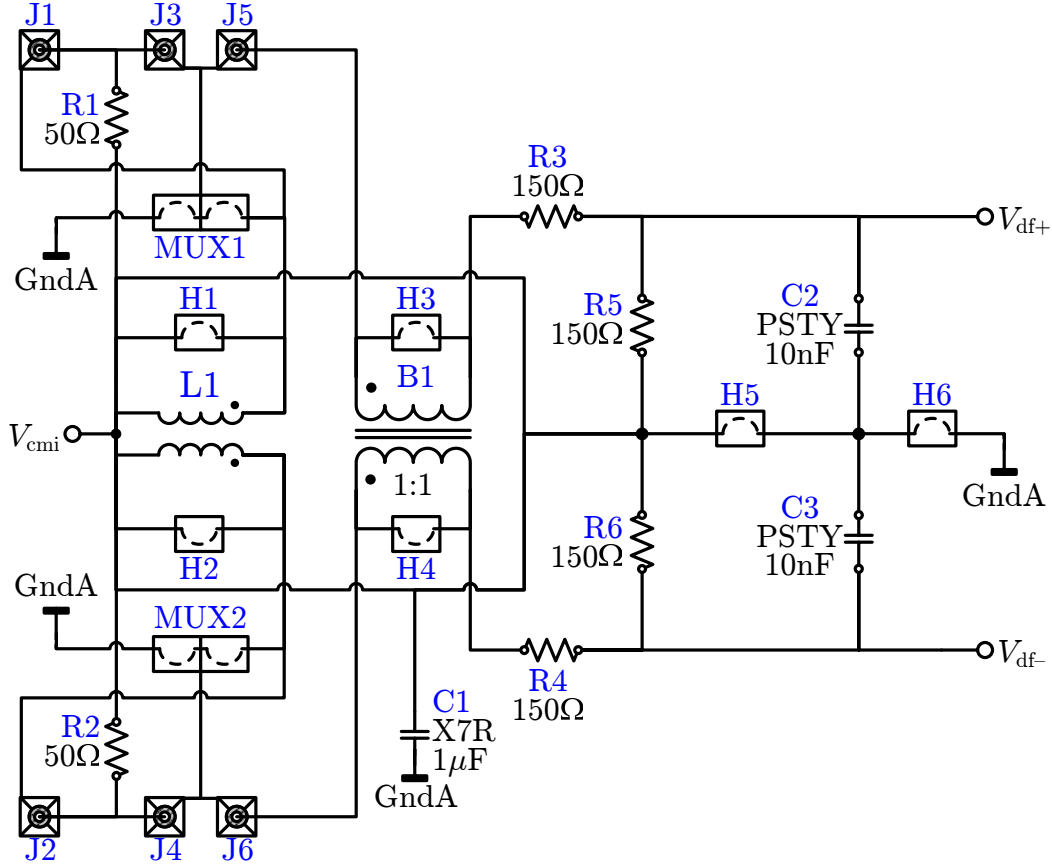


Figure H.3: Schematic of INPDF block, which provides balancing, impedance matching, and noise filtering for high-precision differential signal sources.

INPSE.

Also similar to INPSE is the inclusion of a current-mode balun (B1), to compensate for any imbalance in the DUT input impedance as seen by the source and eliminate common-mode noise currents on the input lines.<sup>10</sup> Since B1 limits the bandwidth of this path, it is implemented with a wideband Coilcraft TTWB1010 RF transformer whose lower 3-dB bandwidth is 3.5 kHz.<sup>11</sup> The trade-off for SMT size and wideband operation is lower inductance, resulting in less common-mode rejection

<sup>10</sup>Balun B1 does not ensure that the voltage at the load is balanced; hence, the need for the INPOS block.

<sup>11</sup>Roll-off in its response below this frequency is de-embedded during calibration of the PCB (cf. Section 6.2.1.3).



than with larger coils. Additionally, since the linearity of this transformer is not published, H3/H4 preserve the option to bypass it.

Once balanced, the input signal is subjected to the 1-pole filter formed by R3–R6 and C2–C3 to attenuate remaining broadband differential noise, including that coupled in by B1 [*Stanford Research Systems, Incorporated*, 1999]. The input impedance (60  $\Omega$  differential) and 3-dB frequency ( $\sim 140$  kHz) of the filter support the use of the SRS DS360 for low-frequency testing (cf. Section 6.2.2.1). Once again, the linearity of polystyrene dielectrics in capacitors C2–C3 is critical, since there is no additional harmonic filtering before the signal reaches the DUT. As in Figure H.2(b), R5/R6 return their current to  $V_{\text{cmi}}$  in order to establish the common-mode voltage of  $V_{\text{df}}$ . However, H5 and H6 provide the option of returning the noise currents of the capacitors to either  $V_{\text{cmi}}$  or GndA, with the latter chosen throughout this testing to avoid corruption of the former.

The final technique for preserving the linearity of the signal source is the use of a high-inductance choke L1—implemented by a Panasonic ELF11M010E line filter—to minimize both common-mode and differential-mode noise currents flowing along the shields of the coaxial cables.<sup>12</sup> Although B1 attenuates common-mode shield noise that returns to the signal source and adds to the input itself, such noise currents would otherwise be provided by RVC1 in the absence of L1. Additionally, L1 presents a large single-ended impedance (30 mH) between each shield and  $V_{\text{cmi}}$ , encouraging differential noise on the former to flow harmlessly back the source rather than onto the PCB. As for B1, the L1 choke can be bypassed by headers H1 and H2, should it prove detrimental.

#### H.1.4 Input Offset Cancellation (INPOS)

The INPOS block of Figure H.1 is used to measure and, if necessary, cancel net DC offset in the signal path, be it residual error in the differential input signal provided from either INPSE or INPDF (depending on the state of MUX1/MUX2 in Figure H.1) or the input-referred offset voltage of the DUT. When enabled, the discrete bipolar

---

<sup>12</sup>MUX1/MUX2 permit the shields to be grounded, rather than driven by the on-board common-mode generator, RVC1. However, this connectivity is not required for the tests described herein.

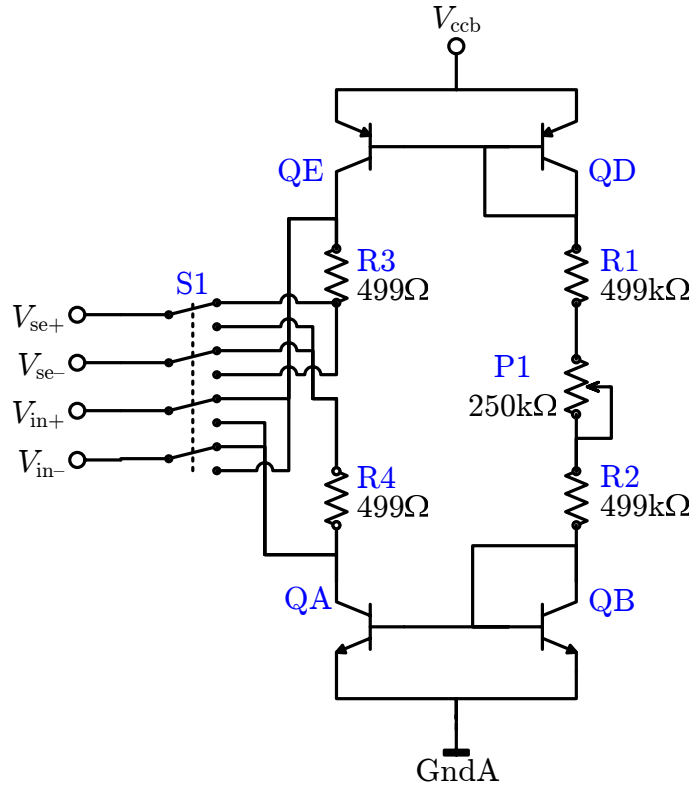


Figure H.4: Schematic of INPOS block, which uses  $I$ - $R$  batteries formed by R3 and R4 to cancel the net input-referred offset of the DUT and on-board signal-path circuitry. Shown with INPSE in use.

array (Intersil HFA3096) and simple current-mirror circuit of Figure H.4 add a DC offset voltage in series with the input signal whose size and polarity are tuned via switch S1 and potentiometer P1, respectively.<sup>13</sup> With a DC input, these are adjusted until the measured difference of the DUT inputs(outputs) goes to zero; the sum of the voltage drops across R3 and R4 then equals the output-referred(input-referred) offset of the (INPSE or INPDF block)DUT.

<sup>13</sup>Since the sum of any offsets from the DUT, the PCB circuitry, and the instrumentation can be quite large, INPOS achieves a range of 3–300 mV by employing a two-tiered scheme: fine tuning is accomplished by means of P1, with coarse steps set by the choice of thru-hole resistors R1 and R2. Not shown is an additional resistor in the same branch that provides overvoltage protection, limiting the master current to 300  $\mu$ A should P1 accidentally clutch with R1 and R2 set to 0  $\Omega$ .

### H.1.5 Output Termination (OUTDF and OUTSE)

As pictured in Figure H.5 the DUT output can be terminated into either a differential RC load (OUTDF) or an active, opamp-based differential-to-single-ended converter serving as the conjugate of the active INPSE path (OUTSE).<sup>14</sup>

#### H.1.5.1 Differential Output

The differential (C1, C2, R1) and common-mode (C3–C6, R2, R3) elements of OUTDF (cf. Figure H.5(a)) are analogous to those at the output of A1 in Figure H.2(b) with the addition of options for thru-hole resistors and high-linearity (NP0) ceramic capacitors in parallel with each polystyrene capacitor to more aggressively filter out-of-band signals prior to sampling. C2, C4, and C6 render the load seen by the DUT at  $V_{\text{out1}}$ , and any performance dependence thereon, independent of which differential instrumentation performs the measurement.

#### H.1.5.2 Single-Ended Output

For single-ended test equipment, the DUT output can instead be taken from  $V_{\text{out2}}$  in Figure H.5(b). The inamp, a Linear LT1167C, offers variable-gain (via P1) to compensate for any attenuation in the input-handling circuitry. Its input can be either AC-coupled above 150 Hz or DC-coupled (via MUX–MUX4) and features passive noise filtering above 2 MHz (via R5/R6 and C3–C5) while its output impedance matches the 50  $\Omega$  load presented by most test equipment.

## H.2 Supplies and References

For ease of use, the characterization PCB is designed to generate all necessary static signals from a single +10 V supply connected to the PWR block.<sup>15</sup> Likewise, the

<sup>14</sup>As opposed to INPSE and INPDF, these blocks are connected in series, using headers not shown in Figure H.1. Only when enabling single-ended output is the connection between them jumpered.

<sup>15</sup>With the exceptions of containing large (330 mF) electrolytic capacitors for board-level decoupling and a master power switch, the implementation of the PWR block is not critical to the overall PCB operation.

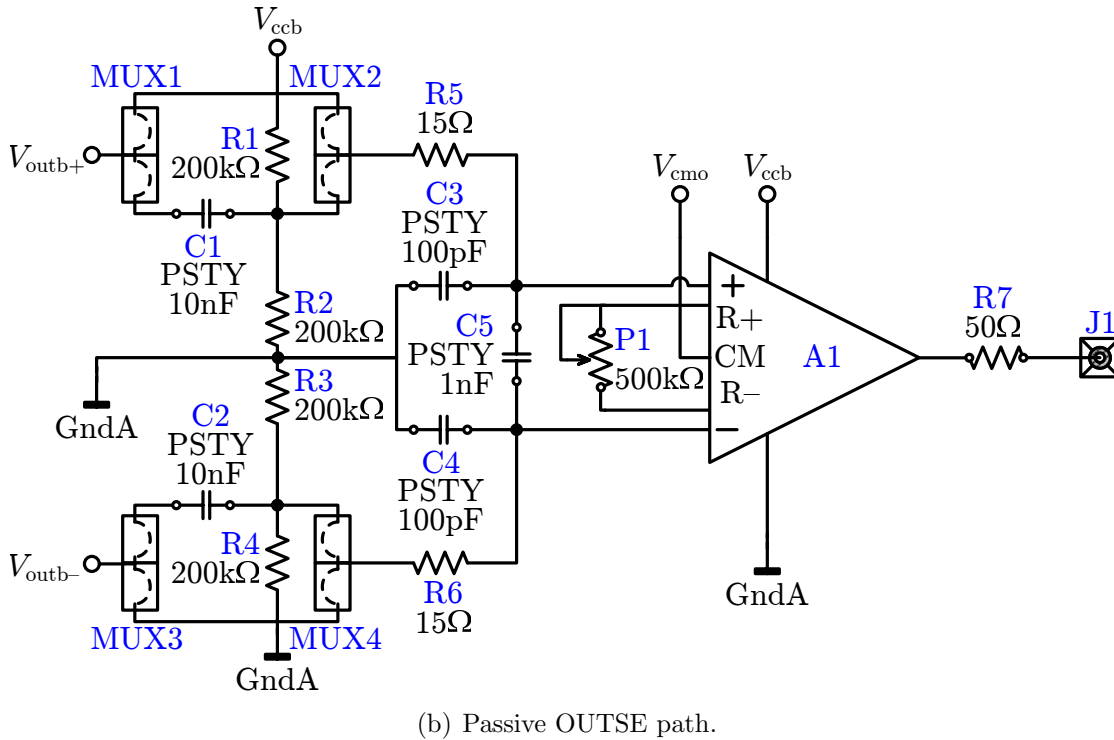
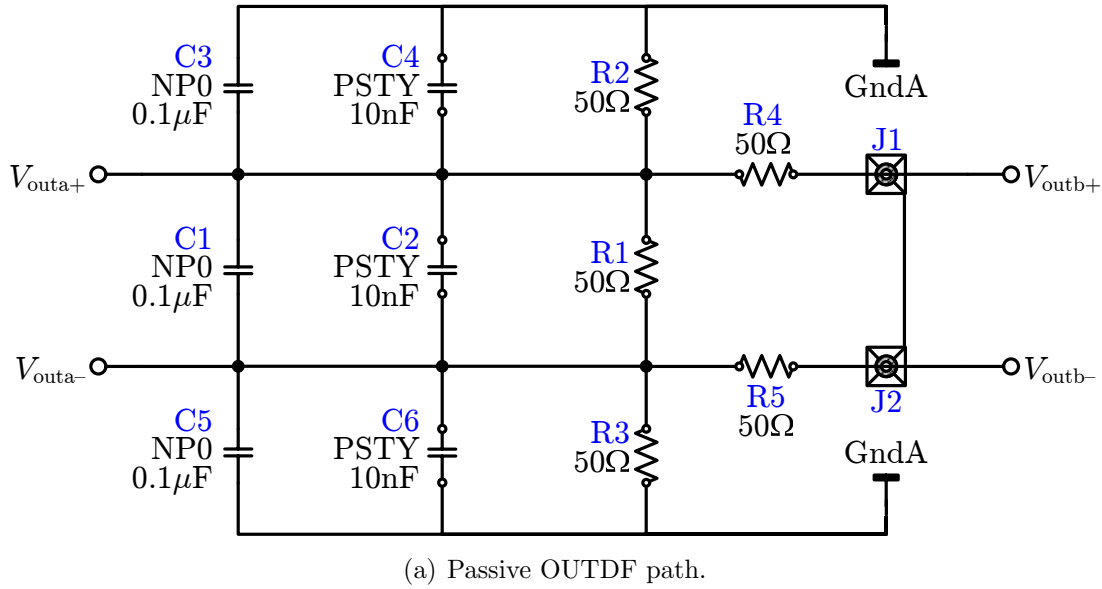


Figure H.5: Schematics of output termination paths. The (a) OUTDF path uses a configuration of passives similar to the loading of Figure H.2(b), whereas (b) OUTSE features differential-to-single-ended amplification.

DUT itself can generate references using on-chip generator rather than relying on those of the PCB. However, as there also exist test conditions under which external references provided to the PCB(DUT) by laboratory instrumentation(board-level generators) are either equally convenient or particularly advantageous, provisions exist to accommodate additional sources for these signals. The subsequent sections detail both methods of supply and reference generation within each block.

### H.2.1 Fixed Supply Regulators (SUPF)

Isolated from the DUT supply domain, analog(digital) components on the PCB that require a fixed supply voltage are powered from the SUPF1(SUPF2 and SUPF3) block. Each SUPF block can derive its power from one of two sources:<sup>16</sup>

#### *External*

Current from a bench-top power supply set to the desired voltage and connected via an SMA jack is filtered by a common-mode choke (TDK ACM4532) and line filter (Panasonic ELKEA33FA) and gated by a 300-mA current-limiting switch (Maxim MAX4793).

#### *Regulator*

The master +10 V supply is line filtered (Panasonic ELKEA33FA) and stepped down to the desired voltage (nominally, +5 V for  $V_{ccb}$  and +3.3 V for  $V_{cca}$  and  $V_{dda}$ ) by a 500-mA low-dropout (LDO) regulator (Linear LT1763).<sup>17</sup>

For all characterization, the on-board regulators are used exclusively. Note that, although equal in value,  $V_{cca}$  and  $V_{dda}$  supply the ADC core and I/O from separate SUPF blocks, mitigating the effects of clock noise.

---

<sup>16</sup>In both cases, Schottky diodes ( $V_F = 0.36$  V) provide flyback protection from the inductive currents of the filters and regulators.

<sup>17</sup>The LT1763 line supports a variety of voltage options; only the LT1763-2.5 (SUPF1) and LT1763-3.3 (SUPF2 and SUPF3) are used here. For maximum precision, each regulator's error amplifier senses the voltage at the overall output rather than that of the regulator itself. In so doing, its feedback loop regulates for parasitic voltage drops between the two nodes.

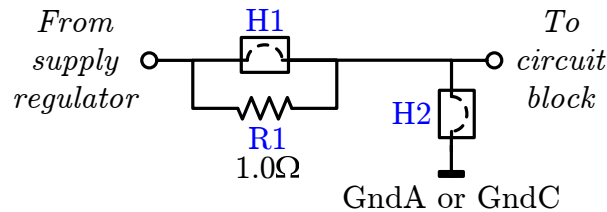


Figure H.6: Schematic of dual-mode power sensing circuit. Depending on the measurement environment, the supply current is measured across H1 either directly (using an ammeter) or indirectly (using a voltmeter and inferring from  $V_{R1}$ ).

### H.2.1.1 Power Measurement

To sense the power drawn from the corresponding SUPF (or SUPA) supply, each block of Figure H.1 interposes the circuit of Figure H.6 along its supply rail(s).<sup>18</sup> With H1 shunted, the voltage reaching the block is measured relative to the appropriate ground plane across H2 and, in the laboratory environment, an ammeter is simply connected across H1 to directly sense the current flowing into the circuit. However, when the measurement equipment is distant from the PCB, the long cables between them are subject to both  $IR$ -drops and ambient noise pickup. This circumstance favors a more accurate technique in which a voltmeter is connected across H1 via a twisted pair cable and the current derived from  $V_{R1}$ . For each block,  $R_1$  is chosen large enough that  $V_{R1}$  exceeds the observed noise but small relative to the voltmeter impedance, minimizing current flow along the cables; empirically, 1–100  $\Omega$  proves sufficient.

## H.2.2 Adjustable Supply Regulators (SUPA)

Elements whose supply voltages may require in-test adjustment, including the DUT, are provided by variable regulators within the SUPA blocks. SUPA1(SUPA2) provides power to the core(I/O ring) of the DUT via  $V_{\text{sup}}(V_{\text{esup}})$  at a nominal level of +2.5 V. SUPA3(SUPA4) controls the logic levels of the ADC input(output) buses, which are nominally referenced to +3.3 V, but can be stepped up or down by level translation

<sup>18</sup>A corresponding version of Figure H.6 consisting of only R1 and H1 is placed in series with the connection between each of the ground buses of SVEPRE (cf. Figure 6.2) and the GndA plane. These ground-interrupt resistors are equally useful for DUT power measurements (cf. Section 6.2.4.1).

circuitry in the ADC block. The contents of each SUPA block are nearly identical to those of SUPF, save for replacing the fixed LT1763 with a variable, 100-mA LDO LT1761 governed by an on-board potentiometer [[Linear Technology, LT1761](#)].

### H.2.3 Reference Currents (RCUR)

Each of the three reference currents supplied to the DUT ( $I_B$ ,  $I_E$ , and  $I_O$ ) is provided by an RCUR block (RCUR1, RCUR2, and RCUR3, respectively) that contains a 50-k $\Omega$  potentiometer to GndA.<sup>19</sup> Depending upon the desired tuning range, this terminates one or both of the corresponding DUT pins (cf. Figure 6.2), working in conjunction with the on-chip diodes described in Section G.2.2.2 to set the current; nominally, each should be 40  $\mu$ A, which requires trimming the corresponding potentiometers to 21–24 k $\Omega$ .

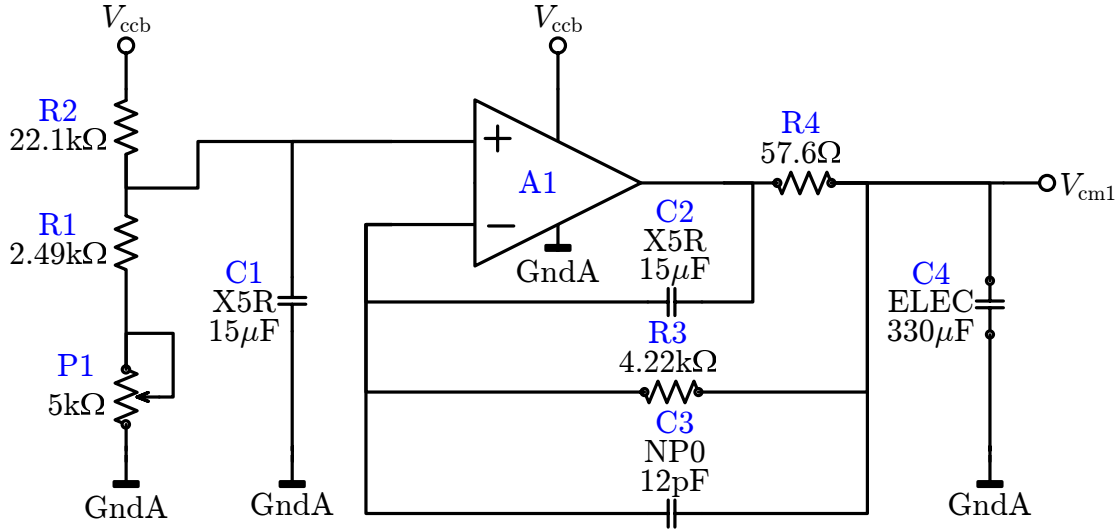
### H.2.4 Reference Voltages (RVLT)

For greater control and higher precision, the tests described in Chapter 6 provide the common-mode reference voltages  $V_{cm1}$  and  $V_{cm2}$  to SVEPRE using external generators, rather than the on-chip alternatives described in Section G.2.2.1. However, the topology of these on-board voltage references—implemented as buffered resistor ladders—is quite similar to their silicon counterparts, as evidenced by Figure H.7.<sup>20</sup>

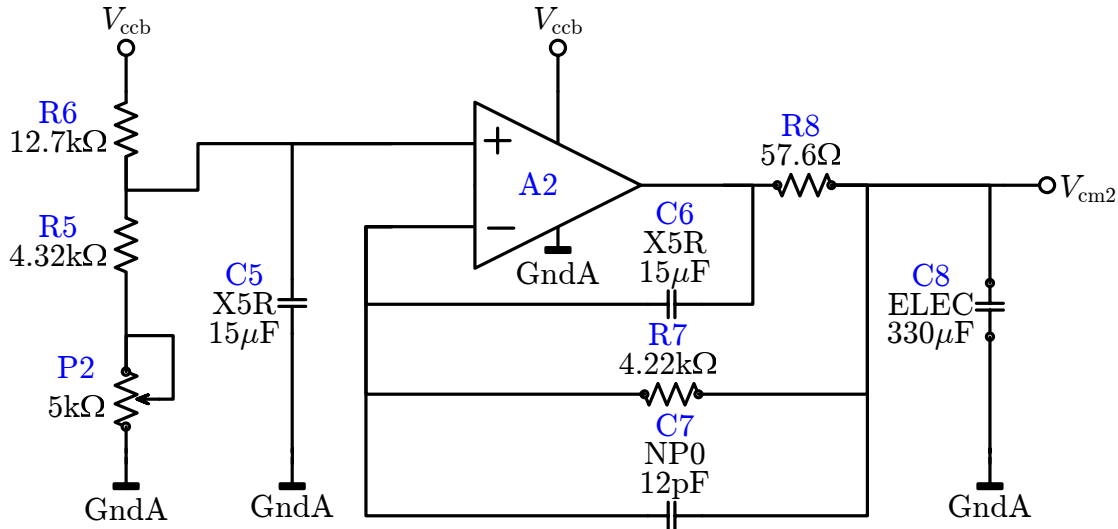
Versions of  $V_{cm1}$  (nominally, +1.0 V) and  $V_{cm2}$  (nominally, +1.75 V) trimmed on separate resistive dividers via overvoltage-protected potentiometers P1 and P2 are buffered by the pair of opamps in a single Maxim MAX4252 dual part so as to

<sup>19</sup>A discrete 5.23 r $\Omega$  resistor in series with this potentiometer prevents overcurrent if it clutches accidentally. In parallel with each potentiometer, a Linear Technology LM334 adjustable current source is also available [[Linear Technology, LM334](#)], but there is sufficient headroom at the Bo, Eo, and Oo pins of all DUTs tested that it proves unnecessary.

<sup>20</sup>Not shown in Figure H.7 are alternative input paths that allow  $V_{cm1}$  and  $V_{cm2}$  to be provided directly from bench-top sources connected either at the inputs or outputs of A1 and A2, depending on buffering requirements. In the absence of any other filtering of these signals, the 10-MHz RC snubber formed by R5 and C6 prevents unwanted interferers from causing ringing on the long traces running to the DUT yet is barely active at the unity gain frequency of the opamps (3 MHz).



(a) RVLT1 block.



(b) RVLT2 block.

Figure H.7: Schematic of blocks for reference voltage generation. Although their reference ladders generate different voltages (nominally, +1V and +1.75V, respectively), the (a) RVLT1 and (b) RVLT2 blocks employ identical buffers, sharing the dual opamps of a MAX4252.



isolate the ladders from the DUT loading or time-dependent fluctuations thereof.<sup>21</sup> Compensation is necessary to ensure the stability of A1(A2) in light of its large input capacitance (11 pF) and the fact that the effective capacitance formed by C4(C8) in parallel with that of the CM1(CM2) DUT pin far exceeds the recommended maximum (400 pF). Isolation resistors R4/R8 and feedback capacitors C2/C3(C6/C7) resolve this difficulty.<sup>22</sup>

---

<sup>21</sup>Noise on the MAX4252 supply pins is common to both opamps and thus of little consequence.

<sup>22</sup>To design compensation networks for the input and load capacitance, three quantities are established at outset:

1. First, conscripting the instance identifiers of Figure H.7(a) in this example, C4 is sized so that the effective opamp load is insensitive to subsequent circuitry and board layout; 330  $\mu$ F comes recommended [*Maxim Integrated Products, AN994*, p.4].
2. Next, observe that in a follower configuration, as opposed to a non-inverting amplifier,  $R_3$  is relatively unconstrained because it does not determine the gain. So as to increase the effective  $e_n$  by no more than 3 dB,  $R_3$  is then selected such that its thermal noise is equal to  $e_{ni}$  of A1 at 10 kHz (8.3 nV/ $\sqrt{\text{Hz}}$ ).
3. Finally, the output resistance of A1,  $R_o$ , must be inferred either from the closed-loop output impedance or the maximum load capacitance given in [*Maxim Integrated Products, MAX4252*]; the former subsumes the effect of shunt feedback, the latter is a proxy for the location of the non-dominant pole at some minimum phase margin (assumed here to be 45°). Both methods concur that  $R_o \simeq 134 \Omega$ .

The goal of the load compensation scheme is that C2 shunts the output signal directly to the inverting opamp input at or below the frequency where the C4 pole rolls off, introducing excess phase. Put another way, the pole at the opamp output

$$p_L = \frac{1}{(R_o + R_4) C_4}$$

must be canceled by the feedback zero

$$z_F = \frac{1}{(R_3 + R_4) C_2}$$

leaving  $L(s)$  unchanged; formally, this dictates  $p_L = z_F$ . Since  $z_L$  also sets the closed-loop bandwidth of the buffer, and since at noise from the reference ladder should be attenuated by at least 30 dB at 100 Hz,  $R_4$  is chosen so that  $p_L = 2.5$  Hz, leaving  $C_2 = 15 \mu\text{F}$ . Note that above  $p_L$ ,  $e_{no}$  (which is equal to  $e_{ni}$ ) is RC-filtered by  $R_4$  and  $C_4$  at 8.4 Hz, which is an order of magnitude below  $f_K$  for this opamp.

With such low closed-loop bandwidth, the pole due the input capacitance is too high to be a stability concern. However, C3 provides a zero to cancel this pole should a reduced load prove advantageous.

### H.2.5 Common-Mode Generators (RVCM)

Details of the circuit that generates the common-mode voltage to which the signal provided by(to) the function generator(measurement equipment) is referenced at the DUT input(output), namely RVCM1(RVCM2), are omitted here since it is functionally identical to that of RVLT2(RVLT1) in Figure H.7(b)(Figure H.7(a)). Only slightly different distribution of the values within their resistor ladders distinguish the two.

## H.3 Programming and Control

To manage the large set of configuration options afforded by the characterization PCB, both manual and automatic systems for programming the DUT and controlling its interface to the test equipment are provided; programming circuits are presented in Section H.3.1 and Section H.3.2, whereas interface management, including the inclusion of an on-board ADC subsystem for digitization, are covered in Section H.3.3 and Section H.3.4.

### H.3.1 Gain Programming (GNADJ)

To set the LNA gain, the GNADJ block implements  $R_d$  as either a discrete 20-k $\Omega$  potentiometer, or a balanced pair of Maxim MAX5483 10-k $\Omega$  digital potentiometers. In exchange for higher distortion, the latter allow the software-controlled test bench to rapidly vary  $R_d$  via signal  $A[0:3]$  on INPHD. However, the demand for maximum linearity favors manual adjustment in all but the most accelerated radiation testing.

### H.3.2 Bandwidth Programming (BWADJ)

To set the AAF bandwidth, the BWADJ block provides the control word  $C[0:1]$  using either manual DIP switches or level-translations of the  $B[0:1]$  signal on INPHD. Since the filter mode is changed infrequently, the alacrity of the latter is typically not required.

### H.3.3 Digital Subsection (ADC, INPCK, SUPF3, SUPF4)

To mimic the operation of a full WBR, a Linear LTC2203 16-bit, 10-MS/s ADC is incorporated into the PCB design, along with the requisite clock and supply generators [*Linear Technology, LTC2203*]. Although an on-board ADC is not necessary to characterize the performance of the DUT,<sup>23</sup> its inclusion renders the characterization PCB a comprehensive example of the mixed-mode complexities faced when engineering a complete plasma wave instrument. Particularly noteworthy in Figure 6.3 is the use of a separate ground plane, GndC, beneath all blocks subject to clock-switching transients, so as to prevent these from coupling into the sensitive DUT via GndA. As a proof-of-concept, the digital section of the characterization PCB demonstrates the integrability of the SVEPRE design.

### H.3.4 Digital Headers (INPHD and OUTHD)

The INPHD(OUTHD) header carrying digital control(data) signals from(to) the instrument controller to(from) the GNADJ, BWADJ, and ADC(ADC) blocks also includes pins for the relevant I/O supply voltage and clock, as well as GndA(GndC) references interlaced as shields between adjacent signals (not pictured), yielding a total width of 32(48) pins.<sup>24</sup> Pertinent to a representative WBR interface, these are not utilized during the SVEPRE characterization.

---

<sup>23</sup>Naturally, though not pursued in this work, the ADC could be employed as part of the characterization process, performing the digitization presently handled by the NI PCI-6052E (cf. Section 6.2.2.1) at rate high enough to support the 100-kHz linearity testing suggested in Section 7.3.

<sup>24</sup>OUTHD contains a pair of headers: one handles the raw ADC outputs whereas the other is fed by to level translators that buffer these buses to drive long test cables.



# Appendix I

## Total-Dose Testing

This appendix summarizes the total-dose testing of the SVEPRE-1 LNA and SVEPRE-3 AAF using both  $^{60}\text{Co}$   $\gamma$ -rays and energetic protons. For each source, it provides an introduction to the test facility and its capabilities, as well as a detailed description of the experiments conducted; such explanatory information is intended as an aide to the interpretation of the radiation results presented in Section 6.4.<sup>1</sup> Section I.1 describes  $^{60}\text{Co}$   $\gamma$ -ray experiments conducted at The Aerospace Corporation in El Segundo, CA, whereas Section I.2 address the use of proton beams of various energies generated by the 88-inch cyclotron at Lawrence Berkeley National Laboratory (LBNL) in Berkeley, CA.

The test procedures described in Section I.1.3 and Section I.2.3 conform to Method 1019.7 of Military Standard 883G, Test Method Standard, Microcircuits [*MIL-STD-883G*, 2006]<sup>2</sup>—referenced simply as the *Military Standard* in the remainder of this appendix—as closely as possible.<sup>3</sup> However, as this dissertation is primarily concerned with investigating the performance of novel circuitry on a small scale, rather than

---

<sup>1</sup>For background on the underlying physics of radiation effects on microelectronic circuits, the reader is directed to Appendix C.

<sup>2</sup>For an introduction to the subject of total dose hardness assurance, including procedural trends throughout the history of the field and the evolution of the governing military standards, the reader is referred to [*Fleetwood and Eisen*, 2003].

<sup>3</sup>Although strictly connoted to apply only to radiation testing with  $^{60}\text{Co}$   $\gamma$ -ray sources [*MIL-STD-883G*, 2006, Sect. 1], procedural elements of the Military Standard not specific to the operation of the source are frequently and readily extended to particle radiation. Testing in support of this work adopts this generalization of the Military Standard conditions as an industrial practice.

qualifying an entire lot of commercial ICs—as is the scope of the Military Standard—research aims take precedence over strict adherence to its stipulations.

In particular, the procedures herein undertake two notable deviations from the Military Standard. First, as described in Section 2.1.2.3, whereas the BiCMOS character of the SVEPRE design and the 3 mrad(Si)/s dose rate expected in the proposed application qualify for low-dose rate (ELDRS) testing according to Section 3.13 of the Military Standard [*MIL-STD-883G*, 2006, Sect. 3.13, Paragraph a], the impracticality of performing the TID tests either at a rate  $\leq 10$  mrad(Si)/s or by accelerating them through elevated temperature as prescribed by Conditions D and E of Section 3.6, precludes such evaluation.

Secondly, in keeping with the same pragmatism, the accelerated annealing test for DUTs potentially vulnerable to time-dependent effects, which also employs elevated temperature [*MIL-STD-883G*, 2006, Sect. 3.12], is eschewed in favor of an extended room-temperature anneal, as per Section 3.11.<sup>4</sup> Furthermore, as the goal of annealing conducted here is merely to discern the causes of radiation-induced degradation from its permanence and the known differences between the annealing rates of  $\Delta N_{ot}$  and  $\Delta N_{it}$  described in Section C.2.4 and Section C.2.6, respectively, it is not necessary to effect worst-case conditions by maintaining static bias throughout.

The Military Standard dictates that characterization of the DUT at the conclusion of a dose step must begin within one hour and be completed within two hours, so as to minimize time dependent effects; however, it is recommended that “these intervals shall be as short as possible” [*MIL-STD-883G*, 2006, Sect. 3.10]. Adherence to this precept motivates the automation of the test benches described in Section 6.2 so as to accelerate the characterization of the DUT between dose steps by eliminating the human element. However, the limiting factor in the available time for—and, thus, the comprehensiveness of—the test bench operation remains the operators: in order to transfer the part from the radiation environment to the characterization PCB, stray radiation levels of the former must first recede below the safety limits dictated by Table C.2. The TID procedures described below are tailored to minimizing both

---

<sup>4</sup>The length of all such annealing conducted in this research is well below the prescribed maximum for the expected environment of one year.

contributions to the delay between dose steps.<sup>5</sup>

## I.1 <sup>60</sup>Co Testing

The <sup>60</sup>Co testing for this work was conducted on April 12–13, 2006 at the headquarters of The Aerospace Corporation in El Segundo, CA. Along with author, the experimenters with The Aerospace Corporation were Steven C. Witczak, James L. Roeder, Jon V. Osborn, Mark A. Turpin, and Robert Garrett. The goal of the testing was not only to confirm that the part maintains performance up to the stated specification of 100 krad(Si), but to determine the maximum survivable dose at which it ceases to properly function. Dose steps up to 200 krad(Si) serving the former objective were carried out on April 12, 2006; after allowing the part to anneal overnight, the sequence of logarithmic steps resumed up to a level of 2 Mrad(Si), at which point the available time expired. No failures of the part were observed.

### I.1.1 Source

An extremely common source for simulating the effects of ionizing radiation on microelectronics, a <sup>60</sup>Co  $\gamma$ -ray chamber produces high-energy photons whose ionizing effects, in terms of  $\Delta N_{\text{ot}}$  and  $\Delta N_{\text{it}}$ ,<sup>6</sup> are nearly identical to those of same dose delivered by radiation-belt protons or electrons [*Holmes-Siedle and Adams, 2002*, p.439]. Much of the popularity of <sup>60</sup>Co chambers stems from their low cost and convenience when contrasted with particle accelerators, such as that of Section I.2.1.<sup>7</sup>

---

<sup>5</sup>The inter-step delay is also governed by a variety of shorter but not insignificant maneuvers, including: populating and depopulating the DUT, transporting the DUT to and from the characterization station, and potentially needing to repeat characterizations should the test benches malfunction. Allowance for these activities is made through safety margins built into the test schedule.

<sup>6</sup>Recall from Section C.3.1.1 that only through inefficient nuclear collisions of secondary electrons can photonic radiation produce displacement damage. Thus, <sup>60</sup>Co is only capable of simulating the ionizing effects of trapped radiation. A more thorough treatment of these phenomena, including definitions of the increased trapped-charge and interface traps densities symbolized by  $\Delta N_{\text{ot}}$  and  $\Delta N_{\text{it}}$ , is offered in Section C.2.

<sup>7</sup>Although low-energy X-ray sources have emerged as even more attractive in these regards, the literature on the correlation between the results obtained with such sources and those using high-energy <sup>60</sup>Co  $\gamma$ -rays—the *de facto* standard—is decidedly mixed [*Dozier and Brown, 1983*; *Oldham*

In this research, the availability of such a facility at headquarters of the Aerospace Corporation provided an expedient means of assessing the robustness of the SVEPRE design prior to engaging the more comprehensive and costly resources of the LBNL cyclotron.

#### I.1.1.1 Theory

The production of  $^{60}\text{Co}$  occurs when stable  $^{59}\text{Co}$  is bombarded by heavy neutron irradiation in a nuclear reactor [[Kerris, 1989](#), p.455]. Typically stored in a concrete or steel cell, rods of  $^{60}\text{Co}$  are unstable with a half-life of 5.27 years—their radioactive decay emits  $\gamma$ -rays with energies of 1.173 MeV and 1.332 MeV [[Holmes-Siedle and Adams, 2002](#), p.439]. However, this initial (and desirable) discrete photon spectrum can be significantly modified by Compton interactions with the materials of the radiation chamber,<sup>8</sup> resulting in a considerable low-energy component (0.1-0.9 MeV) [[Kerris, 1989](#)]. These soft  $\gamma$ -rays can cause not only dramatic dose enhancement [[Brown and Dozier, 1982](#)], but even liberate strong photoelectrons that in turn generate displacement damage (cf. Footnote 6) [[Turinetti et al., 1998](#)].

To mitigate the dosimetry errors associated with this low-energy backscatter, the Military Standard mandates that the radiation bias PCB be enclosed in a lead-aluminum (Pb-Al) container when illuminated by a  $^{60}\text{Co}$  source [[MIL-STD-883G, 2006](#), Method 1019.7, Sect. 3.4]. The outer thickness of lead ( $> 1.5$  mm) filters out the soft  $\gamma$ -rays, whereas the inner cladding of aluminum ( $> 0.7$  mm) shields against energetic secondary particles emitted by this process. Provided the calibration dosimeter is placed within the box as well, an accurate determination of the dose received by the part can be had to within  $\pm 5\%$  [[MIL-STD-883G, 2006](#), Method 1019.7, Sect. 2.1].

---

and [McGarrrity, 1983](#)]. Despite evidence that the ionization mechanism of the two are distinct, proposed methods of converting the dose delivered by the former to an equivalent dose of the latter suggest that it is possible to achieve valid simulation of the expected radiation environment for many applications through careful qualification with X-ray sources [[Benedetto and Boesch, 1986](#); [Fleetwood et al., 1988](#)].

<sup>8</sup>The mechanism of Compton scattering is described in Section [C.2.1.1](#).



### I.1.1.2 Overview

The <sup>60</sup>Co chamber at The Aerospace Corporation [*Witczak et al.*, 2005, p.2603] contains four rods of varying radioactivity sealed in a subterranean concrete cell. Any combination of these rods, which (measured in the SI unit of Curie) possess activities of 1 Ci, 100 Ci, 3500 Ci, and 3500 Ci, can be raised via a pneumatic hoist into the lead-lined bunker where the DUT resides;<sup>9</sup> for this research, the two 3500-Ci rods are extracted, for a total exposure of 7000 Ci and a correspondingly high dose rate necessary to reach the target dose levels.<sup>10</sup>

### I.1.1.3 Dosimetry

The dose rate experienced by the DUT is a function of its proximity to the rods. This distance is controlled by a gauge whose separation from the rods is measured in millimeters. Prior to irradiation, the dose rate of the chamber is calibrated to within  $\pm 5\%$  (as required by the Military Standard) by affixing an ionization chamber to the radiation bias board in place of the DUT and sweeping the gauge distance. The resulting map of the dose rate is provided in Table I.1. Since the dosimeter rests atop the socket, whereas the die itself rests on the floor of the package cavity, it is necessary to correct the measurement by an additional 2 mm to arrive at the properly adjusted values in the final two columns. As indicated in Table I.1, the ionization chamber does not measure dose directly but, rather, exposure. Exposure is a measure of the ability of radiation to ionize dry air at standard temperature and pressure (STP) and, as such is measured in C/kg, or with the non-SI unit of Roentgen ( $1 \text{ R} = 2.58 \times 10^{-4} \text{ C/kg}$ ). The conversion from exposure to dose, whose SI unit is the Gray (cf. Section C.1.2.2) thus requires a measure of the energy required to generate electron-hole pairs in air. This quantity is known as the *W*-value of air, or the mean energy expended per ion pair formed, and is commonly taken to be 33.97 eV/pair or,

---

<sup>9</sup>This bunker, in turn, resides within a room encircled by thick concrete walls. Even in conjunction with the thick lead door at the terminus of the bunker (where the Pb-Al container is loaded), experimenters are barred from the room during exposures; such is the penetrating power of  $> 1\text{-MeV}$   $\gamma$ -rays.

<sup>10</sup>For reference, a source of moderate strength has an activity of about 1000 Ci [*Holmes-Siedle and Adams*, 2002, p.439].

Gauge distance [mm]	Measured exposure rate [kR/hr]	Calculated dose rate		Adjusted dose rate	
		[rad(SiGe)/s]	[rad(Si)/s]	[rad(SiGe)/s]	[rad(Si)/s]
58	333	80.020	80.060	78.098	78.722
60	325	78.098	78.722	75.214	75.816
62	313	75.214	75.816	73.772	74.362
64	307	73.772	74.362	71.369	71.940
66	297	71.369	71.940	70.408	70.971
68	293	70.408	70.971	68.245	68.791
70	284	68.245	68.791	66.323	66.853
72	276	66.323	66.853	65.602	66.127
74	273	65.602	66.127	64.160	64.673
76	267	64.160	64.673	n/a	n/a

Table I.1: Dose rate calibration table for The Aerospace Corporation  $^{60}\text{Co}$  chamber. The adjusted dose rate of the highlighted row applies to the all data obtained for this dissertation.

equivalently, 33.97 J/C. Thus, the relationship between exposure ( $X$ ) and dose in air ( $D_{\text{air}}$ ) is:<sup>11</sup>

$$X = \frac{D_{\text{air}}}{W_{\text{air}}} \quad (\text{I.1})$$

Substituting the aforementioned value of  $W_{\text{air}}$  into (I.1) and applying a series of fundamental conversion factors in order to convert to units of rad allows the conversion

<sup>11</sup>Strictly speaking, (I.1) actually converts between exposure and collisional kerma in air ( $K_c$ ), not dose. Although the latter pair of quantities share the same SI units (J/kg or Gy) collisional kerma(dose) is appropriate for photonic(particle) radiation which is indirectly(directly) ionizing [Attix, 1986, p.21-22]. Since the data in question pertains to  $^{60}\text{Co}$   $\gamma$ -rays, the expected value of the net kinetic energy transferred from the photons to the charged particles of air is actually kerma (Kinetic Energy Released per unit MAass) or  $K$ . It is these secondary particles which then go on to directly ionize the dosimeter material, either through collisions or bremsstrahlung. The fraction of kerma imparted to particles that participate in the in the former method of ionization is known as the collisional kerma and it is this quantity which constitutes the absorbed dose. Thus, even though it is strictly possible only to express  $K_c$ , not  $D$ , in terms of fluence for indirectly ionizing radiation [Attix, 1986, p.27], in this work the very fact that fluence is measured with an ionization chamber ensures that all the pairs generated by  $K$  are measured as absorbed dose in the air, thus implying  $K_c = D$ .

factor from exposure in air (measured in R) to dose (in rad) to be determined as:

$$\xi_{\text{air}} \Big|_{\frac{\text{rad}}{\text{R}}} = \frac{D_{\text{air}} \Big|_{\text{rad}}}{X \Big|_{\text{R}}} = 0.876 \quad (\text{I.2})$$

Ultimately, it is necessary to determine the conversion factor for dose absorbed by the material of the die (for silicon, this is  $\xi_{\text{Si}}$ ). For the same fluence, the ratio of doses between any two target materials simply reflects the ratio of their mass energy-absorption coefficients, defined in Footnote 12 of Appendix C. Thus, for silicon targets:<sup>12</sup>

$$\xi_{\text{Si}} \Big|_{\frac{\text{rad}}{\text{R}}} = \frac{D_{\text{Si}} \Big|_{\text{rad}}}{X \Big|_{\text{R}}} = 0.876 \frac{(\mu_{\text{en}}/\rho)_{\text{Si}}}{(\mu_{\text{en}}/\rho)_{\text{air}}} \quad (\text{I.3})$$

Determining the mass energy-absorption coefficients for die materials is complicated by two factors: the coefficients are not typically tabulated for compounds such as SiO<sub>2</sub> and SiGe; and the coefficients are functions of photon energy of which <sup>60</sup>Co  $\gamma$ -rays exhibit two distinct values. Conventional methods address the former by deriving compound coefficients as a weighted sum of the composite elements in proportion to their atomic masses,<sup>13</sup> and the latter by simply using an average photon energy of 1.25-MeV for <sup>60</sup>Co. Employing these methods yields values of 0.872, 0.875, and 0.803 (all in units of rad/R) for  $\xi_{\text{Si}}$ ,  $\xi_{\text{SiO}_2}$ , and  $\xi_{\text{SiGe}}$ , respectively.

The final conversion factors employed to arrive at the calculated dose rates of Table I.1 are reduced from these ideal values to account for the attenuation of the photon energies as they penetrate the Pb-Al enclosure. Although the calculations for both  $\xi_{\text{Si}}$  and  $\xi_{\text{SiGe}}$  are tabulated, the small amount of germanium present in the bases of the npn BJTs is not significant to their ionizing radiation response (cf. Section 2.1.2). Thus, results hereafter are quoted in units of rad(Si)/s, in keeping with the predilection of the dissertation.

---

<sup>12</sup>As is shown next, similar conversions are possible for SiO<sub>2</sub> and SiGe.

<sup>13</sup>This technique is an application of Bragg's rule, which states the stopping power of a compound is simply the linear combination of the stopping powers of its elements [*Ziegler et al.*, 2008].

### I.1.2 Setup

For  $^{60}\text{Co}$  testing using the chamber of Section I.1.1, a single instance of SVEPRE is inserted in the radiation bias PCB, which is then housed in the Pb-Al box, which is then lidded and mounted into the chamber. A brief review of the particulars of each step comprises the remainder of this section.

#### I.1.2.1 Device-Under-Test

The DUT for these experiments is the SVEPRE-1 LNA, instance 2B. From an external +2.5-V supply, the part is biased to nominal operating conditions with  $G_p = 14$  dB using the on-chip reference generators.

#### I.1.2.2 Circuit Board

The DUT is housed on the radiation bias PCB (cf. Section 6.1.2.2) whose power is supplied by a bench-top source adjacent to the chamber.<sup>14</sup> Being specially designed by Mark A. Turpin of The Aerospace Corporation to match the dimensions of the Pb-Al box,<sup>15</sup> the PCB is firmly screwed into the box such that, between dose steps, the entire assembly is removed from the chamber and the part extracted for transfer to the characterization PCB.<sup>16</sup>

### I.1.3 Procedure

The LNA is exposed to  $^{60}\text{Co}$   $\gamma$ -rays in a series of logarithmic dose steps up to 2 Mrad(Si) according to the schedule of Table I.2. Although the exact dose is

---

<sup>14</sup>A cable feed-through beneath the chamber door guides the BNC cable carrying this power to the radiation PCB.

<sup>15</sup>Due to height limitations imposed by electrolytic capacitors on the radiation bias board, it was necessary to mount it backwards in the Pb-Al box, meaning the  $\gamma$ -rays travel through the PCB and the ceramic package before reaching the die. However, as they are extremely penetrating (not even the thick lead door at the egress of the chamber is sufficient to allow operators in the room while the source is on, as noted in Footnote 9), this trajectory has little effect on the received dose. To be certain, dosimetry was performed in this reversed orientation as well.

<sup>16</sup>Unfortunately, the radiation bias board developed by The Aerospace Corporation features lateral-force rather than zero-insertion force sockets, so populating and depopulating the part between dose steps is a not trivial in the overall time budget for characterization.

computed from the known exposure and duration via the method of Section I.1.1.3, each step is assigned a convenient dose value for record keeping purposes; this is the dose that is referenced when identifying dose steps throughout this chapter.

Between steps, the DUT is removed from the chamber, transported to the characterization PCB in accordance with provisions of the Military Standard for remotely located test equipment [*MIL-STD-883G*, 2006, Sect. 3.9.2],<sup>17</sup> and subjected to characterization via the FR, LN, and PD test benches.

#### I.1.3.1 Irradiation Schedule

To maintain a constant dose-rate throughout the testing,<sup>18</sup> the gauge position is set at 60 mm, achieving an adjusted dose rate of 75.8 rad(Si)/s according to Table I.1. This dose rate falls within the range prescribed by the Military Standard (50 rad(Si)/s to 300 rad(Si)/s), yet is as low as possible so as to still engender time-dependent effects without precluding the accumulation of large total doses in a reasonable amount of time.<sup>19</sup>

#### I.1.3.2 Annealing Schedule

This process of exposure and characterization is repeated up to a maximum dose of 2 Mrad(Si) without part failures; the testing concluded when the contracted time had elapsed. The next day, following an 11-hour, unbiased, room-temperature anneal, the DUT was put through the characterization procedure a final time to determine the degree of recovery, if any. Without material differences from the results of the 2 Mrad(Si) step, these data are omitted.

---

<sup>17</sup>At the headquarters of The Aerospace Corporation in El Segundo, CA, the  $^{60}\text{Co}$  chamber is housed in a separate building from the laboratories and offices of the collaborators. Thus, the DUT must be physically carried from one to the other, and back, between dose steps. The total travel time is less than five minutes.

<sup>18</sup>Technically, the dose rate need not be constant across all dose steps, so long as it varies by less than  $\pm 10\%$  during the irradiation itself [*MIL-STD-883G*, 2006, Sect. 3.6.1]. However, this condition facilitates interpretation of the device performance.

<sup>19</sup>Rather than only test to specified levels, the goal is to reach the highest possible dose in the allotted time and, thereby, stress the part to its limits, as noted at the outset of Section I.1.

Run identification		Exposure duration [min]	Dose rate [rad(Si)/s]	Incremental dose [krad(Si)]	Accumulated dose [krad(Si)]	Assigned dose [krad(Si)]
Date	ID					
12 April 2006	A	0.00	0.00	0.00	0.00	Prerun
12 April 2006	B	0.22	75.82	1.01	1.01	1
12 April 2006	C	0.22	75.82	1.01	2.02	2
12 April 2006	D	0.66	75.82	3.02	5.04	5
12 April 2006	E	1.11	75.82	5.04	10.08	10
12 April 2006	F	2.22	75.82	10.08	20.16	20
12 April 2006	G	6.65	75.82	30.24	50.40	50
12 April 2006	H	11.08	75.82	50.40	100.80	100
12 April 2006	I	22.16	75.82	100.80	201.60	200
13 April 2006	n/a	672.48	0.00	0.00	n/a	Anneal
13 April 2006	J	66.48	75.82	302.40	504.00	500
13 April 2006	K	110.80	75.82	504.00	1008.00	1000
13 April 2006	L	221.59	75.82	1008.00	2016.00	2000

Table I.2: Irradiation schedule for total-dose testing of the SVEPRE-1 LNA using <sup>60</sup>Co  $\gamma$ -rays.

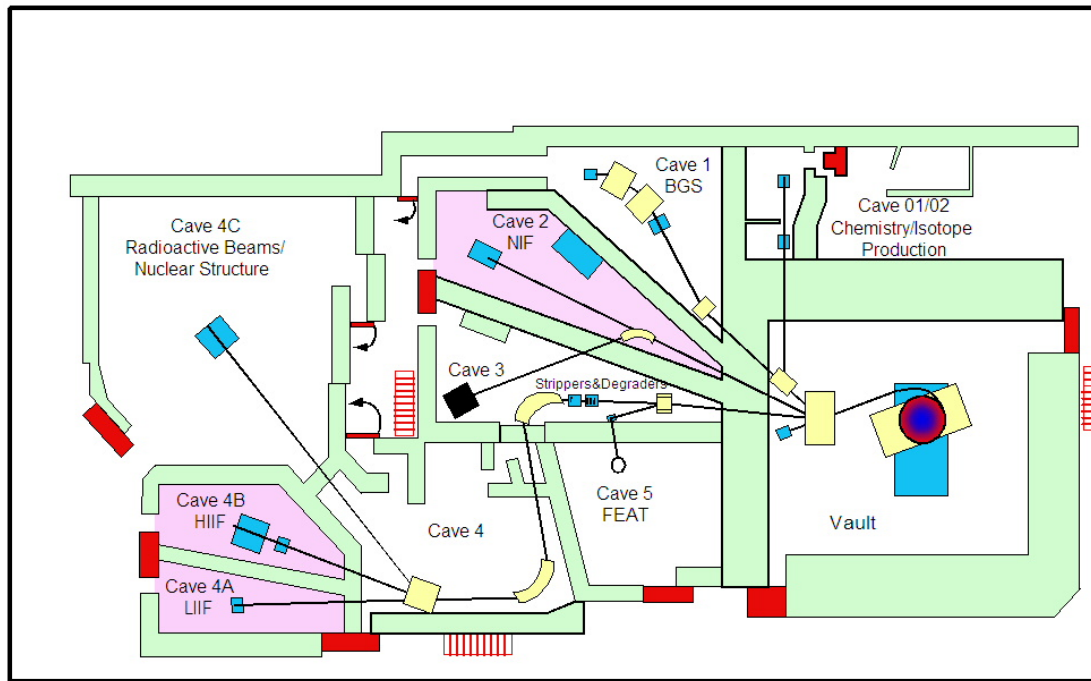


Figure I.1: Map of the BASE facility at the LBNL 88-inch cyclotron. Radiation testing for this work was conducted in Caves 4A and 4B. Reproduced *in toto* from [McMahan, 2005a, p.3].

## I.2 Proton Testing

High-energy proton testing of the LNA was conducted on June 9–10, 2006 in Cave 4A of the Berkeley Accelerator Space Effects (BASE) facility associated with the 88-inch cyclotron at the Lawrence Berkeley National Laboratory (LBNL) in Berkeley, CA. A map of the beam lines at this facility is provided in Figure I.1.<sup>20</sup> Analogous testing of the AAF was conducted from March 28, 2008 to April 1, 2008 at the same facility. Both sessions were arranged under the aegis of Bernie Blake of the Aerospace Corporation. Along with author, the experimenters were Rocky Koga and Jeffrey S.

<sup>20</sup>Each year, the BASE facility conducts 1000–2000 hours of radiation effects testing and is constantly undergoing upgrades. The trends of such testing over the 40-year history of the 88-inch cyclotron as well as planned improvements to the BASE facility in the current decade are nicely summarized by McMahan [2005b]. Although the map of Figure I.1 is only current as of 2006, those areas germane to the tests reported here were essentially configured as depicted at the time of they were conducted.

George with The Aerospace Corporation and Michael B. Johnson with LBNL.<sup>21</sup> The goal of the testing was not only to confirm that the part maintains performance up to the stated specification of 100 krad(Si), but to determine the maximum survivable dose above which it ceases to properly function. For both DUTs, testing terminated when the device exhibited anomalous behavior.

At the 2 Mrad(Si) dose step of the 50-MeV  $H^+$  exposure, the LNA abruptly malfunctioned, exhibiting a sharp drop in supply current and railed outputs. As it was preceded by only minimal and gradual degradations of the measured performance, this unexpected result remains unexplained, pending further test to duplicate the failure signature on additional samples.

At the 500 krad(Si) dose step of the of the 30-MeV  $H^+$  exposure, the AAF outputs became erratic, repeatedly pegging to the rails despite only a slight decrease in the overall power dissipation. Lacking sufficient transparency with the pinout of Figure 6.2 to investigate the inner workings of the AAF, the causes for this behavior can only be theorized.

However, based on simulations indicating that similar behaviors attend circumstances in which the gain of the substrate pnps at the transconductor inputs falls below unity, it is surmised that the total-dose response of these devices is a culprit. As discussed in Section 2.1.2.1, substrate pnp geometries are known to exhibit  $\beta$ -degradation at relatively low doses (cf. Figure 2.15), due to the increased surface conduction associated with their high emitter perimeter-to-area ratios. Since their nominal  $\beta$  is less than four (cf. Section 3.2.1.3), there is little margin to accommodate such degradation should it proceed according to Figure 2.15 and drop over two octaves between 50 krad(Si) and 60 krad(Si). Section 7.3 provides suggested remedies on the basis of this working theory.

### I.2.1 Source

As opposed to  $\gamma$ -ray sources, the high-energy protons derived from particle accelerators or resonance sources accurately simulate both the expected ionizing and

---

<sup>21</sup>For the round of AAF testing, Kirk B. Crawford of The Aerospace Corporation accompanied this team.



displacement damage of the radiation-belt environment during ground tests.<sup>22</sup> In addition, via their activation stopping power,  $\mathcal{S}_a$  (cf. Equation (C.4)) they participate in inelastic nuclear interactions of the class described in Appendix C that can induce radioactivity in (i.e., ‘activate’) the materials within Cave 4A, especially the PCB and device package.<sup>23</sup> With at least 10 MeV required of the incident  $H^+$  for it to surmount the Coulomb barrier of a nuclear proton, interaction probabilities and, hence, the degree of activation, are proportional to particle energy and decline sharply as the beam energy is reduced from 50 MeV to 30 MeV. Thus, after initial exposures of the LNA were conducted at the former energy, AAF testing was performed at the latter in order to reduce the wait before entering the cave between dose steps and maximize the available characterization time.<sup>24</sup>

### I.2.1.1 Overview

Designated for light-ion nuclear reactions, the Light-Ion Irradiation Facility (LIIF) in Cave 4A of the BASE center receives a 20-cm diameter beam<sup>25</sup> of 1–55 MeV protons<sup>26</sup> at fluxes up to  $10^{10}$  protons/cm<sup>2</sup>/s from the 88-inch cyclotron at LBNL [*Johnson et al.*, 2006; *McMahan*, 1999, p.145-146, p.183]. Upon entering the cave, the beam passes through a series of elements responsible for its uniformity and dosimetry; an example of the instrument sequence is depicted Figure I.2.

<sup>22</sup>In this context, ‘high-energy’ describes beam energies between 1–50 MeV, since proton penetration depth in silicon is insufficient below this range while their damage efficiencies fall off as their LET drops above 20 MeV [*Holmes-Siedle and Adams*, 2002, p.447].

<sup>23</sup>Activation is the process by which protons interact with the nuclei of these targets, producing radioactive isotopes whose decay precludes immediate reentry into the cave.

<sup>24</sup>The duration of the overall testing also decreases at lower proton energies because cross-section for electronic stopping power,  $\sigma_{\text{stop,e}}$ , which is governed by interactions with electrons rather than nuclei (cf. Section C.1.2.1) is inversely proportional to particle energy. The resulting increase in LET when transitioning from 50-MeV to 30-MeV protons increases the dose rate for the same particle flux by approximately  $\sqrt{2}$ , reducing the time required to accumulate a given incremental dose in kind.

<sup>25</sup>Whereas the optics of Figure I.2 can focus the beam to a diameter of up to 15-cm upon incidence—limited by the diameter of the ionization chamber [*Johnson et al.*, 2006, p.183]—the beam line running from the cyclotron to the cave is 20 cm in diameter [*McMahan*, 1999, p.146].

<sup>26</sup>Protons are injected into the cyclotron from an electron cyclotron resonance (ECR) source that can produce a range of ions with extremely high energies and charge states. The proton energy range of the initial ECR at LBNL was 55 to 130 MeV, but as newer generations of ECR sources are installed the maximum energy continues to climb [*McMahan*, 1999, p.142].

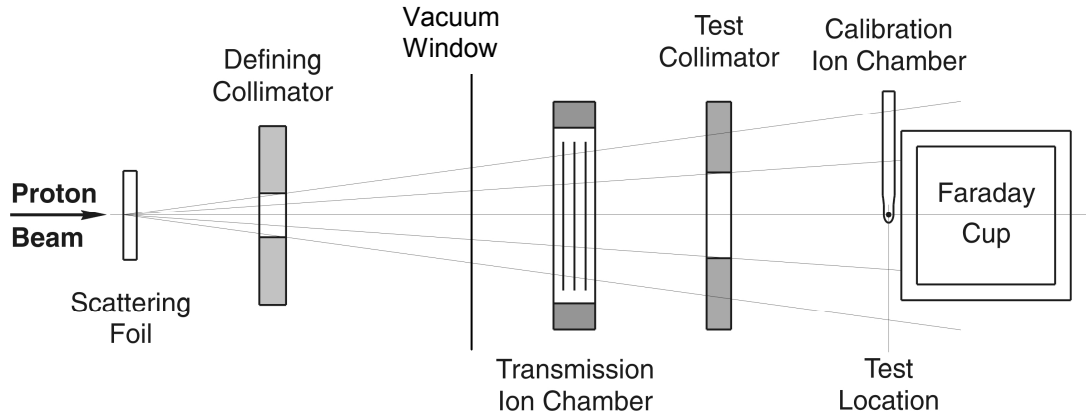


Figure I.2: Example of the equipment sequence at the beam line terminus in Cave 4A. The ion chamber and Faraday cup are only present during initial calibration. All elements to the right of the vacuum window reside in open air. Reproduced *in toto* from [McMahan *et al.*, 2008, p.135].

Whereas the scattering foil and defining collimator lie within the vacuum of the beam line, elements to the right of the vacuum window, including the test location for the DUT, are exposed in air [McMahan, 2005b, p.412]. The segmented, nitrogen-filled transmission ion chamber ensures beam uniformity to within  $\pm 5\%$  [McMahan, 1999, p.146] using flux measurements from seven concentric rings of various diameters (1, 2, 4, 6, 8, and 10 cm) [Johnson *et al.*, 2006, p.184]; when the beam is uniform, all rings see the same flux (normalized for area differences). For the experiments presented in this dissertation, a 1.25-inch thick aluminum plate serves as the test collimator, focusing the beam to a diameter of  $\sim 2.5$  inches at the DUT by means of a narrow aperture.<sup>27</sup>

<sup>27</sup>Standard focusing magnets produce an approximately Gaussian beam distribution. To obtain maximum uniformity, it is recommended that the final beam diameter be restricted to occupy the central 10% of this spatial distribution [McMahan *et al.*, 2008, p.137]; given the 20-inch beam line in Cave 4A (cf. Footnote 25), this rule guides the choice of a 2.5-inch aperture, though collimators with 5-, 7.5- and 10-cm diameters are also available [Johnson *et al.*, 2006, p.185]. Note also that the restrictor plate is carefully designed to limit well-known errors associated with slit scattering [McMahan *et al.*, 2008, p.139].

### I.2.1.2 Dosimetry

A LabView application running on the instrument control computer is responsible for the operation of the proton beam. To deliver a desired dose, it monitors the real-time flux through the transmission ion chamber and adjusts the duration of the exposure until a target fluence is achieved. Since the operator specifies the target fluence, rather than dose, it is necessary to convert the incremental dose at each step of the experiment plan into a corresponding proton fluence to be entered.

To do so, recall from (C.7a) that the total ionizing dose absorbed by a particular target is simply the integral of the mass stopping power of the incident particle (for that target material) over the incident fluence. Assuming as in Section C.1.2.1 that the LET of an incident proton can be equated with its unrestricted electronic mass stopping power,<sup>28</sup> this fundamental relationship between absorbed dose ( $D$ ) and fluence ( $\phi$ ) simplifies to

$$D = \int_{\phi} \mathcal{L}_e d\phi \quad (\text{I.4})$$

If it is further assumed that the particle LET is uniform over the thickness of the sample,<sup>29</sup> and that scattering is negligible, so that all particles pass directly through it, the integral of (I.4) reduces to a product of the surface LET and total fluence,<sup>30</sup>

$$D|_{\text{rad}} = \mathcal{L} \Big|_{\frac{\text{MeV-cm}^2}{\text{mg}}} \times \phi \Big|_{\frac{\text{protons}}{\text{cm}^2}} \times 1.602 \times 10^{-5} \Big|_{\frac{\text{rad-mg}}{\text{MeV}}} \quad (\text{I.5})$$

in which the trailing coefficient handles the dimensional analysis necessary to obtain dose in rads for LET specified in the traditional units [McMahan *et al.*, 2008, p.136].

---

<sup>28</sup>As explained in Footnote 10 of Appendix C, this assumption eliminates the locality restriction on the deposited energy and is equivalent to considering the energy associated with the production of all  $\delta$ -rays, not just those with energy less than a given cutoff.

<sup>29</sup>Although increasing in validity with device scaling, this assumption is a gross oversimplification. That the surface LET can be considerably lower than that deep within the sample is evident in the heavy-ion Bragg curves of Figure J.2. However, in order to replicate the calculations performed by the control software, the method of this section must adopt this equality for protons.

<sup>30</sup>Assumptions treating LET as constant and neglecting scattering amount to considering an infinitely thin sample. Although strictly true only for thin foils [Attix, 1986, p.188], the resulting independence of thickness in (I.5) holds to a good approximation for high-energy protons incident on modern silicon wafers. However, as described in Section J.2.1.2 such cavalier simplifications, to be at all valid, must be invoked with exceptional care in the case of heavier ions.

To arrive at the conversion factor of interest from (I.5), namely  $\eta = D/\phi$ , or

$$\eta \Big|_{\frac{\text{rad-cm}^2}{\text{proton}}} = \frac{D|_{\text{rad}}}{\phi|_{\frac{\text{protons}}{\text{cm}^2}}} = \mathcal{L} \Big|_{\frac{\text{MeV-cm}^2}{\text{mg}}} \times 1.602 \times 10^{-5} \Big|_{\frac{\text{rad-mg}}{\text{MeV}}} \quad (\text{I.6})$$

requires knowledge of the  $\text{H}^+$  surface LET.

For protons of known energy, simulations using the GEANT (GEometry AND Tracking) code [*Holmes-Siedle and Adams, 2002*, p.115] or, more commonly, the SRIM (Stopping Range of Ions in Matter) software package [*Ziegler et al., 2008*], yield a reasonable estimate of this quantity. However, such programs are sensitive to the particle energy at impact, especially at higher energies. As such, it is critical to account for any losses prior to the beam reaching the target. In particular, for the setup of Figure I.2 the impact energy of the beam line protons,  $E_{\text{imp}}$ , is reduced from their nominal energy,  $E_{\text{nom}}$ , due to losses from their passage through:

- The tantalum scattering foil used for magnification and uniformity
- The 5-mil thin-film kapton window of the transmission ion chamber
- The nitrogen within transmission ion chamber itself

according to<sup>31</sup>

$$E_{\text{imp}} = E_{\text{nom}} - \Delta E = E_{\text{nom}} - \Delta E_{\text{foil}} - \Delta E_{\text{window}} - \Delta E_{\text{chamber}} \quad (\text{I.7})$$

Invoking meticulous calibration of the loss terms—each of which is a function of energy—by operators of the BASE facility, (I.7) determines  $E_{\text{imp}}$  of the 30-MeV(50-MeV)  $\text{H}^+$  to be 29.278 MeV(49.518 MeV). Using these values along with the SRIM package, yields estimates of

$$\eta = \begin{cases} 2.363 \times 10^{-7} & , \quad \text{for } E_{\text{nom}} = 30 \text{ MeV} \\ 1.667 \times 10^{-7} & , \quad \text{for } E_{\text{nom}} = 50 \text{ MeV} \end{cases} \quad (\text{I.8})$$

---

<sup>31</sup>Of these contributors, the  $\Delta E_{\text{chamber}}$  tends to dominate, particularly for lower proton energies, where it degrades beam strength by as much as 33% [*McMahan, 2005b*, p.412].

in units of rads/proton/cm<sup>2</sup> that are valid to within the  $\pm 5\%$  accuracy of the SRIM fits.<sup>32</sup>

## I.2.2 Setup

The setup for proton beam irradiation using Cave 4A of the BASE facility is very similar to that of Section I.1.2. Critical distinctions are established in this section, particularly as pertains to alignment of the DUT, which must be precise enough to ensure uniform illumination by the narrow (2.5-inch-diameter) beam.

### I.2.2.1 Device-Under-Test

The DUT for these experiments is the SVEPRE-1 LNA, instance 2H. From an external +2.5-V supply, the part is biased to nominal operating conditions with  $G_p = 14$  dB using the on-chip reference generators. This setup is functionally equivalent to that of the <sup>60</sup>Co testing,<sup>33</sup> permit results comparison.

### I.2.2.2 Circuit Board

The same radiation bias PCB referenced in Section I.1.2.2 is used for proton testing as well, but without the need for enclosure within a Pb-Al box. Instead, the PCB is mounted vertically on a stage at the beam terminus using two C-clamps and aligned by means of a collinear laser focused from the direction opposite the beam (i.e., from the rear wall of the cave) onto the back of the PCB.<sup>34</sup>

---

<sup>32</sup>SRIM is a fit to a finite ensemble of previously measured data sets and, as such, its LET estimates are themselves only good to  $\pm 5\%$  [Ziegler *et al.*, 2008].

<sup>33</sup>The identical bench-top power supply used at The Aerospace Corporation was transported to LBNL along with the rest of the test equipment for characterization.

<sup>34</sup>For this purpose, the DUT was placed in into the central socket on the radiation bias PCB and the laser centered both horizontally and vertically on the thru-hole outline of the socket. Since this mounting strategy lacks a certain degree of robustness, the board is left in place throughout the testing, while the part is inserted and removed in a vertical orientation between dose steps. But, to ensure consistency, the alignment is re-checked with the laser before each illumination.

### I.2.3 Procedure

Prior to irradiation, the baseline performance of the DUT is characterized to ensure desired operation and the critical voltages and currents of both the characterization and radiation bias PCBs recorded.<sup>35</sup> Next, the DUT is exposed to  $H^+$  doses in a series of logarithmic dose steps. Although the exact dose is computed from the known fluence via the method of Section I.2.1.2), each step is assigned a convenient dose value for record keeping purposes; this is the dose that is referenced when identifying dose steps throughout the dissertation. Between steps, the DUT is carefully removed from radiation bias PCB (cf. Footnote 34) and transferred to the neighboring cave (Cave 4B) in which a makeshift laboratory is erected to house the test equipment.<sup>36</sup> Here, it is subject to characterization via the FR, LN, and PD test benches. Finally, at the conclusion of testing, the part is subject to an isothermal anneal after which and its performance is evaluated to assess the degree of recovery.

#### I.2.3.1 Irradiation Schedule

The LNA(AAF) was exposed to 50-MeV(30-MeV) protons in a series of logarithmic dose steps according to the schedule of Table I.3(Table I.4).<sup>37</sup> In both cases, testing terminated when the device exhibited anomalous behavior. Although data from the terminal  $H^+$  dose step for each DUT, being of little probative value, is omitted from the results of Section 6.4.2 and Section 6.4.2, the reported maximum dose exceeds that necessary to confirm performance to the specified level of 100 krad(Si) in both cases.

---

<sup>35</sup>Forgoing the pedagogy, these extensive but largely unremarkable tables are omitted here. It suffices to note that all bias conditions were deemed satisfactory.

<sup>36</sup>This transport is again conducted according to Sect. 3.9.2 of the Military Standard, using conductive foam to short the leads and minimize time-dependent effects.

<sup>37</sup>To reduce the exposure durations for the highest dose steps, Table I.3 indicates the manual enhancement of the dose rate prior to each of the 50 krad(Si), 100 krad(Si), and 200 krad(Si) dose steps for the 50-MeV testing; Table I.4 exhibits a similar rate increase prior to the 50 krad(Si) step for the 30-MeV testing. In both cases, low dose rates were adopted in the early stages of testing until it was confirmed that the part could survive moderate total dose. Later, in the interest of time, higher doses were accumulated more rapidly. Note that since the dose rate during each step does not fluctuate by more than  $\pm 10\%$ , even though the variation between steps is much larger, the dictums of the Military Standard remain satisfied (cf. Footnote 18).

### I.2.3.2 Annealing Schedule

A final round of characterization was performed following a 12-hour(70-hour) unbiased, room-temperature anneal at the conclusion of the 30-MeV(50-MeV) testing to assess the rate at which the LNA(AAF) recovered following the cessation of irradiation. The degree of recovery exhibited by these data is analyzed in [Section 6.4](#).

Run identification		Exposure	Total	Average	Dose	Incremental	Accumulated	Assigned
Date	ID	duration	fluence	flux	rate	dose	dose	dose
		[min]	[cm <sup>-2</sup> ]	[cm <sup>-2</sup> /s]	[rad(Si)/s]	[krad(Si)]	[krad(Si)]	[krad(Si)]
09 June 2006	A	0.00	0.00	0.00	0.00	0.00	0.00	Prerun
09 June 2006	B	3.27	6.24×10 <sup>9</sup>	3.18×10 <sup>7</sup>	5.31	1.04	1.04	1
09 June 2006	C	2.17	5.76×10 <sup>9</sup>	4.43×10 <sup>7</sup>	7.38	0.96	2.00	2
09 June 2006	D	6.87	1.80×10 <sup>10</sup>	4.37×10 <sup>7</sup>	7.28	3.00	5.00	5
09 June 2006	E	12.07	3.00×10 <sup>10</sup>	4.14×10 <sup>7</sup>	6.91	5.00	10.00	10
09 June 2006	F	23.38	6.00×10 <sup>10</sup>	4.28×10 <sup>7</sup>	7.14	10.02	20.02	20
09 June 2006	G	25.00	1.80×10 <sup>11</sup>	1.20×10 <sup>8</sup>	20.00	30.00	50.02	50
09 June 2006	H	5.32	3.00×10 <sup>11</sup>	9.40×10 <sup>8</sup>	156.76	50.01	100.03	100
09 June 2006	I	6.10	6.00×10 <sup>11</sup>	1.64×10 <sup>9</sup>	273.57	100.02	200.05	200
09 June 2006	J	18.35	1.80×10 <sup>12</sup>	1.63×10 <sup>9</sup>	272.56	300.08	500.13	500
09 June 2006	K	44.53	3.00×10 <sup>12</sup>	1.12×10 <sup>9</sup>	187.18	500.14	1000.27	1000
09 June 2006 <sup>a</sup>	L	60.32	6.00×10 <sup>12</sup>	1.66×10 <sup>9</sup>	276.32	1000.00	2000.27	2000
10 June 2006	M	710.72	0.00	0.00	0.00	0.00	n/a	Anneal

<sup>a</sup> Run L was initiated on 09 June 2006 and concluded on 10 June 2006

Table I.3: Irradiation schedule for total-dose testing of the SVEPRE-1 LNA using 50-MeV protons.



Date	Illumination			Total fluence [cm <sup>-2</sup> ]	Dose rate [rad(Si)/s]	Incremental dose [krad(Si)]	Accumulated dose [krad(Si)]	Assigned dose [krad(Si)]
	Start [24-hr]	End [24-hr]	Duration [sec]					
27 March 2008	19:30	20:30	3600	0.00	0.00	0.00	0.00	Prerun
27 March 2008	01:45	01:47	109	2.12×10 <sup>10</sup>	45.94	5.01	5.01	5
27 March 2008	02:58	03:00	90	2.12×10 <sup>10</sup>	55.58	5.00	10.01	10
27 March 2008	04:07	04:11	182	1.69×10 <sup>11</sup>	219.78	40.00	50.01	50
27 March 2008	05:22	05:36	230	2.12×10 <sup>11</sup>	217.57	50.04	100.05	100
27 March 2008	06:44	06:53	518	4.23×10 <sup>11</sup>	193.05	100.00	200.05	200
27 March 2008	08:14	08:24	588	4.23×10 <sup>11</sup>	170.07	100.00	300.05	300
27 March 2008	13:06	13:20	803	8.46×10 <sup>11</sup>	249.07	200.00	500.05	500
31 March 2008	15:01 <sup>a</sup>	13:28 <sup>a</sup>	2.54×10 <sup>5</sup>	0.00	0.00	0.00	n/a	Anneal

<sup>a</sup> Anneal start and end times reflect initiation on 27 March 2008 and conclusion on 31 March 2008

Table I.4: Irradiation schedule for total-dose testing of the SVEPRE-3 AAF using 30-MeV protons.



# Appendix J

## Single-Event Testing

This appendix summarizes the single-event testing of the SVEPRE-1 LNA and AAF via pulsed-laser and heavy-ion beam stimulations. For each source, it provides an introduction to the test facility and its capabilities, as well as a detailed description of the experiments conducted; such explanatory information is intended as an aide to the interpretation of the radiation results presented in Section 6.4.<sup>1</sup> Section J.1 describes experiments conducted at The Aerospace Corporation in El Segundo, CA using a 590-nm pulsed dye laser, whereas Section J.2 address the use of heavy ions generated by the 88-inch cyclotron at Lawrence Berkeley National Laboratory (LBNL) in Berkeley, CA.

### J.1 Pulsed-Laser Testing

SEE evaluations of the SVEPRE-1 ASIC using a picosecond-pulsed laser were performed at the headquarters of the Aerospace Corporation in El Segundo, CA on April 6–7, 2006. Along with author, the experimenters with The Aerospace Corporation were Stephen D. LaLumondiere, James L. Roeder, and Stephanie Brown. The goal of the testing was to diagnosis the SEE-sensitivity of the part prior to engaging the more comprehensive and costly resources of the heavy-ion beam at the

---

<sup>1</sup>For background on the underlying physics of radiation effects on microelectronic circuits, the reader is directed to Appendix C.

LBNL cyclotron (cf. Section J.2.1). On April 6, an initial round of manual scans using high beam energies attempted to induce single-event latchup (SEL)—the absence of which is a *sine qua non* for proceeding to further testing. In addition, regions of high sensitivity to single-event transients (SETs) were noted for further investigation the following day. Having observed no evidence of latchup, a series of SET scans were performed on April 7 in order to determine the most sensitive regions of the die and identify the critical factors, both intrinsic and extrinsic, dictating parameters such as transient amplitude, upset, and recovery time.

### J.1.1 Source

Illuminating silicon ICs with a picosecond-pulsed laser in order to provide a preliminary assessment of SEE vulnerabilities is a well-known method [*Buchner et al.*, 1990; *Koga et al.*, 1993]. Much of its popularity stems from its low cost and convenience when contrasted with particle accelerators, such as that of Section J.2.1; it only requires standard optical laboratory equipment and the instrumentation (along with the experimenters) can be immediately adjacent to the test fixtures [*Moss et al.*, 1995, p.1948].<sup>2</sup> Furthermore, it provides experimenters with the ability to interactively stimulate selected portions of the die, synchronize the upsets with circuit operation, and correlate the resulting performance with the circuitry in these locations so as to directly evaluate the effectiveness of RHBD techniques [*Moss et al.*, 1995, p.1948]; such controlled experiments over focused areas are not possible with ion sources [*Buchner and McMorow*, 2005, p.19]. Indeed, for the investigative aims of this research, such specificity renders the pulsed-laser a critical tool in evaluating the proposed RHBD techniques.

#### J.1.1.1 Theory

Charge generation in semiconductors via laser stimulation occurs when electrons are promoted from the valence to conduction band via photon absorption [*Buchner and*

---

<sup>2</sup>Not to mention the inventory economy achieved since the lack of accumulated ionizing and displacement damage allows the same samples to be subjected to total-dose testing [*Moss et al.*, 1995, p.1948].

[*McMorrow*, 2005, p.31]. When the photon energy is greater(less) than the silicon bandgap, the dominate mechanism, in which one(two) photons are absorbed per  $e^- - h^+$  pair generated, exhibits linear(nonlinear) dependence on intensity [*Buchner and McMorrow*, 2005, p.31].<sup>3</sup> Single-photon absorption obeys Beer's law (cf. Equation (C.2)), in which the beam intensity depends exponentially on depth. Laterally, the width of the beam profile spreads as it penetrates due to the refractive index of silicon [*Melinger et al.*, 1994, p.2575].<sup>4</sup> For two-photon absorption, the rate of carrier generation depends quadratically, rather than linearly, on intensity. Thus, even though both photons have energies smaller than the bandgap of the semiconductor, and thus pass through un-attenuated, if the beam is tuned to narrow pulse width ( $\sim 100$  fs) and spot size ( $\sim 1 \mu\text{m}$ ) the increased irradiance at the focus is sufficient for the pair to be absorbed, generating an  $e^- - h^+$  pair [*Buchner and McMorrow*, 2005, p.37].

In exchange for the diagnostic advantages provided by its spatial and temporal resolution [*Buchner and McMorrow*, 2005, p.28], the pulsed-laser technique suffers from limitations that preclude it from serving as the sole arbiter of SEE hardness. The most often cited disadvantage is the inability of the laser to penetrate the substrate beneath regions covered by metalization [*Melinger et al.*, 1994, p.2582]. However, this issue is most detrimental for the high-density, regularized layouts of digital circuits;<sup>5</sup> analog layout typically contains large regions of exposed substrate since metalization interferes with device matching [*Buchner and McMorrow*, 2005, p.34].<sup>6</sup>

---

<sup>3</sup>To be certain which of these effects is at work, it is not advisable to perform testing with a laser whose wavelength—which is inversely proportional to energy—is very near the Si bandgap [*Melinger et al.*, 1994, p.2577].

<sup>4</sup>The width of the beam is defined by twice the radial distance at which its intensity drops to half of its peak value: the full-width, half-maximum (FWHM) value. Typically, the radial intensity profile normal to its direction of propagation is presumed to be Gaussian [*Melinger et al.*, 1994, p.2574].

<sup>5</sup>Yet, even for highly scaled CMOS technologies with dense metal coverage, simple layout techniques that permit accurate topside illumination have recently been validated [*Balasubramanian et al.*, 2008].

<sup>6</sup>In the absence of such opening above the critical regions, another solution to the impediment of metalization is illuminating the die from the backside using two-photon absorption [*McMorrow et al.*, 2002]. Combined with wafer thinning, the ability to ensure that charge generation only occurs at the focus allows this technique to still probe sensitive junctions near the Si-SiO<sub>2</sub> interface. Using operational amplifiers, it has been shown that topside and through-wafer illumination yield

A second concern is that the lower intensity and wider beam width of the penetrating laser result in a charge track shallower and less dense than that of a heavy ion, along the path of which the charge density is relatively constant [Melinger *et al.*, 1994, p.2576].<sup>7</sup> But, despite differences in the nature of the ion tracks and charge collection of laser illumination when compared to those of heavy-ion passage,<sup>8</sup> a high degree of correlation is repeatedly observed between ASETs generated by the two methods [Buchner *et al.*, 2004a, b] because only a few picoseconds after generation,<sup>9</sup> the spatial distributions of the two types evolve to become indistinguishable [Melinger *et al.*, 1994].<sup>10</sup>

Insofar as the 590-nm dye laser used in this work selects for single-photon absorption, and the SVEPRE layout is devoid of metal over the most sensitive transistors, and the time-constants of the VLF signal path are far shorter than those of charge redistribution along the ionizing tracks, the pulsed-laser technique stands as an expedient predictive tool for the heavy-ion susceptibility of the design in question.

### J.1.1.2 Overview

A schematic of the cavity-dumped, actively mode-locked, 590-nm dye laser housed at The Aerospace Corporation [Moss *et al.*, 1995, p.1950–1951] is depicted in Figure J.1. It begins with an actively mode-locked, frequency-doubled Nd:YAG diode-

---

indistinguishable transient pulses, even for unthinned wafers [McMorrow *et al.*, 2004].

<sup>7</sup>As described in Section C.2.1 and Section C.2.2, the density of the charge track governs the net yield from a given strike and, as described in Section 2.2, the eventual impact of that charge is determined by collection mechanisms that are also dependent on density.

<sup>8</sup>The differences in charge collection are not as pronounced as might be anticipated. Funneling has been shown to play a role both in laser and ion illuminations, though the funnel length of the former is somewhat shorter on account of its lower densities [Buchner *et al.*, 1988]. However, Auger recombination lifetimes are markedly on denser ion tracks [Melinger *et al.*, 1994, p.2580].

<sup>9</sup>Note that the time required for this evolution of the charge deposition must be shorter than the response time of the circuit for this equivalence to hold [Buchner and McMorrow, 2005, p.35].

<sup>10</sup>The degree of correlation between pulsed-laser and heavy-ion data has long been a source of contention. However, “it has been unequivocally demonstrated for the devices investigated to date that the ASET shapes generated by pulsed laser light are identical to those generated by heavy ions. The similarity of the pulse shapes suggests that the differences in the mechanisms responsible for free-carrier generation—Coulomb excitation for charged particles and light absorption for photons—are not important for the devices tested thus far” [Buchner and McMorrow, 2005, p.30].

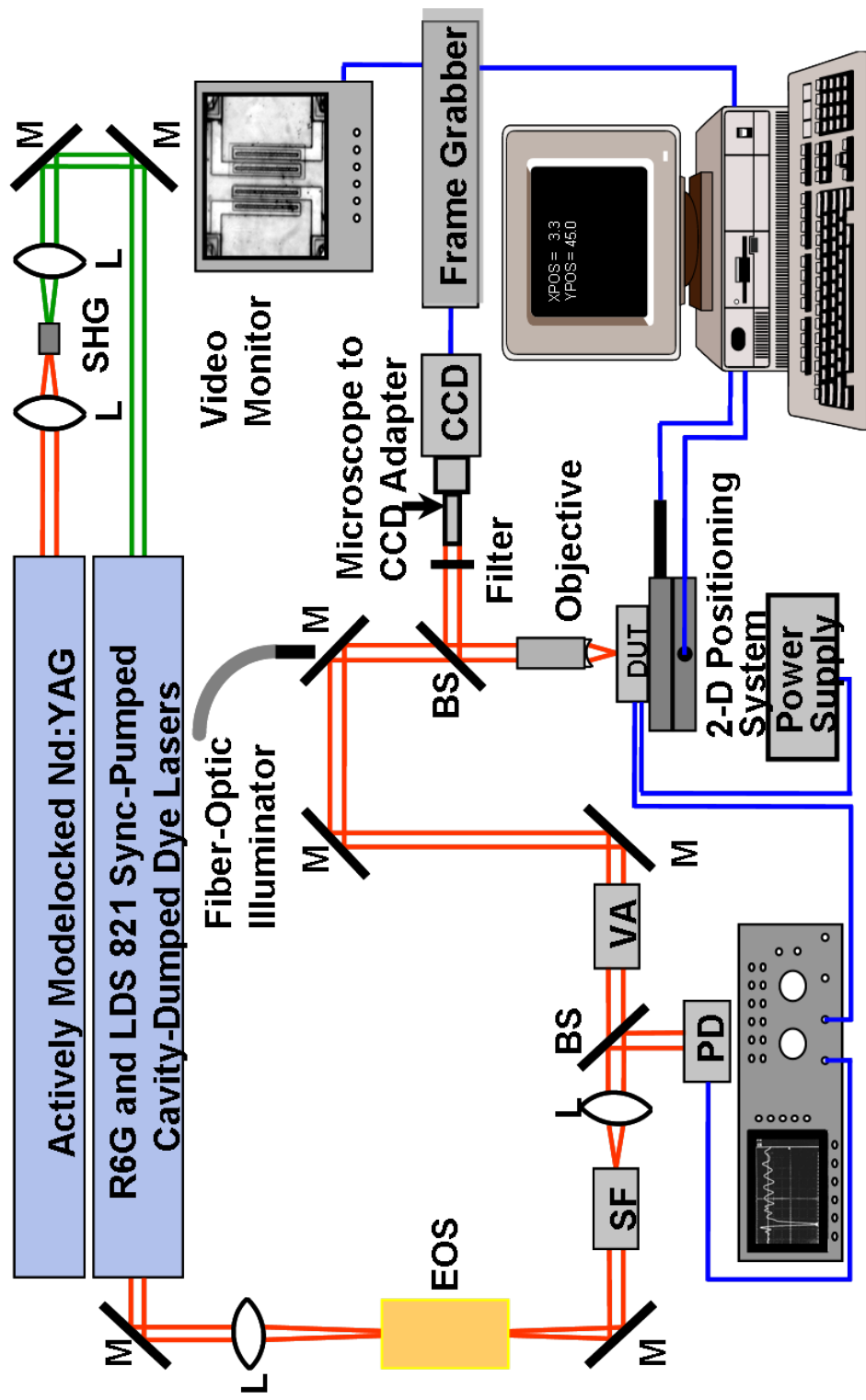


Figure J.1: Diagram of pulsed-laser apparatus at The Aerospace Corporation. Codes: BS—beam splitter; EOS—electro-optical shutter, M—mirror, PD—photodetector, SHG—optical second-harmonic generating crystal, VA—variable optical attenuator. Reproduced *in toto* from [Moss *et al.*, 1995, p.1851].

pumped solid-state (DPSS) laser,<sup>11</sup> which synchronously pumps the cavity-dumped Rhodamine 6G dye laser at 590 nm.<sup>12</sup> To achieve ultra-short pulses and minimize cavity losses while it circulates, this dye laser is cavity dumped by an optical switch that extracts 40 pJ/pulses with FWHM widths of 15 ps at a rate of 1 MHz. The beam ultimately delivered to the DUT is then gated by an electro-optical shutter with a much lower repetition rate (100 Hz), so that the presence(absence) of the pulse stream that is emitted(blocked) when it is open(closed) can be perceived by the operators.<sup>13</sup> The periscope through which the laser is focused incorporates a microscope with objectives from 50 $\times$ –100 $\times$  to support spot diameters from 1  $\mu$ m to 100  $\mu$ m. In addition to the laser light, the periscope also carries incoherent light reflected by the die back up through a dye laser mirror to a CCD imager coaligned with the laser itself so that the location of the latter can be precisely determined and recorded by frame-grabbing software.

A summary of the relevant parameters of the laser is provided in Table J.1. Note that the penetration depth at which the laser reaches  $1/e$  ( $\sim 37\%$ ) of its incident intensity is  $\sim 1.8$   $\mu$ m, which exceeds the diffused depths of the suspected critical junctions, even in a non-epitaxial 0.25- $\mu$ m technology.<sup>14</sup>

### J.1.1.3 Dosimetry

The initial beam energy as the laser leaves the optical cavity,  $E_o$ , is defined in terms of the nominal average power per pulse of the dye laser as measured just prior to the periscope ( $P_o$ ) and the rate at which the dye laser is being cavity-dumped via an

---

<sup>11</sup>To clarify: a solid-state gain medium Nd:YAG ( $\sim 1\%$  neodymium-doped yttrium aluminium garnet crystal) is pumped with a laser diode to produce an infrared transition at 1064 nm. An electro-optical AM modulator synchronizes that action with the cavity round-trip time to lock all the harmonics; such mode-locking permits the generation of picosecond pulse widths. The second harmonic (532 nm) is then obtained from a nonlinear crystal, thereby implementing the frequency-doubling.

<sup>12</sup>Again, a bit of exposition: The gain medium of this second laser, the organic dye Rhodamine 6G, has a wide bandwidth that can be easily tuned. Synchronizing it via pumping of the preceding laser mode-locks its wavelength to 590 nm.

<sup>13</sup>Also for operator convenience, the oscilloscope is automatically synchronized with the shutter because it triggers off a fast PIN diode that is illuminated (via a beam splitter) when the shutter opens.

<sup>14</sup>The remainder of the parameters in Table J.1 are explained in Section J.1.1.3.



Symbol	Property	Value	Units	Notes
<i>Optical fundamentals</i>				
$\lambda$	Wavelength	590	nm	Frequency-doubled Nd:YAG DPSS
$D$	Penetration depth	$\sim 1.8$	$\mu\text{m}$	$1/e$ depth in silicon
<i>Pulse generation</i>				
$t_p$	Pulse width	15	ps	Full-width, half-maximum
$f_w$	Pulse rate	1	MHz	R6G cavity dump rate
$f_R$	Repetition rate	100	Hz	Electro-optical shutter rate
$P_o$	Average power	0.04	mW	Beam Energy: $E_o = P_o f_w$
<i>Optical losses</i>				
$T_{\text{peri}}$	Periscope transmittance	0.2325	W/W	Incl. loss of CCD beam-splitter
$T_{\text{obj}}$	Objective transmittance	0.85/0.9	W/W	For 50 $\times$ objective
$R_{\text{Si}}$	SVEPRE surface reflectivity	0.65	W/W	$T_{\text{Si}} = 1 - R_{\text{Si}}$
$A_x$	Absorbance of ND filters	0.04–1.5	neper	Adjusted separately for $x = 1, 2, 3, 4$
<i>Magnification</i>				
M	Objective magnification	20 $\times$		Overall magnification: 200 $\times$
		50 $\times$		Overall magnification: 500 $\times$
$d_o$	Spot diameter	$\sim 30$	$\mu\text{m}$	For 20 $\times$ objective
		$\sim 1.2$	$\mu\text{m}$	For 50 $\times$ objective

Table J.1: Key parameters of pulsed dye laser setup at The Aerospace Corporation needed to determine the energy/pulse and equivalent LET. A detailed account of the various quantities can be found in Section J.1.1.3.

electro-optical switch ( $f_W$ ) as:

$$E_o = \frac{P_o}{f_W} \quad (\text{J.1})$$

This expression merely reflects the fact that, every time the cavity is dumped, all the beam power accumulated during the preceding regeneration phase is released. Hence, ignoring the width of the pulse itself, the entire time between pulses is used to accumulate laser power for the next pulse, yielding the energy of that pulse when multiplied by the average power of the beam.

To adjust the power of the laser and hence the intensity of illumination at a given spot size, a set of four, adjustable, neutral density filters are placed in series with the laser path prior to the objective, implementing the VA block of Figure J.1. The overall absorbance, denoted  $A$ , is then determined by the sum of the optical densities, or absorbances, of these filters, each denoted  $A_x$  for  $x = 1, 2, 3, 4$  with the lowest subscript indicating the filter closest to the objective. This absorbance is logarithmically related to the transmittance ( $T_A$ ), which is the ratio of the intensity of the transmitted beam,  $I$ , to that of the incident beam,  $I_o$ , by

$$T_A = \frac{I}{I_o} = 10^{-A} = 10^{-(A_1+A_2+A_3+A_4)} \quad (\text{J.2})$$

The neutral density filters are just one of several attenuating elements in the path of the beam. In addition:

- The transmittance  $T_{\text{peri}}$  accounts for loss through the periscope, including that of the beam splitter for the CCD.
- The transmittance  $T_{\text{obj}}$  of the  $50\times$  microscope objective accounts for focusing the spot size. This objective provides an overall magnification of  $500\times$  for the smallest spot sizes ( $\sim 2 \mu\text{m}$ ).
- The reflectivity of the silicon surface,  $R_{\text{Si}} = 1 - T_{\text{Si}}$  accounts for the light which does not penetrate the sample. Prior to testing, it is measured by replacing the CCD with a photodetector and comparing the light reflected by the DUT against that of a fully reflective phantom [*Moss et al.*, 1995, p.1951].

Thus, the net energy (in pJ) of each pulse as it penetrates the die surface,  $E_p$ , can be described by applying the various attenuations to the initial energy  $E_o$  such that<sup>15</sup>

$$E_p = E_o \times T_A \times T_{\text{peri}} \times T_{\text{obj}} \times T_{\text{Si}} \times 10^{12} \quad (\text{J.3})$$

To arrive at an estimate for the equivalent LET of the  $E_p$  in (J.3), the method of *Kim et al.* [1992, p.909] can be applied such that

$$\mathcal{L}_{\text{eqv}} \simeq 3E_p \quad (\text{J.4})$$

Although pulsed-laser results are best considered only in terms of relative, rather than absolute, LET [*Melinger et al.*, 1994, p.2582], this notion of ion-equivalent LET has been proffered in the literature on account of the strong correlations observed between the ASETs excited by pulsed lasers and heavy ions [*Buchner et al.*, 2004a; *Koga et al.*, 1993]. Thus, in this work, the approximation is only used to bound the limits of device performance: if effects are not observed at a particular beam energy, a quoted minimum  $\mathcal{L}_{\text{eqv}}$  for device robustness is established by applying a conservative derating factor to the result of (J.4).

## J.1.2 Setup

For SEE testing using the laser of Section J.1.1, a single instance of SVEPRE is operated under nominal conditions on the characterization bias PCB during illumination with its lid removed. A brief review of the particulars of each step comprises the remainder of this section.

### J.1.2.1 Device-Under-Test

The DUT for these experiments is the SVEPRE-1 LNA, instance 2B. From an external +2.5-V supply, the part is biased to nominal operating conditions with  $G_p = 21$  dB

---

<sup>15</sup>Note that (J.3) assumes that the full beam spot penetrates the substrate and generates carriers; that is, no correction is made for the fact that only a fraction of the spot actually fits within the opening of any given underlying metalization pattern. Without such a correction, the calculated  $E_p$  is an overestimate.

using the on-chip reference generators.

### J.1.2.2 Circuit Board

To leverage the sub-micron precision of the laser, the characterization PCB is mounted onto a motorized 2-D translation stage (1-inch travel in each direction with  $\sim 1 \mu\text{m}$  accuracy) using a custom aluminum back-plate that mates the standoffs of the former to the screws of the latter. Note that use of the characterization PCB, rather than the radiation bias PCB, allows in-beam DUT operation to simulate mission conditions by providing the DUT with the input signal described in Table 6.7 while the DMM(oscilloscope) is monitored for any anomalous supply(output) waveforms.

## J.1.3 Procedure

Manual scans of the SVEPRE-1 die using the pulsed-laser of Section J.1.1 are distinguished by the character of the SEE under investigation according to the divisions of Section 6.2.5.

### J.1.3.1 SEL Scans

During SEL scans, the entire die is surveyed using a beam of maximum spot diameter ( $30 \mu\text{m}$ ) and energy ( $1.3 \text{ nJ/pulse}$ , corresponding to an equivalent LET in excess of  $1000 \text{ MeV-cm}^2/\text{mg}$ ). Although manual scanning cannot ensure complete coverage, the wider diameter permits the majority of the surface area to be examined using a serpentine trajectory that extends out to the edges of the die.<sup>16</sup>

### J.1.3.2 SET Scans

During SET scans, selected sections of the die are probed with the spot diameter reduced to  $\sim 1.2 \mu\text{m}$  and the beam intensity adjusted via the sequence of neutral

---

<sup>16</sup>ESD structures, which are known to be more vulnerable to latchup than core circuitry on account of the higher currents typically observed, are adjacent to each pad. Hence, scanning the periphery of the die was the highest priority in adjusting the pitch of the labyrinthine course of the SEL scan.

density filters described in Section J.1.1.2.<sup>17</sup>

The SET scans are further subdivided, being conducted in two stages. For a given die location, typically a critical transistor array, the initial illumination, known as a *threshold scan*, gradually increases the beam intensity at a narrow spot diameter until an ‘onset threshold’ is reached, at which point transients of sufficient amplitude are observable. Then, the beam intensity is augmented by  $3\times$ , constituting a *high-LET* scan whose impact on the transient amplitude and recovery time are noted. To identify the exact beam position in order to associate it with the corresponding waveform records, a bitmap image is obtained at the conclusion of the high-LET scan by means of the CCD imager focused through the laser objective.<sup>18</sup>

## J.2 Heavy-Ion Testing

Heavy-ion testing of the LNA was conducted on September 26–27, 2006 in Cave 4B of the Berkeley Accelerator Space Effects (BASE) facility associated with the 88-inch cyclotron at the Lawrence Berkeley National Laboratory (LBNL) in Berkeley, CA (cf. Figure I.1). Along with author, the experimenters were Charles C. Wang with Stanford University, and Rocky Koga, Jeffrey S. George, and Van T. Trans with The Aerospace Corporation. The goal of the testing was to validate intimations regarding the SEL and SET tolerance of the part obtained during pulsed-laser evaluations by exposing it to heavy ions representative of the expected orbital profile. A typical choice, the 10 MeV/nucleon cocktail reasonably approximates the plasmaspheric environment: the effects of passing ions with energies below this level (after discounting for any shielding) increases error rates by at most  $\sim 20\%$  [Tylka *et al.*, 1996, p.2762].<sup>19</sup> Species constituting the 10-MeV/nucleon cocktail at LBNL

---

<sup>17</sup>SET scans specifically target regions of the die devoid of metal fill, only training the center of the spot over exposed substrate so that the maximum beam energy is delivered to and generates charge near the collecting junctions.

<sup>18</sup>Recall from Section J.1.1.2 that this image comes courtesy of a dye laser mirror whose reflection about the vertical axis of the raw images is reversed during post-processing, and whose transmittance is taken into account when determining the fraction of the beam energy refracted through the objective in the  $T_{\text{peri}}$  term of (J.3).

<sup>19</sup>Ion with energies less than 10 MeV/nucleon (particular lighter species) violate the underpinnings of rate prediction models that assume constant LET when integrating over the chords of the sensitive

Species	Atomic properties				Effective LET		Range
	$Z$	$A$	Charge state	Energy	0°	60°	
	[#]	[AU]		[MeV]	[MeV-cm <sup>2</sup> /mg]		
B	5	11	+3	108.01	0.89	1.78	305.7
O	8	18	+5	183.47	2.19	4.38	226.4
Ne	10	22	+6	216.28	3.49	6.98	174.6
Si <sup>a</sup>	14	29	+8	291.77	6.09	12.19	141.7
Ar <sup>a</sup>	18	40	+11	400.00	9.74	19.48	130.1
V <sup>a</sup>	23	51	+14	508.27	14.59	29.18	113.4
Cu	29	65	+18	659.19	21.17	42.34	108.0
Kr	36	64	+24	906.45	30.23	60.46	113.1
Y <sup>a</sup>	39	89	+25	928.49	34.73	69.46	102.2
Ag	47	107	+29	1039.42	48.15	96.30	90.0
Xe	54	124	+34	1232.55	58.78	117.56	90.0

<sup>a</sup> Not present in the cocktail at time of reported testing; available upon special request

Table J.2: Properties of species in the 10-MeV/nucleon heavy ion cocktail at the LBNL 88-inch cyclotron. Total energy per ion and charge state are determined from atomic number ( $Z$ ) and mass number ( $A$ ) since the energy/nucleon and mass/charge ratio are approximately constant for a given cocktail. Effective LET given for both normal (0°) and oblique (60°) incidence; range applies to normal incidence. Reproduced from [*LBNL, Lawrence Berkeley National Laboratory, 2009*].

are summarized in Table J.2.

### J.2.1 Source

As opposed to protons, whose low LET favors secondary ionization, the increased mass of heavy ions trades range for higher LET and, thus, they cause direct as well as indirect ionization.<sup>20</sup> Since this combination renders them more effective at volume (cf. Footnote 83 of Chapter 6) since they may come to rest along the chord [*Tylka et al., 1996*, p.2762]. The interplay between the increased LET associated with the Bragg peak and these shorter penetration depths usually belies the presumption of constant LET.

<sup>20</sup>A more complete exposition of these mechanisms is available in Section C.2.1.2.

generating SEEs, heavy ions are preferred over protons for single event testing.<sup>21</sup> Thus, to ascertain the DUT response to a range of LETs, thereby generating cross-section curves as described in Section 2.2.2, the LBNL cyclotron is configured to emit selected heavy ions from the cocktail of Table J.2.<sup>22</sup>

A cocktail is simply a mixture of ions with nearly identical mass-to-charge ratios [McMahan, 1999, p.143];<sup>23</sup> the cyclotron then acts a mass spectrum analyzer to extract a desired component from the cocktail simply by tuning its RF frequency. Since the gyrofrequency of the ions orbiting within the cyclotron magnetic field is linearly and inversely proportional to their mass, á la (A.7), the cyclotron's mass resolution is a function of its RF frequency resolution: for the 88-inch cyclotron, the latter is 2 kHz, so the former is approximately 1/3000 [McMahan, 2005a, p.1].<sup>24,25</sup> The ability to rapidly adjust the RF tuning allows the cyclotron operators at LBNL to select a desired species (and, thus, LET) from the cocktail in about one minute [McMahan, 1999, p.143].

Spanning the range of LETs observed from naturally occurring radiation sources, including those of the cosmic rays (cf. Chapter 2), the heavy ions of the LBNL cocktails (as compared to laser pulses) provide a realistic simulation of the anticipated space environment [Koga, 1996, p.661–662].

---

<sup>21</sup>Motivated by expediency, this preference carries a caveat: devices that do not exhibit single-event errors below a particular heavy-ion LET may nevertheless be susceptible to the lower LETs of protons in environments wherein secondary ionization of the latter proves significant [Rasmussen, 1988, p.1531]. This complication is further highlighted in Footnote 32.

<sup>22</sup>Resulting from ongoing upgrades to the ion sources at LBNL, new cocktails are routinely available. The latest examples, featuring 16-MeV/nucleon and 4.5-MeV/nucleon, respectively, are described by McMahan *et al.* [2004] and Johnson *et al.* [2007].

<sup>23</sup>To produce this amalgamation, the ECR source described in Footnote 26 of Appendix I generates sufficiently high charge states for a large range of ion masses, which are then tuned out together [McMahan, 2005b, p.410].

<sup>24</sup>This resolution is sufficient to separate out most, though not all, of the ions of near-identical mass-to-charge ratio emanating from the ECR source [McMahan, 2005a, p.1].

<sup>25</sup>Similar arguments attend the benefits of its large diameter: since the circular path of ions within the cyclotron is long (200 to 300 turns) [Leitner-Wutte *et al.*, 2002], heavier ions, whose gyroradii are proportional to their masses via (A.8) can be accelerated.

### J.2.1.1 Overview

Designated for heavy-ion nuclear reactions, the Heavy-Ion Irradiation Facility (HIIF) in Cave 4B of the BASE center receives a beam containing heavy ions (from  $^4\text{He}$  through uranium) of varying mass and charge states from the 88-inch cyclotron at LBNL [*McMahan*, 2005b, p.409]. Given the large interaction cross-sections of these species, which are responsible for their high LET, the beam target is housed within a large<sup>26</sup> vacuum chamber that is pumped to down to  $\sim 0.1\text{-mTorr}$  to prevent attenuation and scattering.<sup>27</sup>

Inside the chamber, the circuit board—here, the characterization PCB of Appendix H—is mounted to a motorized, three-dimensional translation stage using a 4.25-inch-square set of screw holes. The computer-controlled stage can tilt the sample relative to the beam through angles from  $0^\circ$  to  $80^\circ$  in order to align it,<sup>28</sup> and/or increase the effective fluence by extending the length of ion paths through the substrate.<sup>29</sup> To communicate with the PCB once the chamber has been pumped down, the side wall is outfitted with four bulkhead connectors containing pass-throughs for BNC, SHV, and ribbon cables.<sup>30</sup>

Upstream of the vacuum chamber, the beam is calibrated, collimated, and controlled by an array of dosimeters, collimators, and shutters located within a diagnostic box [*McMahan*, 1999, p.146]. A diamond of quad photomultiplier tubes monitors the beam flux, reporting the value to the control PC so that the operator can manually regulate it over nine orders of magnitude using a series of attenuator

---

<sup>26</sup>With interior dimensions of 20-by-22-by-38 inches, the chamber is large enough to house not only circuit boards, but even entire systems [*McMahan*, 1999, p.144].

<sup>27</sup>The chamber is specially designed to reach such pressures in only a few minutes [*McMahan*, 1999, p.144]. Nevertheless, the scheduling penalty associated with repeated pressurizing and depressurizing the vacuum chamber is significant enough that experimental design ought minimize these occurrences.

<sup>28</sup>Remote alignment is facilitated by real-time images delivered to the control computer from a CCD imager inside the vacuum chamber that is trained on the stage.

<sup>29</sup>Given mechanical difficulties when the tilt approaches  $90^\circ$ , not to mention shadowing from taller components on the PCB, including the device socket, testing is predominantly restricted to angles below  $60^\circ$ . Hence, the choice of this incidence angle for computing the effective LETs of Table J.2.

<sup>30</sup>Connectors other than these defaults can be accommodated by installing alternate bulkhead plates into the flanges, so long as the total thickness of the cable bundle fits within the 5-inch inner-diameter of the of the flange hole.



grids at the ion source that are inserted/removed on command [Leitner-Wutte *et al.*, 2002]. For these experiments, the collimators are tuned to yield a beam diameter of  $\sim 3$  inches. Finally, the shutter position is governed by the main application on the control PC, whose interface allows the user to specify the duration of the exposure in terms of either the target fluence or elapsed time; the latter is preferred here.

### J.2.1.2 Dosimetry

Since early radiobiological studies demonstrated that, for particles of the same linear energy transfer (LET), “the spectrum of energy losses in primary collision is, to a good approximation, the same” [Neary, 1970], it has been common in the radiation effects community to employ the metric of LET in lieu of a full description of the SEE environment [Koga, 1996, p.662].

However, despite its utility, this simplification is fraught with latent assumptions. First, since it is commonly equated to the unrestricted, linear electronic stopping power, as noted in Section C.1.2.1, the oft-reported LET only measures the energy of the incident particle lost to Coulomb collisions; it does not necessarily account for the true fraction absorbed (ignoring, for example, recombination),<sup>31</sup> nor for the effects of non-local, secondary ionization (via, for example,  $\delta$ -rays),<sup>32</sup> nor for nuclear, activation, nor radiative stopping mechanisms [Koga, 1996, p.662].<sup>33</sup> Secondly, studies confirm that higher energy ions yield more efficient charge collection than lower energy ions of the same LET on account of their lower ion track densities [Stapor *et al.*, 1988, p.1588].<sup>34</sup> Lastly, single-event and total-dose responses can be mistakenly conflated without monitoring the accumulated dose in addition to the LET [Koga, 1996, p.668]. For these reasons, it is necessary to report not only the LET of heavy ions used during SEE testing, but also the ion species, the particle energies (or energy/nucleon, from

---

<sup>31</sup>Naturally, the absorbed energy is the more critical quantity for SEE hardness assurance. Thus, “the observation that energy loss and charge collection are not necessarily correlated highlights the inadequacy of LET as a measure for SEE studies” [Koga, 1996, p.665].

<sup>32</sup>Neglect of secondary ionization, whether in the form  $\delta$ -rays generated by heavy ions [Dicello *et al.*, 1991] or the baryons released as scattering or spallation products of low-LET protons [Nichols *et al.*, 1982] can produce dramatic inconsistencies.

<sup>33</sup>In particular, LET does not encompass the effects of displacement damage [Koga, 1996, p.661].

<sup>34</sup>The dependence of charge collection on ion track density is explicated more fully in Section 2.2.

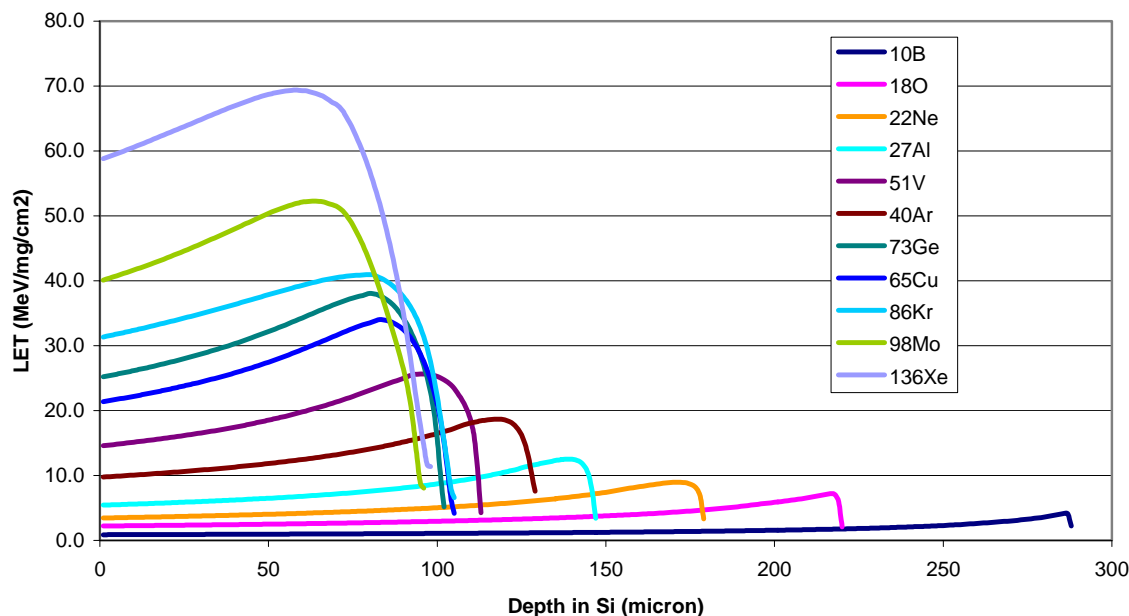


Figure J.2: Bragg curves for species in the 10-MeV/nucleon cocktail at the LBNL 88-inch cyclotron. Reproduced *in toto* from [McMahan, 2005a, p.5].

which they can be easily calculated), and the duration of the exposure.

Furthermore, additional care in the application of the LET concept is mandated by two potential pitfalls stemming from the capabilities of the BASE facility. First, though it is standard practice to assign each species an LET corresponding to its value at the surface of the target (i.e., the surface LET), the curves of LET-vs-depth for the 10-MeV/nucleon cocktail in Figure J.2 indicate substantial variation as ions penetrate into silicon. Known as Bragg curves, these examples exhibit a universally observed shape in which the LET reaches a maximum (the Bragg peak) as result of the increase in its interaction cross-section as the particle loses energy just before it abruptly comes to rest.<sup>35</sup> Given that the LET both increases and, more importantly, sharply plummets at a point defined by the particle range,<sup>36</sup> it is critical that the

<sup>35</sup>Although reporting the surface LET, as is convention, belies this variation *prima facie*, its existence is widely understood and implied *de facto*.

<sup>36</sup>A rigorous definition of range in the context of continuous stopping is provided in Footnote 6 of Appendix C. However, for heavy ions, which deflect minimally, there is little distinction between total path length and mean penetration depth, so the two may be considered equivalent in the context of this section and as pertains to the values of Table J.2.

elements of the cocktail be chosen such that the Bragg peak exceeds—preferably by a comfortable margin—the sensitive depths of the silicon die. Exhibiting ranges beyond 100  $\mu\text{m}$ , those of 10-MeV/nucleon cocktail satisfy this criterion for the integrated circuits in question.

Secondly, to increase the upset rate for a particular beam energy, the DUT translation stage can be tilted from a plane normal to the beam by an angle  $\theta$ , thereby increasing the path length of heavy ions traversing the thickness of the sample. Such geometry leads to the notion of an effective LET,  $\mathcal{L}_{\text{eff}}$ , scaled from that of the normally incident case,  $\mathcal{L}_{\perp}$ , by the increase in the length of the chord through the sensitive collection volume in the substrate as [*Petersen et al.*, 1992, p.1588]:

$$\mathcal{L}_{\text{eff}} = \mathcal{L}_{\perp} \sec(\theta) \quad (\text{J.5})$$

However, this simplistic interpretation makes two dubious assumptions; namely, that the particle LET is constant throughout the depth of the sensitive volume [*Koga*, 1996, p.666], and that this volume is sufficiently thin (relative to its areal dimensions) for geometric effects near its corners to be neglected [*Petersen et al.*, 1992, p.1588]. According the Bragg curves of Figure J.2, the former only holds for lighter ions passing through thin volumes; for heavier ions such as xenon, it is patently false even a few microns below the surface. Limitations based on the sensitive volume geometry, including its depth and whether it can be modeled as rectangular, are only surmounted if these quantities are known *a priori*.<sup>37</sup>

In light of these shortcomings, “the applicability of the effective LET concept is... somewhat limited for many advanced devices” and, so, is “generally inapplicable to the testing of high density microcircuits” [*Koga*, 1996, p.662] as in this work. Instead, as recommended by *Petersen et al.* [1992, p.1590], data is only obtained for

---

<sup>37</sup>However, with this knowledge, simple geometric corrections can be applied to (J.5) so as to avoid erroneously accounting for particle trajectories that only intercept the corners of the sensitive volume. In particular, the methodology proposed by [*Petersen et al.*, 1992, p.1588–1589] proves successful in correcting anomalies in published cross-section curves. But, since their methods have not been universally adopted, the authors recommend that “more credibility should be placed on measurements at normal incidence” [*Petersen et al.*, 1992, p.1590] and that angular dependence is best ascertained by tilting and then rotating the DUT in the plane of the stage.

heavy ions impinging orthogonal to the die surface.

## J.2.2 Setup

The setup for heavy-ion beam irradiation using Cave 4B of the BASE facility is somewhat more complicated than that of Section J.1.2 since the exposure is conducted inside a vacuum chamber. Although the configuration of the DUT and characterization board are functionally equivalent, the necessary modification to the instrument locations and connections, as well as the operation of the SEE test bench (cf. Section 6.2.5), are explained in this section.

### J.2.2.1 Device-Under-Test

The DUT for these experiments is the SVEPRE-1 LNA, instance 2G. The Agilent 6236B DC power supply of Figure 6.12(b) provides 10-V to the PWR block of the characterization PCB, which ensures that the bias and gain ( $G_p = 20$  dB) match those of Section J.1.2.1 as closely as possible, to permit results comparison.

### J.2.2.2 Circuit Board

As for the pulsed-laser, the setup for SEE testing with the heavy-ion beam delivered to Cave 4B of the LBNL facility (cf. Figure I.1) consists of mounting the characterization PCB on a motorized translation stage inside the vacuum chamber so that the DUT can both be operational during the exposure and aligned relative to the beam.

However, it is not uncommon for noise radiated by the stepper motors that control the location of the stage to corrupt the outputs of DUTs that contain sensitive analog circuits. Such is the case for the LNA, requiring the motors to be disabled and preventing vertical translation.<sup>38</sup> In order to align the DUT with the beam, the characterization PCB is instead affixed to the stage via a C-clamp and manually adjusted using a collinear laser observed on the CCD image of the DUT that is transmitted to the beam-control computer. Although a static arrangement

---

<sup>38</sup>Stepper motors cannot maintain torque without power, so the stage drops to the bottom of its track.

only permits normal incidence, thereby limiting the maximum effective LET, a configuration in which the beam trajectory is perpendicular to the plane of the die is preferred over oblique illumination since it eliminates the commonly overlooked ambiguities described in Section J.2.1.2.

### J.2.2.3 Instrumentation

Since the characterization board is placed inside the vacuum chamber (cf. Section J.2.1.1), it must be connected to the instrumentation of Figure 6.12(b) and Figure 6.12(a) via one of four bulkhead connectors that bridge the metallic chamber without breaching the integrity of its vacuum.<sup>39</sup> In addition, experimenters are precluded from the concrete cave housing the chamber, due to high levels of radiation contamination. Since the distance from the chamber bulkhead to the permissible location of the operator stations is approximately 30 feet,<sup>40</sup> the difficulties associated with driving sensitive signals through the bulkhead and down long cables [*Turflinger*, 1996, p.596] drive the partitioning of this instrumentation between the cave itself and the operator station as shown in Figure J.3.

Noteworthy in this configuration is the proximity of the DMMs and oscilloscope to the chamber (videlicet, on a nearby instrument cart), which minimizes the corruption or degradation of their signals otherwise observed over the 30 foot traverse. Since this distance exceeds the limitations of the GPIB interface, which recommends cables less than 4 m [*IEEE Std 488.1-2003*, 2003, Sect. 8.4.2], remote control of the DMMs is accomplished through a pair of National Instruments NI GPIB-140 optical extenders that convert then carry the signals from the SEL station to the bulkhead, and vice versa, over 200 feet of fiber pair (1 transmit, 1 receive). Lacking a GPIB interface, the oscilloscope is remotely commanded via a dedicated PC (SET station) with a PC running the custom Textronix eScope application and connected to the instrument in the cave by a 25-foot Cat6 crossover cable.

---

<sup>39</sup>For this testing, each bulkhead connector features 16 BNC pass-throughs, though only about ten are easily accessible.

<sup>40</sup>Cables running through the bulkhead(cable tray) from the DUT(instruments) inside(on) the vacuum chamber(instrument cart) to equipment on(at) the instrument cart(operator station) travel approximately 10(20) feet.

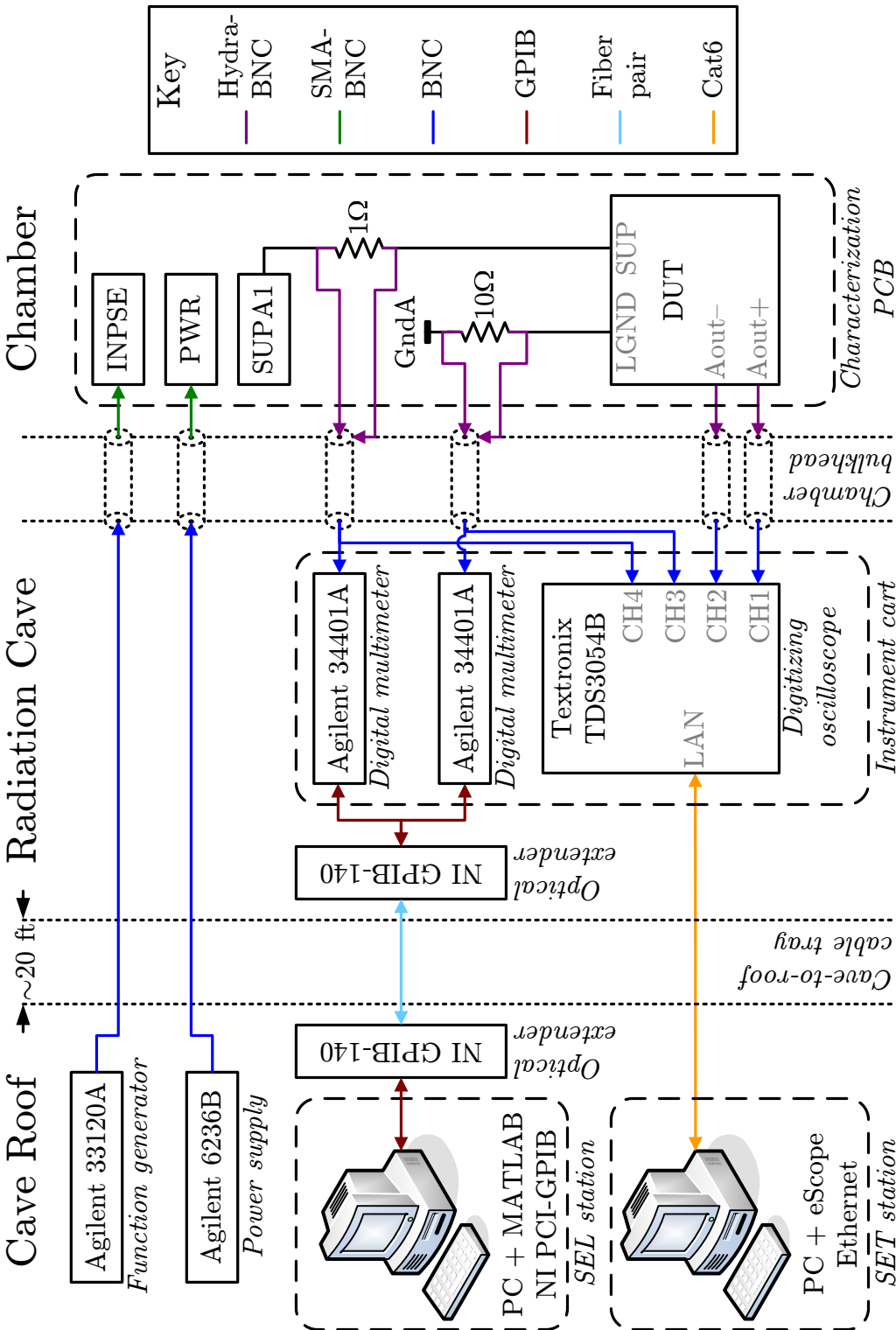


Figure J.3: Location of test equipment for heavy-ion SEE testing. Shields of all bulkhead pass-throughs carry universal ground unless otherwise indicated.

### J.2.3 Procedure

On the day of testing, the species in the 10 MeV/nucleon cocktail spanned an LET range of 3.45 MeV-cm<sup>2</sup>/mg (Neon) to 58.72 MeV-cm<sup>2</sup>/mg (Xenon) (cf. Table J.2).<sup>41</sup> During SET investigations, the DUT is illuminated with ions of progressively higher LET over both variable-length and fixed-interval durations. As explained in Section 6.2.5.3, the former permits synoptic recording of transient waveforms whereas the latter facilitates ‘upset’ counting to produce cross-section distributions.<sup>42</sup> The particular beam conditions during runs of each type are summarized below according to the continuous and discrete data sets obtained.

#### J.2.3.1 Waveform Runs

Table J.3 presents the irradiation schedules for the synoptic recording of representative waveforms when using a free-running beam and an input amplitude of either 30 mV<sub>PP</sub> or 60 mV<sub>PP</sub>. The number and duration of the runs for each species varies with the rate at which the operators were able to identify and download oscilloscope captures of illuminating ASET morphologies. The experiment IDs associate the waveform records with observations gleaned at the time of their acquisition. The beam conditions for the second class of waveforms, those obtained at the conclusion of each 300-s run, are encapsulated by the irradiation schedules for the discrete data sets described below.

#### J.2.3.2 Cross-Section Runs

In order to obtain ‘upset’ distributions for cross-section analyses, LET sweeps were repeated for each of the input signals enumerated in Table 6.7. For each pair of 300-s runs per species performed with a 10 kHz sinusoidal input tone at an effective input amplitude of 30 mV<sub>PP</sub>(60 mV<sub>PP</sub>), the beam conditions are provided in Table J.4(Table J.5). Similarly, the irradiation schedule for DC sweeps of both  $V_{\text{thresh}}$  polarities is summarized in Table J.6.

---

<sup>41</sup>A peculiar dearth of silver in the ion mix on the day of testing explains the reduced Ag fluence values in the irradiation schedules of this section.

<sup>42</sup>Continuous monitoring for SEL phenomena occurs throughout all runs.

Species	Surface LET [MeV-cm <sup>2</sup> /mg]	Illumination			Total fluence [cm <sup>-2</sup> ]	Average flux [cm <sup>-2</sup> /s]	Maximum flux [cm <sup>-2</sup> /s]	Input ampl. [mV <sub>PP</sub> ]	Records [#]
		Start [24-hr]	End [24-hr]	Duration [min]					
Ne	3.45	11:23	11:37	13.94	2.20×10 <sup>7</sup>	2.63×10 <sup>4</sup>	6.80×10 <sup>4</sup>	30	1
								60	2
Ar	9.74	11:38	11:50	11.69	2.69×10 <sup>7</sup>	3.84×10 <sup>4</sup>	1.25×10 <sup>5</sup>	30	3
								60	3
Cu	21.33	12:02	12:22	20.72	3.90×10 <sup>7</sup>	3.14×10 <sup>4</sup>	2.26×10 <sup>5</sup>	30	6
								60	5
Kr	31.28	12:54	13:39	45.15	1.37×10 <sup>8</sup>	5.05×10 <sup>4</sup>	2.16×10 <sup>5</sup>	30	5
								60	6
Ag	48.16	13:21	13:43	22.71	8.62×10 <sup>6</sup>	6.32×10 <sup>3</sup>	1.97×10 <sup>4</sup>	30	5
								60	5
Xe	58.72	13:51	14:09	17.85	3.53×10 <sup>7</sup>	3.30×10 <sup>4</sup>	8.50×10 <sup>4</sup>	30	5
								60	5

Table J.3: Irradiation schedule for waveform acquisition during single-event testing of the SVEPRE-1 LNA using 10-MeV/nucleon heavy ions. Each record represents a single waveform acquisition by the oscilloscope for either a 30 mV<sub>PP</sub> or 60 mV<sub>PP</sub> input sinusoid at 10 kHz.



Species	Surface LET [MeV-cm <sup>2</sup> /mg]	Illumination			Total fluence [cm <sup>-2</sup> ]	Average flux [cm <sup>-2</sup> /s]	Maximum flux [cm <sup>-2</sup> /s]
		Start [24-hr]	End [24-hr]	Duration [s]			
Ne	3.45	10:19	10:24	300.02	$7.39 \times 10^6$	$2.46 \times 10^4$	$6.70 \times 10^4$
		10:27	10:32	300.03	$7.63 \times 10^6$	$2.54 \times 10^4$	$7.12 \times 10^4$
Ar	9.74	06:24	06:29	300.04	$9.53 \times 10^6$	$3.18 \times 10^4$	$5.41 \times 10^4$
		06:34	06:39	300.02	$9.24 \times 10^6$	$3.08 \times 10^4$	$5.22 \times 10^4$
Cu	21.33	07:10	07:15	300.04	$1.30 \times 10^7$	$4.34 \times 10^4$	$2.76 \times 10^5$
		07:19	07:24	300.03	$9.18 \times 10^6$	$3.06 \times 10^4$	$7.80 \times 10^5$
Kr	31.28	07:56	08:01	300.04	$8.26 \times 10^6$	$2.75 \times 10^4$	$9.03 \times 10^4$
		08:05	08:10	300.02	$7.89 \times 10^6$	$2.63 \times 10^4$	$8.63 \times 10^4$
Ag	48.16	09:35	09:45	600.03	$5.34 \times 10^6$	$8.90 \times 10^3$	$3.08 \times 10^4$
		09:49	09:59	600.04	$5.36 \times 10^6$	$8.93 \times 10^3$	$2.82 \times 10^4$
Xe	58.72	08:34	08:39	300.03	$7.31 \times 10^6$	$2.43 \times 10^4$	$7.70 \times 10^4$
		08:42	08:47	300.03	$7.02 \times 10^6$	$2.34 \times 10^4$	$8.02 \times 10^4$

Table J.4: Irradiation schedule for count acquisitions during single-event testing of the SVEPRE-1 LNA using 10-MeV/nucleon heavy ions. Input amplitude: 30 mV<sub>PP</sub>.

Species	Surface LET [MeV-cm <sup>2</sup> /mg]	Illumination			Total fluence [cm <sup>-2</sup> ]	Average flux [cm <sup>-2</sup> /s]	Maximum flux [cm <sup>-2</sup> /s]
		Start [24-hr]	End [24-hr]	Duration [s]			
Ne	3.45	10:00	10:05	300.03	$8.11 \times 10^6$	$2.70 \times 10^4$	$7.04 \times 10^4$
		10:11	10:16	300.04	$7.57 \times 10^6$	$2.52 \times 10^4$	$6.70 \times 10^4$
Ar	9.74	06:16	06:21	300.03	$9.81 \times 10^6$	$3.27 \times 10^4$	$7.89 \times 10^4$
		06:42	06:47	300.02	$1.01 \times 10^7$	$3.36 \times 10^4$	$1.37 \times 10^5$
Cu	21.33	06:52	06:57	300.04	$1.39 \times 10^7$	$4.63 \times 10^4$	$2.81 \times 10^5$
		07:01	07:06	300.04	$1.32 \times 10^7$	$4.41 \times 10^4$	$2.85 \times 10^5$
Kr	31.28	07:37	07:42	300.03	$9.29 \times 10^6$	$3.10 \times 10^4$	$8.55 \times 10^4$
		07:45	07:50	300.02	$8.90 \times 10^6$	$2.97 \times 10^4$	$6.88 \times 10^4$
Ag	48.16	09:04	09:14	600.04	$5.00 \times 10^6$	$8.34 \times 10^3$	$3.30 \times 10^4$
		09:19	09:29	600.03	$5.30 \times 10^6$	$8.84 \times 10^3$	$3.08 \times 10^4$
Xe	58.72	08:17	08:22	300.03	$7.40 \times 10^6$	$2.47 \times 10^4$	$7.41 \times 10^4$
		08:25	08:30	300.03	$7.46 \times 10^6$	$2.49 \times 10^4$	$7.44 \times 10^4$

Table J.5: Irradiation schedule for count acquisitions during single-event testing of the SVEPRE-1 LNA using 10-MeV/nucleon heavy ions. Input amplitude: 60 mV<sub>PP</sub>.

Species	Surface	Illumination			Total	Average	Maximum
	LET	Start	End	Duration	fluence	flux	flux
	[MeV-cm <sup>2</sup> /mg]	[24-hr]	[24-hr]	[s]	[cm <sup>-2</sup> ]	[cm <sup>-2</sup> /s]	[cm <sup>-2</sup> /s]
Trigger level: +30 mV							
Ne	3.45	15:07	15:12	300.04	8.58×10 <sup>6</sup>	2.86×10 <sup>4</sup>	7.67×10 <sup>4</sup>
Ar	9.74	14:49	14:54	300.03	6.08×10 <sup>6</sup>	2.03×10 <sup>4</sup>	4.19×10 <sup>4</sup>
Kr	31.28	14:28	14:33	300.04	1.43×10 <sup>7</sup>	4.75×10 <sup>4</sup>	1.75×10 <sup>5</sup>
Xe	58.72	14:09	14:14	300.03	8.33×10 <sup>6</sup>	2.78×10 <sup>4</sup>	8.52×10 <sup>4</sup>
Trigger level: −30 mV							
Ne	3.45	15:15	15:20	300.03	8.59×10 <sup>6</sup>	2.86×10 <sup>4</sup>	6.53×10 <sup>4</sup>
Ar	9.74	14:58	15:03	300.02	5.20×10 <sup>6</sup>	1.73×10 <sup>4</sup>	2.65×10 <sup>4</sup>
Kr	31.28	14:40	14:45	300.04	1.48×10 <sup>7</sup>	4.92×10 <sup>4</sup>	1.56×10 <sup>5</sup>
Xe	58.72	14:18	14:23	300.03	9.27×10 <sup>6</sup>	3.09×10 <sup>4</sup>	8.37×10 <sup>4</sup>

Table J.6: Irradiation schedule for count acquisitions during single-event testing of the SVEPRE-1 LNA using 10-MeV/nucleon heavy ions. A 0-V DC input is applied for both trigger polarities.

# Appendix K

## Burn-In Testing

This appendix summarizes the burn-in testing of the SVEPRE-3 front-end ASIC as part of qualification for flight opportunities. The goal of burn-in testing is to ensure the reliability of the flight components by subjecting a lot to prolonged thermal stress (hence, the designation ‘burn-in’). Since manufacturing tolerances dictate that the ensemble will exhibit a distribution of failure rates associated with time and stress,<sup>1</sup> it is important to identify those devices that fail far sooner (infant mortality) or far later (lifetime failure) than the lot average.<sup>2</sup> Through burn-in screening, instances that exhibit early failures are eliminated from the pool of flight-worthy parts, thereby improving confidence in the longevity of the flight instrument.

Burn-in testing was performed in June 2008 on a lot of 34 SVEPRE-3 die bonded in the 44-pin SOIC package described by Table 6.1 and serialized as noted in Section 6.1.1. The tests were conducted in accordance with Military Standard 883G, Method 1015.9, Class B [*MIL-STD-883G*, 2006, Method 1015.9]—referenced simply as the *Military Standard* in the remainder of this appendix—by lead experimenter Bob Bumala and engineers Clem Tiller, and Ken Holsworth and supervised by Jack Doolittle at the facilities of the Lockheed Martin Advanced Technology Center in Palo

---

<sup>1</sup>There may also exist “inherent defects [which] would be expected to result in infant mortality or early lifetime failures under use conditions” [*MIL-STD-883G*, 2006, Method 1015.9, Sect. 1].

<sup>2</sup>These outliers populate the edges of the temporal failure rate distribution, which typically resembles a classic ‘bathtub curve’ [*McCormick*, 1981, p.26]. The intention of burn-in is only to screen out parts at the low end of the curve; testing is not carried out long enough to engender fatigue or wear-out failures as this would disqualify too large a fraction of the lot.

Alto, CA.<sup>3</sup> All devices remained functional following a 160-hour burn-in at 125°C with a minimal spread of stress-induced performance variations.<sup>4</sup>

The experimental setup and test procedures for both the thermal portion of the testing and the device characterization are described in Section K.1 and Section K.2, respectively. Based on the results in Section K.3, which summarizes batch characterizations performed before and after burn-in, as well as performance criteria established in Section K.4, the elements of the lot are ranked by serial number. Ultimately, the top 15 devices are allocated to flight inventory.

## K.1 Setup

Along with the availability of an adequate thermal chamber and skilled operators, programmatic concerns dictated the use of a Lockheed Martin test environment distinct from that employed during the baseline and radiation testing. Although input from the author drove the majority of characterization setup described in Section K.1.2 to be functionally equivalent to its previous incarnations, details of chip operation within the thermal chamber merit the attention paid in Section K.1.1.

### K.1.1 Thermal

While in the thermal chamber, the lot of SVEPRE parts is biased under nominal operating conditions using the burn-in board described in Section 6.1.2.3.<sup>5</sup> Each lateral-force socket is supplied with power and reference voltages by means of a global on-board bus that is derived from a single HP6629A DC power supply operating at +2.5 V. At a local level, input and output terminations, reference current generation, programming voltages/resistances, supply decoupling, and fusing are performed by identical replicas of the socket-level circuitry depicted in Figure K.1.

---

<sup>3</sup>All experimenters are with Lockheed Martin Corporation.

<sup>4</sup> Characterization prior to burn-in identified two instances that were ‘dead-on arrival’—unable to pass the acceptance criteria for basic operation on account of their outputs being pinned to the rails. These parts (SN 019 and SN 021) were still subjected to the burn-in procedure but, without viable data to evaluate, are omitted from the subsequent discussion.

<sup>5</sup>Of the 50 available sockets, 16 lie fallow during this testing.

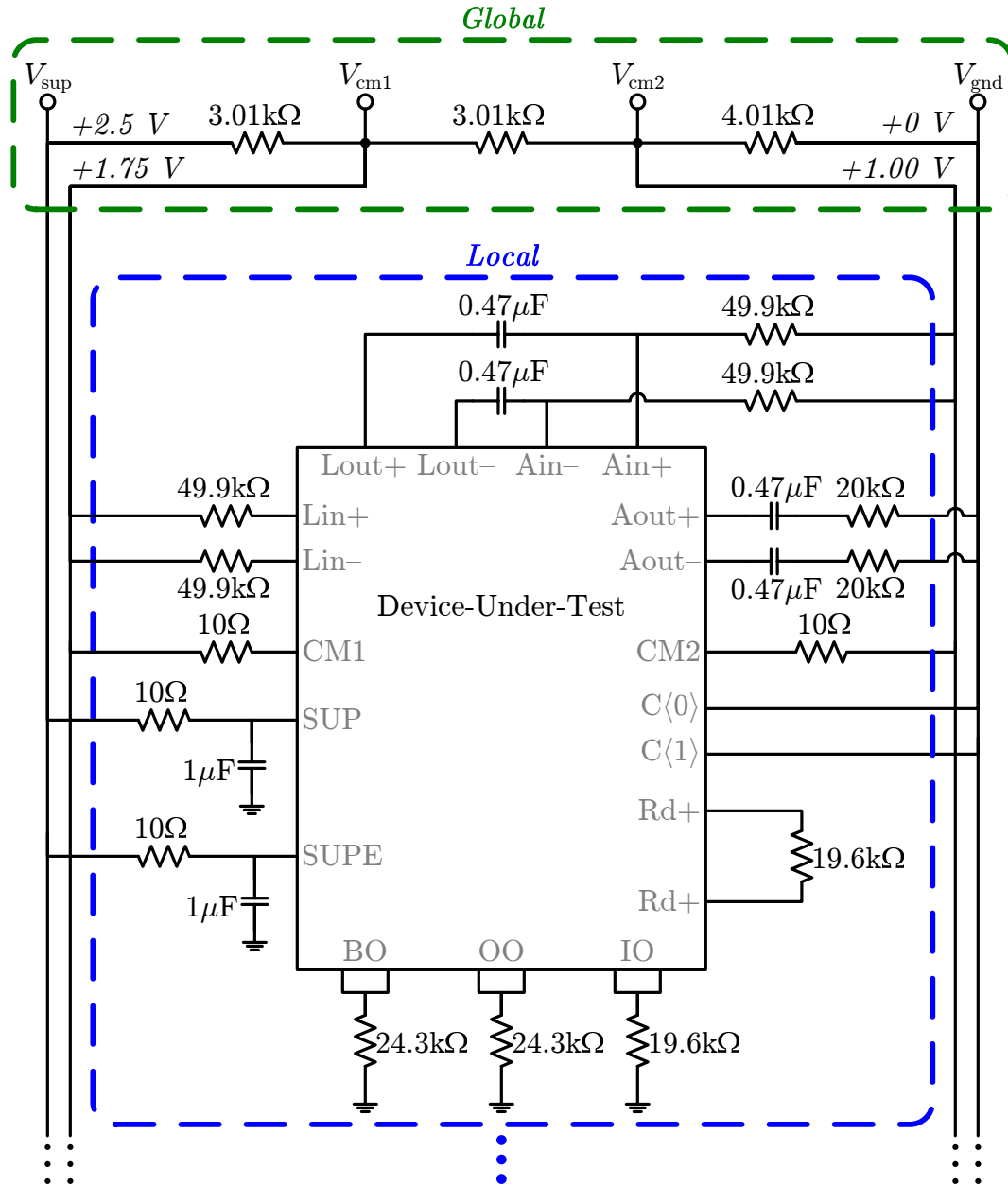


Figure K.1: Schematic of DUT bias configuration for burn-in PCB. Global reference and supply generation, derived from an HP6629A DC power supply (not pictured) is shown in **blue**. Local elements replicated at every socket (an example of which is shown in **green**) provide isolated yet identical biasing environments for each instance.

### K.1.2 Characterization

Before and after the thermal bake, each of the SVEPRE-3 parts is characterized using a modified version of the characterization PCB developed by engineers at Lockheed Martin.<sup>6</sup> During this performance evaluation, the part is biased by off-chip reference voltage and current generators and supplied with inputs by an SRS DS360 function generator. The output of the LNA, which is programmed to a nominal gain of  $G_p = 23$  dB, is AC-coupled to the input of the AAF, which is programmed to Mode A and trimmed to a nominal bandwidth of  $f_{pa} = 35$  kHz.<sup>7</sup> The AAF then feeds the ADC of Wang [2009],<sup>8</sup> which digitizes its outputs to provide all the measurements for the test benches described in Section K.2.<sup>9</sup>

## K.2 Procedure

Conforming to the precepts of the Military Standard for Class Level B, the entire lot is submitted to an uninterrupted, isothermal bake while actively biased [*MIL-STD-883G*, 2006, Method 1015.9, Sect. 3.1]. To assess functionality and performance, each DUT is characterized by modified versions of the FR, LN, and PD test benches before and after this stressor, with the latter occurring inside the prescribed interval following cooling.

---

<sup>6</sup>The modified PCB models a single-channel WBR with a signal path consisting from input to output of: antenna protection and balancing circuitry, first-stage pre-amplification, the SVEPRE-3 front-end, a gain-of-2 buffer, the ADC of Wang [2009], and a control FPGA.

<sup>7</sup>These parameters replicate the anticipated configuration of the plasma-wave WBR model (cf. Footnote 6), thereby imposing a variety of constraints. First, since the overall system gain exceeds  $G_p$  by 4 dB, the former is programmed to 23 dB when a nominal system gain of 27 dB is required. Secondly, since the dynamic range of the target system permits relaxed anti-aliasing, the AAF bandwidth is trimmed to exceed the nominal  $f_{pa}$  thereby widen its passband at the expense of  $A_{min}$ . Finally, to generate an output common-level compliant with the subsequent ADC buffer, the AAF input common-mode is reset by AC-coupling it to the LNA through a resistor ladder.

<sup>8</sup>A gain-of-2 amplifier is interposed between the two chips to counteract the presence of upstream attenuators in the signal path of the model WBR that determine the absolute dynamic range. Aligning the voltage ranges of the two ASICs in this fashion maximizes the performance of the ADC.

<sup>9</sup>Replacing the test equipment of Section 6.1.3 with an ADC is not a trivial matter. It incurs a variety of complications, corresponding solutions for which are presented in Section K.2.2.

### K.2.1 Thermal

Prior to population of the DUT sockets, the temperature of the VWR Scientific thermal chamber is calibrated whilst it is fully loaded with bias PCBs in their unpowered configuration [*MIL-STD-883G*, 2006, Method 1015.9, Sect. 3.1.1].<sup>10</sup> Instances which performed satisfactorily through pre-burn-in characterization (cf. Footnote 4) are then populated in the bias PCB and the pins of each the corresponding sockets probed to ensure delivery of the desired voltages and/or currents [*MIL-STD-883G*, 2006, Method 1015.9, Sect. 3.2.3b]. As per Section 3.2.3b,c of the Military Standard, this verification procedure is carried out again once the board reaches thermal equilibrium at the target temperature of 125°C (for a single socket) and yet again at the conclusion of the bake (for all sockets).<sup>11</sup> In between, the thermal test chamber maintains an internal temperature of 125°C for at least 160 hours. No accelerated burn-in or re-burn-in requirements were imposed.

### K.2.2 Characterization

As per Section 3.2 of the Military Standard, all instances are removed from the bias PCB, individually inserted into the characterization PCB, and measured using the FR, LN, and PD test benches within 96 hours after the removal of bias.<sup>12,13</sup>

---

<sup>10</sup>In addition to the lot of SVEPRE-3 chips, burn-in testing is simultaneously conducted for a lot of 23 of the ADCs designed by Wang [2009, p.447–463]. Thus the thermal chamber contains two bias PCBs during both calibration and operation.

<sup>11</sup>Once it is at temperature, the thermal chamber can be open for no longer than 10 minutes total during bias verification of both the front-end and ADC chips, so time is of the essence in the first case. Thus, only the critical bias voltages and currents, as well as the input and output signals of a single socket, are assessed at the outset of the bake.

<sup>12</sup>In order isolate the performance of the front-end, thereby ascertaining metrics that can be used to satisfy the acceptance criteria for this part, it is necessary that all other elements in the signal path of the modified WBR be held constant with respect to the various device instances. In particular, a single ADC is used to acquire all on the performance of the front-end. Since the batch of latter devices is being subjected to burn-in in parallel with the SVEPRE-3 parts, post-burn-in characterization must be performed on all the ADC devices, and a suitable sample chosen, prior to any post-burn-in testing of SVEPRE-3. Hence, after burn-in, the latter must remain under bias throughout the 96-hour window during which the former are being characterized.

<sup>13</sup>The removal of bias, rather than the return to thermal equilibrium, is used as the burn-in test condition from which this interval is measured. Since the latter occurred much earlier than the former on account of the delay described by Footnote 12, this choice safely satisfies the cool-down

Quantity	Symbol	Mode	Value	Units
LNA Gain	$G_p$	G0	23	dB
		G1	13	dB
		G2	3	dB
Input frequency	$f_o$	F0	100	Hz
		F1	1	kHz
		F2	10	kHz

Table K.1: Burn-in test vectors comprised of select gain and frequency modes. To complete characterization within the allotted time, the FR, PD, and LN test benches are only executed for LNA gain modes G0–G2; similarly, the input tones employed by LN test bench are limited to the fundamentals of frequency modes F0–F2.

Notably, the entire, fully differential front-end signal path is characterized in these experiments, rather than treating the LNA and AAF separately. For each test bench, a comprehensive evaluation is prohibited by this time limit, so an abbreviated range of operating conditions is judiciously examined. The acceptance criteria outlined in Section K.4 is then derived from these parochial measurements.

### K.2.2.1 Test Vectors

The prodigious set of possible amplitude and frequency ranges over which the pre- and post-burn-in performance of the SVEPRE-3 would otherwise be characterized is distilled down to the test vectors of Table K.1 in the interest of time.<sup>14</sup>

Gain modes G0–G2 describe the programmable gain steps of the LNA for which each of the test benches is executed. As Mode G0 is expected to be the worst-case, owing to its processing the largest signals through the front-end, only scalar metrics obtained in this mode are incorporated by the ranking rubric described in Section K.4.<sup>15</sup>

imposed by the Military Standard [*MIL-STD-883G*, 2006, Method 1015.9, Sect. 3.2.1].

<sup>14</sup>Should characterization of the 32 parts consume longer than 96 hours, the entire lot must be re-burned for an additional minimum of 24 hours [*MIL-STD-883G*, 2006, Method 1015.9, Sect. 3.2].

<sup>15</sup>Indeed, the scalar quantities necessary to compute the figure-of-merit described in Section K.4.1 are only extracted and recorded in Mode G0.



Gain mode	Frequency parameters				Amplitude parameters	
	Start [Hz]	Stop [kHz]	Step size [#/dec]	Total steps [#]	$V_{\text{in}}$ [mV <sub>PP</sub> ]	$V_{\text{out}}$ [mV <sub>PP</sub> ]
G0	30	60	10	30	56.57	799.05
G1	30	60	3	9	197.99	884.39
G2	30	60	3	9	565.69	799.05

Table K.2: Sweep parameters for FR test bench during burn-in testing. For reference, the mode-dependent amplitude values on SRS DS360 front panel are converted to differential equivalents at the input ( $V_{\text{in}}$ ) and output ( $V_{\text{out}}$ ) of the SVEPRE front-end using nominal gain values of all signal path components.

Frequency modes F0–F2 describe the fundamental frequencies of the input tones for which the linearity of the front-end is measured by the LN test bench. These sinusoidal signals, whose spectral purity is assured through the use of an SRS DS360 function generator (cf. Section 6.2.2.1), are distributed over the bandwidth of interest since acceptance limits can vary across this passband in conjunction with the scientific data sought.

### K.2.2.2 Frequency Response (FR)

For each of the gain modes identified in Table K.1, the frequency response of the entire signal path, including the front-end under test, is obtained by applying a single-tone sinusoid of fixed amplitude and varying its frequency over the bandwidth of interest using the SRS DS360 logarithmic sweep capability; the parameters of these sweeps are summarized in Table K.2. Assessing the output amplitude at each frequency step and computing its ratio against the input amplitude generates an approximation to a Bode magnitude plot of  $G(f)$  where, at each frequency tested:

$$G(f_o) = \frac{V_{\text{out}}(f_o)}{V_{\text{in}}(f_o)} \quad (\text{K.1})$$

To limit the duration of this portion of the characterization, the number of frequency steps varies with the gain mode. The result is a coarser sampling in

Gain mode	Total steps [#]	$V_{\text{in}}$		$V_{\text{out}}$	
		Start [mV <sub>PP</sub> ]	Stop [mV <sub>PP</sub> ]	Start [mV <sub>PP</sub> ]	Stop [V <sub>PP</sub> ]
G0	21	5.66	84.85	79.91	1.199
G1	23	19.80	265.87	88.44	1.188
G2	21	59.40	831.56	83.90	1.175

Table K.3: Sweep parameters for LN test bench during burn-in testing. For reference, the mode-dependent amplitude values on SRS DS360 front panel are converted to differential equivalents at the input ( $V_{\text{in}}$ ) and output ( $V_{\text{out}}$ ) of the SVEPRE front-end using nominal gain values of all signal path components.

frequency for modes G1 and G2, as evidenced by Table K.2. Note that the input amplitude varies inversely with the gain mode so as to maintain an approximately constant output amplitude: exercising the same decision levels of the ADC in each gain mode prevents its non-linear effects from introducing discrepancies in the data.

### K.2.2.3 Linearity (LN), Gain Compression

For each of the gain modes and fundamental frequencies identified in Table K.1, the gain compression of the entire signal path, including the front-end under test, is obtained by applying a single-tone sinusoid of fixed frequency and varying its amplitude over the signal range of interest. Table K.3 provides the parameters of this amplitude sweep for each gain mode.

Assessing the output amplitude at each input amplitude step and computing their ratio yields a measure of the gain as a function of input amplitude:

$$V_{\text{out}}(f_o) = G(V_{\text{in}}) V_{\text{in}}(f_o) \quad (\text{K.2})$$

In the ideal case, the coefficient of (K.2) would reduce to a constant  $G(V_{\text{in}}) = G$ , so that  $V_{\text{out}} \propto V_{\text{in}}$  and a plot of  $V_{\text{out}}$  against  $V_{\text{in}}$  would be a straight line with slope  $G$ . To assess the compression concomitant with the actual circuit, the degree of deviation from this ideal is determined by developing a first-order least-squares fit to

the  $V_{\text{out}}\text{-vs-}V_{\text{in}}$  curve above, yielding an estimate of the ideal  $V'_{\text{out}}$  given by:

$$V'_{\text{out}}(V_{\text{in}}) = G'V_{\text{in}} + g_o \quad (\text{K.3})$$

where unlike  $G$ ,  $G'$  is constant. Taking the percent difference between these two quantities at each input amplitude produces a series of so-called residuals described by

$$\rho(V_{\text{in}}) = \frac{V'_{\text{out}}(V_{\text{in}}) - V_{\text{out}}(V_{\text{in}})}{V_{\text{out}}(V_{\text{in}})} = \frac{(G' - G_o)V_{\text{in}} + g_o}{GV_{\text{in}}} \quad (\text{K.4})$$

To arrive at arrive at a single number that encapsulates the extent to which the actual gain is nonlinear for a particular set of the test vectors, the RMS average of the residuals over all  $K$  of the discrete input amplitudes defined in Table K.3 is dubbed the residue,  $R$ , and computed as:

$$R = \sqrt{\frac{1}{K} \sum_{k=1}^K \rho^2(V_{\text{in},k})} \quad (\text{K.5})$$

Again, it is critically important amplitudes scale inversely with the gain mode so to isolate the nonlinearities of the front-end from those of the ADC.

#### K.2.2.4 Linearity (LN), SFDR

Using the amplitude sweep parameters of Table K.3 for each combination of the gain and frequency vectors, the SFDR of the entire signal path, including the front-end under test, is also obtained. In contrast to Section 6.2.2.4, the underlying FFT consists of only  $2^{12}$  samples; with the ADC running at 100 kS/s, this equates to a bin width of  $\sim 24$  Hz.<sup>16</sup> As prescribed in (3.6) and (3.7), the peak SFDR over the amplitude sweep is used as the representative measure of harmonic distortion for each combination of test vectors.

---

<sup>16</sup>The SFDR is computed from a PSD spectral estimate based on a modified periodogram using a method similar to that of Section 6.2.2.4, but with two key differences are: no Welch-averaging is performed and the window length matches that of the data record (i.e.,  $N=L$ ).

### K.2.2.5 Power Dissipation (PD)

The power dissipation of  $V_{\text{sup}}$  and  $V_{\text{esup}}$  is measured using a voltmeter to measure the voltage drop across R1 in the circuit of Figure H.6. However, as only negligible power is consumed by the latter,  $P_{\text{sup}}$  is the measure of the total front-end power that best captures the effects of burn-in.

## K.3 Results

Invoking the metrics described in Section K.2.2, Table K.4 and Table K.5 summarize the performance of the DUTs, ordered by serial number (SN), when measured before and after burn-in, respectively. These tables report the departure from the nominal gain  $G_o$  of each mode in Table K.1 given by the gain error

$$G_{\text{err}} = G' - G_o \quad (\text{K.6})$$

rather than the absolute gain, since the ability to accurately set the gain of the device to a known value is more relevant to its utility than the absolute value of that gain. Indeed, this is in part why the G1 and G2 modes are omitted (cf. Section K.2.2.1). Furthermore, given the coarse sampling of the FR test bench, (K.6) derives  $G_{\text{err}}$  from  $G'$ —the slope of the regression obtained as part of compression measurements by the LN test bench—rather than the passband gain of the approximated Bode response.

## K.4 Analysis

Final ranking of the parts is predicted on the formulation of a novel figure-of-merit (FoM) that encapsulates the performance of a single instance relative to all the other members of the population. It is derived from the metrics described in Section K.2.2 and, like them, is computed both before and after burn-in. It should be emphasized that the FoM itself says nothing about the response of a given instance, or indeed a population thereof, to burn-in (or any other experimentally applied) stress. Rather, it is general way of assessing the performance of a single instance relative to all the others

in a population. In so doing, it measures the relative 'goodness' of a particular part against its peers and can, therefore, be used to rank the members of any population.

### K.4.1 Figure of Merit

For device  $x$ , the FoM at fundamental frequency  $f_o$  is defined as a weighted sum of the normalized versions of each of the metrics presented in Table K.4 and Table K.5, in linear units:<sup>17</sup>

$$\text{FoM}(x)|_{f_o} = W_P \frac{P(x)}{\overline{P}} \Big|_{f_o} + W_G \frac{G_{\text{err}}(x)}{\overline{G_{\text{err}}}} \Big|_{f_o} + W_R \frac{R(x)}{\overline{R}} \Big|_{f_o} + W_S \frac{\text{SFDR}(x)}{\overline{\text{SFDR}}} \Big|_{f_o} \quad (\text{K.7})$$

where the normalizing constants are their ensemble averages over the populations (indicated by overbars) and the nominal weighting factors (cf. Table K.6) are described in detail in Section K.4.1.1.

The lower the FoM of an instance, the better its relative performance, as this implies lower power dissipation, lower gain error, lower residual error to the linear fit, and higher SFDR. Enforcing the condition that the weighting factors sum to unity ensures that a device whose performance matches that of the ensemble average for each of the included metrics possesses an FoM of unity.

The FoM of a particular instance is computed for each of the frequency modes in Table K.1, since all of the underlying metrics, save power, depend on  $f_o$ . The ability to evaluate device performance at a particular fundamental independently from all others, is especially valuable if it is known that components in the signal path other than the front-end ASIC dominate its performance over particular bandwidths. However, it is also convenient to encapsulate the device's performance with a single scalar quantity by averaging the FoM over all  $M$  values of  $f_o$  such that

$$\text{AFoM}(x) = \frac{1}{M} \sum_{m=1}^M \text{FoM}(x)|_{f_{o,m}} \quad (\text{K.8})$$

Although more sophisticated weighting can be applied to this Aggregate Figure of

---

<sup>17</sup>Converting the gain error and SFDR from dB to linear units prior to the FoM computation ensures that all the ratio terms, and thus the FoM itself, are unitless.

SN	Power	Mode F0 (100 Hz)			Mode F1 (1 kHz)			Mode F2 (10 kHz)		
		$G_{\text{err}}$	Residue	SFDR	$G_{\text{err}}$	Residue	SFDR	$G_{\text{err}}$	Residue	SFDR
	[mW]	[dB]	[%]	[dB]	[dB]	[%]	[dB]	[dB]	[%]	[dB]
001	48.00	0.39	8.80	44.88	1.11	4.03	48.71	0.73	3.70	48.39
002	48.53	0.03	9.45	45.06	0.80	3.85	50.15	0.23	3.50	48.56
003	48.00	0.29	11.2	45.76	0.90	4.10	48.85	0.45	3.68	48.74
004	48.43	0.22	7.57	45.22	0.13	2.97	48.82	0.02	2.87	49.78
005	48.50	0.23	9.99	45.72	0.82	3.76	49.42	0.68	3.46	49.51
006	48.38	0.03	9.46	45.87	0.62	3.54	48.70	0.09	3.23	49.14
007	48.90	0.31	9.90	45.58	0.40	3.63	48.18	0.28	3.44	48.49
008	47.85	0.10	10.1	46.54	0.45	3.68	48.33	0.09	3.32	48.78
009	48.60	0.26	10.9	46.78	0.96	4.20	48.77	0.74	3.91	49.27
010	48.58	0.00	9.58	45.46	0.63	3.96	48.04	0.17	3.45	48.27
011	48.30	0.41	10.8	47.49	1.01	4.01	48.47	0.57	3.57	49.19
012	48.40	0.11	9.91	46.75	0.47	3.52	48.96	0.08	3.26	49.31
013	48.15	0.34	9.94	45.32	1.02	3.89	49.72	0.58	3.42	49.60
014	48.48	0.14	9.02	45.13	0.64	3.65	48.95	0.25	3.25	48.35
015	48.30	0.11	9.93	46.08	0.56	3.82	49.80	0.52	3.48	49.07
016	48.80	0.11	9.58	47.16	0.79	3.75	49.28	0.17	3.32	49.26
017	48.25	0.10	13.1	44.98	0.82	7.43	45.07	0.68	6.92	43.37
018	47.60	0.37	11.1	45.29	0.26	4.62	48.32	0.11	4.14	48.19
020	48.88	0.17	10.1	45.88	0.98	4.12	48.23	0.57	3.66	50.24
022	48.10	0.48	9.74	46.40	0.19	3.62	47.96	0.00	3.32	47.00
023	48.05	0.62	8.38	46.50	0.96	2.87	49.04	0.68	2.74	49.51
024	47.95	0.37	8.85	46.80	0.87	2.85	48.87	0.27	3.13	49.91
025	48.48	0.19	9.23	46.32	0.94	3.87	48.47	0.66	7.50	49.55
026	48.30	0.59	8.38	46.21	0.05	2.84	47.55	0.70	2.80	48.75
027	48.13	0.17	9.76	46.38	0.82	3.86	47.81	0.76	3.52	48.59
028	48.65	0.51	9.73	45.93	1.25	4.11	47.80	0.88	3.70	49.67
029	48.65	0.31	11.2	44.92	0.78	3.92	48.77	0.19	3.43	49.90
030	48.48	0.25	10.6	44.61	0.40	4.00	47.92	0.16	3.50	46.75
031	48.28	0.01	11.0	46.37	0.67	4.24	48.18	0.19	3.73	48.77
032	47.78	0.05	10.2	45.38	0.69	4.16	48.80	0.45	1.93	48.63
033	48.60	0.17	9.26	45.34	0.64	3.76	48.04	0.69	3.52	50.31
034	48.58	0.01	11.1	46.16	0.63	3.17	49.23	0.27	3.62	48.35
$\mu$	48.34	0.23	0.10	45.88	0.70	0.04	48.54	0.40	0.04	48.79
$\sigma$	0.32	0.17	0.01	0.72	0.29	0.01	0.88	0.27	0.01	1.27

Table K.4: Measured performance of SVEPRE lot before burn-in, ordered by DUT serial number (SN). Ensemble mean ( $\mu$ ) and standard deviation ( $\sigma$ ) computed below for each metric of Section K.2.2.

SN	Power	Mode F0 (100 Hz)			Mode F1 (1 kHz)			Mode F2 (10 kHz)		
		$G_{\text{err}}$	Residue	SFDR	$G_{\text{err}}$	Residue	SFDR	$G_{\text{err}}$	Residue	SFDR
	[mW]	[dB]	[%]	[dB]	[dB]	[%]	[dB]	[dB]	[%]	[dB]
001	48.13	0.35	9.93	45.13	1.07	4.12	47.68	0.72	3.86	48.47
002	48.53	0.26	10.6	46.32	0.82	3.72	48.66	0.25	3.34	49.82
003	47.98	0.19	9.82	45.51	0.95	4.05	48.52	0.47	3.62	49.68
004	48.55	0.49	9.45	45.62	0.13	3.23	48.62	0.01	3.03	49.49
005	48.48	0.08	9.63	46.10	0.80	3.80	48.17	0.65	3.43	48.88
006	48.30	0.15	8.95	45.08	0.58	3.47	48.43	0.05	3.19	48.61
007	48.90	0.44	9.41	45.13	0.38	3.61	47.60	0.23	3.31	48.57
008	47.75	0.18	8.07	46.58	0.45	3.20	49.46	0.08	3.07	49.89
009	48.58	0.38	11.4	46.51	0.98	4.23	49.22	0.76	3.86	47.84
010	48.80	0.18	10.5	45.01	0.55	4.27	48.00	0.21	3.90	47.89
011	48.33	0.29	10.0	45.58	1.06	4.23	48.52	0.63	3.87	48.27
012	48.40	0.31	9.10	47.12	0.45	3.59	48.28	0.09	3.40	49.28
013	48.15	0.30	11.0	45.95	0.86	4.03	49.19	0.53	3.51	50.32
014	48.48	0.09	9.48	45.10	0.61	3.72	47.76	0.24	3.30	48.35
015	48.30	0.22	9.47	45.82	0.58	3.74	49.38	0.53	3.43	49.13
016	48.80	0.15	10.0	46.75	0.80	3.76	48.25	0.18	3.32	48.12
017	48.25	0.10	12.3	45.18	0.87	6.97	46.43	0.72	6.46	43.43
018	47.63	0.68	9.42	45.88	0.24	4.64	47.52	0.13	4.16	48.52
020	48.88	0.19	10.2	46.19	0.98	4.16	48.34	0.60	3.71	50.04
022	48.08	0.52	9.70	45.21	0.20	3.71	47.50	0.00	3.14	47.05
023	48.25	0.27	11.6	45.40	0.90	4.18	48.26	0.63	3.87	48.26
024	48.08	0.00	10.1	46.43	0.83	4.17	48.35	0.23	3.71	49.77
025	48.53	0.17	10.7	45.33	0.92	4.31	48.54	0.64	3.99	48.43
026	48.33	0.72	9.92	45.42	0.04	3.55	48.69	0.75	3.01	48.51
027	48.15	0.05	9.91	46.40	0.83	4.20	48.57	0.77	3.88	48.77
028	48.68	0.47	11.0	44.51	1.23	4.37	48.75	0.87	3.92	50.61
029	48.63	0.23	11.5	46.18	0.81	3.98	48.08	0.17	3.55	50.53
030	48.50	0.63	11.1	44.43	0.37	3.91	48.27	0.12	3.59	47.54
031	48.28	0.01	10.2	46.59	0.79	4.38	47.82	0.20	3.94	48.54
032	47.80	0.02	10.4	45.86	0.70	4.08	48.22	0.48	2.20	49.08
033	48.60	0.05	11.0	45.96	0.61	3.90	47.30	0.41	6.19	49.49
034	48.60	0.12	10.9	45.22	0.62	3.90	48.77	0.27	3.47	49.81
$\mu$	48.36	0.26	0.10	45.73	0.69	0.04	48.29	0.39	0.04	48.78
$\sigma$	0.32	0.20	0.01	0.66	0.29	0.01	0.64	0.27	0.01	1.31

Table K.5: Measured performance of SVEPRE lot after burn-in, ordered by DUT serial number (SN). Ensemble mean ( $\mu$ ) and standard deviation ( $\sigma$ ) computed below for each metric of Section K.2.2.

Metric	Weight	Nominal value
Power	$W_P$	0.2
Gain error	$W_G$	0.4
Compression	$W_R$	0.3
SFDR	$W_S$	0.1

Table K.6: Weighting coefficients for figure-of-merit defined in (K.7), empirically chosen to favor those metrics with the widest variation and least measurement error.

Merit (AFoM), uniformity is preferred here.

#### K.4.1.1 Weighting

The nominal values of the weighting factors in (K.7), which are given in Table K.6, are chosen both to satisfy the normalizing condition and to reflect the importance placed on the relative performance of each device with regard to the corresponding metric.<sup>18</sup> Low-accuracy metrics (e.g., SFDR) receive lower weights since their sample-to-sample variation across the ensemble reflects stems largely from the noise of these measurements rather than actual device discrepancies.

Specifically, the smaller significance attached to the power metric ( $W_P$ ) reflects the fact that it hardly varies at all over the ensemble ( $< 1\%$ ), so its minor fluctuations are dominated by measurement error and, thus, not weighted heavily. Similarly, a low weighting is given to the SFDR metric ( $W_S$ ) because it is an inherently noisy measurement and, also, expresses little variation over the ensemble. In light of these factors, it is evident that performance in terms of gain and compression—metrics that benefit the dynamic range requirements of plasma wave receivers (cf. Section 3.1.2) and carry the least measurement error—dominate the overall FoM of a given instance

<sup>18</sup>Another means of weighting the individual terms in the FoM definition would be to determine the spread of each over the ensemble (defined, for example, as  $\sigma/\mu$ ) and normalize all terms in (K.7) to the spread of any single term so that, on average, each resulting quantity would contribute the same amount to the total. Then, an additional set of weights could be applied to these normalized terms, to formulate the desired relative impacts. However, given that terms with little spread are both insignificant to determining relative performance and likely to be dominated by measurement error, the proposed weighting method is superior to spread normalization in averting the undesired influence of such fluctuations on FoM.



with the selected weights of Table K.6.

### K.4.2 Ranking

Based on the aggregate FoM defined by (K.8), three different ranking schemes are proposed:

#### K.4.2.1 Delta Acceptance

The delta acceptance method merely determines at the difference (or *delta*) in the AFoM of each part before ( $\text{AFoM}_{\text{pre}}$ ) and after burn-in ( $\text{AFoM}_{\text{post}}$ ) and ranks those parts more highly whose delta is smallest. That is, it ranks each instance  $x$  according to the quantity  $\delta(x)$  where

$$\delta(x) = \text{AFoM}_{\text{post}}(x) - \text{AFoM}_{\text{pre}}(x) \quad (\text{K.9})$$

To foster intuition for the efficacy of this method, two assumptions are necessary. The first, which is justified by the data, is that the AFoM does not vary substantially across the ensemble.<sup>19</sup> Secondly, it is presumed that if two parts demonstrate the same percent change in performance, the part whose absolute performance is better should be favored.

Recall that the FoM defines ‘goodness’ relative to all the other instances in the ensemble. So, if a part possesses a lower(better) FoM before burn-in, the same percent increase in FoM after burn-in yields a smaller  $\delta(x)$  than for a part whose pre-burn-in FoM is higher. In other words, parts with a low  $\text{FoM}_{\text{pre}}$  are characterized by lower  $\delta(x)$  than those with a high  $\text{FoM}_{\text{pre}}$  for the same percent change in performance relative to the rest of the population. In this way, those parts with better absolute performance still rise to the top of the delta ranking system, as long as they do not experience larger-than-average percent degradation.

Additionally, the relative nature of the FoM must be considered in any such failure scenario. Namely, if a part with a low  $\text{FoM}_{\text{pre}}$  suffers from a large  $\delta(x)$ , then its

---

<sup>19</sup>If it does, remove the outliers from consideration to improve the tightness of the AFoM scatter.

performance has degraded more so than that of its peers as a result of burn-in. So, by definition, it is a less desirable than one whose position relative to its peers does not change with burn-in. Favoring the latter serves the purpose of burn-in characterization because those parts that are less robust to thermal stress than their peers filter to the bottom of the rankings.

#### K.4.2.2 Epsilon Acceptance

A simple modification to the delta method, epsilon acceptance merely determines the percent difference (or *epsilon*) in the AFoM of each part before and after burn-in rather than the absolute difference embodied in its  $\delta(x)$ . Again, it ranks those parts more highly whose epsilon is smallest. That is, it ranks each instance  $x$  according to the quantity  $\epsilon(x)$  where

$$\epsilon(x) = \frac{\text{AFoM}_{\text{post}}(x) - \text{AFoM}_{\text{pre}}(x)}{\text{AFoM}_{\text{pre}}(x)} = \frac{\delta(x)}{\text{AFoM}_{\text{pre}}(x)} \quad (\text{K.10})$$

Measuring only the relative variation in AFoM for each instance appears desirable, as it isolates the change as a result of burn-in stress from the absolute performance either before or after. But, eliminating dependence on absolute value permits a part with a high  $\text{AFoM}_{\text{post}}$  to rank ahead of one with a lower (and, hence better)  $\text{AFoM}_{\text{post}}$  simply because it underperformed the ensemble average almost exactly as much before burn-in as after.

#### K.4.2.3 Zeta Acceptance

Using zeta acceptance provides an explicit method of adjusting the importance of the absolute AFoM relative to the burn-in-related changes in the final ranking. To do so, it squares the percent difference in the AFoM of each part and adds it back to the  $\text{AFoM}_{\text{post}}$  resulting in a quantity dubbed  $\zeta$ . Again, it ranks those parts more highly whose zeta is smallest. That is, it ranks each instance  $x$  according to the quantity

$\zeta(x)$  where

$$\begin{aligned}\zeta(x) &= \alpha_1 \text{AFoM}_{\text{post}}(x) + \alpha_2 \left( \frac{\text{AFoM}_{\text{post}}(x) - \text{AFoM}_{\text{pre}}(x)}{\text{AFoM}_{\text{pre}}(x)} \right)^2 \\ &= \alpha_1 \text{AFoM}_{\text{post}}(x) + \alpha_2 \epsilon^2(x)\end{aligned}\tag{K.11}$$

Although delta acceptance accounts for both absolute and relative AFoM, the significance of these two factors cannot be adjusted; for a given percent change due to burn-in, there is no way to increase the importance of that discrepancy relative to the absolute FoM levels in the  $\delta(x)$  rankings. In contrast, the zeta rubric affords a straightforward means of separating these two types of measures and then recombining them into a final ranking with control of their weights,  $\alpha_1$  and  $\alpha_2$ .<sup>20</sup> If these coefficients are chosen such that, on average over the ensemble, the first and second terms of (K.11) are of equal size, absolute and relative variations are given equal prominence. For the SVEPRE-3 FoM data, this condition is achieved with  $\alpha_1=0.1$  and  $\alpha_2=7$ .

### K.4.3 Summary

For all frequency modes, Table K.7 provides the  $\text{FoM}_{\text{pre}}$  and  $\text{FoM}_{\text{post}}$  of each SVEPRE instance (identified by serial number, SN), as well as the delta, epsilon, and zeta rankings derived from the cumulative  $\text{AFoM}_{\text{pre}}$  and  $\text{AFoM}_{\text{post}}$ . The ordering corresponds to delta acceptance, with the lowest (read best) rankings at the top. Although delta acceptance is the method selected here, it is evident that the robust burn-in performance of SVEPRE-3 results in nearly identical rankings of the top 15 parts using all three systems.

---

<sup>20</sup>A word of caution: the  $\epsilon^2(x)$  term in (K.11) amplifies the effect of burn-in variations on the final ranking and compensation with only the (linear)  $A_2$  coefficient cannot completely neutralize this effect. Thus, the zeta method exhibits an inherent preference for those devices with minimal burn-in degradation at the expense of absolute performance.

SN	Mode F0 (100 Hz)		Mode F1 (1 kHz)		Mode F2 (10 kHz)		Rankings		
	FOM <sub>pre</sub>	FOM <sub>post</sub>	FOM <sub>pre</sub>	FOM <sub>post</sub>	FOM <sub>pre</sub>	FOM <sub>post</sub>	$\delta(x)$	$\epsilon(x)$	$\zeta(x)$
003	1.043	1.132	1.433	1.433	1.344	1.350	0.032	3.008	0.142
005	1.040	1.130	1.433	1.434	1.360	1.368	0.033	3.106	0.144
008	1.025	1.110	1.406	1.386	1.321	1.321	0.035	3.268	0.139
029	1.054	1.154	1.439	1.441	1.339	1.346	0.036	3.348	0.146
032	1.025	1.125	1.420	1.419	1.324	1.332	0.036	3.489	0.145
027	1.030	1.125	1.433	1.433	1.360	1.373	0.037	3.449	0.146
014	1.032	1.133	1.425	1.426	1.341	1.349	0.037	3.491	0.146
022	1.044	1.148	1.401	1.400	1.327	1.332	0.037	3.495	0.146
007	1.049	1.154	1.426	1.424	1.352	1.357	0.038	3.535	0.148
012	1.030	1.132	1.414	1.412	1.329	1.340	0.038	3.592	0.146
031	1.031	1.126	1.433	1.440	1.338	1.351	0.038	3.565	0.145
017	1.051	1.152	1.490	1.491	1.400	1.413	0.038	3.549	0.151
015	1.031	1.134	1.416	1.412	1.350	1.359	0.039	3.635	0.147
018	1.043	1.145	1.405	1.407	1.326	1.337	0.039	3.619	0.146
006	1.026	1.129	1.422	1.413	1.329	1.335	0.039	3.685	0.146
020	1.042	1.144	1.458	1.456	1.362	1.374	0.039	3.641	0.149
013	1.042	1.147	1.436	1.428	1.348	1.353	0.039	3.681	0.148
011	1.045	1.143	1.445	1.448	1.353	1.371	0.040	3.623	0.147
016	1.032	1.139	1.439	1.440	1.342	1.354	0.040	3.767	0.149
034	1.036	1.146	1.419	1.427	1.347	1.351	0.040	3.803	0.150
002	1.030	1.146	1.431	1.432	1.343	1.347	0.040	3.885	0.152
001	1.037	1.143	1.443	1.447	1.358	1.371	0.041	3.828	0.150
024	1.030	1.123	1.415	1.432	1.326	1.342	0.042	3.802	0.144
028	1.053	1.167	1.468	1.464	1.374	1.384	0.042	3.908	0.153
009	1.045	1.156	1.450	1.445	1.370	1.383	0.043	3.978	0.152
026	1.044	1.163	1.390	1.390	1.353	1.366	0.044	4.110	0.152
025	1.032	1.146	1.444	1.447	1.395	1.377	0.045	4.173	0.153
004	1.027	1.150	1.393	1.394	1.322	1.334	0.046	4.349	0.154
033	1.036	1.142	1.433	1.434	1.360	1.390	0.046	4.174	0.151
030	1.047	1.173	1.423	1.416	1.343	1.350	0.046	4.333	0.155
010	1.029	1.150	1.434	1.437	1.341	1.362	0.048	4.507	0.155
023	1.042	1.153	1.421	1.439	1.345	1.370	0.052	4.628	0.152
$\mu$	1.04	1.14	1.43	1.43	1.35	1.36	0.04	0.04	0.15
$\sigma$	0.01	0.01	0.02	0.02	0.02	0.02	0.00	0.00	0.00

Table K.7: Burn-in rankings of SVEPRE lot using delta acceptance method. Since FoM is relative to ensemble, its mean ( $\mu$ ) and standard deviation ( $\sigma$ ) vary minimally.

# Bibliography

- Abdelmoneum, M. A.; Demirci, M. M.; Li, S.; and Nguyen, C. T. C. “Post-fabrication laser trimming of micromechanical filters”. In *IEEE International Electron Devices Meeting, 2004. IEDM Technical Digest.*, pp. 39–42. IEEE, San Francisco, CA: IEEE Press, 13–14 December 2004. ISBN 0-7803-8684-1. doi:10.1109/IEDM.2004.1419058.
- Abo, A. M. and Gray, P. R. “A 1.5-V, 10-bit, 14.3-MS/s CMOS pipeline analog-to-digital converter”. *IEEE Journal of Solid-State Circuits*, vol. 34, no. 5, pp. 599–606, May 1999. doi:10.1109/4.760369.
- Acosta, L.; Jiménez, M.; Carvajal, R.; Lopez-Martin, A.; and Ramírez-Angulo, J. “Highly linear tunable CMOS  $G_m$ -C low-pass filter”. *IEEE Transactions on Circuits and Systems I: Regular Papers*, vol. 56, no. 10, pp. 2145–2158, October 2009. doi:10.1109/TCSI.2008.2012218.
- Adell, P.; Schrimpf, R. D.; Barnaby, H. J.; Marec, R.; Chatry, C.; Calvel, P.; Barillot, C.; and Mion, O. “Analysis of single-event transients in analog circuits”. *IEEE Transactions on Nuclear Science*, vol. 47, no. 6, pp. 2616–2623, December 2000. doi:10.1109/23.903817.
- Agilent Technologies, Incorporated. *Agilent 33120A 15 MHz Function/Arbitrary Waveform Generator*. Loveland, CO, 6 ed., March 2002.
- Alexander, D. R. “Design issues for radiation tolerant microcircuits for space”. In *1996 IEEE Nuclear and Space Radiation Effects Conference (NSREC) Short Course*, p. Sec. 5. Indian Wells, CA: IEEE NPSS, 15 July 1996.

- Ali, M. I.; Howe, M.; Sánchez-Sinencio, E.; and Ramírez-Angulo, J. “A BiCMOS low distortion tunable OTA for continuous-time filters”. *IEEE Transactions on Circuits and Systems I: Fundamental Theory and Applications*, vol. 40, no. 1, pp. 43–49, January 1993. doi:10.1109/81.215341.
- Analog Devices, Incorporated. *Careful Design Tames High Speed Opamps*. AN257 Application Note, Norwood, MA, 1993.
- . *14-Bit, 40 MSps/65 MSps A/D Converter*. AD6644 Data Sheet, Rev. C, Norwood, MA, May 2003.
- Analog Devices Incorporated. *Low-Distortion Differential ADC Driver*. AD8138 Data Sheet, Rev. F, Norwood, MA, May 2006.
- Anelli, G. *Design and Characterization of Radiation Tolerant Integrated Circuits in Deep Submicron CMOS Technologies for the LHC Experiments*. Ph.D. thesis, Institut National Polytechnique de Grenoble, Padova, Italy, 11 December 2000.
- Anelli, G.; Campbell, M.; Delmastro, M.; Faccio, F.; Floria, S.; Giraldo, A.; Heijne, E.; Jarron, P.; Kloukinas, K.; Marchioro, A.; Moreira, P.; and Snoeys, W. “Radiation tolerant VLSI circuits in standard deep submicron CMOS technologies for the LHC experiments: Practical design aspects”. *IEEE Transactions on Nuclear Science*, vol. 46, no. 6, pp. 1690–1696, December 1999. doi:10.1109/23.819140.
- Anelli, G.; Faccio, F.; Florian, S.; and Jarron, P. “Noise characterization of a 0.25  $\mu\text{m}$  CMOS technology for the LHC experiments”. *Nuclear Instruments and Methods in Physics Research Section A: Accelerators, Spectrometers, Detectors and Associated Equipment*, vol. 457, no. 1-2, pp. 361–368, January 2001. doi:10.1016/S0168-9002(00)00761-0.
- Angelopoulos, V. “The THEMIS mission”. *Space Science Reviews*, vol. 141, pp. 5–34, December 2008. doi:10.1007/s11214-008-9336-1.
- Attix, F. H. *Introduction to Radiological Physics and Radiation Dosimetry*. New York, NY: John Wiley & Sons, 1986. ISBN 0-47-101146-0.

- Ausman, Jr., G. A. and McLean, F. B. “Electron-hole pair creation energy in SiO<sub>2</sub>”. *Applied Physics Letters*, vol. 26, no. 4, pp. 173–175, February 1975. doi:10.1063/1.88104.
- Avant! Corporation. *Avant! Star-Hspice Manual*. Release 1998.2, Fremont, CA, July 1998.
- Azuma, S.; Kawama, S.; Iizuka, K.; Miyamoto, M.; and Senderowicz, D. “Embedded anti-aliasing in switched-capacitor ladder filters with variable gain and offset compensation”. *IEEE Journal of Solid-State Circuits*, vol. 37, no. 3, pp. 349–356, March 2002. doi:10.1109/4.987087.
- Babcock, J. A.; Loftin, B.; Madhani, P.; Xinfen Chen; Pinto, A.; and Schroder, D. K. “Comparative low frequency noise analysis of bipolar and MOS transistors using an advanced complementary BiCMOS technology”. In *IEEE 2001 Conference on Custom Integrated Circuits*, pp. 385–388. IEEE, San Diego, CA: IEEE Press, May 2001. ISBN 0-7803-6591-7. doi:10.1109/CICC.2001.929806.
- Balasubramanian, A.; McMorrow, D.; Nation, S. A.; Bhuva, B. L.; Reed, R. A.; Massengill, L. W.; Loveless, T. D.; Amusan, O. A.; Black, J. D.; Melinger, J. S.; Baze, M. P.; Ferlet-Cavrois, V.; Gaillardin, M.; and Schwank, J. R. “Pulsed laser single-event effects in highly scaled CMOS technologies in the presence of dense metal coverage”. *IEEE Transactions on Nuclear Science*, vol. 55, no. 6, pp. 3401–3406, December 2008. doi:10.1109/TNS.2008.2007295.
- Bale, S. D.; Ullrich, R.; Goetz, K.; Alster, N.; Cecconi, B.; Dekkali, M.; Lingner, N. R.; Macher, W.; Manning, R. E.; McCauley, J.; Monson, S. J.; Oswald, T. H.; and Pulupa, M. “The electric antennas for the STEREO/WAVES experiment”. *Space Science Reviews*, vol. 136, no. 1–4, pp. 529–547, April 2008. doi:10.1007/s11214-007-9251-x.
- Balmain, K. G. “The impedance of a short dipole antenna in a magnetoplasma”. *IEEE Transactions on Antennas and Propagation*, vol. 12, no. 5, pp. 605–617, September 1964.

- . “Impedance of a short dipole in a compressible plasma”. *Journal of research, National Bureau of Standards. Section D, Radio Science*, vol. 69D, no. 4, pp. 559–566, April 1965.
- . “Antennas in plasma: Characteristics as functions of frequency”. *Radio Science*, vol. 7, no. 8–9, pp. 771–775, August–September 1972. doi:10.1029/RS007i008p00771.
- Banerjee, G.; Niu, G.; Cressler, J. D.; Clark, S. D.; Palmer, M. J.; and Ahlgren, D. C. “Anomalous dose rate effects in gamma irradiated SiGe heterojunction bipolar transistors”. *IEEE Transactions on Nuclear Science*, vol. 46, no. 6, pp. 1620–1626, December 1999. doi:10.1109/23.819130.
- Banks, L. M. “Magnetosphere, ionosphere, and atmosphere interactions”. In *Solar System Plasma Physics*, vol. 2, L. J. Lanzerotti; C. F. Kennel; and E. N. Parker, eds., chap. 2.2, pp. 57–104. New York, NY: North-Holland, 1979. ISBN 0-444-85267-0.
- Banu, M. and Tsividis, Y. “Fully integrated active RC filters in MOS technology”. *IEEE Journal of Solid-State Circuits*, vol. 18, no. 6, pp. 644–651, December 1983.
- . “An elliptic continuous-time CMOS filter with on-chip automatic tuning”. *IEEE Journal of Solid-State Circuits*, vol. 20, no. 6, pp. 1114–1121, December 1985.
- Barnaby, H. J.; Cirba, C.; Schrimpf, R. D.; Kosier, S.; Fouillat, P.; and Montagner, X. “Minimizing gain degradation in lateral PNP bipolar junction transistors using gate control”. *IEEE Transactions on Nuclear Science*, vol. 46, no. 6, pp. 1652–1659, December 1999. doi:10.1109/23.819134.
- Barth, J. L.; Dyer, C. S.; and Stassinopoulos, E. G. “Space, atmospheric, and terrestrial radiation environments”. *IEEE Transactions on Nuclear Science*, vol. 50, no. 3, pp. 466–482, June 2003. doi:10.1109/TNS.2003.813131.
- Baumeister, D. *Development and Characterisation of a Radiation Hard Readout Chip for the LHCb-Experiment*. Ph.D. thesis, University of Heidelberg, Germany, Heidelberg, Germany, 29 January 2003.



- Bell, T. F. and Helliwell, R. A. "The Stanford University VLF wave injection experiment on the ISEE-A spacecraft". *IEEE Transactions on Geoscience Electronics*, vol. 16, no. 3, pp. 248–252, July 1978. doi:10.1109/TGE.1978.294556.
- Bell, T. F.; Inan, U. S.; Platino, M.; Pickett, J. S.; Kossey, P. A.; and Kennedy, E. J. "CLUSTER observations of lower hybrid waves excited at high altitudes by electromagnetic whistler mode signals from the HAARP facility". *Geophysical Research Letters*, vol. 31, no. 6, p. 6811, March 2004. doi:10.1029/2003GL018855.
- Benedetto, J. M. and Boesch, H. E. "The relationship between  $^{60}\text{Co}$  and 10-keV X-ray damage in MOS devices". *IEEE Transactions on Nuclear Science*, vol. 33, no. 6, pp. 1317–1323, December 1986. doi:10.1109/TNS.1986.4334599.
- Benedetto, J. M.; Boesch, H. E.; McLean, F. B.; and Mize, J. P. "Hole removal in thin-gate MOSFETs by tunneling". *IEEE Transactions on Nuclear Science*, vol. 32, no. 6, pp. 3916–3920, December 1985. doi:10.1109/TNS.1985.4334043.
- Berthelier, J. J.; Godefroy, M.; Leblanc, F.; Malingre, M.; Menvielle, M.; Lagoutte, D.; Brochot, J. Y.; Colin, F.; Elie, F.; Legendre, C.; Zamora, P.; Benoist, D.; Chapuis, Y.; Artru, J.; and Pfaff, R. "ICE, the electric field experiment on DEMETER". *Planetary and Space Science*, vol. 54, no. 5, pp. 456–471, April 2006. doi:10.1016/j.pss.2005.10.016.
- Berthelier, J. J.; LeFeuvre, F.; Mogilevsky, M. M.; Molchanov, O. A.; Galperin, Y. I.; Karczewski, J. F.; Ney, R. ad Gogly, G.; Guerin, C.; LeVeque, M.; Moreau, J.-M.; and Sene, F. X. "Measurements of the VLF electric and magnetic components of waves and DC electric field on board the AUREOL-3 spacecraft: the TBF-ONCH experiment". *Annales de Géophysique*, vol. 38, no. 5, pp. 643–667, 1982.
- Bilotti, A. and Mariani, E. "Noise characteristics of current mirror sinks/sources". *IEEE Journal of Solid-State Circuits*, vol. 10, no. 6, pp. 516–524, December 1975.
- Birkeland, K. *The Norwegian Aurora Polaris Expedition, 1902–1903: On the Cause of Magnetic Storms and the Origin of Terrestrial Magnetism*, vol. 1. New York, NY: Longmans, Green, & Co., 1908.

- Bittencourt, J. A. *Fundamentals of Plasma Physics*. 2<sup>nd</sup> ed. New York, NY: Springer, 1995. ISBN 8-590-01001-5.
- Boesch, H. E.; McLean, F. B.; Benedetto, J. M.; McGarrity, J. M.; and Bailey, W. E. "Saturation of threshold voltage shift in MOSFET's at high total dose". *IEEE Transactions on Nuclear Science*, vol. 33, no. 6, pp. 1191–1197, December 1986. doi:10.1109/TNS.1986.4334577.
- Bonnell, J. W.; Mozer, F. S.; Delory, G. T.; Hull, A. J.; Ergun, R. E.; Cully, C. M.; Angelopoulos, V.; and Harvey, P. R. "The electric field instrument (EFI) for THEMIS". *Space Science Reviews*, vol. 141, no. 1, pp. 303–341, December 2008. doi:10.1007/s11214-008-9469-2.
- Bortnik, J. *Precipitation of Radiation Belt Electrons by Lightning-Generated Magnetospherically Reflecting Whistler Waves*. Ph.D. thesis, Stanford University, Stanford, CA, May 2004.
- Bougeret, J. L.; Goetz, K.; Kaiser, M. L.; Bale, S. D.; Kellogg, P. J.; Maksimovic, M.; Monge, N.; Monson, S. J.; Astier, P. L.; Davy, S.; Dekkali, M.; Hinze, J. J.; Manning, R. E.; Aguilar-Rodriguez, E.; Bonnin, X.; Briand, C.; Cairns, I. H.; Cattell, C. A.; Cecconi, B.; Eastwood, J.; Ergun, R. E.; Fainberg, J.; Hoang, S.; Huttunen, K. E. J.; Krucker, S.; Lecacheux, A.; MacDowall, R. J.; Macher, W.; Mangeney, A.; Meetre, C. A.; Moussas, X.; Nguyen, Q. N.; Oswald, T. H.; Pulupa, M.; Reiner, M. J.; Robinson, P. A.; Rucker, H.; Salem, C.; Santolik, O.; Silvis, J. M.; Ullrich, R.; Zarka, P.; and Zouganelis, I. "S/WAVES: The radio and plasma wave investigation on the STEREO mission". *Space Science Reviews*, vol. 136, no. 1–4, pp. 487–528, April 2008. doi:10.1007/s11214-007-9298-8.
- Bougeret, J.-L.; Kaiser, M. L.; Kellogg, P. J.; Manning, R.; Goetz, K.; Monson, S. J.; Monge, N.; Friel, L.; Meetre, C. A.; Perche, C.; Sitruk, L.; and Hoang, S. "Waves: The radio and plasma wave investigation on the Wind spacecraft". *Space Science Reviews*, vol. 71, no. 1–4, pp. 231–263, February 1995. doi:10.1007/BF00751331.

- Bracewell, R. N. *The Fourier Transform and Its Applications*. 2<sup>nd</sup>, revised ed. Boston, MA: WCB/McGraw-Hill, 1986. ISBN 0-07-007015-6.
- Brady, F. T.; Maimon, J. D.; and Hurt, M. J. "A scaleable, radiation hardened shallow trench isolation". *IEEE Transactions on Nuclear Science*, vol. 46, no. 6, pp. 1836–1840, December 1999. doi:10.1109/23.819162.
- Brokaw, A. P. and Timko, M. P. "An improved monolithic instrumentation amplifier". *IEEE Journal of Solid-State Circuits*, vol. 10, no. 6, pp. 417–423, December 1975.
- Brown, D. B. "The time dependence of interface state production". *IEEE Transactions on Nuclear Science*, vol. 32, no. 6, pp. 3899–3904, December 1985. doi:10.1109/TNS.1985.4334040.
- Brown, D. B. and Dozier, C. M. "Reducing errors in dosimetry caused by low energy components of Co-60 and flash X-ray sources". *IEEE Transactions on Nuclear Science*, vol. 29, no. 6, pp. 1996–1999, December 1982. doi:10.1109/TNS.1982.4336485.
- Buchner, S.; Howard, Jr., J.; Poivey, C.; McMorow, D.; and Pease, R. "Pulsed-laser testing methodology for single event transients in linear devices". *IEEE Transactions on Nuclear Science*, vol. 51, no. 6, pp. 3716–3722, December 2004a. doi:10.1109/TNS.2004.839263.
- Buchner, S.; Kang, K.; Stapor, W. J.; Campbell, A. B.; Knudson, A. R.; McDonald, P.; and Rivet, S. "Pulsed laser-induced SEU in integrated circuits: A practical method for hardness assurance testing". *IEEE Transactions on Nuclear Science*, vol. 37, no. 6, pp. 1825–1831, December 1990. doi:10.1109/23.101196.
- Buchner, S.; Knudson, A.; Kang, K.; and Campbell, A. B. "Charge collection from focussed picosecond laser pulses". *IEEE Transactions on Nuclear Science*, vol. 35, no. 6, pp. 1517–1522, December 1988. doi:10.1109/23.25490.
- Buchner, S. and McMorow, D. "Single event transients in linear integrated circuits". In *2003 IEEE Nuclear and Space Radiation Effects Conference (NSREC) Short Course*, p. Sec. 4. Seattle, WA: IEEE NPSS, 11 July 2005.

- Buchner, S.; McMorow, D.; Poivey, C.; Howard, Jr., J.; Boulghassoul, Y.; Massengill, L. W.; Pease, R.; and Savage, M. "Comparison of single-event transients induced in an operational amplifier (LM124) by pulsed laser light and a broad beam of heavy ions". *IEEE Transactions on Nuclear Science*, vol. 51, no. 5, pp. 2776–2781, October 2004b. doi:10.1109/TNS.2004.835111.
- Buchner, S. D. and Baze, M. P. "Single event transients in fast electronic circuits". In *2001 IEEE Nuclear and Space Radiation Effects Conference (NSREC) Short Course*, p. Sec. 5. Vancouver, B.C.: IEEE NPSS, 16 July 2001.
- Carpenter, D. L. "Whistler evidence of a 'knee' in the magnetospheric ionization density profile". *Journal of Geophysical Research*, vol. 68, no. 6, pp. 1675–1682, March 1963. doi:10.1029/JZ068i006p01675.
- . "Whistler studies of the plasmopause in the magnetosphere, 1, temporal variations in the position of the knee and some evidence on plasma motions near the knee". *Journal of Geophysical Research*, vol. 71, no. 3, pp. 693–709, February 1966. doi:10.1029/JZ071i003p00693.
- Castello, R.; Montecchi, F.; Alini, R.; and Baschiroto, A. "A very linear BiCMOS transconductor for high-frequency filtering applications". In *Proceedings of the 1990 IEEE International Symposium on Circuits and Systems (ISCAS)*, vol. 2, pp. 1364–1367. IEEE, New Orleans, LA: IEEE Press, 1–3 May 1990. doi:10.1109/ISCAS.1990.112383.
- Cauffman, D. P. and Gurnett, D. A. "Satellite measurements of high latitude convection electric fields". *Space Science Reviews*, vol. 13, no. 3, pp. 369–410, July 1972. doi:10.1007/BF00219164.
- Cazenave, P.; Fouillat, P.; Montagner, X.; Barnaby, H.; Schrimpf, R. D.; Bonora, L.; David, J. P.; Touboul, A.; Calvet, M.-C.; and Calvel, P. "Total dose effects on gate controlled lateral PNP bipolar junction transistors". *IEEE Transactions on Nuclear Science*, vol. 45, no. 6, pp. 2577–2583, December 1998. doi:10.1109/23.736500.

- Chapman, S. "The thermosphere—the Earth's outermost atmosphere". In *Physics of the Upper Atmosphere*, J. A. Ratcliffe, ed., chap. 1, pp. 1–16. New York, NY: Academic Press, 1960.
- Chapman, S. and Ferraro, V. C. A. "A new theory of magnetic storms". *Terrestrial Magnetism and Atmospheric Electricity*, vol. 36, no. 2, pp. 77–97, June 1931. doi: 10.1029/TE036i002p00077.
- Chevalier, T. *Near-Field Characteristics of Electric Dipole Antennas in the Inner Magnetosphere*. Ph.D. thesis, Stanford University, Stanford, CA, October 2007.
- Chincarini, A.; Gemme, G.; Iannuzzi, M.; Parodi, R.; and Vaccarone, R. "Gain and noise analysis of HEMT amplifiers from room temperature to superfluid He". *Classical and Quantum Gravity*, vol. 23, no. 8, pp. S293–S298, 28 March 2006.
- Chung, W.-S. and Cha, H.-W. "Bipolar linear transconductor". *Electronics Letters*, vol. 26, no. 10, pp. 619–621, 10 May 1990. doi:10.1049/el:19900406.
- Chung, W.-S.; Kim, K.-H.; and Cha, H.-W. "A linear operational transconductance amplifier for instrumentation applications". *IEEE Transactions on Instrumentation and Measurement*, vol. 41, no. 3, pp. 441–443, June 1992. doi:10.1109/19.153345.
- Cirrus Logic, Incorporated. *16-, 14- and 12-bit Self-Calibrating A/D Converters*. CS5012A/CS5014/CS5016 Data Sheet, Rev. DS14F9, Austin, TX, August 2005.
- Coilcraft, Incorporated. *ADSL Transformers for Actel, Motorola and TI chip sets*. AS8397-B Data Sheet, Rev. 222-1, Cary, IL, 11 January 2001.
- . *ADSL Transformers for Analog Devices chipsets*. AS8456-A Data Sheet, Rev. 244-1, Cary, IL, 21 January 2003.
- Cressler, J. D. "On the potential of SiGe HBTs for extreme environment electronics". *Proceedings of the IEEE*, vol. 93, no. 9, pp. 1559–1582, September 2005. doi: 10.1109/JPROC.2005.852225.

- Cressler, J. D.; Krithivasan, R.; Zhang, G.; Niu, G.; Marshall, P. W.; Kim, H. S.; Reed, R. A.; Palmer, M. J.; and Joseph, A. J. "An investigation of the origins of the variable proton tolerance in multiple SiGe HBT BiCMOS technology generations". *IEEE Transactions on Nuclear Science*, vol. 49, no. 6, pp. 3203–3207, December 2002. doi:10.1109/TNS.2002.805362.
- Crook, G. M.; Scarf, F. L.; Fredricks, R. W.; Green, I. M.; and Lukas, P. "The OGO-V plasma wave detector: Instrumentation and in-flight operation". *IEEE Transactions on Geoscience Electronics*, vol. 7, no. 2, pp. 120–135, April 1969. doi:10.1109/TGE.1969.271332.
- Curtis, O. L. "Effects of point defects on electrical and optical properties of semiconductors". In *Point Defects in Solids: Semiconductors and Molecular Crystals*, vol. 2, J. H. Crawford, Jr. and L. M. Slifkin, eds., chap. 3, pp. 257–332. New York, NY: Plenum Press, 1975. ISBN 0-306-37511-7.
- Curtis, Jr., O. L. and Srour, J. R. "The multiple-trapping model and hole transport in SiO<sub>2</sub>". *Journal of Applied Physics*, vol. 48, no. 9, pp. 3819–3828, September 1977. doi:10.1063/1.324248.
- Cussac, T.; Clair, M.-A.; Ultré-Guerard, P.; Buisson, F.; Lassalle-Balier, G.; Ledu, M.; Elisabelar, C.; Passot, X.; and Rey, N. "The demeter microsatellite and ground segment". *Planetary and Space Science*, vol. 54, no. 5, pp. 413–427, April 2006. doi:10.1016/j.pss.2005.10.013.
- Czarnul, Z. and Fujii, N. "Highly-linear transconductor cell realised by double MOS transistor differential pairs". *Electronics Letters*, vol. 26, no. 21, pp. 1819–1821, 11 October 1990. doi:10.1049/el:19901164.
- De Lima, J. A. and Dualibe, C. "A tunable triode-MOSFET transconductor and its application to gm-C filters". In *Proceedings of the 1999 IEEE International Symposium on Circuits and Systems (ISCAS)*, vol. 2, pp. 640–643. IEEE, IEEE Press, 2 June 1999. ISBN 0-7803-5471-0. doi:10.1109/ISCAS.1999.780846.

- Deal, B. E. "Standardized terminology for oxide charges associated with thermally oxidized silicon". *IEEE Transactions on Electron Devices*, vol. 27, no. 3, pp. 606–608, March 1980.
- Deen, M. J.; Rumyantsev, S.; Bashir, R.; and Taylor, R. "Measurements and comparison of low frequency noise in npn and pnp polysilicon emitter bipolar junction transistors". *Journal of Applied Physics*, vol. 84, no. 1, pp. 625–633, 1 July 1998. doi:10.1063/1.368066.
- Dicello, J. F.; Wasiolek, M.; and Zaider, M. "Measured microdosimetric spectra of energetic ion beams of Fe, Ar, Ne, and C: Limitations of LET distributions and quality factors in space research and radiation effects". *IEEE Transactions on Nuclear Science*, vol. 38, no. 6, pp. 1203–1209, December 1991. doi:10.1109/23.124094.
- Dodd, P. E.; Shaneyfelt, M. R.; Fuller, E.; Pickel, J. C.; Sexton, F. W.; and Winokur, P. S. "Impact of substrate thickness on single-event effects in integrated circuits". *IEEE Transactions on Nuclear Science*, vol. 48, no. 6, pp. 1865–1871, December 2001. doi:10.1109/23.983144.
- Dozier, C. M. and Brown, D. B. "The use of low energy X-rays for device testing—A comparison with Co-60 radiation". *IEEE Transactions on Nuclear Science*, vol. 30, no. 6, pp. 4382–4387, December 1983. doi:10.1109/TNS.1983.4333142.
- Dressendorfer, P. V. "Radiation effects on MOS devices and circuits". In *Ionizing Radiation Effects on MOS Devices and Circuits*, T. P. Ma and P. V. Dressendorfer, eds., chap. 5, pp. 256–332. New York, NY: John Wiley & Sons, 1989a. ISBN 0-471-84893-X.
- . "Radiation-hardening technology". In *Ionizing Radiation Effects on MOS Devices and Circuits*, T. P. Ma and P. V. Dressendorfer, eds., chap. 6, pp. 333–400. New York, NY: John Wiley & Sons, 1989b. ISBN 0-471-84893-X.
- Duh, K. H. G.; Pospieszalski, M. W.; Kopp, W. F.; Ho, P.; Jabra, A. A.; Chao,

- P.-C.; Smith, P. M.; Lester, L. F.; Ballingall, J. M.; and Weinreb, S. "Ultra-low-noise cryogenic high-electron-mobility transistors". *IEEE Transactions on Electron Devices*, vol. 35, no. 3, pp. 249–256, March 1988. doi:10.1109/16.2448.
- Dungey, J. W. "Electrodynamics of the outer atmosphere". In *The Physics of the Ionosphere: Report of the Physical Society Conference on the Physics of the Ionosphere held at the Cavendish Laboratory, Cambridge, September, 1954*, pp. 229–236. The Physical Society at Cavendish Laboratory, Cambridge, London, U. K.: The Physical Society, September 1954.
- Duque-Carrillo, J. F. "Control of the common-mode component in CMOS continuous-time fully differential signal processing". *Analog Integrated Circuits and Signal Processing*, vol. 4, no. 2, pp. 131–140, September 1993. doi:10.1007/BF01254864.
- Durham, A. M.; Hughes, J. B.; and Redman-White, W. "Circuit architectures for high linearity monolithic continuous-time filtering". *IEEE Transactions on Circuits and Systems II: Analog and Digital Signal Processing*, vol. 39, no. 9, pp. 651–657, September 1992. doi:10.1109/82.193320.
- Dyer, C. "Calculation of radioactivity induced in gamma-ray spectrometers during spaceflight". *Nuclear Instruments and Methods*, vol. 173, no. 3, pp. 585–601, July 1980. doi:10.1016/0029-554X(80)90916-7.
- Enlow, E. W.; Pease, R. L.; Combs, W.; Schrimpf, R. D.; and Nowlin, R. N. "Response of advanced bipolar processes to ionizing radiation". *IEEE Transactions on Nuclear Science*, vol. 38, no. 6, pp. 1342–1351, December 1991. doi:10.1109/23.124115.
- Enlow, E. W.; Pease, R. L.; Combs, W. E.; and Platteter, D. G. "Total dose induced hole trapping in trench oxides". *IEEE Transactions on Nuclear Science*, vol. 36, no. 6, pp. 2415–2422, December 1989. doi:10.1109/23.45457.
- Ergun, R. E.; Carlson, C. W.; Mozer, F. S.; Delory, G. T.; Temerin, M.; McFadden, J. P.; Pankow, D.; Abiad, R.; Harvey, P.; Wilkes, R.; Primbsch, H.; Elphic,



- R.; Strangeway, R.; Pfaff, R.; and Cattell, C. A. "The FAST satellite fields instrument". *Space Science Reviews*, vol. 98, no. 1–2, pp. 67–91, August 2001. doi:10.1023/A:1013131708323.
- Ergun, R. E.; Larson, D.; Lin, R. P.; McFadden, J. P.; Carlson, C. W.; Anderson, K. A.; Muschietti, L.; McCarthy, M.; Parks, G. K.; Reme, H.; Bosqued, J. M.; D'Uston, C.; Sanderson, T. R.; Wenzel, K. P.; Kaiser, M.; Lepping, R. P.; Bale, S. D.; Kellogg, P.; and Bougeret, J.-L. "Wind spacecraft observations of solar impulsive electron events associated with solar type iii radio bursts". *Astrophysical Journal*, vol. 503, no. 1, pp. 435–445, August 1998. doi:10.1086/305954.
- Evans, R. D. *The Atomic Nucleus*. New York, NY: McGraw-Hill, 1955.
- Fahleson, U. "Theory of electric field measurements conducted in the magnetosphere with electric probes". *Space Science Reviews*, vol. 7, no. 2–3, pp. 238–262, October 1967. doi:10.1007/BF00215600.
- Feigl, F. J.; Fowler, W. B.; and Yip, K. L. "Oxygen vacancy model for the  $E'_1$  center in  $\text{SiO}_2$ ". *Solid State Communications*, vol. 14, no. 3, pp. 225–229, February 1974. doi:DOI:10.1016/0038-1098(74)90840-0.
- Ficklin, B. P.; Rorden, L. H.; Mills, M. E.; Stehle, R. H.; and Orsak, L. E. "Description and operation of the instruments for the Stanford University/Stanford Research Institute experiment (5002) to be flown on the POGO satellite". Technical Memorandum 2 L-21858, Stanford Research Institute, Menlo Park, CA, March 1965.
- Fleetwood, D. M. "border traps' in MOS devices". *IEEE Transactions on Nuclear Science*, vol. 39, no. 2, pp. 269–271, April 1992. doi:10.1109/23.277495.
- Fleetwood, D. M. and Eisen, H. A. "Total-dose radiation hardness assurance". *IEEE Transactions on Nuclear Science*, vol. 50, no. 3, pp. 552–564, June 2003. doi:10.1109/TNS.2003.813130.

Fleetwood, D. M.; Kosier, S. L.; Nowlin, R. N.; Schrimpf, R. D.; Reber, Jr., R. A.; DeLaus, M.; Winokur, P. S.; Wei, A.; Combs, W. E.; and Pease, R. L. "Physical mechanisms contributing to enhanced bipolar gain degradation at low dose rates". *IEEE Transactions on Nuclear Science*, vol. 41, no. 6, pp. 1871–1883, Dec 1994a. doi:10.1109/23.340519.

Fleetwood, D. M.; Meisenheimer, T. L.; and Scofield, J. H. " $1/f$  noise and radiation effects in MOS devices". *IEEE Transactions on Nuclear Science*, vol. 41, no. 11, pp. 1953–1964, November 1994b. doi:10.1109/16.333811.

Fleetwood, D. M.; Winokur, P. S.; and Dodd, P. E. "An overview of radiation effects on electronics in the space telecommunications environment". *Microelectronics Reliability*, vol. 40, no. 1, pp. 17–26, January 2000. doi:DOI: 10.1016/S0026-2714(99)00225-5.

Fleetwood, D. M.; Winokur, P. S.; and Schwank, J. R. "Using laboratory X-ray and Cobalt-60 irradiations to predict CMOS device response in strategic and space environments". *IEEE Transactions on Nuclear Science*, vol. 35, no. 6, pp. 1497–1505, December 1988. doi:10.1109/23.25487.

Fleetwood, D. M.; Xiong, H. D.; Lu, Z.-Y.; Nicklaw, C. J.; Felix, J. A.; Schrimpf, R. D.; and Pantelides, S. T. "Unified model of hole trapping,  $1/f$  noise, and thermally stimulated current in MOS devices". *IEEE Transactions on Nuclear Science*, vol. 49, no. 6, pp. 2674–2683, December 2002. doi:10.1109/TNS.2002.805407.

Florida, C. D. "The development of a series of ionospheric satellites". *Proceedings of the IEEE*, vol. 57, no. 6, pp. 867–875, June 1969.

Fried, B. D. and Conte, S. D. *The Plasma Dispersion Function: The Hilbert Transform of the Gaussian*. New York, NY: Academic Press, October 1961.

Gardiner, G. W. "Origin of the term Ionosphere". *Nature*, vol. 224, no. 4386, p. 1096, December 1969. doi:10.1038/195939a0.

- Georgantas, T.; Papananos, Y.; and Tsividis, Y. “A comparative study of five integrator structures for monolithic continuous-time filters—a tutorial”. In *Proceedings of the 1993 IEEE International Symposium on Circuits and Systems (ISCAS)*, pp. 1259–1262. IEEE, IEEE Press, 3–6 May 1993. ISBN 0-7803-1281-3.
- Gilbert, B. “A new wide-band amplifier technique”. *IEEE Journal of Solid-State Circuits*, vol. 3, no. 4, pp. 353–365, December 1968.
- . “The multi-tanh principle: A tutorial overview”. *IEEE Journal of Solid-State Circuits*, vol. 33, no. 1, pp. 2–17, January 1998. doi:10.1109/4.654932.
- Giraldo, A. *Evaluation of Deep Submicron Technologies with Radiation Tolerant Layout for Electronics in LHC Environments*. Ph.D. thesis, Università Degli Studi Di Padova, Padova, Italy, 31 December 1998.
- Gold, T. “Motions in the magnetosphere of the Earth”. *Journal of Geophysical Research*, vol. 64, no. 9, pp. 1219–1224, September 1959. doi:10.1029/JZ064i009p01219.
- Goldstein, R. “A fully integrated micro-magnetometer/microspacecraft for multipoint measurements”. In *Measurement Techniques in Space Plasmas: Fields, Geophysical Monographs*, vol. 103, R. F. Pfaff; J. E. Borovsky; and D. T. Young, eds., pp. 305–310. Washington, DC: American Geophysical Union, 1998. ISBN 0-87590-086-0.
- Gorbachev, O. A.; Konikov, Y. V.; and Khazanov, G. V. “Quasilinear heating of electrons in the Earth’s plasmasphere”. *Pure and Applied Geophysics*, vol. 127, no. 2/3, pp. 545–559, June 1988. doi:10.1007/BF00879825.
- Graeme, J. *Optimizing Opamp Performance*. New York, NY: McGraw-Hill, 1997. ISBN 0-07-024522-3.
- Gray, P. R.; Hurst, P. J.; Lewis, S. H.; and Meyer, R. G. *Analysis and Design of Analog Integrated Circuits*. 2<sup>nd</sup> ed. New York, NY: John Wiley & Sons, 2001. ISBN 0-471-32168-0.

Gregorian, R. and Temes, G. C. *Analog MOS Integrated Circuits for Signal Processing*, chap. Switched-Capacitor Filters, pp. 265–410. Wiley Series on Filters. New York, NY: Wiley-Interscience, 1986. ISBN 0-471-09797-7.

Gringauz, K. I.; Bezrukikh, V. V.; Ozerov, V. D.; and Rybchinskii, R. E. “The study of interplanetary ionized gas, high-energy electrons and corpuscular radiation of the Sun, employing three-electrode charged particle traps on the second Soviet space rocket”. *Planetary and Space Science*, vol. 9, no. 3, pp. 103–107, March 1962. doi:DOI:10.1016/0032-0633(62)90180-0.

Griscom, D. L. “Diffusion of radiolytic molecular hydrogen as a mechanism for the post-irradiation buildup of interface states in SiO<sub>2</sub>-on-Si structures”. *Journal of Applied Physics*, vol. 58, no. 7, pp. 2524–2533, October 1985. doi:10.1063/1.335931.

Grunthaner, F. J.; Grunthaner, P. J.; and Maserjian, J. “Radiation-induced defects in SiO<sub>2</sub> as determined with XPS”. *IEEE Transactions on Nuclear Science*, vol. 29, no. 6, pp. 1462–1466, December 1982. doi:10.1109/TNS.1982.4336387.

Gurnett, D. A. “The Earth as a radio source: Terrestrial kilometric radiation”. *Journal of Geophysical Research*, vol. 79, no. 28, pp. 4227–4238, October 1974. doi:10.1029/JA079i028p04227.

———. “Principles of space plasma wave instrument design”. In *Measurement Techniques in Space Plasmas: Fields, Geophysical Monographs*, vol. 103, R. F. Pfaff; J. E. Borovsky; and D. T. Young, eds., pp. 121–136. Washington, DC: American Geophysical Union, 1998. ISBN 0-87590-086-0.

Gurnett, D. A.; Huff, R. L.; and Kirchner, D. L. “The wide-band plasma wave investigation”. *Space Science Reviews*, vol. 79, no. 1–2, pp. 195–208, January 1997. doi:10.1023/A:1004966823678.

Gurnett, D. A.; Kurth, W. S.; Kirchner, D. L.; Hospodarsky, G. B.; Averkamp, T. F.; Zarka, P.; Lecacheux, A.; Manning, R.; Roux, A.; Canu, P.; Cornilleau-Wehrlin, N.; Galopeau, P.; Meyer, A.; Boström, R.; Gustafsson, G.; Wahlund, J.-E.; Åhlen, L.; Rucker, H. O.; Ladreiter, H. P.; Macher, W.; Woolliscroft, L. J. C.;

- Alleyne, H.; Kaiser, M. L.; Desch, M. D.; Farrell, W. M.; Harvey, C. C.; Louarn, P.; Kellogg, P. J.; Goetz, K.; and Pedersen, A. "The Cassini radio and plasma wave investigation". *Space Science Reviews*, vol. 114, no. 1–4, pp. 395–463, September 2004. doi:10.1007/s11214-004-1434-0.
- Gurnett, D. A. and O'Brien, B. J. "High-latitude geophysical studies with satellite Injun 3. 5, Very Low Frequency electromagnetic radiation". *Journal of Geophysical Research*, vol. 69, no. 1, pp. 65–89, January 1964. doi:10.1029/JZ069i001p00065.
- Gurnett, D. A.; Persoon, A. M.; Randall, R. F.; Odem, D. L.; Remington, S. L.; Averkamp, T. F.; Debower, M. M.; Hospodarsky, G. B.; Huff, R. L.; Kirchner, D. L.; Mitchell, M. A.; Pham, B. T.; Phillips, J. R.; Schintler, W. J.; Sheyko, P.; and Tomash, D. R. "The Polar plasma wave instrument". *Space Science Reviews*, vol. 71, no. 1–4, pp. 597–622, February 1995. doi:10.1007/BF00751343.
- Gurnett, D. A.; Pfeiffer, G. W.; Anderson, R. R.; Mosier, S. R.; and Cauffman, D. P. "Initial observations of VLF electric and magnetic fields with the Injun 5 satellite". *Journal of Geophysical Research–Space Physics*, vol. 74, no. 19, pp. 4631–4648, September 1969. doi:10.1029/JA074i019p04631.
- Gurnett, D. A.; Scarf, F. L.; Fredricks, R. W.; and Smith, E. J. "The ISEE-1 and ISEE-2 plasma wave investigation". *IEEE Transactions on Geoscience Electronics*, vol. 16, no. 3, pp. 225–230, July 1978. doi:10.1109/TGE.1978.294552.
- Gussenhoven, M. S.; Mullen, E. G.; and Brautigam, D. H. "Improved understanding of the Earth's radiation belts from the CRRES satellite". *IEEE Transactions on Nuclear Science*, vol. 43, no. 2, pp. 353–368, April 1996. doi:10.1109/23.490755.
- Halfin, S. "Simultaneous determination of ordering and amplification of cascaded subsystems". *Journal of Optimization Theory and Applications*, vol. 6, no. 5, pp. 356–363, November 1970. doi:10.1007/BF00932582.
- Hall, R. N. "Electron-hole recombination in germanium". *Physical Review*, vol. 87, no. 2, p. 387, July 1952. doi:10.1103/PhysRev.87.387.

- Harvey, P.; Mozer, F. S.; Pankow, D.; Wygant, J.; Maynard, N. C.; Singer, H.; Sullivan, W.; Anderson, P. B.; Pfaff, R.; Aggson, T.; Pedersen, A.; Fälthammar, C.-G.; and Tanskannen, P. "The electric field instrument on the Polar satellite". *Space Science Reviews*, vol. 71, no. 1–4, pp. 583–596, February 1995. doi:10.1007/BF00751342.
- Harvey, P. R.; Curtis, D. W.; Heeterdks, H. D.; Pankow, D.; Rauch-Leiba, J. M.; Wittenbrock, S. K.; and McFadden, J. P. "The FAST spacecraft instrument data processing unit". *Space Science Reviews*, vol. 98, no. 1–2, pp. 113–149, August 2001. doi:10.1023/A:1013135809232.
- Hashimoto, K.; Nagano, I.; Yamamoto, M.; Okada, T.; Kimura, I.; Matsumoto, H.; and Oki, H. "EXOS-D (AKEBONO) very low frequency plasma wave instruments (VLF)". *IEEE Transactions on Geoscience and Remote Sensing*, vol. 35, no. 2, pp. 278–286, March 1997. doi:10.1109/36.563267.
- Hastings, A. *The Art of Analog Layout*. 2<sup>nd</sup> ed. Upper Saddle River, NJ: Prentice Hall, 2006. ISBN 0-13-146410-8.
- Hauser, J. R.; Diehl-Nagle, S. E.; Knudson, A. R.; Campbell, A. B.; Stapor, W. J.; and Shapiro, P. "Ion track shunt effects in multi-junction structures". *IEEE Transactions on Nuclear Science*, vol. 32, no. 6, pp. 4115–4121, December 1985. doi:10.1109/TNS.1985.4334078.
- Häusler, B.; Anderson, R. R.; Gurnett, D. A.; Koons, H. C.; Holzworth, R. H.; Bauer, O. H.; Treumann, R.; Gnaiger, K.; Odem, D.; Harbridge, W. B.; and Eberl, F. "The plasma wave instrument on board the AMPTE IRM satellite". *IEEE Transactions on Geoscience and Remote Sensing*, vol. GE-23, no. 3, pp. 267–273, May 1985. doi:10.1109/TGRS.1985.289526.
- Heidt, H.; Puig-Suari, J.; Moore, A. S.; Nakasuka, S.; and Twiggs, R. J. "CubeSat: A new generation of picosatellite for education and industry low-cost space experimentation". In *14<sup>th</sup> Annual AIAA/USU Conference on Small Satellites*,

- SSC00-V-5. Logan, UT: American Institute of Aeronautics and Astronautics/Utah State University, 21–24, August 2000.
- Helliwell, R. A. *Whistlers and Related Atmospheric Phenomena*. Stanford, CA: Stanford University Press, 1965. ISBN 0-80-470106-7.
- Helms, C. R. “Physical structure and chemical nature of the si-sio<sub>2</sub> interfacial region”. In *The Si-SiO<sub>2</sub> System, Materials Science Monographs*, vol. 32, P. Balk, ed., chap. 3, pp. 77–127. New York, NY: Elsevier Science, 1988. ISBN 0-444-42603-5.
- Hoegy, W. R. and Brace, L. H. “The dumbell electrostatic ionosphere probe: Theoretical aspects”. Scientific Report JS-1, University of Michigan, Ann Arbor, MI, September 1961.
- Holback, B.; Jansson, S.-E.; Åhlén, L.; Lundgren, G.; Lyngdal, L.; Powell, S.; and Meyer, A. “The Freja wave and plasma density experiment”. *Space Science Reviews*, vol. 70, no. 3–4, pp. 577–592, November 1994. doi:10.1007/BF00756887.
- Holmes-Siedle, A. and Adams, L. *Handbook of Radiation Effects*. 2<sup>nd</sup> ed. New York, NY: Oxford University Press, 2002. ISBN 0-19-850733-X.
- Horne, R. B. “The contribution of wave-particle interactions to electron loss and acceleration in the Earth’s radiation belts during geomagnetic storms”. In *The Review of Radio Science 1999–2002*, W. R. Stone, ed., chap. 33, pp. 801–828. New York, NY: Wiley-Interscience, 2002. ISBN 0-471-26866-6.
- Hughes, H. “Historical perspective”. In *Ionizing Radiation Effects in MOS Devices and Circuits*, T. P. Ma and P. V. Dressendorfer, eds., chap. 2, pp. 47–86. New York, NY: John Wiley & Sons, 1989. ISBN 0-471-84893-X.
- Hughes, H. L. and Benedetto, J. M. “Radiation effects and hardening of MOS technology: Devices and circuits”. *IEEE Transactions on Nuclear Science*, vol. 50, no. 3, pp. 500–521, June 2003. doi:10.1109/TNS.2003.812928.

- Hughes, R. C.; EerNisse, E. P.; and Stein, H. J. "Hole transport in MOS oxides". *IEEE Transactions on Nuclear Science*, vol. 22, no. 6, pp. 2227–2233, December 1975. doi:10.1109/TNS.1975.4328110.
- ICRP. "Biological aspects of radiological protection". *Annals of the ICRP*, vol. 21, no. 1–3, pp. 11–25, 1991a. doi:DOI:10.1016/0146-6453(91)90067-Q. Publication 60: The 1990 Recommendations of the International Commission on Radiological Protection.
- . "The conceptual framework of radiological protection". *Annals of the ICRP*, vol. 21, no. 1–3, pp. 25–32, 1991b. doi:DOI:10.1016/0146-6453(91)90068-R. Publication 60: The 1990 Recommendations of the International Commission on Radiological Protection.
- . "Quantities used in radiological protection". *Annals of the ICRP*, vol. 21, no. 1–3, pp. 4–11, 1991c. doi:DOI:10.1016/0146-6453(91)90066-P. Publication 60: The 1990 Recommendations of the International Commission on Radiological Protection.
- . "Summary of recommendations". *Annals of the ICRP*, vol. 21, no. 1–3, pp. 67–77, 1991d. doi:DOI:10.1016/0146-6453(91)90072-O. Publication 60: The 1990 Recommendations of the International Commission on Radiological Protection.
- . "The system of protection for proposed and continuing practices". *Annals of the ICRP*, vol. 21, no. 1–3, pp. 32–49, 1991e. doi:DOI:10.1016/0146-6453(91)90069-S. Publication 60: The 1990 Recommendations of the International Commission on Radiological Protection.
- . "Quantities used in radiological protection". *Annals of the ICRP*, vol. 37, no. 2–4, pp. 61–79, April–June 2007. doi:DOI:10.1016/j.icrp.2007.10.005. Publication 103: The 2007 Recommendations of the International Commission on Radiological Protection.
- ICRU. "Fundamental quantities and units for ionizing radiation". ICRU Report 60,



- International Commission on Radiation Units and Measurements, Bethesda, MD, December 1998.
- IEEE Std 1241-2000. “IEEE standard for terminology and test methods for analog-to-digital converters”. Waveform Measurement and Analysis Technical Committee of the IEEE Instrumentation and Measurement Society, 13 June 2001.
- IEEE Std 488.1-2003. “IEEE standard for higher performance protocol for the standard digital interface for programmable instrumentation”. Technical Committee on Automated Test Systems and Instrumentation (TC-8) of the IEEE Instrumentation and Measurement Society, 12 December 2003.
- Inan, U. S.; Bell, T. F.; Bortnik, J.; and Albert, J. M. “Controlled precipitation of radiation belt electrons”. *Journal of Geophysical Research–Space Physics*, vol. 108, no. A5, p. 1186, May 2003. doi:10.1029/2002JA009580.
- Inan, U. S.; Helliwell, R. A.; and Kurth, W. S. “Terrestrial versus jovian VLF chorus - a comparative study”. *Journal of Geophysical Research*, vol. 88, no. A8, pp. 6171–6180, August 1983. doi:10.1029/JA088iA08p06171.
- Inan, U. S. and Inan, A. S. *Electromagnetic Waves*, chap. Field-Matter Interactions and Elementary Antennas, pp. 414–507. Upper Saddle River, NJ: Prentice Hall, 2000. ISBN 0-201-36179-5.
- Jaffé, G. “Zur theorie der ionisation in kolonnen”. *Annalen der Physik*, vol. 347, no. 12, pp. 303–344, September 1913. doi:10.1002/andp.19133471205.
- Jastrow, R. and Pearse, C. A. “Atmospheric drag on the satellite”. *Journal of Geophysical Research*, vol. 62, no. 3, pp. 413–423, September 1957. doi:10.1029/JZ062i003p00413.
- Jin, Z.; Niu, G.; Cressler, J. D.; Marshall, C. J.; Marshall, P. W.; Kim, H. S.; Reed, R. A.; and Harame, D. L. “ $1/f$  noise in proton-irradiated SiGe HBTs”. *IEEE Transactions on Nuclear Science*, vol. 48, no. 6, pp. 2244–2249, December 2001. doi:10.1109/23.983203.

- Johnson, M. B.; McMahan, M. A.; Galloway, M.; Leitner, D.; Morel, J. R.; Gimpel, T. L.; Ninemire, B. F.; Siero, R.; and Thatcher, R. K. ““super” cocktails for heavy ion testing”. In *IEEE Radiation Effects Data Workshop*, vol. 0, pp. 34–37. IEEE, Honolulu, HI: IEEE Press, July 2007. ISBN 978-1-4244-1464-2. doi:10.1109/REDW.2007.4342537.
- Johnson, M. B.; McMahan, M. A.; Gimpel, T. L.; and Tiffany, W. S. “Berkeley Accelerator Space Effects (BASE) light ion facility upgrade”. In *IEEE Radiation Effects Data Workshop*, pp. 183–187. IEEE, Ponte Vedra Beach, FL: IEEE Press, 17–21 July 2006. ISBN 1-4244-0638-2. doi:10.1109/REDW.2006.295490.
- Johnson, M. P.; Inan, U. S.; Lev-Tov, S. J.; and Bell, T. F. “Scattering pattern of lightning-induced ionospheric disturbances associated with early/fast VLF events”. *Geophysical Research Letters*, vol. 26, no. 15, pp. 2363–2366, August 1999. doi:10.1029/1999GL900521.
- Johnston, A. H. “Super recovery of total dose damage in MOS devices”. *IEEE Transactions on Nuclear Science*, vol. 31, no. 6, pp. 1427–1433, December 1984. doi:10.1109/TNS.1984.4333524.
- . “The influence of VLSI technology evolution on radiation-induced latchup in space systems”. *IEEE Transactions on Nuclear Science*, vol. 43, no. 2, pp. 505–521, April 1996. doi:10.1109/23.490897.
- . “Radiation effects in advanced microelectronics technologies”. *IEEE Transactions on Nuclear Science*, vol. 45, no. 3, pp. 1339–1354, June 1998. doi:10.1109/23.685206.
- Johnston, A. H.; Swift, G. M.; Miyahira, T. F.; and Edmonds, L. D. “A model for single-event transients in comparators”. *IEEE Transactions on Nuclear Science*, vol. 47, no. 6, pp. 2624–2633, December 2000. doi:10.1109/23.903818.
- Jones, D. “Introduction to the S-300 wave experiment onboard GEOS: For GEOS S-300 experimenters”. *Space Science Reviews*, vol. 22, no. 4, pp. 327–332, October 1978. doi:10.1007/BF00210871.

- Jones, R. O. "P-N-P transistor stability". *Microelectronics Reliability*, vol. 6, no. 4, pp. 277–283, November 1967. doi:DOI:10.1016/0026-2714(67)90083-2.
- Jursa, A. S. "Handbook of Geophysics and the Space Environment, 4<sup>th</sup> ed." Tech. Rep. AD/A167000, Air Force Geophysics Laboratory, Hancolm, MA, Dec. 1985.
- Kennel, C. F. and Petscheck, H. E. "Limit on stably trapped particle fluxes". *Journal of Geophysical Research*, vol. 71, no. 1, pp. 1–28, January 1966. doi:10.1029/JZ071i001p00001.
- Kerns, S. E. "Transient-ionization and single-event phenomena". In *Ionizing Radiation Effects on MOS Devices and Circuits*, T. P. Ma and P. V. Dressendorfer, eds., chap. 9, pp. 485–576. New York, NY: John Wiley & Sons, 1989. ISBN 0-471-84893-X.
- Kerns, S. E.; Shafer, B. D.; Rockett, Jr., L. R.; Pridmore, J. S.; Berndt, D. F.; van Vonno, N.; and Barber, F. E. "The design of radiation-hardened ICs for space: A compendium of approaches". *Proceedings of the IEEE*, vol. 76, no. 11, pp. 1470–1509, November 1988. doi:10.1109/5.90115.
- Kerris, K. G. "Source considerations and testing techniques". In *Ionizing Radiation Effects on MOS Devices and Circuits*, T. P. Ma and P. V. Dressendorfer, eds., chap. 8, pp. 443–484. New York, NY: John Wiley & Sons, 1989. ISBN 0-471-84893-X.
- Kim, Q.; Schwartz, H. R.; Edmonds, L. D.; and Zoutendyk, J. A. "Diagnosis of NMOS DRAM functional performance as affected by a picosecond dye laser". *Solid-State Electronics*, vol. 35, no. 7, pp. 905–912, July 1992. doi:DOI:10.1016/0038-1101(92)90317-6.
- Kinchin, G. H. and Pease, R. S. "The displacement of atoms in solids by radiation". *Reports on Progress in Physics*, vol. 18, no. 1, pp. 1–51, 1955. doi:10.1088/0034-4885/18/1/301.

- King, E. E.; Lacoce, R. C.; and Wang-Ratkovic, J. "The role of the spacer oxide in determining worst-case hot-carrier stress conditions for NMOS LDD devices". In *Proceedings of 38<sup>th</sup> Annual IEEE International Reliability Physics Symposium*, pp. 83–92. San Jose, CA: IEEE, 2000. ISBN 0-7803-5680-0. doi:10.1109/RELPHY.2000.843895.
- Kitchin, C. and Counts, L. *A Designer's Guide to Instrumentation Amplifiers*. G02678-15-9/06(B), 3<sup>rd</sup> ed. Analog Devices, Inc., 2006.
- Knudson, A. R. and Campbell, A. B. "Charge collection in bipolar transistors". *IEEE Transactions on Nuclear Science*, vol. 34, no. 6, pp. 1246–1250, December 1987. doi:10.1109/TNS.1987.4337460.
- Knudson, A. R.; Campbell, A. B.; Hauser, J. R.; Jessee, M.; Stapor, W. J.; and Shapiro, P. "Charge transport by the ion shunt effect". *IEEE Transactions on Nuclear Science*, vol. 33, no. 6, pp. 1560–1564, December 1986. doi:10.1109/TNS.1986.4334641.
- Koga, R. "Single-event effect ground test issues". *IEEE Transactions on Nuclear Science*, vol. 43, no. 2, pp. 661–670, April 1996. doi:10.1109/23.490909.
- Koga, R.; Imamoto, S. S.; Katz, N.; and Pinkerton, S. D. "Data processing units for eight magnetospheric particle and field sensors". *Journal of Spacecraft and Rockets*, vol. 29, no. 4, pp. 574–579, August 1992. doi:10.2514/3.25638.
- Koga, R.; Pinkerton, S. D.; Moss, S. C.; Mayer, D. C.; LaLumondiere, S.; Hansel, S. J.; Crawford, K. B.; and Crain, W. R. "Observation of single event upsets in analog microcircuits". *IEEE Transactions on Nuclear Science*, vol. 40, no. 6, pp. 1838–1844, December 1993. doi:10.1109/23.273472.
- Korotkov, A. S.; Hauer, H.; Ponomarev, S. A.; and Morozov, D. V. "Realization of narrow-band SC-filters with low power consumption". In *4<sup>th</sup> European Conference on Circuits and Systems for Communications (ECCSC)*, pp. 69–72. Bucharest, Romania, 10-11 July 2008. ISBN 978-1-4244-2419-1. doi:10.1109/ECCSC.2008.4611648.

- Krabbe, H. "A high-performance monolithic instrumentation amplifier". In *1971 IEEE International Solid-State Circuits Conference. Digest of Technical Papers.*, vol. XIV, pp. 186–187, February 1971.
- Krauss, H. L.; Bostian, C. W.; and Raab, F. H. *Solid State Radio Engineering*. New York, NY: John Wiley & Sons, 1980. ISBN 0-471-03018-X.
- Kuehl, H. H. "Resistance of a short antenna in a warm plasma". *Radio Science*, vol. 1, no. 8, pp. 971–976, August 1966.
- Laaspere, T.; Morgan, M. G.; and Johnson, W. C. "Observations of lower hybrid resonance phenomena on the OGO 2 spacecraft". *Journal of Geophysical Research–Space Physics*, vol. 74, no. 1, pp. 141–152, January 1969. doi:10.1029/JA074i001p00141.
- Lacoe, R. C. "CMOS scaling, design principles, and hardening-by-design methodology". In *2003 IEEE Nuclear and Space Radiation Effects Conference (NSREC) Short Course*, p. Sec. 2. Monterey, CA: IEEE NPSS, 21 July 2003.
- Lacoe, R. C.; Osborn, J. V.; Koga, R.; Brown, S.; and Mayer, D. "Application of hardness-by-design methodology to radiation-tolerant ASIC technologies". *IEEE Transactions on Nuclear Science*, vol. 47, no. 6, pp. 2334–2341, December 2000. doi:10.1109/23.903774.
- Laker, K. R. and Sansen, W. M. C. *Design of Analog Integrated Circuits and Systems*. New York, NY: McGraw-Hill, 1994. ISBN 0-07-036060-X.
- Lakshmikumar, K. R.; Hadaway, R. A.; and Copeland, M. A. "Characterisation and modeling of mismatch in MOS transistors for precision analog design". *IEEE Journal of Solid-State Circuits*, vol. 21, no. 6, pp. 1057–1066, December 1986.
- Langford, D. S.; Tesch, B. J.; Williams, B. E.; and Nelson, Jr., G. R. "A BiCMOS analog front-end circuit for an FDM-based ADSL system". *IEEE Journal of Solid-State Circuits*, vol. 33, no. 9, pp. 1383–1393, September 1998. doi:10.1109/4.711337.

- Langmuir, I. “The interaction of electron and positive ion space charges in cathode sheaths”. *Physical Review*, vol. 33, no. 6, pp. 954–989, June 1929. doi:10.1103/PhysRev.33.954.
- Lanzerotti, L. J. “Impacts of ionospheric/magnetospheric processes on terrestrial science and technology”. In *Solar System Plasma Physics*, vol. 3, L. J. Lanzerotti; C. F. Kennel; and E. N. Parker, eds., chap. 3.2.1, pp. 317–363. New York, NY: North-Holland, 1979. ISBN 0-444-85267-0.
- Lanzerotti, L. J. and Southwood, D. J. “Hydromagnetic waves”. In *Solar System Plasma Physics*, vol. 3, L. J. Lanzerotti; C. F. Kennel; and E. N. Parker, eds., chap. 3.1.3, pp. 109–136. New York, NY: North-Holland, 1979. ISBN 0-444-85267-0.
- Larcher, L.; Paccagnella, A.; Ceschia, M.; and Ghidini, G. “A model of radiation induced leakage current (RILC) in ultra-thin gate oxides”. *IEEE Transactions on Nuclear Science*, vol. 46, no. 6, pp. 1553–1561, December 1999. doi:10.1109/23.819120.
- Lauben, D. S.; Inan, U. S.; and Bell, T. F. “Precipitation of radiation belt electrons induced by obliquely propagating lightning-generated whistlers”. *Journal of Geophysical Research–Space Physics*, vol. 106, no. A12, pp. 29745–29770, December 2001. doi:10.1029/1999JA000155.
- LBNL, Lawrence Berkeley National Laboratory. “The 88-inch cyclotron, heavy ions page”. <http://cyclotron.lbl.gov/subpage2.html> (accessed 21 November 2009), 2009.
- Lee, K. H.-H. *Fault-Tolerant FFT Processor Design for Space Applications*. Ph.D. thesis, Stanford University, Stanford, CA, in preparation.
- Lee, T. H. *The Design of CMOS Radio-Frequency Integrated Circuits*. Cambridge, U. K.: Cambridge University Press, 1998. ISBN 0-521-63922-0.
- Leitner-Wutte, D.; McMahan, M. A.; Aregento, D.; Gimpel, T. L.; Guy, A.; Morel, J. R.; Siero, R.; Thatcher, R. K.; and Lyneis, C. M. “Heavy ion cocktail beams

- at the 88-inch cyclotron". *Lawrence Berkeley National Laboratory*, pp. 1–4, 3 September 2002. Retrived from: <http://www.escholarship.org/uc/item/65x4t87p>.
- Lelis, A. J.; Oldham, T. R.; Boesch, Jr., H. E.; and McLean, F. B. "The nature of the trapped hole annealing process". *IEEE Transactions on Nuclear Science*, vol. 36, no. 6, pp. 1808–1815, December 1989. doi:10.1109/23.45373.
- Lemaire, J. "Plasma distribution models in a rotating magnetic dipole and refilling of plasmaspheric flux tubes". *Physics of Fluids B: Plasma Physics*, vol. 1, no. 7, pp. 1519–1525, July 1989. doi:10.1063/1.858928.
- Lemaire, J. F. and Gringauz, K. I. *The Earth's Plasmasphere*. Cambridge, U. K.: Cambridge University Press, 1998. ISBN 0-521-43091-7.
- Lenahan, P. M.; Bohna, N. A.; and Campbell, J. P. "Radiation-induced interface traps in MOS devices: Capture cross section and density of states of  $p_{b1}$  silicon dangling bond centers". *IEEE Transactions on Nuclear Science*, vol. 49, no. 6, pp. 2708–2712, December 2002. doi:10.1109/TNS.2002.805357.
- Lenahan, P. M. and Conley, Jr., J. F. "What can electron paramagnetic resonance tell us about the Si/SiO<sub>2</sub> system?" *Journal of Vacuum Science and Technology B*, vol. 16, no. 4, pp. 2134–2153, July/August 1998. doi:10.1116/1.590301.
- Lenahan, P. M. and Dressendorfer, P. V. "An electron spin resonance study of radiation-induced electrically active paramagnetic centers at the Si/SiO<sub>2</sub> interface". *Journal of Applied Physics*, vol. 54, no. 3, pp. 1457–1460, March 1983. doi: 10.1063/1.332171.
- . "Hole traps and trivalent silicon centers in metal/oxide/silicon devices". *Journal of Applied Physics*, vol. 55, no. 10, pp. 3495–3499, May 1984. doi:10.1063/1.332937.
- Lide, D. R., ed. *CRC Handbook of Chemistry and Physics*. 89<sup>th</sup> ed. Boca Raton, FL: CRC Press, June 2008. ISBN 142006679X.

- Limotyrakis, S. *Power-Efficient Broadband A/D Conversion*. Ph.D. thesis, Stanford University, Stanford, CA, September 2004.
- Lindqvist, P.-A.; Marklund, G. T.; and Blomberg, L. G. “Plasma characteristics determined by the Freja electric field instrument”. *Space Science Reviews*, vol. 70, no. 3–4, pp. 593–602, November 1994. doi:10.1007/BF00756888.
- Linear Technology. *Constant Current Source and Temperature Sensor*. LM134 Series Data Sheet, Rev. C, Milpitas, CA, 1991.
- . *High-Speed, 16-bit, 333ksps, Sampling A/D Converter with Shutdown*. LTC1604 Data Sheet, Rev. A, Milpitas, CA, 1998.
- . *100mA, Low-Noise, LDO Micropower Regulators in SOT-23*. LT1761 datasheet, Rev. A, Milpitas, CA, 1999.
- . *Low-Noise, Low-Distortion Fully Differential Input/Output Amplifier/Driver*. LT1994 Data Sheet, Rev. A, Milpitas, CA, 2005.
- . *16-bit, 25Msps/10Msps ADCs*. LTC2203/LTC2202 Data Sheet, Rev. A, Milpitas, CA, 2006.
- Lyons, L. R. “Plasma processes in the Earth’s radiation belts”. In *Solar System Plasma Physics*, vol. 3, L. J. Lanzerotti; C. F. Kennel; and E. N. Parker, eds., chap. 3.1.4, pp. 137–164. New York, NY: North-Holland, 1979. ISBN 0-444-85267-0.
- Ma, T. P. and Dressendorfer, P. V., eds. *Ionizing Radiation Effects on MOS Devices and Circuits*. New York, NY: John Wiley & Sons, 1989. ISBN 0-471-84893-X.
- Markas, T. “Hardware implementations of data compression algorithms for aerospace type applications”. In *9<sup>th</sup> AIAA Computing in Aerospace Conference, San Diego, CA, Oct. 19-21, 1993, Technical Papers Pt. 1*, pp. 606–614. Washington, DC: American Institute of Aeronautics and Astronautics, October 1993.



- Mason, S. J. "Feedback theory—some properties of signal flow graphs". *Proceedings of the IRE*, vol. 41, no. 9, pp. 1144–1156, September 1953. doi:10.1109/JRPROC.1953.274449.
- Matsumoto, H.; Nagano, I.; Anderson, R. R.; Kojima, H.; Hashimoto, K.; Tsutsui, M.; Okada, T.; Kimura, I.; Omura, Y.; and Okada, M. "Plasma wave observations with GEOTAIL spacecraft". *Journal of Geomagnetism and Geoelectricity*, vol. 46, no. 1, pp. 59–95, January 1994.
- Maxim Integrated Products. *Reference Voltage for Multiple ADCs*. AN994 Application Note, Sunnyvale, CA, 6 March 2002.
- . *UCSP, Single-Supply, Low-Noise, Low-Distortion, Rail-to-Rail Op Amps*. MAX4252 Data Sheet, Rev. 6, Sunnyvale, CA, 3 November 2003.
- Maxwell Technologies. *16-Bit Latchup Protected Analog-to-Digital Converter*. 7809LP Data Sheet, Ver. 01.11.05, Rev. 7, San Diego, CA, 2005.
- Maynard, N. C.; Bielecki, E. A.; and Burdick, H. F. "Instrumentation for vector electric field measurements from DE-B". *Space Science Instrumentation*, vol. 5, no. 4, pp. 523–534, December 1981.
- Mazur, J. E. "An overview of the space radiation environment". <http://www.aero.org/publications/crosslink/summer2003/02.html> (accessed 21 November 2009), 2003.
- McCormick, N. J. *Reliability and Risk Analysis: Methods and Nuclear Power Applications*. New York, NY: Academic Press, 1981. ISBN 0-12-482360-2.
- McCreary, J. L. "Matching properties, and voltage and temperature dependence of MOS capacitors". *IEEE Journal of Solid-State Circuits*, vol. 16, no. 6, pp. 608–616, December 1981.
- McLean, F. B. "A framework for understanding radiation-induced interface states in SiO<sub>2</sub> MOSstructures". *IEEE Transactions on Nuclear Science*, vol. 27, no. 6, pp. 1651–1657, December 1980. doi:10.1109/TNS.1980.4331084.

- McLean, F. B.; Ausman, Jr., G. A.; Boesch, Jr., H. E.; and McGarrity, J. M. “Application of stochastic hopping transport to hole conduction in amorphous SiO<sub>2</sub>”. *Journal of Applied Physics*, vol. 47, no. 4, pp. 1529–1532, April 1976a. doi:10.1063/1.322767.
- McLean, F. B.; Boesch, H. E.; and McGarrity, J. M. “Hole transport and recovery characteristics of SiO<sub>2</sub> gate insulators”. *IEEE Transactions on Nuclear Science*, vol. 23, no. 6, pp. 1506–1512, December 1976b. doi:10.1109/TNS.1976.4328530.
- McLean, F. B.; Boesch, Jr., H. E.; and Oldham, T. R. “Electron-hole generation, transport, and trapping in SiO<sub>2</sub>”. In *Ionizing Radiation Effects on MOS Devices and Circuits*, T. P. Ma and P. V. Dressendorfer, eds., chap. 3, pp. 87–192. New York, NY: John Wiley & Sons, 1989. ISBN 0-471-84893-X.
- McLean, F. B. and Oldham, T. R. “Charge funneling in N- and P-type Si substrates”. *IEEE Transactions on Nuclear Science*, vol. 29, no. 6, pp. 2017–2023, December 1982. doi:10.1109/TNS.1982.4336489.
- . “Basic mechanisms of radiation effects in electronic materials and devices”. In *1987 IEEE Nuclear and Space Radiation Effects Conference (NSREC) Short Course*, p. Sec. 1. Snowmass, CO: IEEE NPSS, 27 July 1987.
- McMahan, M. A. “Radiation effects testing at the 88-inch cyclotron”. In *Fifth European Conference on Radiation and Its Effects on Components and Systems (RADECS), 1999.*, pp. 142–147. IEEE, Fontevraud, France: IEEE Press, 13–17 September 1999. ISBN 0-7803-5726-4. doi:10.1109/RADECS.1999.858563.
- . “The Berkeley Accelerator Space Effects (BASE) Facility”. In *Proceedings of the Space Nuclear Conference*. San Diego, CA: American Nuclear Society, 5–9 June 2005a. ISBN 0-89448-696-9.
- . “The Berkeley Accelerator Space Effects (BASE) Facility—A new mission for the 88-inch cyclotron at LBNL”. *Nuclear Instruments and Methods in Physics Research Section B: Beam Interactions with Materials and Atoms*, vol.

- 241, no. 1–4, pp. 409–413, December 2005b. doi:doi:10.1016/j.nimb.2005.07.050. The Application of Accelerators in Research and Industry - Proceedings of the Eighteenth International Conference on the Application of Accelerators in Research and Industry (CAARI 2004).
- McMahan, M. A.; Blackmore, E.; Cascio, E. W.; Castaneda, C.; von Przewoski, B.; and Eisen, H. “Standard practice for dosimetry of proton beams for use in radiation effects testing of electronics”. In *IEEE Radiation Effects Data Workshop*, pp. 135–141. IEEE, Tucson, AZ: IEEE Press, 14–18 July 2008. ISBN 978-1-4244-2545-7. doi:10.1109/REDW.2008.31.
- McMahan, M. A.; Leitner, D.; Gimpel, T. L.; Morel, J. R.; Ninemire, B. F.; Siero, R.; Silver, C.; and Thatcher, R. K. “A 16 MeV/nucleon cocktail for heavy ion testing”. In *IEEE Radiation Effects Data Workshop*, pp. 156–159. IEEE, Atlanta, GA: IEEE Press, 22, July 2004. ISBN 0-7803-8697-3. doi:10.1109/REDW.2004.1352923.
- McMorrow, D.; Buchner, S.; Lotshaw, W. T.; Melinger, J.; Maher, M.; and Savage, M. W. “Demonstration of single-event effects induced by through-wafer two-photon absorption”. *IEEE Transactions on Nuclear Science*, vol. 51, no. 6, pp. 3553–3557, December 2004. doi:10.1109/TNS.2004.839106.
- McMorrow, D.; Ferlet-Cavrois, V.; Paillet, P.; Duhamel, O.; Baggio, J.; Boos, J. B.; and Melinger, J. S. “Transient response of semiconductor electronics to ionizing radiation. recent developments in charge-collection measurement”. *IEEE Transactions on Nuclear Science*, vol. 54, no. 4, pp. 1010–1017, August 2007. doi:10.1109/TNS.2007.896345.
- McMorrow, D.; Lotshaw, W. T.; Melinger, J. S.; Buchner, S.; and Pease, R. L. “Subbandgap laser-induced single event effects: Carrier generation via two-photon absorption”. *IEEE Transactions on Nuclear Science*, vol. 49, no. 6, pp. 3002–3008, December 2002. doi:10.1109/TNS.2002.805337.
- McMorrow, D.; Melinger, J. S.; Thantu, N.; Campbell, A. B.; Weatherford, T. R.; Knudson, A. R.; Lan Hu Tran; and Peczalski, A. “Charge-collection mechanisms

- of heterostructure FETs". *IEEE Transactions on Nuclear Science*, vol. 41, no. 6, pp. 2055–2062, December 1994. doi:10.1109/23.340542.
- Meisenheimer, T. L. and Fleetwood, D. M. "Effect of radiation-induced charge on  $1/f$  noise in MOS devices". *IEEE Transactions on Nuclear Science*, vol. 37, no. 6, pp. 1696–1702, December 1990. doi:10.1109/23.101179.
- Melinger, J. S.; Buchner, S.; McMorro, D.; Stapor, W. J.; Weatherford, T. R.; Campbell, A. B.; and Eisen, H. "Critical evaluation of the pulsed laser method for single event effects testing and fundamental studies". *IEEE Transactions on Nuclear Science*, vol. 41, no. 6, pp. 2574–2584, December 1994. doi:10.1109/23.340618.
- Messenger, G. C. "A general proof of the  $\beta$  degradation equation for bulk displacement damage". *IEEE Transactions on Nuclear Science*, vol. 20, no. 1, pp. 809–810, February 1973. doi:10.1109/TNS.1973.4327002.
- . "Collection of charge on junction nodes from ion tracks". *IEEE Transactions on Nuclear Science*, vol. 29, no. 6, pp. 2024–2031, December 1982. doi:10.1109/TNS.1982.4336490.
- Messenger, G. C. and Ash, M. S. *The Effects of Radiation on Electronic Systems*. 2<sup>nd</sup> ed. New York, NY: Van Nostrand Reinhold, 1992. ISBN 0-442-23952-1.
- Meyer, P. and Vernet, N. "Impedance of a short antenna in a warm magnetoplasma". *Radio Science*, vol. 9, no. 3, pp. 409–416, March 1974. doi:10.1029/RS009i003p00409.
- Meyer-Vernet, N. "On natural noises detected by antennas in plasmas". *Journal of Geophysical Research*, vol. 84, no. A9, pp. 5373–5377, 1 September 1979. doi:10.1029/JA084iA09p05373.
- Meyer-Vernet, N.; Meyer, P.; and Perche, C. "Losses due to the inhomogeneous sheath surrounding an antenna in a plasma". *Radio Science*, vol. 13, no. 1, pp. 69–73, January–February 1978. doi:10.1029/RS013i001p00069.

- Meyer-Vernet, N. and Perche, C. "Tool kit for antennae and thermal noise near the plasma frequency". *Journal of Geophysical Research*, vol. 94, no. A3, pp. 2405–2415, March 1989. doi:10.1029/JA094iA03p02405.
- MIL-STD-810G. "Test method standard: Environmental engineering considerations and laboratory tests". U. S. Department of Defense, 31 October 2008.
- MIL-STD-883G. "Test method standard: Microelectronics". U. S. Department of Defense, 28 February 2006.
- Mini-Circuits. *How RF Transformers Work*. AN20-001 Application Note, Brooklyn, NY, 18 October 1999.
- Mlodnosky, R. F. and Garriott, O. K. "The v.l.f. admittance of a dipole in the lower ionosphere". In *Proceedings of the International Conference on the Ionosphere held July 1962 at Imperial College, London*, A. C. Stickland, ed., pp. 484–491. The Institute of Physics and the Physical Society, London, U. K.: The Institute of Physics and the Physical Society, 1963.
- Morioka, A.; Oya, H.; and Kobayashi, K. "Polarization and mode identification of auroral kilometric eadiation by PWS system onboard the Akebono (EXOS-D) satellite". *Journal of Geomagnetism and Geoelectricity*, vol. 42, no. 4, pp. 443–458, 1990.
- Moschytz, G. S., ed. *MOS Switched-Capacitor Filters: Analysis and Design*. IEEE Press Selected Reprint Series. New York, NY: IEEE Press, 1984. ISBN 0-87942-177-0.
- Moss, S. C.; LaLumondiere, S. D.; Scarpulla, J. R.; MacWilliams, K. P.; Crain, W. R.; and Koga, R. "Correlation of picosecond laser-induced latchup and energetic particle-induced latchup in CMOS test structures". *IEEE Transactions on Nuclear Science*, vol. 42, no. 6, pp. 1948–1956, December 1995. doi:10.1109/23.489239.
- Mossawir, B.; Linscott, I. R.; Inan, U. S.; Roeder, J. L.; Osborn, J. V.; Witczak, S. C.; King, E. E.; and LaLumondiere, S. D. "A TID and SEE radiation-hardened,

- wideband, low-noise amplifier”. *IEEE Transactions on Nuclear Science*, vol. 53, no. 6, pp. 3439–3448, December 2006. doi:10.1109/TNS.2006.886219.
- Motchenbacher, C. D. and Fitchen, F. C. *Low-Noise Electronic Design*. New York, NY: John Wiley & Sons, 1973. ISBN 0-471-61950-7.
- Mott-Smith, H. M. and Langmuir, I. “The theory of collectors in gaseous discharges”. *Physical Review*, vol. 28, no. 4, pp. 727–763, October 1926. doi:10.1103/PhysRev.28.727.
- Mozer, F. S. “Analysis of techniques for measuring DC and AC electric fields in the Magnetosphere”. *Space Science Reviews*, vol. 14, no. 2, pp. 272–313, February 1973. doi:10.1007/BF02432099.
- Mozer, F. S.; Cattell, C. A.; Temerin, M.; Torbert, R. B.; von Glinski, S.; Woldorff, M.; and Wygant, J. “The DC and AC electric field, plasma density, plasma temperature, and field-aligned current experiments on the S3-3 satellite”. *Journal of Geophysical Research*, vol. 84, no. A10, pp. 5875–5884, October 1979. doi:10.1029/JA084iA10p05875.
- Nakatani, D. T. and Kuehl, H. H. “Input impedance of a short dipole antenna in a warm anisotropic plasma: I - kinetic theory”. *Radio Science*, vol. 11, no. 5, pp. 433–444, May 1976. doi:10.1029/RS011i005p00433.
- National Semiconductor Corporation. *Noise Specs Confusing?* AN104 Application Note, Santa Clara, CA, May 1974.
- Nauta, B. “A CMOS transconductance-C filter technique for very high frequencies”. *IEEE Journal of Solid-State Circuits*, vol. 27, no. 2, pp. 142–153, February 1992. doi:10.1109/4.127337.
- NCRP. “Ionizing radiation exposure of the population of the united states”. NCRP Report 160, National Council on Radiation Protection and Measurements, Bethesda, MD, 3 March 2009.

- Neary, G. J. "Irradiation of simple biological specimens by charged particles". In *The Uses of Cyclotrons in Chemistry, Metallurgy and Biology: Proceedings of a Conference held at St. Catherine's College, Oxford, 22-23 September 1969*, C. B. Amphlett, ed., pp. 194-203. St. Catherine's College, London, U. K.: Butterworths, 22-23 September 1970. ISBN 0-408-70029-7.
- Nedungadi, A. and Viswanathan, T. "Design of linear CMOS transconductance elements". *IEEE Transactions on Circuits and Systems*, vol. 31, no. 10, pp. 891-894, October 1984.
- Nichols, D. K.; Price, W. E.; and Andrews, J. L. "The dependence of single event upset on proton energy (15-590 MeV)". *IEEE Transactions on Nuclear Science*, vol. 29, no. 6, pp. 2081-2084, December 1982. doi:10.1109/TNS.1982.4336500.
- Nicolet, M. "The properties and constitution of the upper atmosphere". In *Physics of the Upper Atmosphere*, J. A. Ratcliffe, ed., chap. 1, pp. 17-72. New York, NY: Academic Press, 1960.
- Niu, G.; Mathew, S. J.; Banerjee, G.; Cressler, J. D.; Clark, S. D.; Palmer, M. J.; and Subbanna, S. "Total dose effects on the shallow-trench isolation leakage current characteristics in a 0.35 $\mu$ m SiGe BiCMOS technology". *IEEE Transactions on Nuclear Science*, vol. 46, no. 6, pp. 1841-1847, December 1999. doi:10.1109/23.819163.
- Nowlin, N.; Bailey, J.; Turfler, B.; and Alexander, D. "A total-dose hardening-by-design approach for high-speed mixed-signal CMOS integrated circuits". *International Journal of High Speed Electronics and Systems*, vol. 14, no. 2, pp. 367-278, June 2004. doi:10.1142/S0129156404002417.
- Nowlin, R. N.; Enlow, E. W.; Schrimpf, R. D.; and Combs, W. E. "Trends in the total-dose response of modern bipolar transistors". *IEEE Transactions on Nuclear Science*, vol. 39, no. 6, pp. 2026-2035, December 1992. doi:10.1109/23.211400.
- Nowlin, R. N.; McEndree, S. R.; Wilson, A. L.; and Alexander, D. R. "A new total-dose-induced parasitic effect in enclosed-geometry transistors". *IEEE Transactions*

- on Nuclear Science*, vol. 52, no. 6, pp. 2495–2502, December 2005. doi:10.1109/TNS.2005.860713.
- Nuttall, A. “Some windows with very good sidelobe behavior”. *IEEE Transactions on Acoustics, Speech and Signal Processing*, vol. 29, no. 1, pp. 84–91, February 1981.
- Nyquist, H. “Certain topics in telegraph transmission theory”. *Transactions of the American Institute of Electrical Engineers*, vol. 47, no. 2, pp. 617–644, April 1928. doi:10.1109/T-AIEE.1928.5055024.
- O’Brien, B. J.; Laughlin, C. D.; and van Allen, J. A. “Geomagnetically trapped radiation produced by a high-altitude nuclear explosion on July 9, 1962”. *Nature*, vol. 195, no. 4845, pp. 939–943, September 1962. doi:10.1038/195939a0.
- Okwit, S. “An historical view of the evolution of low-noise concepts and techniques”. *IEEE Transactions on Microwave Theory and Techniques*, vol. 32, no. 9, pp. 1068–1082, September 1984.
- Oldham, T. R. *Ionizing Radiation Effects in MOS Oxides*. River Edge, NJ: World Scientific, 1999. ISBN 9810233264.
- . “How device scaling affects single event effects sensitivity”. In *2003 IEEE Nuclear and Space Radiation Effects Conference (NSREC) Short Course*, p. Sec. 4. Monterey, CA: IEEE NPSS, 21 July 2003.
- Oldham, T. R.; Lelis, A. J.; Boesch, H. E.; Benedetto, J. M.; McLean, F. B.; and McGarrity, J. M. “Post-irradiation effects in field-oxide isolation structures”. *IEEE Transactions on Nuclear Science*, vol. 34, no. 6, pp. 1184–1189, December 1987. doi:10.1109/TNS.1987.4337450.
- Oldham, T. R. and McGarrity, J. M. “Ionization of SiO<sub>2</sub> by heavy charged particles”. *IEEE Transactions on Nuclear Science*, vol. 28, no. 6, pp. 3975–3980, December 1981. doi:10.1109/TNS.1981.4335658.



- . “Comparison of  $^{60}\text{Co}$  response and 10 KeV X-ray response in MOS capacitors”. *IEEE Transactions on Nuclear Science*, vol. 30, no. 6, pp. 4377–4381, December 1983. doi:10.1109/TNS.1983.4333141.
- Oldham, T. R. and McLean, F. B. “Total ionizing dose effects in MOS oxides and devices”. *IEEE Transactions on Nuclear Science*, vol. 50, no. 3, pp. 483–499, June 2003. doi:10.1109/TNS.2003.812927.
- Onsager, L. “Initial recombination of ions”. *Physical Review*, vol. 54, no. 8, pp. 554–557, October 1938. doi:10.1103/PhysRev.54.554.
- Oppenheim, A. V.; Schafer, R. W.; and Buck, J. *Discrete-Time Signal Processing*. 2<sup>nd</sup> ed. Upper Saddle River, NJ: Prentice Hall, 1999. ISBN 0-13-754920-2.
- Osborn, J. V.; Lacoe, R. C.; Mayer, D. C.; and Yabiku, G. “Total dose hardness of three commercial CMOS microelectronics foundries”. *IEEE Transactions on Nuclear Science*, vol. 45, no. 3, pp. 1458–1463, June 1998. doi:10.1109/23.685223.
- Papastamatiou, M.; Arpatzanis, N.; Papaioannou, G. J.; Papastergiou, C.; and Christou, A. “Neutron radiation effects in high electron mobility transistors [AlGaAs/GaAs]”. *IEEE Transactions on Nuclear Science*, vol. 44, no. 3, pp. 364–372, March 1997. doi:10.1109/16.556145.
- Park, C. and Schaumann, R. “Design of a 4-MHz analog integrated CMOS transconductance-C bandpass filter”. *IEEE Journal of Solid-State Circuits*, vol. 23, no. 4, pp. 987–996, August 1988. doi:10.1109/4.350.
- Park, C.-S. and Schaumann, R. “A high-frequency CMOS linear transconductance element”. *IEEE Transactions on Circuits and Systems*, vol. 33, no. 11, pp. 1132–1138, November 1986.
- Parker, E. N. “Dynamics of the interplanetary gas and magnetic fields”. *Astrophysical Journal*, vol. 128, pp. 664–676, November 1958. doi:10.1086/146579.
- Parrot, M.; Benoist, D.; Berthelier, J. J.; Błęcki, J.; Chapuis, Y.; Colin, F.; Elie, F.; Fergeau, P.; Lagoutte, D.; Lefeuvre, F.; Legendre, C.; Lévêque, M.; Pinçon, J. L.;

- Poirier, B.; Seran, H.-C.; and Zamora, P. "The magnetic field experiment IMSC and its data processing onboard DEMETER: Scientific objectives, description and first results". *Planetary and Space Science*, vol. 54, no. 5, pp. 441–455, April 2006. doi:10.1016/j.pss.2005.10.015.
- Paschal, E. W. "The design of broad-band VLF receivers with air-core loop antennas". Tech. rep., Stanford University, Stanford, CA, May 1988.
- Pease, R. L. "Total ionizing dose effects in bipolar devices and circuits". *IEEE Transactions on Nuclear Science*, vol. 50, no. 3, pp. 539–551, June 2003. doi:10.1109/TNS.2003.813133.
- Pease, R. L.; Sternberg, A.; Massengill, L.; Schrimpf, R.; Buchner, S.; Savage, M.; Titus, J.; and Turflinger, T. "Critical charge for single-event transients (SETs) in bipolar linear circuits". *IEEE Transactions on Nuclear Science*, vol. 48, no. 6, pp. 1966–1972, December 2001. doi:10.1109/23.983158.
- Pease, R. L.; Turfler, R. M.; Platteter, D.; Emily, D.; and Blice, R. "Total dose effects in recessed oxide digital bipolar microcircuits". *IEEE Transactions on Nuclear Science*, vol. 30, no. 6, pp. 4216–4223, December 1983. doi:10.1109/TNS.1983.4333111.
- Pedersen, A.; Cornilleau-Wehrlin, N.; de La Porte, B.; Roux, A.; Bouabdellah, A.; Décréau, P. M. E.; Lefeuvre, F.; Sene, F. X.; Gurnett, D.; Huff, R.; Gustafsson, G.; Holmgren, G.; Woolliscroft, L.; Alleyne, H. S. C.; Thompson, J. A.; and Davies, P. H. N. "The wave experiment consortium (WEC)". *Space Science Reviews*, vol. 79, no. 1–2, pp. 93–106, January 1997. doi:10.1023/A:1004927225495.
- Pelgrom, M. J. M.; Duinmaijer, A. C. J.; and Welbers, A. P. G. "Matching properties of MOS transistors". *IEEE Journal of Solid-State Circuits*, vol. 24, no. 5, pp. 1433–1439, October 1989. doi:10.1109/JSSC.1989.572629.
- Pennock, J. L. "CMOS triode transconductor for continuous-time active integrated filters". *Electronics Letters*, vol. 21, no. 18, pp. 817–818, 29 August 1985. doi:10.1049/el:19850576.

- Petersen, E. L. “SEE rate calculations using the effective flux approach and a generalized figure of merit approximation”. *IEEE Transactions on Nuclear Science*, vol. 42, no. 6, pp. 1995–2003, December 1995. doi:10.1109/23.489245.
- Petersen, E. L.; Pickel, J. C.; Adams, Jr., J. H.; and Smith, E. C. “Rate prediction for single event effects—a critique”. *IEEE Transactions on Nuclear Science*, vol. 39, no. 6, pp. 1577–1599, December 1992. doi:10.1109/23.211340.
- Pfaff, R. F.; Borovsky, J. E.; and Young, D. T., eds. *Measurement Techniques in Space Plasmas: Particles, Geophysical Monograph*, vol. 102. Washington, DC: American Geophysical Union, 1998. ISBN 0-87590-085-2.
- Pfister, G. and Scher, H. “Dispersive (non-Gaussian) transient transport in disordered solids.” *Advances in Physics*, vol. 27, no. 5, pp. 747–798, September 1978.
- Pierret, R. F. *Field Effect Devices, Molecular Series on Solid State Devices*, vol. 4. 2<sup>nd</sup> ed. Reading, MA: Addison-Wesley, 1990. ISBN 0-201-12298-7.
- Pitman, J. *Probability*. New York, NY: Springer-Verlag, 1993. ISBN 0-387-97974-3.
- Platino, M.; Inan, U. S.; Bell, T. F.; Gurnett, D. A.; Pickett, J. S.; Canu, P.; and Décréau, P. M. E. “Whistlers observed by the Cluster spacecraft outside the plasmasphere”. *Journal of Geophysical Research–Space Physics*, vol. 110, no. A03212, p. 3212, March 2005. doi:10.1029/2004JA010730.
- Plummer, J. D.; Deal, M. D.; and Griffin, P. B. *Silicon VLSI Technology: Fundamentals, Practice, and Modeling*. Upper Saddle River, NJ: Prentice Hall, 2000. ISBN 0-13-085037-3.
- Pospieszalski, M. W. “Extremely low-noise amplification with cryogenic FETs and HFETs: 1970–2004”. *IEEE Microwave Magazine*, vol. 6, no. 3, pp. 62–75, September 2005. doi:10.1109/MMW.2005.1511915.
- Primdahl, F. “Scalar magnetometers for space applications”. In *Measurement Techniques in Space Plasmas: Fields, Geophysical Monographs*, vol. 103, R. F. Pfaff;

- J. E. Borovsky; and D. T. Young, eds., pp. 85–100. Washington, DC: American Geophysical Union, 1998. ISBN 0-87590-086-0.
- Rashkeev, S. N.; Cirba, C. R.; Fleetwood, D. M.; Schrimpf, R. D.; Witczak, S. C.; Michez, A.; and Pantelides, S. T. “Physical model for enhanced interface-trap formation at low dose rates”. *IEEE Transactions on Nuclear Science*, vol. 49, no. 6, pp. 2650–2655, December 2002. doi:10.1109/TNS.2002.805387.
- Rasmussen, R. D. “Spacecraft electronics design for radiation tolerance”. *Proceedings of the IEEE*, vol. 76, no. 11, pp. 1527–1537, November 1988. doi:10.1109/5.90116.
- Ratcliffe, J. A.; Chapman, S.; Nicolet, M.; Newell, Jr., H. E.; Friedman, H.; Bates, D. R.; Booker, H. G.; Weekes, K.; Vestine, E. H.; Greenhow, J. S.; and Lovell, C. B. “Advances during the International Geophysical Year 1957/58”. In *Physics of the Upper Atmosphere*, J. A. Ratcliffe, ed., chap. 12, pp. 551–563. New York, NY: Academic Press, 1960.
- Razavi, B. *Design of Analog CMOS Integrated Circuits*. Boston, MA: McGraw-Hill, 2001. ISBN 0-07-238032-2.
- Reed, R. A.; Marshall, P. W.; Pickel, J. C.; Carts, M. A.; Fodness, B.; Niu, G.; Fritz, K.; Vizkelethy, G.; Dodd, P.; Irwin, T.; Cressler, J. D.; Krithivasan, R.; Riggs, P.; Prairie, J.; Randall, B.; Gilbert, B.; and LaBel, K. A. “Heavy-ion broad-beam and microprobe studies of single-event upsets in 0.20- $\mu\text{m}$  SiGe heterojunction bipolar transistors and circuits”. *IEEE Transactions on Nuclear Science*, vol. 50, no. 6, pp. 2184–2190, December 2003. doi:10.1109/TNS.2003.821815.
- Reiner, M. J.; Fainberg, J.; Kaiser, M. L.; and Stone, R. G. “Type iii radio source located by Ulysses/Wind triangulation”. *Journal of Geophysical Research*, vol. 103, no. A2, pp. 1923–1931, February 1998. doi:10.1029/97JA02646.
- Reinisch, B. W.; Haines, D. M.; Bibl, K.; Cheney, G.; Galkin, I. A.; Huang, X.; Myers, S. H.; Sales, G. S.; Benson, R. F.; Fung, S. F.; Green, J. L.; Boardson, S.; Taylor, W. W. L.; Bougeret, J.-L.; Manning, R.; Meyer-Vernet, N.; Moncuquet,

- M.; Carpenter, D. L.; Gallagher, D. L.; and Reiff, P. "The radio plasma imager investigation on the IMAGE spacecraft". *Space Science Reviews*, vol. 91, no. 1–2, pp. 319–359, January 2000. doi:10.1023/A:1005252602159.
- Revesz, A. G. "Defect structure and irradiation behavior of noncrystalline SiO<sub>2</sub>". *IEEE Transactions on Nuclear Science*, vol. 18, no. 6, pp. 113–116, December 1971. doi:10.1109/TNS.1971.4326421.
- Reznikov, A. E. and Shkliar, D. R. "Single VLF plane wave characteristics and plasma parameter determination by means of amplitude measurements on board a satellite". *Annales de Géophysique*, vol. 38, no. 5, pp. 669–673, 1982.
- Roederer, J. G. "Earth's magnetosphere: Global problems in magnetospheric plasma physics". In *Solar System Plasma Physics*, vol. 2, L. J. Lanzerotti; C. F. Kennel; and E. N. Parker, eds., chap. 2.1, pp. 1–56. New York, NY: North-Holland, 1979. ISBN 0-444-85267-0.
- Rorden, L. H.; Orsak, L. E.; Ficklin, B. P.; and Stehle, R. H. "Instruments for the Stanford University/Stanford Research Institute VLF experiment (4917) on the EOGO satellite". Supplemental Report NASA-CR-139258, Stanford Research Institute, Menlo Park, CA, May 1966.
- Rosenbaum, S. E.; Jelloian, L. M.; Larson, L. E.; Mishra, U. K.; Pierson, D. A.; Thompson, M. S.; Liu, T.; and Brown, A. S. "A 2-GHz three-stage AlInAs-GaInAs-InP HEMT MMIC low-noise amplifier". *IEEE Microwave and Guided Wave Letters*, vol. 3, no. 8, pp. 265–267, August 1993. doi:10.1109/75.242220.
- S-300 Experimenters. "Measurements of electric and magnetic wave fields and of cold plasma parameters on-board GEOS-1. Preliminary results". *Planetary and Space Science*, vol. 27, no. 4, pp. 317–339, April 1979. doi:10.1016/0032-0633(79)90110-7.
- Sagalyn, R. C.; Smiddy, M.; and Wisnia, J. "Measurement and interpretation of ion density distributions in the daytime F region". *Journal of Geophysical Research*, vol. 68, no. 1, pp. 199–211, 1 January 1963. doi:10.1029/JZ068i001p00199.

- Samavati, H.; Hajimiri, A.; Shahani, A. R.; Nasserbakht, G. N.; and Lee, T. H. "Fractal capacitors". *IEEE Journal of Solid-State Circuits*, vol. 33, no. 12, pp. 2035–2041, December 1998. doi:10.1109/4.735545.
- Savage, M. W.; Titus, J. L.; Turflinger, T. L.; Pease, R. L.; and Poivey, C. "A comprehensive analog single-event transient analysis methodology". *IEEE Transactions on Nuclear Science*, vol. 51, no. 6, pp. 3546–3552, December 2004. doi:10.1109/TNS.2004.839107.
- Scarabucci, R. R. "Satellite observations of equatorial phenomena and defocusing of VLF electromagnetic waves". *Journal of Geophysical Research–Space Physics*, vol. 75, no. 1, pp. 69–84, January 1970. doi:10.1029/JA075i001p00069.
- Scarf, F. L. "The AMPTE/CCE plasma wave investigation". *IEEE Transactions on Geoscience and Remote Sensing*, vol. 23, no. 3, pp. 250–252, May 1985. doi:10.1109/TGRS.1985.289522.
- Scarf, F. L.; Crook, G. M.; Green, I. M.; and Virobik, P. F. "Initial results of the Pioneer 8 VLF electric field experiment". *Journal of Geophysical Research–Space Physics*, vol. 73, no. 21, pp. 6665–6686, November 1968. doi:10.1029/JA073i021p06665.
- Scarf, F. L.; Green, I. M.; and Crook, G. M. "The Pioneer 9 electric field experiment: Part 1, near Earth observations". *Cosmic Electrodynamics*, vol. 1, no. 4, pp. 496–512, October 1971.
- Scarf, F. L. and Gurnett, D. A. "A plasma wave investigation for the Voyager mission". *Space Science Reviews*, vol. 21, no. 3, pp. 289–308, December 1977. doi:10.1007/BF00211543.
- Scarf, F. L.; Taylor, W. W. L.; and Virobik, P. F. "The Pioneer Venus Orbiter plasma wave investigation". *IEEE Transactions on Geoscience and Remote Sensing*, vol. GE-18, no. 1, pp. 36–38, January 1980. doi:10.1109/TGRS.1980.350257.

- Schaumann, R. "Design of continuous-time fully integrated filters: A review". *IEEE Proceedings G: Circuits, Devices and Systems*, vol. 136, no. 4, pp. 184–190, August 1989.
- . "Continuous-time integrated filters—a tutorial". In *Integrated Continuous-Time Filters: Principles, Design, and Applications*, Y. P. Tsividis and J. O. Voorman, eds., chap. 1, pp. 3–14. New York, NY: IEEE Press, 1993. ISBN 0-7803-0425-X.
- Schaumann, R. and van Valkenburg, M. E. *Design of Analog Filters*. Oxford, U.K.: Oxford University Press, 2001. ISBN 0-119-511877-4.
- Schiff, M. L. "Impedance of a short dipole antenna in a warm isotropic plasma". *Radio Science*, vol. 5, no. 12, pp. 1489–1496, December 1970. doi:10.1029/RS005i012p01489.
- Schmidt, D. M.; Wu, A.; Schrimpf, R. D.; Fleetwood, D. M.; and Pease, R. L. "Modeling ionizing radiation induced gain degradation of the lateral PNP bipolar junction transistor". *IEEE Transactions on Nuclear Science*, vol. 43, no. 6, pp. 3032–3039, December 1996. doi:10.1109/23.556902.
- Schulz, M. and Lanzerotti, L. J. *Particle Diffusion in the Radiation Belts, Physics and Chemistry in Space*, vol. 7. New York, NY: Springer-Verlag, 1974. ISBN 0-387-06398-6.
- Schunk, R. W. and Watkins, S. D. "Comparison of solutions to the thirteen-moment and standard transport equations for low speed thermal proton flows". *Planetary and Space Science*, vol. 27, no. 4, pp. 433–444, April 1979. doi: DOI:10.1016/0032-0633(79)90120-X.
- Schuster, A. "On the Investigation of Hidden Periodicities with Application to a Supposed 26 Day Period of Meteorological Phenomena". *Terrestrial Magnetism and Atmospheric Electricity*, vol. 3, no. 1, pp. 13–41, 1898. doi:10.1029/TM003i001p00013.

- Schwank, J. R.; Ferlet-Cavrois, V.; Shaneyfelt, M. R.; Paillet, P.; and Dodd, P. E. "Radiation effects in SOI technologies". *IEEE Transactions on Nuclear Science*, vol. 50, no. 3, pp. 522–538, June 2003. doi:10.1109/TNS.2003.812930.
- Schwank, J. R.; Winokur, P. S.; McWhorter, P. J.; Sexton, F. W.; Dressendorfer, P. V.; and Turpin, D. C. "Physical mechanisms contributing to device "rebound"". *IEEE Transactions on Nuclear Science*, vol. 31, no. 6, pp. 1434–1438, December 1984. doi:10.1109/TNS.1984.4333525.
- Scofield, J. H.; Doerr, T. P.; and Fleetwood, D. M. "Correlation between preirradiation  $1/f$  noise and postirradiation oxide-trapped charge in MOS transistors". *IEEE Transactions on Nuclear Science*, vol. 36, no. 6, pp. 1946–1953, December 1989. doi:10.1109/23.45391.
- Sedra, A. S. and Brackett, P. O. *Filter Theory and Design: Active and Passive*. Matrix Series in Circuits and Systems. Beaverton, OR: Matrix Publishers, 1978. ISBN 0-916469-14-2.
- Sentman, D. D. "Thermal fluctuations and the diffuse electrostatic emissions". *Journal of Geophysical Research*, vol. 87, no. A3, pp. 1455–1472, 1 March 1982. doi:10.1029/JA087iA03p01455.
- Sexton, F. W. "Destructive single-event effects in semiconductor devices and ICs". *IEEE Transactions on Nuclear Science*, vol. 50, no. 3, pp. 603–621, June 2003. doi:10.1109/TNS.2003.813137.
- Shaneyfelt, M. R.; Dodd, P. E.; Draper, B. L.; and Flores, R. S. "Challenges in hardening technologies using shallow-trench isolation". *IEEE Transactions on Nuclear Science*, vol. 45, no. 6, pp. 2584–2592, December 1998. doi:10.1109/23.736501.
- Shaneyfelt, M. R.; Pease, R. L.; Schwank, J. R.; Maher, M. C.; Hash, G. L.; Fleetwood, D. M.; Dodd, P. E.; Reber, C. A.; Witczak, S. C.; Riewe, L. C.; Hjalmarson, H. P.; Banks, J. C.; Doyle, B. L.; and Knapp, J. A. "Impact



- of passivation layers on enhanced low-dose-rate sensitivity and pre-irradiation elevated-temperature stress effects in bipolar linear ICs". *IEEE Transactions on Nuclear Science*, vol. 49, no. 6, pp. 3171–3179, December 2002. doi:10.1109/TNS.2002.805365.
- Shannon, C. E. "Communication in the presence of noise". *Proceedings of the IRE*, vol. 37, no. 1, pp. 10–21, January 1949.
- Shawhan, S. D. "Magnetospheric plasma waves". In *Solar System Plasma Physics*, vol. 3, L. J. Lanzerotti; C. F. Kennel; and E. N. Parker, eds., chap. 3.1.6, pp. 211–270. New York, NY: North-Holland, 1979. ISBN 0-444-85267-0.
- Shawhan, S. D.; Gurnett, D. A.; Odem, D. L.; Helliwell, R. A.; and Park, C. G. "The plasma wave and quasi-static electric field instrument (PWI) for Dynamics Explorer-A". *Space Science Instrumentation*, vol. 5, no. 4, pp. 535–550, December 1981.
- Shockley, W. and Read, W. T. "Statistics of the recombinations of holes and electrons". *Physical Review*, vol. 87, no. 5, pp. 835–842, September 1952. doi:10.1103/PhysRev.87.835.
- Shyu, J.-B.; Temes, G. C.; and Krummenacher, F. "Random error effects in matched MOS capacitors and current sources". *IEEE Journal of Solid-State Circuits*, vol. 19, no. 6, pp. 948–956, December 1984.
- Singh, U. P. and Singh, D. P. "Intense low latitude VLF emissions observed aboard Ariel 4". *Journal of Geophysical Research*, vol. 103, no. A9, pp. 20727–20734, September 1998. doi:10.1029/98JA00066.
- Snare, R. C. "A history of vector magnetometry in space". In *Measurement Techniques in Space Plasmas: Fields, Geophysical Monographs*, vol. 103, R. F. Pfaff; J. E. Borovsky; and D. T. Young, eds., pp. 101–114. Washington, DC: American Geophysical Union, 1998. ISBN 0-87590-086-0.

- Snoeys, W. J.; Gutierrez, T. A. P.; and Anelli, G. "A new NMOS layout structure for radiation tolerance". *IEEE Transactions on Nuclear Science*, vol. 49, no. 4, pp. 1829–1833, August 2002. doi:10.1109/TNS.2002.801534.
- Spanjers, G.; Winter, J.; Cohen, D.; Adler, A.; Guarnieri, J.; Tolliver, M.; Ginet, G.; Dichter, B.; and Summers, J. "The AFRL demonstration and science experiments (DSX) for DoD space capability in the MEO". In *Proceedings of the 2006 IEEE Aerospace Conference*, 2.0501. Big Sky, MT, 4–11 March 2006. doi:10.1109/AERO.2006.1655750.
- Spasojević, M. *Global Dynamics of the Earth's Plasmasphere*. Ph.D. thesis, Stanford University, Stanford, CA, October 2003.
- Srour, J. R. and McGarrity, J. M. "Radiation effects on microelectronics in space". *Proceedings of the IEEE*, vol. 76, no. 11, pp. 1443–1469, November 1988. doi:10.1109/5.90114.
- Stanford Research Systems, Incorporated. *Model DS360 Ultra Low Distortion Function Generator: Operating Manual and Programming Reference*. Rev. 1.8, Sunnyvale, CA, January 1999.
- Stapor, W. J.; August, L. S.; Wilson, D. H.; Oldham, T. R.; and Murray, K. M. "Proton and heavy-ion radiation damage studies in MOS transistors". *IEEE Transactions on Nuclear Science*, vol. 32, no. 6, pp. 4399–4404, December 1985. doi:10.1109/TNS.1985.4334131.
- Stapor, W. J.; McDonald, P. T.; Knudson, A. R.; Campbell, A. B.; and Glagola, B. G. "Charge collection in silicon for ions of different energy but same linear energy transfer (LET)". *IEEE Transactions on Nuclear Science*, vol. 35, no. 6, pp. 1585–1590, December 1988. doi:10.1109/23.25502.
- Stassinopoulos, E. G. and Raymond, J. P. "The space radiation environment for electronics". *Proceedings of the IEEE*, vol. 76, no. 11, pp. 1423–1442, November 1988. doi:10.1109/5.90113.

- Stone, R. G.; Bougeret, J. L.; Caldwell, J.; Canu, P.; de Conchy, Y.; Cornilleau-Wehrlin, N.; Desch, M. D.; Fainberg, J.; Goetz, K.; and Goldstein, M. L. "The unified radio and plasma wave investigation". *Astronomy and Astrophysics Supplement Series*, vol. 92, no. 2, pp. 291–316, January 1992.
- Storey, L. R. O. "An investigation of whistling atmospherics". *Philosophical Transactions of the Royal Society of London. Series A—Mathematical and Physical Sciences*, vol. 246, no. 908, pp. 113–141, July 1953.
- Stutzman, W. L. and Thiele, G. A. *Antenna Theory and Design*. 2<sup>nd</sup> ed. New York, NY: John Wiley & Sons, 1998. ISBN 0-471-02590-9.
- Szczepański, S.; Wyszynski, A.; and Schaumann, R. "Highly linear voltage-controlled CMOS transconductors". *IEEE Transactions on Circuits and Systems I: Fundamental Theory and Applications*, vol. 40, no. 4, pp. 258–262, April 1993. doi:10.1109/81.224298.
- Sze, S. M. and Ng, K. K. *Physics of Semiconductor Devices*. 3<sup>rd</sup> ed. Hoboken, NJ: Wiley-Interscience, 2007. ISBN 0-471-14323-5.
- Tascione, T. F. *Introduction to the Space Environment*. 2<sup>nd</sup> ed. Malabar, FL: Krieger, 1994. ISBN 0-89464-044-5.
- Tribble, A. C. *The Space Environment: Implications for Spacecraft Design*. Princeton, NJ: Princeton University Press, 2003. ISBN 0-691-10299-6.
- Troutman, R. R. *Latchup in CMOS Technology: The Problem and Its Cure*. Boston, MA: Kluwer Academic Publishers, 1986. ISBN 0-89838-215-7.
- Tsurutani, B. T. and Lakhina, G. S. "Some basic concepts of wave-particle interactions in collisionless plasmas". *Reviews of Geophysics*, vol. 35, no. 4, pp. 491–501, November 1997. doi:10.1029/97RG02200.
- Turflinger, T. L. "Single-event effects in analog and mixed-signal integrated circuits". *IEEE Transactions on Nuclear Science*, vol. 43, no. 2, pp. 594–602, April 1996. doi:10.1109/23.490903.

- Turflinger, T. L. and Davey, M. V. "Understanding single event phenomena in complex analog and digital integrated circuits". *IEEE Transactions on Nuclear Science*, vol. 37, no. 6, pp. 1832–1838, December 1990. doi:10.1109/23.101197.
- Turflinger, T. L.; Davey, M. V.; and Mappes, B. M. "Single event effects in analog-to-digital converters: Device performance and system impact". *IEEE Transactions on Nuclear Science*, vol. 41, no. 6, pp. 2187–2194, December 1994. doi:10.1109/23.340561.
- Turinetti, J. R.; Kemp, W. T.; and Chavez, J. R. "Spectrum determination and modification of the AFRL Co-60 cell". *IEEE Transactions on Nuclear Science*, vol. 45, no. 6, pp. 2720–2726, December 1998. doi:10.1109/23.736520.
- Tylka, A. J.; Adams, Jr., J. H.; Boberg, P. R.; Brownstein, B.; Dietrich, W.; Flueckiger, E.; Petersen, E. L.; Shea, M. A.; Smart, D. F.; and Smith, E. C. "CREME96: A revision of the cosmic ray effects on micro-electronics code". *IEEE Transactions on Nuclear Science*, vol. 44, no. 6, pp. 2150–2160, December 1997. doi:10.1109/23.659030.
- Tylka, A. J.; Dietrich, W. F.; Boberg, P. R.; Smith, E. C.; and Adams, Jr., J. H. "Single event upsets caused by solar energetic heavy ions". *IEEE Transactions on Nuclear Science*, vol. 43, no. 6, pp. 2758–2766, December 1996. doi:10.1109/23.556863.
- van Bezooijen, A.; Ramalho, N.; and Voorman, J. O. "Balanced integrator filters at video frequencies". In *Proceedings of the 17<sup>th</sup> European Solid-State Circuits Conference (ESSCIRC), 1991*, pp. 1–4. IEEE, Milan, Italy: IEEE Press, September 1991.
- van der Plas, J. "MOSFET-C filter, with low excess noise and accurate automatic tuning". *IEEE Journal of Solid-State Circuits*, vol. 26, no. 7, pp. 922–929, July 1991. doi:10.1109/4.92011.
- van der Ziel, A. *Noise in Solid-State Devices and Circuits*. New York, NY: John Wiley & Sons, 1986. ISBN 0-471-83234-0.

- van Vonno, N.; Lucas, R.; and Thornberry, D. "Total dose hardness of a commercial SiGe BiCMOS technology". In *1999 5<sup>th</sup> European Conference on Radiation and Its Effects on Components and Systems (RADECS)*, pp. 414–417. IEEE, September 1999. ISBN 0-7803-5726-4. doi:10.1109/RADECS.1999.858617.
- Verdonckt-Vandebroek, S.; Wong, S. S.; Woo, J. C. S.; and Ko, P. K. "High-gain lateral bipolar action in a MOSFET structure". *IEEE Transactions on Electron Devices*, vol. 38, no. 11, pp. 2487–2496, November 1991. doi:10.1109/16.97413.
- Victory, J.; McAndrew, C. C.; Hall, J.; and Zunino, M. "A four-terminal compact model for high voltage diffused resistors with field plates". *IEEE Journal of Solid-State Circuits*, vol. 33, no. 9, pp. 1453–1458, September 1998. doi:10.1109/4.711347.
- Vittoz, E. A. "MOS transistors operated in the lateral bipolar mode and their application in CMOS technology". *IEEE Journal of Solid-State Circuits*, vol. 18, no. 3, pp. 273–279, June 1983.
- Vleugels, K. *Broadband Oversampling Analog-to-Digital Conversion for Digital Communications*. Ph.D. thesis, Stanford University, Stanford, CA, February 2002.
- Voldman, S. H. *Latchup*. West Sussex, U.K.: John Wiley & Sons, 2007. ISBN 978-0470-01642-8.
- Voorman, J. O. "Continuous-time analog integrated filters". In *Integrated Continuous-Time Filters: Principles, Design, and Applications*, Y. P. Tsividis and J. O. Voorman, eds., chap. 1, pp. 15–46. New York, NY: IEEE Press, 1993. ISBN 0-7803-0425-X.
- Voorman, J. O.; Brühls, W. H. A.; and Barth, P. J. "Bipolar integration of analog gyrator and laguerre type filters (transconductor-capacitor filters)". In *Proceedings of the 6<sup>th</sup> European Conference on Circuit Theory and Design (ECCTD), 1983*, pp. 108–110. Stuttgart, Germany, 6–8 September 1983. ISBN 3800713276.
- Walt, M. *Introduction to Geomagnetically Trapped Radiation*. Cambridge, U. K.: Cambridge University Press, 1994. ISBN 0-521-43143-3.

- Wang, C. C.-I. *High-Fidelity Analog-to-Digital Conversion for Spaceborne Applications*. Ph.D. thesis, Stanford University, Stanford, CA, September 2009.
- Wang, T. N. C. *VLF Input Impedance Characteristics of an Electric Antenna in an Magnetoplasma*. Ph.D. thesis, Stanford University, Stanford, CA, May 1970.
- Wang, T. N. C. and Bell, T. F. "Radiation resistance of a short dipole immersed in a cold magnetoionic medium". *Radio Science*, vol. 4, no. 2, pp. 167–177, February 1969. doi:10.1029/RS004i002p00167.
- . "Electric dipole radiation at vlf in a uniform warm magneto-plasma". *Revue de Physique Appliquée*, vol. 7, no. 1, pp. 11–20, March 1972. doi:10.1051/rphysap:019720070101100.
- Watkins, G. D. "Intrinsic point defects in semiconductors". In *Handbook of Semiconductor Technology*, vol. 1, K. A. Jackson and W. Schröter, eds., chap. 3, pp. 121–165. Weinheim, Germany: Wiley-VCH, 1999. ISBN 3-527-29834-7.
- Weighton, D. "Note on the design of wide-band low-noise amplifiers". *Proceedings of the IRE*, vol. 43, no. 9, pp. 1096–1101, September 1955. doi:10.1109/JRPROC.1955.277886.
- Welch, P. "The use of Fast Fourier Transform for the estimation of power spectra: A method based on time averaging over short, modified periodograms". *IEEE Transactions on Audio and Electroacoustics*, vol. 15, no. 2, pp. 70–73, June 1967.
- West, G. S.; J., W. J.; and Euler, H. C. "Space and planetary environment criteria for use in space vehicle development, 1977 revision". NASA Technical Memorandum NASA-TM-78119, George C. Marshall Space Flight Center, Marshall Space Flight Center, AL, November 1977.
- Whale, H. A. "The excitation of electroacoustic waves by antennas in the ionosphere". *Journal of Geophysical Research*, vol. 68, no. 2, pp. 415–422, 15 January 1963a. doi:10.1029/JZ068i002p00415.

- . “The impedance of an electrically short antenna in the ionosphere”. In *Proceedings of the International Conference on the Ionosphere held July 1962 at Imperial College, London*, A. C. Stickland, ed., pp. 472–477. The Institute of Physics and the Physical Society, London, U. K.: The Institute of Physics and the Physical Society, 1963b.
- . “Ion sheath effects near antennas radiating within the ionosphere”. *Journal of Geophysical Research*, vol. 69, no. 3, pp. 447–455, 1 February 1964. doi:10.1029/JZ069i003p00447.
- Whelehan, J. J. “Low-noise amplifiers - then and now”. *IEEE Transactions on Microwave Theory and Techniques*, vol. 50, no. 3, pp. 806–813, March 2002. doi:10.1109/22.989964.
- White, R.; Luschas, S.; and Krishnan, S. “Analysis of errors in a comparator-based switched-capacitor biquad filter”. *IEEE Transactions on Circuits and Systems II: Express Briefs*, vol. 56, no. 9, pp. 704–708, September 2009. doi:10.1109/TCSII.2009.2027965.
- Wilcox, J. M. “Solar structure and terrestrial weather”. *Science*, vol. 192, no. 4241, pp. 745–748, May 1976. doi:10.1126/science.192.4241.745.
- Williams, III., L. A. *Modeling and Design of High-Resolution Sigma-Delta Modulators*. Ph.D. thesis, Stanford University, Stanford, CA, August 1993.
- Willingham, S. D.; Martin, K. W.; and Ganesan, A. “A BiCMOS low-distortion 8-MHz low-pass filter”. *IEEE Journal of Solid-State Circuits*, vol. 28, no. 12, pp. 1234–1245, December 1993. doi:10.1109/4.261997.
- Wilson, G. “Linearised bipolar transconductor”. *Electronics Letters*, vol. 28, no. 4, pp. 390–391, 13 February 1992. doi:10.1049/el:19920244.
- Winokur, P. S. “Radiation-induced interface traps”. In *Ionizing Radiation Effects on MOS Devices and Circuits*, T. P. Ma and P. V. Dressendorfer, eds., chap. 4, pp. 193–255. New York, NY: John Wiley & Sons, 1989. ISBN 0-471-84893-X.

- Winokur, P. S.; Sexton, F. W.; Schwank, J. R.; Fleetwood, D. M.; Dressendorfer, P. V.; Wrobel, T. F.; and Turpin, D. C. "Total-dose radiation and annealing studies: Implications for hardness assurance testing". *IEEE Transactions on Nuclear Science*, vol. 33, no. 6, pp. 1343–1351, December 1986. doi:10.1109/TNS.1986.4334603.
- Witczak, S. C.; Lacoe, R. C.; Mayer, D. C.; Fleetwood, D. M.; Schrimpf, R. D.; and Galloway, K. F. "Space charge limited degradation of bipolar oxides at low electric fields". *IEEE Transactions on Nuclear Science*, vol. 45, no. 6, pp. 2339–2351, December 1998. doi:10.1109/23.736453.
- Witczak, S. C.; Lacoe, R. C.; Osborn, J. V.; Hutson, J. M.; and Moss, S. C. "Dose-rate sensitivity of modern nMOSFETs". *IEEE Transactions on Nuclear Science*, vol. 52, no. 6, pp. 2602–2608, December 2005. doi:10.1109/TNS.2005.860709.
- Woolliscroft, L. J. C.; Farrell, W. M.; Alleyne, H. S. C.; Gurnett, D. A.; Kirchner, D. L.; Kurth, W. S.; and Thompson, J. A. "Cassini radio and plasma wave investigation: Data compression and scientific applications". *Journal of the British Interplanetary Society*, vol. 46, no. 3, pp. 115–120, March 1993.
- Wrixon, A. D. "New ICRP recommendations". *Journal of Radiological Protection*, vol. 28, no. 2, pp. 161–168, June 2008. doi:10.1088/0952-4746/28/2/R02.
- Wunderlich, R.; Oehm, J.; Dollberg, A.; and Schumacher, K. "A linear operational transconductance amplifier with automatic offset cancellation and transconductance calibration". In *Proceedings of the 6th IEEE International Conference on Electronics, Circuits and Systems (ICECS), 1999*, vol. 3, pp. 1321–1324. IEEE, Pafos, Cypress: IEEE Press, 5–8 September 1999. ISBN 0-7803-5682-9. doi:10.1109/ICECS.1999.814412.
- Xiong, H. D.; Fleetwood, D. M.; Choi, B. K.; and Sternberg, A. L. "Temperature dependence and irradiation response of  $1/f$ -noise in MOSFETs". *IEEE Transactions on Nuclear Science*, vol. 49, no. 6, pp. 2718–2723, December 2002. doi:10.1109/TNS.2002.805354.



- Xu, M. *Substrate Noise in Mixed-Signal Integrated Circuits*. Ph.D. thesis, Stanford University, Stanford, CA, June 2001.
- Yan, Z.; Deen, M. J.; and Malhi, D. S. “Gate-controlled lateral PNP BJT: Characteristics, modeling and circuit applications”. *IEEE Transactions on Electron Devices*, vol. 44, no. 1, pp. 118–128, January 1997. doi:10.1109/16.555443.
- Young, D. T. “Space plasma particle instrumentation and the new paradigm: Faster, cheaper, better”. In *Measurement Techniques in Space Plasmas: Particles, Geophysical Monographs*, vol. 102, R. F. Pfaff; J. E. Borovsky; and D. T. Young, eds., pp. 1–16. Washington, DC: American Geophysical Union, 1998. ISBN 0-87590-085-2.
- Zhang, S.; Cressler, J. D.; Subbanna, S.; Groves, R.; Niu, G.; Isaacs-Smith, T.; Williams, J. R.; Bakhru, H.; Marshall, P. W.; Kim, H. S.; and Reed, R. A. “An investigation of proton energy effects in SiGe HBT technology”. *IEEE Transactions on Nuclear Science*, vol. 49, no. 6, pp. 3208–3212, December 2002. doi:10.1109/TNS.2002.805361.
- Ziegler, J. F.; Biersack, J. P.; and Ziegler, M. D. *SRIM, The Stopping and Range of Ions in Matter*. Chester, MD: SRIM Co., 2008. ISBN 0-9654207-1-X.
- Zvanut, M. E.; Stahlbush, R. E.; Carlos, W. E.; and Hughes, H. L. “Hydrogen-related  $e'$  centers and positive charge in irradiated oxide films”. In *The Physics and Chemistry of SiO<sub>2</sub> and the Si-SiO<sub>2</sub> Interface*, vol. 2, C. R. Helms and B. E. Deal, eds., chap. 8, pp. 465–471. New York, NY: Plenum Press, 1993. ISBN 0-306-44419-4.